CODEN: JASMAN

The Journal of the Acoustical Society of America

ISSN: 0001-4966

Vol. 109, No. 1 January 2001

(Continued)

THE JOURNAL OF THE ACOUSTICAL SOCIETY OF AMERICA VOL. 109, NO. 1, JANUARY 2001

CONTENTS—*Continued from preceding page*

(Continued)

THE JOURNAL OF THE ACOUSTICAL SOCIETY OF AMERICA VOL. 109, NO. 1, JANUARY 2001

CONTENTS—*Continued from preceding page*

(Continued)

THE JOURNAL OF THE ACOUSTICAL SOCIETY OF AMERICA VOL. 109, NO. 1, JANUARY 2001

CONTENTS—*Continued from preceding page*

ACOUSTICAL NEWS—USA

Elaine Moran
Acoustical Society of America, Suite 1NO1, 2 Huntington Quadrangle, Melville, NY 11747-4502

Editor's Note: *Readers of this Journal are encouraged to submit news items on awards, appointments, and other activities about themselves or their colleagues. Deadline dates for news items and notices are 2 months prior to publication.*

Announcement of the 2001 Election

In accordance with the provisions of the bylaws, the following Nominating Committee was appointed to prepare a slate for the election to take place on 22 May 2001:

James E. West, *Chair* — Allan D. Pierce
Robert E. Apfel — Julia H. Royster
Fredericka Bell-Berti — Alexandra I. Tolstoy

The bylaws of the Society require that the Executive Director publish in the *Journal* at least 90 days prior to the election date an announcement of the election and the Nominating Committee's nominations for the offices to be filled. Additional candidates for these offices may be provided by any Member or Fellow in good standing by letter received by the Executive Director not less than 60 days prior to the election date and the name of any eligible candidate so proposed by 20 Members or Fellows shall be entered on the ballot.

Biographical information about the candidates and statements of objectives of the candidates for President-Elect and Vice President-Elect will be mailed with the ballots.

CHARLES E. SCHMID
Executive Director

The Nominating Committee has submitted the following slate:

FOR PRESIDENT-ELECT

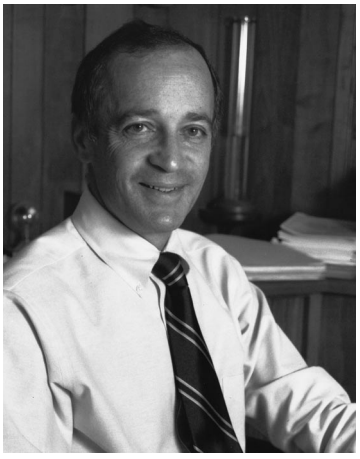

Robert C. Spindel

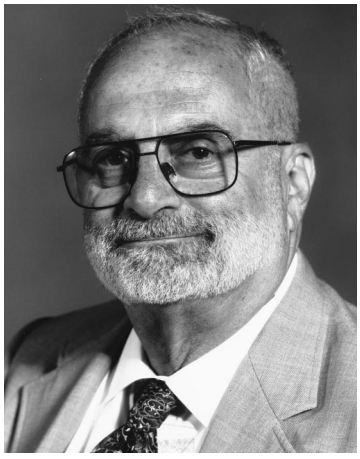

Richard Stern

 0001-4966/2001/109(1)/1/4/$18.00

FOR VICE PRESIDENT-ELECT

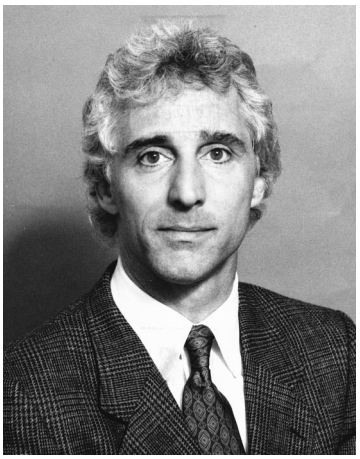

Mark F. Hamilton

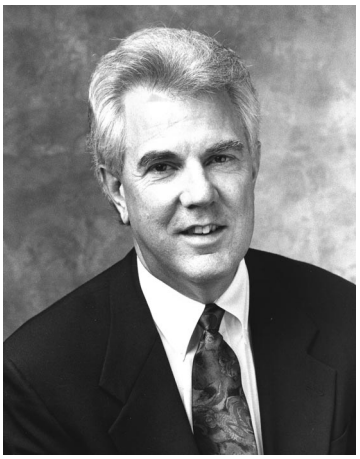

William A. Yost

FOR MEMBERS OF THE EXECUTIVE COUNCIL

Whitlow W. L. Au

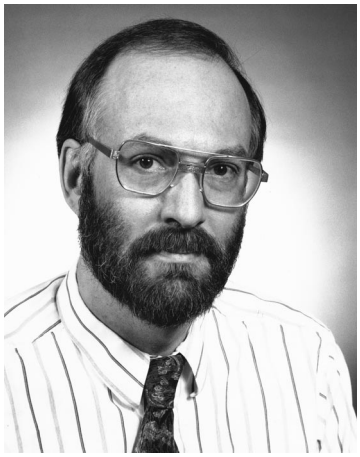

David I. Havelock

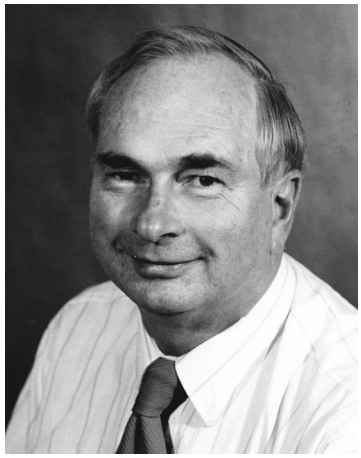

Daniel L. Johnson

Joseph Pope

James M. Sabatier

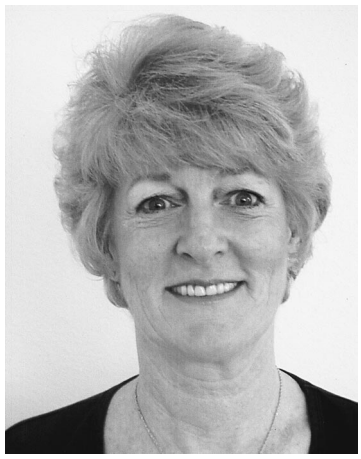

Winifred Strange

Leo L. Beranek receives American Academy of Arts and Sciences award

The American Academy of Arts and Sciences has awarded its first Scholar-Patriot Distinguished Service award to Dr. Leo L. Beranek. Dr. Beranek received the award in honor of his contributions to science, his role in founding Bolt, Beranek and Newman (BBN) and other engineering and media companies, and his service on behalf of the community and the nation.

Academy President James O. Freedman said: ''Leo Beranek's wide-ranging work in science and engineering has helped shape our world. Dr. Beranek is a practical visionary who represents all that this Academy stands for—a scientist and businessman who achieved great distinction in his profession and a concerned citizen who has served countless educational and cultural institutions.''

Dr. Beranek received his Doctorate in Science from Harvard in 1940 and then went on to form Harvard's first World War II research laboratory to study Electro-Acoustics. In 1948, he received the Presidential Certificate of Merit for his war-research contributions, notably advances in the shoring up of the nation's radar defenses. Leo Beranek is an Honorary Fellow of the Acoustical Society of America and served as ASA President from 1954 to 1955. He was awarded the ASA Biennial Award (now R. Bruce Lindsay Award) in 1944, the Wallace Clement Sabine Medal in 1961, and the Gold Medal in 1975.

The Academy also dedicated the Leo L. Beranek Library to honor Dr. Beranek's achievements and his support of the Academy which was founded in 1780 by a small group of scholar-patriots.

M. David Egan awarded honorary doctorate

ASA Fellow M. David Egan (Principal Consultant, Egan Acoustics, Anderson, SC) received an Honorary Doctorate from Clemson University at Graduation Exercises on 12 August 2000. Clemson awards Honorary Doctorates to recognize exemplary achievements and to enhance the reputation of the University. The citation read, in part,

> ''Clemson University Professor Emeritus M. David Egan is a distinguished educator, lecturer, author, and consultant. Born in Trenton, New Jersey, he earned his undergraduate degree from Lafayette College in 1962 and his master's degree from the Massachusetts Institute of Technology in 1966. From 1962 to 1964, he served as a US Army officer commanding Ordnance troops in the Forêt de Trois-Fontaines, France.
>
> In 1972, Professor Egan joined Clemson's faculty in the School of Design and Building. Because of his dedication, expertise, and professionalism in the classroom and consulting, he gained the reputation for being a leader. For more than 30 years, Professor Egan has excelled as an educator in the areas of architectural acoustics, lighting, fire and life safety, and low-energy design. He has authored seven major textbooks [including *Architectural Acoustics*, 1988 and, with Charles W. Tilley, AIA, *Architectural Acoustics Workbook*, 2000] and several sections in reference books for architects and engineers. His textbooks are not only a part of Clemson's curriculum, but also the curricula of more than two hundred schools worldwide.
>
> Professor Egan's service to Clemson University has placed him in high regard among his professional and collegiate peers and has brought credit and recognition to the University and the School of Design and Building. Principally through his teaching [including lectures on acoustics at more than 40 schools in the US and four other countries], writing, and consulting on acoustics [on award-winning projects in North America, Europe, Africa, and the Middle East], his contributions to education and architecture are universally recognized.
>
> His numerous awards include advancement to fellowship in the Acoustical Society of America (ASA), election as vice president of the National Council of Acoustical Consultants (NCAC), board certification by the Institute of Noise Control Engineering (INCE), honorary membership in the American Institute of Architects (AIA), and recognition as Lifetime Distinguished Professor of the Association of Collegiate Schools of Architecture (ACSA).
>
> Professor Egan embodies those ideals that Clemson University values. His wide recognition and respect as a humanitarian, an author, and an educator place him in a unique position to represent Clemson and its mission to audiences throughout the world. Clemson University holds Professor Emeritus M. David Egan and his lifetime achievements in the highest esteem, and it is a distinct privilege to honor him with the presentation of the Doctor of Laws.''

Professor Egan also has served for 15 years on the Advisory Board of The Robert B. Newman Student Award Fund, Lincoln, MA. The Fund awards medals to students for merit in architectural acoustics and the Schultz Grant to suport teachers and researchers in acoustical education. He has taught 14 Newman Medalists at Clemson University and 3 Medalists at the University of North Carolina at Charlotte.

USA Meetings Calendar

Listed below is a summary of meetings related to acoustics to be held in the U.S. in the near future. The month/year notation refers to the issue in which a complete meeting announcement appeared.

2001

4–8 Feb.	Midwinter Meeting, Association for Research in Otolaryngology, St. Petersburg, FL [ARO Office, 19 Mantua Rd., Mt. Royal, NJ 08061, Tel.: 856-423-7222; Fax: 856-423-3420; E-mail: meetings@aro.org; WWW: www.aro.org/mwm/mwm.html].
15–17 March	Annual Meeting, American Auditory Society, Scottsdale, AZ [Wayne J. Staab, Ph.D., American Auditory Society, 512 E. Canberbury Ln., Phoenix, AZ 85022, Tel.: 602-789-0755; Fax: 602-942-1486; E-mail: amaudsoc@aol.com; WWW: www.amauditorysoc.org].
22–25 March	''New Frontiers in the Amelioration of Hearing Loss,'' St. Louis, MO [Sarah Uffman, CID Department of Research, 4560 Clayton Ave., St. Louis, MO 63110, Tel.: 314-977-0278; Fax: 314-977-0030; E-mail: suffman@cid.wustl.edu].
30 Apr.–3 May	2001 SAE Noise & Vibration Conference & Exposition, Traverse City, MI [Patti Kreh, SAE Int'l., 755 W. Big Beaver Rd., Suite 1600, Troy, MI 48084, Tel.: 248-273-2474; Fax: 248-273-2494; E-mail: pkreh@sae.org].
4–8 June	141st Meeting of the Acoustical Society of America, Chicago, IL [Acoustical Society of America, Suite 1NO1, 2 Huntington Quadrangle, Melville, NY 11747-4502, Tel.: 516-576-2360; Fax: 516-576-2377; E-mail: asa@aip.org; WWW: asa.aip.org]. Deadline for receipt of abstracts: 2 February 2001.
9–13 July	2001 SIAM Annual Meeting, San Diego, CA [Society for Industrial and Applied Mathematics (SIAM), Tel.: 215-382-9800; Fax: 215-386-7999; E-mail: meetings@siam.org; WWW: www.siam.org/meetings/an01/].
15–19 Aug.	ClarinetFest 2001, New Orleans, LA [Dr. Keith Koons, ICA Research Presentation Committee Chair, Music Dept., Univ. of Central Florida, P.O. Box 161354, Orlando, FL 32816-1354, Tel.: 407-823-5116; E-mail: kkoons@pegasus.cc.ucf.edu]. Deadline for receipt of abstracts: 15 January 2001.
7–10 Oct.	2001 IEEE International Ultrasonics Symposium Joint with World Congress on Ultrasonics, Atlanta, GA [W. O'Brien, Electrical and Computer Engineering, Univ. of Illinois, 405 N. Mathews, Urbana, IL 61801; Fax: 217-244-0105; WWW: www.ieeeuffc.org/2001].
3–7 Dec.	142nd Meeting of the Acoustical Society of America, Ft. Lauderdale, FL [Acoustical Society of America, Suite 1NO1, 2 Huntington Quadrangle, Melville, NY 11747-4502, Tel.: 516-576-2360; Fax: 516-576-2377; E-mail: asa@aip.org; WWW: asa.aip.org].

2002

3–7 June	143rd Meeting of the Acoustical Society of America, Pittsburgh, PA [Acoustical Society of America, Suite

1NO1, 2 Huntington Quadrangle, Melville, NY 11747-4502, Tel.: 516-576-2360; Fax: 516-576-2377; E-mail: asa@aip.org; WWW: asa.aip.org].

2–6 Dec. Joint Meeting: 144th Meeting of the Acoustical Society of America, 3rd Iberoamerican Congress of Acoustics, and 9th Mexican Congress on Acoustics, Cancun, Mexico [Acoustical Society of America, Suite 1NO1, 2 Huntington Quadrangle, Melville, NY 11747-4502, Tel.: 516-576-2360; Fax: 516-576-2377; E-mail: asa@aip.org; WWW: asa.aip.org/cancun.html].

OBITUARIES

Kerry P. Green • 1955–1998

Kerry P. Green, associate professor of psychology at the University of Arizona and a distinguished speech researcher, died suddenly and unexpectedly in his sleep on Christmas morning, 1998, at his parent's home in Prescott, Arizona. He was just 43 years old. He was engaged to be married in June of 1999. He had just received a major research grant from the National Science Foundation and was surely about to enter the most productive period of an already accomplished academic career.

Kerry began a lifelong interest in the psychology of thought and perception as an undergraduate at Ithaca College, where he conducted experiments on the organization of cognitive categories. He earned a bachelor of arts degree from Ithaca in 1977. His master's and doctoral studies were carried out at Northeastern University, where he earned a Ph.D. in Psychology in 1984. His experimental work at Northeastern focused on the visual processes underlying the recognition of American Sign Language and on the role of vision in spoken language processing. His studies at Northeastern were the beginning of a highly productive line of work that was aimed at understanding the complex problem of how sensory information is integrated across visual and auditory modalities, and on the related problem of how disparate sources of auditory information are integrated to form phonetic percepts. Especially noteworthy was a series of influential papers in collaboration with Joanne Miller that investigated the integration of temporal cues arising from speaking rate with those arising from the relative timing of articulatory gestures.

Following his graduate studies at Northeastern, Kerry moved to the University of Washington as a postdoctoral fellow and, later, as a research associate. What followed was a highly productive series of investigations that exploited the McGurk Effect, a powerful illusion created by presenting subjects with mismatched information in which visual cues signal one speech sound while acoustic cues signal another. In what was arguably his single most important contribution to the field, Kerry, in collaboration with Patricia Kuhl, designed a novel experiment to explore a longstanding problem in phonetic perception. It had long been known that listeners' judgments about the phonetic feature of voicing (e.g., ''b'' versus ''p'') were influenced by the status of a separate phonetic feature related to the place in the vocal tract where the speech sound was produced (e.g., ''b'' versus ''d''). This apparently arcane detail has attracted a great deal of interest over the years because of the very different views about how this integration phenomenon might be explained and because of the considerable theoretical significance attendant to which of those competing views proved to be correct. Although it had never been quite pinned down, there was a widely held belief that there was a relatively straightforward psychoacoustic explanation for this effect. In an ingenious experiment, Green and Kuhl were able to demonstrate that articulatory place judgments influence voicing judgments even when the place of articulation percept is entirely illusory, having been created by the McGurk Effect. This was a powerful demonstration that seemed to reveal the operation of a pattern recognition system far more subtle and complex than many had imagined. The ingenuity and insight that characterize this remarkable study were hallmarks of all of Kerry's experimental work.

Kerry continued his primary focus on auditory-visual integration after a 1989 move to the Psychology Department at the University of Arizona. His interests also expanded to include electrophysiological investigations of the neurophysiology of speech processing, and to studies on the acquisition of the sound pattern of a new language. These cross-language investigations were carried out in collaboration with Mary Zampini, to whom he would later become engaged. His varied work on the psychology of speech perception led to eight research grants, including major awards from the National Institutes of Health and the National Science Foundation.

Kerry was also a model teacher and mentor. Students flocked to his laboratory in part because of his broad expertise in experimental psychology, in part because of his infectious enthusiasm, and in part because of a richly deserved reputation for kindness and generosity.

Kerry had a rich and full life outside of the research laboratory and classroom. He was a fine athlete and an especially fine and fearless skier, having skied both competitively and recreationally from the age of eight. He was also an avid outdoors man, cook, auto mechanic, and card shark. He showed courage in surviving life-threatening surgery to remove a brain tumor, and in patiently enduring the arduous physical and speech therapy that would eventually restore his health.

In addition to Mary Zampini, Kerry is survived by his parents, Justin and Grace of Prescott, Arizona, brother Justin of Breckenridge, Colorado, and sister Allison of Knoxville, Tennessee.

JAMES M. HILLENBRAND

Harry B. Miller • 1916–1999

Harry B. Miller, Fellow of the Acoustical Society of America, died on 8 February 1999 from injuries he sustained in a car accident. Harry loved acoustics and brought a high level of enthusiasm and an unusual degree of ingenuity to all his work over a professional career that spanned 55 years. Harry also loved the Acoustical Society with all its activities and meetings and was a member for 51 years. He worked in many fields of acoustics but specialized in development of electroacoustic transducers and methods for acoustic measurements. He also had a lifelong love of music: playing the viola and piano, singing in various organizations, and taking an interest in studying and improving musical instruments.

After graduation from the Boston Latin School, Harry attended Harvard where he received a bachelor's degree in chemistry. He later earned a master's degree in physics from the Case Institute of Technology.

Harry began his industrial career in 1940 at the Brush Development Company (later the Clevite Corporation) in Cleveland, OH. During this period he worked on a variety of acoustic projects including both air acoustics and underwater acoustics. He participated in development of hearing aids, public address microphones, air-dropped sonobuoys, low side lobe transducers for homing torpedoes, hull-mounted active sonar arrays, and methods for suppression of cavitation. At Clevite he rose to become head of the acoustic engineering department.

In 1960 Harry joined General Dynamics in Rochester, NY as manager of the Advanced Development Electroacoustics Laboratory where he was responsible for development of major sonar systems for the Navy. In 1968 he joined the Naval Underwater Systems Center (NUSC) in New London, CT [now the Naval Undersea Warfare Center (NUWC) in Newport, RI] where he first concentrated on development of new high power transducers for the Navy's latest surface ship active sonar systems. After 27 years and various other sonar projects he retired from NUWC in 1995. Upon his retirement he received the Decibel Award which was established over 50 years ago at the Navy Underwater Sound Laboratory in New London, CT to honor those who have achieved distinction in the fields of sonar or underwater acoustics.

Throughout his long career Harry's broad training in chemistry, physics, and engineering combined with his enthusiasm and ingenuity often led to significant results. One of the best examples is prestressing (or mechanical biasing) of the piezoceramic in longitudinal resonator transducers. Harry developed a method of prestressing for these transducers, which made them much more reliable at high power. Since then prestressing the ceramic has been extended to other transducer types such as the flextensionals.

Another development of Harry's was a method for using stacks of piezoceramic rings in the 33 mode for longitudinal resonator transducers, which allowed more efficient use of the ceramic's electromechanical properties. Combining prestressing with the 33 mode resulted in longitudinal resonator transducers that had greater bandwidth and were more efficient and reliable than they had been before these improvements. The Navy has used such transducers by the thousands in both submarine and surface ship sonar systems.

Harry also displayed his ingenuity in the recording field. In a project for the Civil Aviation Authority he developed an early type of digital processing which resulted in a method of tape recording that was more linear than existing methods. He also developed an antistatic vinyl phonograph record by finding the precise quantity and characteristics of carbon black required to reduce the resistivity of vinyl to the appropriate level.

Harry had a strong interest in acoustic measurements and was one of the first to realize that Seneca Lake in New York offered good conditions for making the measurements needed to evaluate the large transducer arrays that were being developed for the Navy. He played a major role in setting up a measurement barge at Seneca Lake and making such measurements as part of his work in General Dynamics.

At NUWC he continued his work in acoustic measurements by developing dummy load techniques for evaluating individual transducer elements being built as surface ship sonar prototypes. Another concept he initiated at NUWC replaced individual hydrophones in a passive array with small groups of hydrophones in which each group could be adapted to reduce hull-generated noise.

Harry participated in various activities of the Acoustical Society. He served as a member and chair of the Technical Committee on Engineering Acoustics and on the Membership Committee. He arranged and chaired special sessions on a variety of topics at several meetings of the Acoustical Society and was also active in the Narragansett Chapter of the Society.

Over his long career Harry was the author of many papers and reports on a wide variety of acoustical subjects. He also wrote a book on analysis of piezoelectric transducers, and he compiled and edited the book *Acoustic Measurements: Methods and Instrumentation* which is Vol. 16 of *Benchmark Papers in Acoustics*. He wrote entertaining book reviews which not only aroused the interest of prospective readers, but also provided a guide on how to use the book to meet their particular needs. Harry is survived by his wife, Vivian, who he married in 1941.

CHARLES H. SHERMAN

Harry B. Miller • 1916–1999

Harry B. Miller, Fellow of the Acoustical Society of America, died on 8 February 1999 from injuries he sustained in a car accident. Harry loved acoustics and brought a high level of enthusiasm and an unusual degree of ingenuity to all his work over a professional career that spanned 55 years. Harry also loved the Acoustical Society with all its activities and meetings and was a member for 51 years. He worked in many fields of acoustics but specialized in development of electroacoustic transducers and methods for acoustic measurements. He also had a lifelong love of music: playing the viola and piano, singing in various organizations, and taking an interest in studying and improving musical instruments.

After graduation from the Boston Latin School, Harry attended Harvard where he received a bachelor's degree in chemistry. He later earned a master's degree in physics from the Case Institute of Technology.

Harry began his industrial career in 1940 at the Brush Development Company (later the Clevite Corporation) in Cleveland, OH. During this period he worked on a variety of acoustic projects including both air acoustics and underwater acoustics. He participated in development of hearing aids, public address microphones, air-dropped sonobuoys, low side lobe transducers for homing torpedoes, hull-mounted active sonar arrays, and methods for suppression of cavitation. At Clevite he rose to become head of the acoustic engineering department.

In 1960 Harry joined General Dynamics in Rochester, NY as manager of the Advanced Development Electroacoustics Laboratory where he was responsible for development of major sonar systems for the Navy. In 1968 he joined the Naval Underwater Systems Center (NUSC) in New London, CT [now the Naval Undersea Warfare Center (NUWC) in Newport, RI] where he first concentrated on development of new high power transducers for the Navy's latest surface ship active sonar systems. After 27 years and various other sonar projects he retired from NUWC in 1995. Upon his retirement he received the Decibel Award which was established over 50 years ago at the Navy Underwater Sound Laboratory in New London, CT to honor those who have achieved distinction in the fields of sonar or underwater acoustics.

Throughout his long career Harry's broad training in chemistry, physics, and engineering combined with his enthusiasm and ingenuity often led to significant results. One of the best examples is prestressing (or mechanical biasing) of the piezoceramic in longitudinal resonator transducers. Harry developed a method of prestressing for these transducers, which made them much more reliable at high power. Since then prestressing the ceramic has been extended to other transducer types such as the flextensionals.

Another development of Harry's was a method for using stacks of piezoceramic rings in the 33 mode for longitudinal resonator transducers, which allowed more efficient use of the ceramic's electromechanical properties. Combining prestressing with the 33 mode resulted in longitudinal resonator transducers that had greater bandwidth and were more efficient and reliable than they had been before these improvements. The Navy has used such transducers by the thousands in both submarine and surface ship sonar systems.

Harry also displayed his ingenuity in the recording field. In a project for the Civil Aviation Authority he developed an early type of digital processing which resulted in a method of tape recording that was more linear than existing methods. He also developed an antistatic vinyl phonograph record by finding the precise quantity and characteristics of carbon black required to reduce the resistivity of vinyl to the appropriate level.

Harry had a strong interest in acoustic measurements and was one of the first to realize that Seneca Lake in New York offered good conditions for making the measurements needed to evaluate the large transducer arrays that were being developed for the Navy. He played a major role in setting up a measurement barge at Seneca Lake and making such measurements as part of his work in General Dynamics.

At NUWC he continued his work in acoustic measurements by developing dummy load techniques for evaluating individual transducer elements being built as surface ship sonar prototypes. Another concept he initiated at NUWC replaced individual hydrophones in a passive array with small groups of hydrophones in which each group could be adapted to reduce hull-generated noise.

Harry participated in various activities of the Acoustical Society. He served as a member and chair of the Technical Committee on Engineering Acoustics and on the Membership Committee. He arranged and chaired special sessions on a variety of topics at several meetings of the Acoustical Society and was also active in the Narragansett Chapter of the Society.

Over his long career Harry was the author of many papers and reports on a wide variety of acoustical subjects. He also wrote a book on analysis of piezoelectric transducers, and he compiled and edited the book *Acoustic Measurements: Methods and Instrumentation* which is Vol. 16 of *Benchmark Papers in Acoustics*. He wrote entertaining book reviews which not only aroused the interest of prospective readers, but also provided a guide on how to use the book to meet their particular needs. Harry is survived by his wife, Vivian, who he married in 1941.

CHARLES H. SHERMAN

BOOK REVIEWS

P. L. Marston
Physics Department, Washington State University, Pullman, Washington 99164

These reviews of books and other forms of information express the opinions of the individual reviewers and are not necessarily endorsed by the Editorial Board of this Journal.

Editorial Policy: *If there is a negative review, the author of the book will be given a chance to respond to the review in this section of the Journal and the reviewer will be allowed to respond to the author's comments. [See ''Book Reviews Editor's Note,'' J. Acoust. Soc. Am.* ***81****, 1651 (May 1987).]*

Acoustic Phonetics

Kenneth N. Stevens

MIT Press, Cambridge, MA, 1999.
viii+607 pp. Price: $60.00 hc ($35.00 pb).
ISBN: 026219404-X hc (026269250-3 pb).

Acoustic phonetics is a relatively young science, having been systematized with the 1960 publication of Gunnar Fant's *Acoustic Theory of Speech Production*. Fant's text presented the theory buttressed by his own empirical work as well as by modeling efforts by scientists working in the United States, and the field of acoustic phonetics and its many associated disciplines (speech physiology, speech perception, speech synthesis, and automatic speech and speaker recognition, to name a few) was off and running. One of the scientists who performed some of the early, well-known modeling work was Professor Kenneth Stevens of MIT, who with Dr. Arthur House extended some of the concepts of the acoustic theory in novel ways. Now, Professor Stevens has written a text entitled *Acoustic Phonetics*, and it is a remarkable accomplishment. The text not only presents the state-of-the-art 40 years removed from Fant's book, but employs a probing, didactic approach that gives the material the feel of having evolved under the influence of teaching many students. This almost certainly accounts for the linear, crystal-clear way in which the information is developed and applied, and for the very creative use of figures and charts. It seems to me that after reading the ten chapters of this book, a motivated student or interested scientist with little or no previous knowledge of acoustic phonetics would know quite a lot about the subject, and in a fair amount of depth. This reader would also understand, very clearly, Professor Stevens' point of view about this material, summarized in the preface: ''The theme of this book is to explore the(se) relations between the discrete linguistic features and their articulatory and acoustic manifestations'' (p. vii).

Chapter 1 presents an overview of the anatomy and physiology of speech production. The anatomy is much like that presented in many textbooks dealing with the head, neck, and respiratory system, but Stevens also brings in more recent information, specifically on the fine structure of the vocal folds as well as on cross-sectional geometries of the vocal tract and sinuses derived from magnetic resonance imaging studies. The speech physiology section of the chapter is most impressive and to this writer's knowledge unique in the sense of not being available in any other source book on speech production or acoustics. This section contains extensive material on aerodynamic processes and articulatory kinematics, both critical for much of the acoustic modeling presented in subsequent chapters.

Chapter 2 is a treatise on source mechanisms in speech acoustics. The accepted theory of speech acoustics is often referred to as the source–filter theory, because the output of the vocal tract is a combination of source and filter mechanisms; stated in acoustic terms, the acoustic properties of the filter shape the acoustic properties of the source. Sources can be located at lots of different locations throughout the speech mechanism, and include most notably the periodic source generated by the vibrating vocal folds and the various aperiodic sources generated at the level of the larynx and throughout the vocal tract. Stevens devotes a good deal of attention to the theory of vocal-fold vibration and its aerodynamic and acoustic consequences. This fairly complex material is developed as a series of modeling steps that always has one eye on the underlying motions of the vocal folds and the other on the aerodynamic consequences of those motions, the prize being the understanding of how this results in the glottal source spectrum for vowels and other voiced sounds. If I were going to select a passage from the textbook literature as an outstanding example of how to develop a complex set of concepts, the material on pages 56 through 64 would be my choice. Stevens also includes information on how variation in the periodic source is achieved and why those variations result in predictable acoustic consequences. Then, the chapter moves into turbulent noise sources, followed by information on transient sources and even suction sources. This presentation makes extensive use of theoretical calculations derived from circuit models of the source mechanisms; later in the text these calculations are compared with real data.

Chapter 3, ''Basic Acoustics of Vocal Tract Resonators,'' treats the filter part of the theory. Here, the transfer function of the vocal tract—the tube extending from the vocal folds to the lips—is introduced and elaborated in terms that will be familiar to speech scientists. Stevens does, however, add interesting and new details to the story, and in particular follows the all-pole exposition with an analytically and intuitively satisfying account of how zeros modify the transfer function. Coverage of tube resonators is followed by a unique presentation of the theory of tube resonances as modified by local constrictions, commonly referred to in speech science circles as *perturbation theory*. The chapter also includes detailed information on losses in sound transmission through the vocal tract, and excitation of vocal-tract resonators. The special case of coupled resonators is treated with attention to the obvious case of nasals, where the nasal pathways serve as a side branch to the vocal tract, and to the less-often discussed case of coupling to subglottal resonators. The latter has special relevance when vocal-fold vibration is characterized by incomplete closure, as during breathy voicing and the production of some voiceless consonants. The inclusion of detailed material on coupling to subglottal resonators is quite unique among available texts.

Chapter 4, entitled ''Auditory Processing of Speechlike Sounds,'' is meant to prepare the reader for a consideration of how the theory and data of speech acoustics *might* be brought to bear on a theory of speech perception. The material on auditory anatomy, physiology, and psychophysics can serve as a starting point for discussion of the role of general auditory processes in speech perception. The chapter concludes with a review of several experiments that implicate this role directly, and later in the text (Chapters 6–9) other speech perception experiments are mentioned which depend to some extent on information contained in the current chapter.

Chapter 5, ''Phonological Representation of Utterances,'' is the briefest chapter in the text yet it focuses the point of view quoted above from the preface. Stevens compresses much of what has driven speech science research over the past 40 years into the following passage: ''We suppose, then, that words are stored in memory as sequences of segments, and each of these segments is represented as an array of distinctive features. The particular inventory of features that are used to make distinctions between words in languages is determined both by the properties of the articulatory system that generates speech and by the characteristics of the human auditory system that processes speech. *The features have correlates both in the articulatory and in the acoustic and auditory domains*. The features for each segment...define which articulators are to be controlled, and provide a broad specification of how these articulators are to be manipulated. The features also specify the intended attributes of the sound that arises from the articulatory movements. These constraints on the articulation and on the sound pattern determine the detailed pattern of articulatory movements that are needed to implement the features within a segment'' (p. 244, italics added).

The chapter goes on to describe a two-category system of features that neatly summarizes Stevens' concern with the role of linguistics in physiological, acoustic, and perceptual accounts of spoken language.

Chapters 6, 7, 8, and 9 get down to the business of detailed theoretical and empirical accounts of speech sound categories. The chapter on vowels (Chapter 6) explores all aspects of vowels that have been of interest to speech scientists, and does so with liberal use of spectrographic and spectral displays. Great care is taken in the description of these individual examples and the patient reader will be rewarded by spending time with these thoughtfully selected illustrations. In particular, Stevens provides an interesting treatment of the nasalized–non-nasalized distinction for vowels, a topic generally not well covered (or covered at all) in most texts of this genre. Chapter 7 deals with stop consonants, and here the aerodynamic foundations from Chapter 2 are deployed and elaborated with great skill. Intertwined with the presentation of stop acoustics is a novel presentation of the formant transition characteristics of the closure and release phases of stop consonant production; the theoretical and empirical aspects of the transition phenomena should be of great interest to working scientists. Fricatives, affricates, and more information on stops is presented in Chapter 8, where Stevens continues the interplay of theory and data, of underlying mechanism and acoustic result. I was particularly impressed with the material on aspiration, a phenomenon that is used by many languages of the world to signal the distinction between voiceless and voiced consonants (such as English ''p'' [aspirated] vs ''b'' [unaspirated]), but which is also prominent in the ''h'' sound and in breathy voice qualities. Chapter 9 presents information on the class of sounds called *sonorants*, which include nasals (such as ''m'' and ''n''), glides (''w'' and ''y''), and liquids (''r'' and ''l'').

Those familiar with the field of acoustic phonetics and with available textbooks in the discipline will not have encountered the depth of treatment evident in Chapters 6–9, and those of us who have been studying this area for a long time will learn something they didn't know after reading these beautifully crafted chapters. It is almost as if Stevens adopted a ''case-study-in-the-life-of-a-speech-sound'' approach in the writing of these chapters and, like an outstanding investigative reporter, unearthed the many individual characteristics of that life and in so doing produced a whole much larger than the sum of its parts.

Chapter 10, ''Some Influences of Context on Speech Sound Production,'' closes the book with a consideration of how the acoustic characteristics of speech sounds are affected by different aspects of context. In previous chapters there is some of this information, such as the variability in acoustic characteristics of stops depending on vowel context, but Chapter 10 extends the concept by providing discussion of some well-known effects (such as vowel reduction) that have been the focus of a good deal of research.

Stevens' book belongs in the library of any scientist interested in spoken language. It is certainly the best acoustic phonetics textbook available at this time, and will probably assume the mantle of discipline ''bible'' for many years to come. The clarity of writing, careful use of graphics, and comprehensive nature of the presentation are noteworthy, and at least in this opinion set the standard for how a textbook can be written to be truly useful. As a course text, the book is most appropriate for a graduate-level class aimed at students with some engineering background, the more the better. Much of the book can be appreciated without any analytical sophistication, but the substantial and theoretically compelling modeling component will be missed by those without the proper technical background.

GARY WEISMER
Department of Communicative Disorders & Waisman Center
1975 Willow Drive
University of Wisconsin-Madison
Madison, Wisconsin 53706

Low Frequency Scattering

George Dassios and Ralph Kleinman

Oxford University Press, New York: Clarendon Press, 2000.
Price: $115.00 (hardcover) ISBN: 019853678X.

Written by two leading experts on the subject, this book provides a solid treatment of wave scattering by ''small'' objects. Techniques and results are presented in three physical areas: acoustics, electromagnetics, and elastodynamics.

The overriding theme of the book is to cast the low frequency scattering problem into a sequence of simpler potential problems for determining the terms of a power series expansion, and to solve the latter iteratively. Emphasis is placed on three-dimensional boundary value or scattering problems involving interior (referred to in the book as transmission problems) and exterior domains and simple constitutive materials. The presentation is mathematical and theoretically oriented.

The book is organized logically into eight chapters, each of which is divided into sections focusing on one of the three physical fields. Chapters 1 and 2 introduce the relevant theory and results from wave scattering in general; Chaps. 3–6 develop the low frequency expansion method; and Chaps. 7 and 8 present explicit results for simple shapes such as sphere and ellipsoid.

Chapter 1, entitled ''basic theory,'' summarizes the differential equations, boundary conditions, and radiation conditions governing the three types of fields. The scattering problems are carefully defined and categorized. These include boundary value problems with Dirichlet (soft), Neumann (hard), and Robin (impedance) conditions in acoustics; the perfectly conducting and Leontovich (impedance) conditions in electromagnetics; Dirichlet (rigid) and Neumann (cavity) conditions in elasticity as well as transmission problems for homogeneous scatterers in all three areas. The excitation is confined to uniform ''plane waves, point source or superposition of plane waves and/or point source'' (which admit a series expansion in powers of the wave number). The authors also emphasize the distinction between lossless or lossy medium because of differences in the resulting formulations. Viscoelastic media and other complex materials (e.g., anisotropic) are not treated.

Chapter 2, entitled ''integral representation and scattering theorems'' sets out to build the stage for the discussion of low frequency scattering by providing specific formulations from general scattering theory. It covers the relevant forms of integral representations, asymptotic expressions for far fields, and definitions of various terms such as the scattering amplitude and scattering cross section. The derivation of several scattering theorems is also outlined. Enough detail is included so that readers with background in only one of the areas can easily follow the discussion.

Chapter 3, entitled ''low frequency expansions'' is one of the two core chapters in this book (the other being Chap. 5). The authors describe in great detail the techniques and steps used to develop the *complete* low frequency expansion, for all ten problems specified. The key idea in these developments is to substitute in the integral representation the low frequency expansions as the formal solution. This transforms the general scattering problem into problems of finding the expansion coefficients, which are then cleverly cast as potential problems and solved iteratively from low to higher order terms. Attention is paid to the derivation details and to some level of mathematical rigorousness.

The formalism given in Chap. 3 is based on surface integral representation. In Chap. 4, entitled ''the transmission problem revisited,'' the authors provide another derivation of the low frequency expansions for transmission problems using volume integrals. This approach turns out to be more effective, especially for electromagnetic problems. The result for lossy electromagnetic transmission problems, not discussed in Chap. 3, is treated in this chapter using the volume integral approach.

In Chap. 5, entitled ''Rayleigh scattering,'' the authors study a topic of long history by starting with a more formal mathematical definition of Rayleigh scattering as the first or dominant term in the low frequency expansions. Following this idea, the general results obtained in Chaps. 3 and 4 are particularized into more explicit expressions for the Rayleigh terms of relevant quantities of interest, including the scattering amplitudes, differential scattering cross section, and total cross section.

Chapter 6, entitled ''integral equations'' is not intended as a treatment of integral equation techniques *per se*, but concentrates on providing a list of integral equations governing the expansion coefficients. This will prove useful in numerical implementation of the low frequency expansion method.

Chapters 7 and 8, entitled ''the sphere'' and ''the ellipsoid,'' respectively, are a compilation of results for simple 3-D shapes and plane wave excitation. Results for acoustic problems with point source excitation are also provided.

The book also includes a 20-page bibliography and a 7-page list of symbols. As noted in the preface, ''not all aspects of low frequency scatter-

ing are discussed in this book.'' The authors mention several topics left out and provide corresponding references.

On the debit side, the reviewers felt that the authors have neglected two important problems. One is the validity of the low frequency expansion. The authors refer to this question briefly in one sentence on p. 79 by providing two references, which are not easily available. The other is the convergence properties of the resulting series.

In summary, this book has provided by far the most complete and systematic treatment of methods and techniques in low frequency scattering. The unified consideration of acoustic, electromagnetic, and elastic waves has once again proved to be very fruitful. The book is a valuable addition to the literature on wave scattering, and can serve as a good reference book for graduate students and researchers.

KAI DU
212 EES, Department of Engineering Science and Mechanics
Pennsylvania State University
University Park, Pennsylvania 16802

VASUNDARA V. VARADAN
212 EES, Department of Engineering Science and Mechanics
Pennsylvania State University
University Park, Pennsylvania 16802 [S0001-4966(00)03512-8]

Coarticulation: Theory, Data, and Techniques

William J. Hardcastle and Nigel Hewlett (Eds.)

Cambridge University Press, Cambridge, UK, 2000.
xiii+386 pp. Price: $64.95 ISBN: 0521440270.

No phenomena has preoccupied speech research like coarticulation. The term coarticulation refers to the fact that the acoustic and articulatory characteristics of speech segments vary with context. For example, lip position during /s/ in ''see'' is different than the lip rounding for the /s/ in ''Sue'' and as a result the two fricatives have different acoustic spectra. Since its first identification, this context-conditioned variation has shaped both theory and experiment. Liberman (1996), for example, credits the results of an early study on the effects of context on consonant identification for shaping his views on speech perception. In the earliest physiological studies of speech production, the smoothness and continuity of articulation that was evident in recordings so surprised Rousselot that he discarded trials that he couldn't segment easily as recording errors (Tillman, 1994).

Coarticulation remains as elusive today as in Rousselot's time. In part, the enduring nature of the ''problem of coarticulation'' stems from the inaccessibility of the speech articulators and this is evident in Hardcastle and Hewlett's book. Close to one-third of the present volume is dedicated to instrumental techniques that can be used to measure coarticulation during speech production. However, there are conceptual/theoretical reasons that contribute to the persistence and prominence of coarticulation in speech research. A dynamic tension exists between the idea of a sequence of separate phonetic units and the fluidity of motor control and no existing approach can resolve this.

Fluidity is a characteristic of all movements and there is evidence that something akin to coarticulation occurs in any rapid motor sequence. In typing, musical performance, sign language, etc. (e.g., Engel *et al.*, 1997; Moore, 1992; Soechting and Flanders, 1997; Tyrone *et al.*, 1999), movements exhibit smoothness and context sensitivity and are overlapping in time. The speech field and the papers in this volume have tended to ignore the generality of this character of movement and thus there has been little cross-fertilization between the various disciplines studying movements in context.

Coarticulation: Theory, Data and Techniques is still a welcome addition to the literature on this topic. It provides the field with a solid review of the current speech data and speech models. The volume grew from a large-scale research project on coarticulation funded through the European Union's ESPRIT program. The project addressed acoustic and articulatory relations in seven languages (English, French, German, Italian, Irish Gaelic, Swedish, and Catalan) with the aim of using this linguistic diversity to isolate more universal characteristics of coarticulation. Many but not all of the chapters were written by members of this team. The book is divided into four sections: (1) an historical and theoretical overview, (2) a review of coarticulation data for individual articulators (e.g., lingual coarticulation), (3) a so-called ''wider perspectives'' section, and (4) an instrumental techniques section.

The term coarticulation was first coined by Menzerath and de Lacerda in 1933 to describe the continuity in their kymograms of airflow during German consonant–vowel sequences. The opening chapter by Barbara Kühnert and Francis Nolan gives a broad overview of the historical background to the concept of coarticulation, including work prior to 1933 that struggled with the dynamic character of speech as well as the more recent theoretical developments. In the other chapter in this first section, Edda Farnetani and Daniel Recasens provide a comprehensive overview of the different theoretical approaches to the phenomenon. Unfortunately some of the ground covered in the first chapter is repeated here and as well in Farnetani's later chapter on labial coarticulation. In spite of this repetition, the chapter on models of coarticulation provides useful summaries of major approaches and a fair evaluation of strengths and weaknesses of each. They correctly point out that no current theory can account for all of the reported data.

And there are a lot of data! The second section of the book is devoted to the major findings and the minutia of speech coarticulation with separate chapters on coarticulation in the tongue, larynx, velopharyngeal port, lips, and lip/jaw system. These chapters provide excellent summaries of the facts of speech coarticulation from a range of languages and from data derived from many different techniques.

The third section called ''wider perspectives'' contains two very good chapters that presumably did not fit anywhere else. Sharon Manuel describes subtle differences in coarticulation in different languages and considers how these differences can be used to think about linguistic contrast. Mary Beckman discusses the relations between coarticulation and phonological representation.

The final section contains chapters on data recording methods that are used to study coarticulation. The list of techniques is not exhaustive and reflects the interests and laboratories of those involved in the ESPRIT research grant. The section includes chapters on palatography, magnetic resonance and ultrasonic imaging, electromagnetic articulography, electromyography, and acoustic analysis and techniques for studying velopharyngeal and laryngeal articulation. From my perspective, this is the least useful part of the book. The aim of the book is not to act as a speech science primer. Further, techniques change quickly and some of the technique descriptions already could be updated.

In the end, this book is a good milepost in the study of speech coarticulation. It provides thoughtful and balanced summaries of the data and theories as of 1999. However, no final conclusions, no consensus seems to have emerged from the European research project on the nature of coarticulation. Presumably, this will await a more general understanding of rapid motor sequencing.

Engel, K. C., Flanders, M., and Soechting, J. F. (**1997**). ''Anticipatory and sequential motor control in piano playing,'' Exp. Brain Res. **113**, 189–199.
Liberman, A. M. (**1996**). *Speech: A Special Code* (Bradford, Cambridge, MA).
Moore, G. P. (**1992**). ''Piano trills,'' Music Perception **9**, 351–359.
Soechting, J. F., and Flanders, M. (**1997**). ''Flexibility and repeatability of finger movement,'' J. Comput. Neurosci. **4**, 29–46.
Tillmann, H. G. (**1994**). ''Phonetics, early modern, especially instrumental work,'' in *The Encyclopedia of Language and Linguistics*, Vol. 6, edited by R. Asher (Pergamon, Oxford), pp. 3082–3094.
Tyrone, M. E., Kegl, J., and Poizner, H. (**1999**). ''Interarticulator coordination in deaf signers with Parkinson's disease,'' Neuropsychologia **37**, 1271–1283.

K. G. MUNHALL
Department of Psychology
Department of Otolaryngology
Queen's University
Kingston, Ontario K7L 3N6, Canada

REVIEWS OF ACOUSTICAL PATENTS

Lloyd Rice
11222 Flatiron Drive, Lafayette, Colorado 80026

The purpose of these acoustical patent reviews is to provide enough information for a Journal reader to decide whether to seek more information from the patent itself. Any opinions expressed here are those of reviewers as individuals and are not legal opinions. Printed copies of United States Patents may be ordered at $3.00 each from the Commissioner of Patents and Trademarks, Washington, DC 20231.

Reviewers for this issue:

GEORGE L. AUGSPURGER, *Perception, Incorporated, Box 39536, Los Angeles, California 90039*
RONALD B. COLEMAN, *BBN Technologies, 70 Fawcett Street, Cambridge, Massachusetts 02138*
DAVID PREVES, *Songbird Medical, Inc., 5 Cedar Brook Drive, Cranbury, New Jersey 08512*
KEVIN P. SHEPHERD, *M.S. 463, NASA Langley Research Center, Hampton, Virginia 23681*
ERIC E. UNGAR, *Acentech, Incorporated, 33 Moulton Street, Cambridge, Massachusetts 02138*

5,992,215

43.35.Zc SURFACE ACOUSTIC WAVE MERCURY VAPOR SENSORS

Joshua J. Caron *et al.*, assignors to Sensor Research and Development Corporation
30 November 1999 (Class 73/24.01); filed 29 May 1997

Gaseous mercury in air is a dangerous pollutant. The invention makes use of supersonic surface acoustic waves in a sensor design appropriate for *in situ* monitoring. This is a good example of how known acoustical principles can be applied to seemingly unrelated fields. The patent is interesting, clearly written, and includes more than a dozen helpful illustrations.—GLA

5,764,783

43.38.Ja VARIABLE BEAMWIDTH TRANSDUCER

Michael W. Ferralli, assignor to Technology Licensing Company
9 July 1998 (Class 381/160); filed 16 January 1996

The inventor's earlier patents set forth the basic geometry shown. Plane waves from transducer **12** are reflected from curved/conical surface **11**, which is shaped such that a ring-shaped virtual origin is created at **14**.

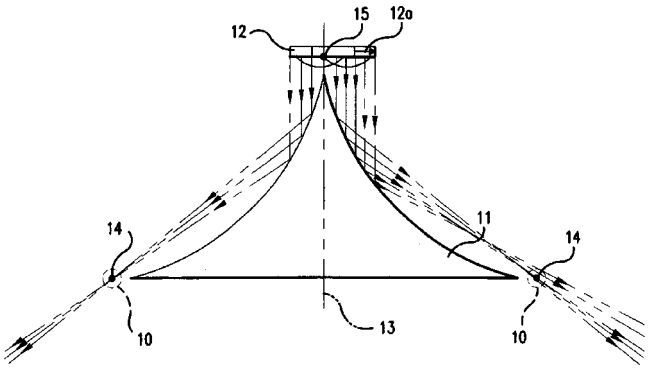

This variant covers the case where the transducer is shifted off-center to location **12a**, which results in an asymmetric coverage pattern.—GLA

5,793,001

43.38.Ja SYNCHRONIZED MULTIPLE TRANSDUCER SYSTEM

Michael W. Ferralli, assignor to Technology Licensing Company
11 August 1998 (Class 181/155); filed 16 January 1996

The geometry of United States Patent 5,764,783 (see preceding patent review) is augmented by an optional second, larger transducer. More importantly, the sound field produced by these transducer/reflector combinations is synchronized with that from a third, nonreflected source—a low-frequency loudspeaker, for example.—GLA

5,988,314

43.38.Ja SOUND OUTPUT SYSTEM

Hirokazu Negishi, assignor to Canon Kabushiki Kaisha
23 November 1999 (Class 181/144); filed in the United Kingdom 9 December 1987

The invention is a variant of Canon's basic ''audio mirror'' geometry in which sound energy from a loudspeaker is bounced off a generally conical reflector. In this case, the directional patterns of symmetrical right and left loudspeaker systems are designed to offset the Haas effect and thus expand the usable listening area for two-channel stereo reproduction.—GLA

6,031,919

43.38.Ja LOUDSPEAKER SYSTEM AND SOUND REPRODUCING APPARATUS

Osamu Funahashi and Norimitsu Kurihara, assignors to Matsushita Electric Industrial Company, Limited
29 February 2000 (Class 381/150); filed in Japan 3 April 1996

In this bandpass speaker system, passive radiator **401** is coupled to driving speaker **402** through air chamber **404**. Notice that subenclosure **406** is supported entirely from main baffle **403a**. This geometry is the inven-

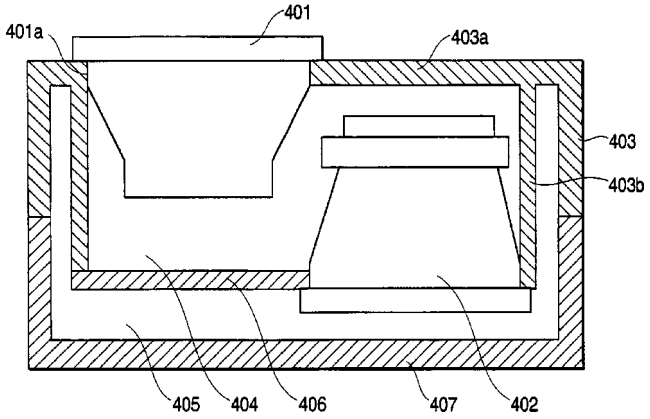

tion's novel feature. Since the top panel is assumed to be more rigid than the other panels (why?), side panel vibration is said to be reduced and sound quality improved.—GLA

6,031,920

43.38.Ja COAXIAL DUAL-PARABOLIC SOUND LENS SPEAKER SYSTEM

David Wiener, Park City, Utah
29 February 2000 (Class 381/160); filed 16 May 1997

Tweeter pod **30** contains three high-frequency transducers **32** whose centers **33** are vertically aligned with the focal point of upper parabolic reflector **20**. Sound energy from low-frequency loudspeaker **36** fires upwardly into sound dispersion lens **38** and then to parabolic reflector **22**. Looking at the diagram, one would expect the large skirt of tweeter pod **30**

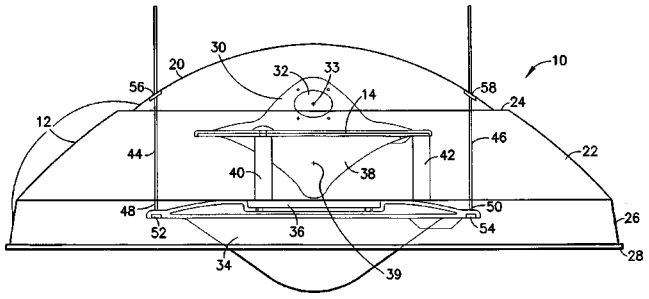

to scatter reflections from upper parabola **20**. Not to worry. ''Particularly, the upper parabolic portion is designed to reflect sound waves emitted by the tweeter drivers around the mid/woofer pod, to thereby reduce any potential interference by the mid/woofer pod with the high frequency sound waves.'' So much for potential interference; what about actual interference?—GLA

6,035,052

43.38.Ja ACOUSTIC TRANSDUCER

Masao Fujihira *et al.*, assignors to Sony Corporation
7 March 2000 (Class 381/401); filed in Japan 31 March 1997

Induction-type loudspeakers date back to the 1930s. The big advantage is that no electrical connections are made to the moving system. The main disadvantage is that induction speakers are notoriously inefficient. In this new Sony design, single-turn coil **7** is bonded to diaphragm **50** and immersed in a cone-shaped magnetic field between pole pieces **15** and **30**.

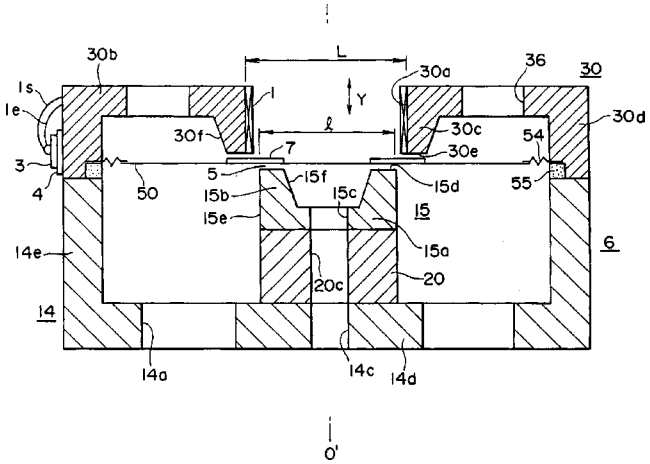

Fixed driving coil **1** is wound in a kind of spiral staircase fashion. Since the primary coil is not contained within the magnetic gap, it can have a great many turns of wire. A variant is described which has additional, tapped primary coils and which can be driven from a digital signal.—GLA

6,068,080

43.38.Ja APPARATUS FOR THE REDISTRIBUTION OF ACOUSTIC ENERGY

Emanuel LaCarrubba, Sausalito, California
30 May 2000 (Class 181/155); filed 13 April 1998

This apparatus in essence is an arrangement of acoustic reflectors intended to distribute sound produced by a transducer relatively uniformly over a broad area. The reflecting surfaces here are portions of ellipsoids of revolution, with the transducer mounted at one of their foci.—EEU

6,016,473

43.38.Md LOW BIT-RATE SPATIAL CODING METHOD AND SYSTEM

Ray M. Dolby, San Francisco, California
18 January 2000 (Class 704/500); filed 7 April 1998

The overnight popularity of music transmission via the internet has stimulated new research into subjectively acceptable low bit-rate encoding. The invention does not attempt to simultaneously reproduce multiple audio channels. Instead, it identifies and then localizes the dominant sound field at any given time. ''Because the system is based on the premise that only sound from a single direction is heard at any instant, the decoder need not apply a signal to more than two sound transducers at any instant.''—GLA

5,946,391

43.38.Si TELEPHONES WITH TALKER SIDETONE

Trevor Dragwidge *et al.*, assignors to Nokia Mobile Phones Limited
31 August 1999 (Class 379/391); filed in the United Kingdom 24 November 1995

The patent document explains that in telephony ''sidetone'' is a desirable effect which occurs when a talker hears a small amount of his own voice in the earpiece. In conventional telephones, the relative sidetone amplitude is held as nearly constant as possible. However, this means that background noise will also be picked up and fed back to the earpiece, which is undesirable. As a matter of fact, the classic Western Electric carbon transmitter did a good job of discriminating between background noise and the talker's voice. Because more modern microphones do not, the invention relies instead on electronic circuitry to control sidetone gain in relation to the magnitude of the input signal. A preprogrammed comparator sets a first

level of gain when the input signal exceeds an upper threshold level, and sets a second level of gain when the signal is less than a lower threshold level.—GLA

5,812,675

43.38.Vk SOUND REPRODUCING ARRAY PROCESSOR SYSTEM

Stephen Francis Taylor, assignor to Taylor Group of Companies, Incorporated
22 September 1998 (Class 381/18); filed 14 December 1993

This invention extends the concepts described in previous Taylor patents. The inventor envisions two-dimensional arrays of ''sound pixels'' combined to form a ''sound bubble'' which can localize various sound events at almost any point in space. A computer-aided design process simplifies the implementation of complex acoustical designs.—GLA

6,021,206

43.38.Vk METHODS AND APPARATUS FOR PROCESSING SPATIALIZED AUDIO

David Stanley McGrath, assignor to Lake DSP Pty Limited
1 February 2000 (Class 381/310); filed 2 October 1996

It seems reasonable that the audio portion of a virtual reality system could be made up of a stereophonic audio signal source, a head tracking device, circuitry capable of ''rotating'' the audio signal, and appropriate conversion of the stereophonic information for reproduction via headphones. This is what has been patented here. A preferred embodiment starts out with the signal encoded in Ambisonic B-format because this simplifies the rotation process.—GLA

5,965,249

43.40.Tm VIBRATION DAMPING COMPOSITE MATERIAL

Stephen P. Sutton *et al.*, assignors to Gore Enterprise Holdings, Incorporated
12 October 1999 (Class 428/304.4); filed 7 August 1997

This patent describes a number of materials in which high damping is achieved by entrapment of highly viscous fluids in the pores of a porous material, such as a fabric or other fibrous substance.—EEU

6,012,346

43.40.Tm LOW VIBRATION MOTION TRANSLATION SYSTEM

Anh Vo, assignor to New Hampshire Ball Bearing, Incorporated
11 January 2000 (Class 74/57); filed 18 September 1998

In tools, such as saber saws, rotational motion of shaft is converted into reciprocating motion by means of ''ball drivers.'' These consist in essence of balls like those used in ball bearings, which ride in noncircumferential grooves in the shaft and in circumferential grooves in the mating reciprocating element. This patent uses a second reciprocating element, actuated by a second ball driver arrangement, to counter-balance the accelerations produced by the primary reciprocating element.—EEU

6,055,317

43.40.Vn ACTIVE VIBRATION DAMPING DEVICE HAVING PNEUMATICALLY OSCILLATED MASS MEMBER WHOSE OSCILLATION AMPLITUDE AS WELL AS FREQUENCY AND PHASE ARE CONTROLLABLE

Atsushi Muramatsu and Yoshihiko Hagino, assignors to Tokai Rubber Industries, Limited
25 April 2000 (Class 381/71.4); filed in Japan 10 February 1998

A pneumatic actuation device is described for suppressing the vibration response of structures to which it is attached. The passive impedance of the device is similar to a traditional reaction-mass shaker. However, forces are imparted into the structure and reaction mass by controlling the air pressure within a volume connecting the two. The oscillating air pressure stretches a mechanical spring connecting the reaction mass to the structure, and transmits control forces into the structure. Pneumatic valves are switched via a computer controller to oscillate the pressure within the actuator. The device appears suited for only tonal rather than broadband control.—RBC

6,058,195

43.40.Vn ADAPTIVE CONTROLLER FOR ACTUATOR SYSTEMS

Wolfgang J. Klippel, Dresden, Germany
2 May 2000 (Class 381/96); filed 30 March 1998

A method is presented to control and linearize the response of generic actuation systems. The major elements of this system are a controller and a parameter detector. The parameter detector operates as an adaptive filter to estimate the electrical characteristics of the actuator. This information, in the form of a parameter vector, is passed to the controller to adapt filter coefficients to minimize a mean-square objective function. The system is said to be applicable for controlling linear as well as nonlinear actuators.—RBC

6,074,208

43.50.Gf NOISE REDUCTION IN FLUID FLOW PASSAGE

Kenneth B. Mitchell, Vancouver, British Columbia, Canada
13 June 2000 (Class 433/91); filed 21 August 1998

In the suction tube of a dental aspirator, which is inserted in a patient's mouth to remove water, etc., high-frequency sound is produced by the air or air/liquid mixture that is being drawn in. A problem also arises when the suction orifice is blocked if it makes contact with the tissue around the operation site. Similar problems also are encountered in other surgical vacuum systems. In order to overcome these problems, the interior of the tube, the edge of the orifice, and a length of the exterior of the tube are provided with an array of bristles that stick out from the tube surfaces. These bristles serve to attenuate the sound and to prevent blocking of the orifice.—EEU

6,076,632

43.50.Gf CROSS FLOW BAFFLE MUFFLER

Kory J. Schuhmacher and Gary D. Goplen, assignors to Nelson Industries, Incorporated
20 June 2000 (Class 181/282); filed 14 December 1998

A box-style muffler for use with an internal combustion engine is designed to minimize acoustic radiation from the flat, exterior surfaces. Exhaust gases initially flow into two internal cavities formed by members **18**

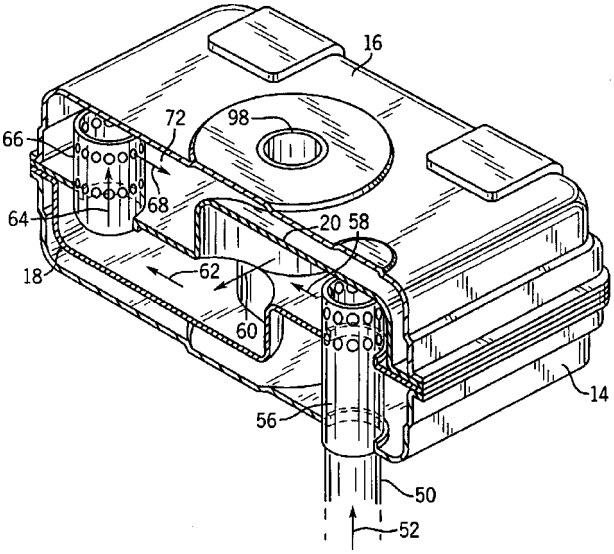

and **20**, before encountering the external cavities formed by **14** and **18**. In order to simplify construction and reduce cost, the two inner baffle members, **18** and **20**, are designed to be physically identical to each other.—KPS

6,041,126

43.50.Ki NOISE CANCELLATION SYSTEM

Kenichi Terai and Hiroyuki Hashimoto, assignors to Matsushita Electric Industrial Company, Limited
21 March 2000 (381/71.6); filed in Japan 24 July 1995

This patent describes an approach for an active telephone handset that reduces the contribution of ambient noise transmitted from the handset, and enhances the ability of the operator to hear his own voice when operated in a noisy environment. The system includes two adaptive least-mean-square (LMS) filters. The first employs a microphone that is located on the outside of the handset, which is sensitive primarily to the ambient noise. The adaptive filter is operated to remove the ambient noise (as characterized by the outside microphone) in the signal from a microphone located inside the earcup. The second adaptive filter operates to remove the ambient noise contribution from the transmitted voice signal. In addition, this nominally noise-free voice signal of the operator is summed with the incoming voice signal so that the operator can hear his own voice when using the handset in a noisy environment.—RBC

6,058,194

43.50.Ki SOUND-CAPTURE AND LISTENING SYSTEM FOR HEAD EQUIPMENT IN NOISY ENVIRONMENT

Christian Gulli and Gerard Reynaud, assignors to Sextant Avionique
2 May 2000 (Class 381/94.8); filed in France 26 January 1996

An active headset for use in noisy environments such as an aircraft is described. The headset includes both disturbance rejections and command-following functionality. The disturbance rejection is achieved via a local feedback loop comprised of a microphone and speaker located within the headset. In this mode, the microphone signal is digitally filtered to produce a drive signal to the loudspeaker in order to minimize the noise at the microphone. The command-following mode is used to enhance intelligibility of signals from other sources (e.g., communications). This is implemented as a traditional servo-system control loop with an additional filter to frequency weight the response at the microphone located within the headset.—RBC

6,061,456

43.50.Ki NOISE CANCELLATION APPARATUS

Douglas Andrea and Martin Topf, assignors to Andrea Electronics Corporation
9 May 2000 (Class 381/71.6); filed 29 October 1992

This extensive patent presents methods and apparatus for reducing unwanted ambient noise in microphones, headsets, and telephone handsets. In contrast to closed-loop feedback system approaches (e.g., United States Patent 6,058,194), an open-loop method is described that relies on sensor placement and orientation to discriminate between desired speech and undesired ambient noise signals. The sensor orientation is used to provide one microphone that senses both speech and ambient noise, while the second microphone senses primarily the ambient noise. These signals are inputs to an operational amplifier that differences these two signals, resulting in an output signal composed primarily of the desired speech signal.—RBC

6,078,673

43.50.Ki APPARATUS AND METHOD FOR ACTIVE CONTROL OF SOUND TRANSMISSION THROUGH AIRCRAFT FUSELAGE WALLS

Andreas H. von Flotow *et al.*, assignors to Hood Technology Corporation
20 June 2000 (Class 381/71.7); filed 3 October 1997

An active control system to reduce aircraft interior noise is described in which acoustic sources are placed in the cavity formed by the outer skin and the inner trim panel of the aircraft. One or more microphones are placed in the vicinity of each acoustic source to provide a feedback control signal,

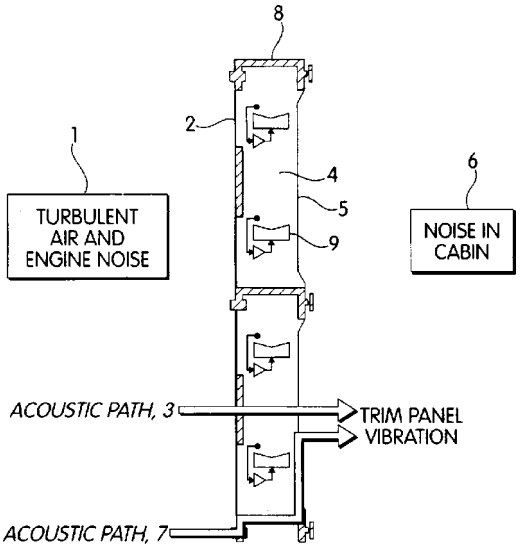

thus reducing the sound pressure in the cavity. Feedback circuitry is described which includes a compensation filter to ensure controller stability.—KPS

6,084,971

43.50.Ki ACTIVE NOISE ATTENUATION SYSTEM

Ian R. McLean, assignor to Siemens Electric Limited
4 July 2000 (Class 381/71.5); filed 10 June 1997

A active noise attenuation system for the air induction ducting of an internal combustion engine is described. The sensors (**40, 42**), electronics **37**, and loudspeaker **32** are contained within an annular pod **16** located within the air inlet duct **10** at the plane of the air intake opening. By placing the loudspeaker at the air intake opening, the loudspeaker sound field de-

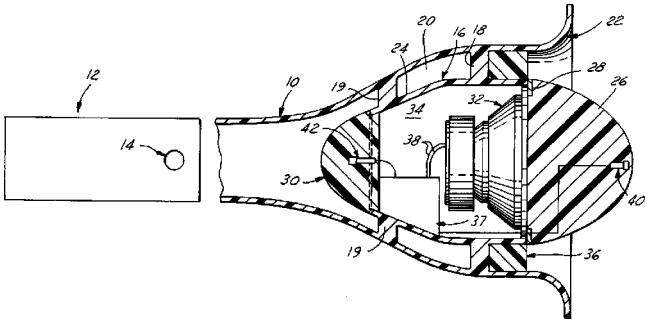

structively interferes with the sound radiating from the annular inlet opening. This results in a cylindrical acoustic doublet source at the inlet. The intent is that this system will reduce the acoustic radiation resistance of the annular inlet and, consequently, reduce acoustic radiation efficiency and radiated power.—RBC

6,072,388

43.50.Lj DRIVELINE SOUND MONITOR

Christos T. Kyrtsos, assignor to Meritor Heavy Vehicle Systems LLC
6 June 2000 (Class 340/439); filed 22 December 1998

A method to monitor the mechanical condition of the drive shaft of a vehicle is described in which one or more acoustic sensors are placed in the vicinity of the drive shaft. Measured signals are compared with expected signals derived from measurements made when the vehicle was known to be in good mechanical condition. Several methods of comparing measured and expected signals are proposed which enable mechanical degradation to be detected, resulting in a warning signal being presented to the vehicle's operator.—KPS

6,029,770

43.55.Ti SOUND DAMPING ELEMENT

Arnold Schneider and Stefan Debold, assignors to Wendt Sit GmbH
29 February 2000 (Class 181/285); filed 20 July 1998

This patent claims to pertain to sound barrier walls for use in buildings, vehicle cabs, and the like. An element according to this patent consists of two thin plates, probably of sheet metal, with the space between these filled with a sound-absorbing material. One of these plates is provided with perforations. The edges of these laminated arrangements are designed so that adjacent arrangements can lock against each other via an airtight elastomeric seal.—EEU

6,088,339

43.66.Ts APPARATUS AND METHOD FOR PROGRAMMING A HEARING AID USING A SERIAL BIDIRECTIONAL TRANSMISSION METHOD AND VARYING CLOCK PULSES

Wolfram Meyer, assignor to Siemens Audiologusche Technik GmbH
11 July 2000 (Class 370/296); filed in Germany 9 December 1996

A single-line, half-duplex data transmission scheme is said to reduce the number of connecting leads between a programming device and a hearing aid. Nonsimultaneous, bi-directional data transmission is described based on variations of amplitude or other parameters of clock pulses. Bi-

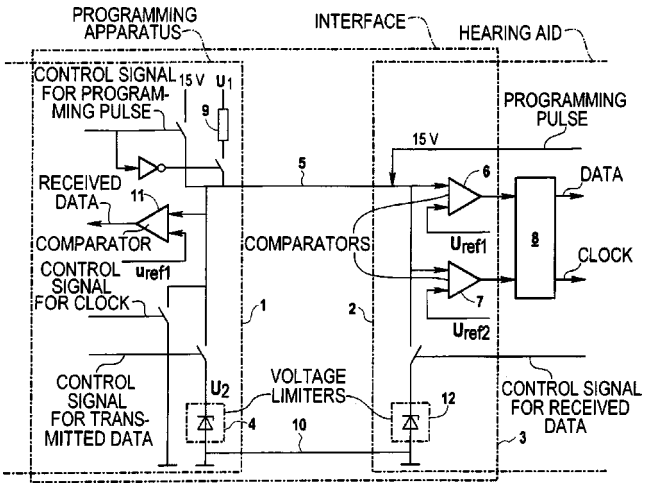

directional transmission of programmable data may occur without cables if a variable rate clock pulse is superimposed with a carrier frequency, thus producing an altered frequency. Using this apparatus, several different hearing aids may be programmed with a single programmer.—DAP

6,088,465

43.66.Ts DOOR-DEPENDENT SYSTEM FOR ENABLING AND ADJUSTING OPTIONS ON HEARING AIDS

William L. Hanright and Sunil Chojar, assignors to Siemens Hearing Instruments, Incorporated
11 July 2000 (Class 381/323); filed 30 April 1996

Conductive strips are attached to the side of a removable hearing aid battery door near the hinge. When the battery door is closed, the conductive strips are in contact with mating conductors on a flexible circuit extension of a programming cable. By using several battery doors with different conduc-

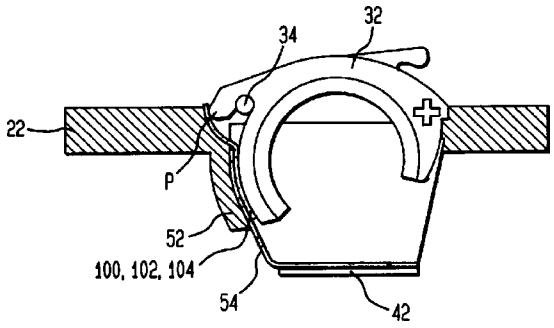

tive patterns, different programmable options may be activated such as filter cutoff frequency, maximum gain value, and maximum output SPL limiting value.—DAP

6,055,495

43.72.Ar SPEECH SEGMENTATION

Roger Cecil Ferry Tucker and Michael John Collins, assignors to Hewlett-Packard Company
25 April 2000 (Class 704/210); filed in European Patent Office 7 June 1996

This patent describes an indexing system, or a sort of directory structure, for voice messages received by a recording device, such as a telephone answering system. Based on the duration of pauses within the various messages, each message is segmented into sections. A kind of map of the sec

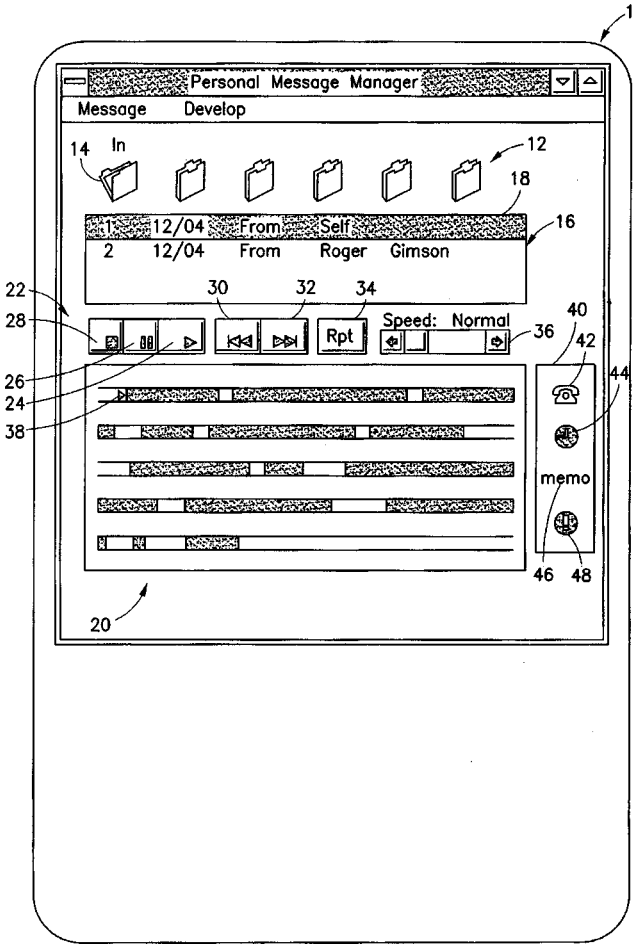

tions is displayed, allowing the user to easily jump to a specific section. The patent goes into considerable detail on the issues involved in reliable pause classification.—DLR

6,055,501

43.72.Ar COUNTER HOMEOSTATIS OSCILLATION PERTURBATION SIGNALS (CHOPS) DETECTION

Robert J. MacCaughelty, Charlotte, North Carolina
25 April 2000 (Class 704/272); filed 3 July 1997

During normal speech, a low-frequency oscillation in the 8- to 12-Hz range, known as microtremor, modulates the various speech musculature controls, affecting focal folds, tract walls, and tongue. As psychological stress increases, muscles tighten and the microtremor amplitude decreases. A few companies have sold devices to detect these microtremor modulations, but only for short utterances such as ''yes'' or ''no'' in response to interrogation. This patent describes a more generally applicable device, able to analyze long-duration utterances and provide more meaningful measured outputs than the stress/nonstress outputs of earlier devices.—DLR

6,061,647

43.72.Ar VOICE ACTIVITY DETECTOR

Paul Alexander Barrett, assignor to British Telecommunications public limited company
9 May 2000 (Class 704/208); filed 29 November 1993

This patent describes a system for estimating the background noise level of a speech signal. In order to make that estimate, it is necessary to know when speech is present, allowing background noise estimation during nonspeech intervals. For this purpose, several steps are performed such as would be used in a speech vocoder system to determine a linear prediction gain value. This value is then compared to a threshold to test for voice activity.—DLR

6,064,956

43.72.Ar METHOD TO DETERMINE THE EXCITATION PULSE POSITIONS WITHIN A SPEECH FRAME

Jonas Svedberg, assignor to Telefonaktiebolaget LM Eriksson
16 May 2000 (Class 704/219); filed in Sweden 12 April 1995

The multipulse method of speech coding represents the linear prediction residual as a series of well-placed pulses such that the reconstructed signal is close to the original speech. In the patented method, two stages of pulse location calculation are performed. The first stage uses a relatively complex calculation, while the second uses a simpler, restricted algorithm. The two computations can be traded off to achieve a desired level of complexity versus quality.—DLR

6,064,962

43.72.Ar FORMANT EMPHASIS METHOD AND FORMANT EMPHASIS FILTER DEVICE

Masahiro Oshikiri *et al.*, assignors to Kabushiki Kaisha Toshiba
16 May 2000 (Class 704/262); filed in Japan 14 September 1995

This linear prediction analysis method uses an increased analysis order to emphasize a particular formant region, thus improving the output quality. However, in order to keep the computational complexity from increasing, the higher-order analysis is implemented as separate first-order low- and high-pass filters. Typically, a first-order low pass with adaptable coefficients is followed by a first-order high pass with fixed coefficients.—DLR

6,067,095

43.72.Ew METHOD FOR GENERATING MOUTH FEATURES OF AN ANIMATED OR PHYSICAL CHARACTER

Damon Vincent Danieli, assignor to Microsoft Corporation
23 May 2000 (Class 345/473); filed 4 February 1997

This system for computing lip positions for a graphical display or a toy uses a vector quantization of linear prediction cepstral features to get lip parameters. Minimum and maximum gain values within a specified interval

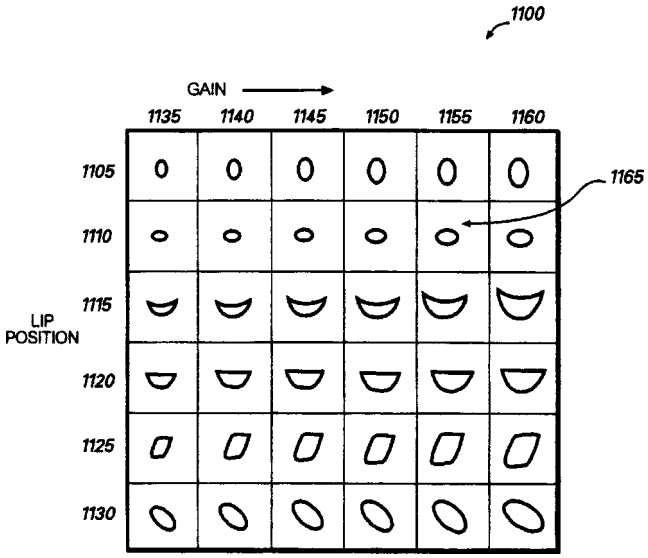

are defined as endpoints for the lip parameters and frame-by-frame values are interpolated according to the quantization code. The figure shows a typical lip parameter space.—DLR

6,067,512

43.72.Ew FEEDBACK-CONTROLLED SPEECH PROCESSOR NORMALIZING PEAK LEVEL OVER VOCAL TRACT GLOTTAL PULSE RESPONSE WAVEFORM IMPULSE AND DECAY PORTIONS

Joseph T. Graf, assignor to Rockwell Collins, Incorporated
23 May 2000 (Class 704/225); filed 31 March 1998

This peak amplitude control system modifies a speech signal so as to reduce the peak-to-average ratio. This is done by adjusting a separate gain control on each of the real and imaginary components of a filtered speech signal. The speech signal, at the gain control point, is delayed by an amount equal to the peak estimation processing time. The amount of gain adjustment is a compromise between peak uniformity and harmonic distortion.—DLR

6,052,665

43.72.Gy SPEECH INPUT TERMINAL AND SPEECH SYNTHESIZING TERMINAL FOR TELEVISION CONFERENCE SYSTEM

Akinori Momii *et al.*, assignors to Fujitsu Limited
18 April 2000 (Class 704/270); filed in Japan 22 November 1995

This patent presents an audio volume control system for use by a television conference system. Two volume controls are available in each unit to adjust the outgoing audio level as well as the normal local sound level. When a conference is started, the terminals perform an audio level test round, during which each terminal adjusts its transmission level according to requests from other terminals, allowing the entire network of terminals to establish a uniform reference level.—DLR

6,061,793

43.72.Gy METHOD AND APPARATUS FOR EMBEDDING DATA, INCLUDING WATERMARKS, IN HUMAN PERCEPTIBLE SOUNDS

Ahmed H. Tewfik *et al.*, assignors to Regents of the University of Minnesota
9 May 2000 (Class 713/176); filed 30 August 1996

This watermark embedding technique buries a recoverable watermark data stream into a digitally sampled audio signal. If the watermark data is not already in a coded form, it is randomized using a pseudo-random sequence. Places are then found in the audio material where watermark data can be hidden using perceptual masking characteristics. After watermark addition to the audio signal, a further temporal masking step is performed to assure that no audible trace remains from the earlier spectral processing steps.—DLR

6,052,666

43.72.Ja VOCAL IDENTIFICATION OF DEVICES IN A HOME ENVIRONMENT

Eric Diehl and Gerard Corda, assignors to Thompson multimedia S.A.
18 April 2000 (Class 704/275); filed in European Patent Office 6 November 1995

This patent addresses the issue of using voice to control multiple devices in the home. For example, both a TV and a VCR might appropriately respond to a request to change the channel. In this system, a central voice manager would direct the commands according to a set of strategies. For feedback, each device would speak with a unique programmed voice characteristic, easily identifiable by the user. If the user did not specifically name a target device for a command and the command would be applicable to multiple devices, the solution presented here is that each applicable device would, in turn, ask whether it was being addressed, until the user acknowledged the intended device.—DLR

6,064,960

43.72.Ja METHOD AND APPARATUS FOR IMPROVED DURATION MODELING OF PHONEMES

Jerome R. Bellegarda and Kim Silverman, assignors to Apple Computer, Incorporated
16 May 2000 (Class 704/260); filed 18 December 1997

A method is described for computing phoneme durations for use in a speech synthesis system. Durations are modeled as a sum of weighted contributions from a variety of contextual factors, such as the identities of surrounding segments, within-word position, phrase boundaries, and speaking rate. The sum is then adjusted by an input/output function, such as shown in the figure. The function may be a straight line for an additive mix, an exponential for a multiplicative mix, or another nonlinear curve.—DLR

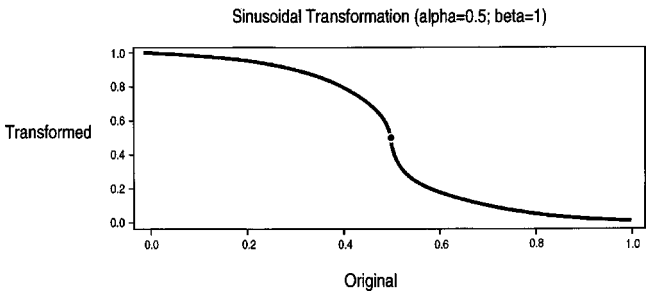

6,067,511

43.72.Ja LPC SPEECH SYNTHESIS USING HARMONIC EXCITATION GENERATOR WITH PHASE MODULATOR FOR VOICED SPEECH

Mark Lewis Grabb *et al.*, assignors to Lockheed Martin Corporation
23 May 2000 (Class 704/223); filed 13 July 1998

This linear prediction vocoding system improves the output speech quality by modulating the phase of individual harmonics in the voiced speech spectrum. Several other techniques for spectral modification are also described. The linear prediction coefficients are first converted to line spectral frequencies. In one version, a 3-bit signal is transmitted with each frame which identifies one of eight voice/noise frequency cutoff boundaries. Harmonics are reconstructed below the cutoff and noise at higher frequencies.—DLR

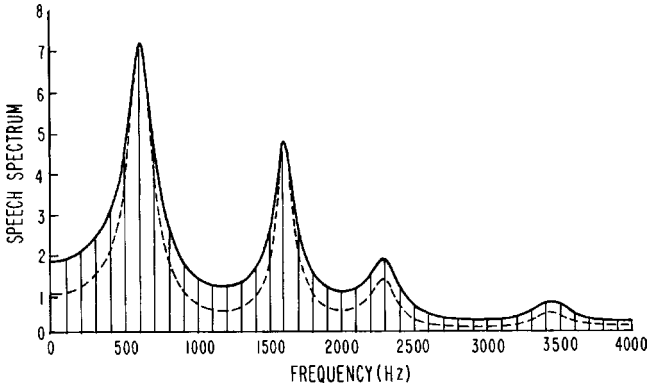

6,055,498

43.72.Ne METHOD AND APPARATUS FOR AUTOMATIC TEXT-INDEPENDENT GRADING OF PRONUNCIATION FOR LANGUAGE INSTRUCTION

Leonardo Neumeyer *et al.*, assignors to SRI International
25 April 2000 (Class 704/246); filed 2 October 1996

The speech recognizer described here performs a variety of tests on a spoken word or phrase to determine the accuracy of pronunciation and to generate a score which characterizes the pronunciation quality. Tests performed include phoneme and syllable durations and goodness of fit to a mixture Gaussian Markov model. The scores from various parts of the word or phrase are combined to determine an overall pronunciation grade.—DLR

6,055,499

43.72.Ne USE OF PERIODICITY AND JITTER FOR AUTOMATIC SPEECH RECOGNITION

Rathinavelu Chengalvarayan and David Lynn Thomson, assignors to Lucent Technologies, Incorporated
25 April 2000 (Class 704/250); filed 1 May 1998

This speech recognition system adds certain voicing analysis parameters to the usual set of cepstral and energy parameters to improve recognition performance. Previous results indicate that simply adding voicing or pitch information to the acoustic vector does not significantly improve the results. In this case, voicing periodicity and jitter are added to the acoustic data, improving the recognition accuracy.—DLR

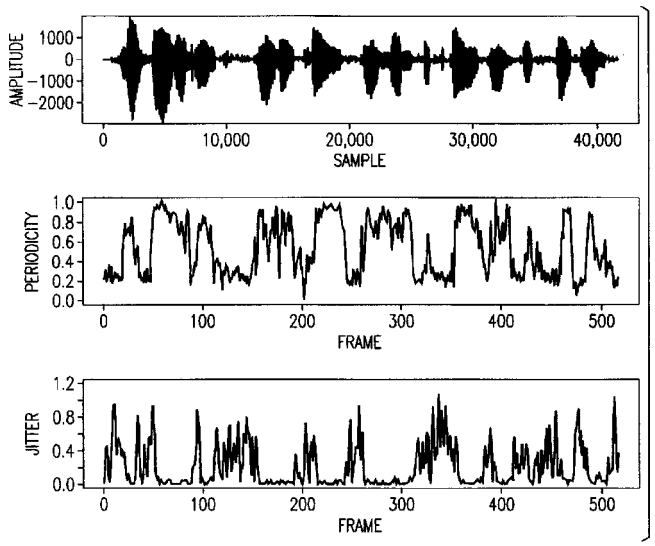

6,058,363

43.72.Ne METHOD AND SYSTEM FOR SPEAKER-INDEPENDENT RECOGNITION OF USER-DEFINED PHRASES

Coimbatore S. Ramalingam, assignor to Texas Instruments, Incorporated
2 May 2000 (Class 704/251); filed 2 January 1997

New utterances, not previously trained in a speech recognition system, are typically detected by an out-of-vocabulary technique known as garbage phrase detection. Speaker-dependent garbage detection works well enough, but uses large amounts of memory. Speaker-independent garbage detection generally does not work well. This speaker-independent garbage detector uses a general-purpose grammar, such as an *n*-gram probabilities model, as a reference. If a penalized general-purpose score exceeds the normal recognition score, the item is classified as out-of-vocabulary.—DLR

6,058,364

43.72.Ne SPEECH RECOGNITION OF CUSTOMER IDENTIFIERS USING ADJUSTED PROBABILITIES BASED ON CUSTOMER ATTRIBUTE PARAMETERS

Randy G. Goldberg *et al.*, assignors to AT&T Corporation
2 May 2000 (Class 704/252); filed 20 November 1997

The patent describes a method for improving the accuracy of a speech recognition system used for customer identification. The initial utterance of the customer's ID, such as a name or account number, is recognized, yielding a list of *n*-best choices. A record of account details, such as account activity and last transaction, is retrieved from a database for each of the *n*-best candidates. Based on the account data, the *n*-best scores are readjusted to determine the most likely customer ID for the caller. —DLR

6,058,365

43.72.Ne SPEECH PROCESSING USING AN EXPANDED LEFT TO RIGHT PARSER

Akito Nagai *et al.*, assignors to ATR Interpreting Telephony Research Laboratories
2 May 2000 (Class 704/257); filed in Japan 16 November 1990

This speech recognizer uses a typical context-free parser, in this case, an LR parser, to accept a sequence of words in the speech input stream. The acoustic features are matched using a hidden Markov model, more or less in

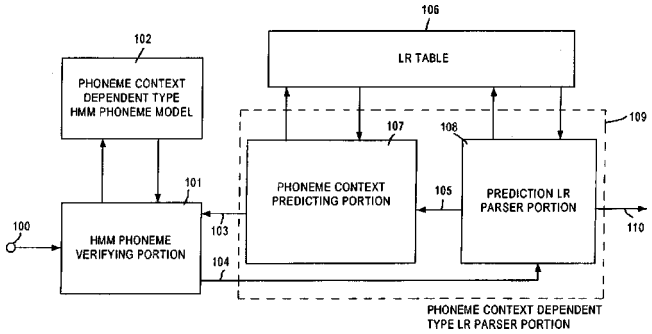

the usual way. However, the probabilities of occurrence for the next phoneme are adjusted according to possible choices for the next word to be allowed by the LR parser.—DLR

6,061,646

43.72.Ne KIOSK FOR MULTIPLE SPOKEN LANGUAGES

Michael John Martino and Robert Charles Paulsen, Jr., assignors to International Business Machines Corporation
9 May 2000 (Class 704/3); filed 18 December 1997

This multi-language speech recognizer is intended for use in a public site, such as an amusement park. An initial recognition dictionary contains a small number of selected ''starter'' words in each of a number of languages. These words are chosen based on the likelihood of their use in an initial question, such as ''how,'' ''where,'' etc. in the case of English. A likely language is determined from the initial recognition. When the language is identified, the input speech is again processed using a larger dictionary for the selected language and a specific-language prompt is generated.—DLR

6,061,651

43.72.Ne APPARATUS THAT DETECTS VOICE ENERGY DURING PROMPTING BY A VOICE RECOGNITION SYSTEM

John N. Nguyen, assignor to Speechworks International, Incorporated
9 May 2000 (Class 704/233); filed 21 May 1996

This speech activity detector is used to determine whether the user is trying to interrupt during the time the processor is generating a prompting utterance. This task is made much more difficult when line echoes from the outgoing prompt interfere with the incoming user speech. This system predicts the line signal based on the original and filtered versions of the outgo-

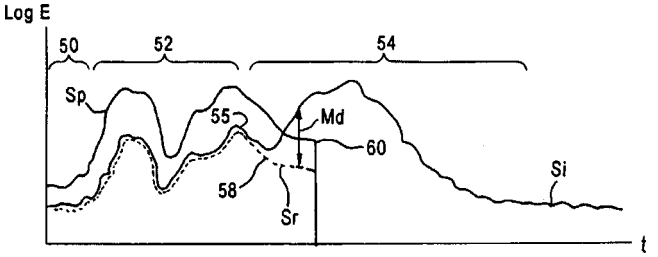

ing signal. The residue after subtraction of this prediction is compared to an energy threshold to determine whether an unpredicted component is present in the signal. Such an unpredictable component is likely to be a user's ''barge-in'' utterance.—DLR

6,061,652

43.72.Ne SPEECH RECOGNITION APPARATUS

Eiichi Tsuboka and Junichi Nakahashi, assignors to Matsushita Electric Industrial Company, Limited
9 May 2000 (Class 704/245); filed in Japan 13 June 1994

This word-spotting speech recognition system performs a cluster analysis on incoming acoustic vectors based on a Kullbach–Leibler divergence (KLD) measure. A hidden Markov model match is performed, fol-

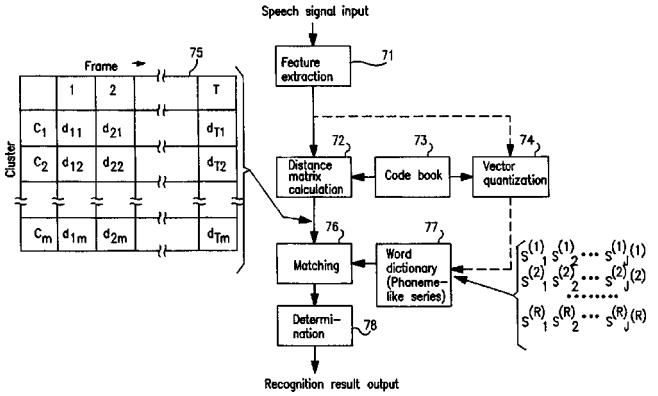

lowed by a dynamic programming alignment with word candidates using the KLD distances.—DLR

6,061,653

43.72.Ne SPEECH RECOGNITION SYSTEM USING SHARED SPEECH MODELS FOR MULTIPLE RECOGNITION PROCESSES

Thomas D. Fisher *et al.*, assignors to Alcatel USA Sourcing, L.P.
9 May 2000 (Class 704/256); filed 14 July 1998

This patent describes an arrangement by which multiple speech recognition processes can make use of a single set of speaker model information. The idea is simply that the speaker model is divided into state-dependent and state-independent parts. The state-independent portion can be read freely by any recognition process. Multiple state-dependent sections are created, one for each recognition process to be run. Each process can then consult its own state-dependent data.—DLR

6,064,959

43.72.Ne ERROR CORRECTION IN SPEECH RECOGNITION

Jonathan Hood Young *et al.*, assignors to Dragon Systems, Incorporated
16 May 2000 (Class 704/251); filed 28 March 1997

This patent gives solutions for some of the problems which can arise while using the speech recognition capability itself to correct errors which may occur during the use of a speech recognition system. In addition to the presence of a command keyword, the correction utterance will have a

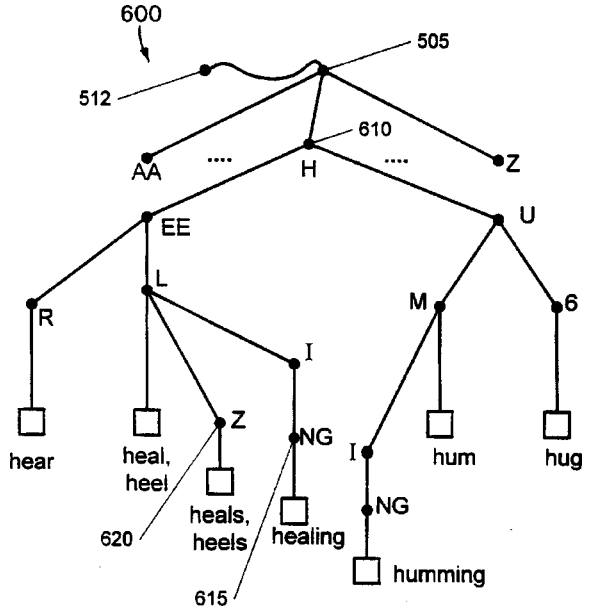

complex pattern of word probabilities, dependent on occurrences of recognized and intended words in the misunderstood utterance. Once a correction utterance is detected, various modes of interaction may be used, such as a display of lists of alternates, etc.—DLR

6,064,957

43.72.Ne IMPROVING SPEECH RECOGNITION THROUGH TEXT-BASED LINGUISTIC POST-PROCESSING

Ronald Lloyd Brandow and Tomasz Strzalkowski, assignors to General Electric Company
16 May 2000 (Class 704/235); filed 15 August 1997

During the training of this speech recognition system, after speaker models have been constructed, the original text is aligned with the recognized text and a series of text correction rules are formulated. The rules thus formed are applied to the recognized text string in several passes, rejecting and reformulating any rules which are not validated. The final set of rules is then applied after normal recognition to correct any errors remaining at the level of the text output.—DLR

6,067,513

43.72.Ne SPEECH RECOGNITION METHOD AND SPEECH RECOGNITION APPARATUS

Shunsuke Ishimitsu, assignor to Pioneer Electronic Corporation
23 May 2000 (Class 704/233); filed in Japan 23 October 1997

This speech recognizer is designed for use in noisy environments, but uses a non-noise speaker model. Just before an utterance is collected for recognition, an interval of the open-mic background noise is collected. A cepstrum representation of the noise signal is saved and then subtracted from the speech cepstral data prior to recognition processing. This results in the deconvolution of the noise spectrum from the speech signal.—DLR

Convergence of poroelastic finite elements based on Biot displacement formulation

Nicolas Dauchez and Sohbi Sahraoui
Laboratoire d'Acoustique UMR CNRS 6613, Université du Maine, 72095 Le Mans cedex 9, France

Noureddine Atalla
GAUS, Mechanical Engineering Department, Université de Sherbrooke, Sherbrooke, Québec J1K 2R1, Canada

(Received 4 April 1999; revised 15 June 2000; accepted 5 July 2000)

The convergence of linear poroelastic elements based on Biot displacement formulation is investigated. The aim is to determine a mesh criterion that provides reliable results under a given frequency limit. The first part deals with 1D applications for which resonance frequencies can be related to Biot wavelengths. Their relative contributions to the motion are given in order to determine if the mesh criteria for monophasic media are suitable for poroelastic media. The imposition of six linear elements per wavelength is found for each Biot wave as a primary condition for convergence. For 3D applications, convergence rules are derived from a generic configuration, i.e., a clamped porous layer. Because of the complex deformation, the previous criterion is shown to be insufficient. Influence of the coupling between the two phases is demonstrated. © *2001 Acoustical Society of America.* [DOI: 10.1121/1.1289924]

PACS numbers: 43.20.Jr, 43.50.Gf, 43.40.Tm, 43.55.Wk [CBB]

I. INTRODUCTION

Biot theory of fluid saturated porous media provides a description of the waves propagating in geophysics materials (Biot, 1956). Several authors have extended this theory to sound-absorbing materials, such as glass wool and polymer foams. A good agreement with measurements has been shown for multilayer systems using analytical methods (Allard, 1993). In order to interpret the modal behavior of finite size structures, 2D and 3D finite element formulations based on extended Biot theory have been developed (Coyette and Wynendaele, 1995; Johansen *et al.*, 1995; Kang and Bolton, 1995; Panneton and Atalla, 1997). These formulations have been validated by comparison with measured or simulated surface impedance of layered media. Several authors have also performed parametric studies. However, the convergence of the different formulations has not been specifically studied.

Because of the biphasic nature of poroelastic elements, a mesh criterion used for elements describing monophasic media (solid or fluid) is *a priori* not valid for poroelastic elements. Such a criterion is essential for designing a suitable mesh that gives reliable results. Moreover, an optimized mesh will result in an important saving of computer time and memory, as poroelastic formulation leads to heavy computation loads. Determination of convergence criterion for poroelastic elements is an objective of this paper.

The finite element formulation used in this study is based on Biot–Johnson–Allard theory (Allard, 1993) and has been implemented by Panneton and Atalla (1997). It is referred to as the (*u,U*) formulation for solid and fluid displacements. Poroelastic elements have six degrees of freedom per node (three translations for each phase). They are based on linear three-dimensional pentaedric or hexaedric elements.

The first part deals with 1D applications for which resonance frequencies can be related to Biot waves. Their relative contributions to the motion are investigated in order to determine whether criteria used for monophasic media are suitable for poroelastic media.

The second part deals with convergence of 3D applications where the finite size of the structure is relevant. In that case, the displacement of both phases can be fairly different and the relation between resonances and wavelengths is no longer direct. Convergence rules are derived from a generic configuration, i.e., a clamped porous layer.

II. CONVERGENCE FOR 1D BEHAVIOR

A. Theoretical analysis

The motion of the poroelastic media is described by the macroscopic displacement of the solid and fluid phases represented by the vectors **u** and **U**. Assuming a harmonic time dependence $e^{j\omega t}$, the equation of motion can be written in the form (Allard, 1993)

$$P\nabla(\nabla\cdot\mathbf{u})-N\nabla\wedge(\nabla\wedge\mathbf{u})+Q\nabla(\nabla\cdot\mathbf{U})+\omega^2(\tilde{\rho}_{11}\mathbf{u}+\tilde{\rho}_{12}\mathbf{U}) = 0, \quad (1)$$

$$Q\nabla(\nabla\cdot\mathbf{u})+R\nabla(\nabla\cdot\mathbf{U})+\omega^2(\tilde{\rho}_{12}\mathbf{u}+\tilde{\rho}_{22}\mathbf{U})=0, \quad (2)$$

where P and R are the bulk modulus of the solid and fluid phases, respectively, N is the shear modulus of the solid phase, and Q quantifies the potential coupling between the two phases. These coefficients are complex: P, N include structural damping in the solid phase and R, Q thermal dissipation. The equivalent mass density coefficients $\tilde{\rho}_{11}$, $\tilde{\rho}_{12}$, $\tilde{\rho}_{22}$ account for inertial and viscous coupling between both the solid and fluid phases.

Coupling between the two phases is described by five parameters according to Johnson–Allard theory (Allard,

1993): ϕ porosity, α_∞ tortuosity, σ air flow resistivity, Λ and Λ' viscous and thermal characteristic lengths, respectively.

1. Properties of Biot waves

As dilatational and rotational waves are uncoupled, the equation of motion can be solved separately for the two types of waves. Scalar potentials for dilatation and vector potentials for shear has been used by Biot to express the displacement of the solid and fluid phases. Two compressional waves characterized by their constant of propagation k_1 and k_2 are found

$$k_1^2=\frac{\omega^2}{2(PR-Q^2)}(P\tilde{\rho}_{22}+R\tilde{\rho}_{11}-2Q\tilde{\rho}_{12}-\sqrt{\Delta}), \tag{3}$$

$$k_2^2=\frac{\omega^2}{2(PR-Q^2)}(P\tilde{\rho}_{22}+R\tilde{\rho}_{11}-2Q\tilde{\rho}_{12}+\sqrt{\Delta}), \tag{4}$$

with

$$\Delta=(P\tilde{\rho}_{22}+R\tilde{\rho}_{11}-2Q\tilde{\rho}_{12})^2-4(PR-Q^2)(\tilde{\rho}_{11}\tilde{\rho}_{22}-\tilde{\rho}_{12}^2).$$

Each wave propagates in both phases with different amplitudes. The ratio μ_i between displacement of fluid and solid phases, respectively denoted U_i and u_i for each wave i, is given by

$$\mu_i=\frac{U_i}{u_i}=\frac{Pk_i^2-\omega^2\tilde{\rho}_{11}}{\omega^2\tilde{r}_{12}-Qk_i^2}, \quad i=1,2. \tag{5}$$

Following the nomenclature used by Allard (1993), the wave that propagates mainly in the fluid is called the fluid-borne wave, and the one that propagates mainly in the solid is called the solid-borne wave. This nomenclature reflects the physical nature of the two waves for acoustical porous materials at low frequencies. The solid-borne wave propagates in the two phases with similar amplitude. The fluid-borne wave propagates mainly in the fluid phase, and is usually strongly damped. Each kind of wave will be identified by overscript *sw* or *fw*, respectively for solid-borne and fluid-borne wave. Note that each wave does not always have the same k_i over the whole frequency range.

One shear wave propagates in the porous medium, characterized by

$$k_3^2=\frac{\omega^2}{N}\left(\frac{\tilde{\rho}_{11}\tilde{\rho}_{22}-\tilde{\rho}_{12}^2}{\tilde{\rho}_{22}}\right) \quad \text{and} \quad \mu_3=-\frac{\tilde{\rho}_{12}}{\tilde{\rho}_{22}}. \tag{6}$$

For each Biot wave i, celerity c_i, wavelength λ_i, and wave damping γ_i are deduced from the following relation:

$$k_i=\frac{\omega}{c_i}-j\gamma_i=\frac{2\pi}{\lambda_i}-j\gamma_i, \quad i=1,2,3. \tag{7}$$

2. Relative contributions of longitudinal Biot waves

Consider a porous layer of thickness l along the x axis (Fig. 1). The displacement of one fluid or solid particle is the contribution of four waves: two waves (*sw* and *fw*) propagating in the x direction, noted by subscript $+$, and two waves propagating in the $-x$ direction, noted $-$. Displacement of solid phase $u(x)$ and fluid phase $U(x)$ of coordinate x is given by

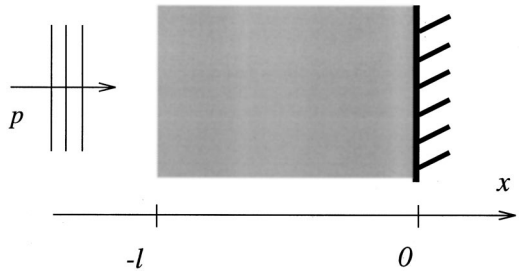

FIG. 1. Porous layer of thickness l, bonded to a rigid impervious wall.

$$u(x)=u_+^{sw}(0)\,e^{-jk^{sw}x}+u_-^{sw}(0)\,e^{+jk^{sw}x}+u_+^{fw}(0)\,e^{-jk^{fw}x}+u_-^{fw}(0)\,e^{+jk^{fw}x}, \tag{8}$$

$$U(x)=\mu^{fw}(u_+^{fw}(0)\,e^{-jk^{fw}x}+u_-^{fw}(0)\,e^{+jk^{fw}x})+\mu^{sw}(u_+^{sw}(0)\,e^{-jk^{sw}x}+u_-^{sw}(0)\,e^{+jk^{sw}x}), \tag{9}$$

where the fluid displacements have been eliminated by using the ratios μ^{sw} and μ^{fw}.

a. Acoustical excitation. The porous layer is first supposed to be bonded to a rigid impervious wall (Fig. 1) at $x=0$, which gives

$$u_+^{sw}(0)=-u_-^{sw}(0), \quad u_+^{fw}(0)=-u_-^{fw}(0). \tag{10}$$

The excitation is an incident plane wave imposing a pressure p at $x=-l$. The stress equilibrium at the surface of the layer is given by

$$-(1-\phi)p(-l)=\sigma_{xx}^s(-l)=P\frac{\partial u(-l)}{\partial x}+Q\frac{\partial U(-l)}{\partial x}, \tag{11}$$

$$-\phi p(-l)=\sigma_{xx}^f(-l)=Q\frac{\partial u(-l)}{\partial x}+R\frac{\partial U(-l)}{\partial x}, \tag{12}$$

where σ_{xx}^s and σ_{xx}^f are, respectively, the stress in the solid and fluid phases. From Eqs. (8)–(12), one can calculate $u_+^{sw}(0)$ and $u_+^{fw}(0)$. Displacements at any position x are given by

$$u(x)=u_+^{sw}(0)\left[2j\sin(-k^{sw}x)+\frac{u_+^{fw}(0)}{u_+^{sw}(0)}2j\sin(-k^{fw}x)\right], \tag{13}$$

$$U(x)=u_+^{fw}(0)\left[2j\mu^{fw}\sin(-k^{fw}x)+\frac{u_+^{sw}(0)}{u_+^{fw}(0)}\mu^{sw}2j\sin(-k^{sw}x)\right], \tag{14}$$

with

$$\frac{u_+^{fw}(0)}{u_+^{sw}(0)}=-\frac{\phi(P+\mu^{sw}Q)-(1-\phi)(Q+\mu^{sw}R)}{\phi(P+\mu^{fw}Q)-(1-\phi)(Q+\mu^{fw}R)}\times\frac{k^{sw}\cos(k^{sw}l)}{k^{fw}\cos(k^{fw}l)}. \tag{15}$$

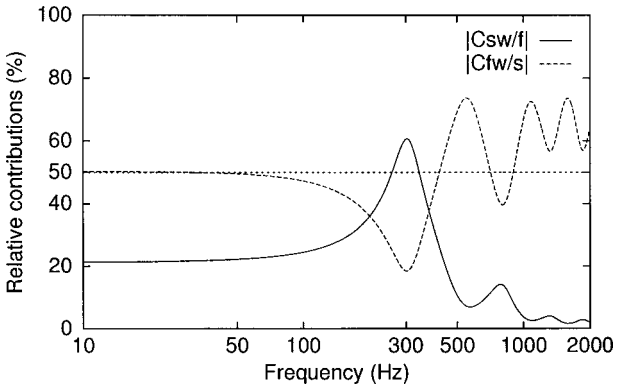

FIG. 2. Relative contributions $|C_{sw/f}|$ and $|C_{fw/s}|$ at the incident face ($x=-l$), for a 10-cm-thick layer of material A (Table I).

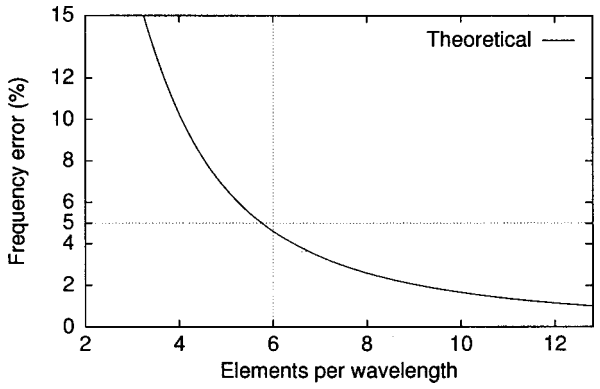

FIG. 3. Convergence rate of 1D linear elastic elements.

Equations (13) and (14) can be rewritten in the form

$$u(x)=u_{+}^{sw}(0)[C_{sw/s}(x)+C_{fw/s}(x)], \tag{16}$$

$$U(x)=u_{+}^{fw}(0)[C_{fw/f}(x)+C_{sw/f}(x)], \tag{17}$$

where $C_{aw/b}(x)$ are contributions of a kind aw of wave on the motion of one phase b (a or b being s for solid or f for fluid) at the abscissa x. Relative contributions are defined by setting that $|C_{sw/b}(x)|+|C_{fw/b}(x)|=100\%$.

Figure 2 gives an example of calculation of relative contributions $|C_{sw/f}|$ and $|C_{fw/s}|$ at the incident face, $x=-l$, for a 10-cm-thick layer of material A (Table I). According to $|C_{sw/f}|$, the motion of the fluid phase is governed at 20% by the solid-borne wave up to 100 Hz. The influence of the solid-borne wave increases strongly at the first λ/4 resonance of the solid phase at 300 Hz. For higher frequencies, because of decoupling, its influence tends to zero. According to $|C_{fw/s}|$, the motion of the solid phase is governed at 50% by the fluid-borne wave up to 100 Hz. But, the influence of the fluid-borne wave decreases to 20% at the first resonance of the solid phase. For higher frequencies, it tends to an asymptotic value of approximately 65%. Except around the first resonance of the solid phase, where the contribution of the fluid-borne wave decreases strongly, both waves must be carefully represented by the finite element discretization.

One can notice that when the solid phase becomes stiffer, μ_{sw} [Eq. (5)] increases and fluid-borne wave governs the motion of the two phases. The solid phase tends to be motionless and the behavior of the porous material can be described by an equivalent fluid model (Allard, 1993).

b. Imposed displacement. In this case, the same displacement is imposed on the phases at the incident face: $u(-l)=U(-l)$. If the layer is bonded to a rigid wall at $x=0$, Eqs. (13) and (14) apply and the coefficients $C_{fw/s}(-l)$, $C_{sw/f}(-l)$ are determined using

$$\frac{u_{+}^{fw}(0)}{u_{+}^{sw}(0)}=-\frac{1-\mu^{sw}\sin k^{sw}l}{1-\mu^{fw}\sin k^{fw}l}. \tag{18}$$

Because μ^{sw} is usually very close to 1 and μ^{fw} is much greater than μ^{sw}, one finds $|C_{fw/s}(-l)|$ close to zero and $|C_{sw/f}(-l)|$ very large. This means that the solid-borne wave governs the motion of the two phases. The criterion would then be related only to this wave. The same conclusion arises if the back face of the layer is free or if the layer has an infinite thickness.

3. Theoretical convergence rate

For purposes of comparison, the theoretical convergence rate has been calculated for a monophasic clamped-free rod of length l, discretized by 1D linear elements (see the Appendix for details). Figure 3 gives the relative error of the calculation of natural frequencies as a function of number of elements per wavelength. The mesh criterion is then defined as follows: with six linear elements per wavelength, the overestimation of natural frequencies is less than 5%.

B. Validation of mesh criterion

In this part, the relation between Biot wavelengths and convergence rate is verified for various configurations and three porous materials. The material properties (Table I) are

TABLE I. Characteristics of materials (ρ_1 is the mass density of the solid phase).

(a)	Material	ϕ	σ (Nm^{-4} s)	α_∞	Λ (μm)	Λ' (μm)
	A	0.98	13 500	1.7	80	160
	B	0.90	25 000	7.8	2.5	2.5
	C	0.96	32 000	1.7	90	165

(b)	Material	ρ_1 (kg m^{-3})	E (kPa)	ν
	A	30	$270(1+j0.1)$	0.3
	B	30	$800(1+j0.25)$	0.4
	C	30	$845(1+j0.1)$	0.3

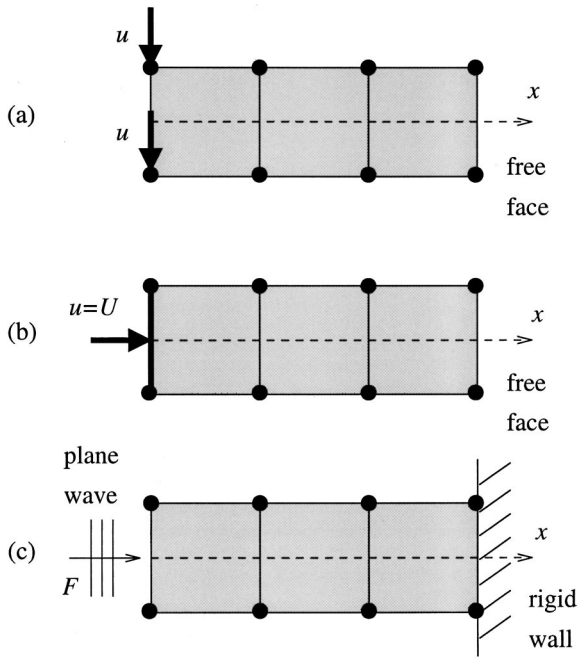

FIG. 4. Mesh of a porous layer: (a) imposed transverse displacement, (b) imposed longitudinal displacement; (c) normal incidence acoustical wave.

chosen so that different behaviors according to the waves characteristics (wavelengths given in Fig. 11) are represented:

(i) material A is a standard polymer foam for which wavelength of the two dilatational waves are of the same order ($\lambda_{sw}=0.61$ m, $\lambda_{fw}=0.51$ m at 200 Hz);
(ii) material B is an overtortuous material so that the fluid-borne wave is much shorter than the solid-borne wave ($\lambda_{sw}=1.24$ m, $\lambda_{fw}=0.05$ m, at 200 Hz); and
(iii) material C is an intermediate material ($\lambda_{sw}=1.00$ m, $\lambda_{fw}=0.42$ m at 200 Hz), corresponding to a usual absorbing material.

Three kinds of excitation and boundary conditions are applied to a poroelastic column of axis x (Fig. 4) in order to excite each type of wave in the most independent way:

(i) excitation only of the shear wave: the direction of the force is normal to axis x and only displacements normal to this axis are allowed;
(ii) excitation mainly of the solid-borne wave: the same displacement along axis x is imposed on both phases, and only displacements along this axis are allowed; and
(iii) excitation of the two longitudinal waves: the column is bonded to a rigid impervious wall and only x displacements are allowed elsewhere. The free face is excited by a longitudinal force F distributed on the surface fraction of each phase: $F_s=(1-\phi)F$ and $F_f=\phi F$. This surface force results from a normal incidence acoustical wave.

Only two nodes are used in the lateral directions and excitation is applied uniformly to get a 1D behavior.

For each configuration, we first verify the relation between converged resonance frequencies and theoretical wavelengths. Converged resonance frequencies are obtained with a great number of elements in the x direction. Then, relative errors on resonance frequencies obtained with coarse meshes are given versus number of elements per wavelength. The frequency range of interest is approximately between 10 and 2000 Hz, in order to observe at least the two first resonances.

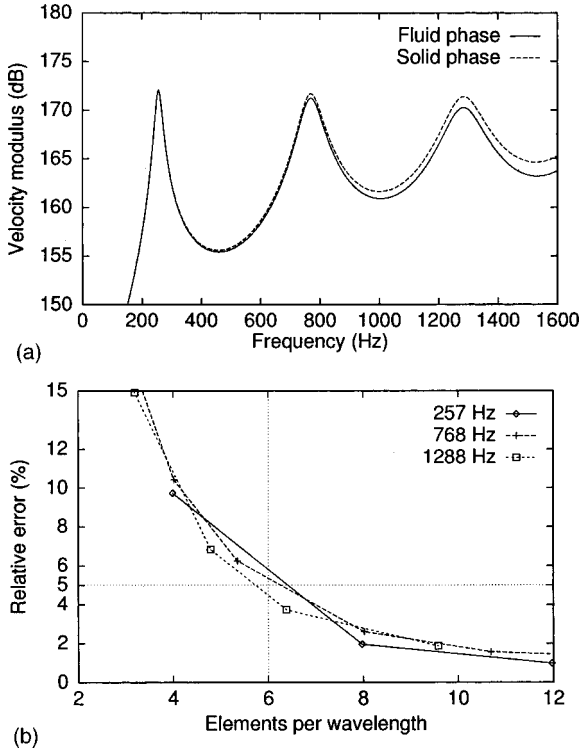

FIG. 5. Shear excited porous column (material C): (a) velocity of the free face; (b) convergence rate.

1. Simple shear displacement

Figure 5(a) shows three resonances at 257, 768, and 1288 Hz, for a 10-cm-thick column of material C. Both phases have almost the same motion at low frequencies. The curves separates slightly as the frequency increases due to progressive decoupling.

Shear wavelengths are 0.399 m at 257 Hz, 0.134 m at 768 Hz, and 0.080 m at 1288 Hz. They are related, respectively, to a $\lambda/4$, $\frac{3}{4}\lambda$, and $\frac{5}{4}\lambda$ resonance.

Figure 5(b) shows that convergence follows the theoretical rate (Fig. 3) when the number of elements is related to the shear wavelength: the criterion is suitable in this case. The same results are found with the other materials.

2. Imposed longitudinal displacement

Figure 6(a) shows two resonances at 500 and 1512 Hz for a 10-cm-thick column of material C. The phases have almost the same motion according to Sec. II A 2. The curves separates slightly as the frequency increases due to progressive decoupling. Solid-borne wavelengths are 0.4017 m at 500 Hz and 0.1335 m at 1512 Hz. They are related, respectively, to a $\lambda/4$ and a $\frac{3}{4}\lambda$ resonance.

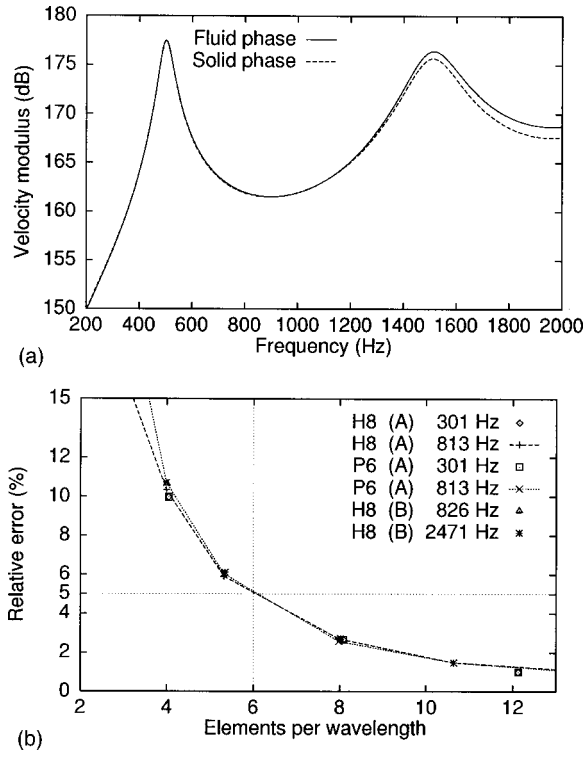

FIG. 6. Mechanically excited porous column: (a) free face velocity (material C); (b) convergence rate for several materials (A and B) and types of element. H8 is related to hexaedric element (brick) and P6 to pentaedric element (straight prism).

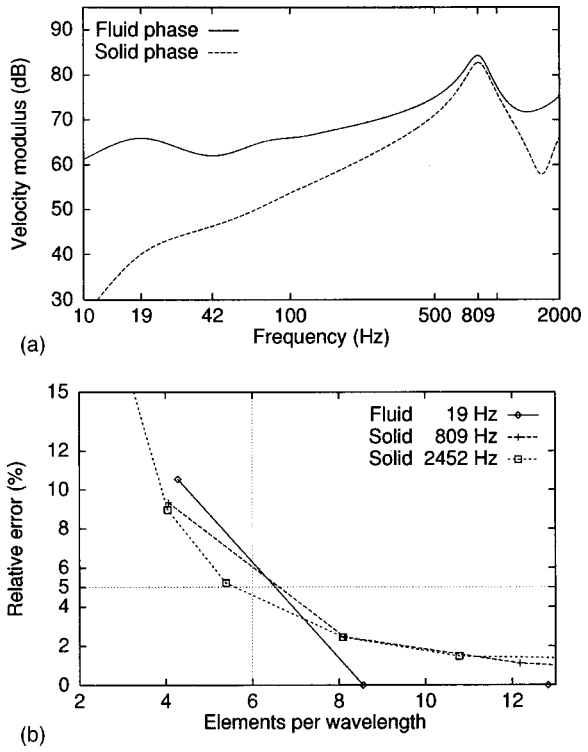

FIG. 7. Acoustically excited 7.5-cm-thick column (material B): (a) velocity of the excited face; (b) convergence rate.

Figure 6(b) presents the convergence rate for the two element shapes and two materials. The convergence follows the theoretical rate (Fig. 3) when the number of elements are related to the solid-borne wavelength: the criterion is verified.

3. Acoustical excitation

Because of very different longitudinal wavelengths, material B is best suited to distinguish phenomena. The thickness of the column is 7.5 cm.

Figure 7(a) shows a resonance at 19 Hz corresponding to a $\lambda/4$ resonance related to the fluid-borne wave. Its wavelength is 32 cm at 19 Hz. Another resonance around 809 Hz corresponds to a $\lambda/4$ resonance related to the solid-borne wave. Its wavelength is 30.6 cm at 809 Hz.

Figure 7(b) presents the convergence rate where the number of elements is related to the appropriate wavelength. Convergence once again follows the theoretical rate. It is less clear for the fluid phase, because only its first resonance is noticeable and its convergence occurs between one and two elements for the whole column. Moreover, because the fluid-borne wave is strongly damped, the determination of the supposed resonance frequency is less accurate.

Because both longitudinal waves are excited, the mesh should verify the criterion for both waves.

a. Mesh optimization. According to Sec. II A 2, situations can be encountered where one of the two longitudinal waves has little influence on the behavior of the porous material. If its wavelength is the longest, less elements are to be used to describe properly the motion.

For example, if the criterion is applied to the 7.5-cm-thick column of material B up to 1100 Hz, two elements are required for the solid-borne wave ($\lambda_{sw}=22.5$ cm), whereas 30 elements are required for the fluid-borne wave (λ_{fw}

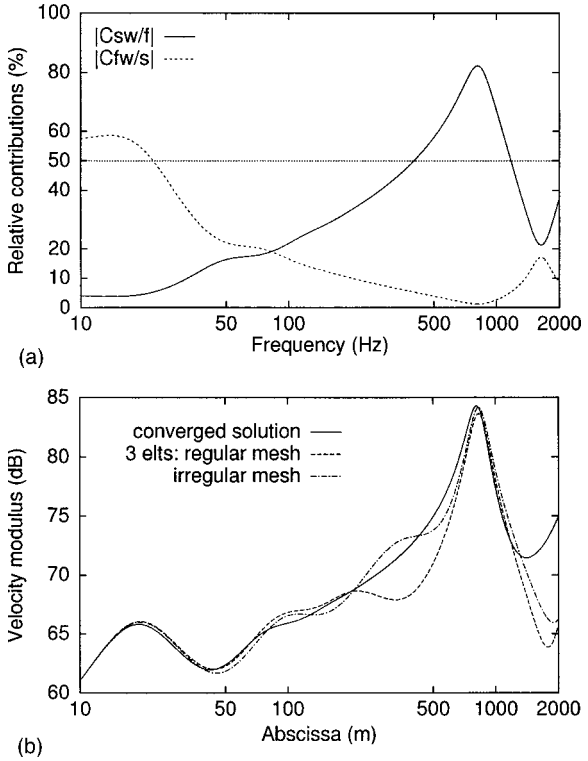

FIG. 8. Acoustically excited 7.5-cm-thick column (material B): (a) $|C_{sw/f}|$ and $|C_{fw/s}|$ ratio at the incident face, for a 7.5-cm-thick layer; (b) velocity of the fluid phase at the free face for several meshes, compared to the converged solution.

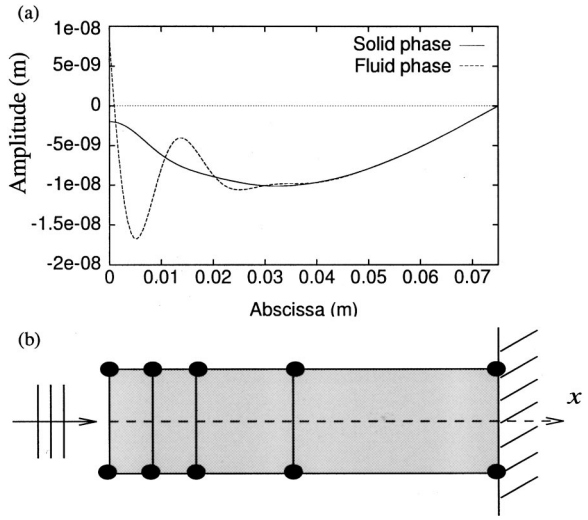

FIG. 9. Acoustically excited porous column: (a) displacement amplitude along axis x of the two phases at first resonance of the solid phase (809 Hz). (b) Example of an irregular mesh.

$=1.5$ cm). However, Fig. 8(a) shows that the contribution of the fluid-borne wave decreases as long as the first resonance related to the solid-borne wave is reached: the contribution of fluid-borne wave $|C_{fw/s}|$ on the solid phase motion is less than 20% after 50 Hz and the contribution of solid-borne wave $|C_{sw/f}|$ on the fluid motion increases up to 80% at 809 Hz. Consequently, with only three elements, the motion of the fluid phase is approximated with an error less than 3 dB, as shown by Fig. 8(b). Above 900 Hz, the error increases slightly due to the decrease of the influence of the solid-borne wave.

b. Irregular mesh. The fluid-borne waves are usually strongly damped. If it corresponds to the shortest wave, a mesh reduction can be achieved by respecting the criterion for this wave only in the area close to the excitation face. Elsewhere, a criterion based on the solid-borne wave will be suitable.

For example, Fig. 9(a) shows a quick variation close to the excited face, corresponding to the fluid phase motion at 809 Hz. This variation is directly related to the fluid-borne wave ($\lambda_{fw}=1.9$ cm, at 809 Hz) which is strongly attenuated. The best results [Fig. 8(b)] are achieved using a mesh with three elements increasing in size from 0.1 to 5 cm [Fig. 9(b)] rather than using three regular-sized elements.

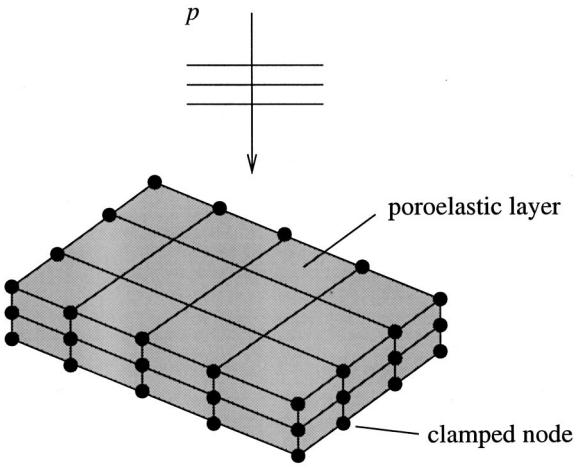

FIG. 10. Clamped poroelastic layer excited by a normal incidence acoustical wave.

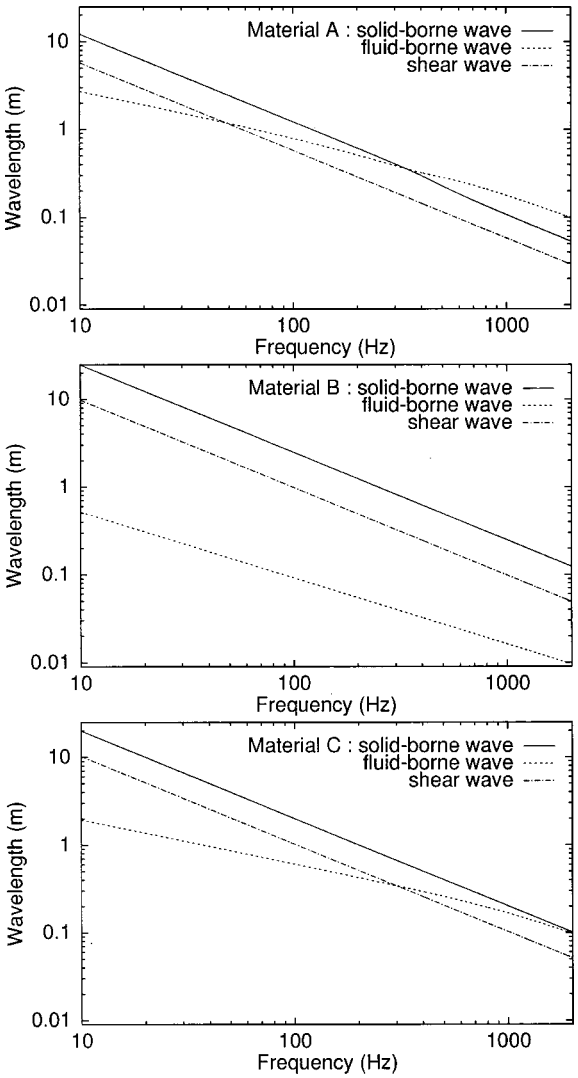

FIG. 11. Biot wavelengths for materials A, B, and C.

The choice of such an irregular mesh can be guided using Eqs. (13) and (14) to calculate the solid- and fluid-phase displacements along x axis.

To summarize, for acoustical excitation, the criterion is applied according to both longitudinal waves, but a mesh optimization can be performed if the shortest wave is not predominant or strongly damped. If the shear wave is relevant in the motion of the poroelastic media, then the criterion has to be applied according to this wave, too. In a general way, the verification of the criterion according to each of the three waves is a necessary condition to insure reliable results.

III. CONVERGENCE FOR 3D BEHAVIOR

For real 3D behavior, the contribution of the Biot waves is difficult to predict. Verification of the criterion for each wave appears to be a necessary condition. Nevertheless, convergence will not necessarily follow the same rules.

TABLE II. Convergence of first bending mode frequency versus number of elements in lateral and thickness directions, for a clamped elastic layer (28 $\times$35$\times$3 cm) equivalent to material A.

	Lateral directions			
Δf (%)	3	6	12	24
Thickness				
1	46	16	10	9
2	45	11	5	3
4	42	9	3	1
8	40	8	2	0

We investigate now the convergence of a generic case in order to specify some convergence rules. The generic case is a clamped porous layer of material A, excited by a plane wave (Fig. 10). The dimensions are 28$\times$35 cm and the thickness is 3 cm. Hexaedric linear elements are used.

A. Convergence of equivalent solid elements

We first consider the behavior without coupling effects. Poroelastic elements are replaced by equivalent solid elements with the same stiffness of the frame and the density of the air-filled porous material. Equivalent element is based on the same hexaedric element used for poroelastic element. The convergence of the frequency of the first bending mode is given by Table II for several meshes refined in lateral and thickness directions. The converged frequency is 48 Hz. It is shown that within an error of 5%, convergence is reached with a 2$\times$12$\times$12 elements mesh. Related to the deformation shape, this yields almost 24 elements per wavelength: it is four times the six element per wavelength criterion.

This slow convergence can be explained by the locking phenomenon of linear elements subject to bending (MacNeal, 1994). Locking induces excessive stiffness for a particular deformation state and is related primarily to interpolation failure. For bending deformation, two kinds of locking are noticed. Shear locking is related to a bad interpolation of the deflection which should be a second-order polynomial. A mesh refinement in the in-plane direction will reduce this locking effect. Dilatation locking is due to a bad interpolation of thickness dilatation, induced by Poisson's effect, which should be a second-order polynomial, too. The phenomenon is more important when ν is close to 0.5. A mesh refinement in the thickness direction will reduce this locking effect.

In order to minimize these effects, selective underintegration (MacNeal, 1994) has been performed for shear strain in our hexaedric element.

B. Convergence of poroelastic elements with coupling effects

Imposition of the 1D criterion for the three waves requires only two elements in lateral directions and less than one element in the thickness at 50 Hz. According to results obtained with equivalent elements, the minimal mesh should be 2$\times$12$\times$12 elements.

Nevertheless, Table III(a) shows that the resonance frequency is overestimated by 10% instead of 5% without coupling effects. Table III(b) shows that convergence of dissipated power by viscous effects D_{cp} is even slower, and very sensitive to a refinement in the thickness. Moreover, when the mesh is too coarse in the thickness, convergence is not always monotonic, as the mesh is refined in the lateral directions.

TABLE III. Convergence of the first bending mode of a clamped porous layer (28$\times$35$\times$3 cm; material A) versus number of elements in lateral and thickness directions: (a) frequency; (b) dissipated power by viscous effect.

		Lateral directions		
(a)	Δf (%)	6	12	24
	Thickness			
	1	40	15	7
	2	36	10	3
	4	35	8	1
	8	34	7	0
		Lateral directions		
(b)	ΔD_{cp} (%)	6	12	24
	Thickness			
	1	89	97	104
	2	84	94	97
	4	64	49	38
	8	54	17	0

IV. CONCLUSION

It has been shown that linear poroelastic elements verify the convergence rate of linear monophasic elements, according to each type of Biot wave. Classical mesh criterion, i.e., six linear elements per wavelength, provides a necessary condition to obtain reliable results.

For real 3D deformations, like bending, the classical criterion gives indications for a minimal mesh but is insufficient because of locking of 3D linear elements and discrepancies of the displacement field of the two phases. A consequent refinement of the mesh is necessary to obtain satisfactory results. Indicators related to the fluid motion have been found to be very sensitive. As a consequence, the minimal number of elements required is difficult to predict.

By nature, the convergence of poroelastic elements is slower than the convergence of either equivalent solid or fluid elements, because of the presence of two different scale phenomena. The discrepancy can be lowered when the behavior of the porous material is dominated by the motion of one phase.

As a consequence, this slow convergence leads to large systems to be solved. Use of higher-order elements together with the (u,p) formulation (Atalla *et al.*, 1996, 1998), that requires only four degrees of freedom per node, would be an efficient way to reduce the size of the systems. Another way would be to design specific models dedicated to particular applications like porous plate bending.

ACKNOWLEDGMENTS

The authors are grateful to PSA Peugeot Citroën and Agence de l'Environnement et de la Maîtrise de l'Energie (Ademe) who have supported this study.

APPENDIX: THEORETICAL CONVERGENCE RATE FOR 1D MONOPHASIC LINEAR ELEMENTS

Consider a clamped-free rod of length l, Young's modulus E, and mass per unit volume ρ. Assuming harmonic longitudinal motion along the x axis, the mode shape r is given by (Blevins, 1995)

$$w_r(x) = w_0 \sin\left(\frac{2r-1}{l}\frac{\pi}{2}x\right), \tag{A1}$$

with natural frequencies

$$\omega_r = \frac{\pi}{2}\sqrt{\frac{E}{\rho l^2}}(2r-1). \tag{A2}$$

Approximation with m linear elements of the same size leads to a system of $m-1$ equations of the form (Géradin and Rixen, 1996)

$$E\frac{m}{l}(-\overline{w}_{i-1}+2\overline{w}_i-\overline{w}_{i+1})-\omega^2\frac{l}{6m}(\overline{w}_{i-1}+4\overline{w}_i+\overline{w}_{i+1}) = 0, \tag{A3}$$

where $\overline{w}_i$ is the displacement of the ith node for $0<i<m$. With a general solution of the form

$$\overline{w}_{i,r} = w_0 \sin(i\overline{k}_r+\theta), \tag{A4}$$

we get wave numbers and approximated natural frequencies

$$\overline{k}_r = \frac{2r-1}{m}\frac{\pi}{2}, \tag{A5}$$

$$\overline{\omega}_r = \frac{1}{\sqrt{3}}\sqrt{\frac{E}{\rho l^2}}m\sqrt{2\frac{1-\cos\left(\frac{2r-1}{m}\frac{\pi}{2}\right)}{2+\cos\left(\frac{2r-1}{m}\frac{\pi}{2}\right)}}, \tag{A6}$$

with $1<i$, $r<m$. The frequency overestimation given by $\overline{\omega}_r/\omega_r$ depends on the ratio $(2r-1)/m$, where $2r-1$ is related to the wavelength λ_r by the expression $\lambda_r = 4l/(2r-1)$. This shows that the frequency error is a function of number of elements per wavelength.

Allard, J.-F. (**1993**). *Propagation of Sound in Porous Media: Modeling Sound Absorbing Materials* (Chapman and Hall, London).

Atalla, N., Panneton, R., and Debergue, P. (**1996**). ''A mixed displacement-pressure formulation for Biot's poroelastic equations,'' J. Acoust. Soc. Am. **99**, 2487.

Atalla, N., Panneton, R., and Debergue, P. (**1998**). ''A mixed displacement-pressure formulation for poroelastic materials,'' J. Acoust. Soc. Am. **104**, 1444–1452.

Bardot, A., Brouard, B., and Allard, J.-F. (**1996**). ''Frame decoupling at low frequency in thin porous layers saturated by air,'' J. Appl. Phys. **79**, 8223–8229.

Biot, M. A. (**1956**). ''The theory of propagation of elastic waves in a fluid-saturated porous solid. I. Low frequency range. II. Higher frequency range,'' J. Acoust. Soc. Am. **28**, 168–191.

Blevins, R. D. (**1995**). *Formulas for Natural Frequency and Mode Shape* (Krieger, Malabar, Florida).

Coyette, J. P., and Wynendaele, H. (**1995**). ''A finite element model for predicting the acoustic transmission characteristics of layered structures,'' Proceedings of Inter-noise 1995, pp. 1279–1282.

Géradin, M., and Rixen, D. (**1996**). *Théorie des Vibrations—Application à la Dynamique des Structures* (Masson, Paris).

Johansen, T. F., Allard, J.-F., and Brouard, B. (**1995**). ''Finite element method for predicting the acoustical properties of porous samples,'' Acta Acust. (China) **3**, 487–491.

Kang, Y. J., and Bolton, J. S. (**1995**). ''Finite element modeling of isotropic elastic porous materials coupled with acoustical finite element,'' J. Acoust. Soc. Am. **98**, 635–643.

MacNeal, R. H. (**1994**). *Finite Elements: Their Design and Performance* (Dekker, New York).

Panneton, R. (**1996**). ''Modélisation numérique 3D par éléments finis des milieux poroélastiques,'' Ph.D. thesis, Université de Sherbrooke, Québec, Canada.

Panneton, R., and Atalla, N. (**1997**). ''An efficient finite element scheme for solving the three dimensional poroelasticity problem in acoustics,'' J. Acoust. Soc. Am. **101**, 3287–3298.

Petyt, M. (**1990**). *Introduction to Finite Element Vibration Analysis* (Cambridge University Press, Cambridge, England).

Free vibration analysis of laminated piezoceramic hollow spheres

W. Q. Chen[a)]
Department of Civil Engineering, Zhejiang University, Hangzhou 310027, People's Republic of China

(Received 20 October 1999; revised 7 May 2000; accepted 14 October 2000)

This paper presents an exact three-dimensional analysis of the general nonaxisymmetric free vibration of a piezoceramic hollow sphere by employing a state-space approach. By introducing three displacement functions and two stress functions, the basic equations of a spherically isotropic piezoelectric medium are eventually turned into two separated state equations with variable coefficients. The solutions of these two equations are then obtained by virtue of Taylor's expansion theorem. Relationships between the state variables at the inner and outer surfaces of a laminated hollow sphere are established. Exact frequency equations corresponding to two independent classes of vibrations are then derived from the free conditions at the spherical boundary surfaces. Numerical results are finally presented. © *2001 Acoustical Society of America.* [DOI: 10.1121/1.1331110]

PACS numbers: 43.20.Bi, 43.20.Ks, 43.88.Fx [CBB]

I. INTRODUCTION

Piezoelectric materials play key roles as active components in many branches of science and technology such as electronics, infranics, and piezoelectric power supplies.[1,2] In practice, piezoelectric components and elements are usually fabricated in a plate or shell configuration and always undergo dynamic forces. Comprehensive studies on dynamic behaviors of piezoelectric plates and shells have been conducted.[3–14] Spherical shells were addressed by Kirichok,[15] who studied the purely radial oscillation of a piezoelectric spherical shell coupled with both inner and outer fluid media. Babaev *et al.*[16] considered the sound radiation by a system of piezoceramic hollow spheres. Shul'ga *et al.*[17–19] investigated the general nonaxisymmetric vibration of a piezoceramic hollow sphere by using a separation technique; they found that the vibration could be divided into two separated classes as the case of a purely elastic hollow sphere. Heyliger and Wu[20] investigated the static and free vibration response of layered piezoelectric spheres; analytic solution was developed only for the simplest case of spherical symmetry. Some other works on piezoelectric hollow spheres/spherical shells not mentioned above are cited in their paper. Of practical interest is the study of piezoelectric spherical resonators conducted by Ko *et al.*[21] and Ko and Pond.[22]

The state space approach is very effective in solving problems of laminated structures. Sosa and Castro[23,24] initiated its application in the plane problem of piezoelectric layered structures. Lee and Jiang[25] and Chen *et al.*[26] independently derived the three-dimensional static state-space formula for transversely isotropic piezoelectricity and analyzed the bending of piezoelectric plates. Chen *et al.*[27] published the dynamic state-space formula and considered the free vibration of a piezoelectric thick plate. Ding *et al.*[28] recently investigated the free axisymmetric vibration of a transversely isotropic piezoelectric circular plate. The above-mentioned state-space formulas are all established in Cartesian or cylindrical coordinates. Shul'ga *et al.*[29] first presented two independent state equations with variable coefficients in spherical coordinates for the vibration of a nonhomogeneous spherically isotropic elastic hollow sphere. However, they have completely overlooked the superiority of the state-space approach in the analysis of laminated spherical shells/hollow spheres; they treated the two state equations just as the simplified ones that were solved by a numerical method.

Most polarized piezoceramic materials exhibit transverse isotropy with the unique axis aligned along with the poling direction. In spherical coordinates, the transverse isotropy has another form, i.e., the spherical isotropy.[15,19] This work presents a state-space method to analyze the free vibration of a laminated piezoceramic hollow sphere. At first, a different system of variables is adopted to rewrite the basic equations that will bring out certain convenience for our analysis. An available separation technique[19,30,31] is then used to derive two independent state equations with variable coefficients. A variable substitution method is employed to transfer the state equations to a form that will facilitate the solutions, which can be obtained by using Taylor's expansion theorem. Allowing for the continuity conditions at each interface, relationships are established between the boundary variables at the inner and outer surfaces of a laminated hollow sphere. Exact frequency equations corresponding to two independent classes of vibrations are presented. For a purely elastic homogeneous hollow sphere, numerical results are compared with those available in the literature and good agreement is obtained. Parametric studies are finally given for a three-layered piezoelectric hollow sphere.

II. GOVERNING EQUATIONS

As pointed out in Toupin,[32] a ceramic shell before polarization is homogeneous and isotropic. However, after the shell is permanently polarized in the radial direction by applying a large static voltage between its inner and outer surfaces, the point symmetry of the material is transversely isotropic with an axis of symmetry in the direction of the radius

a)Electronic mail: caijb@ccea.zju.edu.cn

vector to the center of the spherical shell. This kind of transversely isotropic material is also named as spherically isotropic material in elasticity.[33,34] The basic equations for linear piezoelasticity for spherical isotropy can be found in Refs. 19 and 31, for example. For the sake of the following analysis, we give these equations in this section in a slightly different way. Assuming the center of the spherical isotropy coincident with the origin of spherical coordinates (r,θ,ϕ), the constitutive relations can be rewritten as follows:

$$
\begin{aligned}
&\Sigma_{\theta\theta}=r\sigma_{\theta\theta}=c_{11}S_{\theta\theta}+c_{12}S_{\phi\phi}+c_{13}S_{rr}+e_{31}\nabla_2\Phi,\\
&\Sigma_{\phi\phi}=r\sigma_{\phi\phi}=c_{12}S_{\theta\theta}+c_{11}S_{\phi\phi}+c_{13}S_{rr}+e_{31}\nabla_2\Phi,\\
&\Sigma_{rr}=r\sigma_{rr}=c_{13}S_{\theta\theta}+c_{13}S_{\phi\phi}+c_{33}S_{rr}+e_{33}\nabla_2\Phi,\\
&\Sigma_{r\theta}=r\sigma_{r\theta}=2c_{44}S_{r\theta}+e_{15}\frac{\partial\Phi}{\partial\theta},\\
&\Sigma_{r\phi}=r\sigma_{r\phi}=2c_{44}S_{r\phi}+\frac{e_{15}}{\sin\theta}\frac{\partial\Phi}{\partial\phi},\\
&\Sigma_{\theta\phi}=r\sigma_{\theta\phi}=2c_{66}S_{\theta\phi},\\
&\Delta_\theta=rD_\theta=2e_{15}S_{r\theta}-\varepsilon_{11}\frac{\partial\Phi}{\partial\theta},\\
&\Delta_\phi=rD_\phi=2e_{15}S_{r\phi}-\frac{\varepsilon_{11}}{\sin\theta}\frac{\partial\Phi}{\partial\phi},\\
&\Delta_r=rD_r=e_{31}S_{\theta\theta}+e_{31}S_{\phi\phi}+e_{33}S_{rr}-\varepsilon_{33}\nabla_2\Phi,
\end{aligned}
\tag{1}
$$

where $\nabla_2=r\partial/\partial r$, σ_{ij} is the stress tensor, Φ and D_i are the electric potential and electric displacement vector, respectively, c_{ij}, ε_{ij}, and e_{ij} are the elastic, dielectric, and piezoelectric constants, respectively. A relation $2c_{66}=c_{11}-c_{12}$ holds for the spherical isotropy. S_{ij} in Eq. (1) is the ''generalized strain tensor'' determined by

$$
\begin{aligned}
&S_{rr}=rs_{rr}=\nabla_2u_r,\quad S_{\theta\theta}=rs_{\theta\theta}=\frac{\partial u_\theta}{\partial\theta}+u_r,\\
&S_{\phi\phi}=rs_{\phi\phi}=\frac{1}{\sin\theta}\frac{\partial u_\phi}{\partial\phi}+u_r+u_\theta\cot\theta,\\
&2S_{r\theta}=2rs_{r\theta}=\frac{\partial u_r}{\partial\theta}+\nabla_2u_\theta-u_\theta,\\
&2S_{r\phi}=2rs_{r\phi}=\frac{1}{\sin\theta}\frac{\partial u_r}{\partial\phi}+\nabla_2u_\phi-u_\phi,\\
&2S_{\theta\phi}=2rs_{\theta\phi}=\frac{1}{\sin\theta}\frac{\partial u_\theta}{\partial\phi}+\frac{\partial u_\phi}{\partial\theta}-u_\phi\cot\theta,
\end{aligned}
\tag{2}
$$

where s_{ij} is the strain tensor; u_i $(i=r,\theta,\phi)$ are three displacement components. The equations of motion in terms of stresses can easily be transformed into the following form:

$$
\begin{aligned}
&\nabla_2\Sigma_{r\theta}+\csc\theta\frac{\partial\Sigma_{\theta\phi}}{\partial\phi}+\frac{\partial\Sigma_{\theta\theta}}{\partial\theta}+2\Sigma_{r\theta}+(\Sigma_{\theta\theta}-\Sigma_{\phi\phi})\cot\theta\\
&\quad=\rho r^2\frac{\partial^2u_\theta}{\partial t^2},\\
&\nabla_2\Sigma_{r\phi}+\csc\theta\frac{\partial\Sigma_{\phi\phi}}{\partial\phi}+\frac{\partial\Sigma_{\theta\phi}}{\partial\theta}+2\Sigma_{r\phi}+2\Sigma_{\theta\phi}\cot\theta\\
&\quad=\rho r^2\frac{\partial^2u_\phi}{\partial t^2},
\end{aligned}
\tag{3}
$$

$$
\begin{aligned}
&\nabla_2\Sigma_{rr}+\csc\theta\frac{\partial\Sigma_{r\phi}}{\partial\phi}+\frac{\partial\Sigma_{r\theta}}{\partial\theta}+\Sigma_{rr}-\Sigma_{\theta\theta}-\Sigma_{\phi\phi}\\
&\quad+\Sigma_{r\theta}\cot\theta=\rho r^2\frac{\partial^2u_r}{\partial t^2},
\end{aligned}
$$

where ρ is the density. The charge equation of the electrostatics also can be rewritten as

$$
\nabla_2\Delta_r+\Delta_r+\frac{1}{\sin\theta}\frac{\partial}{\partial\theta}(\Delta_\theta\sin\theta)+\frac{1}{\sin\theta}\frac{\partial\Delta_\phi}{\partial\phi}=0. \tag{4}
$$

III. THE SEPARATION TECHNIQUE AND THE STATE-SPACE FORMULATIONS

It has been shown that by employing certain separation formulas,[19,30,31] not only can the basic equations be decoupled with the order reduced, the followed solving procedure also becomes simpler. The following separation formulas are thus adopted:

$$
u_\theta=-\frac{1}{\sin\theta}\frac{\partial\psi}{\partial\phi}-\frac{\partial G}{\partial\theta},\quad u_\phi=\frac{\partial\psi}{\partial\theta}-\frac{1}{\sin\theta}\frac{\partial G}{\partial\phi},\quad u_r=w, \tag{5}
$$

$$
\Sigma_{r\theta}=-\frac{1}{\sin\theta}\frac{\partial\Sigma_1}{\partial\phi}-\frac{\partial\Sigma_2}{\partial\theta},\quad \Sigma_{r\phi}=\frac{\partial\Sigma_1}{\partial\theta}-\frac{1}{\sin\theta}\frac{\partial\Sigma_2}{\partial\phi}, \tag{6}
$$

where ψ, G, and w are three displacement functions while Σ_1 and Σ_2 are two stress functions. Note that the completeness of the separation formulation for displacements, Eq. (5), has been verified by Hu,[35] and that of Eq. (6) can be similarly demonstrated.

By employing Eqs. (5) and (6), through some lengthy manipulations, we can transfer the basic equations into the following equations:

$$
\nabla_2\begin{Bmatrix}\Sigma_1\\ \psi\end{Bmatrix}=\begin{bmatrix}-2 & -c_{66}(\nabla_1^2+2)+r^2\rho\partial^2/\partial t^2\\ \dfrac{1}{c_{44}} & 1\end{bmatrix}\begin{Bmatrix}\Sigma_1\\ \psi\end{Bmatrix}, \tag{7}
$$

$$
\nabla_2\begin{Bmatrix}\Sigma_{rr}\\ \Sigma_2\\ G\\ w\\ \Delta_r\\ \Phi\end{Bmatrix}=\mathbf{M}(\nabla_1^2,r,\partial^2/\partial t^2)\begin{Bmatrix}\Sigma_{rr}\\ \Sigma_2\\ G\\ w\\ \Delta_r\\ \Phi\end{Bmatrix}, \tag{8}
$$

where $\nabla_1^2=(\partial^2/\partial\theta^2)+\cot\theta(\partial/\partial\theta)+\csc^2\theta(\partial^2/\partial\phi^2)$, $\mathbf{M}$ is an operator matrix, which is related to the material constants,

the partial operators ∇_1^2 and $\partial^2/\partial t^2$, and the radial coordinate r. The nonzero elements of the matrix $\mathbf{M}$ are given as follows:

$$
\begin{aligned}
&M_{11}=2\beta-1,\ M_{12}=\nabla_1^2,\ M_{13}=k_1\nabla_1^2,\\
&M_{14}=-2k_1+r^2\rho\partial^2/\partial t^2,\ M_{15}=2M_{25}=-M_{64}=2\gamma,\\
&M_{21}=\beta,\quad M_{22}=-2,\ M_{23}=k_2\nabla_1^2-2c_{66}+r^2\rho\partial^2/\partial t^2,\\
&M_{24}=-k_1,\quad M_{32}=1/c_{44},\ M_{33}=M_{34}=-M_{55}=1,\\
&M_{36}=e_{15}/c_{44},\quad M_{41}=\varepsilon_{33}/\alpha,\ M_{43}=\beta\nabla_1^2,\ M_{44}=-2\beta,\\
&M_{45}=e_{33}/\alpha,\quad M_{52}=e_{15}\nabla_1^2/c_{44},\ M_{56}=k_3\nabla_1^2,\\
&M_{61}=e_{33}/\alpha,\ M_{63}=\gamma\nabla_1^2,\ M_{65}=-c_{33}/\alpha,
\end{aligned}
\tag{9}
$$

where

$$
\begin{aligned}
&\alpha=c_{33}\varepsilon_{33}+e_{33}^2,\quad \beta=(c_{13}\varepsilon_{33}+e_{31}e_{33})/\alpha,\\
&\gamma=(c_{13}e_{33}-c_{33}e_{31})/\alpha,\ k_1=2(c_{13}\beta+e_{31}\gamma)-(c_{11}+c_{12}),\\
&k_2=k_1/2-c_{66},\quad k_3=\varepsilon_{11}+e_{15}^2/c_{44}.
\end{aligned}
\tag{10}
$$

For the nonaxisymmetric free vibration of a hollow sphere, it is assumed that

$$
\begin{aligned}
&\Sigma_1=\sum_{m=0}^{n}\sum_{n=0}^{\infty}\Sigma_{1n}(r)S_n^m(\theta,\phi)e^{i\omega t},\\
&\psi=\sum_{m=0}^{n}\sum_{n=0}^{\infty}\psi_n(r)S_n^m(\theta,\phi)e^{i\omega t},\\
&\Sigma_{rr}=\sum_{m=0}^{n}\sum_{n=0}^{\infty}\Sigma_{rn}(r)S_n^m(\theta,\phi)e^{i\omega t},\\
&\Sigma_2=\sum_{m=0}^{n}\sum_{n=0}^{\infty}\Sigma_{2n}(r)S_n^m(\theta,\phi)e^{i\omega t},\\
&G=\sum_{m=0}^{n}\sum_{n=0}^{\infty}G_n(r)S_n^m(\theta,\phi)e^{i\omega t},\\
&w=\sum_{m=0}^{n}\sum_{n=0}^{\infty}w_n(r)S_n^m(\theta,\phi)e^{i\omega t},\\
&\Delta_r=\sum_{m=0}^{n}\sum_{n=0}^{\infty}\Delta_{rn}(r)S_n^m(\theta,\phi)e^{i\omega t},\\
&\Phi=\sum_{m=0}^{n}\sum_{n=0}^{\infty}\Phi_n(r)S_n^m(\theta,\phi)e^{i\omega t},
\end{aligned}
\tag{11}
$$

where $S_n^m(\theta,\phi)=P_n^m(\cos\theta)e^{im\phi}$ are the spherical harmonic functions and $P_n^m(x)$ are the associate Legendre polynomials, n and m are integers, ω is the circular frequency. From the following derivations, it will be shown that the integer m will not appear in the resulting ordinary differential equations about the unknown functions $\Sigma_{1n}(r)$ and $\psi_n(r)$ etc., so that it has not been indicated in the subscript of these functions in Eq. (11). It is also clear that Σ_{10}, ψ_0, Σ_{20}, and G_0 all vanish in the final expressions of displacements and stresses so that they can be assumed zero. By virtue of Eq. (11), one obtains from Eqs. (7) and (8)

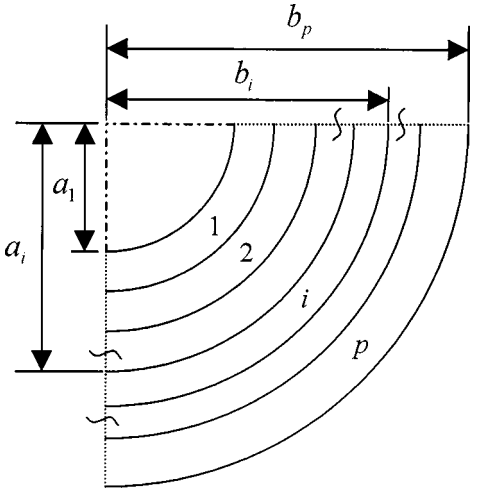

FIG. 1. The geometry of a p-ply hollow sphere.

$$
r\frac{\mathrm{d}}{\mathrm{d}r}\begin{Bmatrix}\Sigma_{1n}\\ \psi_n\end{Bmatrix}=\begin{bmatrix}-2 & c_{66}(l-2)-r^2\rho\omega^2\\ \dfrac{1}{c_{44}} & 1\end{bmatrix}\begin{Bmatrix}\Sigma_{1n}\\ \psi_n\end{Bmatrix},
\tag{12}
$$

$$
r\frac{\mathrm{d}}{\mathrm{d}r}\begin{Bmatrix}\Sigma_{rn}\\ \Sigma_{2n}\\ G_n\\ w_n\\ \Delta_{rn}\\ \Phi_n\end{Bmatrix}=\mathbf{M}(-l,r,-\omega^2)\begin{Bmatrix}\Sigma_{rn}\\ \Sigma_{2n}\\ G_n\\ w_n\\ \Delta_{rn}\\ \Phi_n\end{Bmatrix},
\tag{13}
$$

where $l=n(n+1)$.

For a p-ply hollow sphere as shown in Fig. 1, the following variable substitution is taken for the ith layer

$$
r=a_ie^{\xi}\quad (i=1,2,...,p;0\leqslant\xi\leqslant\xi_i),
\tag{14}
$$

where $\xi_i=\ln(b_i/a_i)$, a_i and b_i are the inner and outer radii of the ith layer, respectively. Substituting Eq. (14) into Eqs. (12) and (13) gives

$$
\frac{\mathrm{d}}{\mathrm{d}\xi}\mathbf{T}_{1ni}=\mathbf{N}_{1ni}\mathbf{T}_{1ni},
\tag{15}
$$

$$
\frac{\mathrm{d}}{\mathrm{d}\xi}\mathbf{T}_{2ni}=\mathbf{N}_{2ni}\mathbf{T}_{2ni},
\tag{16}
$$

where $\mathbf{T}_{1ni}=[t_{1n1},t_{1n2}]_i^T$, $\mathbf{T}_{2ni}=[t_{2n1},t_{2n2},t_{2n3},t_{2n4},t_{2n5},t_{2n6}]_i^T$, with

$$
\begin{aligned}
&t_{1n1}=\Sigma_{1n}/(a_1c_{44}^{(1)}),\quad t_{1n2}=\psi_n/a_1,\quad t_{2n1}=\Sigma_{rn}/(a_1c_{44}^{(1)}),\\
&t_{2n2}=\Sigma_{2n}/(a_1c_{44}^{(1)}),\quad t_{2n3}=G_n/a_1,\quad t_{2n4}=w_n/a_1,\\
&t_{2n5}=\Delta_{rn}/(a_1e_{33}^{(1)}),\quad t_{2n6}=\Phi_n\varepsilon_{33}^{(1)}/(a_1e_{33}^{(1)}),
\end{aligned}
\tag{17}
$$

and

$$\mathbf{N}_{1ni}=\begin{bmatrix} -2 & \dfrac{(l-2)c_{66}}{c_{44}^{(1)}}-J_i \\ \dfrac{c_{44}^{(1)}}{c_{44}} & 1 \end{bmatrix}, \tag{18}$$

$$\mathbf{N}_{2ni}=\begin{bmatrix} 2\beta-1 & -l & -\dfrac{k_1 l}{c_{44}^{(1)}} & -\dfrac{2k_1}{c_{44}^{(1)}}-J_i & \dfrac{2\gamma e_{33}^{(1)}}{c_{44}^{(1)}} & 0 \\ \beta & -2 & -\dfrac{k_2 l+2c_{66}}{c_{44}^{(1)}}-J_i & -\dfrac{k_1}{c_{44}^{(1)}} & \dfrac{\gamma e_{33}^{(1)}}{c_{44}^{(1)}} & 0 \\ 0 & \dfrac{c_{44}^{(1)}}{c_{44}} & 1 & 1 & 0 & \dfrac{e_{15}e_{33}^{(1)}}{c_{44}\varepsilon_{33}^{(1)}} \\ \dfrac{c_{44}^{(1)}\varepsilon_{33}}{\alpha} & 0 & -\beta l & -2\beta & \dfrac{e_{33}e_{33}^{(1)}}{\alpha} & 0 \\ 0 & -\dfrac{e_{15}c_{44}^{(1)}l}{e_{33}^{(1)}c_{44}} & 0 & 0 & -1 & -\dfrac{k_3 l}{\varepsilon_{33}^{(1)}} \\ \dfrac{e_{33}c_{44}^{(1)}\varepsilon_{33}^{(1)}}{\alpha e_{33}^{(1)}} & 0 & -\dfrac{\gamma\varepsilon_{33}^{(1)}l}{e_{33}^{(1)}} & -\dfrac{2\gamma\varepsilon_{33}^{(1)}}{e_{33}^{(1)}} & -\dfrac{c_{33}\varepsilon_{33}^{(1)}}{\alpha} & 0 \end{bmatrix}, \tag{19}$$

where $J_i=\Omega^2\rho_i a_i^2 e^{2\xi}/a_1^2$, $\Omega^2=a_1^2\rho^{(1)}\omega^2/c_{44}^{(1)}$ is the nondimensional frequency, $\rho_i=\rho^{(i)}/\rho^{(1)}$, and, $\rho^{(1)}$, $c_{44}^{(1)}$, and $\varepsilon_{33}^{(1)}$, etc., represent the material constants in the first layer. It is noted here that a nondimensionalization procedure has been used to derive the state equations (15) and (16). Thus, in each lamina we have established two separated state equations with variable coefficients in a dimensionless form. The solutions to these two equations will be presented in the next section.

IV. SOLUTIONS OF STATE EQUATIONS WITH VARIABLE COEFFICIENTS

The solution of a state equation with constant coefficients can be readily obtained by using the matrix theory.[36] Therefore, for the static and dynamic analysis of laminated cylindrical shells, Soldatos and Ye[37] first divided any thick layer into many sublayers with very small thickness and then formulated approximately a state equation with constant coefficients. Ye and Soldatos[38] also applied their method to study the axisymmetric free vibrations of laminated hollow spheres. Here, we directly start from the state equations (15) and (16) with variable coefficients to establish relationships between the state variables at the lower and upper surfaces of each lamina. According to Taylor's expansion theorem, any continuous function can be expressed in terms of a polynomial with coefficients related to the values of its derivatives. We thus have

$$\mathbf{T}_{kni}(\xi)=\mathbf{T}_{kni}(0)+\frac{\mathbf{T}'_{kni}(0)}{1!}\xi+\frac{\mathbf{T}''_{kni}(0)}{2!}\xi^2+\cdots+\frac{\mathbf{T}^{(q)}_{kni}(0)}{q!}\xi^q+\cdots \quad (k=1,2;0\leqslant\xi\leqslant\xi_i). \tag{20}$$

From Eqs. (15) and (16), the higher-order derivatives $\mathbf{T}^{(q)}_{kni}(0)$, $(q=1,2,3,...)$ can be expressed in terms of $\mathbf{T}_{kni}(0)$ as follows:

$$\begin{aligned} \mathbf{T}'_{kni}(0)&=\mathbf{N}_{kni}(0)\mathbf{T}_{kni}(0),\\ \mathbf{T}''_{kni}(0)&=[\mathbf{N}'_{kni}(0)+\mathbf{N}^2_{kni}(0)]\mathbf{T}_{kni}(0),\\ \mathbf{T}'''_{kni}(0)&=\{\mathbf{N}''_{kni}(0)+2\mathbf{N}'_{kni}(0)\mathbf{N}_{kni}(0)+\mathbf{N}_{kni}(0)\\ &\quad\times[\mathbf{N}'_{kni}(0)+\mathbf{N}^2_{kni}(0)]\}\mathbf{T}_{kni}(0). \end{aligned} \tag{21}$$

It is obvious from Eqs. (20) and (21) that

$$\mathbf{T}_{kni}(\xi)=\mathbf{A}_{kni}(\xi)\mathbf{T}_{kni}(0) \quad (k=1,2;0\leqslant\xi\leqslant\xi_i), \tag{22}$$

where

$$\mathbf{A}_{kni}(\xi)=\mathbf{1}+\frac{\mathbf{N}_{kni}(0)}{1!}\xi+\frac{\mathbf{N}'_{kni}(0)+\mathbf{N}^2_{kni}(0)}{2!}\xi^2+\cdots. \tag{23}$$

It is immediately seen that if $\mathbf{N}_{kni}$ are constant matrices, one will obtain $\mathbf{A}_{kni}(\xi)=\exp(\mathbf{N}_{kni}\xi)$. In this case the solution given by Eq. (22) will coincide with the one obtained by using the usual matrix theory.[36]

Setting $\xi=\xi_i$ in Eq. (22) gives

$$\mathbf{T}_{kni}(\xi_i)=\mathbf{A}_{kni}(\xi_i)\mathbf{T}_{kni}(0) \quad (k=1,2;i=1,2,...,p). \tag{24}$$

Thus, the relationships between the state variables at the lower and upper surfaces of each lamina have been established. Further considering the continuity conditions at each interface, one can obtain by virtue of Eq. (24)

$$\mathbf{T}_{1np}(\xi_p)=\mathbf{S}_{1n}\mathbf{T}_{1n1}(0) \quad (n=1,2,3,...), \tag{25}$$

$$\mathbf{T}_{2np}(\xi_p)=\mathbf{S}_{2n}\mathbf{T}_{2n1}(0) \quad (n=1,2,3,...), \tag{26}$$

where $\mathbf{S}_{1n}=\Pi_{i=p}^{1}\mathbf{A}_{1ni}(\xi_i)$ and $\mathbf{S}_{2n}=\Pi_{i=p}^{1}\mathbf{A}_{2ni}(\xi_i)$ are square matrices of the second order and sixth order, respectively.

Through these two matrices, the relations between the state variables at the outer and inner surfaces of a laminated piezoelectric hollow sphere are founded. As mentioned earlier, Σ_{10}, ψ_0, Σ_{20}, and G_0 contribute nothing to the electroelastic field and Eqs. (12) and (13) degenerate to the following one equation only when $n=0$:

$$r\frac{\mathrm{d}}{\mathrm{d}r}\begin{Bmatrix}\Sigma_{r0}\\ w_0\\ \Delta_{r0}\\ \Phi_0\end{Bmatrix}=\begin{bmatrix}2\beta-1 & -2k_1-r^2\rho\omega^2 & 2\gamma & 0\\ \dfrac{\varepsilon_{33}}{\alpha} & -2\beta & \dfrac{e_{33}}{\alpha} & 0\\ 0 & 0 & -1 & 0\\ \dfrac{e_{33}}{\alpha} & -2\gamma & -\dfrac{c_{33}}{\alpha} & 0\end{bmatrix}\times\begin{Bmatrix}\Sigma_{r0}\\ w_0\\ \Delta_{r0}\\ \Phi_0\end{Bmatrix}. \tag{27}$$

We then obtain similarly

$$\mathbf{T}_{20p}(\xi_p)=\mathbf{S}_{20}\mathbf{T}_{201}(0)\quad(n=0), \tag{28}$$

where $\mathbf{S}_{20}$ is a fourth-order square matrix.

V. EXACT FREQUENCY EQUATIONS

For the free vibration problem, we have the following boundary conditions at the inner and outer spherical surfaces:

$$\sigma_{rr}=\sigma_{r\theta}=\sigma_{r\phi}=D_r=0\quad(r=a_1,b_p). \tag{29}$$

Equation (29) can be expressed in terms of the state variables as follows:[19]

$$\Sigma_{rr}=\Sigma_1=\Sigma_2=\Delta_r=0\quad(r=a_1,b_p). \tag{30}$$

Since the completeness of Eq. (6) can be verified,[35] the boundary conditions (30) are adequate for the validity of the boundary conditions (29).

It can be seen that either the controlling equations or the boundary and continuity conditions can be separated into two independent classes: The first one is only related to two state variables Σ_1 and Ψ, while the second one is related to the other six state variables. Utilizing Eq. (30), one gets from Eqs. (25), (26), and (28)

$$\begin{Bmatrix}0\\ t_{1n2}(\xi_p)\end{Bmatrix}_p=\mathbf{S}_{1n}\begin{Bmatrix}0\\ t_{1n2}(0)\end{Bmatrix}_1\quad(n=1,2,3,...), \tag{31}$$

$$\begin{Bmatrix}0\\ 0\\ t_{2n3}(\xi_p)\\ t_{2n4}(\xi_p)\\ 0\\ t_{2n6}(\xi_p)\end{Bmatrix}_p=\mathbf{S}_{2n}\begin{Bmatrix}0\\ 0\\ t_{2n3}(0)\\ t_{2n4}(0)\\ 0\\ t_{2n6}(0)\end{Bmatrix}_1\quad(n=1,2,3,...), \tag{32}$$

$$\begin{Bmatrix}0\\ t_{204}(\xi_p)\\ 0\\ t_{206}(\xi_p)\end{Bmatrix}_p=\mathbf{S}_{20}\begin{Bmatrix}0\\ t_{204}(0)\\ 0\\ t_{206}(0)\end{Bmatrix}_1\quad(n=0). \tag{33}$$

For nontrivial solutions, Eqs. (31)–(33) give the frequency equations of two independent classes of vibrations, respectively

$$S_{1n12}=0\quad(n=1,2,3,...), \tag{34}$$

for the first class, and

$$S_{2012}=0\quad(n=0), \tag{35}$$

$$\begin{vmatrix}S_{2n13} & S_{2n14} & S_{2n16}\\ S_{2n23} & S_{2n24} & S_{2n26}\\ S_{2n53} & S_{2n54} & S_{2n56}\end{vmatrix}=0\quad(n=1,2,3,...), \tag{36}$$

for the second class. In Eqs. (34)–(36), S_{knij} represents the element on the ith row and jth column of the matrix $\mathbf{S}_{kn}$. It should be noted that the frequency equation of the second class for $n=0$, i.e., the purely radial vibration, is shown in Eq. (35) rather than the following equation:

$$\begin{vmatrix}S_{2012} & S_{2014}\\ S_{2032} & S_{2034}\end{vmatrix}=0. \tag{37}$$

This follows because, when the inner spherical surface is free from the normal electric displacement, the outer surface will naturally be free from the normal electric displacement as one can see from Eq. (27) directly. This fact is also obvious from the balance condition of the electric charge. Thus, the third condition in Eq. (33) is automatically satisfied and one should only consider the first condition from which Eq. (35) is derived.

The fact that there exist two independent classes of vibrations of a closed spherical shell has been observed for isotropic elastic materials,[39,40] for spherically isotropic elastic materials,[41–43] and also for spherically isotropic piezoelectric materials.[17,19] Here, we reach the same conclusion starting from the state-space formulations. The first class, which corresponds to an equivoluminal motion of the sphere, is characterized by the absence of a radial component of mechanical displacement and of the electric potential. It is in fact identical to the one of a spherically isotropic elastic hollow sphere.[41,42] For the second class, the mechanical displacement has, in general, both transverse and radial components, but the rotation has no radial component. It is different from the one of an elastic sphere because of the effect of the electric field.

It also can be seen that the integer m, which represents the nonaxisymmetric characteristics of the vibration, does not appear in the frequency equations. The reason is obvious, since any nonaxisymmetric modes of vibrations can be obtained by the superposition of the axisymmetric ones with respect to differently oriented spherical coordinates of an identical natural frequency.[44]

For calculating the mode shapes, once the frequency is obtained, the eigenstate vectors at the inner and/or outer

spherical surfaces can be solved from Eqs. (31)–(33). The state vectors at any interior point can then be calculated by the following formula:

$$\mathbf{T}_{knj}(\xi)=\mathbf{A}_{knj}(\xi)\prod_{i=j-1}^{1}\mathbf{A}_{kni}(\xi_i)\mathbf{T}_{kn1}(0)\ \ (k=1,2;0\leqslant\xi\leqslant\xi_j). \tag{38}$$

Three induced variables $\Sigma_{\theta\theta}$, $\Sigma_{\phi\phi}$, and $\Sigma_{\theta\phi}$ are determined by

$$\begin{aligned}\Sigma_{\theta\theta}-\Sigma_{\phi\phi}&=2c_{66}\left(\nabla_1^2G-2\frac{\partial^2G}{\partial\theta^2}+2\cot\theta\csc\theta\frac{\partial\psi}{\partial\phi}\right.\\&\quad\left.-2\csc\theta\frac{\partial^2\psi}{\partial\theta\partial\phi}\right),\\\Sigma_{\theta\theta}+\Sigma_{\phi\phi}&=2\beta\Sigma_{rr}+2\gamma\Delta_r+k_1\nabla_1^2G-2k_1w,\\\Sigma_{\theta\phi}&=-c_{66}\left(\nabla_1^2\psi-2\frac{\partial^2\psi}{\partial\theta^2}-2\cot\theta\csc\theta\frac{\partial G}{\partial\phi}\right.\\&\quad\left.+2\csc\theta\frac{\partial^2G}{\partial\theta\partial\phi}\right).\end{aligned} \tag{39}$$

To obtain the other two induced variables Δ_θ and Δ_ϕ in terms of the state variables, we first employ the following separation formula:

$$\Delta_\theta=-\frac{1}{\sin\theta}\frac{\partial\Delta_1}{\partial\phi}-\frac{\partial\Delta_2}{\partial\theta},\quad \Delta_\phi=\frac{\partial\Delta_1}{\partial\theta}-\frac{1}{\sin\theta}\frac{\partial\Delta_2}{\partial\phi}. \tag{40}$$

Then, we have

$$\Delta_1=(e_{15}/c_{44})\Sigma_1,\quad \Delta_2=(e_{15}/c_{44})\Sigma_2+k_3\Phi. \tag{41}$$

VI. NUMERICAL STUDIES

From Eq. (23), it is seen that to make the solution converge rapidly, one can assume $\xi_i<1$ or much less than 1. To do this, we can divide each lamina into several sublayers in the numerical calculation. In contrast to the work of Soldatos and Ye,[37,38] each sublayer does not need to be very thin; thus, the number of the sublayers can be greatly reduced. In addition, Soldatos and Ye[37,38] formulated approximately a state equation with variable coefficients in which model error (the difference between the actual structure and the layer-up approximation) was inevitably introduced, although it can be minimized to a desired degree by adopting a larger number of sublayers. On the contrary, such an error does not appear in our method. Instead, only truncated error, which depends on the computer, will be involved in our method.

It is pointed out that there is an infinite number of frequencies for each class of vibration due to the three-dimensional property of the resulting frequency equations. In the numerical calculation, we only present the lowest nonzero natural frequencies ($\Omega>0$) that are of the most importance in practical engineering. Notice that when $n=1$, the rigid body rotation and translation movements exist in the first and second classes of vibrations, respectively. In both cases, the natural frequency equals zero.

For comparison purpose in the future, numerical results are all given in a tabular form.

A. Comparison and convergence studies

Cohen *et al.*[41] presented an exact analysis of the free vibration of spherically isotropic elastic hollow spheres by employing two auxiliary functions. Chen and Ding[42] have also presented an exact analysis of the free vibration of a fluid-filled spherically isotropic elastic spherical shell by introducing three displacement functions. In the absence of fluid medium, the resulting frequency equations of Cohen *et al.*[41] and Chen and Ding[42] are identical, though different methods have been employed. Obviously, the state-space approach suggested in this paper also can be applied easily to the degenerated case, i.e., the purely elastic case. Thus, we can make a numerical comparison between the present method and the former ones[41,42] so that the validity as well as the convergence characteristics of the present method can be assessed. As mentioned earlier, however, the rate of conver-

TABLE I. Comparison with available results for a homogeneous elastic hollow sphere.

n			0	1	2	3	4	5
Present	$q=2$	First class	⋯	4.181 47	2.540 17	3.924 16	5.176 02	6.377 77
		Second class	5.550 99	3.866 45	1.917 67	2.592 47	1.645 31	7.019 24
	$q=3$	First class	⋯	3.431 42	2.407 41	3.728 84	4.926 73	6.075 71
		Second class	5.135 85	3.278 72	1.791 08	2.661 16	7.522 02	8.107 58
	$q=4$	First class	⋯	3.512 31	2.393 92	3.698 65	4.874 34	5.997 71
		Second class	5.157 19	3.360 97	1.782 87	2.497 90	3.016 90	6.802 24
	$q=5$	First class	⋯	3.552 08	2.391 59	3.695 31	4.870 37	5.992 43
		Second class	5.147 67	3.390 53	1.782 33	2.499 11	3.153 42	8.125 55
	$q=6$	First class	⋯	3.556 32	2.391 90	3.696 45	4.872 65	5.996 18
		Second class	5.151 53	3.393 79	1.782 12	2.495 64	3.103 28	3.665 43
	$q=7$	First class	⋯	3.555 98	2.391 92	3.696 60	4.873 12	5.997 24
		Second class	5.151 34	3.393 45	1.782 27	2.496 56	3.106 30	3.686 60
	$q=8$	First class	⋯	3.555 81	2.391 93	3.696 64	4.873 21	5.997 41
		Second class	5.151 42	3.393 36	1.782 24	2.496 15	3.103 96	3.672 31
	$q=9$	First class	⋯	3.555 79	2.391 93	3.696 64	4.873 20	5.997 40
		Second class	5.151 41	3.393 34	1.782 25	2.496 29	3.104 72	3.674 41
Refs. 41 and 42		First class	⋯	3.555 79	2.391 93	3.696 64	4.873 20	5.997 39
		Second class	5.151 41	3.393 34	1.782 24	2.496 26	3.104 48	3.673 32

TABLE II. The piezoelectric effect on the lowest natural frequency (Ω).

n		0	1	2	3	4	5
PZT-4	First class	⋯	3.555 79	0.530 76	0.837 38	1.120 34	1.392 69
	Second class	1.089 33	1.208 22	0.494 66	0.955 07	1.497 19	2.069 08
PZT-4(E)	First class	identical with those for PZT-4					
	Second class	1.069 11	1.181 96	0.489 00	0.935 28	1.458 61	2.009 95

gence of the Taylor's series, Eq. (23), can be improved by dividing each lamina into several sublayers with smaller thickness.

Table I gives the lowest nonzero natural frequencies Ω of a homogeneous elastic hollow sphere with the elastic constants being $c_{11}=20\times10^{10}$ Pa, $c_{12}=12\times10^{10}$ Pa, $c_{13}=2\times10^{10}$ Pa, $c_{33}=2\times10^{10}$ Pa, and $c_{44}=1\times10^{10}$ Pa. The inner and outer radii of the sphere are $a_1=0.5b$ and $b_1=b$, respectively. In the calculation, to make the solution converge rapidly, we divide the homogeneous sphere into five layers with each layer having the thickness $0.1b$. In order to check the convergence characteristics of the Taylor's expansion method, we present the results for $2\leqslant q\leqslant 9$; here, q is the term number in the Taylor's series [Eq. (23)].

As one can see from Table I, the results for $q=8$ and $q=9$ are very close and both are almost identical to the ones obtained by using different exact methods.[41,42] It indicates that the convergence behavior of the Taylor's expansion method is good and the correctness of the present method is also clarified. In the following, we will always take $q=9$ in the numerical calculation. Table I also shows that for the mode number $n<6$, even when $q=6$ is taken, the results are exact enough with the largest relative error smaller than 0.3% ($n=5$, the second class). However, for higher modes a larger q should be employed to obtain accurate frequencies, as one can see from the results of the second class of vibration for mode numbers $n=4$ and $n=5$.

The relation of CPU time versus q depends on many factors involved in programming such as language, algorithm, precision, and the class of vibration, etc. In our case of a MATHEMATICA program, we find the CPU time nearly keeps invariant with q for the first class of vibration and varies almost linearly with q for the second class of vibration in this example.

Numerical calculation is also performed for a homogeneous isotropic hollow sphere with Poisson ratio $\nu=0.3$ and the thickness-to-mean radius ratio $t^*=0.5$. The first three natural frequencies of radial vibration have been calculated by Ye and Soldatos.[38] Our results show that four fictitious layers are sufficient for results to be accurate up to four significant figures, when $q=8$ is adopted, compared to eight fictitious layers in their method.

Numerical comparison is now made between a homogeneous PZT-4 piezoceramic hollow sphere and the corresponding elastic sphere to show the piezoelectric effect. The geometry of the sphere is the same as that in the above example. Table II gives the lowest frequencies (Ω) for these two cases. The elastic results are labeled as PZT-4(E) in Table II indicating that the elastic constants of the corresponding elastic material are the same as those of PZT-4. The material constants of PZT-4 as well as other two piezoelectric materials, ZnO and CdS, are listed in Table III.[45]

As pointed out in the previous section, the piezoelectric effect has completely no effect on the natural frequencies of the first class of vibration. From Table I and Table II, we further find that the natural frequencies for $n=1$ do not vary with the elastic constants. It is theoretically obvious, as we can see from Eq. (18) that the matrix $\mathbf{N}_{1ni}$ is independent of the elastic constants if the sphere is homogeneous. For the second class of vibration, however, the piezoelectric effect will result in differences between the frequencies of a piezoceramic hollow sphere and the corresponding elastic ones. In particular, for a PZT-4 sphere, as shown in Table II, the piezoelectric effect leads to the increasing of the lowest natural frequencies for all modes. This is known as the piezoelectric stiffening effect, as has been reported extensively.[20]

B. Parametric studies

For the parametric study, we consider a three-ply piezoelectric hollow sphere with the inner and outer radii being $a_1=0.5b$ and $b_3=b$, respectively. The first attempt here is to investigate the geometric effect on the natural frequencies. It is assumed that the inner and the outer layers are made of ZnO, and the intermediate one is made of CdS. Numerical results are presented in Table IV for several cases regarding layers' thickness: case (1) $a_2=b_1=0.7b$, $a_3=b_2=0.8b$; case (2) $a_2=b_1=0.7b$, $a_3=b_2=0.9b$; case (3) $a_2=b_1=0.6b$, $a_3=b_2=0.9b$; and case (4) $a_2=b_1=0.6b$, $a_3=b_2=0.8b$. No matter which case is considered, we divide the

TABLE III. Material constants of three piezoelectric materials.

Materials	PZT-4	ZnO	CdS
c_{ij} (10^{10}N/m^2)	$c_{11}=13.9$, $c_{12}=7.8$ $c_{13}=1.4$, $c_{33}=33.64$ $c_{44}=16.25$	$c_{11}=20.97$, $c_{12}=12.11$ $c_{13}=10.51$, $c_{33}=21.09$ $c_{44}=4.25$	$c_{11}=8.565$, $c_{12}=5.32$ $c_{13}=4.62$, $c_{33}=9.36$ $c_{44}=1.49$
e_{ij} (C/m^2)	$e_{15}=12.7$, $e_{31}=-5.2$ $e_{33}=15.1$	$e_{15}=-0.59$, $e_{31}=-0.61$ $e_{33}=1.14$	$e_{15}=-0.21$, $e_{31}=-0.24$ $e_{33}=0.44$
ε_{ij} (10^{-11}F/m)	$\varepsilon_{11}=650$, $\varepsilon_{33}=560$	$\varepsilon_{11}=7.38$, $\varepsilon_{33}=7.83$	$\varepsilon_{11}=7.99$, $\varepsilon_{33}=8.44$
ρ (kg/m^3)	$\rho=7500$	$\rho=5676$	$\rho=4824$

TABLE IV. The geometric effect on the lowest natural frequency (Ω).

n		0	1	2	3	4	5
Case (1)	First class	⋯	2.700 51	1.176 18	1.838 55	2.440 73	3.017 29
	Second class	2.302 28	2.185 76	0.948 66	1.513 34	2.081 67	2.637 84
Case (2)	First class	⋯	2.389 02	1.079 98	1.674 93	2.209 40	2.717 92
	Second class	2.200 45	1.968 08	0.905 24	1.442 17	1.962 65	2.440 93
Case (3)	First class	⋯	2.249 54	1.023 35	1.599 45	2.124 33	2.627 18
	Second class	2.027 43	1.868 83	0.822 53	1.290 62	1.743 70	2.174 90
Case (4)	First class	⋯	2.449 24	1.125 65	1.768 50	2.359 15	2.928 27
	Second class	2.143 14	2.074 28	0.869 98	1.364 71	1.865 68	2.374 35

sphere into five sublayers with each thickness being $0.1b$ in the numerical calculation. For example, for case (3), we divide the intermediate layer only into three equal thickness sublayers.

It is shown from Table IV that amongst the four cases considered, the lowest natural frequencies for case (1) are the largest while those for case (3) are the smallest. This is interesting because for case (1), the thickness of the intermediate layer, i.e., the CdS layer, is the smallest and for case (3), it is the largest. Theoretically, it is because the elastic moduli of ZnO are larger than those of CdS. Thus, a rigid structure of case (1) will give larger natural frequencies than a relatively soft structure of case (3). Though the lowest natural frequencies of the first class for case (4) are always larger than those for case (2), there is no such simple trend considering the second class. It is also observed that the smallest natural frequency of each case always occurs at the mode $n=2$ of the second class. This fact will be very important in the practical designs. Table IV also shows that the lowest natural frequencies of the first class are always larger than the corresponding ones of the second class ($n\neq 0$). However, this could be associated with the use of different materials and/or structures, as we can find from the next example.

In the second example, we study the effect of the arrangement scheme of the laminated structure with the sphere geometry identical with case (1) in the above example. Six different types of material combination are considered: (1) ZnO/CdS/ZnO; (2) ZnO/PZT-4/ZnO; (3) PZT-4/ZnO/PZT-4; (4) PZT-4/CdS/PZT-4; (5) CdS/ZnO/CdS; and (6) CdS/PZT-4/CdS. As one can see, the inner and outer layers are of the same material, with the intermediate layer of different material. The lowest natural frequencies of the first class as well as the second class are listed in Table V. To be comparable, the nondimensional frequency $\Omega^P=a_1\omega\sqrt{\rho^P/c_{44}^P}$ are given there, here, ρ^P and c_{44}^P are the mass density and elastic constant of PZT-4, respectively.

As we can see, the lowest natural frequencies are different for different layer-up schemes. Though it is natural, it can be used in a specified design to obtain a desired frequency. In fact, adopting a proper selection of the structural scheme will possibly improve its dynamic behavior. The analysis method proposed in this paper provides an effective tool to perform the calculations involved with accurate results obtainable.

It is seen from Table V that the lowest natural frequencies of type (3) are always larger than the corresponding ones of type (4). Note that only the intermediate layers in the two types are different, and the elastic constants of ZnO are obviously larger than those of CdS. Without significant difference between the other material constants, the elastic constants will be the main factor for determining the value of the frequency. That is to say, similar to cases (1) and (3) in the last example, a more rigid structure will give larger natural frequencies. This is also the case considering types (2) and (6). Such a fact can make it possible to determine what kind of scheme can be left out of consideration without detailed calculations.

Table V also clearly shows that the frequencies of the second class are larger than the corresponding ones of the first class for certain cases. Thus, for a correct design (in most practical engineering, only the smallest frequency is of significance), the axisymmetric analysis is not enough.[38]

TABLE V. The effect of arrangement scheme on the lowest natural frequency (Ω^P).

n		0	1	2	3	4	5
Type (1)	First class	⋯	1.587 53	0.691 43	1.080 82	1.434 82	1.773 76
	Second class	1.353 43	1.284 93	0.557 68	0.889 64	1.223 74	1.550 69
Type (2)	First class	⋯	2.422 54	0.692 36	1.087 98	1.449 94	1.796 50
	Second class	1.336 99	1.396 22	0.580 54	0.991 15	1.428 70	1.870 46
Type (3)	First class	⋯	2.444 73	0.563 28	0.885 09	1.178 31	1.456 71
	Second class	1.151 21	1.221 09	0.502 16	0.912 47	1.375 52	1.850 53
Type (4)	First class	⋯	1.590 49	0.519 32	0.814 51	1.083 10	1.339 03
	Second class	1.081 10	1.122 38	0.454 65	0.796 50	1.170 62	1.545 99
Type (5)	First class	⋯	1.531 11	0.543 21	0.842 91	1.105 58	1.346 00
	Second class	1.070 50	1.057 47	0.437 74	0.706 84	0.987 38	1.272 05
Type (6)	First class	⋯	1.608 17	0.497 43	0.779 82	1.035 56	1.277 10
	Second class	0.994 26	1.027 15	0.406 28	0.677 38	0.970 02	1.273 46

VII. CONCLUDING REMARKS

This paper develops a three-dimensional analysis of the free vibration of a laminated piezoelectric hollow sphere. Two independent classes of vibrations are observed and exact frequency equations are derived. No matter how many layers the sphere contains, the resulting frequency equations always keep the same order, as shown in Eqs. (34)–(36). The correctness of the analysis is clarified through the numerical comparison.

For the electric condition at the spherical boundaries, the vanishing of the normal electric displacement is assumed. However, one can also adopt the shorted-electrode condition, i.e., $\Phi=0$, at both boundary surfaces and derive the corresponding frequency equations.

For coupled free vibration of a fluid-filled laminated piezoceramic hollow sphere, by introducing a relationship between the normal stress and radial displacement at the inner spherical boundary [Eq. (15) in Ref. 34], one can readily derive the corresponding frequency equations. Note that the frequency equation of the first class will remain unchanged for the purely elastic case.

The present method is mathematically exact, although truncated error must be introduced in the numerical procedure. Disregarding the limitation related to the computer itself, however, one can get the solution as precisely as desired. Thus, the method can be used as a benchmark to check various two-dimensional approximate theories or numerical methods.

The Taylor's expansion method can also be used in the analysis of laminated cylindrical shells/hollow cylinders, as well as in the analysis of plates and shells of functionally graded materials. Recent developments in these topics will be reported in the future.

ACKNOWLEDGMENTS

The work was supported by the National Natural Science Foundation of China (No. 10002016). The author would like to express sincere thanks to Professor Haojiang Ding for his useful discussions. Helpful comments from the reviewers as well as the associate editor are also acknowledged.

[1] D. Berlincourt, ''Piezoelectric ceramics: Characteristics and applications,'' J. Acoust. Soc. Am. **70**, 1586–1595 (1981).
[2] S. S. Rao and M. Sunar, ''Piezoelectricity and its use in disturbance sensing and control of flexible structures: A survey,'' Appl. Mech. Rev. **47**, 113–123 (1994).
[3] H. F. Tiersten, *Linear Piezoelectric Plate Vibrations* (Plenum, New York, 1969).
[4] N. T. Adelman and Y. Stavsky, ''Radial vibration of axially polarized piezoelectric ceramic cylinders,'' J. Acoust. Soc. Am. **57**, 356–360 (1975).
[5] M. C. Dokmeci, ''Recent advances in vibrations of piezoelectric crystals,'' Int. J. Eng. Sci. **18**, 431–448 (1980).
[6] B. A. Auld, ''Wave propagation and resonance in piezoelectric materials,'' J. Acoust. Soc. Am. **70**, 1577–1585 (1981).
[7] R. D. Mindlin, ''Frequencies of piezoelectrically forced vibrations of electroded, doubly rotated, quartz plates,'' Int. J. Solids Struct. **20**, 141–157 (1984).
[8] M. E. Dyubchenko, ''Influence of axisymmetric vibrational modes on the sensitivity and directivity patterns of a piezoceramic sphere,'' Sov. Phys. Acoust. **30**, 286–288 (1984).
[9] P. C. Y. Lee, X. Guo, and M. S. H. Tang, ''Coupled and energy trapped thickness vibrations in piezoelectric crystal plates,'' J. Appl. Phys. **63**, 1850–1856 (1988).
[10] H. S. Tzou and J. P. Zhong, ''A linear theory of piezoelectric shell vibrations,'' J. Sound Vib. **175**, 77–88 (1994).
[11] P. R. Heyliger and D. A. Saravanos, ''Exact free vibration analysis of laminated plates with embedded piezoelectric layers,'' J. Acoust. Soc. Am. **98**, 1547–1557 (1995).
[12] H. S. Paul and K. Natarajan, ''Flexural vibration in a finite piezoelectric hollow cylinder of class 6 mm,'' J. Acoust. Soc. Am. **99**, 373–382 (1996).
[13] H. J. Ding, W. Q. Chen, Y. M. Guo, and Q. D. Yang, ''Free vibrations of piezoelectric cylindrical shells filled with compressible fluid,'' Int. J. Solids Struct. **34**, 2025–2034 (1997).
[14] R. C. Batra and X. Q. Liang, ''The vibration of a rectangular laminated elastic plate with embedded piezoelectric sensors and actuators,'' Comput. Struct. **63**, 203–216 (1997).
[15] I. F. Kirichok, ''Numerical solution of problems of the electroelastic oscillation of a cylinder and a sphere,'' Sov. Appl. Mech. **16**, 121–125 (1980).
[16] A. E. Babaev, V. G. Savin, and A. I. Stadnik, ''Sound radiation by a system of piezoceramic spherical shells under pulse electrical excitation,'' Sov. Appl. Mech. **24**, 967–971 (1988).
[17] N. A. Shul'ga, ''Electroelastic oscillations of a piezoceramic sphere with radial polarization,'' Sov. Appl. Mech. **22**, 497–500 (1986).
[18] I. A. Loza and N. A. Shul'ga, ''Forced axisymmetric vibrations of a hollow piezoceramic sphere with an electrical method of excitation,'' Sov. Appl. Mech. **26**, 812–822 (1990).
[19] N. A. Shul'ga, ''Harmonic electroelastic oscillation of spherical bodies,'' Sov. Appl. Mech. **29**, 812–817 (1993).
[20] P. Heyliger and Y. C. Wu, ''Electroelastic fields in layered piezoelectric spheres,'' Int. J. Eng. Sci. **37**, 143–161 (1999).
[21] S. H. Ko, G. A. Brigham, and J. L. Butler, ''Multimode spherical hydrophone,'' J. Acoust. Soc. Am. **56**, 1890–1898 (1974).
[22] S. H. Ko and H. L. Pond, ''Improved design of spherical multimode hydrophone,'' J. Acoust. Soc. Am. **64**, 1270–1277 (1978).
[23] H. A. Sosa, ''On the modeling of piezoelectric laminated structures,'' Mech. Res. Commun. **19**, 541–546 (1992).
[24] H. A. Sosa and M. A. Castro, ''Electroelastic analysis of piezoelectric laminated structures,'' Appl. Mech. Rev. **46**, s21–s28 (1993).
[25] J. S. Lee and L. Z. Jiang, ''Exact electroelastic analysis of piezoelectric laminae via state space approach,'' Int. J. Solids Struct. **33**, 977–990 (1996).
[26] W. Q. Chen, J. Liang, and H. J. Ding, ''Three dimensional analysis of bending problem of thick piezoelectric composite rectangular plates,'' Acta Mater. Composi. Sin. (in Chinese) **14**, 108–115 (1997).
[27] W. Q. Chen, R. Q. Xu, and H. J. Ding, ''On free vibration of a piezoelectric composite rectangular plate,'' J. Sound Vib. **218**, 741–748 (1998).
[28] H. J. Ding, R. Q. Xu, Y. W. Chi, and W. Q. Chen, ''Free axisymmetric vibration of transversely isotropic piezoelectric circular plates,'' Int. J. Solids Struct. **36**, 4629–4652 (1999).
[29] N. A. Shul'ga, A. Y. Grigorenko, and T. L. Efimova, ''Free nonaxisymmetric oscillations of a thick-walled, nonhomogeneous, transversely isotropic, hollow sphere,'' Sov. Appl. Mech. **24**, 439–444 (1988).
[30] W. Q. Chen and H. J. Ding, ''Exact static analysis of a rotating piezoelectric spherical shell,'' Acta Mech. Sin. **14**, 257–265 (1998).
[31] W. Q. Chen, ''Problems of radially polarized piezoelastic bodies,'' Int. J. Solids Struct. **36**, 4317–4332 (1999).
[32] R. A. Toupin, ''Piezoelectric relations and the radial deformation of a polarized spherical shell,'' J. Acoust. Soc. Am. **31**, 315–318 (1959).
[33] W. T. Chen, ''On some problems in spherically isotropic elastic materials,'' J. Appl. Mech. **33**, 539–546 (1966).
[34] S. G. Lekhnitskii, *Theory of Elasticity of an Anisotropic Body* (Mir, Moscow, 1981).
[35] H. C. Hu, ''On the general theory of elasticity for a spherically isotropic medium,'' Acta Sci. Sin. **3**, 247–260 (1954).
[36] R. Bellman, *Introduction to Matrix Theory* (McGraw-Hill, New York, 1970).
[37] K. P. Soldatos and J. Q. Ye, ''Axisymmetric static and dynamic analysis of laminated hollow cylinders composed of monoclinic elastic layers,'' J. Sound Vib. **184**, 245–259 (1995).
[38] J. Q. Ye and K. P. Soldatos, ''Axisymmetric vibration analysis of laminated hollow spheres composed of transversely isotropic layers,'' Proceedings of Engineering Systems Design and Analysis Conference, Montpellier, France, **9**, 161–169 (1996).

[39] A. E. H. Love, *A Treatise on The Mathematical Theory of Elasticity* (Cambridge University Press, Cambridge, 1927).
[40] A. H. Shah, C. V. Ramakrishnan, and S. K. Datta, ''Three dimensional and shell theory analysis of elastic waves in a hollow sphere, part I. Analytical foundation,'' J. Appl. Mech. **36**, 431–439 (1969).
[41] H. Cohen, A. H. Shah, and C. V. Ramakrishnan, ''Free vibrations of a spherically isotropic hollow sphere,'' Acustica **26**, 329–333 (1972).
[42] W. Q. Chen and H. J. Ding, ''Natural frequencies of a fluid-filled anisotropic spherical shell,'' J. Acoust. Soc. Am. **105**, 174–182 (1999).
[43] H. J. Ding and W. Q. Chen, ''Nonaxisymmetric free vibrations of a spherically isotropic spherical shell embedded in an elastic medium,'' Int. J. Solids Struct. **33**, 2575–2590 (1996).
[44] A. Silbiger, ''Non-axisymmetric modes of vibrations of thin spherical shell,'' J. Acoust. Soc. Am. **34**, 862 (1962).
[45] Y. Y. Tang and K. Xu, ''Exact solutions of piezoelectric materials with moving screw and edge dislocation,'' Int. J. Eng. Sci. **32**, 1579–1591 (1994).

Spatial analysis of torsional wave propagation in a cylindrical waveguide. Application to magnetostrictive generation

Jean-Christian Aime and Michel Brissaud
Laboratoire de Génie Electrique et Ferroélectricité, Institut National des Sciences Appliquées de Lyon, 20, avenue Albert Einstein, 69621 Villeurbanne Cedex, France

Laurent Laguerre
Laboratoire Central des Ponts et Chaussées, Division Reconnaissance et Mécanique des sols, Section Reconnaissance et Géophysique, route de Bouaye, BP 4129, 44341 Bouguenais, France

(Received 8 June 1999; accepted for publication 13 September 2000)

A spatial analysis of the generation and propagation of torsional waves in a cylindrical rod is presented. Starting from the classical linear equation of propagation and assuming a linear medium of propagation, the eigenfunctions of the propagation operator are calculated. Under the hypothesis of separation-of-variables type of solution, two ways of deriving the associated modes are performed. Given the normal mode basis, the behavior of a wavefront generated into the rod is examined. The application to the magnetostrictive generation of torsional waves is studied. Including the influence of eddy currents on the excitation and the geometry waveguide effects on the wave propagation, an analytical expression of mechanical losses during the first steps of propagation is given. A basic model of the interaction between a defect and the torsional guided waves is also proposed. © *2001 Acoustical Society of America.* [DOI: 10.1121/1.1323717]

PACS numbers: 43.20.Bi, 43.20.Ks, 43.38.Ct [ANN]

I. INTRODUCTION

Many authors have studied the mechanical wave propagation into cylindrical waveguides.[1–3] They analyzed the relationships between frequency and wave number related to each type of polarization (longitudinal, flexural, and torsional). Our investigation focuses on estimation of the mechanical energy distribution occurring when torsional waves are generated and propagated inside a cylindrical waveguide. To this end, mechanical energy losses are calculated from spatial modal analysis, showing the spatial filtering effect of the waveguide. To determine the amplitudes connecting each mode, two approaches were used. First, a direct method of expanding the wave amplitudes versus normal mode functions was developed. Second, using Hobson's theorem, this expansion becomes systematic and forms a complete space basis. Then, this development is applied to the case of a magnetostrictive generation of torsional waves in a rod. Spatial filtering effect of the waveguide and related energy losses are shown and the near-field distance is calculated according to the magnetic flux density profile due to eddy currents. Finally, under some restrictions due to mode coupling, we investigate the reflected wave from a simple defect.

II. HARMONIC ANALYSIS OF TORSIONAL WAVE MODE PROPAGATION

The waveguide is assumed to be a linear, homogeneous, and isotropic elastic medium of propagation. We analyzed only the torsional wave behavior. Harmonic analysis is used to calculate the normal modes basis.

Torsional waves in a cylindrical rod, of radius a, involve a circumferential displacement that is independent of θ (Fig. 1). The governing wave equation is

$$\frac{\partial^2 u}{\partial r^2}+\frac{1}{r}\frac{\partial u}{\partial r}-\frac{u}{r^2}+\frac{\partial^2 u}{\partial z^2}=\frac{1}{C_t^2}\frac{\partial^2 u}{\partial t^2}, \tag{1}$$

where u is the displacement polarized in the θ direction and C_t is the shear wave velocity.[1,2] Assuming time-harmonic plane wave propagation the solutions to (1) are of the form

$$u(r,z,t)=\Phi(r)\exp[i(\omega t-kz)], \tag{2}$$

where $\omega=2\pi\nu$ is the angular frequency, ν is the frequency, and k is the wave number. It is worth noting that this hypothesis is more complex than a separation-of-variables type of solution. It implicitly involves the classical plane wave spatiotemporal form.

This form yields the amplitude equation

$$\frac{\partial^2 \Phi}{\partial r^2}+\frac{1}{r}\frac{\partial \Phi}{\partial r}-\frac{\Phi}{r^2}+q^2\Phi=0, \tag{3}$$

wherein

$$q^2=\frac{\omega^2}{C_t^2}-k^2. \tag{4}$$

This equation can be written as an operator equation

$$\left(\frac{\partial^2}{\partial r^2}+\frac{1}{r}\frac{\partial}{\partial r}-\frac{1}{r^2}\right)\Phi=-q^2\Phi. \tag{5}$$

This defines the amplitude evolution operator

$$K=\left(\frac{\partial^2}{\partial r^2}+\frac{1}{r}\frac{\partial}{\partial r}-\frac{1}{r^2}\right). \tag{6}$$

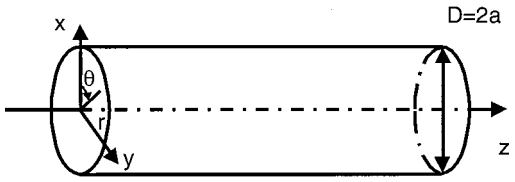

FIG. 1. Coordinates system.

Then, the amplitude equation becomes a classical eigenvalues equation

$$K\Phi = -q^2\Phi. \tag{7}$$

The operator K being a differential one, the eigenfunctions $\{\Phi_n\}$ form an orthonormal basis[4] (i.e., the normal modes of torsional waves in the rod). The Hobson's theorem ensures the basis is a complete one. Any function representing a torsional displacement is fully described as a linear combination of these functions (see Appendixes A and B). At this point a physical interpretation must be made. The orthogonality of the $\{\Phi_n\}$ mathematically states that no energy transfer exists from one mode to another. The completeness of the basis implies no coupling occurs between torsional wave modes and other polarization modes (flexural and longitudinal) during propagation. This is an important property of the basis. As shown in Sec. VI, if the basis is no longer complete, there is mode coupling and a part of the incident mechanical energy is converted into another polarization mode.

A classical analytical approach[1] leads to the general solutions to Eq. (3). These general solutions are of the form

$$\Phi(r) = AJ_1(qr) + CK_1(qr), \tag{8}$$

where J_1 and K_1 represent the Bessel's function of the first type of order 1 and the modified second type Bessel's function of order 1, respectively. As the K_1 function has an infinite value for $r=0$, the only possible solution is obtained for $C=0$. The general solutions are then

$$u(r,z,t) = AJ_1(qr)\exp[i(kz-\omega t)]. \tag{9}$$

The boundary conditions at $r=a$ lead to the equation

$$(qa)J_0(qa) - 2J_1(qa) = 0, \tag{10}$$

which can be simplified as

$$J_2(qa) = 0. \tag{11}$$

The solutions to Eq. (11) form a set of value $\{\beta_n = q_n a\}$ which is the root of the first type of Bessel's function of order 2. It follows that

$$\beta_{n+1} > \beta_n. \tag{12}$$

Allowed values for β_n are

$$\{\beta_n\} = \{0,5.13,8.41,11.62,14.80,17.96,21.11,...\}. \tag{13}$$

From the $\{\beta_n\}$ we can compute the $\{k_n\}$ which gives the eigenvalues of the propagating operator P_z (propagation along the z axis). This operator includes the K operator defined in Eq. (6) and the progressive wave dependence.

The eigenfunctions Ψ_n of P_z are of the form

$$\Psi_n = \Phi_n \exp i\{2\pi\nu t - k_n z_0\}, \tag{14}$$

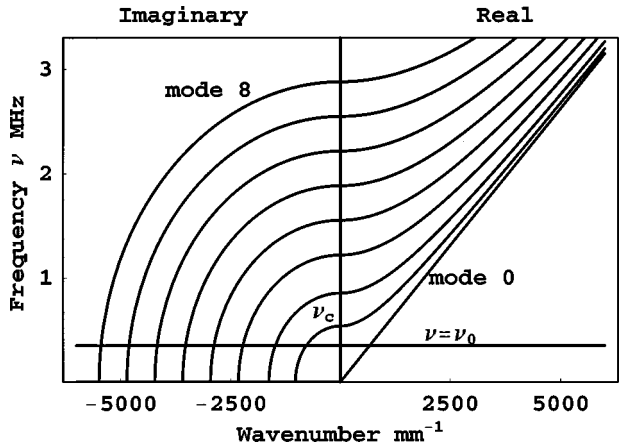

FIG. 2. Real and imaginary parts of dispersion curves for the first nine modes for $a = 5\times10^{-3}$ m.

such as

$$P_z\Psi_n = \exp i\{k_n z\}\Psi_n. \tag{15}$$

At any frequency ν_0, an infinite number of k_n are solutions to the dispersion relation. These are given by the intersection between the line $\nu=\nu_0$ and the branches of the dispersion curves. These curves are displayed in Fig. 2. A real-valued k_n means that, at the frequency ν_0, the nth mode is a propagative one; conversely, an imaginary-valued k_n means that the nth mode is an evanescent one.

The frequency $\nu_c = (C_t/2\pi)\,\beta_1/a$ is the cutoff frequency of the guide. If $\nu < \nu_c$ only the fundamental mode has a real wave number. In this particular case the propagation of the fundamental mode is the classical plane wave.

The Φ_n functions calculated in Appendix B are derived as functions of the variable X, where X is the dimensionless radius r/a varying from the center 0 to 1 (the rod surface).

The Φ_n functions are

$$\Phi_0 = \frac{\sqrt{2}}{\sqrt{\pi}}X,$$
$$\Phi_n = \frac{1}{\sqrt{\pi}}\frac{1}{J_1(\beta_n)}J_1(\beta_n X). \tag{16}$$

The first five modes are shown in Fig. 3. The zeros of Φ_n define circles. These circles are called the nodal circles. The

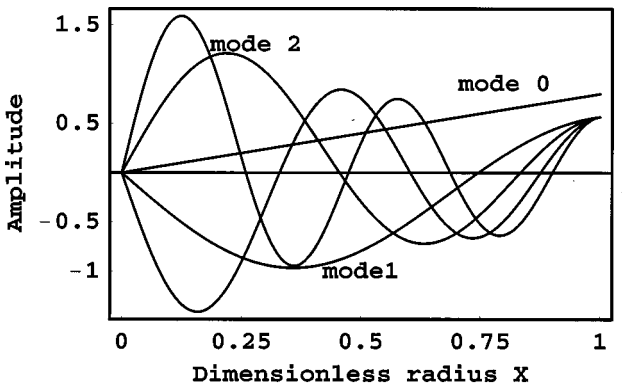

FIG. 3. Amplitude of the first five torsional modes.

number of nodal circles of the nth mode is n.

We now have a complete set of tools to fully analyze the propagation of any arbitrary-shaped wavefront in the cylindrical waveguide.

III. EXCITATION

A. General case

Let us consider a pure torsional displacement source over a rod slice at $z=z_0$ and suppose the amplitude of the source is characterized by a function $f(r)$, independent of θ.

Fundamental hypothesis

The excitation of a particular waveguide mode in a given point of the section is proportional to the values of this mode and the excitation function at this point (for more details on modal analysis methods see the book by Morse and Ingard[5]). The nth mode is excited in an elementary section $\xi\, d\xi\, d\theta$ proportionally to

$$\delta u_n = \Phi_n(\xi) f(\xi) \xi\, d\xi\, d\theta\, \Phi_n(r). \tag{17}$$

This property has a well-known consequence; it is impossible to excite a particular mode of a bar or membrane if the excitation is located at a node of the mode [$\Phi_n(r)=0$ at a node or on a nodal line or circle].

To see how the nth mode is excited over the whole section of the rod, we sum all the contributions of each elementary area. The amplitude Λ_n of the Φ_n function excited by the function $f(r)$ is then

$$\Lambda_n = \int_0^a \int_0^{2\pi} \Phi_n(\xi) f(\xi) \xi\, d\xi\, d\theta. \tag{18}$$

Summing all the mode contributions gives the initial displacement

$$u = \int_0^a \int_0^{2\pi} \sum_{n=0}^{\infty} \delta u_n = \sum_{n=0}^{\infty} \Lambda_n \Phi_n. \tag{19}$$

It is worth noting that the initial displacement is equal to the excitation function according to Eq. (A4). It is true because the $\{\Phi_n\}$ form a complete basis.

Another way of calculating the normal mode expansion of f is to use the algebraic properties of the $\{\Phi_n\}$ directly. The basis being complete, any function representing a torsional displacement is described as a superposition of the Φ_n functions [Appendix A, Eq. (A4)],

$$f(r) = I \cdot f = \sum_n \Phi_n (\phi_n \cdot f), \tag{20}$$

which leads to the integral form

$$f(r) = \sum_n \left(\int_0^a \int_0^{2\pi} \Phi_n(\xi) f(\xi) \xi\, d\xi\, d\theta \right) \Phi_n(r) = u. \tag{21}$$

This emphasizes that the initial displacement created at $z=z_0$ is equal to the excitation function $f(r)$.

Using the condensed form defined in Eq. (19), we have

$$u = \sum_n \Phi_n(r) \Lambda_n. \tag{22}$$

The set $\{\Lambda_n\}$ resulting from the projection of f over the $\{\Phi_n\}$ is the spatial spectrum of the excitation function.

B. Magnetostrictive case

If the rod is now made of a magnetostrictive material, steel for example, we can generate torsional mechanical waves using Wiedeman's[6–8] effect; the equations governing Wiedeman's effect are presented in the following. From a practical standpoint the magnetostrictive transducer is a driving coil encircling the rod. In order to use linear magnetostriction, a static circumferential magnetic biasing field is needed (see Ref. 6 for the technical process) To this end, a dc current along the rod length magnetizes the medium. A dynamic current (transient or sinusoidal) through the driving coil induces a change $B(r,t)$ in flux density. According to the law of magnetostriction, this change produces a stress wave traveling down the rod. In our study we suppose the magnetostrictive effect only occurs at the generating point z_0 and we neglect the inverse magnetostrictive effect along the rod. In this particular case $f(r)$ is related to the spatial distribution of magnetic flux density B in the rod due to eddy currents. The exponential shape of $f(r)$ is a direct consequence of eddy currents[9]

$$B(r,t) = B_0 Y(r-a) \exp\left\{ \frac{r-a}{\delta} \right\} \exp\{2i\pi\nu t\}, \tag{23}$$

where $Y(r)$ is the unit step function or Heaviside function which has the value 1 for $r>0$ and 0 elsewhere. B_0 is the static magnetic flux density and δ the skin thickness which is a function of frequency ν.[9]

The equations for Wiedeman's effect given by Tzannes[5] are

$$\begin{pmatrix} H_z \\ T_{r\theta} \end{pmatrix} = \begin{pmatrix} \dfrac{1}{\mu_r^S} & -2\sqrt{2}\lambda \\ -\dfrac{\lambda}{\sqrt{2}} & G^B \end{pmatrix} \begin{pmatrix} B_z \\ S_{r\theta} \end{pmatrix}. \tag{24}$$

B_z and H_z are the dynamic magnetic flux density and the dynamic magnetic field, respectively, λ is the magnetostrictive constant, G^B the shear modulus at constant magnetic flux density, μ_r^S the permeability at constant strain; T and S are the stress and strain in the medium, respectively. Neglecting the inverse Wiedeman's effect gives the equations

$$\begin{aligned} H_z &= \frac{1}{\mu_r^S} B_z, \\ T_{r\theta} &= -\frac{\lambda}{\sqrt{2}} B_z + G^B S_{r\theta}. \end{aligned} \tag{25}$$

Assuming $S_{r\theta}=0$ at the beginning of the excitation gives the following equation for the excitation function $f(r)$:

$$T_{r\theta} = \frac{\partial f(r)}{\partial r} - \frac{1}{r} f(r) = -U B_z, \tag{26}$$

where U is a function of the magnetic and elastic parameters and λ is the magnetostrictive constant of the material.[6,9]

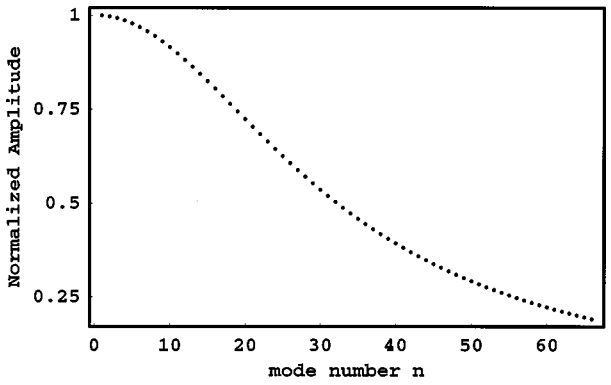

FIG. 4. Spectrum of $f(r)$ for $a=10^{-2}$ m and $\delta=10^{-3}$ m.

Introducing the $B(r)$ expression (21) into (24) leads to a differential equation for $f(r)$

$$\frac{\partial f(r)}{\partial r}-\frac{1}{r}f(r)=-UB_0Y(r-a)\exp\left\{\frac{r-a}{\delta}\right\}. \tag{27}$$

Solving this differential equation gives the expression for the excitation function

$$f(r)=C\exp\left\{-\frac{a}{\delta}\right\}r\int_{-r/\delta}^{\infty}\frac{\exp\{-\eta\}}{\eta}d\eta, \tag{28}$$

where C is an arbitrary constant.

A numerical evaluation of $f(r)$ shows for low δ/a values, a good approximation (less than 1%) of this function is

$$f(r)=C\exp\left\{\frac{r-a}{\delta}\right\}\propto UB_0\exp\left\{\frac{r-a}{\delta}\right\}. \tag{29}$$

With these approximations we found that the excitation function is proportional to the applied magnetic flux density. Figure 4 shows the set $\{\Lambda_n\}$ that is the spatial spectrum of $f(r)$, calculated for $a=10^{-2}$ m and $\delta=10^{-3}$ m.

We have also calculated the spectrum of $f(r)$ for several values of δ. This enables one to estimate the energy distribution on each mode as a function of the skin thickness δ from Eq. (A8). Figure 5 gives the spatial spectra for several values of δ versus β_n values. The projection has the mathematical form of a Hankel's transform (Appendix B). A remarkable property of this transform is the uncertainty relation. The equivalent width product of the function and Hankel's transform is a constant. In our particular case this means the length of the f spatial spectra is proportional to $1/\delta$. Decreasing δ increases the excited modes number.

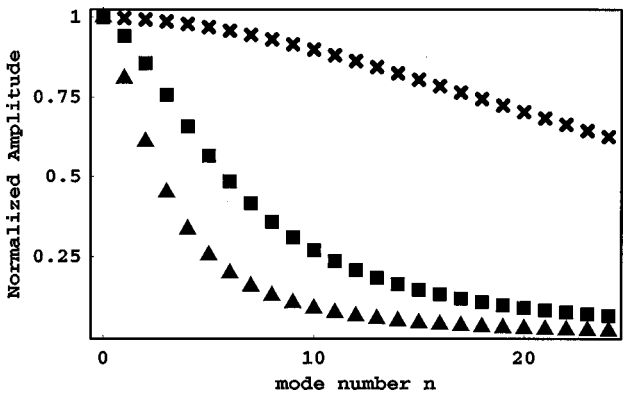

FIG. 5. Spectrum of $f(r)$ for $a=10^{-2}$ with different values of δ (in m). Values are $\delta=10^{-4}$ (cross), 5×10^{-4} (square), and 10^{-3} (triangle).

IV. SPATIAL FILTERING EFFECT OF THE WAVEGUIDE

As mentioned in Sec. III, the initial displacement is interpreted as a linear combination of normal modes Ψ_n. The propagation behavior of these normal modes has been investigated in Sec. II. From these results we derived the displacement evolution along the z propagation axis.

The initial displacement at $z=z_0u(z_0,r,t)$ is of the form

$$u(z_0,r,t)=\sum_n \Lambda_n\Psi_n. \tag{30}$$

Applying P_z to u gives

$$u(z,r,t)=P_z\sum_n \Lambda_n\Psi_n=\sum_n \exp i(k_nz)\Lambda_n\Psi_n. \tag{31}$$

Assuming the working frequency ν is below the cutoff frequency ν_c, only the k_0 wave number is real; higher ones are purely imaginary.

Recalling the expression (4) of k_n

$$k_n=\left[\left(\frac{\omega}{C_t}\right)^2-q_n^2\right]^{1/2}=[k_0^2-q_n^2]^{1/2}. \tag{32}$$

We can study the evolution of mode 1 amplitude as a function of z. For this mode the wave number k_1 is given by

$$k_1=iK_1 \quad \text{and} \quad K_1=\left(q_1^2-\left(\frac{\omega}{C_t}\right)^2\right)^{1/2}. \tag{33}$$

For a radius of 5×10^{-3} m ($C_t=3.3.10^3$ ms^{-1}, $\nu_c=540$ kHz) at a 100-kHz frequency $K_1\approx1000\approx q_1\approx5/a$. Hence, the mode 1 amplitude can be written as follows:

$$u_1=\Lambda_1\Phi_1(r)\exp-\left(\frac{5}{a}z\right). \tag{34}$$

According to $q_{n+1}>q_n$, mode 1 is the last evanescent mode to vanish. At a distance $D=2a$ from the excitation source, the amplitude has been attenuated by a factor $\exp(-10)\approx4.5\times10^{-5}$. The near-field length is very short. Although the excitation is predominantly a surface excitation, beyond a distance $D=2a$ from the source, only the fundamental mode still exists so the wave propagates into the whole guide section. Kaule[10] described this phenomenon experimentally. Figure 6 illustrates this near-field behavior of the generated wave amplitude.

Moreover, we can define the excitation efficiency E_{eff} as the ratio between the energy part which propagates and the total energy E_t brought to the system.

First, we can give a numerical evaluation of the expression for E_{eff}

$$E_{\text{eff}}\propto\frac{\Lambda_0^2}{E_t}=\frac{\Lambda_0^2}{\Sigma\Lambda_n^2}. \tag{35}$$

For $\delta=10^{-4}$ m and $a=10^{-2}$ m and summing over the first 200 terms of the series, we find E_{eff} in dB

$$E_{\text{eff}}=-11.1\text{ dB}. \tag{36}$$

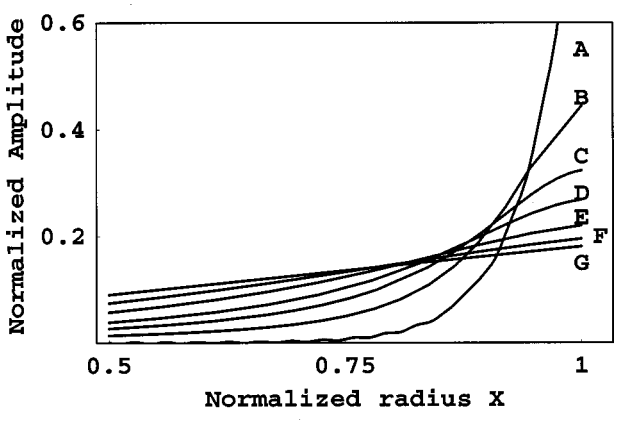

FIG. 6. Near-field amplitudes at several distances from the excitation point for $a=10^{-2}$ m and $\delta=10^{-3}$ m [excitation function is such that $f(1)=1$]. Distances are $z=0$ (A), $z=2a/5$ (B), $z=4a/5$ (C), $z=6a/5$ (D), $z=7a/5$ (E), $z=8a/5$ (F), $z=4a$ (G).

This represents the ratio of total energy which propagates in both the $z>0$ and $z<0$ directions. The ratio of energy, which propagates in the $z>0$ direction, is

$$E_{\text{eff}+}=\frac{E_{\text{eff}}}{2}=-14.1\ \text{dB}. \tag{37}$$

Second, we can deduce from Eqs. (18) and (A8) an analytical expression of E_{eff} as a function of δ and a,

$$\Lambda_0=\frac{\sqrt{2}}{a^2\sqrt{\pi}}C\int_0^{2\pi}\int_0^a \exp\left\{\frac{\xi-a}{\delta}\right\}\xi^2\,d\xi. \tag{38}$$

Assuming $\delta/a\ll 1$, as is the case in practical measurements, leads to

$$\Lambda_0^2=4\pi C^2\delta^2\left(1-2\frac{\delta}{a}+2\left(\frac{\delta}{a}\right)^2\right). \tag{39}$$

Developing expressions of Λ_0^2 and $|f(r)|^2$, we find

$$E_{\text{eff}}=8\frac{\delta}{a}\frac{\left(1-2\dfrac{\delta}{a}+2\dfrac{\delta^2}{a^2}\right)^2}{\left(1-\dfrac{\delta}{2a}\right)}, \tag{40a}$$

which can be expressed as a function of the dimensionless parameter $x=\delta/a$,

$$E_{\text{eff}}=8x\frac{(1-2x+2x^2)^2}{(1-x/2)}\underset{x\to 0}{\approx}8x-28x^2. \tag{40b}$$

With $\delta=10^{-4}$ m and $a=10^{-2}$ m, calculation yields

$$E_{\text{eff}}=-11.2\ \text{dB}. \tag{41}$$

The ratio of energy, which propagates in the $z>0$ direction, is then

$$E_{\text{eff}+}=-14.2\ \text{dB}. \tag{42}$$

These consistent results lead to a major property of the guide: given a rod radius, the closer the excitation is to the rod surface, the more important are the losses. In the particular case of the magnetostrictive generation of torsional waves, the skin thickness is readily related to frequency, so increasing frequency decreases skin thickness and increases losses. These losses could be counterbalanced using some $B(r,t)$ higher magnitudes. Accordingly, high currents at high frequency have to be generated through the driving coil. Regardless of the magnetostrictive efficiency, the latter limitation could possibly explain why it is very difficult to create a high-frequency (more than several hundred kHz) torsional wave pulse in a ferromagnetic rod of several centimeters in diameter using magnetostrictive devices. Conversely, in the case of piezoelectric generation of torsional waves, the excitation is still localized at the rod surface and very high voltage pulses into the piezoelectric devices are needed in order to counteract the propagation filtering effect in the rod.

V. EFFECT OF DEVICE WIDTH IN PULSED MODE

The influence of the device width in magnetostrictive pulsed mode generation and detection of mechanical waves has been studied by Onoe,[8] Rothbart and Rosenberg,[11] and Williams.[12] Major results of these studies can simply gain from the harmonic analysis developed above. To this end, the rod linear medium assumption enables us to apply the harmonic analysis to each frequency composing the pulse, and sum all the frequency contributions. This development is only valid for the wave generated from a coil slice. In the following we suppose that pulse frequency components are below the cutoff frequency of the rod.

Element dz of the coil at $z=z_0$ creates at the frequency ν and in the $z>0$ direction the displacement field

$$u(z,r,t)=\frac{\Lambda_0}{\sqrt{2}}\Phi_0\exp[i(\omega t-k_0(z-z_0))]. \tag{43}$$

The $\sqrt{2}$ coefficient ensures that only half the energy inserted in the guide is considered (i.e., only the wave that propagates in the $z>0$ direction is examined).

Replacing k_0 into the expression, according to the dispersion relation of mode 0, $k_0C_t=\omega$ leads to

$$u(z,r,t)=\frac{\Lambda_0}{\sqrt{2}}\Phi_0\exp\left[i\omega\left(t-\frac{z-z_0}{C_t}\right)\right]. \tag{44}$$

Now, considering a time excitation of the form

$$u(z_0,t)=\Omega(t)=\int_{-\infty}^{+\infty}Z(\omega)\exp(-i\omega t)d\omega, \tag{45}$$

we obtain the displacement created at z by element dz,

$$u(z,r,t)=\int_{-\infty}^{+\infty}\frac{\Lambda_0}{\sqrt{2}}\Phi_0Z(\omega)\exp\left[i\omega\left(t-\frac{z-z_0}{C_t}\right)\right]d\omega. \tag{46}$$

The final form is

$$u(z,r,t)=\frac{\Lambda_0}{\sqrt{2}}\Phi_0\Omega\left(t-\frac{z-z_0}{C_t}\right). \tag{47}$$

The total displacement field created by the coil is the sum of each elementary displacement over the L coil width

$$u(z,r,t)=\int_0^L\frac{\Lambda_0}{\sqrt{2}}\Phi_0\Omega\left(t-\frac{z-z_0}{C_t}\right)dz_0. \tag{48}$$

This integral can be graphically interpreted as a smoothing process. The $\Omega(t)$ function is scanned by an L/C_t time-width rectangular slot. For a 3-mm coil width this corresponds to a bandwidth approximately $C_t/L \approx 1$ MHz low-pass filtering. Accordingly, the effect of the coil width does not affect a signal composed of lower frequencies.

VI. DEFECT INTERACTION

Now, we investigate the interaction between a flaw in the rod and the lowest-order torsional wave mode. We suppose that the flaw is located at a position $z=z_d$ and characterized by a θ-dependent reflection coefficient R. The R reflection function value is 1 over a given cross section and 0 elsewhere. The defect is also assumed to have no z extension.

From the normal mode decomposition, the description of the R function is much more difficult. The R function being θ dependent, the initial wavefront of the reflected wave at $z=z_d$ is a function of both r and θ variables. So, it cannot be described as a superposition of the ψ_n functions. Indeed, the P_z propagation operator is no longer θ independent and the $\{\psi_n\}$ basis is no longer a complete one. In addition to the $\{\psi_n\}$ basis, the new basis involves higher modes and other types of polarization.[1] The $\{\psi_n\}$ becomes the basis of the functions describing only the pure torsional part of the reflected wave.

However, in the case below cutoff frequency propagation, we can calculate the part of the reflected wave that propagates on the lowest torsional mode. The reflected wave at point $z=z_d$ can be expressed as follows:

$$\Pi(r,\theta)=R(r,\theta)\Lambda_0\Phi_0(r,\theta). \tag{49}$$

The reflected wave in the far-field zone ($z \gg 2D$) is

$$(\Phi_0 \cdot \Pi)\Psi_0(r,z_d-z,t). \tag{50}$$

This wave is traveling down the $z<0$ direction. The amplitude of the reflected fundamental mode component Λ_{0r} is given by

$$\Lambda_{0r}=\Phi_0 \cdot [\Lambda_0 R \Phi_0]=\int_0^{2\pi}\int_0^a \Lambda_0 |\Phi_0(r)|^2 R(r,\theta) r\, dr\, d\theta. \tag{51}$$

Expressing Λ_{0r} as a function of Λ_0 gives

$$\Lambda_{0r}=\Lambda_0 \int_0^{2\pi}\int_0^a |\Phi_0(r)|^2 R(r,\theta) r\, dr\, d\theta=\Lambda_0 F. \tag{52}$$

The energy associated with this amplitude is

$$E_r=\Lambda_{0r}^2=\Lambda_0^2 F^2. \tag{53}$$

We are now able to estimate the efficiency of transduction and interaction denoted Γ as the ratio of E_r and E_t as

$$\Gamma=\frac{E_r}{E_t}=\frac{\Lambda_0^2}{E_t}F^2=E_{\text{eff}+}F^2. \tag{54}$$

In order to perform the evaluation of expression F we used a quite simple defect function illustrated in Fig. 7. This function does not represent a particular defect but a very simple model which allows an analytical computation of F. It is defined by three parameters: 1, α, and r_0; 1 is the radial

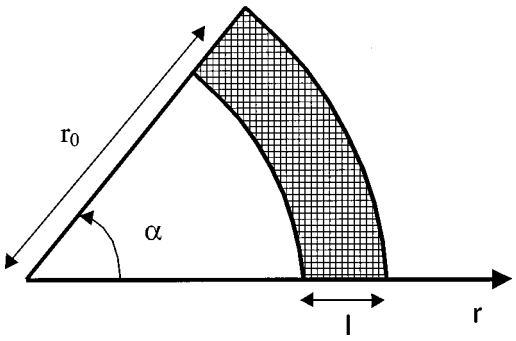

FIG. 7. Defect function.

thickness, α is the angular width, and r_0 is the distance from the axis. Using these parameters, the calculation yields

$$F=\int_0^{\alpha}\int_{r_0-1/2}^{r_0+1/2}\frac{2}{\pi a^4}r^3\, dr\, d\theta=\frac{\alpha l r_0(l^2+4r_0^2)}{2\pi a^4}. \tag{55}$$

Introducing the dimensionless parameters $l_r=l/a$, $r_{r0}=r_0/a$, and $\alpha_r=\alpha/2\pi$ leads to

$$F=2\alpha_r^2 l_r^2 r_{r0}^2(l_r^2+4r_{r0}^2)^2. \tag{56}$$

Now, we can determine the amount of reflected energy from a simple defect model as a function of these parameters. Figure 8 shows the F evolution in dB as a function of l_r and for fixed values of r_{r0} and α_r. It should be noted that for a given F many configurations of the defect function are possible. The measurement of the reflected amplitude is not enough to fully characterize the defect function; this is a typical case of an undetermined inverse problem. We need more measured data to characterize the defect.

VII. CONCLUSION

Although simple, the normal mode model gives rise to some significant results. We showed analytically, despite a wave generation close to the rod surface, that at a short distance from the source of excitation the torsional wave penetrates into the whole guide section. As a consequence, the torsional wave can be useful to search for inner defects.

Then, we showed that the waveguide propagation characteristics induce a spatial filtering effect with associated energy losses. In fact, in the simpler case of pulse where only the fundamental mode is propagating, a fraction of the me-

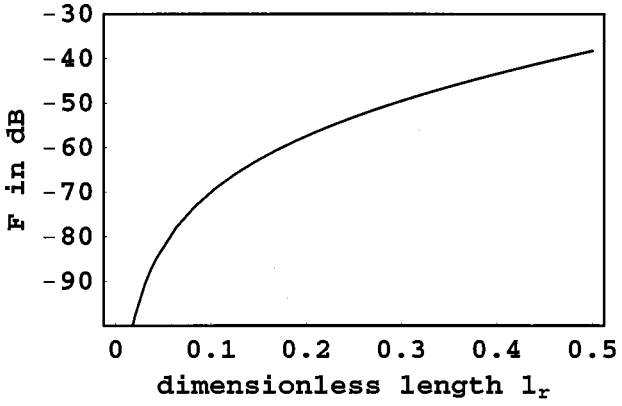

FIG. 8. F in dB for $\alpha_r=1/16$ and $r_{ro}=1/2$ vs l_r.

chanical energy is transferred into evanescent modes in the first steps of propagation, and dissipated into heat.

In the special application of a magnetostrictive excitation to the generation of mechanical stresses in a waveguide, regardless of the magnetostrictive efficiency itself and the purely magnetic losses, we showed the major limitations in the mechanical energy transduction efficiency.

First, we mentioned that these mechanical energy losses are directly related to the skin thickness to the rod radius ratio. Second, given a rod radius and a frequency increase, the proportion of energy transferred to higher evanescent modes increases.

According to the technical difficulty to generate high dynamic density fluxes at increasing frequencies, this latter behavior highlights the problem of the high frequencies generation in such a structure using magnetostrictive excitation.

Even if major results relative to the loss of mechanical energy of torsional guided waves can be generalized, an extension of the present analytical model with respect to other types of polarization mode is needed to fully consider the usefulness of guided waves in the nondestructive testing problems.

The limitation of our approach is mentioned in the case of the reflected wave from the defect using a first-order interaction model. Further studies considering the 2D-coupled propagation equation have to be conducted. For instance, the case of ''longitudinal'' or ''flexural'' waves is not trivial to derive.

ACKNOWLEDGMENTS

This work was supported by the Laboratoire Central des Ponts et Chaussées, route de Bouaye, BP 4129, 44341 Bouguenais, France.

APPENDIX A: LINEAR ALGEBRA, HERMITIAN INNER PRODUCT, AND DIMENSIONLESS VARIABLES

Consider complex functions of the real variables x and θ defined for $x\in[0,1]$ and $\theta\in[0,2\pi]$. These functions define a vectorial space **H**. The Hermitian product of two functions f and g is defined by

$$f(x,\theta)\cdot g(\chi,\theta)=\int_0^{2\pi}\int_0^1 f(x,\theta)g^*(x,\theta)x\,dx\,d\theta, \quad \text{(A1)}$$

where* stands for the complex conjugate. This product defines an associated norm

$$g(x,\theta)\cdot g(x,\theta)=\int_0^{2\pi}\int_0^1 |g(x,\theta)|^2 x\,dx\,d\theta=\|g\|^2. \quad \text{(A2)}$$

The square of the norm can be interpreted as the ''energy'' associated with the function. A vectorial space with an Hermitian product is called an hermitic space. In such a space the eigenfunctions $\{\Phi_n\}$ of a differential operator form an orthonormal basis.

The $\{\Phi_n\}$ has the properties

$$\Phi_n\cdot\Phi_m=\delta_{nm}, \quad \text{(A3)}$$

where δ_{nm} is the Kronecker symbol such that $\delta_{nm}=1$ for $n=m$ and 0 otherwise.

If the basis is complete, any function of **H** can be described as a sum of Φ_n functions

$$f=\sum_n \Phi_n(\Phi_n\cdot f). \quad \text{(A4)}$$

In terms of operators it can be written as

$$\sum_n \Phi_n(\Phi_n\cdot)=I, \quad \text{(A5)}$$

where I stands for the identity operator.

Moreover, the energy of a function can be written as a function of the $\{\Phi_n\}$,

$$f\cdot f=\sum_n \Phi_n(\Phi_n\cdot f)\cdot\sum_m \Phi_m(\Phi_m\cdot f). \quad \text{(A6)}$$

Introducing the quantity $\Lambda_n=\Phi_m\cdot f$, we find the relation

$$f\cdot f=\sum_n |\Lambda_n|^2. \quad \text{(A7)}$$

The energy of the function f is the sum of the energy of all the components of f in the $\{\Phi_n\}$ basis. This result leads to the relation

$$\int_0^{2\pi}\int_0^a |f(r)|^2 r\,dr\,d\theta=\sum_n |\Lambda_n|^2. \quad \text{(A8)}$$

To work with dimensionless variables, we define the orthogonal transform for functions of **H**,

$$e(r,\theta)\leftrightarrow\frac{1}{a}e(X,\theta) \quad \text{with} \quad X=\frac{r}{a}, \quad \text{(A9)}$$

with $r\in[0,a]$ and $X\in[0,1]$. Given this rule, we have the relationship

$$e(r,\theta)\cdot g(r,\theta)=e(X,\theta)\cdot g(X,\theta), \quad \text{(A10)}$$

where the left-hand side denotes the Hermitian product in the space of function defined for r in $[0,a]$ and the right-hand side for functions of X in [0, 1]. The Hermitian product of two functions is conserved under the orthogonal transform $r\leftrightarrow X$.

APPENDIX B: NORMALIZATION OF THE Φ_n FUNCTIONS

The eigenfunctions of the amplitude operator K are the functions

$$\Phi_n(r,\theta)=A_n J_1\left(\beta_n\frac{r}{a}\right), \quad \text{(B1)}$$

where a is the rod radius and β_n are the positive roots of the equation

$$J_2(\beta_n)=0. \quad \text{(B2)}$$

To normalize these functions we compute the Hermitian inner product

$$\Phi_n\cdot\Phi_m=\int_0^{2\pi}\int_0^a A_n A_m J_1(p_n r)J_1(p_m r)r\,dr\,d\theta. \quad \text{(B3)}$$

These integrals are

$$2\pi A_n A_m \int_0^a J_1(p_n r) J_1(p_m r) r\, dr$$

$$= \left[\frac{a}{p_n^2 - p_m^2} \left(\frac{J_1(p_m a)}{a} \right) (J_2(p_n a)) \right]. \tag{B4}$$

Taking into account the boundary conditions, this expression vanishes for $m \neq n$ and we have shown that the $\{\Phi_n\}$ are orthogonal functions. Now, we have to find the constant A_n to normalize $\{\Phi_n\}$. For that we compute the squared norm of Φ_n,

$$\Phi_n \cdot \Phi_n = 2\pi a^2 \int_0^a A_n^2 (J_1(q_n r))^2 r\, dr = 2\pi \frac{a^2}{2} J_1^2(q_n a) A_n^2. \tag{B5}$$

Since the constants A_n are arbitrary, we can choose them so that $\Phi_n \cdot \Phi_n = 1$. This give the A_n values

$$A_n = \frac{1}{\sqrt{\pi}} \frac{1}{a J_1(q_n a)}. \tag{B6}$$

The case $q_n = 0$ must be calculated separately. For that we take the limit of A_n when $q_n \to 0$. The general expressions of the Φ_n written as a function of r are

$$\Phi_0 = \frac{\sqrt{2}}{\sqrt{\pi}} \frac{r}{a^2},$$
$$\Phi_n = \frac{1}{\sqrt{\pi}} \frac{1}{a J_1(q_n a)} J_1(q_n r). \tag{B7}$$

In the dimensionless interval $[0, 1]$, using the transformation rules defined in Eq. (A10), the functions of the dimensionless variable X are

$$\Phi_0 = \frac{\sqrt{2}}{\sqrt{\pi}} X,$$
$$\Phi_n = \frac{1}{\sqrt{\pi}} \frac{1}{J_1(\beta_n)} J_1(\beta_n X). \tag{B8}$$

With the expression (B8) we can interpret the operation giving the values Λ_n defined by

$$\Lambda_n = \Phi_n \cdot f = \int_0^{2\pi} \int_0^a A_n J_1(p_n r) f(r) r\, dr\, d\theta, \tag{B9}$$

as an Hankel transform.[13] The function giving $\Lambda(p_n) = \Lambda_n$ is the Hankel transform of $f(r)$. Let d be the equivalent width of $f(r)$; the uncertainty relationship ensures that the function $\Lambda(p_n)$ has equivalent length of order $1/d$.

APPENDIX C: THE HOBSON'S THEOREM (Ref. 14)

Let $\beta_1, .., \beta_n$ denotes the positive roots of the equation

$$J_{m+1}(\beta) = 0, \tag{C1}$$

where m has any real value $\geqslant 0$.

For any function $f(z)$ defined within the interval $[0,1]$ and $z \in [0,1]$, the Hobson theorem states that the series

$$2(m+1) z^m \int_0^1 f(\xi) \xi^{m+1}\, d\xi$$
$$+ \sum_{r=1}^{\infty} C_r J_m(\beta_r z) \int_0^1 f(\xi) J_m(\beta_r \xi) \xi\, d\xi, \tag{C2}$$

in which C_r denotes

$$C_r = \frac{2}{(J_m(\beta_r))^2}, \tag{C3}$$

converges towards the value

$$\tfrac{1}{2}\{f(z+0) + f(z-0)\}. \tag{C4}$$

This relation assumes that in the neighborhood of z the function $f(z)$ is of limited total fluctuation (*à variation bornée*).[14]

At the boundaries of interval, at $z = 1$ the series converges to the value $f(1-0)$ and at $z = 0$; the series converges to 0. The expression (B2) with $m = 0$ is similar to the expression (A4). This theorem proves analytically that the function f can be written as a series of, and only of, Φ_n functions. This demonstrates that the basis defined in Appendix B is complete.

[1] J. D. Achenbach, *Wave Propagation in Elastic Solids* (North-Holland/American, Elsevier, 1973), Chap. 6.
[2] D. Royer and E. Dieulesaint, *Ondes Élastiques dans les Solides* (Masson, Paris, 1996), Vol. 1, pp. 289–297.
[3] R. N. Thurston, ''Elastic waves in rods and clad rods,'' J. Acoust. Soc. Am. **64**, 1–37 (1978).
[4] P. Benoist-Guetal and M. Courbage, *Mathématiques pour la Physique* (Eyrolles, Paris, 1993), Vol. 3, Chap. 6.
[5] P. M. Morse and K. U. Ingard, *Theoretical Acoustics* (Princeton University Press, Princeton, 1986) pp. 191–222.
[6] N. S. Tzannes, ''Joule and Wiedeman effects. The simultaneous generation of longitudinal and torsional stress pulses in magnetostrictive materials,'' IEEE Trans. Sonics Ultrason. **SU-13**, 33–41 (1966).
[7] H. Kwun and C. Teller, ''Magnetostrictive generation and detection of longitudinal, torsional and flexural waves in a steel rod,'' J. Acoust. Soc. Am. **96**, 1202–1204 (1994).
[8] M. Onoe, ''Theory of ultrasonic delay lines for direct-current pulse transmission,'' J. Acoust. Soc. Am. **34**, 1247–1254 (1962).
[9] R. Bozorth, *Ferromagnetism* (Van Nostrand, Princeton, 1951).
[10] W. Kaule, ''Magnetostrictive ultrasonic testing of materials,'' Proceedings of the 4th International Conference on Nondestructive Testing, London, 1963.
[11] A. Rothbart and L. Rosenberg, ''A theory of pulse transmission along a magnetostrictive delay line,'' Trans. IRE, PGUE-6, 1957.
[12] R. C. Williams, ''Theory of magnetostrictive delay lines for pulse and continuous wave transmission,'' IEEE Trans. Ultrason. Eng. **UE-7**, 16–38 (1959).
[13] F. Roddier, *Distributions et Transformation de Fourier* (Ediscience International, Paris, 1993), Chap. VIII, pp. 129–140.
[14] E. W. Hobson, ''On the representation of a function by series of Bessel's functions,'' Proc. London Math. Soc. **7**(2), 359–388 (1909).

Influence of grazing flow and dissipation effects on the acoustic boundary conditions at a lined wall

Yves Aurégan, Rudolf Starobinski,[a] and Vincent Pagneux
Laboratoire d'Acoustique de l'Université du Maine (I. A. M.), UMR CNRS 6613, Av. O Messiaen, 72085 Le Mans Cedex 9, France

(Received 26 July 1999; revised 10 October 2000; accepted 14 October 2000)

The problem of sound propagation near a lined wall taking into account mean shear flow effects and viscous and thermal dissipation is investigated. The method of composite expansion is used to separate the inviscid part, in the core of the flow, from the boundary layer part, near the wall. Two diffusion equations for the shear stress and the heat flux are obtained in the boundary layer. The matching of the solutions of these equations with the inviscid part leads to a modified specific acoustic admittance in the core flow. Depending on the ratio of the acoustic and stationary boundary layer thicknesses, the kinematic wall condition changes gradually from continuity of normal acoustic displacement to continuity of normal acoustic mass velocity. This wall condition can be applied in dissipative silencers and in aircraft engine-duct systems. © *2001 Acoustical Society of America.* [DOI: 10.1121/1.1331678]

PACS numbers: 43.20.Mv, 43.28.Py [LCS]

I. INTRODUCTION

In this paper, the problem of acoustic propagation in a duct with parallel shear flow and transverse temperature gradient is investigated. The aim is to take into account viscothermal effects in the boundary layer near a lined wall. These effects are accounted for by modifying the boundary condition at the duct wall. The effects of temperature and velocity gradients as well as thoses caused by dissipation are concentrated in a thin layer near the wall. In the core of the flow, the fluid is considered to be an ideal gas and the velocity and the temperature vary only slowly. Finally, a new boundary condition on the wall is obtained for the sound in the core flow.

Several authors[1–8] have addressed the problem of propagation in lined flow ducts for adiabatic, inviscid sound propagation. In these cases, they have assumed continuity of displacement at the wall since it seems to be the more appropriate.[9] Nayfeh[10] has studied how viscothermal effects affect the impedance for the case where the acoustic boundary layer is much thinner than the mean flow boundary layer. In this paper, by taking into account both viscothermal effects near the wall and the effects of large stationary velocity and temperature gradients, it is shown that the effective boundary condition can be continuity of normal acoustic displacement, or continuity of normal acoustic velocity, or a mixed condition depending on the different length scales (acoustic and mean flow boundary layer thicknesses). This wall condition can be applied in lined flow ducts such as dissipative silencers and aircraft engine-duct systems.

The equations of lossy fluid mechanics linearized about a mean state are presented in Sec. II. These equations are simplified by making classical boundary layer assumptions for a flow near a plane wall and scaled to obtain dimensionless equations. An asymptotic representation of these equations is then given in Sec. III. In the core of the flow, the problem reduces to solving the equations of lossless acoustics with mean parallel shear flow and mean transverse temperature gradient. The effects of the boundary layer can be taken into account by a modified admittance of the wall. This modified admittance is found in Sec. IV by solving two diffusion equations (for the shear stress and the heat flux) in the boundary layer. In Sec. V the analysis is extended to the case of rough lined walls.

II. GENERAL EQUATIONS

The situation for the sound propagation being investigated is shown in Fig. 1, where the lined wall lies in the plane $y^*=0$ of a coordinate system (x^*,y^*,z^*). The general equations governing the linear oscillations of a gas with a mean flow are

$$\frac{\partial \rho^*}{\partial t^*}+\rho_0^*\nabla\cdot\mathbf{v}^*+\mathbf{v}_0^*\cdot\nabla\rho^*+\mathbf{v}^*\cdot\nabla\rho_0^*+\rho^*\nabla\cdot\mathbf{v}_0^*=0, \tag{1a}$$

$$\frac{\partial v^*}{\partial t^*}+(\mathbf{v}_0^*\cdot\nabla)\mathbf{v}^*+(\mathbf{v}^*\cdot\nabla)\mathbf{v}_0^*+\frac{1}{\rho_0^*}\nabla p^*+(\mathbf{v}_0^*\cdot\nabla)\mathbf{v}_0^*\frac{\rho^*}{\rho_0^*}=\frac{\mathbf{B}^*}{\rho_0^*}, \tag{1b}$$

$$\frac{\partial s^*}{\partial t^*}+\mathbf{v}_0^*\cdot\nabla s^*+\mathbf{v}^*\cdot\nabla s_0^*=\frac{Q^*}{\rho_0^* T_0^*}, \tag{1c}$$

$$p^*=c_0^{*2}\rho^*+h_0^* s^*, \tag{1d}$$

where the terms without subscript refer to fluctuating components and the subscript 0 refers to mean values $\mathbf{v}^*$ is the velocity, p^* is the pressure, ρ^* is the density, s^* is the entropy. T^* is the temperature, c_p^* is the specific heat of the gas at constant pressure, c_0^* is the adiabatic sound speed

$$c_0^{*2}(y^*)=\left(\frac{\partial p_0^*}{\partial \rho_0^*}\right)_s, \tag{2a}$$

[a]Present address: ''Silencers: Consulting and Engineering,'' Dorotheenstr. 76, Hamburg D-22301, Germany.

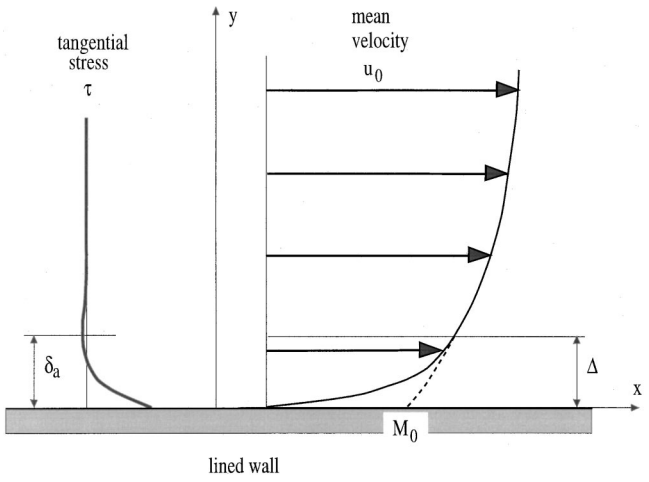

FIG. 1. Schematic description of the geometry.

and, for an ideal gas

$$h_0^*(y^*)=\left(\frac{\partial p_0^*}{\partial s_0^*}\right)_{\rho^*}=\frac{\rho_0^* c_0^{*2}}{c_p^*}. \tag{2b}$$

The sources of forces $\mathbf{B}^*$ and of heat Q^* include all the dissipation terms, and expressions for these are given in the following.

The x axis is chosen to be aligned with the mean velocity. Gradients of v_0^*, ρ_0^*, s_0^*, and p_0^* in the x and z directions are considered negligible in comparison with their gradients in the y direction normal to the wall (assuming a fully developed stationary flow). Furthermore, the stationary pressure is assumed constant in the y direction ($dp_0^*/dy^*=0$). This last assumption leads to

$$\frac{ds_0^*}{dy^*}=-\frac{c_p^*}{\rho_0^*}\frac{d\rho_0^*}{dy^*}=\frac{c_p^*}{T_0^*}\frac{dT_0^*}{dy^*}, \tag{3}$$

and to $d(\rho_0^*/c_0^{*2})/dy^*=0$.

For simplicity the sound is assumed to propagate only in the x direction (an extension to propagation in both x and z directions is straightforward). Then, by introducing dimensionless quantities, the variables may be written as follows:

$$\begin{aligned}
&x^*=xc_a/\omega^*, \quad y^*=yc_a/\omega^*, \quad t^*=t/\omega^*, \quad c_0^*=c_a c_0(y),\\
&u_0^*=c_a u_0(y), \quad u^*=c_a u(y)E,\\
&v_0^*=0, \quad v^*=c_a v(y)E,\\
&p_0^*=\rho_a c_a^2 p_0, \quad p^*=\rho_a c_a^2 p(y)E,\\
&T_0^*=T_a T_0(y), \quad T^*=T_a T(y)E,\\
&\rho_0^*=\rho_a \rho_0(y), \quad \rho^*=\rho_a \rho(y)E,\\
&s_0^*=c_p^* s_0(y), \quad s^*=c_p^* s(y)E,
\end{aligned} \tag{4}$$

where the subscript a refers to dimensional properties in the core of the flow (for instance in the midline), ω^* is the frequency, c_a is the sound speed ($c_a^2=c_p^*(\gamma-1)T_a$), u and v are the velocity components in the x and y directions, and $E=\exp(-i\omega^* t^*+ik^* x^*)=\exp(-it+ikx)$ where $k=k^* c_a/\omega^*$ is the wave number.

Using expressions (4) with the above assumptions, Eqs. (1) are transformed to

$$-i\Omega\rho+\rho_0\left(iku-i\Omega\frac{d\xi}{dy}+ik\frac{du_0}{dy}\xi\right)-i\Omega\frac{d\rho_0}{dy}\xi=0, \tag{5a}$$

$$-i\Omega u-i\Omega\frac{du_0}{dy}\xi+\frac{ikp}{\rho_0}=\frac{\delta_a^2}{2}\frac{\rho_w}{\rho_0}B_x, \tag{5b}$$

$$-i\Omega v+\frac{1}{\rho_0}\frac{dp}{dy}=\frac{\delta_a^2}{2}\frac{\rho_w}{\rho_0}B_y, \tag{5c}$$

$$-i\Omega s+i\Omega\frac{1}{\rho_0}\frac{d\rho_0}{dy}\xi=\frac{\delta_a^2}{2}\frac{\rho_w}{\rho_0}\frac{Q}{T_0}, \tag{5d}$$

$$p=c_0^2\rho+s, \tag{5e}$$

where $\Omega=1-ku_0$ and $\xi=-v/i\Omega$ is the acoustical displacement in the y direction, $\delta_a=(2\mu_a\omega^*/\rho_w^* c_a^2)^{1/2}$ is the dimensionless acoustic boundary layer thickness, $\rho_w^*=\rho_a\rho_w$ is the density at the wall, and μ_a is the dynamic viscosity of the fluid. For simplicity the dynamic viscosity and the thermal conductivity are assumed to be constant and the bulk viscosity is assumed to be equal to zero; then, the dissipation terms B_x, B_y and Q are given by

$$B_x=\frac{d^2u}{dy^2}+\frac{1}{3}ik\frac{dv}{dy}+\frac{4}{3}k^2u, \tag{6a}$$

$$B_y=\frac{4}{3}\frac{d^2v}{dy^2}+\frac{1}{3}ik\frac{du}{dy}-k^2v, \tag{6b}$$

$$Q=\frac{1}{\sigma^2}\left(\frac{d^2T}{dy^2}-k^2T\right)+2(\gamma-1)\frac{du_0}{dy}\left(\frac{du}{dy}+ikv\right), \tag{6c}$$

where $\sigma^2=c_p^*\mu_a/\kappa_a$ is the Prandtl number; κ_a is the thermal conductivity. By retaining only the two variables ξ and p, Eqs. (5) lead to

$$\frac{d\xi}{dy}+\left[1-\left(\frac{c_0 k}{\Omega}\right)^2\right]p=-\frac{\rho_w\delta_a^2}{2i\rho_0\Omega}\left[\frac{Q}{T_0}+\frac{k}{\Omega}B_x\right], \tag{7a}$$

$$\frac{dp}{dy}-\left(\frac{\Omega}{c_0}\right)^2\xi=\frac{\delta_a^2}{2}B_y. \tag{7b}$$

The propagation equations, Eqs. (7), must be applied with boundary conditions at the wall. The most appropriate choice to express the boundary conditions would be to use the compliance of the wall which links pressure and normal displacement. But, the liner characteristics are more usually given in terms of the wall admittance. Thus, the boundary condition at the wall is written

$$Y=\frac{\rho_0 c_a v^*(0)}{p^*(0)}=\frac{v(0)}{p(0)}, \tag{8}$$

where Y is the specific acoustic admittance of the wall.

III. ASYMPTOTIC REPRESENTATION

For simplicity, it is helpful to separate the problem into two regions: (1) the core of the flow, where the dissipation effects can be neglected; (2) a thin layer near the wall, within which the viscous and thermal dissipation effects are confined.

Thus, the problem is amenable to asymptotic analysis. With the method of composite expansions,[11] the solution for any quantity $q(y)$, where $q=u,v,\xi,p,T,\rho$ is expressed as $q=q_c(y)+q_b(\zeta)$ with $\zeta=y/\delta_a$. The second term with subscript b (representing boundary layer terms near the wall $y=0$) tends to zero as $\zeta\to\infty$. The gradients of mean velocity and temperature are assumed to be non-negligible in the boundary layer. Then, it is convenient to express them, respectively, as $u_a=M_c(y)+M_b(\zeta)$ and $T_o=\Theta_c(y)+\Theta_b(\zeta)$, where the terms with subscript b account for the significant gradients near the wall.

The first terms (inviscid terms in the core of the flow) can be obtained from Eqs. (5) without dissipation and without large gradients near the wall. In the core of the flow, Eqs. (7) lead to the convected wave equation for the outer pressure p_c

$$\frac{d}{dy}\left[\left(\frac{c_0 c}{\Omega_c}\right)^2\frac{dp_c}{dy}\right]+\left[1-\left(\frac{c_{0c}k}{\Omega_c}\right)^2\right]p_c=0, \tag{9}$$

where $\Omega_c=1-kM_c$ and $c_{0c}^2=\Theta_c$. This equation may also be written[10]

$$\frac{d^2p_c}{dy^2}+\left(\frac{1}{\Theta_c}\frac{d\Theta_c}{dy}-\frac{2k}{\Omega_c}\frac{dM_c}{dy}\right)\frac{dp_c}{dy}+\left(\frac{\Omega_c^2}{\Theta_c}-k^2\right)p_c=0, \tag{10}$$

which is the classical Pridmore-Brown[12] equation with temperature gradient. An effective admittance could be defined for the outer region by

$$Y_c=\frac{v_c(0)}{p_c(0)}, \tag{11}$$

while the relationship between the normal velocity and the normal pressure gradient given by Eq. (5c) can be simplified as $i\Omega_c v_c=dp_c/dy$.

In the boundary layer, taking the limit $\delta_a\to 0$, Eqs. (7) reduce to

$$\frac{d\xi_b}{d\zeta}=-\frac{\rho_w\delta_a}{2i\rho_0\Omega}\left[\frac{Q_b}{T_0}+\frac{k}{\Omega}B_b\right], \tag{12a}$$

$$\frac{dp_b}{d\zeta}=0, \tag{12b}$$

where

$$B_b=\frac{d^2u_b}{d\zeta^2}, \tag{13a}$$

and

$$Q_b=\frac{1}{\sigma^2}\frac{d^2T_b}{d\zeta^2}+2(\gamma-1)\frac{dM_b}{d\zeta}\frac{du_b}{d\zeta}. \tag{13b}$$

The solution of Eq. (12b) (which tends to zero as $\zeta\to\infty$) is $p_b=0$. Thus, the pressure is constant across the boundary layer to the first order in δ_a.

Integration of Eq. (12a) leads to

$$\xi_b(0)=-\delta_a\int_0^\infty\frac{\rho_w}{2i\rho_{0b}(\zeta)\Omega_b(\zeta)}\times\left[\frac{Q_b}{\Theta_c(0)+\Theta_b(\zeta)}+\frac{kB_b}{\Omega_c(0)+\Omega_b(\zeta)}\right]d\zeta. \tag{14}$$

Without any dissipation, the kinematic condition in the case of a vanishing stationary boundary thickness is continuity of acoustic normal displacement.[9] Using the above notation, this means that $\xi_b(0)=0$. Equation (14) shows that this condition does not hold when there is dissipation, and that an added normal displacement $\xi_b(0)$ is introduced by the viscothermal effects.[13] The expression for the added displacement may be simplified if $\Delta\Theta_0=\Theta_0-\Theta_w$ [where $\Theta_0=\Theta_c(0)$ and $\Theta_w=\Theta_c(0)+\Theta_b(0)$ is the wall temperature] and $M_0=M_c(0)$ are small compared to 1. To the first order in the parameters M_0 and $\Delta\Theta_0$, the added displacement may be written

$$\xi_b(0)=-\frac{i\delta_n}{2}\left(\frac{1}{\Theta_w\sigma^2}\frac{dT_b}{d\zeta}(0)+k\frac{du_b}{d\zeta}(0)\right). \tag{15}$$

The added displacement $\xi_b(0)$, which needs to be included in the boundary conditions, is defined only in terms of the heat flux $q=dT_b/d\zeta$ and the shear stress $\tau=du_b/d\zeta$ at the wall. How these are determined is shown in the next section.

IV. DETERMINATION OF THE ADDED DISPLACEMENT

The diffusion of momentum and heat has to be determined in the boundary layer to find the kinematic condition which can be applied. The momentum equation in the x direction Eq. (5b) becomes, to the first order in M_0 and $\Delta\Theta_0$

$$\frac{d^2u_b}{d\zeta^2}+2iu_b=-2iu_c(0)-\frac{2i}{\delta_a}\frac{dM_b}{d\zeta}\xi_c(0)+2ik\frac{p_c(0)}{\rho_w}. \tag{16}$$

This equation may be transformed into an expression for the shear stress $\tau=du_b/d\zeta$ which is involved in the added displacement

$$\frac{d^2\tau}{d\zeta^2}+2i\tau=\frac{df}{d\zeta}, \tag{17}$$

where

$$f(\zeta)=-\frac{2i}{\delta_a}\frac{dM_b}{d\zeta}\xi_c(0)+2ik\frac{p_c(0)}{\rho_w}. \tag{18}$$

The boundary conditions associated with Eq. (17) are $\tau\to 0$ when $\zeta\to\infty$ and $u(0)=u_b(0)+u_c(0)=0$, which can be transformed using Eq. (16) into $d\tau/d\zeta(0)=f(0)$.

The shear waves described by Eq. (17) is excited in two ways. In the first way, a shear wave is excited by the acoustics in the core of flow [i.e., the second term in the definition of $f(\zeta)$]. This wave is the classical one found in dynamic boundary layers near a rigid wall. The second way [which corresponds to the first term in the definition of $f(\zeta)$] is very weak when the wall is rigid [$\xi(0)=0$]. It corresponds to waves induced by changes to the stationary velocity and by the normal displacement near the wall.

Equation (17), subject to the boundary conditions, leads to

$$\tau(0)=-\frac{1}{\tau_1'(0)}\int_0^\infty f(\zeta)\frac{d\tau_1}{d\zeta}d\zeta, \tag{19}$$

where $\tau_1=\exp[(-1+i)\zeta]$ is the solution of the homogeneous part of Eq. (17) vanishing at infinity. Then, the shear stress at the wall is

$$\tau(0)=(1-i)k\frac{p_c(0)}{\rho_w}+\frac{2i}{\delta_a}M_{\text{eff}}\xi_c(0), \tag{20a}$$

where

$$M_{\text{eff}}=\int_0^\infty \frac{dM_b}{d\zeta}\exp[(-1+i)\zeta]d\zeta \tag{20b}$$

is the effective mean velocity involved in the added displacement. This effective velocity may be seen[14] as an average of the mean velocity over the boundary layer weighted by τ_1 and can be written $M_{\text{eff}}=\beta_v M_0$, where $M_0=M_c(0)$ with $0\leqslant|\beta_v|\leqslant 1$.

In the same way, the conservation of energy [Eq. (5d)] leads to a value for the heat flux $q=dT_b/d\zeta$ at the wall

$$\frac{1}{\sigma^2}q(0)=\frac{1-i}{\sigma}(\gamma-1)\frac{p_c(0)}{\rho_w}+\frac{2i}{\delta_a}\Delta\Theta_{\text{eff}}\xi_c(0), \tag{21a}$$

where

$$\Delta\Theta_{\text{eff}}=\int_0^\infty \frac{d\Theta_b}{d\zeta}\exp[(-1+i)\sigma\zeta]d\zeta \tag{21b}$$

is the effective difference between mean temperature and wall temperature involved in the added displacement and can be written $\Delta\Theta_{\text{eff}}=\beta_t\Delta\Theta_0$, where $\Delta\Theta_0=\Theta_0-\Theta_w$ with $0\leqslant|\beta_t|\leqslant 1$.

The added displacement may be written

$$\xi_b(0)=\frac{(1+i)\delta_a}{2\rho_w}\left(\frac{\gamma-1}{\sigma\Theta_w}+k^2\right)p_c(0)-\left(kM_{\text{eff}}+\frac{\Delta\Theta_{\text{eff}}}{\Theta_w}\right)\xi_c(0), \tag{22}$$

which leads to a relation giving the modified admittance

$$\left(1-(1-\beta_v)kM_0+\frac{\Delta\Theta_0}{\Theta_w}\beta_t\right)Y_c=Y+\frac{1-i}{2\rho_w}\left(\frac{\gamma-1}{\sigma}+k^2\right)\delta_a. \tag{23}$$

It can be seen from Eq. (23) that the effect of the classical shear and thermal waves (induced by the acoustics in the core of the flow) which leads to the second term on the right-hand side of (23) is weak (of the order δ_a). Since Y is much larger than δ_a for a typical lined wall, this term is only important for a hard wall and will be neglected in front of Y in what follows.

When β_v and $\beta_t\to 0$, Eq. (23) is equivalent to the continuity of acoustic normal displacement across the boundary layer: $\xi_b(0)=0$ or $Y_c=Y/(1-kM_0)$. When β_v and $\beta_t\to 1$, Eq. (23) is transformed in a condition of conservation of the normal mass velocity across the boundary layer: $\rho_c(0)v_c(0)=\rho_w v(0)$ or $\Theta_0 Y_c=\Theta_w Y$.

This behavior is illustrated here for three simplified mean velocity profiles with a constant temperature. The outer mean velocity is taken as constant, i.e., $M_c(y)=M_0$. The slope at the origin is the same for all three profiles: $du_0/dy(0)=M_0/\Delta$ where Δ is the stationary boundary layer thickness [see Fig. 2(b)]. The ratio of the acoustic over the stationary boundary layer thickness is called $\delta^*=\delta_a/\Delta$.

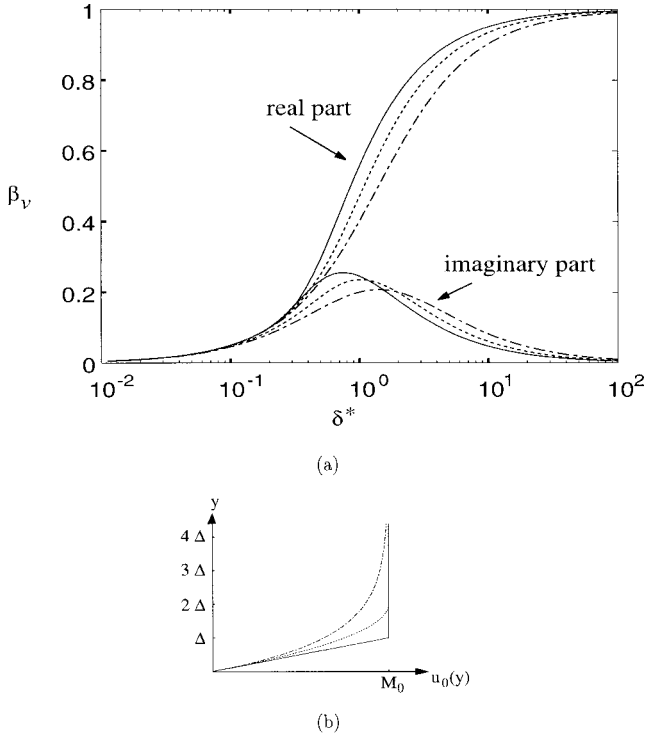

FIG. 2. (a) Variation of the effective velocity divided by the core velocity, β_v, as a function of the ratio of the acoustic and stationary boundary layer thicknesses, δ^*, for three mean velocity profiles. Solid line: linear; dashed line: quadratic, and dash-dot line: exponential. (b) Mean velocity profiles.

(1) For the first profile, the inner mean velocity is linear

$$M_b(\zeta)=-M_0(1-\delta^*\zeta)\quad \text{for } 0\leqslant\zeta\leqslant 1/\delta^*,$$

$$M_b(\zeta)=0\quad \text{for } \zeta>1/\delta^*,$$

and in this case

$$\beta_v=\frac{(1+i)\delta^*}{2}\left[1-\exp\left(\frac{-1+i}{\delta^*}\right)\right]. \tag{24}$$

(2) The second profile is quadratic

$$M_b(\zeta)=-M_0(1-\delta^*\zeta/2)^2\quad \text{for } 0\leqslant\zeta\leqslant 2/\delta^*,$$

$$M_b(\zeta)=0\quad \text{for } \zeta>2/\delta^*,$$

and in this case

$$\beta_v=\frac{i\delta^*}{2}\left[\left(\exp\left(\frac{2(-1+i)}{\delta^*}\right)-1\right)\frac{\delta^*}{2}-(-1+i)\right]. \tag{25}$$

(3) The last profile is exponential, i.e., $M_b(\zeta)=-M_0\exp(-\delta^*\zeta)$, and in this case $\beta_v=\delta^*/(\delta^*+1-i)$.

The real and imaginary parts of β_v as a function of δ^* are plotted in Fig. 2(a) for the three profiles. When the acoustic boundary layer thickness, δ_a, is small compared to the stationary boundary layer thickness Δ (i.e., $\delta^*\ll 1$), β_v goes to zero. In this case, continuity of displacement can be applied across the boundary layer. On the other hand, when $\delta^*\gg 1$, β_v goes to 1, which means that continuity of velocity is applicable across the boundary layer. For a given station-

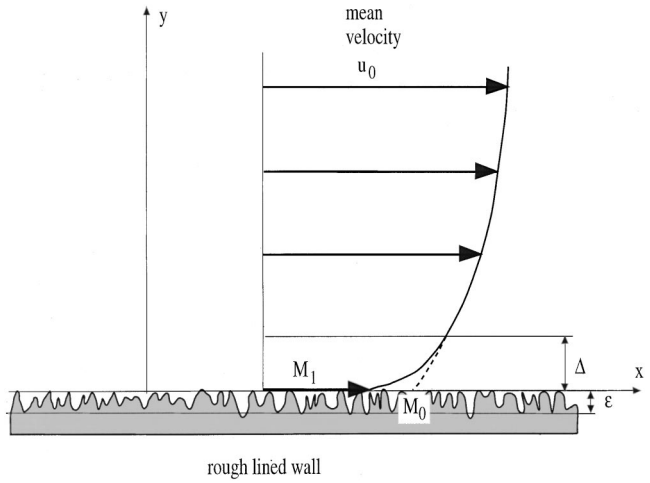

FIG. 3. Schematic description of the rough wall geometry.

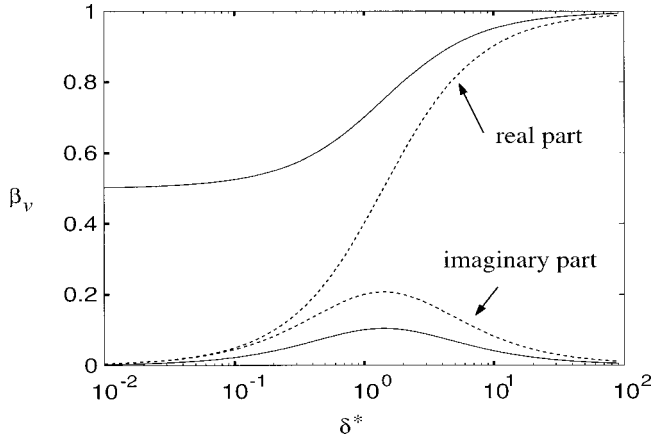

FIG. 4. Variation of the effective velocity divided by the core velocity, β_v, as a function of the ratio of the acoustic and stationary boundary layer thickness, δ^*, for a rough wall with an exponential mean velocity profile. Solid line: rough wall; dashed line: smooth wall [same as Fig. 2(a)].

ary boundary layer thickness, Δ, continuity of displacement applies at high frequencies while continuity of mass velocity applies at low frequencies. For a given frequency, continuity of displacement applies at low Mach number (i.e., giving a thick stationary boundary layer), while continuity of mass velocity applies at high Mach number (i.e., resulting in a thin stationary boundary layer). These findings are in qualitative agreement with the experimental observations of Ingard and Singhal.[15]

It should be noted that, when both acoustic and stationary boundary layer thicknesses are of the same order $\Delta \simeq \delta_a$, β_v and β_t are complex, so they not only change the value but also the character of the admittance.

It may be seen from Eq. (20a) that the most important part of the acoustic shear stress comes from the transfer, by the normal fluctuating displacement, of axial momentum from the stationary flow into the lined wall,[16] this effect being induced by viscosity. The parameter β_v controls this transfer from $\beta_v=0$ (no transfer) to $\beta_v=1$ (full transfer). β_v can be seen from Eq. (20b) to be the ratio of the mean velocity in the layer where the shear wave is significant over the core mean velocity. The same reasoning holds for the thermal flux and the parameter β_t.[14]

V. ADMITTANCE OF A ROUGH LINED WALL

The mean velocity profiles of turbulent flow over a rough wall is schematically depicted in Fig. 3. Compared to a smooth wall profile, the main difference is the slip velocity M_1 at the outer boundary of the equivalent roughness thickness. This slip velocity depends on the equivalent roughness and on the core velocity.[17]

Taking into account the above analysis of the viscous effects, the axial momentum linked to the slipping velocity M_1 is transferred into the roughness of the wall even if the acoustic boundary layer thickness is small compared to Δ. Then, the continuity of mass velocity must be applied over a distance equal to the roughness of the wall.[13] This can be written as $\rho_1 v(0)=-i(1-kM_1)\rho_1\xi(0)=\rho_w Y p(0)$, where ρ_1 and ρ_w are the density corresponding, respectively, to the $y=0$ and to the wall temperature. The origin of the coordinates y and ζ is taken at the outer boundary of the equivalent roughness thickness ϵ. Assuming that the axial acoustic velocity is equal to 0 at $y=0$, Eq. (23) then becomes

$$\left(1-(1-\tilde{\beta}_v)kM_0+\frac{\Delta\Theta_a}{\Theta_w}\tilde{\beta}_t\right)Y_c=Y, \tag{26}$$

where

$$\tilde{\beta}_v=\frac{1}{M_0}\left(M_1+\int_0^\infty \frac{dM_b}{d\zeta}\exp[(-1+i)\zeta]d\zeta\right), \tag{27a}$$

and

$$\tilde{\beta}_t=\frac{1}{\Delta\Theta_0}\left(\Delta\Theta_1+\int_0^\infty \frac{d\Theta_b}{d\zeta}\exp[(-1+i)\sigma\zeta]d\zeta\right); \tag{27b}$$

$\Delta\Theta_1=\Theta_w-\Theta_1$ is the difference between the wall temperature and the temperature at $y=0$.

The effect of roughness is illustrated for the case of an exponential velocity profile with a slip velocity, in the case of a constant temperature. The stationary velocity profile takes the form $M_b(\zeta)=-(M_0-M_1)\exp(-\delta^*\zeta)$ and in this case $\beta_v=(\delta^*+(1-i)M_1/M_0)/(\delta^*+1-i)$.

The real and imaginary parts of $\tilde{\beta}_v$ as a function of δ^* are plotted in Fig. 4 for $M_1=0.5M_0$. It can be seen that continuity of normal displacement ($\tilde{\beta}_v=0$) is never attained for a rough wall (solid line in Fig. 4). When the acoustic boundary layer thickness δ_a is small compared to the stationary boundary layer thickness Δ (i.e., $\delta^*\ll 1$), $\beta_v \rightarrow M_1/M_0$, and the boundary condition is $Y_c=Y/(1-kM_1)$ instead of $Y_c=Y/(1-kM_0)$ for the case of a smooth wall (i.e., continuity of displacement).

VI. CONCLUSIONS

The effective acoustic admittance of a liner, taking account of viscothermal effects, can be computed for the case where acoustic and stationary boundary layer thicknesses are small compared to the wavelength. The main effect of viscosity is the transfer of axial momentum and heat flux of the stationary flow into the lined wall. The effective admittance is given as a function of two coefficients β_v and β_t which mainly depend on the ratio of the acoustic and stationary

boundary layer thicknesses. When the acoustic boundary layer thickness is small compared with the stationary boundary layer thickness, continuity of normal displacement applies across the boundary layer. On the other hand, when the acoustic boundary layer thickness is large compared with the stationary boundary layer thickness, it is continuity of mass velocity which applies across the boundary layer. If the lined wall is rough, normal displacement continuity never applies. In this paper, only molecular diffusion effects (described by the dynamic viscosity and the thermal conductivity) are taken into account. Further work is needed to include the turbulent diffusion effects which can be incorporated in a complex effective viscosity and which will depend both on the normal coordinate and on frequency.

[1] D. H. Tack and R. F. Lambert, ''Influence of shear flow on sound attenuation in a lined duct,'' J. Acoust. Soc. Am. **38**, 655–666 (1965).
[2] W. Eversman, ''Effect of boundary layer on the transmission and attenuation of sound in an acoustically treated lined duct,'' J. Acoust. Soc. Am. **49**, 1372–1380 (1971).
[3] S. H. Ko, ''Sound attenuation in acoustically lined circular ducts in the presence of uniform flow and shear flow,'' J. Sound Vib. **54**, 192–210 (1973).
[4] M. E. Goldstein and E. Rice, ''Effect of shear on duct wall impedance,'' J. Sound Vib. **30**(1), 79–84 (1972).
[5] B. J. Tester, ''The propagation and attenuation of sound in lined ducts containing uniform or plug flow,'' J. Sound Vib. **28**(2), 151–203 (1973).
[6] B. J. Tester, ''Some aspects of sound attenuation in lined ducts containing inviscid mean flows with boundary layers,'' J. Sound Vib. **28**(2), 217–245 (1973).
[7] R. S. Brand and R. T. Nagel, ''Reflection of sound by a boundary layer,'' J. Sound Vib. **85**(1), 31–38 (1982).
[8] R. T. Nagel and R. S. Brand, ''Boundary layer effects on sound in a circular duct,'' J. Sound Vib. **85**(1), 19–29 (1982).
[9] A. H. Nayfeh, J. E. Kaiser, and D. P. Telionis, ''Acoustics of aircraft engine-duct systems,'' AIAA J. **13**(2), 130–153 (1975).
[10] A. H. Nayfeh, ''Effect of acoustic boundary layer on the wave propagation in ducts,'' J. Acoust. Soc. Am. **54**, 1737–1742 (1973).
[11] A. H. Nayfeh, *Perturbation Methods* (Wiley, New York, 1973), Chap. 4.
[12] D. C. Pridmore-Brown, ''Sound propagation in a fluid flowing through an attenuating duct,'' J. Fluid Mech. **4**, 393–406 (1958).
[13] R. Starobinski, ''Sound propagation in lining duct with essentially nonuniform distribution of velocity and temperature,'' in *Jet Engine Noise, Transactions of the Central Institute of Aviation Engine* (CIAM, N 752, Moscow, 1978), pp. 155–181 (in Russian).
[14] R. Starobinski, ''Theory and synthesis of the silencers for intake and exhaust systems of internal combustion engine,'' D. of Sc. thesis, Togliatti University, 1983 (in Russian).
[15] U. Ingard and V. Singhal, ''Upstream and downstream sound radiation into a moving fluid,'' J. Acoust. Soc. Am. **54**, 1343–1346 (1973).
[16] J. Rebel and D. Ronneberger, ''The effect of shear stress on the propagation and scattering of sound in flow ducts,'' J. Sound Vib. **158**(3), 469–496 (1992).
[17] H. Schlichting, *Boundary Layer Theory*, 7th ed. (McGraw-Hill, New York, 1979).

Structural-acoustic coupling in a partially opened plate-cavity system: Experimental observation by using nearfield acoustic holography

Sea-Moon Kim and Yang-Hann Kim[a)]
Center for Noise and Vibration Control (NOVIC), Department of Mechanical Engineering, Korea Advanced Institute of Science and Technology (KAIST), Science Town, Taejon 305-701, Korea

(Received 1 August 1999; revised 21 April 2000; accepted 29 August 2000)

In order to understand the cause and effect relation between a structure and a fluid, many studies on structural-acoustic coupling have been done. However, the studies were restricted to the interaction between only a structure and a fluid located on one or the other side of the structure. It is our aim to understand the coupling mechanism of a generally coupled system that has direct interaction between a finite interior fluid and a semi-infinite exterior one. We believe that this configuration allows the structure to interact with the fluid of the finite volume and that of the infinite one, thus providing a more general structure-fluid coupling (or structural-acoustic coupling) mechanism. For this purpose, we selected a partially opened plate-cavity system which has two different modally reacting boundary conditions: a plate and a hole. In order to understand the physical coupling phenomena of the selected system, visualization of the sound fields was performed experimentally. We used near field acoustic holography to estimate sound field variables, such as pressures and intensities. Examining the acoustic variables, we found that there are two types of coupling mechanisms depending on frequency and associated wavelength. One is where the plate and the cavity are so strongly coupled that the plate can be considered as a source. In this case, the system radiates acoustic energy effectively through the plate. The other is where the coupling interaction behavior decreases the radiation efficiency. The frequencies that determine whether the plate is a good or bad radiator are found to be around the natural frequencies of the plate. [DOI: 10.1121/1.1320476]

PACS numbers: 43.20.Tb, 43.40.Rj [CBB]

I. INTRODUCTION

When solving acoustic problems, in many cases, we often assume that the boundary is rigid or locally reacting for simplicity. However, if a flexible structure is attached at the boundary, then this assumption is no longer valid. In this case we have to consider a modally reacting boundary caused by the interaction between the flexible boundary and acoustic fields.

Numerous analytical and experimental investigations have been performed in this area. For example, Dowell and Voss[1] studied the effect of a cavity on panel vibration, and Lyon[2] focused on the noise reduction in an enclosure with a flexible wall. A few years later, Pretlove[3,4] analyzed free and forced responses of a cavity-backed plate with *in vacuo* modes of the plate. All these studies were based on the assumption that there is interaction only between a cavity and a flexible structure. In the late 1960s Morse[5] considered transmission of sound through a circular membrane and in the late 1970s Guy[6] investigated sound transmission from an exterior field to an interior field through a panel. There have also been studies on structural-acoustic coupling in a system having more complex shapes. Fuller and Fahy[7] investigated the interaction between cylindrical elastic shells filled with fluid. Nefske *et al.*[8] used an FEM based model to discover the coupling mechanism in an irregular shaped system. Pan *et al.*[9,10] even tried to reduce the noise transmitted through a panel into a cavity by using an active noise control (ANC) technique. Recently studies on coupling in high and medium frequency ranges have been done.[11,12] Sum and Pan also investigated an analytical model for band-limited response.[13]

These studies, however, were restricted to the interaction between a structure and a cavity [see Fig. 1(a)] or a structure and the infinite dimension of acoustic fields [see Fig. 1(b)]. If one combines these two typical coupling systems, then the system may look like the one in Fig. 1(c). The flexible structure may control the acoustic coupling between a finite size cavity and a semi-infinite acoustic domain; the structure is a communicator. One typical example of this kind would be a large speaker system in which higher order modes are likely to be generated in the speaker box. One flexible structure may easily introduce other types of coupling mechanisms other than between a finite cavity and a semi-infinite fluid system so that one can investigate the general coupling mechanism.

It is our aim to understand the coupling mechanism between the structure and fluid as illustrated in Fig. 2(a). In this system, acoustic fields can be divided into two parts. One is finite and the other is semi-infinite. The former makes the acoustic cavity, covered by a finite size structure. The structure faces two different domains, which we call the ''outer domain'' and ''inner domain.'' The inner domain will be reverberant, and the outer field would be well expressed by a propagating field, or a radiating field. This configuration ex-

a)Electronic mail: yhkim@sorak.kaist.ac.kr

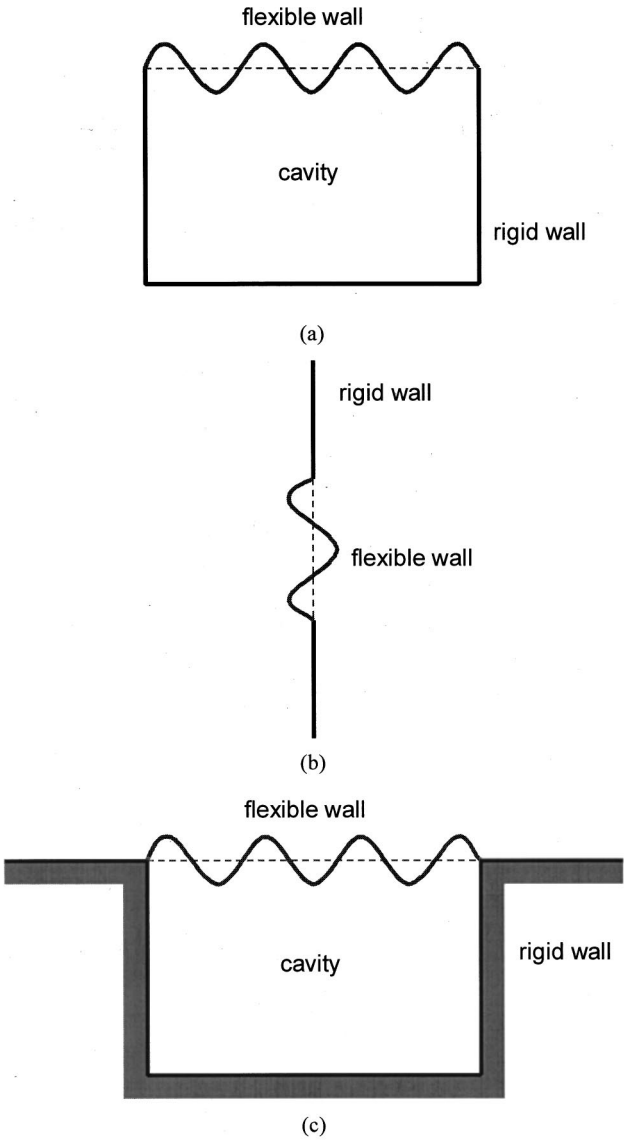

FIG. 1. Three examples of structural-acoustic coupling problems. (a) Interaction of a structure with a finite acoustic field, (b) interaction of a structure with infinite acoustic fields, (c) interaction of a structure with a finite acoustic field and an infinite acoustic field.

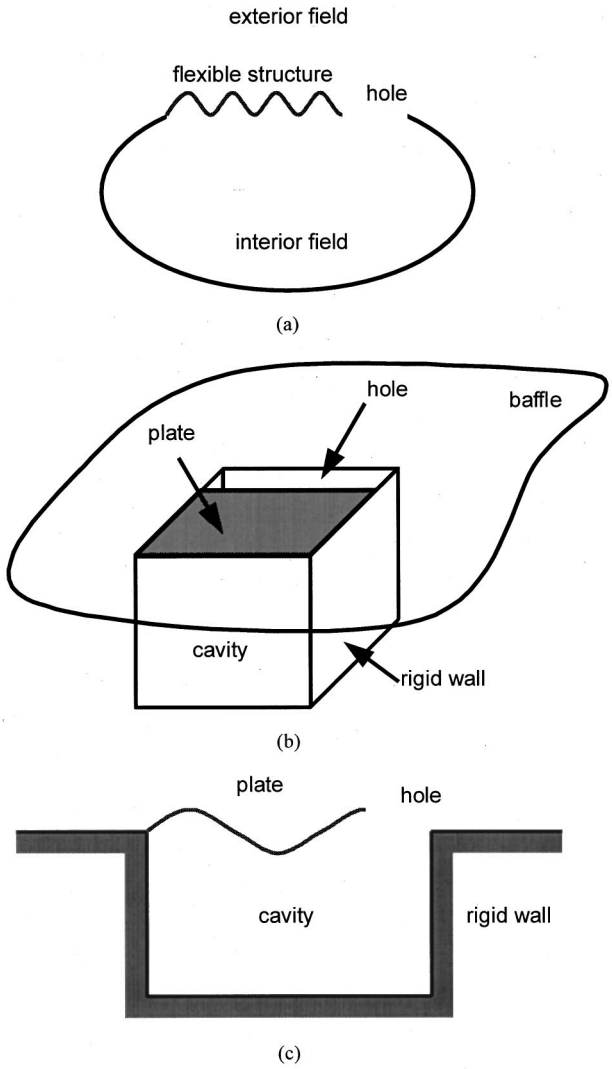

FIG. 2. The structural-acoustic coupling model to be considered. (a) A general model, (b) the plate-cavity system with a hole (prospective view), (c) the plate-cavity system with a hole (side view).

hibits general coupling phenomena between the structure, the inner domain and the outer fluid. We also allow discontinuity on the top of the cavity; the structure only covers part of the opening of the inner domain so as to make the problem more general. This allows the inner domain to interact with the outer domain through two different media: a structure and a fluid. This configuration provides a good representation of the general coupling behavior between a structure and acoustic fields. One of the good applications of this kind of system can be a musical instrument which has vibrating plates and a cavity with a hole.[14]

This paper studies coupling phenomena in the system of rectangular geometry [Figs. 2(b) and (c)] because of its simplicity. Nearfield acoustic holography[15] was used to estimate acoustic parameters such as pressure, particle velocity, and sound intensity. The results are analyzed in terms of frequency and wavelength.

II. EXPERIMENTAL SETUP

In order to visualize the interaction among three subsystems (a structure, an interior field, and an exterior field), we selected a partially opened plate-cavity system as shown in Fig. 3(a). The size of the cavity was 16 cm(x)$\times$12 cm(y)$\times$13 cm(z). The upper side of the cavity was partially covered by a rectangular plate which was made from galvanized iron with a thickness of 0.3 mm. The area covered by the plate was 14 cm(x)$\times$12 cm(y) and the area of uncovered part was 2 cm(x)$\times$12 cm(y). The uncovered part (or a hole) enabled direct interaction between the interior and exterior fields. Three sides of the plate were fixed by steel plates having a thickness of 2 mm so that the boundary condition was considered as clamped. The other side had a free boundary condition. The remaining five walls of the cavity were made from transparent acrylic resin with a thickness of 2 cm, which was considered as a rigid wall. A rigid baffle of 3.30 m(x)$\times$2.44 m(y) was located on the same level of the plate. The system was excited by a horn driver which was located slightly off the center of the side wall in order to make as many internal modes as possible. The horn driver

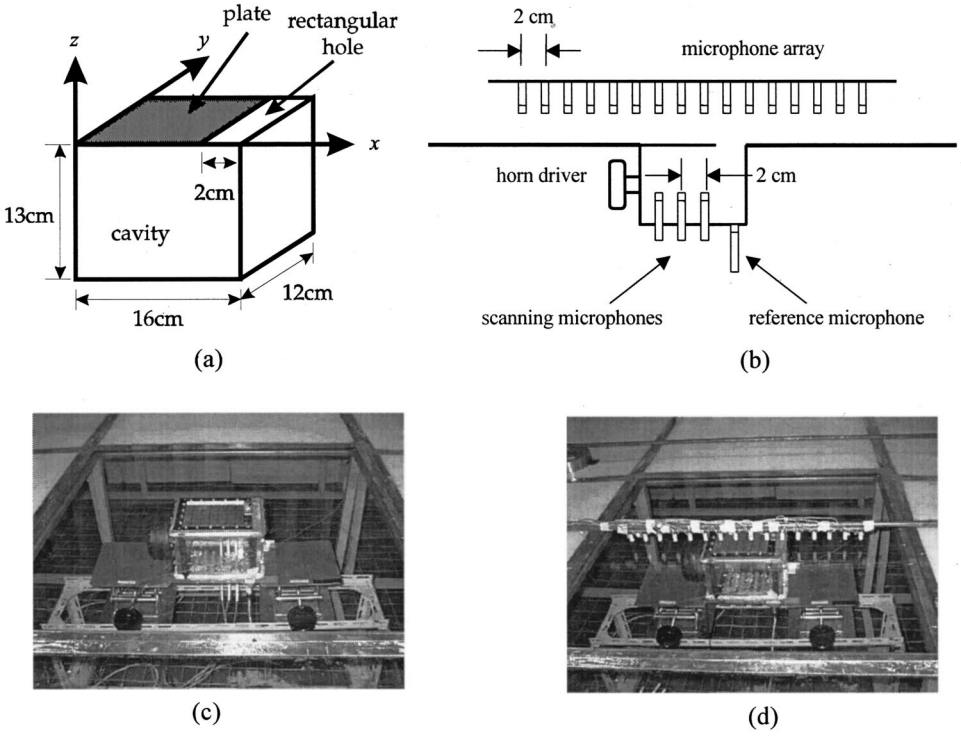

FIG. 3. Experimental setup. (a) Plate-cavity system: plate (14 cm×12 cm, galvanized iron sheet, 0.3 mm thickness), cavity (16 cm×12 cm×13 cm, acrylic resin wall with the thickness of 2 cm), (b) measurement setup (inside the cavity: 2 cm spacing, 7×5×7 pts, outside the cavity: 2 cm spacing, 32×32 pts, distance between the microphone array and the system: 2.5 cm), (c) photograph of internal field measurement, (d) photograph of external field measurement.

was flush mounted and its diameter was 1.9 cm. For the measurement of sound pressures inside and outside the cavity, we set up microphone systems as shown in Fig. 3(b). For the interior field the pressures were measured at $7(x)\times5(y)\times7(z)$ points with 2 cm spacing by using three 1/4 inch microphones. (The scattering effect by the internal microphones could be ignored at the frequency range of interest. The details are explained in Appendix A.) For the exterior field, we measured pressures at $32(x)\times32(y)$ points with 2 cm spacing by a line array of 16 microphones. The distance between the line array and the plate or the baffle was 2.5 cm. One more microphone, which was flush mounted at the bottom, was used to obtain reference signals. The experiments were performed in an anechoic chamber (100 Hz cutoff). The results were obtained by the swept-sine method in a frequency range between 90 Hz and 3 kHz. The range of 0 Hz through 90 Hz was excluded because of the poor performance of the horn driver. Figures 3(c) and (d) are the photographs of the experimental setup.

III. FREQUENCY CHARACTERISTICS—COMPARISON WITH AN UNCOUPLED SYSTEM

Comparing the acoustic characteristics between uncoupled and coupled systems will greatly enhance our understanding of the coupling behavior. Thus, we obtained the frequency response of the uncoupled system, which was made by putting thick clay on the plate so that the cavity interacts only with the exterior field through the hole. The mass per unit area of the clay was 19.1 kg/m^2, which was about 10 times greater than that of the plate. Table I shows the resonance frequencies of both the uncoupled and coupled systems. The results are based on the pressure signal of the reference microphone. The resonance frequencies between the two systems show little difference in the high frequency range. However, in the low frequency range the coupled system exhibits two other resonance frequencies (110 Hz and 167 Hz). This fact illustrates the fact that the main coupling effect occurs in the low frequency range. Theoretical values assuming the top boundary as rigid and in a pressure release condition are also shown for comparison. The results certainly lead us to the conclusion that the boundary conditions of the coupled and uncoupled systems are somewhere between rigid and pressure release. Interestingly, we could not find the cavity mode (1,0,1) in the experiment. We suspect that the reason could be that the source position was not good for generating that mode. The other modes up to 3 kHz were found clearly.

TABLE I. The measured resonance frequencies of the coupled and uncoupled systems (l,m,n: number of nodal surfaces in the x, y, and z directions, respectively, spectral resolution between 90–200 Hz: 0.5 Hz, spectral resolution above 200 Hz: 2 Hz) and theoretical values of the natural frequencies of two ideal systems having rigid and pressure release boundary conditions for the top.

	Experimental values			Theoretical values	
Mode (l,m,n)	Coupled system	Uncoupled system	Difference between them	Rigid condition	Pressure release condition
	110,[a] 167,[a] 113.5,[b] 171[b]				
(0,0,0)	256	240	+16	0	731
(1,0,0)	1122	1118	+4	1064	1291
(0,0,1)	1352, 1388	1368	−16, +20	1302	1493
(0,1,0)	1474	1472	+2	1462	2193
(1,0,1)				1681	1833
(1,1,0)	1832	1834	−2	1808	2437
(2,0,0)	2180	2178	+2	2128	2250
(2,0,1)	2570	2568	+2	2494	2599

[a]Peak frequencies.
[b]Trough frequencies.

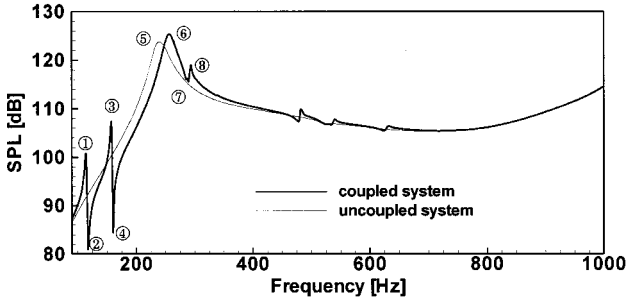

FIG. 4. The sound pressure levels measured by the reference microphone for the uncoupled and coupled systems (frequency resolution between 90–200 Hz: 0.5 Hz, frequency resolution between 200–1000 Hz: 2 Hz), ①, ③: first and second peaks in the coupled system (110 Hz, 167 Hz), ②, ④: first and second troughs in the coupled system (113.5 Hz, 171 Hz), ⑤: frequency of the Helmholtz resonator mode in the uncoupled system (240 Hz), ⑥: frequency of the Helmholtz resonator mode in the coupled system (256 Hz), ⑦, ⑧: first trough and peak over the frequency of the Helmholtz resonator mode (290 Hz, 294 Hz).

Figure 4 shows the power spectra of the reference microphone signals of both the coupled and uncoupled systems up to 1 kHz. Above 1 kHz, the two responses are so close to each other that we cannot distinguish them. The major difference between them is in the low frequency range. Therefore, this paper concentrates the analysis of the results in the frequency range below 1 kHz. The results in Fig. 4 obviously contain information on coupling mechanisms. However, it is also obvious that exploring the meaning of the two curves without having any guidelines or a reference system, which we understand better than the system we attempt to analyze, would be very difficult. For this reason, we first introduce a simplified model which exhibits the basic coupling mechanisms under investigation.

A. A simplified model

Figure 5 shows the simplified structural-acoustic coupling model obtained by changing the plate and the hole to corresponding 1-DOF systems. The whole system is harmonically excited by a piston source. Let us assume that the exciting frequency is so low that the dimension of the cavity is much smaller than the wavelength; then the acoustic pressure p inside the cavity can be obtained as a constant magnitude throughout the cavity. For small variations in p and V, we can obtain[16]

$$-\frac{p}{(\Delta V/V_0)}=B, \tag{1}$$

where V_0 is the volume when no disturbance occurs and B is the bulk modulus of the media in the cavity. The motions of the 1-DOF systems can be expressed by impedance Z_1 and Z_2:

$$\frac{pS_1}{v_1}=Z_1, \tag{2a}$$

$$\frac{pS_2}{v_2}=Z_2, \tag{2b}$$

where v_i, S_i, and Z_i are velocity, surface area, and mechanical impedance of the ith system, respectively. By using the

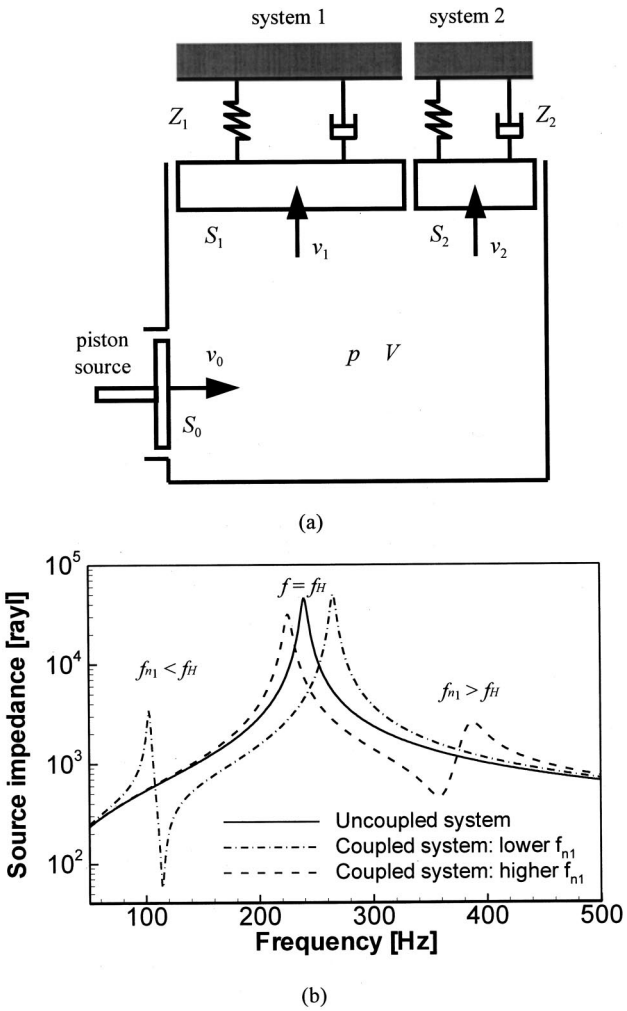

FIG. 5. A simplified model of the partially opened plate-cavity coupled system and its simulation result (f_H: frequency for the Helmholtz resonator mode, f_{n1}: the natural frequency of system 1). (a) A simplified lumped model under the assumption of low frequency, (b) simulation result: comparison between the models for the uncoupled and coupled systems.

notation M_i, C_i, and K_i for mass, damping, and stiffness of the ith system, we can express the impedance as

$$Z_1=j\omega M_1+C_1+\frac{K_1}{j\omega}, \tag{3a}$$

$$Z_2=j\omega M_2+C_2+\frac{K_2}{j\omega}. \tag{3b}$$

For harmonic excitation with a frequency of ω, the rate of volume change can be derived as

$$j\omega\Delta V=v_1S_1+v_2S_2-v_0S_0, \tag{4}$$

where v_0 and S_0 are the velocity and the surface area of the piston. With Eqs. (1), (2), and (4), we can readily obtain the source impedance z,

$$z = \frac{p}{v_0} = \frac{1}{j\omega(V_0/BS_0) + (S_1/Z_1)(S_1/S_0) + (S_2/Z_2)(S_2/S_0)}. \quad (5)$$

The first term of the denominator represents the admittance of the cavity. The following two terms mean the admittance of the 1-DOF systems. This equation says that the total admittance is equal to the summation of the admittance of each system. Because system 2 models the hole in the coupled system, the spring element, K_2, can be regarded as negligible. Then the imaginary part of the last term in the denominator has a negative value and the magnitude decreases as the frequency increases. On the contrary, the imaginary part of the first term has a positive value and increases as the frequency goes up. When system 1 is fixed so that the admittance is zero, the whole simplified model represents an uncoupled system. In this case, the source impedance z has the maximum absolute value at the frequency where the summation of the imaginary parts of the first and last terms cancel out. This frequency corresponds to the Helmholtz resonator mode of the uncoupled system. The solid line in Fig. 5(b) illustrates the frequency response of the uncoupled system. The peak around 240 Hz represents the Helmholtz resonator mode. For the coupled system the second term has either a positive or negative imaginary value depending on the frequency. At the natural frequency of system 1, it has a maximum value so that the impedance z or pressure p becomes very small. The frequency characteristics of the coupled system depend on the natural frequency of system 1 (f_{n1}). In a frequency range lower than the frequency for the Helmholtz resonator mode, f_H, the summation of the first and last terms has a negative imaginary value. Therefore, the zero value of the imaginary part of the denominator occurs when $\mathrm{Im}\{1/Z_1\} > 0$. This happens at a frequency lower than the natural frequency of system 1. At this frequency, the magnitude of the source impedance becomes very large. Thus, as the frequency around f_{n1} goes up, the source impedance and the pressure first have maximum values and then minimum values. The dashed–dotted line in Fig. 5(b) shows the result. On the contrary, if the natural frequency, f_{n1} is higher than f_H, the summation of the first and last terms has a positive imaginary value. Therefore, the imaginary part of the denominator becomes zero at a frequency higher than f_{n1}. In this case, z and p first have minimum values and then maximum values. The dashed line in Fig. 5(b) shows the result.

Because of the interaction of system 1 with the cavity, the peak frequency, f_H, which corresponds to the Helmholtz resonator mode also changes. When f_{n1} is lower than f_H, the second term has a negative imaginary value at the frequency f_H. Therefore, the imaginary part of the summation of the first and last terms must have a positive value for cancellation. This phenomenon occurs at a frequency higher than f_H. Similarly we can find that the peak frequency f_H shifts lower when f_{n1} is higher than f_H. Based on these simulation results we can easily explain the coupling effect for the experimental results.

B. Experimental results

Figure 4 demonstrates that several peak and null responses appear in the coupled system and the peak frequency 240 Hz is shifted to a higher frequency. This change in frequency responses are obviously results from the coupling effect between the plate and the two acoustic fields. Note that the arrangements of peaks and troughs in the frequency range below 240 Hz are different from those in the frequency range above 240 Hz. In the lower frequency range, peaks appear first, then troughs, but they do so in reverse order in the higher frequency range. These coupling phenomena are the same as those in the simulation results described in the preceding section. The differences are the number of peaks and troughs and their positions. The frequency shift of the peak for the Helmholtz resonator mode to higher means that the effect of the lower modes are dominant over the effect of the higher modes. It is noteworthy that the bandwidths of lower peaks and troughs (①, ②, ③, and ④ in Fig. 4) are narrower than those of higher ones (⑦ and ⑧ in Fig. 4). This is because the damping effect of the plate becomes larger as the frequency increases. [See the simulation results of the simplified model for the coupled system (Fig. 5)]. In the experimental result, the peak corresponding to the Helmholtz resonator mode is broader than those obtained by the simulation. This is because the simplified model disregards the exterior acoustic field; therefore, the energy loss occurs only by the damping element in system 2 (Fig. 5). However, in the experiment, the exterior field also plays the role of an effective energy absorbent. This is the reason the peak for the Helmholtz resonator mode has a broader bandwidth than the other peaks or troughs. It is clear that the acoustic behaviors of the selected system well represent the typical characteristics of coupling in the low frequency range, especially around the frequency of the Helmholtz resonator mode.

IV. MEASURED AND ESTIMATED SOUND FIELDS

A. Measured pressure distribution

In order to see how the coupled system behaves at those frequencies mentioned above, we examined the pressure distribution of the interior and exterior sound fields. Figure 6 shows the contour plots for the measured pressures at four frequencies: 110 Hz, 113.5 Hz, 167 Hz, and 171 Hz. Two of them (110 Hz and 167 Hz) correspond to the peaks (peak responses) and the others (113.5 Hz and 171 Hz) to the troughs (null responses) in Fig. 4. The pressures are normalized by the pressure at the reference microphone, p_{ref}. All the interior pressure distributions shown in the left-hand side have almost the same magnitude throughout the cavity. This is because the size of the cavity is much smaller than the wavelength. However, the distributions show that interior pressures near the hole have lower values than those at the opposite positions. This is consistent with what we expect: pressure has a higher value around the rigid wall than near the open end. In other words higher impedance induces higher pressure.

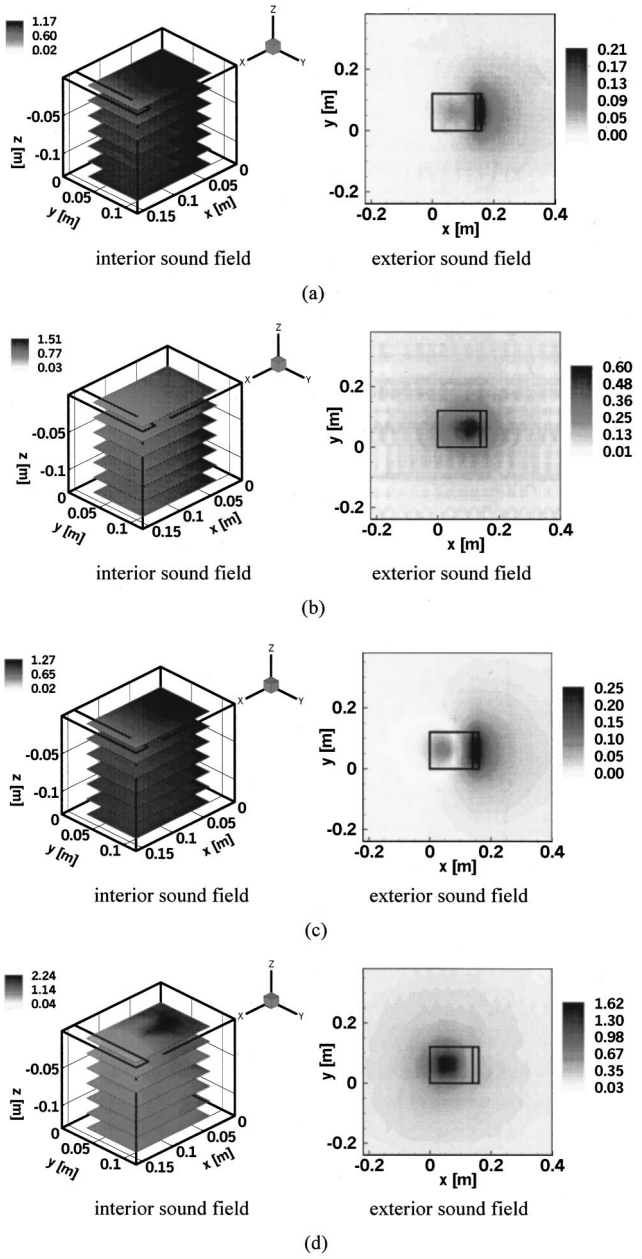

FIG. 6. The measured pressure normalized by the pressure at the reference microphone. The left figures show the interior sound field and the right figures the exterior one. (a) 110 Hz (the first peak frequency), (b) 113.5 Hz (the first trough frequency), (c) 167 Hz (the second peak frequency), (d) 171 Hz (the second trough frequency).

The figures on the right-hand side of Fig. 6 show the measured pressure distribution of the exterior field. Figures 6(a) and (c) have the pressure distributions where the pressure over the hole is much greater than over the plate. These two correspond to the peak responses ① and ③ in Fig. 4. In these cases the cavity has a larger direct interaction with the exterior field through the hole. On the other hand, Figs. 6(b) and (d) show the pressure distributions where pressure over the plate is greater than over the hole. These correspond to the null responses ② and ④ in Fig. 4. In these cases the cavity has a larger direct interaction with the exterior field through the plate. These frequencies are related to the natural frequencies of the plate [see Appendix B]. Note that the maximum values of normalized pressures are higher than those obtained in the peak responses. More details are presented in the next sections.

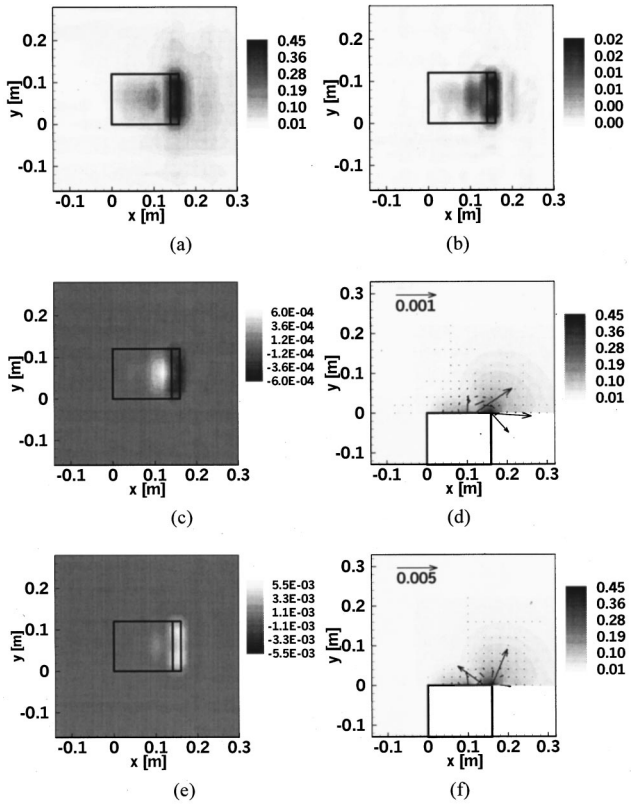

FIG. 7. Various normalized acoustic properties at the first frequency of peak response (110 Hz) (pressure, velocity, and intensity are normalized by p_{ref}, $p_{\mathrm{ref}}/\rho c$, and $p_{\mathrm{ref}}^2/\rho c$). (a) Normalized pressure, (b) normalized z-directional velocity, (c) normalized z-directional active intensity, (d) normalized pressure and normalized active intensity, (e) normalized z-directional reactive intensity, (f) normalized pressure and normalized reactive intensity.

B. Estimated sound fields in the exterior field-pressure, particle velocity, and intensity

To see more details, all acoustic variables such as pressure, particle velocity, and intensity were estimated from the measured pressures in the exterior field by using nearfield acoustic holography. To reduce the estimation error, zero padding was used in the forward prediction and the window that minimizes the associated errors[17] was applied during backward prediction. Figures 7 and 8 show the estimated acoustic values at the frequencies of the first null and peak responses. As mentioned before, the pressure is normalized by the pressure at the reference microphone, p_{ref}. The particle velocity and intensity are normalized by $p_{\mathrm{ref}}/\rho c$ and $p_{\mathrm{ref}}^2/\rho c$, respectively.

Figure 7(a) represents the estimated pressure fields on the source plane ($z=0$) at the frequency of the first peak response (110 Hz). They are very similar to the measured distribution [the figures on the right-hand side of Fig. 6(a)] except that the levels are higher. Figure 7(b) shows the estimated z-directional particle velocity on the source plane. The patterns of their distributions are similar to those of Fig. 6(a). Figures 7(c) and (e) represent the z-directional active and reactive intensities on the source plane. In the figures, white

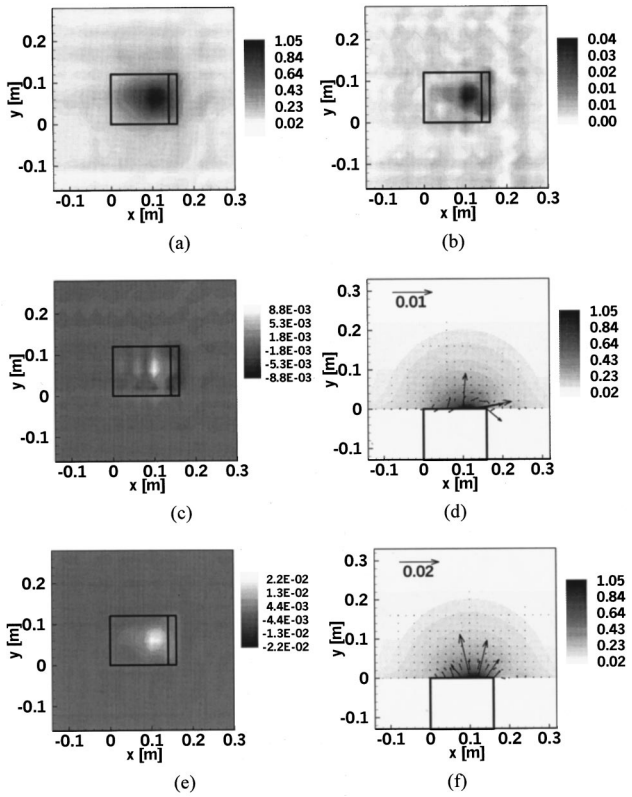

FIG. 8. Various normalized acoustic properties at the first frequency of null response (113.5 Hz) (pressure, velocity, and intensity are normalized by p_{ref}, $p_{\mathrm{ref}}/\rho c$, and $p_{\mathrm{ref}}^2/\rho c$). (a) Normalized pressure, (b) normalized z-directional velocity, (c) normalized z-directional active intensity, (d) normalized pressure and normalized active intensity, (e) normalized z-directional reactive intensity, (f) normalized pressure and normalized reactive intensity.

indicates the intensity going out to the positive z direction and black indicates the intensity going down to the negative z direction. If the baffle used in the experiment was rigid, then the intensity must be zero. The figures show that the values at the baffle are close to zero. The result shows both positive and negative values of the active intensity around the hole. Since the active intensity means the time-averaged energy flow, we can say that most of the acoustic energy averaged in time circulates through the plate and hole. Reactive intensity is related to the fluctuating energy in half a period.[18] It has a larger value near acoustic sources. The results show a positive value near the hole which means that there is a fluctuating energy flow through the hole. The active and reactive intensities on the vertical plane ($y=0.04$ m) are shown in Figs. 7(d) and (f). The contour plot of the pressure is also shown in the same figures. The reactive intensity is much greater than the active intensity since the size of the hole, which looks like an acoustic source when it is seen from the exterior field, is much smaller than the wavelength and the hole radiates the acoustic energy ineffectively. These intensity plots show that there is more energy flow between the interior and exterior sound fields than there is between the structure and the fluid. The sound field distributions at other frequencies with a peak response have similar characteristics to the one at 110 Hz.

Figure 8 shows the various acoustic values at 113.5 Hz

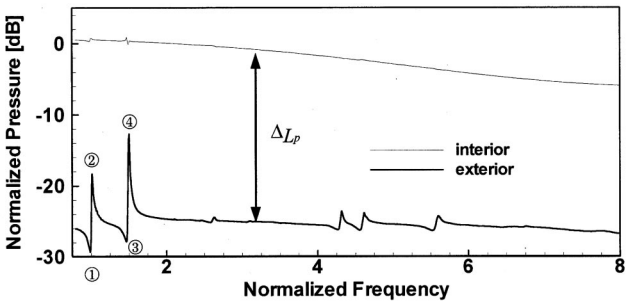

FIG. 9. The average values of normalized sound pressure levels between interior and exterior fields measured, ①, ③: first two trough frequencies (110 Hz and 167 Hz, which correspond to the frequencies of peak response, ① and ③ in Fig. 4), ②, ④: first two peak frequencies (113.5 Hz and 171 Hz, which correspond to the frequencies of null response, ② and ④ in Fig. 4).

which corresponds to the lowest frequency with a null response. The estimated pressure on the plate is much greater than the one on the hole. Velocity and active and reactive intensities have similar behavior. Contrary to the results at 110 Hz, the magnitudes of active and reactive intensities have comparable values and the values on the plate are greater. This means that the energy exchange between internal and external energy occurs to a great extent through the plate. We can say that there is strong coupling between the plate and the surrounding acoustic fields. The sound field distributions at other frequency with a null response have characteristics similar to those at 113.5 Hz.

V. SPATIALLY AVERAGED ACOUSTIC VARIABLES

A. Average pressures of the interior and the exterior fields

Examining the average pressure values between the interior and exterior fields is a good way to understand the coupling mechanism. Figure 9 shows the results. The average was taken over all the measured pressures. The pressures were normalized by the pressure at the reference microphone as done in Sec. IV. Frequency was normalized by 114 Hz, the fundamental natural frequency of the plate. This normalization will tell us the relative frequency ratio respect to the fundamental natural frequency of the plate. The thin line indicates the averaged pressure of the interior field and the thick line is for the exterior field. In the frequency range shown, the averaged interior pressure slowly decays with respect to the frequency. The reason is that as the frequency goes up the pressure distribution in the cavity varies more rapidly. That is, the size of the cavity relative to the wavelength becomes greater, although it still has a value smaller than one. Note that the first natural mode (1,0,0) of the cavity occurs above 1 kHz (Table I). This observation can be confirmed by examining a partially opened enclosure as shown in Fig. 10(a). When the frequency or wave number is nearly zero, the pressure distribution is almost constant throughout the cavity [Fig. 10(b)]. In this case the average value of the pressure is

$$(p^2)_{\mathrm{avrg}} \approx (p_{\max})^2, \tag{6}$$

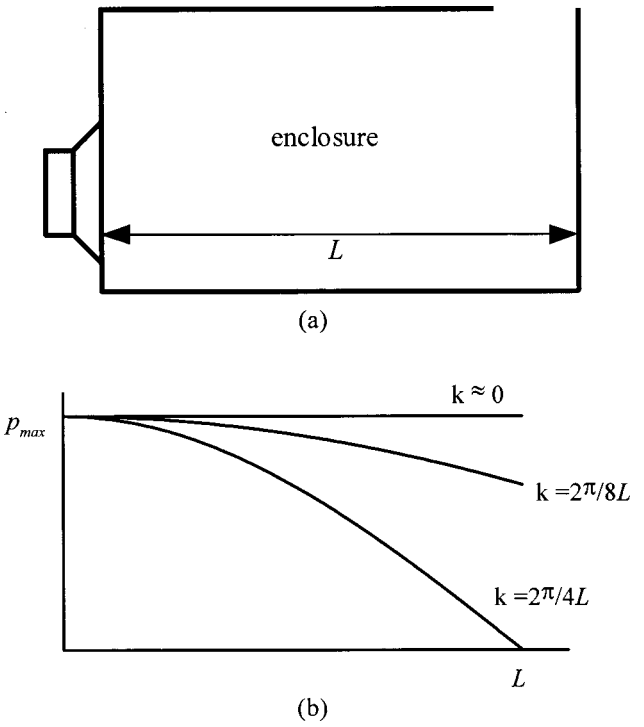

FIG. 10. (a) A partially opened enclosure excited by a speaker located at a side wall. (b) Pressure distribution in the enclosure at three frequencies: a frequency close to zero ($k \approx 0$), the frequency at which L is equal to 1/8 of wavelength ($k = 2\pi/8L$), and the frequency at which L is equal to quarter wavelength ($k = 2\pi/4L$).

where $p_{\max}$ is the maximum value. As the frequency goes up from zero to the frequency corresponding to a quarter of the wavelength [Fig. 10(b)], the average value slowly goes down to

$$(p^2)_{\text{avrg}} = \tfrac{1}{2}(p_{\max})^2 \tag{7}$$

which is the minimum value for the frequency of a quarter of the wavelength. It is 3 dB lower than the maximum pressure. If we consider a pressure drop in three directions, we can obtain a bigger pressure drop as obtained in the experiment.

The shape of the line for the exterior pressure is completely different from the one for the interior field. There are several peak and null responses which correspond to those in Fig. 4. The major difference is in the order of the peaks and troughs. This is because the pressures are normalized by p_{ref}. The level difference between the two values, ΔL_p, can be considered as a transmission loss. At the frequencies of peak response ② and ④ in Fig. 9, the acoustic energy radiates more effectively to the exterior field. On the other hand, at the frequencies of null response, ① and ③, the sound radiates ineffectively. These frequencies correspond to the frequencies of peak response in Fig. 4. This result indicates that the coupled system can be used as an efficient noise control element for narrow band noise.

B. Average acoustic variables on the plate and the hole

It would also be very interesting if we examine the spatially averaged acoustic values on the hole and the plate. This information certainly shows the roles of the plate and the hole which bridge the cavity and the exterior field.

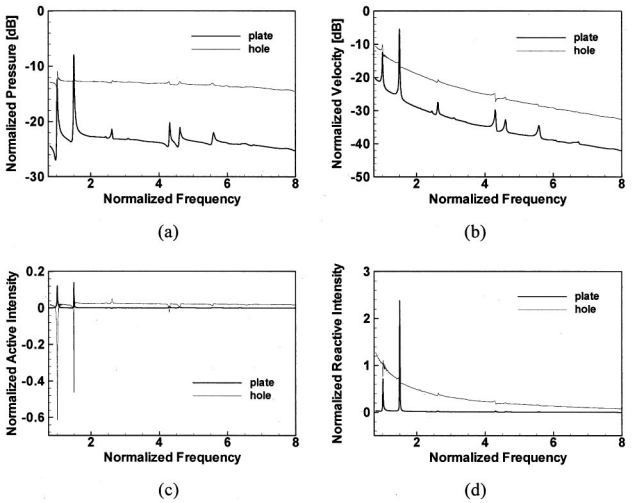

FIG. 11. Comparison between average values of normalized acoustic properties (pressure, velocity, and intensity are normalized by p_{ref}, $p_{\text{ref}}/\rho c$, and $p_{\text{ref}}^2/\rho c$). (a) Normalized pressures, (b) normalized velocities, (c) normalized active intensity, (d) normalized reactive intensity.

Figure 11 shows the average acoustic properties on the hole and the plate. Figures 11(a) and (b) show the average pressure and z-directional velocity levels. The acoustic values on the hole do not vary much according to frequency. However, the graphs for the plate have several peaks. These peaks correspond to the troughs in Fig. 4. At the peak frequencies the differences between the average pressure and velocity levels on the plate is small. Even at the second peak, the levels on the plate are greater than the ones on the hole. As mentioned before, this is because the strong coupling occurs at these peak frequencies. Figures 11(c) and (d) are the graphs for active and reactive intensities. As the results in Figs. 11(a) and (b) demonstrate, there exist several peaks at the same locations. The interesting result is that the coupling effect at the frequencies of peak response in Fig. 4 is negligible, which means the coupling mechanism is weak at those frequencies.

VI. CONCLUDING REMARKS

We experimentally studied a coupling system (a cavity system coupled with a plate and an exterior acoustic field) excited by an acoustic source at a wall of the cavity. The cavity is excited by a source and its behavior is affected by the plate and the exterior acoustic field. The movement of the plate is also affected by the cavity and the exterior field. The exterior acoustic field is constructed by the energy going out through the plate and the hole. This system is selected to express a coupling system that exhibits typical and general coupling phenomena.

From the results we found that the frequency characteristics are totally dependent on the properties of the plate, especially at the low frequency region where the cavity mode does not occur. The presence of the plate gives additional peaks and troughs in the frequency response. Their corresponding frequencies are related to the natural frequency of

the plate, at which the impedance becomes small. These are the well-known characteristics of a structural-acoustic coupling system. At those frequencies the exterior sound field has a complex pattern around the plate, whereas the sound field inside the cavity has a smooth pattern. The reason is that the acoustic wavelength is much greater than the wavelength of the plate. The interesting thing we found is the arrangement of the peaks and troughs. Below the peak frequency for the Helmholtz resonator mode, peaks appear first and then troughs. However, above the peak frequency the order is reversed. This is because the combination of the masslike or springlike behavior of the hole and the cavity differs in those two regions and plays different roles on the plate. The frequency shift of the peak for the Helmholtz resonator mode to higher frequency is another main coupling effect. This phenomenon results from the effect of the lower frequency modes of the plate, which have masslike behavior at that peak frequency. Therefore, the magnitude of the admittance increases by the mass effect and physically the coupled system appears to have a smaller effective mass, which leads to a Helmholtz resonator mode at a higher frequency.

Around the peaks and troughs, the coupling phenomena vary with frequency and can be classified into two categories: weak and strong coupling. At frequencies where the movement of air near the hole is dominant over the plate, the plate can be considered as rigid and most of the energy goes through the hole. This is weak coupling between the plate and the cavity. At frequencies where the plate vibrates more intensively so that the sources look like they are distributed over it, more energy flows through the plate than through the hole. These findings, in fact, highlight the study on the general coupling phenomena. The cavity can be a place where we have to put a noise source and we often have to design a means of noise control by using an additional structure but allowing some space so that the machine can take fluid from the outside. This study offers a guideline for designing noise control devices.

As frequency goes up to the region where the cavity mode occurs, the wavelength of the plate becomes smaller so that the rigidity and impedance of the plate increase. Therefore, the plate behaves as if it were a rigid wall. The figure which shows the difference between the coupled and uncoupled systems supports this fact. In other words, we can find small differences in the high frequency range but much smaller than those in the low frequency range. Therefore, the cavity appears to interact with the exterior field only, that is, the coupling with the plate is very weak and only the hole radiates sound, not the plate.

ACKNOWLEDGMENTS

This paper is performed with financial support by the Korea Science and Engineering Foundation (KOSEF, Project Number 98-0200-06-01-3), the Korea Institute of Science and Technology Evaluation and Planning (KISTEP, ''National Research Laboratory'' Project), and the Ministry of Education (''Brain Korea 21'' Project).

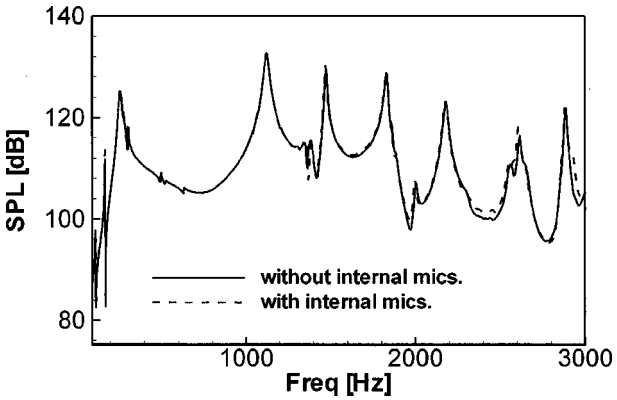

FIG. A1. Comparison of the reference microphone signals (solid line: measured SPL when there is no internal microphone in the cavity, dashed line: measured SPL when the internal microphones were put into the cavity).

APPENDIX A: THE SCATTERING EFFECT OF THE INTERNAL MICROPHONES ON THE SOUND FIELD IN THE CAVITY

In order to determine the scattering effect of the internal microphones on the sound field in the cavity, we performed a simple experiment with the coupled system used in this study. First, we measured the frequency response function (the pressure signal at the reference microphone relative to the voltage input of the horn driver) in the absence of the internal microphones. After putting the internal microphones into the cavity, we measured the frequency response function again. Figure A1 shows the results. Comparing the results we concluded that we can ignore the scattering effect up to about 2 kHz which is much higher than the highest frequency of our interest (1 kHz).

APPENDIX B: MODAL TESTING OF THE PLATE

We did modal testing of the plate by using an accelerometer and an impulse hammer. The bottom wall of the cavity was removed in order to reduce the cavity effect. The accelerometer was fixed at one corner of the end (having a free boundary condition) of the plate during the experiment. The number of impact points was 7(x) by 5(y) and the spacing was 2 cm. Table BI shows the resonance frequencies of the plate. The analysis by using simplified model described in Sec. III A shows that the response of the coupled system has a trough at around the natural frequency of the uncoupled lumped system (system 1). However, the trough frequencies in Fig. 4, where we observed very strong structural coupling, are not exactly the same as those of the natural frequencies of the plate alone (Table BI). This discrepancy

TABLE BI. First four resonance frequencies of the plate in the absence of the bottom wall of the cavity (l,m: number of nodal lines in the x and y directions, spectral resolution: 1 Hz).

Mode (l,m)	Resonance frequency (Hz)
(0,0)	114
(1,0)	165
(0,1)	281
(1,1)	348

comes from the modeling errors. Fluid loading effect on the structure and damping effect are only two of them. The model used here is devised to qualitatively explain the coupling between structure and fluid. More accurate model that can consider the coupling effect more precisely has to be developed and this is beyond this paper's objectives.

[1] E. H. Dowell and H. M. Voss, ''The effect of a cavity on panel vibration,'' AIAA J. **1**, 476–477 (1963).
[2] R. H. Lyon, ''Noise reduction of rectangular enclosures with one flexible wall,'' J. Acoust. Soc. Am. **35**, 1791–1797 (1963).
[3] A. J. Pretlove, ''Free vibrations of a rectangular panel backed by a closed rectangular cavity,'' J. Sound Vib. **2**, 197–209 (1965).
[4] A. J. Pretlove, ''Forced vibrations of a rectangular panel backed by a closed rectangular cavity,'' J. Sound Vib. **3**, 252–261 (1966).
[5] P. M. Morse, ''Transmission of sound through a circular membrane in a plane wall,'' J. Acoust. Soc. Am. **40**, 354–366 (1966).
[6] R. W. Guy, ''The steady state transmission of sound at normal and oblique incidence through a thin panel backed by a rectangular room—a multi-modal analysis,'' Acustica **43**, 295–304 (1979).
[7] C. R. Fuller and F. J. Fahy, ''Characteristics of wave propagation and energy distribution in cylindrical elastic shells filled with fluid,'' J. Sound Vib. **81**, 501–518 (1982).
[8] D. J. Nefske, J. A. Wolf, Jr., and L. J. Howell, ''Structural-acoustic finite element analysis of the automobile passenger compartment,'' J. Sound Vib. **80**, 247–266 (1982).
[9] J. Pan, C. H. Hansen, and D. A. Bies, ''Active control of noise transmission through a panel into a cavity: I. Analytical study,'' J. Acoust. Soc. Am. **87**, 2098–2108 (1990).
[10] J. Pan and C. H. Hansen, ''Active control of noise transmission through a panel into a cavity: II. Experimental study,'' J. Acoust. Soc. Am. **90**, 1488–1492 (1991).
[11] J. Pan and D. A. Bies, ''The effect of fluid-structural coupling on acoustical decays in a reverberation room in the high-frequency range,'' J. Acoust. Soc. Am. **87**, 718–727 (1990).
[12] K. S. Sum and J. Pan, ''An analytical model for bandlimited response of acoustic-structural coupled systems. I. Direct sound field excitation,'' J. Acoust. Soc. Am. **103**, 911–923 (1998).
[13] K. S. Sum and J. Pan, ''A study of the medium frequency response of sound field in a panel-cavity system,'' J. Acoust. Soc. Am. **103**, 1510–1519 (1998).
[14] N. H. Fletcher and T. D. Rossing, *The Physics of Musical Instruments* (Springer-Verlag, New York, 1991), pp. 216–217.
[15] D. Maynard, E. G. Williams, and Y. Lee, ''Nearfield acoustic holography: I. Theory of generalized holography and development of NAH,'' J. Acoust. Soc. Am. **78**, 1395–1413 (1985).
[16] L. E. Kinsler *et al.*, *Fundamentals of Acoustics*, 3rd ed. (Wiley, New York 1982), p. 101.
[17] Hyu-Sang Kwon and Yang-Hann Kim, ''Minimization of bias error due to windows in planar acoustic holography using a minimum error window,'' J. Acoust. Soc. Am. **98**, 2104–2111 (1995).
[18] F. J. Fahy, *Sound Intensity* (Elsevier Applied Science, New York, 1989), Chap. 4.

Numerical simulation of acoustic wave phase conjugation in active media

S. Ben Khelil and A. Merlen[a)]
Laboratoire de Mécanique de Lille ura CNRS 1441 Cité scientifique, 59655 Villeneuve d'Ascq, France

V. Preobrazhensky
Wave Research Center of General Physics Institute Academy sc., 38 Vavilova Street, 117942 Moscow, Russia

Ph. Pernod
Institut d'Electronique et Microelectronique du Nord, DOAE, umr CNRS 8520, 59655 Villeneuve d'Ascq, France

(Received 18 January 2000; revised 18 September 2000; accepted 3 October 2000)

Godunov-type computation schemes are applied to numerical simulations of wave propagations in time-dependent heterogeneous media (solids and liquids). The parametric phase conjugation of a wide band ultrasound pulse is considered. The supercritical dynamics of the acoustic field is described for one-dimensional systems containing a parametrically active solid. The impulse response function, numerically calculated for a finite active zone in an infinite medium above the threshold of absolute parametric instability, is in a good agreement with the analytical asymptotic theory. The supercritical evolution of the acoustic field spatial distribution is studied in detail for parametric excitations in an active zone of a solid layer, loaded by a semi-infinite liquid on one side and free on the other. © *2001 Acoustical Society of America.* [DOI: 10.1121/1.1328794]

PACS numbers: 43.25.Dc, 43.25.Lj [MFH]

I. INTRODUCTION

The problem of wave propagation in a nonstationary medium when parameters depend on time is of fundamental interest because of its various applications in acoustics and solid state physics. The parametric wave phase conjugation (WPC) in photorefractive media is an example of such applications.[1] In acoustics, parametric WPC has been studied for liquids and solids (water and water with gas bubbles,[2,3] piezoelectrics,[4,5] magnetics,[6] and piezo-semiconductor systems[7]). The modulation of the acoustic parameters of solids is usually carried out by means of rf, microwave, or optical pumping, distributed almost homogeneously in the active zone of the medium. There are no exact analytical solutions to the general problem of parametric WPC. The perturbation theory is applicable for relatively weak parametric interactions under the threshold of absolute parametric instability. Above the threshold (in a supercritical mode), multiscale asymptotic expansion methods (MSAE) can be used to describe narrow band resonance parametric interactions.[4,8] Recently the problem of WPC has been discussed extensively in the context of ultrasound time reversal transformation for applications in nondestructive testing and medicine.[6,9] Acoustic signals of wide relative frequency band are of practical interest, though the applicability of MSAE methods under such conditions becomes problematical.

For this reason, the development of numerical methods adapted to the problem seems to be a productive research direction. On the basis of the propagation properties involved in the phenomenon it is possible to show that the mathematical problem falls within the scope of hyperbolic partial differential systems. Therefore the numerical background developed in the last decade within the frame of unsteady aerodynamics can be applied to this problem and, particularly, all the Godunov family schemes[10] including the weighted average flux method (WAF) of Toro.[11]

The present paper represents the first application of this approach to the problem of wave propagation in nonstationary medium. An example of supercritical parametric WPC of a wide band acoustic pulse is considered. In order to compare numerical results with analytical solutions[4,8] the model of localized active zone in infinite solid is studied for narrow band pumping. The time evolution of the elastic stress distribution is presented. The shape of the phase conjugate pulse is in satisfactory agreement with the analytical calculation. The problem is also adapted to generic experimental conditions, when the active solid is loaded by a liquid medium on one flat boundary and is free on the opposite one. The parametric amplification of ultrasound reverberations observed earlier in experiments[12] is correctly described by the numerical simulation.

II. MATHEMATICAL FORMULATION

A. Fluid media

The basic idea of the present numerical approach comes from the natural formation of acoustics in fluids. It is well known that in a nondissipative fluid, the linearized Euler equation can be written:

$$\frac{\partial \rho}{\partial t} + \rho_0 \nabla \cdot \mathbf{V} = 0, \quad \frac{\partial \mathbf{V}}{\partial t} + \frac{1}{\rho_0} \nabla p = 0, \quad \frac{dp}{d\rho} = c^2, \tag{1}$$

where ρ, p, $\mathbf{V}$, and c are, respectively, the density, pressure, fluid velocity, and sound speed in the medium.

a)Electronic mail: Alain.merlen@univ-lille1.fr

The active medium is defined by a given function $C(t)$ such as

$$c = C(t).$$

Hence, since $\partial\rho/\partial t = (1/c^2)(\partial p/\partial t)$, system (1) rewritten for p and $\mathbf{V}$ reduces to

$$\frac{1}{\rho_0 c}\frac{\partial p}{\partial t} + c\,\boldsymbol{\nabla}\cdot\mathbf{V} = 0, \quad \frac{\partial \mathbf{V}}{\partial t} + c\left[\frac{1}{\rho_0 c}\nabla p\right] = 0. \tag{2}$$

The acoustic equations usually follow from the change of variable

$$\theta = \frac{p - p_0}{p_0 c},$$

where p_0 is the uniform steady pressure of the medium at rest. Here system (1) becomes

$$\frac{\partial \theta}{\partial t} + c\,\boldsymbol{\nabla}\cdot\mathbf{V} = -\frac{\theta}{c}\frac{\partial c}{\partial t}, \quad \frac{\partial \mathbf{V}}{\partial t} + c\nabla\theta = 0. \tag{3}$$

If c were a constant, this would be the classical system of acoustics in fluids but, in this case, a source term appears on the right-hand side. In fact, function $C(t)$ is nothing but a small modulation of c_0, the sound velocity of the medium at rest. In the following, $C(t)$ is assumed, for all practical purposes, to be given by

$$C(t)^2 = c_0^2(1 + m\cos(\Omega t + \Psi)),$$

where m is a small parameter ($m \ll 1$) referred as the ''modulation depth.'' It is clear that system (3) can be linearlized and replaced by

$$\begin{aligned} &\frac{\partial \theta}{\partial t} + c_0\,\boldsymbol{\nabla}\cdot\mathbf{V} = m\Omega\frac{\theta}{2}\sin(\Omega t + \Psi), \\ &\frac{\Omega \mathbf{V}}{\partial t} + c_0\nabla\theta = 0. \end{aligned} \tag{4}$$

The source term reflects the active effect that becomes sensitive for high frequencies. The left-hand side term is the linear advection operator, which is the basic linear hyperbolic system. All the numerical methods for compressible fluids have been tested on this advection system and, particularly, all the Godunov-type schemes. Owing to flux splitting techniques, these finite volume schemes are essentially a sequence of one-dimensional operators. Therefore, the one-dimensional problem is crucial for numerical methods. Moreover, this corresponds to an unavoidable first step in a detailed physical description of the process that can only be provided by numerical methods if these are sufficiently accurate. In many respects, a numerical solution of

$$\begin{aligned} &\frac{\partial \theta}{\partial t} + c_0\frac{\partial v}{\partial x} = m\frac{\Omega\theta}{2}\sin(\Omega t + \Psi), \\ &\frac{\partial v}{\partial t} + c_0\frac{\partial \theta}{\partial x} = 0, \end{aligned} \tag{5}$$

gives more information on the efficiency of the methods and on the physical behavior of solutions that a direct resolution of a three-dimensional (3D) case with all the unessential features caused by purely geometrical effects or by mesh problems. Moreover, the physics involved in the 3D effect is well known: it is essentially the conversion between longitudinal and transverse waves when reflections occur. In this case, the most important goal is the physical understanding of the pumping effects. This means that the source term is more essential than the advection operator. Therefore, a highly refined one-dimensional (1D) simulation is more reliable for a first attempt than a 3D case, which is inevitably less refined because of the limited capacity of the computers. Local refinement techniques are less helpful here than in other applications since the high frequencies of the spatial variations are not localized as in the case of shock waves in fluid mechanics. In such a case, rapid spatial variations concern the whole computational domain.

Matters become clearer in 1D, and as a result upgrading to a 3D becomes an engineering problem which is not trivial but generally carried out well by developers. In the frame of flux splitting techniques, this consists in building the 3D operator as a sequence of 1D.

Introducing new variables $w_1 = v + \theta$, $w_2 = v - \theta$, Eq. (5) can be rewritten:

$$\begin{aligned} &\frac{\partial w_1}{\partial t} + c_0\frac{\partial w_1}{\partial x} = m\frac{\Omega}{4}(w_1 - w_2)\sin(\Omega t + \Psi), \\ &\frac{\partial w_2}{\partial t} + c_0\frac{\partial w_2}{\partial x} = -m\frac{\Omega}{4}(w_1 - w_2)\sin(\Omega t + \Psi). \end{aligned} \tag{6}$$

The problem finally comes down to two advection equations in opposite directions coupled by linear source terms. Apparently the numerical treatment of such problems is well known but the need to manage high frequencies makes it less trivial than it seems at a first glance. The scheme has to be robust and very weakly dissipative.

Before beginning the numerical treatment, it is worth extending the approach to elastic active solid media. In this field, experimental works and analytical theories are much more developed than for fluids.

B. Elastic solid media

For linear elasticity, the formulation in the previous form is less natural. Let it be assumed that the stress tensor is

$$\boldsymbol{\sigma} = \lambda(t)\,\boldsymbol{\nabla}\cdot\mathbf{u}\mathbf{I} + 2\mu(t)\boldsymbol{\varepsilon}.$$

Vector $\mathbf{u}$ is the displacement and $\boldsymbol{\varepsilon}$ the small deformation tensor:

$$\boldsymbol{\varepsilon} = \tfrac{1}{2}(\nabla\mathbf{u} + (\nabla\mathbf{u})^T).$$

Here, the Lame coefficients λ and μ can depend on time but not on the space coordinates. Consequently the classical deviation of the wave equations from the Navier equation for constant λ and μ still holds.

Briefly, by splitting $\mathbf{u}$ in $\mathbf{u}_l = \nabla\psi$ and $\mathbf{u}_t = \boldsymbol{\nabla}\times\mathbf{A}$ (Helmholtz decomposition), the momentum equation $\rho(\partial^2\mathbf{u})/(\partial t^2) = \boldsymbol{\nabla}\cdot\boldsymbol{\sigma}$ gives

$$\Delta\psi - \frac{1}{c_l^2}\frac{\partial^2\psi}{\partial t^2} = 0, \tag{7}$$

$$\Delta \mathbf{A} = -\frac{1}{c_t^2}\frac{\partial^2 \mathbf{A}}{\partial t^2} = 0 \tag{8}$$

with $c_l^2 = (\lambda + 2\mu)/(\rho)$ and $c_t^2 = \mu/\rho$.

Starting with the compression wave $\mathbf{u}_l$, the following change of variables is introduced:

$$\theta_l = -\frac{1}{c_l}\frac{\partial^2 \psi}{\partial t^2}, \quad \mathbf{v}_l = \frac{\partial \mathbf{u}_l}{\partial t} = \nabla \frac{\partial \psi}{\partial t},$$

and consequently,

$$\nabla \theta_l = -\frac{1}{c_l}\frac{\partial \mathbf{v}_l}{\partial t}, \tag{9}$$

Moreover the wave equation (7) becomes

$$\theta_l + c_l \boldsymbol{\nabla}\cdot\mathbf{u}_l = 0 \tag{10}$$

or

$$\frac{\partial \theta_l}{\partial t} + c_l \boldsymbol{\nabla}\cdot\mathbf{u}_l = -\boldsymbol{\nabla}\cdot\mathbf{u}_l \frac{\partial c_l}{\partial t}, \tag{11}$$

which can be rewritten according to (10):

$$\frac{\partial \theta_l}{\partial t} + c_l \boldsymbol{\nabla}\cdot\mathbf{u}_l = \frac{\theta_l}{c_l}\frac{\partial c_l}{\partial t}. \tag{12}$$

Therefore, Eqs. (9) and (12) once again give system (3) but with a source term of the opposite sign.

In one-dimensional (1D) problems and after linearization around the sound velocity c_{0_l} of the medium at rest, the system becomes

$$\begin{aligned} &\frac{\partial w_1}{\partial t} + c_{0_l}\frac{\partial w_1}{\partial x} = -m\frac{\Omega}{4}(w_1 - w_2)\sin(\Omega t + \Psi), \\ &\frac{\partial w_2}{\partial t} + c_{0_l}\frac{\partial w_2}{\partial x} = m\frac{\Omega}{4}(w_1 - w_2)\sin(\Omega t + \Psi). \end{aligned} \tag{13}$$

The sign of the source term is irrelevant for the amplitude evolution and corresponds only to a phase shift of π between solids and fluids. This difference arises from the fact that, in fluids, the dilatation rate $\boldsymbol{\nabla}\cdot\mathbf{V}$ is not directly related to pressure variations by a constitutive law but indirectly, through the mass conservation, by an unsteady thermodynamic process $dp = c^2(t)d\rho$. Conversely, for solids, in the one-dimensional assumption ($\mathbf{u} = \mathbf{u}_l$, $\partial/\partial y = \partial/\partial z = 0$), it is easy to verify from expressions of $\boldsymbol{\sigma}$ and c_l that the normal stress in direction x is

$$\sigma_{xx} = -\frac{\lambda + 2\mu}{c_l}\theta_l = -\theta_l \rho c_l.$$

Hence Eq. (10) is just the reduction of the constitutive law for normal stress in direction x. Obviously, solids differ from fluids, even in 1D, by the fact that the stress tensor is not isotropic for solids, the normal stress in the y and z directions being $-\lambda\,\theta_l/c_l$.

The case of shear waves can be treated identically but with the variables

$$\boldsymbol{\theta}_t = -\frac{1}{c_t}\frac{\partial \mathbf{u}_t}{\partial t} \quad \text{and} \quad \mathbf{T}_t = \boldsymbol{\nabla}\mathbf{u}_t.$$

Nevertheless, in one dimension, no mode changes are expected even at the interfaces, and consequently, no shear waves appear unless they exist initially in the medium. For the clarity of the analysis, we now suppose that this condition is fulfilled.

C. Numerical method

Systems (6) and (13) can be written symbolically

$$\begin{aligned} &\frac{\partial U}{\partial t} + \frac{\partial F(U)}{\partial x} = S, \quad \forall x \in \mathbb{R}, t \geqslant 0, \\ &U(x,0) = U_0(x) \quad \forall x \in \mathbb{R} \end{aligned} \tag{14}$$

and

$$F(U) = \begin{pmatrix} c_0 w_1 \\ -c_0 w_2 \end{pmatrix}, \quad U = \begin{pmatrix} w_1 \\ w_1 \end{pmatrix},$$

and

$$S = \pm \begin{pmatrix} m\dfrac{\Omega}{4}(w_1 - w_2)\sin(\Omega t + \Psi) \\ -m\dfrac{\Omega}{4}(w_1 - w_2)\sin(\Omega t + \Psi) \end{pmatrix},$$

depending on the case (solid or fluid). System (14) is solved by an explicit finite volume method. The spatial domain is shared in N cells of length Δx and the time step is Δt. The numerical solution $U_i^n = U(i\Delta x, n\Delta t)$ is obtained at time $(n+1)\Delta t$ by

$$U_i^{n+1} = U_i^n - \frac{\Delta t}{\Delta x}[f_{i+1/2}(U^n) - f_{i-1/2}(U^n)] + \Delta t S(U_i^n), \tag{15}$$

where the numerical fluxes $f_{i+1/2}$ and $f_{i-1/2}$ determine the scheme. This is a first-order accurate method for time integration. Second-order methods are of course available but not of great interest here since the time step is determined more by physical than numerical reasons. It must be emphasized that the pumping is a very quick oscillation of frequency 2×10^7 Hz, leading to characteristic times of order 10^{-8} s. Time steps of order 10^{-9} s are therefore necessary for a good description of the phenomenon. As long as the simulation is 1D the advantage of a second-order time marching technique is not clear since, for the physical reasons mentioned, the time step cannot be one order of magnitude higher and conversely the numerical procedure can be more time consuming. Moreover, for a first simulation of the phenomenon, the first-order time marching method was unavoidable, at least as a reference.

The choice of the numerical fluxes f at the cell interface characterizes the scheme and particularly the spatial accuracy, which is much more important that the accuracy of the time procedure because it is linked to the dissipation properties of the scheme. Tests have been performed with the basic first-order Godunov scheme[10] and its extension to second-order using the monotone upstream centered scheme for conversion laws[13] approach with limiters. Finally the second-order WAF[11] (weighted average flux) and the superbee

limiter[14] appeared to be the most accurate combination for the problem treated here. Hence, the numerical fluxes are

$$f_{i+1/2}(U_{i+1}^n, U_i^n) = \alpha_1 F(U_i^n) + \alpha_2 (U_{i+1}^n) \tag{16}$$

with α_1 and α_2 obtained by

$$\alpha_1 = \tfrac{1}{2}(1+\nu)$$

and

$$\alpha_2 = \tfrac{1}{2}(1-\nu),$$

where $\nu = c_0 \Delta t/\Delta x$ is the Courant number associated with the wave speed c_0. The partial fluxes $F(U_i^n)$ and $F(U_{i+1}^n)$ represent the upwind and the downwind parts of the total flux. The weights α_1 and α_2 control the contributions of the partial fluxes; α_1 is responsible for stability while α_2 is responsible for accuracy and oscillations. The flux limiter has the role of limiting the contribution of the downwind term. Denoting a flux limiter by $B_{i+1/2}$ the weights α_1 and α_2 are modified in Eq. (16) as follows:

$$\overline{\alpha_1} = \alpha_1 + (1 - B_{i+1/2})\alpha_2, \quad \overline{\alpha_2} = \alpha_2 B_{i+1/2}. \tag{17}$$

The flux limiter used here is the so-called superbee. The corresponding limiting function is

$$B_{i+1/2} = \begin{cases} (1-2(1-|\nu|))/|\nu|, & r_i \geqslant 2 \\ (1-r_i(1-|\nu|))/|\nu|, & 1 \leqslant r_i \leqslant 2 \\ 1, & \tfrac{1}{2} \leqslant r_i \leqslant 1 \\ (1-2r_i(1-|\nu|))/|\nu|, & 0 \leqslant r_i \leqslant \tfrac{1}{2} \\ 1/|\nu|, & r_i \leqslant 0 \end{cases} \tag{18}$$

with

$$r_i = \frac{u_i^n - u_{i-1}^n}{u_{i+1}^n - u_i^n} \tag{19}$$

and $\nu = 0.6$.

D. The interface problem in 1D

Numerical simulations help to explain phenomena which could not be accounted for by experiments or analytical results. For instance, the instantaneous stress field inside a sample of active medium is not available in experiments, or the effect of wave reflections on the sample boundary requires very complicated theoretical developments in the frame of purely analytical analysis. This latter issue is easily treated in the present approach by solving the classical problem of ''resolution of a discontinuity,'' which provides the numerical fluxes in the Godunov family scheme under the name of the ''Riemann problem.''

The interface separates two nonactive media: R (right) and L (left). Equations (6) and (13) are then strictly identical, and, for the 1D case, solid and fluid are hence treated in the same way. In medium R, of sound velocity c_R, the initial state is (U_R, θ_R) and (U_L, θ_L) in medium L with c_L as sound velocity (Fig. 1). In Fig. 1, under characteristic C_0^-, the left-hand side remains in its original state because no information comes from the interface. The same happens under characteristic C_0^+ on the right-hand side. Between C_0^- and the interface i, the uniform solution 1 gives the state on the left-hand side where C^+ comes from state R and C^- from the interface where the variables are unknown. Solution 2 is the equivalent of 1 for the right-hand side. Nevertheless, characteristics C^- in sector 1 and C^+ in sector 2 gives no information. The missing relations for the determination of states 1 and 2 are supplied by the continuity of stresses and normal velocities at the interface, of velocity v_i. This gives

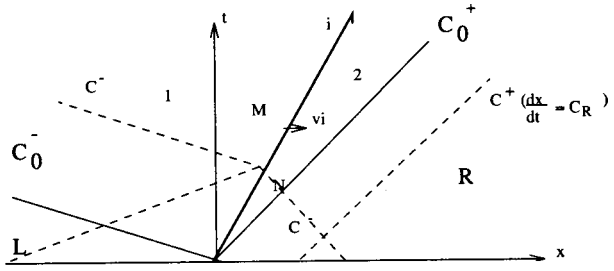

FIG. 1. Riemann problem at the interface. Characteristics C_0^+ and C_0^- limit the unperturbed zones R and L. Zones 1 and 2 are the uniform states at each side of the interface i.

$$\theta_2 = \tau\theta_1, \quad v_2 = v_1 = v_i,$$

where $\tau = \rho_L c_L/\rho_R c_R$ is the transmission coefficient. Subscript 1 corresponds to the solution in the medium originally in state L and subscript 2 in the medium originally in state R. For all the C^+ characteristics coming from sector L, the invariant relation gives

$$v_1 + \theta_1 = v_L + \theta_L$$

and for all the C^- coming from sector R:

$$v_2 - \theta_2 = v_R + \theta_R.$$

Since $v_1 = v_2 = v_i$ and $\theta_2 = \tau\theta_1$, elimination of θ_1 between these four equations leads to

$$v_1 = v_2 = v_i = \frac{1}{1+\tau}[\tau v_L + v_R] + \frac{1}{1+\tau}[\tau\theta_L - \theta_R]$$

and consequently,

$$\theta_1 = \frac{1}{1+\tau}[v_L - v_R] + \frac{1}{1+\tau}[\theta_L + \theta_R].$$

When $\tau = 1$ the solution corresponds to the Riemann problem of the linear advection system in an homogeneous medium as given by Godunov. For $\tau \to 0$, medium R is infinitely rigid ($c_R \to \infty$) and the solution is $\theta_1 = v_L + \theta_L$, $v_1 = v_i = v_2 = 0$, which corresponds to the ''half Riemann'' problem often used for reflective boundary conditions for the linear advection system. When $\tau \to \infty$, medium R is a vacuum and $\theta_1 = \theta_2 = 0$, $v_1 = v_2 = v_L + \theta_L$.

The present solution provides all the data needed for computing the fluxes at interfaces between nonactive zones in any 1D situation.

The boundary between active and passive zones is simulated in a very straightforward way by switching off the source terms in the passive zone. The same is done in an active zone as soon as the pumping is stopped.

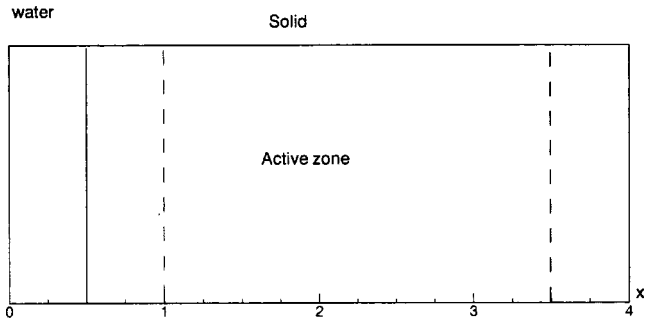

FIG. 2. Computational domain: The active zone (length 2.5 cm) is limited by dashed lines, the interface water–solid is at abscissa 0.5 cm, the boundary at 0 cm is nonreflective, and the boundary at 4 cm is stress free (vacuum).

III. RESULTS AND DISCUSSION

The numerical method and the interface problem have been tested on the configuration presented in Fig. 2. From $x=0-0.5$ cm the medium is water and the sample of magnetoacoustic ferrite is situated between $x=0.5$ cm and $x=4$ cm. The active zone lies between $x=1$ cm and $x=3.5$ cm. The mesh contains 1000 points in water and 7000 points in the sample. This global refinement is only possible in 1D and underlines the great interest of these simulations in terms of reference for further multidimensional computations. For 2D or symmetry of revolution, a direct extrapolation of the present numerical method is still possible but for 3D the number of points would be too high. Even local refinement–derefinement methods are of little use because the refinement would be needed almost everywhere in the computational domain. A productive research direction is a numerical simulation of the amplitude of the wave without the quick oscillation, the main issue here being the derivation of suitable conditions at the interface.

In this case, the boundary condition at $x=0$ cm is nonreflective as if the domain $x<0$ were filled by water too. At $x=4$ cm an absence of stress can be assumed as if a vacuum existed for $x>4$ cm. The initial condition is given in the following form:

$$W_1 = 2\sin\left(\frac{2\pi}{\lambda}(x-x_L)\right) \quad \text{for } x_L<x<0.5,$$

$$W_2 = 0 \quad \text{for } x_L<x<0.5, \tag{20}$$

$$W_1 = W_2 = 0 \quad \text{elsewhere.}$$

Abscissa x_L is chosen such as $(0.5-x_L)=3\lambda$, λ being the wavelength: $\lambda = 2\pi c_0 \omega$ with $\omega = 2\pi 10^7$ s^{-1} and $c_0 = 1500$ m/s.

Figure 3 shows this initial condition and the reflection process after 3.75 μs is presented in Fig. 3(b). The wave in water is traveling back to $x=0$ cm after partial reflection on the interface at $x=0.5$ cm while part of the wave enters the sample traveling to the right-hand side. In Fig. 3(b), the normal stress in the x direction is presented after the wave has entered the active zone but before the pumping was switched on. The pumping is applied when the incident wave has covered about one-third of the length of the active zone. Figures 4 and 5 show the next stage of the phenomenon. In Figs. 4 and 5 the beginning of the pumping is taken as the origin of the time. In order to produce the phase conjugation, the pumping frequency is fixed at $\Omega = 2\omega$.[1] The duration of the pumping is $T=19$ μs and Ψ is equal to π. Figure 4 shows the normal stress field at different times for $m = 4.1\times 10^{-2}$. In Fig. 4(a) the pumping has just been initiated and the direct amplified wave begins from the edge of the active zone. In Fig. 4(b) the conjugate wave can be clearly observed in the fluid. In the solid, the incident wave is just reflecting at the end of the sample. Figure 4(c) illustrates the amplification process and the emission of the conjugate wave in the fluid. The incident wave or its reflection on the edges of the sample is no longer visible due to the high level of amplification of the conjugate and direct waves. In Fig. 4(d) the pumping is finished and all the waves are to be evacuated through the interface toward the fluid after many reflections between the end of the sample and the interface. This is a long process, as shown in Figs. 4(e) and (f).

From the numerical point of view, this test has been very productive. It can be noticed that the scheme succeeds in propagating the waves for a long period without damping their amplitudes. Moreover our boundary conditions work without generation of spurious oscillations, for instance, Figs. 4(a) and (b) show no artificial numerical reflections at $x=0$ cm and no oscillations at $x=4$ cm for the reflective boundary. At the interface $x=0.5$ cm, the modified Rieman solver, which respects the continuity of stress and velocity, allows a smooth treatment of the change of amplitude and

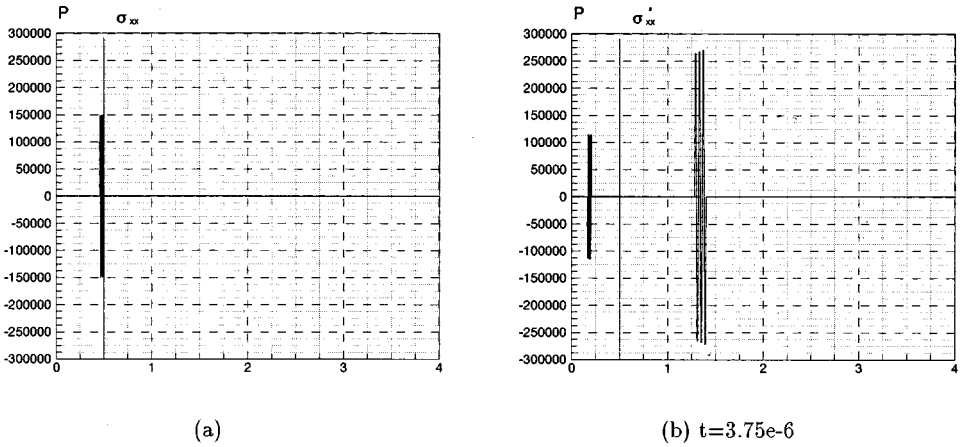

FIG. 3. Initial solution. (a) The initial pressure wave in the water zone. (b) The state when the pumping is initiated (pressure unit: Pa).

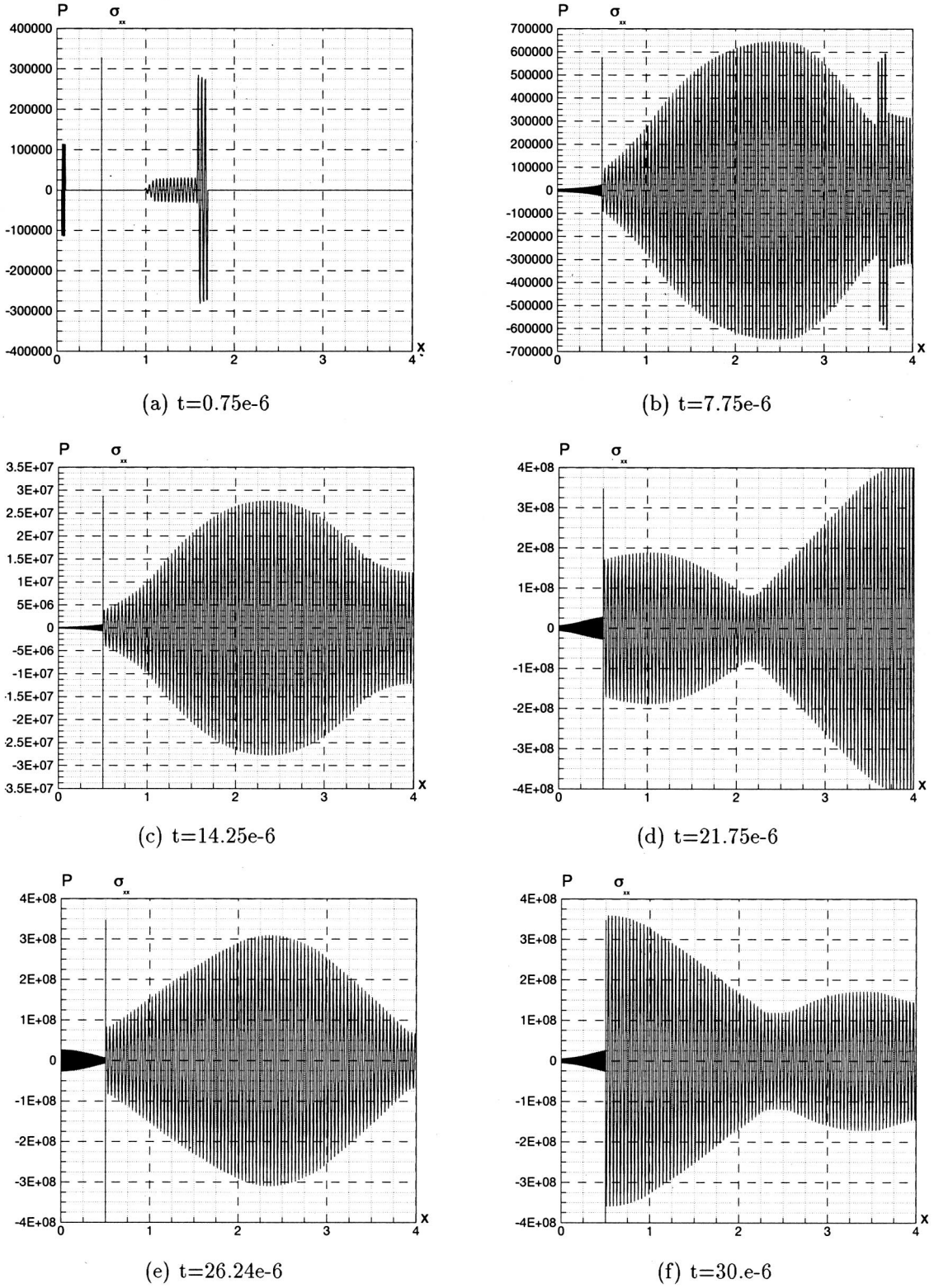

FIG. 4. Numerical solution: Spatial pressure and normal stress repartitions in a finite domain water–sample–vacuum at different stages of the process (stress unit: Pa).

sound velocity due to the different impedances on both sides.

As to the physical point of view, this test is still too complicated to be compared with analytical results. Another test has thus been performed on an infinite sample with the same active zone and the same pumping conditions except $m=3.2\times10^{-2}$. The initial wave in the active zone is the same as in previous case. Figures 5(a)–(f) show the evolution of the process. The quasisymmetrical behavior of the direct amplified wave and the conjugate one is not disturbed by the interfaces. At the end of the process, both waves are evacuated in opposite directions. Figures 5(c) and (d) present the situation just before and just after the end of the pump-

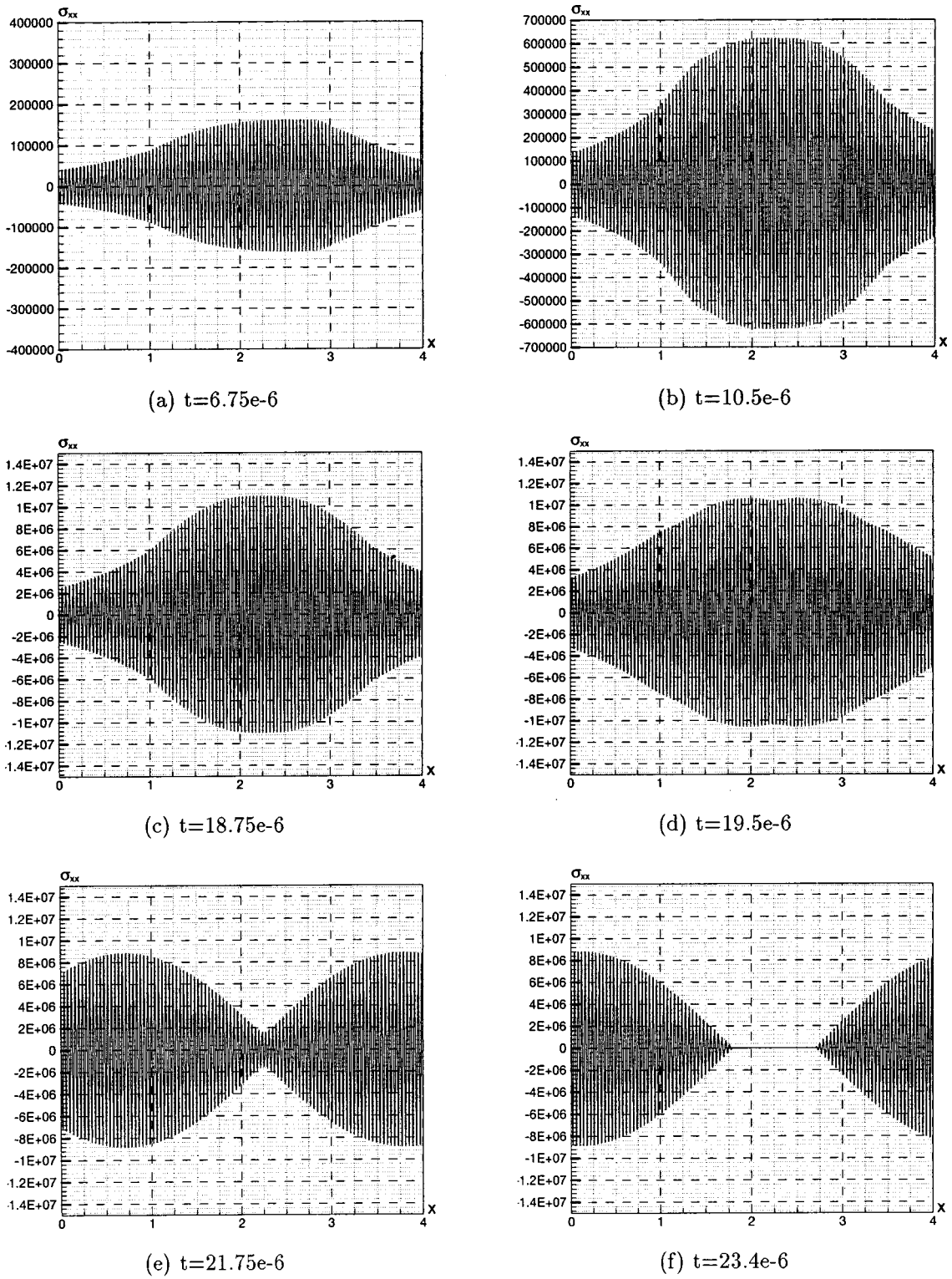

FIG. 5. Numerical solution: Normal stress repartitions in an infinite sample at different stages of the process.

ing. The amplification stops immediately and the separation of both waves starts.

This process corresponds to the ideal situation that gave rise to an analytical solution for the amplitude of the conjugate wave versus time. This analytical solution still holds in a more realistic situation where the sample is bounded on the left by water and is infinite on the left-hand side. No reflections on the left-hand edge disturb the emission of the conjugate wave in the liquid and, hence, the comparison between analytical solution and experiments is relevant for the pressure measurements in water until the first reflection of the right edge reaches the left interface in the experiments. Figure 6 presents the pressure in water for a semi-infinite sample limited on the left by the liquid. It shows total agreement with the results of the supercritical mode theory.[4,8] In accordance with the theory of impulse response,[8] the first

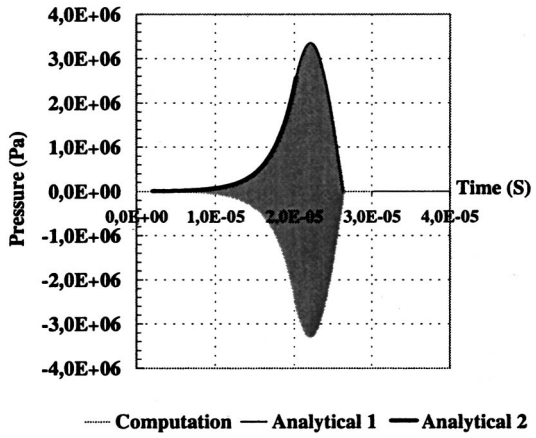

FIG. 6. Comparison of the analytical and numerical solutions: Time evolution of the pressure in water due to the conjugate wave at the interface water solid. The sample is semi-infinite, the boundary at 4 cm is nonreflective. Curve ''analytical 1'' is a partial sinus wave corresponding to the evacuation of the conjugate wave after the end of the pumping. Curve ''analytical 2'' is the exponential growth.

part of the envelope of the phase conjugate wave corresponds to the supercritical amplification stage due to the presence of electromagnetic pumping. It can be described asymptotically by an exponential function of time with gain Γ.[4] The second part of the signal observed after the end of the pump excitation, can be correlated with the spatial amplitude distribution of the acoustic conjugate wave inside the active zone at the moment the pump is suppressed.

In the case of a finite sample, the evolution in time of the acoustic pressure in the fluid side of the interface $x=0.5$ cm is presented in Fig. 7. Numerous reflections at the end of the sample explain the successive rebounds of the signal. The succession of pairs of rebounds having the same intensity is noticeable. This corresponds to conjugate waves and direct

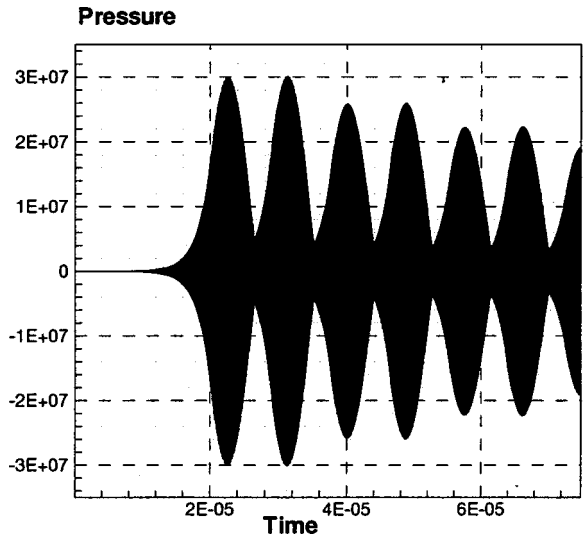

FIG. 7. Time evolution of the pressure in water at the left edge of the finite sample. The boundary at 4 cm is stress free. The conjugate wave (first burst) is followed by the reflection of the direct wave on the right edge (second burst) and next by its own reflection on the left and right edges (third burst), the equivalent double reflection of the direct wave explains burst four. The difference of the amplitude between the first and the second couple of bursts is due to the transmission of energy into water at each reflection on the left interface. The process continues until complete damping of the reflections.

amplified waves having the same number of reflections at the interface $x=0.5$ cm. The reflections on $x=0.5$ cm are the only origin of the intensity decay for the waves inside the sample. At the end ($x=4$ cm) no energy is lost by the reflected waves. Hence the number of rebounds depends only on τ. It is clear that in a real situation this number would be dramatically reduced by the 3D effects and by the fact that the direct wave is not as coherent with the conjugate one as in our 1D simulation.

IV. CONCLUSION

The computation scheme developed in the present paper provides, in principle, direct integration of various problems of wave propagation in nonstationary media. The first results of these numerical simulations of parametric WPC by this scheme clearly show the supercritical dynamics of the acoustic field in the active medium and demonstrate a good agreement with the analytical theory. The method can be easily generalized to the description of the nonlinear stage of parametric WPC (Ref. 15) taking into account pumping depletion and multiple reflections of parametrically coupled waves at the boundaries of the active medium. The problem of wideband pumping is of special interest for applications of the proposed approach because, in contrast with asymptotic methods, it is free of limitations on speed of sound velocity variations. The problem of reverberation noise amplification in parametric WPC under double pumping, recently studied experimentally,[12] also does not require considerable modification of the computational technique either. Thus, the computation method proposed in the present paper can find various applications in parametric dynamics of continuous media. Nevertheless, if the extension in 2D is possible through standard numerical techniques like flux splitting, the 3D case cannot be solved without a loss of precision because of the necessary limitation of the number of cells. A fruitful research direction is the derivation of an ''amplitude formulation'' by a hybrid asymptotic-numerical approach, including a suitable treatment of the boundary conditions which would give only the amplitude evolution.

[1] B. Ya. Zel'dovich, N. F. Pilipetskii, and V. V. Shkumov, *Principles of Phase Conjugation* (Springer, Berlin, 1985).
[2] F. V. Bunkin, D. V. Vlasov, and Yu. A. Kravtsov, ''On problem of sound wave phase conjugation with amplification of conjugate wave,'' Sov. J. Quantum Electron. **11**, 687–688 (1981).
[3] F. V. Bunkin *et al.*, ''Wave phase conjugation of sound in water with bubbles,'' Sov. Phys. Acoust. **29**, 169–171 (1983).
[4] R. B. Thomson and C. E. Quate, ''Nonlinear interaction of microwave electric fields and sound in $LiNbO_3$,'' J. Appl. Phys. **42**, 907–919 (1971).
[5] M. Ohno and K. Takagi, ''Enhancement of the acoustic phase conjugate reflectivity in nonlinear piezoelectric ceramics by applying static electric or static stress fields,'' Appl. Phys. Lett. **69**, 3483–3485 (1996).
[6] A. P. Brysev, L. M. Krutyianskii, and V. L. Preobrazhenskii, ''Wave phase conjugation of ultrasonic beams,'' Phys. Usp. **41**, 793–805 (1998), Reviews of topical problems.
[7] A. A. Chaban, ''On one nonlinear effect in piezoelectric semiconductors,'' Sov. Phys. Solid State **9**, 3334–3335 (1967).
[8] D. L. Bobroff and H. A. Haus, ''Impulse response of active coupled wave systems,'' J. Appl. Phys. **38**, 390–403 (1967).
[9] M. Fink, ''Time reversal of ultrasonic fields,'' IEEE Trans. Ultrason. Ferroelectr. Freq. Control **39**, 555–592 (1996).

[10] S. K. Godunov, ''A finite difference method for numerical computation of discontinuous solutions of the systems of the equations of fluid dynamics,'' Mat. Sb. **47**, 357–393 (1959).
[11] E. F. Toro, ''The weighted average flux method applied to the Euler equations,'' Philos. Trans. R. Soc. London, Ser. A **341**, 499–530 (1992).
[12] V. L. Preobrazhensky and P. Pernod, ''Compression and decompression of ultrasonic echoes by means of parametric wave phase conjugation,'' Proceedings of the 1998 IEEE Ultrasonic Symposium, Sendaï, Japan, 1998, Vol. 1, p. 889–891.
[13] B. Van Leer, ''Towards the ultimate conservative difference scheme V. A second order sequel to Godunov's methods,'' J. Comput. Phys. **32**, 101–136 (1979).
[14] P. Roe, ''Some contributions to the modeling of discontinuous flows,'' Proceedings of the 15th AMS-SIAM Summer Seminar on Applied Mechanics, Lect. Appl. Math. SIAM **22**, 169–193 (1985).
[15] A. P. Brysev, F. V. Bunkin, M. F. Hamilton, L. M. Krutyianskii, K. B. Cunningham, V. L. Preobrazhensky, Yu. V. Pyl'nov, A. D. Stakhovskii, and S. J. Younghouse, ''Nonlinear propagation of quasi-plane conjugate ultrasonic beam,'' Acoust. Phys. **44**, 641–650 (1998).

Thermal wave harmonics generation in the hydrodynamical heat transport in thermoacoustics

Vitalyi Gusev[a)]
Laboratoire de Physique de l'Etat Condensé, UPRESA-CNRS 6087, Université du Maine, Avenue O. Messiaen, 72085 Le Mans Cedex 9, France

Pierrick Lotton, Hélène Bailliet, Stéphane Job, and Michel Bruneau
Laboratoire d'Acoustique de l'Université du Maine, UMR CNRS 6613, Université du Maine, Avenue O. Messiaen, 72085 Le Mans Cedex 9, France

(Received 17 April 2000; accepted for publication 16 October 2000)

It is demonstrated that the temperature oscillations near the edge of the thermoacoustic stack are highly anharmonic even in the case of harmonic acoustic oscillations in the thermoacoustic engines. In the optimum regime for the acoustically induced heat transfer, the amplitude of the second harmonic of the temperature oscillations is comparable to that of the fundamental frequency. [DOI: 10.1121/1.1332383]

PACS numbers: 43.25.Gf, 43.35.Ud, 43.35.Ty [MFH]

I. INTRODUCTION

Nowadays there exists an understanding that the thermal waves in the thermoacoustic devices (such as prime movers and refrigerators) are, in general, anharmonic (i.e., periodic, but including higher harmonics than the fundamental).[1–3] However, the only physical mechanism of the thermal wave harmonics excitation which has been investigated analytically until now is the one related to the acoustic nonlinearity in the thermoacoustic resonators.[1–3] In fact, it has already been established in the classical experiments[1] that the nonlinear acoustic effect (i.e., cascade process of harmonics generation in acoustic wave propagation) influences the thermoacoustic effect in a resonant tube. The theoretical explanation[2] of the experimental observations takes into account that the pressure oscillations at higher frequencies are necessarily accompanied by temperature oscillations at the same frequencies, and, consequently, the interaction of acoustic and thermal waves at the higher (but equal) frequencies provides a nonzero time-average contribution to the heat flux. The thermal wave harmonics accompanying nonlinear standing acoustic waves have also been taken into account later in the analysis of the performance of a large thermoacoustic engine.[3] The hydrodynamical temperature flux is described by the nonlinear term $(\mathbf{v}\cdot\boldsymbol{\nabla})T$ (the so-called convective derivative) in the equations for the energy transport in hydrodynamics.[4] Here, $\mathbf{v}$ and T denote the fluid velocity and the fluid temperature fields, respectively (note that in the standing acoustic wave considered in our paper the hydrodynamical temperature flux is proportional both to the second-order heat flux and to the second-order enthalpy flux). It is evident that the interaction of the acoustic and thermal waves described by this nonlinearity, $(\mathbf{v}\cdot\boldsymbol{\nabla})T$, is not only the source of the nonzero time-average temperature flux (i.e., the physical origin of the thermoacoustic effect), but also the source of the higher thermal wave harmonics. This physical mechanism of thermal wave harmonic generation is additional to the one described in Refs. 1–3 (i.e., one associated with the acoustic nonlinearity). The nonlinear term $(\mathbf{v}\cdot\boldsymbol{\nabla})T$, which describes hydrodynamical (advective) transport of temperature, generates thermal wave harmonics even in the absence of the higher harmonics of the acoustic field.

The goal of the present work is to investigate analytically thermal wave harmonic excitation in the process of hydrodynamical temperature transport and to demonstrate that accounting for this phenomenon may be important for the analysis of thermoacoustic devices. The form of the nonlinear term $(\mathbf{v}\cdot\boldsymbol{\nabla})T$ indicates that the existence of the high spatial temperature gradients should favor thermal wave harmonic generation. That is why the present research is concentrated on the analysis of the temperature field near one of the ends of the thermoacoustic stack. In fact, by both numerical[5] and analytical[6,7] approaches, it has been demonstrated recently that near the stack termination the characteristic spatial scale of temperature variations can be of the order of (or even less than) the particle displacement amplitude u_0 in the acoustic wave. Consequently, from the point of view of classical thermoacoustic theory (where the particle displacement amplitude is considered to be sufficiently small in order to assume all the spatial variations along the x direction of the acoustic waves propagation take place at scales significantly larger than u_0), the region near the stack end may be the most important source of thermal wave harmonics. For a review of the classical approach in thermoacoustics, see Ref. 8.

II. THEORY

In order to get the basic physical insight to the process of thermal wave harmonic generation near the stack termination, it is highly desirable to proceed in the analysis as far as possible by analytical means. For this purpose, the viscosity of the medium and the dependence of the thermophysical parameters on the temperature are neglected here. It is assumed that the blockage of the fluid flux by the stack is negligible and, thus, even near the stack termination, the ve-

a)Electronic mail: vitali.goussev@univ-lemans.fr

locity field is unidirectional (only the component v of the velocity field, which is directed along the x axis, effectively contributes to the advective transport). The equation for the temperature[9,8] takes the form

$$\frac{\partial T'}{\partial t}+v\frac{\partial T'}{\partial x}=\frac{T_0}{p_0}\left(\frac{\partial p}{\partial t}+v\frac{\partial p}{\partial x}\right)+D_0\left(\frac{\partial^2}{\partial x^2}+\nabla_\tau^2\right)T'. \quad (1)$$

In Eq. (1), T' denotes the deviation of the temperature from the characteristic value T_0, p denotes the pressure variation, p_0 is the characteristic pressure ($p_0=\rho_0 c_p/\beta$, where ρ_0 is the undisturbed density, c_p is the isobaric heat capacity, and β is the thermal expansion coefficient), D_0 is the thermal diffusivity, and ∇_τ^2 denotes the transverse part of the Laplace operator. The second term on the right-hand side of Eq. (1) contains, in comparison with the first one, an additional small parameter of the order of magnitude u_0/λ (where λ is the acoustic wavelength), which is much less than 1 and, thus, can be neglected. The conduction heat transfer in the axial direction (described by the term $D_0\partial^2 T'/\partial x^2$) is considered to be negligible in comparison with the hydrodynamical temperature transport (described by the term $v\partial T'/\partial x$).[6–8] Since (in the absence of viscosity and blockage) the velocity v of the particles does not depend on the transverse coordinate, Eq. (1) can easily be integrated over a cross section S of a pore in the thermoacoustic stack

$$\frac{\partial \overline{T'}}{\partial t}+v\frac{\partial \overline{T'}}{\partial x}=\frac{T_0}{p_0}\frac{\partial_p}{\partial t}+\frac{D_0}{S}\oint\frac{\partial T'}{\partial n}d\Pi. \quad (2)$$

In Eq. (2), $\overline{T'}$ denotes the average temperature of the gas in a cross section of a pore, and the integral term on the right-hand side of Eq. (2) denotes integration over the perimeter II of the pore ($\partial T'/\partial n$ is the temperature derivative along the internal normal to the stack surface). In the present investigation, the heat flux at the gas/stack interface is described by Newton's law of cooling[9] of the form

$$k_s\frac{\partial T_s'}{\partial n}=h(T_s'-\overline{T'}), \quad (3)$$

where k_s is the thermal conductivity of the stack, T_s' is the variation of the stack surface temperature, and h is the convection heat transfer coefficient.[4,9] However, in the absence of the transverse components of velocity field, the advective transport of temperature in the transverse direction is absent and, consequently, at the interface

$$k_s\frac{\partial T_s'}{\partial n}=k_0\frac{\partial T'}{\partial n}. \quad (4)$$

Here, k_0 is the gas thermal conductivity. Combining Eqs. (2), (3), and (4), the equation for the average gas temperature becomes

$$\frac{\partial \overline{T'}}{\partial t}+v\frac{\partial \overline{T'}}{\partial x}=\frac{T_0}{p_0}\frac{\partial_p}{\partial t}-\frac{\Pi h}{S\rho_0 C_p}\left(\overline{T'}-\frac{1}{\Pi}\oint T_s' d\Pi\right). \quad (5)$$

The last term on the right-hand side of Eq. (5) provides coupling with the equation of heat diffusion inside the stack.[7] In the present short communication, we follow the model proposed in Ref. 5 and treat the simplest case, with zero longitudinal temperature gradient within the plates (as if the plates were made of a solid with infinite thermal conductivity and heat capacity). Thus, it is assumed here that $T_s'\equiv 0$, and Eq. (5) becomes a closed equation for the heat transfer in the gas. It should be mentioned, however, that Newton's law of cooling [Eq. (3)] is not a solution for the problem of transverse heat exchange between the gas and the plates, but is rather its reformulation, because the precise determination of the heat transfer coefficient h itself demands the solution of the convection heat transfer problem (see, for example, Ref. 6). But, concentrating attention on the physics of the nonlinear phenomena, we treat here the parameter h as phenomenological. The coefficient $(\Pi/S)(h/\rho_0 C_p)$ on the right-hand side of Eq. (5) has a physical meaning of the inverse thermal relaxation time $1/\tau_R$.[10] The relaxation time approximation for the transverse heat exchange is quite frequently used in the analysis of cyclic flow refrigerators (see Refs. 11, 12, and references therein). In the present work, the relaxation time approximation is combined with precise analytical treatment of the advective axial transport of heat.

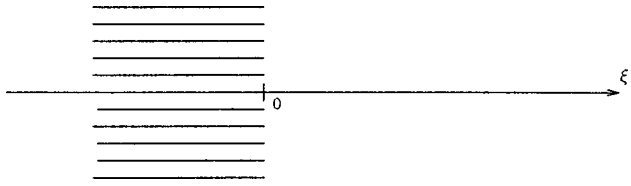

FIG. 1. Stack configuration.

We use the following description for the harmonic acoustic field in a half-wavelength resonator:

$$v=\omega u\sin(\omega t),\quad u\equiv u_0\sin(2\pi x/\lambda),$$
$$p=\rho_0(\lambda\omega^2/2\pi)u_0\cos(2\pi x/\lambda)\cos(\omega t). \quad (6)$$

The variation of v and p with coordinate x in Eq. (6) is much slower than the spatial variation of temperature in Eq. (5) near the stack end. Because of this, by introducing the dimensionless temperature $\theta=\overline{T'}/T_c$

$$(T_c=-T_0(\rho_0/p_0)(\lambda\omega^2/2\pi)u_0\cos(2\pi x/\lambda)),$$

the dimensionless variables $\tau=\omega t$, $\xi=x/u$, and the dimensionless relaxation parameter $R=\omega\tau_R$, Eq. (5) can be rewritten as

$$\frac{\partial\theta}{\partial\tau}+\sin\tau\frac{\partial\theta}{\partial\xi}=\sin\tau-\frac{\theta}{R}. \quad (7)$$

The solutions of Eq. (7) depend on the coordinate inside the resonator only parametrically via the adopted normalization. When the position of the stack is fixed, it is suitable to shift the origin of the ξ axis to the edge of the stack. Thus, in the following, it is considered that the stack occupies the region $\xi\leqslant 0$, while in the region $\xi>0$ the temperature relaxation is absent [adiabatic region of the acoustic field, $R(\xi>0)=\infty$]. This simplest configuration is presented in Fig. 1. In the region $\xi\leqslant 0$, the magnitude of the relaxation parameter R controls the regime of the hydrodynamical flow (it is quasi-isothermal for $R\ll 1$ and it is quasiadiabatic for $R\gg 1$). The partial differential equation (7) is equivalent[13] to the system of two ordinary differential equations

$$\frac{d\xi}{d\tau}=\sin\tau, \quad \frac{d\theta}{dt}=\sin\tau-\frac{\theta}{R}.$$

The solution of these equations inside the stack region ($\xi\leqslant 0$, $R\neq\infty$) is

$$\xi=-\cos\tau+c_1^-,$$
$$\theta=\frac{R}{1+R^2}\sin\tau-\frac{R^2}{1+R^2}\cos\tau+c_2^-\exp\left(-\frac{\tau}{R}\right). \tag{8}$$

The solution outside the stack region ($\xi\geqslant 0$, $R=\infty$) (for which we introduce the notation ξ^+, θ^+) is

$$\xi^+=-\cos\tau+c_1^+, \quad \theta^+=-\cos\tau+c_2^+. \tag{9}$$

The relation between the integration constants $c_{1,2}^{\pm}$ can be found from the condition of continuity of temperature distribution across the boundary ($\theta=\theta^+$ when $\xi=\xi^+=0$)

$$\frac{R}{1+R^2}\sin\tau-\frac{R^2}{1+R^2}\cos\tau+c_2^-\exp\left(-\frac{\tau}{R}\right)=-\cos\tau+c_2^+, \tag{10}$$

$$-\cos\tau+c_1^-=-\cos\tau+c_1^+=0. \tag{11}$$

It follows from Eq. (11) that $c_1^-=c_1^+$, that Eq. (11) can be satisfied only if $|c_1^-|\leqslant 1$, and if $|c_1^-|\leqslant 1$ then Eq. (11) is satisfied twice at each period of oscillations. From a physics point of view this formal mathematics corresponds to the fact that not all fluid particles can cross the boundary $\xi=0$ (but only a part of those that are close to the stack edge), and that if the particle of fluid crosses $\xi=0$ then it does it twice in a cycle. At a period $-\pi\leqslant\tau\leqslant\pi$, two solutions of Eq. (11) are $\tau_{\pm}=\pm\arccos(c_1^-)$. Substitution of $\tau_{\pm}$ into Eq. (10) provides two relations between c_1^-, c_2^-, and c_2^+. Excluding c_2^+, the relation between c_1^- and c_2^- is obtained. Substitution in the latter relation of the constants c_1^- and c_2^- from Eq. (8) provides the following solution for the temperature:

$$\theta=\frac{R}{1+R^2}\sin\tau-\frac{R^2}{1+R^2}\cos\tau + \frac{R}{1+R^2}\frac{\sin[\arccos(\xi+\cos\tau)]}{\sinh\left[\dfrac{\arccos(\xi+\cos\tau)}{R}\right]}\exp\left(-\frac{\tau}{R}\right). \tag{12}$$

In accordance with the derivation, Eq. (12) is valid only in the region $-2\leqslant\xi\leqslant 0$ where a part of the fluid can reach the stack edge and only at the times $|\xi+\cos\tau|\leqslant 1$ when the temperature in a point ξ is controlled by the particles of fluid crossing the boundary $\xi=0$. Outside the indicated regions the temperature is controlled by the particles never leaving the stack and (as a consequence) it does not depend on the coordinate. The precise solution is given by the second part of Eq. (8), where in addition $c_2^-=0$ from the condition of periodicity $[\theta(\tau)=\theta(\tau+2\pi)]$. The same result formally follows from Eq. (12) if the last term is considered to be equal to zero when the arccosine function is undetermined in real numbers (i.e., outside the region $|\xi+\cos\tau|\leqslant 1$). Consequently, under this agreement, the solution (12) is valid in the whole region $\xi\leqslant 0$ for all $-\pi\leqslant\tau\leqslant\pi$. A less formal (more physical) and more detailed version of the derivation of Eq. (12) is presented in the Appendix.

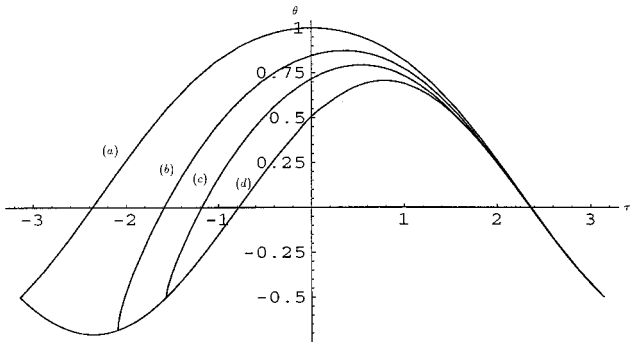

FIG. 2. Profile of the temperature oscillations at different distances ξ from the stack edge [optimal regime $R=1$, (a) $\xi=0$; (b) $\xi=-0.5$; (c) $\xi=-1$; (d) $\xi=-2$].

The third term on the right-hand side of Eq. (12) contributes to the solution only when the $\arccos(\xi+\cos\tau)$ function is defined in the real space (i.e., if $-1\leqslant\xi+\cos\tau\leqslant 1$). In particular, the third term does not contribute to the solution in the region $\xi<-2$ at any τ. Thus, at distances from the stack edge larger than the maximum particle displacement (i.e., $2u$), the temperature field is purely harmonic and the time-average temperature is equal to zero, $\langle\theta\rangle=0$. Here, $\langle ...\rangle$ denotes averaging over the period of oscillations. However, there exists a nonzero axial temperature flux, which in the nondimensional form can be described as $J=\langle\theta\sin\tau\rangle=R/2(1+R^2)$. Note that in the standing wave of Eq. (6) the same nondimensional presentation is valid also for the heat flux and for the enthalpy flux. Consequently, the maximum thermoacoustic heat flux along the stack is expected for $R=1$. This prediction qualitatively correlates with the classical predictions[8] that the optimum regime for pumping heat is intermediate between adiabatic and isothermal.

In the region $-2<\xi<0$ the temperature oscillations are anharmonic. In Fig. 2 the profiles of the temperature oscillations, Eq. (12), are presented at different distances ξ ($-2\leqslant\xi\leqslant 0$) from the stack edge for the particular (optimal) regime $R=1$. It is evident that the temperature oscillations are anharmonic everywhere except at the coordinate $\xi=-2$ (from the point $\xi=-2$, the fluid particle can reach the stack edge but cannot cross it). The temperature profiles in Fig. 2 include also the contribution from the average temperature field.[14] The amplitudes of the sine and cosine components [denoted by (θ_n^s) and (θ_n^c), respectively] are derived from Eq. (12)

$$\theta_n^s=\frac{R}{1+R^2}\left[\delta_{n,1}-\frac{2}{\pi}\int_0^{\arccos(-1-\xi)}\frac{\sin[\arccos(\xi+\cos\tau)]}{\sinh\left[\dfrac{\arccos(\xi+\cos\tau)}{R}\right]} \times\sinh\left(\frac{\tau}{R}\right)\sin(n\tau)\,d\tau\right], \tag{13}$$

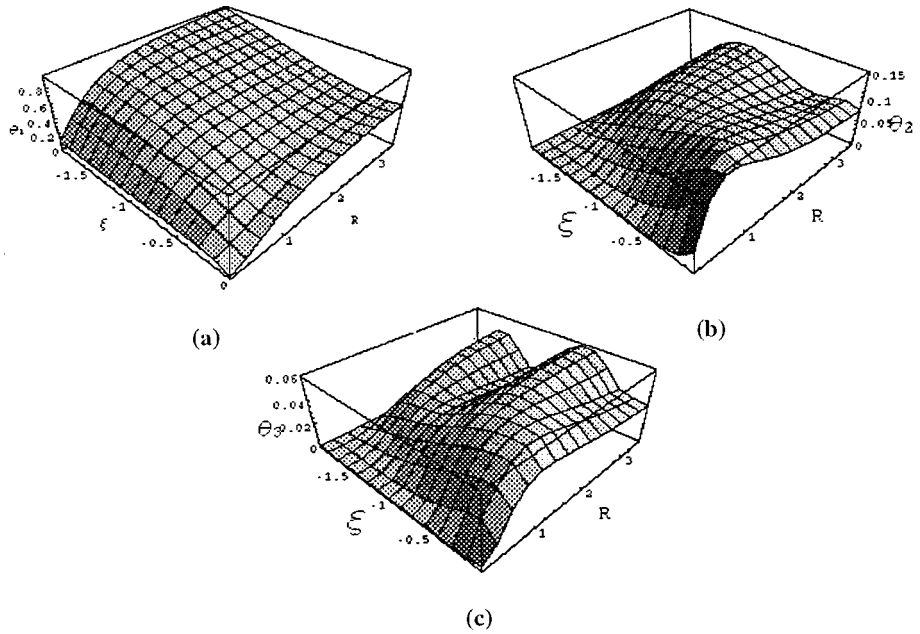

FIG. 3. Spatial distribution of the temperature: (a) fundamental frequency; (b) second harmonic; (c) third harmonic.

$$\theta_n^c = \frac{R}{1+R^2}\left[-R\,\delta_{n,1} + \frac{2}{\pi}\int_0^{\arccos(-1-\xi)} \frac{\sin[\arccos(\xi+\cos\tau)]}{\sinh\left[\dfrac{\arccos(\xi+\cos\tau)}{R}\right]} \times \cosh\left(\frac{\tau}{R}\right)\cos(n\tau)\,d\tau \right]. \tag{14}$$

Here, $n=1,2,3,\ldots$. The absence of the sine component at the fundamental frequency at the edge of the stack [$\theta_1^s(\xi=0)=0$] correlates with the necessary absence of the axial heat flux into the adiabatic region $\xi>0$ [$J(\xi=0)=0$]. The spatial distribution of the fundamental frequency oscillations ($n=1$) and of the second and third harmonics $\theta_n=\sqrt{(\theta_n^s)^2+(\theta_n^c)^2}$ is presented in Fig. 3 as functions of relaxation parameter R. The data presented in Figs. 2 and 3 provide evidence for the anharmonic character of temperature oscillation. In accordance with Fig. 3, the nonlinear effects are most important around the optimum regime ($R=1$) of the heat pump performance. It can be seen, for example, that in this regime the amplitude of the second harmonic near the stack termination ($\xi=0$) is of the same order of magnitude as the amplitude of the fundamental frequency.

The behavior of the harmonics in the quasiadiabatic regime $R\gg 1$ (see the region $R\geqslant 3$ in Fig. 3) deserves special discussion. When analyzing the possibility of the experimental observation of the predicted distributions of harmonics in space, it should be taken into account that when $R\gg 1$ the acoustically induced heat flux is relatively small ($J\approx 1/2R\ll 1$). Consequently, the characteristic time for the ''accumulation'' of the predicted temperature distribution (i.e., the time for the approach to the periodic temperature oscillations) can be relatively long. And then, the neglected ordinary diffusive heat conduction in the axial direction can be important.

At the stack termination ($\xi=0$) Eqs. (13) and (14) can be expressed in terms of special functions. In the quasiadiabatic regime ($R\gg 1$)

$$\theta_n^s(\xi=0)=0, \theta_n^c \cong \frac{1}{\pi}(\mathrm{Si}[(n+1)\pi]-\mathrm{Si}[(n-1)\pi])-\delta_{n,1}, \tag{15}$$

where Si denotes sine integral. In the quasi-isothermal regime ($R\ll 1$)

$$\theta_n^s(\xi=0)=0, \quad \theta_n^c \cong \frac{2R}{\pi}\frac{(-1)^{n+1}-1}{n^2-1}. \tag{16}$$

In particular, in accordance with Eq. (16), the contribution of the fundamental frequency and its odd harmonics to the temperature oscillations at the edge of the quasi-isothermal stack is negligible.

Finally, it should be mentioned that, when averaged over a period of the oscillations, Eq. (12) provides the distribution of the mean temperature near the stack termination.[14] This solution for the mean temperature, or Eq. (12) itself, can be applied to establish the mathematical condition for the negligence of the molecular heat transport in the direction of the x axis in comparison with acoustically induced heat flux [see the assumptions used for the derivation of Eq. (12)]. However, in Ref. 14 it is demonstrated that the solution for the mean temperature that follows from Eq. (12) does not differ significantly from one obtained in the mean-field approximation and because of that the required condition can be presented in a simple form

$$\frac{D_0}{D_{ac}} \ll \min\left\{R, \frac{8}{1+R^2}\right\}, \tag{17}$$

where $D_{ac}\equiv u^2\omega/4$ is the acoustically induced thermal diffusivity in the regime where $R=1$. The condition (17) can always be satisfied for sufficiently high level of the acoustic

oscillations in the resonator. In particular, in most of the currently operating thermoacoustic engines, this condition is usually satisfied.[3,8]

III. CONCLUSION

The analytical description of Eqs. (13)–(16) confirms the highly nonlinear character of the temperature oscillations up to distances of the order of the particle displacement from the stack edge. This result indicates that the mean-field approximation, which is traditionally used for the analytical analysis of the thermoacoustic heat flux, may not be valid near the stack termination. The results of the evaluation of the validity of the mean-field approximation in thermoacoustics, as well as the results of the application of the proposed equation (7) for the analysis of thermoacoustic heat transfer between two adiabatically separated stacks, is reported elsewhere.[14]

In summary, the developed theoretical model for the acoustically induced heat transfer near the edge of a stack in a thermoacoustic engine and its analysis indicate that (at the scale of the particle displacement in the acoustic wave) the temperature oscillations are highly nonlinear. Their evaluation requires a theoretical approach which is not based on the ''classical'' mean-field approximation.

Finally, it is obvious that the possible analytical extensions of the developed theory should include, first of all, the analysis of the influence of the viscosity and of the partial blockage of the fluid motion by the stack edges on the thermal wave harmonics excitation. The effect of the viscosity on the predicted excitation of the thermal wave harmonics in the vicinity of the stack termination is not expected to be strong [in our opinion, the viscosity cannot significantly suppress the process of harmonics generation associated with the term $v(\partial T'/\partial x)$ in Eq. (5)]. Moreover, currently we cannot exclude even the possibility that the presence of the viscosity increases the anharmonicity of the temperature oscillations near the stack edge. In fact, both numerical solution of the basic equations[5] and their analytical investigation in the frame of the mean-field approximation[6,7] demonstrate that the characteristic values of the mean temperature axial derivative near the stack edge (i.e., the steepness of the temperature distribution) diminishes with the increase of the Prandtl number. However, at the same time, an effective value of v contributing to the advective nonlinearity $v(\partial T'/\partial x)$ increases. The reason for the latter effect has been recently explained in Ref. 15. The presence of the viscosity changes the particle velocity profile in the cross section of the stack channel. In the viscous case, the gas near the wall of the channel does not move. By continuity, the gas in the center of the channel must have a higher velocity relative to the inviscid case. This conclusion is supported by the analytical formulas presented in Refs. 15 and 16, for example. In both the viscous and nonviscous cases, the gas near the wall is pinned to the temperature of the wall. Therefore, it is the gas at the distance exceeding (or of the order of) the thermal boundary layer thickness, whose oscillations are sufficiently nonisothermal, which contributes to the thermoacoustic effects. But, the oscillations of the particle velocity at these distances can be bigger in the viscous case (relative to the inviscid case) and consequently, the effective cross-sectional average v contributing to $v(\partial T'/\partial x)$ can increase in the presence of the viscosity. There are examples in Ref. 15 showing that the viscosity increases the thermoacoustic power production. To derive definite conclusions on the role of the viscosity in the thermal wave harmonics excitation, it is necessary to modify the theory developed here significantly. However, from the inviscid-case theory presented here it follows that the characteristic amplitudes of the temperature oscillations at the fundamental frequency and at the harmonics are all linearly proportional to the particle displacement amplitude (or the particle velocity amplitude). Consequently, it can be expected that in the first approximation the influence of the viscosity on the effective velocity will cause proportional change of all spectral components of the temperature oscillations and will not change the importance of the harmonics relative to the fundamental frequency. This is the reason why we do not expect any strong influence of the viscosity on the particular process of the thermal wave harmonics excitation described in the present paper. At the same time, the role of the possible vortex shedding[17] is not clear at the moment. Thus, the analysis of the phenomena which are currently not included in the simplest nonlinear theory presented here provides the perspective for future research.

APPENDIX

In this Appendix we demonstrate how the formal mathematics[13] leading to the solution of the derived equations can be described in words and, as a result, can be understood better from a physical point of view. We are going to solve the system

$$\theta_\tau + \sin\tau\,\theta_\xi = \sin\tau - \frac{\theta}{R}, \quad \text{if } \xi<0, \tag{A1}$$

$$\theta_\tau + \sin\tau\,\theta_\xi = \sin\tau, \quad \text{if } \xi>0. \tag{A2}$$

It is written in Euler coordinates. The presentation of these partial differential equations as the system of ordinary differential equations is, in fact, equivalent to the transformation to Lagrange coordinates. When Eqs. (A1) and (A2) are written in the equivalent form of the sets of the ordinary differential equations

$$\frac{d\theta}{d\tau} = \sin\tau - \frac{\theta}{R}, \tag{A3}$$

$$\frac{d\xi}{d\tau} = \sin\tau, \tag{A4}$$

if $\xi<0$, and

$$\frac{d\theta}{d\tau} = \sin\tau, \tag{A5}$$

$$\frac{d\xi}{d\tau} = \sin\tau, \tag{A6}$$

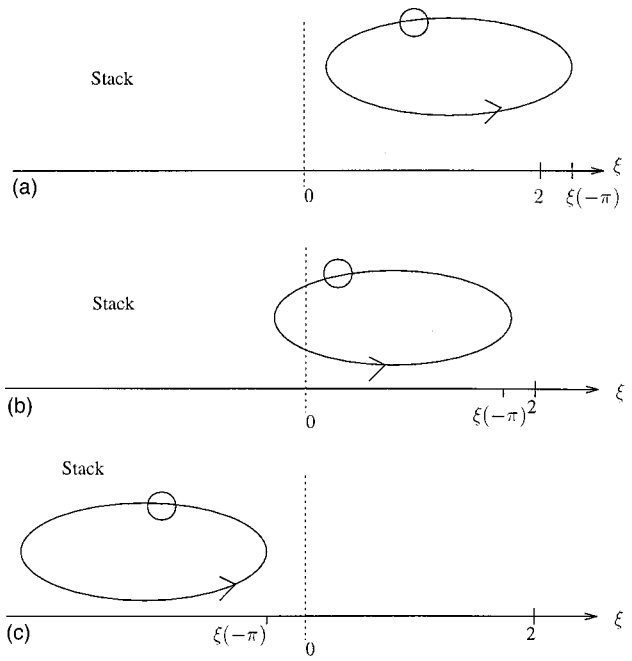

FIG. A1. (a) Displacement of a particle with $\xi(-\pi)>2$. (b) Displacement of a particle with $0\leqslant\xi(-\pi)\leqslant 2$. (c) Displacement of a particle with $\xi(-\pi)<0$.

if $\xi>0$, Eqs. (A4) and (A6) describe the change of the coordinate of a fixed particle of fluid. By integrating Eqs. (A4) and (A6), we get

$$\xi = c - \cos\tau, \tag{A7}$$

where the constant c is a marker for the chosen particle. For the analysis of our periodic process, it is sufficient to find a solution during an interval of 2π. We fix for the analysis a period $-\pi\leqslant\tau\leqslant\pi$ and we denote $c\equiv\xi(\tau=-\pi)+1$. Then, Eq. (A7) takes the form

$$\xi = \xi(\tau=-\pi) - 1 - \cos\tau. \tag{A8}$$

So, $\xi(\tau=-\pi)$ describes the initial coordinate of the particle (at the beginning $\tau=-\pi$ of the period). It is clear that in accordance with Eq. (A8) all the particles first move left during the period when $-\pi\leqslant\tau\leqslant 0$ and then they return when $0\leqslant\tau\leqslant\pi$. We can identify three types of particles (Fig. A1).

The particles with $\xi(-\pi)>2$ [see Fig. A1(a)] will never arrive inside the stack and they will never contribute to temperature inside the stack.

The particles with $0\leqslant\xi(-\pi)\leqslant 2$ [see Fig. A1(b)] cross the stack termination twice and they contribute to temperature variations inside the stack ($\xi\leqslant 0$).

The particles with $\xi(-\pi)<0$ [see Fig. A1(c)] do not cross the stack termination but they contribute to temperature variation inside the stack. The integration of the ordinary differential equations (A3) and (A5) gives

$$\theta = \frac{R}{1+R^2}\sin\tau - \frac{R^2}{1+R^2}\cos\tau + c_2^-\exp\left(-\frac{\tau}{R}\right), \tag{A9}$$

if the particle is inside the stack ($\xi\leqslant 0$), and gives

$$\theta = -\cos\tau + c_2^+, \tag{A10}$$

if the particle is outside the stack ($\xi\geqslant 0$). In Eqs. (A9) and (A10), c_2^- and c_2^+ denote constants of integration. In this Lagrange approach, Eq. (A8) describes the position of the particle in space as a function of time, at the same time Eqs. (A9) and (A10) describe the temperature of the particle also as a function of time. The constants c_2^- and c_2^+ can be different for different particles, i.e., they depend on the marker $\xi(-\pi)$ (which we are using to specify the particle of the fluid). So, for the description of each particle we have two unknowns, c_2^- and c_2^+. The constant c_2^- is important for the description of particle temperature in the stack ($\xi\leqslant 0$); the constant c_2^+ is important for the description of the particle temperature outside the stack ($\xi\geqslant 0$). From Fig. A1 it is clear that there is a relation between c_2^- and c_2^+ only if the particle crosses the stack termination [i.e., only for the particles of the type Fig. A1(b)]. However, it is also clear that a particle of the type presented in Fig. A1(b) crosses the stack termination twice, and, consequently, we have two boundary conditions to find c_2^- and c_2^+ because the temperatures described by Eqs. (A9) and (A10) should be equal twice over a single period (once when the particle enters the stack and the second time when the particle leaves the stack). To find the moments when the particles cross the stack termination, we assume $\xi=0$ in Eq. (A8) and solve the trigonometric equation to find

$$\tau_\pm = \pm\arccos[\xi(-\pi)-1]. \tag{A11}$$

Equation (A11) describes two solutions in the interval $-\pi\leqslant\tau\leqslant\pi$ if

$$0\leqslant\xi(-\pi)\leqslant 2. \tag{A12}$$

The meaning of the inequality (A12) is clear: only the particles which at $\tau=-\pi$ are closer than two particle displacement amplitudes from the stack termination and are located to the right from the stack [i.e., the particles of the type Fig. A1(b)] are crossing the interface $\xi=0$. The particles with the initial coordinate $\xi>2$ (or $\xi<0$) cannot enter (or leave) the stack. For the latter particles, mathematically the $\arccos[\xi(-\pi)-1]$ is undefined in real numbers. For them the constant c_2^- can be defined easier and by a different approach (see below). For the particles of the type Fig. A1(b) [satisfying Eq. (A12)] we equate the right-hand sides of Eqs. (A9) and (A10) at two moments $\tau=\tau_+$ and $\tau=\tau_-=-\tau_+$

$$\frac{R}{1+R^2}\sin\tau_+ - \frac{R^2}{1+R^2}\cos\tau_+ + c_2^-\exp\left(-\frac{\tau_+}{R}\right) = -\cos\tau_+ + c_2^+,$$

$$-\frac{R}{1+R^2}\sin\tau_+ - \frac{R^2}{1+R^2}\cos\tau_+ + c_2^-\exp\left(\frac{\tau_+}{R}\right) = -\cos\tau_+ + c_2^+.$$

Taking the difference, we get

$$\frac{2R}{1+R^2}\sin\tau_+ + c_2^-\left[\exp\left(-\frac{\tau_+}{R}\right) - \exp\left(\frac{\tau_+}{R}\right)\right] = 0,$$

and, consequently

$$c_2^- = \frac{R}{1+R^2}\,\frac{\sin\tau_+}{\sinh(\tau_+/R)}. \tag{A13}$$

Substituting Eq. (A13) into Eq. (A9) we get the description of the particle temperature when the particle is inside the stack

$$\theta = \frac{R}{1+R^2}\sin\tau - \frac{R^2}{1+R^2}\cos\tau + \frac{R}{1+R^2}\,\frac{\sin[\arccos(\xi(-\pi)-1)]}{\sinh\left[\dfrac{\arccos(\xi(-\pi)-1)}{R}\right]}\exp\left(-\frac{\tau}{R}\right). \tag{A14}$$

The derived solutions Eqs. (A8) and (A14) provide the description of the temperature of the particle inside the stack in the Lagrange coordinates. To return to the Euler coordinates we note that in the Euler coordinates we are interested to know how the temperature depends on time in a fixed point of space, that is, when we fix a coordinate ξ and allow to come to a point ξ different particles carrying each their own temperature. In accordance with Eq. (A8) the temperature in a fixed point ξ at a moment τ is associated with a particle having a marker

$$\xi(-\pi) = \xi + 1 + \cos\tau. \tag{A15}$$

Substituting Eq. (A15) into Eq. (A14) we arrive at the Euler description of temperature

$$\theta = \frac{R}{1+R^2}\sin\tau - \frac{R^2}{1+R^2}\cos\tau + \frac{R}{1+R^2}\,\frac{\sin[\arccos(\xi+\cos\tau)]}{\sinh\left[\dfrac{\arccos(\xi+\cos\tau)}{R}\right]}\exp\left(-\frac{\tau}{R}\right). \tag{A16}$$

This result is valid only if $-2\leqslant\xi\leqslant 0$, because the particles crossing the interface contribute to temperature changes only in this region of the stack. Moreover, this result is valid only if $|\xi+\cos\tau|\leqslant 1$ when the $\arccos(\xi+\cos\tau)$ is defined in real numbers. If $|\xi+\cos\tau|>1$ then at the time moments τ satisfying the latter inequality the temperature in the point $\xi\leqslant 0$ is ''carried'' by the particles of the type Fig A1(c) which never cross the stack termination. For these particles the solution is simpler. For them the constant in Eq. (A9) is equal to zero because of the condition of periodicity $\theta(\tau=-\pi)=\theta(\tau=\pi)$. Accordingly,

$$\theta = \frac{R}{1+R^2}\sin\tau - \frac{R^2}{1+R^2}\cos\tau \tag{A17}$$

for all $\xi\leqslant 0$ satisfying the inequality $|\xi+\cos\tau|>1$. Combining Eqs. (A16) and (A17) we can say that the solution Eq. (A16) is valid for all $\xi\leqslant 0$ if we assume the third term in Eq. (A16) to be equal to zero when and where the $\arccos(\xi+\cos\tau)$ is undefined in real numbers. This is precisely the same solution as presented in Eq. (8) of the main text. A physical interpretation of the derived solution Eq. (A16) is the following. In a fixed point $\xi<-2$ [where $\arccos(\xi+\cos\tau)$ is always undefined] the temperature is purely harmonic and is controlled by the arrival of the particles of the type Fig. A1(c). In a fixed point between $-2\leqslant\xi\leqslant 0$, starting $\tau=-\pi$ first arrive the particles of the type Fig. A1(c), then the particles of the type Fig. A1(b), and then again (at the end of the period) the particles of the type Fig. A1(c). The derived solution is periodic and is anharmonic.

[1] P. Merkli and H. Thomann, ''Thermoacoustic effects in a resonance tube,'' J. Fluid Mech. **70**(1), 161–177 (1975).
[2] N. Rott, ''The heating effect connected with nonlinear oscillations in a resonance tube,'' Z. Angew. Math. Mech. **25**, 619–634 (1974).
[3] G. W. Swift, ''Analysis and performance of a large thermoacoustic engine,'' J. Acoust. Soc. Am. **92**, 1551–1563 (1992).
[4] L. D. Landau and E. M. Lifshitz, *Fluid Mechanics* (Pergamon, Oxford, 1982).
[5] N. Cao, J. R. Olson, G. W. Swift, and S. Chen, ''Energy flux density in a thermoacoustic couple,'' J. Acoust. Soc. Am. **99**, 3456–3464 (1996).
[6] G. Mozurkewich, ''Time average temperature distribution in a thermoacoustic stack,'' J. Acoust. Soc. Am. **103**, 380–388 (1998).
[7] G. Mozurkewich, ''A model for transverse heat transfer in thermoacoustics,'' J. Acoust. Soc. Am. **103**, 3318–3326 (1998).
[8] G. W. Swift, ''Thermoacoustic engines,'' J. Acoust. Soc. Am. **84**, 1145–1180 (1988).
[9] F. P. Incropera and D. P. De Witt, *Introduction to Heat Transfer*, 3rd ed. (Wiley, New York, 1985, 1996 reissue).
[10] J. R. Brewster, R. Raspet, and H. Bass, ''Temperature discontinuities between elements of thermoacoustic devices,'' J. Acoust. Soc. Am. **102**, 3355–3360 (1997).
[11] J. H. Xiao, ''Thermoacoustic theory for cyclic flow regenerators. I. Fundamentals,'' Cryogenics **32**, 895–901 (1992).
[12] B. J. Huang and C. W. Lu, ''Linear network analysis of regenerator in a cyclic flow system,'' Cryogenics **35**, 203–207 (1995).
[13] R. Courant, *Partial Differential Equations*, Vol. II of *Method of Mathematical Physics*, by R. Courant and D. Hilbert (Interscience Wiley, New York, 1989).
[14] V. Gusev, P. Lotton, H. Bailliet, S. Job, and M. Bruneau, ''Relaxation-time approximation for the evaluation of temperature field in thermoacoustic stacks and heat exchangers,'' J. Sound Vib. **235**(5), 711–726 (2000).
[15] G. Petculescu and L. A. Wilen, ''Thermoacoustics in a single pore with an applied temperature gradient,'' J. Acoust. Soc. Am. **106**, 688–694 (1999).
[16] W. P. Arnott, H. E. Bass, and R. Raspet, ''General formulation of thermoacoustics for stacks having arbitrary shaped pore cross sections,'' J. Acoust. Soc. Am. **90**, 3228–3237 (1991).
[17] A. S. Worlikar and O. M. Knio, ''Numerical simulation of a thermoacoustic refrigerator. I. Unsteady adiabatic flow around the stack,'' J. Comput. Phys. **127**, 424–451 (1996).

Acoustic waveform inversion with application to seasonal snow covers

Donald G. Albert[a)]
US Army Cold Regions Research and Engineering Laboratory, 72 Lyme Road, Hanover, New Hampshire 03755-1290

(Received 10 March 1997; revised 16 August 1997; accepted 2 October 2000)

The amplitude and waveform shape of atmospheric acoustic pulses propagating horizontally over a seasonal snow cover are profoundly changed by the air forced into the snow pores as the pulses move over the surface. This interaction greatly reduces the pulse amplitude and elongates the waveform compared to propagation above other ground surfaces. To investigate variations in snow-cover effects, acoustic pulses were recorded while propagating horizontally over 11 different naturally occurring snow covers during two winters. Two inversion procedures were developed to automatically match the observed waveforms by varying the snow-cover parameters in theoretical calculations. A simple frequency-domain technique to match the dominant frequency of the measured waveform suffered from multiple solutions and poor waveform matching, while a time-domain minimization method gave unique solutions and excellent waveform agreement. Results show that the effective flow resistivity and depth of the snow are the parameters controlling waveform shape, with the pore shape factor ratio of secondary importance. Inversion estimates gave flow resistivities ranging from 11 to 29 kN s m^{-4}, except for two late-season cases where values of 60 and 140 were determined (compared to 345 for the vegetation-covered site in the summer). Acoustically determined snow depths agreed with the measured values in all but one case, when the depth to a snow layer interface instead of the total snow depth was determined. Except for newly fallen snow, the pore shape factor ratio values clustered near two values that appear to correspond to wet (1.0) or dry (0.8) snow. [DOI: 10.1121/1.1328793]

PACS numbers: 43.28.En, 43.28.Fp, 43.60.Pt [LCS]

I. INTRODUCTION

The interaction of sound energy with the ground is an important effect in understanding outdoor sound propagation.[1–3] It affects predictions of traffic, industrial, or blasting noise levels, which are becoming increasingly important in mitigating or preventing community noise problems and assessing environmental impacts of various activities. Snow is of interest in these applications since it is the most absorbent, naturally occurring ground cover. The presence of a snow cover has a large effect on acoustic pulse propagation, causing increased attenuation and marked waveform changes compared with propagation over grassland.[4] This article reports on measurements that were undertaken during two winters to investigate a wide range of snow covers and to examine the effect of snow cover properties on acoustic pulse propagation outdoors. The feasibility of using acoustic measurements to automatically determine properties of the snow itself is also examined.

Although it has long been known that a snow cover strongly absorbs sound, there are still significant experimental data gaps limiting the understanding and ability to predict acoustic wave interaction with snow.[5] Early papers on acoustics and snow were rather infrequent, and primarily reported that snow strongly absorbed audible acoustic waves, either through anecdotal reports,[6,7] simple measurements,[8] or simple calculations.[9] In all of these papers, the effect of various snow properties or structures was ignored. It was not recognized until the 1950's that the physical properties of the snow and snow metamorphism had an effect on the acoustic properties of the snow. Careful experimental measurements were reported by a number of Japanese researchers,[10–18] who conducted short-range acoustic measurements using loudspeakers and continuous wave (CW) sources in and above a snow cover, and reported differences between the propagation characteristics of ''new'' and ''compact'' snow. This work is summarized in Refs. 11 and 19. Short range measurements were also reported by Tillotson.[20] Gubler[21] reported on measurements of peak amplitude decay for propagation experiments on a shallow snow cover using an explosion source.

Johnson[22] was the first to apply Biot's[23–25] complete and comprehensive treatment of wave propagation in a porous medium to snow. However, for acoustic waves propagating above a snow cover, the full Biot theory is not necessary, since treating the snow as a rigid-framed porous material is sufficient to describe the air flow within the pores, and the elastic properties of the ice grain bonds have little effect. This simplified theory has been widely used to treat ground effects in outdoor sound propagation over soils and grass.[26] Various formulations have been developed to model the acoustic effects of the rigid porous material; Delaney and Bazley[27] developed an empirical relation that is widely used; Attenborough's[28] four-parameter model (the parameters are effective flow resistivity, porosity, and two shape factors) is theoretically based. These rigid-frame models have been

a)Electronic mail: dalbert@crrel.usace.army.mil

used to analyze data from short-range, high-frequency CW measurements over snow,[29,30] pulse measurements at longer ranges and lower frequencies,[31] and laboratory measurements on snow samples;[32,33] the physically based model has been shown to give better agreement than the Delaney–Bazley empirical model.

In this paper, experimental measurements of acoustic pulse propagation over seasonal snow covers are reported. The measurements were conducted over two winters to investigate the variations in acoustic response caused by naturally occurring variations in the snow-cover parameters. The next section of this paper discusses the experimental approach. A waveform inversion method is developed to determine the snow-cover parameters from the acoustic measurements and applied in the following section, and the acoustically determined parameters of the snow are compared to the directly observed snow properties. These results are discussed and summarized in the final section.

II. EXPERIMENTAL MEASUREMENTS

The experimental objective was to determine the acoustic response and its variability for typical New England seasonal snow covers. To accomplish this goal, broadband acoustic pulses were recorded as they propagated horizontally above the soil or snow surface at an undisturbed site in Hanover, NH. As the snow-cover properties changed during two winters, the measurements were repeated at the same location with an identical experimental setup. Careful characterization measurements were also done to allow the acoustic results to be compared to the snow-cover properties and other environmental conditions. Snow-cover characteristics change, and not only as a result of deposition from storms or melting during thaw periods. Snow continually metamorphoses as a result of temperature and vapor gradients within it,[34] and one of the goals of these experiments was to investigate how such physical changes within the snowpack affect the acoustic response.

A handheld .45-caliber blank pistol fired 1 m above the soil or snow surface was used as the source of the acoustic waves. The acoustic pulses were monitored using a linear array of 4.5-Hz Mark Products model L-15B geophones and Globe model 100C low-frequency microphones located at the soil or snow surface at distances up to 90 m away from the source. In addition, two Bruel & Kjaer type 4165 microphones were used to record the source pulse. A Bison model 9048 digital seismograph, triggered by a microphone located near the pistol, was used to record the waveforms at a sampling rate of 5 kHz per channel. The useful bandwidth of the measurements is estimated as 5–500 Hz and is limited mainly by the source output and the high frequency roll-off of the Globe microphones (see Fig. 1).

For each winter experiment, a snow characterization pit was used to determine the temperature, density, wetness, grain size, and crystal type for each layer present, using standard techniques.[35] Snow and frost depths were also measured throughout the test site. The ground was always frozen to at least 0.10 m depth during the winter measurements.

Meteorological data were collected using a Campbell Scientific model 21X data logger. Temperatures were measured within the ground and snow and at heights of up to 5 m in the air. Wind speeds at 1- and 3-m heights were also recorded, along with relative humidity and barometric pressure. All of the experiments were conducted on days of light or no wind and over short propagation ranges, so the atmospheric conditions introduced little variability in the acoustic measurements.

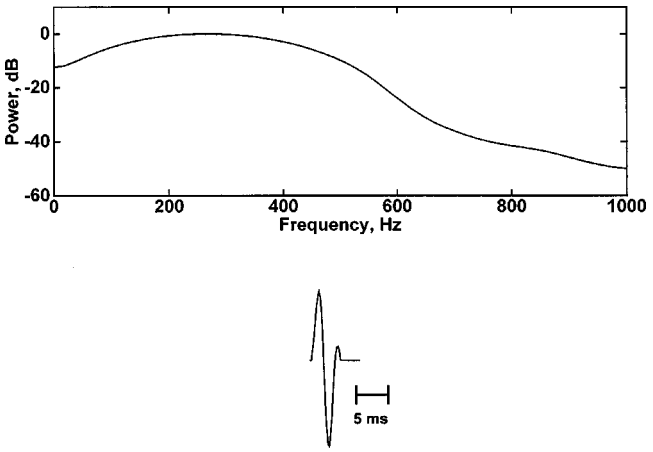

FIG. 1. Estimated source pulse from the blank pistol (bottom) and calculated power spectral magnitude (top). Because measurements of the source pulse made using a microphone 10 m away were influenced by ground reflections (and were often clipped), this source pulse is *estimated* by smoothing a measured waveform. The source spectrum shows the frequency bandwidth of the measurements.

Seismic refraction measurements taken under summer conditions indicated a compressional wave velocity of 265 $\mathrm{m\,s^{-1}}$ at the surface, with the velocity rapidly increasing to about 400 $\mathrm{m\,s^{-1}}$ within the upper meter. Laboratory analysis of soil samples showed that the soil type throughout the test area was a silty sand. The soil moisture content during the summer experiment was 25%.

Figure 2 summarizes the experimental measurements obtained. The figure shows the normalized pressure waveform recorded by a surface microphone 60 m away from the source location, for 11 different snow covers and for grass-covered ground. The waveforms recorded over snow are all elongated to various degrees, and exhibit relatively stronger low-frequency content than those recorded without snow present. This change in waveform shape when snow is present is mainly attributable to the existence of an acoustic surface wave above the highly absorbing snow surface.[36] The differences in the recorded waveforms are caused by changes in the snow-cover properties, which are also shown schematically in Fig. 2 and listed in Table I. These waveform changes will be examined more closely below when the inversion method is developed.

Two of the tests, experiments 11 and 12, occurred during the spring melt period. For these tests, the entire snowpack had ''ripened''; it had been at the melting point for some time, allowing the ice grains to become very large, and was rapidly melting. The snow cover was becoming very nonuniform in depth and discontinuous in some areas as the melt season progressed. These measurements showed the smallest waveform elongations recorded during the winter.

For each of the experiments, the peak pressure of the

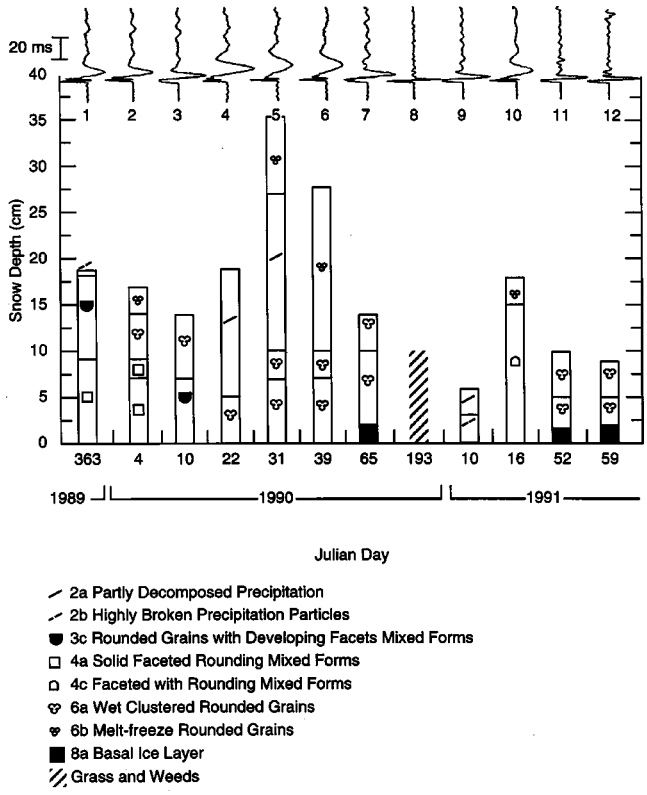

FIG. 2. Chronological evolution of snow-cover properties and the acoustic pulses measured after propagating from a source 60 m away. The snow-cover stratigraphy and crystal type are shown below the acoustic waveforms; additional snow-cover properties are listed in Table I. The microphone pressure waveforms are normalized. Experiment numbers indicated on the figure are in chronological order and are used in Tables I–III.

pulses, the amplitude decay with distance, and the acoustic-to-seismic coupling ratio, defined as the ratio of induced particle velocity in the snow to the incident acoustic pressure, were determined from the data and are listed in Table II. With the exception of the two measurements made during the melt period, the peak pressure at 60 m range was smaller by a factor of 3–7 than the peak pressure measured in the summer. This reduction in peak pressure is caused by increased transmission of sound energy into the subsurface as the pulses interact with the highly permeable snow cover in the winter.

The amplitude decay as a function of range was determined by least-squares fitting of the data from the surface microphones at all ranges to the expression

$$A(r)=A_1 r^{\alpha}, \tag{1}$$

where r is the propagation distance in m, $A(r)$ is the peak amplitude in Pa at range r, A_1 is the source amplitude at a reference distance r_1, and α is the distance attenuation exponent. The coefficient α for snow (Table II) is about -1.8 over snow (slightly lower during the melt period) compared to a value of -1.4 for the grass- and weed-covered ground in the summer. These values agree with previous longer-range pulse measurement values of -1.9 for snow and -1.2 for grass-covered soil.[4]

The acoustic-to-seismic coupling was determined from the collocated surface vertical component geophones and surface microphones (Table II). These ratios vary from 2 to $16\times10^{-6}\,\mathrm{m\,s^{-1}\,Pa^{-1}}$ and are in agreement with previous measurements.[4,37–40]

III. ACOUSTIC WAVEFORM ANALYSIS

The experimental data collected show that the acoustic pulse shapes are greatly affected by the presence of a snow cover. In this section, a method for automatically modeling these waveform changes and using this model to determine the physical characteristics of the snow cover is developed.

A. The forward problem: Calculating pulse shapes from known surface properties

Although most previous work in outdoor sound propagation used continuous wave sources, a few studies have used pulses, which are a much more stringent test of related acoustic theories. A method of calculating pulse shapes based on the Delaney–Bazley empirical model[27] of ground impedance has been developed[41–44] and applied to investigations of soil properties.[41,42,45,46] This work has been extended[31] by including a more complicated but physically based model of ground impedance.[28] The new model gave better agreement with observed measurements for snow, primarily because of its increased accuracy at low frequencies compared to the empirical model.

The procedure for calculating theoretical acoustic pulse waveforms from known (or assumed) surface properties is briefly outlined here. For a monofrequency source in the air and a receiver on the surface, the acoustic pressure P a slant distance r away from the source is given by

$$\frac{P}{P_0}=\frac{e^{ikr}}{kr}(1+Q)e^{-i\omega t}, \tag{2}$$

where P_0 is a reference source level, k is the wave number in air, and Q is the spherical wave reflection factor representing the effect of the ground. At high frequencies ($kr\gg1$), Q can be written as[47–49]

$$Q=R_P+(1-R_P)F(w), \tag{3}$$

where R_P is the plane wave reflection coefficient, F is the boundary loss factor, and w is a numerical distance, all of which depend on the specific surface impedance Z of the ground. The impedance is itself dependent upon frequency; thus, so is Q. [The elongation and relatively stronger low frequency content of the measured waveforms in Fig. 2 can be explained theoretically by the decrease in R_P at high frequencies and the enhancement of $F(w)$ at low frequencies (see Ref. 31, Fig 4).] For a particular frequency f_n (denoted by subscript n), once Q_n is determined, the response P_n can be written as

$$P_n=\frac{P_0}{4\pi r}S_n W_n(1+Q_n)e^{i2\pi f_n r/c}, \quad n=0,1,2,\ldots,N-1 \tag{4}$$

where S_n and W_n represent the source and instrument effects, respectively, and c is the speed of sound in air. An inverse FFT

TABLE I. Snow cover properties.

Experiment number	Date/ Julian day	Air temperature, °C	Height above base, cm	Snow temperature, °C	Grain classification[a]	Grain size, mm	Density, kg m^{-3}	Wet snow? (Dye test)
1	12-29-89	−13.5	0–9	−5.0	4a	4	170	N
	363		9–18	−9.5	3c	2	150	N
			18–18.5	−13.5	2b	1.5		N
2	1-4-90	4.0	0–7	0	4a	3	220	⋯
	4		7–9	0	4a	3	220	⋯
			9–14	0	6b	2	200	⋯
			14–17	0	6a	1	260	Y
3	1-10-90	1.5	0–7	−1.0	3c	3	240	N
	10		7–14	0	6b	2	280	Y
4	1-22-90	−5.0	0–5	−2.5	6b	0.5	210	N
	22		5–12	−3.0	2a	0.5	130	N
			12–19	−3.0	2a		100	N
5	1-31-90	−3.0	0–7	0	6b	1.0	260	N
	31		7–10	−0.5	6b	0.8	240	N
			10–27	−2.5	2a	0.25	120	N
			27–35.5	0	6a	0.25	140	N
6	2-8-90	5.0	0–7	0	6b	2	180	N
	39		7–10	0	6b	2	220	Y[b]
			10–19	0	6a	2	200	Y[b]
			19–28	0	6a		150	Y[b]
7	3-6-90	−2.0	0–2	−1.0	8c	⋯	>400	N
	65		2–10	−1.0	6b	1	290	N
			10–14	0	6b	1	340	N
8	7-12-90	18.0	0–10	Grass and weed covered soil				
	193							
9	1-10-91	−10.5	0–3	−5.0	2b	1	100	N
	10		3–6	−6.0	2a	4	100	N
10	1-16-91	2.0	0–5	−0.5	4c	0.5	190	N
	16		5–10	−0.5	4c	0.5	150	N
			10–15	−0.5	4c	0.75	140	N
			15–18	−0.5	6a	1	210	Y
11	2-21-91	6.0	0–1.5	0	8c	⋯	>400	Y
	52		1.5–5	0	6b	12	310	Y
			5–10	0	6b	8	270	Y
12	2-28-91	1.0	0–2	0	8c	⋯	>400	Y
	59		2–5	0	6b	4	220	Y
			5–9	0	6b	7	250	Y

[a]Snow grain types are given in accordance with the international standard; see Ref. 35. See Fig. 1 caption for grain types.
[b]During the acoustic experiments, which were conducted in the morning, the snow cover was cold and no liquid water was present. The snow warmed up considerably by the time the snow pit was done at noon.

$$P_m = \frac{1}{N}\sum_{n=0}^{N-1} P_n e^{-i2\pi mn/N}, \quad m = 0,1,2,...,N-1 \tag{5}$$

is used to construct theoretical pulse waveforms in the time domain. Nicolas *et al.*[29] have shown that an explicitly layered model of the ground must be used to represent thin snow covers, and this was done in the calculations presented here using (omitting the frequency subscripts)

$$Z = Z_2 \frac{Z_3 - iZ_2 \tan k_2 d}{Z_2 - iZ_3 \tan k_2 d}, \tag{6}$$

where d is the snow layer thickness, k_2 is the wave number in the layer, and Z_2 and Z_3 are the impedances of the snow layer and substratum, respectively (Ref. 50, p.17).

The acoustic behavior of the soil or snow is specified by the specific impedance Z_2 and wave number k_2, which are used in Eqs. (3) and (6) to find the theoretical waveform. A number of models are available in the literature to calculate these parameters.[51] In this paper, the parameters were calculated using Attenborough's[28] four-parameter model of ground impedance. The four input parameters are the effective flow resistivity σ, the porosity Ω, the pore shape factor ratio s_f, and the grain shape factor n'. The snow depth d and the substrate properties are also required in a layered model.

Attenborough's model describes propagation in the porous medium via the propagation constant k_2 and the characteristic impedance Z_c (which is the same as the surface impedance for a locally reacting material)

$$k_2 = \frac{\omega}{c_0} q \frac{C^{1/2}}{B^{1/2}}, \tag{7}$$

$$\frac{Z_c}{\rho_0 c_0} = \frac{q}{\Omega} \frac{1}{B^{1/2} C^{1/2}}, \tag{8}$$

where

TABLE II. Range decay coefficient and acoustic-to-seismic coupling ratio measured for air waves. The error bounds are 95% confidence intervals.

Experiment number	Date	Range decay coefficient α		Acoustic-to-seismic coupling ratio, $m\,s^{-1}\,Pa^{-1}$		Peak amplitude at 60 m Pa
		Number of points	α	Number of points	Ratio $\times 10^{-6}$	
1	363-89	32	-1.9 ± 0.4	31	1.9 ± 0.2	3.7
2	04-90	13	-1.8 ± 0.4	60	3.1 ± 0.3	5.3
3	10-90	18	-1.7 ± 0.2	80	2.9 ± 0.2	5.0
4	22-90	42	-1.6 ± 0.3	42	5.6 ± 0.7	2.1
5	31-90	40	-1.8 ± 0.4	40	16.2 ± 1.5	2.3
6	39-90	35	-1.7 ± 0.3	35	7.3 ± 0.5	2.0
7	65-90	18	-1.8 ± 0.3	36	3.1 ± 0.3	3.3
9	10-91	68	-1.9 ± 0.2	59	2.9 ± 0.3	4.0
10	16-91	50	-1.8 ± 0.2	50	10.8 ± 0.8	2.9
11	52-91	91	-1.6 ± 0.1	89	3.6 ± 0.2	6.6
12	59-91	76	-1.4 ± 0.1	76	4.7 ± 0.3	7.3
8	193-90	48	-1.4 ± 0.2	27	4.1 ± 0.9	13.8

$$B=\left[1-\frac{2}{D}T(D)\right],\quad C=\left[1-\frac{2(\gamma-1)}{N_{\mathrm{Pr}}^{1/2}D}T(N_{\mathrm{Pr}}^{1/2}D)\right],$$

$T(x)=[J_1(x)]/[J_0(x)]$
is the ratio of cylindrical Bessel functions,

$$\lambda=\frac{1}{s_f}[(8\rho_0 q^2\omega)/(\Omega\sigma)]^{1/2},\quad D=\lambda\sqrt{i},$$

$q^2=\Omega^{-n'}=$tortuosity,

γ=the ratio of specific heats (=1.4 for air), N_{Pr}=Prandtl number (=0.71 for air), and $\omega=2\pi f$.

For all of the calculations in this paper, the grain shape factor n' was set to 0.5 corresponding to spherical grains, and the porosity Ω was determined from the measured density of the snow. Parameters for the frozen soil beneath the snow were fixed at $\sigma=3000$ kN s m^{-4}, $\Omega=0.27$, $s_f=0.73$, and $n'=0.5$.[31] The effective flow resistivity σ, the snow depth d, and the pore shape factor ratio s_f were varied in the inversions discussed below.

B. The inverse problem: Finding snow parameters to match the observed acoustic waveforms

The previous section discussed the *forward* problem, using a rigid-ice-frame porous model of snow to calculate the expected waveform shape when the snow properties are measured or assumed. Through trial-and-error calculations, good agreement between the calculated and observed waveforms can often be obtained.[31] However, this procedure is time consuming and tedious, and does not provide information about the uniqueness of the waveform match or the sensitivity of the calculated waveforms to the snow parameters. In this section, the *inverse* problem is investigated, where the observed waveform is used to determine automatically the acoustic parameters of the snow. Two inversion strategies, one in the frequency domain and one in the time domain, were investigated in an attempt to match the experimentally observed waveforms.

1. Frequency-domain inversion

The elongated, low-frequency acoustic surface wave is a dominant characteristic of the pulse waveforms observed propagating over a snow cover (see Fig. 2). The first inversion attempt, therefore, was to try to match the dominant frequency of the observed waveform, since this frequency should sensitively depend on the snow-cover properties responsible for the acoustic surface wave shape. If successful, this inversion procedure would be extremely rapid, since the broadband time-domain waveform would not need to be calculated as part of the search procedure. Fast methods of finding the peak frequency from a given set of assumed acoustic parameters could be developed to further reduce the calculation times.

Unfortunately, problems were encountered when this inversion strategy was tested. Figure 3 shows a simplified example of the inversion. In this figure, the snow depth was held at the measured value of 0.28 m at the sensor location, and the pore shape factor ratio s_f is fixed at a value of 0.8. Only the effective flow resistivity σ was allowed to vary in calculating the theoretical peak frequency. The figure shows that there are two solutions; that is, there are two values of the flow resistivity that give agreement with the observed peak frequency. This *nonuniqueness* of solutions is a common feature of inversions, and indicates that the information content of the measurements is not enough to require a single parameter value to obtain agreement. There are a number of approaches one can take to investigate this nonuniqueness.[52]

However, these approaches were not considered because the problem is more serious than just finding multiple solutions. Figure 4 shows a comparison of the observed and theoretical waveforms; the agreement is very poor. Apparently, the frequency-domain representation of the observed waveform has a very broad spectral maximum. Thus, matching this parameter is not sufficiently sensitive to yield good waveform agreement as had been hoped. Although the method had the promise of very rapid calculations and inversions, it had to be abandoned because of its poor accuracy.

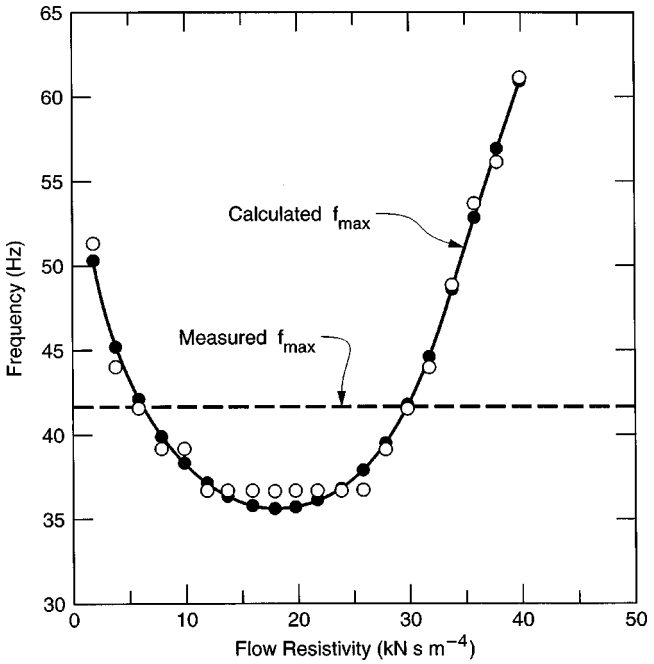

FIG. 3. A simplified example of the frequency-domain inversion for the acoustic waveform for experiment 6. The dashed line indicates the peak frequency found by Fourier analysis of the measured waveform, about 42 Hz. The symbols indicate theoretical peak frequencies, open circles represent the FFT bin, and filled circles (connected by the solid line) the interpolated frequency value. The x axis is the flow resistivity σ used to calculate the theoretical peak frequency. The snow depth is held at the measured value of 0.28 m at the sensor, and pore shape factor ratio s_f is fixed at a value of 0.8. Only the effective flow resistivity σ is allowed to vary.

2. Time-domain waveform inversion

In this section, an inversion procedure for directly matching the normalized, time-aligned microphone waveform is discussed. Theoretical waveforms are calculated using Attenborough's[28] model of ground impedance and Eqs. (2)–(6) as discussed above. For the snow, a single snow layer is used, with the effective flow resistivity σ, the snow depth d, and the pore shape factor ratio s_f being allowed to vary; parameters for the frozen soil below the snow are fixed at $\sigma=3000$ kN s m^{-4}, $\Omega=0.27$, $s_f=0.73$, and $n'=0.5$. For the summer case, a half-space model of the ground with the same variable parameters is used.

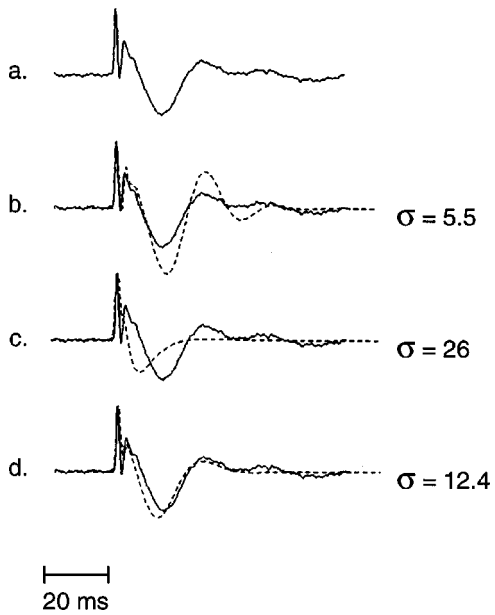

FIG. 4. Comparison of the observed (solid lines) and calculated (dashed lines) waveforms. (a) Measured pulse. (b), (c) Using the frequency domain inversion procedure and the parameters determined from Fig. 3. The agreement is very poor. (d) Using the time-domain inversion procedure shows much better agreement.

In setting up an inverse problem, one has a choice of a norm (or measure) of what is considered to be a good solution. Solutions are then compared using that norm, with the best solution having the minimum value. In this case, the norm was chosen to directly match the theoretical and observed waveforms. The best-fitting waveform was selected under the L_1 norm criterion (i.e., the sum of the absolute value of the differences between the calculated and observed waveforms over a fixed time window) by minimizing

$$\text{Error}=\sum_{t=0}^{\text{waveform}} |P_t^{\text{obs}}-P_t^{\text{calc}}|. \tag{9}$$

A least-squares criterion, the L_2 norm, was avoided because it heavily weights, and tries to reduce, the maximum misfit. Since the source pulse in the calculations is an estimated one, and not actually measured for each experiment, this approach allows for errors in this estimated source pulse to be ignored while accurately fitting the overall, low-frequency portion of the measured waveforms. However, as will be shown below, the waveform agreement turned out to be so close that the choice of norm had no effect on the results, and tests done using the L_2 norm gave the same results.

Before discussing the actual results of this inversion method, a simpler two-parameter inversion example is examined as an illustration. In the actual inversions, the pore shape factor ratio parameter had a small effect on the waveform fits, so it was held constant for this example. Changes in the effective flow resistivity and snow depth had a much larger effect on the theoretical waveform shape. Figure 5 shows these effects by comparing the observed waveform with calculated waveforms for a subset of values of the flow resistivity and snow depth parameters. The best parameters, $\sigma=12.5$ kN s m^{-4} and $d=0.19$ m, are easy to determine by eye and give excellent waveform agreement.

Figure 6 shows the error surface calculated for this experiment as the snow depth and effective flow resistivity were varied in the theoretical calculations. Even over this very large range of parameters, the surface is smooth and has only a single minimum. The appearance of this surface is very encouraging and unusual for an inverse problem, since the single minimum shows that there is only one best solution, and the smoothness of the surface indicates that it will be easy to find that solution, as apparently no local minima exist that could confuse a search procedure.

To find the best waveform fit, a simplex iterative search procedure[53] was implemented, with three variables: the effective flow resistivity σ, the snow depth d, and the pore shape factor ratio s_f. The waveform comparison was calculated for three initial triplets (with unrealistic starting parameter values), and these values were then used to estimate the gradient of the surface and select the next points to be tested.

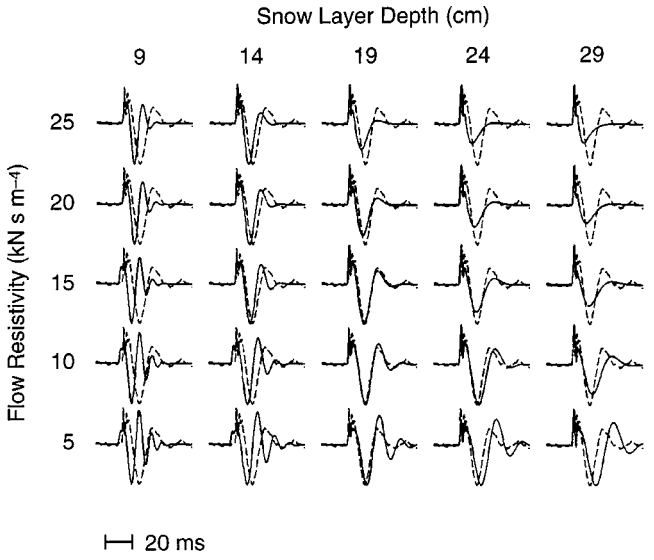

FIG. 5. Visual comparison of the agreement between the observed (dashed lines) and theoretical (solid lines) waveforms for experiment 4. The best fit occurs when the snow depth is 0.19 m and the effective flow resistivity is about 12.5 kN s m^{-4}, in agreement with the surface minimum shown in Fig. 6.

The algorithm moved smoothly and directly to the solution in all cases; restarts with different initial values led to the same final solution. The results of the inversions presented below indicate that the smooth shape of the error surface with a single minimum, as shown in Fig. 6, appears to be a general property, as all of the data waveforms were inverted without encountering any uniqueness or convergence problems. Because of the smoothness of the error surface, a less-conservative convergence procedure would probably work well and increase the search speed. Figure 4 shows the improvement in waveform matching obtained using the time-domain search procedure instead of the frequency-domain inversion.

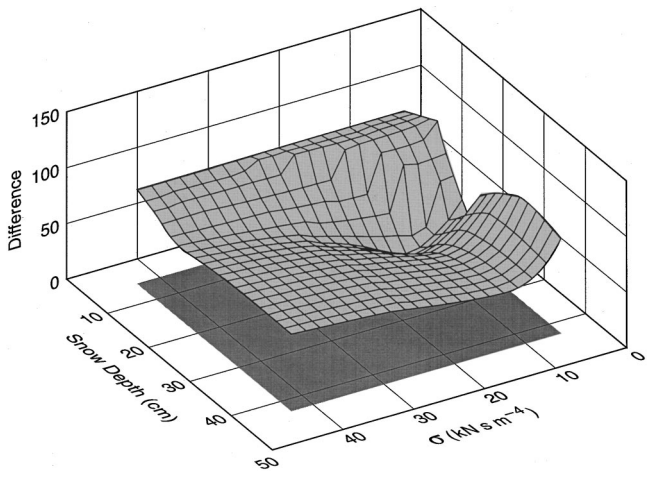

FIG. 6. Comparison of the agreement between observed and theoretical waveforms for experiment 4, using the norm given by Eq. (9). The snow depth and effective flow resistivity are varied in calculating the theoretical waveforms. The best waveform agreement occurs at the minimum of this smooth surface, and the goal of the inversion procedure is to find that minimum.

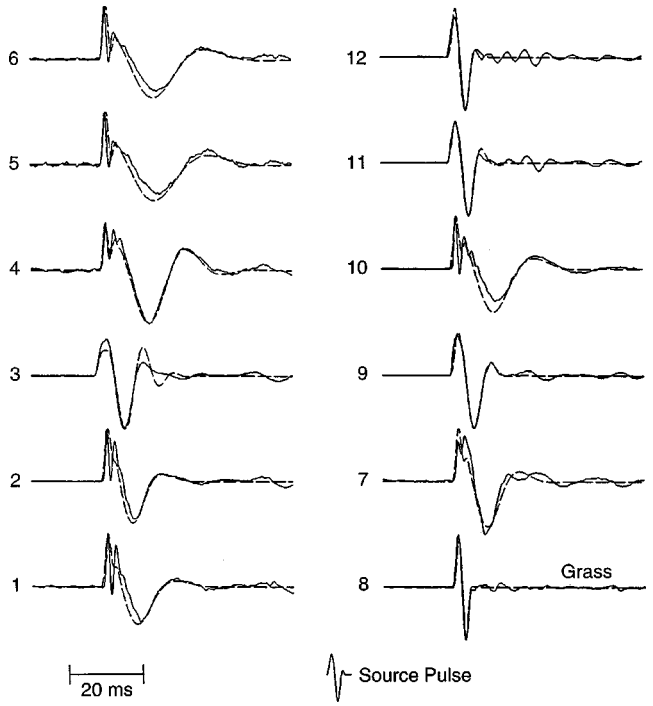

FIG. 7. Comparison of observed (solid lines) and acoustically determined theoretical waveforms (dashed lines) at a propagation distance of 60 m for all of the experiments. The agreement is excellent in all cases. Table II lists the snow parameters found using the waveform inversion procedure.

IV. RESULTS

Figure 7 shows the measured and the theoretical waveforms for all of the experiments. The inversion procedure has been able to automatically match waveforms of quite different appearance, and the agreement is excellent in all cases. Table III gives the snow parameters determined from the acoustic waveform inversion, listed in order of increasing pore shape factor ratio.

The acoustically determined snow depths agree well with the directly measured values. In most cases the agreement is within 0.02 m, which is less than the 0.05-m or greater variation in snow layer thickness along the actual propagation path caused by wind crusts and slight topographic variations. The worst error is 0.05 m, for the thickest snow cover (experiment 5, 0.35 m). In all but one case, the full snow depth was determined. This is not a surprising result considering the large acoustic wavelengths compared to the snow layer thickness. In the exception, experiment 3, the depth to a snow layer interface was determined. An ice layer was not noted at that depth in the snow pit, as might be expected, but a transition occurred from a fine-grained layer above to a coarse-grained layer beneath. This situation has been termed a ''capillary barrier'' to melt water flow through a soil or snow cover.[54,55] Since the daytime high air temperatures had risen to above 0 °C for a few days before this experiment, some melting may have occurred. The melt water would not have penetrated this interface because of the difference in capillary forces, and a very thin ice crust may have formed at this depth, which was overlooked in the snow pit but affected the acoustic wave penetration.

Figure 8 shows the relationship between the half-period

TABLE III. Snow parameters from waveform inversion.

Experiment number	Effective flow resistivity σ, kN s m^{-4}	Acoustic snow depth, cm	Measured snow depth, cm	Pore shape factor ratio, s_f	Wet snow?
6	12	30	28	0.75	Y[a]
7	24	17	14	0.79	N
4	12	19	19	0.80	N
5	11	30	35	0.81	N
1	27	16	18	0.84	N
2	26	14	17	0.93	Y
3	14	9[b]	14	0.97	Y
12	137	3	1–9	0.98	Y
10	11	21	20	0.99	Y
11	58	5	4–10	1.02	Y
9[c]	29	5	6	1.39	N
8[d]	345	⋯	⋯	1.00	N

[a]The snow was wet when the snow pit observations were made, but dry when the acoustic measurements were done earlier that morning.
[b]Depth to a snow layer interface.
[c]Newly fallen snow.
[d]Grass and weed covered ground; no snow present.

of the pressure waveform, defined as the time interval between the peak positive and negative pressures, and the snow depth. This plot shows a strong relationship between the waveform elongation and the snow depth.

The effective flow resistivity values in Table III range from 11 to 29 kN s m^{-4}, except for two late-season cases of discontinuous and very variable snow covers, where values of 58 and 137 were determined. For the grass-covered site in the summer, a value of 345 kN s m^{-4} was determined. These values agree with previous outdoor measurements on snow and soil.[1,3,29–31,56–58] The values also agree with Attenborough and Buser's directly measured values[32,33] of 5 to 17 kN s m^{-4} for alpine snow.

The results listed in Table III for the pore shape factor ratio s_f are of interest, since the values seemed to cluster into two groups, one near 1.0 and the other near 0.8. The value for the only measurement over newly fallen snow was vastly different at 1.4. This parameter is defined as

$$s_f^2 = \frac{8\eta q^2}{\Omega \sigma r_n^2}, \tag{10}$$

where η is the dynamic viscosity of air, q^2 is the tortuosity, Ω is the porosity, σ is the effective flow resistivity, and r_h is the hydraulic radius, defined as twice the area divided by the circumference of the pore cross-sectional shape.

The pore shape factor ratio was clearly secondary in importance, compared to the effective flow resistivity and snow depth, in determining the waveform fits. These two parameters caused very large changes in the waveform shape as they were varied, as can be seen from Fig. 5. The pore shape factor ratio did seem to influence the waveform shapes independently of the other parameters, causing the relative amplitudes of the peaks and troughs to vary, while leaving the overall shape and elongation unchanged. The clustering of the determined values indicates that this parameter may contain information about the pore structure and not just be a free parameter varied randomly to improve the waveform fits.

In all but one experiment, the presence or absence of liquid water in the snow corresponded with the two values of 1.0 and 0.8 (Table III). For the single exception, experiment 6, a closer examination of the field notes and meteorological data (including snow temperature) showed that the snow was wet when the snow pit observations were made, but still cold and dry when the acoustic measurements were done earlier that morning. The presence of liquid water within the snow pack, which tends to gather in the smallest pore necks because of surface tension, could be a physical change responsible for the observed changes in this parameter. The snow pores have complicated shapes and a wide distribution of sizes. Filling the smallest pores with liquid water would remove them from the acoustic interactions, which occur only

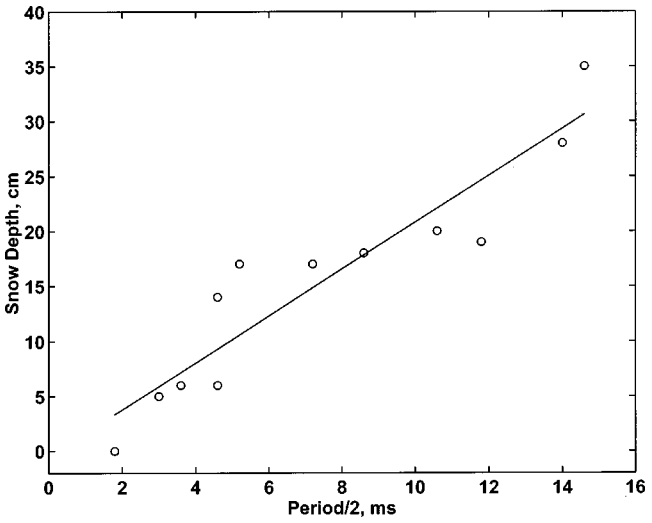

FIG. 8. Half-period of the acoustic waveform vs measured snow depth.

in air-filled pores, perhaps causing the measured change in the pore shape factor ratio parameter. For the newly fallen snow (experiment 9), the pore structure is expected to be quite different because of the much-flatter grain shapes.

Although originally derived as an index of cross-sectional shape, for uniform pores, later work[51,59,60] has shown that the pore shape factor ratio s_f should approach a value of 1 at low frequencies. In addition, comparison with measured data has shown that s_f varies with frequency. Models of acoustic wave propagation in porous materials that explicitly include the effect of pore-size distribution[61–63] have shown that the range of pore sizes present in a material can have measurable effects on the propagation. For these measurements on snow, the determined values of the pore shape factor ratio may be indirectly indicating differences, not in the pore shapes, but in the pore-size distribution. Confirming this hypothesis is left for future work.

Figure 8 shows that the wave elongation is proportional to the snow depth. Are there any other connections between waveform appearance and snow-cover properties? The waveforms for the measurements where the surface layer of the snow was grain type 6a (experiments 2, 5, 6, and 10) are all similar, with a sharp initial pulse followed by a low-frequency surface wave. Also, when the snow surface layer was grain type 6b (experiments 3, 7, 11, and 12), the initial part of the pulse was much more rounded. However, measurements over surface snow of type 2 grains (experiments 1, 4, and 9) have both types of waveforms. Snow-cover depth does consistently divide this set of waveforms into the sharp initial front (experiments 1, 2, 4, 5, 6, and 10) and rounded initial front (3, 7, 9, 11, and 12) classes, depending on whether the snow depth was greater or less than 0.15 m, respectively.

However, the reader is cautioned that these observations are extremely tentative, and must be confirmed by additional observations. In the author's opinion, a much more likely explaination is that atmospheric conditions may control the initial appearance of the waveforms. A slight headwind or upward-refracting temperature gradient would tend to bend the direct ray upwards, reducing its amplitude relative to the surface wave propagating along the surface, while a downwind or downward-refracting condition would tend to enhance this wave.

A subsequent measurement in Alaska[64] showed a dramatic example of this atmospheric effect. Figure 9 shows five waveforms recorded at a range of 202 m over a 3-min interval. The sun had set shortly before the measurements were made, and a strong temperature inversion was rapidly forming. The cooling caused a large amplitude refracted arrival to appear during the course of the measurements, ''sharpening'' the initial part of the waveform, while the surface wave pulse remained unchanged. The snow-cover properties did not change during the short time period of these measurements and cannot have been responsible for the observed waveform changes.

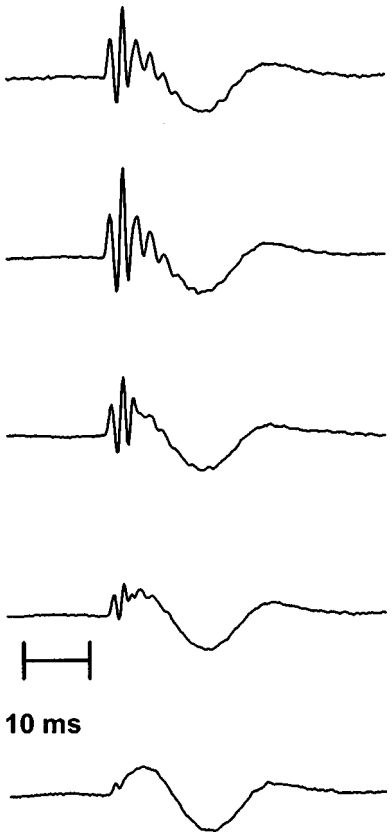

FIG. 9. Blank pistol shot waveforms recorded at a distance of 202 m. These measurements were done over a 3-min period (from bottom to top) in Alaska during the development of an atmospheric inversion layer shortly after sunset. An arrival that is refracted through the air above the snow cover appears and becomes stronger with time as the air cools. (Modified from Ref. 64.)

V. CONCLUDING REMARKS

In this paper, the results of 11 separate measurements of the effects of New England seasonal snow cover on acoustic pulse propagation in the atmosphere have been presented. The measurements show that, when a snow cover is present, the acoustic waveform shape, peak sound-pressure levels, and sound attenuation rates are very different from those measured under summer conditions. An automatic waveform inversion method was successfully implemented and was able to determine unique snow parameters that gave excellent agreement between the measured and calculated acoustic waveforms. The effective flow resistivities determined using this automatic inversion method agree with previous acoustic measurements on snow. The acoustically determined snow depths agreed with the directly measured depths, except for a single case where the depth to a snow layer interface was found. Also, except for a single measurement over newly fallen snow, the pore shape factor ratios determined by the inversion procedure clustered into two groups that may indicate the presence or absence of liquid water within the snowpack. Additional measurements will be made over snow and other winter ground conditions to continue this investigation of environmentally induced variations in acoustic propagation.

In the future, the theoretical approach will be improved in three ways. First, the inversion method will be expanded to include layers within the snow, rather than treating it as a single layer. This modification may allow the snow cover stratigraphy to be determined acoustically. However, the

unique solution found for a single layer may disappear when multiple layers are included. The second improvement will be to implement a jumping approach[65] to select the next parameters in the inversion search. Because the error surface is smooth, this approach should significantly speed up the calculations needed to match the waveforms. Finally, incorporating rigid porous ground impedance models that explicitly include the pore-size distribution as a parameter may offer an improved understanding of the results and additional knowledge of the properties of the snow cover.

Since the effective flow resistivity is proportional to the dynamic viscosity of air divided by the snow permeability, this acoustic waveform inversion method may lead to a useful method of determining snow permeability, a parameter that is currently difficult to measure but of great importance in snow science. Acoustic measurements also have the advantage of determining a spatially averaged permeability value at a scale selectable by the propagation path. This capability is an improvement over current laboratory and field measurements, which are limited to point samples and small sample sizes. Scales could be selected on the basis of the geophysical parameter of interest, and measurements along different directions could be used to investigate, for example, the influence of sastrugi (large surface wind crusts) on snow or firn ventilation for ice core studies. Direct comparison of acoustically determined and conventionally measured[66,67] snow permeabilities are planned in the near future.

ACKNOWLEDGMENTS

These experiments could not have been conducted without the assistance of many of my co-workers. Nancy Greeley provided all the meteorological data, did much of the snow characterization, and assisted with the experiments. Steve Decato was the primary shooter and provided much additional support. Dave Gaskin helped to arrange for the use of the test site and Jim Cragin provided access to a heated shelter for the equipment and personnel. Their assistance is greatly appreciated. Thanks are also due to LT Karen Faran, Gus Greeley, SSG Tommie Hall, Mark Moran, and Frank Perron for their help. Technical reviews were provided by Gilles Daigle and Mark Moran. The author especially appreciated comments from the Associate Editor, Lou Sutherland, and two anonymous reviewers, which greatly improved the clarity of the paper. This work is supported by the Directorate of Research and Development, U.S. Army Corps of Engineers.

[1] K. Attenborough, ''Ground parameter information for propagation modeling,'' J. Acoust. Soc. Am. **92**, 418–427 (1992).
[2] T. F. W. Embleton, J. E. Piercy, and N. Olson, ''Outdoor sound propagation over ground of finite impedance,'' J. Acoust. Soc. Am. **59**, 267–277 (1976).
[3] T. F. W. Embleton, J. E. Piercy, and G. A. Daigle, ''Effective flow resistivity of ground surfaces determined by acoustical measurements,'' J. Acoust. Soc. Am. **74**, 1239–1244 (1983).
[4] D. G. Albert and J. A. Orcutt, ''Observations of low frequency acoustic-to-seismic coupling in the summer and winter,'' J. Acoust. Soc. Am. **86**, 352–359 (1989).
[5] R. A. Sommerfeld, ''A review of snow acoustics,'' Rev. Geophys. Space Phys. **20**, 62–66 (1982).
[6] G. Seligman, ''Sound absorption of snow,'' Nature (London) **143**, 1071 (1939).
[7] S. W. Colliander, ''Russian ski patrols in action,'' Befael **37**(1), 22–25 (1954).
[8] G. W. C. Kaye and E. J. Evans, ''Sound absorption of snow,'' Nature (London) **143**, 80 (1939).
[9] R. B. Watson, ''On the propagation of sound over snow,'' J. Acoust. Soc. Am. **20**, 846–848 (1948).
[10] T. Ishida and S. Onodera, ''Sound absorption by a snow layer,'' Low Temp. Sci., Ser. A **12**, 17–24 (1954).
[11] T. Ishida, ''Acoustic impedance of a snow layer,'' Low Temp. Sci., Ser. A **15**, 81–91 (1956).
[12] T. Ishida, ''Acoustic impedance of a snow layer II,'' Low Temp. Sci., Ser. A **16**, 241–248 (1957).
[13] T. Ishida and H. Shimizu, ''Resistance to air flow through snow layers (Part 1),'' SIPRE Translation 60 [Translation of Low Temp. Sci., Ser. A **14**, 32–42 (1955)] (1958).
[14] T. Ishida, ''Acoustic properties of snow,'' Low Temp. Sci., Ser. A **20**, 23–63 (1965).
[15] H. Oura, ''Reflection of sound at snow surface,'' Seppyo **12**, 273–275 (1950).
[16] H. Oura, ''Sound velocity in snow cover,'' Low Temp. Sci. Ser. A **9**, 171–178 (1953).
[17] H. Oura, ''Reflection of sound at snow surface and mechanism of sound propagation in snow,'' Low Temp. Sci. Ser. A **9**, 179–186 (1953).
[18] H. Oura, ''A study on the optical and the acoustical properties of the snow cover,'' General Assembly of Rome, 1954, IASH Publication No. 4, pp. 71–81 (1954).
[19] S. M. Lee and J. C. Rodgers, ''Characterization of snow by acoustic sounding: A feasibility study,'' J. Sound Vib. **99**, 247–266 (1985).
[20] J. G. Tillotson, ''Attenuation of sound over snow-covered fields,'' J. Acoust. Soc. Am. **39**, 171–173 (1965).
[21] H. Gubler, ''Artificial release of avalanches by explosives,'' J. Glaciol. **19**, 419–429 (1977).
[22] J. B. Johnson, ''On the application of Biot's theory to acoustic wave propagation in snow,'' Cold Regions Sci. Technol. **6**, 49–60 (1982).
[23] M. A. Biot, ''Theory of propagation of elastic waves in a fluid-saturated porous solid. I. Low-frequency range,'' J. Acoust. Soc. Am. **28**, 168–178 (1956).
[24] M. A. Biot, ''Theory of propagation of elastic waves in a fluid-saturated porous solid. II. Higher frequency range,'' J. Acoust. Soc. Am. **28**, 179–191 (1956).
[25] M. A. Biot, ''Mechanics of deformation and acoustic propagation in porous media,'' J. Appl. Phys. **33**, 1482–1498 (1962).
[26] K. Attenborough, ''Review of ground effects on outdoor sound propagation from continuous broadband sources,'' Appl. Acoust. **24**, 289–319 (1988).
[27] M. E. Delaney and E. N. Bazley, ''Acoustical properties of fibrous absorbent materials,'' Appl. Acoust. **3**, 105–116 (1970).
[28] K. Attenborough, ''Acoustical impedance models for outdoor ground surfaces,'' J. Sound Vib. **99**, 521–544 (1985).
[29] J. Nicolas, J.-L. Berry, and G. A. Daigle, ''Propagation of sound above a finite layer of snow,'' J. Acoust. Soc. Am. **77**, 67–73 (1985).
[30] H. M. Moore, K. Attenborough, J. Rogers, and S. Lee, ''*In situ* acoustical investigations of deep snow,'' Appl. Acoust. **33**, 281–301 (1991).
[31] D. G. Albert and J. A. Orcutt, ''Acoustic pulse propagation above grassland and snow: Comparison of theoretical and experimental waveforms,'' J. Acoust. Soc. Am. **87**, 93–100 (1990).
[32] O. Buser, ''A rigid frame model of porous media for the acoustic impedance of snow,'' J. Sound Vib. **111**, 71–92 (1986).
[33] K. Attenborough and O. Buser, ''On the application of rigid-porous models to impedance data for snow,'' J. Sound Vib. **124**, 315–327 (1988).
[34] S. C. Colbeck, ''An overview of seasonal snow metamorphism,'' Rev. Geophys. Space Phys. **20**(1), 45–61 (1982).
[35] S. Colbeck, E. Akitaya, R. Armstrong, H. Gubler, J. Lafeuille, K. Lied, D. McClung, and E. Morris, ''International Classification for Seasonal Snow on the Ground,'' International Comm. Snow and Ice (IAHS), World Data Center A for Glaciology, University of Colorado, Boulder (1990).
[36] D. G. Albert, ''Observations of acoustic surface waves propagating above a snow cover,'' *Proceedings of the Fifth International Conference on Long Range Sound Propagation* (The Open University, Milton Keynes, England, 1992), pp. 10–16.
[37] H. A. J. M. van Hoof and K. W. F. M. Doorman, ''Coupling of airborne sound in a sandy soil,'' TNO/LEOK Rep. No. TR 1983-09, Netherlands

Organization for Applied Scientific Research, Laboratory for Electronic Developments for the Armed Forces, Oegstgeest, NL (1983).
[38] C. Madshus and A. M. Kanyia, ''Ground response to propagating airblast,'' *Inter-Noise 96* (Institute of Acoustics, Liverpool, UK, 1996), pp. 1433–1438.
[39] H. E. Bass, L. N. Bolen, D. Cress, J. Lundien, and M. Flohr, ''Coupling of airborne sound into the earth: Frequency dependence,'' J. Acoust. Soc. Am. **67**, 1502–1506 (1980).
[40] J. M. Sabatier, H. E. Bass, and L. N. Bolen, ''Acoustically induced seismic waves,'' J. Acoust. Soc. Am. **80**, 646–649 (1986).
[41] A. J. Cramond and C. G. Don, ''Reflection of impulses as a method of determining acoustic impedance,'' J. Acoust. Soc. Am. **75**, 382–389 (1984).
[42] C. G. Don and A. J. Cramond, ''Soil impedance measurements by an acoustic pulse technique,'' J. Acoust. Soc. Am. **77**, 1601–1609 (1985).
[43] R. Raspet, H. E. Bass, and J. Ezell, ''Effect of finite ground impedance on the propagation of acoustic pulses,'' J. Acoust. Soc. Am. **74**, 267–274 (1983).
[44] R. Raspet, J. Ezell, and H. E. Bass, Additional comments on and erratum for ''Effect of finite ground impedance on the propagation of acoustic pulses'' [J. Acoust. Soc. Amer. **74**, 267–274 (1983)], J. Acoust. Soc. Am. **77**, 1955–1958 (1985).
[45] A. J. Cramond and C. G. Don, ''Effects of moisture content on soil impedance,'' J. Acoust. Soc. Am. **82**, 293–301 (1987).
[46] C. G. Don and A. J. Cramond, ''Impulse propagation in a neutral atmosphere,'' J. Acoust. Soc. Am. **81**, 1341–1349 (1987).
[47] K. Attenborough, S. I. Hayek, and J. M. Lawther, ''Propagation of sound above a porous half-space,'' J. Acoust. Soc. Am. **68**, 1493–1501 (1980).
[48] K. U. Ingard, ''On the reflection of a spherical wave from an infinite plane,'' J. Acoust. Soc. Am. **23**, 329–335 (1951).
[49] I. Rudnick, ''Propagation of an acoustic wave along a boundary,'' J. Acoust. Soc. Am. **19**, 348–356 (1947).
[50] L. M. Brekhovskikh, *Waves in Layered Media*, 2nd ed. (Academic, New York, 1980).
[51] J. F. Allard, *Propagation of Sound in Porous Media* (Elsevier, London, 1993), p. 284.
[52] S. C. Constable, R. L. Parker, and C. G. Constable, ''Occam's inversion: A practical algorithm for generating smooth models from electromagnetic sounding data,'' Geophysics **52**, 289–300 (1987).
[53] W. H. Press, B. P. Flannery, S. A. Teukolsky, and W. T. Vetterling, *Numerical Recipes: The Art of Scientific Computing* (Cambridge University Press, New York, 1986).
[54] R. Jordan, ''Effects of capillary discontinuities on water flow and water retention in layered snow covers,'' International Symposium on Snow and Related Manifestations, Manali, India (1994).
[55] D. Hillel and R. S. Baker, ''A descriptive theory of fingering during infiltration into layered soils,'' Soil Sci. **146**, 51–56 (1988).
[56] H. M. Hess, K. Attenborough, and N. W. Heap, ''Ground characterization by short-range propagation measurements,'' J. Acoust. Soc. Am. **87**, 1975–1986 (1990).
[57] J. M. Sabatier, H. Hess, W. P. Arnott, K. Attenborough, M. J. M. Roemkens, and E. H. Grissinger, ''*In situ* measurements of soil physical properties by acoustical techniques,'' Soil Sci. Soc. Am. J. **54**, 658–672 (1990).
[58] Care is needed in comparing these values with other work, since in many cases a different definition of effective flow resistivity is used. For example, Hess *et al.* (Ref. 56) use $\sigma_{pe}=\frac{1}{4}s_f^2\Omega\sigma$. Reducing the values reported here according to the above definition gives agreement with Hess *et al.*'s low reported values of 1 to 3 kN s m^{-4}.
[59] Y. Champoux and M. R. Stinson, ''On acoustical models for sound propagation in rigid frame porous materials and the influence of shape factors,'' J. Acoust. Soc. Am. **92**, 1120–1131 (1992).
[60] M. R. Stinson and Y. Champoux, ''Propagation of sound and the assignment of shape factors in model porous materials having simple pore geometries,'' J. Acoust. Soc. Am. **91**, 685–695 (1992).
[61] K. Attenborough, ''Models for the acoustical properties of air-saturated granular media,'' Acta Acust. (China) **1**, 213–226 (1993).
[62] D. K. Wilson, ''Relaxation-matched modeling of propagation through porous media, including fractal pore structure,'' J. Acoust. Soc. Am. **94**, 1136–1145 (1993).
[63] T. Yamamoto and A. Turgut, ''Acoustic wave propagation through porous media with arbitrary pore size distribution,'' J. Acoust. Soc. Am. **83**, 1744–1751 (1988).
[64] D. G. Albert, ''Environmental effects on acoustic wave propagation at Ft. Greely, Alaska,'' *1998 Meeting of the IRIS Specialty Group on Acoustic and Seismic Sensing* (Johns Hopkins University, Laurel, MD, 1999), pp. 273–280.
[65] P. R. Shaw and J. A. Orcutt, ''Waveform inversion of seismic refraction data and applications to young Pacific crust,'' Geophys. J. R. Astron. Soc. **82**, 375–414 (1985).
[66] E. F. Chacho, Jr. and J. B. Johnson, ''Air permeability of snow,'' EOS Trans. Am. Geophys. Union **68**, 1271 (abstract) (1987).
[67] J. P. Hardy and D. G. Albert, ''The permeability of temperate snow: Preliminary links to microstructure,'' Proceedings of the 50th Eastern Snow Conference, Quebec, Canada (1993), pp. 149–156.

Perturbation theory applied to sound propagation in flowing media confined by a cylindrical waveguide

M. Willatzen[a)]
IN-EV, Danfoss A/S, DK-6430, Nordborg, Denmark and Mads Clausen Institute for Product Innovation, University of Southern Denmark, Gundtvigs Alle 150, DK-6400 Sønderborg, Denmark

(Received 23 November 1999; revised 10 October 2000; accepted 16 October 2000)

First-order perturbation theory is employed to examine sound propagation in flowing media confined by a cylindrical waveguide. The use of perturbation theory allows examination of mode phase-speed changes due to any radially dependent flow $w(r)$ as long as the flow magnitude is sufficiently small. The condition to be fulfilled is satisfied in the flow range: 0–0.3 m/s for the specific values of cylinder radius, ultrasound frequency, and sound speed analyzed in the present work [in the general case, however, the condition in Eq. (1) of the present work must be fulfilled]. This freedom of choice, i.e., the possibility to handle any radial flow profile, is used to analyze two flow profile cases: (1) where $w(r)$ is a linear combination of a laminar flow profile and a flat profile corresponding to turbulent flow, and (2) where $w(r)$ is a linear combination of a laminar flow profile and a more realistic logarithmic-dependent turbulent flow profile. In both cases, it is shown that large errors may result in ultrasound flow measurements if several modes are excited by the transmitting transducer, and that a logarithmic flow profile in the turbulent regime leads to somewhat larger measurement errors at high flow values as compared to assuming a simple flat profile in the turbulent regime. © *2001 Acoustical Society of America.* [DOI: 10.1121/1.1331676]

PACS numbers: 43.28.Py [LCS]

I. INTRODUCTION

In ultrasonic flow metering based on reciprocal ultrasound systems, measurements are usually carried out by performing two-signal exchanges, one where an ultrasound pulse travels upstream with respect to flow, and the other corresponds to the reverse case where an ultrasound pulse travels downstream with respect to flow.[1] Such a sequential measurement allows determination of the mean flow without any prerequired knowledge of the transmission medium, if the fundamental acoustic mode is the only mode excited in the cylindrical waveguide confining the sound (and flow) between the two transducers. This was suggested by Lechner[2–4] (although his conclusions on mode phase speed changes with flow are wrong) and the present author.[5] Both analyses are based on the original work by Sodha *et al.* on a flow $w(r)$ that can be described by the radial dependence: $w(r)=w_0[1-(1-\tau)(r^2/R^2)]$, where τ is the so-called profile parameter.[6] However, as will be shown in the present work, first-order perturbation theory allows *any* dependence $w=w(r)$ to be analyzed in terms of mode phase-speed changes with flow. Common to the present method based on perturbation theory as well as Sodha *et al.*'s method is that the flow must be sufficiently small so that the condition

$$\left(\frac{\omega R}{c_0'}\right)^2 \frac{\overline{w}}{c_0'} \ll 1, \tag{1}$$

is fulfilled, where ω, R, c_0', and $\overline{w}$ denote the angular frequency, cylinder radius, medium sound speed, and mean flow, respectively. The freedom to examine any radially dependent flow $w(r)$ by perturbation theory is next used to compare two flow cases: (1) where the flow profile is a linear combination of a laminar profile and a flat profile describing fully developed turbulence, and (2) where the flow profile is a linear combination of a laminar flow profile and a more realistic logarithmic profile describing fully developed turbulence.[7] Consequences for accurate ultrasonic flow measurements are discussed for both flow cases.

II. PERTURBATION THEORY APPLIED TO SOUND PROPAGATION IN CYLINDRICAL WAVEGUIDES

In a quiescent medium (liquid), the time-dependent wave equation for sound propagation can be written as

$$\frac{\partial^2 \Phi}{\partial t^2} - c_0'^2 \nabla^2(\Phi) = 0, \tag{2}$$

where Φ is the scalar potential field. In the case of continuous operation, $\Phi(t) \propto \exp(i\omega t)$ and Eq. (2) simplifies to

$$\nabla^2 \Phi + \frac{\omega^2}{c_0'^2}\Phi = 0, \tag{3}$$

with the general solution using the separation-of-variables method[8]

$$\Phi(r,\theta,z;t) = \sum_{m,n} d_{mn} \Psi_{mn}(r)\, \eta_m(\theta) Z_n(z) \exp(i\omega t), \tag{4}$$

where

$$\frac{d^2 Z_n}{dz^2} = (k_n^2 - k_0^2) Z_n = -\beta_n^2 Z_n, \tag{5}$$

$$\frac{1}{r}\frac{d}{dr}\left(r\frac{d\Psi_{mn}}{dr}\right) + \left(k_n^2 - \frac{m^2}{r^2}\right)\Psi_{mn} = 0, \tag{6}$$

a)Electronic mail: mwillatzen@danfoss.dk

$$\frac{d^2\eta_m}{d\theta^2} = -m^2\eta_m. \tag{7}$$

In Eq. (5), the wave number $k_0=\omega/c_0'$ has been introduced. The constants d_{mn}, k_n (at this point unspecified) are determined by the inlet flow conditions and the boundary conditions at the cylinder wall, respectively. The second expression in Eq. (5) serves to define β_n, i.e., $\beta_n=\sqrt{k_0^2-k_n^2}$. The functions $\Psi_{mn}(r)$, $\eta_m(\theta)$, and $Z_n(z)$ represent the (functional) dependencies of $\Phi(r,\theta,z;t)$ on r, θ, and z, respectively.

If axisymmetric solutions are sought, Φ must be independent of θ, i.e., $m=0$, and $\eta_m=1$ can be chosen. Then, Eq. (6) reduces to

$$\frac{1}{r}\frac{d}{dr}\left(r\frac{d\Psi_n}{dr}\right)+k_n^2\Psi_n=0, \tag{8}$$

with the well-known solution

$$\Psi_n(r)=J_0(k_nr), \tag{9}$$

where J_0 is Bessel's zeroth-order function.

Furthermore, if the cylinder wall is assumed rigid, the velocity vanishes at $r=R$, where R is the cylinder radius, equivalent to

$$\mathbf{v}|_{r=R}=\boldsymbol{\nabla}\Psi_n|_{r=R}=0, \tag{10}$$

such that $k_n=j_{1n}/R$, and j_{1n} are the discrete set of zero points of Bessel's first-order function J_1. The most general solution to Eq. (2) now becomes

$$\Phi(r,\theta,z;t)=\sum_n d_nJ_0\left(\frac{j_{1n}}{R}r\right)\exp(i(\omega t+\beta_nz)), \tag{11}$$

where

$$\beta_n=\sqrt{\omega^2/c_0'^2-j_{1n}^2/R^2}. \tag{12}$$

The constants d_n are fixed by the boundary conditions at the cylinder inlet face.

III. WAVE EQUATION UNDER FLOW

Consider the medium to be homogeneous in terms of the density and in equilibrium but allow for a radially dependent sound speed $c(r)$ due to an underlying axial flow. Equation (3) is then modified to (see Ref. 9)

$$\boldsymbol{\nabla}^2\Phi+\frac{\omega^2}{c(r)^2}\Phi=0, \tag{13}$$

where

$$c(r)=c_0'+w(r), \tag{14}$$

and $w(r)$ is the fluid velocity assumed independent of azimuthal angle as well as the axial coordinate z.

Under typical conditions,

$$w(r)\ll c_0', \tag{15}$$

and the equation replacing Eq. (8) becomes

$$\frac{1}{r}\frac{d}{dr}\left(r\frac{d\Psi_n'}{dr}\right)+\left[k_0^2\left(1-\frac{2w(r)}{c_0'}\right)-\beta_n'^2\right]\Psi_n'=0, \tag{16}$$

where Ψ_n' and β_n' denote the corresponding solutions and eigenvalues to Eq. (16) subject to the rigid wall boundary condition: $\mathbf{v}|_{r=R}=\boldsymbol{\nabla}\Psi_n'|_{r=R}=0$. Note that primed variables correspond to the perturbed case (with flow), whereas unprimed variables correspond to the unperturbed case (without flow). The other equation describing the axial part of the total solution: Z_n is left unchanged as compared to the case without a medium flow except that β_n must be replaced by β_n' in Eq. (5).

The differential equation (16) cannot be solved analytically in the general case where $w(r)$ is an arbitrary function of r. It is, however, possible to find expressions by use of first-order perturbation theory that link β_n' to β_n and $\Psi_n'(r)$ to $\Psi_n(r)$ as a function of $w(r)$ if the term proportional to $w(r)$ in Eq. (16) is small enough. What ''small enough'' means becomes clear in the discussion that follows.

The analysis starts out by defining the differential operator L by

$$L=\frac{1}{r}\frac{d}{dr}\left(r\frac{d}{dr}\right)+k_0^2. \tag{17}$$

Equation (3) can now be rewritten as

$$L\Psi_n=\beta_n^2\Psi_n, \tag{18}$$

and in order to satisfy orthonormality

$$\int_0^R\Psi_k(r)\Psi_n(r)r\,dr=\delta_{kn}. \tag{19}$$

Ψ_n must be specified as

$$\Psi_n(r)=\frac{\sqrt{2}}{J_0(j_{1n})R}J_0(k_nr). \tag{20}$$

A differential operator L' is also introduced

$$L'=L(r)+W(r)=L+W, \tag{21}$$

where

$$W(r)=-2k_0^2\frac{w(r)}{c_0'}. \tag{22}$$

Note that W is the operator term due to the *flow perturbation*. This term must be added to the original operator L in the differential equation for the radial part of the potential scalar field [Eq. (18)] in the presence of a background flow.

In terms of L', Eq. (16) reads

$$L'\Psi_n'=\beta_n'^2\Psi_n'. \tag{23}$$

Since $w(r)\ll c_0'$, the appearance of a superimposed flow only slightly modifies the sound propagation problem, equivalent to stating that

$$W\ll L. \tag{24}$$

The new wave functions Ψ_n' can therefore be written as

$$\Psi_n'=\sum_p c_p\Psi_p, \tag{25}$$

where $c_p \ll c_n$, if $p \neq n$. In Eq. (25), p runs over all mode indices ($p=1,2,3,\ldots$) and c_p ($p \neq n$) is different from zero only if the perturbation due to flow results in new wave functions (i.e., new modes) being a mixture of the original wave functions (original modes) corresponding to zero flow. Substituting this expansion in Eq. (23), we obtain

$$L'\Psi_n' = \beta_n'^2 \sum_p c_p \Psi_p = \sum_p c_p(\beta_p^2 + W)\Psi_p \approx \sum_p (c_p \beta_p^2 \Psi_p) + W\Psi_n, \tag{26}$$

since $c_p W$ ($p \neq n$) is small to second order and can be neglected. Also, $c_n W \approx W$ up to second order. Multiplying by Ψ_k (k is any of the mode indices: 1,2,3,...) and integrating over r yields

$$c_k(\beta_n'^2 - \beta_k^2) = W_{kn}, \tag{27}$$

where

$$W_{kn} = \int_0^R \Psi_k(r) W(r) \Psi_n(r) r\, dr. \tag{28}$$

The change in β_n caused by the underlying flow therefore reads

$$\Delta\beta_n^2 = \beta_n'^2 - \beta_n^2 = W_{nn}, \tag{29}$$

again neglecting second-order terms. Furthermore, an expression for c_k can now be given

$$c_k = \frac{W_{kn}}{\beta_n^2 - \beta_k^2}, \tag{30}$$

if $k \neq n$. The coefficient c_n still remains arbitrary, but can be found from the requirement that Ψ_n' must be normalized up to and including terms of first order in W. Since

$$\left| \Psi_n + \sum_k{}' \frac{W_{kn}}{\beta_n^2 - \beta_k^2} \Psi_k \right|^2 \tag{31}$$

differs from unity by a quantity of the second order of smallness, we must have $c_n = 1$, and

$$\Psi_n' = \Psi_n + \sum_k{}' \frac{W_{kn}}{\beta_n^2 - \beta_k^2} \Psi_k. \tag{32}$$

Note that the prime (Σ_k') means that the term with $k=n$ is omitted from the sum. Another point should be mentioned: The condition that $c_k (k \neq n)$ must be small for the approximations above to hold is equivalent to [from Eq. (30)]

$$|W_{kn}| \ll |\beta_n^2 - \beta_k^2|, \quad k \neq n. \tag{33}$$

Whenever Eq. (33) is fulfilled, first-order perturbation theory can be used. In the following section, sound propagation in flowing media confined by a cylindrical waveguide will be examined in two cases of flow profiles using perturbation theory as described above.

IV. PHASE-SPEED CHANGES WITH FLOW IN CASES WHERE THE FLOW PROFILE CAN BE DESCRIBED AS A MIXTURE OF LAMINAR AND TURBULENT FLOW PROFILES

In this section, perturbation theory will be used to examine the influence of laminar, mixed, and turbulent flow profiles for the various mode phase speeds. Particular attention is given to the effect of a more realistic logarithmic flow profile describing fully developed turbulence as compared to the assumption of a simple flat profile on mode phase-speed changes with flow.

Phase-speed changes with flow due to a combination of a simple flat profile in the turbulent regime and a laminar (parabolic) flow profile is described elsewhere by solving the wave equation directly in cases where Eq. (1) is satisfied. The analysis carried out in Refs. 2–6 is *restricted* to flow profiles that correspond to a linear combination of a flat profile and a parabolic profile, whereas perturbation theory, as described in the present work, can be applied to *any* flow profile $w(r)$. This freedom allows us to compare phase-speed changes with flow in the two cases where the flow profile can be written as

$$w_1(r) = \alpha w(r)_{\text{lam}} + (1-\alpha) w(r)_{\text{turb}}^{\text{fp}}, \tag{34}$$

corresponding to the case studied in Refs. 2–6 and

$$w_2(r) = \alpha w(r)_{\text{lam}} + (1-\alpha) w(r)_{\text{turb}}^{\text{log}}, \tag{35}$$

where

$$w(r)_{\text{lam}} = 2\overline{w}\left(1 - \frac{r^2}{R^2}\right), \tag{36}$$

$$w(r)_{\text{turb}}^{\text{fp}} = \overline{w}, \tag{37}$$

$$w(r)_{\text{turb}}^{\text{log}} = \overline{w}\left(1 + \frac{2.652 + 1.768\ln(1-r/R)}{3.48 - 1.74\ln(41.7\text{Re}^{-0.9})}\right), \tag{38}$$

and

$$\alpha(\text{Re}) = \frac{1}{1 + (\text{Re}/\text{Re}_0)^n}, \tag{39}$$

$$\text{Re} = 2\frac{\rho \overline{w} R}{\mu}. \tag{40}$$

Note that the difference between the flow profiles $w_1(r)$ and $w_2(r)$ is that the former (latter) describes a flat (logarithmic) profile in the strongly turbulent region. At low Re values, corresponding to laminar flow, both flow profiles are parabolic. In the expressions above, ρ, μ, and $\overline{w}$ are the medium mass density, medium viscosity, and mean flow, respectively. In this example, $\text{Re}_0 = 2000$ and $n=4$ are chosen corresponding to a relatively sharp transition region located around $\text{Re}_0 = 2000$, but again any dependence $\alpha = \alpha(\text{Re})$ can be chosen. The logarithmic flow profiles given by Eqs. (35) and (38) are due to Nikuradse.[7] Although the logarithmic profile dependence does not hold very close to and at the cylinder wall where a laminar boundary layer exists [and, actually $\ln(1-r/R) \to -\infty$ as $r \to R$], it is possible to assume in the calculations that $w(r)$ follows the $\ln(1-r/R)$ depen-

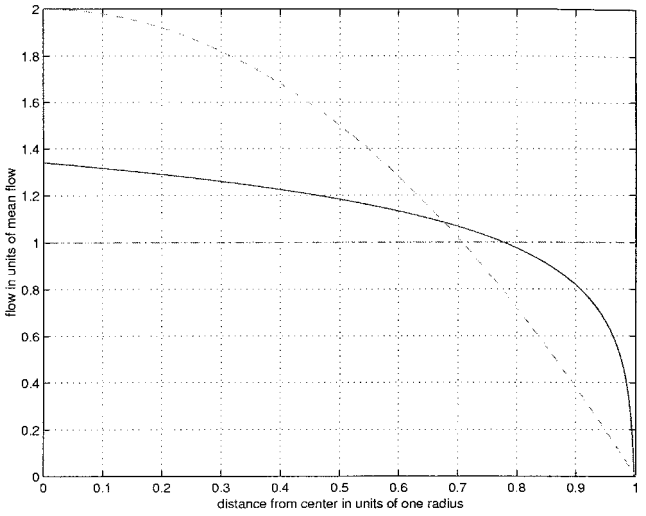

FIG. 1. Contour curves illustrating the parabolic profile for a laminar flow situation (dashed), a simple flat profile assumed for fully developed turbulent flows (dashed-dotted), and a more realistic logarithmic-dependent flow profile describing fully developed turbulence (solid).

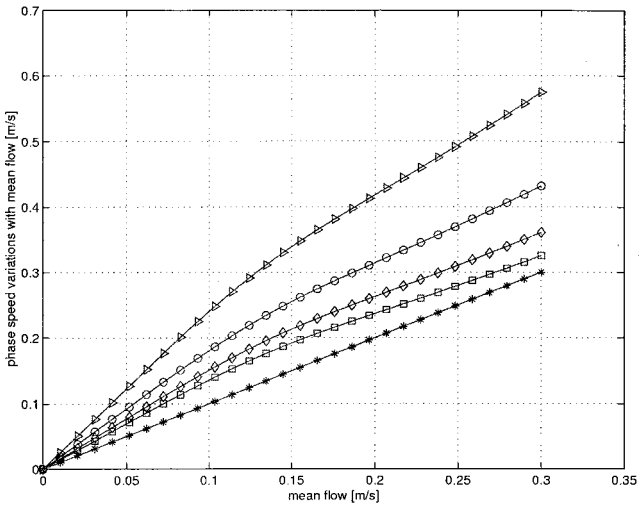

FIG. 2. Calculated phase speeds for the first five modes as a function of the mean flow corresponding to a flow profile which is a linear combination of a parabolic laminar profile and a simple flat profile describing fully developed turbulence. Phase speeds as a function of mean flow for mode 2, mode 3, mode 4, and mode 5 correspond to the rectangle-solid, diamond-solid, circle-solid, and triangle-solid curves, respectively. Parameter values used in the calculations are: $c_0'=1500$ m/s, $\omega=2\pi\cdot 10^6$ rad/s, $R=0.0055$ m.

dence very close to, and at, $r=R$. This is so, since the integral in Eq. (28) is well-defined in spite of the divergence of $w(r)$ at $r=R$, and is a reasonable assumption if the laminar boundary layer can be neglected. This will, nevertheless, be assumed in the following.

In Fig. 1, the profiles $w(r)_{\text{lam}}$, $w(r)_{\text{turb}}^{\text{fp}}$, and $w(r)_{\text{turb}}^{\text{log}}$ are shown.

The phase-speed changes with flow can now be found by insertion of Eqs. (34) and (35), respectively, into Eq. (28), i.e., by evaluating the integrals

$$W_n^i=\int_0^R \Psi_n(r)W_i(r)\Psi_n(r)r\,dr, \tag{41}$$

where

$$W_i(r)=-2k_0^2\frac{w_i(r)}{c_0'}, \tag{42}$$

and $i=1,2$. The functions $\Psi_n(r)$ are defined in Eq. (20).

Having determined W_n^i, the phase speeds c_{pn}^i can easily be found

$$c_{pn}^i(r)=\frac{\omega}{\sqrt{\dfrac{\omega^2}{c_0'^2}-\dfrac{j_{1n}^2}{R^2}+W_n^i}}. \tag{43}$$

In Fig. 2, calculated data for c_{pn}^1 for the first five modes ($n=1-5$) are shown as a function of the mean flow $\overline{w}$ for a mean flow varying between 0 and 0.3 m/s. The following parameter values are used in the calculations: $c_0'=1500$ m/s, $\omega=2\pi\cdot 10^6$ rad/s, $R=0.0055$ m, which are typical values for a 0.6–1.5 m^3/h flow meter used in district heating systems (water as medium). Numerical calculations confirmed that the condition in Eq. (33) is fulfilled in the flow interval 0–0.3 m/s. Also, inserting the parameter values above and a mean flow of 0.3 m/s into Eq. (35) shows that the flow speed becomes approximately 1% (in absolute value) of the sound speed at $r=0.9999R$, i.e., perturbation theory holds well in the range $0\leqslant r\leqslant 0.9999R$ where the flow speed is less than 1% of the sound speed. In a real flow situation, however, the fluid velocity must be zero at the cylinder wall as the fluid sticks to the wall. It must therefore be checked that differences in W_n^i are negligible for the two cases: (a) $w(r)$ is given by Eqs. (35) and (38) in the range $0\leqslant r<0.9999R$ and $w(r)=0$ for $0.9999R\leqslant r\leqslant R$; (b) $w(r)$ is given by Eqs. (35) and (38) in the whole range $0\leqslant r\leqslant R$. A simple analytical calculation shows that this difference is approximately 0.01% for all five modes analyzed in the worst case where mean flow equals 0.3 m/s. Consequently, the present analysis is accurate to within at least 0.01% if flow is given by Eq. (35) being sufficient for a perturbative analysis.

It is evident that the phase speed of the fundamental mode satisfies

$$c_{p1}^1=c_0'+\overline{w}, \tag{44}$$

i.e., phase-speed changes with flow equal the mean flow for the fundamental mode if $w(r)=w_1(r)$. Generally speaking, as $J_0((j_{11}/R)\,r)=1$, phase-speed changes with flow for the fundamental mode depend on mean flow only while being independent of the flow profile. It also follows that mode phase-speed changes with flow for all other modes *depend* on the flow profile, i.e., depend on the value of α. Furthermore, mode phase-speed changes with flow are generally higher than the mean flow if $n\geqslant 2$. It should be pointed out that the calculated phase speeds agree to within numerical accuracy with the values found by direct solution of the differential equation given in Eq. (16) as described in Refs. 5 and 6 In particular, the present results using perturbation theory show that mode phase speeds change sign as the flow direction is reversed in agreement with the conclusions in

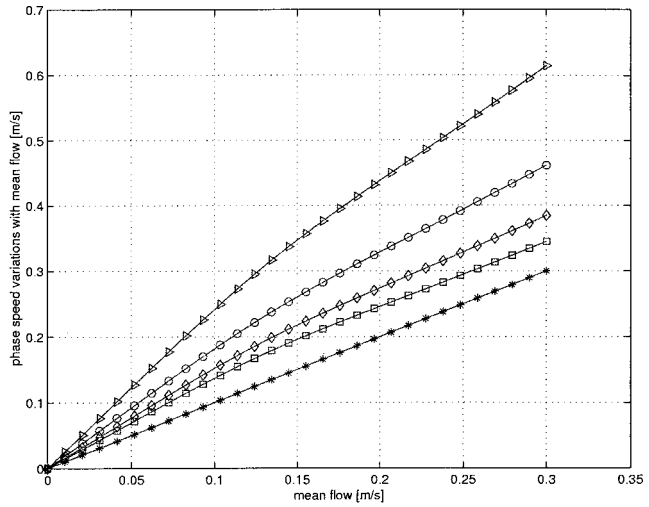

FIG. 3. Calculated phase speeds for the first five modes as a function of the mean flow corresponding to a flow profile which is a linear combination of a parabolic laminar profile and a more realistic logarithmic dependent flow profile describing fully developed turbulence. All parameters and line codings are the same as for Fig. 2.

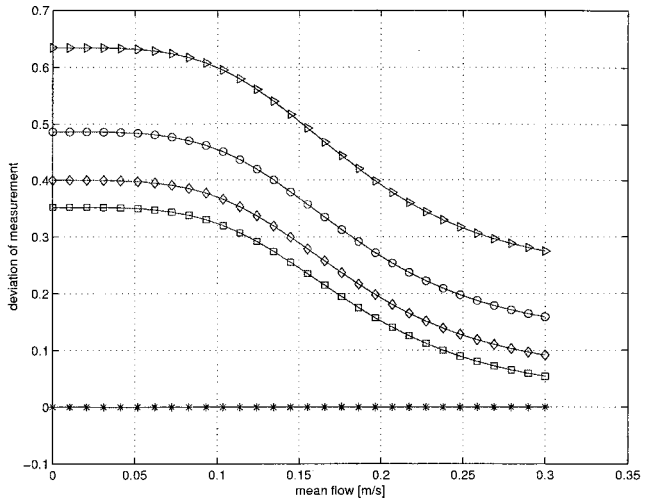

FIG. 4. Deviation of measurement E_n^1 for the first five modes as a function of the mean flow corresponding to a flow profile which is a linear combination of a parabolic laminar profile and a simple flat profile describing fully developed turbulence. All parameters and line codings are the same as for Fig. 2.

Ref. 5, and therefore in disagreement with the claims made in Refs. 2–4.

In Fig. 3, mode phase-speed changes with flow are depicted in the case where the turbulent part of the flow profile is a logarithmic function of the radial coordinate, i.e., $w(r) = w_2(r)$. As already mentioned, the fundamental mode phase speed changes by an amount equal to the mean flow independent of the flow profile. All other modes are characterized by phase speeds that depend on the profile (or α) and phase-speed changes with flow are generally larger than the mean flow if $w(r) = w_2(r)$ similar to the conclusions found when $w(r) = w_1(r)$. Notice, however, that phase-speed changes with flow deviate stronger from the mean flow value in the turbulent regime if the flow profile follows a logarithmic dependence as compared to the case with a flat profile.

In the remaining part of the paper, consequences due to differences in flow profiles for flow measurement based on phase-speed changes shall be addressed. Traditionally, flow measurements are based on changes in phase speed between two successive measurements, one where sound is propagated along the flow direction and the other then corresponds to the case where sound propagates against the flow direction. As a result of the flow-profile-dependent phase-speed change for any mode except from the fundamental mode, flow measurements inevitably suffer from measurement errors if the transmitting transducer excites any of the higher-order modes. This is so because flow measurements ideally must be independent of the flow profile, i.e., dependent on the mean flow only.

Let us define the phase-speed difference $\Delta\phi_n$ between an upstream and a downstream sound propagation situation, in which the nth mode is the only mode excited, as

$$\Delta\phi_n = \omega b_a \left(\frac{1}{c_{pn}^-} - \frac{1}{c_{pn}^+} \right), \tag{45}$$

where b_a denotes the distance between the two transducers (the two transducer axes are assumed aligned with the cylinder axis), and c_{pn}^- and c_{pn}^+ are the phase speeds corresponding to an upstream sound propagation situation and a downstream sound propagation situation, respectively. The transit time difference Δt_n between the two successive sound propagation situations then becomes

$$\Delta t_n = \frac{\Delta\phi_n}{\omega}, \tag{46}$$

and the so-called deviation of measurement E_n^i can be written as

$$E_n^i = \frac{\Delta t_n - 2b_a\overline{w}/c^2}{2b_a\overline{w}/c^2}, \tag{47}$$

where $2b_a\overline{w}/c^2$ is the transit time difference of the fundamental mode and $i=1$ ($i=2$) if $w(r) = w_1(r)$ ($w(r) = w_2(r)$). This definition implies, of course, that a transducer exciting the fundamental mode only in the cylindrical waveguide leads to error-free measurements, and, in particular, independence of flow-profile variations.

In Fig. 4, the deviation of measurement E_n^1 is shown for the first five modes as a function of mean flow corresponding to the case where $w(r) = w_1(r)$. The data presented in Fig. 4 are calculated using the data presented in Fig. 2 for c_{pn}^+ and the fact that $c_{pn}^- = 2c_{pn} - c_{pn}^+$, where c_{pn} denotes the nth mode phase speed in a quiescent medium. This linear relationship between c_{pn}^+ and c_{pn}^- holds true as long as first-order perturbation theory can be applied. It is evident that E_n^1 can be quite large in the near-laminar regime. As the flow approaches values for which fully developed flat-profile turbulence exists, E_n^1 becomes smaller. These results clarify as well that large errors may be induced whenever several mode components are excited by the transmitting transducer as the various mode-phase speeds depend *differently* on flow.

In Fig. 5, the deviation of measurement E_n^2 is depicted for the case where $w(r) = w_2(r)$ based on the data values for

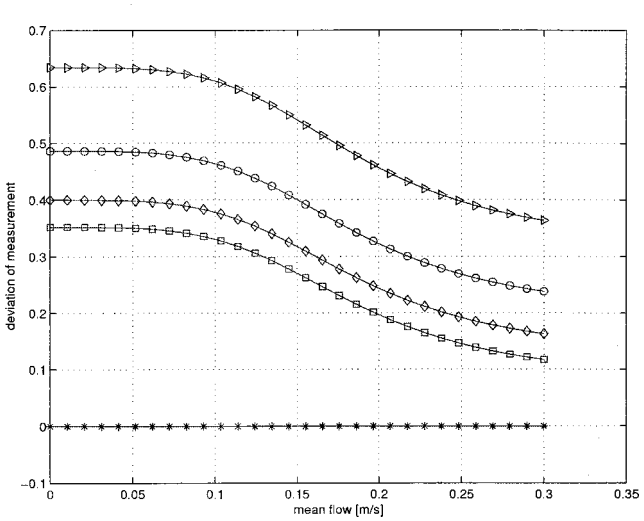

FIG. 5. Deviation of measurement E_n^2 for the first five modes as a function of the mean flow corresponding to a flow profile which is a linear combination of a parabolic laminar profile and a logarithmic-dependent profile describing fully developed turbulence. All parameters and line codings are the same as for Fig. 2.

c_{pn}^+ shown in Fig. 3, and the fact that $c_{pn}^- = 2c_{pn} - c_{pn}^+$. Again, large errors in the laminar and near-laminar flow regime are found and E_n^2 becomes smaller at higher flows. However, E_n^2 is larger than E_n^1 for the higher-order modes in the turbulent regime due to the logarithmic-dependent flow profile as compared to a flat-profile turbulence.

V. CONCLUSIONS

First-order perturbation theory has been applied to the sound propagation problem in flowing media confined by a cylindrical waveguide. The use of perturbation theory allows changes in mode phase speeds to be determined for *any* possible radial dependence of the flow $w(r)$ as long as $w(r)$ is sufficiently small. In practice, flow values ranging from 0 to approximately 1 m/s can be treated by this method. The fact that $w(r)$ may be any function of r is exploited to examine two cases of flow profiles: (1) where $w(r)$ is a linear combination of a laminar flow profile and a flat profile describing fully developed turbulence, and (2) where $w(r)$ is a linear combination of a laminar flow profile and a more realistic logarithmic-dependent profile describing fully developed turbulence. In both cases, it is shown that only the fundamental mode is characterized by a phase speed that depends on the mean flow but not on the flow profile. This conclusion suggests that for ultrasound flow meter applications, where the mean flow must be determined, accurate flow measurement requires that only the fundamental mode is excited by the transmitting transducer. It is shown that the deviation of measurement can be quite large in all flow regimes if higher-order modes contribute to the sound field. It is also found that at high flow values, where it is particularly important to minimize relative measurement errors, the deviation of measurement is somewhat larger for the case where a logarithmic-dependent flow profile characterizes the turbulent regime as compared to the case with a flat profile describing fully developed turbulence.

[1] L. C. Lynnworth, ''Ultrasonic Flowmeters,'' in *Physical Acoustics*, edited by W. P. Mason and R. N. Thurston (Academic, New York, 1979), Vol. 14, Chap. 5, pp. 407–525.
[2] H. Lechner, ''Ultrasonic flow metering based on transit time differentials which are insensitive to flow profile,'' J. Acoust. Soc. Am. **74**, 955–959 (1983).
[3] H. Lechner, ''Ultrasonic measurement of volume flow independent of velocity distribution,'' ACTA IMEKO, pp. 279–288 (1982).
[4] H. Lechner, ''Stroemungsprofilunabhaengige Durchflussmessung mit Ultraschall,'' Landis & Gyr Mitteilungen 28, pp. 16–18 (1981).
[5] M. Willatzen, ''Comments on 'Ultrasonic flow metering based on transit time differentials which are insensitive to flow profile' '' [J. Acoust. Soc. Am. **74**, 955–959 (1983)], *ibid.* **107**, 1762–1765 (2000).
[6] M. S. Sodha, A. Kumar, I. C. Goyal, and A. K. Ghatak, ''Sound wave propagation in cylindrical inhomogeneous waveguides,'' Acustica **41**, 232–237 (1979).
[7] J. Nikuradse, ''Gesetzmaessigkeiten der turbulenten Stroemung in glatten Rohren,'' Forschungsheft 356, Forschung auf dem Gebiete des Ingenieurwesens, Volume B, No. 3, September/October (1932).
[8] G. Arfken, *Mathematical Methods for Physicists*, 3rd ed. (Academic, Orlando, 1985), pp. 113–115.
[9] L. D. Landau and E. M. Lifshitz, *Fluid Mechanics*, 2nd ed. (Pergamon, Oxford, 1987), p. 292.

Aeroacoustics of diffusers: An experimental study of typical industrial diffusers at Reynolds numbers of $O(10^5)$

L. van Lier, S. Dequand, and A. Hirschberg
Eindhoven University of Technology, Postbus 513, 5600 MB Eindhoven, The Netherlands

J. Gorter
Nederlandse Gasunie N.V., Postbus 19, 9700 MA Groningen, The Netherlands

(Received 10 July 1999; revised 10 September 2000; accepted 29 September 2000)

Diffusers as used in gas transport systems have an optimal pressure recovery but are unstable due to marginal flow separation. Coupling of diffuser flow oscillation with acoustic modes in a pipe has been demonstrated in a recent work by Kwong and Dowling [J. Fluids Eng. **116**, 842 (1994)] to drive flow unsteadiness. Considered here in addition to the diffuser at a pipe termination is the aeroacoustic response of a diffuser in a long pipe. In both cases reflection coefficient measurements show that at moderate and low amplitudes of the acoustical particle velocity compared to the main flow velocity, diffusers are aeroacoustic sources similar to the whistler nozzle and the horn. This confirms the observations of Kwong and Dowling. At higher acoustical velocity amplitudes diffusers become strong absorbers, which can be explained in terms of a quasistationary flow model. Finally, an indication is provided for possible remedial measures when a stable flow is needed. [DOI: 10.1121/1.1329618]

PACS numbers: 43.28.Ra, 43.50.Nm [LCS]

I. INTRODUCTION

Typical gas-transport systems have been designed for low-flow velocities ($U_0 < 20$ m/s). There is a strong tendency to increase this velocity in existing manifolds of compressor stations, mixing stations, and measuring stations. Velocities up to 80 m/s are allowed locally to increase the capacity of existing facilities. Such changes might induce strong self-sustained pulsations of the flow due to coupling between vortex shedding and acoustical standing waves. In earlier studies, closed side branches have been identified as crucial elements forming both perfect reflectors at specific frequencies and as sources of sound (Bruggeman,[1] Kriesels,[2,3] Ziada,[4] Hofmans[5]). The main source of sound is due to the vortices shed from the upstream edge of the junction between the side branch and the main pipe. Quantitative models have been obtained to describe the sound production. These theories have led to the design of spoilers (sharp edges) placed at the upstream edge of the junction between the closed side branch and the main pipe.[1] Reduction of the pulsation levels by 60 dB were observed when strong pulsations occurred. Such strong pulsations correspond to acoustic velocity amplitudes u' of the order of the mean flow velocity U_0. The corresponding pressure amplitudes p' are of the order of $\rho_0 c_0 U_0$ with ρ_0 the mean gas density and c_0 the speed of sound. Such strong pulsations are not common. In most cases one observes pulsations with amplitudes of the order of the dynamic pressure $\frac{1}{2}\rho_0 U_0^2$. It is obvious that with an increase in U_0 by a factor of 4, moderate amplitude pulsations can become a major problem. Typical diffusers have a ratio S_d/S_u of the downstream and the upstream cross-sectional areas of about 2 and are therefore not very effective acoustical reflectors, in contrast with closed side branches. However, optimal diffusers, i.e., in the regime of maximal pressure recovery, show marginal flow separation and are therefore rather unstable (Blevins[6]). The work of Kwong and Dowling[7] has demonstrated that typical diffusers placed at the end of a pipe can sustain significant pressure fluctuations. In their experiments the sound source at the diffuser corresponds to 5% fluctuation in dynamic pressure. Coupled to a resonator with a quality factor Q of the order of 10, this would result in amplitude fluctuations of the order of the mean dynamic pressure $\frac{1}{2}\rho U_0^2$. The study of Kwong and Dowling is limited to the self-sustained oscillations observed for a diffuser at an open pipe termination. This corresponds in gas-transport systems to diffusers at the junction of a pipe with a reservoir or with a pipe of a much larger cross section. In gas-transport systems, diffusers are often placed significantly upstream of such junctions. In this paper we investigate the aeroacoustic response of two diffusers which are typically used in gas-transport systems as shown in Fig. 1. Both diffusers have an area ratio $S_d/S_u = 25/9$. The first has an opening or diverging angle $\theta = 28°$ and the second has $\theta = 14°$ (Fig. 1).

The reflection coefficient of three diffuser/pipe combinations was measured. Comparison of these results with the theoretical reflection coefficient for a diffuser/pipe combination without flow separation provides quantitative information about the energy production or absorption at the diffuser.

We investigate both the response of the diffuser to moderate amplitudes $u'/U_0 = O(10^{-2})$ and to high amplitudes $u'/U_0 = O(1)$. The results present unexpected aspects related to the essential nonlinearity of the aeroacoustic behavior. This effect will be discussed in terms of a quasistationary model. Finally, we will propose a remedial measure.

II. EXPERIMENTAL METHOD

The experimental setup used is essentially the setup described by Peters[8] and Hofmans.[5] The upstream main pipe diameter is $D_u = 3.0013$ cm with a wall roughness of the or-

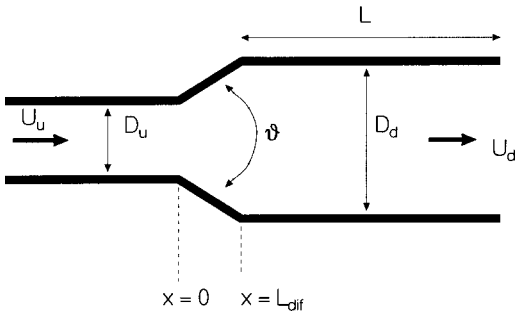

FIG. 1. Diffuser geometry.

der of 0.1 μm and a wall thickness of 5 mm. A siren placed 200 diameters upstream of the diffuser is used as a source of sound. A fixed pulsation frequency $f=289$ Hz was used in all experiments. This corresponds to a ratio of the pipe diameter to the acoustical wavelength of 3×10^{-2} which is much lower than the cutoff frequency for higher-order modes. The Strouhal number $Sr=\pi D_u f/U_0$ was varied by changing the flow velocity. The amplitude of the pulsation velocity u' at the diffuser was determined by using a variable bypass of the siren. The flow Mach number was varied in the range $0<M<0.3$ corresponding to Reynolds numbers $U_0 D_u/\nu$ up to 2×10^5. The flow velocity U_0 upstream of the diffuser was determined from volume flow measurements by means of a turbine meter corrected for pressure and temperature changes. The accuracy in the velocity is of the order of 0.5%. Dry air was used (dewpoint -40 °C). The atmospheric pressure was measured within an accuracy of 0.1% by means of a mercury manometer. The flow temperature was calculated from wall temperature measurements with an accuracy of 0.1 °C assuming an adiabatic wall turbulent recovery factor. The acoustic pressure was measured by means of piezoelectrical microphones, placed randomly within 1 meter upstream of the diffuser. The microphone positions measured from the diffuser were: $x_1=-0.1097$ m, $x_2=-0.2135$ m, $x_3=-0.4107$ m, $x_4=-0.5084$ m, and $x_5=-0.6977$ m. These microphones (type PCB 116A) were coupled to charge amplifiers (Kistler type 5007) with a bandwidth $0.1\text{ Hz}<f<3$ kHz. The positions x_i of the microphones were measured within 0.2 mm. The signals were transferred to a HP 3565S data acquisition system. FFT transform was carried out with a frequency discretization of $\Delta f\leqslant0.06$ Hz and a Hann window. This provided the transfer functions $H_{ij}=\hat{p}_i/\hat{p}_j$ between microphones at positions x_i and x_j. Only data with a coherence equal to 1 within the accuracy of the measurement (10^{-4}) were used. The reflection coefficient R just before the diffuser $x=0$ was determined by using microphone j as reference and using the formulas

$$(e^{ik^- x_j}-H_{ji}e^{ik^- x_i})R=(H_{ji}e^{-ik^+ x_i}-e^{-ik^+ x_j}), \tag{1}$$

where k^+ and k^- are the wave numbers calculated by means of the formula

$$k^{\pm}=\frac{1}{1\pm M}\left(\frac{\omega}{c_0}-i\alpha_0 Z\right), \tag{2}$$

where $M=U_0/c_0$ is the mean flow Mach number, α_0 is the damping coefficient (m^{-1}) without mean flow (Kirchhoff), and Z is the normalized wall impedance as measured by Ronneberger[9] and Peters.[8] We used for Z a fit of Ronneberger's data proposed by Aurégan.[10] The set of four equations (1) for the single unknown R was solved in the least-square sense. The reference microphone and the number of microphones used were determined by trial and error to achieve the optimal least-square fit (typical standard deviations are of the order of 0.008). Typical reproducibility of the data in R is better than 0.2%. The absolute accuracy in R was confirmed by measurements on closed pipes of different lengths and is about 0.2%. The pipe downstream of the diffuser has a diameter of $D_d=4.99$ cm and a quality similar to the pipe upstream of the diffuser. Special care was taken to have a sharp-edged open pipe termination allowing use of the experimental data of Peters[8] and the theory of Cargill[11,12] to predict the reflection coefficient R at the open pipe termination. Three pipe segments of different lengths were used downstream of the diffuser:

(i) $(L_d)_1=0.0237$ m or $(L_d)_1/D_d=0.5$;
(ii) $(L_d)_2=0.7049$ m or $(L_d)_2/D_d=14$; and
(iii) $(L_d)_3=1.2558$ m or $(L_d)_3/D_d=29$.

In the first configuration we are close to a pipe terminated by a diffuser as in the work of Kwong and Dowling.[7] The two other pipe lengths have been chosen close to a half and to one wavelength, respectively, so that the diffuser inlet is close to a pressure node of the acoustic standing wave pattern. In that case, since the sound production by vortices in low subsonic flow is dominated by a dipole contribution,[13] we expect an optimal interaction between vortex shedding at the diffuser and the acoustic field.

III. THEORY

A. Prediction of the reflection coefficient

Rather than the pressure reflection coefficient R, we represent data for the reflection coefficient R_B of the acoustic ''enthalpy'' as defined by Howe[14] which is given by

$$R_B=|R|\frac{c_0-U_0}{c_0+U_0}. \tag{3}$$

The square $(R_B)^2$ of this reflection coefficient corresponds to an energy reflection coefficient. Strictly speaking, when entropy variations occur, as we expect with flow separation, the acoustical variable $B'=U_0u'+p'/\rho_0$ used here is not the enthalpy fluctuation (Aurégan[10]). We compare the measured data with a theoretical value of $(R_B)_{th}$ obtained by assuming a frictionless quasi-one-dimensional flow in the diffuser. The transfer matrix for acoustic waves across the diffuser is calculated by means of the low Mach number approximation $(U_0/c_0)^2\ll1$ proposed by Eashwaran and Munjal[15] and by means of a quasistationary approximation assuming an abrupt pipe expansion at arbitrary Mach numbers (see the Appendix). The modulus of the reflection coefficient R_{out} at the open pipe termination is calculated from

$$|R|_{\text{out}}=(1+\mathcal{A}M)\left(1-\frac{1}{2}\left(\frac{\pi f D_d}{c_0}\right)^2\right), \tag{4}$$

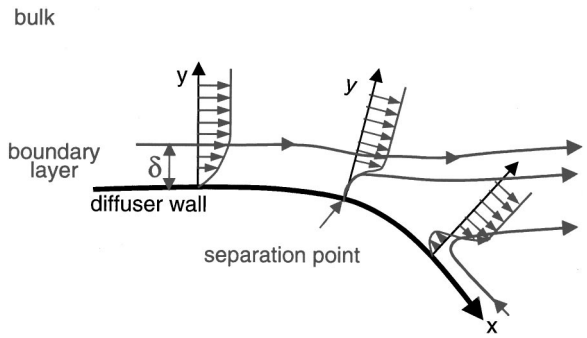

FIG. 2. Flow separation at the wall of a diffuser.

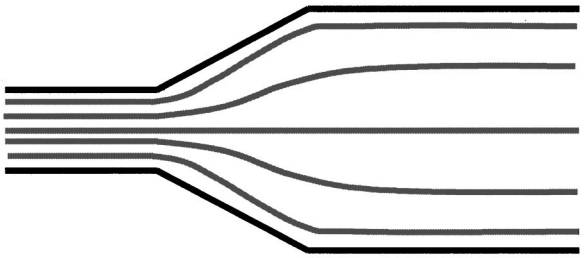

FIG. 3. Flow in an ideal diffuser without flow separation.

where $\mathcal{A}$ is a fit of the theory of Cargill[11,12] proposed by Hofmans[5]

$$\mathcal{A}(Sr_d)=\begin{cases}\dfrac{Sr_d^2}{3}, & 0\leqslant Sr_d<1\\ \dfrac{2Sr_d-1}{3}, & 1\leqslant Sr_d<1.85\\ 0.9, & 1.85\leqslant Sr_d,\end{cases} \tag{5}$$

with

$$Sr_d=\frac{\pi f D_d}{U_d}, \tag{6}$$

the Strouhal number for the wide pipe downstream of the diffuser. The end corrections $\delta\approx 0.3D_d$ measured by Peters[8] were used to determine the phase of the reflection coefficient at the pipe termination defined as

$$R_{\text{out}}=|R|_{\text{out}}\exp(-2ik\delta). \tag{7}$$

B. Flow separation and vortex sound

Before continuing, we give some information about flow separation in a diffuser. A discussion of various flow conditions as a function of the diffuser angle and length is provided by Blevins.[6] We provide here a qualitative discussion of the phenomenon which should support some later arguments.

We call flow separation the departure of particles of fluid from the wall towards the interior of the flow field. In a stationary flow, separation occurs when the wall streamline shows a bifurcation at a point where the normal gradient of the tangential velocity component $\partial u/\partial y$ vanishes at the wall $[(\partial u/\partial y)_{\text{wall}}=0]$ (Fig. 2). In an unsteady flow, as in the case of an acoustically perturbated flow, there is no simple criterion for separation because the particle path depends on the flow history. In this case, the criterium $(\partial u/\partial y)_{\text{wall}}=0$ is not sufficient.

To begin a quantitative discussion, we consider a flow with a high Reynolds number $O(10^5)$. In such a case, the bulk of the flow is frictionless and flow separation is controlled by the interaction between a narrow region at the wall (in which friction is important) and the main flow. This viscous region is the boundary layer.[16] We consider first a flow in an ideal diffuser without flow separation (Fig. 3). In the frictionless bulk of the flow (designated by the index ∞), there is an equilibrium between inertia and pressure forces which is described along the pipe axis by the x component of the momentum conservation equation (Euler)

$$\rho\left(\frac{\partial u_\infty}{\partial t}+u_\infty\frac{\partial u_\infty}{\partial x}\right)=-\frac{\partial p}{\partial x}. \tag{8}$$

For an incompressible steady flow, this equation can be integrated to yield the equation of Bernoulli in the simplified form

$$p+\tfrac{1}{2}\rho_0 u_\infty^2=\text{constant}. \tag{9}$$

Complementing this equation with the corresponding one-dimensional equation for mass conservation

$$\rho_0 S u_\infty=\text{constant}, \tag{10}$$

we see that when we travel through the diffuser u_∞ decreases because S increases. As a consequence of the decrease of u_∞, the equation of Bernoulli indicates that the pressure p increases. The fluid particle uses its kinetic energy $\frac{1}{2}\rho u^2$ to overcome the adverse pressure gradient $\partial p/\partial x>0$. We now discuss the flow in the viscous boundary layers.

Boundary layers are so thin that the flow velocity is dominated by the tangential component along the wall. This implies that the momentum conservation law, written in the direction normal to the wall, reduces to the condition of uniform pressure $\partial p/\partial y=0$ in the boundary layer. Hence, the mean flow imposes its pressure to the boundary layer and also the adverse pressure gradient $\partial p/\partial x>0$.

At the wall, the velocity **v** vanishes due to viscosity. The boundary layer provides a smooth transition $u(y)$ from the main friction flow velocity u_∞ towards $u(0)=0$ at the wall. This implies that fluid particles at the wall do feel the adverse pressure gradient but do not have any kinetic energy $(\frac{1}{2}\rho_0 u^2(0)=0)$. It becomes difficult therefore to understand why a fluid particle near the wall would flow in the main flow direction. This occurs because of viscous drag of those fluid particles by the particles in the main flow. This is of course more efficient if there is an efficient mixing between the fluid in the boundary layer and the main flow. Such a mixing is found in turbulent boundary layers which are therefore much more stable than laminar boundary layers. Surface roughness therefore plays an important role in determining the performance of a diffuser. For a laminar boundary layer of thickness δ, the characteristic time for diffusion of momentum from the bulk towards particles near the wall is δ^2/ν, where ν is the kinematic viscosity of the fluid. When the characteristic deformation time $|(1/u_\infty)(\partial u_\infty/\partial t)+\partial u_\infty/\partial x|^{-1}$ becomes smaller than δ^2/ν, the main flow is not able to drag the fluid particles near the wall and back

flow is initiated along the wall. Such a back flow and subsequent flow separation usually has a dramatic effect on the volume flow through the diffuser. Hence, flow separation affects the value of u_∞. This will, in turn, affect the separation. This is a highly nonlinear phenomenon which cannot be predicted without taking this interaction into account.

In the absence of an acoustical perturbation, very complex phenomena are observed including a breakdown of the symmetry of the flow.[6] The acoustic field will make the situation more complex because the flow is essentially unsteady. At low frequencies, however, when plane waves are dominant, the perturbation may keep the symmetry of the separation phenomenon. In extreme cases [when $u'/U_0 = O(1)$], we found that the acoustical perturbation alternatively completely suppresses separation when $\partial u'/\partial t > 0$ while a full separation occurs when $\partial u'/\partial t < 0$. This alternates each half oscillation period of the acoustical perturbation.

Following Blevins,[6] diffusers with opening angles less than 8° show no flow separation. In industry, angles of 14° or even 28° are commonly used. In the first case ($\theta = 14°$), we expect only marginal flow separation and the position of the flow separation point will be very sensitive to acoustical perturbations. In the second case ($\theta = 28°$), a very significant flow separation will occur and for low amplitudes u'/U_0 the separation point position will not be very sensitive to acoustical perturbations. In the extreme case of an abrupt sharp-edged pipe expansion, the separation will remain at the sharp edge independent of the acoustical perturbation amplitude.

Flow separation involves the formation of a shear layer which is a transition between the main irrotational flow and the back flow region near the wall. The shear layer contains rotation ($\partial u/\partial y \neq 0$). Such a layer is unstable and tends to break down into discrete vortices. Modulation of the vorticity induced by acoustical perturbations can trigger such an instability. When the perturbations are very weak ($u'/U_0 \ll 1$), the instability grows exponentially with the distance from the flow separation point, which corresponds to a linear response to the acoustical perturbation.

At moderate perturbation amplitudes [$u'/U_0 = O(10^{-1})$], the exponential growth is very soon followed by a saturation corresponding to a breakdown of the shear layer into discrete vortices. However, the strength of these vortices will be almost independent of the acoustical amplitude. Bruggeman[1] calls this the moderate amplitude region. In this region, we expect the effect of vortices to be described by a dipole of pressure fluctuation Δp across the diffuser which scales as $\frac{1}{2}\rho_0 U_0^2$. This fluctuation is triggered by the acoustical flow, but has a magnitude which is independent of the acoustical amplitude. At high amplitudes [$u'/U_0 = O(1)$], the acoustic field strongly affects the strength of shed vortices.

A more formal discussion of the sound generated by vortices is provided by Howe.[13] Using this theory, whistling phenomena can be understood at least qualitatively. While acoustical perturbation of the shear layer at the flow separation point involves sound absorption, the vortex formed can, half a period later, generate more sound than has been absorbed initially. The average of the produced acoustical power $\langle \mathcal{P}_{ac} \rangle$ over one period of oscillation is given by the formula of Howe[13] for low Mach number flows

$$\langle \mathcal{P}_{ac} \rangle = -\left\langle \rho_0 \int_V (\boldsymbol{\omega} \times \mathbf{v}) \cdot \mathbf{u}'_{ac}\, dV \right\rangle, \tag{11}$$

where $\mathbf{u}'_{ac}$ is the unsteady potential flow component of the fluid flow velocity $\mathbf{v}$, and $\boldsymbol{\omega}$ is the vorticity $\nabla \times \mathbf{v}$. The brackets indicate a time averaging. When the integral is carried out over a compact source region where $\boldsymbol{\omega} \neq 0$, this formula stresses the dipole character of the source which will not produce acoustical energy if $\mathbf{u}'_{ac} = \mathbf{0}$ (at a pressure antinode). In the formula, the convection velocity $\mathbf{v}$ (of the vorticity) is of the order of magnitude of the mean flow velocity U_0 and is almost independent of the acoustical velocity $\mathbf{u}'_{ac}$ if $u'/U_0 \ll 1$. At very low acoustic velocity amplitudes compared to the mean flow velocity, the unsteady component of $\boldsymbol{\omega}$ scales with $\mathbf{u}'_{ac}$ so that $\langle \mathcal{P}_{ac} \rangle$ scales with $(u'_{ac})^2$. This corresponds to a reflection coefficient $|R_B|$ independent of the amplitude.

For larger amplitudes, we expect a decrease in the produced acoustical power due to saturation of the perturbation of $\boldsymbol{\omega}$ to a limit value scaling with U_0 as we discussed above (moderate amplitudes).

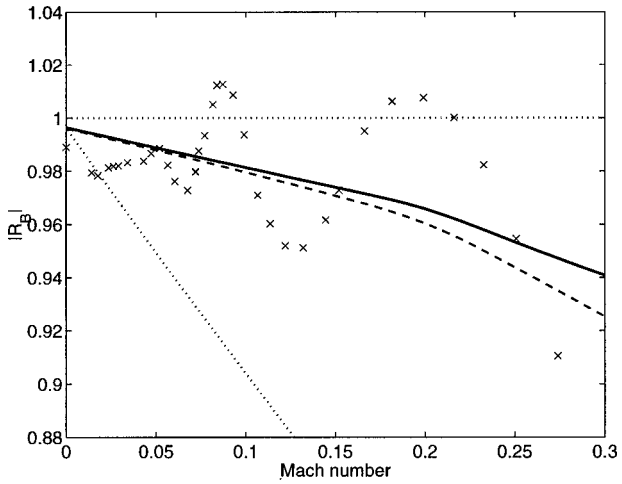

FIG. 4. Enthalpy reflection coeficient R_B of the 28° diffuser as a function of the mean flow Mach number. $f = 289$ Hz and $u'/U_0 \approx 0.1$. × measurements: —— quasistationary compressible theory without flow separation; ··· quasistationary compressible theory with flow separation; - - - analytical low Mach number theory.

IV. RESULTS

A. Short pipes [$(L_d)_1$]

We present in Figs. 4 and 5 the data measured for $u'/U_0 = O(10^{-2})$ for both diffusers, terminated by a short pipe segment $(L_d)_1$. The wide diffuser (diverging angle $\theta = 28°$, Fig. 4) shows spectacular oscillations of R_B with maxima at critical Strouhal numbers $Sr_u = \pi f D_u / U_u$ corresponding to the values observed by Powell[17] and Peters[8] for a horn. We clearly see maxima at $Sr_u = 1.60$, 0.90, and 0.44 ($M = 0.06$, 0.09, and 0.19) corresponding to three hydrodynamic modes of the diffuser. In particular, for the first two hydrodynamic modes $Sr_u = 0.44$ and $Sr_u = 0.90$ the sound production is obvious because R_B exceeds unity. The intensity I^- of the reflected wave is larger than the intensity I^+ of the incident wave. For other modes comparison with the

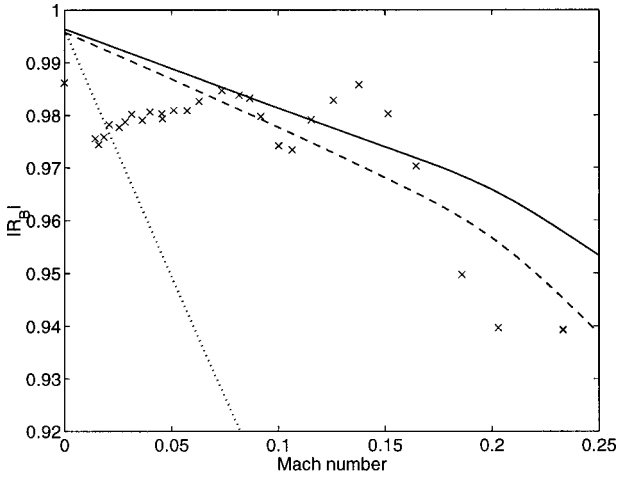

FIG. 5. Enthalpy reflection coefficient R_B of the 14° diffuser as a function of the mean flow Mach number. $f=289$ Hz and $u'/U_0\approx 0.1$. × measurements: —— quasistationary compressible theory without flow separation; ··· quasistationary compressible theory with flow separation; - - - analytical low Mach number theory (Ref. 15).

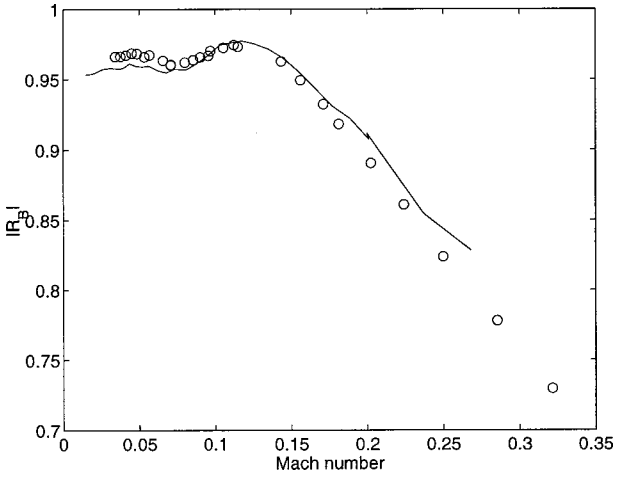

FIG. 6. Enthalpy reflection coefficient $|R_B|$ of the 28° diffuser with two different pipe lengths placed behind and $u'/U_0\approx 0.1$: ○ $(L_d)_2$; —— $(L_d)_3$.

theory for an ideal diffuser (Eashwaran[15]) and quasisteady model also clearly demonstrates sound production. For the narrow diffuser ($\theta=14°$) we observe a similar, but less spectacular effect (Fig. 5). Only two hydrodynamic modes can be observed and R_B remains smaller than unity. However, at critical Strouhal numbers, the reflection coefficient R_B deviates more than 2% from the theory assuming a nonseparated flow. For a diffuser with a diverging angle $\theta=14°$, vortex shedding is also a clear powerful source of sound. This sound production at critical Strouhal numbers can be explained conveniently by the vortex sound theory of Howe[14] [Eq. (10)]. For whistler nozzles and horns, a discussion is given by Hirschberg[18] and Dupère and Dowling[19] assuming that:

(i) the separation point, where the vortices are formed, is fixed; and
(ii) the formation of a new vortex is triggered each time the acoustical velocity passes through zero turning from pipe inwards to pipe outwards.

The same criteria were used quite successfully for closed side branches (Bruggeman[1]) and Helmholtz resonators (Nelson,[20,21] Hirschberg[22]) at moderate amplitudes. The observed phenomenon can be understood by assuming a fixed separation point.

Please note that the difference between theory and experiments at $M=0$, which we see in Fig. 4, is expected to be due to acoustic resonances in the laboratory, as observed already by Peters[8] in his study of reflection at open pipe terminations.

At low Mach number we observe that measured values are significantly lower than theoretical prediction. This could be due to relatively low Reynolds numbers $O(10^4)$ for $M\leqslant 0.05$. At such low Reynolds numbers, diffuser performance decreases with decreasing Reynolds number.[6] The difference between theory and experiments is of the order of the difference between theory with and without flow separation. We therefore expect that there is permanent flow separation at those low Mach numbers due to the low Reynolds number effect. As a reference we give results of the quasisteady theory assuming flow separation at an abrupt pipe expansion.[23] We find a fair agreement between measurements and this theory for $M\leqslant 0.02$ (Fig. 4 and Fig. 5).

B. Long pipes [$(L_d)_2$ and $(L_d)_3$]

While the diffuser behavior at an open pipe termination observed by Kwong and Dowling[7] is similar to our previous experience, we would like to know whether a marginal flow separation can induce sound production at a diffuser in a long pipe. As we expect from the dipole character of vortex sound sources, a condition for vortex sound production is a large acoustic velocity. We therefore choose pipe lengths L_d downstream of the diffuser which are close to integral multiples of half an acoustic wavelength ($L_d f/c_0\approx 0.5$ and 1). As shown in Fig. 6, we observe for a wide diffuser ($\theta=28°$) at both pipe lengths roughly the same oscillation in R_B indicating some sound production for $u'/U_0\leqslant O(10^{-1})$ independently of the distance from the pipe termination. This is therefore clearly a sound production localized at the diffuser. We further found that the reflection coefficient R_B is independent of the amplitude u'/U_0 in the range $10^{-2}\leqslant u'/U_0\leqslant 10^{-1}$. At moderate amplitudes $u'/U_0=O(10^{-1})$ a significant decrease of the oscillations in R_B with increasing amplitude is observed (see Fig. 7). This can be explained by a saturation of the sound source due to discrete vortex formation which we discussed above. In other words, because the oscillating total enthalpy defect ΔB across the diffuser is amplitude independent, the acoustical energy dissipation $\Delta I=(\rho_0 u'+\rho' U_0)\Delta B$ is linear in u', while the intensity I^+ of incident waves scales with u'^2 so that

$$1-R_B^2=\frac{\Delta I}{I^+}\sim\frac{U_0}{u'}. \tag{12}$$

As observed by Kriesels[3] at higher pulsation amplitudes $u'/U_0=O(1)$, the simple model mentioned in the previous paragraph fails for closed side branches. The vortex formation shifts in phase relative to the acoustic oscillation. In the case of a marginal flow separation we expect that at high

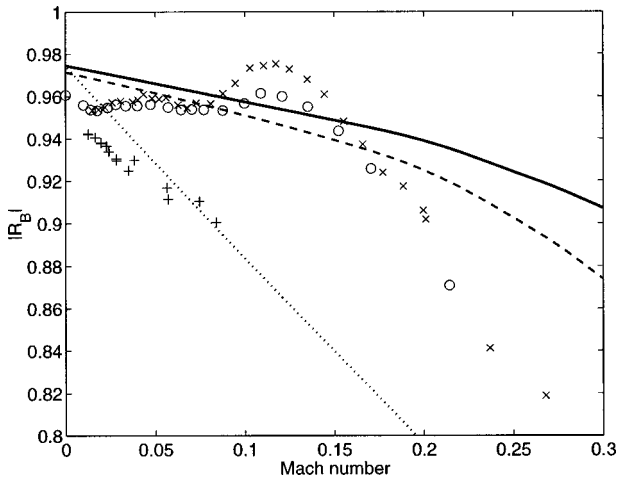

FIG. 7. Amplitude dependence of $|R_B|$ of the 28° diffuser with a long pipe downstream $[(L_d)_3]$. × $u'/U_0=0.1$; ○ $u'/U_0=0.4$; + $u'/U_0=1.0$. Theories as in Fig. 4.

acoustic amplitudes $u'/U_0=O(1)$ the positive acoustic pressure gradient upon acoustic acceleration can even suppress flow separation while flow separation certainly becomes dramatic in the acoustic deceleration phase. This can induce a phase shift of $\pi/2$ of the initialization of vortex shedding and limits the vortex shedding to about half the oscillation period. Indeed, we do observe in Fig. 7 a dramatic change in the behavior of R_B for amplitudes $u'/U_0=O(1)$. In the limit of separated flow during the entire oscillation period, we can calculate R_B by using the quasisteady theory proposed by Ronneberger[23] (see the Appendix). We indicate the results of this theory in Fig. 7 by the dotted line. This strong absorption at high amplitudes is quite different from the behavior of a horn as observed by Hofmans:[5] in the case of the horn, the whistling phenomenon persists at high amplitudes.

In order to support the conclusions of this section, we show in Fig. 8 measurements obtained with a sharp-edged sudden pipe expansion ($\theta=180°$). We see that up to Strouhal numbers of the order of unity corresponding to the very low Mach numbers ($M=0.02$), the quasistationary theory predicts the observed behavior and that there are no oscillations of $|R_B|$. Hence, the interaction of vortices generated at the expansion with the open pipe termination is indeed negligible.

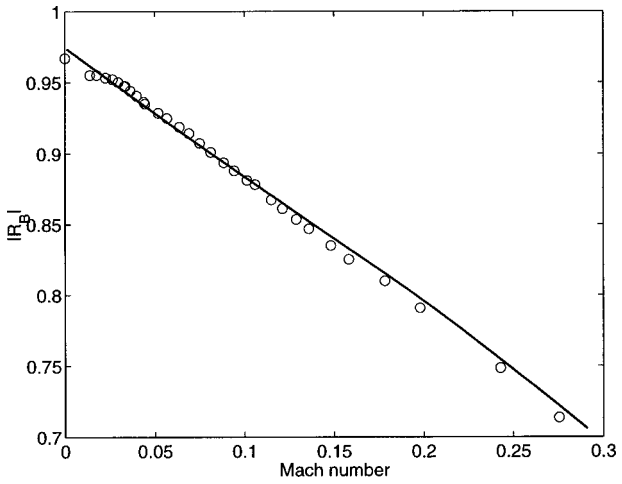

FIG. 8. Enthalpy reflection coefficient $|R_B|$ as a function of the Mach number at an abrupt expansion with $\sigma=25/9$; $L_{\text{pipe}}=1.2558$ m; $f=289$ Hz. The solid line is the solution of the quasistationary model with flow separation.

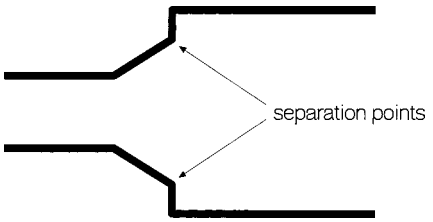

FIG. 9. Modified diffuser geometry to fix the separation points.

V. CONCLUSIONS AND PROPOSED REMEDIAL MEASURES

Comparison of our experimental data for the enthalpy reflection coefficient R_B with the theory for an ideal diffuser clearly demonstrates that at low and moderate pulsation amplitudes $u'/U_0\leqslant 0.1$ a diffuser is a source of sound at critical Strouhal numbers. A diffuser with $S_d/S_u=25/9$ and diverging angle $\theta\geqslant 14°$ placed close to an open pipe end is a very powerful sound source which can drive pulsations of moderate amplitudes $p'=O(\frac{1}{2}\rho U_0^2)$. A diffuser with $\theta\geqslant 14°$ placed in a long pipe is a much weaker sound source but can induce some flow instabilities by coupling of vortex shedding with acoustical resonances. At high pulsation amplitudes $[u'/U_0=O(1)]$ a diffuser becomes a sound absorber. In the case of moderate and low pulsation amplitudes, the behavior of the diffuser seems to be explained by a flow separation at a fixed point. Because the initial sound absorption associated with the vortex shedding is very weak, there is a net sound production (see Hirschberg[18]). Due to saturation of the aeroacoustic source at moderate amplitudes $u'/U_0=O(10^{-1})$, the acoustical energy production or loss scales with u'/U_0 while a fixed value of the enthalpy reflection coefficient would correspond with a $(u'/U_0)^2$ dependence, as explained in our discussion of vortex sound theory based on Eq. (11). This implies a decrease of the effect of the aeroacoustic source on R_B with increasing u'/U_0 at moderate amplitudes. At lower amplitudes $10^{-2}\leqslant u'/U_0\leqslant 10^{-1}$ the reflection coefficient R_B is independent of the amplitude.

The flow separation point can further be fixed by using a cutoff of the divergent part of the diffuser using an abrupt pipe widening at the end of the diffuser (see Fig. 9). Vortex shedding at the sharper edge will now induce a stronger initial absorption, reducing the net sound production. This modified geometry would prevent the use of expensive narrow diffusers. Such a modified geometry can only be used, however, when the diffuser is placed in a long pipe. When the diffuser is at a pipe termination it is more logical to use a shorter diffuser or a narrower diffuser. For narrow diffusers ($5°\leqslant\theta\leqslant 10°$) and area ratios $S_d/S_u\leqslant 2$ flow separation is not observed, even in a pulsating flow (Roozen[24]). As our experiments were limited to moderately high Reynolds numbers ($\text{Re}_D=U_0D/\nu\leqslant 2\times 10^5$), it would be interesting to carry out experiments at higher Reynolds numbers relevant for gas-transport systems.

ACKNOWLEDGMENTS

This work has been carried out within the framework of the EuroBrite project ''Flow Duct Acoustics'' (Flodac; No. BRPR CT97-10394) and with the support of Gasunie N.V. (Dr. H. Riezebos). The authors especially wish to acknowledge the contributions of Jan Gorter of Gasunie Research (now deceased), to this particular work. His sustained effort in understanding self-sustained pulsations in gas-transport systems has been a continuous source of inspiration for our research in the last 20 years. He drew our attention to typical unsteadiness in flows which he associated with diffusers. His contributions to the other papers of our research group during all those years have been immeasurable.

APPENDIX: QUASISTEADY RESPONSE OF A SUDDEN PIPE EXPANSION

In this Appendix, we describe the quasisteady theory of compact diffusers used for comparison with our experimental data.

1. Compact diffuser without flow separation

The flow in the one-dimensional approximation is described by the mass conservation law

$$\Phi_m=\rho_u u_u S_u=\rho_d u_d S_d\,, \tag{A1}$$

and the equation of Bernoulli applied to an ideal gas with constant specific heat ratio γ

$$B_0=\frac{1}{2}u_u^2+\frac{\gamma}{\gamma-1}\left(\frac{p_u}{\rho_u}\right)=\frac{1}{2}u_d^2+\frac{\gamma}{\gamma-1}\left(\frac{p_d}{\rho_d}\right), \tag{A2}$$

completed by the isentropic gas relation

$$\frac{p_u}{p_d}=\left(\frac{\rho_u}{\rho_d}\right)^{\gamma}. \tag{A3}$$

Φ_m and B_0 are constants for a given imposed upstream condition. Elimination of u_d and p_d yields a single nonlinear equation for ρ_d

$$\frac{1}{2}\frac{\Phi_m^2}{S_d^2}\rho_d^{-2}+\frac{\gamma}{\gamma-1}\frac{p_u}{\rho_u^{\gamma}}\rho_d^{\gamma-1}=B_0\,, \tag{A4}$$

which can easily be solved for given upstream conditions.

In order to determine the acoustical linear transfer matrix **T** of the diffuser

$$\begin{pmatrix} p_u' \\ u_u' \end{pmatrix}=\mathbf{T}\cdot\begin{pmatrix} p_d' \\ u_d' \end{pmatrix}, \tag{A5}$$

we calculated the solution (p_d^0,u_d^0,ρ_d^0) for a given steady condition (p_u^0,u_u^0,ρ_u^0).

We then calculated the solution A for a small perturbation $(u_u')_A$ in the velocity while we maintain p_u^0 and ρ_u^0 fixed $[(p_u')_A=0,(\rho_u')_A=0]$. A second calculation B was then carried out for $u_u'=0$ and a given pressure perturbation $(p_u')_B$ [from which we calculated $(\rho_u')_B=(1/\gamma)\rho_u^0[(p_u')_B]/p_u^0$]. Subtracting from these two perturbated solutions the reference solution for (p_u^0,u_u^0,ρ_u^0), we obtain a set of four linear equations with coefficients T_{ij} of **T** as unknowns

$$0=T_{11}(p_d')_A+T_{12}(u_d')_A\,, \tag{A6}$$

$$(u_u')_A=T_{21}(p_d')_A+T_{22}(u_d')_A\,, \tag{A7}$$

$$(p_u')_B=T_{11}(p_d')_B+T_{12}(u_d')_B\,, \tag{A8}$$

$$0=T_{21}(p_d')_B+T_{22}(u_d')_B\,. \tag{A9}$$

Once **T** is known, we can obtain a theoretical prediction of the reflection coefficient of a diffuser placed at a distance L_d upstream from an open pipe termination. We use Eqs. (4) and (5) to predict the open-end acoustical response.

2. Compact diffuser with flow separation

When flow separation occurs, a free jet is formed at the inlet of the diffuser. We assume that in this jet the pressure is equal to the pressure in the stagnant surrounding. For typical flow conditions considered here, the jet mixes turbulently with the surrounding after a few pipe diameters. We assume that this process is adiabatic and that friction at the wall is negligible. Under such conditions, we have still the same mass and energy conservation laws as in the previous case

$$\Phi_m=\rho_u u_u S_u=\rho_d u_d S_d\,, \tag{A10}$$

$$B_0=\frac{1}{2}u_u^2+\frac{\gamma}{\gamma-1}\left(\frac{p_u}{\rho_u}\right)=\frac{1}{2}u_d^2+\frac{\gamma}{\gamma-1}\left(\frac{p_d}{\rho_d}\right). \tag{A11}$$

Those equations are completed now by the integral momentum conservation law applied to the mixing region

$$\mathcal{P}_0=S_d p_u+S_u\rho_u u_u^2=S_d p_d+S_d\rho_d u_d^2, \tag{A12}$$

where $\mathcal{P}_0$ is a constant for a given upstream state (p_u,u_u,ρ_u). The solution for a subsonic case is

$$u_d=\frac{\gamma\mathcal{P}_0-\sqrt{\gamma^2\mathcal{P}_0^2-2(\gamma^2-1)B_0\Phi_m^2}}{\Phi_m(\gamma+1)}, \tag{A13}$$

$$\rho_d=\frac{\Phi_m}{S_d u_d}, \tag{A14}$$

$$p_d=\left(B_0-\frac{1}{2}u_d^2\right)\frac{\gamma-1}{\gamma}\rho_d\,. \tag{A15}$$

The transfer matrix **T** is obtained numerically in an analogous way as in the case without flow separation. Please note that Ronneberger[23] provides a detailed discussion of the linear solution in the low Mach number limit.

[1] J. C. Bruggeman, A. Hirschberg, M. E. H. van Dongen, A. P. J. Wijnands, and J. Gorter, ''Self-sustained aero-acoustic pulsations in gas transport systems: Experimental study of the influence of closed side braches,'' J. Sound Vib. **150**, 371–393 (1991).

[2] P. C. Kriesels, M. C. A. M. Peters, A. Hirschberg, A. P. J. Wijnands, A. Iafrati, G. Riccardi, R. Piva, and J. C. Bruggeman, ''High amplitude vortex-induced pulsations in a gas transport system,'' J. Sound Vib. **184**, 343–368 (1995).

[3] P. C. Kriesels, G. C. J. Hofmans, M. C. A. M. Peters, and A. Hirschberg, ''Flow induced pulsation in pipe systems,'' *Flow Induced Vibration*, edited by P. W. Bearman (1995), pp. 505–514.

[4] S. Ziada and E. T. Bühlman, ''Self-excited resonances of two side braches in close proximity,'' J. Fluids and Struct. **6**, 583–601 (1992).

[5] G. C. J. Hofmans, ''Vortex Sound in Confined Flows,'' Ph.D. thesis, Technische Universiteit Eindhoven, 1998.

[6] R. D. Blevins, *Applied Fluid Dynamics Handbook* (Van Nostrand Reinhold, New York, 1984).

[7] A. H. M. Kwong and A. P. Dowling, ''Unsteady flow in diffusers,'' J. Fluids Eng. **116**, 842 (1994).

[8] M. C. A. M. Peters, ''Damping and reflection coefficient measurements for an open pipe at low Mach and low Helmholtz numbers,'' J. Fluid Mech. **256**, 499–534 (1993).
[9] D. Ronneberger and C. D. Ahrens, ''Wall shear stress caused by small amplitude perturbations of turbulent boundary-layer flow: An experimental investigation,'' J. Fluid Mech. **83**, 433–464 (1977).
[10] Y. Aurégan, Laboratoire d'Acoustique de l'Université du Maine, private communication, 1999.
[11] A. M. Cargill, ''Low-frequency sound radiation and generation due to the interaction of unsteady flow with a jet pipe,'' J. Fluid Mech. **121**, 59–105 (1982).
[12] A. M. Cargill, ''Low frequency acoustic radiation from a jet pipe—A second order theory,'' J. Sound Vib. **83**, 339–354 (1982).
[13] M. S. Howe, *Acoustics of Fluid–Structure Interactions* (Cambridge University Press, Cambridge, England, 1998).
[14] M. S. Howe, ''Contributions to the theory of aerodynamic sound, with application to excess jet noise and the theory of the flute,'' J. Fluid Mech. **71**, 625–673 (1975).
[15] V. Eashwaran and M. L. Munjal, ''Plane wave analysis of conical and exponential pipes with incompressible mean flow,'' J. Sound Vib. **152**(1), 73–93 (1992).
[16] H. Schlichting and K. Gersten, *Boundary Layer Theory*, 8th ed. (Springer, Berlin, 2000).
[17] W. K. Blake and A. Powell, ''The development of contemporary views of flow-tone generation,'' in *Recent Advances in Aeroacoustics* (Springer, New York, 1983).
[18] A. Hirschberg, J. C. Bruggeman, A. P. J. Wijnands, and N. Smits, ''The whistler nozzle and horn as aeroacoustic sound sources in pipe systems,'' Acustica **68**, 157–160 (1989).
[19] I. D. J. Dupère and A. P. Dowling ''The absorption of sound near abrupt area expansions,'' Presented as AIAA 98-2303 at the 4th AIAA/CEAS Aeroacoustics Conference, Toulouse, France, 2–4 June 1998.
[20] P. A. Nelson, N. A. Halliwell, and P. E. Doak, ''Fluid dynamic of a flow excited resonance,'' J. Sound Vib. **78**, 15–38 (1981).
[21] P. A. Nelson, N. A. Halliwell, and P. E. Doak, ''Fluid dynamic of a flow excited resonance,'' J. Sound Vib. **91**, 375–402 (1983).
[22] A. Hirschberg, J. Kergomard, and G. Weinreich, *Mechanics of Musical Instruments* (Springer, New York, 1995).
[23] D. Ronneberger, ''Experimentelle Untersuchungen zum akustischen Reflexionsfaktor von unstetigen Querschnittsänderungen in einem luftdurchströmten Rohr,'' Acustica **19**, 222–235 (1967).
[24] N. B. Roozen, M. Bockholts, P. van Eck, and A. Hirschberg, ''Vortex sound in bass-reflex ports of loudspeakers,'' J. Acoust. Soc. Am. **104**, 1914–1919 (1998).

Numerical modeling of the spectral broadening of sodar echoes by winds perpendicular to the axis of a finite beamwidth antenna

Frank Quintarelli and Andreas Bergstrom
Katestone Scientific, PO Box 2184, Toowong, Queensland 4066, Australia

(Received 30 June 1999; revised 6 October 2000; accepted 14 October 2000)

A simple model for determining the amount of spectral broadening in acoustic sounder echoes caused by winds traveling perpendicular to the antenna beam is presented. Key features of the model are that the wind profile is described by an analytic function and the antenna radiation pattern is included in the calculations. The model was restricted to the situation where the antenna was aligned in the vertical direction and the winds were horizontal. The effects of refraction by temperature and wind velocity gradients were neglected. The radiation pattern used in the model was the sinc(θ) or $\sin(\theta)/\theta$ function. The wind profiles which were used were a constant windspeed between the antenna and the scattering height, a profile where the windspeed increases linearly with height, and a logarithmic profile. Here, the amount of spectral broadening or spectral width of the echo is calculated by treating the amplitude spectrum of the echo as a probability distribution and determining the standard deviation of this distribution. It was found that the relationship between the standard deviation of the echo, σ, and windspeed, u, was closely described by a linear relationship, $\sigma = Bu$, with the value of B ranging from 0.05 to 0.08 for the situations modeled here. Observational data are presented. The data were obtained with a sounder whose radiation pattern was approximated with the sinc function. The observed relationship between σ, and u, was essentially linear, agreeing favorably with the model predictions; however, the value of the proportionality constant B was 0.04. A possible explanation for this is that the radiation pattern for the antenna may have been underestimated since the effects of the sound absorbing shielding surrounding the antenna are unknown. [DOI: 10.1121/1.1331677]

PACS numbers: 43.28.Tc [LCS]

I. INTRODUCTION AND BACKGROUND

The spectrum of an echo received by an acoustic sounder resembles a broad distribution, the mean of which is taken to represent the Doppler shift of the echo and the width, which may be represented by either the variance (σ^2) or standard deviation (σ) of this distribution, is attributed to numerous factors including artifacts of the technique employed in obtaining the spectrum and the finite duration of the transmitted pulse, both of which are well understood and can be accounted for in subsequent analyses. Others include atmospheric turbulence and broadening by winds traveling in a direction perpendicular to the beam axis. Any processing which involves the spectral moments of the echo must take into account the contribution from each of the above mechanisms. For example, it has been shown that the component due to atmospheric turbulence is a direct measure of the dissipation rate of turbulent kinetic energy—one of the more fundamental measures of atmospheric turbulence (Ref. 1); therefore, an experiment designed to measure the dissipation rate from the spectral width of the echo must also take into account the contributions from the other sources of broadening.

This paper presents the results of a numerical modeling investigation to determine the spectral broadening of an echo caused by winds traveling perpendicular to the antenna beam axis. The model developed for this investigation differs significantly from the approach adopted by other researchers (Phillips *et al.*,[2] Georges and Clifford,[3,4] Spizzichino,[5,6] and Leelananda and Mathews[7]) in two aspects—first, the wind profile is represented by an analytic function, and second, the antenna radiation pattern is included in the calculations.

The major task in investigations of this type is computing the path of a ray in a moving medium. The technique generally employed is to divide the atmosphere into a number of horizontal slices and compute the path of the ray through each slice using Snell's law,[2,7] allowing the ray path to be traced for any observed wind profile as the number of slices determines the accuracy with which the profile can be represented. A discussion of the theory of sound propagation in the atmosphere will be omitted here as it has been exhaustively covered in the literature (see, for example, Phillips *et al.*,[2] Georges and Clifford[3]).

The effects of the antenna radiation pattern have been neglected, or at best very poorly treated, in the models found in the literature. Phillips *et al.*[2] have summarized this tendency in their statement: ''the ray path is interpreted as the path of a biased mean of all energy radiated,'' proceeding then to determine the effects of refraction on this single ray. In this investigation, the effects of the antenna radiation pattern are taken into account by summing the response of the antenna to all the rays lying within the beam of the antenna for both the transmission and reception phases of the sodar operation. It is essentially a numerical integration over the solid angle representing the beamwidth of the antenna.

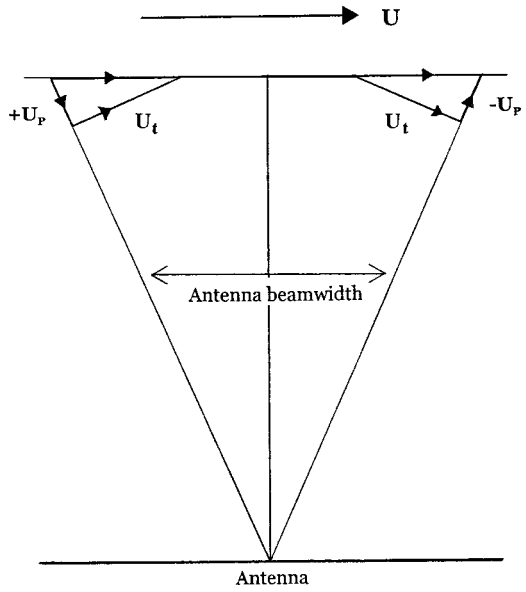

FIG. 1. Physical situation giving rise to spectral broadening of the echo. The transverse wind contains a component parallel to the rays at the periphery of the beam, thereby giving rise to Doppler shifts in the scattered energy.

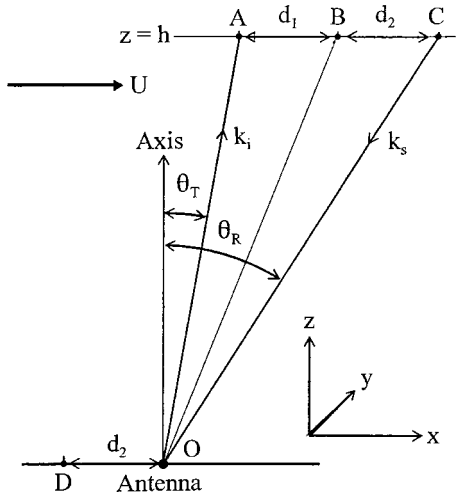

FIG. 2. Model geometry. The transmitted ray travels towards point A, is translated to point B where scattering occurs. Only radiation scattered in the direction of point D arrives back at the antenna, appearing to emanate from point C. The dotted curves represent the ray paths.

II. PHYSICAL CONSIDERATIONS

To gain an appreciation of the mechanism which gives rise to spectral broadening, consider the situation shown in Fig. 1. Here, an antenna with a nonzero beamwidth transmits vertically. For the rays located at the edges of the beam, the horizontal wind velocity vector can be viewed as having components parallel, $\mathbf{u_p}$, and transverse, $\mathbf{u_t}$, to the ray. The component labeled $+\mathbf{u_p}$ gives rise to positive Doppler shifts upon scattering and the component labeled $-\mathbf{u_p}$ gives rise to negative Doppler shifts. To glean an insight into the magnitude of the Doppler shift associated with these peripheral rays, for a ray transmitted 9 deg from the vertical and a horizontal windspeed of 10 m/s at the scattering site, the Doppler shift associated with this ray would correspond to a radial windspeed of about 1.6 m/s. When all possible rays within the beam of the antenna are taken into account, we find a range of values for $\mathbf{u_p}$ ranging from -1.6 to $+1.6$ m/s, and when these are combined at the receiver, the result is a spectrally broadened echo. Consider now the propagation of sound in a moving medium. Referring to Fig. 2, an antenna transmits a pulse of sound at an angle θ_T from the vertical. As the sound propagates upwards it is also advected a distance d_1 by the horizontal wind. The resulting path or ray is now a curve, the exact shape depending on the wind profile. Also, the group and phase velocity vectors are no longer parallel.

At the scattering height, the sound is effectively reradiated in all directions; however, only rays scattered at the correct angle will arrive back at the antenna. As the sound propagates downwards, it will be advected a distance d_2 by the horizontal wind. For an observer located at the antenna, the rays are transmitted at an angle θ_T from the vertical and upon reception the echo appears to emanate from point C, corresponding to an angle θ_R from the vertical. Note that the distances d_1 and d_2 are not the distances traveled by the scatterers during the transmission/reception cycle of the sounder but the advection of the sound pulse as it propagates to the scattering height and back, respectively.

At this stage, a discussion of the assumptions which have been made is appropriate. First, refraction due to temperature variations in the atmosphere and propagation in a moving medium have been neglected. In the mixed layer, which is the practical range of interest for studies involving acoustic sounders, the temperature decreases with altitude at the average rate of 10 deg per km—known as the adiabatic lapse rate. This temperature profile constitutes a change in refractive index of the air, thus changing the ray path from a straight line to a curve. For the situation modeled in this study, the radius of curvature of the resulting rays is several tens of kilometers.[8] The resulting deviation from a straight line (about 0.5 m) is negligible for the situation modeled here. Refraction due to a moving medium can be analyzed in terms of an equivalent temperature profile.[9] For the situation modeled here, it can be shown that the equivalent temperature profile is 6 deg per km, or about one half of the effect due to an adiabatic lapse rate discussed previously. In both cases, the deviation of the ray path from a straight line, and hence refraction, is negligible; consequently, it has been assumed that the rays travel in a straight line.

The second assumption incorporated in these analyses is that the horizontal advection on the upwards leg of the journey is equal to the advection on the downwards leg of the journey. Strictly, the advections are not equal; however, for the situation modeled here, it can be shown using simple geometry that the error incurred in making this assumption is of the order of 0.1 percent.

III. THE MODEL

For the following discussion, it has been assumed that the antenna is pointed in a vertical direction, transverse winds are the horizontal winds, and the prevailing wind direction is constant with height. For convenience, the prevail-

ing wind direction was set along the x axis, the z axis represented the vertical, and the y axis direction transverse to the prevailing wind.

Referring to Fig. 2, the model equations are derived as follows. The antenna transmits acoustic energy in the form of a pulse of finite duration. As this pulse travels up through the atmosphere, it is also displaced horizontally a distance d_1 by the horizontal wind. After scattering, the energy directed back towards the antenna will again be displaced horizontally, this time a distance d_2 by the horizontal wind. For scattered energy to impinge on the center of the antenna, the scattering angle must be such that the scattered ray is directed to a location which is a distance d_2 upwind of the antenna.

The horizontal displacement d of a ray for the upwards leg of the journey can be found by evaluating the following integral (hence the requirement for an analytical expression for the wind profile):

$$d = \frac{1}{C_0 \cos(\theta)} \int_0^h u(z)dz, \tag{1}$$

where h is the scattering height, $u(z)$ is the variation of windspeed with height, and the term $C_0 \cos(\theta)$ is the vertical component of the speed of the acoustic energy as it propagates to the scattering height. As stated previously, the displacements for both legs of the journey were set equal to each other, resulting in a total horizontal displacement of $2d$.

In terms of the symbols in Fig. 2, the line segment OA represents the direction of propagation of the transmitted ray at the instant of initiating transmission. The ray is displaced horizontally as it propagates up to the scattering height at point B where scattering occurs. Only rays scattered in the direction of point D will impinge on the center of the antenna. To an observer located at the antenna, the scattered ray will appear to emanate from point C.

Turning now to the angles of transmission and reception (θ_T and θ_R), the transmission angle is known since it is the independent variable in the process. The angle of reception can be determined from the horizontal displacement ($2d$) which in turn is determined by the wind profile. Once the angles of transmission and reception have been determined, the response of the antenna to radiation from these directions can be found and incorporated into the calculations.

The Doppler shift which occurs during the scattering process is given by

$$\delta f = \frac{1}{2\pi}(\mathbf{k}_s - \mathbf{k}_i) \cdot \mathbf{u}, \tag{2}$$

where $\mathbf{k}_i$ and $\mathbf{k}_s$ are, respectively, the incident and scattered vector wave numbers with magnitude $2\pi/\lambda$ and directions given by unit vectors along OA and CO and $\mathbf{u} = (u(z),0,0)$ is the horizontal wind vector. The direction of the prevailing wind is restricted to the x axis as stated previously.

IV. WIND PROFILES AND RADIATION PATTERN

The spectral broadening resulting from several wind profiles were examined. In all the profiles, the windspeed was zero at the antenna ensuring that the phase and group velocity vectors are parallel, a necessary condition if the antenna were to respond to the incoming radiation according to the radiation pattern.

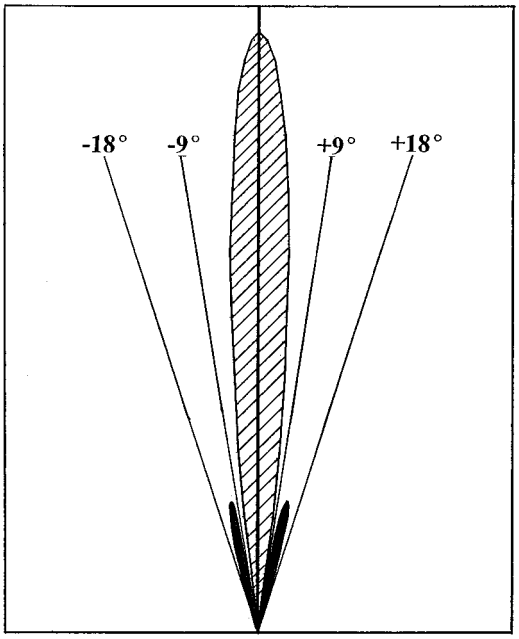

FIG. 3. Radiation pattern (amplitude response) of the antenna used in this analysis. The pattern has nodes at 9 and 18 deg from the axis.

The profiles that were considered were

$$u(z) = u_0 \quad [\text{with } u(0) = 0],$$
$$u(z) = Az, \tag{3}$$
$$u(z) = A \ln\left(1 + \frac{z}{z_0}\right) \quad (\text{with } z_0 = 0.1 \text{ m}),$$

where A is a constant.

The first and second profiles can be observed during convective and near neutral conditions;[10] the third profile is a logarithmic profile which can be observed in conditions of neutral stability.

Antenna radiation patterns are both difficult to measure and calculate for real antenna systems; consequently, various workers have suggested simple analytic functions such as the Gaussian[11] and the Bessel function.[12] The antenna whose characteristics were used in this study consisted of a circular parabolic dish constructed from glass-reinforced plastic with a transducer mounted at the focus. The dish was surrounded by a pentagonal noise shield 2.5 m high. The internal walls of the shield were lined with sound-absorbing foam. To minimize the possibility of noise being diffracted over the edge of the shielding, foam-lined serrated sections were attached to the top edges of the shield. The effects of the addition of the internal foam and serrated edges on the radiation pattern were unknown; however, the authors believe that this would result in partial or total removal of the sidelobes from the radiation pattern (see Ref. 13).

To arrive at an amenable solution we note that the radiation pattern for a circular dish is a Bessel function and for a square dish it is a sinc function. As the sinc function is the broader of the two (for an antenna of equal diameter) it was

TABLE I. Model predictions of mean standard deviation of the echo spectrum for the three wind profiles for a radiation pattern which does not contain sidelobes.

	Constant		Linear		Logarithmic	
u (m/s)	Mean (m/s)	Std. dev. σ (m/s)	Mean (m/s)	Std. dev. σ (m/s)	Mean (m/s)	Std. dev. σ (m/s)
0	0.00	0.00	0.00	0.00	0.00	0.00
2	−0.000 14	0.10	−0.000 80	0.10	−0.000 094	0.10
4	−0.000 41	0.20	−0.000 27	0.21	−0.000 40	0.21
6	−0.000 87	0.30	−0.000 44	0.31	−0.000 76	0.30
8	−0.001 4	0.39	−0.000 81	0.41	−0.001 4	0.40
10	−0.002 4	0.48	−0.001 7	0.51	−0.002	0.49

decided to use it, knowing that it would yield an overestimate (hence an upper limit) to the amount of broadening. Spectral broadening was determined for the cases where the radiation pattern contained no sidelobes and only the first sidelobes. This was achieved by truncating the sinc function at the appropriate angle. The radiation pattern for the antenna is shown in Fig. 3.

V. IMPLEMENTATION DETAILS

Implementing the model can be performed in either polar or Cartesian coordinates. It was found that the implementation was greatly simplified if the Cartesian coordinate system was employed. As previously mentioned, the evaluation consisted of integrating all rays emitted within the beamwidth of the antenna. However, instead of varying the transmission angle, the x and y coordinates of point A in Fig. 2 were varied such that the entire beam was covered in increments of 0.02 deg.

Setting the antenna axis coincident with the z axis, and the x and y axes parallel and perpendicular to the prevailing wind direction, the vector **OA** (Fig. 2) can be written as

$$\mathbf{OA}=(x,y,h), \tag{4}$$

where h is the height at which scattering occurs. This is a very convenient formulation since the unit vector

$$\widehat{\mathbf{OA}}=\frac{(x,y,h)}{\sqrt{x^2+y^2+h^2}}, \tag{5}$$

also defines the direction of the incident vector wave number $\mathbf{k}_i$. The transmission angle θ_T is thus given by

$$\sin\theta_T=\sqrt{\frac{x^2+y^2}{x^2+y^2+h^2}}. \tag{6}$$

Again referring to Fig. 2, since the scattered ray appears to emanate from point C, the vector **CO** defines the direction of the scattered energy which impinges on the antenna. Writing this vector as

$$\mathbf{CO}=-(x+2d,y,h), \tag{7}$$

similar expressions for the scattered wave number vector $\mathbf{k}_s$ and the reception angle θ_R can be obtained.

The compilation of the echo spectrum (i.e., the frequency domain representation of the echo) was achieved as follows. For each ray, the angles, antenna response (for both transmission and reception angles), and Doppler shift were determined. The Doppler shift was used as an index into an array which represented the echo spectrum. The appropriate array element was then updated by adding to it the energy represented by that ray. The energy, E, added to each element was determined from the radiation pattern of the antenna

$$E=R(\theta_T)\cdot R(\theta_R), \tag{8}$$

where $R(\theta)$ is the response of the antenna to radiation impinging on it at angle θ from the beam axis.

The statistics of the echo spectrum were then determined using the same methods as used in the sounder *viz*. the array was treated as a histogram, each array element was a bin of the histogram, and the contents of each bin represented the probability of observing the Doppler shift corresponding to that bin or array element. Since the final result is essentially a probability distribution, the mean and standard deviation of this distribution can be readily obtained. The bin width was 0.25 Hz or 0.025 m/s.

TABLE II. Model predictions of mean standard deviation of the echo spectrum for the three wind profiles for a radiation pattern which contains sidelobes.

	Constant		Linear		Logarithmic	
u (m/s)	Mean (m/s)	Std. dev. σ (m/s)	Mean (m/s)	Std. dev. σ (m/s)	Mean (m/s)	Std. dev. σ (m/s)
0	0.00	0.00	0.00	0.00	0.00	0.00
2	−0.000 29	0.17	−0.000 15	0.17	−0.000 23	0.17
4	−0.001 2	0.33	−0.000 57	0.34	−0.000 92	0.33
6	−0.002 3	0.49	−0.001 1	0.50	−0.002 0	0.49
8	−0.003 9	0.64	−0.002 0	0.66	−0.003 6	0.65
10	−0.006 0	0.79	−0.003 2	0.83	−0.005 4	0.80

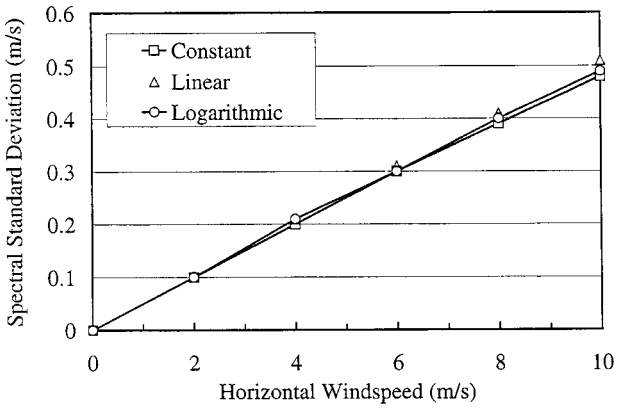

FIG. 4. Plot of the standard deviation of the echo spectrum against windspeed for the radiation pattern without sidelobes.

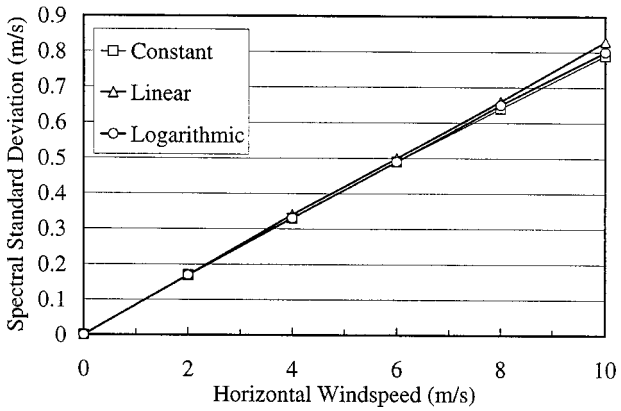

FIG. 5. Plot of the standard deviation of the echo spectrum against windspeed for the radiation pattern with sidelobes.

VI. RESULTS AND DISCUSSION

The physical situation which was modeled in this investigation consisted of an acoustic sounder operating at a frequency of 1675 Hz. The sodar was a three-axis monostatic system with one antenna oriented vertically (described previously) and the other two inclined 30 deg from the vertical in northerly and easterly directions in order to obtain the horizontal wind components. A transmit/receive sequence consisted of transmitting a 500-ms cosine bell modulated pulse, switching the sodar circuitry to the receive mode and using a time gate to select echoes from the appropriate range. After appropriate signal processing (i.e., filtering, amplification, etc.), the received echoes were digitized and the fast Fourier transform algorithm was used to calculate the spectrum.

In the model, the parameters were chosen to coincide with operational settings of the sodar and the prevailing meteorological conditions—a scattering height of 500 m and windspeeds ranging from 0 to 10 m/s. As a point of interest, when the horizontal windspeed exceeds about 10 m/s, the noise thus generated (e.g., rustling of leaves, grass, etc.) increasingly interferes with reception, giving rise to a spectrally noisy echo from which it is difficult to extract reliable data.

Since the model calculates the spectrum of the echo, both the mean and the standard deviation, σ, can be readily obtained. The predictions of the model are shown in Tables I and II and in Figs. 4 and 5. Table I presents results consisting of the mean and standard deviation of the spectrum for the three wind profiles at various windspeeds for a radiation pattern which does not contain sidelobes. Table II presents corresponding results for a radiation pattern where the sidelobes have been included. It is evident from the results that the standard deviation, σ, with windspeed, u, can be closely described using a linear relationship $\sigma = B \cdot u$ with the value of B ranging from about 0.08 for the case with sidelobes to 0.05 for the case without sidelobes.

The model also predicts a negative bias in the echo spectrum which will be interpreted by the echo analysis software in the sounder as an updraft of a few millimeters per second. In practice, such a small bias is extremely difficult to detect. It is interesting to note that Spizzichino[5,6] also reports a bias in the vertical windspeed estimate due to the presence of a horizontal wind. However, care should be exercised when comparing the results presented in Spizzichino[5,6] with the results presented here. The results presented in Spizzichino[5,6] are for a single ray, whereas the results presented here are the sum of a very large (ideally an infinite) number of rays.

Figure 6 presents observed data obtained with the above-mentioned sounder and parameters. The scatter plot shows σ plotted against u for convective conditions where the wind profile is approximately constant. The prominent feature is that the points do not pass through the origin. This is due to the finite duration of the transmitted pulse. Since the transmitted pulse has finite duration, its Fourier transform has a finite width, σ_{TX}, in the frequency domain. In practice, the variance of the echo which is received is the sum of the variances of the spectrum of the transmit pulse, that due to transverse winds, atmospheric turbulence, noise, etc. For the situation where only a horizontal wind is present, the observed spectral standard deviation of the echo is given by

$$\sigma_{\text{observed}} = \sqrt{(Bu)^2 + \sigma_{TX}^2} \tag{9}$$

The above equation therefore defines a lower limit for the

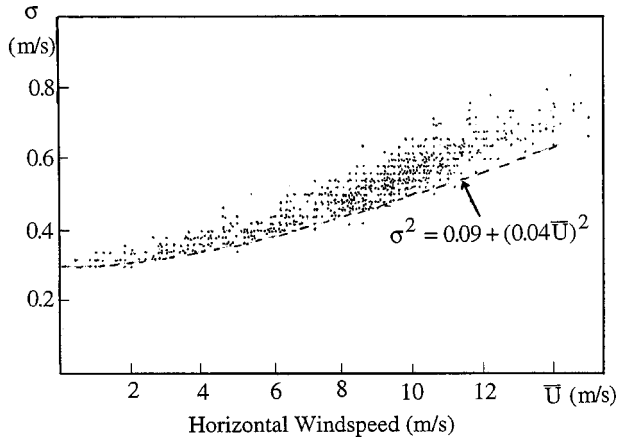

FIG. 6. Observed spectral widths of echoes plotted against value of the windspeed at the scattering height. The intercept at 0.3 represents the spectral variance due to the finite duration of the transmitted pulse. Data were obtained at Alice Springs (subtropical desert environment) during May (autumn) 1985 when the atmosphere was generally unstable. Data were averaged over 30-min intervals throughout the day.

data points in Fig. 6 and the intercept of this lower limit with the vertical axis is σ_{TX}. All points above this limit represent the total broadening due to all the mechanisms previously mentioned. Note that had the spectral width of the transmitted pulse been zero, the standard deviation of the echo would have been directly proportional to the windspeed, with the value of the constant being about 0.04, which is not unreasonable given that the radiation pattern for this antenna system was not accurately known. Note again that, above about 10 m/s, the quality and reliability of the data has begun to decrease due to the presence of environmental noise.

VII. CONCLUDING REMARKS

A very simple model for determining the spectral broadening of sodar echoes due to winds moving transverse to the antenna beam axis has been presented. The salient features of the model are that the wind profile has been described by an analytic function and that the radiation pattern of the antenna has been included in the calculations. The model parameters were chosen to represent realistic operational situations. Simplifying assumptions included restricting the geometry to a vertically pointing antenna and horizontal winds. The effects of refraction due to temperature and wind profiles were neglected. For temperature profiles which are likely to be encountered in practice, the deviation of the ray path from a straight line is about 0.5 m for a scattering height of 500 m. Refraction due to a moving medium amounted to about one half of that caused by the temperature profile.

The model predicts that (to first order) the contribution to the standard deviation of the echo spectrum by a horizontal wind is directly proportional to the horizontal windspeed at the scattering site, a prediction which compared favorably with observation. The value of the constant predicted by the model would depend on the radiation pattern of the antenna and ranged from 0.05 to 0.08 for the cases investigated here. The value of the constant deduced from the observed data was 0.04.

Improvements to the model include incorporating the effects of refraction and allowing for nonvertical antenna orientation (in which case a new set of model equations would need to be derived). Last, determining the radiation pattern of the antenna still presents a major difficulty, whether this is achieved through theoretical calculations or physical measurements.

ACKNOWLEDGMENTS

The authors would like to thank Professor I. Bourne for providing the observational data obtained with the sounder whose antenna characteristics were modeled herein.

[1] R. C. Srivastava and D. Atlas, ''Effect of finite radar pulse volume on turbulence measurements,'' J. Appl. Meteorol. **13**, 472–480 (1974).
[2] P. D. Phillips, H. Richner, and W. Nater, ''Layer model for assessing acoustic refraction effects in acoustic sounding,'' J. Acoust. Soc. Am. **62**, 277–285 (1977).
[3] T. M. Georges and S. F. Clifford, ''Acoustic sounding in a refractive atmosphere,'' J. Acoust. Soc. Am. **52**, 1397–1405 (1972).
[4] T. M. Georges and S. F. Clifford, ''Estimating refractive effects in acoustic sounding,'' J. Acoust. Soc. Am. **62**, 277–285 (1974).
[5] A. Spizzichino, ''La refraction des ondes acoustiques dans l'atmosphere et son influence sur les mesures du vent par sodar,'' Ann. Telecommun. **29**, 301–310 (1974).
[6] A. Spizzichino, ''Discussion on the operating conditions of a Doppler sodar,'' J. Geophys. Res. **29**, (No 36), 5585–5591 (1974).
[7] S. A. Leelananda and T. Mathews. ''A method of correcting wind profiles obtained using Doppler acoustic radar,'' in *Proceedings of the International Symposium on Acoustic Remote Sensing of the Atmosphere and Oceans* (University of Calgary, Calgary, Alberta, Canada).
[8] U. Ingard, ''A review of the influence of meteorological conditions on sound propagation,'' J. Acoust. Soc. Am. **25**, 405–411 (1953).
[9] D. C. Pridmore-Brown, ''Sound propagation in a temperature and wind stratified medium,'' J. Acoust. Soc. Am. **18**, 438–443 (1946).
[10] *Atmospheric Turbulence and Air Pollution Modelling*, edited by F. T. Nieustadt and H. Van Dop (Reidel, Dordrecht, 1982).
[11] A. Weill, C. Klapisz, B. Strauss, F. Baudin, C. Jaupart, P. Van Grunderbeek, and J. P. Goutourbe, ''Measuring heat flux and structure functions of temperature fluctuations with an acoustic Doppler sounder,'' J. Appl. Meteorol. **19**, 199–205 (1980).
[12] The Boulder Low-level Intercomparison Experiment, Report No. 2, edited by J. C. Kaimal, H. W. Baynton, and J. E. Gaynor, NOAA/ERL, Boulder, CO.
[13] E. Hecht and A. Zajac, *Optics* (Addison-Wesley, Reading, MA).

Backscattering from buried sediment layers: The equivalent input backscattering strength model

Laurent Guillon[a)]
Laboratoire de Mécanique et d'Acoustique, UPR CNRS 7051, 31, chemin Joseph Aiguier, 13402 Marseille Cedex 20, France

Xavier Lurton[b)]
IFREMER, Service Acoustique et Sismique, BP 70, 29280 Plouzané, France

(Received 27 March 2000; revised 31 July 2000; accepted 5 October 2000)

Signals received by low-frequency multibeam echosounders are strongly affected by sound penetration inside the upper sediment layers and by backscattering from buried layers down to depths of a few meters; this may lead to serious ambiguities and misinterpretations of experimental data. These phenomena are modeled here using a concept of *equivalent input backscattering strength* (EIBS), based on a combination of classical models of local backscattering strength and propagation inside fluid layered media. The local backscattering strength at a buried interface is expressed first to account for the impedance adaptation due to the overlying layers, for the angular refraction effects due to the velocity profile, and for the layered structure of the underlying medium. It is then transferred to the upper water–sediment interface, accounting for propagation inside the layered stack; the transfer coefficient is obtained from the classical theory of plane wave propagation in layered media. The volume backscattering effects are processed in the same way and account for the finite thickness of the layers. The various contributions are finally summed to give the backscattering strength, at the upper interface, that features the various effects of propagation and attenuation inside the layered structure. © *2001 Acoustical Society of America.*
[DOI: 10.1121/1.1329622]

PACS numbers: 43.30.Gv, 43.30.Hw, 43.30.Ma, 43.30.Pc [DLB]

I. INTRODUCTION

Deep-sea multibeam echosounders are widespread tools in marine geology studies since they can readily provide bathymetry and sonar images of large seafloor areas. A geologist's first interpretation can be formed from these images by combining the recorded backscattering strength with the seafloor nature and assuming a one-to-one relation between these two variables. Classically, backscattering strength is modeled as the sum of one contribution from the rough surface and one from the semi-infinite volume below it (see, e.g., Ref. 1). But, at low frequencies (typically 10–15 kHz for deep-water systems), the signal may significantly penetrate into the seafloor. Since the geological context may be very complex in the first meters of sediment, the stratification effects on the overall response should be taken into account. Simple two-component models are not able to describe the recorded backscattering strength so using them may lead to ambiguities in data interpretation.[2] There is therefore a need for geoacoustic models predicting the backscattering strength of layered seafloors.

Although many studies have dealt with the influence of sediment stratification on the reflection and transmission coefficients (see, e.g., Refs. 3–5), only a few have been devoted to backscattering by layered media. One of the earliest works was Ivakin's model[6] of volume backscattering for stratified sediments, which is based on a small perturbation approach over a Green's function description of the acoustical field inside the sediment. Later works by Ivakin[7–9] and Tang[10] proposed unified approaches of backscattering by volume and buried interfaces in layered media. They showed that if a buried interface is considered as a perturbation of the surrounding medium, the two contributions may be expressed under a single formulation.

As opposed to these ''global'' methods considering the problem in its generality, some authors tried to model the effects of stratification upon backscattering strength in particular configurations. Solutions were proposed for the backscattering strength of a single isotropic layer upon a basement: McDaniel[11] took into account the layer roughness and Essen[12] the shear wave in the basement. They showed notable effects near the critical angle but they did not include volume backscattering strength in their models. Moreover, their exact formulations cannot be generalized to more complex geological configurations.

Various more pragmatic approaches to the problem may be found.[2,13–15] In particular, Lyons *et al.*[15] proposed a backscattering strength model for layered seafloors, in which every layer is characterized by its own individual backscattering strength (based on Jackson's model); the global backscattering strength is the sum of all the layer contributions individually modified by the layering. The layering effects, however, were not fully detailed in this attractive approach since those authors focused on volume backscattering modeling.

The principle of our equivalent input backscattering strength (EIBS) model[16–19] is basically an extension of that

a)Electronic mail: guillon@lma.cnrs-mrs.fr
b)Electronic mail: lurton@ifremer.fr

of Lyons *et al.*[15] Starting from the same intuitive description of local contributions from buried layers ''seen'' through the filter of an overlying sediment stack, we account for stratification effects in a more rigorous way and under a more easily generalizable formalism, (1) by carefully accounting for the local modifications of backscattering strength due to burying and (2) by using a classical model of plane wave propagation inside a fluid layered medium. Finally, the ultimate ambition of our EIBS model is to provide results in good agreement (despite their narrower generality) with those obtained from more global approaches such as Ivakin's.[9]

II. THE CONCEPT OF EQUIVALENT INPUT BACKSCATTERING STRENGTH

A. Geoacoustic model

In the following, the seafloor is described by a two-part geoacoustic model (Fig. 1):

(i) A fluid dissipative sedimentary layer of thickness h, split into n elementary layers. Each layer l is characterized by its sound speed c_l, density ρ_l, attenuation coefficient α_l, its thickness d_l, and its own individual backscattering cross section (BCS) $\sigma_l(\theta_0)$, considered at its upper boundary.

(ii) A semi-infinite fluid dissipative basement, with parameters c_{n+1}, ρ_{n+1}, and α_{n+1}, and its BSC $\sigma_{n+1}(\theta_0)$.

Note that the concept of ''basement'' here relates only to the acoustical penetration, meaning that there is no significant return of energy from the medium below interface $n+1$. It is not related to a particular geological structure.

In the following, to define its individual BCS, each layer is first considered as having its upper boundary overlaid with water. We found this convention convenient for numerous practical configurations in which one has to compare backscattering strength levels from the same boundary either outcropping or buried under a stratified sediment layer. An initial local BCS is defined under this assumption, classically split into two components (surface roughness and volume inhomogeneities) and is then modeled using a local backscattering strength model such as Jackson's.[1]

B. The equivalent input backscattering strength

Calculating the total BCS features two steps. First, the local individual BCS $\sigma_l(\theta_0)$ are defined taking into account the effects due to layering: changes in impedance contrasts, influence of underlying layers, volume limitation, and refraction. These various effects are detailed in Sec. III. The modified individual BCS for each layer l is written $\tilde{\sigma}_l(\theta_{l-1})$; this notation includes the angle changes due to refraction. The second step of the process is to calculate the transfer coefficients accounting for sound propagation inside the stack. The contribution of each layer l is weighted by a coefficient $C_{pl}(\theta_0)$ determined by the acoustic field inside the layered structure. Under a small perturbation hypothesis, these coefficients can be obtained by a classical plane wave approach of sound transmission in layered media (see, e.g., Ref. 20).

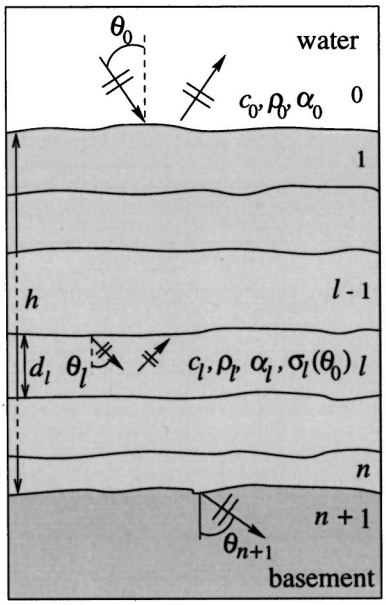

FIG. 1. Geoacoustic model.

These two steps finally lead to the ''equivalent input backscattering strength'' at the upper water/sediment interface.[18] This term was chosen by analogy with the concept of ''equivalent input impedance'' in the theories of electric circuits or sound propagation in layered media.[20] Thereafter, under the hypothesis of single scattering, the various contributions are summed to provide the total BCS of the geoacoustic configuration:

$$\sigma_t(\theta_0) = \sum_{l=1}^{n+1} C_{pl}(\theta_0)\tilde{\sigma}_l(\theta_{l-1}). \tag{1}$$

The global backscattering strength for the stack is finally $10\log[\sigma_t(\theta_0)]$.

Two hypotheses are necessary for establishing this expression of the total BCS. First, a small perturbation approach is used here: the scattered wave has second-order magnitude relative to the incident field, so one can deal with plane wave propagation inside the stack. This approximation is usually admitted in sediment backscattering models.[1,6,21,22] Second, a single-scattering approach, related to the former hypothesis, is needed. The multi-scattered field is considered as negligible relative to the single-scattered echo (whose backwards propagation accounts for the complete description of phenomena associated with layered media). Consequently, one can make a single summation of the various contributions. This second hypothesis is valid if each layer's backscattering strength is low enough. This is true outside the ''specular'' regime, typically for incidence angles greater than 20 degrees; on the other hand, at low incidences, backscattering strength may be large enough to allow multiple scattering. Consequently, for angles close to the vertical incidence, the model must be considered as a first approximation of the problem and further calculations should be done to extend it exactly to the whole angular range.

TABLE I. Number of parameters used for the equivalent input backscattering strength model of an n-layer sediment stack.

Parameters	No. of parameters
Geoacoustic configuration	
c_l: sound speed	$n+1$
ρ_l: density	$n+1$
α_l: attenuation	$n+1$
d_l: thickness	n
Backscattering parameters	
Surface	$2\times(n+1)$
Volume	$n+1$
Total	$7n+6$

C. Number of parameters and discussion

For every layer, the composite roughness model[1] served to determine the individual interface BCS. We used the two classical parameters γ and β_J defining the roughness spectrum as $W_s(\mathbf{K})=\beta_J K^{-\gamma}$, and a single parameter σ_v for the volume contribution.

Table I features the parameters involved in this model for the geoacoustic configuration presented in Fig. 1, showing that $7n+6$ input parameters are needed for an n-layer configuration. For example, a simple two-layer model (a basement below two sediment layers) requires 20 input parameters. The effective number of independent parameters can be reduced by taking into account relations between some of them (see, e.g., Ref. 23), but the array size will nevertheless remain large.

III. LOCAL DESCRIPTION OF THE INDIVIDUAL BCS

Our objective was to model the modifications of the backscattering strength due to layering. To do so, we used the model of Jackson[1] for the local backscattering strength of a given layer but other models could have been used. In the following, the changes induced by layering on the individual layer BCS are illustrated by numerical applications computed on a geoacoustic model with two layers (mud and medium sand) overlying a coarse sand basement. The layering effects are visualized on the figures representing the backscattering strength of the medium-sand layer. The configuration parameters are given in Table II. The acoustical parameters (c, ρ, and α) are from data compilations by Hamilton.[23] The values for β_J and γ are from Mourad and Jackson.[24] The volume backscattering strength coefficient was based on typical values obtained on real data. The signal frequency is 13 kHz.

TABLE II. Input parameters of the geoacoustic model used for illustrating the numerical applications in Secs. III and IV.

Layers	Water	Mud	Medium sand	Coarse sand
c ($\mathrm{m\cdot s^{-1}}$)	1500	1550	1650	1840
ρ	1	1.3	1.43	2.2
α (dB/λ[a])	0	0.2	0.87	0.9
γ	⋯	3.25	3.25	3.25
β_J ($\mathrm{cm^4}$)	⋯	4×10^{-4}	30×10^{-4}	60×10^{-4}
σ_v ($\mathrm{dB\cdot m^{-3}}$)	⋯	−43	−35	−30
d (cm)	⋯	20	10	⋯

[a]λ is the wavelength.

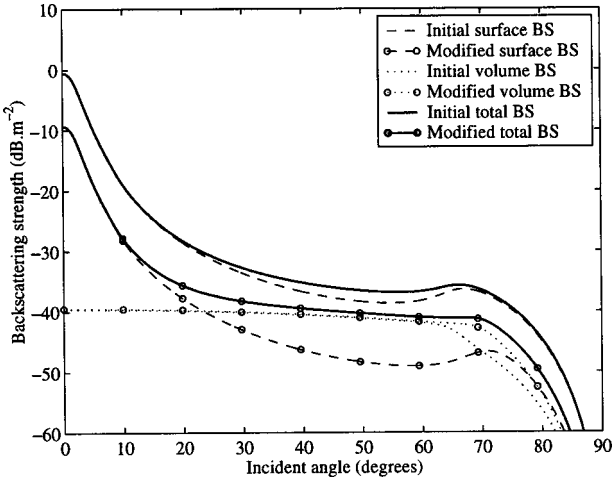

FIG. 2. Effect of impedance contrast changes for the medium sand backscattering strength (BS). The model used is Jackson's (Ref. 1) with input parameters given in Table II. The curves labeled ''Initial BS'' are computed for the medium-sand layer covered with water whereas the curves labeled ''Modified BS'' are computed for this layer covered with mud.

A. Local backscattering strength definition

As said above, for each layer l ($l>1$), the individual initial BCS is first defined as having its interface overlaid with water. Now, when this layer is inside the sediment stack, some changes obviously occur. First, the presence of the upper sediment layer $l-1$ decreases the impedance contrast associated with the backscattering phenomenon, and this decrease modifies the local reflection and transmission coefficients. Because these coefficients are used in the local backscattering models, the individual BCS will be modified accordingly, providing a new local BCS.

As an example, Fig. 2 shows the effect of this impedance contrast change on the backscattering strength of the medium-sand layer and its clear dependence on incident angle.

At steep incidence, the backscattering process is dominated by the roughness contribution; it is modeled, in Jackson's approach,[1] using Kirchhoff's approximation, as follows:

$$\sigma_k(\theta_0)=\frac{R^2(0)}{8\pi\cos^2\theta_0\sin^2\theta_0}\int_0^\infty \exp(-qu^{\gamma-2})J_0(u)\,u\,du, \tag{2}$$

where q is a function of θ_0, k, γ, and β_J, and $R(\theta_0)$ is the amplitude reflection coefficient for the water–sediment boundary for incident angle θ_0.

This BCS expression is proportional to the squared pressure reflection coefficient $R(0)$ upon the interface; hence a change from the water–sand boundary $[R(0)=0.222]$ to the mud–sand boundary $[R(0)=0.079]$ leads to a decrease of $20\log(0.079/0.222)=-9.0$ dB, which is clear in Fig. 2. This is an impedance matching effect: the decrease in impedance contrast lowers the scattered energy.

At oblique incidence, the combination of surface and volume contributions makes the interpretation more difficult. In Ref. 24, the roughness scattering at large incidence is expressed using the composite roughness model[1] with the local BCS written as follows:

$$\sigma_{cr}(\theta_0) = 4k^4 \cos^4\theta_0 |Y(\theta_0)|^2 W_s(2k_0 \sin\theta_0), \tag{3}$$

where

$$Y(\theta_0) = \frac{(\rho-1)^2 \sin^2\theta_0 + \rho^2 - \kappa^2}{[\rho\cos\theta_0 + P(\theta_0)]^2}. \tag{4}$$

In Eq. (4), $\rho = \rho_1/\rho_0$, $\kappa = k_1/k_0$, and $P(\theta_0) = k_{z1}/k_0$, where $k_{z1} = \sqrt{k_1^2 - k_0^2 \sin^2(\theta_0)}$; ρ_0 and k_0 are the density and wave number in water, these are respectively ρ_1 and k_1 in sediment. Figure 2 shows that roughness scattering at oblique incidence is also affected by the impedance matching.

For volume backscattering, we used the expression from the model of Jackson and Briggs:[25]

$$\sigma_{sv}(\theta_0) = \frac{|1-R^2|^2 \cos^2\theta_0}{4k_0 \mathcal{I}[P(\theta_0)]|P(\theta_0)|^2} \sigma_v. \tag{5}$$

The effect of an impedance contrast change on volume backscattering strength is weak because $|1-R^2|^2$, which features the two-way transmission losses through the water–sediment interface, varies little with the impedance contrast. More important is the angular dependence effect: lowering the impedance contrast increases the critical angle, as shown in Fig. 2 and described in Sec. III D.

To summarize, the balance between the local BCS components is modified: the surface BCS is lowered (impedance matching effect) whereas the volume BCS is almost unchanged. Consequently, burying the various layers may strongly affect their BCS. Results then depend on the respective proportion of surface and volume backscattering strength in the initial BCS.

B. Influence of underlying layers

The change in impedance contrast affects the backscattering strength through the local reflection and transmission coefficients. But the underlying stratified structure also modifies these coefficients in a global way which also changes the backscattering strength. This was shown by Moe and Jackson[26] for a stratified structure underlying a rough surface. In the following we used their expression for the resulting BCS:

$$\sigma_s(\theta_0) = \left(\frac{k_0}{4}\right)^4 |1+R_L|^4 \left|1 - \frac{\kappa^2}{\rho} + \left(1 - \frac{1}{\rho}\right) \times \left[\sin^2\theta_0 + \rho\cos^2\theta_0 \left(\frac{1-R_L}{1+R_L}\right)^2\right]\right|^2 W_s(2k\sin\theta_0), \tag{6}$$

where R_L is now the amplitude reflection coefficient for the layered media (see, e.g., Ref. 20). Figure 3 presents this calculation for the medium-sand layer; to make interpretation easier the impedance contrast changes described earlier were omitted. The strong oscillations between 50 degrees and 60 degrees are caused by the reflection on the medium-sand layer.

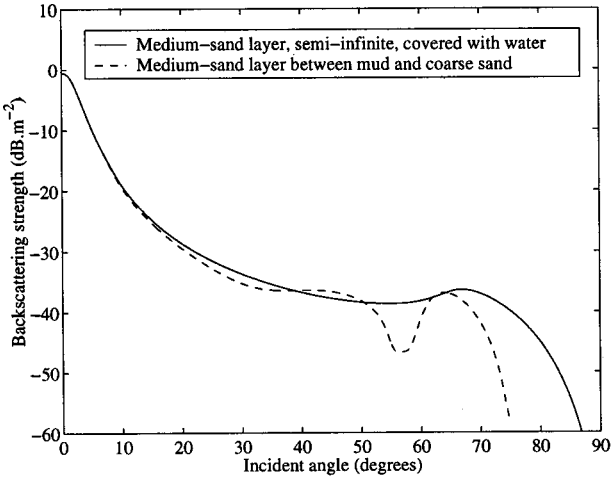

FIG. 3. Roughness backscattering strength of the medium sand layer with parameters provided in Table II. The solid curve is the initial roughness backscattering strength, and the dashed curve corresponds to this layer inside the sediment stack, using Eq. (6).

C. Volume limitation

The volume contribution to the backscattering process is classically[25] modeled with a single parameter σ_v, which is the local BCS associated with a unit volume. This BCS is not ''seen'' directly, but rather through the interface. Equation (5) given above is based on the hypothesis that the scattering medium is semi-infinite. However, for a given sediment layer, this is not true any more. To take into account this volume limitation, expression (5) now becomes

$$\sigma_{sv} = \frac{|1-R^2|^2 \cos^2(\theta_0)}{4k_1 \mathcal{I}[P(\theta_0)]|P(\theta_0)|^2} [1 - e^{-4\mathcal{I}(k_{zl})d_l}] \sigma_v, \tag{7}$$

where $\mathcal{I}(k_{zl})$ is the imaginary part of the vertical component of the wave vector inside the sediment. The bracketed corrective term in Eq. (7) features the attenuation effect along the layer thickness d_l.

Figure 4 presents this effect of thickness limitation on the volume backscattering strength of the medium-sand layer. Backscattering strength is lowered, with a maximum influence at steep angles. Beyond the critical angle, this effect disappears because penetration becomes negligible; the energy is conducted only by an evanescent lateral wave.[20] The layer thickness is then of little importance.

D. Refraction and attenuation

Sound propagation inside the sediment layers implies two consequences for local individual BCS. First, the incident wave is refracted. At each interface, the Snell–Descartes relation gives

$$k_{l-1}\sin\theta_{l-1} = k_l \sin\theta_l = k_0 \sin\theta_0, \tag{8}$$

so layer l is now ''seen'' at incident angle θ_{l-1} instead of at the in-water original angle θ_0. This modifies the backscattering strength angular dependence by a kind of ''anamorphosis.'' Second, the sediment layers are dissipative. Their at-

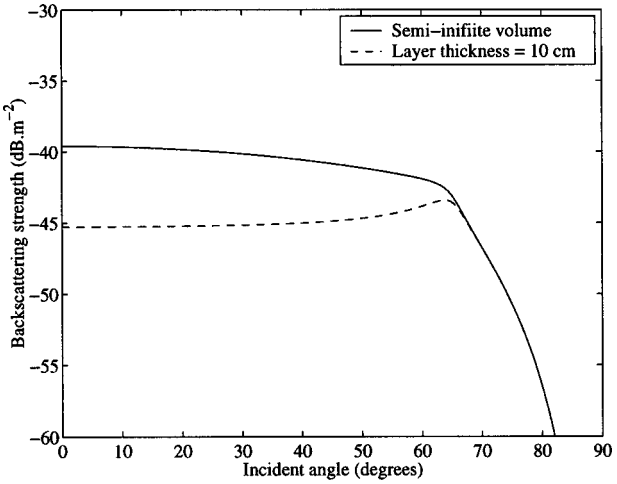

FIG. 4. Volume limitation effect on the medium-sand layer backscattering strength. Solid curve is computed with Eq. (5) whereas the dashed one corresponds to Eq. (7).

tenuation lowers the backscattered level, as seen from Eq. (7). This effect is all the stronger as the incident angle is large (the acoustical path is longer) and the layer is deep.

E. Local backscattering strength synthesis

Figure 5 summarizes the various effects described earlier that affect the individual backscattering strength of the buried medium-sand layer. On most of the angular range there is a global lowering, between 5 and 10 dB, relative to the water-overlaid case. Moreover, the cutoff angle effect is steeper than previously. This change in critical angle is due to refraction as described in Sec. II D. The underlying stratification influence [Eq. (6)] is weak in this case because the dominant effect in this angular range is volume scattering rather than interface roughness.

IV. COMPUTATION OF THE TRANSFER COEFFICIENTS

Now that every layer's local BCS is defined and specified, it has to be transferred upwards to the water–sediment interface in a way correctly accounting for the propagation inside the sedimentary medium. In the following, the transfer coefficient $C_{pl}(\theta_0)$ quantifies, for each buried layer l, the total energy incident at angle θ_0 transmitted inside the sediment down to layer l and backscattered to the sonar in the same direction θ_0. The computation of these transfer coefficients is first presented for the simple case of a single sediment layer overlying a basement and then for the general multilayered case. In the following $R_{i,j}$, or $T_{i,j}$, denotes the reflection, or transmission, coefficient from medium i to medium j. The complex wave number $k_l=\omega/c_l+i\alpha_l/8.686\lambda$ (with α_l in dB/wavelength) accounts for sound attenuation in layer l. The vertical, or horizontal, projection of the wave vector $\mathbf{k}_l$ is k_{z_l}, or k_{x_l}.

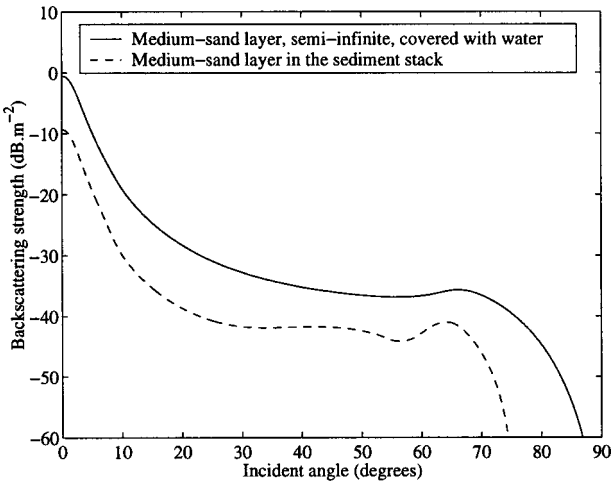

FIG. 5. Medium-sand backscattering strength as a semi-infinite medium covered with water (solid curve) and as a layer inside the sedimental stack (dashed curve). The parameters used are given in Table II.

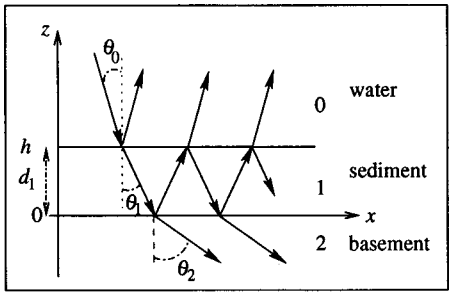

FIG. 6. Geometry for the incident path.

A. A single-sediment layer

We develop here the basement transfer coefficient: $C_{p2}(\theta_0)$. The calculation is split into two parts: we expressed first the energy incident from the water to the basement and then the energy transmitted back to the receiver.

1. Incident path

Figure 6 depicts the first part of this approach. Under the small perturbation hypothesis, only plane waves are considered inside the sediment layers.

The acoustical pressure field in the three media may be written as follows:

$$\begin{aligned} p_0&=[e^{-ik_{z_0}(z-h)}+R_a e^{ik_{z_0}(z-h)}]e^{ik_x x}e^{-i\omega t},\\ p_1&=[A_1 e^{-ik_{z_1}z}+B_1 e^{ik_{z_1}z}]e^{ik_x x}e^{-i\omega t},\\ p_2&=T_a e^{-ik_{z_2}z}e^{ik_x x}e^{-i\omega t}, \end{aligned} \tag{9}$$

where R_a is the reflection coefficient at the water–sediment interface for the whole sediment stack. Here T_a is the global transmission coefficient from water to basement ($T_{0,2}$):[20]

$$T_a=\frac{4Z_1Z_2}{(Z_2-Z_1)(Z_1-Z_0)e^{i\xi_1}+(Z_2+Z_1)(Z_1+Z_0)e^{-i\xi_1}}, \tag{10}$$

where $Z_l=\rho_l\omega/k_{z_l}$ is the plane wave impedance in layer l and $\xi_l=d_l k_{z_l}$. For notation convenience, the time dependence $e^{-i\omega t}$ and the horizontal components $e^{ik_x x}$ are suppressed in the following, and the incident acoustical pressure is normalized to 1. The acoustical continuity conditions at the basement boundary are used to express coefficient A_1, which is the relative amplitude of the incident wave on the considered scattering boundary:

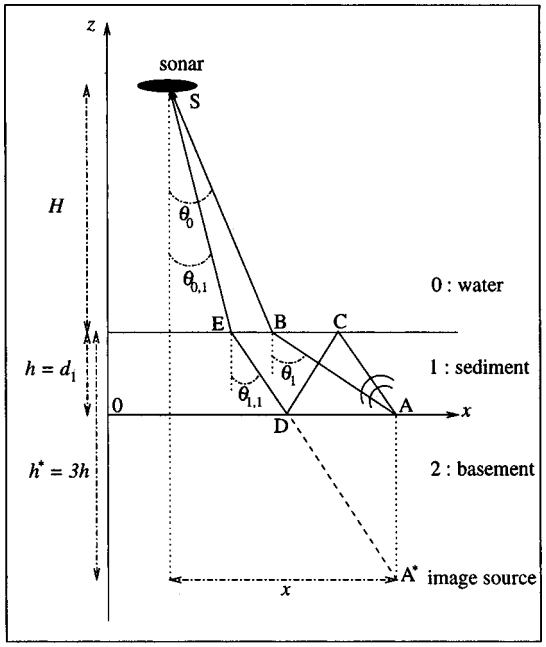

FIG. 7. Backscattered spherical wave: direct and first multiple path.

$$A_1 = T_a \frac{Z_2 + Z_1}{2Z_1} = \frac{T_a}{T_{1,2}}. \tag{11}$$

The incident acoustical intensity on the sediment ($z = h$) is

$$I_{i0} = \frac{\cos\theta_0}{2\rho_0 c_0}. \tag{12}$$

On the basement, the incident intensity is

$$I_{i1} = \frac{|A_1|^2 \Re(k_{z_1})}{2\omega\rho_1}, \tag{13}$$

with $\Re(k)$ denoting the real part of the complex number k.

2. Backscattered wave

The incident acoustical wave is scattered in all directions by the basement roughness; the angular dependence is given by a scattering function.[27] The energy scattered upwards through the sediment layer can therefore follow various paths back to the receiver, with different angles corresponding to image-sources due to successive reflections inside the layer; the mth-order image source is at depth $z_m = -2mh$. Figure 7 depicts the direct path (ABS) from a scatterer at point A to the sonar and, for instance, the first multiple path (ACDES) from the first-order image source A* at depth $z = -2h$.

The field emitted from A and transmitted to S may therefore be written as the summation of these image-source contributions:

$$p_s(\theta_0) = \sum_{m=0}^{\infty} \frac{T_{1,0}(\theta_{1,m}) R_{1,0}^m(\theta_{1,m}) R_{1,2}^m(\theta_{1,m})}{\mathcal{R}_m} e^{i[k_0 r_{0,m} + k_1 r_{1,m}]}. \tag{14}$$

For the mth image source, $r_{0,m}$ and $r_{1,m}$ are the path lengths in media 0 and 1, $\theta_{1,m}$ is the incident angle inside medium 1, and $1/\mathcal{R}_m$ is the spherical loss from the image source to the receiver. The difference in phase terms φ_m for source (m) in Eq. (14) and φ_0 for the direct path ABS is obtained by

$$\begin{aligned}\varphi_m - \varphi_0 &= k_0(r_{0,m} - r_0) + k_1(r_{1,m} - r_1) \\ &= k_0 H\left(\frac{1}{\cos\theta_{0,m}} - \frac{1}{\cos\theta_0}\right) + k_1 h\left(\frac{2m+1}{\cos\theta_{1,m}} - \frac{1}{\cos\theta_1}\right),\end{aligned} \tag{15}$$

where θ_0 and θ_1 are angles in media 0 and 1 for the direct path.

Since $h \ll H$ (in a typical deep-water echosounding configuration, h is a few meters whereas H is 1 to 5 km), angle $\theta_{0,m}$ may be considered as a small perturbation of θ_0 according to variations of $2mh$. Developing Eq. (15) to the first order gives (see details in the Appendix):

$$\varphi_m - \varphi_0 = 2mk_1 h \cos\theta_{1,m}. \tag{16}$$

The condition $h \ll H$ allows the spherical loss to be approximated as $1/\mathcal{R}_0 \approx 1/\mathcal{R}_1 \approx 1/\mathcal{R}_2 \approx \cdots$, meaning that the extra range and the refraction effect raised by the layer are negligible in the geometrical divergence loss. Also, the reflection and transmission coefficients may be approximated as $T_{1,0}(\theta_1) \approx T_{1,0}(\theta_{1,1}) \approx T_{1,0}(\theta_{1,2}) \approx \cdots$ and $R_{1,0}(\theta_1) \approx R_{1,0}(\theta_{1,1}) \approx R_{1,0}(\theta_{1,2}) \approx \cdots$ because of the very slight variation of the incident angle. This leads to the following expression for Eq. (14):

$$p_s(\theta_0) = \frac{T_{1,0}(\theta_1)}{\mathcal{R}_0} e^{i\varphi_0} \sum_{m=0}^{\infty} R_{1,0}^m(\theta_1) R_{1,2}^m(\theta_1) e^{2ik_1 hm\cos\theta_1}, \tag{17}$$

which features the classical expression[20] for a transmission coefficient in a layered medium. Hence, the backscattered wave will be considered as one plane wave emitted upwards in direction θ_1 (Fig. 8).

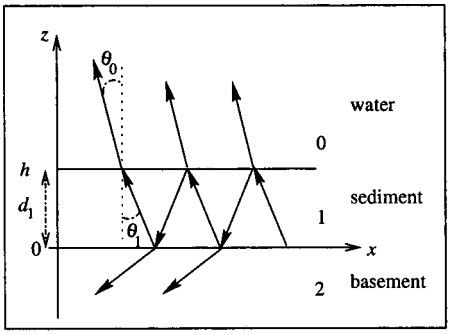

FIG. 8. Geometry for the backscattered wave.

The water-transmitted field is now determined from

$$\begin{aligned} p_0 &= De^{ik_{z_0}(z-h)}, \\ p_1 &= Fe^{ik_{z_1}z} + Ce^{-ik_{z_1}z}. \end{aligned} \tag{18}$$

For computational convenience, it is now supposed that the system depicted in Fig. 8 is generated by a virtual plane wave coming from the basement with amplitude L. Thus, $F = T_{2,1}L$ and $D = T_r L$, where T_r is the transmission coefficient from basement to water ($T_{2,0}$) that can be obtained with

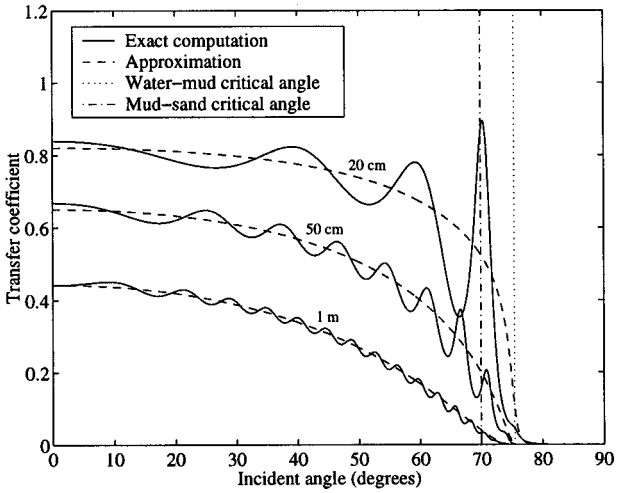

FIG. 9. Transfer coefficients computed from sand layer to water, for different mud thicknesses according to exact formulation [Eq. (24)] (solid curves) or to approximate expression [Eq. (25)] (dashed curves).

Eq. (10) by inverting indices 0 and 2. The following relation between D and F is obtained:

$$D = F\frac{T_r}{T_{2,1}}. \tag{19}$$

Inside the sediment layer, the basement-backscattered field is linked with the incident field by the relation

$$I_d = \tilde{\sigma}_2(\theta_1) I_{i1}, \tag{20}$$

with the intensity $I_d = |F|^2 \Re(k_{z_1})/2\omega\rho_1$. Using Eq. (13), one obtains

$$|F|^2 = |A_1|^2 \tilde{\sigma}_2(\theta_1). \tag{21}$$

The outgoing intensity is written

$$I_s = \frac{|D|^2 \cos\theta_0}{2\rho_0 c_0} = |D|^2 I_{i0}. \tag{22}$$

3. Synthesis

Using relations (21), (22), and (19), one can write for the intensity backscattered and transmitted back to the water

$$I_s = \tilde{\sigma}_2(\theta_1)|A|^2 \left|\frac{T_r}{T_{2,1}}\right|^2 I_i. \tag{23}$$

Referring to Eqs. (1) and (11), the transfer coefficient for the basement underlying a single-sediment layer is finally

$$C_{p2} = \left|\frac{T_a}{T_{1,2}}\right|^2 \left|\frac{T_r}{T_{2,1}}\right|^2. \tag{24}$$

If one neglects the multiple reflected paths inside the sediment stack, this transfer coefficient becomes

$$\check{C}_{p2} = |T_{1,0}|^2 |T_{0,1}|^2 e^{-4h\mathcal{I}(k_1)/\cos\theta_1}. \tag{25}$$

Figure 9 presents the computation results of Eqs. (24) and (25) for a medium-sand layer covered with various thicknesses of mud, for parameters given in Table II.

The transfer coefficients are maximum at steep incidences and decrease until the cutoff imposed by the critical angles of the various interfaces. These coefficients tend to zero beyond the highest critical angle. Oscillations associated with the resonant character of sound propagation inside layers are superimposed over this global trend. The density of these oscillations depends on the number of resonant angles at a given frequency, whereas their levels depend on the relative levels of interfering multipaths and hence upon attenuation across the dissipative layers. These oscillations therefore get closer and smoother when the layer thickness increases. In the case shown in Fig. 9, the effect of multipath interference is clearly negligible for the 1-m thickness, and the simple expression (25) is then a good approximation. On the other hand, for thinner mud layers, Eq. (25) is less acceptable, especially close to the critical angle cutoff where the oscillation effect becomes dominant. These oscillatory interference effects are obviously encountered in the resulting transferred backscattering strengths. Experimental evidence of such oscillations may be found in the literature (see, e.g., Ref. 13).

B. General case

In the case of a multilayered seafloor as sketched in Fig. 1, the transfer coefficients are obtained by generalizing the single-layer case. Thus, for layer l the transfer coefficient can be written as

$$C_{pl} = |A_{l-1}|^2 \left|\frac{T_{l,0}}{T_{l,l-1}}\right|^2, \tag{26}$$

where A_{l-1} is the incident amplitude on layer l, obtained from the following recursive relations:

$$\begin{aligned} A_{l-1} &= \frac{A_l e^{-i\xi_l}}{T_{l-1,l}} + B_l e^{i\xi_l}\frac{Z_l - Z_{l-1}}{2Z_l}, \\ B_l &= A_{l-1}\frac{Z_{l-1} - Z_l}{2Z_{l-1}} + B_{l-1}\frac{e^{i\xi_{l-1}}}{T_{l,l-1}}, \end{aligned} \tag{27}$$

with

$$A_n = \frac{T_a}{T_{n,n+1}}, \quad B_n = T_a\frac{Z_{n+1} - Z_n}{2Z_{n+1}}.$$

Now T_a is the transmission coefficient from water to basement ($T_{0,n+1}$) for the whole sediment stack:[20]

$$T_a = \prod_{j=n+1}^{1} \frac{Z_{in}^{(j)} + Z_j}{Z_{in}^{(j)} + Z_{j-1}} e^{i\xi_j}, \tag{28}$$

with

$$Z_{in}^{(j)} = Z_j \frac{Z_{in}^{(j+1)} - iZ_j \tan\xi_j}{Z_j - iZ_{in}^{(j+1)} \tan\xi_j}; \tag{29}$$

and $Z_{in}^{(n+1)} = Z_{n+1}$. $Z_{in}^{(2)}$ is the input impedance of the system.

Figure 10 presents the sand-to-water and basement-to-water transfer coefficients. The former is limited by the water–mud critical angle, and the angle range of the latter is narrower because of the steeper angle associated with the water–sand contrast. The differences in global levels are easily accounted for by the respective sediment thicknesses considered.

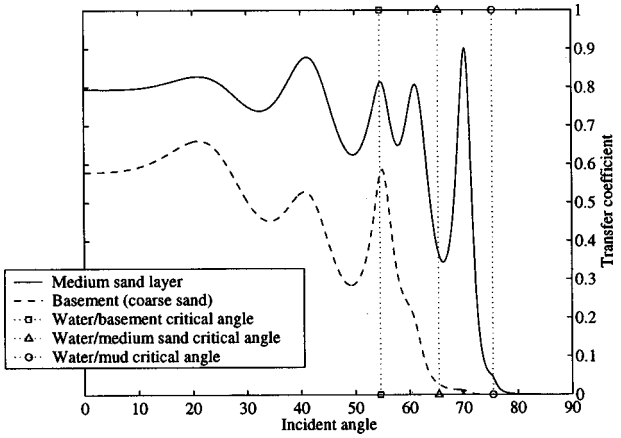

FIG. 10. Transfer coefficients for Table II configuration, computed from sand layer to water (solid curve) and from basement to water (dashed curve).

All the above was developed for the case of depth-invariant characteristics inside each layer, for which the propagating waves are plane, thus making the reflection and transmission coefficients straightforward to compute. Note that the same method of transfer coefficient computation may be readily adapted to the case of layers featuring depth-varying sound speed, density, and attenuation. This was evoked in Refs. 18 and 19 and will be presented with more details in a future paper.

V. NUMERICAL EXAMPLES

A. Practical application

The total EIBS of a geoacoustic configuration may be readily computed from the various elements presented in the previous sections. Several steps are necessary. After the acoustical parameters of each layer are defined (see an example in Table II), the individual BCS (related to their nature and to the geological context) are computed at the various interfaces by using a backscattering model such as Eqs. (3)–(5). Then these individual BCSs are modified according to the acoustical parameters of the sediment stack in order to define the local BCS, as described in Sec. III A and using Eqs. (6) and (7). The anamorphosis effect due to refraction is accounted for by applying Eq. (8). Next, the transfer coefficients from the various layers to the upper interface $C_{pl}(\theta_0)$ are computed using Eqs. (26)–(29). Finally, the total equivalent BCS is obtained by summing all the layer contributions using Eq. (1).

B. Two-layer model

The first example is the geoacoustic configuration presented in Table II. The results are in Figs. 11 and 12.

The total backscattering strength follows the modified basement backscattering strength on a wide angular range. The strong oscillation at 55 degrees is due to the transfer coefficient C_{p4} of the basement near the water/basement critical angle (see Fig. 10). Beyond this critical angle, the total backscattering strength decreases rapidly and finally follows the mud layer backscattering strength.

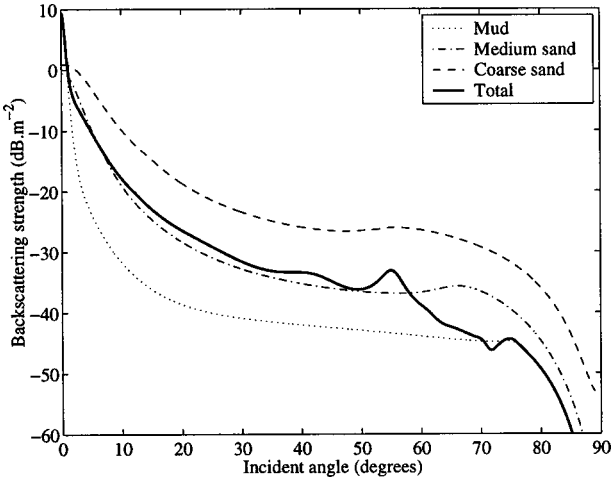

FIG. 11. Individual backscattering strength (dotted curves) with reference to water, and EIBS (solid curve) for the geoacoustic configuration presented in Table II.

C. Comparison with Ivakin's model

It is interesting to compare, both formally and in their results, our EIBS model and the ''unified approach'' proposed by Ivakin.[9] While his is theoretically far more general than ours, a ground of comparison may be found in the limit case presented by Ivakin as the first-order approximation of his model. In this case corresponding to single-scattering, the two approaches provide nearly identical expressions [see his Eqs. (64) and (65) in Ref. 9].

The two numerical models were compared in various test cases.[28] We present here a computation of roughness backscattering by a two-layer seafloor (clay and silt layers over a sandy basement) with parameters provided in Table III.

The computation of this seafloor backscattering strength through Ivakin's first-order model is presented in Fig. 13, and computation with the EIBS model is presented in Fig. 14.

The two models are in very good agreement, especially for the location and the amplitudes of the oscillations. There

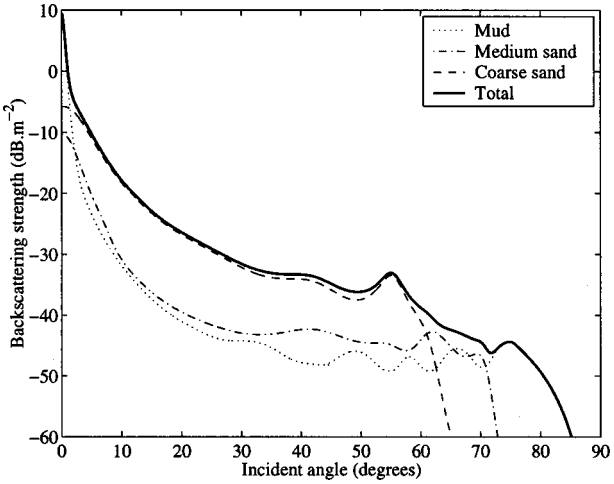

FIG. 12. Local backscattering strength (dotted curves) weighted by their transfer coefficient and EIBS (solid curve) for the geoacoustic configuration presented in Table II.

TABLE III. Geoacoustic parameters of the second numerical example (comparison with Ivakin's model).

Layers:	Water	Clay	Silt	Sand
c (m·s^{-1})	1500	1580	1650	1750
ρ	1	1.5	1.8	2
α (dB/λ)	0	0.3	0.5	0.6
γ	···	3.25	3.25	3.25
β_J (cm^4)	···	4×10^{-4}	10^{-3}	2×10^{-3}
d (cm)	···	50	20	···

are small differences in the prediction of the backscattering strength amplitudes from the two buried interfaces, but the two computation results are very close.

VI. DISCUSSION

The EIBS model proposed in this article offers a wide potential for the interpretation of experimental backscattered data, in particular those obtained with low-frequency multibeam echosounders on soft sedimentary seafloors for which penetration phenomena are notable. Actually its results have already been compared to experimental data obtained with a 13-kHz multibeam echosounder in two configurations,[17,19] revealing effects associated with sediment layering.

However, one has to be careful in using such a model for experimental data validation, since its input parameters are numerous and its output is very sensitive to small variations of the configuration. Its modular structure makes it possible to account for complex sedimentary structures. On the other hand, increasing the complexity of the description increases the number of input parameters needed, which may make it difficult to provide the model with numerical values, and may make its results risky to interpret. This raises several issues. First, establishing a geoacoustic model for a given real configuration unavoidably implies relying upon available geological data; however, these are seldom usable directly for the acoustical modeling purpose. For instance, data obtained from geological analyses and geotechnical measurements of sample cores are often very detailed, and they must be simplified to make the acoustical model practicable. Also, the parameters coming from classical geological investigations have to be transformed into usable acoustical parameters, using intermediate models.[23] Moreover some of the parameters needed in an acoustical model of layered sediments are not accessible to measurement; for example, it is practically impossible today to measure the *in situ* roughness of buried layers. Finally, because of the high number of input parameters and the limited information usually obtainable from the echosounder experimental data, ambiguities may affect the interpretation: several different layered structures may provide more or less the same response measured as an average intensity level.[19]

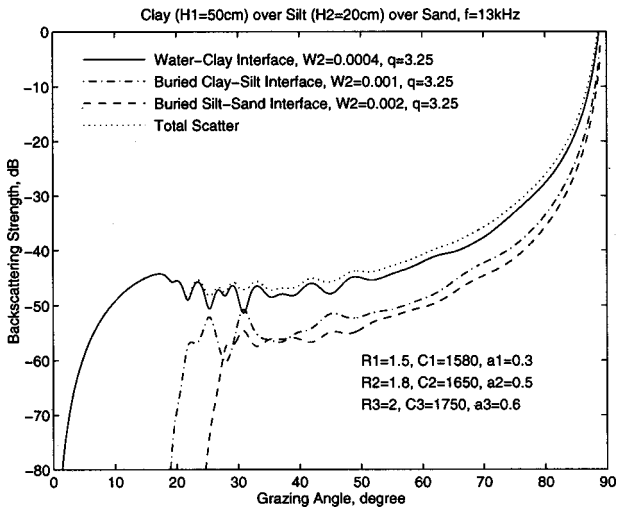

FIG. 13. Local and total backscattering strength for the seafloor model presented in Table III computed with the first order of Ivakin's model (Ref. 9). (This figure is taken from Fig. 1a in Ref. 28 by Ivakin.)

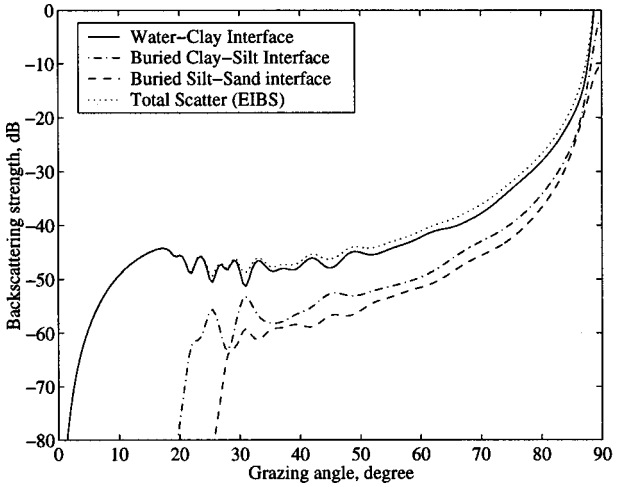

FIG. 14. Local and total backscattering strength for the seafloor model presented in Table III computed with the EIBS model.

The theoretical limitations of the approach should also be kept in mind. On one hand its overall validity depends on the model used for local phenomena, and the transferred backscattering strength cannot be expected to be more accurate than the initial local one. We did not propose anything new in this respect; we just present the local modifications to be applied to a given classical model. Moreover, the EIBS model itself is defined under the limitation of small perturbations and single scattering, and hence its results should be taken cautiously in the regimes of high-level scattering such as the near-specular incidences.

To summarize, the EIBS model presented is basically a formalization of a physically intuitive approach, that makes it possible to describe the backscattering strength associated with buried layers, considered as local phenomena filtered by the overlying sediment structure. Such a physical concept has already been presented and exploited (see, e.g., Refs. 2, 13, and 15), but we believe that the EIBS approach is more general and easier to use because of its detailed description of the local backscattering phenomena modifications, its easy extension to any number of layers, and its potential for processing sedimentary characteristics that continuously vary with depth. On the other hand, it agrees in a satisfactory way with developments obtained from a general theoretical approach of the problem.[9] The EIBS model is then proposed as a practical compromise between a pragmatic approach of the

physical problem and a rigorous treatment of the backscattering phenomena.

ACKNOWLEDGMENTS

The authors wish to thank Anatoliy Ivakin (Andreev Acoustics Institute, Moscow) for making his own results available for publication here, and for many fruitful discussions. We also thank Bruno Lombard and Joel Piraux (LMA–CNRS) for their comments and suggestions about this paper.

APPENDIX: PHASE DIFFERENCE FOR BACKSCATTERED WAVE

Considering an image source A* at depth h^* (cf. Fig. 7 but the following is valid whatever the image-source order), the phase difference between paths AS and A*S is developed as

$$\Delta\varphi = k_0 H\left(\frac{1}{\cos\theta_{0,1}} - \frac{1}{\cos\theta_0}\right) + k_1\left(\frac{h^*}{\cos\theta_{1,1}} - \frac{h}{\cos\theta_1}\right)$$
$$= k_0 H\left(\frac{1}{\cos\theta_{0,1}} - \frac{1}{\cos\theta_0}\right) + k_1 h^*\left(\frac{1}{\cos\theta_{1,1}} - \frac{1}{\cos\theta_1}\right)$$
$$+ k_1(h^*-h)\frac{1}{\cos\theta_1}. \quad \text{(A1)}$$

Taking into account that $H \gg h$, variations in h will slightly modify θ_0 and θ_1. Therefore, the difference $1/\cos\theta^* - 1/\cos\theta$ may be written as the differential $(\partial/\partial\theta) \times (1/\cos\theta)$. Equation (A1) becomes

$$\Delta\varphi = k_0 H\frac{\sin\theta_0}{\cos^2\theta_0}\partial\theta_0 + k_1 h^*\frac{\sin\theta_1}{\cos^2\theta_1}\partial\theta_1$$
$$+ k_1(h^*-h)\frac{1}{\cos\theta_1}. \quad \text{(A2)}$$

Neglecting the second-order terms leads to the following expression for the phase difference:

$$\Delta\varphi = k_0 H\frac{\sin\theta_0}{\cos^2\theta_0}\partial\theta_0 + k_1(h^*-h)\frac{1}{\cos\theta_1}. \quad \text{(A3)}$$

The relation between variations in h and θ is obtained from the expression of horizontal range x:

$$x = H\tan\theta_0 + h\tan\theta_1, \quad \text{(A4)}$$

the differential of which gives, neglecting the second order-terms,

$$\partial\theta_0 = -\tan\theta_1\cos^2\theta_0\frac{\partial h}{H}. \quad \text{(A5)}$$

Using Eq. (A5) in Eq. (A3) leads to

$$\Delta\varphi = -k_0\sin\theta_0\tan\theta_1\partial h + k_1\frac{h^*-h}{\cos\theta 1}. \quad \text{(A6)}$$

Rewriting this expression with the use of the Snell–Descartes relation [Eq. (8)] gives

$$\Delta\varphi = -k_1\frac{\sin^2\theta_1}{\cos\theta_1}\partial h + k_1\frac{h^*-h}{\cos\theta_1}$$
$$= k_1\cos\theta_1(h^*-h) = k_{z_1}(h^*-h). \quad \text{(A7)}$$

Hence, the phase difference between an image-source geometrical path and the direct path is simply approximated by the corresponding plane wave phase difference. Since for image (m), $h^* = (2m+1)h$, it becomes

$$\Delta\varphi_m = 2k_{z_1}mh. \quad \text{(A8)}$$

[1] D. R. Jackson, D. P. Winnebrenner, and A. Ishimaru, ''Application of the composite roughness model to high frequency bottom backscattering,'' J. Acoust. Soc. Am. **79**, 1410–1422 (1986).
[2] J. V. Gardner *et al.*, ''Ground-truthing 6.5 kHz side scan sonographs: what are we really imaging?'' J. Geophys. Res. **96**, 5955–5974 (1991).
[3] M. Stern, A. Bedford, and H. R. Millwater, ''Wave reflection from a sediment layer with depth-dependent properties,'' J. Acoust. Soc. Am. **77**, 1781–1788 (1985).
[4] M. A. Ainslie, ''Reflection and transmission coefficients for a layered fluid sediment overlying a uniform solid substrate,'' J. Acoust. Soc. Am. **99**, 893–902 (1996).
[5] R. Carbo, ''Wave reflection from a transitional layer between the seawater and the bottom,'' J. Acoust. Soc. Am. **101**, 227–232 (1997).
[6] A. N. Ivakin, ''Sound scattering by random inhomogeneities of stratified ocean sediments,'' Sov. Phys. Acoust. **32**, 492–496 (1987).
[7] A. N. Ivakin, ''Sound scattering by rough interfaces and volume inhomogeneties of a layered seabed,'' J. Acoust. Soc. Am. **95**, 2884–2885(A) (1994).
[8] A. N. Ivakin, ''A unified approach to volume and roughness scattering,'' J. Acoust. Soc. Am. **98**, 2988(A) (1994).
[9] A. N. Ivakin, ''A unified approach to volume and roughness scattering,'' J. Acoust. Soc. Am. **103**, 827–837 (1998).
[10] D. Tang, ''A note on scattering by a stack of rough interfaces,'' J. Acoust. Soc. Am. **99**, 1414–1418 (1996).
[11] S. McDaniel, ''Effect of surficial sediment layering on high-frequency seafloor reverberation,'' J. Acoust. Soc. Am. **91**, 1353–1356 (1992).
[12] H. H. Essen, ''Scattering from a rough sedimental seafloor containing shear and layering,'' J. Acoust. Soc. Am. **95**, 1299–1310 (1994).
[13] Q. J. Huggett *et al.*, ''Interference fringes on Gloria side-scan sonar images from the Bering Sea and their implications,'' Mar. Geophys. Res. **14**, 47–63 (1992).
[14] N. C. Mitchell, ''A model for attenuation of backscatter due to sediment accumulations and its application to determine sediment thickness with GLORIA sidescan sonar,'' J. Geophys. Res. B **98**, 22477–22493 (1993).
[15] A. P. Lyons, A. L. Anderson, and F. S. Dwan, ''Acoustic scattering from the seafloor: Modeling and data comparison,'' J. Acoust. Soc. Am. **95**, 2441–2451 (1994).
[16] L. Guillon and X. Lurton, ''Rétrodiffusion de signaux de sondeurs grands fonds: influence du volume sédimentaire,'' in *Actes du 4ème Congrès Français d'Acoustique*, edited by G. Canévet, G. Mangiante, and S. Meunier (Teknea, Toulouse, France, 1997), pp. 1121–1124 (in French).
[17] L. Guillon and X. Lurton, ''Backscattering by layered media: Modeling and comparison with data,'' J. Acoust. Soc. Am. **103**, 2900(A) (1998).
[18] L. Guillon, ''Contribution à l'interprétation géoacoustique de la rétrodiffusion des fonds marins,'' Ph.D. thesis (text in French), Université du Maine, Le Mans, France, 1999.
[19] X. Lurton and L. Guillon, ''Seafloor characterization using a low-frequency multi-beam echo-sounder: Ambiguities in backscattering strength interpretation,'' J. Acoust. Soc. Am. **105**, 1206(A) (1999).
[20] L. M. Brekhovskikh and O. A. Godin, *Acoustics of Layered Media. I: Plane and Quasi-Plane Waves* (Springer-Verlag, Berlin, 1990).
[21] P. C. Hines, ''Theoretical model of acoustic backscatter from a smooth seabed,'' J. Acoust. Soc. Am. **88**, 324–334 (1990).
[22] T. Yamamoto, ''Acoustic scattering in the ocean from velocity and den-

sity fluctuations in the sediments,'' J. Acoust. Soc. Am. **99**, 866–879 (1996).
[23] E. L. Hamilton, ''Geoacoustic modeling of the sea floor,'' J. Acoust. Soc. Am. **68**, 1313–1340 (1980).
[24] P. D. Mourad and D. R. Jackson, ''High-frequency sonar equation models for bottom backscatter and forward loss,'' in *Proceedings of Oceans'89* (IEEE, New York, 1989), pp. 1168–1175.
[25] D. R. Jackson and K. B. Briggs, ''High-frequency bottom backscattering: Roughness versus sediment volume scattering,'' J. Acoust. Soc. Am. **92**, 962–977 (1992).
[26] J. E. Moe and D. R. Jackson, ''First-order perturbation solution for rough surface scattering cross section including the effects of gradients,'' J. Acoust. Soc. Am. **96**, 1748–1754 (1994).
[27] L. M. Brekhovskikh and Yu. P. Lysanov, *Fundamentals of Ocean Acoustics*, 2nd ed. (Springer-Verlag, Berlin, 1991), pp. 210–212.
[28] A. Ivakin, ''Modelling of Medium Frequency Acoustic Scattering from Marine Sediments with Buried Interfaces,'' Contract Ifremer No. 98 2311227DITI/SM/ASM, Report of the Andreyev Acoustics Institute (1999).

Bubble clouds and their transport within the surf zone as measured with a distributed array of upward-looking sonars

Peter H. Dahl[a)]
Applied Physics Laboratory, College of Ocean and Fishery Sciences, 1013 N.E. 40th Street, Seattle, Washington 98105-6698

(Received 1 June 2000; revised 25 September 2000; accepted 10 October 2000)

A collaborative, multi-institute experiment called the Scripps Pier Experiment was conducted in the vicinity of the Scripps pier in La Jolla, California, in March 1997 to study the fate of bubbles in the surf zone and the effects of these bubbles on acoustic propagation. This paper discusses data gathered by the Applied Physics Laboratory, University of Washington, using a set of four upward-looking sonars (frequency 240 kHz), which simultaneously measured vertical profiles of acoustic volume scattering from bubbles at four locations. The transport of bubbles via rip currents emerged as an important, though episodic and localized, feature of the acoustic environment in the surf zone. Images of volumetric backscattering strength vs time and depth reveal the episodic events (of increased scattering level) lasting between 5 and 10 min caused by the passage of bubble clouds over the sonar. Time lags for the onset of increased scattering at the four locations are consistent with a seaward velocity of the bubble clouds of order 10 cm/s, and the length scales of these bubble clouds in the seaward direction are inferred to be in the range 50–100 m. The influence of the incoming surface wave field is also discussed.
[DOI: 10.1121/1.1331108]

PACS numbers: 43.30.Ft, 43.30.Pc [DLB]

I. INTRODUCTION

The surf zone is an extremely challenging environment for the operation of sonars. Although its shallowness means that sound transmission through the surf zone must invariably include interaction with its surface and bottom boundaries, the defining acoustic characteristic of the surf zone is the high concentration of bubbles. The process of bubble generation in the surf zone has been studied by Deane,[1,2] whose focus has been on the sound produced by bubbles associated with individual breaking waves. Deane showed through the analysis of photographic images taken within the active wave-breaking region of the surf zone (or breaker zone) that air entrainment by shallow-water breaking wavecrests forms bubbles whose radii a span the range $O(10)$ μm to $O(10)$ mm, and that these bubbles can be organized into clouds which commonly extend a meter into the water column within the breaker zone (or about half the total depth).

Immediately seaward of the breaker zone within which bubble generation occurs, rip currents, which are narrow strong return flows directed seaward,[3,4] can play a important role in determining the fate of bubbles in the surf zone. The Scripps Pier Experiment was conducted during the first 2 weeks of March 1997, off the Scripps pier in La Jolla, California. Its primary objective was to measure properties of bubbles within the outer region of the surf zone, such as bubble concentration and size distribution, the spatial and temporal scales of organized bubble clouds, and the transport and diffusion of bubbles as mediated by rip currents. To accomplish this objective, instruments for measuring bubbles, ambient noise, and surface waves were assembled by the Naval Research Laboratory at the Stennis Space Center (NRL-SSC), the Institute of Ocean Sciences (IOS), the Scripps Institute of Oceanography (SIO), and the Applied Physics Laboratory, University of Washington (APL-UW). These instruments were deployed 10 m off the north side of the Scripps pier, nominally 50 to 100 m seaward of the breaker zone, depending on tidal stage.

This paper discusses the measurements made by APL-UW during the Scripps Pier Experiment, using a distributed array of four upward-looking sonars, each called a SALMON unit, for Shallow water Acoustic Lightweight MONitor. When combined into an array, these units simultaneously measured vertical profiles of acoustic volume scattering from bubbles at their respective locations within the measurement field. The experiment and measurement system are described further in Sec. II. In Sec. III we briefly discuss the topic of acoustic scattering from bubbles to make clear the nature of our measurements, the corrections applied in the initial data processing, and our notation. Also discussed in this section is a new way of quantifying the range of bubble radii that contributes to backscattering as function of acoustic frequency. Observations are presented in Sec. IV. These are in the form of images of volumetric backscattering strength versus time and depth, which reveal the effects of seaward advection of large-scale bubble clouds by rip currents. Additionally, time averages of the data are presented, which yield estimates of the bubble concentration and the characteristic depth to which the bubbles have been dispersed during the course of their advection. A summary is given in Sec. V.

a)Electronic mail: dahl@apl.washington.edu

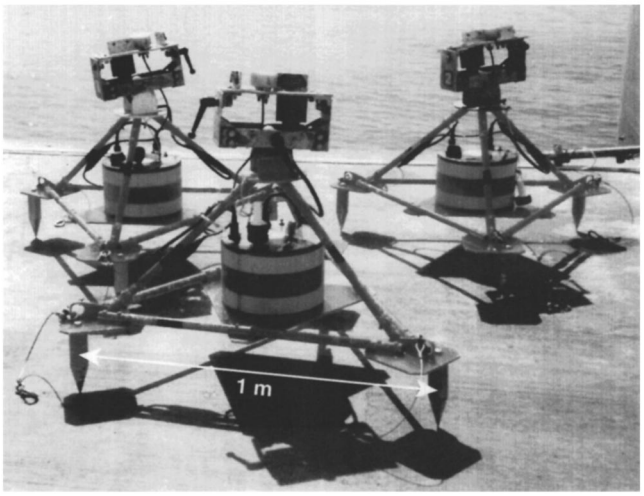

FIG. 1. Photograph of three of the four SALMON units made just prior to their deployment in surf zone waters off the Scripps pier.

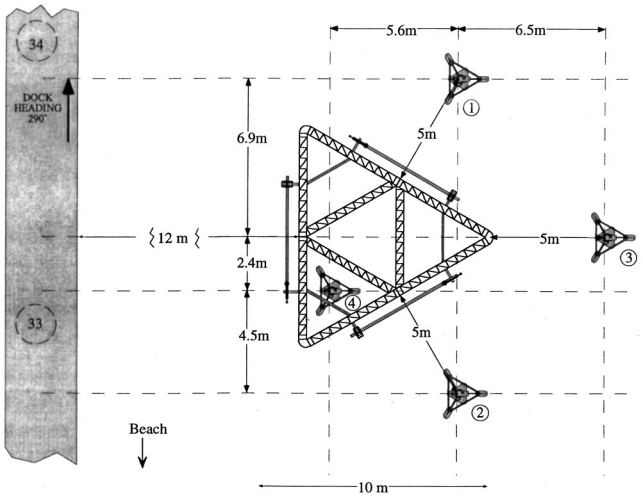

FIG. 2. Plan view and grid of the experimental area showing the delta frame and locations of the four SALMON units, labeled 1–4. Bubbles entrained in the seaward flow of rip currents were first seen on unit 2, then 4, 3, and 1.

II. EXPERIMENTAL MEASUREMENT SYSTEM

Figure 1 shows three of the four SALMON units prior to their 10-day deployment in the surf zone off the Scripps pier. Each unit consists of a stout frame housing a transducer and instrument case containing transmitting and receiving electronics, a pressure wave gauge, and a tilt meter. The units were controlled from a base on the Scripps Pier via underwater cables, and important system diagnostics, e.g., tilt, could be ascertained remotely. The units were hand carried and lowered into the water for final positioning by divers from NRL-SSC and operated on demand throughout the 10-day deployment in the punishing underwater environment of the surf zone.

The four transducers transmitted simultaneously (with a source level of 179 dB *re* μPa at 1 m) at 0.5-s intervals a rectangular pulse of width of 0.1 ms and center frequency 240 kHz, giving a vertical resolution of approximately 8 cm. The one-way half-power beamwidth of all four transducers was 6°. The face of each transducer was placed 0.67 m above the seabed, and data recording started after a time delay equivalent to a range of 0.7 m to ensure that measurements were made in the transducer's far field ($\sim$0.5 m). Data from the pressure gauges were recorded simultaneously along with the acoustic data, but at 0.25-s intervals. These pressure measurements were converted to sea surface elevation above each sensor unit, assuming the measured pressure field was hydrostatic. In addition to wave height and wave spectral information, the pressure data were used to establish the location of the air/sea interface during periods of severe acoustic attenuation from bubbles.

The NRL-SSC delta frame,[5] an equilateral triangle with sides of approximately 10 m, established the primary locus of measurement activity. The delta frame was placed 10 m north of the Scripps pier between pier pilings 33 and 34. Figure 2 shows the location of the delta frame with respect to the Scripps pier and the four SALMON units. Two of the four units (units 1 and 2) were located along a line parallel to the anticipated seaward flow of bubbles, and two units (units 3 and 4) were offset on either side of this line. This layout was intended to maximize the ability to measure the larger spatial scales of a bubble field as it advected over the delta frame.

More information concerning the delta frame is given by Caruthers *et al.*,[5] who discuss the results of the multifrequency sound propagation and attenuation measurements made by NRL-SSC during the Scripps Pier experiment. Also, Vagle *et al.*,[6] Farmer *et al.*,[7] and Terrill and Melville[8] discuss measurements made by IOS and SIO which included horizontal-looking sonars directed shoreward from the Scripps pier and instruments for measuring the bubble size distribution in the breaker zone. These works, along with this paper and one by Rouseff *et al.*,[9] constitute a developing set of archival works covering the 1997 Scripps Pier Experiment. The observations of bubbles presented in this paper complement those presented in Refs. 5–9 insofar as our measurements reveal information on the vertical distribution of bubbles, as measured at four locations, and the seaward flow speeds of organized bubble clouds, as inferred from the time delay between the arrival of the increased scattering associated with these bubble clouds at each sensor location.

III. ACOUSTIC SCATTERING FROM BUBBLES

Our measurements of bubbles are in the form of the backscattering cross section per unit solid angle, or $s_v\,[\mathrm{m}^{-1}]$, which is defined by the integral

$$s_v = \int \sigma_{bs}(a) N(a)\, da, \tag{1}$$

where $\sigma_{bs}(a)$ is the backscattering cross section of a single bubble, and $N(a)$ is the bubble size distribution function giving the number of bubbles per cubic meter per unit radius for radii between a and $a+da$. For $\sigma_{bs}(a)$ we use (e.g., cf. Ref. 10)

$$\sigma_{bs}(a) = \frac{a^2}{[(f_R/f)^2 - 1]^2 + \delta^2} \tag{2}$$

which is valid for $ka \ll 1$, where k is the acoustic wave number; δ is the total damping coefficient, f is the frequency, and f_R is the resonant frequency. The resonant frequency is related to the bubble radius and depth z by $f_R = 3.25\sqrt{1+0.1z}/a$, where all units are in MKS. We report the decibel equivalent, $S_v = 10\log_{10} s_v$, in dB *re* m^{-1}. The sonar equation is used to compute initial estimates of s_v vs range from the sonar, which are then corrected for the effects of excess attenuation from bubbles. Knowledge of the bubble size distribution is required for this procedure, and thus we incorporate information about $N(a)$ derived from the multifrequency attenuation measurements made during the Scripps Pier experiment by Caruthers *et al.*[5] and Terrill and Melville.[8] Specifically, Caruthers *et al.* report estimates of $N(a)$ for bubbles with radii in the range 16 to 100 μm. Below is a good representation of all six $N(a)$ functions shown in their Figs. 10–15, expressed here as $n(a)$; $n(a)$ differs from $N(a)$ by a multiplicative constant scaling factor q, which can be set with either a known void fraction or s_v:

$$n(a) = 1, \quad 16\ \mu\mathrm{m} \leqslant a \leqslant 40\ \mu\mathrm{m}, \tag{3a}$$

$$n(a) = (a/40\ \mu\mathrm{m})^{-3.4}, \quad 40\ \mu\mathrm{m} < a \leqslant 100\ \mu\mathrm{m}. \tag{3b}$$

For small bubbles, we postulate that $n(a)$ behaves as

$$n(a) = (a/16\,\mu\mathrm{m})^{3}, \quad a < 16\ \mu\mathrm{m}. \tag{3c}$$

For large bubbles, we take the a^{-5} power law behavior reported by Terrill and Melville, giving

$$n(a) = (a/100\,\mu\mathrm{m})^{-5}, \quad a > 100\ \mu\mathrm{m}. \tag{3d}$$

The range of bubble radii a is such that $1\,\mu\mathrm{m} \leqslant a \leqslant 200\ \mu$m. It is not surprising that the $N(a)$ associated with bubbles near the delta frame measurement area is quite different from the one that Deane estimated from photographic evaluation of nascent bubbles in the active breaker zone, e.g., as in Fig. 7 of Ref. 1. By the time bubbles have advected from the breaker zone where they are generated to the delta frame, they have existed for $O(10)$ min.

Corrections for bubble-mediated excess attenuation commence at a range of 1 m from the sonar. The value of S_v at that point, called S_{v_0}, is used for correcting S_v in the next range bin, and so on up to the sea surface, which produces a distinctive reflection. A new scaling factor q is computed at each of the range bins, which are separated by $dR = 3$ cm. For example, at the starting range, where no correction is applied,

$$q_1 = \frac{10^{S_{v_0}/10}}{\int_{1\ \mu\mathrm{m}}^{200\ \mu\mathrm{m}} \sigma_{bs}(a) n(a)\, da}. \tag{4}$$

Next, the bubble-mediated attenuation α_1 (in dB/m) that is applied to the uncorrected S'_{v_1} in the next range bin is given by

$$\alpha_1 = 4.34 q_1 \int_{1\ \mu\mathrm{m}}^{200\ \mu\mathrm{m}} \sigma_e(a) n(a)\, da, \tag{5}$$

where $\sigma_e(a)$ is the extinction cross section per unit volume and equals $(4\pi\delta/ka)\sigma_{bs}$. We proceed to convert uncorrected values S'_{v_j} to corrected values S_{v_j} via

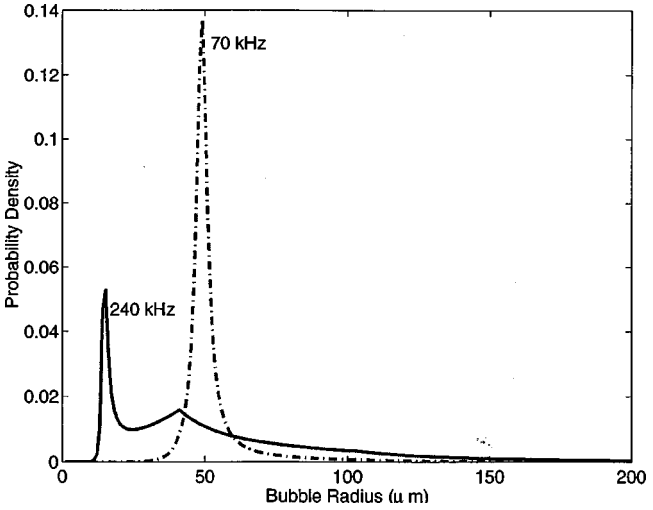

FIG. 3. Probability density function (PDF) for the variable a_s, defined as the radius of a bubble contributing to the backscatter for a set acoustic frequency. Two PDFs are shown, one for an acoustic frequency of 70 kHz and one for 240 kHz.

$$S_{v_j} = S'_{v_j} + 2dR \sum_{j=1}^{N} \alpha_j. \tag{6}$$

Note that there are a few instances where the bubble concentration is sufficiently high as to nearly extinguish the sound pulse and prevent backscatter from the sea surface. Under these circumstances, the correction procedure, which is essentially a first-order multiple scattering representation,[11] is no longer valid. The air/sea interface, however, can still be located using the pressure time series. Note that for strong, but otherwise measurable, backscatter, e.g., for $S_v = -25$ dB, α equals about 0.5 dB/m, which is comparable to direct measurements of attenuation made at 244 kHz by Caruthers *et al.*[5]

It is useful to evaluate how backscattering measurements made at 240 kHz respond to this bubble size distribution. For this we define the probability density function (PDF) $p(a_s)$ by recognizing that the positive quantities $\sigma_{bs}(a)$ and $n(a)$ can be combined into a PDF for the variable a_s. (On the basis of the Lebesgue decomposition theorem,[12] any nonnegative function that integrates to unity can be identified as a PDF for some variable.) The variable a_s is defined as the radius of a bubble contributing to the backscatter at a specified acoustic frequency, where

$$p(a_s) = \frac{\sigma_{bs}(a_s) n(a_s)}{\int_{1\ \mu\mathrm{m}}^{200\ \mu\mathrm{m}} \sigma_{bs}(a) n(a)\, da}, \tag{7}$$

and the sample space over which a_s is defined is the same as the range for a (1–200 μm). Figure 3 shows the PDF corresponding to the $n(a)$ described above and a frequency of 240 kHz, along with one based on a frequency of 70 kHz; note the dominant effect of scattering by resonant-sized bubbles at the lower frequency. We shall call the expected value $E(a_s)$ the *scattering centroid*, or sc, and the square root of the variance $E(a_s - sc)^2$ the *scattering spread*, or δsc. With the above representation of $n(a)$, then $sc = 55\,\mu$m and $\delta sc = 39\,\mu$m at 240 kHz, and $sc = 53\,\mu$m and $\delta sc = 15\,\mu$m at 70 kHz. A good measure of the central tendency of volumetric

backscattering from bubbles *vis-à-vis* bubble radius is to take a range $\pm \delta sc$ about sc. For example, at 240 kHz approximately 90% of the scattered intensity is due to bubbles with radii of 16 to 94 μm, while at 70 kHz this range narrows to 38 to 68 μm. Importantly, these sc and δsc values for 240 kHz are relatively insensitive to alternative representations of the behavior of $n(a)$ at the bubble radii of <16 μm that we have postulated.

Finally, S_v is mapped to void fraction, defined as the ratio of the volume of air to the volume of the sample region. The mapping assumes a sonar frequency of 240 kHz plus the $n(a)$ defined above for bubble radii between 1 and 200 μm, and is as follows:

$$\log_{10} \text{void fraction} = 0.1 S_v - 3.67. \tag{8}$$

Since $n(a)$ goes as a^{-5} for larger bubble radii, smaller bubbles are more important for determining void fraction (see Ref. 1 for further discussion on this point). This mapping produces a higher void fraction (by about a factor of 7) for a given S_v than the result given by Dahl and Jessup[13] for the same frequency, obtained in studies of ambient oceanic bubble populations. One expects this, however, since most studies of ambient oceanic bubble populations, e.g., those reported by Vagle and Farmer,[14] show $n(a)$ reaching a maximum in the vicinity of 20 μm.

IV. OBSERVATIONS

Acoustic transmissions from the SALMON units were coordinated with measurement periods of the other instruments located on or near the delta frame to prevent interference. A synchronized measurement run lasted typically 5000 s, or 83 min and 20 s. In this paper, as in Ref. 5, we discuss results from measurement run 7, which began at 1426 PST on 8 March. As noted in Ref. 5, rip currents were more prevalent during periods of low tide, which produced active surf breaking and swash in the region nominally 100–150 m shoreward of the delta frame measurement area. A spring tide was in effect on 8 March, with the start of run 7 coinciding with the low water point and the beginning of the incoming tide. The mean water depth at unit 2 (as determined from the pressure data after time averaging to remove wave effects) at the start of run 7 was 4 m, which increased to 4.25 m over the next 80 min.

Figure 4 shows a surface wave height frequency spectrum from run 7, as determined by the pressure data from unit 3. The rms wave height is about 0.3 m, and there is a broad peak in the vicinity of 0.1 Hz. Interestingly, there is also a significant peak near 0.06 Hz, which is possibly associated, through nonlinear interaction,[15] with the peak near 0.18 Hz. Given the mean water depth of 4 m, the peak at 0.1 Hz corresponds, via finite-depth linear theory, to a wavelength of 61 m. However, the time series of surface elevation show nonlinear effects such as an extended duration of the trough phase compared to that of the peak phase. Using the dispersion relation for finite-depth, nonlinear Stokes waves[16] and taking a typical wave amplitude to be 0.4 m puts the wavelength at 0.1 Hz closer to 63 m. (The influence of these nonlinear waves on the structure of bubble clouds is illustrated in Fig. 7.)

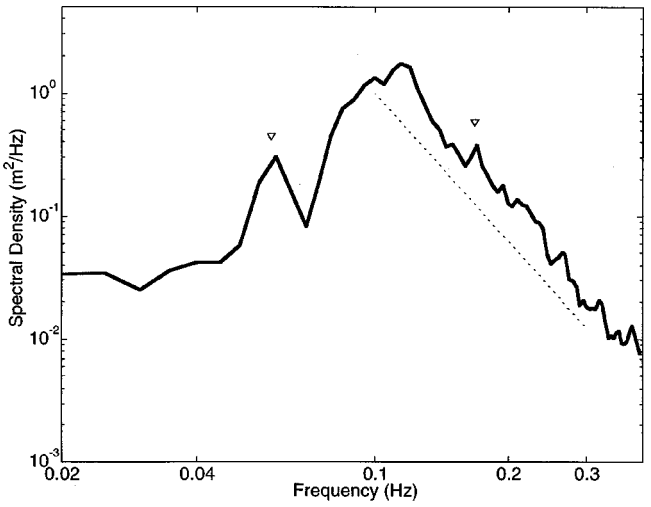

FIG. 4. Frequency spectrum corresponding to run 7, measured by the pressure sensor located at SALMON unit 3. For reference, the dotted line shows a slope of f^{-4}. A significant peak near 0.06 Hz and its third harmonic, 0.18 Hz, are identified by the markers.

Figure 5 shows an 80-min display of S_v (with the above corrections for bubble attenuation applied) versus depth and time (representing 96% of run 7). The plots in Fig. 5 are arranged such that their order, from top to bottom, represents units 2-4-3-1, or increasing distance in the seaward direction (see Fig. 2). The sea surface is represented on each plot by the brown color indicative of intense backscatter (essentially reflection) from the air/sea interface, and the vertical depth scale on each plot is referenced to a nominal mean still-water level. Although rip currents do carry a sediment load which increases optical turbidity (see, e.g., Smith and Largier[17]), we shall assume, based on the huge scattering advantage of bubbles over that of suspended particulates, that scattering from within the water column is associated primarily with entrained bubbles. As remarked earlier, our procedure for correcting bubble attenuation is not applicable when bubbles are in such high concentration that the sound pulse is nearly extinguished owing to bubble scattering and absorption. This condition is shown in the top plot between minutes 14 and 17 and in the third-from-top plot between minutes 15 and 17.

Letters A–E, shown only in the uppermost plot, identify five sustained periods of increased bubble scattering, which we have classified as episodic events and interpret as the passage of organized, large-scale, bubble clouds. This classification is somewhat arbitrary; e.g., events C and D have early and late phases, each of which could constitute a separate event. However, we choose to define an event as the existence of a well-defined scattering front caused by a rapid increase in scattering level that (1) first appears in the data from unit 2, and (2) then in the data from the other three units located seaward of unit 2, with approximately the same scattering strength and duration but with increasing delay with increasing seaward location of the sensor unit. The one exception is event B, in which the front arrives at unit 3 about 30 s before it arrives at unit 4, just shoreward of unit 3. These same five events can be identified in Fig. 6 of Caruthers *et al.*,[5] which shows five periods of sustained high bubble attenuation (including the early and late phases of

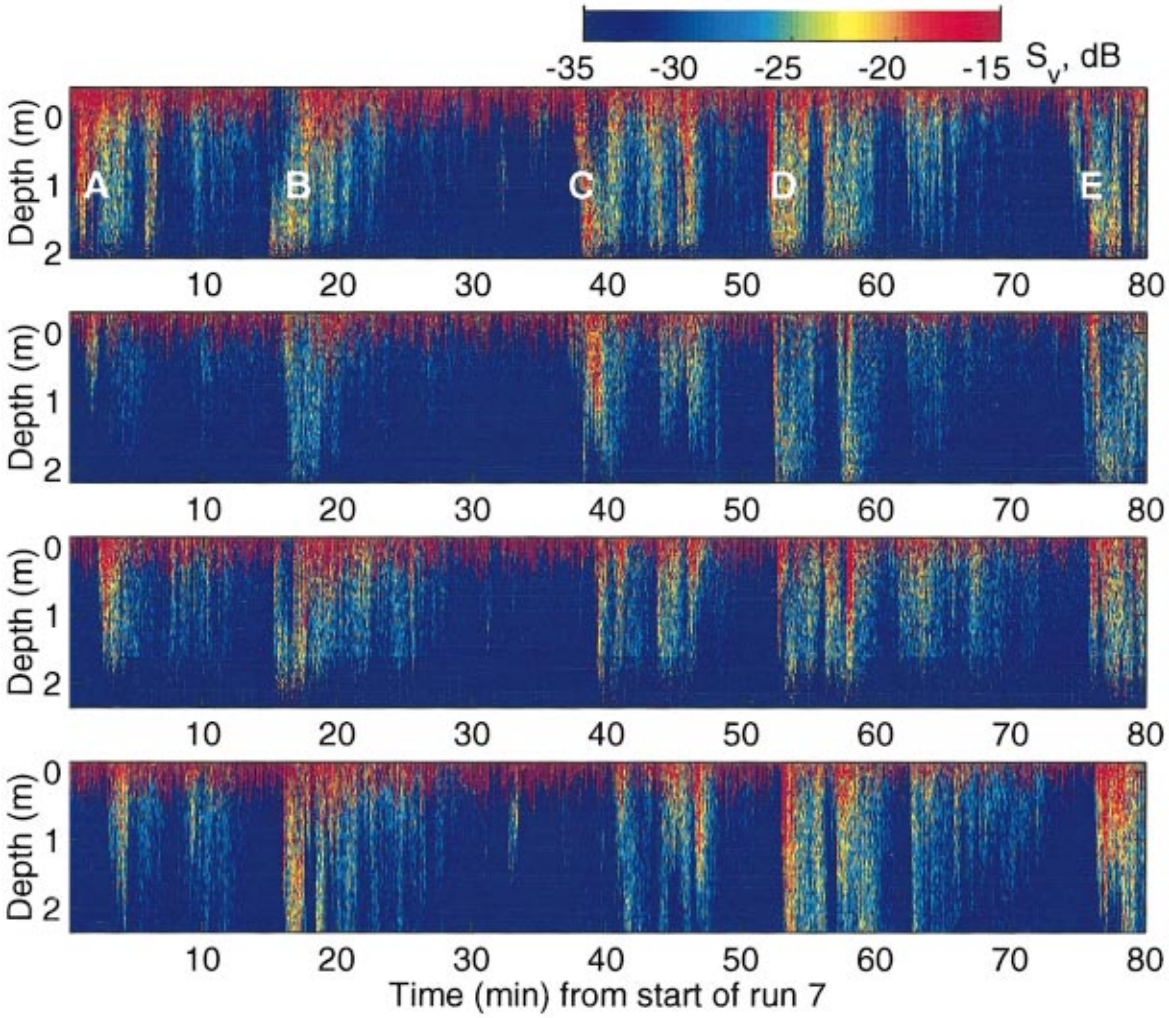

FIG. 5. Depth-versus-time display of decibel equivalent of the backscattering cross section per unit volume, or S_v in dB. The 80-min duration represents 96% of run 7. The four plots are arranged such that their order, from top to bottom, represents data from SALMON units 2-4-3-1, or increasing distance in the seaward direction, as shown in Fig. 2. The sea surface is represented on each plot by the brown color. The depth axis is relative to a nominal mean still-water level. The letters A–E, shown only in the top plot, identify five sustained periods of increased bubble scattering that are classified as events.

events C and D). Based on the time delay between the arrival of these fronts at the three units located seaward of unit 2, we estimate the seaward advection speed V_{df} at the delta frame site to be 7, 19, 7, 17, and 20 cm/s for events A–E, respectively.

The delay effect is best viewed with a less compressed time scale such as that in Fig. 6, which shows a 25-min subset of the data shown in Fig. 5 including the fronts associated with events C and D. The small white triangles in the top and bottom plots each point to a smaller scattering feature about 45 s in duration seen only on inner unit 2 and, 55 s later, on outer unit 1. We postulate that this scattering feature originates from the same discrete bubble cloud, and the inferred seaward velocity of this bubble cloud is 0.25 m/s. If we invoke Taylor's frozen turbulence hypothesis, the 45-s duration implies that the cloud's extent, or outer scale, in the seaward direction L_S (parallel to the pier) is ~11 m. The fact that the cloud is detected only by units 2 and 1 implies that the cloud's extent in the longshore direction L_L (perpendicular to the pier) is <12 m. Using similar arguments, we find that the larger organized bubble clouds associated with scattering events A–E all have $L_L > 12$ m, based on the fact that these events eventually produce a simultaneous scattering response on all four units. Their seaward extents can also be inferred by the scattering duration, which ranges from about 5 to 10 min, combined with their inferred velocities; these results put L_S in the range of 50 to 100 m. Thus, area coverage of these organized bubble clouds is in the range of 500 to 1000 m^2. Finally, there are intermittent periods of temporal variation in S_v that appear to be related to the dominant frequency of the surface waves. (For example, as depicted in the bottom plot of Fig. 6 near the label C.) Mechanisms for this variation may be, in part, similar to those discussed by Dahl and Plant.[18] This will be investigated in more detail in future work.

Figure 7 shows 65 s of data from inner unit 2 (top plot) and outer unit 1 (middle plot) corresponding to the passage of the discrete bubble cloud seen only by these two units and identified by the white triangles in Fig. 6. The time scale for the middle plot has been shifted by 55 s in order to compare the data. The bold white line on the top and middle plots shows the location of the air/sea interface as determined from the pressure records. At both times and locations, the cloud's bottom contour with respect to a fixed reference

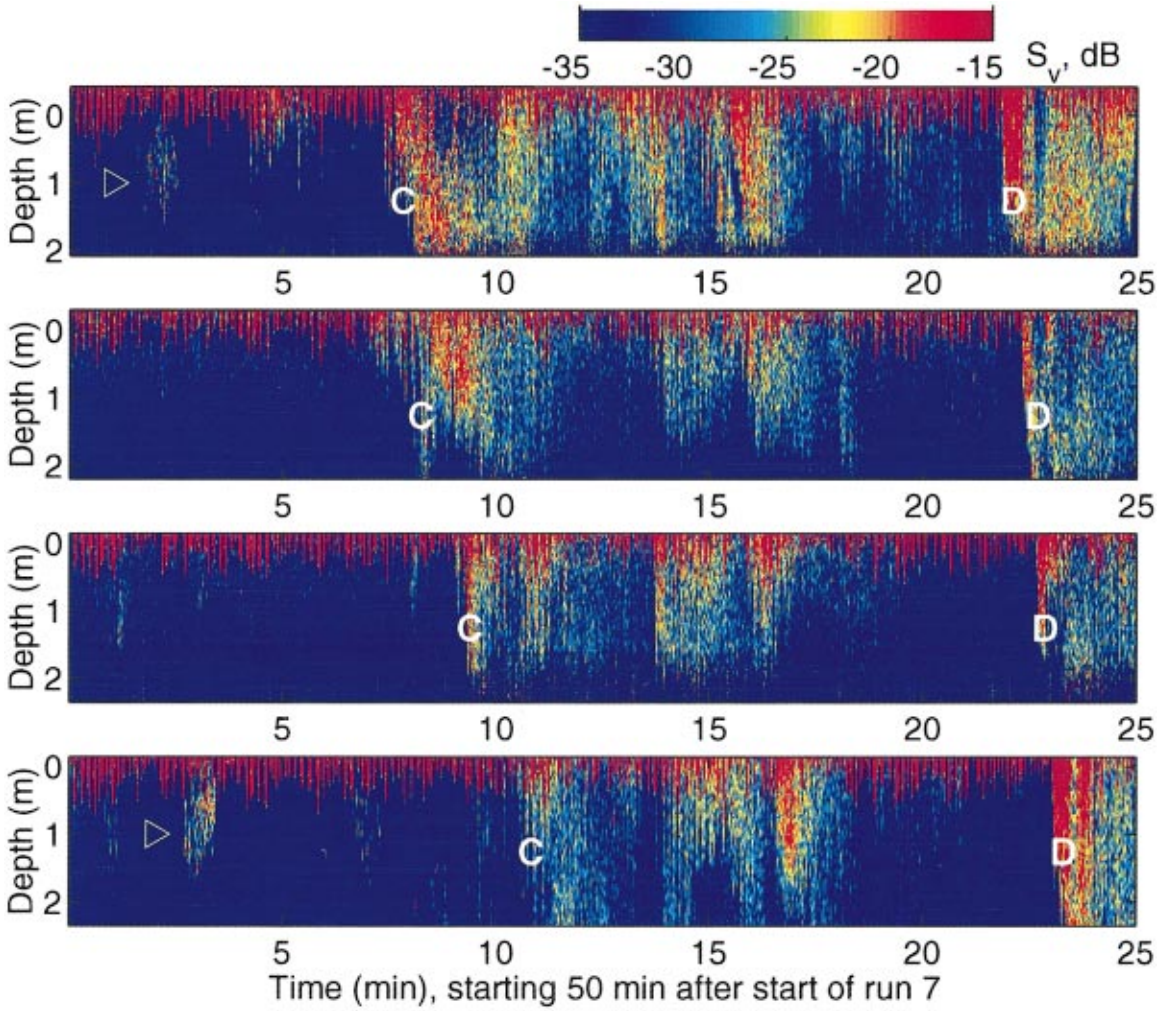

FIG. 6. Same as Fig. 5, but display of S_v starts 50 min after start of run 7, and duration is 25 min. Events C and D are now identified on the data displays of all four SALMON units. The two white triangles mark a scattering feature seen only on inner unit 2 and, 55 s later, on outer unit 1.

frame is governed by water column displacements associated with the dynamics of surface waves. The surface wave field above the outer sensor (and 55 s later) provides a particularly nice illustration of nonlinearities in the surface waves. The dashed line in the middle plot tracing a portion of the cloud's bottom contour at the location of unit 1 is simulated vertical displacement associated with a finite-depth Stokes wave. The parameters for this wave are wave period 11 s, wave amplitude a 0.35 m, and depth 4.4 m, which corresponds to a wave number of 0.0869 radians/m, or a wavelength of 72 m. (Note that the wave amplitude is such that $2a$ corresponds to the peak-to-trough height of the Stokes wave.) The equation for vertical displacement giving the dashed line is derived from Whitham's[16] equation for the velocity potential of a finite-depth Stokes wave, carried out to $O(a^2)$.

Finally, the bottom plot of Fig. 7 shows the depth-averaged s_v (in dB) of the bubble cloud measured at each location. This processing largely removes differences due to the variation in the surface wave field, and the two depth-averaged time series now appear quite similar, lending further credence to our assertion that these are indeed the same bubbles. Again, assuming that a Taylor's frozen turbulence hypothesis applies, and using an advection speed of 0.25 m/s, we see that coherent structure on scales of order 1 m in the seaward dimension is preserved in the course of advection over the delta frame site.

Figure 8 shows a time series of void fraction as measured by the sonar located on SALMON unit 2. The void fraction estimate was calculated from Eq. (8), using $S_v = 10 \log_{10}\langle s_v \rangle_z$, where in this case $\langle s_v \rangle_z$ is a depth average over a 0.25-m-thick layer centered at 1 m (thick gray line) and 2 m (thick dashed line) below the time-varying sea surface (with sea surface elevation determined by the pressure data). Upon taking the depth average, the result was then time averaged over a 30-s window equivalent to 60 sonar pulses. Letters A–E corresponding to the five primary bubble-scattering events first depicted in Fig. 5 are also shown in this figure. A characteristic time scale for the events, defined as a sustained high void fraction that exceeds 10^{-7}, ranges between 5 and 10 min. Alternatively, event B is particularly suited to using an exponential decay law to describe the decay in void fraction after its initial sharp onset. Here, the time constant of the exponential is 4 min, and the decay law is shown by the dotted-dashed line.

The void fraction within the layer centered at 1 m is, for the most part, greater than or equal to that found in the layer centered at 2 m. A notable exception is the start of event B,

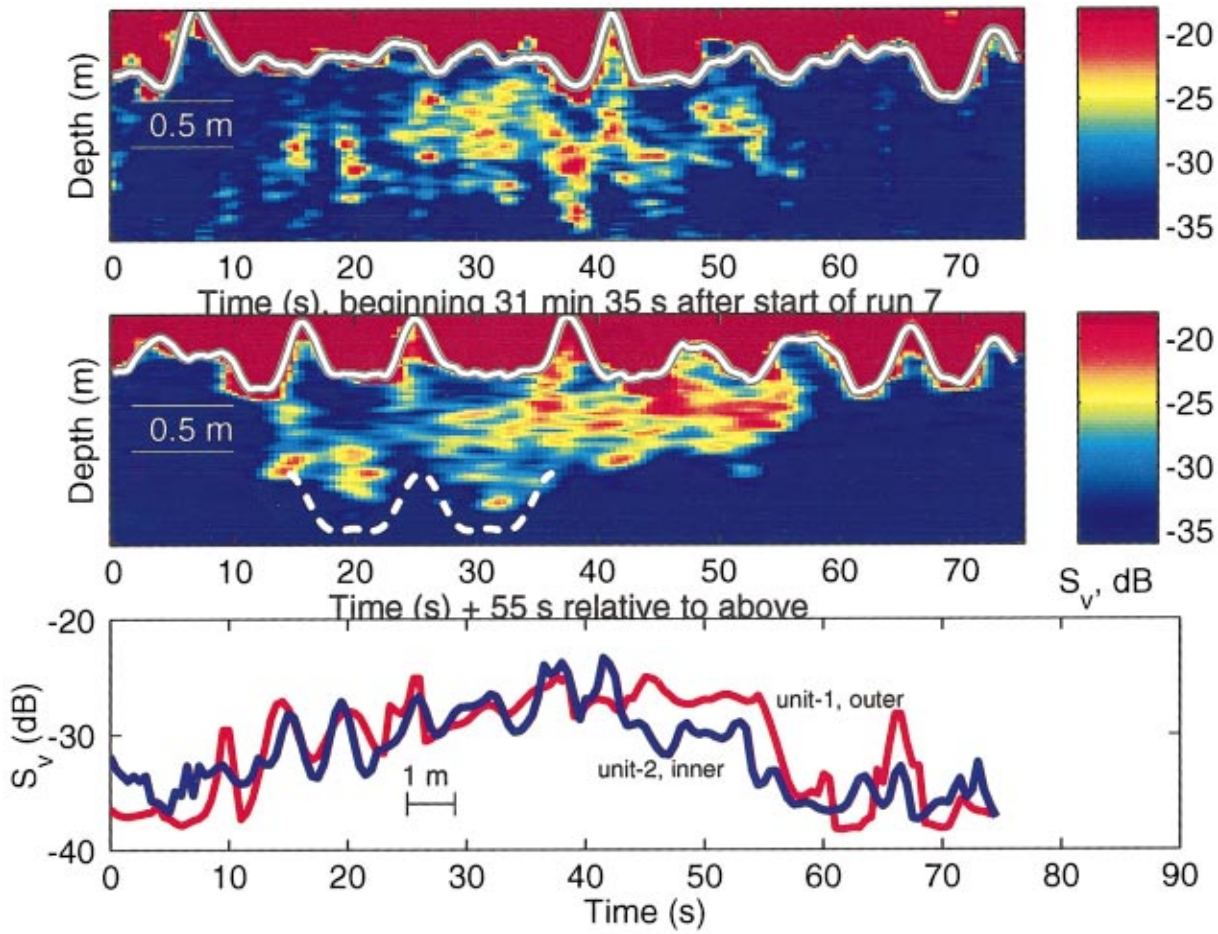

FIG. 7. Expanded view of depth-versus-time display of S_v showing 65 s of data from inner unit 2 (top plot) and outer unit 1 (middle plot). Note that the time scale for the middle plot is shifted by 55 s. The bold white lines in the top and middle plots represent the air/sea interface as determined from the pressure gauges located within each unit. The dashed line shown in the middle plot is simulated vertical displacement based on a finite-depth Stokes wave. The bottom plot shows depth-averaged s_v (expressed in dB) versus time, which removes the effect of a time-varying air/sea interface. The 1-m scale represents length in the seaward dimension based on an advection speed of 0.25 cm/s.

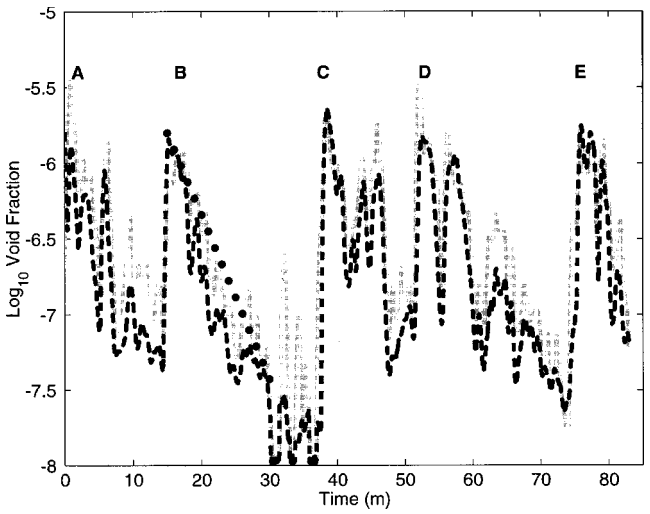

FIG. 8. Time series of void fraction measured by the sonar located on SALMON unit 2. The letters A–E correspond to the same events identified in Fig. 5. The dashed line corresponds to a 0.25-m-thick layer centered 2 m below the time-varying sea surface, and the solid, gray line corresponds to a 0.25-m-thick layer centered 1 m below the time-varying sea surface. The dotted line plotted over the data in the vicinity of event B is an exponential decay model with a time scale of 4 min.

where as remarked earlier the signal in the upper region of the water column is reduced owing to bubble attenuation. Also, the smaller bubble cloud seen near the surface and discussed in Fig. 7 produces an abrupt jump in void fraction seen only in the 1-m data shortly after min 31. Thus, this cloud would not have been detected by instruments mounted on the delta frame.

To evaluate further the dependence of void fraction on depth, the void fraction is averaged over a time window corresponding (approximately) to the uninterrupted time span during which the void fraction exceeds 10^{-7} for each event. Figure 9 shows the time-averaged void fraction vs depth beneath the time-varying sea surface for the five events (plots labeled A–E, along with their advection speeds) and their overall average (plot labeled AVG along with the average advection speed). The event time averages are computed for each sensor separately, with data from each sensor shown by the thick, colored lines. The overall average (thick, black line in the lower right plot) corresponds to an average over all four sensor units and all five events. A background time-averaged void fraction versus depth for each unit is also shown (thin, dashed colored lines), along with the average

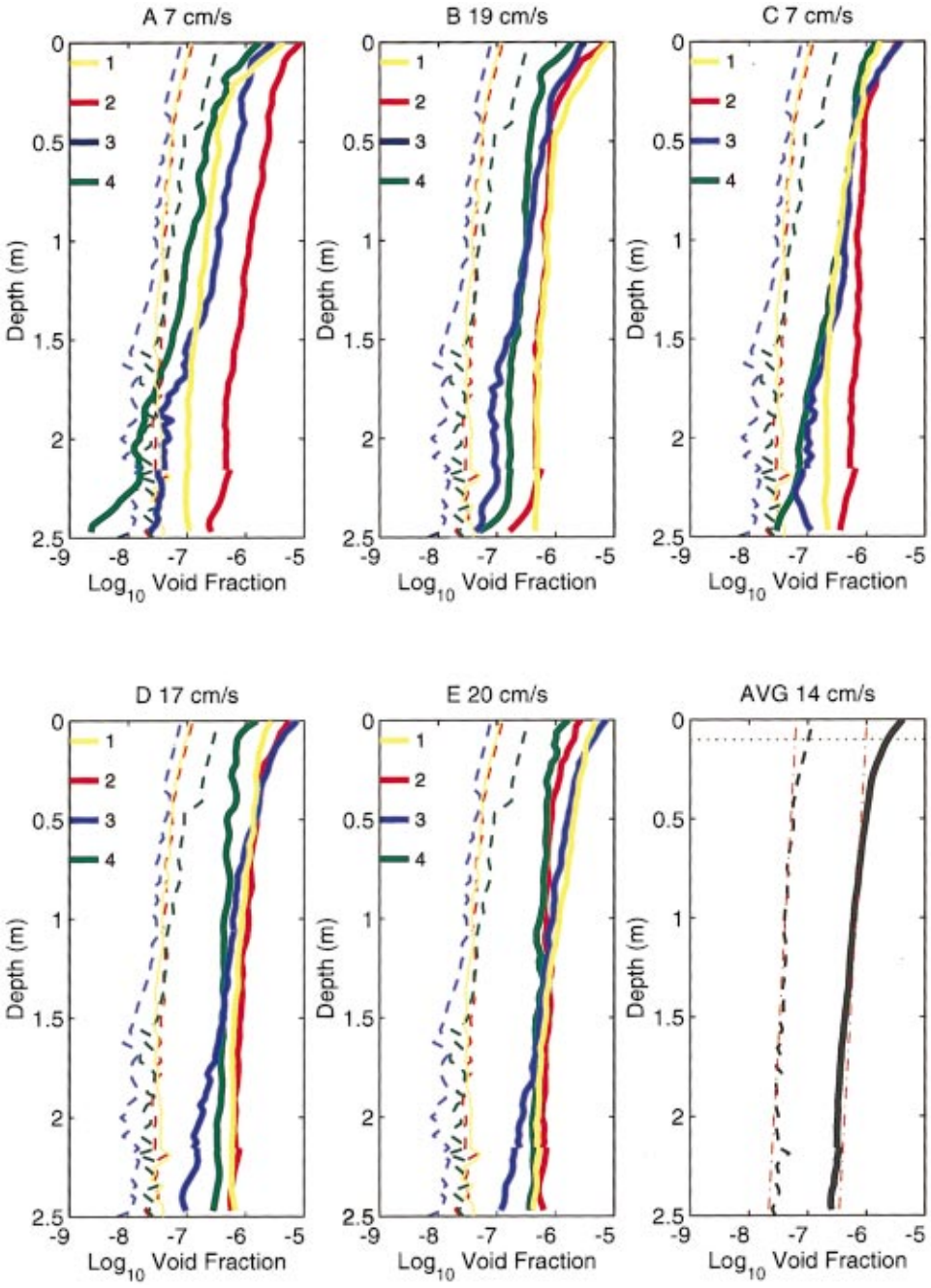

FIG. 9. Time-averaged void fraction versus depth beneath the time-varying sea surface for the five events (plots labeled A–E, along with their advection speeds) and their overall average (plot labeled AVG along with the average advection speed). The event time averages computed for each sensor separately are shown by the thick, colored lines. The overall average corresponds to an average over all four sensor units and all five events and is shown by the thick, black line in the lower right plot. A background time-averaged void fraction versus depth for each unit is also shown (thin, dashed colored lines), along with the average over all four units (thin, dashed black line in the lower right plot). Dotted horizontal line in the lower right plot corresponds to a depth of 10 cm and marks beginning of a region of ambiguity in surface resolution as determined by pulse length. The dotted lines plotted over the averaged data are simple exponential decay representations of the averaged data.

over all four units (thin, dashed black line) in the plot at the lower right. The background estimates are derived by averaging over times (such as in the vicinity of minute 30 in Fig. 5) between high-scattering events.

With exception of event A, where the data from unit 4 (green line) and unit 2 (red line) are significantly lower and higher, respectively, than data from the other two units, the data from the four units display a central tendency in both level and depth scale. This tendency is illustrated in the overall average shown in the lower right plot. The average background void fraction during run 7 is about $10^{-7.5}$, which itself is acoustically significant, and the void fraction increases by roughly an order of magnitude owing to the influx of bubbles advected by a rip current. The dashed red lines plotted over the average results are simple representations based on an exponential reduction in void fraction with distance z beneath the time-varying surface elevation. This representation is

$$\beta(z) = \beta_0 e^{-z/L_z}, \tag{9}$$

where β is the average void fraction, L_z is the exponential depth scale, which is 2.3 m and applies to both background and events, and β_0 is the average void fraction just below the air–sea interface, which is $10^{-7.2}$ for the background and 10^{-6} for the events. The dashed horizontal line at 10 cm in the lower right plot marks the point where pulse resolution limits our ability to reliably distinguish between volume scattering from entrained bubbles and surface scattering from the air–sea interface. Thus, averaged data above this line are of questionable value. We would expect reality to lie between the averaged data and the exponential decay law.

Finally, we can make a crude estimate of the time T over which bubbles have undergone advection, starting from their generation within the breaker zone and ending at the delta frame measurement site, by projecting the estimated rip-current speeds back toward the breaker zone. For this we shall assume that most of the rip-current field between the breaker zone and the delta frame is confined within a fixed-width channel and that the current undergoes minimal lateral expansion in the longshore dimension. This inner part of the rip-current field is called the neck. At a point farther seaward, the current does expand laterally, becoming more eddylike, and this outer part of the current is called the rip head.[19] If we assume, furthermore, that the flow is uniform in depth at least within the neck region,[20,21] then by mass conservation the speed of the seaward current increases with distance X from the delta frame in the direction toward the breaker zone, and goes as $V(X)=4V_{df}/[4-X\tan(1.2°)]$, where V_{df} is the current speed estimated at the delta frame, 1.2° is the nominal bottom slope,[6] and 4 m is the water depth at sensor unit 2.

We take the nominal distance from the delta frame to the breaker zone to be 75 m, giving $T\approx 300$ s when V_{df} is 20 cm/s and $T\approx 870$ s when V_{df} is 7 cm/s. Next, we estimate the magnitude of the average vertical eddy diffusivity, k_v, based on bubbles mixing to depth L_z over a time scale T, using $k_v \sim L_z^2/2T$. This puts k_v in the range 0.003 to 0.009 m^2/s, and varying linearly with V_{df} within this range. These magnitude estimates for k_v are reasonably consistent with more precisely modeled estimates of k_v recently computed by Vagle *et al.*[6] based on a turbulent boundary layer model. We expect to carry out more detailed comparisons between the depth-dependent void fraction estimates presented here and the model for bubble diffusion in the surf zone discussed in Ref. 6.

V. SUMMARY

Bubble clouds within the outer region of the surf zone have been studied using a distributed array of four upward-looking sonars as part of the 1997 Scripps Pier experiment involving several organizations. The bubble clouds were created in the inner, or breaker zone, region of the surf zone by shoaling waves, and the bubbles reached the measurement site through the process of seaward advection by rip currents. This study demonstrates how the seaward transport of bubbles via rip currents can dramatically alter the acoustic environment in the outer region of the surf zone, when this outer region is fed by rip currents which are themselves both episodic and localized.

The sonar measurements were in the form of volumetric backscattering strength S_v (in dB) versus depth and time and were made at an acoustic frequency of 240 kHz. A function, proportional to the size distribution of bubbles transported by rip currents into the outer region of the surf zone, was defined. This function, $n(a)$, where a is bubble radius, represents an amalgamation of multifrequency bubble attenuation measurements, which were more sensitive to bubble radius, made by other members of the experimental collaboration. The relation between $n(a)$ and frequency-dependent volumetric backscattering was also quantified by way of a PDF for the contribution to backscattering as a function of bubble radius at a specific acoustic frequency. At our frequency of 240 kHz, for example, bubble radii within the range 16 to 94 μm contributed 90% of the backscattered acoustic energy.

Depth-versus-time images of S_v revealed episodes of high scattering, called scattering events, associated with the passage of large-scale bubble clouds over the four measurement locations. Five of such events, each of duration $O(100)$ s, were identified in the 83 min of continuous measurements examined here. Based on a mapping between S_v and void fraction, which depends on $n(a)$, the average void fraction over the duration of these events was of $O(10^{-6})$, with a somewhat higher void fraction observed over periods lasting a few seconds. We emphasize that our void fraction estimates depend on a mapping between our observable, s_v, and the void fraction, based on the form for the bubble size distribution, $n(a)$, discussed in this paper. The speed of seaward advection of these bubble clouds was estimated from the delay between the arrival of the event's front at each of the four sonar locations. These speeds ranged from 7 to 20 cm/s, although the speed associated with a smaller scattering feature, seen only on two of the four sonar units, was estimated to be 25 cm/s.

The outer length scales in the seaward direction L_S of the bubble clouds associated with the high-scattering events were estimated from their duration time and the seaward advection speed. These calculations put L_S in the range of 50–100 m. In terms of the outer length scale in the longshore direction (L_L), this estimate was bounded by $L_L > 12$ m, since the events were eventually seen simultaneously at units 3 and 4, which were separated in the longshore direction by 12 m. A characteristic depth scale for the bubble clouds was estimated to be ~2.3 m. Using this value along with T, the time over which bubbles have undergone advection and vertical mixing, in the range 300–870 s, puts an estimate of the vertical eddy diffusivity k_v in the range 0.003–0.009 m^2/s.

The incoming wave field at the location of each unit was measured with a pressure gauge. The peak period of the frequency spectrum for the incoming wave field was close to 10 s, which translates to wavelengths of about 63 m according to finite-depth nonlinear wave theory. The influence of this wave field was illustrated by modeling the time-varying interface between the organized bubble cloud and the surrounding water, which had a much lower concentration of bubbles, with a finite-depth Stokes wave.

ACKNOWLEDGMENTS

I wish to thank R. Drever and M. Welsh of APL-UW for critical engineering and field support in carrying out the Scripps Pier Experiment. I also thank Dr. S. Stanic of NRL-SSC and the entire field crew and dive team from NRL-SSC for their assistance in the field. The discussions with Dr. G. Deane of SIO and Dr. L. Crum and Dr. F. Henyey of APL-UW are also much appreciated. This work was supported by the Office of Naval Research, Code 321 Ocean Acoustics, via Contract Nos. N00039-91-C-0072 and N00014-96-1-0325.

[1] G. B. Deane, ''Sound generation and air entrainment by breaking waves in the surf zone,'' J. Acoust. Soc. Am. **102**, 2671–2689 (1997).
[2] G. B. Deane, ''Acoustic hot-spots and breaking wave noise in the surf zone,'' J. Acoust. Soc. Am. **105**, 3151–3167 (1999).
[3] D. R. Basco, ''Surfzone current,'' Coastal Eng. **7**, 331–355 (1983).
[4] F. P. Shepard and D. L. Inman, ''Nearshore water circulation related to bottom topography and wave refraction,'' Trans., Am. Geophys. Union **31**, 196–212 (1950).
[5] J. W. Caruthers, S. J. Stanic, P. A. Elmore, and R. R. Goodman, ''Acoustic attenuation in very shallow water due to the presence of bubbles in rip currents,'' J. Acoust. Soc. Am. **106**, 617–625 (1999).
[6] S. Vagle, D. M. Farmer, and G. B. Deane, ''Bubble transport in rip currents,'' J. Geophys. Res. (submitted).
[7] D. M. Farmer, G. B. Deane, and S. Vagle, ''The influence of bubble clouds on acoustic propagation in the surf zone,'' IEEE J. Oceanic Eng. (to be published).
[8] E. J. Terrill and W. K. Melville, ''Bubbles and surf zone oceanography,'' in Proceedings of the 16th International Congress on Acoustics and the 135th Meeting of the Acoustical Society of America, 1998, pp. 703–704.
[9] D. Rouseff, F. Henyey, J. W. Caruthers, and S. J. Stanic, ''Tomographic reconstruction of shallow water bubble fields,'' IEEE J. Oceanic Eng. (to be published).
[10] C. S. Clay and H. Medwin, *Acoustical Oceanography* (Wiley, New York, 1977).
[11] A. Ishimaru, *Wave Propagation and Scattering in Random Media* (Academic, New York, 1978), Vol. I.
[12] K. L. Chung, *A Course in Probability Theory* (Academic, New York, 1974), see Theorem 1.3.2.
[13] P. H. Dahl and A. T. Jessup, ''On bubble clouds produced by breaking waves: An event analysis of ocean acoustic measurements,'' J. Geophys. Res. **100**, 5007–5020 (1995).
[14] S. Vagle and D. M. Farmer, ''A comparison of four methods for bubble size and void fraction measurements,'' IEEE J. Oceanic Eng. **23**, 211–222 (1998).
[15] S. Elgar and R. T. Guza, ''Shoaling gravity waves: Comparison between field observations, linear theory, and a nonlinear model,'' J. Fluid Mech. **158**, 47–70 (1985).
[16] G. B. Whitham, *Linear and Nonlinear Waves* (Wiley, New York, 1974).
[17] J. A. Smith and J. L. Largier, ''Observations of nearshore circulation: Rip currents,'' J. Geophys. Res. **100**, 10967–10975 (1995).
[18] P. H. Dahl and W. J. Plant, ''The variability of high-frequency acoustic backscatter from the region near the sea surface,'' J. Acoust. Soc. Am. **101**, 2596–2602 (1997).
[19] F. B. Shepard, *Submarine Geology* (Harper, New York, 1948).
[20] F. B. Shepard, with chapters by D. L. Inman and E. D. Goldbert, *Submarine Geology*, 2nd ed. (Harper & Row, New York, 1963).
[21] C. Miller and A. Barcilon, ''The dynamics of the littoral zone,'' Rev. Geophys. Space Phys. **14**, 81–91 (1976).

Acoustic scattering by internal solitary waves in the Strait of Gibraltar

Christopher O. Tiemann, Peter F. Worcester, and Bruce D. Cornuelle
Scripps Institution of Oceanography, University of California at San Diego, La Jolla, California 92093

(Received 13 March 2000; revised 18 September 2000; accepted 6 October 2000)

High-frequency underwater acoustic transmissions across the Strait of Gibraltar were used to examine acoustic scattering caused by the unique internal wave field in the Strait. Internal solitary waves of 100 m in amplitude propagate along the interface between an upper layer of Atlantic water and a lower layer of Mediterranean water. The interface is also strongly modulated by internal tides of comparable amplitude. As internal solitary waves cross the acoustic path, they cause sharp soundspeed gradients which intermittently refract acoustic rays away from normal sound channels. Internal tides vertically shift soundspeed profiles for additional travel time variability. Although the acoustic scattering is quite complicated, it is also surprisingly robust, making it a good candidate for modeling. Key features of the acoustic arrival pattern can be accounted for in some detail by a model description of the complex hydraulics in the Strait.
[DOI: 10.1121/1.1329624]

PACS numbers: 43.30.Re, 43.30.Ft, 43.30.Cq [DLB]

I. INTRODUCTION

The Strait of Gibraltar Acoustic Monitoring Experiment was conducted in April 1996 as a joint project between the Scripps Institution of Oceanography and the Institut für Meereskunde, University of Kiel. One goal of the experiment was to explore the acoustic scattering caused by the internal wave field in the Strait of Gibraltar. This article addresses that goal by describing a physical model used in the forward scattering problem that reproduces much of the observed acoustic channel impulse response.

The scattering effects of internal waves on acoustic transmissions in deep water are now reasonably well understood (Flatté *et al.*, 1979; Flatté, 1983). Internal wave effects on shallow water transmissions have received much attention recently despite the difficulties associated with shallow water acoustics, such as bottom interactions and range-dependent oceanography (Apel *et al.*, 1997; Preisig and Duda, 1997; Tang and Tappert, 1997; Lynch *et al.*, 1996; Rubenstein and Brill, 1991; Zhou *et al.*, 1991). The study of the interactions of acoustic transmissions with internal solitary waves and internal tides is important because internal solitary waves and internal tides are now known to be common in shallow water, straits, and gulfs, and scattering from internal waves is one of the factors limiting the use of acoustics in these interesting places.

In shallow water, internal waves are frequently observed as packets of solitary waves with well-defined wavelengths. Several studies have modeled acoustic transmissions through simulated packets of internal solitary waves with shapes similar to those observed on continental shelves (Duda and Preisig, 1999; Preisig and Duda, 1997; Tielburger, 1997; Rubenstein and Brill, 1991; Zhou *et al.*, 1991; Baxter and Orr, 1982). Common to most of these studies was their focus on normal mode fluctuations and mode coupling caused by internal waves. The shallowness of the waters under study also made the acoustic effects of internal waves difficult to isolate because of surface and bottom interactions, and several were hindered by insufficient environmental data. In this work, a geometric ray approach was best suited for the high-frequency, broadband, forward scatter problem, but the sound channel impulse response could have been calculated using normal mode code as the equivalence of travel time variance of geometric rays and a truncated sum of acoustic modes has been shown (Traykovski, 1996).

This article offers another example of modeling acoustic transmissions through moving internal solitary waves, but several features make the Gibraltar data set unique among all other internal wave studies. First, it clearly isolates the effects of internal solitary waves on high-frequency acoustic transmissions without the added complexity of surface and bottom interactions. This data set can identify the passing of an internal solitary wave over the instruments, making it possible to distinguish between acoustic effects which are most likely internal wave related and those which are tide related. Though quite complicated, the acoustic travel time variability is surprisingly robust in that it is repeated on every tidal cycle, simplifying the identification of key features to reproduce in the forward problem. Furthermore, the geometry of the Gibraltar experiment provides valuable insight into the feasibility of acoustic remote sensing of internal solitary waves, a topic which has previously been discussed only briefly (Zhou *et al.*, 1991; Essen *et al.*, 1983).

This article is organized as follows. Section II provides a general overview of both the environment of the Strait of Gibraltar and the experiment instrumentation. In Sec. III acoustic data from two different acoustic paths are presented along with a discussion of the most interesting features. In Sec. IV we describe the construction of the range- and time-dependent soundspeed field used in the forward problem. In Sec. V experimental data and theoretical predictions are compared.

II. OVERVIEW

An understanding of the physical processes in the Strait of Gibraltar is required before attempting to reproduce the

observed acoustic data. The two largest contributors to acoustic scattering are trains of internal solitary waves and the internal tide. Here the internal tide is defined as vertical fluctuations in the depth of the interface between two main water layers. The Gibraltar experiment was designed to acoustically sample this interface and the internal waves which propagate there.

A. Environment

The basic circulation in the Strait of Gibraltar is relatively simple. An upper layer of relatively warm, fresh Atlantic water about 100 m thick flows east into the Mediterranean Sea. After evaporation and cooling in the Sea, the dense water mass sinks and a lower layer of relatively salty, cold Mediterranean water flows back west through the Strait into the Atlantic. This mean flow is modulated by large semidiurnal tidal flows and is also subject to hydraulic controls at the shallowest sill (Camarinal Sill on the west side of the Strait) and narrowest constriction (Tarifa Narrows). Furthermore, there are tidal fluctuations in the depth of the interface between the upper Atlantic and lower Mediterranean water layers (Armi and Farmer, 1988; Farmer and Armi, 1988). Perhaps the most interesting feature, though, is the propagation of internal bores which are released at the Camarinal Sill at the relaxation of most high tides and propagate east down the Strait.

These internal bores are the result of interaction between tidal currents and topography. A lee wave in the form of an internal hydraulic jump appears behind the Camarinal Sill during strong westward tidal flows. When the tide relaxes, this wave crosses the sill and moves east as an internal bore along the density gradient marking the interface between Atlantic and Mediterranean waters. The bore eventually disintegrates into a train of internal solitary waves. As the train moves east, the amplitudes of the solitary waves decrease, more waves are added to the packet, and the interface level deepens behind the passing train.

Packets of internal solitary waves in the Strait of Gibraltar have been observed in several experiments by echo sounders, thermistors, surface radar, airplanes, and satellites (Armi and Farmer, 1988; Farmer and Armi, 1988; Watson and Robinson, 1990; Watson, 1994; Richez, 1994; Alpers and La Violette, 1993; Ziegenbein, 1970), and though there is much variability in individual packets, some general descriptions can be made. First, internal bores are released from the Camarinal Sill on almost every spring tide but less often during neap tides. They can have vertical amplitudes of 100 m and wavelengths from 0.5 to 2.5 km. They are found at approximately the interface depth, and a single bore can eventually evolve into as many as 12 solitons traveling together in a packet with a phase speed from 1 to 2.6 m/s (Armi and Farmer, 1988; Farmer and Armi, 1988; Watson and Robinson, 1990; Richez, 1994; Ziegenbein, 1970; Frassetto, 1964).

Synthetic aperture radar (SAR) images of the Strait of Gibraltar taken by the ERS-1 satellite during the days of the experiment provide information on the structure of the internal wave packets. One of those SAR images is shown in Fig. 1 where a packet of internal solitary waves exiting the Strait to the east is visible to the SAR as distinctive surface roughness patterns. Further examples and discussions of SAR images of the Strait of Gibraltar are available from Alpers and Richez (Alpers and La Violette, 1993; Richez, 1994).

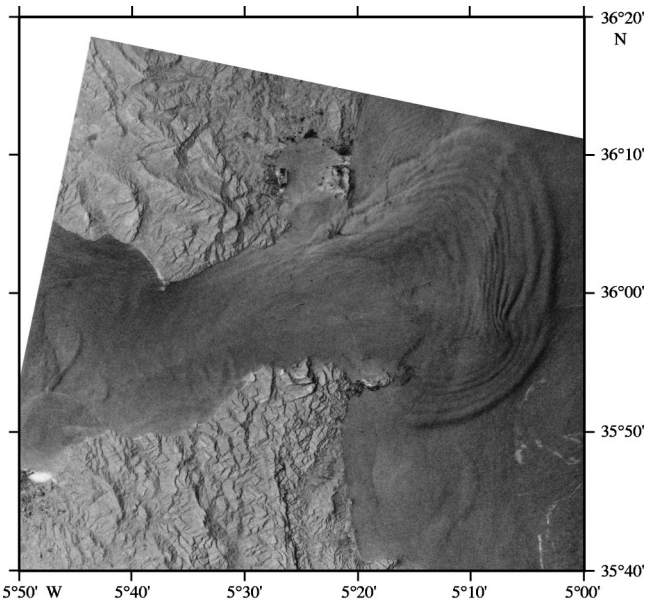

FIG. 1. SAR image of a train of internal solitary waves exiting the Strait of Gibraltar. Image was taken by the ERS-1 satellite during the experiment. Courtesy of John Apel, Global Ocean Associates. Copyright ESA 1996.

B. Experimental approach

The Gibraltar experiment was designed to test whether high-frequency (2 kHz) acoustic ray paths across the Strait are resolvable, identifiable, and stable. Geometries were selected so that lower ray paths would be confined to the lower layer of Mediterranean water, while upper ray paths traversed the interface between Atlantic and Mediterranean water layers. Three transceivers (labeled T1, T2, and T3 in

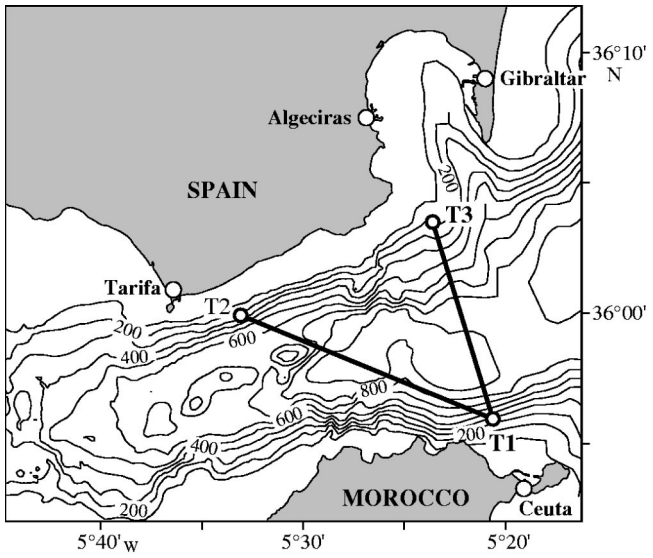

FIG. 2. Bathymetry of the Strait of Gibraltar with instrument positions and acoustic paths indicated. Due to inaccuracies in bathymetry, depth contours do not exactly match instrument depths.

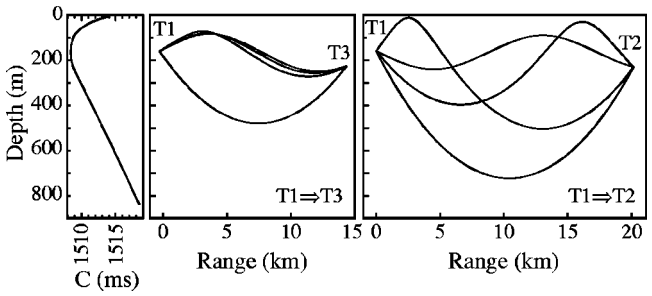

FIG. 3. Predicted ray paths for transmissions from a source at T1 to receivers at T2 and T3 assuming a historic mean range-independent soundspeed profile.

Fig. 2) were installed at the endpoints of two acoustic paths, just above the bottom at about 200-m depth. The T1–T3 path was perpendicular to the flow with a length of 14.60 km, and the T1–T2 path had a component parallel to the flow with a length of 20.15 km. The predicted ray paths between the instruments, assuming a historic mean soundspeed profile, are shown in Fig. 3 and best illustrate the differences between ''upper'' and ''lower'' rays.

Pulses were transmitted by all three instruments every 2 min. Pulse compression techniques were used to improve the signal-to-noise ratio (SNR) of the received signal without appreciably sacrificing resolution in time of the multipath arrivals. The transmitted signal was a nonlinear frequency sweep with a center frequency of 2272.72 Hz (440 μs period), extending from 1136.36 to 3409.09 Hz, and lasting 25.0 ms. The signal spectrum was designed to yield about 0.7-ms resolution after processing.

Instrument positions were surveyed using a ship-mounted interrogator and transponders on the instruments. The estimated uncertainties of the differential GPS were too small for a successful survey solution, so a constant GPS uncertainty of 10 m was used. Because this work focuses on changes in ray travel times, knowing the absolute ranges between instruments is not so critical. The final surveyed positions and uncertainties for the three instruments' receivers are shown in Table I. An instrument's source is 1.13 m deeper than its receiver.

The tilts and orientations of the moorings were measured every 5 min and used to compute the displacements of the instruments as a function of time so that the acoustic travel times could be corrected for mooring motion. Close examination of the T1 instrument tilt data showed brief but violent tilts occurring roughly every 12 h. These kicks are due to the passing of an internal solitary wave over the instrument and are now being used to time the internal wave crossings. They also provide a hint as to where to look in the acoustic data for internal wave effects.

The environmental sampling strategy was designed to account for the large tidal variability in the Strait. Measurements of temperature, salinity, and velocity fields were obtained using a conductivity-temperature-depth (CTD) sensor and an acoustic Doppler current profiler (ADCP), both along and perpendicular to the acoustic paths, and at several tidal phases during spring and neap tides. Three current meter moorings provided data spanning the Strait close to and parallel to the T1–T3 acoustic path. An extensive analysis of the Gibraltar experiment's current meter data is available by Baschek *et al.* (2000).

III. ACOUSTIC DATA

The data examined in this article were taken from two weeks during which the moored transponders remained at their surveyed locations, and those days include both a neap and a spring tide. The absolute acoustic travel times to the T2 and T3 instruments, corrected for both mooring motion and onboard clock drift, are shown in Fig. 4 as dot plots. Times of internal solitary wave crossings, as provided by the instrument tilt data, are indicated by thin vertical lines. In both cases, the earliest arrival is from the lower ray path and is stable over the duration of the experiment, but the earliest arrival of the T1–T2 path has a much stronger tidal signal. This is expected because tidal currents are aligned approximately along the axis of the Strait, perpendicular to the T1–T3 path, and so have little effect on ray travel times for the T1–T3 path.

At both T2 and T3, the several ray arrivals following the earliest one are from upper ray paths which traverse the interface between the Atlantic and Mediterranean water layers. The travel time fluctuations of these rays are more complex and less sinusoidal than for the lower ray paths, and again the tidal signal is stronger for the T1–T2 path due to current effects. Much of the travel time variability seen in the T1–T3 case is not due to currents but rather shifts in the soundspeed field over a tidal cycle. Times of neap and spring tides can be seen, with a minimum tidal signal on about yearday 118 and a maximum tidal signal on about yearday 125. The times of internal solitary wave crossings confirm that they occur regularly during spring tides and less often during neap tides.

By using travel times of lower rays recorded at all three instruments, sum and difference travel times for reciprocal transmissions along both acoustic paths were calculated, and they are proportional to the integrated temperature and current, respectively (Munk *et al.*, 1995). The difference travel times along the T1–T3 path are much smaller than those of the T1–T2 path, confirming that any current effects on travel time are weaker in the T1–T3 case. Because the T1–T3 difference travel time series had a swing of at most ± 2 ms during spring tides, this path was chosen to be modeled first in hopes that the current effects could be neglected. Further analysis of the Gibraltar experiment's sum and difference travel times can be found in the paper by Send *et al.* (2000).

Close examination of the T1–T3 travel time data during spring tides shows a sudden decrease in travel times, for both the deep and shallow rays, coinciding with the clock of internal solitary wave crossings at the T1 instrument. Although the acoustic scattering following each crossing is slightly different, some large scale features are regularly repeated with each spring tide (Tiemann *et al.*, 1998). To illustrate this, the expanded view of Fig. 4 shows acoustic data from six spring semidiurnal tidal cycles. Note how upper ray paths routinely disappear over parts of the tidal cycle. The travel times of persistent upper rays have a sawtooth shape and a variability of 15 ms over a tidal cycle, and for part of every tidal cycle the upper and lower rays have nearly identical travel times. It is the repeatability of such acoustic features,

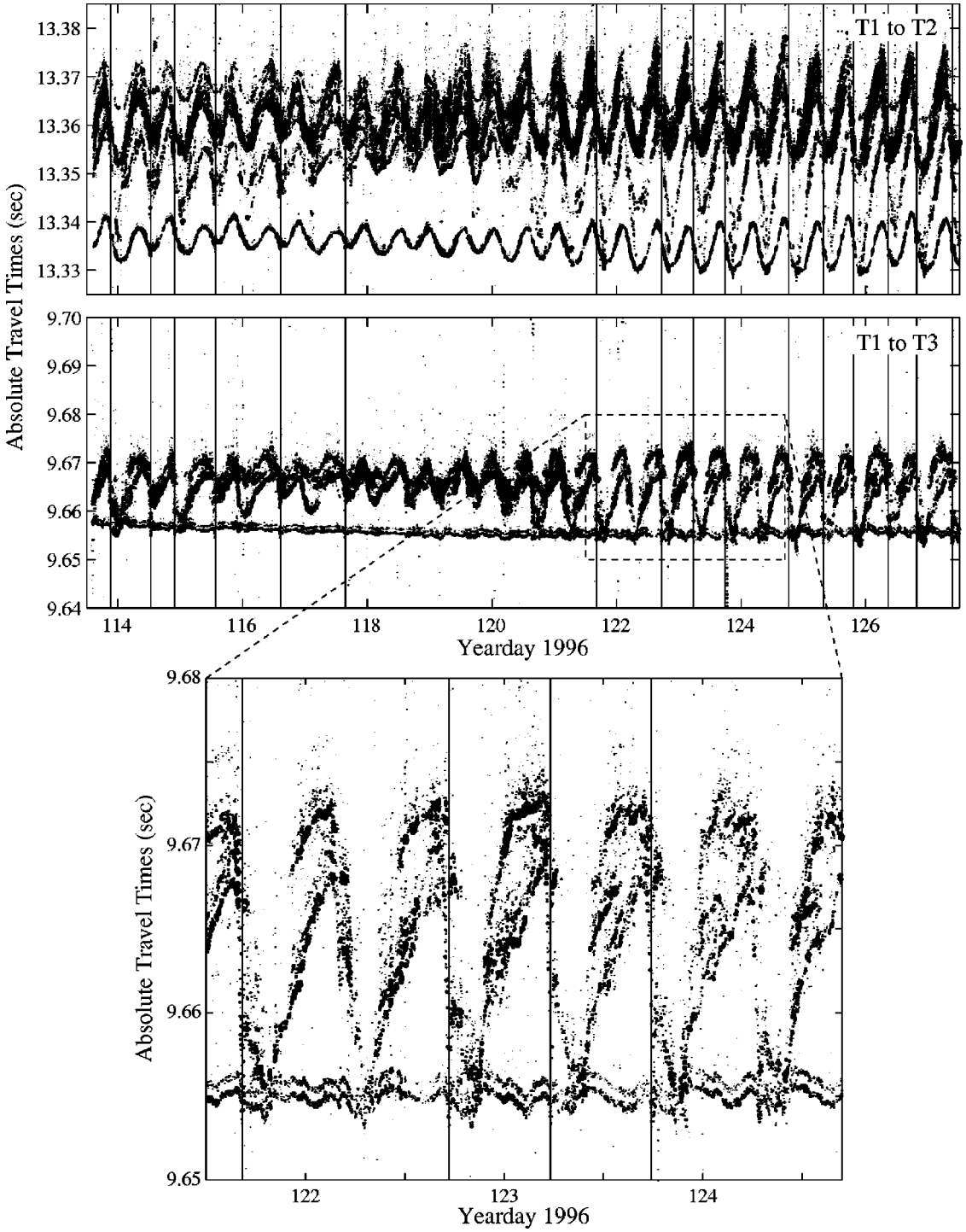

FIG. 4. Absolute travel times as a function of yearday 1996 for transmissions from T1 to T2 and T3. Each arrival peak is plotted as a dot, with size proportional to SNR. Vertical lines indicate times of internal solitary waves crossing the T1 instrument. The expanded box focuses on transmissions from T1 to T3 during six spring tidal cycles.

despite their complexity, that make the Gibraltar data set so interesting and a good candidate for modeling.

IV. FORWARD PROBLEM

Constructing a range- and time-dependent soundspeed field to use in acoustic propagation studies of the Strait is difficult given the strong tides, internal wave field, and uncertainty in the background soundspeed field. However, those three components can all be modeled independently and their cumulative perturbations to the soundspeed field combined. In order to match measured travel times to predicted ray travel times output by an acoustic propagation program, a model was constructed consisting of a range-dependent background soundspeed field perturbed by both an internal tide and internal waves over a simulated 12-h tidal cycle. The model's background soundspeed field was constructed using CTD measurements taken during the experiment (Sec. IV A) and then vertically shifted by a mode 1 internal tide (Sec. IV B). Finally, soundspeed perturbations

TABLE I. Surveyed instrument positions and uncertainties.

Instrument	Latitude (deg N)	Longitude (deg W)	Receiver depth (m)	Uncertainty N/S (m)	Uncertainty E/W (m)	Uncertainty depth (m)
T1	35.932 329	5.343 448	164.852	0.741	0.594	0.734
T2	35.998 661	5.551 346	215.919	0.758	0.580	0.540
T3	36.058 256	5.390 321	202.261	1.463	1.045	0.856

due to internal solitary waves crossing the acoustic path were applied. The vertical and horizontal shapes for the modeled internal solitary waves were derived from echosounder and satellite observations of the Strait (Sec. IV C).

After a range- and time-dependent soundspeed field was made, the ray-tracing program RAY (Bowlin *et al.*, 1992) was used to predict ray paths and travel times from the T1 source to the T3 receiver. A limitation of the ray-tracing program used here is that it cannot account for changes in travel time due to currents. Because of this limitation, only the T1–T3 acoustic path is being modeled since any current-related effects along this path should be relatively small in comparison to the total travel time variability.

A. Background soundspeed field

Perhaps the biggest limitation of the Gibraltar model is the uncertainty in the background soundspeed field due to insufficient environmental data, and, unfortunately, historical average soundspeed profiles available for the Strait do not closely resemble those observed by this experiment's CTD measurements. Rapid CTD casts over a 12-h tidal period were obtained at three stations along the T1–T3 acoustic path, at ranges 1.5, 7.8, and 10.7 km, during both spring and neap tides. Those CTD casts show that during much of the tidal cycle a single soundspeed profile for a particular station appears to be shifting vertically over time, as the Atlantic/Mediterranean interface depth shifts vertically from internal tides. Such vertical shifting of a single soundspeed profile was observed at all three ranges across the Strait. As an example, Fig. 5 shows 12 consecutive soundspeed profiles seen at the CTD station at 1.5 km along the T1–T3 path. The middle six profiles (solid lines) most closely resemble each other and were used in construction of a ''representative'' soundspeed profile for that station. It is recognized that in doing so, agreement between modeled and measured soundspeed profiles would be less at the very top and bottom of the tidal cycle.

Temperature and salinity profiles from all three CTD stations show sharp steps in the profiles which cause double minimums in soundspeed profiles to appear at about depths 80 and 170 m. Because the temperature or salinity profiles from any one CTD station all had a similar shape, but were offset vertically from each other, taking an average of all the profiles from any one station resulted in a profile that was too smooth to capture the important features of the magnitudes and depths of the steps. However, when the temperature and salinity profiles from a station were vertically aligned to a common salinity at a common depth (37.8 psu at 130-m depth), the profiles overlaid each other closely and their shape was again obvious. Figure 6 demonstrates this, showing the aligned temperature and salinity profiles for the six CTD casts highlighted in Fig. 5. Averages of the aligned profiles as in Fig. 6 did capture the important features of the temperature and salinity profiles, except in the shallowest

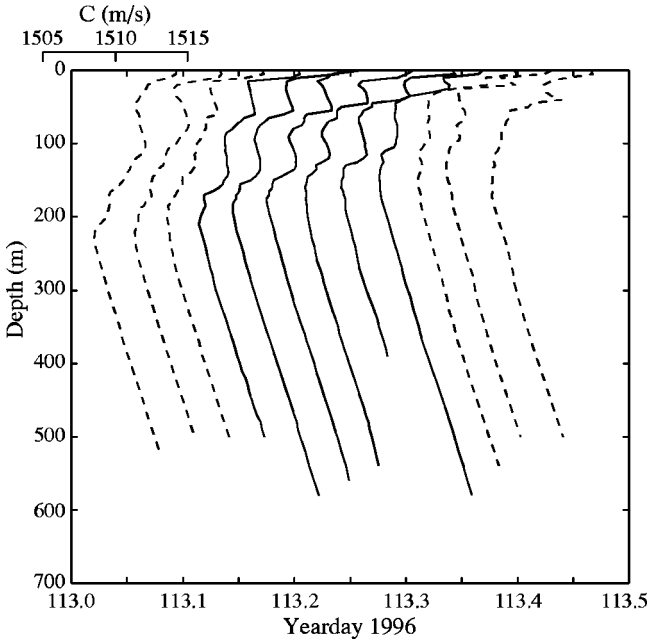

FIG. 5. Twelve consecutive soundspeed profiles from CTD station at 1.5 km along T1–T3 path. Highlighted profiles (solid lines) are used in construction of a representative profile for that station. Scale for profile values is the same for all profiles but offset in time.

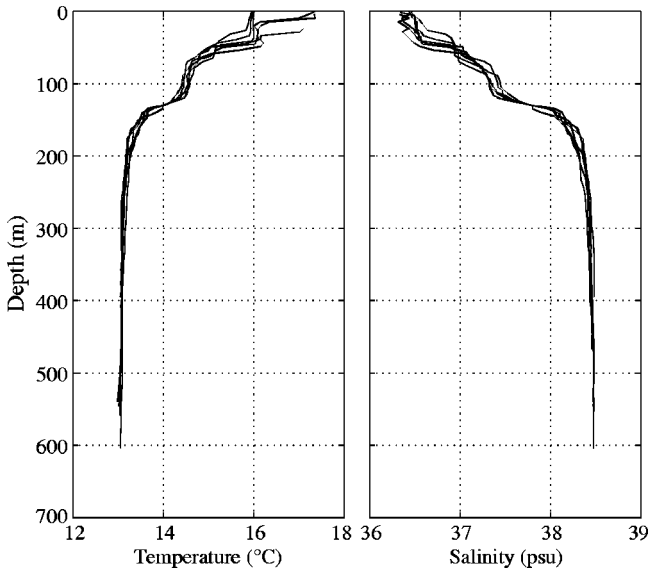

FIG. 6. Temperature and salinity profiles from the highlighted CTD casts of Fig. 6 aligned at 37.8 psu and 130-m depth to demonstrate their similar step structure.

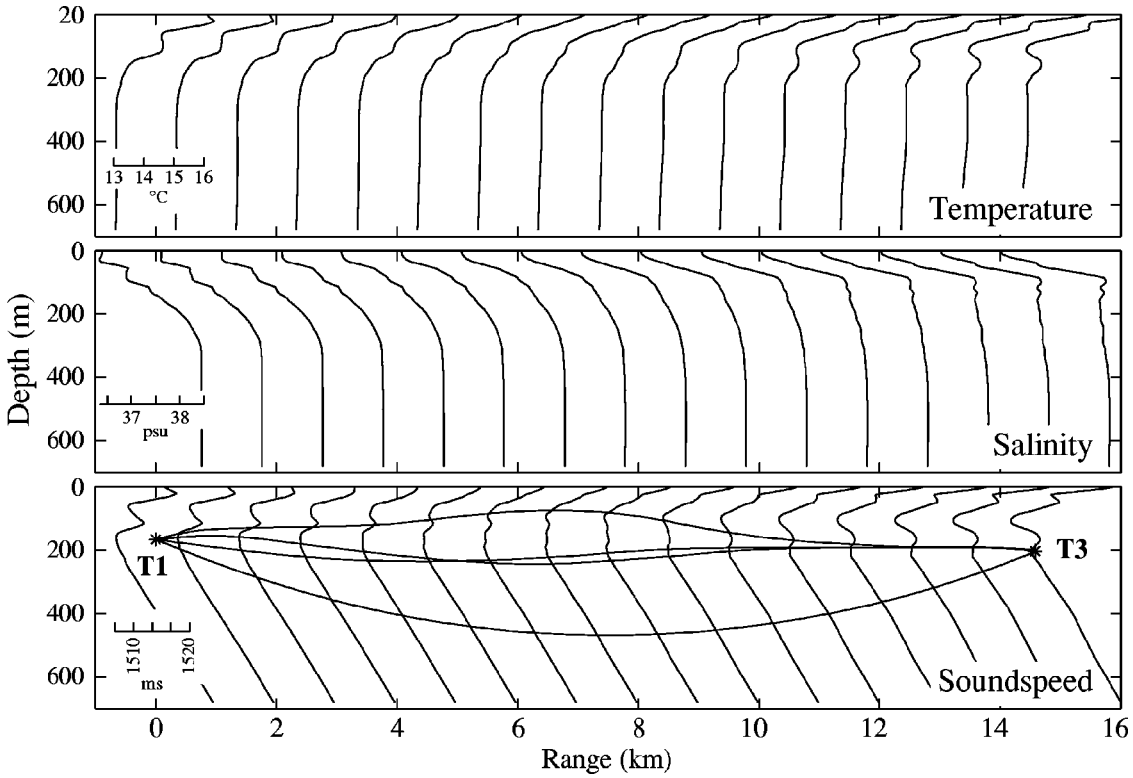

FIG. 7. Unperturbed background temperature, salinity, and soundspeed profiles used in the model. Ray paths from instrument T1 to T3 are overlaid on the soundspeed profiles. Scale for profile values is the same for all profiles but offset in range.

60 m where many cases of no data (due to vertical shifting), and widely varied data, caused the average to be erratic. The top 60 m of the average profiles were manually smoothed, resulting in representative temperature and salinity profiles for the three CTD stations.

Soundspeed profiles at more than three ranges along the acoustic path are necessary when applying the perturbations from internal tides and internal waves to the model. In order to construct a background temperature and salinity field over the whole path, linear fits at each depth through values at the three CTD stations were used to interpolate or extrapolate new profiles at 1-km range steps along the acoustic path. From these interpolated temperature and salinity profiles, a smoothly varying soundspeed field, with double minimums at all ranges, was constructed and declared the background soundspeed field. Figure 7 shows the background temperature, salinity, and soundspeed fields used, along with the predicted acoustic ray paths for the given soundspeed field. It is encouraging that the ray paths show a single lower ray and multiple upper rays with no surface or bottom bounces, as is expected from the acoustic data, despite all the uncertainties and approximations made during soundspeed field construction.

B. Internal tides

The depth of the interface between the upper and lower water layers in the Strait of Gibraltar can shift by as much as 150 m with the semidiurnal tides in some parts of the Strait, but fluctuations of 50 to 70 m are more common at locations near the middle of the T1–T3 path (Bray *et al.*, 1990; Candela *et al.*, 1990; Boyce, 1975; Watson and Robinson, 1991). Such tidal fluctuations of the interface are greater on the southern side of the Strait than the north, and the cross-strait slope of the interface changes with the tides as well (Bray *et al.*, 1990). These characteristics of the interface depth were also observed in this experiment's environmental data from CTD casts and moorings (Baschek *et al.*, 2000).

The vertical shifting of soundspeed profiles with the changing interface depth requires time dependence be added to the Gibraltar model's background soundspeed field. It was noted earlier that in almost every CTD cast, the soundspeed profiles showed double minimums at depths of about 80 and 170 m. Although these minimums shift up or down in unison over a tidal cycle, their separation is not constant; the shallower soundspeed minimum has a smaller vertical swing than the deeper minimum. This nonlinearity of the tidal shifting is also seen in Fig. 5 and can be accounted for in soundspeed field construction as well.

To model the tidal swings, sinusoidal vertical offsets with a frequency of 2 cpd were applied to the background temperature and salinity profiles, and new soundspeed profiles were then recalculated. The amount of vertical offset to apply to profiles varied with both range and time. A sinusoidal swing of ± 40-m amplitude was assigned to the southernmost profiles at the source; a ± 25-m swing was applied to the northernmost profiles at 15-km range. With these two sinusoids serving as endpoints, tidal offsets at 1-km range steps were linearly interpolated between the two endpoints and at several phases over one tidal cycle. The tidal offsets calculated in this way are consistent with observations of the interface depth fluctuations over a tidal cycle (Bray *et al.*, 1990; B. Baschek, personal communication).

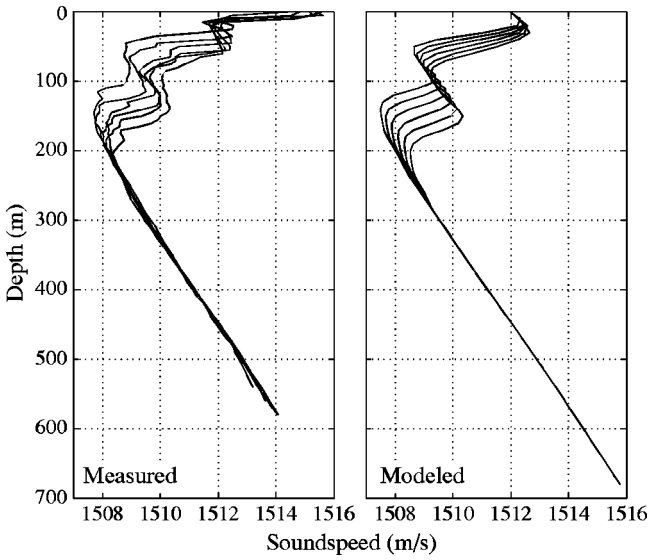

FIG. 8. Measured soundspeed profiles from 1.5 km along the T1–T3 path (also highlighted in Fig. 5) and modeled soundspeed profiles at that same range.

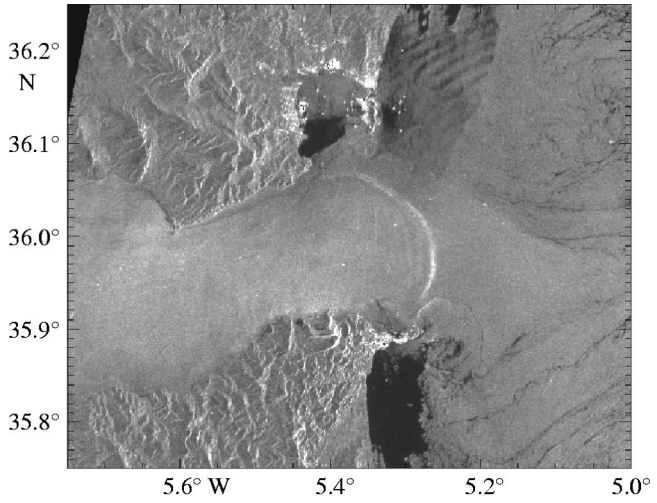

FIG. 9. SAR image from March 1998 of a wavefront crossing the T1–T3 path. Copyright ESA 1998.

The calculated tidal offsets were the maximum displacements added to temperature and salinity profiles at a particular range and time. The maximum tidal displacements were scaled with depth according to a vertical mode 1 function determined from range-dependent buoyancy frequency profiles. Nonlinear vertical shifting of profiles was done by adding the vertically-scaled tidal displacement to the depth indices of the background temperature and salinity profiles. Soundspeed profiles recalculated at each range- and time-step captured the most important features of data from the CTD measurements, i.e., the multiple minimums and maximums between 50- and 200 m-depth. Although agreement between measured and modeled soundspeeds is not perfect, the advantage of this model is that all the effects of a range- and time-dependent internal tide can be defined with just a few parameters. Figure 8 shows a comparison between the six soundspeed profiles from the CTD station at 1.5 km, as highlighted earlier in Fig. 5 but now overlaid on each other, with modeled soundspeed profiles for that same station. The largest error between the two occurs in the upper 20 m, but this should not affect the acoustic propagation comparisons as the rays do not travel in water that shallow.

C. Internal solitary waves

After creating a background soundspeed field that includes the internal tides, perturbations from internal solitary waves must then be applied to complete the model. However, the large variability in observed shapes of solitary waves' vertical displacements and horizontal wavefronts makes choosing a ''typical'' solitary wave perturbation difficult. Furthermore, the range dependence across the Strait of a single wave's vertical amplitude has not been directly observed.

Satellite, airplane, and surface radar observations of the surface manifestations of solitary wave packets in the Strait show that their wavefronts are not straight as they leave the narrows; the wavefront has curvature as it crosses over the acoustic path (Alpers and La Violette, 1993; Richez, 1994; Watson and Robinson, 1990). A model was therefore constructed such that any initial wavefront shape, starting position, and along-axis speed as a function of range across the Strait can be specified. As the model steps through time, the wavefront propagates over the acoustic path and can evolve in shape. Of the many SAR images of wavefronts in the Strait, the one that most clearly shows a wavefront over the T1–T3 acoustic path is provided by ESA from March 1998, as seen in Fig. 9. The model approximates this shape during the time the wavefront is over the acoustic path with the following equation of wavefront position along the axis of the Strait $[x\,(\mathrm{m})]$ as a function of range along the acoustic path $[r\,(\mathrm{km})]$ and time $[t\,(\mathrm{sec})]$:

$$x(r,t)=(-0.0043r^2+0.046r+2.48)(t+900)-25\,000. \quad (1)$$

Figure 10 shows a planview of the modeled wavefront position at several times in intervals of 30 min; the acoustic path is defined as the line $x=0$ km.

The modeled wavefront moves with a speed of about 2.5 m/s over the acoustic path. While average wavefront speeds through the length of the Strait are much slower, 2.5 m/s is consistent with observations of internal solitary waves exiting the narrows (Richez, 1994; Armi and Farmer, 1988; Farmer and Armi, 1988; Ziegenbein, 1970).

Vertical displacements caused by a passing internal solitary wave packet in the Strait have been measured in numerous echo sounder and thermistor observations (Armi and Farmer, 1988; Farmer and Armi, 1988; Watson, 1994; Wesson and Gregg, 1988; Ziegenbein, 1970; Frassetto, 1964). Of those observed in the narrows near the acoustic path, the internal bore has usually evolved into a packet of four or more solitary waves. Any vertical displacement history for a solitary wave packet can be supplied to the model, and an echosounder observation from Armi and Farmer (1988, Fig. 12.5), taken near the middle of the T1–T3 acoustic path, was used because of its clarity and proximity to the location under study. The bottom panel of Fig. 10 shows a vertical section of the internal solitary wave packet input into the model. Within the model, the vertical shape of the packet

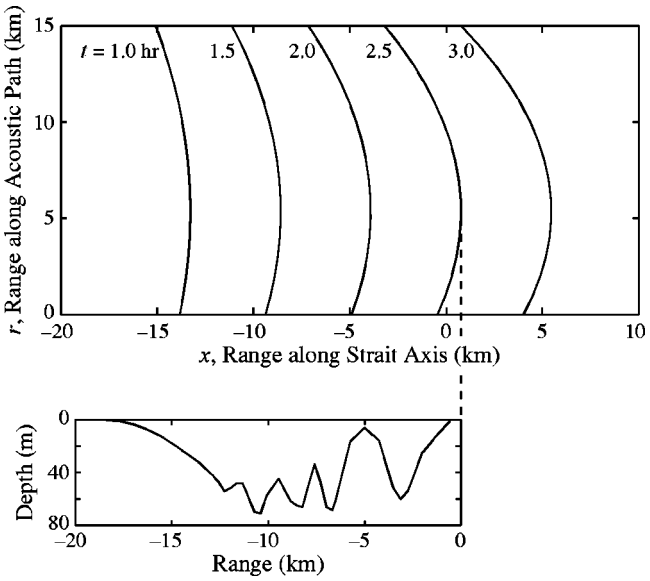

FIG. 10. A planview of modeled wavefront position at 30-min intervals as defined by Eq. (1), and a vertical section of the modeled solitary wave packet. Direction of propagation is to the right (east). The head of the packet (at range = 0 km) is shown aligned with the propagating wavefront curve at the time = 2.5 h position.

does not evolve during the time it moves over the acoustic path, but this same simplification has been made in several other internal wave studies (Duda and Preisig, 1999; Preisig and Duda, 1997; Zhou *et al.*, 1991; Baxter and Orr, 1982).

While the vertical shape of a solitary wave packet is the same at all ranges along the acoustic path, the model allows the amplitude of the solitary waves to be scaled as a function of range across the Strait. Although there are no direct observations of internal wave amplitude as a function of cross-Strait range, Watson (1994) reports that the amplitude of the waves is comparable to the depth of the upper Atlantic water layer. Because the upper layer deepens from north to south across the Strait, an increasing scaling was applied to the internal wave amplitude in the same direction. Bray *et al.* (1995) report the average interface depth in the eastern part of the Strait to be between 75 and 100 m; the upper limit of those average depths is used as the average internal wave amplitude in the model in an effort to reproduce the oceanography of spring tides, when internal waves are biggest. A cross-Strait salinity contour at 37.6 psu taken from the interpolated background salinity profiles passes through 100-m depth in the middle of the acoustic path and has endpoints at 70- and 125-m depth. The slope defined by that contour is in agreement with other observations of the sloping interface (Send *et al.*, 2000; Bray *et al.*, 1995), and the difference of the endpoint depths, 55 m, is within the range of values reported by Watson and Robinson (1991). Therefore, within the model, internal solitary wave packets were assigned a maximum vertical amplitude of 70 m on the northern side of the acoustic path and a maximum amplitude of 125 m on the southern side.

Once defined, the horizontal wavefront shape and the wave packet's vertical shape are combined within the model. The head of the wave packet is placed on the horizontal wavefront, and the wavefront is allowed to propagate over the acoustic path as the model steps through time, moving the packet with it. The result was a vertical displacement, due to internal solitary waves, as a function of cross-Strait range and time. In order to add depth dependence, the displacement was then scaled by a vertical mode 1 function, as calculated from range-dependent buoyancy frequency profiles. Next, the scaled displacement was multiplied by the potential soundspeed gradient (dc/dz) profile for its range to determine soundspeed perturbations at each depth. Finally, the soundspeed perturbations were added to the tidally shifting background soundspeed profiles, giving range-, depth-, and time-dependent soundspeeds for use in the acoustic propagation calculations.

D. Acoustic propagation calculations

The acoustic ray-tracing code RAY was used to find eigenrays between the T1 and T3 instruments through range- and time-dependent soundspeed profiles constructed by the Gibraltar model. Ray traces through a 12-h tidal cycle were calculated with increments in time of 5 min. In searching for eigenrays, the program used a fan of 400 rays with launch angles from the T1 instrument of -6 degrees to $+7$ degrees from horizontal.

V. MODEL RESULTS

Predicted travel times output by the acoustic propagation code were first compared to acoustic data from times of spring tides. Several important features of the data were successfully matched by the model, and examination of modeled ray paths throughout a tidal cycle provides valuable insight into how passing internal waves and tidal swings are affecting acoustic propagation. As a further test of the model, some input parameters were changed to simulate a neap tidal cycle, the forward problem recalculated, and comparisons made between predicted and measured neap tide travel times.

A. Spring tide travel times

Predicted ray travel times during one modeled tidal cycle are shown in Fig. 11 along with a typical 12 h of spring tide acoustic data from the T3 instrument for comparison. The following key features, labeled in Fig. 11(b) for identification, are seen repeatedly in the real data and were successfully reproduced in the simulation:

(a) A nearly constant travel time for the earliest arrival, the lower ray.
(b) Multiple later arrivals of upper rays at the beginning and end of the tidal cycle.
(c) A sudden and drastic decrease, then brief increase, in travel times of both upper and lower rays as an internal wave packet crosses the acoustic path.
(d) A brief and isolated cloud of upper ray arrivals at hour 4.75.
(e) Upper and lower rays with similar travel times during the middle of the tidal cycle.
(f) The absence of multiple late-arriving upper rays during the middle of the tidal cycle which reappear at hour 9.

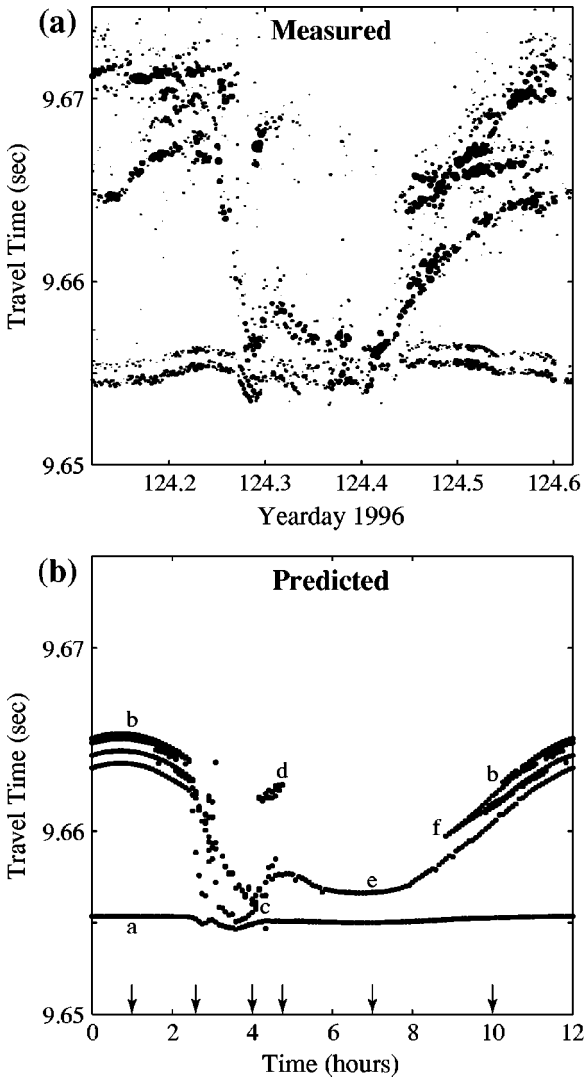

FIG. 11. (a) and (b) Measured and predicted ray travel times over a 12-h spring tidal cycle. The labels in (b) (''a'' through ''f'') identify key features of the model output which match the recorded data and are described in the text. Small arrows indicate times for which ray paths are shown in Fig. 12.

The largest discrepancy between the measured and predicted travel times is the time separation between arrivals of lower and upper rays at the beginning of the tidal cycle, which is greater than shown in the simulated data. This is probably due to errors in the background soundspeed profiles; environmental data was limited during profile construction, and the modeled profiles are known to be less accurate at the extremes of the tidal swing. The current-induced effects on travel time along the T1–T3 path, assumed to be negligible, could account for some error as well. The measured acoustic data also shows two lower ray arrivals at T3, the earlier at 9.655 s being stronger, while the modeled data only shows one lower ray arrival. The second, weaker ray arrival may be due to a bottom reflection very near one of the instruments as such a second arrival is not seen in the reciprocal acoustic data at T1 nor has it been reproduced in any modeling attempt.

B. Spring tide ray paths

Figure 12 shows the evolution over a spring tidal cycle of both the soundspeed field and resulting acoustic ray paths

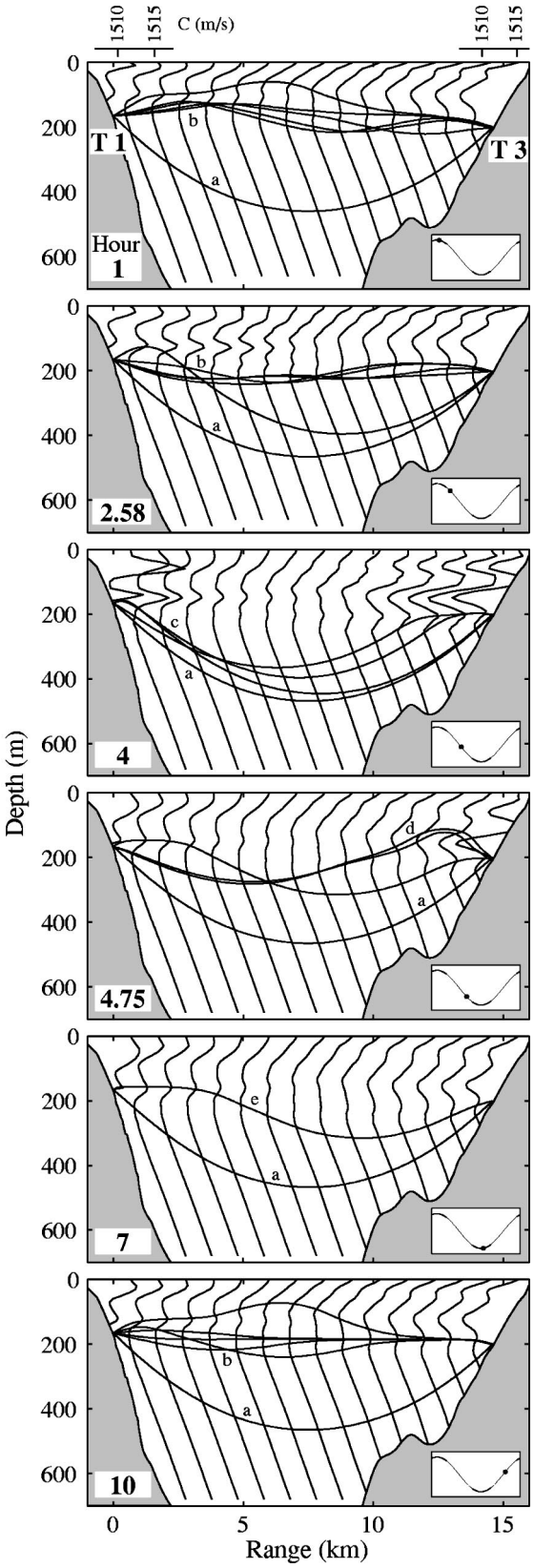

FIG. 12. Vertical sections along the T1–T3 acoustic path showing background soundspeed profiles and predicted ray paths at several times in a 12-h spring tidal cycle. Inset shows phase within the tidal cycle. The view is looking west with the southern T1 source on the left. The ray identifiers (''a'' through ''e'') correspond to the same labels of Fig. 11(b). Scale for profile values is the same for all profiles but offset in range.

from the T1 to T3 instruments. Each ray path will have a corresponding dot in Fig. 11(b) indicating its travel time, and the same labels used in Fig. 11(b) (''a'' to ''e'') are also used in identifying the corresponding ray paths of Fig. 12. Together, Figs. 11 and 12 can describe a ray by its path and travel time.

At the start of the tidal cycle (Fig. 12, hour 1), the soundspeed profiles are unperturbed by any internal solitary waves but are at a maximum tidal displacement upward. A single lower ray (a) and several upper rays (b) are seen, and their travel times can be found using the same labels on Fig. 11(b) at time=1 hour. For example, the travel time for the lower ray path (a) is 9.655 s. One upper ray travels briefly in a very shallow sound channel near 80-m depth while other upper rays are trapped in a channel near 150-m depth. These double soundspeed minimums are critical to reproducing the wide spread in the upper ray travel times. When smooth soundspeed profiles with only one minimum are used in the model, all upper rays arrive with almost identical travel times which does not agree with the recorded data.

At hour 2.58, the wavefront of the internal solitary wave packet is starting to cross the southern end of the acoustic path near the source at T1. The soundspeed profiles of Fig. 12, hour 2.58, show how gradients in the southern profiles are increasing as warm shallow water is being displaced deeper by the passing internal waves, and the gradient beneath the shallowest soundspeed minimum is now strong enough to refract shallow rays away from it soon after they leave the source. While the single deep ray (a) and main cluster of shallow rays (b) follow similar paths as before, the ray that used to travel in the shallowest sound channel has been refracted down to a much deeper path. The disappearance of the latest ray arrival at time=2.58 h in Fig. 11(b) confirms that the very shallow ray path no longer exists.

Due to the curvature of the propagating wavefront, at hour 4 the perturbations of the solitary wave packet are felt mainly at the endpoints of the acoustic path and less so in the middle of the path. Figure 12, hour 4, represents this as very strong soundspeed gradients in the northern- and southernmost profiles. The soundspeed gradient is now so strong near the source that all rays that used to be upper rays (c) are immediately refracted down to follow paths very similar to the lower ray (a). Rays that follow similar paths should have similar travel times, and that is confirmed in Fig. 11(b) as all ray arrivals are within 2 ms of each other at time=4 h. The rapid decrease in travel times from hours 2.58 to 4 is not caused by a single soliton crossing the acoustic path, but rather is the cumulative effect of an entire packet of solitary waves, on a curved wavefront, crossing the acoustic path. A modeled wavefront speed of about 2.5 m/s is necessary to match the observed duration of the sharp travel time decrease, confirming measurements of internal wave phase speed in this region of the Strait.

Both the measured and predicted travel time data show a brief and isolated group of late ray arrivals shortly following the sudden decrease in travel times. These rays are labeled ''d'' in Fig. 11(b) at time=4.75 h, and Fig. 12, hour 4.75, shows why they appear. At that time, the packet of internal solitary waves has moved past the source at T1, but because of the curvature of the wavefront, the packet is still present at the T3 receiver. The large soundspeed gradients it causes directly over the receiver are strong enough to refract a group of upper rays (d) down relatively quickly to hit the receiver from above. With the passing of the solitary wave packet, the strong soundspeed gradients over the receiver will disappear along with the ray paths they allow; this is confirmed in Fig. 11(b) with the end of the ray arrivals at ''d.''

At hour 7, the solitary wave packet has moved completely over the acoustic path and is no longer causing any soundspeed perturbations. However, this is the hour of maximum downward internal tide displacement which can be visualized by comparing the soundspeed profiles of Fig. 12, hour 7, with those of hour 1. At hour 7, the lower ray (a) persists, along with a single upper ray (e). The single upper ray explains the absence of multiple late arrivals in Fig. 11(b) between time=5 h to time=9 h. The changes in upper ray travel time during those hours are due entirely to the internal tide shifting the background soundspeed field. A ray may stay within the same sound channel over much of the tidal cycle, but a ray's path length must change in order to remain within that shifting channel, resulting in changes in its travel time. Because tidal soundspeed perturbations are scaled by a vertical mode 1 function, the deepest parts of the soundspeed profiles are changed only slightly, and thus the lower ray travel time does not change significantly.

By hour 10, the tidal cycle is nearing completion. Internal tide displacements are increasing in the upward direction, and there are no internal solitary wave perturbations. Figure 12, hour 10, shows that several upper rays (b) are again using the main sound channel at 170-m depth, and access to the shallowest sound channel has returned as well. Multiple late arrivals are present again in Fig. 11(b) at time=10 h, and the upper ray travel times will continue to increase to their maximum with the increasing internal tide displacements.

C. Neap tide travel times

While the Gibraltar model was created to aid in understanding acoustic propagation during the more interesting spring tides when internal bores are present and internal tides are strongest, a good test of the model would be to explore how well it can also reproduce neap tide travel times. Figure 13(a) shows 12 h of acoustic travel time data from the T3 instrument, taken during a neap tide. Typically, the neap tide acoustic data does not show the sudden drop in travel times as internal solitary wave packets are much smaller in amplitude or nonexistent. Furthermore, the amplitude of the internal tide is less during neap tides, so the travel time variability between the top and bottom of a tidal cycle should be less as well.

A new unperturbed background soundspeed profile was not constructed for the model's neap tide test, but model parameters describing internal solitary wave and internal tide amplitudes were adjusted. Because the acoustic data shows minor fluctuations in upper ray travel times, the internal solitary wave amplitude was not set to 0% but rather 5% of the spring tide amplitude. However, this may just be a crude way of modeling some background internal wave activity and not

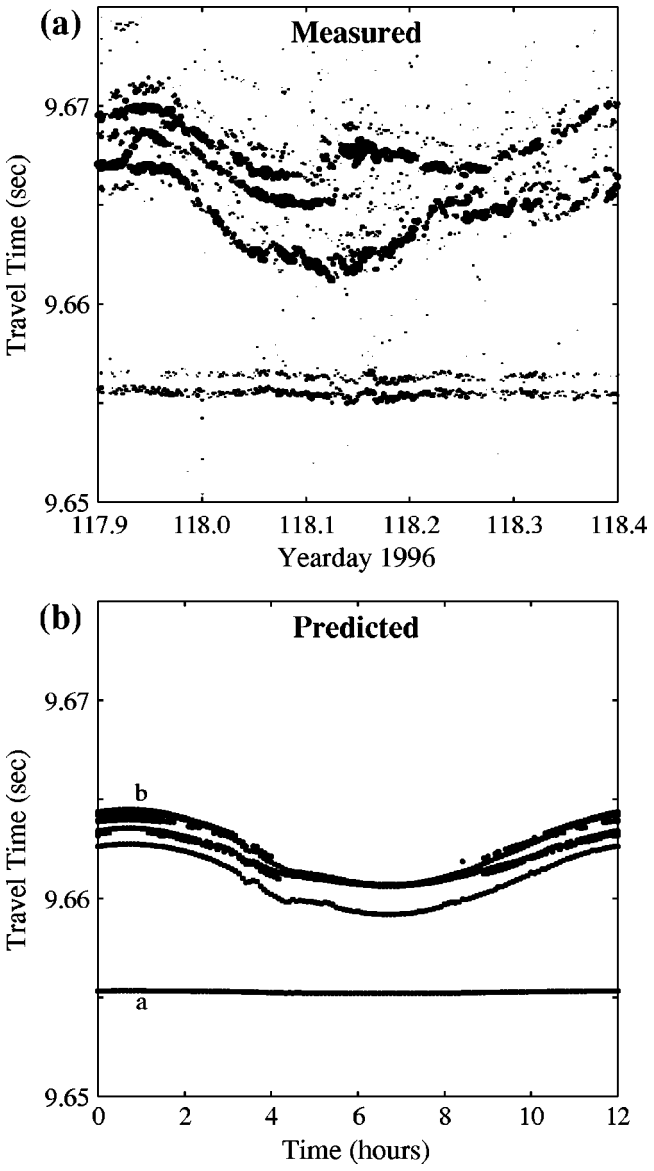

FIG. 13. (a) and (b) Measured and predicted ray travel times over a 12-h neap tidal cycle. The labels in (b) (''a'' and ''b'') identify key features of the model output which match the recorded data and are described in the text.

necessarily a propagating packet of internal solitary waves. Tidal amplitude was reduced to a ± 20-m tidal swing at the source and ± 10-m swing at the receiver, approximately half the spring tide amplitudes.

Figure 13(b) shows the predicted travel times from one neap tidal cycle as output by the acoustic propagation code, and fortunately, it has reproduced many key features of the measured neap tide data. The lower ray travel time (a) is constant over the tidal cycle, and multiple upper ray arrivals (b) are present at all times, some even with minor fluctuations. Unlike the spring tide case, there is no absence of upper rays during the middle of the tidal cycle nor any sharp decrease in travel times, and the predicted overall travel time variability is less due to smaller tidal amplitudes. Again, the biggest discrepancy between the real and predicted data is in the time separation of lower and upper ray travel times, but this is probably due to the same reason mentioned earlier for the spring tide case.

VI. SUMMARY

Given the complexity of both the Gibraltar experiment's data set and the environment of the Strait, the challenge is to explain the acoustic observations in terms of physical processes. The model discussed in this article is a valuable tool for doing so. To construct a range- and time-dependent soundspeed field for use in acoustic propagation calculations, internal tides and propagating internal solitary waves are modeled separately and their perturbations to a background soundspeed field combined.

Forward problem calculations over a simulated tidal cycle were successful in reproducing many important features of the acoustic data at times of both spring and neap tides. Furthermore, the evolution of the modeled background soundspeed field and acoustic ray paths as they change due to internal wave and internal tide perturbations provides a qualitative explanation for the observed acoustic scattering. For example, this work has shown how the arrival of an internal solitary wave can deny rays access to previously used sound channels. The vertical shifting of soundspeed profiles by internal tides further increases travel time variability.

Work with the model has shown that both internal wave and internal tide effects must be combined to reproduce the observed acoustic channel impulse response; either one individually cannot explain all the travel time variability. Comparison between the spring and neap tide cases emphasizes the significant acoustic scattering in the presence of a large-amplitude internal solitary wave packet, and the Gibraltar experiment has isolated the scattering effects of a packet to just 2 h out of a tidal cycle. These results also suggest that it may be feasible to use acoustics for remote sensing of internal solitary waves.

ACKNOWLEDGMENTS

U. Send was the principal investigator for the Gibraltar Acoustic Monitoring Experiment at the University of Kiel. B. Baschek provided analysis of the environmental data taken during the experiment. T. Birdsall and K. Metzger designed the 2-kHz signals and signal processing. M. Dzieciuch assisted with the data analysis. J. Apel acquired and processed the SAR image of Fig. 1. R. J. Small provided the SAR image of Fig. 9. D. Farmer and L. Armi participated in many helpful discussions during the design and analysis of the experiment. The first phase of the field work was conducted with the able assistance of the crew of the German research vessel F/S POSEIDON. The 2-kHz instruments were recovered by the Spanish Naval research vessel MALASPINA, which was generously made available to us by the Spanish Navy, with J. Rico (Instituto Hidrografico de la Marina, Cádiz, Spain) as Chief Scientist. The acoustic instrumentation was designed, fabricated, tested, and fielded by L. Day, K. Hardy, D. Horwitt, D. Peckham, and A. Rivera. B. Betts prepared the illustrations. This work was supported by the Office of Naval Research (ONR Grant No. N00014-95-1-0072) and the European Community MAST

program (EC MAST-3 Contract No. MAS3-CT96-0060). C. Tiemann was supported by an ONR AASERT grant (ONR Grant No. N00014-95-1-0795).

Alpers, W., and La Violette, P. (**1993**). ''Tide-generated nonlinear internal wave packets in the Strait of Gibraltar observed by the synthetic aperture radar aboard the ERS-1 satellite,'' in *Proceedings of the First ERS-1 Symposium*, Eur. Space Agency Spec. Publ. ESA-SP 359(2), edited by B. Kaldeich (ESA Publications Division, Noordwijk, The Netherlands), pp. 753–758.

Apel, J., Badiey, M., Chiu, C., Finette, S., Headrick, R., Kemp, J., Lynch, J., Newhall, A., Orr, M., Pasewark, B., Tielbuerger, D., Turgut, A., von der Heydt, K., and Wolf, S. (**1997**). ''An overview of the 1995 SWARM shallow-water internal wave acoustic scattering experiment,'' IEEE J. Ocean Eng. **22**(3), 465–500.

Armi, L., and Farmer, D. M. (**1988**). ''The flow of Mediterranean water through the Strait of Gibraltar,'' Prog. Oceanogr. **21**, 1–105.

Baschek, B., Send, U., Lafuente, J. G., and Candela, J. (**2000**). ''Transport estimates in the Strait of Gibraltar with a tidal inverse model,'' J. Geophys. Res. (submitted).

Baxter, L., and Orr, M. (**1982**). ''Fluctuations in sound transmission through internal waves associated with the thermocline: A computer model for acoustic transmission through sound velocity fields calculated from thermistor chain, CTD, XBT, and acoustic backscattering,'' J. Acoust. Soc. Am. **71**, 61–66.

Bowlin, J., Spiesberger, J., Duda, T., and Freitag, L. (**1992**). ''Ocean Acoustical Ray-Tracking Software RAY,'' Woods Hole Oceanographic Institution Technical Report WHOI-93-10.

Boyce, F. (**1975**). ''Internal waves in the Straits of Gibraltar,'' Deep-Sea Res. Oceanogr. Abstr. **22**, 597–610.

Bray, N., Ochoa, J., and Kinder, T. (**1995**). ''The role of the interface in exchange through the Strait of Gibraltar,'' J. Geophys. Res. **100**(C6), 10755–10776.

Bray, N., Winant, C., Kinder, T., and Candela, J. (**1990**). ''Generation and kinematics of the internal tide in the Strait of Gibraltar,'' in *The Physical Oceanography of Sea Straits*, edited by L. Pratt (Kluwer Academic, Dordrecht), pp. 477–491.

Candela, J., Winant, C., and Ruiz, A. (**1990**). ''Tides in the Strait of Gibraltar,'' J. Geophys. Res. **95**(C5), 7313–7335.

Duda, T., and Preisig, J. (**1999**). ''A modeling study of acoustic propagation through moving shallow-water solitary wave packets,'' IEEE J. Ocean Eng. **24**(1), 16–32.

Essen, H., Schirmer, F., and Sirkes, S. (**1983**). ''Acoustic remote sensing of internal waves in shallow water,'' Int. J. Remote Sens. **4**(1), 33–47.

Farmer, D. M., and Armi, L. (**1988**). ''The flow of Atlantic water through the Strait of Gibraltar,'' Prog. Oceanogr. **21**, 1–105.

Flatté, S. (**1983**). ''Wave propagation through random media: Contributions from ocean acoustics,'' Proc. IEEE **71**, 1267–1294.

Flatté, S., Dashen, R., Munk, W., Watson, K., and Zachariasen, F. (**1979**). *Sound Transmission Through a Fluctuating Ocean* (Cambridge University Press, Cambridge, England).

Frassetto, R. (**1964**). ''Short period vertical displacements of the upper layers in the Straits of Gibraltar,'' Technical Report, SACLANT A.S.W. Research Center, La Spezia.

Lynch, J. F., Guoliang, J., Pawlowicz, R., Ray, D., Plueddemann, A. J., Chiu, C., Miller, J. H., Bourke, R. H., Parsons, A. R., and Muench, R. (**1996**). ''Acoustic travel time perturbations due to shallow water internal waves and internal tides in the Barents Sea polar front: theory and experiment,'' J. Acoust. Soc. Am. **99**, 803–821.

Munk, W., Worcester, P., and Wunsch, C. (**1995**). *Ocean Acoustic Tomography* (Cambridge University Press, Cambridge, England).

Preisig, J., and Duda, T. F. (**1997**). ''Coupled acoustic mode propagation through continental-shelf internal solitary waves,'' IEEE J. Ocean Eng. **22**(2), 256–269.

Richez, C. (**1994**). ''Airborne synthetic aperture radar tracking of internal waves in the Strait of Gibraltar,'' Prog. Oceanogr. **33**, 93–159.

Rubenstein, D., and Brill, M. H. (**1991**). ''Acoustic variability due to internal waves and surface waves in shallow water,'' in *Ocean Variability and Acoustic Propagation*, edited by J. Potter and A. Warn-Varnas (Kluwer Academic, Dordrecht), pp. 215–228.

Send, U., Worcester, P. F., Cornuelle, B. D., Tiemann, C. O., and Baschek, B. (**2000**). ''Integral measurements of mass transport and heat content in straits from acoustic transmissions,'' Deep Sea Research (submitted).

Tang, X., and Tappert, F. D. (**1997**). ''Effects of internal waves on sound pulse propagation in the Straits of Florida,'' IEEE J. Ocean Eng. **22**(2), 245–255.

Tielburger, D., Finette, S., and Wolf, S. (**1997**). ''Acoustic propagation through an internal wave field in a shallow water waveguide,'' J. Acoust. Soc. Am. **101**, 789–808.

Tiemann, C. O., Worcester, P. F., Cornuelle, B. D., and Send, U. (**1998**). ''Effects of internal waves and bores on acoustic transmissions in the Strait of Gibraltar,'' in ONR Workshop on Internal Solitary Waves in the Ocean: Their Physics and Implications for Acoustics, Biology, and Geology, Victoria, B. C., Canada, 27–29 October 1998, Woods Hole Oceanographic Institution Technical Report WHOI-99-07.

Traykovski, P. (**1996**). ''Travel-time perturbations due to internal waves: Equivalence of modal and ray solutions,'' J. Acoust. Soc. Am. **99**, 822–830.

Watson, G. (**1994**). ''Internal waves in a stratified shear flow: The Strait of Gibraltar,'' J. Phys. Oceanogr. **24**(2), 509–517.

Watson, G., and Robinson, I. (**1990**). ''A study of internal wave propagation in the Strait of Gibraltar using shore-based marine radar images,'' J. Phys. Oceanogr. **20**, 374–395.

Watson, G., and Robinson, I. (**1991**). ''A numerical model of internal wave refraction in the Strait of Gibraltar,'' J. Phys. Oceanogr. **21**(2), 185–204.

Wesson, J. C. and Gregg, M. C. (**1988**). ''Turbulent dissipation in the Strait of Gibraltar and associated mixing,'' in *Small-Scale Turbulence and Mixing in the Ocean*, edited by J. Nihoul and B. Jamart (Elsevier, Amsterdam), pp. 201–212.

Zhou, J., Zhang, X., and Rogers, P. H. (**1991**). ''Resonant interaction of sound wave with internal solitons in the coastal zone,'' J. Acoust. Soc. Am. **90**, 2042–2054.

Ziegenbein, J. (**1970**). ''Spatial observations of short internal waves in the Strait of Gibraltar,'' Deep-Sea Res. Oceanogr. Abstr. **17**, 867–875.

A least squares method of estimating length to target strength relationships from *in situ* target strength distributions and length frequencies

Patrick L. Cordue, Roger F. Coombs, and Gavin J. Macaulay
National Institute of Water and Atmospheric Research, P.O. Box 14-901, Wellington, New Zealand

(Received 22 May 2000; revised 25 September 2000; accepted 4 October 2000)

A least squares method is presented for estimating length to target strength relationships for a target species and associated species using a series of target strength distributions and associated trawl catches. A by-product of the estimation procedure is an objective determination of the correspondence between modal lengths in the trawl catches and the modal lengths in the associated target strength distributions. The method is illustrated by applying it to a data set collected to determine the length to target strength relationship for hoki (*Macruronus novaezelandiae*). © *2001 Acoustical Society of America.* [DOI: 10.1121/1.1329621]

PACS numbers: 43.30.Sf, 43.30.Gv, 43.80.Jz [DLB]

I. INTRODUCTION

The estimation of a length to target strength relationship for a given species can be done in several ways. Indirect methods use models of the acoustic scattering properties of the target species and an assumed tilt angle distribution to estimate the tilt averaged target strength for any given length (Coombs and Cordue, 1995; McClatchie and Ye, 2000). Direct methods use measurements of target strength obtained from individuals of the target species. This has been done by using live or dead fish in the laboratory or, more commonly, by collecting acoustic data from the target species *in situ* (MacLennan and Simmonds, 1992). The latter approach has two inherent difficulties: identifying which echoes are from single targets, and identifying the species mix and size distribution of the single targets.

The first problem is overcome by using a reliable single target detection algorithm (e.g., Soule *et al.*, 1997). Acoustic data collected from an aggregation of fish can then be used to produce a distribution of single targets. The identification of the species mix and size distribution of the single targets is usually done by sampling targeted trawl catches. However, if there is a mix of species present or a single species with several size classes, then it can be difficult to decide how the species and size classes relate to the target strength distribution. The usual approach to overcome this difficulty is to find primarily single species aggregations of the target species which have a uni-modal length distribution. The mode in the length frequency is then taken to correspond to the main mode in the target strength distribution. Data are collected from as many aggregations as possible and the resulting pairs of modal lengths and modal target strengths are used in a regression to estimate the length to target strength relationship (Foote, 1987).

This approach should work well if a sufficient number of suitable aggregations can be found over a wide enough range of length modes. However, for some species it may be difficult to find suitable aggregations and the norm will be for the target strength distribution to be multi-modal and for there to be several species and size classes present in the trawl catches. Such data can still be used to produce pairs of modal lengths and modal target strengths for use in a regression. However, the choice of which target strength mode corresponds to a length mode of the target species is usually done in a sequential and subjective fashion. Thus an error in the interpretation of an ''early'' data set can lead to further errors as modes in ''new'' data sets are misassigned based on the earlier interpretation.

In this article we present a method of estimating length to target strength relationships for a target species and associated species using a series of target strength distributions and associated trawl catches. A by-product of the estimation procedure is an objective determination of the correspondence between modal lengths in the trawl catches and the modal lengths in the associated target strength distributions. The method is illustrated by applying it to a data set collected to determine the length to target strength relationship for hoki (*Macruronus novaezelandiae*).

II. METHODS

The estimation method is the focus of this section; the data collection methods for the illustrative data set and the application of the estimation procedure to it are also described, but these descriptions are kept as brief as possible.

A. Estimation procedure

The estimation procedure assumes that there are one or more target strength (TS) distributions, and that for each TS distribution there are associated length frequencies for one or more species. There are three main steps in the procedure: determination of the TS modes; determination of the length frequency modes; and minimization of a sum of squared residuals. In the sum of squares the observed values are the TS and length frequency modes, and the predicted values are those obtained from a simple model whose unknown parameters are the true length frequency modes and the coefficients of the length to TS relationships of all species in the length frequencies.

Assume that there are n TS distributions and denote the jth mode in the ith TS distribution as T_{ij} and let m_i be the number of TS modes in the ith distribution. Further, let L_{isk} denote the kth mode for species s in the ith length frequency, and let m_{is} be the number of length frequency modes for species s in the ith length frequency. Note that some of the m_{is} may be equal to zero for some species.

The model assumes for each species a log linear relationship between TS and length:

$$\mathrm{TS}_s(l) = a_s + b_s \log_{10}(l)$$

and that the true length modes l_{isk} may differ from the observed length modes:

$$l_{isk} = L_{isk} + \alpha_{isk}$$

where α_{isk} is an unknown error.

The independent unknown parameters in the model are therefore the a_s, the b_s, and the l_{isk}. They are estimated by minimizing the following sum of squares:

$$\sum_{isk} u_{isk}[l_{isk} - L_{isk}]^2 + w_{isk}[\mathrm{TS}_s(l_{isk}) - \mathrm{TS}_{isk}]^2,$$

where the u_{isk} and w_{isk} are specified weights and TS_{isk} is the T_{ij} which is closest to $\mathrm{TS}_s(l_{isk})$ in terms of minimum absolute difference. The rationale behind this approach is the hope that each length frequency mode will contribute to a mode in the corresponding TS distribution which on average is not too far away from the modal TS corresponding to the length frequency mode. Because the assignment of TS modes to length frequency modes is done simultaneously with the estimation of the length to TS parameters, the consistency of the assignments is guaranteed to the extent that the data are consistent (with the assumed model).

The use of weights in the sum of squares is to allow for different levels of sampling effort, or other measures of ''quality'' with regard to the data used in the TS distributions and length frequencies. In general, the better the ''quality'' of a distribution the higher the weight it should be given. With regard to the length frequencies, the higher the weight assigned to a mode the closer the predicted mode will be to the observed mode.

The minimization of the sum of squares is technically somewhat problematic. As a function of the unknown parameters the sum of squares is continuous and differentiable. However, for most data sets the surface will contain numerous local minima. This is because for any particular association of length modes with TS modes there will be a region of best fit which produces a local minimum (it may not be a ''good'' fit, but locally it is the best). The minimization of the sum of squares is therefore a problem of *global* minimization. The solution used in this article was to randomly select a large number of starting points for the minimizer, and to determine the minimum over all of the minimizer runs. The model was implemented using C++ classes which use the Autodif libraries (Otter Research, 1992). Autodif uses automatic differentiation classes and has a quasi-Newton minimizer.

The determination of modes from the TS distributions and length frequencies is a necessary part of the estimation procedure, but the method by which they are determined is not central to this article. However, there are a few important points to note. Estimation of the modes ''by eye'' is subjective. It is preferable to use an algorithm which produces modes which, ''by eye,'' appear to be sensibly positioned on a histogram of the distribution. For the TS distributions it is important to include all modes including ''shoulders'' [that is a mode which is half covered by another mode; see Fig. 1(b)]. For the length frequencies, it is better to exclude a doubtful mode than to include it. The reason for the different treatments of TS distributions and length frequencies is that each length mode must be explained by a TS mode (in the sum of squares), but superfluous TS modes can be ignored.

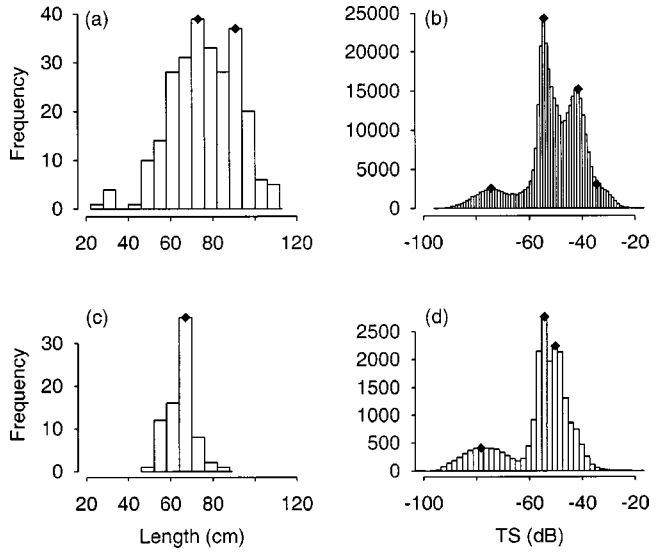

FIG. 1. Examples of modes and a shoulder [see (b)] for hoki length frequencies and associated target strength distributions used in the estimation procedure: (a) hoki length frequency from the KAHAROA voyage, station 9; (b) TS distribution after single target filtering for KAHAROA set 2; (c) hoki length frequency from the TANGAROA voyage, station 131; and (d) TS distribution after single target filtering for TANGAROA set 6.

To obtain a measure of the confidence of the TS parameter estimates, a simple nonparametric bootstrap procedure is proposed. For any given species for which a length to target strength relationship is estimated, there is a set of observed and predicted length modes, and a set of observed and predicted TS modes. These then yield a set of length mode residuals and TS mode residuals. The bootstrap procedure involves doing a large number of simulation runs. On each run a simulated set of ''observed'' length modes and TS modes is generated. Using the simulated data, a weighted least squares regression is done to estimate a length to TS relationship. The coefficients of the relationship are stored; then for any given length, a distribution of TS values can be generated (one from each relationship) and a confidence interval on TS can be obtained for that length. This can be done over a range of lengths and so a confidence region can be obtained.

A simulated set of observed length modes is obtained by adding a random length mode residual to each predicted length mode, and a simulated set of observed TS modes is obtained by adding a random TS mode residual to each predicted TS mode. The sampling of the length residuals and the

TABLE I. Descriptive details for the target strength distributions with the station numbers of the associated trawls.

Voyage	TS distribution	Collection period (h)	No. of single echoes (thousand)	Associated trawls (station no.)
KAH9911	K1	2.5	153	7, 8
(Cook Strait)	K2	4.5	381	9, 10, 11
	K3	5.1	88	12, 13
TAN9901	T1	3.4	31	117, 118, 119
(Chatham Rise)	T2	3.1	31	120, 121, 122
	T3	1.2	16	130
	T4	1.2	12	133
	T5	1.2	10	132
	T6	2.5	21	131
	T7	3.1	34	141, 142

TS residuals should be done independently. The length and TS residuals from the original estimation will actually be negatively correlated. For example, if a predicted TS mode is higher than the corresponding observed TS mode, then the predicted length mode will be less than the observed length mode (to the extent that it can be given the weights in the sum of squares) because a shorter length yields a lower TS (which gives a better fit). However, the correlation caused by the estimation procedure should not be used in generating the simulated data as there is no reason to suppose that the observation errors of the length modes should be correlated with the observation errors of the TS modes.

B. Hoki data set

Hoki are a commercially important species to the New Zealand fishing industry and the research program on hoki has included acoustic biomass surveys since the mid-1980s. Early attempts at estimating the length to TS relationship for hoki were done using simple swimbladder modeling techniques (Do and Surti, 1990; Coombs and Cordue, 1995). A reanalysis of the early data using more sophisticated swimbladder models (Grimes *et al.*, 1997) cast some doubt on the assumed relationship, and *in situ* data have recently been collected to help in its determination.

The data analyzed in this article were collected during two voyages in 1999. The first voyage was a trawl survey of the Chatham Rise in January conducted by NIWA's research vessel TANGAROA (a 70-m stern trawler). From 22–26 January, at the end of the trawl survey component of the voyage, acoustic data and trawl data were collected from layers containing hoki. A calibrated 38-kHz split beam echo sounder (Coombs, 1994) was used with the transducer in a towed body which was deployed within 30 to 70 m of the layer. Length frequency and species mix data were collected from the layers by trawling (on one occasion a mid-water trawl was used, on all other occasions the standard hoki bottom trawl was used; see Hurst and Bagley, 1994). The acoustic data were filtered using a single target detection algorithm based on the methods of Soule *et al.* (1997). Consideration is given to several echo characteristics: the width of the combined beam, the relative widths of the four beams, the phase stability of the combined beam and of the individual beams, the proximity of other echoes, the similarity of amplitudes between beams, and the angle of arrival of the echo (see Macaulay and Grimes, 2000).

The second voyage was an acoustic survey of spawning hoki biomass in Cook Strait during July and August conducted by NIWA's other open seas research vessel KAHAROA (a 28-m stern trawler). Target strength data were collected from 3–10 August using a nearly identical acoustic system to that used in the January survey. The same data collection and single target filtering methods were used. Layers were also sampled by trawling, except that a mid-water trawl was used (during the spawning season in Cook Strait hoki are normally in mid-water in and around canyon features).

C. Application of the estimation procedure to the hoki data set

On each of the voyages, there were some occasions on which more than one trawl sampled the layer from which target strength data were collected. In the fitting procedure, each trawl was used separately; that is the target strength distribution was paired with each of the corresponding trawls in turn. A reasonable alternative to this approach is to use the trawls to construct a single combined species and size distribution for the layer. However, it is not clear how to weight the different trawl catches and it may be that some loss of information would occur if the catches were combined.

A parametrized algorithm was used to define modes in the target strength distributions and the length frequencies; different parameters were used depending on the number of samples in each distribution. Details of the algorithm are in the Appendix.

For the length frequencies, all species for which samples of 50 or more were measured were used in the analysis. The algorithm detected the ''main modes,'' one or two modes in each hoki length frequency, and only one mode for each bycatch species. As a sensitivity test, an alternative result was obtained by using different parameter values which for some stations gave up to four hoki modes (but still only one mode for each bycatch species).

The specified weights for the sum of squares were calculated as the product of a (trawl) station weight and a constant ''length frequency weight'' (for the length mode portion of the sum of squares) or the station weight and a constant ''target strength weight'' (for the target strength portion of the sum of squares). The ''length frequency weight'' was 0.5 and the ''target strength weight'' was 1. The station weights were either 0.1 (when the hoki catch was less than 100 kg, and the hoki length frequency was used on that station), 2.0 for length frequency sample sizes from 500 to 700, or 1.0 for sample sizes up to 400 (see Table II). In an alternative weighting scheme the weights of 0.1 were replaced by weights of 1.

The baseline estimation used the ''main modes'' with the weighting scheme which down-weighted stations with low hoki catch. Two sensitivity runs were also done. Both used the alternative simpler weighting scheme, one with the ''main modes,'' and the other using the larger set of length frequency modes (''all modes'').

TABLE II. For each trawl station, the station weight used in the sum of squares, the catch of hoki, the percentage of hoki in the total catch (by weight), the number of hoki measured, and the catch of the main bycatch species. CBO: Bollen's rattail, COL: Oliver's rattail, GSH: ghost shark, LDO: lookdown dory, RBM: Ray's bream, SPD: spiny dogfish, and SPE: sea perch.

Trawl station	Station weight	Hoki catch (ton)	Hoki catch/ total catch (%)	No. of hoki measured	Bycatch species catch (when ⩾80 kg)
7	2	1.1	79	608	SPD 273
8	1	0.3	81	160	
9	1	0.4	99	257	
10	1	0.5	99	393	
11	1	0.4	97	260	
12	2	0.5	85	666	
13	2	0.4	85	586	
117	2	2.4	80	617	LDO 114, SPD 107, SPE 88
118	2	1.3	78	612	SPD 95
119	0.1	0.04	32	91	
120	2	4.2	91	679	GSH 147
121	2	2.3	76	626	SPD 175, SPE 243
122	2	0.4	82	516	RBM 88
130	2	1.2	70	629	CBO 168, COL 82
131	0.1	0.07	36	76	
132	0.1	0.09	32	103	
133	1	0.03	18	40	
141	1	0.2	49	254	
142	1	0.4	64	372	

In each of the three estimation runs, the slope of the hoki target strength relationship was estimated within the interval [5,95]. This interval was partitioned into nine or ten subintervals and each subinterval was used to bound the hoki slope while an estimation was done using 300 random starting values for the minimizer. This procedure was done for two or three further narrow subintervals (including a forced hoki slope of 20) so that the general trend in the sum of squares surface was determined for each run. In the baseline run, a further estimation was done using bounds on the hoki slope which included the best estimate from the initial runs. In this final estimation, 5000 random starting values were used and the global minimum was determined. The bootstrap procedure was only applied to the baseline estimation results and 1000 simulations were used to determine a 99% confidence region for the hoki regression line.

III. RESULTS

A total of about 30 h of target strength data was collected during the two voyages. There were three target strength sets on the KAHAROA voyage (KAH9911) and seven on the TANGAROA voyage (TAN9901), and there were 19 associated trawl stations (Table I). The KAHAROA target strength sets were very successful in the number of detected single echoes, with between about 80 000 and 380 000 targets being accepted in each of the three sets (Table I).

Hoki was the primary catch for most of the trawl stations with most hoki catches being greater than 200 kg and making up 70% or more of the total catch by weight (Table II). Hoki catches of less than 100 kg were made on four of the stations. In the baseline analysis, three of these stations were down-weighted (Table II). Station 133 was not down-weighted as the hoki length frequency was not used (since only 40 hoki were measured). For the small hoki catches, all of the hoki were measured. When larger catches were made, subsamples were taken with typically between 250 and 700 hoki being measured (Table II).

In total, the largest bycatch over the trawl stations came from spiny dogfish, with sea perch making the next largest contribution (Table II). On the TANGAROA trawl stations a bottom trawl was used and much of the bycatch came from what are probably bottom-dwelling species which would therefore make little contribution to the acoustic backscatter. Sea perch, lookdown dory, and ghost shark would fall within

TABLE III. The length frequency sample size for each trawl station for the bycatch species used in the analysis. ''–'' indicates that less than 50 were measured for that station. FRO: frost fish, CBI: two-saddle rattail, JAV: javelin fish, COL: Oliver's rattail, and CBO: Bollen's rattail.

Species code	Station no.								
	12	13	121	130	131	132	133	141	142
FRO	53	53	–	–	–	–	–	–	–
CBI	50	100	–	–	–	–	–	–	–
JAV	–	–	119	122	60	82	79	112	100
COL	–	–	–	103	86	135	97	69	–
CBO	–	–	–	115	–	76	–	87	60

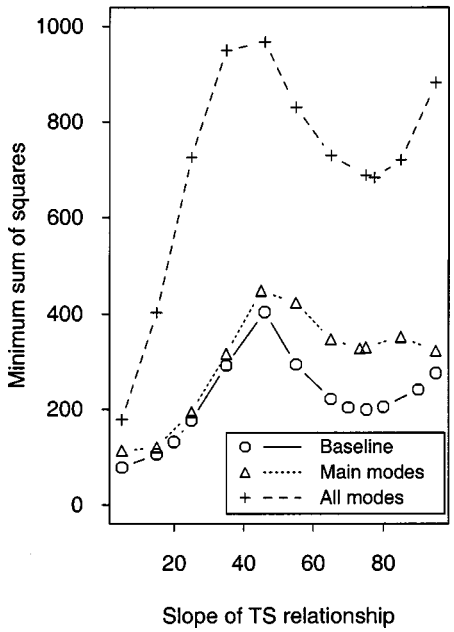

FIG. 2. The general trend in the shares of the sums of squares surfaces, with regard to the slope in the length to TS relationship for hoki, for the baseline run and the two sensitivity runs. ''Main modes'' uses the same length modes as the baseline but with a different weighting scheme. ''All modes'' uses the same weights as ''Main modes'' but with a much larger number of length modes.

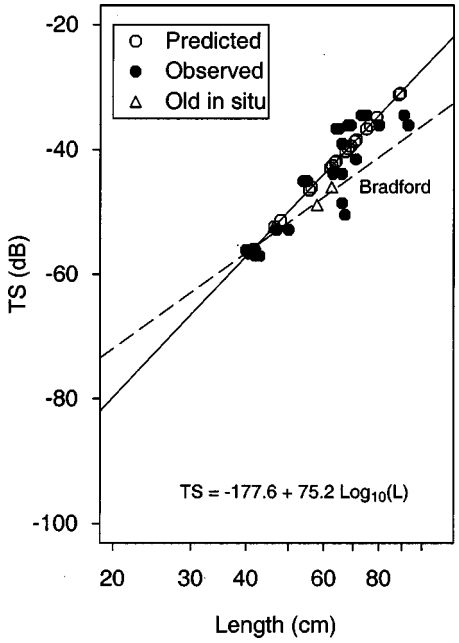

FIG. 3. The fitted length to target strength relationship for hoki in the baseline case (solid line). The relationship for hoki derived by Bradford (1999) is also shown (dashed line) with the three previously accepted *in situ* data points (triangles).

this category. For the bycatch species the length frequency sample sizes were typically less than 100 and there were no common species between the KAHAROA and TANGAROA voyages (Table III).

Two examples of the hoki length frequencies and associated target strength distributions used in the analysis are given in Fig. 1. In the baseline analysis only the main modes were used [e.g., for station 9 the possible mode at 30 cm was used in a sensitivity run but excluded from the baseline run [Fig. 1(a)]. A small length frequency sample size does not necessarily mean that the length modes are not well defined. Arguably, the single mode for station 131 is better defined than the two modes for station 9 [Figs. 1(a) and (c)] despite the lower sample size (see Table II). The second KAHAROA TS set has a very smooth distribution when a cell width of 1 dB is used [Fig. 1(b)]. This is due to its enormous sample size (381 000). In comparison, the sixth TANGAROA set with a moderate sample size (21 000) is only relatively smooth when a cell width of 2 dB is used [Fig. 1(d)].

In the baseline run and the two sensitivity runs the global minimum for the sum of squares occurred when the slope of the hoki length to TS relationship was 5, being the lowest value of the range considered (Fig. 2). Such a low value is implausible and it should be noted that a slope of 0 will yield an even better fit. In each of the three runs there was a general dip in the sum of squares when the hoki slope was near to 75. However, for hoki slopes of about 20, a better fit can be achieved in each of the three runs than is possible for hoki slopes of about 75 (Fig. 2).

When the minimization was done in each of the three runs, while restricting the hoki slope to between 65 and 85, the best fits were obtained at hoki slopes from 73.3 to 77.5 (Table IV). Estimates of the length to TS relationships for the bycatch species were stable across the three runs except for frostfish (Table IV). However, for two-saddle rattail the estimated slope was always at the lower bound imposed during the estimation, and for Bollen's rattail the estimated slope was always at the upper bound.

In the baseline case (with the estimated hoki slope at about 75) the fit to the associated pairs of length and TS modes appears reasonable (Fig. 3). The relationship is also consistent with three previously estimated *in situ* points (Fig. 3). The previously estimated hoki TS relationships of ''Ma-

TABLE IV. The estimated length to TS relationships for hoki and the bycatch species in the baseline and sensitivity runs (''Intc.''=intercept).

	Baseline		Main modes		All modes	
Species	Intc.	Slope	Intc.	Slope	Intc.	Slope
Hoki	−177.6	75.2	−174.8	73.3	−183.9	77.5
Frostfish	−77.8	18.9	−161.8	49.4	−156.4	46.4
Two-saddle rattail	−100.1	18.0	−100.1	18.0	−100.1	18.0
Javelin fish	−137.5	37.4	−137.4	37.2	−137.4	37.2
Oliver's rattail	−81.4	20.9	−82.4	21.5	−82.4	21.5
Bollen's rattail	−206.8	80.0	−206.5	80.0	−206.5	80.0

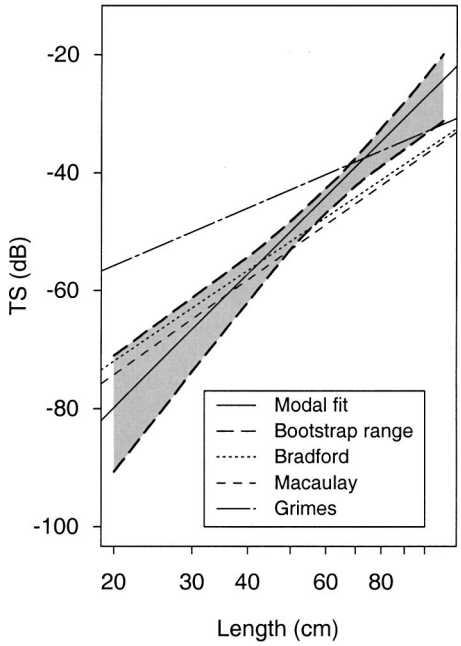

FIG. 4. The fitted length to target strength relationship for hoki in the baseline case (solid line) with a 99% confidence region. The relationships for hoki derived by Bradford (1999), and Macaulay and Grimes (2000) are also shown. The ''Macaulay'' relationship used *in situ* data and the ''Grimes'' relationship was from swimbladder modeling which used a neutral buoyancy assumption.

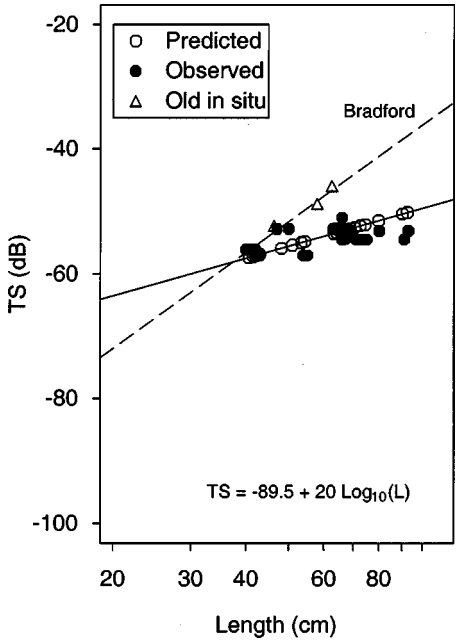

FIG. 5. The fitted length to target strength relationship for hoki when a slope of 20 is assumed (solid line). The relationship for hoki derived by Bradford (1999) is also shown (dashed line) with the three previously accepted *in situ* data points (triangles).

caulay'' (Macaulay and Grimes, 2000) and Bradford (1999) are on the edge of the estimated confidence region (Fig. 4). The estimate of ''Grimes'' (Macaulay and Grimes, 2000) from the latest swimbladder modeling results, which has a neutral buoyancy assumption, is clearly inconsistent with the modal estimate (Fig. 4).

When a hoki slope of 20 is imposed on the minimization, the resultant fit is also reasonable, except that the predicted values for lengths above 70 cm are all higher than the observed values (Fig. 5). However, this relationship is not consistent with the previous *in situ* points (Fig. 5) or with any of the other estimated relationships (Fig. 6).

For three of the five bycatch species there is very little contrast in the modal lengths used in the analysis (Fig. 7). For this reason the estimates for frostfish, two-saddle rattail, and Bollen's rattail are highly dubious. The estimated relationships for javelin fish and Oliver's rattail are based on a wider range of lengths, but because of the paucity of data, the estimates can only be described as preliminary.

IV. DISCUSSION

A. Estimation method

For any estimation method it is important to understand the strengths and limitations of the method in terms of the reliability of the estimates that it provides. The method proposed in this article assumes that there is a one-to-one correspondence between length frequency modes and TS modes for each species for which a length to target strength relationship is estimated. It is known that for some species that such a relationship does not necessarily hold. On occasion, a single species layer with a uni-modal length frequency has been seen to produce a bimodal TS distribution and it has been shown that such an occurrence can be predicted from swimbladder modeling results (Williamson and Traynor, 1984). The method proposed in this article will not work well with such species. However, the same type of modeling approach can still be used.

A natural extension of the method, consistent with the

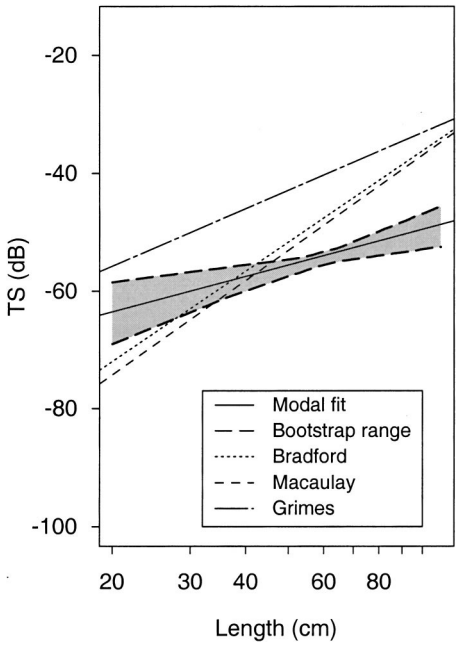

FIG. 6. The fitted length to target strength relationship for hoki when a slope of 20 is assumed (solid line) with a 99% confidence region. The relationships for hoki derived by Bradford (1999), and Macaulay and Grimes (2000) are also shown. The ''Macaulay'' relationship used *in situ* data and the ''Grimes'' relationship was from swimbladder modeling which used a neutral buoyancy assumption.

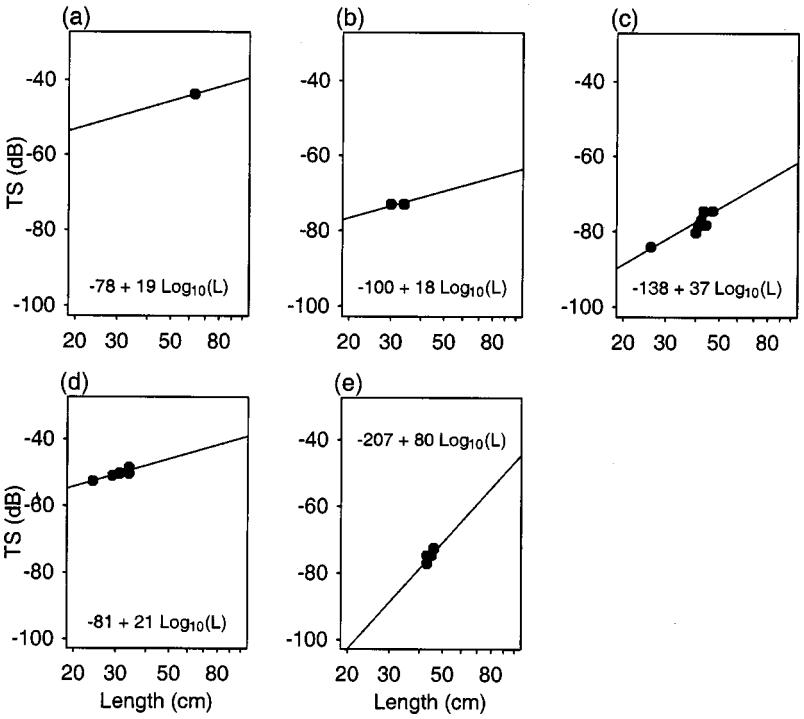

FIG. 7. The fitted length to TS relationships for the species other than hoki used in the analysis: (a) frostfish, (b) two saddle rattail, (c) javelin fish, (d) Oliver's rattail, and (e) Bollen's rettail.

underlying philosophy, is to use a more complicated estimation model which uses length frequencies to predict TS distributions. Fitting TS distributions to obtain estimates of parameters of interest is not new in the acoustic literature, but it has generally only been done in a restricted setting where many of the parameters are assumed to be known (e.g., Chu *et al.*, 1993; Foote and Traynor, 1988; MacLennan and Menz, 1996). Of course, depending on what data are available, the use of a more complex model (with more parameters) may or may not yield better estimates than the current approach.

Another issue with using TS modes in a regression to obtain a length to tilt-averaged TS relationship is that the backscattering cross section corresponding to the modal TS is not generally equal to the tilt-averaged backscattering cross section. This is due to the transformation between log space (TS) and linear space (backscattering cross section) and that the averaging of TS must be done in linear space (Burczynski, 1979). In the case when a ''modal TS distribution'' (being the distribution associated with a single mode) is normal, then the backscattering cross section is lognormal and the ratio of the average backscattering cross section ($\mathrm{E}[t]$) to the backscattering cross section of the TS mode (m) is

$$\frac{\mathrm{E}[t]}{m} = e^{[(1/2)((\log_e(10)\sigma)/10)^2]},$$

where σ is the standard deviation of the modal TS distribution.

An observed modal TS distribution will contain a contribution of variance from the size composition of the targets responsible for the mode and from their tilt angle distribution. For a particular species, it is the contribution of variance due to the tilt angle distribution which is determinant in whether a regression on TS modes will yield an adequate approximation for a length to tilt-averaged TS relationship. In the above equation, values of σ from 1 to 3 give ratios of 1.03 to 1.27; the ratio is about 2 when $\sigma=5$, and is greater than 5 when $\sigma=8$. If the observed TS modes in a data set typically have a large variance, then the proposed method would be expected to under estimate true TS. The method could still be applied, using ''corrected'' modes, if it were possible to estimate appropriate factors based on the variances of modal TS distributions. However, it may be better to use a more complex estimation model as suggested in the case of species which may produce bimodal TS distributions from a uni-modal length distribution.

The estimation method used in this article is fairly robust to TS modes caused by species not used in the estimation procedure. Provided that the model assumptions are satisfied and there is not too much observation error, the method allows any number of spurious TS modes to be ignored in favor of those modes which yield the best fit. If there is too much observation error, then TS modes may not be assigned to the correct species. However, if the data set includes stations from single species layers with a uni-modal length frequency, then the estimation of the length to TS relationship for these species will be much more robust, especially so if such layers cover a large length range.

The proposed boot-strapping procedure provides a useful indication of the confidence that can be placed in the estimates for a given species. However, it underestimates the level of uncertainty in the relationship because it does not allow for alternative correspondences between length and TS modes. A better method would be to bootstrap the full estimation procedure, but this is somewhat problematic because an allowance would need to be made for all of the species which contributed to the TS modes (i.e., not just those species which are represented in the length frequencies). One possibility would be to attribute TS modes which were not

assigned to the represented species to the minimum number of unknown species which would explain them.

B. Hoki data set

The use of the proposed method on the hoki data set is probably acceptable in regard to the issue of whether there is a one-to-one correspondence between hoki length modes and hoki TS modes. We used the early swimbladder modeling results of Grimes *et al.* (1997) to create simulated TS distributions for uni-modal length frequencies with a range of tilt angle distributions. All of the simulated TS distributions were uni-modal because there was sufficient variation in the TS response at angle for fish of the same length. In simulations which did not include variation in response at angle for a given fish length, it was easy to generate a bimodal TS distribution from a uni-modal length frequency. Sufficient conditions were that the tilt angle distribution extended beyond the occurrence of the first nulls (or very low TS values) and that the TS response at angle was symmetric about the mode of the tilt angle distribution.

The variance in individual modal TS distributions was examined visually for each TS mode which was associated with a hoki length mode (in the baseline run). The standard deviations ranged from about 3 to 5 dB. Given that this variation is due to variation in length, possible multiple species composition, sampling variance, and the *tilt angle* distribution, it was considered that there would be little error in using modal TS as a proxy for tilt averaged TS.

The estimated slope of about 75 for the hoki TS relationship seems dubious given estimates of slopes for other fish species and the rather common practice of assuming a slope of 20 (Foote, 1979). McClatchie *et al.* (1996) provide a range of estimates for regressions of maximum dorsal aspect TS using a large collection of published data. Their slope estimates range from about 10 to 25, and the 95% confidence intervals for the slopes of any of the species do not extend beyond 30. They do note that hoki is atypical of gadoids having a small swimbladder relative to its length because of a long tapering tail. This explains why it may have a lower TS at length than a typical gadoid, but does not suggest that the slope of the length to TS relationship would be steeper than that of other gadoids.

When a slope of 20 was imposed in the modal fitting for the hoki data set, the fit was better than at a slope of 75. However, the regression line was inconsistent with the early *in situ* data points accepted by Bradford (1999), the early swimbladder modeling results (Grimes *et al.*, 1997) and the regression line from modal association by eye (Macaulay and Grimes, 2000) (see Figs. 5 and 6). In contrast, the regression with the slope at 75 was consistent with these results (see Figs. 3 and 4). The most recent swimbladder modeling results made a neutral buoyancy assumption to determine how much to inflate the swimbladders (Macaulay and Grimes, 2000). The higher intercept and the flatter slope of this relationship compared to the other estimated relationships (see Fig. 4) suggest that the neutral buoyancy assumption is incorrect, and that smaller hoki maintain a higher magnitude of negative buoyancy than larger hoki.

It is possible that the estimated slope of about 75 is correct for hoki. Part, but not all, of the steep slope can be explained by the relative growth rates of the swimbladder and the fish length (the early swimbladder modelling results gave an estimated slope of about 55). The additional steepness could be explained by a trend in tilt angle distribution with length. Smaller hoki are more vulnerable to predators than larger hoki and therefore could be expected to maintain a greater level of negative buoyancy to enable a quicker dive response when threatened. However, this is somewhat speculative and more data will be required before hoki TS can be estimated with confidence.

ACKNOWLEDGMENTS

We thank Ian Doonan, Sam McClatchie, and other members of NIWA's acoustic group for useful discussions on this work. Thanks also to two anonymous referees who provided useful comments on an earlier draft of this article. Funding for this work was provided by the Ministry of Fisheries through Project No. HOK9803.

APPENDIX: DETERMINATION OF TS AND LENGTH FREQUENCY MODES

The modes in the target strength distributions and the length frequencies were determined algorithmically. The same algorithm was used on all of the data (target strength and length frequencies), but different parameters were used depending on the number of samples in each distribution.

The algorithm ''get.modes'' is given below in S/S+code (''←'' denotes assignment, ''[ ]'' addresses subcomponents of vectors, ''c( )'' concatenates numbers to form vectors, ''#'' prefixes comments):

```
get.modes←function(counts, breaks, crit, crit1, p){
    # counts is the vector of cell frequencies, breaks is the vector of breakpoints
    # crit, crit1, and p are the parameters controlling assignment of modes
    n←length(counts)
    totct←sum(counts)
    midpts←(breaks[2:(n+1)]+breaks[1:n])/2
    modeid←NULL
    for (i in 1:n)
      if (counts[i]/totct>p and bigdrop(counts, i, crit, crit1))
        modeid←c(modeid,i)
    modes←midpts[modeid]
    return(modes)}
```

The essentials of the Boolean function ''bigdrop'' are as follows.

- If (counts[i]⩾counts[i−1] and counts[i]⩾counts[i+1]) then the ith cell is proposed as a ''mode.''
- If {counts[i]>counts[i−1] and counts[i]<counts[i+1] and (counts[i]−counts[i−1])/(counts[i+1]−counts[i])<crit1} or {counts[i]>counts[i+1] and counts[i]<counts[i−1] and (counts[i]−counts[i+1])/(counts[i−1]−counts[i])<crit1} then the ith cell is proposed as a ''shoulder.''
- For a proposed mode or shoulder, let counts[v] be the cell count in the nearest ''valley.'' If

(counts[v]/counts[i]<crit) then the proposed mode or shoulder is accepted (and bigdrop returns TRUE).

For the target strength distributions, cell widths (the distance between breakpoints) varied from 1 to 2 dB. The smallest width was used for the largest KAHAROA distributions which had hundreds of thousands of samples. The largest width was used for all of the TANGAROA distributions; these had tens of thousands of samples. Note, larger cell widths give smoother distributions; if a distribution is too ''spikey,'' then there will be many spurious modes. A p value of 0.003 was used for all target strength distributions (it is relatively low because of the relatively large sample sizes). The value of crit1 was almost always 0.1, but it was increased to 0.3 on two occasions to allow the selection of shoulders which were obvious by eye (but not selected at the stricter level of 0.1). The value of crit was always 0.8, but this could have been set much lower without affecting the results (it should not be too low, otherwise a mode with modes on either side of it will not be selected).

For the length frequencies, all species for which samples of 50 or more were measured were used in the analysis. The cell widths were either 6 cm (sample sizes up to 400) or 4 cm (sample sizes from 500 to 700). A strict value of 0.05 was used for p and crit1 to ensure that only ''main modes'' were accepted and shoulders were virtually eliminated. As for the target strength distributions, a value of 0.8 was used for crit, but this could have been set much lower without affecting the results. These parameters lead to either one or two modes being accepted for hoki length frequencies, and only one mode for each bycatch species. As a sensitivity test, an alternative result was obtained by using lower p and crit1 values, which for some stations gave up to four hoki modes (but still only one mode for each bycatch species).

Bradford, E. (**1999**). ''Acoustic target strength of hoki,'' NIWA, Wellington, Final Research Report for Ministry of Fisheries Research Project HOK9703, Objective 2. p. 25.

Burczynski, J. (**1979**). ''Introduction to the use of sonar systems for estimating fish biomass,'' F.A.O. Technical Paper 191, p. 89.

Chu, D., Foote, K. G., and Stanton, T. K. (**1993**). ''Further analysis of target strength measurements of Antarctic krill at 38 and 120 kHz: Comparison with deformed cylinder model and inference of orientation distribution,'' J. Acoust. Soc. Am. **93**, 2985–2988.

Coombs, R. F. (**1994**). ''An adaptable acoustic data acquisition system for fish stock assessment,'' in *International Conference on Underwater Acoustics*, 5–7 December 1994, Australian Acoustical Society, Univ. of New South Wales, Sydney, pp. 18–22.

Coombs, R. F., and Cordue, P. L. (**1995**). ''Evolution of a stock assessment tool: acoustic surveys of hoki (*Macruronus novaezelandiae*) off the west coast of the South Island, New Zealand, 1985–1991,'' New Zealand J. Marine Freshwater Res. **29**, 175–194.

Do, M. A., and Surti, A. M. (**1990**). ''Estimation of dorsal aspect target strength of deep-water fish using a simple model of swimbladder backscattering,'' J. Acoust. Soc. Am. **87**, 1588–1596.

Foote, K. G. (**1979**). ''On representations of length dependence of acoustic target strengths of fish,'' J. Fish. Res. Board Can. **36**, 1490–1496.

Foote, K. G. (**1987**). ''Fish target strengths for use in echo integration surveys,'' J. Acoust. Soc. Am. **82**, 981–987.

Foote, K. G., and Traynor, J. J. (**1988**). ''Comparison of walleye pollock target strength estimates determined from *in situ* measurements and calculations based on swimbladder form,'' J. Acoust. Soc. Am. **83**, 9–17.

Grimes, P. J., McClatchie, S., and Richards, L. (**1997**). ''A re-calculation of target strength from hoki swimbladder casts using original data from Do and Surti (1990) and Coombs and Cordue (1995),'' NIWA, Wellington, Final Research Report for Ministry of Fisheries Research Project POAC04, Objective 2, p. 14.

Hurst, R. J., and Bagley, N. W. (**1994**). ''Trawl survey of middle depth and inshore bottom species off Southland, February–March 1993 (TAN9301),'' NIWA, Wellington, New Zealand Fisheries Data Report 52, p. 58.

Macaulay, G. J., and Grimes, P. J. (**2000**). ''Estimation of acoustic target strength of hoki using *in situ* data and swimbladder modelling,'' NIWA, Wellington, Research Progress Report for Ministry of Fisheries Research Project HOK9803, Objective 2, p. 19.

MacLennan, D. N., and Menz, A. (**1996**). ''Interpretation of *in situ* target-strength data,'' ICES J. Mar. Sci. **53**, 233–236.

MacLennan, D. N., and Simmonds, E. J. (**1992**). *Fisheries Acoustics* (Chapman and Hall, London), p. 325.

McClatchie, S., Alsop, J., and Coombs, R. F. (**1996**). ''A re-evaluation of relationships between fish size, acoustic frequency, and target strength,'' ICES J. Mar. Sci. **53**, 780–791.

McClatchie, S., and Ye, Z. (**2000**). ''Target strength of an oily deep-water fish, orange roughly (*Hoplostethus atlanticus*) Part II. Modeling,'' J. Acoust. Soc. Am. **107**, 1280–1285.

Otter Research Ltd. (**1992**). ''AUTODIF. A C++ array language extension with automatic differentiation for use in nonlinear modelling and statistics,'' Otter Research Ltd., Nanaimo BC, Canada.

Soule, M., Barange, M., Solli, H., and Hampton, I. (**1997**). ''Performance of a new phase algorithm for discriminating single and overlapping echoes in a split-beam echosounder,'' ICES J. Mar. Sci. **54**, 934–938.

Williamson, N. J., and Traynor, J. J. (**1984**). ''*In situ* target-strength estimation of Pacific whiting (*Merluccius productus*) using a dual-beam transducer,'' J. Cons., Cons. Int. Explor. Mer **41**, 285–292.

A design study of an acoustic system suitable for differentiating between orange roughy and other New Zealand deep-water species

Richard Barr
National Institute of Water and Atmospheric Research Ltd., P.O. Box 14-901, Kilbirnie, Wellington, New Zealand

(Received 21 February 2000; revised 25 September 2000; accepted 6 October 2000)

Using the simple slab-cylinder acoustic model for fish, developed by Clay and Horne [J. Acoust. Soc. Am. **96**, 1661–1668 (1994)], the target strengths of three of New Zealand's deep-water fish species, namely orange roughy, black oreos, and smooth oreos, have been derived. The target strengths derived for the model fish have been found to be in reasonable agreement with currently accepted target strength values. These three model fish were used in a study to test the species discrimination of a chirp sonar system. Chirps of center frequencies 40, 80, and 160 kHz and bandwidth of 10, 20, and 40 kHz have been used to acoustically illuminate the three fish species listed above and the matched, filtered responses to the chirps determined. The effect of the response of transducer or system bandwidth has also been investigated. It has been found that the bandwidth of the chirp is much more important for resolving detail in a fish target than the chirp center frequency. A bandwidth of at least 20 kHz, and preferably 40 kHz, produces matched filtered responses for black and smooth oreos and orange roughy which are quite clearly species specific. Results suggest that with orange roughy it may be possible to size and even sex the targets acoustically. © *2001 Acoustical Society of America.* [DOI: 10.1121/1.1332381]

PACS numbers: 43.30.Sf, 43.20.Fn, 43.30.Ft [DLB]

I. INTRODUCTION

Orange roughy (*Hoplostethus Atlanticus*) are but one of a number of deep-water fishes which feed the valuable deep-water fishing industry around New Zealand. Reliable estimates of the absolute biomass of the major deepwater species are an ongoing requirement for effective management of this national resource (Clark and Tracy, 1994). Acoustic surveys are now thought to provide the most effective means of assessing the absolute biomass of these dominant deep-water species (Do and Coombs, 1989; Elliot and Kloser, 1993; Cordue, 1996; Kloser *et al.*, 1996). However acoustic assessment of deep-water species has unique problems that sets it apart from the simpler acoustic stock assessment of species living in more shallow regions (McClatchie *et al.*, 1999).

In order to assess the absolute biomass of any particular species, one has to know the acoustic target strength for that species. While this is difficult enough with fishes living in shallow waters, the problems are exacerbated for deep-water fishes like orange roughy (McClatchie *et al.*, 1999). It is difficult to bring live fish to the surface from such great depths without damaging them in some way. Working with dead orange roughy has even more problems associated with it and it was the uncertainties of estimating the target strengths from dead orange roughy that led McClatchie *et al.* (1999) to attempt to capture live orange roughy for target strength measurements. Even working with orange roughy *in situ*, at great depths, has its problems. Orange roughy exhibit strong avoidance reactions to both towed and falling objects (Koslow *et al.*, 1995) and this orientation change tends to bias target strength estimates (McClatchie *et al.*, 1999). Finally, orange roughy usually occur in nature in association with other deep-water species which have much higher target strengths, for example black and smooth oreos (*Allocytus niger* and *Pseudocyttus maculatus*) (Doonan *et al.*, 1998). Such species mixing could significantly bias biomass estimates.

The reason for the significant difference in target strength between orange roughy and black and smooth oreos is that orange roughy do not have an air-filled swimbladder. Foote (1980) showed that for fish in dorsal aspect, air-filled swimbladders were responsible for 90% to 95% of the acoustic backscattering cross section. Orange roughy maintain their buoyancy by using a swimbladder filled with wax esters (Phleger and Grigor, 1990). As the waxy esters have a density only slightly less than that of seawater, and as the velocity of sound in the esters is not significantly different from that in seawater (McClatchie *et al.*, 2000), the acoustic impedance of an orange roughy is not significantly different from the surrounding sea water. An orange roughy is thus not a very strong acoustic scatterer. In fact, acoustically it might almost be considered a ''stealth'' fish. The air-filled swimbladders of black and smooth oreos, on the other hand, have acoustic impedances tens of times smaller than that of seawater. Their air bladders are thus almost perfect acoustic reflectors in seawater.

The fact that the acoustic scattering characteristics of the orange roughy are so different from its swimbladdered colleagues suggests that orange roughy could make an ideal candidate for target identification using acoustic techniques. With reliable identification of orange roughy in their natural environment, many of the problems of target strength evaluation listed above could be avoided. Reliable identification of

orange roughy targets could therefore lead to significant improvements in biomass estimation.

Many varied techniques have been employed in attempts to differentiate between fish species acoustically. However, there are broadly two different approaches. The approach most commonly used tries to identify schooling fish by looking at the characteristics of fish schools (LeFeuvre *et al.*, 2000; Rose and Legget, 1988; Scalabrin *et al.*, 1996). This approach has the advantage that it can use the same acoustic sounding instrumentation as that used in the standard biomass surveys and thus can be used concurrently. It has the disadvantage that very few features of fish shoals exhibit high species discrimination (Scalabrin *et al.*, 1996).

The second approach is to try and identify individual fish on the edge of large schools (Koslow and Kloser, 1999). By using towed transducers near fish schools, it is possible to obtain *in situ* target strengths of individual fish (Do and Coombs, 1989; Cordue, 1996). By measuring the target strength at three discrete frequencies, Koslow and Kloser (1999) claim to have some success in discriminating between myctophidae, orange roughy, and whiptails. Koslow and Kloser (1999) provide no modeling data on the species between which they discriminated. They merely combined the signals from the three different frequencies in an empirical fashion until species-specific outputs were obtained.

This paper uses the second approach in that it tries to identify individual fish of a particular species. However, rather than using an empirical system based on three arbitrarily chosen frequencies, we have adopted an acoustic modeling approach. First, we have produced three simple anatomically based acoustic backscatter models for orange roughy and black and smooth oreos. Then, we have theoretically insonified these target fish with frequency-modulated pulses (chirps) in an attempt to optimize the parameters of an acoustic sounding system capable of differentiating between the three fish groups. In this way we are effectively applying to fishes the technique which Chu and Stanton (1998) used with such success on zooplankton.

By alternately transmitting chirp and standard target strength pulses from a towed body, it should be possible to identify individual fishes and then measure their *in situ* target strength.

II. MODELING

A. Frequency range

When performing target strength studies on orange roughy or oreos *in situ*, it is necessary to work at short ranges from the fish (typically <100 m) using a narrow-beam transducer. This is to ensure we record a reasonable number of echoes from single fish targets. As orange roughy, during the spawning season, typically congregate around sea mounts at a depth of $\sim$1000 m, this also means deploying the acoustic sounding system from a towed body. To maintain both a narrow beamwidth and still have a towed body of manageable size limits operation to frequencies above about 20 kHz, and we typically use a frequency of 38 kHz for acoustic surveys of deep-water fish. As we therefore work at frequencies above 20 kHz, in our study we have only modeled the high-frequency response of fish, thereby avoiding the extra complications resulting from swimbladder resonances (Clay, 1992; Ye, 1997). Ye (1997) has found large discrepancies in the target strength estimates of gas-filled prolate spheroids at resonance evaluated using different numerical techniques.

TABLE I. Physical parameters for spheroidal model black oreo, total length 30 cm.

Parameter	Units	Swimbladder	Fish body	Sea water
Length	cm	5.2	22.5	n/a
Height	cm	2.3	13.5	n/a
Width	cm	2.3	5.0	n/a
Velocity of sound	m/s	335.0	1548	1484
Density	kg/m^3	126	1060	1032
Orientation	deg.	22.0	0.0	n/a

Using the formula for air-bubble resonance frequency provided by Medwin and Clay (1998), one can evaluate the approximate bladder resonance of smooth and black oreos. At a depth of 1000 m the black and smooth oreos, described in Tables I and II, respectively, would have bladder resonances at $\sim$2.2 and 3.3 kHz, respectively. The target strength data presented here for black and smooth oreos, which ignore such resonance, should thus not be used below 10 kHz.

Although bladder resonance will not make a significant contribution above 10 kHz to the target strength (TS) for our larger species, one should bear in mind that myctophidae, which are a common fish on the Chatham Rise, New Zealand and in the Eastern and Southern fishing zones of Australia (Koslow and Kloser, 1999), have a much smaller swimbladder than oreos. In deep water a 7-cm-long myctophid could be expected to have a bladder resonance near 10 kHz. In fact, such a resonance may provide a physical reason for the success of the three-frequency technique of Koslow and Kloser (1999) in distinguishing between myctophidae and whiptails, both of which have swimbladders.

B. Anatomically based acoustic backscatter models

A drawing of a black oreo, a smooth oreo, and an orange roughy are shown in the upper half of Fig. 1 (from Paul, 1986). In the lower half of Fig. 1 the three smaller panels show the acoustical ray paths through a simple spheroidal model of these fish (shown in the lateral aspect). The first of the three panels shows the rays incident on and reflected from the fish body. This panel applies to all three fish types. The middle panel of the three shows the extra rays incident on and reflecting from an air-filled swimbladder. This panel is applicable to black and smooth oreos. Note, because of the

TABLE II. Physical parameters for spheroidal model smooth oreo, total length 30 cm.

Parameter	Units	Swimbladder	Fish body
Length	cm	2.9	22.4
Height	cm	1.65	12.4
Width	cm	1.65	4.4
Velocity of sound	m/s	335	1548
Density	kg/m^3	126	1060
Orientation	deg.	22.0	0.0

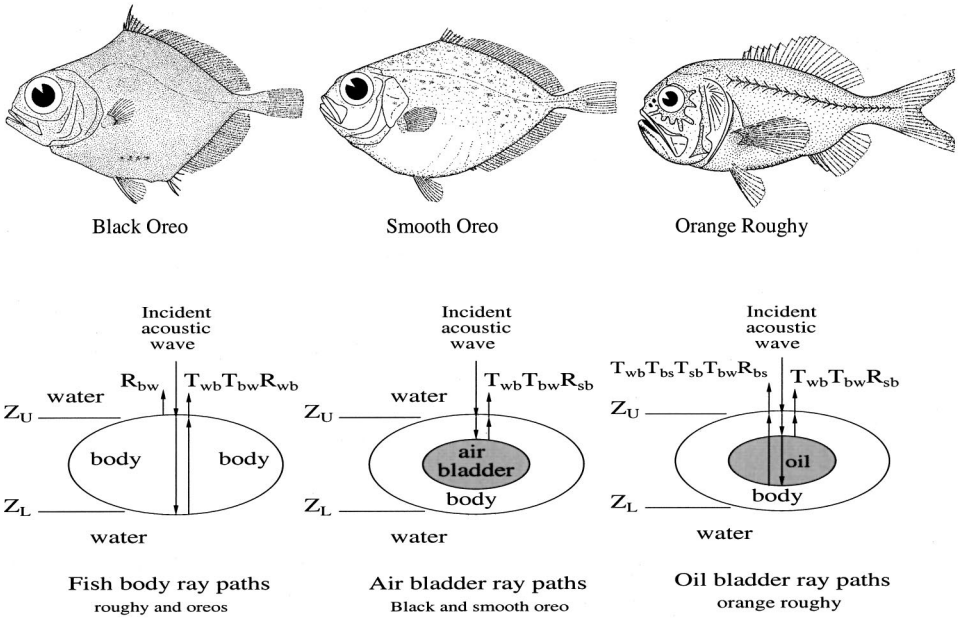

FIG. 1. Upper panel: Drawing of a black oreo, a smooth oreo and an orange roughy (from Paul, 1986). Lower panel: Ray paths through our anatomically based, acoustic backscatter fish models.

almost perfect acoustic reflection at the fish-body/air interface, no ray paths are shown into and through the air-filled swimbladder. The final panel shows the rays incident on and transmitted through an oil-filled swimbladder. This model applies to the orange roughy. The impedance contrast between the body of the roughy and the oil bladder is of the same order as that between the fish body and seawater. As a result the reflection at the upper surface of the oil-filled swimbladder is much weaker than at the upper surface of the air bladder of an oreo. We therefore now have to also include ray paths that are transmitted through the swimbladder and are reflected from its lower surface.

In transverse section the bodies of all our fish are modeled as half-cylinder tops over half-cylinder bottoms, joined by straight vertical sections (see Fig. 2). The diameter of the cylindrical elements, at any point along the longitudinal axis of the fish (line joining mouth to center of tail) is effectively defined by the width of the fish, as seen in the dorsal aspect, at that point along the longitudinal axis. This fish model is an idealized version of the cod models of Clay and Horne (1994), who effectively reduced the acoustic scattering of cod to a summation over typically 11 cylindrical elements (see also Medwin and Clay, 1998). Because of the analytical nature of our fish models we can easily expand the number of cylindrical elements used. We have typically used 200 elements which corresponds to digitization steps of $\sim\lambda/40$, where λ is the acoustic wavelength in seawater. This resolution gives backscatter amplitudes within 0.1 dB and backscatter phases within 0.5° of the limiting values obtained with infinitesimal digitization steps.

The swimbladders of the fish are modeled with a spheroidal model similar to that used for the fish body, the overall size and axes ratios being chosen to best fit the biological data for the species under study. Jech and Horne (1998) investigated the sensitivity of acoustic scattering cross section of swimbladders to the coarseness of swimbladder digitization but did not relate the results directly to wavelength. Their results can be reinterpreted to show that acoustic backscatter cross sections, indistinguishable to plotting accuracy, can be obtained with digitization intervals $<\lambda/3$.

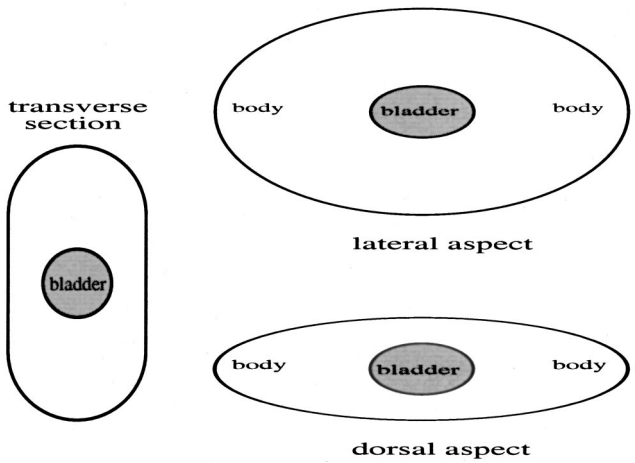

FIG. 2. Anatomically based, acoustic backscatter fish model from three aspects.

C. Data sources for anatomically based fish models

One can see from Figs. 1 and 2 how the simple spheroidal fish model is a reasonable fit to the body of oreos and roughy. In a similar way the two x rays in Fig. 3 of black and smooth oreos and the sagittal section of a frozen male orange roughy (from Phleger and Grigor, 1990) show the legitimacy of our simple spheroidal model for the swimbladders. For the smooth oreo in particular, the spheroidal model seems particularly apposite. The x rays in Fig. 3 were enhanced by injecting the swimbladders of the oreos with a barium-loaded epoxy resin. This technique had the advantage that after dissection of the fish, the bladder casts could be sliced for use in more accurate target strength estimations using the Kirchhoff approximation (Medwin and Clay, 1998; McClatchie *et al.*, 1996). Also note that from the sagittal frozen section and the two x rays it is possible to determine the angle between the

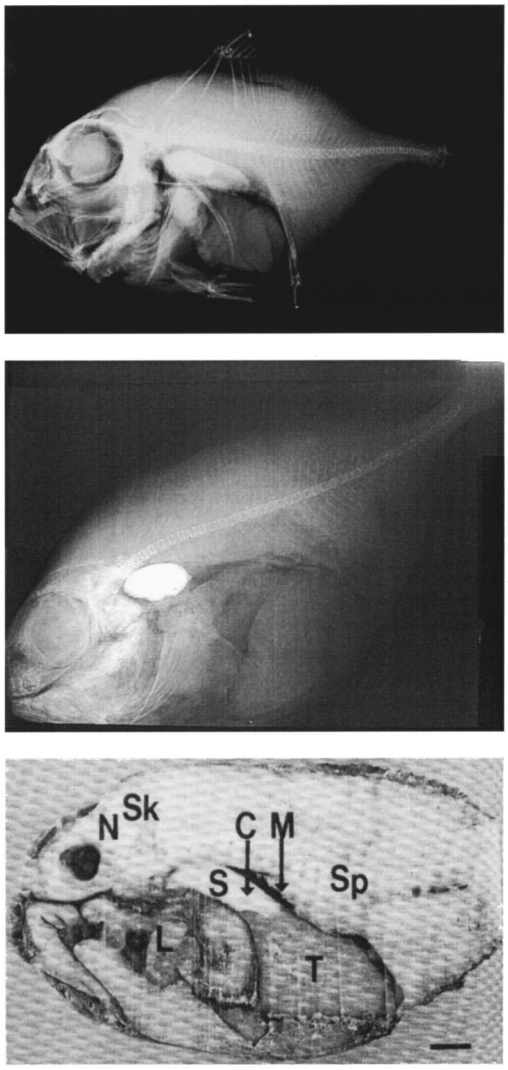

FIG. 3. Upper panel: x ray of a black oreo with a ''barium-loaded'' swimbladder. Middle panel: x ray of a smooth oreo with a barium-loaded swimbladder. Lower panel: frozen saggittal section of a male orange roughy (from Phleger and Grigor, 1990). Swimbladder marked with letter ''S.''

longitudinal axis of the fish and the longitudinal (major) axis of the spheroidal swimbladders, hereinafter termed the *orientation* of the swimbladder. We define the orientation angle as positive if the fish needs to swim in a head-down configuration to make the major (longitudinal) axis of its swimbladder horizontal.

As oreos are recovered from very deep water the swimbladders are subject to very great stress as the fish are brought to the surface. In general the smaller smooth oreo swimbladders tend to survive the trauma intact but the black oreo swimbladders more often than not burst under the strain. There is, therefore, much more uncertainty in the black oreo swimbladder data than there is in the smooth oreo data. The overall inflation level of injected swimbladders was based on the total swimbladder volume required to make the fish neutrally buoyant (Hart, 2000).

In a 1998 New Zealand oreo survey (Doonan *et al.*, 1998), the mean total lengths of smooth oreo males was 35.9 cm and females 38.9 cm. The black oreos were smaller at males 31.3 cm and females 31.9 cm. However, though a larger fish, a smooth oreo of a given length typically has a swimbladder only ~2/3 the length of that of a black oreo of the same length total length (Barr, 2000).

TABLE III. Physical parameters for spheroidal model orange roughy, standard length 35 cm.

Parameter	Units	Swimbladder	Fish body
Length	cm	7.5	30.5
Height	cm	1.85	16.5
Width	cm	1.85	7.1
Velocity of sound	m/s	1525	1548
Density	kg/m^3	903	1050
Orientation	deg.	18.0	0.0

Tables I and II provide model data based on the body and bladder dimensions of one black and one smooth oreo linearly scaled to a total length of 30 cm. The length of the fish, presented in Tables I and II, will be seen to be significantly less than the stated total length of 30 cm. This is because the dimensions given in Tables I and II are those of the ''best-fit'' spheroidal fish model, as described in Fig. 1, which we consider most closely approximated our black and smooth oreos of total length 30 cm. This best-fit spheroidal fish model takes no account of the tail of the fish.

Since this paper was first written, swimbladder data from many more black and smooth oreos have become available. Doonan *et al.* (2000) have made measurements on 27 smooth and 22 black oreo swimbladder casts from fish with total lengths ranging from 22 to 53 cm. However, the ''average swimbladders'' derived from these data sets and scaled to a total length of 30 cm are not significantly different from our two specimens described in Tables I and II. As a result we have continued to use these original fish in our modeling. It can also be argued with some justification that one will never get an ''average fish'' as a target.

For our spheroidal orange roughy model we have assumed a standard length of 35 cm, this being the modal size for commercially exploited orange roughy in New Zealand (Clark, 1995). We derived the shape of our orange roughy from Fig. 1 of McClatchie and Ye (2000) and the details of the swimbladder from Phleger and Grigor (1990). These authors indicate that the orange roughy is a very oily fish, the majority of the oil being located in the flesh and beneath the skin. The oil-filled swimbladder is the second most significant oil source in the fish. Figure 1 of Phleger and Grigor (1990), duplicated here as the lower panel of Fig. 3, shows that the orientation angle of the swimbladder is ~18°. This means that were a fish to swim so that the longitudinal axis of its swimbladder were horizontal, its head would be tilted down 18° below the horizontal. The model parameters extracted from the above references are listed in Table III.

The remainder of the information in Tables I–III was derived as follows. The sound velocity in water was computed using the simplified formula of Mackenzie (1981). It has been evaluated for a salinity of 34.5 parts per thousand and a temperature of 4.3 °C, these being the conditions representative in New Zealand's Chatham Rise, deep-water fishery (Doonan, 2000). The velocity of sound in air and the density of air are taken from the CRC (1973) handbook. The

density of seawater is computed from the International Equation of State of Seawater 1980 (UNESCO, 1981). The velocity of sound in fish flesh, and the flesh density are each averages of 27 measurements presented by Shibata (1969). The constants in the tables are assumed to be valid at a depth of 1000 m.

Finally, it should again be stressed that these are very basic model fish. We are *not* trying to accurately model the absolute target strengths of orange roughy and oreos or their intraspecies variability. We are merely trying to ascertain if it may be possible to distinguish between different fishes acoustically using chirp technology. In this study we only wish to set realistic limits on the design parameters of such a system.

III. SOUND SCATTERED BY THE ACOUSTIC MODELS

If we assume our fish is insonified with a plane incident sound wave of amplitude P_{inc}, then the scattered sound pressure, P_{scat}, at a distance R from the fish is given in the time domain by

$$P_{\text{scat}}(t,R)=[P_{\text{inc}}(t-R/c)/R]*l_s(t), \tag{1}$$

where, l_s, is the scattering length of the fish in the time domain and the symbol ''*'' denotes convolution. In the frequency domain the scattered sound pressure, P_{scat}, at the frequency, f, is given by

$$P_{\text{scat}}(f,R)=[P_{\text{inc}}(f)/R]L_s(f), \tag{2}$$

where L_s is the scattering length of the fish in the frequency domain.

The absolute square of the scattering length, $\sigma_{\text{bs}}(f)$, is termed the backscattering cross section and the target strength, TS(f), is related to the scattering length by the expression

$$\text{TS}(f)=20\log_{10}|L_s(f)/L_0|, \tag{3}$$

where L_0 is the reference length, usually 1 m.

There are many ways to compute the scattering lengths of fish. To determine the scattering length of a fish body in seawater, $L_{\text{bod}}(f)$, or an oil swimbladder in the fish, $L_{\text{blad}}(f)$, we have chosen the low-contrast fluid-cylinder models developed by Stanton *et al.* (1993) and Clay and Horne (1994), as presented by Medwin and Clay (1998). To determine the scattering length of an air-filled swimbladder in a fish body, we have used the work of Clay (1992) as summarized by Medwin and Clay (1998). The total scattering length of our fish models in the frequency domain, $L_s(f)$, can then be simply derived by coherently adding the scattering lengths of the fish body to that of the fish bladder, be it air- or oil filled

$$L_s(f)=L_{\text{bod}}(f)+L_{\text{blad}}(f), \tag{4}$$

the equivalent form in the time domain being

$$l_s(t)=l_{\text{bod}}(t)+l_{\text{blad}}(t). \tag{5}$$

This simple analysis neglects the effect of the swimbladder on the rays through the fish body, but as the area of the swimbladder in dorsal aspect is typically only 4% of the area of the fish body, errors in the target strength of the fish body from this source should be small. In the case of an air-filled

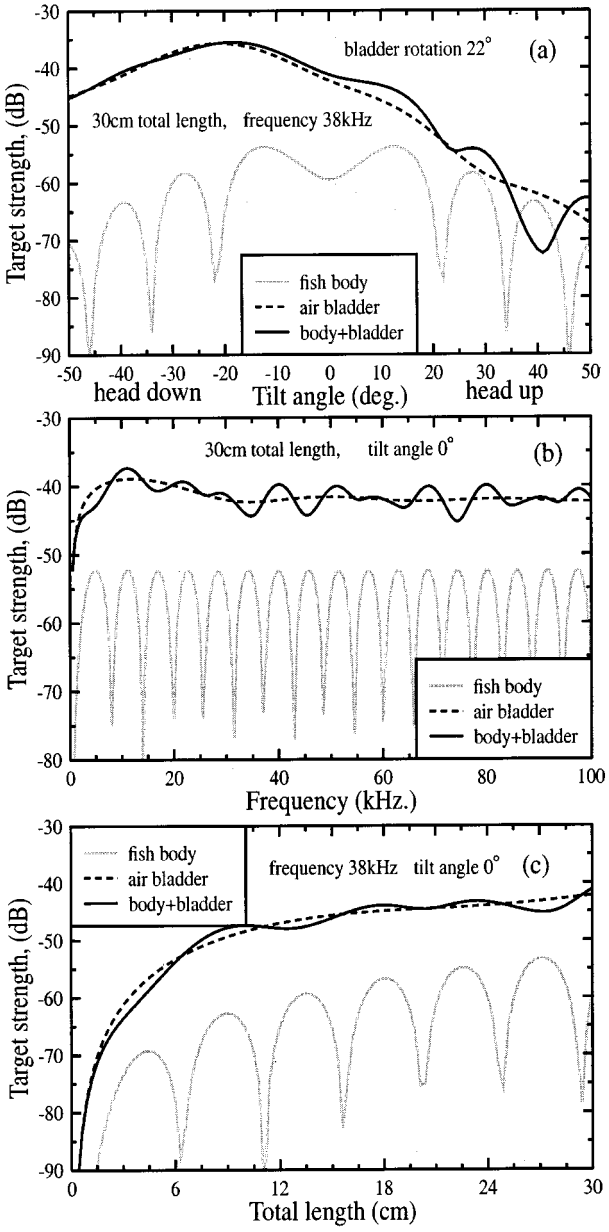

FIG. 4. Target strength of model black oreo.

bladder, because of its almost perfect acoustic reflectivity, we can expect an air-filled swimbladder to contribute 90%–95% of the total scattering cross section of the fish (Foote, 1980). A 4% error in scattering from the fish body will thus have a negligible effect on the total scattering cross section of the fish. In the case of an oil-filled bladder, the correction should also be negligible as the transmission coefficient of sound through the bladder will be almost 100% and the velocity of sound in the swimbladder is not significantly different from that of the fish body.

A. Black oreo target strength

Figure 4(a) shows the target strength, as a function of the tilt angle, of our model black oreo of total length 30 cm, as described in Fig. 1 and Table I, in the dorsal aspect. Due to the symmetry of the fish body the target strength of the fish body is also symmetrical, about a tilt angle of 0°. Like-

wise, the target strength plot of the swimbladder is symmetrical, but about an angle of −22° due to the orientation of the swimbladder relative to the fish body.

At 38 kHz and in the dorsal aspect the target strength of the black oreo peaks at ~−35.7 dB, when swimming head down with the body tilted 22° below the horizontal plane. The dominant contributor to the backscatter is the air-filled swimbladder. This maximum target strength value is very near the value of −35.6 dB presented by Barr (2000), which was derived from a linear least-squares fit of the target strength of 22 black oreo swimbladder casts to the total length of the fish from which the casts were extracted, evaluated at a total length of 30 cm. The target strength of the 22 casts was derived using the Kirchhoff surface integral technique (Medwin and Clay, 1998; McClatchie *et al.*, 1996) and the fish ranged in length from 26 to 37 cm (Coombs *et al.*, 2000). The agreement to within 0.1 dB is probably just good fortune, bearing in mind the ontogenetic changes and intraspecific variability in black oreos, but it adds support to the validity of the software used to derive the target strengths. The maximum scattering from the fish body is typically ~−53 dB, some 17 dB smaller than the scattering from the air bladder. This ratio is somewhat greater than the value of ~11 dB obtained by Foote (1980) comparing similar-shaped fish (cod and mackerel) with and without swim bladders.

Figure 4(b) shows how the target strength, in the dorsal aspect and at zero fish tilt, varies with frequency. (Note that in our calculations swimbladder resonances are not included.) It is clear that the contribution from the swimbladder is almost independent of frequency, whereas that of the fish body is oscillatory in nature, due to the interference between the signals reflected from the upper and lower surfaces of the fish body. These results are similar to those obtained by Clay and Horne (1994) modeling Atlantic cod. It should be noted that in a real fish, the uniform periodic variation with frequency of the target strength of the fish body will be destroyed somewhat by the irregular shape of a real oreo and the presence of the internal organs.

Finally, Fig. 4(c) shows how one can expect the target strength to vary with the total length of the fish. In this model it is assumed that all dimensions of the body and the bladder scale uniformly.

B. Smooth oreo target strength

The physical parameters we have chosen for our acoustic model smooth oreo, shown in the middle upper panel of Fig. 1, are listed in Table II. The three panels in Fig. 5(a) show the target strength computed for this model smooth oreo in the dorsal aspect. The fish has been scaled to a total length of 30 cm, the same as the model black oreo (Sec. III A) in order to facilitate comparisons. Like the black oreo the target strength of the smooth oreo is dominated by the air-filled swimbladder component, but at a level only ~12 dB greater than the maximum target strength of the fish body. This result is very similar to the value of ~11 dB obtained by Foote (1980) as the difference in target strength between similar fish with and without swimbladders.

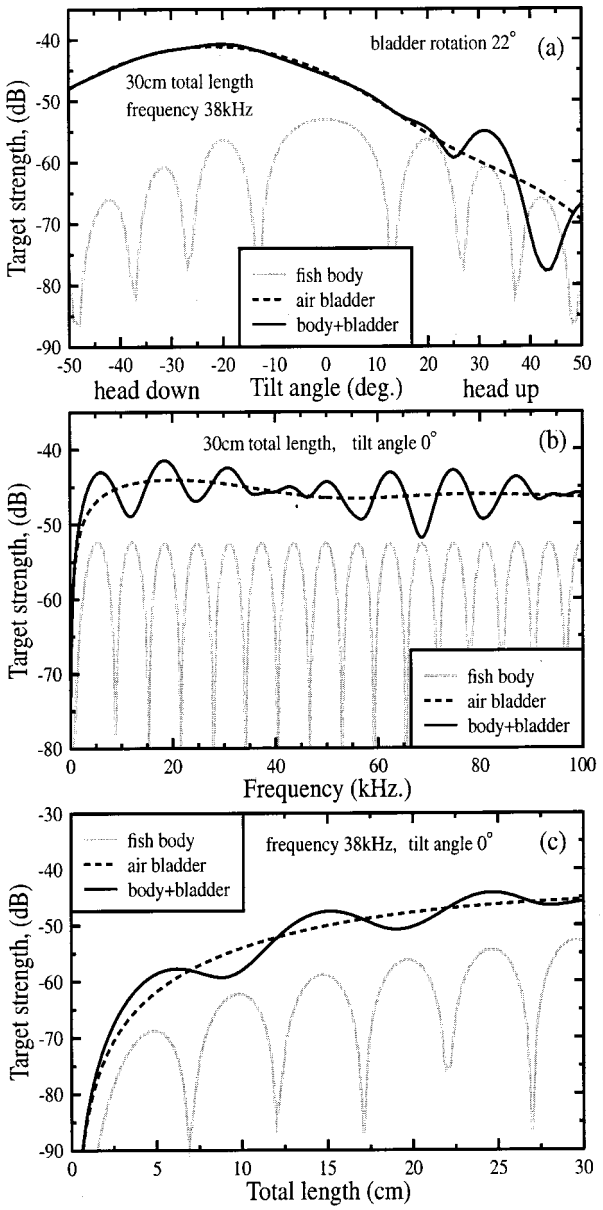

FIG. 5. Target strength of model smooth oreo.

The maximum target strength for the smooth oreo swimbladder in our 30-cm model evaluates to −41.1 dB [Fig. 5(a)]. This target strength value is near the value of −42 dB presented by Barr (2000) which was derived from a linear least-squares fit of the target strength of 23 smooth oreo swimbladder casts to the total length of the fish from which the casts were extracted, evaluated at a total length of 30 cm. The target strength of the 23 casts was derived using the Kirchhoff surface integral technique (Medwin and Clay, 1998; McClatchie *et al.*, 1996) and the fish ranged in length from 22 to 36 cm (Coombs *et al.*, 2000). This again supports the validity of our model.

Figure 5(b) shows how the target strength of the smooth oreo varies with frequency. The total target strength of the smooth oreo can be seen to fluctuate more than that of the black oreo due to the smaller difference between the backscatter from the swimbladder and fish body. For a similar reason the plot of smooth oreo target strength as a function

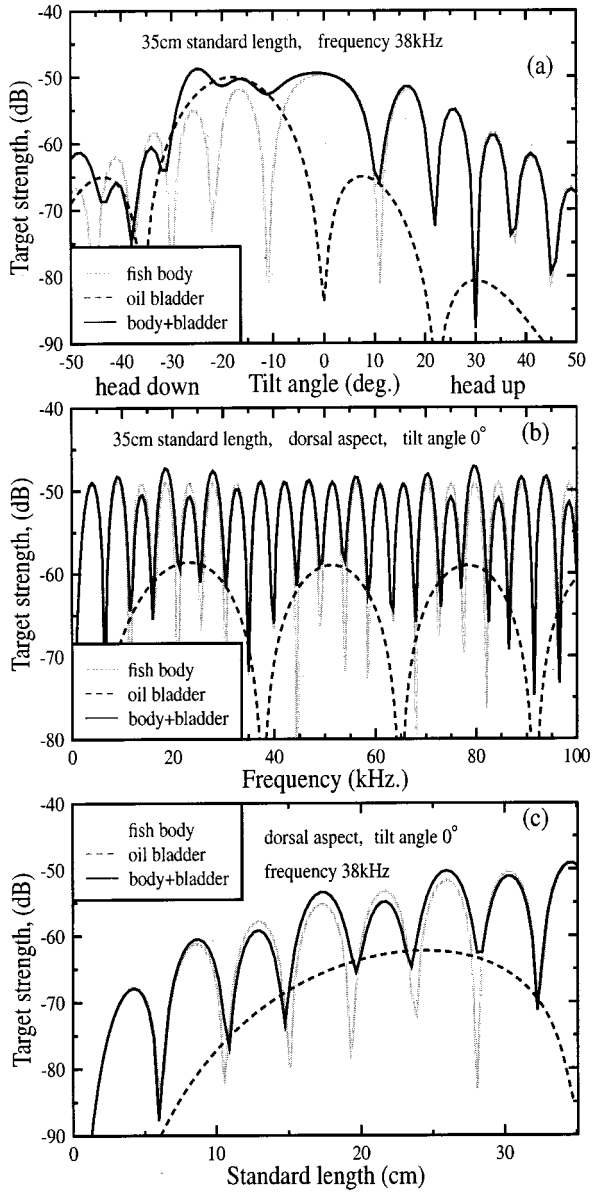

FIG. 6. Target strength of model orange roughy.

of total fish length [Fig. 5(c)] oscillates about the target strength of the swimbladder alone by about ±2.5 dB

As the behaviors of the target strength of the black and smooth oreo with frequency are very similar, it would be difficult to differentiate them just by looking at the variation of target strength with frequency (Koslow and Kloser, 1999). A small black oreo would look very much like a larger smooth oreo, especially when intraspecific variability is taken into account. However, it is clear that the relative contributions of swimbladder and fish body are different between black and smooth oreos and a technique based on this difference may show some species discrimination.

C. Orange roughy target strength

Figure 6(a) shows the target strength (in the dorsal aspect) as a function of tilt angle of the orange roughy described in Table III at a frequency of 38 kHz. It can be seen that unlike the oreo target strengths [Fig. 6(a)], the peak backscatter from the swimbladder (now oil filled) and the fish body are similar at around −50-dB maximum. It can also be seen that the shape of the fish body and swimbladder responses is similar, the differences being largely ones of horizontal scale, a direct result of the difference in height of the swimbladder and the fish body. Also, due to the orientation of the swimbladder in the fish body the swimbladder response peaks at fish tilt angle of −18°, whereas the response of the fish body peaks at zero tilt. As a result the response of the fish body and swimbladder combine to give an almost constant target strength over the tilt angle range from +5° to −28.° However, slight changes in the size of the fish body, or a small vertical displacement or rotation of the swimbladder, would significantly alter the relative phasing of target strength contributions from swimbladder and fish body and hence the appearance of the total fish backscatter [see Fig. 6(a)], where contributions from the swimbladder and fish body are similar in amplitude.

Figure 6(b) shows how the target strength of our model orange roughy, in the dorsal aspect and zero tilt angle, varies with frequency. The variations of target strength for fish body and swimbladder can be seen to be of similar shape but they differ in amplitude and horizontal scale due to the 18° tilt of the swimbladder relative to the fish body and the difference in height of the fish body and swimbladder, respectively. The target strength for the fish body varies ~5.6 times more rapidly with frequency simply due to the fish body having a height ~5.6 times that of the effective height of the rotated swimbladder.

The heavy solid line in Fig. 6(b) shows the target strength of the whole fish. This can be seen to undergo rapid amplitude variations, mainly due to constructive and destructive interference between the acoustic signals scattered back from the upper and lower surfaces of the fish body. An irregular and smaller scale target strength variation results from interference between the dominant scatter from the fish body and the weaker scatter from the tilted swimbladder. Figure 6(c) shows how one might expect the target strength of an orange roughy, measured at 38 kHz, in the dorsal aspect and zero tilt angle, to vary with its overall length. Note that although the target strength undergoes a periodic amplitude variation, at standard lengths near 33.6 cm, the average standard length of male and female orange roughy observed by Kloser *et al.* (2000) during target strength experiments on roughy plumes, our model gives target strength values of ~−51 dB. Kloser *et al.* (2000) obtained values between −51 and −52.1 dB. This agreement, superficially at least, gives some confidence in our model but the rapid variation of target strength with fish length and frequency [Figs. 6(c),(b)] suggests that this agreement might be almost fortuitous.

The rapid variations of target strength with fish length shown in Fig. 6(c) were derived assuming a continuous wave excitation at 38 kHz. A typical target strength pulse is only ~315 μs long and therefore has a bandwidth of ~3 kHz. Were the target strength values in Fig. 6 to be derived by using such a broadband pulse, the effect would be a weighted integration over the regions of rapid fluctuation which would probably reduce the perceived target strength somewhat, but

would also reduce the severity of the target strength fluctuations. This effect is to be the topic of an independent study.

The complex nature of the variation of orange roughy target strength with standard length given in Fig. 6(c) also suggests there may be some additional problems in the acoustic biomass assessment of this species which are not present for the more common air-swimbladdered fish like black oreos [Fig. 6(c)]. For biomass estimation pulse lengths are typically ~1 ms long and have a narrower bandwidth than the target strength pulse. As a result the integrating effects typical of wide bandwidth target strength pulses will be less apparent. However, in large schools, where the backscatter from individual fish add in a random manner, the integrating effects of the addition of a continuous range of fish sizes will tend to smooth out the maxima and minima in Fig. 6(c). This should provide an effective smooth variation of average acoustic backscatter with standard length similar in nature to Fig. 4(c).

The target strength of smooth oreos is dominated by the air-filled swimbladder component, but at a level only ~12 dB greater than the target strength for the fish body. The target strength of the black oreo air-filled swimbladder was typically ~17 dB greater than the target strength of the fish body, whereas the target strength of the oil-filled swimbladder and fish body of orange roughy were of the same order. These target strength differences suggest it may be possible to discriminate between these three species acoustically, and the remainder of this paper is devoted to determining the parameters of an acoustic system capable of such discrimination.

IV. MATCHED-FILTER ANALYSIS

Our objective is to be able to acoustically differentiate between different fish targets in the presence of background noise. The most efficient filter for discriminating between white noise and a desired signal is a time-reversed sequence of the original transmitted signal (Chu and Stanton, 1998). Our design problem therefore revolves around finding the best spectrum to transmit for differentiating between targets of different fish species.

When investing in real estate the most important parameters are said to be location, location, and location. In a similar way, when trying to differentiate between different targets, using either radio waves and radar, or acoustic waves and sonar, the most important parameters for success might be said to be bandwidth, bandwidth, and bandwidth. The simplest form of wideband pulse transmission is the chirp signal. A chirp has an instantaneous frequency that changes linearly with time, as given by the equation

$$c(t)=\begin{cases}\cos(\omega_0+\alpha t)t, & 0\leqslant t\leqslant T,\\ 0, & \text{otherwise},\end{cases} \tag{6}$$

where ω_0, α, and T are the initial angular frequency of the pulse, sweep rate, and pulse duration, respectively. This pulse type has been used with some success by Chu and Stanton (1998) to differentiate between different anatomical groups in zooplankton. They used chirps of 400-kHz bandwidth, B, scanning from 300 to 700 kHz in 200 μs. At such high frequencies the attenuation in sea water is very large, precluding measurements at any significant range. Such high frequencies were needed to see spatial structure in the plankton which typically had a maximum length of only 30 mm. A 400-kHz bandwidth, B, converts to a time resolution, $1/B$ of 2.5μS which corresponds to a range resolution of ~2 mm in sea water.

The chirp signal scattered from a fish target, $v(t)$, is a convolution of the chirp pulse, $c(t)$, given in Eq. (6) with the scattering impulse response of the fish target, $l_s(t)$, given in Eq. (5), and the impulse response of the transducer, $b(t)$. It can be expressed as

$$v(t)=c(t)*l_s(t)*b(t), \tag{7}$$

where the symbol ''*'' denotes convolution.

To generate a filter exactly matched to the target and transducer response is not very practical, especially as in any practical case we do not know the target. In the work that follows, therefore, we have presented data filtered by a time-reversed version of the transmitted pulse [described in Eq. (6)]. Chu and Stanton (1998) prefer to describe this technique as pulse compression (PC) rather than matched filtering (MF). The compressed pulse response, $p(t)$, is then given by

$$p(t)=c(t)*c(-t)*l_s(t)*b(t), \tag{8}$$

which reduces to

$$p(t)=r_{ss}(t)*l_s(t)*b(t), \tag{9}$$

where, $r_{ss}(t)$, is the autocorrelation function of the chirp signal.

In fact, the transducer and fish backscatter responses have been evaluated in the frequency domain and thus we have evaluated the right-hand side of Eq. (9) in the frequency domain before taking the inverse transform to produce the pulse-compressed or matched-filter impulse response $p(t)$ as given below

$$p(t)=\mathfrak{T}^{-1}\{|C(f)|^2L(f)B(f)\}, \tag{10}$$

where $C(f)$, $L(f)$, and $B(f)$ are the Fourier spectra of the chirp pulse, the backscatter response of the fish target, and the transducer frequency response, respectively.

A. Standard targets

In order to test the matched-filter software we first computed the filtered chirp response of a 10-cm-long spheroidal air bladder, of diameter 1 cm. For our chirp pulses we chose a center frequency of 40 kHz (near 38 kHz, the most commonly used frequency for acoustic surveys), a bandwidth of 40 kHz (20–60-kHz sweep) and a duration of 8 ms. Figure 7 shows the response of the air bladder to this chirp pulse, after matched filtering with a time-reversed version of the pulse.

The computations for Fig. 7 include the effect of a theoretical transducer frequency response. The transducer response is assumed to be that of a single resonant circuit (used once in the transmit path and once in the receive path) whose Q value is different in each panel of Fig. 7. With a transducer Q of 0.25 the bandwidth of the transducer, δf, is 160 kHz and so it has very little effect on the matched-filter response

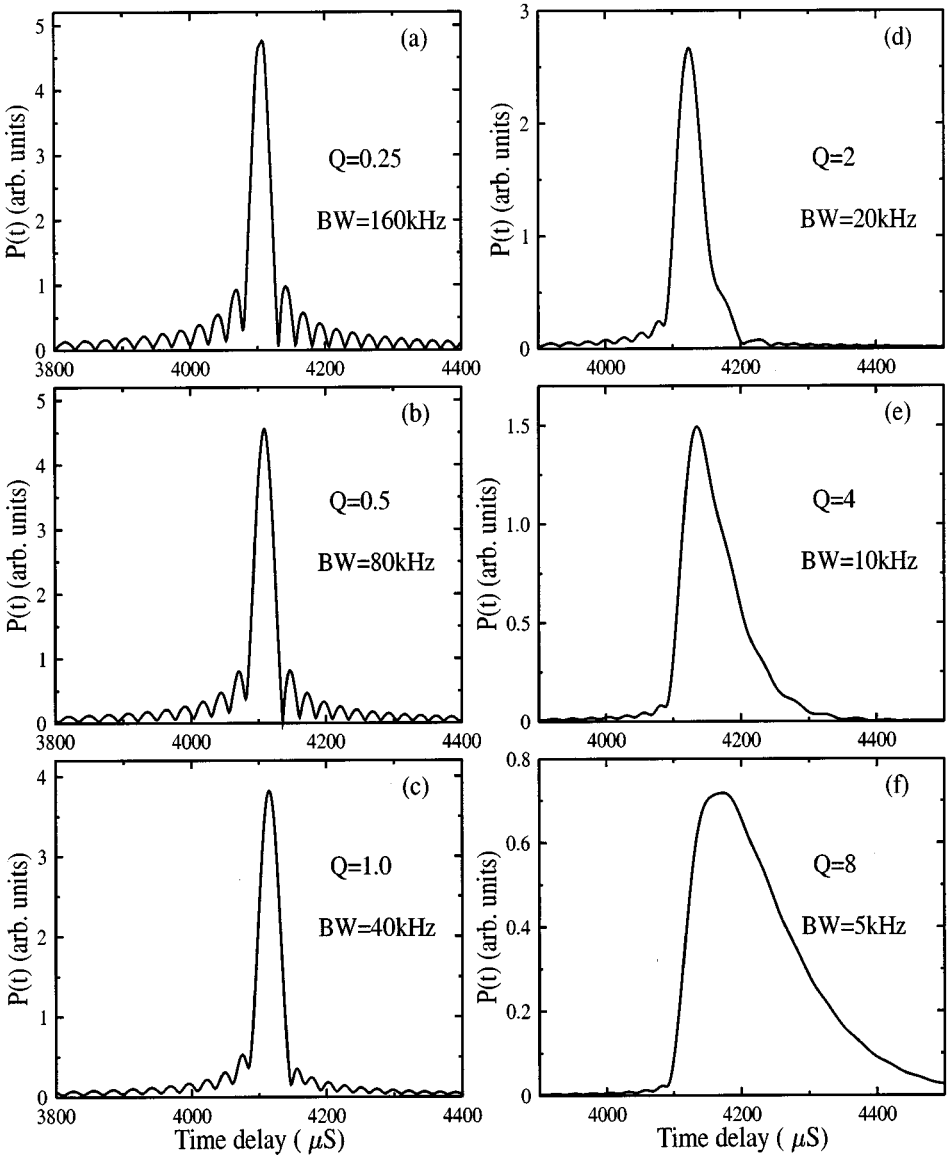

FIG. 7. ''Matched-filter response'' of long, thin air-filled spheroid to chirp pulse showing the effect of the system/transducer bandwidth.

of the chirp, as shown in Fig. 7(a), where the sidelobe structure of the response can be seen quite clearly. The sidelobe structure is a result of the sharp switch on and off of the chirp pulse, which has undergone little modification in passing through such a low Q transducer (see Fig. 2 of Chu and Stanton, 1998). As the Q of the transducer is increased, and hence the system bandwidth reduced, the amplitude at the beginning and end of the chirp pulse is reduced and hence also the sidelobe structure. This is seen clearly in moving from Fig. 7(a) through to Fig. 7(c). Any further reduction in bandwidth [Figs. 7(d)–(f)] not only further reduces the sidelobe amplitude but also has a significant adverse effect on the time resolution of the system. This is due to the reduced system bandwidth effectively shortening the chirp duration and hence the system resolution. Note that in Fig. 7 the amplitude scales in each of the six panels have been adjusted to produce approximately equal peak response amplitudes to facilitate the comparison of pulse shapes.

The decrease in temporal symmetry with respect to the peak response of the compressed pulse response in Fig. 7, with decreasing transducer bandwidth, results from the fact that the time-reversed chirp used in the processing is not matched to the phase response of the transducer. This is confirmed in Fig. 8, which is a repeat of Fig. 7 but with the matched filtering again being performed with a time-reversed chirp but with added phase compensation for the transducer response. All the curves can now be seen to show time symmetry. Figures 7 and 8 show that with low Q transducers ($Q<\sim 1$) the phase response of the transducer has little effect on the ''matched-filter'' response. However, at higher Q values, which are in fact more representative of practical transducers, using a filter matched to the phase response of the transducer could have advantages in simplifying the interpretation of backscatter from more complex targets. It also appears that the optimum Q for a transducer, or for the overall transmit–receive system if the system is not transducer limited, is equal to the frequency of the chirp divided by its bandwidth. At this setting we get some sidelobe suppression without incurring too much loss in temporal resolution. This optimal setting will be used in all the following analyses. As a typical transducer Q is more likely to be ~ 6 than the value of unity required for optimum resolution; it may also be

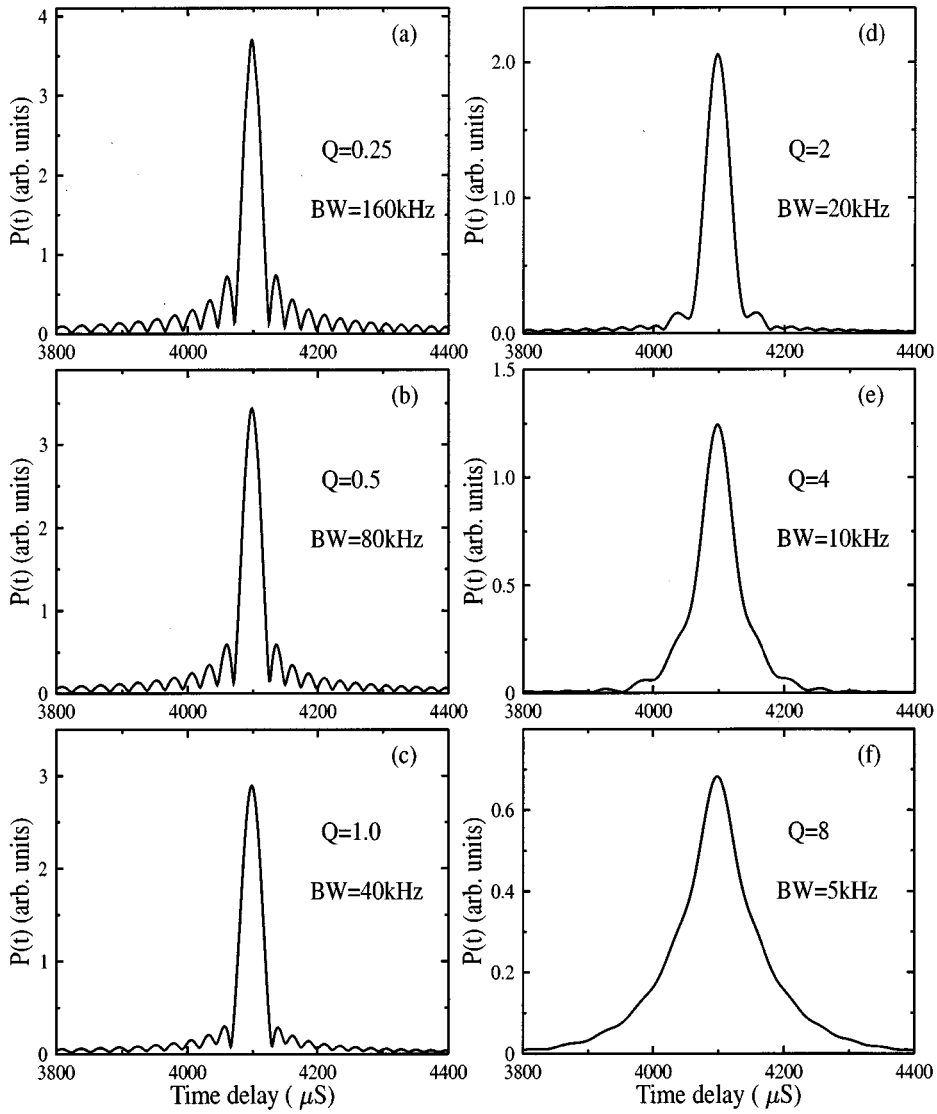

FIG. 8. Matched-filter response of long, thin air-filled spheroid to chirp pulse showing the effect of system/transducer bandwidth. Matched filter compensated for phase response of the system/transducer.

advantageous to use compensation for both the amplitude and phase response of the transducer in a practical target identification system.

In our case we wish to employ target identification techniques when we are surveying deep-water species in ''the target strength mode.'' In this mode we ''fly'' the acoustic transducer in a towed body, at a typical depth of 800 m, at a range of 10 to 100 m above the fish being studied. This gives us a reasonable chance of getting a significant number of echoes from single fish targets. At these comparatively short ranges it will also be possible to use high frequencies, with their accompanying increased attenuation loss, without too much return path signal loss. If one assumes that acoustic transducers have an approximately constant Q factor, then the maximum usable transducer bandwidth at any frequency, and hence the spatial resolution of our system, should be proportional to the mean frequency transmitted.

Having tested the matched-filter software against a simple spheroidal bladder target, we can now use the chirp software to derive the response of the fish models, developed in Sec. III, to insonification by chirp signals.

B. Model fish target responses

A theoretical black oreo, of total length 30 cm, as described in Table I and Figs. 1 and 2, was illuminated (in the dorsal aspect and zero tilt) by a series of 8-ms chirps of center frequencies (f_0), of 40, 80, and 160 kHz and bandwidths 10, 20, and 40 kHz. The theoretical matched response to these transmitted pulses is shown in the nine panels of Fig. 9. It can be seen that the dominant parameter of the chirp is the bandwidth, the chirp center frequency having only a second-order effect. The greater the chirp bandwidth, the better the spatial resolution. A comparison of Figs. 9(a), (d), and (g) for the black oreo, with Fig. 8(c) for the air-filled swimbladder, shows that the effect of the fish body is to produce small sidelobes on each side of the main response peak. The amplitude of the sidelobes is about 15 dB below that of the main peak. The small contribution of the fish body to the total response agrees with the target strength plot of the black oreo given in Fig. 3 which shows the target strength of the fish body to be about 17 dB below that of the swimbladder at 38 kHz.

Figure 10 shows the chirp response of our model smooth

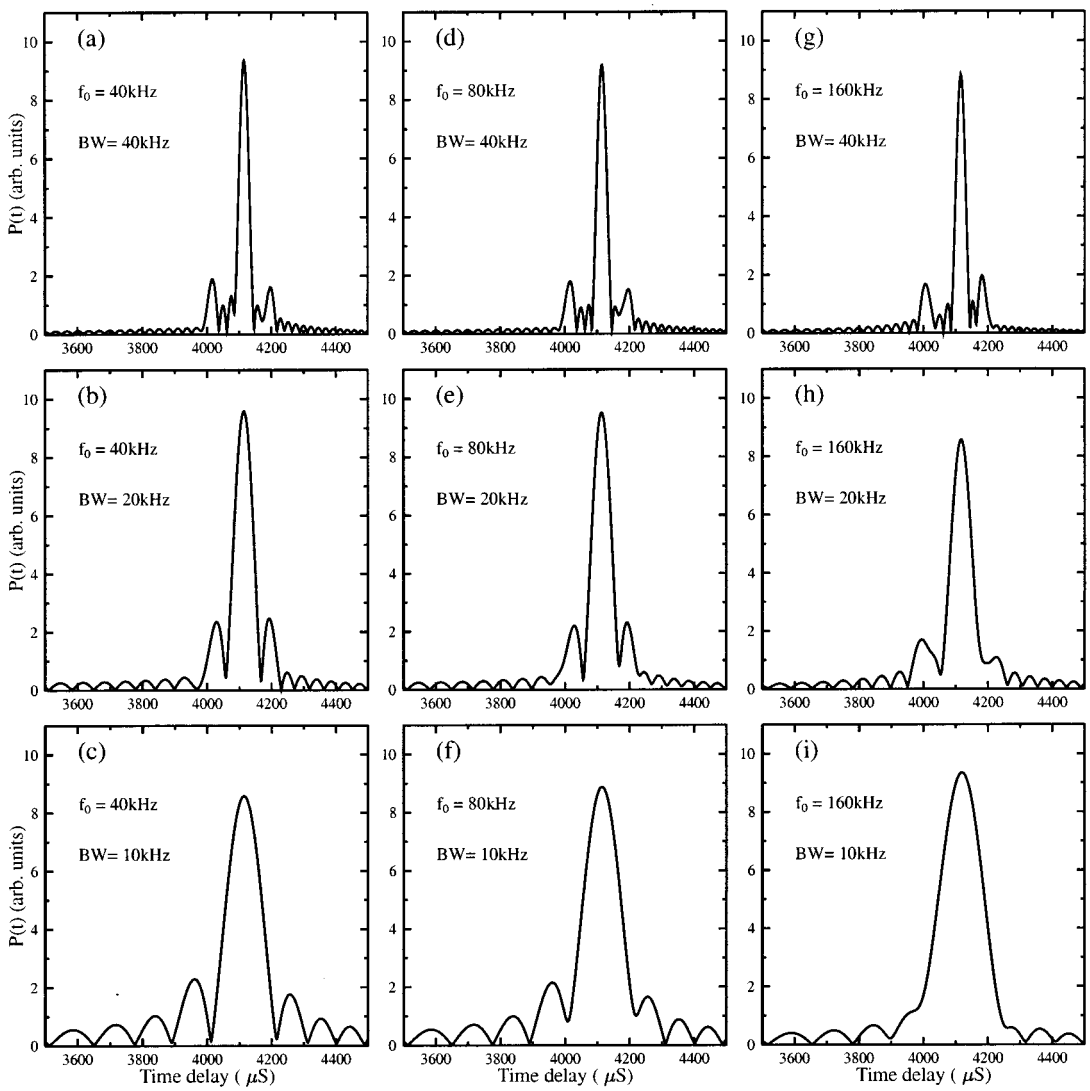

FIG. 9. Response of model black oreo to a range of chirp pulses.

oreo, as described in Table II and Figs. 1 and 2. It can be seen to be very similar to the response of the black oreo shown in Fig. 9 but with enhanced sidelobes. For both fishes the dominant scattering center is the upper surface of the air bladder. However, due to the smaller relative size of the bladder in the smooth oreo the pulse response of the bladder is reduced relative to that of the fish body, enhancing the relative importance of the sidelobes to about 11 dB. In fact, when using the response to chirps for target identification on air-bladdered fish, the most useful species specific data will probably be derived from the separation of the sidelobes, and the height of the sidelobes relative to the peak response. The spacing of the sidelobes should give information on fish size, and the height of the central peak should give information on the air-bladder backscatter without the obfuscating interference effects between body and bladder responses present in the normal target strength assessment [Figs. 4(c), 5(c), 6(c)].

To check the validity of this assumption, the ratio of the peak response to the sidelobe response of the matched and filtered backscatter from black and smooth oreos, ranging in length from 10 to 50 cm, has been plotted in Fig. 11. Due to the presence of some sidelobe asymmetry, the sidelobe amplitude was taken as the geometric mean of the amplitude of the upper and lower sidelobes. The data were obtained using an 8-ms chirp of center frequency 160 kHz and 40-kHz bandwidth. The data assume all the fish dimensions scale linearly. It can be seen that the peak to sidelobe response ratio is clearly different between the two fish groups, the ratio in blacks being typically 3 dB greater than smooths. The periodic fluctuations in the peak/sidelobe ratio are thought to be due the periodic oscillations in the pules response [see, for example, Figs. 7(a), (b), (c)]. This effect may be less marked when using a lower system bandwidth. Note that over the same range of fish lengths the target strength of large smooth oreos would have been the same as the target strength of smaller black oreos, making species-discriminatory decisions based on target strength alone ambiguous. However, it should be noted that no account is taken of ontogenetic changes and intraspecific variability in these comparisons. Such effects, together with the effects of fish tilt, will tend to blur out the distinctions between the two species. Regardless of theses effects, however, the technique still has more species discrimination than target strength alone.

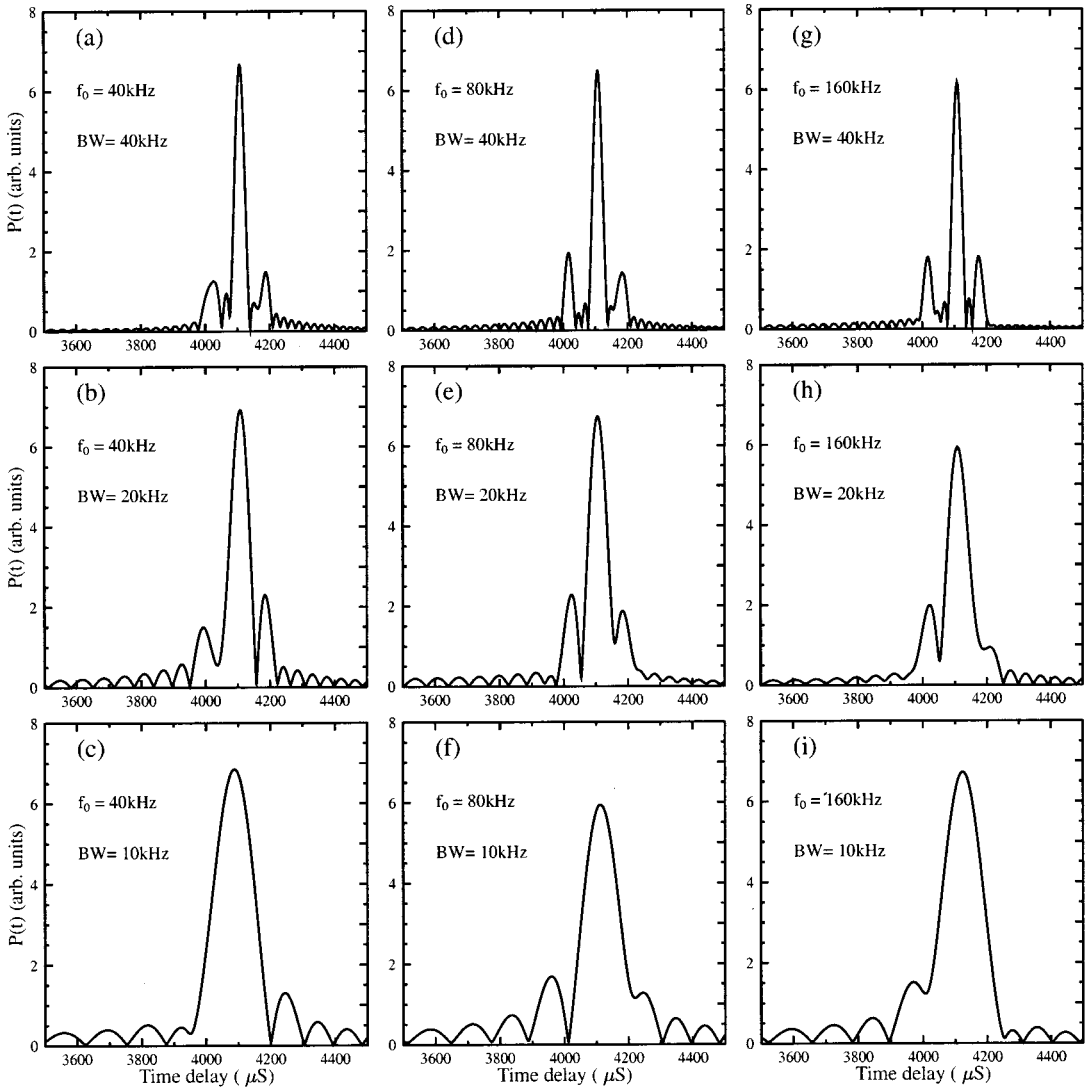

FIG. 10. Response of model smooth oreo to a range of chirp pulses.

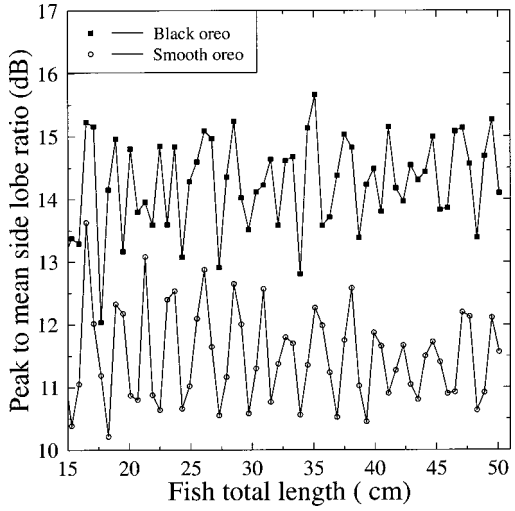

FIG. 11. Ratio of peak response to sidelobe response, plotted as a function of fish total length. Comparison of black and smooth oreo models.

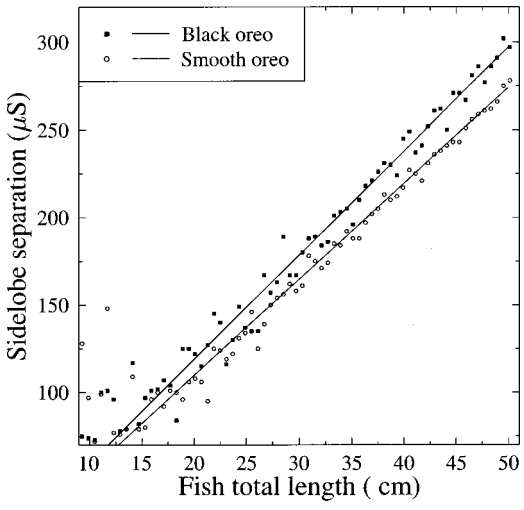

FIG. 12. Sidelobe separation in matched-filter response of black and smooth oreo models, plotted as a function of model fish total length.

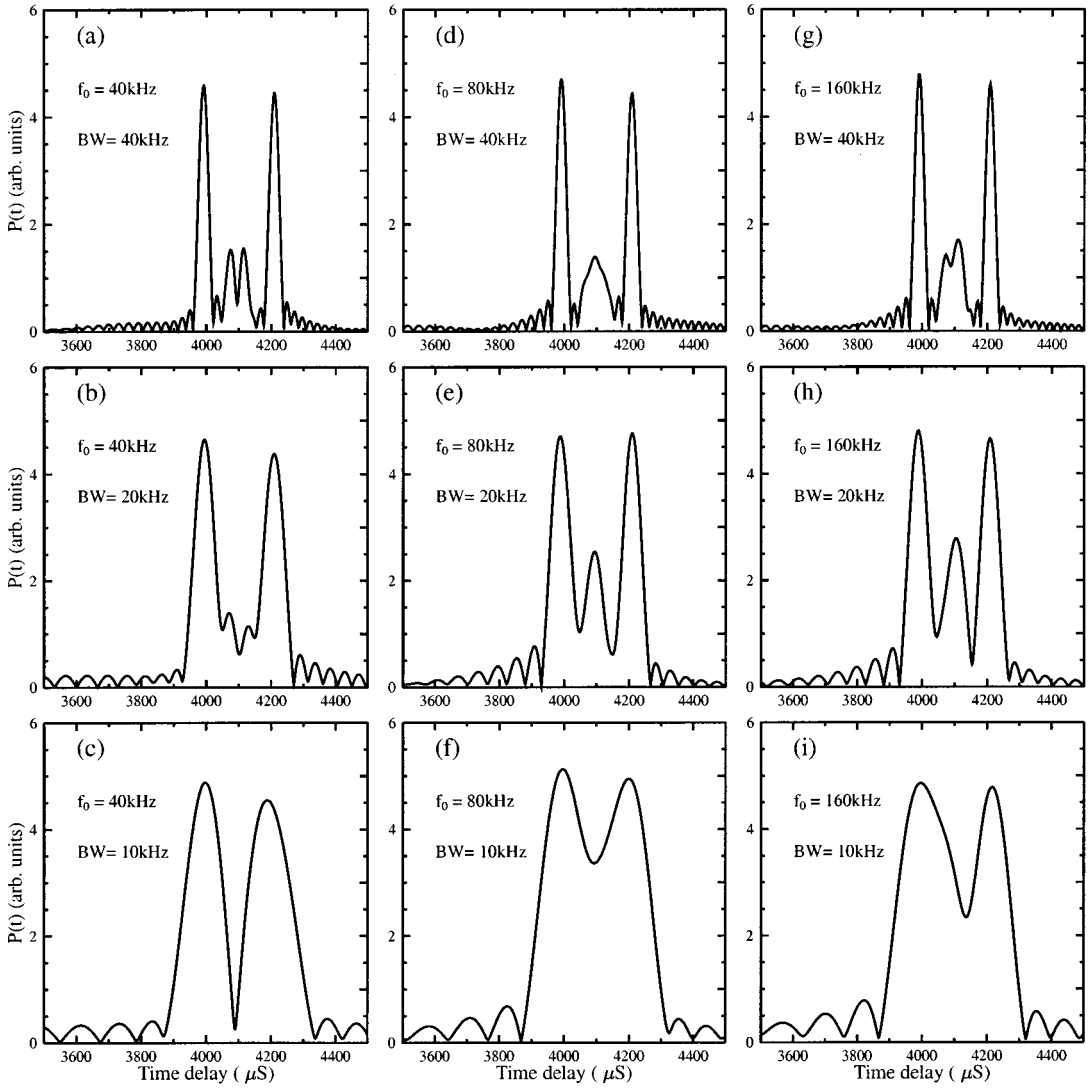

FIG. 13. Response of model orange roughy to a range of chirp pulses.

Figure 12 shows a plot of sidelobe separation for black and smooth oreo as a function of fish length, derived from the same data set as Fig. 11. It shows that the sidelobe separation of matched-filter chirp responses should be a useful method of estimating fish size. It should be remembered that the heights of our black and smooth oreos differ by only ~9% and as such they represent a difficult case study for target discrimination.

It could be argued that the sidelobe data could also be provided by a standard single-frequency acoustic pulse of sufficiently short duration. At 38 kHz a standard acoustic survey pulse has 1-ms duration and a target strength pulse (12 cycles) ~315 μS duration. Even the target strength pulse would only be able to resolve features ~25 cm apart. To resolve the upper and lower body echoes from a 20-cm oreo (height ~8.5 cm) one would need pulses of duration <110 μS or about 4 cycles of a 38-kHz signal. However, working with such short duration, and hence wide bandwidth pulses, with commonly available narrow-band transducers could not be expected to produce the signal-to-noise ratios one can achieve using an 8-ms chirp (see Chu and Stanton, 1998).

The filtered response of our model orange roughy, described in Table III and Figs. 1 and 2, is shown in Fig. 13. Calculations have again been presented for three different chirp bandwidths (40, 20, and 10 kHz) and three center frequencies (40, 80, and 160 kHz). It is clear the finer detail in the orange roughy model is more effective for comparing the spatial resolution of the nine chirp–pulse combinations than was the model black oreo. All three chirps with a bandwidth of 40 kHz are able to resolve both the upper and lower reflections from the fish body and also separate reflections from the oil swimbladder. However, only the 40- and 160-kHz chirps are able to resolve the reflections from the upper and lower surfaces of the swimbladder. The superior discrimination of the chirp with the 40-kHz center frequency is thought to be due to the fact that the 40-kHz chirp senses the target with waves ranging over a factor of 3:1 in wavelength (20 to 60 kHz). In contrast the 80-kHz chirp only covers a wavelength range of 1.66:1 and the 160-kHz chirp a range of 1.29:1. The 20-kHz bandwidth chirps clearly show the reflections from the upper and lower surfaces of the fish body and give some evidence of the presence of the swimbladder.

Again, only the chirp with a 40-kHz center frequency manages to resolve the swimbladder reflections. The 10-kHz bandwidth chirps are only capable of resolving the reflections from the fish body. Note, however, that even with a chirp of only 10-kHz bandwidth the responses of black oreos [Figs. 9(c), (f), (i)] and smooth oreos [Figs. 10(c), (f), (i)] are quite distinct, irrespective of the chirp center frequency, from the chirp response of orange roughy [Figs. 13(c), (f), (i)].

Phleger and Grigor (1990) state that most of the oil in an orange roughy lies in the flesh and just under the skin, so it is possible that in a real-life orange roughy the fish body echoes could be somewhat enhanced over those shown in Fig. 13. The orange roughy also has a large bony skull and spine, these together contain 20% of the total oil content of the fish. These extra scattering centers will add extra reflections to those shown in Fig. 13, making the response of a real orange roughy even more complex. However, this added complexity should make it even easier to distinguish between a diffuse target like the orange roughy and a localized target like the black oreo. Also, as the gonads of orange roughy are a significant fraction of total body volume during the spawning season, they should make up a measurable component in the chirp response. It may thus be possible to remotely sense the sex of orange roughy and even their gonad stage using a chirp sonar system.

V. SUMMARY

Using the simple slab-cylinder acoustic model for fish, developed by Clay and Horne (1994), we have derived the target strengths of three of New Zealand's deep-water fish species, namely orange roughy, black oreos, and smooth oreos. The target strengths derived from our models have been found to be in reasonable agreement with currently accepted target strength values. Unlike some earlier studies on black and smooth oreos, our calculations have included scattering effects due to the body of the fish as well as the air-filled swimbladder.

The scattering results for black oreos are very similar to earlier work of Foote (1980) on gadoids and mackerel in that 90% of the scattered energy comes from the air-filled swimbladder rather than the fish body. The dominant scattering source in the black oreo is localized to the surface of the air-filled bladder. In contrast, the oil-filled swimbladder of the orange roughy scatters at a similar level to the rest of the fish body. All body parts in the roughy, having different densities or supporting different propagation velocities for sound waves, contribute in roughly similar amounts to the scattering cross section. The roughy is thus a much more distributed scattering source. The smooth oreo, with its smaller air-filled swimbladder, exhibits scattering with values between the extremes presented by the black oreo and the orange roughy. The air bladder in the smooth oreo scatters with about 3 times the efficiency of the fish body.

The above three fish models have been used in a study to test the ability of a chirp sonar system to discriminate between fish of different species. Chirps of duration 8 ms, center frequencies of 40, 80, and 160 kHz and bandwidths of 10, 20, and 40 kHz have been used to model the insonification of the three fish species listed above, and the matched-filter responses to the chirps have been determined. The effect of the response of transducer (system bandwidth) has also been investigated. We have found:

The bandwidth of the chirp is much more important for resolving detail in a target fish than the chirp center frequency.

A chirp bandwidth of at least 20 kHz, and preferably 40 kHz, produces matched-filter responses for black and smooth oreos and orange roughy which are quite clearly specie specific.

The matched-filter chirp response can also be used to distinguish between black and smooth oreos themselves, the ratio of peak response to mean sidelobe response being the species-specific parameter. However, the difference is small and in the real world the distinction will be blurred by variability of the fish population and also by fish tilt. However, it must also be remembered that black and smooth oreos are similar fish in comparison to say, oreos and hoki, where the same parameter may provide more effective discrimination.

The sidelobe spacing can provide direct information on fish size.

The more complex chirp response of orange roughy holds the possibility of even more target-specific information. It may even be possible with chirp sonar to monitor remotely both the sex and gonad stage of orange roughy during the spawning season.

ACKNOWLEDGMENTS

I would like to thank Roger Coombs and my colleagues in the acoustics and fisheries groups for useful discussions. I would like to thank Di Tracy for pointing me to useful biological papers on orange roughy and Alan Hart for injecting the smooth oreo swimbladders with barium-loaded epoxy resin. I would also like to thank Sam McClatchie for helpful comments on the first draft of the paper. Funding for this research was provided by the New Zealand Ministry of Fisheries under Project Nos. OEO9801 and ORH9801.

Barr, R. (**2000**). ''Black and smooth oreo target strength developments,'' slides presented to Deep Water Fishery Assessment Working Group, Greta Point, 20 April 2000, Document number 00/41, held by Ministry of Fisheries, Wellington.

Chu, D., and Stanton, T. K. (**1998**). ''Applications of pulse compression techniques to broadband acoustic scattering by live individual zooplankton,'' J. Acoust. Soc. Am. **104**, 39–55.

Clark, M. (**1995**). ''Experience with management of orange roughy (*Hoplostethus Atlanticus*) in New Zealand waters, and the effects of commercial fishing on stock over the period 1980–1993,'' in *Deepwater Fisheries of the North Atlantic Oceanic Slope*, edited by A. G. Hopper (Kluwer Academic, Dordrecht).

Clark, M., and Tracy, D. M. (**1994**). ''Changes in a population of orange roughy, *Hoplostethus Atlanticus*, with commercial exploitation on the Challenger Plateau, New Zealand,'' Fish. Bull. **92**, 236–253.

Clay, S. C. (**1992**). ''Composite ray-mode approximations for backscattered sound from gas-filled cylinders and swimbladders,'' J. Acoust. Soc. Am. **92**, 2173–2180.

Clay, S. C., and Horne, J. K. (**1994**). ''Acoustic models of fish: The Atlantic cod (*Gadus morhua*),'' J. Acoust. Soc. Am. **96**, 1661–1668.

Coombs, R. F., Barr, R., and Hart, A. C. (**2000**). ''Target strength of black and smooth oreos,'' unpublished draft paper, part of Doonan *et al.* (2000) listed below, held by Ministry of Fisheries, Wellington.

Cordue, P. L. (**1996**). ''On the feasibility of using acoustic techniques to estimate orange roughy and oreo biomass on underwater hills,'' New Zealand Fisheries Assessment Research Document 96/22.

CRC (**1973**). *Handbook of Chemistry and Physics* (CRC Press, Boca Raton).
Do, M. A., and Coombs, R. F. (**1989**). ''Acoustic measurements of the population of orange roughy (*Hoplostethus Atlanticus*) on the north Chatham Rise, New Zealand,'' New Zealand J. Mar. Freshwater Res. **23**, 225–237.
Doonan, I. J., Coombs, R. F., McMillan, P. J., and Dunn, A. (**1998**). ''Estimate of the absolute abundance of black and smooth oreo in OEO 3A and 4 on the Chatham Rise,'' Final research report for the New Zealand Ministry of Fisheries Research Project No. OEO9701, NIWA.
Doonan, I. J., Hart, A., McMillan, P. J., and Coombs, R. F. (**2000**). ''Oreo abundance estimates from the October 1998 survey of the south Chatham Rise, OEO 4,'' Final research report for the New Zealand Ministry of Fisheries Research Project No. OEO9801, NIWA.
Doonan, I. J. (**2000**). Private communication.
Elliot, N. G., and Kloser, R. J. (**1993**). ''Use of acoustics to assess a small aggregation of orange roughy, *Hoplostethus Atlanticus* (Collet), off eastern coast of Tasmania,'' Aust. J. Mar. Freshwater Res. **44**, 407–413.
Foote, K. G. (**1980**). ''Importance of the swimbladder in acoustic scattering by fish: A comparison of gadoid and mackerel target strengths,'' J. Acoust. Soc. Am. **67**, 2084–2089.
Hart, A. (**2000**). Private communication.
Jech, J. M., and Horne, J. K. (**1998**). ''Sensitivity of acoustic scattering models to fish morphometry,'' J. Acoust. Soc. Am. **103**, 2958(A).
Kloser, R. J., Koslow, J. A., and Williams, A. (**1996**). ''Acoustic assessment of the biomass of a spawning aggregation of orange roughy (*Hoplostethus Atlanticus*, Collet) off Southeastern Australia, 1990–93,'' Mar. Freshwater Res. **47**, 1015–1024.
Kloser, R. J., Ryan, T. E., Williams, A., and Soule, M. (**2000**). ''Development and implementation of an acoustic survey of orange roughy in the Chatham Rise Spawning box from the commercial factory trawler, Amaltal Explorer,'' Report 597.64, CSIRO Marine Research, Hobart, Tasmania.
Koslow, J. A., Kloser, R., and Stanley, C. A. (**1995**). ''Avoidance of a camera system by a deepwater fish, orange roughy (*Hoplostethus Atlanticus*),'' Deep-Sea Res., Part I **42**, 233–244.
Koslow, J. A., and Kloser, R. J. (**1999**). ''Development of acoustic methods to survey orange roughy in the Eastern and Southern Zones,'' Report FRDC 95/031, CSIRO Division of Marine Research, Hobart, Tasmania.
LeFeuvre, P., Rose, G. A., Gosine, R., Hale, R., Pearson, W., and Kahn, R. (**2000**). ''Acoustic species identification in the Northwest Atlantic using digital image processing,'' Fisheries Res. **47**, 137–147.
Mackenzie, K. V. (**1981**). ''Nine-term equation for sound speed in the oceans,'' J. Acoust. Soc. Am. **70**, 808–812.
McClatchie, S., Aslop, J., Ye, Z., and Coombs, R. F. (**1996**). ''Consequence of swimbladder model choice and fish orientation to target strength of three New Zealand fish species,'' ICES J. Mar. Sci. **53**, 847–862.
McClatchie, S., Macauly, G., Coombs, R. F., Grimes, P., and Hart, A. (**1999**). ''Target strength of an oily deep-water fish, orange roughy (*Hoplostethus Atlanticus*). I. Experiments,'' J. Acoust. Soc. Am. **106**, 1–12.
McClatchie, S., and Ye, Z. (**2000**). ''Target strength of an oily deep-water fish, orange roughy (*Hoplostethus Atlanticus*). II. Modeling,'' J. Acoust. Soc. Am. **107**, 1280–1285.
McClatchie, S., (**2000**).
Medwin, H., and Clay, S. C. (**1998**). *Fundamentals of Acoustical Oceanography* (Academic, London).
Paul, L. J. (**1986**). *New Zealand Fishes: An Identification Guide* (Reed Methuen, Auckland, New Zealand).
Phleger, C. F., and Grigor, M. R. (**1990**). ''Role of wax esters in determining buoyancy in *Hoplostethus Atlanticus* (Beryciormes: Trachichthyidae),'' Mar. Biol. (Berlin) **105**, 229–233.
Rose, G. A., and Leggett, W. C. (**1988**). ''Hydroacoustic signal classification of fish schools by species,'' Can. J. Fish. Aquat. Sci. **45**, 597–604.
Scalabrin, C., Diner, N., Weill, A., Hillion, A., and Mouchot, M. (**1996**). ''Narrowband acoustic identification of monospecific fish shoals,'' ICES J. Mar. Sci. **53**, 181–188.
Shibata, K. (**1969**). ''Study on details of ultrasonic reflection from individual fish,'' thesis submitted for the degree of Doctor of Fisheries at the Hokkaido University.
Stanton, T. K., Clay, C. S., and Chu, D. (**1993**). ''Ray representation of sound scattering by weakly scattering deformed fluid cylinders: Simple physics and applications to zooplankton,'' J. Acoust. Soc. Am. **94**, 3454–3462.
UNESCO (**1981**). ''Background papers and supporting data on the International Equation of State of Seawater 1980,'' UNESCO Technical papers in marine science.
Ye, Zhen (**1997**). ''Low-frequency acoustic scattering by gas-filled prolate spheroids in liquids,'' J. Acoust. Soc. Am. **101**, 1945–1952.

Dynamic measurements of the thermal dissipation function of reticulated vitreous carbon

L. A. Wilen[a)]
Department of Physics and Astronomy, Ohio University, Athens, Ohio 45701

(Received 8 March 2000; revised 10 October 2000; accepted 20 October 2000)

A volume modulation technique is employed to measure the complex compressibility of a gas in reticulated vitreous carbon (RVC). The complex compressibility depends on the geometry-dependent thermal coupling between the gas and the solid walls, and is related to the thermoacoustic function f_κ, or equivalently $F(\lambda_T)$. By measuring samples of different cross section and length, all external boundary effects are eliminated, so that $F(\lambda_T)$ corresponding to bulk RVC is determined. Working down to very low frequencies achieves a wide range of values for the ratio of the thermal penetration depth to the mean pore size. As a test of the concept of ''capillary-based porous media,'' the results are compared to analytical solutions for $F(\lambda_T)$ in circular, parallel plate and pin-array geometries. Measurements made at peak-to-peak gas displacement amplitudes exceeding the pore size in at least half of the sample showed no observable deviation from the small-amplitude results. © *2001 Acoustical Society of America.* [DOI: 10.1121/1.1333422]

PACS numbers: 43.35.Ud, 43.20.Mv, 43.20.Ye [SGK]

I. INTRODUCTION

Novel stack geometries have the potential to improve the efficiency of thermoacoustic devices. Recent tests with reticulated vitreous carbon[1] showed that it can perform comparably to conventional parallel-plate stacks in prime-movers and refrigerators.[2] RVC is a highly porous rigid open-cell foam structure composed of vitreous (amorphous) carbon. It has the desirable properties of low thermal conductivity, high melting point, and ease of construction. In order to characterize the thermoacoustic properties of novel stacks, we have recently developed techniques which can directly measure some of the relevant thermoviscous functions for a sample.[3,4] These techniques were successfully tested on pores of simple geometry (circular, rectangular, etc.) for which the analytical solution was known. A similar technique was also employed by Hayden and Swift[5] to measure the thermal dissipation function, $F(\lambda_T)$, for the pin-array geometry. Here we present measurements of $F(\lambda_T)$ for RVC, the first application of such techniques to a random porous media. These results are useful in determining the optimal operating frequency for thermoacoustic devices using RVC of a specified nominal pore size. Our results can also be used to test the ideas of ''capillary-based porous media.'' These ideas, first pioneered by Rayleigh,[6] model a complex porous material as an array of parallel circular tubes or parallel plates. For these cases, analytic solutions can be found for the complex compressibility and complex density. Later workers developed more sophisticated techniques by defining ''shape factors'' or by finding analytical solutions to more complicated geometries such as pin-arrays and crossed pin-arrays.[7,8] We compare some of the results of these capillary-based models to our measurements of the complex compressibility of RVC. By measuring a material with two different pore sizes, we demonstrate that scaling holds so that our results should be applicable to RVC of any pore size. Finally, we explore a high-amplitude regime of operation where the displacement of the gas is larger than the nominal pore size.

II. EXPERIMENTAL TECHNIQUE

The apparatus is very similar to the ones described in Refs. 3 and 4. The setup is shown in Fig. 1. A 4-in. woofer, driven by the reference output of a lock-in (buffered with a power amplifier), modulates an electro-formed bellows attached to one side of a porous sample. The motion of the bellows is monitored by bouncing a laser beam off a mirror on the speaker cone onto a position-sensitive detector (United Detector Technology model LSC/5D). The resulting pressure oscillations are sensed with a silicon pressure gauge (Honeywell Microswitch model 24PCAFA1G). The position and pressure signals are detected simultaneously with two digital vector lock-in amplifiers (Stanford Research Systems models SR850 and SR830) locked to the same reference frequency. The drive frequency is stepped from 0.5 to 96 Hz in 71 equal increments of $f^{1/2}$. The complex pressure response is then divided by the complex displacement response for all measured frequencies. This normalized pressure response will be referred to throughout the article as $p(\omega)$.

The setup was designed so that different sample lengths and geometries could easily be inserted (and sealed) or removed. Before taking data for each sample, the cell was first flushed with dry nitrogen gas for 30 min and then sealed off under approximately one atmosphere of nitrogen. The static pressure in the cell was determined by measuring the outside pressure with a mercury barometer and the pressure difference between the inside and outside with the silicon pressure gauge, which was calibrated separately. The cell was allowed to equilibrate to room temperature, which was measured with a mercury thermometer. A complete run for one pore took 35 min, during which time the drift in pressure and temperature was typically less than 1.5 torr and 0.1 °C, respectively.

a)Electronic mail: Wilen@helios.phy.ohiou.edu

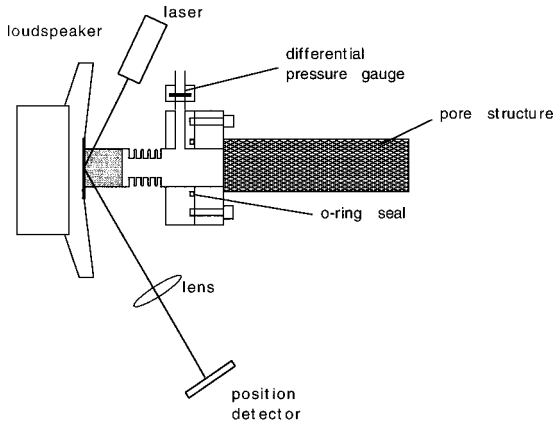

FIG. 1. Schematic diagram of the experimental setup.

Typically, two or three runs were made with a given pore to check that the data were reproducible.

Measurements were made on samples of different size. These measurements determined the thermoacoustic function $F(\lambda_T)$ corresponding to bulk RVC, as discussed below. The dimensions and shapes of the different samples used in the experiment are shown in Fig. 2.

III. THEORY

In the low-frequency limit, the pressure response can be considered spatially uniform. To first order, the pressure and volume of the cell can be written as

$$P(t)=P_0+P_1(\omega)\exp(-i\omega t),$$
$$V(t)=V_0+V_1(\omega)\exp(-i\omega t), \tag{1}$$

where P_0 and V_0 are the equilibrium values and P_1 and V_1 are the acoustic variations. The complex compressibility is defined in terms of these quantities as

$$C(\omega)=-\frac{1}{V_0}\frac{V_1(\omega)}{P_1(\omega)}. \tag{2}$$

Throughout this article, it will prove more convenient to work with the dimensionless quantity, $P_0C(\omega)$. Also for convenience, the term ''compressibility'' will be used to refer to the normalized value. The compressibility is related to the experimentally measured normalized pressure response, $p(\omega)$, as follows:[3]

$$P_0C(\omega)=\frac{p(0)}{p(\omega)}. \tag{3}$$

In addition, the volume of the cell can be expressed as[3]

$$V_0=-\frac{P_0A_{\text{eff}}}{p(0)}, \tag{4}$$

where A_{eff} is the effective cross-sectional area of the bellows. The thermoacoustic function $F(\lambda_T)$ for a sample is defined in terms of the complex compressibility as follows:[9]

$$F(\lambda_T)=\frac{\gamma}{\gamma-1}[1-P_0C(\omega)], \tag{5}$$

where

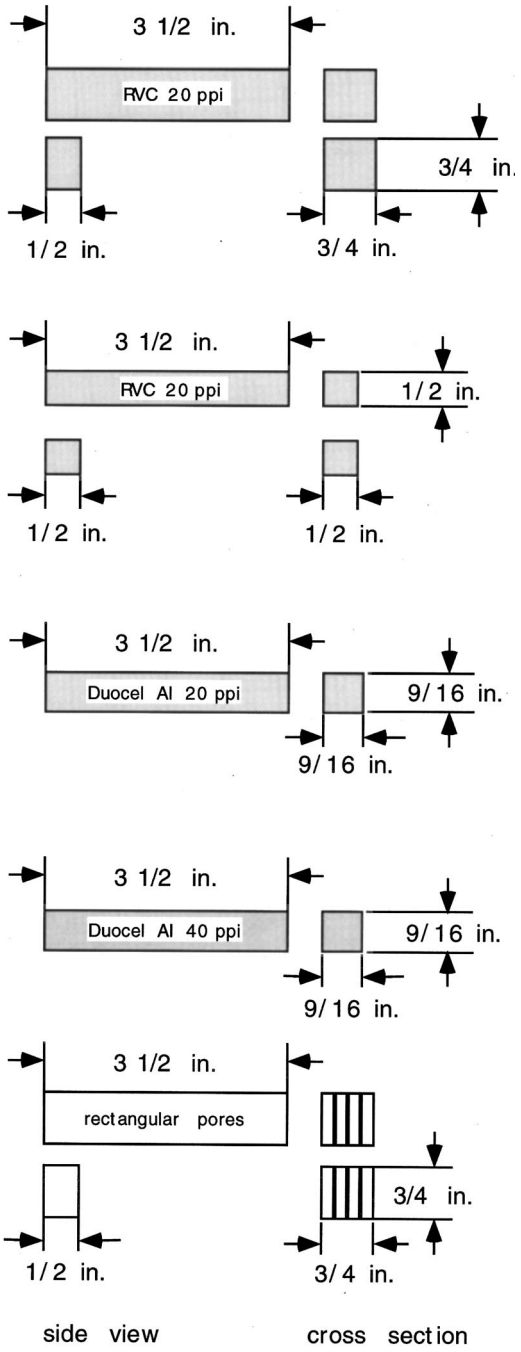

FIG. 2. Geometry and outside dimensions of the samples used in the experiment. The wall thickness of the brass tubes was 0.028 in.

$$\lambda_T=R\sqrt{\frac{\rho_0\omega c_p}{\kappa}}. \tag{6}$$

Here γ is the usual ratio of specific heats, ρ_0 is the gas density, c_p is the isobaric heat capacity, and κ is the thermal conductivity. R is the characteristic pore radius which is defined (for pores of uniform cross section) as twice the transverse pore area divided by the pore perimeter. Because this quantity is unknown for RVC, we will use the nominal pore size specified by the manufacturer.[10]

In previous work, we showed that by measuring two lengths of a single pore, we can determine the compressibility corresponding to an infinite-length pore.[3] The measured

compressibility is the sum of the compressibilities of the uniform middle part of the pore and the ends of the pore which contain the bellows, pressure gauge, etc., each weighted by their respective volumes. Two pores of different lengths have the same contribution from the ends, and the proper subtraction yields the compressibility from the middle part alone. The same subtraction can be performed with two samples of RVC. However, because of the larger diameter of bellows used in the present experiment, it is necessary to analyze the data in a slightly different way than was done previously. The reason is the following: with a large-diameter bellows, the gas in the bellows (and also the open region adjacent to it on the right) does not undergo isothermal oscillations until extremely low frequencies are reached. Consequently, the procedure we used previously to find P_0C, which involved extrapolating to the zero frequency limit of the pressure response, was more difficult here. Fortunately, it is possible to rearrange the equation describing the subtraction procedure to show that the subtraction can be done first on the raw data, followed by an extrapolation to zero frequency to get the same final result. The formula for the subtraction is given by

$$[P_0C(\omega)]_\infty = \frac{V_a[P_0C(\omega)]_a - V_b[P_0C(\omega)]_b}{V_a - V_b}, \tag{7}$$

where the subscript (∞) refers to a sample which is infinite in its length but not in its cross section. Combining this with Eqs. (4) and (5), this expression can be recast as

$$[P_0C(\omega)]_\infty = \frac{h(\omega)}{h(0)}, \tag{8}$$

where the function $h(\omega)$ is defined as follows:

$$h(\omega) = P_a/p_a(\omega) - P_b/p_b(\omega). \tag{9}$$

Here P_a and P_b are the static pressures for each of the runs. $h(\omega)$ is fully determined from experimentally measured quantities. Furthermore, $h(\omega)$ can be easily extrapolated to zero frequency because the troublesome bellows part of the response has already been subtracted out. Strictly speaking, Eq. (9) is correct only when the static pressure and temperature is the same for both runs, i.e., $P_a = P_b$, $T_a = T_b$. However, we can take advantage of scaling properties to relate two runs taken at different static pressures and temperatures (denoted by α and β):[11,12]

$$p_\alpha(\omega) = \frac{P_\alpha}{P_\beta} p_\beta\left(\omega \frac{P_\alpha T_\beta c_p(T_\alpha)\kappa(T_\beta)}{P_\beta T_\alpha c_p(T_\beta)\kappa(T_\alpha)}\right). \tag{10}$$

In practice, we always scale the run taken for the short pore to have the same pressure and temperature as that of the long pore. The pressure and temperature do not vary greatly in the laboratory and this scaling correction never exceeded 2%. The thermal response function is calculated from the compressibility according to Eq. (5).

Performing the above subtraction on two different-length samples of RVC yields the thermal response function for a sample of ''infinite'' length (i.e., with no end effects present). However, this is not the desired final result because there are still ''perimeter'' corrections due to the plane boundaries between the RVC and the brass tube holding the sample. The pores adjacent to the tube walls will not have the same thermal behavior as pores in the middle. To eliminate this effect, we perform measurements on two pairs of samples. Each pair consists of a short ($\frac{1}{2}$ in.) and a long ($3\frac{1}{2}$ in.) sample of RVC in a square tube, but the tube cross section is different for each pair. The usual subtraction is first performed for each pair. Because each pair has a different volume-to-area ratio, it is then possible to perform a third subtraction to eliminate all effects of the perimeter to achieve the true bulk result. The details are as follows: assume that there is a region of width d near the walls of the tube where the compressibility is modified due to the RVC/wall interface. The volume of this region is A^*d, where A is the total area of the outside boundary. We associate with this region an ''areal'' thermal response function $F_A(\lambda_T)$. In the interior of the sample, the thermal response function is the one for bulk, denoted by $F_B(\lambda_T)$. As usual, the measured response function is the sum of response functions weighted by their relative volumes:

$$F(\lambda_T)_\infty = \frac{(V - Ad)F_B(\lambda_T) + AdF_A(\lambda_T)}{V}. \tag{11}$$

If we now take the ''infinite'' results from two pairs having different values for V/A, we can solve to find the bulk result which we denote $F_B(\lambda_T)$. Let F_{p1}, V_{p1}, A_{p1}, and F_{p2}, V_{p2}, A_{p2} denote the response function, volume, and area, from the first and second pairs, respectively. Then

$$F_B(\lambda_T) = \frac{(V_{p1}/A_{p1})F_{p1}(\lambda_T) - (V_{p2}/A_{p2})F_{p2}(\lambda_T)}{V_{p1}/A_{p1} - V_{p2}/A_{p2}}. \tag{12}$$

Technically, there is also a correction to the thermal response at the edges of the tube where the faces meet in lines at 90 degrees. We will see that the areal corrections are already quite small, so that it is reasonable to neglect these ''line'' corrections.

Finally, in order to get the most accurate results for $F(\lambda_T)$, it is necessary to correct for the finite length of the pore relative to an acoustic wavelength. In past work, we have seen small discrepancies between experiment and theory at higher frequencies. This was attributed to the fact that the pressure oscillations are not perfectly uniform throughout the sample cell. In effect, there are deviations due to the ''tail'' of the first resonance in the tube. Here, we correct for this effect using the following procedure. We model the cell as an assembly of ducts of the appropriate cross section and length. We solve for the acoustic pressure at the position of the pressure gauge as a function of the velocity of the speaker cone using the boundary conditions at the ends of, and between, ducts. We assume that the wave vector k is given by the adiabatic plane wave value,

$$k = \frac{\omega}{c}, \tag{13}$$

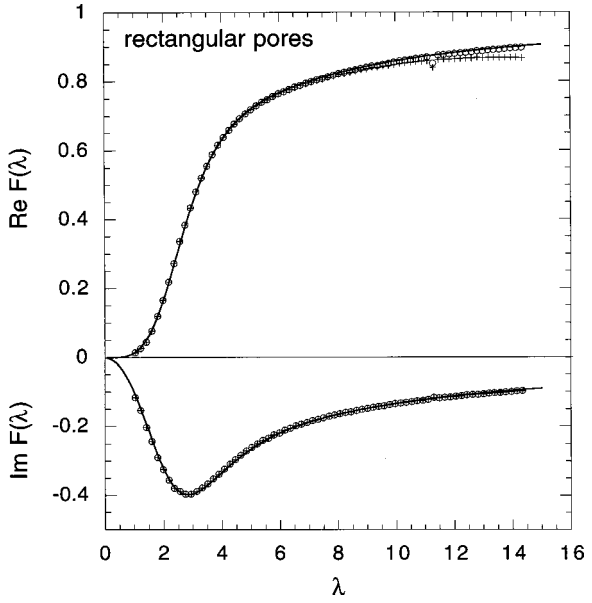

FIG. 3. $F(\lambda_T)$ vs λ_T plotted for the results from rectangular pores. The circles include the finite kL correction and the plusses are uncorrected. The solid lines are the results of the theory for this specific rectangular geometry.

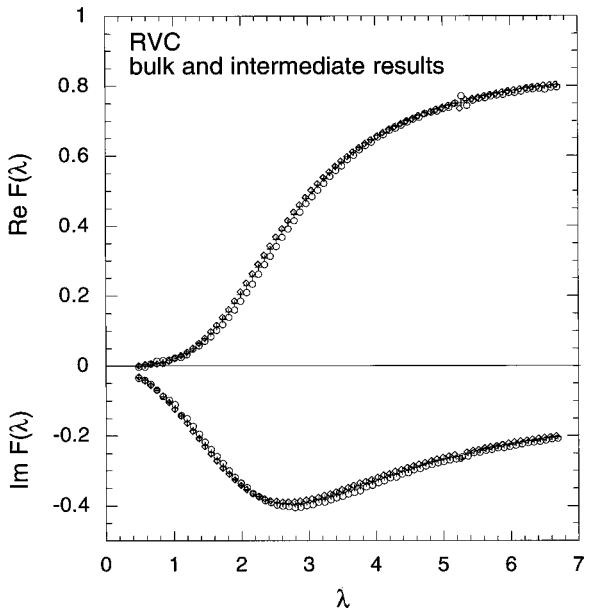

FIG. 4. $F(\lambda_T)$ vs λ_T plotted for RVC. The circles are the final result for bulk RVC. The diamonds are the intermediate ''infinite'' results from the $\frac{1}{2}$ -in. tubes and the plusses are the intermediate ''infinite'' results from the $\frac{3}{4}$ -in. tubes.

where c is the adiabatic speed of sound. We then normalize the acoustic pressure at the gauge by the value obtained by setting $k=0$. The resulting expression is a ''finite kL'' correction factor that we use to correct the measured pressure oscillations. This correction factor is approximate in the following sense. The wave vector is not strictly given by Eq. (13), but depends on the complex compressibility and complex density of the gas.[8,9,13] However, the finite kL correction is extremely small except at the highest frequencies measured, where Eq. (13) is a reasonable approximation. In the lower frequency range, the correction term has negligible effect on the data.

To test this procedure, we measured $F(\lambda_T)$ for an array of rectangular pores, depicted in Fig. 3. The results are displayed with and without the correction, compared to the theory for this geometry. These results give us confidence that this procedure is valid. All the remaining results for $F(\lambda_T)$ have been corrected in this fashion.

IV. RESULTS AND DISCUSSION

In Fig. 4, the bulk result for 20 ppi RVC is shown along with the intermediate ''infinite'' results for each of the sample pairs. The small anomaly observed in all the experimental curves is due to pickup at 60 Hz. The experimental data for F are plotted against $\lambda_T=(\rho_0\omega c_p/\kappa)^{1/2}R$, where R is the nominal pore size specified by the manufacturer. (In this case, $R=\frac{1}{20}$ in.) Note that the ''infinite'' results are already very close to the bulk results. In particular, the position of the dip in the imaginary part is at almost the same position in all three curves.

In Fig. 5, we plot the bulk RVC results along with the theory for parallel plates, circular pores, and pin-arrays.[14] For pin-arrays, the theory depends on the ratio of the pin diameter to pin spacing. We chose this ratio by taking the pin diameter to be the same as the web thickness of the RVC, and the pin spacing to be given by the pore spacing in the RVC ($\frac{1}{20}$ in.). For each comparison, we adjusted the value of R for the RVC so that the position of the minimum in the measured curve for Im[F] lined up with that of the theory. The value of R used for RVC in each case is included in the figure. These results are useful for both porous media studies and thermoacoustics. Note that it is a good approximation to model RVC by parallel plates whose spacing is about 15% larger than the average RVC pore size. This can be thought of as a validation of the ideas of ''capillary-based porous media,'' at least as far as the complex compressibility is concerned. For thermoacoustic applications, these results can be used to determine what size pores should be chosen for a device operating at a particular frequency, or vice versa. Within the inviscid, short stack approximation, Arnott *et al.*[9] have shown that the power of a prime-mover is proportional to $-\mathrm{Im}[F(\lambda_T)]$. So, for example, for pores the same size as those used here (20 ppi), the optimal frequency of operation for a thermoacoustic prime-mover would be set by $\lambda_T \approx 2.8$, with R given by $\frac{1}{20}$ in. (1.25 mm). This corresponds to 17 Hz for N_2 at atmospheric pressure and room temperature (22 °C). The similarity between the RVC response and that for parallel plates of spacing on the order of 1/#ppi is consistent with the results found by Adeff *et al.*[2] in their comparisons of the performance of thermoacoustic devices employing parallel plates and RVC.

If these results are to be applicable to other studies, we must establish that our measurements can be ''scaled'' to describe RVC with other pore sizes. For example, if we study RVC with half the pore spacing, we should get the same result for $F(\lambda_T)$ if all dimensions of the RVC scale with the pore size.

Due to sample availability, measurements to test scaling were performed with two sizes (20 and 40 ppi) of an aluminum material having a geometry very similar to RVC.[15] For

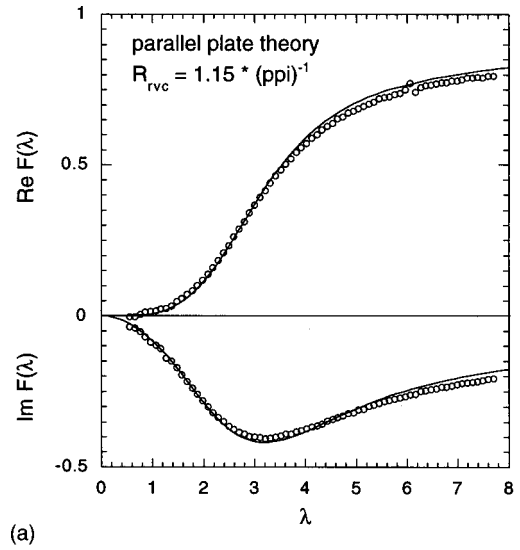

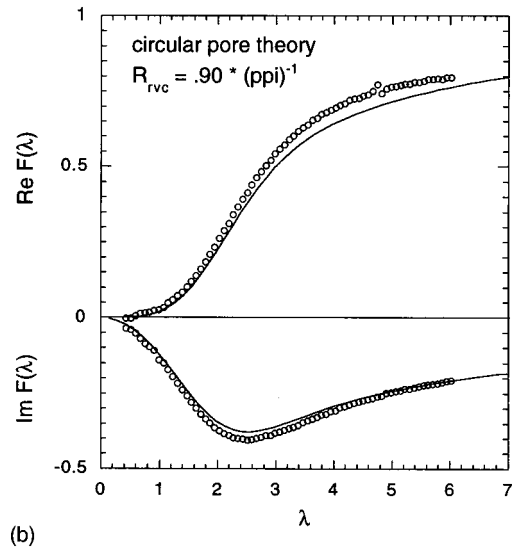

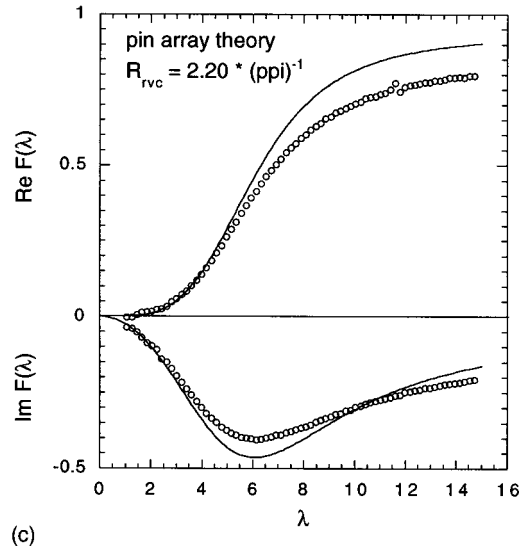

FIG. 5. $F(\lambda_T)$ vs λ_T plotted for the results of bulk RVC compared with (a) circular pores, (b) parallel plates, and (c) pin-arrays.

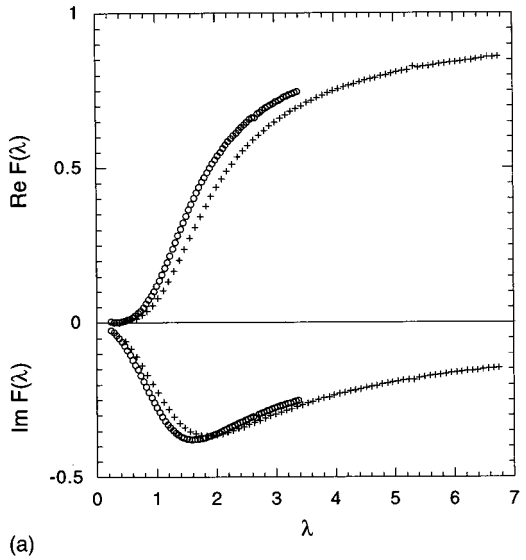

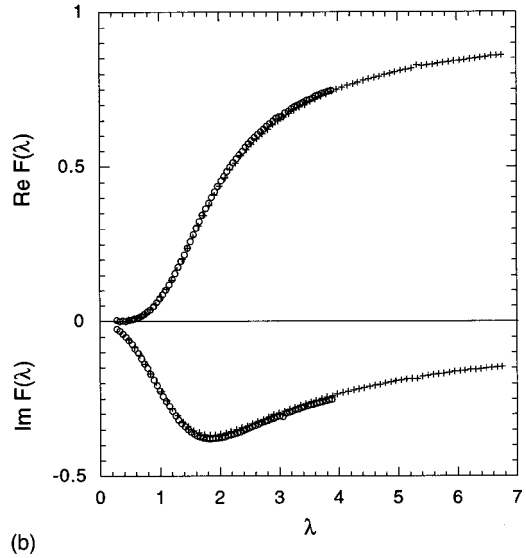

FIG. 6. $F(\lambda_T)$ vs λ_T plotted for two pore sizes of Duocel aluminum. The circles and plusses are the results for 40 and 20 ppi, respectively. In (a) lambda is calculated from the pore sizes specified by the manufacturer. In (b), the pore size of the finer sample is allowed to vary to give the best fit, which is achieved for $R = 1/(35\ \text{ppi})$.

this comparison, we did not use the full subtraction procedure described earlier. Instead, for each sample, the short pore was simply a flange which ''blanked off'' the bellows portion of the cell. No attempt was made to eliminate the corrections due to the perimeter boundaries. However, from our above results, and other comparisons performed, we know that these simpler measurements are still a fairly good approximation to the true bulk results.

Figure 6(a) shows the results. Although the curves have a similar shape, they do not line up particularly well. In Fig. 6(b), we show the results when the pore size of the finer (40 ppi) sample is allowed to vary. An acceptable fit occurs for a value of 35 ppi, which is not unreasonable considering that the manufacturer's numbers are ''nominal'' values.

Finally, we performed a simple measurement to search for possible nonlinear effects. We guessed that when the gas displacement amplitude became comparable to the pore size,

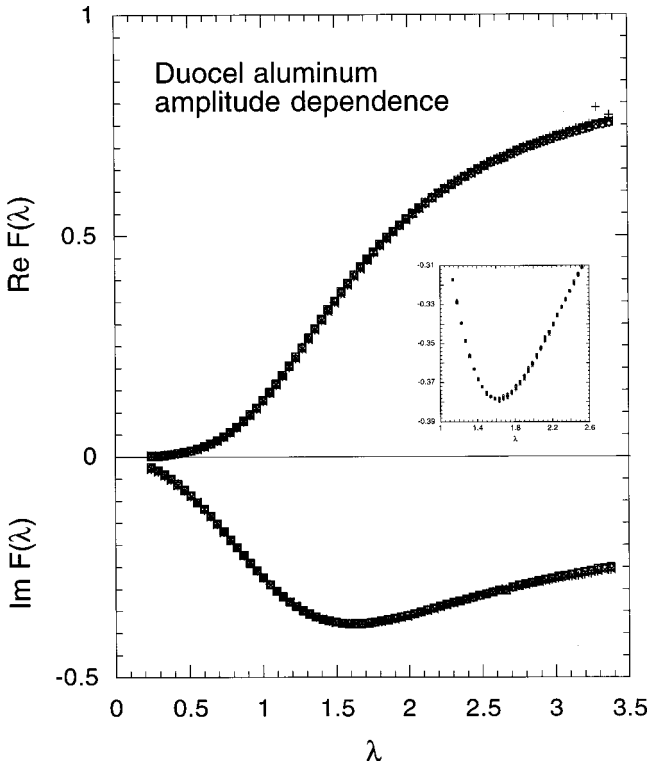

FIG. 7. $F(\lambda_T)$ vs λ_T plotted at different drive amplitudes. The results are almost indistinguishable. The inset shows a blowup of the region around the minimum in Im$[F(\lambda_T)]$.

the thermal coupling to the solid walls might change. For this test, we used the 40-ppi Al sample (pore size=0.635 mm) and the simple subtraction with the blank-off flange. The displacement amplitude at the loudspeaker (measured at 0.5 Hz) was varied from 0.25 to 1.06 mm in five steps. The displacement amplitude of gas in the pores varied correspondingly from 0.23 to 0.98 mm at the left end of the sample and decreased linearly to zero at the right end.[16] At the highest drive, the peak-to-peak displacement was larger than the pore size in over half of the sample. (This is the cross-sectional average of the displacement; the local displacements are even higher since gas near solid boundary is fixed.) For each amplitude, $F(\lambda_T)$ was measured. Figure 7 shows the results. No amplitude-dependent effects whatsoever were observed.

The maximum uncertainty in the data points in all of the runs due to systematic effects is estimated to be about 0.004 in absolute units for the imaginary component and 0.02 for the real component. The statistical errors in most cases are smaller than this, except at the very lowest frequencies where some scatter is observed.

V. CONCLUSIONS

Accurate measurements of $F(\lambda_T)$ for reticulated vitreous carbon have been performed. The results are compared with the theory derived for various analytically solvable geometries. RVC behaves similarly to parallel plates. Scaling between samples was shown to hold reasonably well, allowing the results here to be applied to RVC with other pore sizes. No nonlinear effects were observed at high driving amplitudes.

Experiments are currently in progress to measure the complex density for RVC. The results of these new experiments, combined with those presented here, should provide a complete and accurate test of the ideas of capillary-based porous media theories. In addition, they will provide information on the relevant viscous properties needed to characterize a thermoacoustic stack constructed of this material.

ACKNOWLEDGMENTS

I gratefully acknowledge support from the Office of Naval Research. I would like to thank the thermoacoustics group at the National Center for Physical Acoustics for RVC samples, and Energy Research and Generation, Inc. for supplying samples of both RVC and Duocel aluminum. I would also like to thank K. Attenborough for helpful comments and suggestions.

[1] Reticulated vitreous carbon (RVC) is manufactured by Energy Research and Generation, Inc., 900 Stanford Avenue, Oakland, CA 94608.
[2] J. A. Adeff, T. J. Hofler, A. A. Atchley, and W. C. Moss, ''Measurements with reticulated vitreous carbon stacks in thermoacoustic prime movers and refrigerators,'' J. Acoust. Soc. Am. **104**, 32 (1998).
[3] L. A. Wilen, ''Measurements of thermoacoustic functions for single pores,'' J. Acoust. Soc. Am. **103**, 1406–1412 (1998).
[4] G. Petculescu and L. A. Wilen, ''Thermoacoustics in a single pore with an applied temperature gradient,'' J. Acoust. Soc. Am. **106**, 688–694 (1999).
[5] M. E. Hayden and G. W. Swift, ''Thermoacoustic relaxation in a pin array stack,'' J. Acoust. Soc. Am. **102**, 2714–2722 (1997).
[6] J. W. Strutt (Lord Rayleigh), *Theory of Sound*, 2nd ed. (Dover, New York, 1945), Vol. II, Sec. 351.
[7] M. A. Biot, ''Theory of propagation of elastic waves in a fluid-saturated porous solid,'' J. Acoust. Soc. Am. **28**, 168–191 (1956).
[8] K. Attenborough, ''Acoustical characteristics of porous materials,'' Phys. Rep. **82**, 179–227 (1982).
[9] W. P. Arnott, H. E. Bass, and R. Raspet, ''General formulation of thermoacoustics for stacks having arbitrarily shaped pore cross sections,'' J. Acoust. Soc. Am. **90**, 3228–3237 (1991).
[10] The manufacturer specifies the pore size in ''pores per inch,'' or ppi. For RVC samples, we take $R=1/\#\text{ppi}$.
[11] L. Wilen, ''Measurements of scaling properties for acoustic propagation in a single pore,'' J. Acoust. Soc. Am. **101**, 1388–1397 (1997).
[12] J. R. Olson and G. W. Swift, ''Similitude in thermoacoustics,'' J. Acoust. Soc. Am. **95**, 1405–1412 (1991).
[13] M. R. Stinson, ''The propagation of plane sound waves in narrow and wide circular tubes, and the generalization to uniform tubes of arbitrary cross-sectional shape,'' J. Acoust. Soc. Am. **89**, 550–558 (1991).
[14] G. W. Swift and R. M. Keolian, ''Thermoacoustics in pin-array stacks,'' J. Acoust. Soc. Am. **94**, 941–943 (1993).
[15] Duocel aluminum foam, manufactured by Energy Research and Generation, Inc., 900 Stanford Ave., Oakland, CA 94608. It should be noted that the 20-ppi aluminum samples had pores which were noticeably larger (upon visual inspection) than those of the 20-ppi RVC samples. This is consistent with the position of the minimum in Im$[F]$ in the curves. The 40-ppi aluminum sample had pores approximately half as big as the 20-ppi sample, so the nominal pore size seems to be fairly consistent within one type of material, but not between types.
[16] The actual displacement amplitude at the left end of the pore is not constant as a function of frequency. It varies because the speaker amplitude varies with frequency (at constant drive voltage), but also because the compressibility of the gas in the ''bellows'' region has a different functional form from that in the pores. The total variation due to these two effects is less than 25%. To be conservative, the numbers we specify here represent the *minimum* displacement amplitude for each run.

Beamforming for a circular microphone array mounted on spherically shaped objects

Jens Meyer[a)]
Technical University of Darmstadt, Institute for Telecommunications, Merckstrasse 25, 64283 Darmstadt, Germany

(Received 5 June 2000; revised 29 September 2000; accepted 6 October 2000)

This paper will discuss the concept of phase modes to generate a desired beam pattern for a circular microphone array mounted around a rigid sphere. The method will be described for arrays consisting of omnidirectional and dipole sensors. The sound diffraction caused by the sphere is taken into account. It will be seen that the method allows, with some restrictions, the design of a wide variety of broadband beam patterns for a given elevation which usually will be the plane of the array. The directivity index is used to characterize the three-dimensional behavior of the array. Simulations show the realization of different beam patterns, based on a 16-element circular array located at the equator of a sphere with radius 0.085 m. The frequency range of this array is from 300 Hz to 5 kHz. Especially at low frequencies, a very good combination of the directivity index and the white noise gain is achieved which cannot be realized with ''conventional'' beamforming for an array of similar dimensions. The simulations are verified by means of a measurement. © *2001 Acoustical Society of America.* [DOI: 10.1121/1.1329616]

PACS numbers: 43.38.Hz, 43.72.Kb, 43.66.Ts [SLE]

I. INTRODUCTION

Two beamforming concepts can be distinguished for circular arrays. First, beamforming based on phase compensation or amplitude tapering and second, beamforming based on the concept of phase modes. Although the second method also requires different complex weights for the sensors, the design approach is different. While in the first case the goal usually is to optimize some characteristics of the beam pattern (e.g., the sidelobe level, the 3-dB beamwidth), the second method is very powerful for designing a desired beam pattern.

The beamforming method described in this paper is based on the second approach, the concept of phase modes. A good overview of this topic can be found in Ref. 1. It seems that this method was first described in Ref. 2 for continuous circular arrays. In Ref. 3 it is applied to discrete elements. The concept can be used for other array geometries as well.[4] Several other authors made further contributions to the phase-mode concept for circular arrays. (e.g., Refs. 5–7). It allows the synthesis of a desired pattern for one elevation. Usually the elevation will be $\vartheta_0 = \pi/2$ (see Fig. 1), which equals the plane of the array. The synthesis is based on a simple spatial Fourier analysis. The basic steps for designing a beam pattern are (a) determine the desired pattern; (b) do a spatial Fourier analysis of this pattern; and (c) convert the resulting Fourier coefficients to the required beamformer weights. Details of the phase modes will be stated in Sec. III.

The drawback of the phase-mode concept for some applications is that the beam pattern is specified only for one elevation. In contrast to other design procedures, the sensitivity for directions off this plane cannot be easily predicted in the design process. There is not much in literature that deals with this problem. In the present paper the directivity index is used to analyze the three-dimensional characteristics of the beam pattern. Broadband beamforming can also be a problem. As described in Ref. 8, this can be overcome by using directional array elements.

All contributions mentioned deal with a uniform circular array (UCA) in free field. In the present paper the UCA is located around a rigid sphere. As will be seen, this improves the broadband performance and the noise susceptibility. The phase-mode concept will be described for omnidirectional array elements and for dipole elements. Furthermore, a combination of both will be pointed out. This will improve the control of the three-dimensional beam pattern.

An application for the sphere baffled circular array might be a steerable conference microphone in the center of a large table. The look direction can be steered to any direction in the horizontal plane without changing the shape of the beam pattern significantly. For automatically steering the beam pattern, direction-finding algorithms[9,10] based on the phase-mode concept can be implemented. As will be seen, the described array setup is especially advantageous for low frequencies. The directivity index achieved here in combination with the good white noise gain cannot be realized with conventional array geometries of similar dimensions.

Another application might be in hearing aid technology. Here, microphone arrays are attractive for improving the acoustical signal-to-noise ratio resulting in an improved speech intelligibility for hearing-impaired persons.[11] Typically the arrays are located on the frame of a pair of glasses. The close distance to the head causes a degradation of the directivity index (e.g., Ref. 12). The circular array around the head might be a new approach that allows the head to be included in the beam-pattern design.

This paper will start with a brief review of the acoustics of a spherical scatterer. Then, the phase-mode concept is applied to the spherical scatterer problem assuming a circular array with omnidirectional elements. Equations for the white

a)Electronic mail: J.Meyer@uet.tu-darmstadt.de

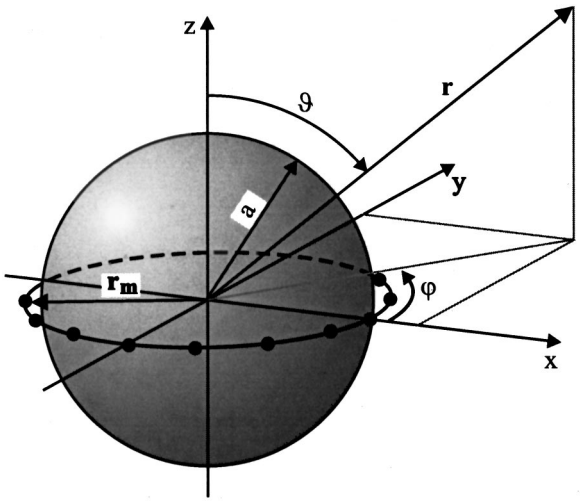

FIG. 1. Description of the setup.

noise gain are derived. Then, simulations are performed and the three-dimensional beam pattern is analyzed. The method is then extended to dipole sensors. The relationship between first-order differential arrays and the described method is discussed. Measurement results for sphere and head-mounted circular arrays are given. The paper will conclude with a summary.

II. THE SPHERICAL SCATTERER

The sound field around a scattering object will be a superposition of the incoming sound wave and the scattered sound field. For an acoustically hard spherical scatterer, the equation describing the resulting sound pressure in spherical coordinates is[13]

$$p(r,\vartheta)=p_i+p_s$$
$$=A\sum_{n=0}^{\infty}(2n+1)(-i)^n \times\left(j_n(kr)-\frac{j_n'(ka)}{h_n'(ka)}h_n(kr)\right)P_n(\cos(\vartheta)). \quad (1)$$

This assumes an impinging plane wave from the z direction. The orientation of the coordinates can be seen in Fig. 1. The magnitude of the impinging sound wave is A. The time dependency is omitted. The symbols in the above equations have the following meaning:

- a ≙radius of the sphere;
- k ≙wave number;
- r,ϑ ≙spherical coordinates of the observation point;
- P_n ≙Legendre function;
- j_n ≙spherical Bessel function;
- j_n' ≙first derivative of spherical Bessel function with respect to the argument;
- h_n ≙spherical Hankel function (Bessel function of the third kind);
- h_n' ≙first derivative of spherical Hankel function with respect to the argument.

Equation (1) shows only an r and ϑ dependency because of the rotational symmetry if a wave impinges from the z direction. For use with multisensor arrangements, it is more convenient to have an expression for the sound pressure at the location $[r_m,\varphi_m,\vartheta_m]$ if the plane wave impinges from $[\varphi,\vartheta]$. This can be achieved by using the following expression for the Legendre functions:[13]

$$P_n(\cos\Theta)=\sum_{l=-n}^{n}\frac{(n-|l|)!}{(n+|l|)!}P_n^{|l|}(\cos\vartheta) \times P_n^{|l|}(\cos\vartheta_m)e^{il(\varphi-\varphi_m)}, \quad (2)$$

where $P_n^{|l|}$ are the associated Legendre functions. Here, Θ is the angle between the direction of the incoming wave $[\varphi,\vartheta]$ and the radius vector of the observation point $[r_m,\varphi_m,\vartheta_m]$. Substituting Eq. (2) in Eq. (1) yields

$$g=\sum_{n=0}^{\infty}b_n(ka,kr_m)\sum_{l=-n}^{n}\frac{(n-|l|)!}{(n+|l|)!}P_n^{|l|}(\cos\vartheta) \times P_n^{|l|}(\cos\vartheta_m)e^{il(\varphi-\varphi_m)}. \quad (3)$$

To simplify notation, b_n was introduced

$$b_n(ka,kr_m)=(2n+1)(-i)^n \times\left(j_n(kr)-\frac{j_n'(ka)}{h_n'(ka)}h_n(kr)\right). \quad (4)$$

The quantity g is normalized by A and can be seen as the acoustical transfer function from a source at point $[\varphi,\vartheta]$ to the sensor at location $[\varphi_m,\vartheta_m,r_m]$.

So far, only plane wave incident is assumed. The following considerations will show that this assumption is valid for the suggested applications. In array theory the common rule of thumb to determine the distance at which the far-field approximations begin to be valid is $R=2L^2/\lambda$.[14] Here, L corresponds to the diameter of the sphere, and λ is the acoustical wavelength. Assuming a sphere of radius 0.085 m (average radius of a head) and a frequency of 6 kHz (upper frequency for high speech quality), R becomes 1 meter. This distance will typically be exceeded in applications such as hearing aids or conference microphones. In the latter case the sphere can be made even smaller, which will shift the far field towards smaller distances.

For applications where the near field has to be considered, an extension to spherical wave incident[13] can be incorporated.

III. CONCEPT OF PHASE MODES

Assume a continuous circular sensor located in a plane parallel to the $x-y$ plane. This position is described by $[\varphi,\vartheta_m,r_m]$. The circular sensor is centered around a sphere of radius a $(a\leqslant r_m)$ located at the origin (see Fig. 1). The aperture weighting function of the sensor is $w(\varphi)$. Since $w(\varphi)$ has to be 2π periodic, it can be expanded in a Fourier series

$$w(\varphi,f)=\sum_{p=-N}^{N}a_p(f)e^{ip\varphi}. \quad (5)$$

The beam pattern caused by the pth term $(a_p(f)e^{ip\varphi})$ of the

aperture weighting function, the pth phase mode, may be represented as follows:

$$D_p(\varphi,\vartheta,f)=\frac{1}{2\pi}\int_0^{2\pi} w_p(\varphi_m,f)g(\varphi_m,\vartheta_m,r_m,f)d\varphi_m, \quad (6)$$

where $g(\varphi_m,\vartheta_m,r_m,f)$ is the source–sensor transfer function from $[\varphi,\ \vartheta]$ to $[\varphi_m,\vartheta_m,r_m]$. If a spherical scatterer is present, this function is given by Eq. (3). This results in the following beam pattern:

$$D_p(\varphi,\vartheta,f)=a_p(f)\underbrace{\sum_{n=|p|}^{\infty} b_n(ka,kr_m)\frac{(n-|p|)!}{(n+|p|)!}P_n^{|p|}(\cos\vartheta)P_n^{|p|}(\cos\vartheta_m)}_{c_p(\vartheta,f)}e^{ip\varphi}. \quad (7)$$

Notice that the pth mode of the aperture weighting function determines the pth mode of the resulting beam pattern. The overall pattern is

$$D(\varphi,\vartheta,f)=\sum_{p=-N}^{N}\hat{a}_p(f)c_p(\vartheta,f)e^{ip\varphi}. \quad (8)$$

With $\hat{a}_p(f)$ equal to $a_p(f)/c_p(\vartheta_0,f)$, this becomes the same as the aperture weighting function for sound impinging from elevation ϑ_0: $D(\varphi,\vartheta_0,f)=w(\varphi,f)$. Of course, D will also depend on the radius r_m and the elevation ϑ_m as can be seen in Eq. (7). These will be assumed as fixed parameters and be omitted for better readability of the equations.

Now, the continuous sensor will be sampled at equispaced angles resulting in the sensor weights

$$w_m(f)=\sum_{p=-N}^{N}\hat{a}_p(f)e^{ip(2\pi/M)m}, \quad m=0,...,M-1, \quad (9)$$

where m determines the mth sensor and M is the total number of sensors. A mathematical expression for the error introduced in the beam pattern due to sampling the continuous aperture can be derived. In Ref. 1 this is done for a circular array in free field. As long as the sampling theorem is fulfilled $(M>2ka)$ this error can be neglected.

As can be seen in Eq. (7), the terms $c_p(\vartheta,f)$ play an important role in the beamforming process. They can be thought of as the strength with which each mode is present at a given frequency f and elevation ϑ for the impinging sound wave. These terms will now be analyzed in more detail. Figure 2 shows the magnitude of $c_p(\vartheta_0,f)$ over ka, with $\vartheta_0=\pi/2$. The sensors are located at $r_m=a$ and $\vartheta_m=\pi/2$, which means they are put on the equator of the sphere. As one would expect, at very low ka only the omnidirectional mode is present, meaning that no directivity can be achieved. The higher ka gets, the more modes emerge. The interesting thing is that unlike a circular array of omnidirectional sensors in free field[1] there are no zeros in the mode amplitude. This is an advantage for broadband applications such as speech pickup. This result is similar to circular arrays in free field consisting of cardioid sensors.[8] Once a mode has reached a certain amplitude it can be used to form the beam pattern. How strong a mode has to be before it can be used for the beam pattern depends on the minimum white noise gain allowed for the application. This will be discussed in the next section.

Figure 3 shows the mode amplitude over mode number. Each curve corresponds to a different ka. For $ka=0.47$ one can see that the fundamental mode is dominant. Mode one is down by 8 dB and mode two is down by 27 dB. The higher ka gets, the more modes are present and the mode magnitude becomes more constant. For each ka there are roughly ka modes present.

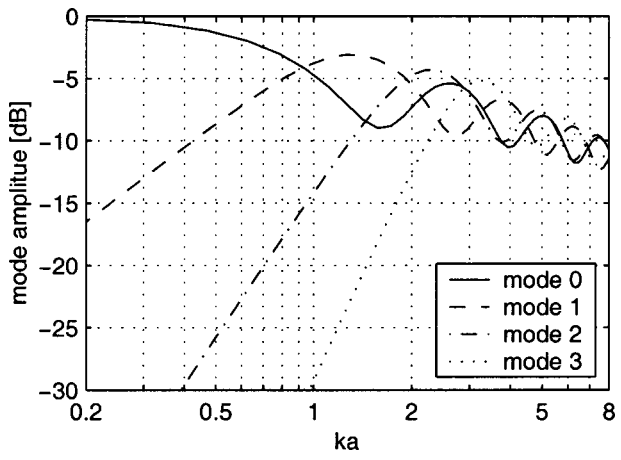

FIG. 2. Mode amplitude versus ka for a circular array of omnidirectional elements located on the equator of a sphere.

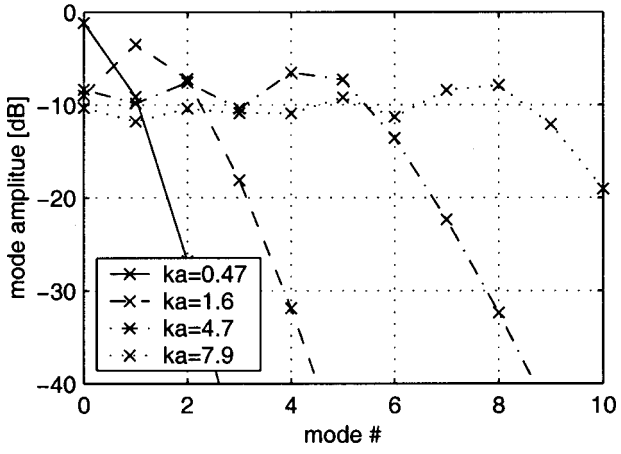

FIG. 3. Mode amplitude versus mode number p for a circular array of omnidirectional elements located on the equator of a sphere.

IV. WHITE NOISE GAIN

As soon as it comes to the implementation of a beamformer, its susceptibility to random errors in the weights and positions of the sensors is important. A measure commonly used is the white noise gain (WNG),[15] here labeled K. The WNG is defined as

$$K(f)=\frac{\mathbf{w}(f)^H\mathbf{g}_0(f)\mathbf{g}_0(f)^H\mathbf{w}(f)}{\mathbf{w}^H(f)\mathbf{w}(f)}, \tag{10}$$

where $\mathbf{w}$ is the vector of the sensor weights, given by Eq. (9), $\mathbf{g}_0$ is the vector of the source–sensor transfer function for the look direction $[\varphi_0,\vartheta_0]$, and H denotes the Hermitian transpose. The WNG can be interpreted as the improvement of the SNR at the sensor output over the SNR at the sensors, where N is the uncorrelated sensor noise. In Ref. 16 it is shown that this can be used as a measure for the robustness of the array.

Using Eq. (9) the denominator will become

$$\mathbf{w}^H\mathbf{w}=M\sum_{p=-N}^{N}|\hat{a}_p|^2. \tag{11}$$

For simplicity the frequency dependence will no longer be stated explicitly. $\mathbf{w}^H\mathbf{g}_0$ is the array output for sound impinging from the look direction

$$\mathbf{w}^H\mathbf{g}_0=M\sum_{p=-N}^{N}a_p. \tag{12}$$

Using Eqs. (11) and (12), K becomes

$$K=M\frac{|\Sigma_{p=-N}^{N}a_p|^2}{\Sigma_{p=-N}^{N}|\hat{a}_p|^2}. \tag{13}$$

Equation (13) can be simplified for two important cases. First, assume that $N\leqslant ka$. For this case c_p is approximately constant (see Fig. 3). Therefore, $\hat{a}_p$ can be approximated by a_p/c. Here, c is the average magnitude of c_p for the desired frequency, e.g., from Fig. 3 it is found that for $ka=4.7$ c is about -8 dB. This simplifies Eq. (13) to

$$K\approx M|c|^2\frac{|\Sigma_{p=-N}^{N}a_p|^2}{\Sigma_{p=-N}^{N}|a_p|^2}. \tag{14}$$

It is interesting to notice that the WNG mainly depends on the Fourier coefficients of the desired pattern. As long as the a_p's are real, the noise susceptibility will be better with the more modes used for the pattern. This makes sense, because every mode used in the pattern will pick up more energy from the sound field. As the frequency increases the energy is distributed over more modes. Therefore, c will decrease with frequency. This means that if the pattern remains constant over frequency (meaning that the same modes are used to form the pattern), the WNG will decrease with frequency because c will decrease. It can also be seen in Eq. (14) that the WNG will increase with the number of microphones used in the array.

Another simplification can be introduced to Eq. (13) for $N>(ka+1)$. This case is especially important for low frequencies, where one might also want to use weak modes in order to get a reasonable directivity. If the Fourier coefficients are chosen to be approximately identical, the WNG is dominated by the highest mode

$$K\approx\frac{1}{2}M\left|\frac{c_N}{a_N}\right|^2\left|\sum_{p=-N}^{N}a_p\right|^2. \tag{15}$$

This can be derived by keeping in mind that $|c_{p+1}|^2\ll|c_p|^2$ for $p>(ka+1)$ (see Fig. 2).

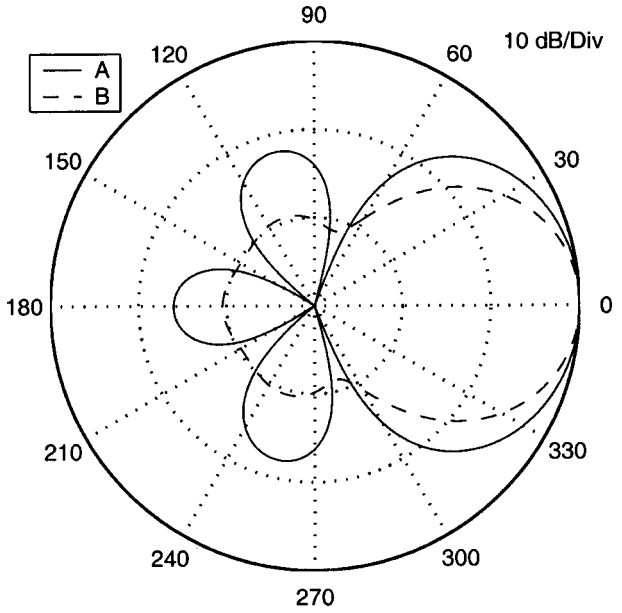

FIG. 4. Desired beam pattern to be realized using the described method.

V. SIMULATIONS

The simulations are done with an equispaced circular array of 16 omnidirectional microphones located on the equator of a sphere with radius 0.085 m. The 16 sensors allow sound pickup up to $ka=8$. This results in an upper limit for the frequency of 5.1 kHz. With this array two more or less arbitrarily selected beam patterns will be generated. These beam patterns are shown in Fig. 4. These two patterns will show some characteristics of the sphere baffled circular array. Both patterns will be kept frequency invariant. Their Fourier coefficients are:

(A) $\mathbf{a}_a(0)$, $\mathbf{a}_a(1)$, $\mathbf{a}_a(2)=1,1,1$;
(B) $\mathbf{a}_b(0),\ldots,\mathbf{a}_b(6)=8.73,\ 4.87,\ 3.84,\ 2.5,\ 1.24,\ 0.35,\ 0.09$.

The coefficients $\mathbf{a}(-1),\ldots,\mathbf{a}(-N)$ equal $\mathbf{a}(1),\ldots,\mathbf{a}(N)$, N being 2 and 6 for pattern A and B, respectively. Equation (9) is used to calculate the filter weights. As an example, the filter weights for $ka=1$ to generate pattern A are given in Fig. 5.

Figure 6 shows the simulated beam pattern in the plane of the array. As one can see they match the desired patterns very closely. The error at the back of the patterns for $ka=7.9$ is due to the sampling of the continuous pattern. Mode 9 and higher cause aliasing problems.

The phase-mode excitation concept allows the design of a desired beam pattern for one given elevation ϑ_0. For many practical applications it is also desired to have control over

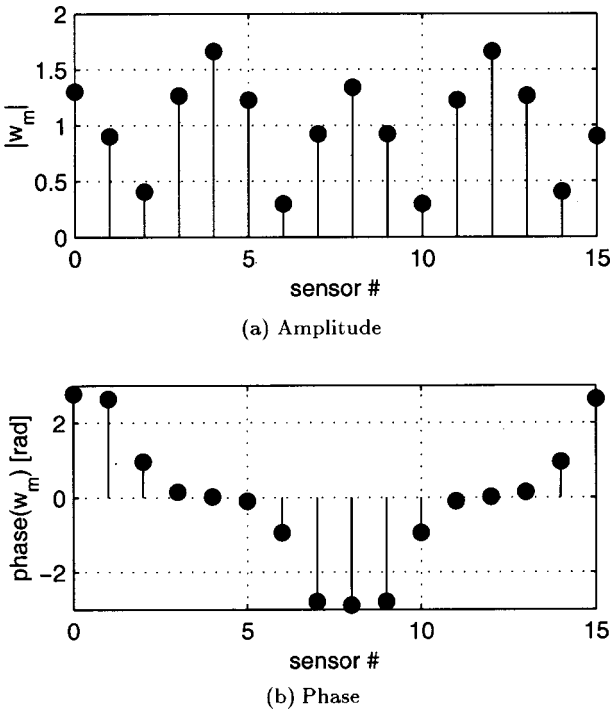

FIG. 5. Filter weights for $ka=1$ to generate beam pattern A.

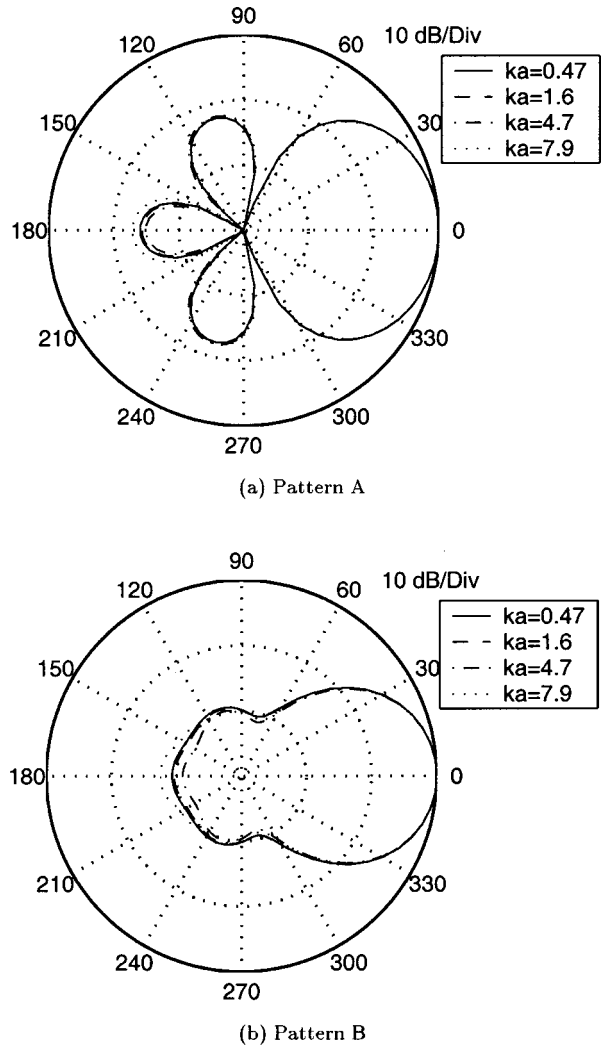

FIG. 6. Simulated beam pattern for a circular array of 16 omnidirectional elements located on the equator of the sphere.

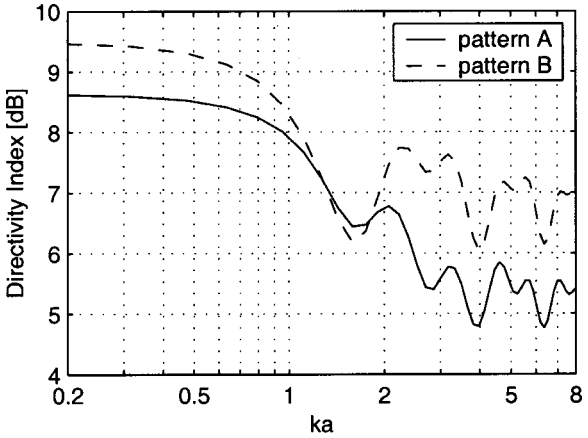

FIG. 7. Directivity index of a circular array of 16 omnidirectional elements located on the equator of a sphere for two different weight vectors.

the three-dimensional beam pattern of the array, e.g., to avoid unwanted high sidelobes. Equation (8) describes the three-dimensional sensitivity. Unfortunately, φ and ϑ cannot be controlled independently. This means that a desired pattern at ϑ_0 determines the complete three-dimensional pattern. Since Eq. (8) does not allow an easy insight into the three-dimensional behavior of the array, the directivity index (DI) will be used to describe the three-dimensional characteristics. The DI is defined as the acoustical SNR improvement of the array over an omnidirectional microphone under the assumption of an isotropic noise field. The array and the omnidirectional microphone have the same sensitivity for the look direction. Figure 7 shows the DI for the two coefficient sets. For $ka=0.5$ (for $a=0.085\,\mathrm{m}$, this is 300 Hz) the DI is 8.5 and 9.3 dB for pattern A and B, respectively. These values can be explained with the relation to differential arrays (see Sec. VIII). Figure 8 shows the three-dimensional (3D) beam pattern for $ka=0.47$.

For $ka=1.6$ both DIs have a local minimum. A comparison with Fig. 2 shows that mode 0 also has a minimum at $kr=1.6$. As a result, this mode has to be amplified [$\hat{a}_0(ka=1.6)$ will be relatively large] to have the modes either at equal strength (pattern A) or in the desired relation (pattern B). Because mode 0 is the only one which contributes to the sensitivity at $\vartheta=0$ and $\vartheta=\pi$, it can be expected that the

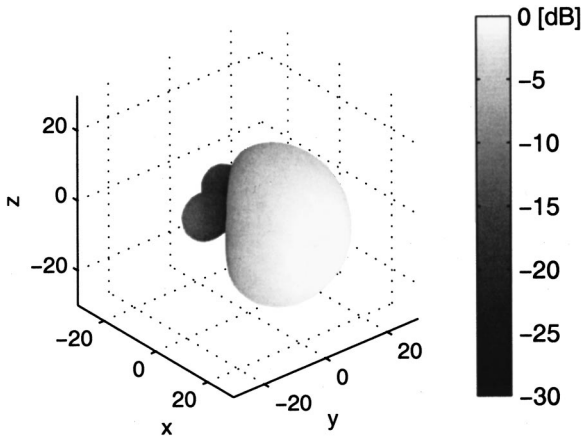

FIG. 8. 3D beam pattern (type A) for $ka=0.47$.

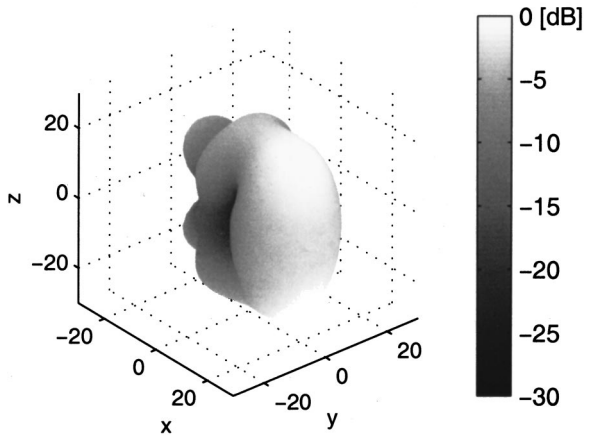

FIG. 9. 3D beam pattern (type A) for $ka=4$.

sensitivity from these directions will be relatively high, resulting in a broad beamwidth for the pattern in the $x-z$ plane. A similar effect can be seen in Fig. 9, which shows the 3D pattern for $ka=4$ for the array with coefficients A. At $ka=4$ mode 0 and 2 do have a minimum. Notice that the pattern in the $x-y$ plane is still the desired one.

Figure 10 shows the WNG for the two beam patterns. For low kr the WNG increases with $6N$ dB/oct, where N is the number of the highest mode used to form the desired beam pattern. This is 12 dB/oct for beam pattern A and 36 dB/oct for beam pattern B. This agrees with Sec. IV, where it was found that for superdirectivity the WNG is mainly determined by the highest mode. From Fig. 2 it can also be seen that the modes rise with $6p$ dB/oct for $ka<p$, where p is the mode number. For the $ka=0.47$, beam pattern A has a WNG of about -4 dB. This means that the equivalent sound-pressure level (ESPL) of the array would be the ESPL of the single microphones plus 4 dB. The allowable WNG depends on the desired sound quality and the ESPL of the single microphones. For a reasonable sound quality and common microphone capsules, the WNG should be above -10 dB. This is also the minimum value to allow some tolerances in the array setup without blowing up the beam pattern.

It can also be seen in Fig. 10 that if the mode coefficients are kept constant over frequency the WNG will drop for higher ka (see Sec. IV).

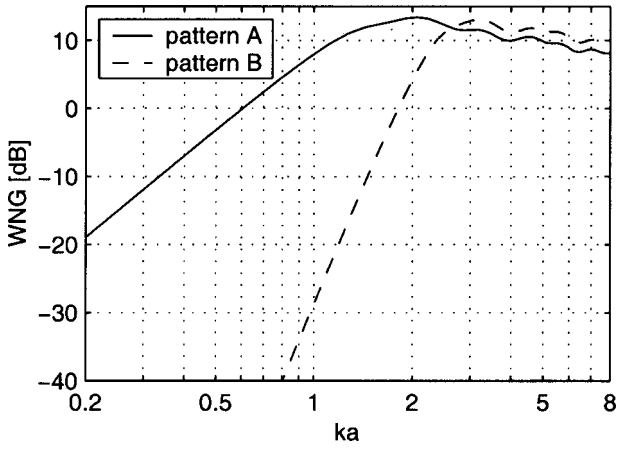

FIG. 10. White noise gain of a circular array of 16 omnidirectional elements located on the equator of a sphere for two different weight vectors.

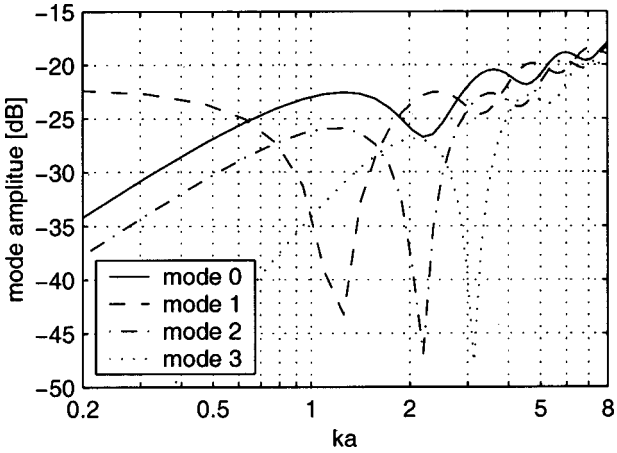

FIG. 11. Mode amplitude (normalized by k) vs ka for a circular array of dipole sensors oriented in the r direction located 5 mm in front of the equator of a sphere ($a=0.085$ m).

VI. ARRAY WITH DIPOLE SENSORS

At first glance it looks attractive to use dipole sensors instead of omnidirectional microphones. If the dipoles are oriented in a way that the zero faces towards $\vartheta=0$ and $\vartheta=\pi$, no sound will be picked up from these directions by the array. This will reduce unwanted high sidelobes and it can be expected that this will increase the DI, especially for higher frequencies. Two orientations of the dipole sensors will be investigated: (1) the dipole picks up the pressure gradient in radial direction, and (2) the dipole picks up the pressure gradient in the circumferential direction.

A. Dipole with radial orientation

From Eq. (1), one gets for the radial pressure gradient

$$\frac{\delta p}{\delta r}=A\sum_{n=0}^{\infty}(2n+1)(-i)^n k \times\left(j_n'(kr)-\frac{j_n'(ka)}{h_n'(ka)}h_n'(kr)\right)P_n(\cos(\Theta)). \quad (16)$$

Therefore, the pth phase mode beam pattern is still described by Eq. (7), but with a different b_n

$$b_n'(ka,kr_m)=(2n+1)(-i)^n k \times\left(j_n'(kr)-\frac{j_n'(ka)}{h_n'(ka)}h_n'(kr)\right). \quad (17)$$

Figure 11 shows the resulting magnitude for different modes for the radial pressure gradient. The radius of the sphere is $a=0.085$ m and the radius of the array is $r_m=0.09$ m. The array is located around the equator of the sphere ($\vartheta_m=\pi/2$). The magnitude of the modes are normalized by k. Unlike the modes for the sound pressure, these modes do have a zero.

The same simulations as in Sec. V were undertaken with an array of 16 dipole sensors equispaced around the equator of a sphere. The radius of the array is 0.09 m and the radius

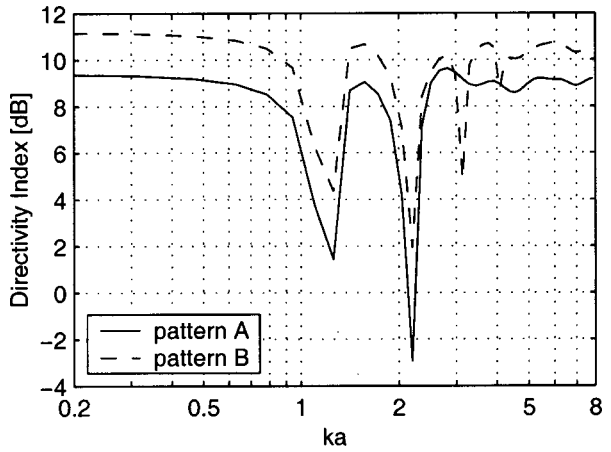

FIG. 12. Directivity index of a circular array of 16 dipole sensors oriented in the r direction located 5 mm in front of the equator of a sphere ($a = 0.085$ m) for two different weight vectors.

of the sphere is 0.085 m. The dipoles are directed towards the radial direction. The patterns A and B (Fig. 4) were used as the desired patterns. As would be expected, the desired patterns can be generated for a desired elevation ϑ_0 without problems.

The resulting DI is shown in Fig. 12. It can be seen that a zero in a required mode causes a deep dip in the DI. The reason for this becomes obvious in Fig. 13. This plot shows the 3D beam pattern with coefficient set A for $ka = 2.2$. For this frequency, mode number 2 is very weak. Therefore, it has to be amplified very strongly to achieve the desired pattern in the $x-y$ plane. This blows up the pattern off the $x-y$ plane. Therefore, care has to be taken to choose the right modes to generate a pattern for broadband application. For example, pattern A can be generated for $ka > 3$ without causing problems. The DI for these frequencies is quite constant at about 9 dB (see Fig. 12). Figure 14 shows the 3D plot of the beam pattern with coefficients A at $ka = 3.9$. It can be seen that the maximum sensitivity is towards the desired direction. For sound impinging from the z direction the sensitivity is zero. From all other directions off the main beam the sensitivity is attenuated by at least 10 dB. It has to be kept in mind that the real acoustical SNR improvement will typically be much better than the DI predicts. This is because

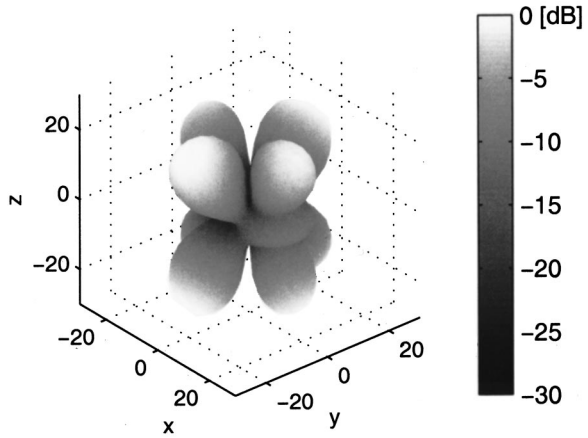

FIG. 13. 3D beam pattern (type A) for $ka = 2.2$.

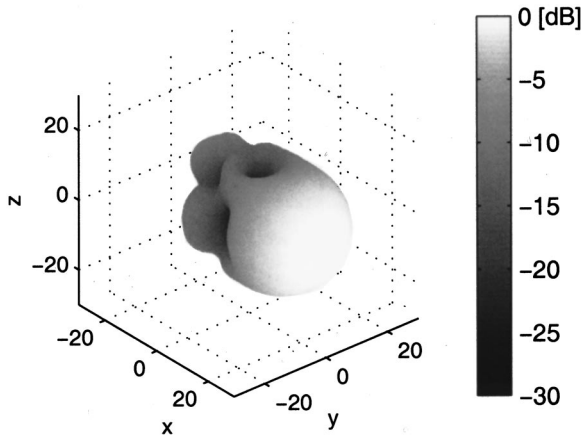

FIG. 14. 3D beam pattern (type A) for $ka = 3.9$.

for many applications it can be assumed that the dominant noise sources impinge under the angle ϑ_0. Since for this angle the pattern can be controlled very well, these noise sources can be attenuated to a high extent.

Figure 15 shows the WNG of the described array for the two patterns. For small ka the WNG has the same slopes as for the omnidirectional sensors. For large ka the slope is 12 dB/oct minus some dB because not all modes are used to form the beam pattern. One might expect a 6-dB/oct rise as is typical for first-order gradient sensors. But, since the dipoles are located in front of a sphere the standing wave in front of the obstacle will change the first-order gradient to a second-order gradient sensor. This effect is similar to a first-order gradient sensor in front of a reflecting wall.[17] This will cause a 12-dB/oct rise of the WNG. The dips in the WNG are caused by the zeros in the modes used in the pattern.

The WNG depicted in Fig. 15 assumes ideal dipole sensors that pick up the pressure gradient. If the dipole is built up using two omnidirectional microphones (and subtracting their outputs) it picks up only the pressure difference. Therefore, the given WNG has to be reduced by $20\log(d)$, where d is the distance between the two sensors. If d is assumed to be 1 cm this results in a subtraction of 40 dB. This means that in applications this kind of array can be used only for frequen-

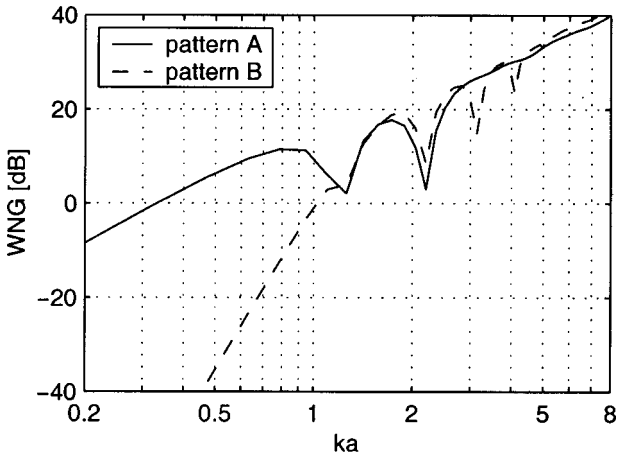

FIG. 15. White noise gain of a circular array of 16 dipole sensors oriented in the r direction located 5 mm in front of the equator of a sphere ($a = 0.085$ m) for two different weight vectors.

cies above $ka=4$ which corresponds to $f=2500$ Hz for a sphere with radius 0.085 m.

A promising approach to improve the 3D performance of the circular array is the combination of pressure modes and radial velocity modes. Unlike in free field the directional pattern of the array element will change with frequency. This is desirable in a way that for low frequencies the pressure modes are dominant and for high frequencies the velocity modes are dominant. First simulations show that it is possible to achieve a constant DI between 8 and 9 dB (using the pattern type A for the plane of the array) over a frequency band from 300 Hz to 5 kHz with a reasonable WNG. Easy-to-use design rules will be developed in the future.

B. Dipole with circumferential orientation

The dipole oriented in the φ direction will pick up the pressure gradient in this direction. Therefore, the modes can be easily derived from the pressure modes: The modes are the Fourier series coefficients of the underlying spatial sound pressure or sound-pressure gradient distribution. Therefore, taking the derivative of the sound pressure with respect to φ results in multiplying the pressure modes (Fig. 2) with jp, where p is the mode number. This means that the constant mode will vanish and the other modes experience a phase shift of $\pi/2$ and a scaling by a factor p.

VII. MEASUREMENTS

The measurement was performed with a sphere of radius 0.1085 m. To cover a frequency range up to 6 kHz, an array of 24 omnidirectional microphones located equispaced on the equator of the sphere was used. The microphones had a thickness of 8 mm. This makes the radius of the array $r=0.1165$ m. The pattern of each microphone was measured in the plane of the array. The filtering and summation was done off-line on a PC.

Figure 16 shows the resulting beam patterns. Pattern type A shows a very good agreement with the selected pattern (Fig. 4). As expected for pattern type B the high noise susceptibility for $ka<1.6$ will destroy the pattern design for these ka's. From $ka=1.6$, which equals a WNG of -10 dB, the pattern starts to become realizable. For higher ka the main beam shows a very good match with the desired beam (Fig. 4). Off the main beam there are some deviations but the attenuation remains above the desired 20 dB.

Figure 17 shows the measured pattern for a 16-element array mounted on two different artificial heads (KEMAR and B&K head). The sensors were mounted every 22.5° around the surface of the head. The plane in which the sensors were put was right above the eyebrow. The pattern was measured in the plane of the array. Although the shape of the head differs from the shape of the sphere and the sensors are no longer placed on a ''round circle'' and are not in the equatorial plane, the agreement between the desired pattern and the measured pattern is fairly good. Especially at low ka, there is a very good match. As ka increases the deviation between the desired and the measured pattern increases. This was expected because as the wavelength decreases the differences in the scattering between the head and the sphere

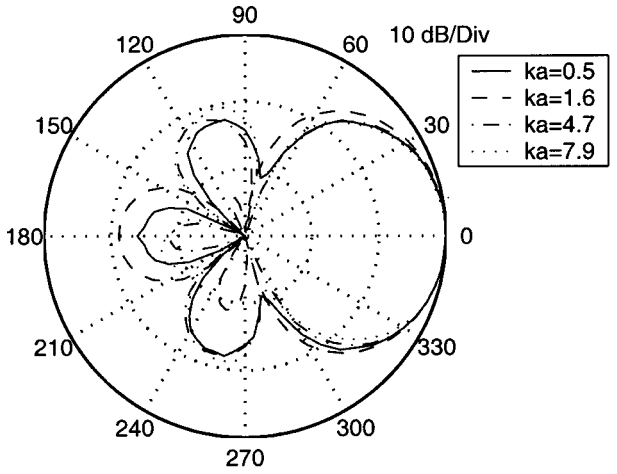

(a) Pattern A

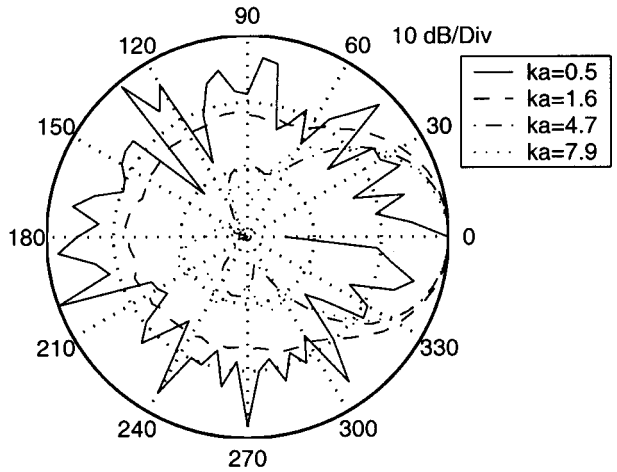

(b) Pattern B

FIG. 16. Measured beam pattern for a circular array of 24 omnidirectional sensors located on the equator of a sphere ($a=0.1$ m).

increase. This is the reason why pattern type B can not be realized. The necessary higher modes modeled for the sphere differ greatly from the head shape.

An approach to improve the results can be to include the measured data in the coefficient design. Another idea is to use the theory of an elliptical array instead of a circular array. These will be left as future tasks.

VIII. RELATION BETWEEN DIFFERENTIAL AND CIRCULAR ARRAYS

This section will point out the similarity between a circular array using the phase-mode excitation concept and first-order differential arrays (FOD) consisting of two omnidirectional sensors. As mentioned before, FODs pick up the pressure gradient. Most commonly used differential arrays are set up using two pressure sensors. The pressure gradient is then approximated by the pressure difference between the two sensors. This is valid as long as the distance d between the two pressure sensors is very small compared to the wavelength.[18] Therefore, $kd/2$ will be small (much less than π). For a circular array it was seen that for $ka<1$ only the modes 0 and ±1 will be present. This means that

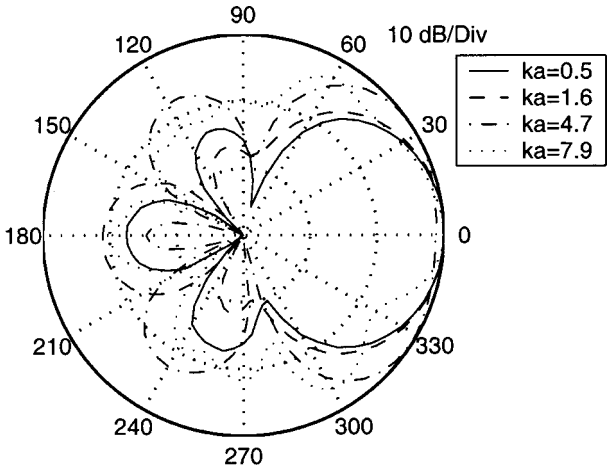

(a) Mounted on KEMAR

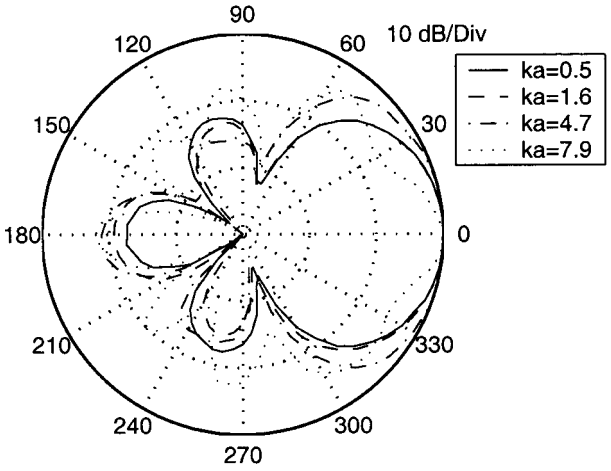

(b) Mounted on B&K Head

FIG. 17. Measured beam pattern (type A) for a head-mounted ''circular'' array of 16 omnidirectional elements.

two microphones will be sufficient to sample the modes and determine the directivity pattern. Therefore, the circular array can be seen as a special case of the FOD (for $ka<1$). Compared to the differential microphone array the sphere baffled array has the advantage that the effective phase difference between the two sensors at the front and the back is $3ka$ for $(ka)^2 \ll 1$,[19] which is 50% larger than the difference in free field. Because the ka is a major parameter for the WNG, this explains why the sphere baffled circular array has a superior performance at low frequencies.

IX. SUMMARY

A microphone array setup is described in combination with the phase-mode concept that allows the analytic implementation of a beam pattern for one elevation ϑ_0 of sound incidence. It has a good white noise gain characteristic that allows high directivity even at low frequencies. Although the method determines the pattern only for one elevation ϑ_0, it was found that the three-dimensional characteristics are also good. Here, the right choice of the single sensor beam pattern is important. A very promising approach seems to be the combination of pressure sensors and radial velocity sensors. With limited accuracy the method can also be applied to head-mounted arrays. Possible changes to the concept are mentioned which may improve the results for this application.

ACKNOWLEDGMENTS

The author would like to thank G. M. Sessler and G. W. Elko for their assistance and helpful discussions. Special thanks are due to B. Kubli for setting up the measurements.

[1] D. E. N. Davies, ''Circular arrays,'' in *The Handbook of Antenna Design* (Peregrinus, London, 1983), Vol. 2, Chap. 12.
[2] W. R. LePage, C. S. Roys, and S. Seely, ''Radiation from circular current sheets,'' Proc. IRE **38**, 1069–1072 (1950).
[3] T. T. Taylor, ''A synthesis method for circular and cylindrical antennas composed of discrete elements,'' IRE Trans. Antennas Propag. **3**, 251 (1952).
[4] R. H. Du Hamel, ''Patterns synthesis for antenna arrays on circular, elliptical and spherical surfaces,'' Technical Report 16, Electrical Engineering Research Laboratory, University of Illinois, Urbana, 1952.
[5] C. E. Hickman, H. P. Neff, and J. D. Tillman, ''The theory of single-ring circular antenna array,'' Trans. Am. Inst. Electr. Eng. **80**, 110–115 (1961).
[6] G. Ziehm, ''Optimum directional pattern synthesis of circular arrays,'' Radio Electron. Eng. **28**, 341–355 (1964).
[7] I. D. Longstaff, P. E. K. Chow, and D. E. N. Davies, ''Directional properties of circular arrays,'' Proc. IEE **114**, 713–717 (1967).
[8] T. Rahim and D. E. N. Davies, ''Effect of directional elements on the directional response of circular arrays,'' Proc. IEE Pt. H **129**, 18–22 (1982).
[9] C. P. Mathews and M. D. Zoltowski, ''Eigenstructure techniques for 2D angle estimation with uniform circular arrays,'' IEEE Trans. Signal Process. **42**, 2395–2407 (1994).
[10] H. D. Griffiths, ''The use of circular arrays for direction finding applications,'' in IEE Colloquium on Passive Direction Finding, 1989, pp. 7/1–7/4.
[11] W. Soede, A. J. Berkhout, and F. A. Bilsen, ''Development of a directional hearing instrument based on array technology,'' J. Acoust. Soc. Am. **94**, 785–798 (1993).
[12] J. M. Kates and M. R. Weiss, ''A comparison of hearing-aid array-processing techniques,'' J. Acoust. Soc. Am. **99**, 3138–3148 (1996).
[13] J. J. Bowman, T. B. A. Senior, and P. E. Uslenghi, *Electromagnetic and Acoustic Scattering by Simple Shapes* (Hemisphere, New York, 1987).
[14] C. A. Balanis, *Antenna Theory: Analysis and Design* (Wiley, New York, 1997).
[15] H. Cox, R. M. Zeskind, and T. Kooij, ''Practical supergain,'' IEEE Trans. Acoust., Speech, Signal Process. **34**, 393–398 (1986).
[16] E. N. Gilbert and S. P. Morgan, ''Optimum design of directive antenna arrays subject to random variations,'' Bell Syst. Tech. J. **34**, 637–663 (1955).
[17] G. W. Elko, J. E. West, and R. A. Kubli, ''Image-derived second-order differential microphones,'' J. Acoust. Soc. Am. **95**, 1991–1997 (1994).
[18] G. W. Elko, ''Superdirectional microphone arrays,'' in *Acoustic Signal Processing for Telecommunication* (Kluwer Academic, Dordrecht, 2000), Chap. 10.
[19] G. F. Kuhn, ''Model for the interaural time differences in the azimuthal plane,'' J. Acoust. Soc. Am. **62**, 157–167 (1977).

Optimization of asymmetric bimorphic disk transducers

Shuo Hung Chang[a] and B. C. Du
Department of Mechanical Engineering, National Taiwan University, Taipei, Taiwan, Republic of China

(Received 16 February 1999; accepted for publication 10 July 2000)

The dynamic and static characteristics of asymmetric bimorphic disk transducers that consist of a piezoelectric layer laminated with an unequal radius elastic disks are optimized. An electroelastic laminated plate theory is developed to analyze the mechanical, electrical and electromechanical behaviors. Close form solutions are obtained for the mechanical displacement and electric potential in terms of Bessel functions. Special focus is on the electromechanical coupling coefficients (EMCC) that are shown sensitive to geometric variables, such as thickness and radius ratios of the piezoelectric and elastic materials. Optimum configurations to reach the maximum values of the EMCC or static displacement sensitivity and influence of material and geometric properties are presented. Experiments are conducted to verify the theoretical results with good agreement. [DOI: 10.1121/1.1310669]

PACS numbers: 43.40.At [PJR]

I. INTRODUCTION

Certain piezoelectric materials with their strong electromechanical coupling effects were used in the scope of sensors and actuators. Thus, materials with piezoelectric effects are the most important and potential candidates of intelligent materials that incorporate the ability of actuation, control, and sensing. The devices based on piezoelectricity have been expanded rapidly in the applications from audio transducer,[1] control of vibration,[2] control of shape,[3] ultrasonic transducer,[4] and detection of distance[5] to precision positioning mechanisms.[6]

The elastic structures laminated with piezoelectric or piezofilm layers were reported for static solution,[7] torsion and bending solution,[8] and extension and bending vibrations.[9,10] The thin piezofilms[3,8,11,12] were used for vibration applications. The vibration characteristics of piezoelectric disks were studied by the finite-element method[13] and the optimum thickness-radius ratio for axisymmetric modes was discussed.[14] The bimorphic disks consist of one piezoelectric and one metal layer with the same radius[15] and with different radii[16] were studied, assuming the Poisson's ratios of the different layer materials equal, but usually this hypothesis is suitable for limited applications.

In this paper we study the static displacements and electromechanical coupling coefficient (FMCC) of piezoelectric-elastic laminated disks and optimizes them by changing the proportion of piezoelectric and elastic parts in the disk. To evaluate the piezoelectric element, the efficiency of energy conversion between elastic and dielectric ones is an essential index. The piezoelectric-elastic disk consists of an isotropic elastic metal disk and an unequal radius piezoelectric disk. The major motion of the disk is the bending type under a sinusoidal electrical excitation.

An electroelastic laminated plate theory is developed first to analyze the static and dynamic behaviors of the composite piezoelectric plates, including static displacements, resonance frequencies, antiresonance frequencies, and EMCC. This theory was formulated by modifying the ordinary plate theory to include the piezoelectric effects. To simplify the problem, it was assumed that the distributed form of electric potential and electric displacement in the thickness direction for each piezoelectric layer were, respectively, quadratic and constant with respect to the thickness coordinate. These characteristics are therefore numerically evaluated for different values of geometric variables, such as thickness and radius ratios of the piezoelectric and elastic materials. Optimum settings of geometric variables where the laminated disk has the maximum EMCC value or maximum static displacement at a central point were obtained.

II. THEORY

A. Basic electroelastic theory

A complete electroelastic theory consists of the equilibrium equations, the strain-displacement relationships, the constitutive relations, and the electrostatic equations. For piezoelectric materials of class 6 mm and polarized in the thickness direction α_3, the constitutive relations are[17]

$$
\begin{aligned}
&S_{11}=s_{11}^{E}T_{11}+s_{12}^{E}T_{22}+s_{13}^{E}T_{33}+d_{31}E_3,\\
&S_{22}=s_{12}^{E}T_{11}+s_{11}^{E}T_{22}+s_{13}^{E}T_{33}+d_{31}E_3,\\
&S_{33}=s_{13}^{E}(T_{11}+T_{22})+s_{33}^{E}T_{33}+d_{33}E_3,\\
&S_{23}=s_{44}^{E}T_{23}+d_{15}E_2,\\
&S_{13}=s_{44}^{E}T_{13}+d_{15}E_1,\quad S_{12}=s_{66}^{E}T_{12},\\
&D_1=d_{15}T_{13}+\epsilon_{11}^{T}E_1,\quad D_2=d_{15}T_{23}+\epsilon_{11}^{T}E_2,\\
&D_3=d_{31}(T_{11}+T_{22})+d_{33}T_{33}+\epsilon_{33}^{T}E_3,
\end{aligned}
\tag{1}
$$

where S_{ij}, T_{ij}, D_i, and E_i denote the components of strain, stress, electric displacements, and electric fields, respectively, and s_{ij}^{E}, d_{ij}, and ϵ_{ij}^{T} denote the elastic compliance constants at a constant electric field, the piezoelectric constants, and the dielectric constants at a constant stress field,

[a]Electronic mail: shchang@ccms.ntu.edu.tw

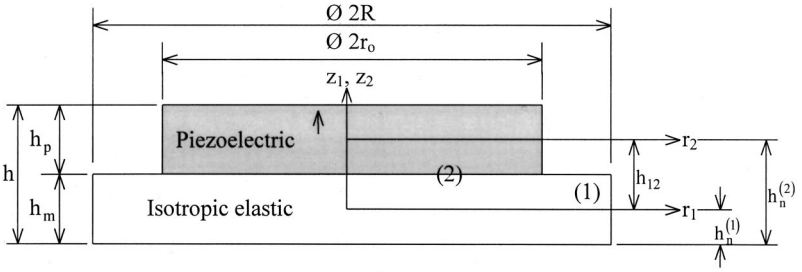

FIG. 1. The configuration of the two-layered bimorphic disk transducer.

respectively. The strain–stress relations for isotropic elastic materials are

$$
\begin{aligned}
S_{11}&=\frac{1}{E}(T_{11}-\nu_m T_{22}-\nu_m T_{33}),\\
S_{22}&=\frac{1}{E}(T_{22}-\nu_m T_{11}-\nu_m T_{33}),\\
S_{33}&=\frac{1}{E}(T_{33}-\nu_m T_{11}-\nu_m T_{22}),\\
S_{23}&=\frac{2(1+\nu_m)}{E}T_{23},\\
S_{13}&=\frac{2(1+\nu_m)}{E}T_{13},\quad S_{12}=\frac{2(1+\nu_m)}{E}T_{12},
\end{aligned}
\tag{2}
$$

where E and ν_m are the Young's modulus and Poisson's ratio of the elastic material. The general electroelastic equations are

$$
\nabla\cdot\vec{D}=0,\quad \vec{E}=-\nabla\psi, \tag{3}
$$

where ψ is the electrical potential. Having chosen the mutually perpendicular lines on the middle surface as coordinates α_1 and α_2, and the normal to the middle surface as the third coordinate α_3, for flat plates without surface traction, the equilibrium equations are

$$
\begin{aligned}
&\frac{1}{A_1}\frac{\partial T_{11}}{\partial\alpha_1}+\frac{1}{A_2}\frac{\partial T_{12}}{\partial\alpha_2}+\frac{1}{A_1A_2}\frac{\partial A_2}{\partial\alpha_1}(T_{11}-T_{22})\\
&\quad+\frac{2T_{12}}{A_1A_2}\frac{\partial A_1}{\partial\alpha_2}+\frac{\partial T_{13}}{\partial\alpha_3}=\rho\frac{\partial^2U_1}{\partial t^2},\\
&\frac{1}{A_2}\frac{\partial T_{22}}{\partial\alpha_2}+\frac{1}{A_1}\frac{\partial T_{21}}{\partial\alpha_1}+\frac{1}{A_1A_2}\frac{\partial A_1}{\partial\alpha_2}(T_{22}-T_{11})\\
&\quad+\frac{2T_{12}}{A_1A_2}\frac{\partial A_2}{\partial\alpha_1}+\frac{\partial T_{23}}{\partial\alpha_3}=\rho\frac{\partial^2U_2}{\partial t^2},\\
&\frac{1}{A_1}\frac{\partial T_{13}}{\partial\alpha_1}+\frac{1}{A_2}\frac{\partial T_{23}}{\partial\alpha_2}+\frac{1}{A_1A_2}\frac{\partial A_2}{\partial\alpha_1}T_{13}+\frac{1}{A_1A_2}\frac{\partial A_1}{\partial\alpha_2}T_{23}\\
&\quad+\frac{\partial T_{33}}{\partial\alpha_3}=\rho\frac{\partial^2U_3}{\partial t^2},
\end{aligned}
\tag{4}
$$

where A_i, U_i, and ρ are the Lame parameters, the components of displacements, and material density, respectively. The strain–displacement relationships are

$$
\begin{aligned}
S_{11}&=\frac{1}{A_1}\left(\frac{\partial U_1}{\partial\alpha_1}+\frac{U_2}{A_2}\frac{\partial A_1}{\partial\alpha_2}\right),\\
S_{22}&=\frac{1}{A_2}\left(\frac{\partial U_2}{\partial\alpha_2}+\frac{U_1}{A_1}\frac{\partial A_2}{\partial\alpha_1}\right),\quad S_{33}=\frac{\partial U_3}{\partial\alpha_3},\\
S_{12}&=\frac{A_1}{A_2}\frac{\partial}{\partial\alpha_2}\left(\frac{U_1}{A_1}\right)+\frac{A_2}{A_1}\frac{\partial}{\partial\alpha_1}\left(\frac{U_2}{A_2}\right),\\
S_{13}&=\frac{\partial U_1}{\partial\alpha_3}+\frac{1}{A_1}\frac{\partial U_3}{\partial\alpha_1},\quad S_{23}=\frac{\partial U_2}{\partial\alpha_3}+\frac{1}{A_2}\frac{\partial U_3}{\partial\alpha_2}.
\end{aligned}
\tag{5}
$$

B. Hypotheses

To simplify the electroelastic problem, four assumptions are proposed. The first two are Kirchhoff–Love hypotheses used in the classical plate theory for an elastic layer and the others are used particularly for a piezoelectric layer. The first hypothesis is that the normal stress acting on the surface elements parallel to the middle surface is small and can be neglected as compared to the other stresses:

$$
T_{33}=0. \tag{6}
$$

The second hypothesis is that a line normal to the middle surface before deformation remains perpendicular to the strained surface and is not extended after deformation:

$$
S_{13}=S_{23}=0. \tag{7}
$$

The third hypothesis is that the electrical potential varies with thickness in the quadratic form:[17]

$$
\psi=\phi_0+\phi_1\alpha_3+\phi_2\alpha_3^2, \tag{8}
$$

where functions ϕ_0, ϕ_1, and ϕ_2 denote coefficients of the constant term (α_3^0), linear term (α_3^1), and quadratic term (α_3^2), respectively. Due to the fact that electric charges should be equal on both electrodes, the fourth hypothesis is that the electric displacement is constant along the plate thickness:

$$
D_3=D_3^0, \tag{9}
$$

where D_3^0 is a function denoted coefficient of the constant term (α_3^0) and is independent of α_3. Besides, the membrane forces N_{ij} and bending moments M_{ij} are considered instead of stress in this electroelastic theory and are defined as

$$
N_{ij}=\int_{\alpha_3}T_{ij}\,d\alpha_3,\quad M_{ij}=\int_{\alpha_3}T_{ij}\alpha_3\,d\alpha_3. \tag{10}
$$

C. Theory for asymmetric bimorphic disk transducers

Thus, an electroelastic laminate plate theory can be derived from Eqs. (1)–(10), but only those relations for particular piezoelectric–elastic disks are shown in this paper. Figure 1 shows a two-layered laminated piezoelectric–elastic disk transducer. This transducer consists of an isotropic elastic disk and a piezoelectric disk. The radius of a piezoelectric disk is not larger than that of the elastic disk. The Poisson's ratios of piezoelectric and elastic layers are not necessarily identical. The piezoelectric disk is fully covered by approximately 10 μm thick electrodes whose thickness can be neglected. It is polarized in the thickness direction and isotropic transversely. The elastic disk is treated as an electrode of the piezoelectric disk. If the distance between the reference plane and the bottom surface of the elastic layer is h_n, the electrical boundary conditions can be expressed as

$$\psi|_{\alpha_3=h-h_n}=V, \quad \psi|_{\alpha_3=h_m-h_n}=-V. \tag{11}$$

Under this kind of configuration and the applied electric potential, the major motion of the disk caused by the in-plane extension of the piezoelectric disk is the bending vibration when under a sinusoidal electrical excitation. Due to transverse isotropy, the cylindrical coordinates r, θ, and z can be used to reformulate equations of the disk. In addition, the dynamic responses in the θ direction is omitted due to axis symmetry:

$$\frac{\partial f}{\partial \theta}=0, \tag{12}$$

where f is any physical property quantity of the transducer. The coordinates r and z are shown in Fig. 1. Moreover, the entire disk is divided into two sections according to the radius r_0 of the piezoelectric disk. The section (1) is the proportion whose radius is larger than r_0 and consists of the elastic layer only, and the section (2) is composed of all piezoelectric layers and part of the elastic layer. Since the material property is symmetric for the section (1) but asymmetric for the section (2), the locations of chosen reference planes may not be the same. The physical quantities of two sections are related by the kinematic and static matching conditions at the boundary between them:

$$\begin{aligned}
&u_z^{(1)}|_{r=r_0}=u_z^{(2)}|_{r=r_0},\\
&u_r^{(1)}|_{r=r_0}=u_r^{(2)}|_{r=r_0}-h_{12}\beta_r^{(2)}|_{r=r_0},\\
&\beta_r^{(1)}|_{r=r_0}=\beta_r^{(2)}|_{r=r_0},\\
&N_{rr}^{(1)}|_{r=r_0}=N_{rr}^{(2)}|_{r=r_0}\\
&N_{rz}^{(1)}|_{r=r_0}=N_{rz}^{(2)}|_{r=r_0},\\
&M_{rr}^{(1)}|_{r=r_0}=M_{rr}^{(2)}|_{r=r_0}+h_{12}N_{rr}^{(2)}|_{r=r_0},
\end{aligned} \tag{13}$$

where

$$\beta_r^{(i)}=-\frac{\partial u_z^{(i)}}{\partial r}, \tag{14}$$

and h_{12} is the distance between reference planes of section one and two as shown in Fig. 1, and upperscripts (1) and (2) denote that physical quantities belong to sections (1) and (2), respectively. To determine the dynamic responses, boundary conditions of the disk should be denoted. If the disk is free, the boundary conditions are

$$N_{rr}^{(2)}|_{r=R}=0, \quad N_{rz}^{(2)}|_{r=R}=0, \quad M_{rr}^{(2)}|_{r=R}=0. \tag{15}$$

By using Eqs. (1)–(12), the equilibrium equations can be simplified. The procedure is stated as follows. From Kirchhoff–Love hypotheses, the displacement in the α_i direction, U_i, in any place of plates can be expressed as

$$\begin{aligned}
&U_1(\alpha_1,\alpha_2,\alpha_3)=u_1(\alpha_1,\alpha_2)+\alpha_3\beta_1(\alpha_1,\alpha_2),\\
&U_2(\alpha_1,\alpha_2,\alpha_3)=u_2(\alpha_1,\alpha_2)+\alpha_3\beta_2(\alpha_1,\alpha_2),\\
&U_3(\alpha_1,\alpha_2,\alpha_3)=u_3(\alpha_1,\alpha_2),
\end{aligned} \tag{16}$$

where u_i is the displacement in the α_i direction of the reference plane in the thickness direction. Using cylindrical coordinates for which $\alpha_3=z$ and substituting Eqs. (12) and (16) into Eq. (5), the strains are expressed as

$$S_{rr}=S_{rr}^0+zk_{rr}, \quad S_{\theta\theta}=S_{\theta\theta}^0+zk_{\theta\theta}, \tag{17}$$

where membrane strains S_{ij}^0 are

$$S_{rr}^0=\frac{\partial u_r}{\partial r}, \quad S_{\theta\theta}^0=\frac{u_r}{r}, \tag{18}$$

bending strains k_{ij} are

$$k_{rr}=\frac{\partial \beta_r}{\partial r}=-\frac{\partial^2 u_z}{\partial r^2}, \quad k_{\theta\theta}=\frac{\beta_r}{r}=-\frac{1}{r}\frac{\partial u_z}{\partial r}. \tag{19}$$

To simplify equilibrium equations, we first change coordinates of Eq. (4) into cylindrical ones and combine Eqs. (6), (7), (12), and (16) into Eq. (4), then integrate Eq. (4) with respect to z, and finally multiply Eq. (4) by z and integrate results with respect to z. At the same time, Eq. (10) is used to make derived equations more clearly. Besides, plates in this paper are thin and the rotating inertia is omitted. After the above procedures, the equilibrium equations can be expressed as

$$\begin{aligned}
&\frac{\partial N_{rr}^{(i)}}{\partial r}+\frac{1}{r}(N_{rr}^{(i)}-N_{\theta\theta}^{(i)})=R_0^{(i)}\frac{\partial^2 u_r^{(i)}}{\partial t^2}+R_1^{(i)}\frac{\partial^2 \beta_r^{(i)}}{\partial t^2},\\
&\frac{1}{r}\frac{\partial}{\partial r}(rN_{rz}^{(i)})=R_0^{(i)}\frac{\partial^2 u_z^{(i)}}{\partial t^2}, \quad i=1,2,
\end{aligned} \tag{20}$$

where

$$\begin{aligned}
N_{rz}^{(i)}&=\frac{\partial M_{rr}^{(i)}}{\partial r}+\frac{1}{r}(M_{rr}^{(i)}-M_{\theta\theta}^{(i)})-R_1^{(i)}\frac{\partial^2 u_r^{(i)}}{\partial t^2},\\
R_0^{(1)}&=\rho_m h_m,\\
R_0^{(2)}&=\rho_m h_m+\rho_p(h-h_m),\\
R_1^{(1)}&=\tfrac{1}{2}\rho_m h_m(h_m-2h_n^{(1)}),\\
R_1^{(2)}&=\tfrac{1}{2}[\rho_m h_m(h_m-2h_n^{(2)})+\rho_p(h-h_m)\\
&\quad\times(h+h_m-2h_n^{(2)})],
\end{aligned} \tag{21}$$

and ρ_m and ρ_p are the density of elastic and piezoelectric material, respectively. By combining Eqs. (1), (2), (3), (8),

(9), and (17) into Eq. (10) and using cylindrical coordinates, the bending moments can be expressed as

$$\begin{bmatrix} N_{rr}^{(i)} \\ N_{\theta\theta}^{(i)} \\ M_{rr}^{(i)} \\ M_{\theta\theta}^{(i)} \end{bmatrix} = \begin{bmatrix} A_{11}^{(i)} & A_{12}^{(i)} & B_{11}^{(i)} & B_{12}^{(i)} \\ A_{12}^{(i)} & A_{11}^{(i)} & B_{12}^{(i)} & B_{11}^{(i)} \\ B_{11}^{(i)} & B_{12}^{(i)} & D_{11}^{(i)} & D_{12}^{(i)} \\ B_{12}^{(i)} & B_{11}^{(i)} & D_{12}^{(i)} & D_{11}^{(i)} \end{bmatrix} \cdot \begin{bmatrix} S_{rr}^{(i)} \\ S_{\theta\theta}^{(i)} \\ k_{rr}^{(i)} \\ k_{\theta\theta}^{(i)} \end{bmatrix} + \begin{bmatrix} E_{11}^{(i)} \\ E_{11}^{(i)} \\ F_{11}^{(i)} \\ F_{11}^{(i)} \end{bmatrix} \cdot V, \quad i=1,2, \tag{22}$$

where for section one,

$$\begin{aligned} A_{11}^{(1)} &= \frac{E_m h_m}{1-\nu_m^2}, \quad A_{12}^{(1)} = \frac{E_m \nu_m h_m}{1-\nu_m^2}, \\ B_{11}^{(1)} &= \frac{E_m h_m (h_m - 2h_n^{(1)})}{2(1-\nu_m^2)}, \\ B_{12}^{(1)} &= \frac{E_m \nu_m h_m (h_m - 2h_n^{(1)})}{2(1-\nu_m^2)}, \\ D_{11}^{(1)} &= \frac{E_m h_m [h_m^2 - 3h_m h_n^{(1)} + 3(h_n^{(1)})^2]}{3(1-\nu_m^2)}, \\ D_{12}^{(1)} &= \frac{E_m \nu_m h_m [h_m^2 - 3h_m h_n^{(1)} + 3(h_n^{(1)})^2]}{3(1-\nu_m^2)}, \\ E_{11}^{(1)} &= 0, \quad F_{11}^{(1)} = 0, \end{aligned} \tag{23}$$

and for section (2),

$$\begin{aligned} A_{11}^{(2)} &= \frac{E_m h_m}{1-\nu_m^2} + \frac{h_p}{S_{11}^E (1-\nu_p^2)}, \\ A_{12}^{(2)} &= \frac{E_m \nu_m h_m}{1-\nu_m^2} + \frac{\nu_p h_p}{s_{11}^E (1-\nu_p^2)}, \\ B_{11}^{(2)} &= \frac{E_m h_m (h_m - 2h_n^{(2)})}{2(1-\nu_m^2)} + \frac{(h-h_m)(h+h_m-2h_n^{(2)})}{2s_{11}^E (1-\nu_p^2)}, \\ B_{12}^{(2)} &= \frac{E_m \nu_m h_m (h_m - 2h_n^{(2)})}{2(1-\nu_m^2)} + \frac{\nu_p (h-h_m)(h+h_m-2h_n^{(2)})}{2s_{11}^E (1-\nu_p^2)}, \\ D_{11}^{(2)} &= \frac{E_m h_m [h_m^2 - 3h_m h_n^{(2)} + 3(h_n^{(2)})^2]}{3(1-\nu_m^2)} \\ &\quad + \frac{h-h_m}{12 s_{11}^E (1-\nu_p^2)(1-2B)} \{-3B(1+\nu_p)(h+h_m \\ &\quad - 2h_n^{(2)})^2 + 4[(h^2 + hh_m + h_m^2) - 3(h+h_m)h_n^{(2)} \\ &\quad + 3(h_n^{(2)})^2] \times (1 - B + B\nu_p)\}, \\ D_{12}^{(2)} &= \frac{E_m \nu_m h_m [h_m^2 - 3h_m h_n^{(2)} + 3(h_n^{(2)})^2]}{3(1-\nu_m^2)} \\ &\quad + \frac{h-h_m}{12 s_{11}^E (1-\nu_p^2)(1-2B)} \{-3B(1+\nu_p)(h+h_m \\ &\quad - 2h_n^{(2)})^2 + 4[(h^2 + hh_m + h_m^2) - 3(h+h_m)h_n^{(2)} \\ &\quad + 3(h_n^{(2)})^2] \times (\nu_p + B - B\nu_p)\}, \\ E_{11}^{(2)} &= \frac{2d_{31}}{s_{11}^E (1-\nu_p)}, \quad F_{11}^{(2)} = \frac{d_{31}(h+h_m-2h_n^{(2)})}{s_{11}^E (1-\nu_p)}, \end{aligned} \tag{24}$$

where

$$\begin{aligned} B &= \frac{d_{31}^2}{\epsilon_{33}^T s_{11}^E (1-\nu_p)} = \frac{1}{2} k_p^2, \\ \nu_p &= -\frac{s_{12}^E}{s_{11}^E}. \end{aligned} \tag{25}$$

We assume that displacements of the reference planes are

$$\begin{aligned} u_r^{(i)}(r,t) &= W_r^{(i)}(r) e^{j\omega t}, \\ u_z^{(i)}(r,t) &= W_z^{(i)}(r) e^{j\omega t}, \end{aligned} \tag{26}$$

where W_r and W_z denote the displacement amplitudes in the r and z directions, and ω is the angular frequency of vibration of the disk. Finally, substituting Eqs. (18), (19), (22), and (26) into Eq. (20), the governing equations for each section of the disk can be expressed as

$$\begin{bmatrix} L_{11}^{(i)} & L_{12}^{(i)} \\ L_{21}^{(i)} & L_{22}^{(i)} \end{bmatrix} \cdot \begin{bmatrix} W_r^{(i)} \\ W_z^{(i)} \end{bmatrix} = \begin{bmatrix} 0 \\ 0 \end{bmatrix}, \quad i=1,2, \tag{27}$$

where

$$\begin{aligned} L_{11}^{(i)} &= \left(\frac{\partial^2}{\partial r^2} + \frac{1}{r}\frac{\partial}{\partial r} - \frac{1}{r^2} \right) + (\lambda_r^{(i)})^2, \\ L_{12}^{(i)} &= -b_{rz}^{(i)} \left(\frac{\partial^3}{\partial r^3} + \frac{1}{r}\frac{\partial^2}{\partial r^2} - \frac{1}{r^2}\frac{\partial}{\partial r} \right) - \frac{R_1^{(i)}}{A_{11}^{(i)}} \omega^2 \frac{\partial}{\partial r}, \\ L_{21}^{(i)} &= -b_{zr}^{(i)} \left(\frac{\partial^3}{\partial r^3} + \frac{2}{r}\frac{\partial^2}{\partial r^2} - \frac{1}{r^2}\frac{\partial}{\partial r} + \frac{1}{r^3} \right) \\ &\quad - \frac{R_1^{(i)}}{D_{11}^{(i)}} \omega^2 \left(\frac{\partial}{\partial r} + \frac{1}{r} \right), \\ L_{22}^{(i)} &= \left(\frac{\partial^4}{\partial r^4} + \frac{2}{r}\frac{\partial^3}{\partial r^3} - \frac{1}{r^2}\frac{\partial^2}{\partial r^2} + \frac{1}{r^3}\frac{\partial}{\partial r} \right) - (\lambda_z^{(i)})^4, \end{aligned} \tag{28}$$

and

$$\begin{aligned} (\lambda_r^{(i)})^2 &= \frac{R_0^{(i)}}{A_{11}^{(i)}} \omega^2, \quad (\lambda_z^{(i)})^4 = \frac{R_0^{(i)}}{D_{11}^{(i)}} \omega^2, \\ b_{rz}^{(i)} &= \frac{B_{11}^{(i)}}{A_{11}^{(i)}}, \quad b_{zr}^{(i)} = \frac{B_{11}^{(i)}}{D_{11}^{(i)}}. \end{aligned} \tag{29}$$

To solve Eq. (27), the governing equations are simplified further by selecting the location of the reference plane. The location of the reference plane is determined by letting

TABLE I. Piezoelectric material properties.

	PZT-4	PZT-5A	PZT-7A	PZT-8	C-82	$BaTiO_3$	ZnO
$\epsilon_{33}^T/\epsilon_0$	1300	1700	425	1020	3400	1700	12.29
$d_{31}(\times 10^{-12}\,\mathrm{C/N})$	−123	−171	−60	−97.4	−260	−78	−5.22
$s_{11}^E(\times 10^{-12}\,\mathrm{m^2/N})$	12.3	16.4	10.7	11.5	16.95	9.1	7.86
$s_{12}^E(\times 10^{-12}\,\mathrm{m^2/N})$	−4.05	−5.74	−3.2	−3.38	−5.76	−2.7	−3.43
$\rho_p\,(\mathrm{kg/m^3})$	7500	7750	7700	7600	7400	5700	5676
k_{31}	0.3269	0.3442	0.2990	0.3022	0.3640	0.2108	0.2524
k_p	0.5645	0.6037	0.5051	0.5087	0.6335	0.3554	0.3362

$$R_1^{(i)}=0, \tag{30}$$

and the chosen results from Eq. (21) are

$$h_n^{(1)}=\tfrac{1}{2}h_m,$$
$$h_n^{(2)}=\frac{1}{2}\,\frac{h_m^2+(h^2-h_m^2)\rho_p/\rho_m}{h_m+(h-h_m)\rho_p/\rho_m}. \tag{31}$$

By substituting Eq. (31) into Eqs. (23), (24), and (28), the governing equations of the extensional and flexural motions of section (1) are decoupled, and their general solutions are

$$W_r^{(1)}=C_1^{(1)}J_1(\lambda_r^{(1)}r)+C_2^{(1)}Y_1(\lambda_r^{(1)}r),$$
$$W_z^{(1)}=C_3^{(1)}J_0(\lambda_z^{(1)}r)+C_4^{(1)}I_0(\lambda_z^{(1)}r)+C_5^{(1)}Y_0(\lambda_z^{(1)}r)+C_6^{(1)}K_0(\lambda_z^{(1)}r), \tag{32}$$

where J_n and Y_n are Bessel functions of the first and second kinds of order n, respectively, and I_n and K_n are modified Bessel functions of the first and second kinds of order n, respectively. But for the section (2), $B_{11}^{(2)}$ is not zero for the chosen reference plane, and the extensional and flexural motions are still coupled. The tedious procedure is similar to the paper in Ref. 18 and omitted here. The general solutions for the governing equations of section (2) are[18]

$$W_r^{(2)}=C_1^{(2)}P_1J_1(\lambda_1 r)+C_2^{(2)}P_2J_1(\lambda_2 r)-C_3^{(2)}P_3I_1(m_3 r)+C_4^{(2)}P_1Y_1(\lambda_1 r)+C_5^{(2)}P_2Y_1(\lambda_2 r)+C_6^{(2)}P_3K_1(m_3 r),$$
$$W_z^{(2)}=C_1^{(2)}J_0(\lambda_1 r)+C_2^{(2)}J_0(\lambda_2 r)+C_3^{(2)}I_0(m_3 r)+C_4^{(2)}Y_0(\lambda_1 r)+C_5^{(2)}Y_0(\lambda_2 r)+C_6^{(2)}K_0(m_3 r), \tag{33}$$

where

$$P_1=\frac{b_{rz}^{(2)}\lambda_1^3}{(\lambda_r^{(2)})^2-\lambda_1^2},$$
$$P_2=\frac{b_{rz}^{(2)}\lambda_2^3}{(\lambda_r^{(2)})^2-\lambda_2^2},$$
$$P_3=\frac{-b_{rz}^{(2)}m_3^3}{(\lambda_r^{(2)})^2+m_3^2},$$
$$\lambda_1=\frac{1}{R}(\mu_1)^{1/2},\quad \lambda_2=\frac{1}{R}(\mu_2)^{1/2}, \tag{34}$$
$$m_3=\frac{1}{R}|\mu_3|^{1/2},\quad \mu_1>\mu_2>\mu_3,$$

and μ_i, $i=1,3$ are the roots of the following equation:

$$(1-b_{rz}^{(2)}b_{zr}^{(2)})\mu^3-(R\lambda_r^{(2)})^2\mu^2-(R\lambda_z^{(2)})^4\mu+(R\lambda_r^{(2)})^2(R\lambda_z^{(2)})^4=0. \tag{35}$$

By substituting general solutions of section (1) and section (2) into Eqs. (14) and (16), the matrix form of algebraic equations for coefficients $C_j^{(i)}$ can be written as

$$[A]\cdot\{C\}=\{F\}, \tag{36}$$

where

$$\{C\}=\{C_1^{(1)},C_2^{(1)},C_3^{(1)},C_4^{(1)},C_5^{(1)},C_6^{(1)},C_1^{(2)},C_2^{(2)},C_3^{(2)}\}^T, \tag{37}$$

and $[A]$ is a nine-order square matrix, and $\{F\}$ is a 9×1 matrix. In the above equations, coefficients $C_4^{(2)}$, $C_5^{(2)}$ and $C_6^{(2)}$ vanish due to that of section (2) is a disk without a central hole. From Eq. (36), coefficients $C_j^{(i)}$ can be found and the resonance frequencies where the electrical impedance is minimized, can be determined by solving

$$\det([A])=0. \tag{38}$$

Besides, from the developed theory, the electric current I of the laminated disk shown in Fig. 1 can be expressed as

$$I=-\frac{j\pi\omega d_{31}}{s_{11}^E(1-\nu_p)}(1+h_m-2h_n)\cdot\left[-\frac{2}{1+h_m-2h_n}r_0W_r^{(2)}|_{r=r_0}-r_0\beta_r^{(2)}|_{r=r_0}+\frac{2\epsilon_{33}^T(1-2B)}{F_{11}^{(2)}(1-h_m)}r_0^2V\right], \tag{39}$$

and the antiresonance frequencies where the electrical impedance is minimized, can be determined by solving

$$I=0. \tag{40}$$

TABLE II. Isotropic elastic material properties.

	Glass	Al	Cu	Fe
$E_m(\times 10^9\ \mathrm{N/m^2})$	46.2	70	119	207
ν_m	0.245	0.33	0.326	0.292
$\rho_m\ (\mathrm{kg/m^3})$	2600	2700	8900	7800

D. Static sensitivity

In addition to dynamic characteristics, displacement sensitivity due to static voltage is another important design factor. Under a static situation, by letting $\omega=0$, Eq. (28) becomes

$$
\begin{aligned}
L_{11}^{(i)} &= \left(\frac{\partial^2}{\partial r^2}+\frac{1}{r}\frac{\partial}{\partial r}-\frac{1}{r^2}\right),\\
L_{12}^{(i)} &= -b_{rz}^{(i)}\left(\frac{\partial^3}{\partial r^3}+\frac{1}{r}\frac{\partial^2}{\partial r^2}-\frac{1}{r^2}\frac{\partial}{\partial r}\right),\\
L_{21}^{(i)} &= -b_{zr}^{(i)}\left(\frac{\partial^3}{\partial r^3}+\frac{2}{r}\frac{\partial^2}{\partial r^2}-\frac{1}{r^2}\frac{\partial}{\partial r}+\frac{1}{r^3}\right),\\
L_{22}^{(i)} &= \left(\frac{\partial^4}{\partial r^4}+\frac{2}{r}\frac{\partial^3}{\partial r^3}-\frac{1}{r^2}\frac{\partial^2}{\partial r^2}+\frac{1}{r^3}\frac{\partial}{\partial r}\right).
\end{aligned}
\tag{41}
$$

Since the terms including $R_1^{(i)}$ are disappeared, matching the condition of Eq. (30) is not necessary and the location of reference plane is determined by letting

$$B_{11}^{(i)}=0. \tag{42}$$

The calculated results are

$$
\begin{aligned}
h_n^{(1)} &= \tfrac{1}{2}h_m,\\
h_n^{(2)} &= \frac{1}{2}\frac{h_m^2+(h^2-h_m^2)\,\eta_k}{h_m+(h-h_m)\,\eta_k},
\end{aligned}
\tag{43}
$$

where

$$\eta_k=\frac{(1-\nu_m^2)}{Es_{11}^E(1-\nu_p^2)}. \tag{44}$$

By this arrangement, the terms $b_{rz}^{(i)}$ and $b_{zr}^{(i)}$ in Eq. (41) are reduced to zero, and the static governing equations of section one and section two have the same form and are decoupled. The general solutions under the static situation are

$$
\begin{aligned}
W_r^{(i)} &= B_1^{(i)}r+\frac{B_{-1}^{(i)}}{r},\\
W_z^{(i)} &= B_2^{(i)}r^2+B_0^{(i)}+B_e^{(i)}\ln r+\frac{B_{-2}^{(i)}}{r^2},
\end{aligned}
\tag{45}
$$

where coefficients $B_1^{(i)}$, $B_{-1}^{(i)}$, $B_2^{(i)}$, $B_0^{(i)}$, $B_e^{(i)}$, $B_{-2}^{(i)}$ can be found by meeting boundary conditions. Thus, static displacement sensitivity of transducers can be solved.

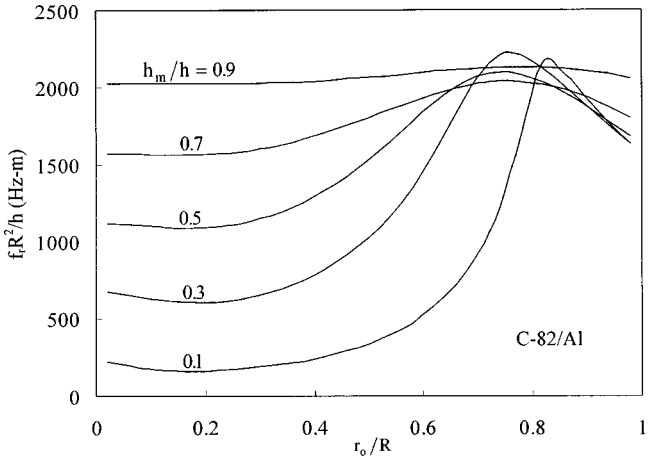

FIG. 2. The first resonance frequency constant f_rR^2/h versus the thickness ratio h_m/h and radius ratio r_0/R for material combination of C-82 and Al.

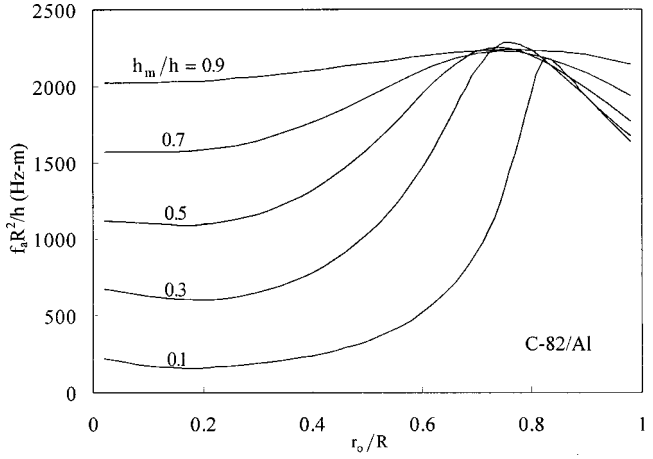

FIG. 3. The first antiresonance frequency constant f_aR^2/h versus the thickness ratio h_m/h and radius ratio r_0/R.

E. EMCC

For piezoelectric transducers, the EMCC is an important characteristic. There are several different definitions of EMCC. When vibration frequency is near the resonance region, the dynamic electromechanical coupling coefficient k_d is found by using the formula[19]

$$k_d^2=\frac{f_a^2-f_r^2}{f_a^2}, \tag{46}$$

where f_r and f_a are the resonance and antiresonance frequencies, respectively.

III. NUMERICAL RESULTS

To illustrate the relationship between characteristics, material properties, and geometric variables such as the thickness and radius ratio, the dynamic responses of a particular two-layered piezoelectric–elastic disk transducer were numerically calculated as an example. In this numerical analysis, a variety of piezoelectric and elastic materials whose properties are listed in Tables I and II are selected for study. The mathematical software MATLAB was used to handle the tedious computations. The calculated first resonance frequency constant, f_rR^2/h, the first antiresonance frequency constant, f_aR^2/h, and the dynamic EMCC, k_d, for C-82 piezoelectric and Al materials are shown in Figs. 2–4, respectively. From the numerical results, it is shown that characteristics depend on thickness ratio h_m/h and radius ratio r_0/R in a complex manner. Figures 2 and 3 show the

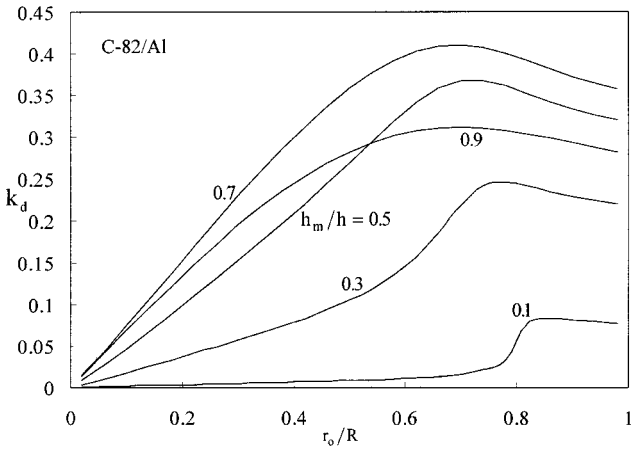

FIG. 4. The EMCC k_d near the first resonance region versus the thickness ratio h_m/h and radius ratio r_0/R.

similar tendency of resonance and antiresonance frequency constants, but the EMCC has a totally different tendency. It is seen that near the radius ratio of approximately 0.7, the maximum values of the resonance and antiresonance frequencies exist for a large range of thickness ratio of greater than 0.3.

Figure 4 show the existence of a maximum EMCC value. From numerical analysis, the EMCC reaches a maximum value of 0.41 when the thickness and radius ratios are 0.68 and 0.69, respectively. Obviously, the optimized values of geometric variables change with material properties. Figure 5 shows the first three mode shapes for the optimized geometric configurations. The optimization results for the maximum dynamic EMCC for all considered materials are obtained and listed in Table III. Taking PZT-4 and glass for example, the optimum EMCC (Kd) of 0.3476, corresponding to $k_d/k_p=0.6158$, is obtained at $h_m/h=0.7939$ and $r_0/R=0.6946$. We conclude that for the considered combination of materials, the optimized value of k_d/k_p is between 57% and 69%. These tables are useful for the design of electroacoustic devices such as microphones, speakers, and filters.

To study the relationship between static displacements and geometric variables, materials C-82 and Fe are used in a

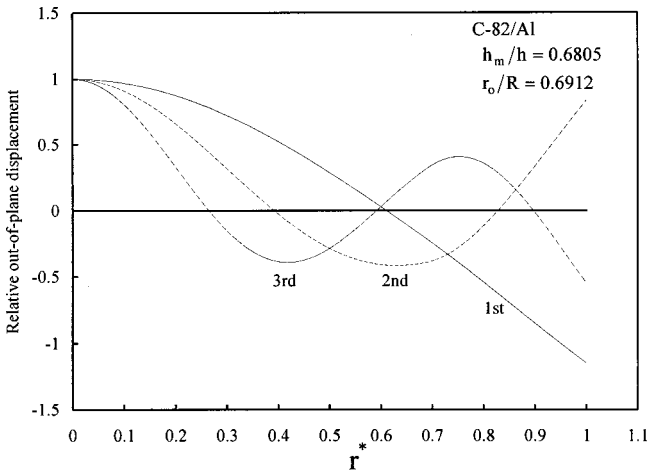

FIG. 5. The first three mode shapes at optimum geometry.

TABLE III. Optimization results for dynamic characteristics.

	PZT-4	PZT-5A	PZT-7A	PZT-8	C-82	$BaTiO_3$	ZnO
				(a) Optimized h_m/h			
Glass	0.7939	0.7616	0.8007	0.7896	0.7592	0.8111	0.8584
Al	0.7167	0.6827	0.7237	0.7115	0.6805	0.7343	0.7900
Cu	0.6313	0.5976	0.6378	0.6255	0.5958	0.6479	0.7071
Fe	0.5507	0.5191	0.5564	0.5446	0.5177	0.5652	0.6234
				(b) Optimized r_0/R			
Glass	0.6946	0.6918	0.6961	0.6961	0.6920	0.7027	0.7007
Al	0.6939	0.6909	0.6955	0.6956	0.6912	0.7035	0.7009
Cu	0.7148	0.7140	0.7164	0.7171	0.7139	0.7217	0.7156
Fe	0.7155	0.7139	0.7173	0.7180	0.7139	0.7244	0.7184
				(c) Optimized k_d			
Glass	0.3476	0.3792	0.3066	0.3103	0.4014	0.2103	0.1945
Al	0.3563	0.3885	0.3145	0.3184	0.4111	0.2160	0.1992
Cu	0.3685	0.4015	0.3257	0.3297	0.4245	0.2240	0.2062
Fe	0.3788	0.4117	0.3353	0.3393	0.4349	0.2313	0.2131
				(d) Optimized k_d/k_p			
Glass	0.6158	0.6281	0.6070	0.6100	0.6336	0.5917	0.5785
Al	0.6312	0.6435	0.6226	0.6259	0.6489	0.6078	0.5925
Cu	0.6528	0.6651	0.6448	0.6481	0.6701	0.6306	0.6133
Fe	0.6710	0.6820	0.6638	0.6670	0.6865	0.6508	0.6338

numerical analysis and results are shown in Fig. 6. The maximum displacements at the central point of the disk exist at the radius ratio of 1. Under the optimized configuration, the changes of the optimized thickness ratio with respect to the changes of material properties are shown in Fig. 7. Obviously, a strong influence of the elastic compliance constant s_{11}^E and Young's modulus E are found. Table IV lists the optimized configurations for the maximum central displacements of the disk.

In some studies,[15,16,20,21] the Poisson's ratios of elastic and piezoelectric materials were treated identical in order to simplify analytical procedures. In this study, we calculate the frequency constants for the cases that the Poisson's ratios of glass and ZnO are and not equal. Table V lists the calculated results at the optimum geometry. In this table, the errors induced by this assumption for the first resonance and antiresonance frequencies are about 8%. For the higher modes, errors of 6.75% in frequency constants, and of 16.12% in EMCC are found.

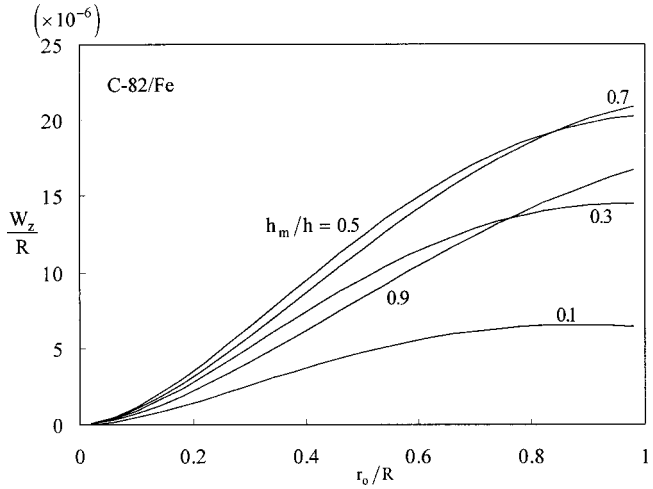

FIG. 6. Nondimensional central displacements W_z/R versus the thickness ratio h_m/h and radius ratio r_0/R.

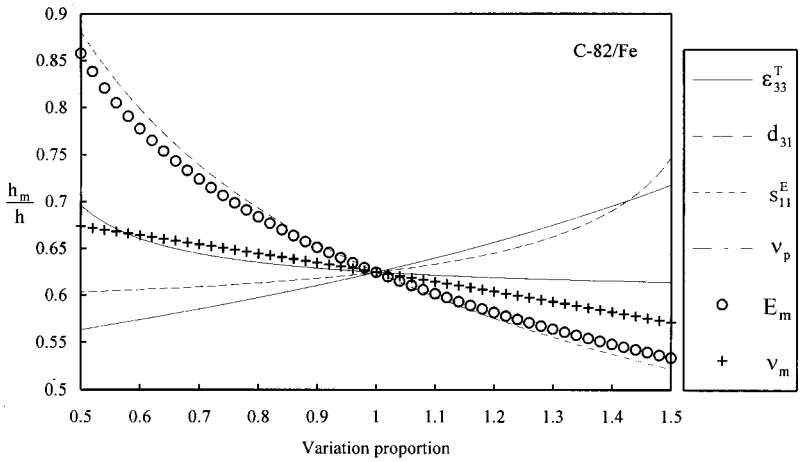

FIG. 7. The influence of material properties on optimization results for the maximum EMCC (K_d).

TABLE IV. Optimization results for static characteristics.

	PZT-4	PZT-5A	PZT-7A	PZT-8	C-82	$BaTiO_3$	ZnO
			(a) Optimized h_m/h				
Glass	→1.0	→1.0	→1.0	→1.0	→1.0	→1.0	→1.0
Al	→1.0	→1.0	→1.0	→1.0	→1.0	→1.0	→1.0
Cu	0.9259	0.7921	0.9999	0.9372	0.7750	→1.0	→1.0
Fe	0.7021	0.6334	0.7299	0.7037	0.6245	0.7864	→1.0
			(b) Optimized W_z/R ($\times 10^{-6}$) under unit voltage				
Glass	43.86	47.19	23.53	35.28	68.37	35.85	3.47
Al	25.69	27.64	13.78	20.67	40.04	21.00	2.03
Cu	15.35	18.05	8.16	12.31	26.72	12.43	1.20
Fe	11.53	14.45	5.88	9.21	21.52	8.28	0.73

TABLE V. Errors of frequency constants induced by $\nu_m = \nu_p$ for $h_m/h = 0.8584$, $r_0/R = 0.7007$, and the use of ZnO and glass.

	Frequency constants (Hz m)								
	Resonance			Antiresonance			Dynamic EMCC		
	1	2	3	1	2	3	1	2	3
$\nu_m \neq \nu_p$	2122	8190	17997	2164	8192	18013	0.1945	0.0242	0.0420
$\nu_m = \nu_p$	2293	8741	19132	2338	8744	19148	0.1944	0.0281	0.0413
error (%)	8.06	6.73	6.31	8.07	6.75	6.31	−0.051	16.12	−1.67

TABLE VI. A comparison of experimental and theoretical results.

	Theory (Hz)			Experiment (Hz)			Error (%)		
				Mode					
Specimen	1	2	3	1	2	3	1	2	3
				(a) Resonance frequency					
1	657	2487	5243	673	2444	5178	2.36	−1.75	−1.24
2	1147	4330	9945	1156	4306	9740	0.81	−0.55	−2.06
3	1339	4916	10 336	1425	4775	10 000	6.42	−2.87	−3.25
				(b) Antiresonance frequency					
1	678	2582	5244	682	2553	5213	0.52	−1.14	−0.59
2	1223	4446	9966	1261	4438	9845	3.13	−0.19	−1.21
3	1465	4959	10 347	1475	4825	10 100	0.68	−2.70	−2.39

IV. EXPERIMENTS

To verify the numerical results, some experiments were conducted. Material of C-82 piezoceramics made by Fuji Inc. Japan and Al were selected for experiments. Three specimens were made with dimensions in mm: $h_m = 0.189$, 0.383,0.388, $h = 0.401$,0.594,0.589, $r_0 = 30$,30,45, and $R = 60$,60,60, respectively. The experimental setup uses an impedance analyzer to measure the impedance spectrum. In the impedance spectrum, the frequencies of local minimum and maximum values of impedance indicate resonance and antiresonance frequencies, respectively. The experimental results compared with theoretical values for vibration modes 1–3 are listed in Table VI. The maximum errors of 6.42% in resonance frequency and 3.13% in antiresonance frequency are found. Some errors may be induced by noncompletely free boundary conditions and the fabrication process. This suggests the acceptance of the proposed theory.

V. CONCLUSIONS

The electroelastic plate theory and optimization of a two-layer bimorphic disk transducer are presented. The dynamic and static optimized configurations for the maximum EMCC value and maximum static displacements are presented. The variations of material property results in changes of optimized configurations and the influence are studied. Numerical results for different hypotheses on Poisson's ratio are compared and the errors of 6.31%–8.07% are found in our examples. The developed easy-to-use figures and tables are useful for the design of the laminated piezoelectric actuators and sensors, such as microphones, speakers, and filters.

ACKNOWLEDGMENT

This work was supported by the National Science Council, Taiwan, Republic of China, under Grant No. NSC86-2212-E-002-007.

[1] M. Pedersen, R. Schellin, W. Olthuis, and P. Bergveld, ''Electroacoustical measurements of silicon microphones on wafer scale,'' J. Acoust. Soc. Am. **101**, 2122–2128 (1997).
[2] H. S. Tzou and M. Gadre, ''Theoretical analysis of a multi-layered thin shell coupled with piezoelectric shell actuators for distributed vibration controls,'' J. Sound Vib. **132**, 433–450 (1989).
[3] R. C. Batra and X. Q. Liang, ''The vibration of a rectangular laminated elastic plate with embedded piezoelectric sensors and actuators,'' Comput. Struct. **63**, 203–216 (1997).
[4] R. Mitra, ''On the performance characterization of ultrasonic air transducers with radiating membranes,'' IEEE Trans. Ultrason. Ferroelectr. Freq. Control **43**, 858–863 (1996).
[5] J. J. Bernstein, S. L. Finberg, K. Houston, L. C. Niles, H. D. Chen, L. E. Cross, K. K. Li, and K. Udayakumer, ''Micromachined high frequency ferroelectric sonar transducers,'' IEEE Trans. Ultrason. Ferroelectr. Freq. Control **44**, 960–969 (1997).
[6] S. H. Chang and B. C. Du, ''A precision piezodriven micropositioner mechanism with large travel range,'' Rev. Sci. Instrum. **69**, 1785–1791 (1998).
[7] L. S. Lee and L. Z. Jiang, ''Exact electroelastic analysis of piezoelectric laminae via state space approach,'' Int. J. Solids Struct. **33**, 977–990 (1996).
[8] C. K. Lee and F. C. Moon, ''Laminated piezopolymer plates for torsion and bending sensors and actuators,'' J. Acoust. Soc. Am. **85**, 2432–2439 (1989).
[9] S. H. Chang and C. C. Chou, ''Electromechanical analysis of an asymmetric piezoelectric/elastic laminated structure: Theory and Experiment,'' IEEE Trans. Ultrason. Ferroelectr. Freq. Control **46**, 441–451 (1999).
[10] S. H. Chang and Y. C. Tung, ''Electro-elastic characteristics of asymmetric rectangular piezoelectric laminae,'' IEEE Trans. Ultrason. Ferroelectr. Freq. Control **46**, 950–960 (1999).
[11] D. Ricketts, ''The frequency of flexural vibration of completely free composite piezoelectric polymer plates,'' J. Acoust. Soc. Am. **80**, 723–726 (1986).
[12] J. S. Yang, R. C. Batra, and X. Q. Liang, ''The vibration of a simply supported rectangular elastic plate due to piezoelectric actuators,'' Int. J. Solids Struct. **33**, 1597–1618 (1996).
[13] N. Guo, P. Cawley, and D. Hitchings, ''The finite element analysis of the vibration characteristics of piezoelectric discs,'' J. Sound Vib. **159**, 115–138 (1992).
[14] H. A. Kunkel, S. Locke, and B. Pikeroen, ''Finite-element analysis of vibrational modes in piezoelectric ceramic disks,'' IEEE Trans. Ultrason. Ferroelectr. Freq. Control **37**, 316–328 (1990).
[15] S. I. Rudnitskii, V. M. Sharapov, and N. A. Shul'ga, ''Vibration of a bimorphic disk transducer of the metal-piezoceramic type,'' Prikl. Mekh. **26**, 973–980 (1991).
[16] Yu. B. Evseichik, S. I. Rudnitskii, V. M. Sharapov, and N. A. Shul'ga, ''Sensitivity of a metal-piezoceramic bimorph transducer,'' Prikl. Mekh. **26**, 1174–1181 (1991).
[17] N. N. Rogacheva, *The Theory of Piezoelectric Shells and Plates* (CRC Press, Boca Raton, 1994).
[18] Y. Stavsky and R. Loewy, ''Axisymmetric vibrations of isotropic composite circular plates,'' J. Acoust. Soc. Am. **49**, 1542–1550 (1971).
[19] W. P. Mason, *Piezoelectric Crystals and Their Application to Ultrasonics* (Van Nostrand, New York, 1950).
[20] N. T. Adelman and Y. Stavsky, ''Flexural-extensional behavior of composite piezoelectric circular plates,'' J. Acoust. Soc. Am. **67**, 819–822 (1980).
[21] Z. Chaudhry, F. Lalande, and C. A. Rogers, ''Modeling of induced strain actuation of shell structures,'' J. Acoust. Soc. Am. **97**, 2872–2877 (1995).

The radiation efficiency grouping of free-space acoustic radiation modes

Kenneth A. Cunefare and M. Noelle Currey
The George W. Woodruff School of Mechanical Engineering, Georgia Institute of Technology, Atlanta, Georgia 30332-0405

M. E. Johnson and S. J. Elliott
Institute of Sound and Vibration Research, The University of Southampton, Southampton SO17 1BJ, United Kingdom

(Received 26 January 1998; revised 12 September 2000; accepted 13 September 2000)

The use of a modal representation for the exterior acoustic field of a structure has received increasing attention in recent years. This modal approach generally seeks a set of orthogonal functions, representing independent surface velocity distributions, termed acoustic radiation modes, which diagonalize a radiation operator in the exterior domain of the structure. These orthogonal acoustic radiation modes may be found, among other methods, through an eigenvalue analysis of a radiation operator and possess a corresponding set of eigenvalues that are proportional to the radiation efficiencies of the acoustic radiation modes. In free space, the acoustic radiation modes of a sphere display a grouping characteristic in their radiation efficiencies, where each acoustic radiation mode's radiation efficiency within a group has the same frequency dependency. This is a consequence of the fact that the acoustic radiation modes of a sphere are the spherical harmonics. Further, the acoustic radiation modes of an arbitrary three-dimensional structure exhibit the same frequency grouping as those for the sphere. The basis for the arbitrary structure's grouping follows from the sphere's grouping. The observation that the acoustic radiation modes of an arbitrary body are dominated by spherical harmonics provides insight on the behavior of such modes. These results have significance for various applications of acoustic radiation modes, including active noise control design, radiation modeling, etc.
[DOI: 10.1121/1.1323236]

PACS numbers: 43.40.Rj, 43.20.Rz, 43.20.Tb [CBB]

I. INTRODUCTION

In this paper, we examine certain aspects of the frequency dependency of the acoustic radiation modes of structures in free space. Specifically, we are interested in exploring an observed ''grouping'' dependency of these acoustic radiation modes at long wavelengths, where we see quantization of the acoustic radiation modes into groups of acoustic radiation modes with the same frequency dependency for their radiation efficiencies. In the remainder of this Introduction, we briefly review the development of the acoustic radiation modes concept. Some of the elements of the topic we discuss in this paper have appeared in a number of the references cited below, but their significance has gone unremarked. As a further note, throughout this paper, we use the full expression ''acoustic radiation modes,'' rather than some abbreviated term, so as to clearly distinguish between what we are interested in and other common interpretations of the use of the word ''mode.'' This will occasionally lead to some clumsy prose, but we do not wish to leave any confusion between acoustic radiation modes and such more commonly encountered items as structural vibration modes and acoustic cavity modes.

The modal approach for characterizing exterior acoustic radiation from an arbitrary, vibrating structure has seen rapid development and application since its introduction in 1990.[1] In one of the many implementations of this approach, any velocity distribution on a structure may be constructed by superimposing contributions from a set of independent acoustic velocity modes. To each such velocity mode there corresponds an acoustic pressure mode. This modal description pertains whether the representation is obtained using surface or field pressure or surface or field velocity considerations. We here consider the representation to yield surface velocity modes.

The acoustic radiation modes are obtained through a modal decomposition of a discretized radiation operator, dependent only on the geometry of the structure and frequency of interest. The term ''radiation operator'' represents a functional that describes some aspect of exterior acoustic radiation from a structure, the form of which being dependent upon the particular avenue chosen to derive the operator. Applying an eigenvalue or related analysis to the radiation operator yields a set of orthogonal vectors, representing linearly independent velocity distributions. Each of these acoustic radiation modes has an associated eigenvalue, proportional to the radiation efficiency of the corresponding velocity distribution. The principal advantage of a modal approach is in replacing the coupled structural modes in the radiation field at long wavelengths with the uncoupled acoustic radiation modes, thereby simplifying the radiation analysis. Further, as a direct result of the orthogonality of the acoustic radiation modes, the total power radiated by a structure is simply obtained by summing the radiation efficiencies

in a proportion dictated by the contributions from individual velocity patterns to an actual surface velocity.

Typically, one finds only a limited set of the acoustic radiation modes acting as efficient radiators, with higher modes' efficiencies dropping off precipitously with increasing mode index. If one plots acoustic modal radiation efficiency versus modal index, one observes a ''plateau'' of efficiencies for low-order acoustic radiation modes, with higher-order modes' efficiencies rolling off steeply. This plateau in the efficiencies (at constant frequency) is only observed if one or more of the acoustic radiation modes exceeds some coincidence criteria (i.e., supersonic wave number components). Note that under the right geometric conditions for the structure under consideration (symmetry and unity aspect ratios), such a single-frequency plot will show the grouping characteristics with which we are interested here.

While a number of different modal techniques have been implemented, most are used to determine measures of radiated power or radiation efficiencies so as to better understand or characterize the radiation from structures. Borgiotti[1] was the first to develop a modal representation for the acoustic radiation from a vibrating structure, using singular value decomposition (SVD). The SVD of the radiation operator resulted in a set of singular values and singular vectors, which were interpreted as radiation efficiencies and singular velocity patterns, respectively. Borgiotti's work included a figure with the single-frequency efficiency plateau described above, but because the surface did not have the requisite near-unity aspect ratio, grouping was not evident. Borgiotti also had a sphere example, and he remarked upon resulting degeneracies in the radiation efficiencies. The consequence of this degeneracy was not discussed. Photiadis[2] investigated the connection between SVD and wave vector filtering, providing information on the physical contributions of the individual subsonic and supersonic elements radiated by a structure. In his example 2, Photiadis addressed the acoustic radiation modes of the sphere, and identified them as the spherical harmonics with a phase dependency. He further noted that the sphere's acoustic radiation modes' efficiencies are degenerate with respect to an index for the spherical harmonics. This degeneracy, in fact, is the grouping for the modes of a sphere, but this was not further remarked on nor explored by Photiadis. Sarkissian[3] applied an eigenvalue technique to a radiation operator obtained from the surface acoustic resistance of a sphere and a cylinder. For spheres, the grouping characteristic may be deduced from careful examination of Sarkissian's Fig. 1, coupled with the definition of the spherical harmonics, but this characteristic was not remarked on by Sarkissian. Borgiotti and Jones[4] demonstrated the usefulness of the SVD by using the singular velocity patterns as spatial filters in an active noise control scheme to obtain a broadband reduction in noise radiation. Borgiotti *et al.*[5] and Kim and Ih[6] further showed that the SVD of the radiation field applied directly to acoustic holography by reconstructing the surface velocity from near-field or far-field pressure measurements.

Baumann *et al.*[7,8] developed an active noise control implementation with a feedback controller to minimize the radiated power by suppressing only the most efficiently radiating modes, with the modes developed through consideration of the surface acoustic resistance. Chen and Ginsberg[9] extended Sarkissian's method by developing a radiation operator based on the surface acoustic impedance. Separate eigenvalue analyses were performed on the real and imaginary portions of the radiation operator, resulting in eigenvalues that were proportional to the ''radiated'' and ''reactive'' powers, respectively.

Cunefare[10] performed an eigenvalue analysis on an operator formulated for the radiation efficiency of a baffled finite beam. Elliott and Johnson[11] demonstrated the connection between the acoustic radiation modes derived from structural modes and those obtained through discrete elemental radiators. Further, they developed a structural active noise control formulation for reducing the total radiated sound power from baffled panels. They demonstrated global minimization of the radiated power by controlling the weighted sum of squared outputs from a bank of sensors mounted on the surface of the structure. The selected weightings yielded estimates of the contribution of each acoustic radiation mode. Grouping of the radiation modes' efficiencies may be observed in Fig. 9 of their paper,[11] evidenced by multiple modes' radiation efficiencies having equal slopes versus frequency. Johnson and Elliott[12] extended their earlier work by showing that a substantial reduction in the radiated power on planar structures was obtained at long wavelengths by volume velocity cancellation, clearly demonstrating a close relationship between volume velocity control and control of the dominant acoustic radiation mode. Naghshineh and Koopmann[13,14] applied the technique to structural active noise control, with the objective of forcing the structure to respond in a forced mode of vibration that coincided with an inefficient acoustic radiation mode (termed a ''weak radiator''). Naghshineh *et al.*[15] demonstrated a design optimization technique such that a subject structure would naturally respond in a structural mode of vibration coinciding with a weak radiation mode, representing an application of the acoustic modal technique to passive control. Burdisso and Fuller[16] used the eigenvalue analysis developed by Cunefare[10] along with an eigenvalue assignment technique to implement a feed-forward active noise control algorithm for tonal and broadband disturbances.

The limiting behavior and characteristics of the acoustic modal technique have received somewhat less attention. We speak here with regard to such factors as the role of discretization, functional representation, convergence, and frequency dependence on the modal technique. Elements of these considerations may be found, to greater or lesser extent, in many of the papers cited above. Cunefare and Currey[17] demonstrated that the manner of representation strongly influences the accuracy and convergence of the acoustic radiation modes. Further, they demonstrated that the acoustic radiation modes are almost independent of frequency over a broad frequency range, while the modes' radiation efficiencies were simple functions of frequency over the same range. The grouping characteristics are again seen in their Figs. 2 and 3, and in the associated curve fits, but the significance of this was unremarked on at the time. Johnson[12]

and Currey[18] have recently further addressed aspects of these issues, including grouping.

The above illustrates the breadth of derivations and applications of the acoustic modal technique. It further demonstrates that multiple authors, including the authors of the present work, encountered the grouping phenomena and did not remark upon its uniqueness. We here seek to rectify this omission. We undertake in this paper a detailed examination of the long wavelength grouping behavior of exterior acoustic modal techniques. In the following, we briefly introduce the mathematical foundation of the technique, and then apply the technique to the analysis of a number of geometric configurations intended to demonstrate the grouping characteristics of the acoustic radiation modes. First, we demonstrate that the spherical harmonics are the analytical acoustic radiation modes for spheres, and that these harmonics display well-characterized grouping behavior. Then, we consider the radiation modes of a rectangular solid, or box, illustrating that it exhibits grouping behavior analogous to that of the sphere. We also demonstrate that the radiation modes of the box are not merely spherical harmonics mapped to the surface of the box. Finally, we demonstrate that the radiation modes of arbitrary distributions of point sources also exhibit grouping behavior.

II. DEVELOPMENT

This study of a modal decomposition technique applied to exterior acoustic radiation is not concerned with the physical characteristics of the radiating structure, such as the material thickness or fluid loading. Likewise, this study is independent of the source of excitation. This analysis is only a function of a particular frequency of interest and the wetted geometry. Throughout this work a harmonic time dependence of the form $e^{i\omega t}$ is assumed but is omitted in the notation. Note that we include the following development only for completeness, as aspects of it have appeared in many prior works.[1–5,10–19]

A. Surface velocity

Consider an arbitrary structure vibrating in free space at a single frequency. We may represent any arbitrary normal velocity distribution on the surface as

$$\hat{u}(\mathbf{x}_S) = \mathbf{u}^T \boldsymbol{\phi}(\mathbf{x}_S), \tag{1}$$

where $\mathbf{u}$ is a column vector of unknown velocity amplitude coefficients, $\boldsymbol{\phi}$ is a column vector of ''basis'' functions on the surface S, and $\mathbf{x}_S$ is a point on the surface. The vectors $\mathbf{u}$ and $\boldsymbol{\phi}$ are length N, where N denotes the total degrees of freedom included in the summation. The choice of basis functions, whether global or local, in representing the surface velocity, is arbitrary. By a global representation, we mean one where the chosen functions are ''complete'' and span the entire surface, as used by Chen and Ginsberg[9] or Cunefare.[10] A local basis function approach is one where the body is discretized, and the basis functions only have local impact, such as through the use of the boundary element method (BEM).[20–22] For the local approach, the surface velocity is simply given by a vector $\mathbf{u}$, where each component of the vector represents a velocity amplitude at a particular location on the structure. Alternatively, one may use discrete radiator approaches, such as those of Elliott and Johnson.[11]

B. Pressure field

The pressure field is determined from the Helmholtz integral equation as[23]

$$\hat{p}(\mathbf{x})\alpha(\mathbf{x}) = \int_s (\hat{p}(\mathbf{x}_S)\nabla G(\mathbf{x}|\mathbf{x}_S) - G(\mathbf{x}|\mathbf{x}_S)\nabla \hat{p}(\mathbf{x}_S)) \cdot \mathbf{e}_n dS, \tag{2}$$

where $\mathbf{e_n}$ is a unit vector pointing in the direction normal to the surface, $\mathbf{x}$ is the receiver point, $G(\mathbf{x}|\mathbf{x}_S)$ is the constant frequency Green's function, and the factor α is zero for an interior point, one for an exterior point, and one half for a point on a continuous body. Brebbia *et al.*[20] and Seybert *et al.*[21] provide a representation of the Helmholtz integral equation for surface discontinuities, such as edges or corners, where α becomes $\delta\Omega/4\pi$ for a receiver point on the surface, given that $\delta\Omega$ is the outer solid angle at that point.

C. Radiated power

The acoustic power radiated by the vibrating structure is determined from the velocity and pressure. The power is expressed in matrix-vector notation dependent on the quadratic expression for the surface velocity, using global or local basis functions, as

$$W = \mathbf{u}^{\mathbf{T}}\mathbf{C}\mathbf{u}, \tag{3}$$

where $\mathbf{C}$ is a coupling matrix.

Before proceeding further, we digress here momentarily to discuss some subtleties of the coupling matrix. For analysis methods that yield reciprocal impedance matrices (e.g., global basis function methods, and discrete source or elemental radiator methods), the coupling matrix is guaranteed by reciprocity to be strictly real, symmetric, and positive-definite. However, using nonvariational-principle-based boundary element methods, we find the form of the impedance matrix is not symmetric (i.e., not reciprocal), and therefore the resulting coupling matrix $\mathbf{C}$ is Hermitian, but still positive-definite. The impedance relationship is not symmetric in the BEM due to the differences in element area associated with each node in the discretized model. A unit velocity at a node on a large element has a much greater impact upon the pressure at a node on a small element than the reciprocal condition.

Returning to the development at hand, an eigenvalue analysis may be applied directly to Eq. (3) to obtain a set of acoustic radiation modes and their corresponding powers.[3] However, in this work, we use radiation efficiency as the basis for the modal representation.

D. Radiation efficiency

We express the radiation efficiency of a vibrating structure as

$$\sigma = \frac{W}{\rho c S \langle |\hat{u}(\mathbf{x}_S)|^2 \rangle}, \tag{4}$$

where ρ is the density of the surrounding fluid, c is the speed of sound in that fluid, S is the wetted surface area, and $\langle|\hat{u}(\mathbf{x}_S)|^2\rangle$ is the spatial mean-square velocity on the surface of the structure,

$$\langle|\hat{u}(\mathbf{x}_S)|^2\rangle = \frac{1}{2S}\int_S |\hat{u}(\mathbf{x}_S)|^2 dS = \mathbf{u}^T\mathbf{V}\mathbf{u}. \tag{5}$$

In Eq. (5), the velocity matrix $\mathbf{V}$ is real, symmetric, and positive-definite. If the basis functions used to represent $\hat{u}$ are orthonormal, $\mathbf{V}$ is the identity matrix.

The radiation efficiency is evaluated by substituting Eqs. (3) and (5) into (4), yielding

$$\sigma(\mathbf{u}) = \frac{\mathbf{u}^\mathbf{T}\mathbf{C}'\mathbf{u}}{\mathbf{u}^\mathbf{T}\mathbf{V}\mathbf{u}}, \tag{6}$$

where σ is an explicit function of $\mathbf{u}$ and we have absorbed the leading coefficients $1/\rho cS$ into the coupling matrix $\mathbf{C}'$.

E. Eigenvalue analysis

The acoustic modal representation may be obtained by a generalized eigenvalue problem applied to the coupling and velocity matrices contained in Eq. (6). This is illustrated by Cunefare[10] through the Lagrange multiplier theorem, where the radiated power is minimized subject to the constraint of a finite, nonzero, spatial mean-square velocity. The eigenvalue solution for an N degree of freedom system yields a set of real eigenvalues and a corresponding set of orthogonal eigenvectors, ordered as $\lambda_N \leqslant \ldots \leqslant \lambda_2 \leqslant \lambda_1$ and $\boldsymbol{\psi}_N \ldots \boldsymbol{\psi}_2, \boldsymbol{\psi}_1$ for convenience.

The eigenanalysis yields an orthogonal array of velocity eigenvectors $\boldsymbol{\Psi}$ such that any arbitrary velocity distribution is the summed contribution of the individual eigenvectors $\boldsymbol{\psi}$. This arbitrary velocity is represented though the expansion theorem as

$$\mathbf{u} = \boldsymbol{\Psi}\mathbf{c}, \tag{7}$$

where $\mathbf{c}$ is a vector of nondimensional participation coefficients. Each element in $\mathbf{c}$ represents the contributions of the individual eigenvectors in $\boldsymbol{\Psi}$ to the velocity vector $\mathbf{u}$.

Note that for BEM-derived, Hermitian $\mathbf{C}'$ matrices, the eigenvalue analysis requires the use of only the real part of this matrix (recall that variational-based methods or simple-source-based methods yield real symmetric $\mathbf{C}'$ matrices). Otherwise, the resulting eigenvectors are complex, with the phases of the elements within the vector unequal, even though the eigenvalues are real. These complex eigenvectors are nonphysical, in that they do not represent an observable velocity distribution. However, restricting the analysis to just the real component of Hermitian $\mathbf{C}'$ matrices does yield real-valued eigenvectors, eigenvectors that satisfy all the requirements of the analysis. Again, note that this real-component restriction only applies to coupling matrix generation methods that yield Hermitian matrices.

As a consequence of the real and symmetric forms of $\mathbf{C}'$ and $\mathbf{V}$, the eigenvalues are real and the eigenvectors in $\boldsymbol{\Psi}$ are linearly independent and orthogonal with respect to the energy inner product constraint $\boldsymbol{\psi}_n^T\mathbf{V}\boldsymbol{\psi}_m = \delta_{nm}$, where δ_{nm} is the Kronecker delta. The eigenvectors diagonalize the combination of the coupling and velocity matrices such that

$$\boldsymbol{\Lambda} = \boldsymbol{\Psi}^{-1}(\mathbf{V}^{-1}\mathbf{C}')\boldsymbol{\Psi}, \tag{8}$$

where $\boldsymbol{\Lambda}$ is a diagonal matrix of real eigenvalues, λ.

As described by Eq. (7), any arbitrary velocity distribution on a structure may be decomposed into individual contributions from the acoustic velocity modes through a set of participation coefficients. This allows the power radiated by the structure to be determined by combining these participation coefficients with the eigenvalues.[1] Therefore, for an arbitrary surface velocity $\mathbf{u}$, the radiated acoustic power is obtained by substituting Eq. (7) in (3) to yield $W = \mathbf{c}^\mathbf{T}\boldsymbol{\Psi}^\mathbf{T}\mathbf{C}\boldsymbol{\Psi}\mathbf{c}$, and then using Eq. (8) and the definition of $\mathbf{C}'$ to obtain

$$W = (\rho cS)\mathbf{c}^\mathbf{T}\boldsymbol{\Lambda}\mathbf{c} = (\rho cS)\sum_{n=1}^{N} c_n^2\lambda_n. \tag{9}$$

With $\boldsymbol{\Psi}^\mathbf{T}\mathbf{V}\boldsymbol{\Psi}$ constrained to be the identity matrix, an arbitrary velocity distribution's radiation efficiency from Eq. (6) is

$$\sigma = \frac{\mathbf{c}^\mathbf{T}\boldsymbol{\Psi}^\mathbf{T}\mathbf{C}'\boldsymbol{\Psi}\mathbf{c}}{\mathbf{c}^\mathbf{T}\boldsymbol{\Psi}^\mathbf{T}\mathbf{V}\boldsymbol{\Psi}_\mathbf{c}} = \frac{\mathbf{c}^\mathbf{T}\boldsymbol{\Lambda}\mathbf{c}}{\mathbf{c}^\mathbf{T}\mathbf{c}} = \frac{\sum_{n=1}^{N} c_n^2\lambda_n}{\sum_{n=1}^{N} c_n^2}. \tag{10}$$

When all participation coefficients in Eq. (7) except one are zero, the resulting velocity distribution is identical to an eigenvector, representing a single acoustic radiation mode. In this case the radiation efficiency in Eq. (10) is identical to the eigenvalue of that acoustic radiation mode. In the paper at hand, the participation coefficients are assumed to adhere to $\mathbf{u} = \boldsymbol{\psi}$. Therefore, for N degrees of freedom, the eigenvectors are the acoustic radiation modes denoted by $\mathbf{u}_N \ldots \mathbf{u}_2, \mathbf{u}_1$. Likewise, the eigenvalues are identically the radiation efficiencies, $\sigma = \lambda$, ordered as $\sigma_N \leqslant \ldots \leqslant \sigma_2 \leqslant \sigma_1$.

Note that one may perform analogous developments to the above for distributions of elemental sources,[19] where the elements of the resulting eigenvectors are interpreted as source strengths for each of the sources. Such a development, not presented in detail here as it is not significantly distinct from the above, will be used as part of our investigation presented below.

III. ANALYTICAL FREE-SPACE GROUPING FOR A SPHERE

We consider here a detailed acoustic modal analysis of a sphere. This will demonstrate that the spherical harmonics are the acoustic radiation modes of a sphere, and that they exhibit well-defined grouping characteristics. The subject sphere has radius a, as depicted in Fig. 1.

A. Theory development

The spherical harmonics are the analytical solutions to the modal acoustic radiation from a finite sphere. Being orthogonal and complete, we may use a global basis function set composed of these functions, representing pressure distributions on the surface as

$$\hat{p}(\mathbf{r}_s) = \mathbf{p}^\mathbf{T}\boldsymbol{\phi}_\mathbf{p}(\mathbf{r}_S), \tag{11}$$

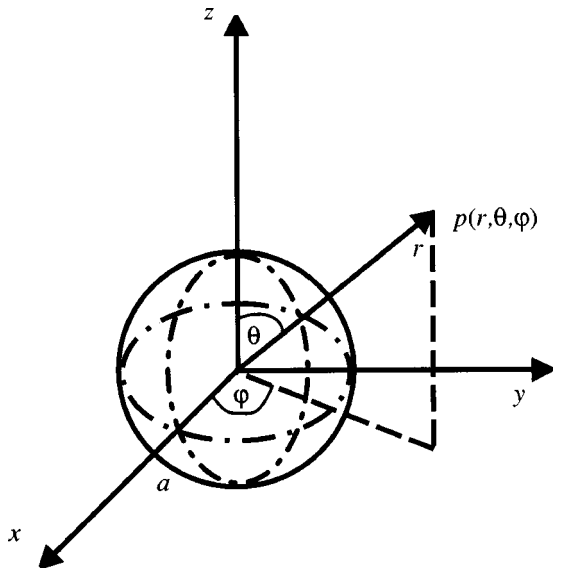

FIG. 1. Finite sphere in a free space.

where $\mathbf{p}$ and $\boldsymbol{\phi}_\mathbf{p}$ are column vectors of length $N(2M-1)$ of unknown pressure coefficients and pressure basis functions, respectively. These pressure basis functions are

$$\phi_{pnm}(\mathbf{r}_S)=h_n^{(1)}(kr_S)Y_n^m(\theta_S,\varphi_S) \tag{12}$$

for $n=0,1,...,N-1$ and $m=-M+1,...,-1,0,1,...,M-1$, where Y_n^m is a spherical harmonic[24] on the surface of the sphere. The spherical harmonics are

$$Y_n^m(\theta_S,\varphi_S)=\cos(m\varphi_S)P_n^m(\cos(\theta_S)) \tag{13}$$

and

$$Y_n^{-m}(\theta_S,\varphi_S)=\sin(m\varphi_S)P_n^m(\cos(\theta_S)), \tag{14}$$

where P_n^m is the associated Legendre polynomial of the first kind, degree n, and order m for n and m positive integers or zero. The associated Legendre polynomials are zero unless $n\geqslant m$, therefore, we assume in the subsequent analysis that this condition is true. The spherical Hankel's functions $h_n^{(1)}$ are of the first kind and order n, given as $h_n^{(1)}(kr_s)=j_n(kr_s)+i\eta_n(kr_s)$, where j_n and η_n are the spherical Bessel's functions of the first and second kinds, respectively.

We determine the normal surface velocity from Euler's equation. Therefore, we may represent the velocity field in vector form as

$$\hat{u}(\mathbf{r}_S)=\mathbf{u}^\mathbf{T}\boldsymbol{\phi}_\mathbf{u}(\mathbf{r}_S), \tag{15}$$

where the column vectors $\mathbf{u}$ and $\boldsymbol{\phi}_\mathbf{u}$ are the unknown velocity coefficients and the velocity basis functions, respectively. Both vectors are of length $N(2M-1)$, where the velocity field basis functions also contain the spherical harmonics as

$$\phi_{unm}(\mathbf{r}_S)=\frac{\partial h_n^{(1)}(kr_S)}{\partial(kr_S)}Y_n^m(\theta_S,\varphi_S) \tag{16}$$

for $n=0,1,...,N-1$ and $m=-M+1,...,-1,0,1,...,M-1$, where

$$\frac{\partial h_n(kr_S)}{\partial(kr_S)}=\frac{1}{2n+1}[nh_{n-1}(kr_S)-(n+1)h_{n+1}(kr_S)]. \tag{17}$$

Furthermore, the nmth element of the unknown pressure and velocity vectors are proportional as

$$p_{n,m}=i\rho c u_{n,m}. \tag{18}$$

Since the solutions for the unknown velocity coefficients are orthogonal eigenvectors, Eq. (18) indicates that the pressure field due to a given acoustic radiation mode is identical to the mode scaled by $i\rho c$.

Using the acoustic pressure and velocity, we obtain the radiated power in terms of a surface integration of the acoustic intensity as

$$W=\frac{1}{2}\mathrm{Re}\left(\mathbf{p}^\mathbf{T}\left[\int_S\boldsymbol{\phi}_\mathbf{p}\boldsymbol{\phi}_\mathbf{u}^\mathbf{H}dS\right]\mathbf{u}^*\right), \tag{19}$$

where the superscript H indicates complex conjugate transpose of a vector. We represent the power in the same form as Eq. (3), where the coupling matrix is

$$\mathbf{C}=\mathrm{Re}\left(\frac{i\rho c}{2}\int_0^{2\pi}\int_0^{\pi}\boldsymbol{\phi}_\mathbf{p}\boldsymbol{\phi}_\mathbf{u}^\mathbf{H}r_S^2\sin(\theta_S)d\theta_S d\varphi_S\right). \tag{20}$$

The integrands of the coupling matrix are

$$\phi_{pnm}\phi_{upq}^*=h_n^{(1)}(kr_S)\frac{\partial h_p^{(2)}(kr_S)}{\partial(kr_S)}Y_n^m(\theta_S,\varphi_S)Y_p^q(\theta_S,\varphi_S), \tag{21}$$

where $h_p^{(2)}$ are the spherical Hankel's functions of the second kind, given as $h_p^{(2)}=h_p^{(1)*}$. Evaluation of the polar angle integral yields

$$\int_0^{\pi}P_n^m(\cos(\theta_S))P_p^q(\cos(\theta_S))\sin(\theta_S)d\theta_S = \begin{cases}\dfrac{2}{2n+1}\dfrac{(n+m)!}{(n-m)!} & n=p\quad m=q\\ 0 & n\neq p\quad m\neq q\end{cases}, \tag{22}$$

indicating that the off-diagonal coupling coefficients integrate identically to zero.[25] The diagonal elements are

$$C_{nmnm}=\mathrm{Re}\left(i\rho c a^2 h_n^{(1)}(ka)\times\frac{\partial h_n^{(2)}(ka)}{\partial(ka)}\frac{2\pi}{2n+1}\frac{(n+m)!}{(n-m)!}\right). \tag{23}$$

Therefore, the coupling matrix is diagonal and composed of only real-valued components.

We develop the radiation efficiency expression for the sphere from Eq. (6), where the spatial mean-square velocity on the surface is

$$\langle|\hat{u}(\mathbf{r}_S)|^2\rangle=\frac{1}{8\pi a^2}\mathbf{u}^\mathbf{T}\left[\int_S\boldsymbol{\phi}_\mathbf{u}\boldsymbol{\phi}_\mathbf{u}^\mathbf{H}dS\right]\mathbf{u}. \tag{24}$$

For the analytical case of the sphere the form of the velocity matrix is real and diagonal, where the diagonal terms are

$$V_{nmnm}=\frac{1}{8\pi a^2}\frac{\partial h_n^{(1)}(ka)}{\partial(ka)}\frac{\partial h_n^{(2)}(ka)}{\partial(ka)}\frac{2}{2n+1}\frac{(n+m)!}{(n-m)!}. \tag{25}$$

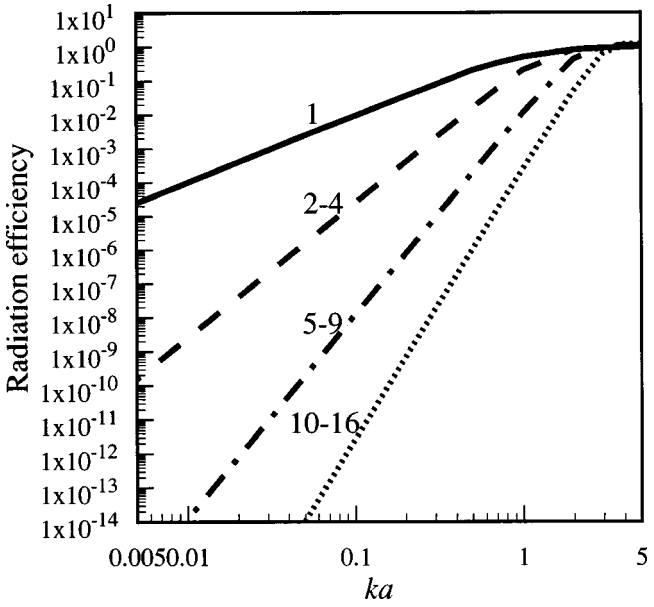

FIG. 2. Radiation efficiencies for the 16 most efficient modes of a free space sphere.

The coupling and velocity matrices are real and diagonal; therefore, the radiation efficiencies are real. We obtain the radiation efficiencies for this representation by using Eqs. (23) and (25) in (6), where the nmth radiation efficiency is

$$\sigma_{n,m}=\frac{\mathrm{Re}\left(ih_n^{(1)}(ka)\dfrac{\partial h_n^{(2)}(ka)}{\partial(ka)}\right)}{\dfrac{\partial h_n^{(1)}(ka)}{\partial(ka)}\dfrac{\partial h_n^{(2)}(ka)}{\partial(ka)}}. \tag{26}$$

As noted by Photiadis,[2] the radiation efficiencies are independent of the index m but are degenerate with respect to that index. This degeneracy produces radiation efficiencies dependent on the index n only, with the order of degeneracy being $2n+1$. This degeneracy leads to the grouping characteristic, with the number of modes within each group ordered as 1, 3, 5, 7, 9, etc.

Since the coupling and velocity matrices are diagonal, the acoustic radiation mode shapes are identically spherical harmonics. The acoustic radiation modes are complex due to the contributions of the Hankel's functions. However, the imaginary portions of the modes are constant relative to the real portions, representing pure phase shifts over the surface. This was noted by Photiadis.[2] Normalizing the unknown velocity coefficients to the complex Hankel's function contributions result in real acoustic radiation mode shapes identical to spherical harmonics.

B. Radiation efficiencies

Figure 2 depicts the radiation efficiencies as a function of frequency for the 16 most efficient acoustic radiation modes of the sphere, forming four radiating groups at long wavelengths. The most efficient acoustic radiation mode has a radiation efficiency dependent on frequency to the power of two. The next three modes have degenerate radiation efficiencies with a frequency dependence to the power of four, while the next five degenerate radiation efficiencies have a frequency dependence to the power of six. This regular pattern of increasing number of acoustic radiation modes per group continues for all higher radiation efficiencies.

The long wavelength behavior of the radiation efficiencies for the sphere in free space is obtained analytically from the substitution of the small-argument asymptotic relationship for the Hankel's functions in Eq. (26) as

$$\lim_{ka\to 0}\sigma_{n,m}\simeq\frac{1}{(n+1)^2}\frac{1}{(\Pi_{i=1}^{n}(2i-1))^2}(ka)^{2n+2}. \tag{27}$$

This relationship explains the behavior of the radiation efficiencies with respect to frequency evident in Fig. 2. There is one radiation efficiency proportional to $(ka)^2$, corresponding to the spherical harmonic Y_0^0 and representing the only mode in the first group. There are three radiation efficiencies proportional to $(ka)^4$, corresponding to the spherical harmonics Y_1^0, Y_1^1, and Y_1^{-1}, representing the three radiation modes in the second group. There are five radiation efficiencies proportional to $(ka)^6$, corresponding to the spherical harmonics Y_2^0, Y_2^1, Y_2^{-1}, Y_2^2, and Y_2^{-2} in the third group. This pattern continues for all positive n and m, where $m\geqslant n$.

Note that in Fig. 2, had we plotted the efficiencies of further less efficient acoustic radiation modes, they would have all been below the lines for the 10th through 16th modes, with steeper slopes. In addition, had we generated a plot of acoustic modal efficiencies versus mode index at, say, $ka=2.0$ (as would be obtained along a vertical line at $ka=2.0$ in Fig. 2), we would observe the exact same sort of ''plateau'' in the distribution of efficiencies amongst the modes as observed by others. Conversely, a similar plot at, for example, $ka=0.1$, would not exhibit such a plateau in mode efficiencies, as none of the acoustic radiation modes have passed coincidence, though there would still be the rapid decrease in efficiencies from mode to mode (degenerate modes would produce local plateaus, but there would not be a plateau of highly efficient modes). We use ''coincidence'' here to imply the wave number at which a mode becomes efficient (radiation efficiency approximately 1), in analogy to the coincidence wave number for waves on plates.

The asymptotic long wavelength frequency behavior of the radiation efficiencies dictates the grouping among their respective acoustic radiation modes. The impact of the frequency grouping behavior of the radiation efficiencies is demonstrated in Fig. 3. In this figure the mode number of the radiation efficiencies is plotted with respect to the specific group number to which each corresponding acoustic radiation mode belongs. Specifically, the first acoustic radiation mode's radiation efficiency stands alone (group number one) with a frequency dependence of $(ka)^2$. The second through fourth acoustic radiation modes' radiation efficiencies are grouped with a frequency dependence of $(ka)^4$ (group number two), while the fifth through ninth acoustic radiation modes are grouped as $(ka)^6$ (group number three), etc.

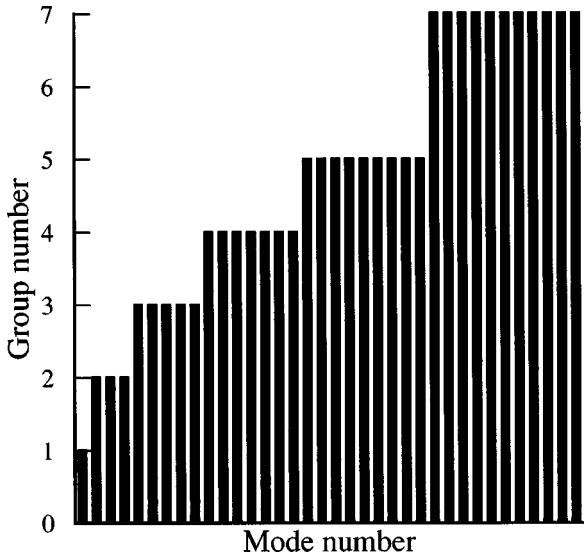

FIG. 3. Grouping of acoustic mode radiation efficiencies for an object (e.g., sphere) in a free space.

C. Acoustic radiation modes

The acoustic radiation mode shapes of the free-space sphere are the individual spherical harmonics. The magnitudes of the spherical harmonic surface distributions for the nine most efficient modes of the free-space sphere are provided in Fig. 4. The first acoustic radiation mode shape, Fig. 4(a), represents a uniform velocity across the surface and acts as a monopole. Figures 4(b) through (d) correspond to identical dipole radiators rotated on three orthogonal axes and circumscribed by a single nodal band. This further illustrates the degeneracy among the corresponding radiation efficiencies, as there is no difference between these acoustic radiation modes other than their spatial orientation. Figure 4(e) is a longitudinal quadrapole, while four other mode shapes, Figs. 4(f) through (i), represent a set of lateral quadrapoles, where there are two nodal bands on each sphere.

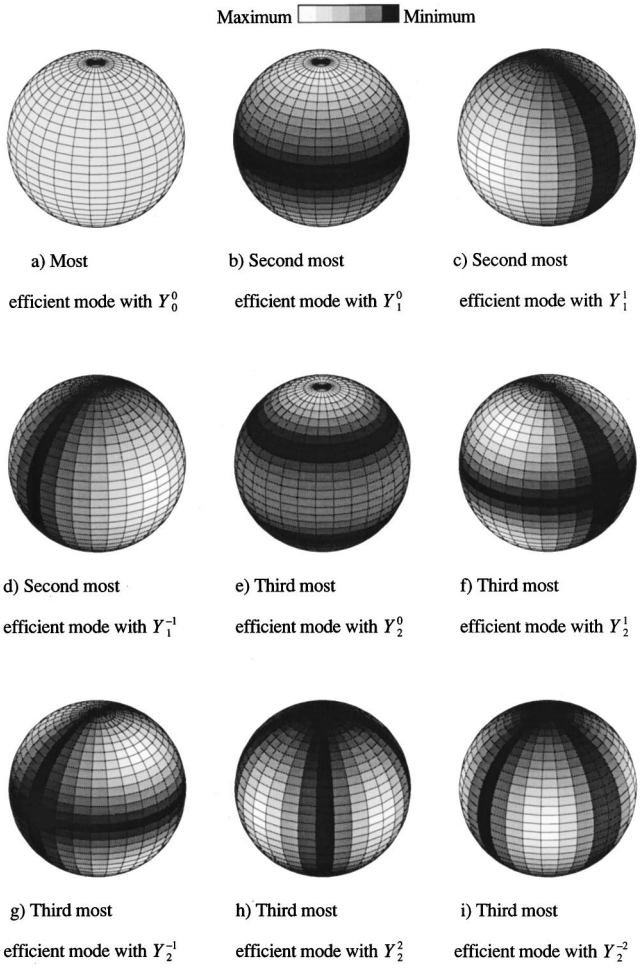

FIG. 4. Surface normal velocity distributions of first nine radiation modes for a sphere.

IV. RECTANGULAR STRUCTURE GROUPING

The acoustic radiation modes of spheres clearly group. Here, we demonstrate that the radiation modes of a more arbitrary structure, a rectangular solid, also exhibit grouping. We consider a rectangular box in free space, as depicted in Fig. 5. The box has length l, width w, and height h, with aspect ratios $w/l=4/5$ and $h/l=2/5$. We use a boundary element model with 150 linear quadrilateral elements, representing a local basis function approach, to obtain the acoustic radiation modes.

A. Frequency characteristics of acoustic modal radiation efficiencies

The frequency dependency of the first nine radiation efficiencies of the free-space, rectangular box are depicted in Fig. 6, where k is the acoustical wave number. At short wavelengths ($kl>1$) the radiation efficiencies approach a value of one. At long wavelengths ($kl<1$) the radiation efficiencies are linear on a logarithmic scale, have a dependence on wave number to even integer powers, and exhibit frequency grouping as was evident for the sphere. There, grouping is evident in that there are sets of acoustic radiation modes each with the same dependency on wave number, as evidenced by the clusters of parallel lines. As with the

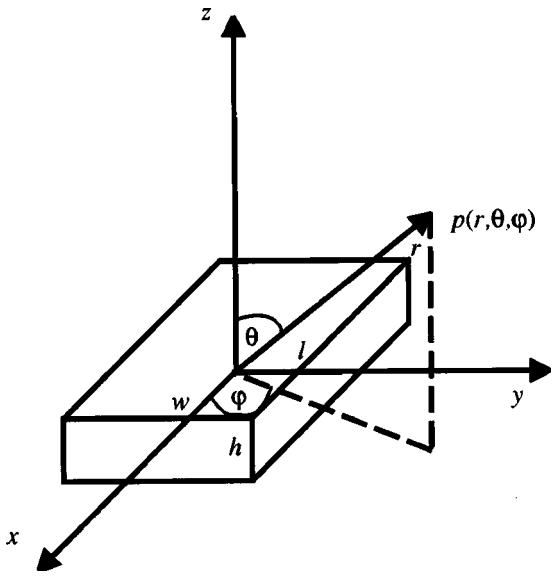

FIG. 5. Finite, rectangular box in a free space.

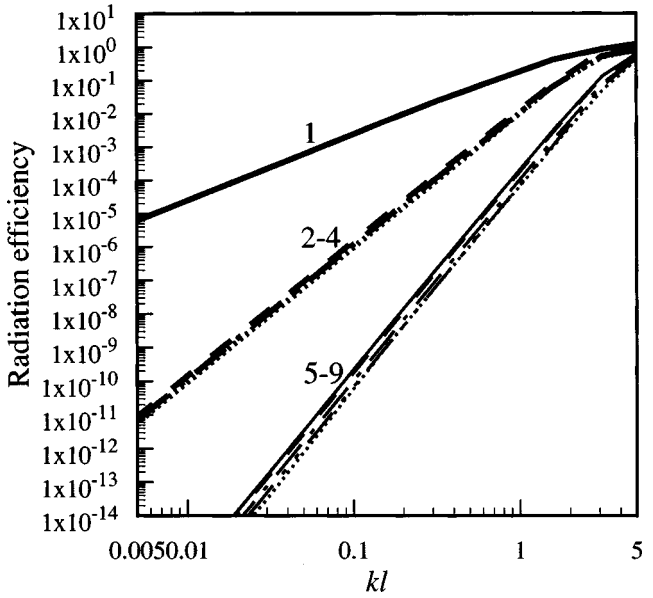

FIG. 6. Radiation efficiencies for the nine most efficient modes of a free space, rectangular box.

sphere, the first mode stands alone (group of 1 mode), the second through fourth modes are grouped (group of 3 modes), the fifth through the ninth modes are grouped (group of 5 modes), etc. The grouping pattern for this example structure follows that of the sphere.

This long wavelength frequency behavior and grouping is further illustrated by examining curve fits to the radiation efficiencies for these nine most efficient modes in Fig. 6. We present these fits in Table I and indicate the group to which each of these modes belong. The frequency dependency evidenced by these curve fits follows those of the sphere, as does the grouping pattern (i.e., modes per group numbered as 1, 3, 5, etc.). Note that the first mode has a frequency dependence as wave number squared, the second group as wave number to the fourth, the third group as wave number to the sixth, etc. As with the sphere, the modes within lower numbered groups prove to be more efficient radiators than the acoustic radiation modes within higher numbered groups. This is apparent in that the members of the higher numbered groups have a higher-order dependency on kl (significant because $kl<1$ here), in addition to noting that the radiation efficiency equations for the members of the lower numbered groups have larger leading coefficients than those for higher groups.

TABLE I. Radiation efficiency expressions for the nine most efficient modes of a rectangular box in free space.

Mode number	Curve fit	Group
1	$\sigma_1 = 2.4\times10^{-1}(kl)^{2.0}$	1
2	$\sigma_2 = 1.4\times10^{-2}(kl)^{4.0}$	2
3	$\sigma_3 = 1.1\times10^{-2}(kl)^{4.0}$	2
4	$\sigma_4 = 9.3\times10^{-3}(kl)^{4.0}$	2
5	$\sigma_5 = 2.2\times10^{-4}(kl)^{6.0}$	3
6	$\sigma_6 = 1.7\times10^{-4}(kl)^{6.0}$	3
7	$\sigma_7 = 1.0\times10^{-4}(kl)^{6.0}$	3
8	$\sigma_8 = 6.7\times10^{-5}(kl)^{6.0}$	3
9	$\sigma_9 = 6.5\times10^{-5}(kl)^{6.0}$	3

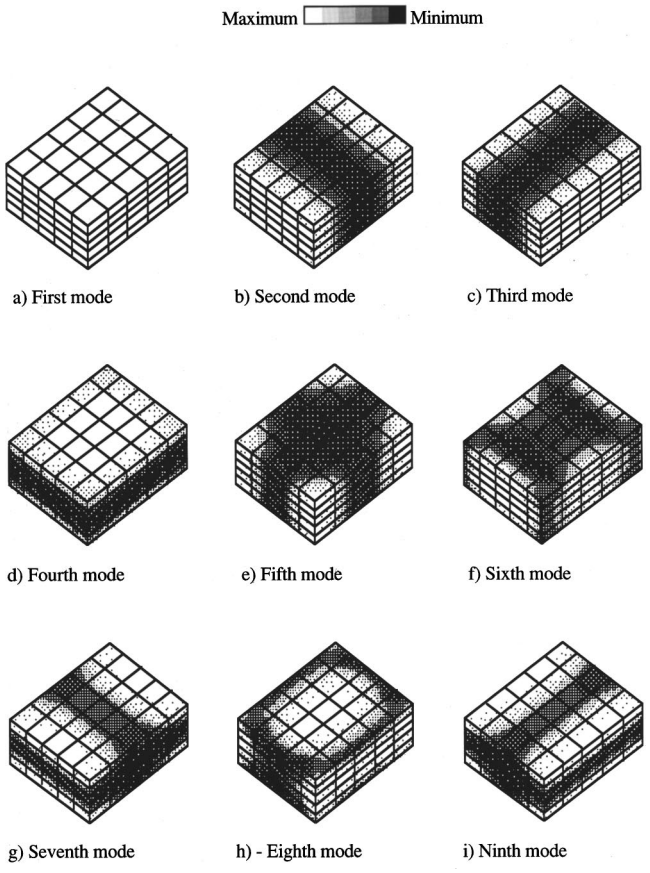

FIG. 7. Surface normal velocity distributions of first nine box radiation modes.

Had the aspect ratios of the box been unity, so that the box had been a cube, then some of the curve fits within each group would have been identical. This is a manifestation of degenerate eigenvalues for the modes within a group. For the example we consider here, the leading coefficient for each of the curve fits is different within each group as a consequence of the nonunity aspect ratios of the box.

B. Acoustic radiation modes

In the low-frequency limit, where the radiation efficiencies behave linearly on a logarithmic frequency scale, the shapes of the acoustic radiation modes of the rectangular box are essentially constant with frequency. Similar observations have been made with respect to the modes for panels and beams,[17,26] with an explanation for such behavior provided in terms of the nature of the coupling matrix. Similar considerations apply here. Under long wavelength conditions the shape of the magnitudes of the nine most efficient acoustic radiation modes for a rectangular box in free space is depicted in Fig. 7. The first acoustic radiation modal velocity distribution in Fig. 7(a), which is the most efficient acoustic radiation mode, is uniform across the entire surface of the box, suggestive of a monopole. The next three acoustic radiation mode shapes, Figs. 7(b) through (d), are characterized by a single nodal band around the axis planes of the box. The second most efficient acoustic radiation mode shape, Fig. 7(b), has a nodal velocity band in the y-z plane, corresponding to the width and height of the box being less

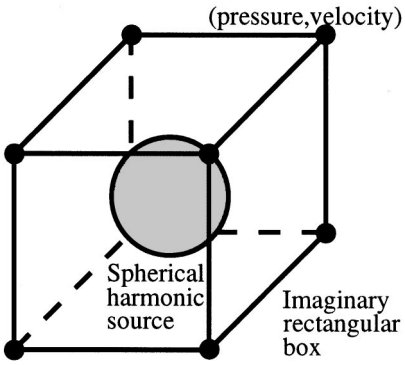

FIG. 8. Imaginary, rectangular box excited by an internal, spherical source.

than the length. The third most efficient acoustic radiation mode shape, Fig. 7(c), has a nodal velocity band in the x-z plane, because the height of the box is less than the width. Last, the fourth most efficient acoustic radiation mode shape, Fig. 7(d), has a nodal velocity band in the x-y plane. The second through fourth acoustic radiation modes constitute a set of three dipole distributions. Figures 7(e) through (f) represent acoustic radiation mode shapes with two nodal velocity bands, forming a set of five quadrapole radiators. The ability of one acoustic radiation mode within a group to radiate more efficiently than another is due to the relative efficiency of hydrodynamic short-circuiting across adjacent nodal bands.[27]

These acoustic radiation modes for the box are suggestive of radiation fields due to a multipole distribution.[23] In addition, the shape and grouping of these velocity distributions are quite similar to that of spherical harmonic distributions.

The striking similarity in the low-frequency limit between the acoustic radiation mode shapes of the rectangular box, Fig. 7, and those of the sphere, Fig. 4, begs the question: are the box's acoustic radiation modes simply spherical harmonics mapped onto the surface of the box at long wavelengths? We address this question in the following.

V. ACOUSTIC RADIATION MODES OF RECTANGULAR SOLID VERSUS SPHERICAL HARMONICS

A. Mapped spherical harmonics

In the low-frequency limit, the rectangular box's acoustic radiation modes' shapes are suggestive of the spherical harmonics on the free-space sphere. This is a direct result of the large wavelength size relative to the structure size. As we shall demonstrate, the box's acoustic radiation mode shapes are not identical to, but are quite similar to, the spherical harmonics mapped onto the surface of the box.

To demonstrate this point, we place a small free-space sphere with its origin at the center of an imaginary box that possesses the same exterior geometry as the actual, rectangular box, as depicted in Fig. 8. We align the polar axis of the sphere with the z axis of the box, and align the axis defining the 0° azimuth with the x axis of the box. This alignment is done consciously, so as not to confound geometric effects of axes orientation with the purpose of this exposition. The chosen source alignment ensures that individual radiation modes on the sphere produce patterns aligned with the similar mode on the box.

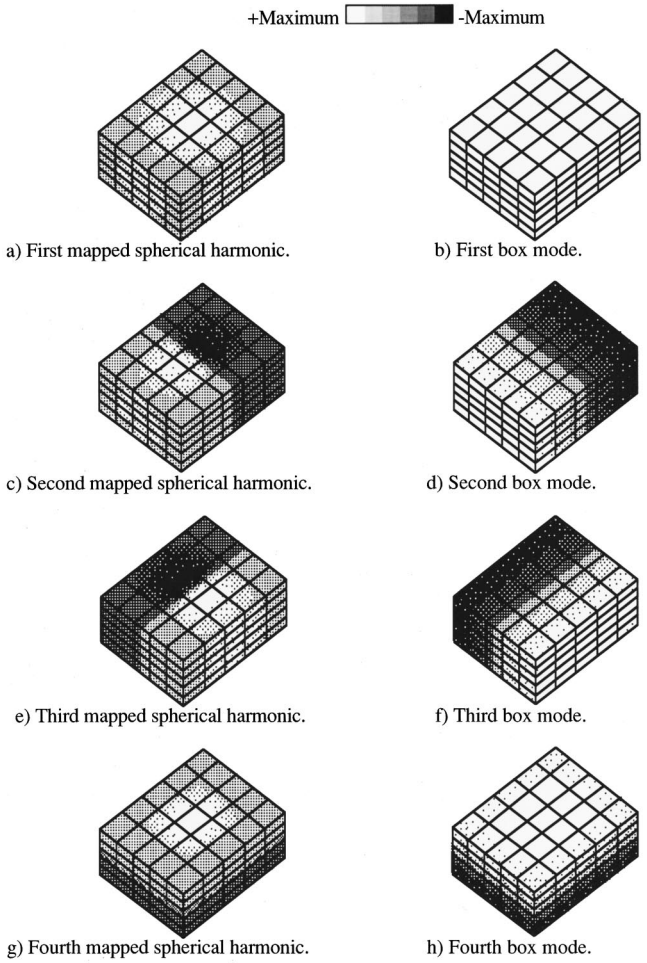

FIG. 9. Comparison of surface velocity distributions between mapped spherical harmonics and box radiation modes.

The sphere is assumed to be vibrating at a single frequency with a single spherical harmonic velocity distribution from Eq. (16), which then generates a velocity and pressure profile on the imaginary box. This process effectively ''maps'' the spherical harmonic onto the surface of the box. We use the velocity profile as a boundary condition for a BEM analysis with the internal source removed and the imaginary surface replaced by the actual box. The pressure profile from the spherical harmonic becomes a means of checking the profile produced by the BEM solution. This is the equivalent to the acoustic mesh calibration technique common in boundary element methods,[21,28] except we use higher-order calibration sources.

As illustration that the box's acoustic radiation mode shapes at long wavelengths are similar to the spherical harmonics mapped onto the surface of the rectangular box, we generate the first 16 spherical harmonics mapped to the surface as described above. The velocities of the mapped spherical harmonics are complex due to the spherical Hankel's functions. As the frequency approaches zero, however, the imaginary contributions to the mapped spherical harmonics will approach zero. The real component of the first four

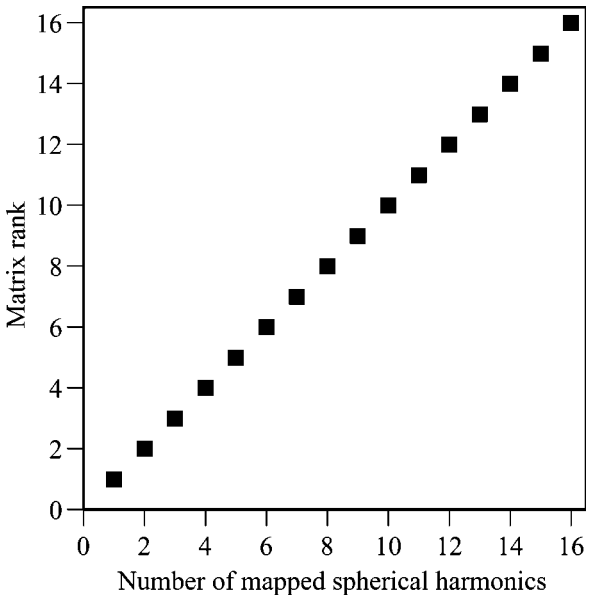

FIG. 10. Matrix rank for added mapped spherical harmonics.

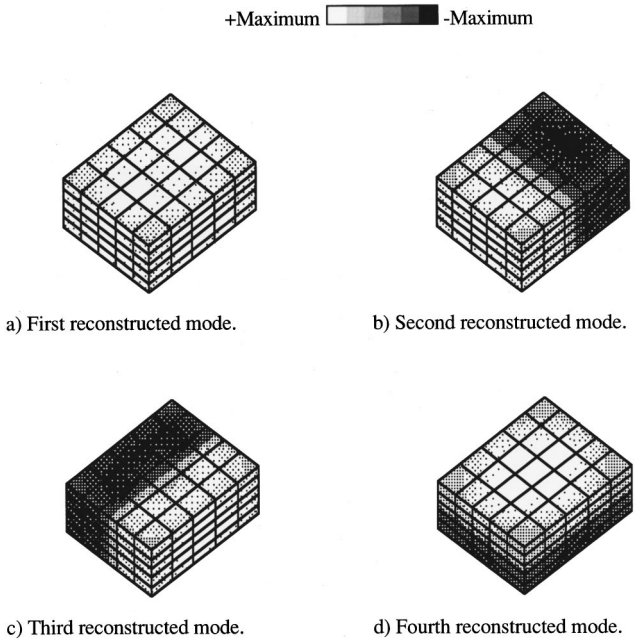

FIG. 11. Box mode shapes reconstructed from mapped spherical harmonics.

mapped spherical harmonics and the corresponding box's true acoustic radiation mode shapes are shown in Fig. 9 for $kl=0.1$. These velocity distributions are not depicted in magnitude terms, because the resolution in shading needed for observing the mapped spherical harmonics can not be achieved with the particular drawing program used.

The first spherical harmonic Y_0^0 produced the box velocity depicted in Fig. 9(a). This mapped spherical harmonic is similar in shape to that of the box's first actual acoustic radiation mode in Fig. 9(b). The velocity distributions are similar, but not identical: there are greater amplitude regions at the centers of the box faces due to the physical proximity of the box to the internal spherical harmonic source. The second mapped spherical harmonic Y_1^1 in Fig. 9(c) is similar to the box's second mode in Fig. 9(d), again with greater amplitude spots at the faces' centers. The same is true for the third mapped spherical harmonic Y_1^{-1} and fourth mapped spherical harmonic Y_1^0 in Figs. 9(e) and (g), respectively, which correspond well to the box's acoustic radiation modes in Figs. 9(f) and (b). We note that the mapped spherical harmonics do not produce the same surface velocity distributions as the box's true acoustic radiation modes. Therefore, we conclude that the box's modes are not simply mapped spherical harmonics.

B. Spherical harmonics as a basis for acoustic radiation modes

In the previous section we demonstrated that the box's acoustic radiation modes are not identical to mapped spherical harmonic velocity distributions on the surface. However, these mapped spherical harmonics do form a second linearly independent velocity set on the box. This point is shown by forming a matrix $\mathbf{U}$, where the individual columns $\mathbf{u}_{\text{map}}$ are the velocity amplitude vectors of M mapped spherical harmonics. Since the number of rows N in $\mathbf{U}$ represents the number of global nodes used in the boundary element model used here, the matrix is of size $(N\times M)$ and may be non-square. To demonstrate that the mapped spherical harmonics form a linearly independent set, the rank of the $\mathbf{U}$ matrix is taken with respect to added mapped spherical harmonics or columns, as depicted in Fig. 10. For each added velocity vector $M+1$, the rank of the matrix is $M+1$ so that it is always full rank.[29] Therefore, the mapped spherical harmonics are linearly independent on the surface of the rectangular box.

Since the mapped spherical harmonics are linearly independent, we may use them in turn as a basis to reconstruct the rectangular box's acoustic radiation modes through the expansion theorem. With a truncated series of 16 mapped spherical harmonics, we may decompose an acoustic radiation mode of the box, $\boldsymbol{\psi}$, using a least-squares technique[29] as

$$\boldsymbol{\Psi}=\mathbf{U}\mathbf{c}. \tag{28}$$

Here, $\boldsymbol{\psi}^{\mathrm{T}}\boldsymbol{\psi}=1$ and $\mathbf{U}$ is normalized such that the Euclidean norm of the individual columns is unity. The least-squares solution is unique, because the mapped spherical harmonics are linearly independent. The first four reconstructed acoustic radiation mode shapes for the box, using 16 mapped spherical harmonics, are depicted in Fig. 11. These reconstructed velocity distributions still bear some characteristics of the mapped spherical harmonics, particularly the higher amplitude regions. However, these reconstructed mode shapes for the box are approaching the true mode shapes. While a single mapped spherical harmonic is not equivalent to a single acoustic radiation mode for the box, each of the box's modes may be represented as a superposition of mapped spherical harmonics. We find this not particularly surprising, as it essentially is a statement of multipole methods.[30] Indeed, one perspective on the matter at hand is that it confirms the validity of multipole and related methods.

TABLE II. Modal participation coefficients of reconstructed box modes.

	First mode	Second mode	Third mode	Fourth mode
Y_0^0	1.04	$0.06+0.01i$	-0.59	0.45
Y_1^1		-0.94		
Y_1^{-1}			-1.00	-0.01
Y_1^0			-0.01	-1.13
Y_2^{-2}			0.01	
Y_2^2		-0.01		
Y_2^1				
Y_2^0	-0.19	0.55	0.12	-0.09
Y_2^{-1}				
Y_3^3		-0.11		
Y_3^{-3}			$-0.28-0.01i$	
Y_3^2				-0.13
Y_3^{-2}				0.54
Y_3^1				
Y_3^{-1}			$0.41+0.01i$	
Y_3^0			0.01	$1.21+0.04i$

C. Demonstration of spherical harmonics as a basis for grouping

We have shown that the mapped spherical harmonics serves as a basis for representing the acoustic radiation mode shapes of the box, when suitably mapped onto its surface. Therefore, we may use the long wavelength efficiency behavior of the spherical harmonics to understand the radiation efficiency behavior of the box's acoustic radiation modes.

To demonstrate this point, we consider the radiated power from one acoustic radiation mode of the rectangular box at long wavelengths. The power may be any real, finite, and positive value, as determined by the normalization of that mode in Eq. (9). We constrain this mode's power to be unity at a single frequency, $W_{\text{box}}=1$, leading to a particular normalization for that mode. We then constrain the radiated power from each individual free-space sphere acoustic radiation mode to be unity at the same single frequency as well. This normalization scheme provides a means of generating a mapped spherical harmonic with an amplitude such that it has the same radiated acoustic power as the corresponding acoustic radiation mode of the box. Therefore, the power of the sphere's mode is identical to that generated on the surface of the box by the corresponding mapped spherical harmonic and to the box's own mode, given as $W_{\text{sphere}}=W_{\text{box}}$. We perform this normalization so that we may use the expansion theorem, Eq. (7), in such a fashion that the participation coefficients are direct measures of the contribution to the total power for each free-space sphere mode.

With this normalization scheme applied to the first 16 mapped spherical harmonics, and using the least-squares approach as before, the resulting participation coefficients for the mapped spherical harmonics in the box's four most efficient acoustic radiation modes are presented in Table II. The empty entries in this table denote participation coefficients values of less than 10^{-3}. This table clearly shows that the box's individual acoustic radiation modes are dominated by their respective mapped spherical harmonics of equivalent order, as indicated by the dominance of the first four diagonal entries. Note that the sign of the coefficient only indicates phase. Further, the complex-valued contributions of the mapped spherical harmonics to the modal reconstruction are becoming significant, as indicated by the complex entries in Table II. We note that as the wave number is increased, these values become increasingly significant. Table II clearly indicates that the box's radiation modes are dominated by a single spherical harmonic, though other modes contribute, as well.

To further illustrate the significance of the above, we may then obtain the power due to a reconstructed box acoustic radiation mode through the use of Eq. (28) in (3), or

$$W_{\text{box}}=\mathbf{c}^{\mathbf{T}}\mathbf{U}^{\mathbf{T}}\mathbf{C}\mathbf{U}\mathbf{c}=\sum_{n=1}^{N}\sum_{m=1}^{N}c_n\mathbf{u}_{\mathbf{map}_n}^{\mathbf{T}}\mathbf{C}\mathbf{u}_{\mathbf{map}_m}c_m. \tag{29}$$

Since a mode for the box is dominated by a single spherical harmonic, at long wavelengths the radiated power of the box's nth acoustic radiation mode is approximately

$$W_{\text{box}_n}\approx c_n^2\mathbf{u}_{\text{map}_n}^{\mathbf{T}}\mathbf{C}\mathbf{u}_{\mathbf{map}_n}=c_n^2W_{\text{sphere}_n}. \tag{30}$$

Using each body's acoustic radiation mode's power and their respective spatial mean-square velocities and areas, the radiation efficiency expression for the box's nth acoustic radiation mode is approximately

$$\boldsymbol{\sigma}_{\text{box}_n}\approx c_n^2\boldsymbol{\sigma}_{\text{sphere}_n}\frac{\langle|\hat{u}_{\text{sphere}_n}|^2\rangle}{\langle|\hat{u}_{\text{box}}|^2\rangle}\frac{A_{\text{sphere}}}{A_{\text{box}}}\propto\boldsymbol{\sigma}_{\text{sphere}_n}. \tag{31}$$

This result proves that the corresponding radiation efficiencies of the rectangular box behave as those of the free-space sphere in the low-frequency limit, explaining the existing frequency dependence and grouping of the box's radiation efficiencies.

VI. GROUPING BEHAVIOR FOR DISTRIBUTIONS OF POINT SOURCES

The above sections have demonstrated that the radiation modes of spheres and rectangular solids exhibit grouping behavior. Here, we address the more general question as to the grouping behavior, if any, of arbitrary geometries. For this purpose, we use the radiation mode concept as developed for distributions of point sources.[19] The benefit of using this method for our purposes here is that it permits the rapid generation and analysis of many distributions of sources, many more so than could be evaluated in an equivalent time using boundary element methods. However, as noted by Johnson,[19] since there is no ''radiation efficiency'' definition equivalent to Eq. (4) for point-source distributions, the eigenvalues of the point-source radiation coupling matrix are what is of interest to us here. Nonetheless, the use of the point-source method does not reduce the generality of the results, as a consequence of the well-established modeling methods based on the use of superposition of radiation contributions from such sources, e.g., Refs. 31–33.

For the following, we consider the radiation modes of two source distributions. Each distribution has 100 point sources. The first distribution has the sources randomly distributed on the surface of a rectangular solid, excluding the ends. That is, the sources are distributed only on the sides, not on the top or bottom. We will refer to this distribution as the ''open box'' distribution. The second distribution has its

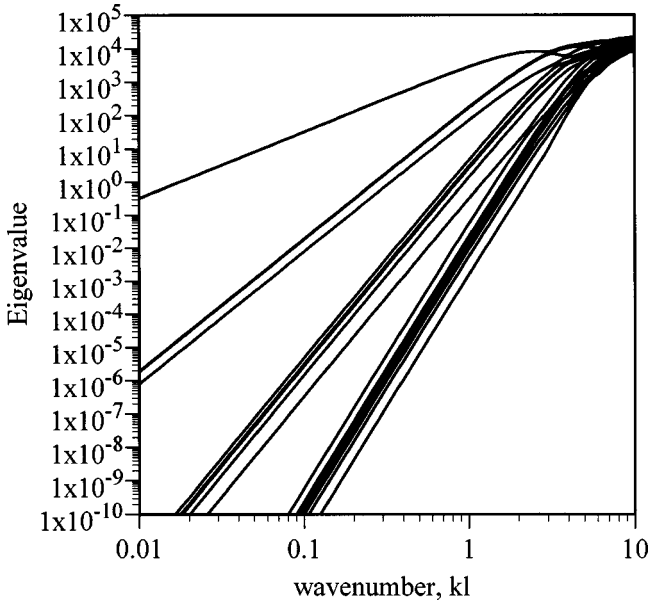

FIG. 12. Eigenvalues of the first 16 radiation modes for the open-box distribution of 100 point sources.

points randomly distributed throughout a rectangular volume with an aspect ratio of 100:1:1. We will refer to this distribution as the ''line'' distribution. Both distributions have a common characteristic length l that is used to generate a dimensionless wave number kl for plotting purposes.

Figures 12 and 13 depict the eigenvalues as a function of kl for the source distributions described above. Figure 12 clearly indicates that the open-box distribution clearly exhibits the same frequency grouping of the point-source modes as did the BEM-derived analyses presented earlier. Figure 13, for the line distribution, at first glance does not immediately support the existence of grouping, *but nonetheless it is present*. The modes still group as to their dependency on *wave number*, while the relative values of the eigenvalues within each group depend on the aspect ratio of the source distribution: the more strongly a distribution deviates from unity aspect ratio, the more strongly the eigenvalues within each group are differentiated.

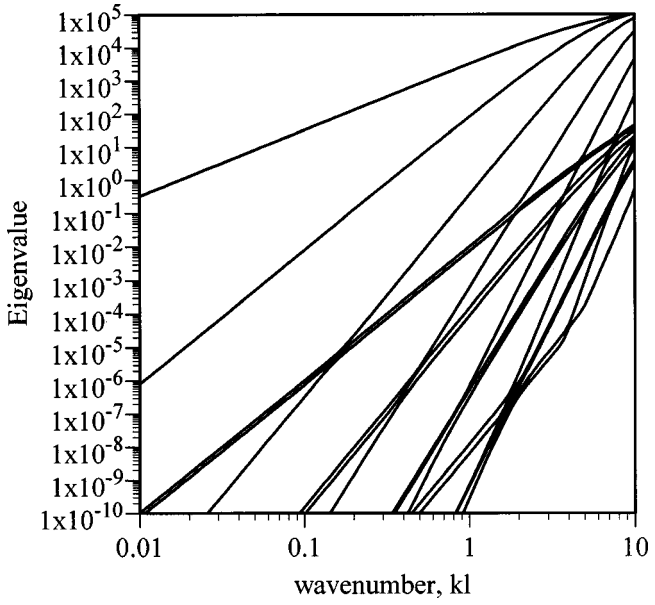

FIG. 13. Eigenvalues of the first 16 radiation modes for the line distribution of 100 point sources.

While we could present eigenvalue versus wave number figures for many more source distributions than the two we have included here, such would add nothing of benefit to this exposition: Every source distribution we have analyzed exhibits grouping behavior.

VII. CONCLUSIONS

We have demonstrated here that the so-called acoustic radiation modes for three-dimensional bodies exhibit a grouping characteristic under long wavelength conditions. The radiation efficiencies of modes within these groups follow frequency dependencies very close to those for spherical harmonics. All acoustic radiation modes within a group have wave number dependencies to the same even power. If $n+1$ represents the group number, then there are $2n+1$ modes within the group, and the wave number dependency goes as wave number to the power $2n+2$ for $n=0,1,2,\ldots$. This grouping is evident based on spherical harmonics, and on the multipole expansion,[24] though we note that multipoles do not, in general, radiate independently.

We have shown that the modal radiation characteristics of a rectangular box in a free space are related to the modal radiation characteristics of a sphere in a free space at long wavelengths. We observe the same grouping behavior in the acoustic radiation modes of distributed point sources, regardless of the geometry of the distribution. Because of the ability to model finite continuous structures with point sources, we therefore expect that such bodies will also exhibit grouping behavior for their radiation modes. Within a group, the relative magnitudes of the radiation efficiencies (or eigenvalues) of the acoustic radiation modes in the low-frequency limit are dependent on the aspect ratios of the structure.

To what consequence is this grouping? The application of the acoustic radiation modes to active noise control leaps immediately to the forefront. It has been proposed that the number of efficiently radiating modes determines the desired order of the control. Depending on the structure's aspect ratio, however, the number of sensors and actuators will increase as the number of acoustic radiation modes in the groups increase. That is, if more than just control of the first acoustic radiation mode is required, then due to the grouping of the next three acoustic radiation modes, the control of four acoustic radiation modes may be required. This is a worst case scenario for a unity aspect ratio object, but the implications are clear. In addition, this grouping concept may provide avenues to reduce the effort required for simulations, by limiting the modeling effort to consideration of only a restricted number of efficiently radiating modes.

ACKNOWLEDGMENTS

This research was supported by NASA, Langley Research Center, through the Graduate Researchers Program, Grant No. NGT-51115. Also, support was provided by NATO Cooperative Research Grant No. 950187.

[1] G. V. Borgiotti, ''The power radiated by a vibrating body in an acoustic fluid and its determination from boundary measurements,'' J. Acoust. Soc. Am. **88**(4), 1884–1893 (1990).
[2] D. M. Photiadis, ''The relationship of singular value decomposition to wave-vector filtering in sound radiation problems,'' J. Acoust. Soc. Am. **88**(2), 1152–1159 (1990).
[3] A. Sarkissian, ''Acoustic radiation from finite structures,'' J. Acoust. Soc. Am. **90**(1), 574–578 (1991).
[4] G. V. Borgiotti and K. E. Jones, ''Frequency independence property of radiation spatial filters,'' J. Acoust. Soc. Am. **96**(6), 3516–3524 (1994).
[5] G. V. Borgiotti, A. Sarkissian, E. G. Williams, and L. Schuetz, ''Conformal generalized near-field acoustic holography for axisymmetric geometries,'' J. Acoust. Soc. Am. **88**(1), 199–209 (1990).
[6] B.-K. Kim and J.-G. Ih, ''On the reconstruction of the vibro-acoustic field over the surface enclosing an interior space using the boundary element method,'' J. Acoust. Soc. Am. **100**(5), 3003–3016 (1996).
[7] W. T. Baumann, W. S. Saunders, and H. H. Robertshaw, ''Active suppression of acoustic radiation from impulsively excited structures,'' J. Acoust. Soc. Am. **90**(6), 3202–3208 (1991).
[8] W. T. Baumann, F.-S. Ho, and H. H. Robertshaw, ''Active structural acoustic control of broadband disturbances,'' J. Acoust. Soc. Am. **92**(4), 1998–2005 (1992).
[9] P.-T. Chen and J. H. Ginsberg, ''Complex power, reciprocity and radiation modes for submerged bodies,'' J. Acoust. Soc. Am. **98**(6), 3343–3341 (1995).
[10] K. A. Cunefare, ''The minimum multimodal radiation efficiency of baffled finite beams,'' J. Acoust. Soc. Am. **90**(5), 2521–2529 (1991).
[11] S. J. Elliott and M. E. Johnson, ''Radiation modes and the active control of sound power,'' J. Acoust. Soc. Am. **94**(4), 2194–2204 (1993).
[12] M. E. Johnson and S. J. Elliott, ''Active control of sound radiation using volume velocity cancellation,'' J. Acoust. Soc. Am. **98**(4), 2174–2186 (1995).
[13] K. Naghshineh and G. H. Koopmann, ''A design method for achieving weak radiator structures using active vibration control,'' J. Acoust. Soc. Am. **92**(3), 856–870 (1992).
[14] K. Naghshineh and G. H. Koopmann, ''Active control of sound power using acoustic basis functions as surface velocity filters,'' J. Acoust. Soc. Am. **93**(5), 2740–2752 (1993).
[15] K. Naghshineh, G. H. Koopmann, and A. D. Belegundu, ''Material tailoring of structures to achieve a minimum radiation condition,'' J. Acoust. Soc. Am. **92**(3), 841–855 (1992).
[16] R. A. Burdisso and C. R. Fuller, ''Design of active structural acoustic control systems by eigenproperty assignment,'' J. Acoust. Soc. Am. **96**(3), 1582–1591 (1994).
[17] M. N. Currey and K. A. Cunefare, ''The radiation modes of baffled finite plates,'' J. Acoust. Soc. Am. **98**(3), 1570–1580 (1994).
[18] M. N. Currey, ''On the exterior acoustic radiation modes of structures,'' Ph.D. dissertation, The Georgia Institute of Technology, 1996.
[19] M. E. Johnson, ''Active control of sound transmission,'' Ph.D. dissertation, The University of Southampton, 1996.
[20] C. A. Brebbia, J. C. Telles, and L. C. Wrobel, *Boundary Element Techniques, Theory and Applications in Engineering* (Springer-Verlag, Heidelberg, Germany, 1984).
[21] A. F. Seybert, B. Soenarko, F. J. Rizzo, and D. J. Shippy, ''An advanced computational method for radiation and scattering of acoustic waves in three dimensions,'' J. Acoust. Soc. Am. **77**(2), 362–367 (1985).
[22] A. F. Seybert, B. Soenarko, F. J. Rizzo, and D. J. Shippy, ''Application of the BIE method to sound radiation problems using an isoparametric element,'' Trans. ASME, J. Vib., Acoust., Stress, Reliab. Des. **106**(3), 414–420 (1984).
[23] A. D. Pierce, *Acoustics: An Introduction to Its Physical Principles and Applications* (Acoustical Society of America, Woodbury, New York, 1989).
[24] P. M. Morse and K. U. Ingard, *Theoretical Acoustics* (McGraw-Hill, New York, 1968).
[25] T. M. MacRobert, *Sperical Harmonics: An Elementary Treatise on Harmonic Functions with Applications* (E. P. Dutton, New York, 1927).
[26] K. A. Cunefare and M. N. Currey, ''On the exterior acoustic radiation modes of structures,'' J. Acoust. Soc. Am. **96**(4), 2302–2312 (1994).
[27] M. C. Junger and D. Feit, *Sound, Structures, and Their Interaction* (MIT Press, Cambridge, MA, 1986).
[28] K. A. Cunefare, ''The design sensitivity and control of acoustic power radiated by three-dimensional structures,'' Ph.D. dissertation, The Pennsylvania State University, 1990.
[29] D. S. Watkins, *Fundamentals of Matrix Computations* (Wiley, New York, 1991).
[30] M. Ochmann, ''The source simulation technique for acoustic radiation problems,'' Acustica **81**(6), 512–527 (1995).
[31] J. B. Fahnline and G. H. Koopmann, ''A numerical solution for the general radiation problem based on the combined methods of superposition and singular value decomposition,'' J. Acoust. Soc. Am. **90**(5), 2808–2819 (1991).
[32] M. Heckl, ''Bemerkung zur Berechnung der Schallabstrahlung nach der Methode der Kugelfeldsynthese,'' Acustica **68**, 251–257 (1989).
[33] G. H. Koopmann, L. Song, and J. B. Fahnline, ''A method for computing acoustic fields based on the principle of wave superposition,'' J. Acoust. Soc. Am. **86**(6), 2433–2438 (1989).

Isolating the auditory system from acoustic noise during functional magnetic resonance imaging: Examination of noise conduction through the ear canal, head, and body[a)]

Michael E. Ravicz
Eaton-Peabody Laboratory, Massachusetts Eye and Ear Infirmary, 243 Charles Street, Boston, Massachusetts 02114
and Research Laboratory of Electronics, Massachusetts Institute of Technology, 77 Massachusetts Avenue, Cambridge, Massachusetts 02139

Jennifer R. Melcher
Eaton-Peabody Laboratory, Boston, Massachusetts 02114
and Department of Otology and Laryngology, Harvard Medical School, Boston, Massachusetts 02115

(Received 7 November 1999; revised 16 August 2000; accepted 19 September 2000)

Approaches were examined for reducing acoustic noise levels heard by subjects during functional magnetic resonance imaging (fMRI), a technique for localizing brain activation in humans. Specifically, it was examined whether a device for isolating the head and ear canal from sound (a ''helmet'') could add to the isolation provided by conventional hearing protection devices (i.e., earmuffs and earplugs). Both subjective attenuation (the difference in hearing threshold with versus without isolation devices in place) and objective attenuation (difference in ear-canal sound pressure) were measured. In the frequency range of the most intense fMRI noise (1–1.4 kHz), a helmet, earmuffs, and earplugs used together attenuated perceived sound by 55–63 dB, whereas the attenuation provided by the conventional devices alone was substantially less: 30–37 dB for earmuffs, 25–28 dB for earplugs, and 39–41 dB for earmuffs and earplugs used together. The data enabled the clarification of the relative importance of ear canal, head, and body conduction routes to the cochlea under different conditions: At low frequencies ($\leqslant$500 Hz), the ear canal was the dominant route of sound conduction to the cochlea for all of the device combinations considered. At higher frequencies ($>$500 Hz), the ear canal was the dominant route when either earmuffs or earplugs were worn. However, the dominant route of sound conduction was through the head when both earmuffs and earplugs were worn, through both ear canal and body when a helmet and earmuffs were worn, and through the body when a helmet, earmuffs, and earplugs were worn. It is estimated that a helmet, earmuffs, and earplugs together will reduce the most intense fMRI noise levels experienced by a subject to 60–65 dB SPL. Even greater reductions in noise should be achievable by isolating the body from the surrounding noise field. [DOI: 10.1121/1.1326083]

PACS numbers: 43.50.Hg, 43.66.Vt, 43.50.Ki [MRS]

I. INTRODUCTION

Functional magnetic resonance imaging (fMRI) is widely used to map the activity patterns of the human brain during sensory stimulation or the performance of a cognitive task. However, the high-level sound, or ''acoustic noise,'' produced by the imaging equipment can be problematic for some fMRI investigations, particularly those focused on the central auditory system. Typically, subjects wear standard hearing protection devices during fMRI (i.e., earmuffs or earplugs; Savoy *et al.*, 1999), but this is not sufficient for achieving the quiet conditions more typical of physiological and psychophysical studies of hearing. The noise can be loud enough to mask the perception of sound stimuli (Shah *et al.*, 1999; Eden *et al.*, 1999), even when earmuffs and earplugs are worn. In addition, the noise itself can evoke brain activity, which can then obscure the activity produced by the intended stimuli (Bandettini *et al.*, 1998; Ulmer *et al.*, 1998; Talavage *et al.*, 1999; Edmister *et al.*, 1999). fMRI paradigms that modify the timing of image acquisitions can be used to reduce the influence of the noise on brain activation (e.g., Edmister *et al.*, 1999; Hall *et al.*, 1999), but these modified paradigms compromise the temporal resolution or data-taking efficiency of the fMRI technique (see Melcher *et al.*, 1999, for a discussion).

Acoustic noise in the imaging environment can arise from several sources. The most intense noise is from the imager gradient coils that produce spatially and temporally varying magnetic fields used in acquiring an image (e.g., Cohen, 1998). This ''gradient noise'' occurs synchronously with each image acquisition and has the same predominant frequency as the current driving the gradient coils (e.g., Hurwitz *et al.*, 1989; Schmitt *et al.*, 1998; Ravicz *et al.*, 2000).

[a)]Portions of this material were presented at the 1997 American Speech-Language-Hearing Association meeting, Boston, MA, 23 November 1997, the Twentieth and Twenty-first Midwinter Meetings of the Association for Research in Otolaryngology, St. Petersburg Beach, FL, 5 February 1997 and 18 February 1998, and the Fourth International Conference on Functional Mapping of the Human Brain, Montreal, PQ Canada, 11 June 1998.

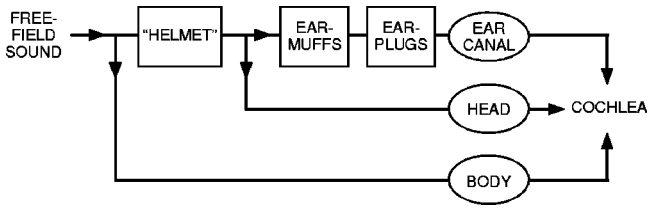

FIG. 1. Block diagram of sound conduction from the free field to the cochlea. Sound is conducted along three routes, labeled with ovals: along the ear canal, through the head, and through the body. As indicated, earmuffs and earplugs reduce sound conduction along the ear-canal route. A helmet enclosing the head is expected to reduce conduction along both the head and ear-canal routes.

We found that peak gradient-noise levels during fMRI reached 123 dB $re\ 20\ \mu$Pa in a 1.5-Tesla (T) imager and 138 dB in a 3-T imager; the gradient-noise spectra (calculated over a 10-ms window coinciding with the highest-amplitude noise) showed a prominent maximum at 1 kHz for the 1.5-T imager (115 dB SPL) and at 1.4 kHz for the 3-T imager (131 dB SPL—Ravicz *et al.*, 2000).[1] (Figure 4 contains examples of noise waveforms.) Other sources of noise include (a) a pump for liquid helium used to cool the imager's static magnet, and (b) the air-handling system in the imager room. Pump and air-handling noise levels at our installation were 71 dB(A) (80 dB SPL unweighted) with spectral peaks at 125, 240, and 490 Hz (Ravicz *et al.*, 2000). Other authors have reported similar gradient and background noise levels for comparable imagers (e.g., Prieto *et al.*, 1998).

Earmuffs and earplugs cannot reduce fMRI acoustic noise to subaudible levels because there is a fundamental limit to their effectiveness. The limit arises because there are multiple routes by which sound is conducted to a subject's cochlea (e.g., von Gierke, 1956). These multiple routes are shown schematically in Fig. 1. Earmuffs and earplugs reduce conduction along the ear canal; however, sound impinging on a subject can still be conducted through the subject's head and body to the cochlea (von Gierke, 1956; Zwislocki, 1957; Berger, 1983).[2] This sound can be conducted (a) directly to the cochlea; (b) to the middle ear and then to the cochlea; or (c) through the walls of the ear canal and along the ear canal to the middle ear and cochlea (Khanna *et al.*, 1976). When no hearing protection devices are worn, sound at the external ear conducted along the ear canal dominates the perceived sound. However, when earmuffs and earplugs are used together to reduce conduction along the ear canal, conduction through the subject's head and body can become significant (Zwislocki, 1957; Berger, 1983), and protecting the ears further will not reduce the level of perceived sound. Shielding the head and body as well as the ears should, however, produce reductions (von Gierke, 1956).

The sound attenuation provided by earmuffs and earplugs has been reported in several previous studies (Berger, 1983; Berger and Kerivan, 1983; Berger *et al.*, 1998; Casali *et al.*, 1995), but the efficacy of devices for shielding the head or body remains largely unexamined. In subjects wearing earmuffs and earplugs, Nixon and von Gierke (1959) found that cotton applied over the head (but not the earmuffs) could attenuate the perceived level of free-field sound (confirming that the attenuation provided by earmuffs and earplugs was indeed limited by conduction through the head). However, they did not examine the degree of isolation that might be achieved by shielding the ear as well as the head, nor did they attempt to test a shielding device for use in practice.

The objective of the present study was to build on the experiments of Nixon and von Gierke by testing a device for isolating both the ear canal and the head from sound (Fig. 1). Because our particular interest was to reduce the imaging noise perceived by subjects during fMRI, we designed a head-shielding device (a ''helmet'') that could eventually be used during imaging experiments. We investigated the attenuation provided by (a) a helmet used with earmuffs, and (b) a helmet used with earmuffs and earplugs together. We measured both (1) subjective attenuation, the attenuation of perceived sound (an indicator of the attenuation of sound reaching the cochlea), and (2) objective attenuation, the attenuation of sound pressure in the ear canal. To determine whether or not the helmet could provide substantial additional attenuation beyond that provided by earmuffs and earplugs, it was necessary to assess the attenuation provided by earmuffs and earplugs under the same experimental conditions (even though the attenuation of earmuffs and earplugs has been examined previously, e.g., Berger *et al.*, 1998).

The data gathered in these investigations provided an opportunity to clarify the relative importance of the various sound conduction routes to the cochlea, particularly at high frequencies where fMRI noise levels are highest. While it is known that ear canal, head, and body conduction can all contribute to perceived sound, the relative importance of these routes at a quantitative level remains largely unresolved. From an fMRI standpoint, we were interested in understanding the conduction routes because this information can be used to design further noise reduction strategies.

II. METHODS

A. Subjects

Subjects were adult volunteers (eight men, two women) with no auditory complaints or known hearing loss. Measurements were generally made in one ear; in three subjects, measurements were made in both ears. Experiments were conducted in accordance with a protocol approved by the Human Studies Committee of the Massachusetts Eye and Ear Infirmary, and informed consent was obtained from all subjects.

B. Devices tested

We tested several devices for isolating a subject's ears and head from sound: earplugs, earmuffs, and helmets.

The earplugs and earmuffs tested were commercial models commonly used for hearing protection. Earplugs were chosen from among five models of compressible foam earplugs of different sizes and Noise Reduction Ratings (NRRs; EPA,1979): E·A·R E·Z·Fit (NRR=28 dB), Howard Leight Max-Lite (NRR=33 dB), Howard Leight Laser-Lite (NRR=32 dB), Lab Safety Supply Sound Defense (NRR =29 dB), Moldex Spark Plug (NRR=31 dB). Earplug

model and size were chosen by the investigators and subject for a snug yet comfortable fit in the ear canal. Preliminary tests indicated that other types of earplugs, such as PVC, molded rubber/plastic, clay, or cotton/fiberglass, were almost always less comfortable and often less effective for subjects. Earmuffs were Howard Leight QM-26 dielectric muffs (NRR = 25 dB), nonmetallic, and therefore MRI compatible, which included a hard thermoplastic shell and PVC-covered foam cushions.

Two helmets for reducing sound transmission to a subject's head were tested. The first helmet was large enough to fit loosely over the head of a subject wearing earmuffs (Fig. 2). This free-standing helmet consisted of a sheet of foam–barrier–foam composite (Netwell FBF-1), comprising a layer of 1/4-in. acoustic foam, a heavy barrier layer of 1/8-in.-thick vinyl (1 lb/in.^{2}), and a layer of 1-in. acoustic foam. The composite was rolled into a cylinder (1-in. foam layer inside) and sealed top and bottom with a circular piece of the same composite. The bottom of the helmet was removable and was slit to allow installation around a subject's neck. Any gaps between the subject's neck and the helmet were filled by a laboratory towel. There was no contact between the helmet and earmuffs and no contact between the helmet and the subject except at the neck and shoulders. A second, larger helmet (which fit over and was supported by a mockup of an imager head coil) was constructed from a barrier–foam composite without the 1-in. foam layer (E·A·R E-0-10-25). The composite was oriented so the 1/4-in. foam layer was between the barrier layer and the mock head coil. This second helmet was also sealed at the top and bottom as described above for the first helmet. Ventilation air for the subject (8–9 l/min.) was provided through a long (~8 m) tube running from a bottle of medical-grade compressed air through the wall of the helmet near the subject's neck to the space under the helmet and exhausted through the towel.

The materials used for the helmets were chosen for (1) a high attenuation rating [STC = 27–34 (Sound Transmission Class, e.g., Warnock and Quirt, 1998)]; (2) a barrier layer that is among the heaviest available in standard products; and (3) a foam decoupling layer. (The foam layer of the second helmet isolated the barrier layer from the mock head coil.) Although we did not explicitly try different materials, we do not expect that other, similar commercially available materials will provide significantly more attenuation unless their STC is higher. Because the helmets were constructed of composites with similar attenuation ratings,[3] we expected that the two helmets would provide similar attenuations. In fact, they did, so we do not distinguish between the two helmets in the results.

C. Measurement techniques

The effect of each isolation device or combination of devices (earmuffs, earplugs, helmet) was assessed two ways. ''Subjective'' attenuation was computed from differences in behavioral threshold to various sound stimuli [Sound Field Real Ear At Threshold (REAT)]. ''Objective'' attenuation was computed from measurements of sound pressure magnitude in a subject's ear canal [Insertion Loss by Microphone

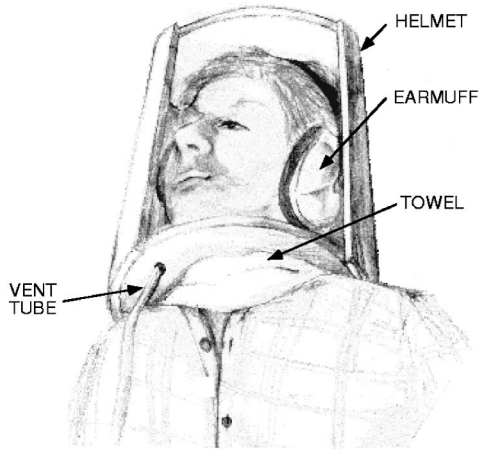

FIG. 2. Realistic view of a subject wearing the first helmet and earmuffs. The helmet is shown cut away to illustrate how it fit loosely over the head of a subject wearing earmuffs; in actuality, it enclosed the subject's entire head.

In Real Ear (MIRE)—Berger, 1986b]. In each case, measurements made with the subject wearing one or more isolation devices were compared with measurements with no devices worn (see Fig. 3). Subjective attenuations were computed from measurements of behavioral threshold (in dB) as

$$\textit{Subjective attenuation}\ (\text{in dB}) = \textit{Threshold with device} - \textit{Threshold with no device}. \tag{1a}$$

Similarly, objective attenuations were computed from measurements of ear-canal sound pressure P_{EC} (normalized by stimulus level) as

$$\textit{Objective attenuation}\ (\text{in dB}) = 20 \times \log_{10}\ (P_{EC}\ \textit{with no device} / P_{EC}\ \textit{with device}). \tag{1b}$$

Measurements were performed with a subject seated in a soundproofed, acoustically deadened chamber at the Eaton-Peabody Laboratory in Boston, MA. Background noise levels were 0 dB SPL or less above 200 Hz (Vér *et al.*, 1975). Sound stimuli were played over a wide-range loudspeaker (Radio Shack #40-1354) located approximately 45 cm from a subject's ear (usually the left) at an azimuth of 90° from the midline and 0° elevation [Fig. 3(A)].[4] A foam earplug was inserted by the experimenter into the ear canal opposite the loudspeaker (to approximately the depth of a ''standard insertion,'' Berger, 1983, 1986b), where it remained throughout the experiment.[5]

Sound pressure P_{EC} was measured in the ear canal closest to the loudspeaker. A short, thin, stiff plastic probe tube (~22 mm length, 1.14-mm inner diameter, 1.57-mm outer diameter) was attached to a hearing aid microphone (Knowles EK-3027) with cyanoacrylic cement. The microphone was inserted into the subject's concha so the probe tube extended approximately 15 mm into the ear canal. The

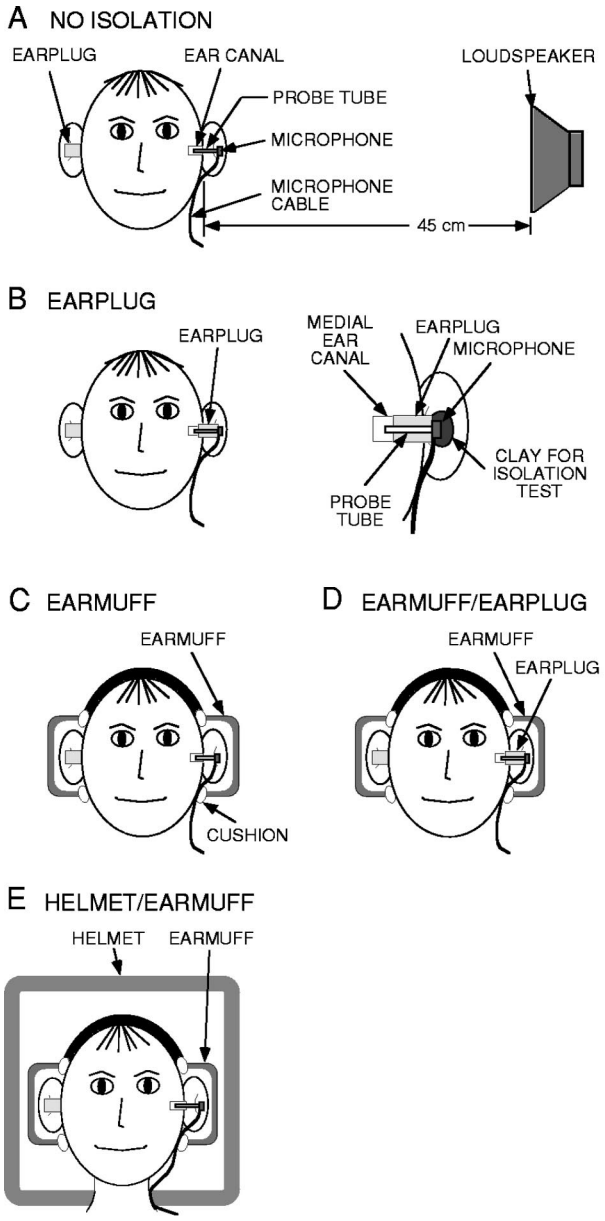

FIG. 3. Diagram of techniques used to measure sound pressure in the ear canal and behavioral thresholds. Measurements were made with no isolation (A) and with different combinations of test devices: earplugs (B, left panel), earmuffs (C), earmuffs and earplugs together (D), a helmet and earmuffs together (E), and a helmet with earmuffs and earplugs together (not shown). Details of the attachment between the earplug, microphone, and probe tube are shown in (B), right panel; also shown is the position of the clay used to test whether the microphone was acoustically isolated from the sound field outside the ear.

microphone was taped to the tragus to hold it in place. Care was taken not to obstruct the entrance to the ear canal and to keep the tip of the probe tube away from the ear-canal wall. For configurations that included an earplug as a test device [Figs. 3(B) and (D)], the probe tube was threaded through a hole in the earplug made with a hypodermic needle such that only the microphone remained outside the earplug [Fig. 3(B), right panel].[6] The earplug was inserted by the experimenter into the ear canal. A standard insertion was always attempted; however, because the probe tube, microphone, and microphone cable increased the difficulty of inserting the earplug, a lesser insertion was realized in some cases (i.e., a ''partial insertion,'' Berger, 1983, 1986b).[7] After P_{EC} was measured with the test earplug in place, the earplug was removed from the ear, and the microphone and probe tube were extracted intact from the earplug and reinserted in the ear canal at approximately the same location. To be sure that the characteristics of the microphone and probe tube were unaffected by these procedures, we checked that the calibration of the microphone with its probe tube was the same at the beginning and the end of each experiment. For the calibration, the microphone with probe tube was sealed to the end of a custom-made acoustic source and the microphone output was measured in response to a broadband chirp stimulus (see Sec. D).

For configurations that included earmuffs as a test device [Figs. 3(C), (D), and (E)], the earmuffs were positioned by the subject to maximize comfort, with assistance by the experimenter, who ensured that there was a seal between earmuff cushion and head. The microphone cable was routed between the earmuff cushion and the subject's head. For configurations that included a helmet [Figs. 3(E) and (F)], the helmet was positioned by the experimenter. The microphone cable was routed along the subject's neck.

For each combination of devices, P_{EC} was measured first to assess the fit of the noise reduction device(s). The subject's behavioral thresholds were then determined in response to imager noise and tone-burst stimuli (described in Sec. D below). Subjects were provided with a push button that controlled a buzzer in the control area outside the soundproofed room and were instructed to keep the button pressed as long as they heard one stimulus presentation per second. Stimuli were initially presented at approximately 20 dB SL. Stimulus level was then reduced in 3-dB steps at approximately 3-s intervals as long as the button was pressed. Once the subject released the button, stimulus level was increased in 3-dB steps until the subject again responded. Three response/no-response cycles were usually sufficient to establish a reliable threshold. Typically, the first sound pressure and threshold measurements in each session were made with multiple noise reduction devices in place [e.g., Fig. 3(E)]; devices were then removed progressively until the last measurement was made with no device in place.

D. Stimuli

For ear-canal sound-pressure measurements, broadband chirps (12 Hz–14 kHz) were played over the loudspeaker at 80–95 dB SPL (as measured in the subject's ear canal) for approximately 90 s. For behavioral threshold measurements, we chose test stimuli based directly on fMRI acoustic noise.[8] Two types of stimuli were used: (1) 650-ms segments of previously digitized 1.5- and 3-T imager noise (including gradient noise—Fig. 4), and (2) tone bursts (50-ms duration) at 1 and 1.4 kHz (the predominant frequencies of the gradient noise in the 1.5-T imager and the 3-T imager, respectively), 2 and 2.8 kHz (second harmonics, also prominent in the noise spectra), and 500 Hz (a prominent lower-frequency peak in the noise spectra). Each imager noise segment cor-

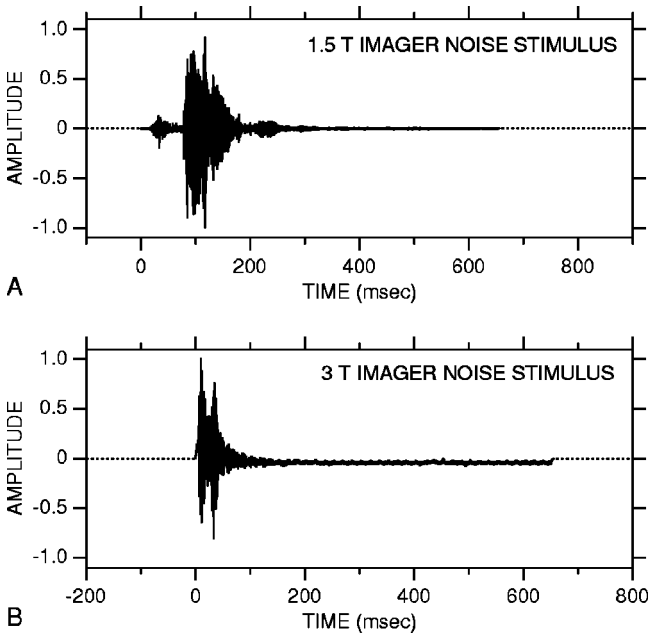

FIG. 4. Imager noise stimuli. In each panel, the waveform from 0 to 650 ms is imager noise recorded in 1.5-T (A) and 3-T imagers (B); the remainder is zero padding (dotted line) for a 1-s presentation period. The high-intensity portions of the noise waveforms [e.g., 80–150 ms in (A), 5–40 ms in (B)] are due to gradient coil activity. The waveforms have been normalized to their respective peaks.

responded to a single image acquisition (Ravicz *et al.*, 2000). All stimuli had 5-ms rise–fall times and were presented at a rate of 1/s.

E. Some potential sources of measurement error

One potential source of error in earplug objective attenuation measurements is sound conducted directly to the microphone through the microphone case rather than the probe tube. During measurements of ear-canal pressure with an earplug in place, the microphone [outside the ear—Fig. 3(B)] is in a more intense sound field than the tip of the probe tube in the ear canal medial to the earplug. If sound conducted through the microphone case to the microphone were comparable to or greater than ear-canal sound pressure, earplug attenuations would be artifactually low. While measuring ear-canal pressure with an earplug in place, we encased the microphone in a heavy clay [Fig. 3(B), right panel], thereby isolating it from the sound field outside the ear. Adding the clay produced no difference in the microphone output. This indicates that sound conduction through the microphone case to the microphone did not contaminate our measurements of earplug attenuation.

We considered whether physiological noise in the ear canal might result in errors in our subjective attenuation measurements. This consideration was prompted by reports that masking of auditory stimuli by higher levels of physiological noise in the occluded versus unoccluded ear canal[9] could cause overestimations of the attenuation of earmuffs and earplugs (Berger and Kerivan, 1983). The amount of overestimation was shown by Berger and Kerivan to be insignificant for measurements of earplug and earmuff attenuation at 500 Hz and above. Since the frequency range of our subjective attenuation measurements was $\geqslant$500 Hz, we assume that any such overestimations did not cause significant errors in our measurements.

A second potential source of error in the subjective attenuation measurements arises because different routes of sound conduction are important with different configurations of isolation devices. For no devices [Fig. 3(A)], behavioral thresholds presumably are indicative of sound reaching one cochlea (on the side closest to the loudspeaker). However, for device configurations where head and/or body conduction contributes significantly to the perceived sound (see Secs. III C, D, E), behavioral thresholds could reflect sound reaching both cochleae rather than only one. The implication is that behavioral thresholds with certain devices may be artificially low (because threshold reflects sound reaching both cochleae instead of only one), in which case subjective attenuation would be artifactually low [see Eq. (1a)]. We estimated that the threshold might differ by as much as 3 dB depending on whether sound was detected with one or both cochleae (based on the difference between minimum audible pressure and minimum audible field; Moore, 1997). Therefore, it is possible that subjective attenuations may have been underestimated by as much as 3 dB in circumstances where head and/or body conduction was important (see also Berger and Kerivan, 1983). We took this into consideration in deducing the dominant routes of sound conduction for different device configurations (Sec. III) as follows: In our deductions (which are based on comparisons of objective and subjective attenuations and comparisons of subjective attenuations for different device configurations) we consider only differences in excess of 3 dB.

III. RESULTS

A. Overview

Objective and subjective attenuations were measured for the four configurations of isolation devices shown in Figs. 3(B)–(E) and for a fifth combination comprising earmuffs, earplugs, and a helmet. The subjective attenuations for each of the device combinations are listed in Table I. Both objective and subjective attenuations are shown in Figs. 5–8. The helmet/earmuff combination provided higher objective and subjective attenuations than the earmuff/earplug combination. The helmet/earmuff/earplug combination provided the highest objective and subjective attenuations of all configurations tested.

B. Earmuffs or earplugs

1. Objective and subjective attenuations

Attenuations for earmuffs [Fig. 3(C)] are shown in Fig. 5(A). The mean objective attenuation for earmuffs[10] [solid line in Fig. 5(A)] increased with increasing frequency up to approximately 1 kHz. (Note that increasing attenuation is plotted downward.) Above 1 kHz, objective attenuation ranged from 29–41 dB. The lesser attenuation at low compared to high frequencies is characteristic of passive attenuation devices (e.g., Nixon, 1979; Berger, 1983). Mean subjective attenuations for tone-burst stimuli [1, 1.4, 2, 2.8 kHz; circles in Fig. 5(A); see Table I] were between 32 and 37 dB

TABLE I. Summary of subjective attenuation measurements in this study and previous reports using similar earmuffs and earplugs. Attenuations are specified in dB (mean±1 standard deviation). Attenuations for this study are based on data in *N* ears; the datum for each ear is the average of 1–3 measurements. The previous studies of earmuff attenuation used Bilson UF-1 earmuffs,[a] presented mean results for several types of earmuffs,[b] or did not specify the type used.[c] The previous studies of earplug attenuation used E·A·R® Classic® foam earplugs[a] or did not specify the type used.[c]

		Subjective attenuation of various sound stimuli (dB)						
		Stimuli						
		Imager noise		Tone bursts				
Isolation device This study	Number of ears *N*	1.5-T (1 kHz)	3.0-T (1.4 kHz)	500 Hz	1 kHz	1.4 kHz	2 kHz	2.8 kHz
Earmuffs	5	30±6.0	37±3.9	···	32±6.9	37±4.7	34±7.9	35±3.8
Earplugs	3	26±6.1	25±0.8	···	28±4.2	27±6.8	35±2.4	41±1.0
Earmuff/earplug combination	8	41±68	39±4.0	41±8.6	41±6.5	39±6.5	47±7.1	48±5.8
Helmet/earmuff combination	3	47±2.7	52±1.7	···	50±0	58±6.9	56±10.4	64±6.4
Helmet/earmuff/earplug combination	5	57±9.7	63±9.9	58±5.5	55±7.3	63±9.7	66±5.8	82±2.1
		Stimuli: 1/3-octave bandwidth noise bursts except as noted						
Other studies		125 Hz	250 Hz	500 Hz	1 kHz	1.4 kHz	2 kHz	3.15 kHz
Earmuffs, ''Subject fit''[a]		7.4±3.6	14.0±3.4	20.7±3.3	29.2±3.8	···	31.7±4.2	···
Earmuffs, mean of several studies[a]		9±3.6	12±4.0	19±4.7	27±4.9	···	28±5.2	···
Earmuffs[b] Stimuli: pure tones		13±4.5	19±5.5	26±5.5	34±7.0	···	32±6.5	33±8.0
Earplugs, ''Subject fit''[a]		21.4±7.8	22.0±7.8	24.2±7.8	25.2±6.9	···	31.0±4.7	···
Earplugs, mean of several studies[a]		17±9.0	17±8.7	20±9.2	22±8.5	···	29±8.3	···
Earmuff/earplug combination[c]		37.5±4.6	41.8±5.1	51.3±6.7	47.8±4.2	···	37.3±3.5	46.8±4.5

[a]Compiled by Berger *et al.*, 1998.
[b]Casali *et al.*, 1995.
[c]Berger, 1983, for ''small-volume'' earmuffs and earplugs inserted to ''standard depth'' (50%–60% of earplug in ear canal).

and were 1–5 dB lower than objective attenuations at corresponding frequencies,[11] but these differences were not statistically significant ($p>0.2$ for all four frequencies, Student's unpaired *t* test; Press *et al.*, 1988). The subjective attenuation for 1.5-T imager noise [30 dB; square in Fig. 5(A)] did not differ significantly from the subjective attenuation for tone bursts at the predominant frequency of the 1.5-T gradient noise (1 kHz; $p>0.6$). Similarly, the subjective attenuation for 3-T imager noise [37 dB; triangle in Fig. 5(A)] did not differ significantly from the subjective attenuation for tone bursts at the predominant frequency of the 3-T gradient noise (1.4 kHz; $p>0.9$). All of the results indicate that earmuffs provide approximately 35 dB of attenuation in the frequency range of imager gradient noise (1–1.4 kHz).

Attenuations for earplugs [Fig. 3(B)] are shown in Fig. 5(B). Data from all of the earplug types tested (of different sizes and NRRs) have been combined. Mean objective attenuation [solid line in Fig. 5(B)] generally increased with increasing frequency up to approximately 3 kHz where it reached a maximum of 41 dB. At still higher frequencies, objective attenuation decreased slightly as frequency increased. Mean subjective attenuations for tone bursts at 1, 1.4, 2, and 2.8 kHz (27–41 dB; see Table I) did not differ significantly from objective attenuations at corresponding frequencies (1–3-dB difference; $p>0.7$ for all four frequencies). Subjective attenuations for imager noise (26 and 25 dB for 1.5- and 3-T noise, respectively) did not differ significantly from those for tone bursts at the predominant frequencies of the gradient noise ($p>0.6$). In the frequency range of the gradient noise, all of the results indicate that earplugs provide approximately 27 dB of attenuation.

2. Comparison with previous studies

Our measurements of earmuff and earplug attenuations are in general agreement with previous reports (Casali *et al.*, 1995; Royster *et al.*, 1996; Berger, 1983; Berger and Kerivan, 1983; Berger *et al.*, 1996, 1998).[12] Our objective attenuations for earplugs are within the range of Berger and Kerivan's (1983) ''partial insertion'' earplug data over the frequency range that the two sets of measurements have in common (125 Hz–2 kHz). Our objective attenuations for earmuffs are also within the range of previously reported values (125 Hz–3.15 kHz), with some exceptions. They are less than attenuations reported by Casali *et al.* (1995) in Bilsom earmuffs below 500 Hz and less than attenuations reported by Berger and Kerivan (1983) in David Clark 19A earmuffs below 1 kHz. A possible reason for these discrepancies is that the earmuffs used by Casali *et al.* and Berger and Kerivan may have had a larger volume than ours—large-

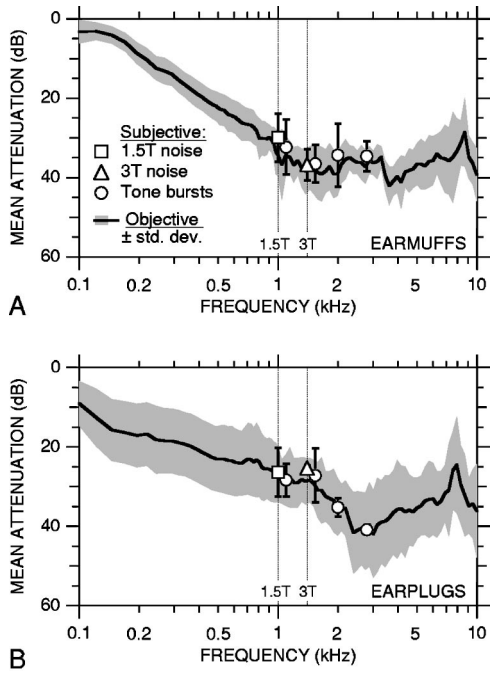

FIG. 5. Attenuation of earmuffs (A) and earplugs (B). In both panels, the solid curve is the mean objective attenuation for nine ears (in seven subjects—earmuffs; six subjects—earplugs); shading indicates ±1 standard deviation (s.d.). Symbols indicate mean subjective attenuations in five subjects (earmuffs) or three subjects (earplugs); error bars indicate ±1 s.d. Subjective attenuations for tone bursts, 1.5-T imager noise, and 3-T imager noise are indicated by circles, squares, and triangles, respectively. For earplugs, ±1 s.d. was less than the dimensions of the symbols indicating the mean subjective attenuations for 3-T imager noise and 2.8-kHz tone bursts. Subjective attenuations for imager noise are plotted at the predominant gradient noise frequencies indicated by vertical dotted lines (1.5 T: 1 kHz; 3 T: 1.4 kHz). Subjective attenuations for tone bursts at 1 and 1.4 kHz have been offset horizontally to the right for clarity.

volume earmuffs have been shown to provide greater attenuation at low frequencies than small-volume earmuffs (Berger, 1983). Our subjective attenuations for earmuffs and earplugs are in close agreement with previous reports (Table I).

3. Dominant conduction route

The fact that our objective and subjective attenuations do not differ significantly for either earmuffs or earplugs indicates that sound in the ear canal fully accounts for the sound perceived by subjects wearing either earmuffs or earplugs. Therefore, conduction through the head and body to the cochlea is not important with these devices: *for earmuffs or earplugs, the dominant sound conduction route is along the ear canal.*

C. Earmuffs and earplugs in combination

1. Objective and subjective attenuations

The attenuation provided by earmuffs and earplugs used together [Fig. 3(D)] is shown in Fig. 6(A). Objective attenuation for this ''earmuff/earplug combination'' generally increased with increasing frequency up to approximately 65 dB at 3–4 kHz and then decreased. Subjective attenuations for tone bursts (0.5, 1, 1.4, 2, and 2.8 kHz—see Table I) were between 39 and 48 dB. At 1.4, 2, and 2.8 kHz, subjective attenuations were significantly less than objective attenuations (by 7–15 dB; $p<0.02$). Subjective attenuations for 1.5- and 3-T imager noise (41 and 39 dB) did not differ significantly from the subjective attenuations for 1- and 1.4-kHz tone bursts, respectively ($p>0.9$). The subjective attenuation for 3-T imager noise was significantly less than the objective attenuation at 1.4 kHz ($p<0.004$). Thus, subjective attenuations for frequencies $\geqslant$1.4 kHz were less than the objective attenuations at corresponding frequencies.

2. Comparison of earmuff/earplug combination with earmuffs or earplugs alone

The attenuations provided by the earmuff/earplug combination can be compared to the attenuations for earmuffs or earplugs alone using Fig. 6(A) and Table I. Objective attenuations for the earmuff/earplug combination exceeded the attenuation provided by either device alone at all frequencies ($p<0.007$), except that the attenuation of the earmuff/earplug combination was not significantly greater than that for earplugs alone near 125 Hz ($p>0.1$). Subjective attenuations for the earmuff/earplug combination significantly exceeded the subjective attenuations for earmuffs or earplugs alone in most cases (by 9–15 dB; $p<0.05$). The exceptions are the 3-T imager noise and 1.4-kHz tone bursts, for which there was no significant difference in attenuation between the earmuff/earplug combination and earmuffs alone ($p>0.3$), and 2.8-kHz tone bursts, for which the difference in attenuation between the earmuff/earplug combination and earplugs alone was not significant ($p>0.1$).

3. Dominant conduction routes

a. Comparison of objective and subjective attenuations. As a first step toward identifying the dominant routes of sound conduction to the cochlea in subjects wearing both earmuffs and earplugs, we compared objective and subjective attenuations in Fig. 6(A). The reasoning that motivated this comparison was as follows: If the ear canal were the dominant sound conduction route, all the sound reaching the cochlea would pass through the earmuff and then the earplug, and objective attenuations would equal subjective attenuations. Thus, a difference between objective and subjective attenuations would indicate that a significant amount of sound reaching the cochlea bypassed the ear canal, i.e., was conducted through the head and body to the middle or inner ear (the ''ossicular'' or ''middle ear'' and ''inner ear'' components described in Khanna *et al.*, 1976). At 500 Hz, the difference between the mean subjective and objective attenuations was insignificant (1 dB), suggesting that the ear canal was the dominant conduction route at 500 Hz. At 1 kHz, subjective and objective attenuations differed to a greater degree (by 6 dB), but not significantly ($p>0.1$). At 1.4 kHz and above, subjective attenuations were 7–15 dB less than objective attenuations, and the differences were significant ($p<0.02$). The discrepancy between objective and subjective attenuations indicates that a significant portion of the sound reaching the cochlea at and above 1.4 kHz bypassed the ear canal, i.e., was conducted through the head and/or body to the middle ear and cochlea.[13]

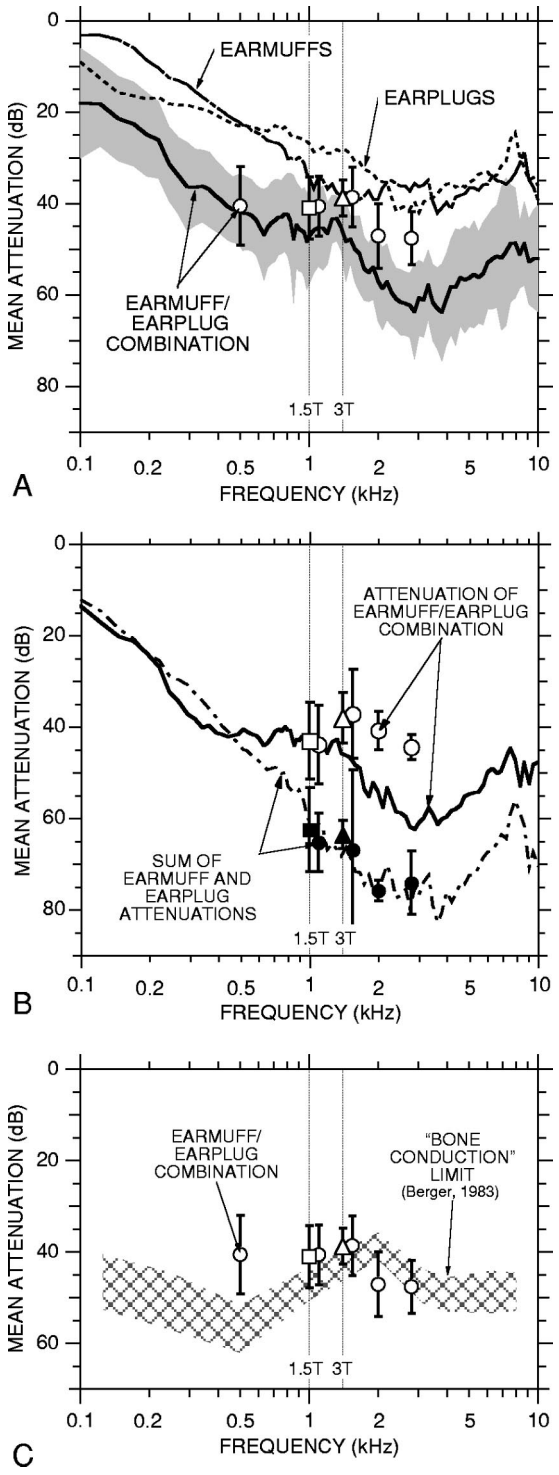

FIG. 6. (A) Objective and subjective attenuations for the earmuff/earplug combination. The solid curve is the mean objective attenuation for 12 ears (in nine subjects; shading indicates ±1 s.d.); symbols are mean subjective attenuations in eight subjects (error bars indicate ±1 s.d.). Key to symbols and vertical lines as in Fig. 5. Also shown are mean objective attenuations for earmuffs and earplugs from Fig. 5 (thin dot-dashed and dotted curves, respectively). (B) Sum of mean earmuff and earplug attenuations (dot-dashed curve and filled symbols) and attenuation for the earmuff/earplug combination (solid curve and open symbols). The results shown in this panel are based only on the ears in which measurements were made in all three of the following conditions: earmuffs alone, earplugs alone, and the earmuff/earplug combination (objective: eight ears in six subjects; subjective: three subjects). (C) Subjective attenuations for the earmuff/earplug combination (symbols) compared to the mean ''bone conduction limit'' ±1 s.d. measured by Berger (1983) in subjects wearing special highly attenuating earmuffs and deeply inserted earplugs (hatched area).

b. Comparison of earmuff/earplug attenuation to summed earmuff and earplug attenuations. To further examine the routes of sound conduction for the earmuff/earplug combination, we (a) calculated what the attenuations for the earmuff/earplug combination would be if the ear canal were the only important sound conduction route, and (b) compared the calculations with our measurements of attenuation for the earmuff/earplug combination. If the ear canal were the only important route, all of the sound reaching the ear canal and cochlea would pass through the earmuff and then the earplug (Fig. 1). In this case, the attenuation for the earmuff/earplug combination would be the sum (in dB) of the individual earmuff and earplug attenuations, assuming that there is no interaction between earmuff and earplug.[14] Therefore, as a test of whether the ear canal was the dominant route, we added the attenuations for earmuffs and earplugs alone and compared the result with the measured attenuation for the earmuff/earplug combination. The idea was that any significant discrepancies would indicate sound conduction via routes other than the ear canal route.

The summed earmuff and earplug objective attenuations are shown in Fig. 6(B) along with the objective attenuation measured for the earmuff/earplug combination. The attenuation for the earmuff/earplug combination (solid line) does not differ significantly from the sum of the earmuff and earplug objective attenuations (dashed line) below 500 Hz ($p>0.4$). This result supports the view that most low-frequency sound reaches the cochlea along the ear canal route, not through the head or body.[15] In contrast, at high frequencies (>500 Hz), the measured attenuation for the earmuff/earplug combination was significantly less than the sum of the objective attenuations for earmuffs and earplugs ($p<0.003$). The difference was greatest (20 dB) near 1.4 kHz. An interpretation of this disparity at high frequencies is that sound was conducted through the head and/or body to the ear canal medial to the earplug [Khanna *et al.*'s (1976) ''external ear component''] when the earmuff/earplug combination was worn.

Summed earmuff and earplug subjective attenuations are also shown in Fig. 6(B) along with subjective attenuations measured for the earmuff/earplug combination. The subjective attenuations for the earmuff/earplug combination (open symbols) were significantly less than the sum of the subjective attenuations for earmuffs and earplugs alone (filled symbols), by 20–35 dB for 1-, 1.4-, 2-, and 2.8-kHz tone bursts and imager noise ($p<0.03$ for all stimuli except 1.5-T imager noise and 1.4-kHz tone bursts—$p<0.06$). Thus, at high frequencies (>500 Hz), both subjective and objective attenuations for the earmuff/earplug combination were less than the summed earmuff and earplug attenuations. These comparisons support the view that, at high frequencies (>500 Hz), *sound conducted to the cochlea via the head and/or body limits the attenuation of earmuffs and earplugs when both are worn.*

c. Comparison with Berger's ''bone conduction limit.'' The importance of head and body conduction for the earmuff/earplug combination at high frequencies but not at low is further supported by a comparison of earmuff/earplug attenuations and Berger's (1983) ''bone conduction limit.''[16]

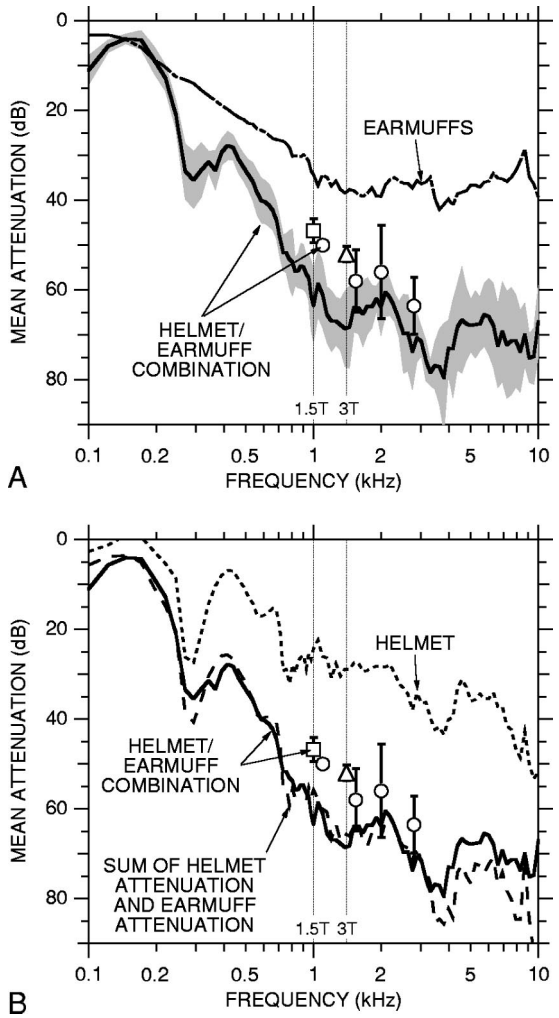

FIG. 7. (A) Mean objective and subjective attenuations for the helmet/earmuff combination ±1 s.d. (objective: solid curve and shading, six ears in six subjects; subjective: symbols and error bars, three subjects). Key to symbols and vertical lines as in Fig. 5. Also shown is the mean objective attenuation for earmuffs from Fig. 5(A) (dot-dashed curve). (B) Mean objective and subjective attenuations for the helmet/earmuff combination [solid curve and symbols from (A)], sum of mean earmuff and helmet objective attenuations (dashed curve), and mean objective attenuation for the helmet alone (dotted curve; six ears in six subjects).

Berger (1983) estimated his bone conduction limit by measuring subjective attenuations in subjects wearing deeply inserted earplugs and large lead earmuffs that presumably blocked sound conduction along the ear canal so that any perceived sound was conducted through the head and body (see also Zwislocki, 1957; Nixon and von Gierke, 1959).[17] Hence, the bone conduction limit is an upper bound on the noise reduction possible using hearing protection that treats only sound conduction along the ear canal (Berger, 1983, 1986a). At 500 Hz, subjective attenuation for the earmuff/earplug combination was below Berger's bone conduction limit [Fig. 6(C)], which further supports the idea that the ear canal was the dominant conduction route to the cochlea at 500 Hz. At 1 kHz and above, subjective attenuations were similar to Berger's bone conduction limit [Fig. 6(C)] which further supports the conclusion that head and/or body conduction are important at high frequencies (>500 Hz) when both earmuffs and earplugs are worn.

d. Summary. Our data are consistent with the view that, at low frequencies (≤500 Hz), the ear canal is the dominant sound conduction route to the cochlea when the earmuff/earplug combination is worn. Comparisons between objective and subjective attenuations and between individual and combined attenuations indicate that, *at higher frequencies, sound conduction through the head and/or body contributes significantly to the sound perceived by subjects wearing the earmuff/earplug combination*. Above 500 Hz, the sound is conducted through the head and/or body to the ear canal; at 1.4 kHz and above, sound is also conducted to the middle ear and cochlea.

D. Helmet and earmuffs in combination

1. Objective and subjective attenuations

To investigate whether reducing sound conduction through the head would lead to further attenuation with earmuffs beyond that possible with earplugs, we measured the attenuation provided by a ''helmet'' worn over earmuffs [Fig. 3(E)]. The mean objective attenuation for the ''helmet/earmuff combination'' [solid line in Fig. 7(A)] generally increased with increasing frequency up to approximately 1 kHz. Above 1 kHz, objective attenuations ranged from approximately 60–80 dB. Mean subjective attenuations for tone-burst stimuli [1, 1.4, 2, 2.8 kHz, circles in Fig. 7(A)] and imager noise (square and triangle) ranged from 47–64 dB. Subjective attenuations for 1.4-, 2-, and 2.8-kHz tone bursts were not significantly different from objective attenuations at corresponding frequencies, but subjective attenuations for all other stimuli were significantly less than objective attenuations at corresponding frequencies (by 11–16 dB; $p<0.02$). Our subjective attenuation data indicate that the helmet/earmuff combination reduced perceived sound by 47–58 dB in the frequency range of the imager noise (1–1.4 kHz)—see Table I.

2. Comparison of helmet/earmuff combination with earmuffs alone and with the earmuff/earplug combination

The helmet/earmuff combination provided more attenuation than earmuffs alone in most instances. For example, the mean objective attenuation for the helmet/earmuff combination was significantly greater than that for earmuffs at 250 Hz and above [$p<0.002$; Fig. 7(A)]. The mean subjective attenuations for the helmet/earmuff combination exceeded those for earmuffs alone by 15–29 dB ($p<0.005$; see Table I).

The helmet/earmuff combination also provided more attenuation at high frequencies than the earmuff/earplug combination. Mean objective attenuation was significantly greater for the helmet/earmuff combination at 1 kHz and above ($p<0.03$), except near 2 kHz ($p>0.1$). For 3-T imager noise and 1-, 1.4-, and 2.8-kHz tone bursts, mean subjective attenuations were significantly greater for the helmet/earmuff combination (9–19 dB) as compared to the earmuff/earplug combination ($p<0.04$; see Table I).

3. Reduction in sound conduction through the head and ear canal at high frequencies (>500 Hz)

Three lines of evidence indicate that the helmet/earmuff combination reduced sound conduction through the head as well as through the ear canal. First, the helmet/earmuff combination provided more subjective attenuation than the earmuff/earplug combination for 1-, 1.4-, and 2.8-kHz tone bursts and for 3-T imager noise. This is relevant because the attenuation provided by the earmuff/earplug combination at high frequencies (>500 Hz) was limited by conduction through the head and/or body, so the greater attenuation provided by the helmet/earmuff combination could be achieved only by a reduction in conduction through the head (since the helmet did not enclose the body). Second, subjective attenuations for the helmet/earmuff combination exceeded the estimated upper limit for ear canal attenuation [i.e., exceeded Berger's ''bone conduction limit'' in Fig. 6(C)] for most of the test stimuli (3-T imager noise and 1.4-, 2-, and 2.8-kHz tone bursts). This indicates that the helmet reduced sound transmission along an additional route, i.e., through the head. Third, the objective attenuation for the helmet/earmuff combination was approximately equal to the sum of the individual objective attenuations of the helmet and earmuffs [Fig. 7(B)], which indicates that little or no sound reached the ear canal by passing through the body, head, and ear canal walls.[18] In short, *the helmet proved effective in its intended function, reducing sound conduction through the head as well as the ear canal*.

4. Dominant conduction routes

Our deductions concerning the dominant routes of sound conduction for the helmet/earmuff combination are as follows. Our reasoning is based on our previous conclusion that, when earmuffs alone are worn, sound is conducted to the cochlea primarily along the ear canal rather than through the head or body. Placing the helmet over earmuffs presumably reduced the sound reaching the ear canal and head to the same degree and therefore did not alter the relative importance of the ear canal versus head conduction routes. This implies that sound conducted through the head contributed negligibly to the perceived sound when the helmet/earmuff combination was worn. Instead, the perceived sound was presumably dominated by sound conducted through the ear canal, body, or both.

The relative importance of ear canal vs body conduction at high frequencies (>500 Hz) can be deduced by considering the relationship between objective and subjective attenuations if only the ear-canal route were important and comparing this hypothetical situation with our data. If only ear-canal conduction were important, sound pressure in the ear canal would fully account for the sound perceived by a subject wearing the helmet/earmuff combination, so subjective and objective attenuations would be the same. Alternatively, if body conduction were important as well, objective and subjective attenuations would not necessarily be equal because subjects could hear sound conducted to the cochlea that bypassed the ear canal. Hence, any significant discrepancy between measured objective and subjective attenuations would imply that conduction through the body was important

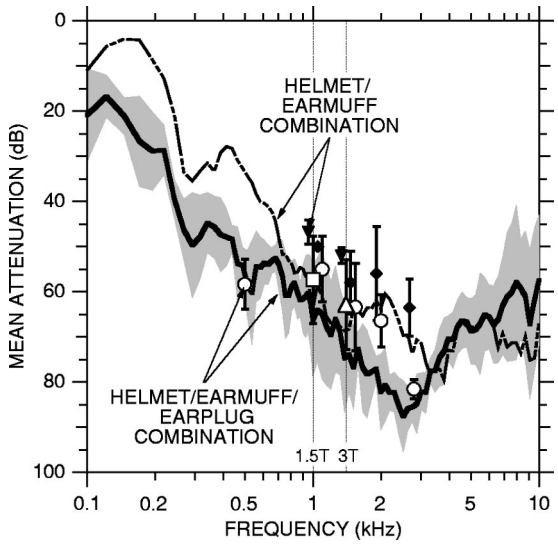

FIG. 8. Mean objective and subjective attenuations for the helmet/earmuff/earplug combination ±1 s.d. (objective: solid curve and shading, five ears in five subjects; subjective: symbols and error bars, five subjects). Key to symbols and vertical lines as in Fig. 5. Mean attenuations for the helmet/earmuff combination from Fig. 7(A) are shown for comparison [objective: dashed curve; subjective: solid inverted triangles (gradient noise) and solid diamonds (tone bursts)]. Solid symbols are offset slightly to the left for clarity.

(see Sec. III C 3). In fact, subjective and objective attenuations for the helmet/earmuff combination did differ significantly for 1-kHz tone bursts and 1.5- and 3-T imager noise, by 11–16 dB. Thus, conduction through the body apparently contributed to the sound heard when the helmet/earmuff combination was worn, at least at some frequencies. The fact that adding earplugs to the helmet/earmuff combination tended to increase subjective attenuations (see Sec. III E 2) supports the idea that conduction along the ear canal also contributed to the perceived sound when the helmet and earmuffs were worn. In short, we conclude that, *for the helmet/earmuff combination, the dominant routes of sound conduction to the cochlea at high frequencies (>500 Hz) are through the ear canal and body*.

In contrast to the situation at high frequencies, our data suggest that the ear canal is the dominant sound conduction route at low frequencies when the helmet/earmuff combination is worn. The reasoning follows from the earlier conclusion that the attenuation for the earmuff/earplug combination at low frequencies (≤500 Hz) was not limited by conduction through the head and body, i.e., conduction was mainly along the ear canal (Sec. III C 3). This conclusion, coupled with the fact that the objective attenuation for the helmet/earmuff combination was less than that for the earmuff/earplug combination at most low frequencies [compare solid lines in Figs. 6(A) and 7(A)], suggests that the ear canal was also the dominant conduction route for low-frequency sound when the helmet/earmuff combination was worn. Thus, *when the helmet/earmuff combination is worn, further low-frequency attenuation should be possible by reducing conduction along the ear canal*.

E. Helmet, earmuffs, and earplugs in combination

1. Objective and subjective attenuations

The attenuation provided by a helmet, earmuffs, and earplugs used together is shown in Fig. 8. Objective attenuation

increased with increasing frequency to a maximum of 87 dB near 2.5 kHz and then decreased with increasing frequency. Subjective attenuations for tone bursts at 0.5, 1, 1.4, and 2.8 kHz did not differ significantly from objective attenuations at corresponding frequencies ($p>0.1$ for all frequencies)—see Table I. However, the subjective attenuation for tone bursts at 2 kHz was significantly less ($p<0.008$). Subjective attenuations for 1.5- and 3-T imager noise (57 and 63 dB) did not differ significantly from the attenuations for tone bursts at 1 and 1.4 kHz (55 and 63 dB), respectively ($p>0.1$). All of our subjective attenuation data indicate that the helmet/earmuff/earplug combination reduces the perceived sound by approximately 60 dB in the frequency range of the imager noise (1–1.4 kHz).

2. Comparison of helmet/earmuff/earplug combination with helmet/earmuff and earmuff/earplug combinations

The attenuations provided by the helmet/earmuff/earplug combination and the helmet/earmuff combination can be compared using Fig. 8. For frequencies below 500 Hz and near 2–3 kHz, objective attenuations for the helmet/earmuff/earplug combination were significantly higher than those for the helmet/earmuff combination ($p<0.008$); near 1 and 1.4 kHz and above 3 kHz there was no significant difference ($p>0.5$). The mean subjective attenuations for the helmet/earmuff/earplug combination (open symbols in Fig. 8) were systematically higher than those for the helmet/earmuff combination (filled symbols), although the difference in attenuation was significant only for 1.5-T imager noise ($p<0.05$; Fig. 8, Table I; note that no subjective data were taken at 500 Hz for the helmet/earmuff combination). Overall, the addition of earplugs to the helmet/earmuff combination tended to increase attenuation at most frequencies.

The subjective attenuations provided by the helmet/earmuff/earplug and earmuff/earplug combinations can be compared using Table I. For every stimulus, attenuations were substantially greater (5–18 dB) for the helmet/earmuff/earplug combination. This result allows a refinement of the earlier conclusion that the head and/or body conduction routes are important at high frequencies when the earmuff/earplug combination is worn (Sec. III C 3). The substantial increase in subjective attenuation that is produced by adding a helmet to the earmuff/earplug combination indicates that *it is specifically head conduction that dominates at high frequencies when earmuffs and earplugs are worn together*.

3. Dominant conduction routes

Our deductions concerning sound conduction routes at high frequencies (>500 Hz) for the helmet/earmuff/earplug combination begin with a previous conclusion: For the helmet/earmuff combination, the dominant routes of sound conduction at high frequencies were through the ear canal and body. When earplugs were added to the helmet/earmuff combination (yielding the helmet/earmuff/earplug combination), sound conduction through the ear canal was presumably reduced substantially, by an amount equal to the objective attenuation of earplugs [23–41 dB for frequencies >500 Hz; Fig. 5(B)] making conduction through the ear canal negligible compared to conduction through the body. Thus, *the dominant route by which high-frequency sound was conducted to the cochlea for the helmet/earmuff/earplug combination was probably through the body*.

Two results provide information about the dominant routes of sound conduction at low frequencies ($\leqslant$ 500 Hz) for the helmet/earmuff/earplug combination: (1) At 500 Hz, the subjective attenuation for the helmet/earmuff/earplug combination was approximately equal to the objective attenuation (Fig. 8), indicating that sound primarily reached the cochlea via the ear canal. (2) Adding earplugs to the helmet/earmuff combination increased objective attenuation significantly at low frequencies (Fig. 8). In fact, the increase was approximately equal to the attenuation measured for earplugs alone [Fig. 5(B)]. This additivity suggests that (a) most low-frequency sound was conducted along the ear canal, and (b) conduction to the ear canal through the head or body was not important at low frequencies when the helmet/earmuff/earplug combination was worn.

IV. DISCUSSION

Our experiments demonstrated that a helmet shielding the head can provide substantial additional attenuation beyond that provided by conventional devices for isolating individuals from sound, namely earmuffs and earplugs. In the course of these demonstrations, we systematically determined both objective (ear canal) and subjective attenuations for various combinations of isolating devices. These data enabled deductions concerning the relative importance of three different sound conduction routes to the cochlea: along the ear canal, through the head, and through the body.

A. Relative importance of sound conduction routes

1. High frequencies

Our measurements were focused on high frequencies (>500 Hz), where fMRI noise levels are highest. At high frequencies, routes other than the ear canal were clearly important for several device configurations: the earmuff/earplug combination, the helmet/earmuff combination, and the helmet/earmuff/earplug combination.

The relative importance of the various conduction routes can be estimated quantitatively by combining our attenuation data with the model in Fig. 1. Estimates of sound conduction for the frequency range of the predominant gradient noise (1–1.4 kHz) are given in Fig. 9. For each combination of isolation devices, and for no isolation, estimates of sound conduction for the ear canal, head, and body routes are given in dB relative to conduction through the ear canal when no isolation devices are worn.

The estimates of ear canal, head, and body conduction in Fig. 9 were made as follows. When no isolation devices are worn, the *ear canal* is the dominant route of sound conduction to the cochlea, and the level of ear-canal conduction is set to 0 dB, the maximum (Fig. 9, far left). When there are various combinations of earmuffs, earplugs, or helmet (Fig. 9, four right-most columns), ear-canal conduction is reduced from maximum by the total attenuation along the ear-canal route. For earmuffs or earplugs, this is just the earmuff or earplug attenuation in the frequency range of the predomi-

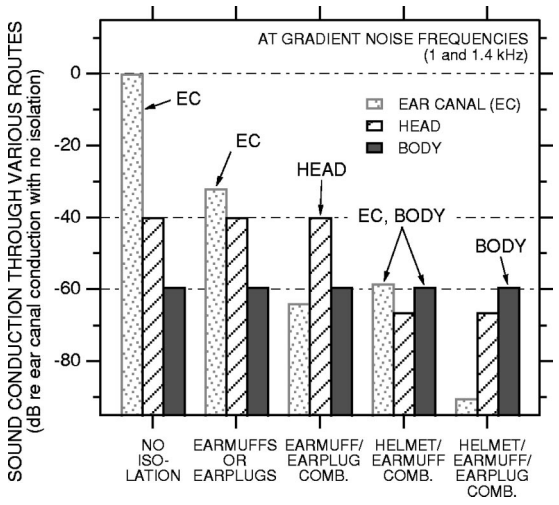

FIG. 9. Estimates of sound conduction to the cochlea through the ear canal, head, and body at frequencies of imager gradient noise, for five conditions: no isolation devices, earmuffs or earplugs, the earmuff/earplug combination, the helmet/earmuff combination, and the helmet/earmuff/earplug combination. Contribution from each route to the perceived sound is indicated in dB relative to conduction along the ear canal with no isolation. Labels above bars indicate the dominant route(s) of sound conduction for each condition (EC: ear canal).

nant gradient noise (the estimates in Fig. 9 are based on an average of the attenuations at 1 and 1.4 kHz). When there are multiple devices, we assumed that the total ear-canal attenuation was the sum of objective attenuations (in dB) provided by each individual device since sound passes through the various devices serially on its way to and along the ear canal (Fig. 1; e.g., for the helmet/earmuff/earplug combination, ear-canal attenuation was calculated as the sum of the individual helmet, earmuff, and earplug objective attenuations).[19]

The level of sound conducted through the *head* was estimated from our subjective attenuation data for the earmuff/earplug combination. For this device configuration, we concluded that sound conduction along the ear canal was reduced to the point that conduction through the head dominated the perceived sound (Secs. III C 3 and III E 2). Therefore, in Fig. 9 the head contribution for this configuration is below the ear-canal contribution with no isolation (0 dB) by an amount equal to the earmuff/earplug subjective attenuation (approximately 40 dB). For the purposes of this figure, we assume that the amount of sound conducted through the head (relative to maximum) is the same for no isolation as for the earmuff/earplug combination.[20] For the device configurations that included the helmet, head conduction in Fig. 9 was reduced by an amount equal to the objective attenuation of the helmet (based on the assumption that the helmet reduced conduction to the head and ear canal by the same amount).

The level of sound conduction through the *body* when there is no isolation was estimated from our subjective attenuation data for the helmet/earmuff/earplug combination. For this device configuration, we concluded that sound conduction along the ear canal and through the head was reduced to the point where conduction through the body dominated the perceived sound. Therefore, in Fig. 9 the body contribution is below maximum by an amount equal to the helmet/earmuff/earplug attenuation (approximately 60 dB). Presumably, none of the devices we studied affected the body route to the cochlea, so the amount of sound conducted through the body (relative to maximum) is the same for all of the situations in Fig. 9.

The relative importance of ear canal, head, and body conduction to the cochlea for various device configurations can be seen from Fig. 9. When there is no isolation (Fig. 9, far left), the ear canal is by far the dominant route of sound conduction. Even when conduction along the ear canal is reduced by earmuffs or earplugs (Fig. 9, second from left), the ear canal remains the dominant route. However, when earmuffs and earplugs are used together, conduction along the ear canal is reduced to the point that head conduction is most important (Fig. 9, middle). For the helmet/earmuff combination, the helmet reduced conduction through the head as well as along the ear canal; consequently, the head route is less important than the ear canal and body routes, and the ear canal and body routes are comparable in importance (Fig. 9, second from right). When earplugs are added to the helmet/earmuff combination, ear-canal conduction is reduced, and the dominant route of conduction is through the body.

2. Low frequencies

Our attenuation data at low frequencies ($\leqslant$ 500 Hz) are consistent with the idea that the ear canal was the dominant conduction route for every device configuration considered. However, it is likely that other routes would have become important if we had attempted to explore the limits of attenuation achievable at low frequencies. For instance, the low-frequency attenuations we measured for the earmuff/earplug combination are less than the maximum achievable because we used earplug insertion depths typical of everyday use, rather than the maximum insertion depth possible. Berger (1983) has shown that conduction through routes other than the ear canal can be significant at low frequencies as well when earmuffs are used with deeply inserted earplugs. In these circumstances, the helmet should still provide additional low-frequency attenuation.

B. Sound conduction to the cochlea under imaging conditions

The conditions under which our measurements were made differ from those in an imager, which raises the possibility that the relative importance of the ear canal, head, and body routes might be different during imaging. For our measurements, the subject was seated in a chair, their head was unsupported, and sound was delivered from a point source some distance away. In the imager, the subject's position and the acoustic environment are different: (1) the subject typically lies supine on a patient table with their head in a head coil. The subject's head rests on the head coil, and there may be cushioning material packed between the head and the head coil to prevent the head from moving. Additionally, the subject may hold a bite bar, which is rigidly attached to the head coil, in his/her mouth to keep the head still. (2) Gradient noise comes from gradient coils surrounding the subject rather than from a point source. (3) The patient table may

vibrate in response to gradient coil or coolant pump activity. Consequently, unlike the experimental conditions of the present study, vibrations may be transmitted to the subject's head through the head coil or bite bar or to the head or body through the patient table. Hence, the importance of the head and body conduction routes relative to the ear canal could be higher in the imager than in the experimental setup in the soundproof room.

C. Achieving further noise reduction

1. Gradient noise

As we have seen, at the predominant frequencies of imager gradient noise, sound conduction through the head limits the effectiveness of devices that treat only the ear canal (e.g., earmuffs, earplugs, ''noise-canceling'' headsets—see the next section), and sound conduction through the body limits the effectiveness of the helmet (which treats only the head and ear canal). Thus, reductions at gradient noise frequencies beyond those demonstrated here will require reducing noise reaching the subject's body as well as the head and ear canal.

One way to achieve further noise reduction would be to enclose the entire subject in sound-attenuating material—a logical extension of the helmet. The idea is that the subject would lie in a sound-attenuating enclosure during imaging. The enclosure would contain integral ventilation, monitoring, and communication equipment. In fact, using the enclosure might be more expedient for imaging purposes than fitting a subject with a helmet. If the enclosure were double-walled, the attenuation provided might be increased further by drawing a vacuum between the inner and outer walls and isolating the inner wall mechanically from the outer wall, perhaps with active vibration isolation mounts. The attenuation provided by such an enclosure used with earmuffs and earplugs would presumably be greater than that provided by the helmet/earmuff/earplug combination because the enclosure, unlike the helmet, would reduce transmission to the body as well as the head.

An alternative to the enclosure just described is to modify the imager to reduce noise transmission from the gradient coils to the subject (Ravicz *et al.*, 1999, 2000). The feasibility of this approach was demonstrated in a preliminary experiment which showed that lining the imager patient tube (in which the subject lies) with acoustic barrier–foam composite reduced gradient noise levels in the imager by approximately 12 dB (Ravicz *et al.*, 1999). This represents only a simple imager treatment; further reductions should be possible with additional treatment.

2. Pump and air-handling noise

Even with the helmet/earmuff/earplug combination, the ear canal was probably still the dominant sound conduction route in the frequency range of the pump and air-handling noise ($\leqslant$ 500 Hz; see Sec. III E 3), so additional reduction in the noise heard at these frequencies should be achievable by further reducing sound conducted along the ear canal. Additional reduction should be achievable by inserting the earplugs more deeply into the ear canal than they were in this study (e.g., Berger, 1983). A second approach for achieving further reductions is active noise reduction (ANR or ''active cancellation''), which involves generating an inverted copy of the noise waveform and introducing it at or near the ear to interfere destructively with the noise (e.g., Elliott and Nelson, 1993). ANR can typically provide 10–20 dB of attenuation at low frequencies when applied in a small volume such as that under an earmuff (e.g., Casali and Berger, 1996; McKinley *et al.*, 1996), and ANR systems have been developed for MRI applications (Goldman *et al.*, 1989; Pla *et al.*, 1995; Palmer, 1998). It is unlikely that substantial additional reductions can be achieved through design improvements to earmuffs or earplugs because the technology of these devices is relatively mature. In fact, most commercially available earmuffs and earplugs provide nearly as much attenuation as experimental devices optimized for noise reduction (at the expense of comfort or practicality—Zwislocki, 1957; Berger, 1983). Of course, the enclosure described in the previous section for reducing gradient noise would also presumably reduce pump and air-handling noise.

D. Noise reduction during imaging versus other high-noise situations

Because the imaging environment has different demands of noise reduction than most industrial environments, more noise reduction options are available during fMRI. For most industrial environments, earmuffs or earplugs may be the only acceptable options for noise reduction because: (1) any noise attenuation devices must be comfortable to wear for a work shift; (2) the devices cannot limit the worker's mobility; and (3) noise attenuation must not be so high that a worker's awareness of his/her surroundings and ability to communicate are impaired. In contrast, for fMRI (1) noise attenuation devices need be comfortable only for the duration of the imaging experiment (e.g., 1–3 h); (2) the subject is immobile, so any contraints that mobility places on devices are not applicable; and (3) maintaining the subject's awareness of his/her surroundings is less important (in fact, some subjects may be more comfortable if they are less aware of their surroundings), and communication can be maintained through a headset (e.g., Savoy *et al.*, 1999). Hence, for noise reduction during imaging, the emphasis can be more on maximal noise isolation without the compromises for comfort, mobility, awareness, and communication required in industrial environments. People exposed to high noise levels in other environments in which the constraints listed above do not apply may benefit from the noise reduction techniques discussed in this paper.

E. Predicted imager noise levels experienced by subjects

Our attenuation data can be combined with measurements of fMRI noise levels to estimate the effective noise levels experienced by subjects wearing various combinations of isolation devices. Estimates for a given device combination were obtained by subtracting the measured subjective attenuations to 1.5- and 3-T imager noise for the device combination from gradient noise levels measured in 1.5- and 3-T

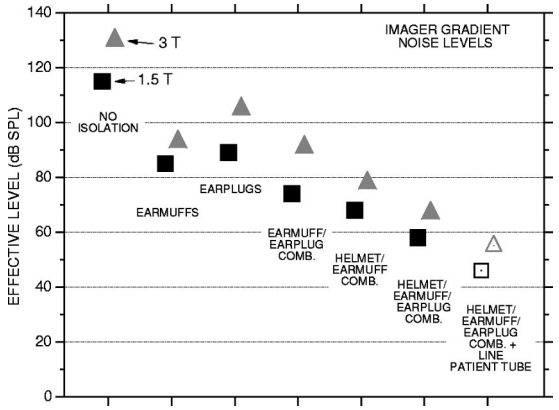

FIG. 10. Effective gradient noise levels experienced by subjects during fMRI in 1.5-T and 3-T imagers (squares and triangles, respectively). The levels shown were measured directly (no isolation) or computed for various devices or combinations of devices (filled symbols). Also shown are estimated noise levels for the helmet/earmuff/earplug combination with the imager patient tube lined with acoustic barrier–foam composite (open symbols).

imagers, respectively. With no isolation, gradient noise levels were 115 dB SPL in the 1.5-T imager and 131 dB SPL in the 3-T imager (Fig. 10; Ravicz *et al.*, 2000).[21] With the combination of the helmet, earmuffs, and earplugs, we estimate that the effective gradient noise levels experienced by a subject would be reduced to approximately 58 dB SPL in the 1.5-T imager and 68 dB SPL in the 3-T imager. If, in addition, the imager patient tube is lined with acoustic barrier–foam composite (such as that used for helmet construction; Ravicz *et al.*, 1999), effective gradient noise levels may be reduced further to 46–56 dB SPL for the 1.5- and 3-T imager, respectively.[22]

Two important points are illustrated by Fig. 10: (1) Substantial reductions in the noise levels experienced by subjects can be achieved using a combination of conventional hearing protection devices and other devices (such as the helmet) that isolate subjects from the imager noise. (2) Even if all of the isolation methods described in this paper are used simultaneously, imager noise levels will still be well within the audible range. Achieving quiet experimental conditions during fMRI may require that less noise be produced by the imager.

V. SUMMARY AND CONCLUSIONS

(1) Even when earmuffs and earplugs are used together to reduce acoustic noise levels during fMRI, the levels are high enough to interfere with investigations of the central auditory system.

(2) We determined that further reductions in imager noise can be achieved using a helmet enclosing the head, in addition to earmuffs and earplugs. In the frequency range of the most intense imager noise (i.e., gradient noise), the attenuation provided by earmuffs and earplugs is limited by sound conduction through the head. The helmet can be used to overcome this limit because it shields the head as well as the ear canal from sound.

(3) When a helmet, earmuffs, and earplugs are used together, the remaining gradient noise heard by a subject is conducted mainly through the body. This indicates that the level of noise experienced by a subject could be reduced even further by shielding the entire body from the surrounding noise field.

(4) Using a combination of attenuation techniques, it is possible to bring the conditions during fMRI substantially closer to the quiet conditions more typical of physiological and psychophysical studies of hearing.

ACKNOWLEDGMENTS

The authors wish to extend their sincere thanks to the subjects for the attenuation experiments. We also wish to thank: Dr. Laurie Heller at the Naval Submarine Medical Research Laboratory and Dr. Christopher Halpin of the MEEI Audiology Dept. for helpful discussions on military and government noise exposure standards and hearing protection; Susan E. Voss for technical assistance with earplugs; Elliott H. Berger at E·A·R for helpful comments; John Guinan, Greg Huang, Nelson Kiang, Bill Peake, John Rosowski, and Susan Voss at the Eaton-Peabody Laboratory for comments on earlier versions of the manuscript; Knowles Electronics for supplying microphones; Irina Sigalovsky for creating the illustration in Fig. 2; Barbara E. Norris for help with figures; and the staff of the Eaton-Peabody Laboratory. Supported in part by NIH NIDCD Grant No. P01 DC00119.

[1]These were General Electric imagers outfitted for echo-planar imaging by ANMR, Inc.

[2]In this paper we consider sound conduction through the head separately from sound conduction through the rest of the body.

[3]The ratings are similar because both composites used for the helmets contain the same barrier layer (and the barrier layer, rather than foam layer(s), primarily determines attenuation). The heavy vinyl barrier layer in the composites provides an impedance mismatch that reduces sound transmission. The foam layer mechanically decouples the barrier layer from surfaces touching the composite.

[4]We located the sound source at 90° because we had no access to a suitable reverberant room [as specified in ANSI S12.6 (1996)]. The results we obtained for earmuffs and earplugs were similar to those obtained by others in reverberant rooms (e.g., Berger *et al.*, 1998)—see Sec. III. Since our experiments compared noise reduction devices rather than rating the performance of any one device, and since the experimental conditions did not change between measurements with different devices or combinations of devices, our conclusions should be unaffected by the discrepancy between our measurement conditions and those specified in ANSI S12.6.

[5]This experimental configuration was used so that objective and subjective attenuations would reflect sound reaching the same ear [i.e., the subject's left in Fig. 3(A)] for no isolation [Fig. 3(A)], earplugs [Fig. 3(B)], or earmuffs [Fig. 3(C)]. Sound-pressure measurements were always made in the ear canal closest to the loudspeaker. We assumed that behavioral thresholds would be indicative of the levels of sound reaching the cochlea closest to the loudspeaker for the ''no isolation,'' ''earmuff,'' and ''earplug'' configurations because (a) the ear furthest from the loudspeaker was ''shadowed'' by the head over the frequency range of our threshold measurements (e.g., by 3–6 dB at 500 Hz, 9–12 dB at 2 kHz—Feddersen *et al.*, 1957; Shaw, 1966, 1974); (b) for ''no isolation'' or ''earmuffs,'' more sound attenuation material was present on the ear furthest from the loudspeaker, and (c) the ear canal was the dominant sound conduction route to the cochlea (Sec. III A). (See Sec. II E for a discussion of the situation when the ear canal is not the dominant route.)

[6]In all cases, the earplug expanded to form a tight seal between the outer probe tube wall and the earplug.

[7]Though a ''deep'' earplug insertion (Berger, 1983, 1986b) may have been more appropriate for studies of conduction routes at low frequencies (i.e., $\leqslant$ 500 Hz) because more attenuation could be achieved, the differences in attenuation between a partial, standard, and deep insertion were expected to be small in the frequency range of gradient noise (1 kHz and above), especially when used in combination with earmuffs (Berger, 1983).

[8]We chose these stimuli to provide the most direct test of the attenuation of imager noise. They differ from the stimuli specified for use in assessing the attenuation of hearing protection devices (i.e., octave or 1/3 octave band noise; ANSI S12.6—1997). An alternative approach in keeping with standard procedures would have been to (a) measure the attenuation with standard stimuli, and (b) infer the attenuation of imager noise from these measurements and the noise spectrum. The similarity of our earmuff and earplug results to those obtained with standard stimuli suggests that the two methods are equivalent in our case (see Sec. III B).

[9]This masking is one manifestation of the ''occlusion effect'' described in the audiological literature (e.g., Goldstein and Newman, 1994). The occlusion effect refers to the observation that the sound pressure within the ear canal generated by vibration of the ear canal walls increases when the ear canal is occluded (e.g., Goldstein and Hayes, 1965; Schroeter and Poesselt, 1986). Causes of ear-canal wall vibration include physiological processes (e.g., Berger and Kerivan, 1983) or externally applied sound or vibrations conducted through the head (e.g., Khanna *et al.*, 1976).

[10]The objective attenuation curves throughout this paper have been interpolated above 1 kHz from the linear frequency spacing of the stimulus chirp (12 Hz) to a logarithmic frequency spacing (15 pts./octave).

[11]The objective attenuations used for these comparisons were calculated as follows. First, for each studied ear, the objective attenuation data were interpolated as described in Footnote 10. The attenuation at a given frequency was the geometric mean of three points on the interpolated curve, centered at the frequency of interest. The attenuations calculated in this way for each studied ear were then averaged, yielding a mean and standard deviation of the objective attenuation that was then compared with subjective attenuation.

[12]Note that most of these studies measured subjective attenuation using third-octave-band noise rather than tone bursts as we did. The use of tone pulses (longer in duration and with longer rise/fall times than our tone bursts) rather than noise was shown in one set of studies to overestimate broadband attenuation by 2–4 dB (Waugh, 1974, 1984; Berger, 1986b). However, another study showed that pure tones on average underestimated the attenuation of earmuffs by 2.1 dB at 500 Hz and above (Casali *et al.*, 1995). These over- or underestimations are in almost every case less than the standard deviations in our measurements.

[13]Khanna *et al.* (1976) reached a similar conclusion in experiments examining conduction through the head to the ear canal, middle ear, and cochlea. They delivered vibratory stimuli to two subjects' foreheads and determined the level and phase of an acoustic stimulus required to cancel the subject's perception of the vibratory stimulus. They concluded that conduction through the head to the middle ear and cochlea became dominant above 3 kHz. In addition, they argued that the frequency range of Carhart's notch (a decrease in clinical bone conduction sensitivity in cases of otosclerotic fixation of the stapes that is most significant between 1 and 2 kHz; e.g., Robinette, 1994) indicates that conduction to the middle ear is negligible above 2 kHz.

[14]Sources of interaction between earmuffs and earplugs that have been proposed are (1) an increase in sound pressure lateral to earplugs due to an increase in the ear canal radiation impedance by earmuffs; (2) an increase in sound pressure medial to earmuffs due to an increase in the ear canal input impedance by earplugs (see Schroeter and Poesselt, 1986); and (3) vibrational coupling through the tissue lining the ear canal (Shaw, 1982). To our knowledge, no definitive evidence exists that there is an interaction between earmuffs and earplugs, and evidence in the present study indicates that any interaction is negligible at 500 Hz and below (see Footnote 15). We anticipate that any interaction at higher frequencies would not be important for the following reasons: (1) The magnitude of the radiation impedance is comparable to the impedance of the volume under earmuffs above about 1 kHz (Schroeter and Poesselt, 1986); (2) the volume occupied by an earplug is only a few percent of the total volume under earmuffs; and (3) as frequency increases, the mass of the tissue lining the ear canal should limit its vibration. (This last point is supported by the fact that the occlusion effect decreases to near zero above about 1.5 kHz.)

[15]The fact that the objective attenuation for the earmuff/earplug combination does not differ significantly from the sum of the earmuff and earplug objective attenuations below 500 Hz also indicates that any interaction between earmuffs and earplugs is negligible in this frequency range.

[16]Note that Berger's ''bone conduction limit'' applies to sound conducted from air to the head, as opposed to the bone conduction commonly referred to by clinicians, which applies to vibrations coupled to the head mechanically (e.g., Dirks, 1994).

[17]Results similar to Berger's were obtained by Schroeter and Poesselt (1986) in unoccluded ears (''MAFB–MAF'') using large-volume earmuffs in concert with active noise reduction at low frequencies and foam earplugs at high frequencies.

[18]No subjective attenuation data were taken with the helmet alone because the ventilation air produced a masking noise. This noise could not be heard by subjects wearing earmuffs or earplugs, so it was not a problem for measurements of subjective attenuations for the helmet/earmuff or helmet/earmuff/earplug combinations.

[19]Again, we assume that interactions between devices are negligible.

[20]The contribution of sound conduction through the head may be overestimated in the case where no isolation is used, due to the occlusion effect (see Footnote 9), because sound conduction through the head was determined from measurements with the ear canal occluded. For sound conducted from a free field, the magnitude of the occlusion effect (measured behaviorally) is about 5–10 dB at 1–1.25 kHz and negligible at 1.6 kHz and above (though as high as 20–25 dB at low frequencies; ''subjective OE,'' Schroeter and Poesselt, 1986). The magnitude of the occlusion effect is similar for earmuffs and for earplugs inserted only into the cartilaginous ear canal, as ours were (Berger and Kerivan, 1983; Schroeter and Poesselt, 1986). For simplicity, we have chosen to use the same value of sound conduction through the head for both the open and occluded cases. Because all other configurations shown include earmuffs and/or earplugs, the occlusion effect is taken into account.

[21]The levels given are time-average levels calculated over a 10-ms window that included the peak in the gradient noise. These levels (115 dB for 1.5 T, 131 dB for 3 T) are unweighted and change by less than 1 dB if an A- or C-frequency weighting is applied. (These weightings account for the frequency dependence of human equal-loudness curves, e.g., Earshen, 1986.)

[22]This assumes that the 12-dB reduction in noise achieved by lining the patient tube would add to the attenuation provided by the helmet/earmuff/earplug combination.

ANSI (**1997**). ANSI S12.6-1997, ''Methods for measuring the real-ear attenuation of hearing protectors'' (American National Standards Institute, New York).

Bandettini, P. A., Jesmanowicz, A., Van Kylen, J., Birn, R. M., and Hyde, J. S. (**1998**). ''Functional MRI of brain activation induced by scanner acoustic noise,'' Magn. Reson. Med. **39**, 410–416.

Berger, E. H. (**1983**). ''Laboratory attenuation of earmuffs and earplugs both singly and in combination,'' Am. Ind. Hyg. Assoc. J. **44**, 321–329.

Berger, E. H. (**1986a**). ''Hearing protection devices,'' in *Noise and Hearing Conservation Manual*, edited by E. H. Berger, J. C. Morrill, W. D. Ward, and L. H. Royster (American Industrial Hygiene Association, Akron, OH), pp. 319–382.

Berger, E. H. (**1986b**). ''Methods of measuring the attenuation of hearing protection devices,'' J. Acoust. Soc. Am. **79**, 1655–1687.

Berger, E. H., Franks, J. R., Behar, A., Casali, J. G., Dixon-Ernst, C., Kieper, R. W., Merry, C. J., Mozo, B. T., Nixon, C. W., Ohlin, D., Royster, J. D., and Royster, L. H. (**1998**). ''Development of a new standard laboratory protocol for estimating the field attenuation of hearing protection devices. III. The validity of using subject-fit data,'' J. Acoust. Soc. Am. **103**, 665–672.

Berger, E. H., Franks, J. R., and Lindgren, F. (**1996**). ''International Review of Field Studies of Hearing Protector Attenuation,'' in *Scientific Basis of Noise-Induced Hearing Loss*, edited by A. Axelsson, H. M. Borchgrevink, R. P. Hamernik, P. A. Hellstrom, D. Henderson, and R. J. Salvi (Thieme, New York), pp. 361–377.

Berger, E. H., and Kerivan, J. E. (**1983**). ''Influence of physiological noise and the occlusion effect on the measurement of real-ear attenuation at threshold,'' J. Acoust. Soc. Am. **74**, 81–94.

Casali, J. G., and Berger, E. H. (**1996**). ''Technology advancements in hearing protection circa 1995: Active noise reduction, frequency/amplitude sensitivity, and uniform attenuation,'' Am. Ind. Hyg. Assoc. J. **57**, 175–185.

Casali, J. G., Mauney, D. W., and Burks, J. A. (**1995**). ''Physical vs psychophysical measurement of hearing protector attenuation—a.k.a. MIRE vs REAT,'' Sound Vib. **29**(7), 20–27.

Cohen, M. (**1998**). ''Theory of echo-planar imaging,'' in *Echo-Planar Imaging: Theory, Technique and Application*, edited by F. Schmitt, M. K. Stehling, and R. Turner (Springer, Berlin), pp. 11–30.

Dirks, D. D. (**1994**). ''Bone-conduction threshold testing,'' in *Handbook of Clinical Audiology*, edited by J. Katz (Williams and Wilkins, Baltimore), pp. 132–146.

Earshen, J. J. (**1986**). ''Sound measurement: Instrumentation and noise descriptors,'' in *Noise and Hearing Conservation Manual*, edited by E. H. Berger, W. D. Ward, J. C. Morrill, and L. H. Royster (American Industrial Hygiene Association, Akron, OH), pp. 37–95.

Eden, G. F., Joseph, J. E., Brown, H. E., Brown, C. P., and Zeffiro, T. A. (**1999**). ''Utilizing hemodynamic delay and dispersion to detect fMRI signal change without auditory interference: The behavior interleaved gradients technique,'' Magn. Reson. Med. **41**, 13–20.

Edmister, W. B., Talavage, T. M., Ledden, P. J., and Weisskoff, R. M. (**1999**). ''Improved auditory cortex imaging using clustered volume acquisitions,'' Hum. Brain Mapping **7**, 89–97.

Elliott, S. J., and Nelson, P. A. (**1993**). ''Active noise control,'' IEEE Signal Process. Mag. **10**(4), 12–35.

EPA (**1979**). ''Noise labeling requirements for hearing protectors,'' Environmental Protection Agency, Fed. Regist. 44(190): 40CFR Part 21, pp. 56120–56147.

Feddersen, W. E., Sandel, T. T., Teas, D. C., and Jeffress, L. A. (**1957**). ''Localization of high-frequency tones,'' J. Acoust. Soc. Am. **29**, 988–991.

Goldman, A. M., Gossman, W. E., and Friedlander, P. C. (**1989**). ''Reduction of sound levels with antinoise in MR imaging,'' Radiology **171**, 549–550.

Goldstein, D. P., and Hayes, C. S. (**1965**). ''The occlusion effect in bone conduction hearing,'' J. Speech Hear. Res. **8**, 137–148.

Goldstein, B. A., and Newman, C. W. (**1994**). ''Clinical masking: A decision-making process,'' in *Handbook of Clinical Audiology*, edited by J. Katz (Williams and Wilkins, Baltimore), pp. 109–131.

Hall, D. A., Haggard, M. P., Akeroyd, M. A., Palmer, A. R., Summerfield, A. Q., Elliott, M. R., Gurney, E., and Bowtell, R. W. (**1999**). ''Sparse' temporal sampling in auditory fMRI,'' Hum. Brain Mapping **7**, 213–223.

Hurwitz, R., Lane, S. R., Bell, R. A., and Brant-Zawadzki, M. N. (**1989**). ''Acoustic analysis of gradient-coil noise in MR imaging,'' Radiology **173**, 545–548.

Khanna, S. M., Tonndorf, J., and Queller, J. E. (**1976**). ''Mechanical parameters of hearing by bone conduction,'' J. Acoust. Soc. Am. **60**, 139–154.

McKinley, R. L., Steuver, J. W., and Nixon, C. W. (**1996**). ''Estimated Reductions in Noise-Induced Hearing Loss by Application of ANR Headsets,'' in *Scientific Basis of Noise-Induced Hearing Loss*, edited by A. Axelsson, H. M. Borchgrevink, R. P. Hamernik, P. A. Hellstrom, D. Henderson, and R. J. Salvi (Thieme, New York), pp. 347–360.

Melcher, J. R., Talavage, T. M., and Harms, M. P. (**1999**). ''Functional MRI of the Auditory System,'' in *Medical Radiology, Diagnostic Imaging and Radiation Oncology: Functional MRI*, edited by C. Moonen and P. Bandettini (Springer, Berlin), pp. 393–406.

Moore, B. C. J. (**1997**). *An Introduction to the Psychology of Hearing* (Academic, London).

Nixon, C. W. (**1979**). ''Hearing protective devices: Ear protectors,'' in *Handbook of Noise Control*, edited by C. M. Harris (McGraw-Hill, New York), pp. 12-1–12-13.

Nixon, C. W., and von Gierke, H. E. (**1959**). ''Experiments on the bone-conduction threshold in a free sound field,'' J. Acoust. Soc. Am. **31**, 1121–1125.

Palmer, A. R. (**1998**). Personal communication to M.E.R.

Pla, F. G., Sommerfeldt, S. D., and Hedeen, R. A. (**1995**). ''Active control of noise in magnetic resonance imaging,'' *Proceedings of Active 95* (Noise Control Foundation: Poughkeepsie, NY), pp. 573–582.

Press, W. H., Flannery, B. P., Teukolsky, S. A., and Vetterling, W. T. (**1988**). *Numerical Recipes in C* (Cambridge University Press, Cambridge).

Prieto, T. E., Bennett, K., and Weyers, D. (**1998**). ''Acoustic noise levels in a head gradient coil during echo planar imaging,'' Proceedings of the International Society for Magnetic Resonance in Medicine, Sixth Scientific Meeting and Exhibition, p. 750.

Ravicz, M. E., Melcher, J. R., and Kiang, N.Y.-S. (**2000**). ''Acoustic noise during functional magnetic resonance imaging,'' J. Acoust. Soc. Am. **108**, 1683–1696.

Ravicz, M. E., Melcher, J. R., and Wald, L. L. (**1999**). ''Reducing acoustic noise transmission from gradient coils to subject during fMRI: An approach and preliminary results,'' NeuroImage **9**, S1.

Robinette, M. S. (**1994**). ''Integrating audiometric results,'' in *Handbook of Clinical Audiology*, edited by J. Katz (Williams and Wilkins, Baltimore), pp. 181–194.

Royster, J. D. (**1996**). ''Occupational and forensic audiology,'' Curr. Opin. Otolaryngol. Head Neck Surgery **4**, 345–352.

Royster, J. D., Berger, E. H., Merry, C. J., Nixon, C. W., Franks, J. R., Behar, A., Casali, J. G., Dixon-Ernst, C., Kieper, R. W., Mozo, B. T., Ohlin, D., and Royster, L. H. (**1996**). ''Development of a new standard laboratory protocol for estimating the field attenuation of hearing protection devices. I. Research of Working Group 11, Accredited Standards Committee S12, Noise,'' J. Acoust. Soc. Am. **99**, 1506–1526.

Savoy, R. L., Ravicz, M. E., and Gollub, R. (**1999**). ''The Psychophysiological Laboratory in the Magnet: Stimulus Delivery, Response Recording, and Safety,'' in *Medical Radiology, Diagnostic Imaging and Radiation Oncology: Functional MRI*, edited by C. Moonen and P. Bandettini (Springer, Berlin), pp. 347–365.

Schmitt, F., Irnich, W., and Fischer, H. (**1998**). ''Physiological side effects of fast gradient switching,'' in *Echo-Planar Imaging: Theory, Technique and Application*, edited by F. Schmitt, M. K. Stehling, and R. Turner (Springer, Berlin), pp. 201–252.

Schroeter, J., and Poesselt, C. (**1986**). ''The use of acoustical test fixtures for the measurement of hearing protector attenuation. II. Modeling the external ear, simulating bone conduction, and comparing test fixture and real-ear data,'' J. Acoust. Soc. Am. **80**, 505–527.

Shah, N. J., Jäncke, L., Grosse-Ruyken, M.-L., and Müller-Gärtner, H. W. (**1999**). ''Influence of acoustic masking noise in fMRI of the auditory cortex during phonetic discrimination,'' JMRI **9**, 19–25.

Shaw, E. A. G. (**1966**). ''Earcanal pressure generated by a free sound field,'' J. Acoust. Soc. Am. **39**, 465–470.

Shaw, E. A. G. (**1974**). ''The transformation of sound pressure level from the free field to the eardrum in the horizontal plane,'' J. Acoust. Soc. Am. **56**, 1848–1861.

Shaw, E. A. G. (**1982**). ''Hearing Protector Design Concepts and Performance Limitations,'' in *Personal Hearing Protection in Industry*, edited by P. W. Alberti (Raven Press, New York), pp. 51–68.

Talavage, T. M., Edmister, W. B., Ledden, P. J., and Weisskoff, R. M. (**1999**). ''Quantitative assessment of auditory cortex responses induced by imager acoustic noise,'' Hum. Brain Mapping **7**, 79–88.

Ulmer, J. L., Biswal, B. B., Yetken, F. Z., Mark, L. P., Mathews, V. P., Prost, R. W., Estkowski, L. D., McAuliffe, T. L., Haughton, V. M., and Daniels, D. L. (**1998**). ''Cortical activation response to acoustic echo planar scanner noise,'' J. Comput. Assist. Tomogr. **22**, 111–119.

Vér, I. L., Brown, R. M., and Kiang, N. Y. S. (**1975**). ''Low-noise chambers for auditory research,'' J. Acoust. Soc. Am. **58**, 392–398.

von Gierke, H. E. (**1956**). ''Personal protection,'' Noise Control **2**, 37–44.

Warnock, A. C. C, and Quirt, J. D. (**1998**). ''Airborne Sound Transmission,'' in *Handbook of Acoustical Measurements and Noise Control*, edited by C. M. Harris (Acoustical Society of America, Woodbury, NY), Chap. 31.

Waugh, R. (**1974**). ''Pure-tone, third-octave, and octave-band attenuation of ear protectors,'' J. Acoust. Soc. Am. **56**, 1866–1869.

Waugh, R. (**1984**). ''Simplified hearing protector ratings—an international comparison,'' J. Sound Vib. **93**, 289–305.

Zwislocki, J. (**1957**). ''In search of the bone-conduction threshold in a free sound field,'' J. Acoust. Soc. Am. **29**, 795–804.

Active noise control in a free field with virtual sensors

Colin D. Kestell, Ben S. Cazzolato, and Colin H. Hansen
Department of Mechanical Engineering, University of Adelaide, South Australia 5005, Australia

(Received 6 October 1999; revised 21 September 2000; accepted 25 September 2000)

The zone of local control around a ''virtual energy density sensor'' is compared with that offered by an actual energy density sensor, a single microphone, and a virtual microphone. Intended as an introduction to the concept of forward difference prediction and a precursor to evaluating the virtual sensor control algorithms in damped enclosures, this paper investigates an idealized scenario of a single primary sound source in a free-field environment. An analytical model is used to predict the performance of the virtual error sensors and compare their control performance with their physical counterparts. The model is then experimentally validated. The model shows that in general the virtual energy density sensor outperforms the actual energy density sensor, the actual microphone, and the virtual microphone in terms of centering a practically sized zone of local control around an observer who is remotely located from any physical sensors. However, in practice, the virtual sensor algorithms are shown to be sensitive (by varying degrees) to short wavelength spatial pressure variations of the primary and secondary sound fields.
[DOI: 10.1121/1.1326950]

PACS numbers: 43.50.Ki [CBB]

I. INTRODUCTION

The simplest strategy for active noise control within an enclosure is to minimize the squared pressure at a single microphone location by means of a secondary control source. However, the zone where the noise attenuation is evident may be so small and limited to the immediate vicinity of the error sensor, that a nearby observer may not perceive any improvement in noise reduction [Fig. 1(a)].

However, energy density is more spatially uniform than squared pressure and can also be measured at single locations. In numerical simulations, Sommerfeldt and Nashif (1991) found that minimizing the energy density at a discrete location significantly outperformed the minimization of squared pressures in terms of the size of the attenuation zone around the error sensor. Total energy density, which is the summation of kinetic energy density and potential energy density, can be easily calculated via the measurement of particle velocity (proportional to the acoustic pressure gradient) and pressure. Elliott and Garcia-Bonito (1995) and Garcia-Bonito and Elliott (1995) demonstrated that in a diffuse sound field, minimizing both the pressure and pressure gradient along one axis rather than simply pressure, resulted in a significant increase in the size of the 10-dB ''zone of quiet.''

Nashif (1992) applied the principle of energy density minimization to a one-dimensional enclosure, also demonstrating that the use of an energy density sensor can overcome the observability difficulties (such as pressure nodes) that are inherent in the use of microphones as error sensors in active noise control systems. Since a phase difference of 90° exists between the velocity nodes and pressure nodes of any enclosure resonance, the weighted summation of pressure and velocity are much more spatially uniform. Parkins (1998) extended the work to a three-dimensional enclosure, verifying the previous findings.

Remotely placed energy density sensors used for active noise control can extend the zone of local control sufficiently to encompass a nearby head, but the size of the zone is frequency dependent on the maximum attenuation still occurring at the sensor location [Fig. 1(b)].

An alternative approach has been to move the location of maximum attenuation away from the error sensor by using a ''virtual microphone.'' This involves estimating the cost function at some desired location (the occupant's head) via a remotely placed physical microphone [Fig. 2(a)]. Garcia-Bonito *et al.* (1996) and Garcia-Bonito *et al.* (1997) modified the pressure measured from an error sensor to estimate the pressure at a nearby desired (virtual) location. They state that at low frequencies the spatial rate of pressure change due to the primary field is small enough to assume that the primary source pressure component is the same at both the virtual and actual location. Close to the secondary sound source the actual sensor and the virtual error sensor to secondary source transfer impedance functions are significantly different. The prior measurement of this difference can then be used as an operator on the actual error signal to estimate the pressure at the virtual location. Rafaely *et al.* (1999) showed that this principle could also be applied to the active control of broadband noise. However, in enclosures, higher-order modes may significantly affect the spatial rate of pressure change, even over relatively small distances with respect to wavelength. Therefore, the assumption that the primary source pressure component is the same at both the actual and virtual error sensor locations may not be accurate. It is also possible that any movement within the vicinity of the sensors will significantly alter the impedance transfer functions. Carme and De Man (1998) also used a virtual microphone to improve the performance of a pair of ANC ear defenders using the same transfer function prediction techniques developed by Garcia-Bonito *et al.* (1997). However, while improving the performance of a pair of ear defenders they still restrict the occupant to the use of ear defenders and all of the problems associated with them.

Using the development of a new virtual microphone extrapolation technique (different to that described earlier) and

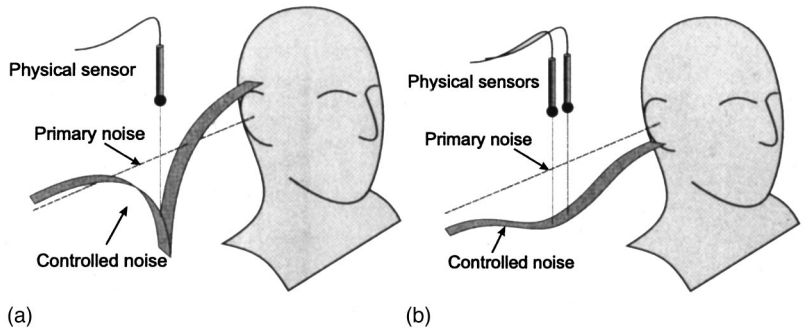

FIG. 1. A schematic representation of the local region of control that may occur around either a single microphone error sensor or an energy density error sensor. (a) A single microphone error sensor, (b) an energy density cost function.

combining the benefits of an energy density sensor, the study described here investigates the use of a ''virtual energy density sensor'' to improve the zone of localized noise attenuation offered by existing active control systems [Fig. 2(b)].

While a virtual microphone may be capable of placing a very high level of attenuation at the observer location, the zone may be impractically small and would not allow for any head movement. It will therefore be shown that it is not only possible to extend the zone of quiet around an observer beyond that offered by either the virtual microphone technique or remotely placed energy density sensors, but to also track any movement of an observer and thus continue to place the center of maximum noise attenuation at his or her location (Fig. 3).

The final objective of the research is to develop a nonintrusive virtual error sensor for use in a highly damped enclosure such as a light aircraft cabin. To fully investigate the concept and its limitations, the virtual sensors are initially evaluated analytically under the ideal condition of a single tonal noise source in a free-field environment. Future research shall extend the system complexity to reactive enclosures so that it is applicable to a light aircraft cabin.

II. THEORY

In practical applications of active noise control it is not always possible to locate an error sensor at the desired control location, usually the observer's head. Transducers located immediately adjacent to the ears may be even more restrictive than the use of personal hearing protection. However, moving the error sensor away from the desired control location often leads to very poor local control at the observer location. The virtual microphone sensor developed by Garcia-Bonito *et al.* (1996) predicts the pressure at the observer's head but requires measuring the secondary source to virtual microphone pressure transfer function prior to implementing a control algorithm. The modified squared pressure cost function also tends to produce a small zone of local control.

An alternative approach to the Garcia-Bonito *et al.* (1996) transfer function based virtual microphone is to use forward difference extrapolation (Fig. 4). The sound pressure at the observer (virtual microphone) location is estimated in real time by extrapolating the signal from remotely placed microphones. This eliminates the need for the prior measurement of the complex acoustic transfer impedance function and allows the prediction technique to adapt to any physical system changes such as head movement or any other mechanism that may alter the error sensor to control source complex acoustic transfer impedance function.

The theory for a first-order (two-microphone) and a second-order (three-microphone) forward difference extrapolation virtual microphone will now be derived. The same approach will be extended to a first-order (two-microphone) and a second-order (three-microphone) virtual energy density sensor with the intention of achieving a broader zone of local control to allow a practical amount of comfortable head movement.

A. Virtual microphone

The spatial rate of change of the sound pressure between relatively closely spaced locations (in terms of wavelength) in free space, in a duct, or in an enclosure will be small and hence predictable. By fitting either a straight line or a curve between pressures measured at fixed locations, the pressures at other locations may be estimated by either interpolation or extrapolation. Since in this research it is intended that an observer is to be remote from the physical sensors, rather than between them, the following equations are extrapolation based.

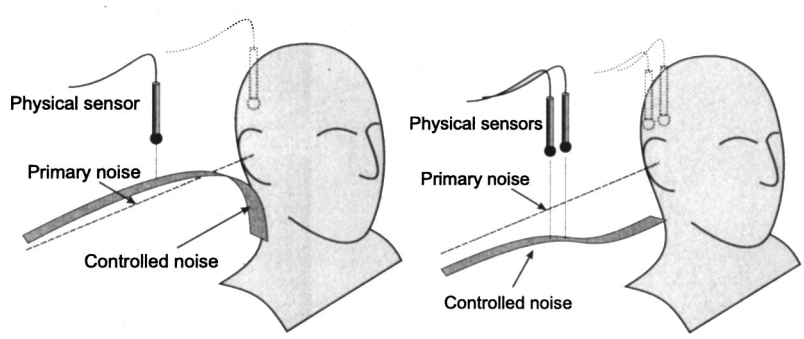

FIG. 2. A schematic representation of the region of control that may occur by estimating a cost function at the observer location. The ghosted sensors represent the ''virtual sensor'' location.

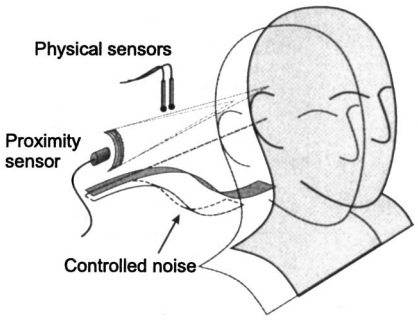

FIG. 3. The concept of movement tracking.

1. Two-microphone first-order pressure prediction

Figure 4(a) illustrates that the pressure at location x can be approximated by the first-order finite difference estimate ($p=(dp/dx)x+c$, where dp/dx is constant) from two remote microphones, separated by a distance of $2h$ by measuring pressures p_1 and p_2, respectively, at the two microphone locations as follows:

$$p_x=\frac{(p_2-p_1)}{2h}x+p_2. \tag{1}$$

To maintain consistency when comparing this method to the three-microphone second-order method (discussed later), $2h$ is chosen as a separation distance.

If $x=0$, or if $x=-2h$, then Eq. (1) reduces to $p_x=p_2$ or p_1, respectively, as expected. But more practically, if the separation distance x between the observer and the nearest transducer is equal to $+h$ then Eq. (1) reduces to

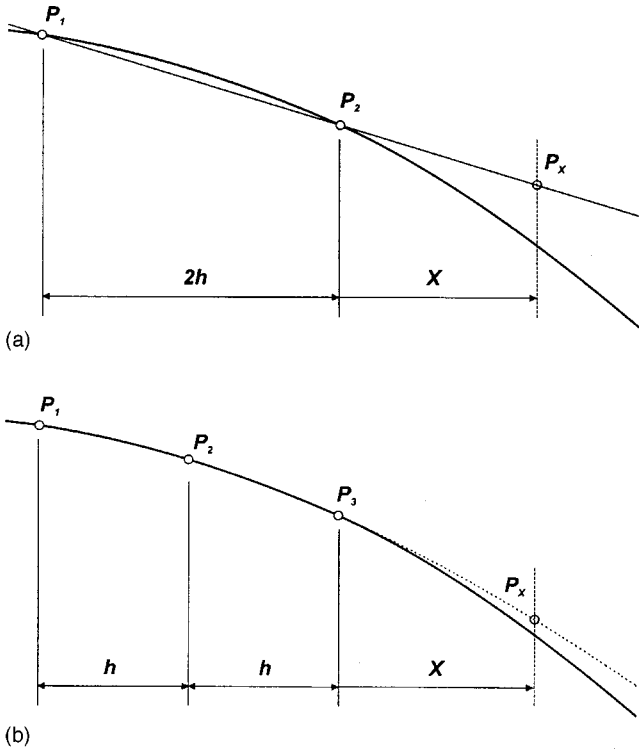

FIG. 4. Forward difference prediction. (a) First-order forward prediction, (b) second-order forward prediction.

$$p_x=\frac{p_2-p_1}{2}+p_2=\frac{1}{2}(3p_2-p_1); \tag{2}$$

if the separation distance is increased to $x=2h$ then,

$$p_x=2p_2-p_1. \tag{3}$$

2. Three-microphone second-order pressure prediction

The use of a third intermediately placed microphone allows an estimation of the rate of change of the pressure gradient, which enables a greater prediction accuracy [Fig. 4(b)]. This second-order approximation, where d^2p/dx^2 is assumed constant (a constant rate of pressure gradient change), can be integrated to determine the relationship between the pressure (p_x) at the virtual location (x) and the pressures measured at the three actual microphone locations p_1, p_2, and p_3 as follows:

$$\begin{aligned} p_x&=\int\int\frac{d^2p}{dx^2}\cdot(dx)(dx)\\ &=\int\int k_1\cdot(dx)(dx)\\ &=\int(k_1x+k_2)\cdot(dx)=\frac{k_1x^2}{2}+k_2x+k_3. \end{aligned} \tag{4}$$

The constants of integration k_1, k_2, and k_3 can be found by applying Eq. (4) to the pressure and location of each of the three microphones at $x_3=0$, $x_2=-h$, and $x_1=-2h$; thus,

$$\begin{aligned} p_3&=k_3,\\ p_2&=\frac{k_1}{2}h^2-k_2h+k_3,\\ p_1&=2k_1h^2-k_2h+k_3. \end{aligned} \tag{5}$$

Solving the equations allows the value for each of these constants to be calculated. When substituted into Eq. (4) this yields

$$p_x=\left(\frac{p_1-2p_2+p_3}{h^2}\right)\frac{x^2}{2}+\left(\frac{p_1-4p_2+3p_3}{2h}\right)x+p_3. \tag{6}$$

Collecting like terms to calculate the weighting factors for each actual microphone (which is more practical for hardware design), results in the pressure at location x being expressed as

$$p_x=\frac{x(x+h)}{2h^2}p_1+\frac{x(x+2h)}{-h^2}p_2+\frac{(x+2h)(x+h)}{2h^2}p_3. \tag{7}$$

Once again, in order to confirm the equation, if $x=0$, or, $x=-h$ or $x=-2h$, then Eq. (7) reduces to $p_x=p_3$, p_2, or p_1, respectively.

If $x=+h$, then Eq. (7) reduces to

$$p_x=p_1-3p_2+3p_3=p_1+3(p_3-p_2). \tag{8}$$

If $x=2h$, then Eq. (7) reduces to

$$p_x=3p_1-8p_2+6p_3=p_1-2(p_2-p_1)+6(p_3-p_2). \tag{9}$$

In the next section this forward prediction approach is adapted to derive a virtual energy density sensor, with the aim of achieving broad zones of reduced noise centered around the head of the observer.

B. Virtual energy density sensor

Using the same forward difference prediction method as introduced in the previous section, the pressure gradient at some point located away from the sensing microphones may also be estimated and this can be used to derive the equations to define a first and second-order ''virtual energy density sensor.''

1. Two-microphone first-order prediction

For the two-microphone sensor shown in Fig. 4(a), the best estimate of pressure at a distance x from the second microphone is given by Eq. (1), i.e., $p_x=((p_2-p_1)/2h)x+p_2$, and the particle velocity is obtained from the best estimate of the pressure gradient given by

$$\frac{dp}{dx}=\frac{p_2-p_1}{2h}. \tag{10}$$

Euler's equation relates particle velocity to spatial pressure gradient with the general relationship

$$\frac{dp}{dx}=-\rho\frac{dv}{dt}, \tag{11}$$

which for monotone sound fields reduces to

$$v=-\frac{1}{j\omega\rho}\frac{dp}{dx}. \tag{12}$$

Therefore, at any given frequency ω (radians/s), the particle velocity estimate for a two-microphone sensor is obtained by multiplying the pressure gradient in Eq. (10) by $-1/j\rho\omega$, i.e.,

$$v_x=-\frac{1}{j\rho\omega}\left(\frac{dp}{dx}\right)=\frac{p_2-p_1}{j2h\rho\omega}. \tag{13}$$

The instantaneous energy density [Nashif and Sommerfeldt (1992)], which is the sum of instantaneous potential and kinetic energy density at a point x, is given as

$$E_{D_x}=\frac{p_x^2}{2\rho c}+\frac{\rho v_x^2}{2}=\frac{1}{2\rho c^2}[p_x^2+\rho^2c^2v_x^2]. \tag{14}$$

It should be noted that the terms outside of the square brackets equally weight both the pressure and the velocity. The terms inside the square brackets define the relative magnitude of the pressure and velocity components and must therefore be accurately incorporated in the design of any energy density sensor.

Substituting the pressure [Eq. (1)] and velocity [Eq. (13)] estimates into Eq. (14) and simplifying with $k=\omega/c$, an estimate for the energy density at some virtual location (x) in terms of the sound pressures at the two microphones is obtained,

$$\begin{aligned}E_{D_x}&=\frac{1}{2\rho c^2}\left[\left(\frac{(p_2-p_1)}{2h}x+p_2\right)^2+\rho^2c^2\left(\frac{p_2-p_1}{j2h\rho\omega}\right)^2\right]\\&=\frac{1}{2\rho c^2}\left[\left(1+\frac{x}{2h}\right)^2p_2^2-\frac{x}{h}\left(1+\frac{x}{2h}\right)p_1p_2\right.\\&\quad\left.+\left(\frac{x}{2h}\right)^2p_1^2-\frac{1}{(2hk)^2}(p_2^2-2p_1p_2+p_1^2)\right].\end{aligned} \tag{15}$$

For a separation distance between the nearest transducer and the observer of $x=0$ this reduces to

$$E_{D_x}=\frac{1}{2\rho c^2}\left[p_2^2-\frac{1}{(2hk)^2}(p_2^2-2p_1p_2+p_1^2)\right], \tag{16}$$

or for $x=h$,

$$\begin{aligned}E_{D_x}&=\frac{1}{2\rho c^2}\left[\left(\left(\frac{3}{2}\right)^2p_2-\left(\frac{3}{2}\right)p_1p_2+\left(\frac{1}{4}\right)p_1^2\right)\right.\\&\quad\left.-\frac{1}{(2hk)^2}(p_2^2-2p_1p_2+p_1^2)\right],\end{aligned} \tag{17}$$

or if $x=2h$,

$$E_{D_x}=\frac{1}{2\rho c^2}\left[4p_2-4p_1p_2+p_1^2-\frac{1}{(2hk)^2}(p_2^2-2p_1p_2+p_1^2)\right]. \tag{18}$$

2. Three-microphone second-order prediction

For the three-microphone sensor shown in Fig. 4(b), the pressure gradient estimate is obtained by differentiating the pressure estimate shown in Eq. (6), i.e.,

$$\begin{aligned}\frac{dp}{dx}&=\frac{d}{dx}\left[\left(\frac{p_1-2p_2+p_3}{h^2}\right)\frac{x^2}{2}+\left(\frac{p_1-4p_2+3p_3}{2h}\right)x+p_3\right]\\&=\left[\left(\frac{p_1-2p_2+p_3}{h^2}\right)x+\left(\frac{p_1-4p_2+3p_3}{2h}\right)\right]\\&=\frac{1}{h^2}\left[\frac{2x+h}{2}p_1-(2x+2h)p_2+\frac{2x+3h}{2}p_3\right].\end{aligned} \tag{19}$$

In the same manner as the two-microphone method, the particle velocity estimate for the three-microphone sensor is obtained by multiplying the pressure gradient in Eq. (19) by $1/j\rho\omega$. This can then be substituted into Eq. (14) along with the virtual pressure estimate [Eq. (7)], to estimate the virtual energy density [Eq. (20)].

$$\begin{aligned}E_{D_x}&=\frac{1}{2\rho c^2}\left[\left(\frac{x(x+h)}{2h^2}p_1+\frac{x(x+2h)}{-h^2}p_2\right.\right.\\&\quad\left.+\frac{(x+2h)(x+h)}{2h^2}p_3\right)^2\\&\quad+\rho^2c^2\left(\frac{1}{j\rho\omega h^2}\left(\frac{2x+h}{2}p_1-(2x+2h)p_2\right.\right.\\&\quad\left.\left.\left.+\frac{2x+3h}{2}p_3\right)\right)^2\right]\\&=\frac{1}{2\rho c^2}\left[\left(\frac{x(x+h)}{2h^2}p_1+\frac{x(x+2h)}{-h^2}p_2\right.\right.\end{aligned}$$

$$+\frac{(x+2h)(x+h)}{2h^2}p_3\Bigg)^2 - \frac{1}{k^2}\left(\frac{2x+h}{2h^2}p_1-\frac{2x+2h}{h^2}p_2+\frac{2x+3h}{2h^2}p_3\right)^2\Bigg]. \tag{20}$$

This may also be customized for various set distances of x in terms of h.

C. Higher-order prediction methods

From Eq. (1) and Fig. 4(a) it is evident that the two-sensor prediction method is fundamentally based on the assumption of a constant pressure gradient between the sensor locations and the observer, or that the estimate has a constant *first-order derivative*. The two-microphone forward difference prediction method is therefore described as a ''first-order'' estimate. In the three-sensor prediction method [Eq. (7) and Fig. 4(a)], it is assumed that the pressure gradient changes at a constant rate, or that the *second-order derivative* is constant. Three sensor forward difference predictions are therefore termed ''second-order'' estimates. From Figs. 4(a) and (b), it can be seen that the second-order method is theoretically more accurate than the first-order method at defining a waveform that is remote from the sensors. This indicates that the theoretical prediction accuracy increases with the order of the prediction method. In fact, any waveform ($f(x)$) can be explicitly defined by a Taylor series expansion,

$$f(x+h)=f(x)+h\cdot f'(x)+\frac{h^2}{2!}f''(0)+\frac{h^3}{3!}f'''(0)+\cdots. \tag{21}$$

While Eq. (21) has an infinite number of terms, it can be estimated by using n terms in the following equation:

$$f(x+h)=f(x)+h\cdot f'(x)+\frac{h^2}{2!}f''(0)+\frac{h^3}{3!}f'''(0) +\cdots\frac{h^n}{n!}f^{(n)}(0). \tag{22}$$

Introducing higher-order terms to theoretically improve the accuracy of a cost function estimate at the observer location will require that the number of sensors proportionally increase to $n+1$. However, this theory does not consider any practical issues associated with implementation that may adversely affect the prediction accuracy. Therefore, in the chapters that follow, only first- and second-order virtual error sensors shall be evaluated and compared, in order to observe the practical benefits of using higher-order terms in the estimation of the cost function at the observer location.

D. Movement tracking

The first- and second-order methods of forward difference prediction presented in the previous sections all depend on the measurement of pressure from physical sensors placed at some distance x from the observer. It therefore follows that if a varying separation distance were measured (via an ultrasonic sensor for example), then the prediction algorithm could be continually updated to effectively make the sound field minimum follow the observer. Although only a fixed virtual location is considered here, tracking an observer's head movement may provide the basis of future research.

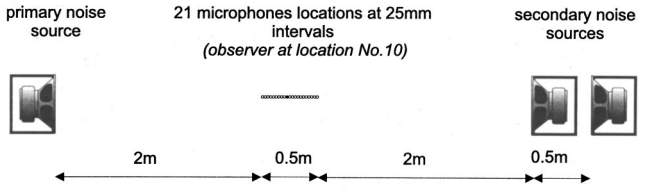

FIG. 5. A schematic diagram of the modeled system.

III. METHOD

The system investigated consisted of a single frequency primary noise source located in a free field. Twenty-one measurement locations were chosen 2 m away, along a 0.5-m length at intervals of 25 mm (referred to as h) and the control

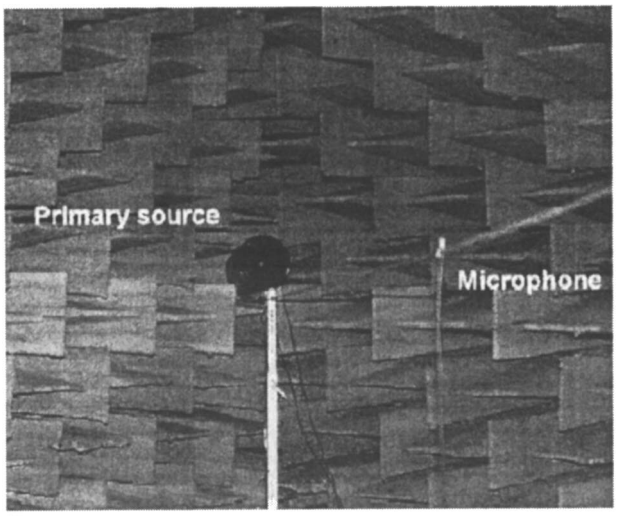

(a)

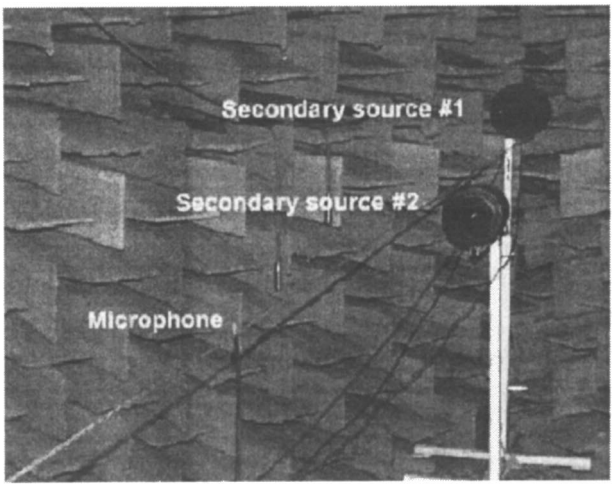

(b)

FIG. 6. The experimental configuration in the anechoic chamber. (a) The primary sound source and the measurement microphone, (b) the two secondary sound sources and the measurement microphone (foreground).

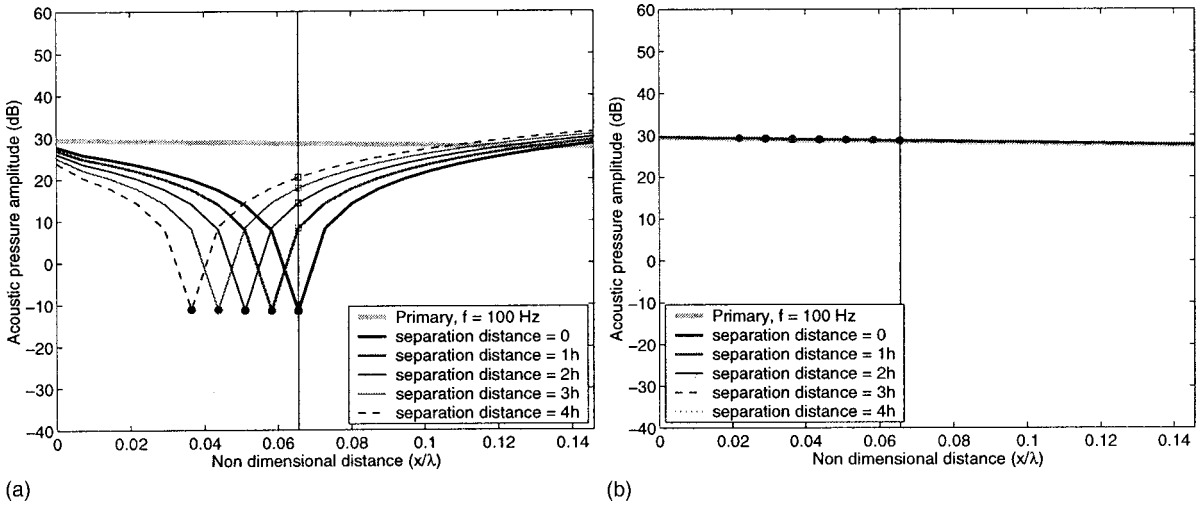

FIG. 7. Comparing the pressure minimization at a single location with energy density control using only one control source. The vertical line is the observer (desired control) location and the physical sensor locations are shown with a circle. (a) A single microphone error sensor, with increasing separation distances from the observer, (b) energy density control, with increasing separation distances from the observer.

noise sources (control speakers) were positioned at 4.5 and 5 m from the primary source (Fig. 5). The system was initially modeled and then the results were experimentally validated.

A. The model

The system was modeled with the primary and control sources represented as point monopoles with a spherical pressure amplitude radiation pattern [Hansen and Snyder (1997)], which is defined by

$$p_r = \frac{j\omega\rho_0 q e^{-jkr}}{4\pi r}, \tag{23}$$

where p is the pressure amplitude measured at a distance r from the source, ω is the rotational frequency, ρ_0 is the air density, q is the source signal strength, and k is the wave number.

The primary sound field was initially modeled and transfer functions were obtained between the sound pressure calculated at each source location and the sound pressure calculated at each of the 21 measurement locations. These locations were at 25-mm intervals (h) along a 0.5-m length, 2 m from the nearest source (Fig. 5). The procedure was repeated for each individually modeled control source sound field. The relevant cost functions at the error sensor location were then minimized via quadratic optimization.

B. The experiment

The physical system (representative of the previously discussed model) consisted of a single frequency primary noise source located in an anechoic chamber. The location of the measurement sensors and the 150-mm diameter enclosed primary source and control source speakers were identical to those locations used in the model (Fig. 6).

In each experiment, while only the primary noise source was driven with broadband random noise, transfer functions were measured between the signal from a microphone in the rear chamber of the primary noise source and the signal from the measurement microphone at each of the 21 locations. The procedure was repeated for each individually driven control source. To allow a direct comparison between the active noise control results from each model and its respective experiment and to eliminate any further differences that may be associated with the performance of a practical ANC controller, the cost functions in the experiment (either from the physical sensors or the virtual sensors) were also minimized via quadratic optimization.

In theory, infinite attenuation may be achieved at an error sensor when using quadratic optimization. In practice, active noise control systems would have inherent errors that would limit the amount of noise attenuation that could be achieved. Therefore, to force the optimization results to a more realistic magnitude and emulate the uncertainty that occurs in practice, transfer function errors were incorporated into the control algorithm limiting the amount of control to less than 40 dB.

C. The number of control sources

To control pressure at a single location only requires one control source; additional sources are redundant [Fig. 7(a)]. In a single control source system, however, there is little advantage in trying to minimize energy density if one is trying to activate local control [Cazzolato (1999)]. Attempts to minimize the pressure gradient can result in a local sound pressure increase. Using the free-field model data as an example, Fig. 7(b) shows that while the control source magnitude and phase (with respect to the primary noise source) can be optimized to produce a zero pressure gradient between the two sensors, it is at the expense of constructive wave summation that results in an increase in the sound pressure level throughout the region of interest.

Therefore, to effectively minimize energy density, the independent control of pressure and pressure gradient (i.e., independent control of pressure at two locations) requires the use of a second control source.

Minimizing energy density in a two-control source and two-sensor system, is the result of minimizing the acoustic

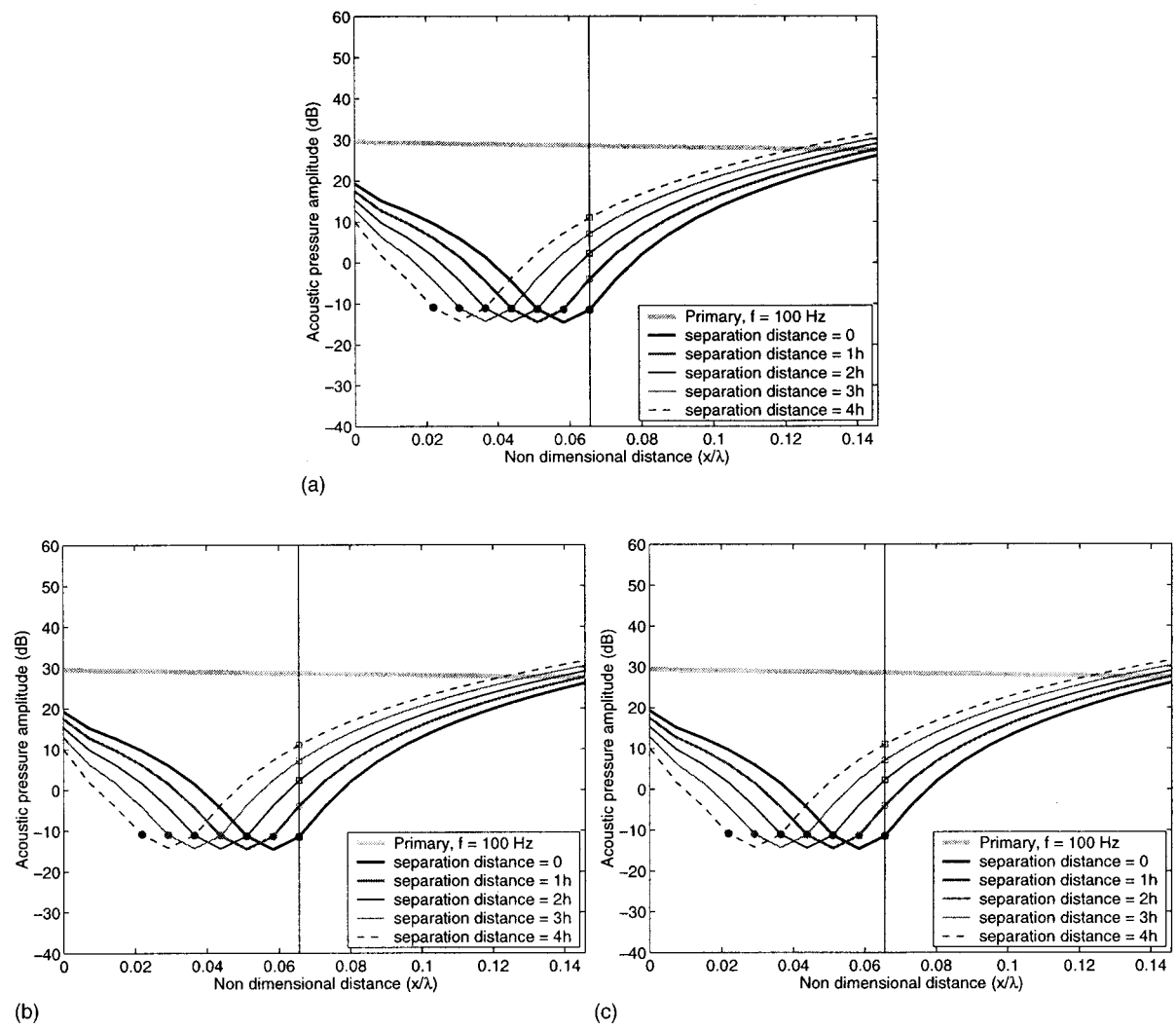

FIG. 8. A comparison of the primary and controlled sound pressure levels for first-order virtual energy density control at the observer location, first-order energy density control at the sensors, and minimizing the acoustic pressure at the two error sensors. There are two control sources and a primary noise tone at 100 Hz. The vertical line is the observer (desired control) location and the physical sensor location is shown with a circle. The minima are shown between two of these in each case. (a) First-order virtual energy density minimization at the observer location, (b) energy density control at the sensors, (c) pressure minimization at the two sensors.

pressure gradient between the two sensors and the mean acoustic pressure measured between them [Eq. (14)]. In the idealized systems considered here, where it is possible to equally minimize the signal from the two sensors, energy density control estimated via two microphones [Fig. 8(a)] is identical to simply minimizing the pressures at the two-microphone locations [Fig. 8(b)]. Practical systems would have more complex wave interaction and inherent errors and it is therefore unlikely that both pressures would be significantly equally minimized while the pressure gradient is also minimized. In a first-order virtual energy density sensor the pressure gradient is assumed to be spatially constant, i.e., the same at the sensor and observer locations (Fig. 4). Because the pressure at the virtual location is also at a minimum when the the two error sensor pressures are at a minimum [Eq. (1)], first-order virtual energy density control [Fig. 8(a)] will be identical to minimizing the energy density at the sensor location [Fig. 8(b)] or the pressure at the two error sensor locations [Fig. 8(c)].

A second-order system that involves estimating the remote pressure and pressure gradient with three sensors results in a more accurate prediction of both pressure and pressure gradient (in the absence of noise). The pressure at the observer location is estimated by extrapolating the pressure profile from three sensors and the pressure gradient is no longer considered constant, but assumed to have a constant rate of change. The use of only two control sources, however, is still pertinent since (in these examples) the energy density has two independent contributors; namely pressure and pressure gradient.

In the examples that follow, the use of a single control source will therefore be limited to observing the acoustic pressure minimization via a single microphone, a first-order virtual microphone, and a second-order virtual microphone. Energy density minimization (identical to two-point pressure control and first-order virtual energy density control) and second-order virtual energy density control will be evaluated with two control sources.

At system excitation frequencies of 100 and 400 Hz, the performance of the following error sensors, with increasing

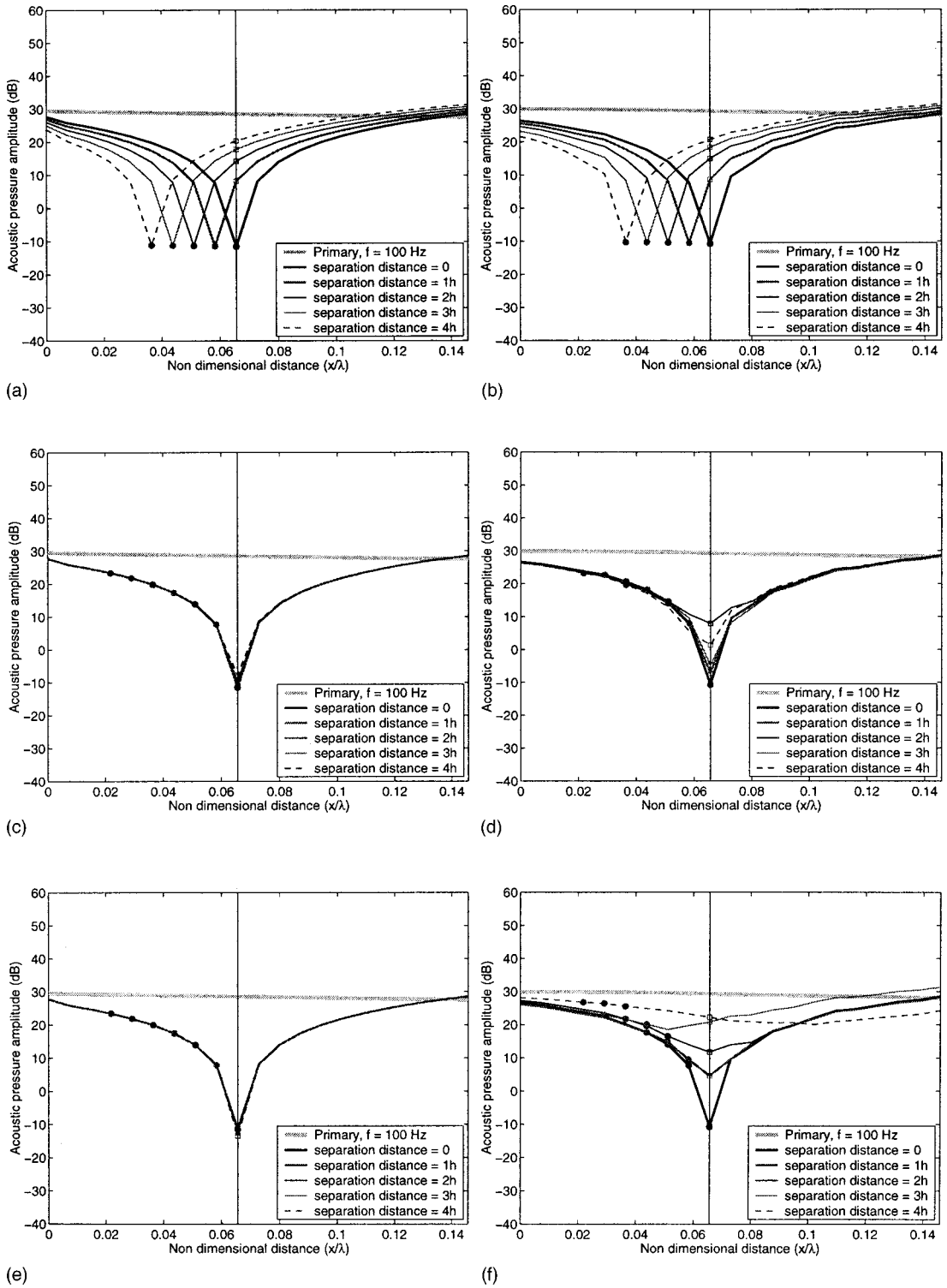

FIG. 9. A 100-Hz primary sound source controlled via one control source. Measured along a 0.5-m length in an anechoic chamber, the actual sensors are marked with a circle and the observer location by a vertical line. (a) Analytical model—pressure control at one microphone location; (b) experimental results—pressure control at one microphone location; (c) analytical model—first-order virtual microphone; (d) experimental results—first-order virtual microphone; (e) analytical model—second-order virtual microphone; (f) experimental results—second-order virtual microphone.

separation distances between the physical sensors and the observer, are compared and discussed:

(1) A single microphone,
(2) A first-order virtual microphone,
(3) A second-order virtual microphone,
(4) First-order virtual energy density control (or two-point pressure minimization or energy density control), and
(5) second-order virtual energy density.

IV. RESULTS

A. Control of a 100-Hz sinusoidal wave

Figure 9 shows the results that are obtained when controlling a 100-Hz monotone in both the free-field model and

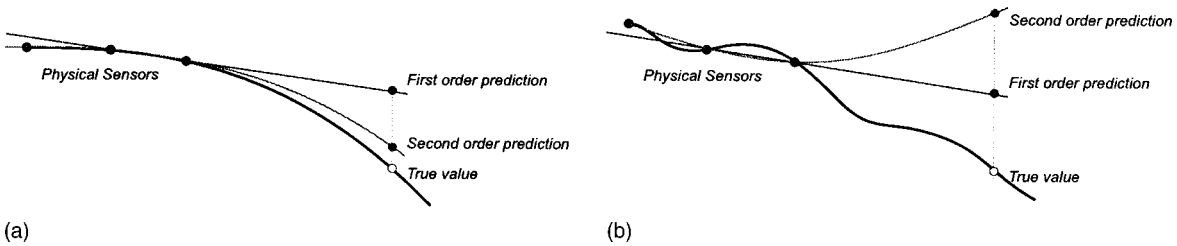

FIG. 10. Examples of extrapolation (prediction) error. (a) An example of the greater theoretical accuracy of a second-order extrapolation technique in the absesnce of short wavelength noise; (b) an example of when the first-order method may be more accurate in the presence of short wavelength noise.

the anechoic chamber experiment. Figures 9(a) and (b) compare the modeled and experimental results for a conventional pressure squared cost function, where the sensor is incrementally moved farther from the observer location. These demonstrate that as the error sensor is moved away from the observer, the attenuation at the observer location decreases. Both figures are similar and show that the attenuation at the observer location reduces from 40 to 8 dB as the observer/sensor separation distance increases from $0h$ to $4h$ (100 mm).

In Figs. 9(c) and (d) the modeled and experimental results for the first-order virtual microphone are compared. Since the algorithm adapts to an increasing separation distance there is only a negligible reduction in attenuation at the observer location. What small error there is, is due to the decrease in estimation accuracy as the separation distance increases. As the sensor is moved farther away, the sound pressure at the observer location is estimated by way of extrapolation. Both the model and the experiment show similar results, although the experiment shows that as the observer/

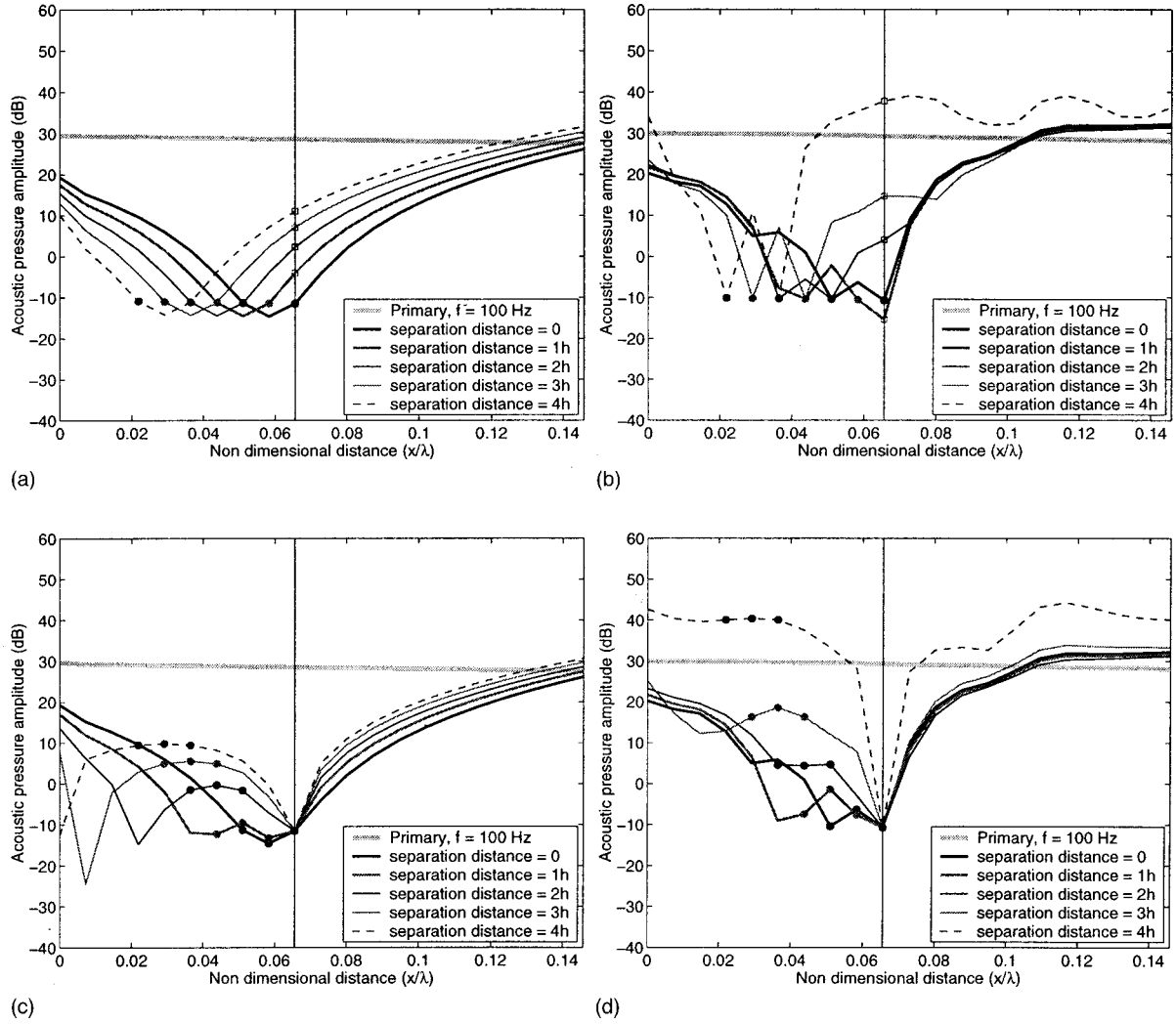

FIG. 11. A 100-Hz primary sound source controlled via two control sources. Measured along a 0.5-m length in an anechoic chamber, the actual sensors are marked with a circle and the observer location by a vertical line. (a) Analytical model—energy density control (and first-order virtual energy density control); (b) experimental results—energy density control (and first-order virtual energy density control); (c) analytical model—second-order virtual energy density control; (d) experimental results—second-order virtual energy density control.

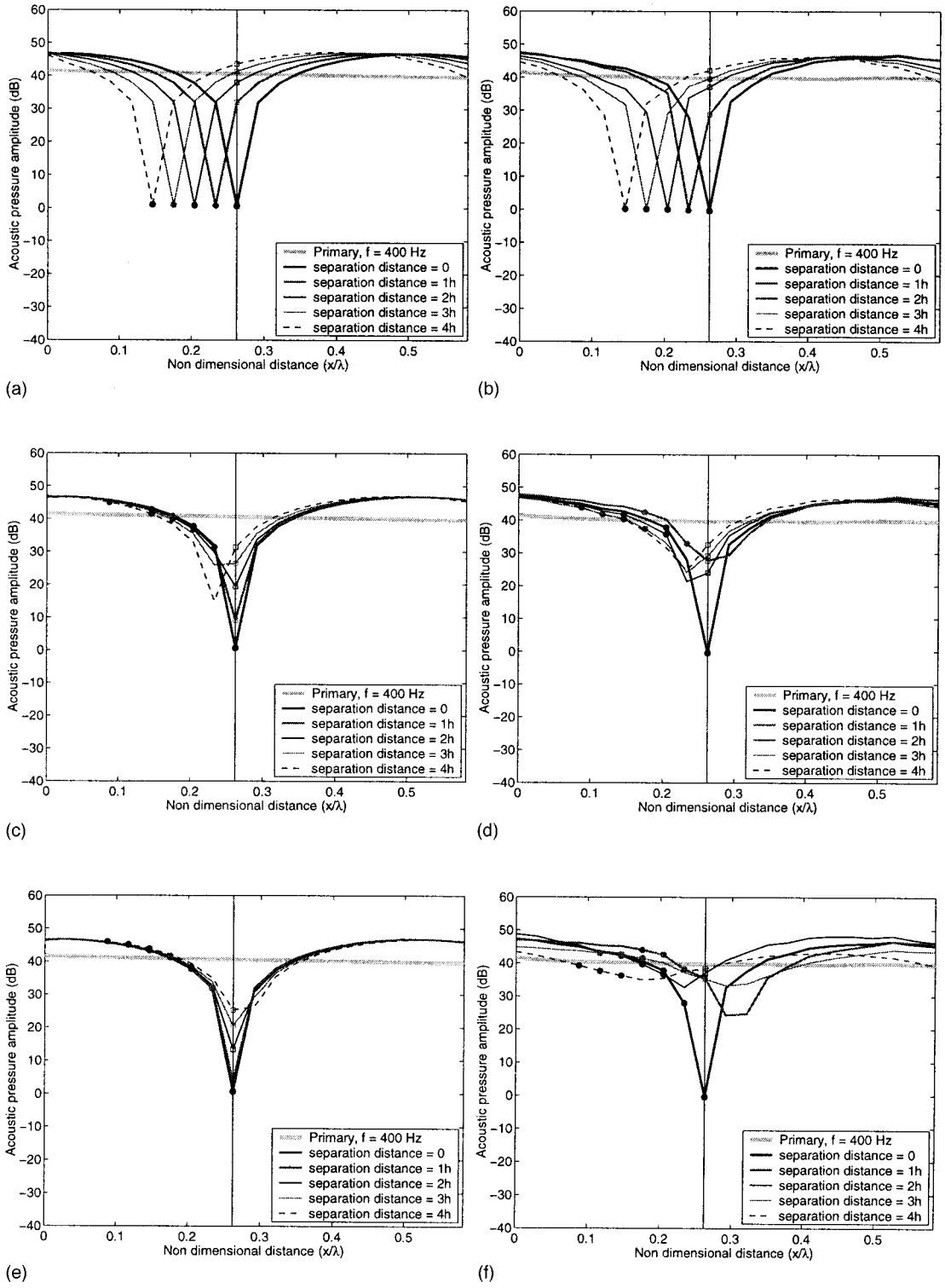

FIG. 12. A 400-Hz primary sound source controlled via one control source. Measured along a 0.5-m length in an anechoic chamber, the actual sensors are marked with a circle and the observer location by a vertical line. (a) Analytical model—pressure control at one microphone location; (b) experimental results—pressure control at one microphone location; (c) analytical model—first-order virtual microphone; (d) experimental results—first-order virtual microphone; (e) analytical model—second-order virtual microphone; (f) experimental results—second-order virtual microphone.

sensor separation distance increases to 100 mm, attenuation at the observer location reduces from 40 to 22 dB compared to only a negligible reduction in the performance of the model. However, this control strategy still demonstrates a practical advantage over the conventional remotely placed single microphone [Fig. 9(b)].

Figure 9(e) illustrates that in theory second-order prediction is more accurate for the forward difference prediction of a pressure squared cost function, but in practice the experiment shows it is less accurate than the first-order method. The model (theory) is based on sound fields that smoothly reduce at a rate of 6 dB per doubling in separation distance from the source whereas in practice there are likely to be relatively small spatial pressure variations due to reflections

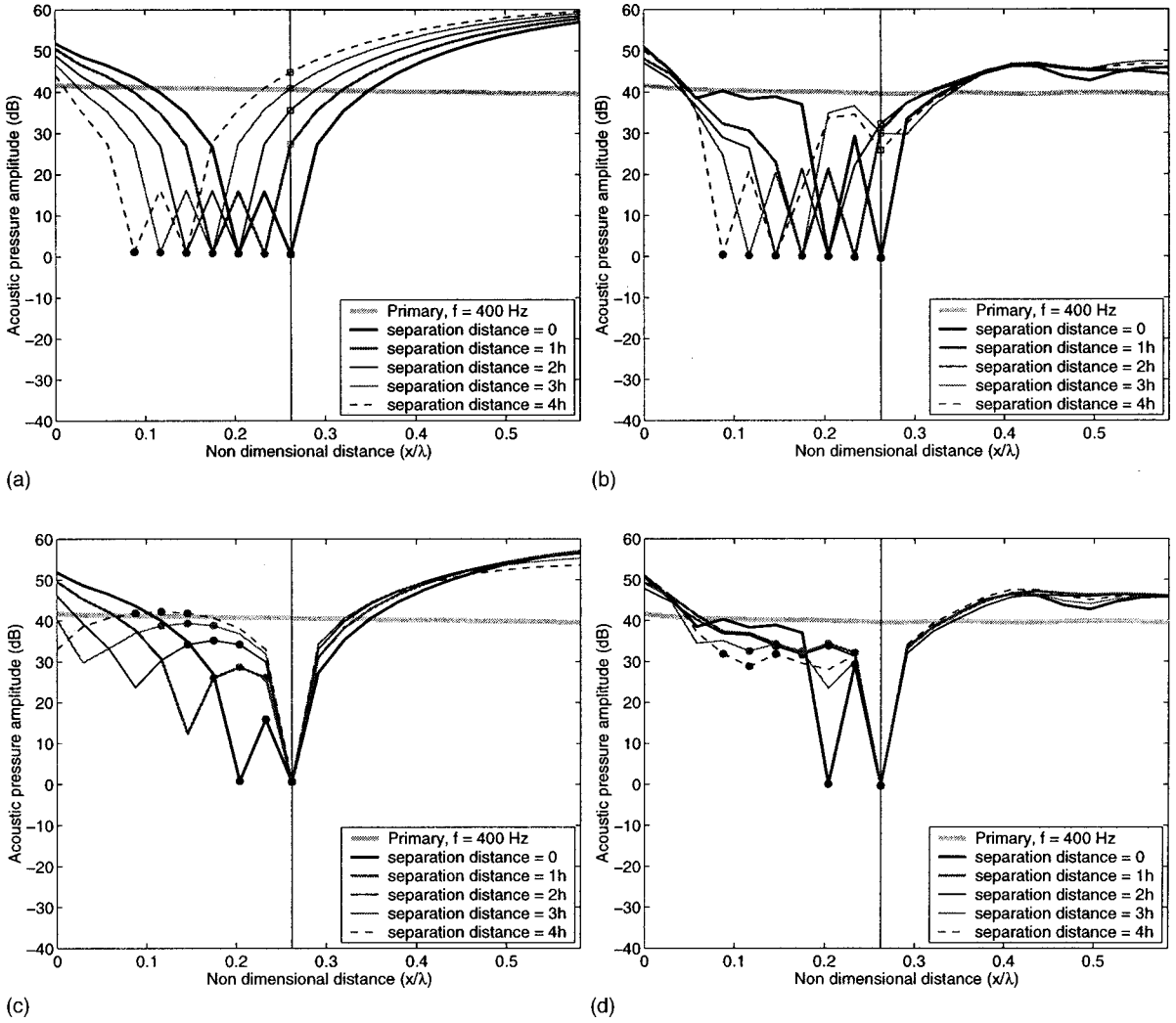

FIG. 13. A 400-Hz primary sound source controlled via two control sources. Measured along a 0.5-m length in an anechoic chamber, the actual sensors are marked with a circle and the observer location by a vertical line. (a) analytical model—energy density control (and first-order virtual energy density control); (b) experimental results—energy density control (and first-order virtual energy density control); (c) analytical model—second-order virtual energy density control; (d) experimental results—second-order virtual energy density control.

inside the chamber as well as signal noise. These small spatial pressure variations can introduce errors into the extrapolation and the effect of these errors are amplified in the more sensitive second-order method [Fig. 10(b)], resulting in poorer performance in practice than achieved when using the first-order method.

Results obtained by either controlling the pressure at two sensor locations or controlling direct or virtual first-order energy density (Sec. III C) are shown in Figs. 11(a) and (b). This cost function produces a broader region of control (when compared to that obtained using a single microphone and a single source) and hence maintains an attenuation envelope around the observer location as the sensors are moved farther away. This attenuation, however, reduces from 35 to 18 dB (at a separation distance of 100 mm) at the observer location in the model. The cost function prediction in the experiment appears to be fairly stable up to an observer/sensor separation distance of 75 mm, but prediction inaccuracies result in a gain of 8 dB when the observer/sensor separation distance increases to 100 mm.

In Figs. 11(c) and (d) the performance of the modeled and actual second-order virtual energy density sensors are compared. The experiment shows that the energy density cost function is more rugged in the presence of small spatial pressure variations and maintains the maximum attenuation at the observer location within a broad and practically sized zone of attenuation.

B. Control of a 400-Hz sinusoidal wave

In Fig. 12 the results obtained when controlling a 400-Hz monotone in both the model and the experiment are shown. Figures 12(a) and (b) again illustrate that the conventional pressure squared cost function produces similar results in both the model and the experiment. The size of the attenuation zone has been reduced with the increased frequency, so that the attenuation at the observer location now becomes a gain of 4 dB for an observer/sensor separation distance of 100 mm.

The modeled and experimental results for the first-order virtual microphone are compared in Figs. 12(c) and (d). The results of both the model and experiment show similar at-

tenuation. For an observer/sensor separation distance of 100 mm, this control strategy shows an experimental improvement of approximately 10 dB when compared to the conventional single microphone error sensor [Fig. 12(b)].

In Fig. 12(f) it is shown that the second-order virtual microphone control strategy is sensitive to higher-order spatial pressure variations, with no resulting improvement in control when compared to results obtained using the conventional pressure squared cost function.

In Figs. 13(a) and (b) the achievable active noise control results for a 400-Hz monotone with an energy density cost function and two control sources is shown. Once again (as in the 100-Hz example), energy density control produces a broader region of control than achieved when using a single microphone and control source. The experiment shows that as the observer/sensor separation distance increases to 100 mm, the attenuation at the observer location is still approximately 8 dB, compared to an observer gain of 4 dB that occurs when using a single remotely placed microphone. The experimental performance appears somewhat better than theoretically possible (when compared to the model). This is merely due to the more fortunate destructive wave interference of the experiment's slightly more erratic pressure profiles for both the primary and secondary sound fields. The second-order virtual energy density sensor continues to contribute toward a superior control strategy [Figs. 13(c) and (d)] with the maximum attenuation remaining at the observer location for relatively large observer/sensor separation distances.

C. Conclusions

All of the virtual microphone systems investigated show the potential to outperform their physical counterpart, offering a higher level of attenuation at the observer location than by minimizing pressure at an equivalent observer/sensor separation distance.

For the frequencies analyzed and for this particular environment, it has been demonstrated that the *first-order virtual microphone* (based on forward difference prediction) outperforms a conventional microphone (in terms of noise reduction at the observer location) with an equivalent observer/sensor location separation distance.

While the highest attenuation in the model and at the observer location was in general achieved by using a *second-order virtual microphone*, the size of the attenuation zone was narrow. The theoretically more precise prediction method of a *second-order virtual microphone* was found to be more sensitive to shorter wavelength spatial variations in an actual sound field, offering only a small practical advantage to using a conventional microphone.

It has been shown that first-order prediction methods for energy density estimation at a remote location (the observer) offer no advantage to controlling energy density directly at the remote sensor.

In terms of both a high level of attenuation and a broad control zone around the location of the observer, the second-order virtual energy density probe produced the most favorable results.

Carme, C., and De Man, P. (**1998**). ''How to improve an ANC headset by using a virtual microphone,'' in *Proceedings of InterNoise 98*, Christchurch.

Cazzolato, B. S. (**1999**). ''Sensing systems for active control of sound transmission into cavities,'' Ph.D. thesis, The University of Adelaide, Adelaide, South Australia, April.

Elliott, S. J., and Garcia-Bonito, J. (**1995**). ''Active cancellation of pressure and pressure gradient in a diffuse sound field,'' J. Sound Vib. **186**(4), 696–704.

Garcia-Bonito, J., and Elliott, S. J. (**1995**). ''Strategies for local active control in diffuse sound fields,'' in *Proceedings of Active 95*, pp. 561–572.

Garcia-Bonito, J., Elliott, S. J., and Boucher, C. C. (**1996**). ''A virtual microphone arrangement in a practical active headrest,'' in *Proceedings of InterNoise 96*, pp. 1115–1120.

Garcia-Bonito, J., Elliott, S. J., and Boucher, C. C. (**1997**). ''Generation of zones of quiet using a virtual microphone arrangement,'' J. Acoust. Soc. Am. **101**(6), 3498–3516.

Hansen, C. H., and Snyder, S. D. (**1997**). *Active Control of Noise and Vibration* (E and FN Spon, London).

Nashif, P. J. (**1992**). ''An energy density based control strategy for minimizing the sound field in enclosures,'' Ph.D. thesis, Penn State University.

Nashif, P. J., and Sommerfeldt, S. D. (**1992**). ''An active control strategy for minimizing the energy density in enclosures,'' in *Proceedings of InterNoise 92*, pp. 357–361.

Parkins, J. W. (**1998**). ''Active minimization of energy density in a three dimensional enclosure,'' Ph.D. thesis, Penn State University.

Rafaely, B., Garcia-Bonito, J., and Elliott, S. J. (**1999**). ''Broadband performance of an active headrest,'' J. Acoust. Soc. Am. **106**(2), 787–793.

Sommerfeldt, S. D., and Nashif P. J. (**1991**). ''A comparision of control strategies for minimizing the sound field in enclosures,'' in *Proceedings of Noise-Con 91*, pp. 299–306.

On the annoyance caused by impulse sounds produced by small, medium-large, and large firearms[a)]

Joos Vos
TNO Human Factors, P.O. Box 23, 3769 ZG Soesterberg, The Netherlands

(Received 23 May 2000; accepted for publication 26 September 2000)

A laboratory study was designed in which the annoyance was investigated for 14 different impulse sound types produced by various firearms ranging in caliber from 7.62 to 155 mm. Sixteen subjects rated the annoyance for the simulated conditions of (1) being outdoors, and (2) being indoors with the windows closed. In the latter case, a representative outdoor-to-indoor reduction in sound level was applied. It was anticipated that the presumed additional annoyance caused by the ''heaviness'' of the impulse sounds might be predicted from the difference between the C-weighted sound exposure level (CSEL; L_{CE}) and the A-weighted sound exposure level (ASEL; L_{AE}). In the outdoor rating conditions, the annoyance was almost entirely determined by ASEL. The explained variance, r^2, in the mean ratings by ASEL was 0.95. In the indoor rating conditions, however, the explained variance in the annoyance ratings by (outdoor) ASEL was significantly increased from $r^2=0.87$ to $r^2=0.97$ by adding the product $(L_{CE}-L_{AE})(L_{AE}-\alpha)$ as a second variable. In combination with a 12-dB adjustment for small firearms, the present results showed that for the entire set of impulse sounds rated indoors with windows closed, the rating sound level, L_r, is given by $L_r=L_{AE}+12\,\mathrm{dB}+\beta(L_{CE}-L_{AE})(L_{AE}-\alpha)$, with $\alpha=45\,\mathrm{dB}$ and $\beta=0.015\,\mathrm{dB}^{-1}$. For the outdoor rating condition, the optimal parameter values were equal to $\alpha=57\,\mathrm{dB}$ and, again, $\beta=0.015\,\mathrm{dB}^{-1}$. In validation studies, in which the effects of the present rating procedure will be compared to field data, it has to be determined to what extent the constants α and β have to be adjusted. © *2001 Acoustical Society of America.* [DOI: 10.1121/1.1327576]

PACS numbers: 43.50.Pn, 43.50.Ba, 43.50.Qp, 43.66.Lj [MRS]

I. INTRODUCTION

Determination of the rating sound level for shooting sounds produced at fire ranges is complicated by the fact that, in general, the sounds may have been produced by a variety of firearms. From the results obtained in various field and laboratory studies, it can be concluded that at least the sounds produced by small and large firearms cannot be rated in the same way.

For impulse sounds produced by small firearms (muzzle reports), the annoyance has been investigated in many field, laboratory, and quasifield studies. In a review of these studies (Vos, 1995a), it has been shown that, overall, an adjustment of 12 dB has to be added to the (outdoor) A-weighted sound exposure level (ASEL; L_{AE}) to equate the ASEL of the shooting sound to the ASEL of an equally annoying vehicle sound.

For impulse sounds produced by large firearms, the number of studies in which the annoyance caused by the shooting sounds is directly compared with the annoyance caused by road-traffic sounds is very limited. For *simulated* artillery fire produced by blasting charges, the annoyance increases more rapidly with level than that caused by vehicle passby sounds (Schomer, 1994; Schomer *et al.*, 1994). For such heavy bangs, the adjustment increases with level. With the level expressed as outdoor ASEL, the adjustment may extend to 20–30 dB.

For impulse sounds produced by the relatively broad category of medium-large weapons (calibers between 20 and 100–110 mm), the information reported in the literature is very limited as well. For firearms with calibers of 20–35 mm, adjustments to ASEL between 13 and 16 dB have been found (Buchta, 1994; Schomer and Wagner, 1995).

In a laboratory experiment, Meloni and Rosenheck (1995) compared the annoyance caused by the (muzzle) sounds from a 7.5-mm rifle, a 83-mm antitank missile, and a 155-mm howitzer. For the simulated condition of being indoors with the windows open, the annoyance was determined by ASEL, regardless of whether the sounds were produced by the rifle, the antitank missile, or the howitzer. For the simulated condition of being indoors with the windows closed, the data imply that at equal outdoor ASELs, the annoyance caused by the howitzer sounds was higher than that of the other two sound types, and that this difference increased with increasing ASEL. Again, no significant differences were obtained between the ratings for the rifle and antitank missile sounds, suggesting that at least for these categories a fixed single adjustment would suffice.

For lack of detailed information about the annoyance caused by medium-large weapon sounds, a laboratory study was designed in which the annoyance was investigated for 14 different impulse sound types produced by various firearms ranging in caliber from 7.62 to 155 mm. In addition to an overall effect of sound level, it was expected that the annoyance would increase with firearm caliber. A possible predictor for the presumed additional annoyance caused by the ''heaviness'' of the impulse sounds might be the differ-

[a)]Preliminary results of the present research were presented at Internoise '96, Liverpool, United Kingdom, 30 July–2 August 1996, and are included in the Proceedings, Book 5, pp. 2231–2236.

TABLE I. Description of the sources that produced the various impulse types. M=muzzle bang, P=projectile bang, R=reflection. The slope of the high-pass (HP) filter was equal to −18 dB/octave. The ''effective'' signal duration was measured at the ears of the subjects. The rise time was determined for free-field (recording) and for indoor (room) conditions.

No.	Firearm/ammunition	Component	Modification	Signal duration (ms)	Rise time (ms)	
					Recording	Room
1	Pistol 9 mm	M	···	260	<1	6
2	Rifle 7.62 mm	M	···	340	1	15
3	Rifle 0.30 in.	M	···	430	<1	10–50
4	Howitzer 155 mm, charge 5M4	M	HP 315 Hz	200	4	5
5	Cannon 25 mm DST 127	P, M	···	190	5[a]	15[a]
6	Machine gun 0.5 in.	M	···	360	2	10–40
7	Howitzer 155 mm, charge 5M4	M	HP 100 Hz	500	4	5
8	Cannon 35 mm	P, M, R	···	220	<1[a]	6[a]
9	Cannon 35 mm	P, M	···	140	8[a]	10[a]
10	Cannon 35 mm	M	···	430	<1	8
11	Howitzer 155 mm, charge 5M4	M	HP 63 Hz	460	16	85
12	Hand grenade	detonation	···	380	22	80
13	Antitank weapon 84 mm	M	···	410	15	70
14	Howitzer 155 mm, charge 5M4	M	···	370	15	70

[a]Rise times for the projectile bang.

ence ($L_{CE}-L_{AE}$) between the C-weighted sound exposure level (CSEL; L_{CE}) and ASEL (Buchta, 1996; Krahé and Buchta, 1994). For more continuous sounds at several work places, Kjellberg *et al.* (1997) showed that addition of the difference between the (indoor) C- and A-weighted average levels resulted in a small but significant increase in the predictability of the annoyance. In the present experiment the various firearms were selected in such a way that for the entire range of $L_{CE}-L_{AE}$ (from −1 to about 30 dB), a balanced distribution of the number of events was obtained. Sixteen subjects rated the annoyance for the simulated conditions of (1) being outdoors, and (2) being indoors with the windows closed. Since the outdoor-to-indoor reduction in sound level is highly dependent on frequency, and the sounds to be rated varied considerably in spectral content, inclusion of these two listening conditions was considered to be very relevant.

II. METHODS

A. Stimuli

In addition to muzzle bangs produced by small (impulse types 1, 2, and 3 in Table I), medium-large (impulse types 6 and 10), and large firearms (impulse types 12, 13, and 14), the experiment also included combinations of muzzle and projectile bangs (impulse types 5, 8, and 9) and spectral modifications of the 155-mm howitzer muzzle bang (impulse types 4, 7, and 11). For the relevant impulse types, digital recordings (sampling rate 48 kHz, amplitude resolution 16 bits) were made at source–receiver distances ranging from 100–200 m for the small firearms to 800–900 m for the medium-large and large firearms. Larger recording distances would have resulted in poor signal-to-noise ratios.

The recorded sounds were sampled down to 16.1 kHz and stored as files on the hard disk of a personal computer. Various versions of the impulse sound were prepared from each recording. For the outdoor rating condition there were four such versions per impulse type, yielding 56 (14 types×4 levels) different impulses. The (outdoor) ASELs ranged from 40 to 70 dB. The corresponding sound quality of the impulses, which is among other things dependent on the distance between the source and the receiver, was simulated both by broadband attenuation (geometric spreading) and by attenuation of the high-frequency components (air absorption). The phase relations in the various impulse type versions were not affected. To simulate the outdoor-to-indoor noise reduction in the indoor rating condition (windows closed), a further spectral reduction of the impulses was equal to 13 dB for the 16-Hz and 31.5-Hz octave bands, and linearly increased from 13 dB for the latter octave band up to 35 dB for the 8-kHz octave band. The adopted (rather conservative) frequency-dependent façade attenuation was based on the outdoor-to-indoor airborne noise reduction characteristics for various kinds of single- and double-glazed windows that might be regarded as typical for Dutch dwellings (Brackenhoff *et al.*, 1981). Within a few decibels, such a reduction was also found to be representative of houses located in the greater Washington, DC area (Yaniv *et al.*, 1982). In some countries, such as in Switzerland, application of special window glazing might, at least for frequencies higher than about 50 Hz, result in higher sound-level reductions (Meloni and Rosenheck, 1995).

The attenuation of the signals (geometric spreading, air absorption, and façade reduction) was performed with the help of a finite impulse response (FIR) filter on a DSP card. The filter was also used to compensate, as much as possible, for both the resonances due to room dimensions and the nonflat frequency characteristics of the loudspeakers and the audio chain. At the subject's listening position, the response was flat within 3–5 dB over a frequency range from 25 to 4000 Hz.

For the set of 56 impulses presented in the outdoor rating condition, 21 impulses were not or were hardly audible after application of the outdoor-to-indoor noise reduction. As a result, the number of impulses included in the indoor rating condition was reduced to 35.

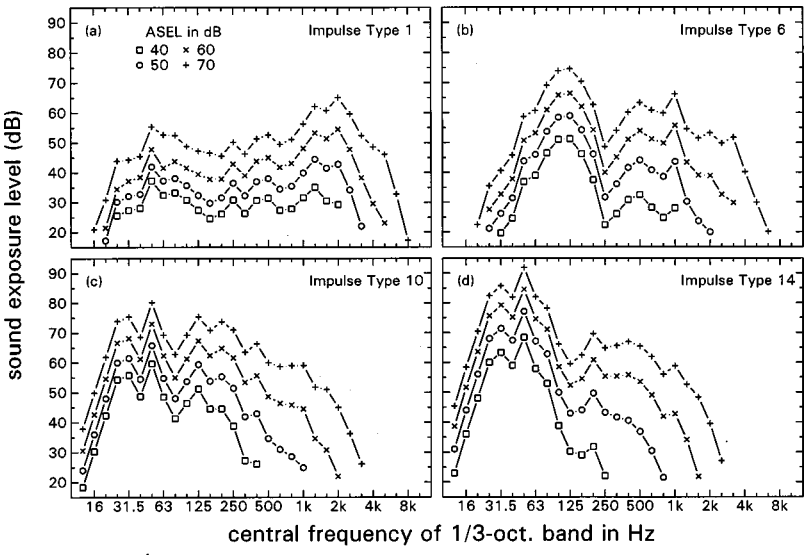

FIG. 1. Sound exposure levels in the various 1/3-octave bands for the muzzle bang from (a) a 9-mm pistol; (b) a 0.5-in. machine gun; (c) a 35-mm cannon; and (d) a 155-mm howitzer, as determined at the ears of the subjects in the simulated outdoor condition. For each impulse type, the four spectra correspond to overall ASELs of 40, 50, 60, or 70 dB.

Figure 1 shows the linear sound exposure level (SEL) in the various 1/3-octave bands for the four versions of the muzzle bang from a 9-mm pistol, a 0.5-in. machine gun, a 35-mm cannon, and a 155-mm howitzer, as determined at the ears of the subjects in the outdoor rating condition. Especially for the pistol bangs [Fig. 1(a)] presented at relatively high overall levels (L_{AE} equal to 60 and 70 dB), the spectral content is dominated by the energy in the frequency bands between about 800 and 2500 Hz, whereas for all howitzer bangs [Fig. 1(d)], the spectral content is dominated by the energy in frequency bands between about 20 and 100 Hz. For frequencies lower than 25 Hz, the sound levels of the howitzer bangs drop by about 35 dB/octave. Results from outdoor measurements reported in Kerry *et al.* (1996), show that for a similar bang produced by a 155-mm howitzer, the sound level in this low-frequency band drops by about 6 dB/octave. The discrepancy between our spectra and those reported by Kerry *et al.* (1996) might for a relevant part be explained by the limitations of our audio system noted above.

For the machine gun [Fig. 1(b)] and the 35-mm cannon [Fig. 1(c)], the spectrum contains both lower and higher frequency components at a significant sound level. For all impulse types, Fig. 1 also shows that due to air absorption, the relative contribution of the higher frequency components decreases with overall level.

The rise time of the impulses, defined as the time interval necessary for the sound to increase from 10% to 90% of the maximum amplitude, as measured at the ears of the subjects, varied from 5 ms for the relatively light bangs to about 80 ms for the heavy bangs (last column in Table I). For impulse types 3 and 6, the exact rise time could not be determined. For bangs with multiple components (impulse types 5, 8, and 9) only the rise time of the first component, which was the projectile bang in all cases, could be measured. In general, the rise time strongly depended on the measurement position in the room. In free-field conditions the rise times were considerably shorter (see the next-to-last column in Table I).

The sound quality of the impulse sounds was improved by fading out the signals after the first 500–1500 ms. The ''effective'' signal duration, defined here as the time interval between the moments at which the temporal envelope was higher than 10% of the maximum amplitude, ranged from about 150 to 500 ms (Table I).

Various experts from the Ministry of Defense, who had been working on infantry or artillery firing ranges, confirmed that the bangs sounded realistic. This held true also for the heavy bangs produced by the hand grenade, the 84-mm antitank weapon, and the 155-mm howitzer. Given that for frequencies higher than 25 Hz the frequency response was flat, it is not *a priori* evident that our experimental results would have been different if we had been able to reproduce the sound levels reported in Kerry *et al.* (1996) for frequencies lower than 25 Hz.

In order to make the acoustic environment more realistic as well, a background noise of remote road traffic was continuously present throughout the experiment at an A-weighted average level of 35 and 40 dB in the indoor and the outdoor conditions, respectively. In both conditions, the spectral content was dominated by energy in the frequency range between 25 and 125 Hz. For higher frequencies, the spectral envelope slope was −7 dB/octave in the outdoor, and −9 dB/octave in the indoor condition.

B. Apparatus

The experiment was entirely computer controlled. The sounds were reproduced in the listening room ($w \times l \times h = 3.5 \times 5.9 \times 3.3$ m) by means of two amplifier/speaker sets, one set for frequencies lower than, and one set for frequencies higher than 150 Hz. The speakers were hidden behind a curtain. The reverberation time of the room corresponded to that of a normal living room. Hearing thresholds were determined with the help of a Madsen Memory Threshold Audiometer (MTA 86).

C. Subjects

Sixteen subjects, nine males and seven females, between 18 and 27 years of age, participated in the experiment. Be-

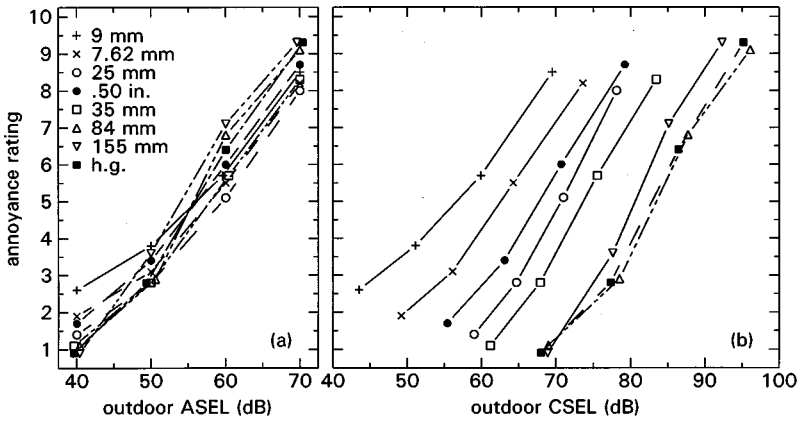

FIG. 2. Mean annoyance ratings in the outdoor condition, as a function of (a) outdoor ASEL and (b) outdoor CSEL, for various impulse sound types.

fore the experimental sessions, their hearing thresholds were determined with pure tones between 250 and 8000 Hz. Thirteen subjects had hearing levels $\leqslant$15 dB in any part of the audiogram (best ears). Three subjects with hearing levels $\leqslant$5 dB for frequencies up to 4000 Hz had local hearing losses of 20–25 dB at 6000 Hz. Since frequencies higher than 4000 Hz were considered to be irrelevant to the present study, these three subjects were regarded as suitable participants. The subjects were paid for their services.

D. Experimental design

The independent variables were: (1) listening condition (acoustic simulation of an outdoor situation such as in the garden or on the balcony or terrace, versus a simulation of an indoor situation with the windows closed); (2) impulse type (14 types produced by firearms ranging in caliber from 7.62 to 155 mm; see Table I); (3) sound level (outdoor ASELs of 40, 50, 60, or 70 dB). In Sec. II A, it was explained that with respect to sound level, we have an incomplete factorial design. All three factors were varied within subjects. Each of the 56 outdoor and 35 indoor conditions was presented twice for rating.

E. Procedure

Eight subjects started with the outdoor condition and the other eight started with the indoor condition. After each trial, in which a specific stimulus was presented twice within about 8 s, the subjects responded to the question ''How annoying would you find the sound if you heard it at home [(a) in the garden or on the balcony, or (b) in the living room, workroom, or study with the windows closed] on a regular basis?'' They were encouraged to use the whole range of the rating scale with values from 1 (''not annoying at all'') to 10 (''extremely annoying'').

The 56 stimuli in the outdoor condition were assigned to four blocks of 14 stimuli each. Both for the first and for the second ratings, presentation order of these blocks was balanced by means of Latin squares. The 35 stimuli in the indoor condition were assigned to two blocks which were again presented twice, and in a balanced order. Presentation order of the stimuli within the blocks was randomized. Before the experimental sessions, the subjects received six practice trials. The total duration of the experimental session was about 4 h, including breaks in between. The background noise was continuously present without interruption.

III. RESULTS

The annoyance ratings will first be related to ASEL and, for the sake of comparison, to CSEL of the impulses. In the indoor rating condition, the annoyance will be related to indoor levels and, since in noise zoning it is mandatory to express the noise dose as levels measured outdoors, also to the corresponding outdoor levels.

A. Outdoor ratings

The annoyance ratings were subjected to an analysis of variance [16 (subjects) $\times$ 14 (impulse type) $\times$ 4 (sound level) $\times$ 2 (replication), all repeated measures]. The procedure for the analysis of data collected in such a repeated measures design, as well as the meaning of the F tests, the relevant degrees of freedom df_1 and $df_2[F(df_1,df_2)]$, and the estimated level of significance (p), is described in, for example, Keppel (1973). The ratings significantly[1] increased with increasing ASEL [$F(3,45)=620$, $p<0.000\,001$] and were significantly affected by impulse type [$F(13,195)=10.5$, $p<0.000\,001$]. A *post hoc* Tukey test (Winer, 1970) showed that averaged across sound level, the bangs from impulse types 1, 3, 6, 7, 11–14 were all more annoying than the bangs from impulse types 8 and 9 ($p\leqslant0.05$). Moreover, there was a significant interaction effect between impulse type and sound level [$F(39,585)=8.2$, $p<0.000\,001$]: At low ASELs the impulses produced by small firearms were more annoying than those produced by medium-large and large firearms, whereas at high ASELs the impulses produced by the small firearms were less annoying than those produced by the large firearms.

This interaction effect is shown in Fig. 2(a), where the ratings, averaged across subjects and replications, are plotted as a function of outdoor ASEL for 8 of the 14 impulse types.

On the basis of the mean annoyance ratings given in columns 2–5 of Table II, it can be verified that the nature of the interaction effect described above also holds for the impulse types that were not included in Fig. 2(a).

For the total set of 56 impulses, 95% of the variance in the mean ratings could be explained by ASEL. From the data shown in Fig. 2(b), it can be concluded that, relative to ASEL, outdoor CSEL is an inadequate predictor of the an-

TABLE II. Annoyance ratings, averaged across subjects and replications, for the 14 impulse types, and the outdoor measured ASELs (dB) in the two listening conditions.

Impulse type no.	Listening condition						
	Outdoors				Indoors		
	ASEL: 40	50	60	70	50	60	70
1	2.6	3.8	5.7	8.5	···	3.4	5.6
2	1.9	3.1	5.5	8.2	···	3.0	5.9
3	2.0	3.6	6.2	8.7	···	3.7	6.5
4	1.8	3.3	5.1	8.1	···	3.2	5.5
5	1.4	2.8	5.1	8.0	···	3.4	5.9
6	1.7	3.4	6.0	8.7	···	3.7	6.7
7	1.3	3.5	6.1	8.6	···	4.2	7.3
8	1.3	2.7	4.9	7.9	1.5	3.4	5.9
9	1.0	2.4	4.7	7.4	1.0	3.3	5.8
10	1.1	2.8	5.7	8.3	1.2	3.7	7.1
11	1.2	3.2	6.4	9.0	1.7	4.6	7.7
12	0.9	2.8	6.4	9.3	1.6	4.6	8.1
13	1.1	2.9	6.8	9.1	1.6	5.2	7.9
14	0.9	3.6	7.1	9.3	1.8	5.2	8.3

noyance. For the total set, the portion of the variance in the mean ratings explained by (outdoor) CSEL was as small as 54%. Table III shows the outdoor CSELs for the 56 conditions.

B. Indoor ratings as a function of outdoor levels

The annoyance ratings were subjected to two analyses of variance. In the first analysis, the ratings given for the 14 impulse types that were presented at outdoor ASELs of 60 and 70 dB were included. In the second analysis, only the ratings given for impulse types 8–14 were included; in this case all three outdoor ASELs could be considered. In both analyses, the ratings significantly increased with increasing ASEL [in the first analysis $F(1,15)=272$, in the second analysis $F(2,30)=340$; in both cases $p<0.000\,001$]. Again, there was a significant effect of impulse type [in the first analysis $F(13,195)=20.1$, in the second analysis $F(6,90)=20.2$; in both cases $p<0.000\,001$].

TABLE III. Outdoor CSEL for the 56 conditions included in the experiment.

Impulse type no.	Outdoor ASEL			
	40	50	60	70
1	43.5	51.1	59.9	69.5
2	49.2	56.1	64.3	73.6
3	52.5	60.4	68.7	77.8
4	46.4	55.4	64.7	73.9
5	59.0	64.7	71.0	78.1
6	55.4	63.0	70.7	79.2
7	61.2	67.3	73.6	80.3
8	55.4	62.1	70.1	78.8
9	59.9	65.1	71.7	79.3
10	61.3	67.9	75.5	83.4
11	65.9	73.4	80.3	86.8
12	68.0	77.3	86.4	95.2
13	69.0	78.5	87.7	96.1
14	68.9	77.6	85.1	92.3

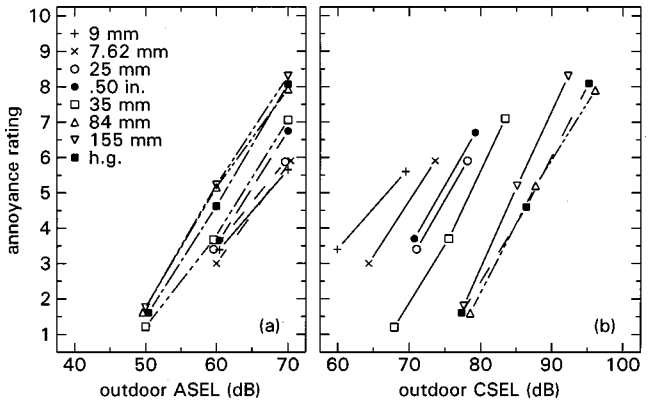

FIG. 3. Mean annoyance ratings in the indoor condition, as a function of (a) outdoor ASEL and (b) outdoor CSEL, for various impulse sound types.

Two *post hoc* Tukey tests showed that averaged across sound level, the bangs from impulse types 1–6, 8, and 9 were significantly less annoying ($p<0.01$) than the bangs from impulse types 11–14.

Again, there was a significant effect between impulse type and sound level [in the first analysis $F(13,195)=2.8$, $p<0.002$; in the second analysis $F(12,180)=8.2$, $p<0.000\,001$].

As shown in Fig. 3(a) for 8 of the 14 impulse types, the increase in the annoyance with outdoor ASEL was larger for the impulses produced by the large firearms than for those produced by the smaller firearms. On the basis of the mean annoyance ratings given in columns 6–8 of Table II, it can be verified that the nature of the interaction effect just described also holds for the impulse types that were not included in Fig. 3(a).

For the total set of 35 impulses, 87% of the variance in the mean ratings could be explained by outdoor ASEL. From the data shown in Fig. 3(b), it must again be concluded that outdoor CSEL is less effective as a predictor of the annoyance. For the total set, the portion of the variance in the mean ratings explained by outdoor CSEL was only 50%.

C. Indoor ratings as a function of indoor levels

For eight impulse types, Fig. 4(a) shows the mean indoor annoyance ratings as a function of indoor ASEL determined at the ears of the subjects. For equal indoor ASELs the impulses produced by the smaller firearms were more annoying than those produced by the medium-large and large firearms.

Columns 2–4 of Table IV list the indoor ASELs for the various outdoor levels and the 14 impulse types. For the total set of the 35 impulses, 88% of the variance in the mean ratings could be explained by indoor ASEL.

From the data shown in Fig. 4(b), it must be concluded that indoor CSEL is a less effective predictor of the annoyance than indoor ASEL. For the total set, the portion of the variance in the mean ratings explained by outdoor CSEL was as small as 33%.

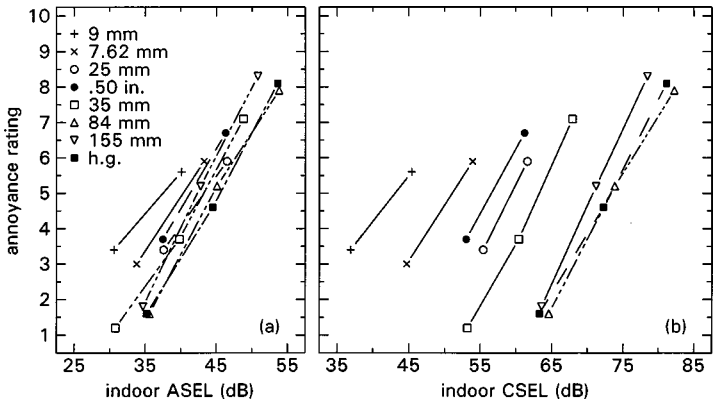

FIG. 4. Mean annoyance ratings in the indoor condition, as a function of (a) indoor ASEL and (b) indoor CSEL, for various impulse sound types.

IV. FEATURES OF A NEW RATING PROCEDURE FOR A GREAT VARIETY OF SHOOTING SOUNDS

A. The additional adjustment for heavy bangs

To obtain ASEL of equally annoying vehicle sounds, ASEL for impulse sounds produced by small firearms ($L_{CE}-L_{AE}\sim 0$ dB) has to be increased by an adjustment of 12 dB (Vos, 1995a). Since at the relevant receiver points the differences between the spectra for the sounds from small firearms and the spectra for (local) road-traffic sounds are relatively small, the 12-dB adjustment holds both for indoor (windows closed or opened) and for outdoor rating conditions (Schomer *et al.*, 1994; Schomer and Wagner, 1995; Vos, 1995a).

Both in the outdoor and in the indoor rating conditions, significant interaction effects between impulse type and sound level were found (Sec. III). Consequently, for rating shooting sounds in general, in addition to the 12-dB adjustment, a second level-dependent adjustment is required. This latter adjustment will now be quantified on the basis of the results of the present experiment.

1. Indoor ratings as a function of outdoor levels

The maximum size of the second adjustment is shown in Fig. 5(a), where the indoor ratings are plotted as a function of outdoor ASEL for the three heavier firearms (impulse types 12–14), with the ratings for the pistol as a reference.

TABLE IV. Indoor ASELs and CSELs, as determined at the ears of the subjects, for impulse type and outdoor ASEL.

Impulse type no.	ASEL (dB)			CSEL (dB)		
	ASEL: 50	60	70	50	60	70
1	···	30.6	40.1	···	36.9	45.4
2	···	33.8	43.3	···	44.7	53.9
3	···	35.9	45.2	···	50.9	59.8
4	···	36.1	45.4	···	41.9	50.6
5	···	37.6	46.5	···	55.4	61.6
6	···	37.5	46.3	···	53.0	61.2
7	···	38.4	47.0	···	58.0	64.1
8	29.2	38.7	48.1	46.2	52.8	60.5
9	29.5	38.7	47.9	50.3	56.0	62.2
10	30.8	39.8	48.8	53.2	60.4	67.9
11	33.0	40.8	48.7	58.9	65.7	72.0
12	35.2	44.5	53.6	63.3	72.2	81.1
13	35.6	45.1	53.8	64.6	73.8	82.2
14	34.7	42.8	50.8	63.6	71.2	78.4

With respect to the difference between outdoor CSEL and outdoor ASEL, the bangs produced by these heavier firearms were clearly distinct from the other bangs: For $L_{AE}=50$ dB, $L_{CE}-L_{AE}>27$ dB, and for $L_{AE}=70$ dB, $L_{CE}-L_{AE}>22$ dB (see Table III). These values of $L_{CE}-L_{AE}$ are comparable to those predicted by Hirsch (1998).

In addition to equally high values of $L_{CE}-L_{AE}$, the bangs from these heavier firearms also yielded about the same indoor annoyance ratings (y) at comparable ASELs: the regression line fitted to the data ($y=-14.4+0.322L_{AE}$) explains 99% of the variance in the mean ratings. Relative to the dose-response relation for the pistol bangs ($y=-9.8+0.22L_{AE}$), the additional adjustment for the heavier bangs increases from 5 dB at an outdoor ASEL of about 51 to 10 dB at an outdoor ASEL of 66 dB. The general equation for the additional adjustment, P_a in decibel, follows from the slopes and intercepts of the two functions, and is given by $P_a=-20.82+0.464L_{AE}$, or $P_a=0.46(L_{AE}-45)$ dB.

2. Outdoor ratings

The outdoor ratings for the bangs from the three heavier firearms and the pistol are shown in Fig. 5(b). Again, the annoyance caused by the heavier bangs is well predicted by a single regression line. The equation of the function is given by $y=-10.64+0.285L_{AE}$, $r^2=0.98$. Relative to the function for the pistol bangs ($y=-5.63+0.196L_{AE}$; $r^2=0.97$), the additional adjustment for the heavier bangs increases

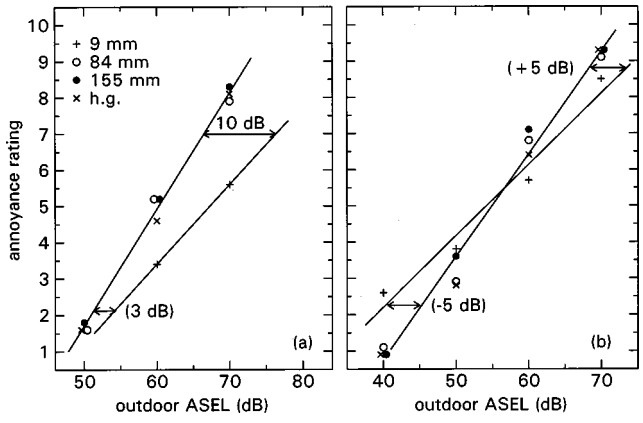

FIG. 5. Mean annoyance ratings as a function of outdoor ASEL for the bangs from the three heavier firearms (impulse types 12–14) and the bangs from the pistol as references. Inserted solid lines are regression functions. (a) Indoor ratings; (b) outdoor ratings.

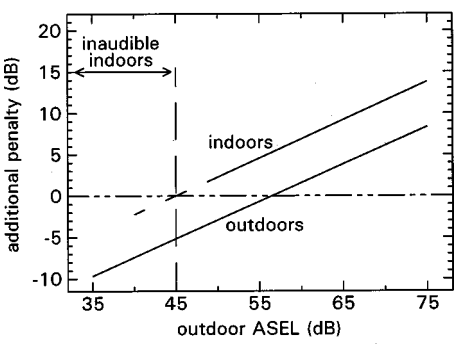

FIG. 6. Additional adjustments for the heavier bangs, as a function of outdoor ASEL for the indoor and outdoor rating conditions, separately.

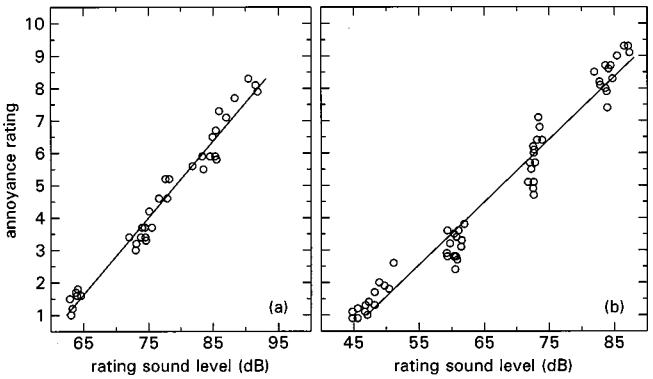

FIG. 7. Mean annoyance ratings as a function of the rating sound level. Inserted lines are regression functions. (a) Indoor ratings; (b) outdoor ratings.

from −5 dB at an outdoor ASEL of 45 to +5 dB at an outdoor ASEL of 68 dB. The general equation is given by $P_a = 0.45(L_{AE} - 56.5)$ dB.

3. A comparison of the results obtained in the two rating conditions

Figure 6 shows the additional adjustment for the heavier bangs as a function of outdoor ASEL for the indoor and outdoor rating conditions, separately. The additional adjustment for the heavier bangs is consistently 5 dB lower for the outdoor than for the indoor conditions. For $L_{AE} < 57$ dB in the outdoor rating condition, the additional adjustment is smaller than 0 dB, yielding an overall adjustment that is smaller than the 12-dB penalty for the impulses from small firearms. At an outdoor ASEL of 40 dB, outdoor listeners are still able to hear the impulse sounds. With respect to the annoyance, however, the overall adjustment to ASEL is reduced to 5 dB.

For the indoor rating conditions, negative additional adjustments are not relevant, because in general, bangs from large firearms with an outdoor $L_{AE} < 45$ dB are either inaudible or result in a sensation that is too low to elicit an annoyance reaction.

B. Determination of the rating sound level for single events

1. Indoor ratings

In Sec. IV A 1, it was shown that for the bangs from the large firearms, the additional adjustment was equal to $P_a = 0.46(L_{AE} - 45)$ dB. For these bangs, $L_{CE} - L_{AE}$ was 28.5 dB at the maximum (see Table III, columns 3–5). For bangs with lower values of $L_{CE} - L_{AE}$, the additional adjustment must be smaller. Lower adjustments might be obtained by introducing the term $(L_{CE} - L_{AE})/\max(L_{CE} - L_{AE})$. With maximum $L_{CE} - L_{AE}$ set to the rounded figure of 30 dB, the equation reduces to $P_a = 0.015(L_{CE} - L_{AE})(L_{AE} - 45)$ dB.

The validity of this modification is demonstrated by means of a multiple linear regression analysis performed on the 35 mean indoor ratings (dependent variable) and on corresponding outdoor ASELs and products of CSEL-ASEL and ASEL as predictors. With ASEL, r^2 was equal to 87%. With $(L_{CE} - L_{AE})(L_{AE} - 45)$ added as the second predictor, (multiple) r^2 increased to 97%. Statistically, this increase of 10 percent points in the explained variance was highly significant ($p < 0.000\,001$).

The rating sound level for any single impulsive event is given by

$$L_r = L_{AE} + 12\ \text{dB} + \beta(L_{CE} - L_{AE})(L_{AE} - \alpha)\ \text{dB}, \qquad (1)$$

in which $\alpha = 45$ dB and $\beta = 0.015\ \text{dB}^{-1}$.

Figure 7(a) shows the indoor annoyance ratings as a function of the proposed rating sound level for all 35 impulses. As expected, the solid regression line included in Fig. 7(a) explained 97% of the variance in the annoyance ratings. With a perfect rating procedure, all data points were to coincide the regression line. Expressed as decibel values, the root-mean-square of the differences between the obtained rating sound level and the rating sound level predicted by the regression line for the same annoyance rating was as small as 1.6 dB.

2. Outdoor ratings

In Sec. IV A 2, it was shown that for the bangs from the large firearms, the additional adjustment was equal to $P_a = 0.45(L_{AE} - 56.5)$ dB. In line with the procedure described for the indoor ratings, the additional adjustment is given by $P_a = 0.015(L_{CE} - L_{AE})(L_{AE} - 56.5)$ dB.

In Sec. III A it had already been shown that 95% of the variance in the mean ratings could be explained by ASEL. By means of a multiple linear regression analysis performed on the 56 mean outdoor ratings $(L_{CE} - L_{AE})(L_{AE} - 56.5)$ was added as a second predictor. The explained variance increased from 95% to 96%. The small increase of 1 percent point was statistically significant ($p < 0.001$).

The rating sound level for any single impulsive event is given by Eq. (1) with α and β set to 56.5 and 0.015 dB^{-1}, respectively. Figure 7(b) shows the outdoor annoyance ratings as a function of the proposed rating sound level for all 56 impulses. Expressed as decibel values, the root-mean-square of the differences between the obtained rating sound level and the rating sound level predicted by the regression line for the same annoyance rating was 2.8 dB.

V. DISCUSSION

A. Integration of the results for the indoor and outdoor rating conditions

In Sec. IV, it was shown that the additional adjustment for the heavier bangs was consistently 5 dB lower for the outdoor than for the indoor rating conditions. At present, detailed information about the extent to which the overall annoyance is determined by indoor and outdoor experienced annoyance is lacking.

The relation between indoor and outdoor annoyance has been researched in laboratory or quasilaboratory studies, in which the sounds were produced by subsonic (Robinson *et al.*, 1963; Bishop, 1966; Bowsher *et al.*, 1966; Kryter, 1970; Gunn *et al.*, 1981) or supersonic aircraft (Kryter, 1970; Johnson and Robinson, 1966), and by light-heavy vehicles (Watts and Nelson, 1993; Vos, 1997a). The indoor annoyance was always lower than the outdoor annoyance, provided that the outdoor sound levels were the same. Field surveys on the annoyance caused by railway (Peeters *et al.*, 1984) or road-traffic sounds (Myncke *et al.*, 1977) showed that the annoyance was lower with the windows closed than with the windows open.

In most studies, however, the differences were smaller than what would be expected on the basis of the façade attenuation. This may imply that the listeners were more tolerant of the sounds in outdoor than in indoor conditions. For the various laboratory studies, the estimated difference in tolerance ranged from 0 dB (Gunn *et al.*, 1981) up to 15–18 dB (Robinson *et al.*, 1963; Bishop, 1966). Since the results may have been affected by the range of both the levels of the sounds and the response scale used by the listeners (Poulton, 1989), it is impossible to estimate the differences precisely.

In field surveys it is less likely that range effects will influence the results. In the field study on the annoyance caused by railway noise (outdoor A-weighted equivalent level, L_{Aeq}, between 40 and 70 dB), the respondents were more tolerant of the sounds as heard indoors with the windows open than as heard indoors with the windows closed (Peeters *et al.*, 1984). For outdoor $L_{\mathrm{Aeq}}<70$ dB, comparable results were obtained in the field study on the annoyance caused by road-traffic sounds (Myncke *et al.*, 1977). For very high outdoor levels ($70<L_{\mathrm{Aeq}}<80$ dB) included in the latter study, such differences in tolerance could not be observed.

In the field survey reported by Myncke *et al.* (1977), the respondents were also asked to rate their overall annoyance. Both for the respondents in Antwerp and for those in Brussels, the overall annoyance was in between the annoyance rated in the conditions with closed and the conditions with open windows. This indicates that the overall annoyance was determined by both conditions. A comparable result was obtained in a field survey reported by Birnie *et al.* (1980). From multiple linear regression analyses performed on annoyance ratings for aircraft and road-traffic sounds, they concluded that both the outdoor and the indoor ratings significantly contributed to the overall annoyance. Unfortunately, they did not give final regression weights for the two rating conditions.

If the annoyance in the indoor and outdoor conditions would contribute equally to the overall annoyance, then the intercept of the appropriate function for the additional adjustment to the heavier bangs should be 1.8 dB lower $[10\log(0.5\cdot 10^{0/10}+0.5\cdot 10^{-5/10})=-1.8\,\mathrm{dB}]$ than the function for the indoor rating condition (Fig. 6), which results in a change of α in Eq. (1) from 45 to 49 dB. If the relative contribution of the annoyance in the indoor and outdoor conditions to the overall annoyance would be equal to 3:1, then the appropriate value for α would be 47 dB.

B. Future research topics

Especially for the shooting sounds produced by medium-large and large firearms, there have been various discussions about which acoustic measure, or which frequency weighting, would be more appropriate, ASEL or CSEL (Buchta, 1996; Bullen *et al.*, 1991; Meloni and Rosenheck, 1995; Schomer, 1977; Schomer and Sias, 1998; Vos, 1995b).

The present results led to an efficient and general method for rating shooting sounds: (1) there is no need to develop separate procedures for different categories of firearm calibers, and (2) both ASEL and CSEL are needed for an adequate prediction of the annoyance.

Although the present study adopts (outdoor) ASEL as the principal predictor of annoyance, the experimental results show that inclusion of (outdoor) CSEL results in a small improvement of the prediction of the annoyance for outdoor rating conditions (see Sec. IV B 2), and in a large improvement of the prediction of the annoyance for indoor rating conditions (see Sec. IV B 1).

The benefit of using both A-weighted and C-weighted sound levels (either measured with the time constant of 125 ms, or expressed as sound exposure levels) has also been shown by Buchta (1996) for explaining differences in the annoyance caused by the impulses produced by rifles, 20–35-mm cannons, and various detonations, and by Schomer and Sias (1998) for explaining differences in the annoyance caused by sonic booms and blast sounds.

To explore the general validity of the proposed rating procedure, and to enhance its applicability, a number of topics must be investigated in the future. Three topics will be discussed briefly below.

1. Determination of the appropriate α- and β values in validation studies

In the present laboratory study, the predictability of the annoyance was considerably enhanced by adding $\beta(L_{\mathrm{CE}}-L_{\mathrm{AE}})(L_{\mathrm{AE}}-\alpha)$ as a second predictor. In field surveys, such a functional relationship between annoyance and the two acoustic measures could never have been found, simply because in the field (a) the respondents are required to give annoyance ratings on the basis of relatively long periods of time, and (b) the stimulus conditions to which they respond are usually very complex. However, it remains to be seen to what extent the values of α, and more importantly, the value of β, as estimated on the basis of the laboratory results, may be applied for obtaining the adequate rating sound level. Re-

call the general aim that numerically equal rating sound levels for shooting and road-traffic sounds should correspond to a similar degree of community response.

As mentioned in the previous section, the annoyance score obtained in the laboratory for a specific stimulus may be affected at least in part by the range of the stimulus levels and by the range of the response scale used (Poulton, 1989). As a result, these annoyance ratings cannot simply be interpreted in an absolute way. Recently, the relevance of comparing the effects of procedures developed on the basis of laboratory or quasilaboratory study results has been demonstrated for the community response to high-energy impulsive sounds. With the sound levels determined in free-field conditions, application of Schomer's level-dependent conversion procedure (Schomer, 1994) might lead to an underestimation of the rating sound level for artillery sounds by about 15 dB (Vos, 1997b, 2000; Buchta and Vos, 1998, 1999; Schomer, 1999). For rating impulse sounds produced by small firearms, however, the discrepancy between the average impulse noise adjustments derived from field and laboratory studies was not greater than about 3 dB (Vos, 1995a).

It might be further hypothesized that the poor fit between the laboratory and field data, as noted for artillery sounds, is in part related to the heightened annoyance response to the impulsive sounds heard during the night: The subjective effects due to nighttime shooting are included in the community response determined in field surveys, but to the knowledge of the present author, these effects have not really been included in the pertinent laboratory studies. The much better fit between the laboratory and field data for impulse sounds from small firearms can be understood from the fact that at the small firearm ranges included in the various field surveys, nighttime shooting occurred rarely if ever.

For a validation of the present procedure, detailed information about receiver levels (both ASEL and CSEL) of all relevant shooting sounds in various meteorological conditions, and, preferably for the same respondents, the A-weighted equivalent level of road-traffic sounds, is needed. If the corresponding community response is based on overall ratings, the problem raised in Sec. V A about the relative importance of the annoyance experienced indoors and outdoors may be avoided.

2. Exploring the usefulness of the rating procedure for other façade attenuation characteristics

Only in the indoor rating conditions was the predictability of the annoyance considerably enhanced by adding $\beta(L_{CE}-L_{AE})(L_{AE}-\alpha)$ as a second predictor. The simulated frequency-dependent façade attenuation represented the average of noise reduction characteristics that is frequently found for Dutch dwellings with the windows closed (Sec. II A).

It is of interest to verify the relevance of the second predictor both for lower and higher façade attenuation types. Lower outdoor-to-indoor noise reductions are relevant to residents who prefer their bedroom windows slightly opened for the major part of the year, and their living room windows open in the summer. Higher noise reductions are relevant to countries where special window glazing is generally applied for improving thermal isolation.

Preliminary results suggest that the benefit of the second predictor increases with increasing overall façade attenuation (Vos, 1998).

3. Determination of ASEL and CSEL in the field

The dynamic ranges of modern DAT recorders and sound-level meters allow reliable ASEL and CSEL measurements at relevant source–receiver distances. Wind-generated noise affects ASEL and CSEL measurements to the same extent (Schomer, 1986). However, at least at greater source–receiver distances, background noise from other environmental sounds, such as those from road traffic, may interfere with ASEL measurements for the impulses produced by large firearms and with CSEL measurements for the impulses produced by small firearms.

Consequently, if high-level background noise is continuously present, appropriate propagation models are required. Descriptions of a practical model that satisfactorily predicts the 16-Hz to 4-kHz-octave-band levels for distances up to 15 km may be found in Salomons *et al.* (1994) and in van den Berg *et al.* (1996).

VI. GENERAL CONCLUSIONS

(1) For the whole set of impulse sound types produced by various firearms ranging in caliber from 7.62 to 155 mm, the annoyance rated in outdoor conditions was almost entirely determined by (outdoor) ASEL of the impulses. The explained variance, r^2, in the mean ratings by ASEL was 0.95. The relation between outdoor annoyance and CSEL was much weaker ($r^2=0.54$).

(2) Similarly, the annoyance rated indoors with the windows closed was much better predicted from outdoor ASEL($r^2=0.87$) than from outdoor CSEL($r^2=0.50$). However, on the basis of both ASEL and the product $(L_{CE}-L_{AE})(L_{AE}-\alpha)$, an almost perfect prediction of the annoyance was obtained (multiple $r^2=0.97$).

(3) For the entire set of impulses rated indoors with the windows closed, the rating sound level, L_r, is given by $L_r=L_{AE}+12\,\text{dB}+\beta(L_{CE}-L_{AE})(L_{AE}-\alpha)$, with $\alpha=45\,\text{dB}$ and $\beta=0.015\,\text{dB}^{-1}$. For the outdoor annoyance ratings, the optimal parameter values were equal to $\alpha=57\,\text{dB}$ and, again, $\beta=0.015\,\text{dB}^{-1}$.

(4) The present laboratory results led to an efficient general method for rating a great variety of shooting sounds. There is no need to develop separate procedures for different categories of firearm calibers. There are just two relevant acoustic measures: ASEL and CSEL.

(5) In validation studies, in which the effects of the present rating procedure will be compared to existing data reported in field surveys on the annoyance caused by shooting and road-traffic sounds, it has to be determined to what extent the constants α and β have to be adjusted.

ACKNOWLEDGMENTS

This research was financed by the Netherlands Ministry of Defense. The preparation of the present paper was further supported by Grant No. D99-101 from TNO Human Factors.

[1]In this example, the null hypothesis (H_0) was that the four conditions with different ASELs would yield identical annoyance ratings. The alternative hypothesis (H_1) was that the ratings would depend on ASEL. To test H_0 against H_1 requires the construction of an F ratio between a specific mean square in the numerator (with the degrees of freedom represented by df_1) and a mean square in the denominator (with the degrees of freedom represented by df_2). These mean squares are calculated in the analysis of variance. Under H_0, the expected value of the F ratio is unity. In the present example, the F ratio is equal to 620. The decision rules in the statistical test are with respect to the rejection or nonrejection of H_0. If the decision rules reject H_0 when in fact H_0 is true, the rules lead to an erroneous decision. The probability of making this kind of error is at most equal to the level of significance (p) of the test. In the present research area, the risk one is willing to take in rejecting the tested hypothesis falsely is given by $\alpha = 0.05$ or $\alpha = 0.01$. Since, in the present example, the estimated level of significance ($p = 0.000\,001$) is much smaller than criterion α, it is concluded that the ratings were indeed affected by ASEL.

Birnie, S. E., Hall, F. L., and Taylor, S. M. (**1980**). ''The contribution of indoor and outdoor effects to annoyance at noise in residential areas,'' in Proceedings Internoise 1980, Miami, pp. 975–978.

Bishop, D. E. (**1966**). ''Judgments of the relative and absolute acceptability of aircraft noise,'' J. Acoust. Soc. Am. **40**, 108–122.

Bowsher, J. M., Johnson, D. R., and Robinson, D. W. (**1966**). ''A further experiment on judging the noisiness of aircraft in flight,'' Acustica **17**, 245–267.

Brackenhoff, H. E. A., Buis, P. M., and von Meier, A. (**1981**). *Handleiding Meten en Rekenen Industrielawaai [Guide for Measuring and Calculating Industrial Noise]* (Leidschendam, The Netherlands), ICG-Report IL-HR-13-01 (in Dutch).

Buchta, E. (**1994**). *Belästigung durch Kanonen- und Straßenverkehrslärm* (Institut für Lärmschutz, Düsseldorf, Germany).

Buchta, E. (**1996**). ''Annoyance caused by shooting noise—determination of the penalty for various weapon calibers,'' in *Proceedings Internoise 1996* (Institute of Acoustics, St. Albans, U.K.), Book 5, pp. 2495–2500.

Buchta, E., and Vos, J. (**1998**). ''A field survey on the annoyance caused by sounds from large firearms and road traffic,'' J. Acoust. Soc. Am. **104**, 2890–2902.

Buchta, E., and Vos, J. (**1999**). Response to ''Comments on 'A field survey on the annoyance caused by sounds from large firearms and road traffic' '' [J. Acoust. Soc. Am. **106**, 1594–1597], J. Acoust. Soc. Am. **106**, 1598–1601.

Bullen, R. B., Hede, A. J., and Job, R. F. S. (**1991**). ''Community reaction to noise from an artillery range,'' Noise Control Eng. J. **37**, 115–128.

Gunn, W. J., Shigehisa, T., Fletcher, J. L., and Shepherd, W. T. (**1981**). ''Annoyance response to aircraft noise as a function of contextual effects and personality characteristics,'' J. Aud. Res. **21**, 51–83.

Hirsch, K.-W. (**1998**). ''Prediction of the difference between CSEL and ASEL of blast sounds for purposes of predicting annoyance,'' in Proceedings of the 16th ICA and 135th Meeting ASA, edited by P. K. Kuhl and L. A. Crum (University of Washington, Seattle, WA), Vol. I, pp. 478–458.

Johnson, D. R., and Robinson, D. W. (**1967**). ''The subjective evaluation of sonic bangs,'' Acustica **18**, 241–258.

Keppel, G. (**1973**). *Design and Analysis. A Researcher's Handbook* (Prentice-Hall, Englewood Cliffs, NJ).

Kerry, G., Ford, R. D., and James, D. (**1996**). ''Bandwidth limitation effects on low-frequency impulse noise prediction and assessment,'' Appl. Acoust. **47**(4), 331–344.

Kjellberg, A., Tesarz, M., Holmberg, K., and Landström, U. (**1997**). ''Evaluation of frequency-weighted sound level measurements for prediction of low-frequency noise annoyance,'' Environ. Int. **23**(4), 519–527.

Krahé, D., and Buchta, E. (**1994**). ''Bestimmung der Lästigkeit von impulsartigen Geräuschen auf Basis der Lautheit,'' in *Fortschritte der Akustik—DAGA 1994* (Bad Honnef, BRD: DPG-GmbH, 1994), pp. 1117–1120.

Kryter, K. D. (**1970**). *The Effects of Noise on Man* (Academic, Orlando).

Meloni, T., and Rosenheck, A. (**1995**). ''Choice of frequency weighting for the evaluation of weapon noise,'' J. Acoust. Soc. Am. **97**, 3636–3641.

Myncke, H., Cops, A., and Gambart, R. (**1977**). ''Traffic noise measurements in Antwerp and Brussels. Part II: Enquiry concerning annoyance,'' in Proceedings 9th I.C.A.-Congress (Madrid, Spain), Paper E19.

Peeters, A. L., Kaper, J. P., de Jong, R. G., and Tukker, J. C. (**1984**). *Hinder door Spoorweggeluid in de Woonomgeving [Railroad Noise Annoyance in Residential Areas]* (Leidschendam, The Netherlands), ICG-Report RL-HR-03-03 (in Dutch).

Poulton, E. C. (**1989**). *Bias in Quantifying Judgments* (Erlbaum Associates, Hove, U.K.).

Robinson, D. W., Bowsher, J. M., and Copeland, W. C. (**1963**). ''On judging the noise from aircraft in flight,'' Acustica **13**, 324–336.

Salomons, E. M., van den Berg, F. H. A., and Brackenhoff, H. E. A. (**1994**). ''Long-term average sound transfer through the atmosphere: predictions based on meteorological statistics and numerical computations of sound propagation,'' in Proceedings of the 6th International Symposium on Long Range Sound Propagation, Ottawa, Canada, pp. 209–228.

Schomer, P. D. (**1977**). ''Evaluation of C-weighted L_{dn} for assessment of impulse noise,'' J. Acoust. Soc. Am. **62**, 396–399.

Schomer, P. D. (**1986**). ''High-energy impulsive noise assessment,'' J. Acoust. Soc. Am. **79**, 182–186.

Schomer, P. D. (**1994**). ''New descriptor for high-energy impulsive sounds,'' Noise Control Eng. J. **42**, 179–191.

Schomer, P. D. (**1999**). ''Comments on 'A field survey on the annoyance caused by sounds from large firearms and road traffic' '' [J. Acoust. Soc. Am. **104**, 2890–2902], J. Acoust. Soc. Am. **106**, 1594–1597.

Schomer, P. D., and Sias, J. W. (**1998**). ''On spectral weightings to assess human response, indoors, to blast noise and sonic booms,'' Noise Control Eng. J. **46**, 57–71.

Schomer, P. D., and Wagner, L. R. (**1995**). ''Human and community response to military sounds–II. Results from field-laboratory tests of sounds of small arms, 25-mm cannons, helicopters, and blasts,'' Noise Control Eng. J. **43**, 1–13.

Schomer, P. D., Wagner, L. R., Benson, L. J., Buchta, E., Hirsch, K.-W., and Krahé, D. (**1994**). ''Human and community response to military sounds: Results from field-laboratory tests of small-arms, tracked-vehicle, and blast sounds,'' Noise Control Eng. J. **42**, 71–84.

van den Berg, F. H. A., Kinneging, N. A., and Salomons, E. M. (**1996**). ''An overview of a method to predict average propagation of shooting noise in order to create computer-generated noise contours around shooting ranges,'' in *Proceedings Internoise 1996* (Institute of Acoustics, St. Albans, U.K.), Book 2, pp. 579–582.

Vos, J. (**1995a**). ''A review of research on the annoyance caused by impulse sounds produced by small firearms,'' in Proceedings Internoise 1995, Newport Beach, CA, Vol. 2, pp. 875–878.

Vos, J. (**1995b**). ''Technical note: On the comparability of community responses to noise from artillery and rifle ranges, as determined in two Australian studies,'' Noise Control Eng. J. **43**, 39–41.

Vos, J. (**1997a**). ''Annoyance caused by sounds of military tracked vehicles, for indoor and outdoor conditions,'' in Proceedings Internoise 1997, Budapest, Hungary, Vol. II, pp. 1003–1008.

Vos, J. (**1997b**). ''A re-analysis of the relationship between the results obtained in laboratory and field studies on the annoyance caused by high-energy impulsive sounds,'' Noise Control Eng. J. **45**, 123–131.

Vos, J. (**1998**). ''A further test of the relevance of ASEL and CSEL in the determination of the rating sound level for shooting sounds,'' in Proceedings of the 16th ICA and the 135th Meeting ASA, edited by P. K. Kuhl and L. A. Crum (University of Washington, Seattle, WA), Vol. I, pp. 459–460.

Vos, J. (**2000**). ''Comments on a procedure for rating high-energy impulsive sounds: Analyses of previous and new data sets, and suggestions for a revision,'' Noise Vib. Worldwide **31**, 18–29.

Watts, G. R., and Nelson, P. M. (**1993**). ''The relationship between vehicle noise measures and perceived noisiness,'' J. Sound Vib. **164**, 425–444.

Winer, B. J. (**1970**). *Statistical Principles in Experimental Design* (McGraw-Hill, London).

Yaniv, S. L., Danner, W. F., and Bauer, J. W. (**1982**). ''Measurement and prediction of annoyance caused by time-varying highway noise,'' J. Acoust. Soc. Am. **72**, 200–207.

Enhancing maximum measurable sound reduction index using sound intensity method and strong receiving room absorption

V. Hongisto,[a] M. Lindgren, and J. Keränen
Turku Regional Institute of Occupational Health, Laboratory of Ventilation and Acoustics, Lemminkäisenkatu 14-18 B, FIN-20520 Turku, Finland

(Received 26 October 1999; revised 9 October 2000; accepted 16 October 2000)

The sound intensity method is usually recommended instead of the pressure method in the presence of strong flanking transmission. Especially when small and/or heavy specimens are tested, the flanking often causes problems in laboratories practicing only the pressure method. The purpose of this study was to determine experimentally the difference between the maximum sound reduction indices obtained by the intensity method, $R_{I,\max}$, and by the pressure method, $R_{\max}$. In addition, the influence of adding room absorption to the receiving room was studied. The experiments were carried out in an ordinary two-room test laboratory. The exact value of $R_{I,\max}$ was estimated by applying a fitting equation to the measured data points. The fitting equation involved the dependence of the pressure-intensity indicator on measured acoustical parameters. In an empty receiving room, the difference between $R_{I,\max}$ and $R_{\max}$ was 4–15 dB, depending on frequency. When the average reverberation time was reduced from 3.5 to 0.6 s, the values of $R_{I,\max}$ increased by 2–10 dB compared to the results in the empty room. Thus, it is possible to measure wall structures having 9–22 dB better sound reduction index using the intensity method than with the pressure method. This facilitates the measurements of small and/or heavy specimens in the presence of flanking. Moreover, when new laboratories are designed, the intensity method is an alternative to the pressure method which presupposes expensive isolation structures between the rooms. [DOI: 10.1121/1.1332377]

PACS numbers: 43.55.Rg, 43.55.Nd [JDQ]

I. INTRODUCTION

The purpose of this study was to determine experimentally the difference, Δ, between the maximum measurable sound reduction index using the intensity method, $R_{I,\max}$, and using the pressure method, $R_{\max}$. In addition, the effect of receiving room absorption as a means to increase the value of $R_{I,\max}$ and Δ was studied experimentally. The value of $R_{I,\max}$ was determined by applying mathematical fitting to the measured data. Therefore, the criteria for the maximum allowed pressure-intensity indicator, F_{pI}, will be studied theoretically and experimentally before the presentation of the main results.

The determination of sound insulation using the pressure method is difficult if the isolation between the test rooms is not sufficient. This is usual when small and/or heavy specimens are tested. The flanking via other surfaces than the specimen can cause an overestimation of the radiated sound power from the specimen. This leads to underestimation of the sound reduction index (sound transmission loss).

Using the pressure method, it is common practice that a correction is made to the apparent sound reduction index of the specimen, R', to take into account the effect of flanking transmission.[1,2] The corrected sound reduction index, R, is calculated by

$$R = -10\ \log\left(10^{-R'/10} - 10^{-R'_T/10}\right)\ \mathrm{dB}, \tag{1}$$

where R'_T is the apparent sound reduction index when the specimen is covered with an additional panel. The panel is used to completely prevent the sound transmission through the specimen. Thus, R'_T is the apparent sound reduction index when flanking is the dominant transmission path.

The correction of Eq. (1) can be made reliably when $R'_T - R' > 6$ dB. Otherwise, the uncertainty of R will be considerably increased. Thus, the maximum measurable sound reduction index using the pressure method, $R_{\max}$, is determined by

$$R_{\max} = R'_T - 6\ \ \mathrm{dB}. \tag{2}$$

The value of $R_{\max}$ depends on the structures of the test laboratory and the specimen area.

The sound intensity method is usually recommended instead of the pressure method especially when flanking transmission causes problems.[3–5] In this study, the sound reduction index obtained by the intensity method is designated by R_I while the pressure method is designated by R. It could be expected that the maximum measurable sound reduction index using the intensity method, $R_{I,\max}$, is larger than $R_{\max}$. However, the determination of $R_{I,\max}$ is not as simple as the determination of $R_{\max}$ because one heavy specimen with a high sound reduction index can suffice to determine R'_T correctly.

The value of $R_{I,\max}$ has to be determined at the limit where sound intensity measurements become invalid. It is well known that the validity of intensity measurements is determined by the pressure-intensity indicator, F_{pI}. Thus,

[a]Electronic mail: valtteri.hongisto@occuphealth.fi

the value of $R_{I,\max}$ is determined at the point where F_{pI} equals the maximum allowed value of F_{pI}. In principle, it is necessary to find a specimen that exactly represents the value of $R_{I,\max}$ at every frequency band. This is a difficult task even for a single frequency band. To avoid a large number of measurements, the value of $R_{I,\max}$ was estimated by using mathematical fitting on measured data. The mathematical fitting equation involves the dependence of F_{pI} on R_I and certain physical and acoustical parameters.

Machimbarrena and Jacobsen recently studied the classical problem concerning the difference in the sound reduction index obtained with the pressure and the intensity methods.[6] They found that, using the latest intensity measurement equipment with very small phase mismatch,[7] and sufficiently large and diffuse transmission rooms, where also the pressure method produces true results at low frequencies, the difference between the methods was below 1 dB throughout the frequency range 80–6300 Hz. No Waterhouse correction was needed. It was concluded that the only significant difference between the pressure and intensity methods was that the intensity method could not be used when the specimen is sound-absorbing on the receiving room side.

In our opinion, there is another, and even more important, difference between the pressure method and the intensity method. It is probable that the maximum measurable sound reduction index using the intensity method, $R_{I,\max}$ is considerably larger than $R_{\max}$. This can be anticipated because the intensity method is insensitive to stable extraneous sound sources. In addition, strong receiving room absorption should increase the value of $R_{I,\max}$ because it decrease the intensity of extraneous noise. This should mean that wall structures with higher sound reduction index could be measured with the intensity method than with the pressure method. However, there are no theoretical or experimental reports available where the value of $R_{I,\max}$ has been determined. The purpose of this study is to fill this gap in the literature.

II. FACTORS AFFECTING THE PRESSURE-INTENSITY INDICATOR

The quality of intensity measurements is largely determined by the pressure-intensity indicator

$$F_{\mathrm{pI}}=L_p-L_I \ \mathrm{dB}, \tag{3}$$

where L_p is the average sound pressure level (*re* 20 μPa) and L_I is the average sound intensity level (*re* 1 pW/m^2) at the measurement surface. The value of F_{pI} depends on the sound field and the phase mismatch of the two-channel measurement equipment. It is desirable that the phase mismatch of the equipment is very small so that F_{pI} depends mainly on the sound field.

Gade[8] showed that there is a maximum allowed value of F_{pI}, which should not be exceeded during measurements as follows:

$$F_{\mathrm{pI}}<L_d=\sigma_{\mathrm{pI},0}-K \ \mathrm{dB}, \tag{4}$$

where L_d is the dynamic capability of the measurement device and $\sigma_{\mathrm{pI},0}$ is the pressure-residual intensity index of the measurement equipment. The bias error factor $K=7$ dB was used in this study. This guarantees that the error due to phase mismatching of the measurement equipment is smaller than 1.0 dB.[9] When the condition of Eq. (4) is applied, the residual intensity does not contaminate the intensity measurements and the value of F_{pI} depends on the properties of the sound field.

It is important to know the factors affecting the value of F_{pI} because F_{pI} is used to estimate the value of $R_{I,\max}$. There are eight factors due to the sound field and the environment. These factors will be introduced below, including a review of the related literature.

(1) The absorption area of the receiving room A_2. Absorption decreases the reverberant component of the extraneous noise. The extraneous noise comprises three components: flanking sound, direct sound (after the first reflection), and background noise. It is well known that the effect of the reverberation time on the intensity sound reduction index is below 1 dB.[10–13] Unfortunately, these investigations were made using specimens with a low sound reduction index. Thus, the flanking ratio was negligible.

Jonasson determined the maximum allowed value of F_{pI} during the sound insulation test tests.[13] Two intensity measurements were made with equal sound power in the source room. During the first measurement, the receiving room was empty. During the second measurement, the reverberation time of the receiving room was considerably reduced. The intensity levels were almost equal in these two cases when the equation

$$F_{\mathrm{pI}}<10 \ \mathrm{dB} \tag{5}$$

was valid. This result agreed with the previous results of Cops *et al.*[11] Unfortunately, the dynamic capability index of the intensity measurement equipment was not reported. It cannot be estimated whether Eq. (5) was in conformance with Eq. (4) or not. Therefore, Eq. (5) cannot be generalized. In a physical sense, Eq. (4) is the correct condition for F_{pI}.[8] According to Fahy, who also applied Eq. (4), the maximum allowed value of F_{pI} was 13 dB.[14]

It should also be noted that the phase matching of new sound intensity probes has improved a lot during the last 10 years. According to Machimbarrena and Jacobsen,[6] the value of L_d was between 12–24 dB, when Eq. (4) was applied. Thus, high values of the dynamic capability index enable reliable intensity measurements in very reactive environments. This should considerably increase the value of $R_{I,\max}$ compared to the 10-dB limitation of Eq. (5) or the 13-dB limitation given by Fahy.

(2) The area of the specimen S. The larger the area of the specimen the smaller the area of the flanking constructions and the larger the proportion of the direct sound. Thus, F_{pI} increases with decreasing specimen area. The sound pressure level in the receiving room increases by approximately 3 dB if the area of the specimen is doubled, provided that the flanking ratio is small. Fahy presented a simple theory, which described the dependence of F_{pI} on the absorption area of receiving room A_2 and specimen area S, as follows:[14]

$$F_{\mathrm{pI}} \cong 9 + 10 \log \frac{S}{A_2} \ \mathrm{dB}. \tag{6}$$

Acceptable values are obtained when $S/A_2 < 2.5$ holds. It was concluded that ''in any case, the introduction of a few square meters of absorbent blanket into a receiving room will usually ensure that the bias error is negligible.'' However, Eq. (6) does not consider the effect of flanking and a more developed model is needed to calculate the value of F_{pI}.

(3) The flanking ratio h_F. Van Zyl and Erasmus[15] studied theoretically the effect of the receiving room absorption A_2, the specimen size S, and the flanking ratio h_F on F_{pI}. The flanking ratio was determined as the ratio of sound powers radiated by flanking surfaces and specimen. It was clearly shown that the effect of flanking on the pressure-intensity indicator (reactivity) is very strong. Unfortunately, no measurement results were presented to verify the theory. The flanking ratio increases with increasing sound reduction index of the specimen provided the flanking via specimen is constant. In this study, this theory will be applied in the calculation of $R_{I,\max}$ and the theory will be verified with different values of h_F and A_2.

(4) The geometric near-field effect. The value of F_{pI} was reduced with increasing measurement distance. Hongisto and Saine studied the sound power of a large diesel engine ($7\times2\times2$ m) using intensity and pressure methods.[16] The measurements were done at a distance of 0.5 m because of the small space around the engine. It was found that the pressure method resulted in systematically higher values of sound power than the intensity method. The average value of F_{pI} was 3 dB higher than expected on the basis of the acoustical environment. It was suggested that the reason was geometric near-field effects. The value of F_{pI} was increased because the intensity probe detected strong intensity components, which were not in the direction of the probe axis. The radiation of the source was not uniformly distributed. Near-field effects can also be expected to affect sound insulation measurements using the intensity method, which involves near-field measurements of a large surface. For example, Lai and Qi studied the effect of measurement distance on F_{pI}.[12] Because of geometric near-field effects, the value of F_{pI} would not reach zero even though the receiving room were anechoic and the surface radiated uniformly. Zero can be obtained only in a free field for a propagating plane wave. However, the effect of near-fields is probably small, a few decibels. It can be expected that the geometric near field affects the values of F_{pI} only when the strongest contributors of F_{pI}, reverberation time and flanking, are negligible. Otherwise, reverberation and flanking mask the effect of the geometric nearfield.

(5) The absorption coefficient of the specimen on the receiving room side, α_S. Van Zyl, Erasmus, and van der Merwe[17] and van Zyl, Erasmus, and Andersson[18] presented a theory for assessing the intensity measurement error caused by a sound-absorbing test specimen. A sound-absorbing specimen leads to underestimation of the true sound intensity if the intensity of extraneous sound is sufficiently high. This leads to overestimation of the sound reduction index. The error was shown to depend on flanking ratio, absorption coefficient of specimen, specimen area, and receiving room absorption. Low absorption coefficient of the specimen can also cause underestimation of the true intensity if the extraneous noise is strong. A few experiments were presented to validate the theory. A sound-absorbing specimen decreases the value of F_{pI} compared to a hard specimen because the amplitude of the reflected extraneous intensity is reduced.

Hongisto *et al.*[19] and Hongisto[20] studied several specimens using the intensity method. The average value of F_{pI} increased from 2 to 10 dB when the sound reduction index increased from 15 to 65 dB, respectively. The increase of F_{pI} was caused by the increased contribution of flanking transmission to the receiving room. The reverberation time of the receiving room was very short because of a sound-absorbing backwall. The effect of the sound-absorbing specimen on the accuracy of intensity measurements was calculated according to van Zyl *et al.*[18] According to the calculations, a typical hard wall with a sound absorption coefficient of approximately 0.05 did not cause sound intensity measurement errors larger than 0.5 dB. It was obvious that the intensity measurement error would occur, if the specimen were strongly sound-absorbing.

Machimbarrena and Jacobsen[6] studied the effect of a sound-absorbing specimen on sound insulation measurements using the intensity method. When the specimen was covered with a 70-mm layer of glasswool in the receiving room, the results obtained with the intensity method overestimated the result by as much as 5 dB. F_{pI} decreased by a few decibels, which agreed with the theory.

(6) Vortices (recirculating intensity) can increase the value of F_{pI} when the distance between the measurement surface and the specimen is small (below 50–100 mm).[12,14] Typically, vortices cause strong fluctuations in sound intensity and also local negative values of sound intensity, but they do not contribute to the radiated power in the far field. This factor was not considered in this study because the measurement distances were over 100 mm.

(7) Inherent background noise of the room. Background noise may be a problem when specimens with a high sound insulation are tested and the source room level is not sufficiently high. This factor was taken into account in this study because the source room levels were sufficient.

(8) The shape of the receiving room. It has been observed that when strong standing waves occur in the receiving room between the specimen and the backwall, negative values of F_{pI} can be obtained.[19,21] Standing waves are typical especially at low frequencies. This factor was not taken into account in this study because negative values were not observed in this laboratory.

III. MATERIALS AND METHODS

A. The calculation of F_{pI} under different measurement conditions

The purpose of this section is to present a model for calculating the value of F_{pI} under different measurement conditions. This model will be applied in the results, to extrapolate the measured data and to facilitate the determina-

tion of $R_{I,\max}$. In the following model, the factors 1, 2 and 3 presented in Sec. II are studied theoretically. This model was introduced by van Zyl and Erasmus.[15]

The pressure-intensity indicator at the measurement surface is defined as the ratio between the total pressure P (Pa) and the intensity to be measured at the measurement surface I (W/m^2) as follows:

$$F_{\mathrm{pI}} = 10 \log \frac{P^2/\rho c}{I} \mathrm{dB}, \tag{7}$$

where ρ is the density of air (kg/m^3) and c is the speed of sound in air (m/s). The fraction h of the total energy W (W) in the receiving room is transmitted through the test specimen. The direct intensity is thus

$$I = \frac{hW}{S}, \tag{8}$$

where S is the area of the specimen (m^2). According to the plane wave model, the sound pressure caused by the specimen is

$$P_S^2 = \frac{hW\rho c}{S}. \tag{9}$$

The reverberant field contains both flanking sound and sound radiated by the specimen itself. The energy of the reverberant sound field is $(1-\alpha_2)W$ when the reduction in sound energy during the first reflection from the walls is encountered.[22] The average reverberant pressure in the middle of the room is approximated by

$$P_R^2 = \frac{4W(1-\alpha_2)\rho c}{A_2}, \tag{10}$$

where α_2 is the average absorption coefficient of the receiving room. Near the test specimen, the total pressure is the sum of the direct sound radiated by the specimen, P_S, and reverberant sound, P_R. Because of the interference caused by a rigid specimen, 3 dB can be added to the reverberant contribution and the result is

$$P^2 = P_S^2 + 2P_R^2. \tag{11}$$

If the specimen is sound-absorbing, the 3-dB addition is an overestimate. The sound absorption coefficient of the specimen on the receiving room side was assumed to be zero. This was justified because most wall structures are acoustically hard. Because the flanking ratio was high, causing a potential intensity measurement error even in the case of negligible specimen absorption, this subject will be returned to in the discussion.

Assuming that the average absorption of the receiving room boundaries is small ($\alpha_2 \ll 1$), we obtain

$$P^2 = \left(\frac{h}{S} + \frac{8}{A_2} \right) W\rho c, \tag{12}$$

and the pressure-intensity indicator at the surface of the test specimen becomes

$$F_{\mathrm{pI}} = 10 \log \left(1 + \frac{8S}{hA_2} \right) = 10 \log \left[1 + 8(h_F + 1) \frac{S}{A_2} \right] \mathrm{dB}. \tag{13}$$

The flanking ratio h_F is determined as the ratio of the energies radiated by the flanking surfaces W_F and the specimen W_S as follows:

$$h_F = \frac{W_F}{W_S} = \frac{1-h}{h} = 10^{(R_I - R_T')/10}. \tag{14}$$

When the flanking ratio is negligible, Eq. (13) is practically equal to Eq. (6). The flanking transmission was assumed to be constant in this study. This was justified because all measurements were carried out in the same test opening. Thus, the flanking ratio could simply be adjusted by varying the sound reduction index of the specimen.

According to the first fitting trials, Eq. (13) systematically overestimated the values of F_{pI} by 0–2 dB compared to the measured F_{pI}. (The first fitting trials were performed in a similar way as will be explained below.) The bias increased as the receiving room absorption increased and R_I decreased. As mentioned in Sec. II, it is probable that near-field effects are independent of h_F and A_2, but they can depend on the measurement distance from the specimen. The dependence is unknown and difficult to determine. A simple linear adaptation parameter NF corresponding to the near-field effects was added to Eq. (13) as follows:

$$F_{\mathrm{pI}} = \mathrm{NF} + 10 \log \left[1 + 8(10^{(R_I - R_T')/10} + 1) \frac{S}{A_2} \right] \mathrm{dB}. \tag{15}$$

NF was not directly measurable, unlike the other parameters of this equation. Thus the value of NF was allowed to float during the mathematical fitting.

Equation (15) describes the dependence of F_{pI} on acoustical conditions. In addition, F_{pI} depends on the dynamic capability L_d of the intensity measurement system because there is always a small residual intensity component originating from the phase mismatch of the measurement system.[8] However, the effect of the residual intensity component is smaller than 1 dB when Eq. (4) is valid.[23] Because the range $F_{\mathrm{pI}} > L_d$ is beyond the scope of this study, Eq. (15) was found to be adequate to make the mathematical fitting.

B. Determination of $R_{I,\max}$ using nonlinear least squares fitting

The nonlinear least squares fitting procedure, based on the Levenberg–Marquardt algorithm, was used to fit Eq. (15) to the measured (R_I, F_{pI}) data.[24] This is the method usually used to fit a mathematical expression to the measured data. The calculation was done using Origin 6.0 software. The quality of fitting results was monitored by the chi square parameter defined by

$$\chi^2 = \sum_{i=1}^{N} \frac{(F_{\mathrm{pI,meas}}^i - F_{\mathrm{pI,pred}}^i)^2}{N-1}, \tag{16}$$

where $F_{\mathrm{pI,pred}}$ is the predicted value given by Eq. (15) and $F_{\mathrm{pI,meas}}$ is the measured value. N is the total number of data points (specimens) used in the fitting. The software calcu-

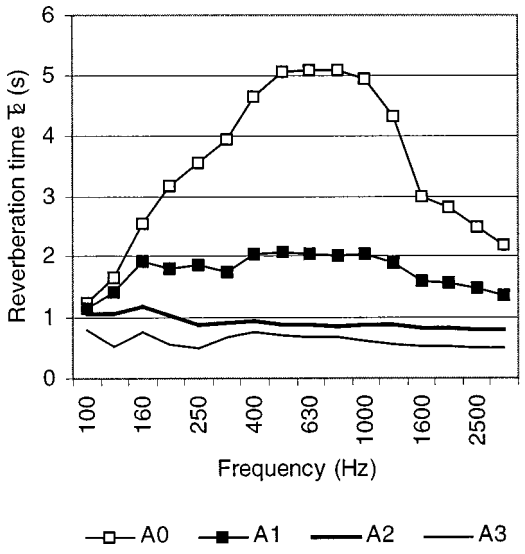

FIG. 1. The reverberation time of the receiving room in the four different cases of receiving room absorption A0, A1, A2 and A3.

lates the optimum parameters of NF to Eq. (15), which give the smallest possible value of the χ^2 parameter. The smaller the value of the χ^2 parameter, the better the fit found between the fitted curve and the measured data. Small χ^2 means that there are probably no other physical factors explaining the value of F_{pI} than those presented in Eq. (15).

When the floating parameter NF was calculated, the value of $R_{I,\max}$ was determined. Equation (4) was used as the boundary condition for F_{pI} in Eq. (15). Thus, the result is

$$R_{I,\max} = R_I|_{(F_{\mathrm{pI}}=L_d)} = 10\log\left[\frac{10^{(L_d-\mathrm{NF})/10} - 8\dfrac{S}{A_2} - 1}{8\dfrac{S}{A_2}}\right] + R'_T \ \mathrm{dB}. \tag{17}$$

The main benefit of this equation was that the graphical determination of $R_{I,\max}$ could be avoided.

C. The materials used for adjusting the sound absorption in the receiving room

Four different reverberation times of the receiving room were used to study the effect of absorption area on $R_{I,\max}$. The notations A0, A1, A2, and A3 were used to label four different cases. The areas of additional absorbents were 0, 5.7, 15.0, and 21.7 m^2, respectively. The reverberation times T_2 in cases A0–A3 are presented in Fig. 1. The corresponding absorption areas A_2 are presented in the results. Mobile mineral wool elements of size $2900\times1600\times100$ mm^3 were mainly used. The absorbents were distributed throughout the room against the walls and the floor to make the diffusion as high as possible.

TABLE I. The summary of sound insulation measurements in decibels in the different cases of receiving room absorption A0–A3. The first four columns represent the intensity method and the fifth column represents the pressure method. The superscript shows the number of frequency bands, which were rejected due to flanking. The surface mass m and the thickness h of the specimens are presented in the final columns.

Method	$R_{I,w}$				R_w	m	h
Case	A0	A1	A2	A3	A0	($\mathrm{kg/m^2}$)	(mm)
Specimen							
1	40	40	40		39	21	50
2	75^{12}	73^{11}	73^{4}		59^{16}	67	290
3	78^{15}		80^{10}		59^{16}	125	310
4	49	49	49		48	78	60
5	64	65	65	65	59^{7}	44	120
6	72^{3}	72^{3}		73	59^{15}	102	250
7	77^{16}	78^{14}		80^{7}	59^{16}	138	390
8	28	28		28	26	10	50

D. The test specimen used in sound insulation measurements

Eight specimens were investigated to adjust the degree of flanking sound in the receiving room. A total of 24 measurements were made with the intensity method and 8 measurements with the pressure method. Each specimen was measured once with the pressure method (A0) and two to four times with the intensity method, using different cases of receiving room absorption (A0–A3). The specimen was not removed between cases A0 and A3 to guarantee repeatability conditions. For specimens 1–4, only cases A0–A2 were used. For specimens 5–8, case A2 was replaced by case A3 to get lower values of F_{pI} and higher acceptable values of R_I.

The size of the test specimen was constantly $S = 2.5\,\mathrm{m}^2$. The specimens were mounted in the small test opening of the same size. The use of the small specimen size was justified by the fact that flanking problems occur more often with small specimen size.

It was essential to obtain a large range of R_I and F_{pI} values to have a broad basis of data for the mathematical fitting procedure. It was also important to have sufficient data points close to L_d to obtain a better accuracy of $R_{I,\max}$. Therefore, half of the specimens were thick and heavy ($R_w > 70\,\mathrm{dB}$) so that high values of F_{pI} due to strong flanking could be obtained.

The surface masses of the specimens were within 21–138 $\mathrm{kg/m^2}$ (see Table I). The specimens comprised 1–5 panels with (sound-absorbing) cavities between them. The total thickness of the specimen varied in the range 50–390 mm. There were no sound-absorbing faces on the receiving room side of the specimen. The sound reduction indices were in the range 11–106 dB, depending on the frequency.

In this study, the flanking ratio was adjusted by using specimens with different sound reduction index. It could be possible to make the adjustment by using artificial sound sources in the receiving room. Thus, only one specimen would be sufficient. This approach was not used because the results obtained by artificial flanking would not be very convincing in the long term.

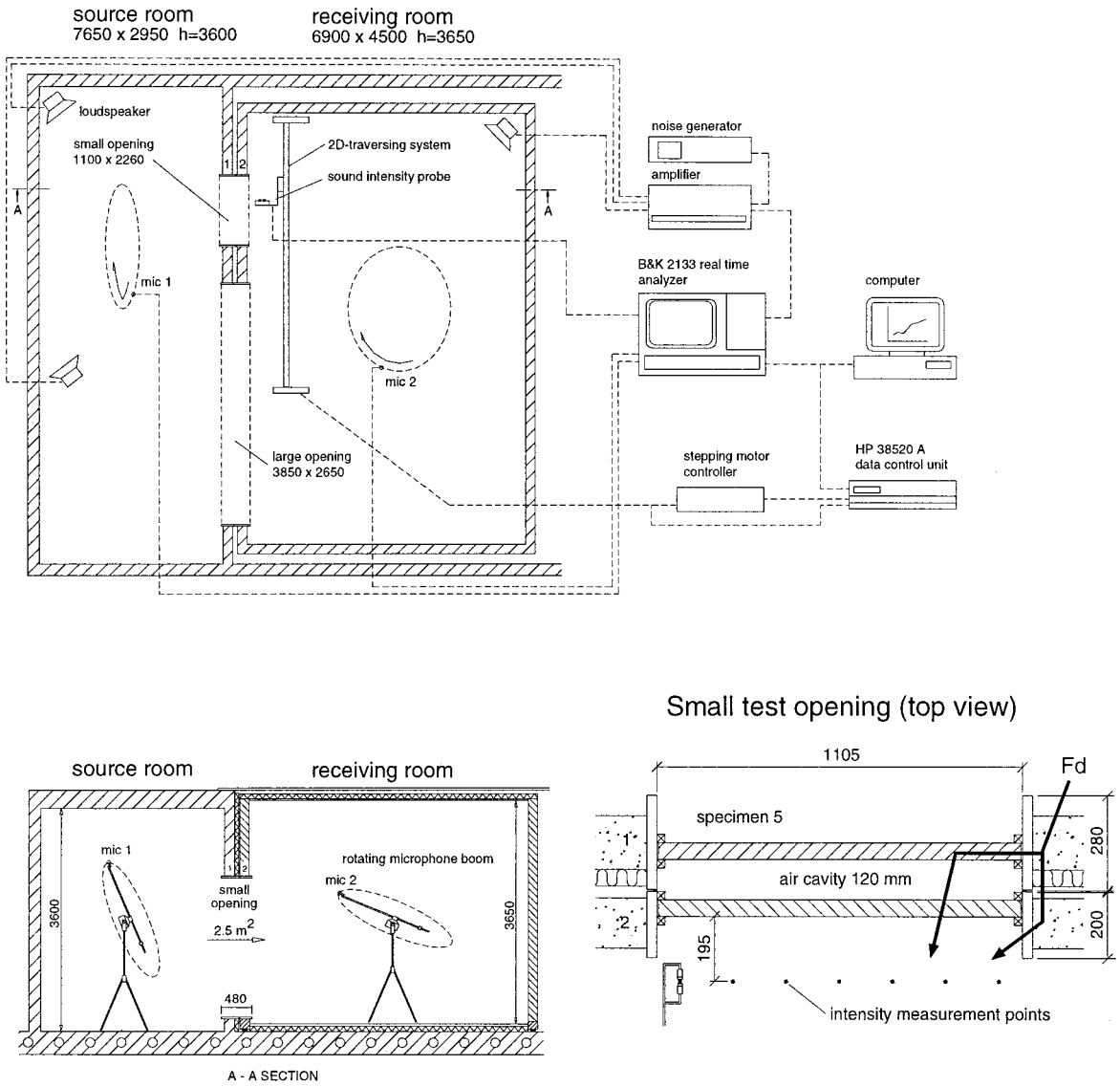

FIG. 2. Top: The layout drawing of the test rooms including the measurement device. The volumes of the rooms were 81 and 113 m^3. Left: Section layout A-A through the small test opening. Right: The top view of the small test opening including the schematic structure of specimen 5.

E. The test laboratory

The test laboratory, the measurement equipment, and the small test opening used in this study are presented in Fig. 2. The walls of the source room were made of 160-mm concrete, the ceiling was made of 190-mm concrete, and the floor was a 265-mm hollow concrete slab which extended uniformly below the test rooms. The receiving room was isolated from the building, unlike the source room. The structural isolation of the receiving room reduced the background noise level by 15–25 dB compared to the source room. The walls of the receiving room were made of 150-mm-thick porous concrete and they were isolated from the common intermediate floor using 45 small rubber isolators. The ceiling was lightweight and supported above the walls. The floating floor was made of chipboard on top of mineral wool plates. The space between the rooms was 70–80 mm and it was filled with mineral wool plates.

Two separate test openings were built to couple the rooms. A small test opening ($S=2.5\,m^2$) was used in this study. The frames of the opening were made of 26-mm-thick plywood plates. The frames in walls 1 and 2 were separated by a 10-mm-thick air cavity, which was sealed with rubber seal and tape. The large test opening (10 m^2) was covered during this study with a 480-mm-thick multilayer structure. According to intensity measurements, the flanking was smoothly distributed to the room surfaces.

F. Sound insulation measurements using the pressure method

The apparent sound reduction index R' was determined by[1]

$$R'=L_{p1}-L_{p2}+10\log\frac{S}{A_2}\text{dB},\quad A_2=\frac{0.16V_2}{T_2},\tag{18}$$

where L_{p1} and L_{p2} are the average sound pressure levels in the source room and receiving room, respectively, and V_2 is the volume (m^3) of the receiving room. Equation (1) was

used to calculate the final sound reduction index R, if $R' < R'_T - 15$ dB.

All sound signals were analyzed using a two-channel real time analyzer (Brüel & Kjær 2133). The test signal of the source room was generated using two loudspeakers driven by two uncorrelated noise generators. The sound pressure levels were 100–105 dB at each third octave band. The sound pressure levels in both rooms were measured simultaneously using a condenser microphone (Brüel & Kjær 4165 equipped with preamplifier 2669). Both microphones were mounted on a rotating microphone boom (Brüel & Kjær 3923) with a rotating radius of 100 cm. The averaging time was 64 s, the same as the rotation time of the boom. The background noise level was always at least 6 dB lower than the level of the test signal.

The reverberation time in the receiving room was measured using two loudspeaker positions and six microphone positions for each loudspeaker position. Altogether 12 decays were averaged using the decay range -5 dB to -25 dB. All pressure measurements were done without additional room absorption (A0).

G. Sound insulation measurements using the intensity method

The intensity sound reduction index R_I was determined by[5]

$$R_I = L_{p1} - 6 - L_I + 10 \log\left(1 + \frac{S_2 \lambda}{8 V_2}\right) \text{ dB}, \tag{19}$$

where L_I is the sound intensity level at the measurement surface, S_2 is the total area of receiving room surfaces (m^2), and λ is the wavelength of sound in air (m). The last term, or the Waterhouse correction, was applied to all intensity measurements to make R_I more comparable with R.

The sound pressure level in the source room was determined as above. The sound intensity radiated by the test specimen was measured using a two-dimensional traversing system specified previously.[19] The sound intensity probe (Brüel & Kjær 3545) comprised two phase-matched condenser microphones (Brüel & Kjær 4181) separated by a 12-mm spacer. Both the source room microphone and the sound intensity microphones were calibrated using a pistonphone calibrator (Brüel & Kjær 4220). The pressure-residual intensity indicator of the probe $\sigma_{\text{pI},0}$ was determined using a small calibration chamber (Brüel & Kjær 3541). The results are shown in Table II.

Discrete intensity measurement points were used. The measurement grid comprised 14 vertical points and 7 horizontal points throughout this study. The horizontal and vertical distances between adjacent measurement points were 16.1 and 15.7 cm, respectively. A planelike measurement surface was used. The measurement surface was in the vicinity of the niche so that no leakages or gaps were formed between the measurement surface and the test opening. The measurement distance d from the specimen varied in the range 12–35 cm because the measurement grid was fixed and the thickness of the specimen varied. The variation in d could also affect the exposure to geometric near-field effects.

TABLE II. The dynamic capability index of the intensity measurement equipment L_d and the maximum measurable sound reduction index using the pressure method R_{max}. They were determined from the measured values, $\sigma_{\text{pI},0}$ and R'_T according to Eqs. (4) and (2), respectively.

f (Hz)	$\sigma_{\text{pI},0}$ (dB)	L_d (dB)	R'_T (dB)	R_{max} (dB)
100	13.2	6.2	36.4	30.4
125	14.8	7.8	41.9	35.9
160	16.8	9.8	47.0	41.0
200	18.6	11.6	52.5	46.5
250	21.2	14.2	56.5	50.5
315	22.5	15.5	61.6	55.6
400	22.6	15.6	65.4	59.4
500	21.4	14.4	70.3	64.3
630	19.3	12.3	75.3	69.3
800	18.7	11.7	78.8	72.8
1000	17.8	10.8	82.1	76.1
1250	18.5	11.5	83.9	77.9
1600	18.5	11.5	84.4	78.4
2000	17.8	10.8	86.2	80.2
2500	17.5	10.5	86.9	80.9
3150	17.9	10.9	90.4	84.4

It is recommended that d should be between 0.1 and 0.3 m, and that the distance between adjacent points should be smaller than d.[5] This rule was not obeyed for specimen 7, having $d = 12$ cm. It is very unlikely that this caused intensity measurement errors because the radiation of the sound was uniformly distributed.

H. Absorption coefficient of the specimen

The normal incidence acoustic absorption coefficient was measured using the standing wave method.[25] The sound pressure level inside the standing wave tube (Acoumet) was measured using a condenser microphone (Brüel & Kjær 4165) placed inside a moving trolley. The sound was transmitted to the trolley via a hollow rod ($\varnothing = 3$ mm). The sound pressure level was analyzed in $\frac{1}{3}$-octave bands. It has been found to be possible to measure absorption coefficients between 0.02 and 0.996 with this tube.

IV. RESULTS

A. Overview of the measurements

Eight specimens were studied. Eight tests were carried out using the pressure method and 24 tests using the intensity method. The measured raw data, R_I, F_{pI} and R', are not presented in this article, but a summary is presented in Table I. The result of each test is summarized in the form of weighted sound reduction index.[26] The number of rejected frequency bands is indicated in superscript. In the presence of rejected bands, the declared value was an underestimate. In the case of the pressure method, the rejected bands were those bands where the apparent sound reduction index R' exceeded the maximum measurable sound reduction index R_{max} [see Eq. (2) and Table II]. In the case of the intensity method, the rejected bands were those bands where the surface pressure-intensity indicator F_{pI} exceeded the dynamic capability index L_d [see Eq. (4) and Table II].

The number of rejected bands was much lower with the intensity method. It is also obvious that the number of these

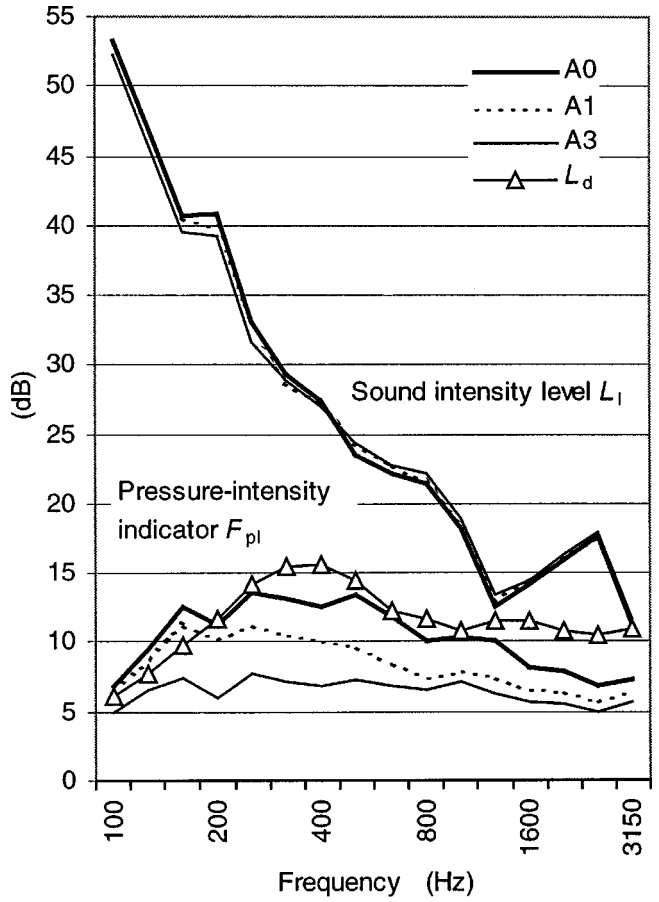

FIG. 3. The sound intensity levels L_I (upper curves) and the corresponding pressure-intensity indicators F_{pI} (lower curves) measured for specimen 6 with three different room absorptions A0, A1, and A3. The source room level was constant in each case. The dynamic capability index L_d is also presented.

bands decreased as the amount of absorbent increased.

B. The maximum allowed F_{pI}

The dependence of the measured sound intensity on the receiving room absorption was studied. The sound intensity through one of the heaviest specimens (specimen 6) was measured with varying receiving room absorption (A0, A1, and A3) and constant source room level. The results are presented in Fig. 3. The most accurate case was assumed to be case A3 because Eq. (4) was fulfilled at each frequency and the reverberation time was shortest. The largest overall difference between the cases occurred at 200 Hz, where the difference between case A0 and the case A3 was 1.6 dB. Above 200 Hz, the largest differences from the case A3 were below 1.0 dB. The intensity levels were overestimated when Eq. (4) was violated. Therefore, the intensity levels decreased with increasing A_2 at low frequencies as shown in Fig. 3.

The sound intensity was practically independent of the reverberation time and F_{pI} when F_{pI} was below 13 dB. Several examples could be presented, which lead to the same conclusion. Therefore, there is no actual reason to use the condition of Eq. (5). Instead, Eq. (4) was applied as proposed in Sec. II. As a result, higher values of $R_{I,\max}$ can be obtained

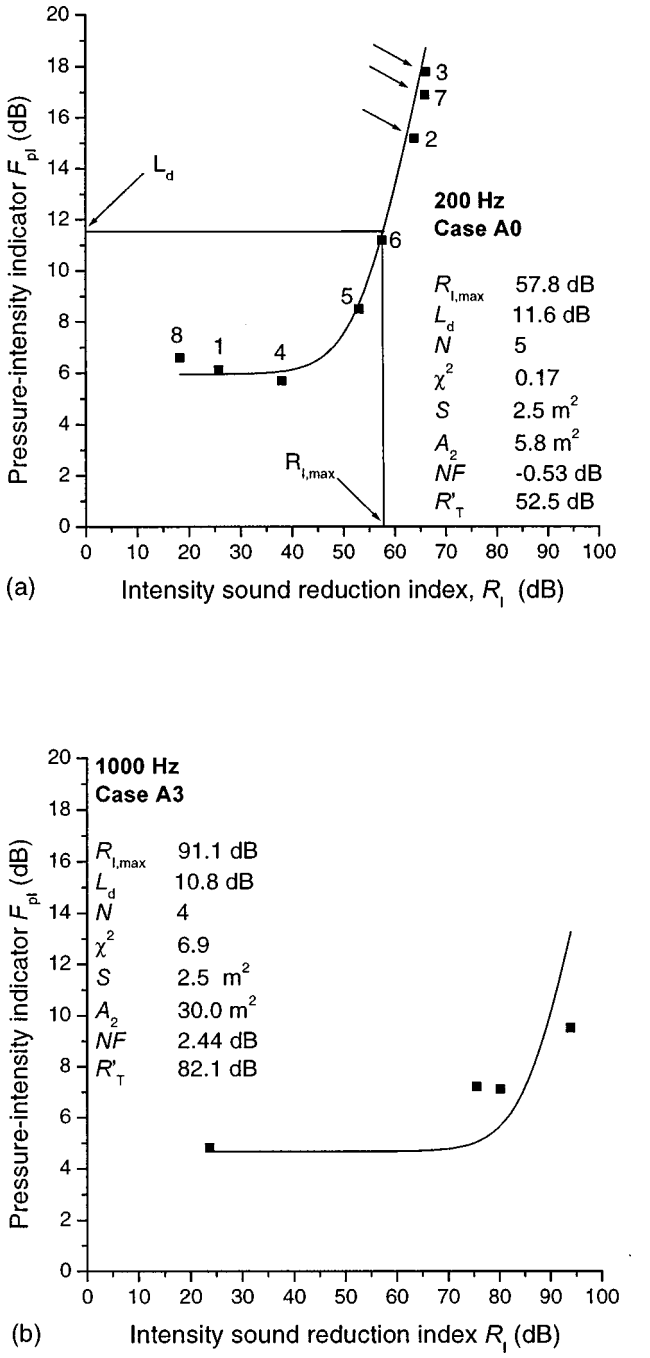

FIG. 4. Two examples of the fitting results. (■) measured points. (———) The nonlinear fitting curve according to Eq. (15). Graph (a) is an example of the graphic determination of $R_{I,\max}$. Data points marked by an arrow were removed from the fitting data as Eq. (4) was violated.

because the intensity method can be reliably used in the presence of stronger extraneous noise or flanking.

C. The pressure method, R_{max}

The maximum measurable sound reduction index $R_{\max}$ was determined by Eq. (2) on the basis of specimens 2, 3, 5, 6, and 7. For these specimens, R_w remained constant while $R_{I,w}$ varied within 64–80 dB. It was not possible to measure values higher than $R_w = 59$ dB using the pressure method. Thus, the average sound pressure in the receiving room was entirely determined by flanking. The values of R'_T and $R_{\max}$

TABLE III. The fitting results according to Eq. (15) in cases A0–A3. The number of performed tests in cases A0, A1, A2, and A3 were 8, 7, 5, and 4, respectively.

	Case A0				Case A1				Case A2				Case A3			
f (Hz)	A_2 (m^2)	NF (dB)	χ^2	N	A_2 (m^2)	NF (dB)	χ^2	N	A_2 (m^2)	NF (dB)	χ^2	N	A_2 (m^2)	NF (dB)	χ^2	N
100	14.7	−0.56	0.21	5	15.7	0.24	0.36	6	17.3	−0.19	0.40	4	23.1	−0.12	0.08	3
125	11.0	−0.70	0.56	4	12.7	−0.80	0.29	5	17.3	−0.45	0.13	4	33.3	0.39	0.81	3
160	7.1	−0.68	0.52	4	9.4	−0.91	1.17	4	15.4	−0.72	1.07	3	23.8	−1.15	2.89	3
200	5.8	−0.53	0.17	5	10.1	−0.20	0.07	5	17.7	−0.16	0.00	3	33.2	−0.47	2.34	4
250	5.1	−1.49	0.77	5	9.8	−1.20	0.54	6	20.3	−0.83	1.51	5	37.3	−0.41	2.09	4
315	4.6	−1.38	1.35	5	10.4	−1.03	1.67	7	20.2	−0.44	0.89	5	27.2	−0.53	2.65	4
400	3.9	−1.36	1.51	5	8.9	−0.98	1.15	5	19.0	0.11	0.41	3	23.6	−1.24	4.36	4
500	3.6	−0.81	1.52	5	8.8	−0.41	1.09	5	20.4	−0.20	7.60	4	26.2	0.01	4.08	4
630	3.6	−0.12	0.90	5	8.9	0.38	0.65	5	20.4	1.93	0.09	4	26.3	1.09	5.09	4
800	3.6	−0.22	0.33	5	9.1	0.65	0.32	5	21.5	2.57	0.30	3	27.2	2.74	0.36	3
1000	3.7	0.48	0.12	5	8.9	1.14	0.17	5	20.5	1.89	4.84	4	30.0	2.44	6.90	4
1250	4.2	0.08	0.03	5	9.6	−0.12	2.57	7	20.8	1.04	3.43	5	31.6	2.01	2.79	4
1600	6.1	0.22	0.72	6	11.4	0.64	1.30	6	21.6	1.61	1.33	5	34.9	2.23	0.73	4
2000	6.5	0.50	0.18	6	11.5	1.29	0.16	6	21.8	2.11	0.79	5	34.9	2.60	0.60	4
2500	7.3	−0.07	0.28	7	12.3	0.75	0.16	6	22.6	2.01	0.21	5	36.6	2.07	0.37	4
3150	8.3	0.67	0.23	6	13.4	1.40	1.56	6	22.6	2.95	2.60	5	37.2	3.24	2.05	4

are presented in Table II. They are valid for the small test aperture used in this study. The third-octave-band values of R'_T were combined from the highest values observed for specimens 2, 3, and 7, representing the specimens with highest sound insulation.

D. The intensity method, $R_{I,\max}$

The maximum measurable sound reduction index using the intensity method $R_{I,\max}$ was determined separately in four cases of receiving room absorption, A0–A3. Two examples of a total of 64 fitting curves according to Eq. (15) are presented in Fig. 4. The complete fitting data are shown in Table III.

Figure 4(a) shows, graphically, the principle for determining the value of $R_{I,\max}$. Each data point is marked by a number indicating the specimen from which the data have been obtained. The data of specimens 2, 7, and 3 were removed from the fitting data because of their violation of Eq. (4). Thus, the fitting was based on five data points.

The value of $R_{I,\max}$ was determined at the point where the value of F_{pI} equals L_d. This is the condition of Eq. (4). In Fig. 4(a), the determination of $R_{I,\max}$ could have been reasonably accurate using visual deduction, without the need for a fitting function. In several cases, as shown in Fig. 4(b), this was not possible because there were no measured data points close to the limit $F_{\mathrm{pI}}=L_d$. Thus, the use of mathematical fitting was justified. It can be seen in Fig. 4(b) that the fitting curve results in overestimated rather than underestimated values of F_{pI}. According to visual estimation of 64 fitting curves, this was finding was valid in most cases. As a result, the values of $R_{I,\max}$ were not overestimated by the mathematical fitting method.

The values of $R_{I,\max}$ for each case, A0, A1, A2, and A3, were calculated according to Eq. (17) using the data in Table III. The results of $R_{I,\max}$ are presented graphically in Fig. 5. The values of the maximum measurable sound reduction index using the pressure method, $R_{\max}$, are shown as a reference. The maximum correction of Eq. (1), +1.3 dB, was included in $R_{\max}$.

The difference between the maximum measurable sound reduction indices using the intensity method and the pressure method, abbreviated by Δ, was calculated for cases A0 and A3. When the intensity method was combined with strong receiving room absorption (A3), it was possible to measure 9–22 dB higher values of the sound reduction index than with the pressure method, depending on the frequency. In the case of the empty receiving room (A0), it was possible to measure 4–15 dB higher values of the sound reduction index than with the pressure method. Thus, the influence of adding room absorption was 2–10 dB.

The exact numerical values obtained for Δ are not directly applicable to all laboratories because the specimen areas and receiving room absorption areas can be very different. However, the main trends of the results are directly applicable to all laboratories, independent of the $R_{\max}$ of the laboratory. Wall structures with higher sound insulation can be measured when the intensity method is used. This result is of practical value for laboratories where the structural isolation between the rooms is not sufficient to carry out pressure measurements for specimens with high sound insulation. In addition, this result is of great value to any laboratory when small specimens are tested.

V. DISCUSSION

At the beginning of the study, the predictions of Eq. (6) were compared to the experimental values of F_{pI}. Figure 6 includes the measured F_{pI} of the heaviest specimen 7 and the lightest specimen 8 in cases A0 and A3. The only test that to some extent agreed with Eq. (6) was the light specimen 8 in case A0 when flanking was negligible and receiving room absorption low. Otherwise, flanking seemed to be the main factor in defining the value of F_{pI}. When the flanking ratio

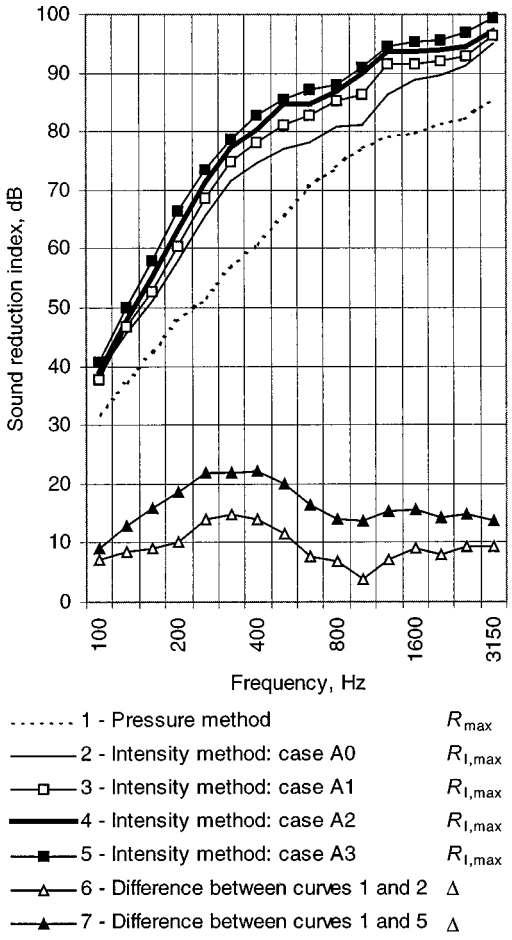

FIG. 5. The maximum measurable sound reduction index $R_{I,\max}$ using the intensity method in the different cases of receiving room absorption A0–A3. The maximum measurable sound reduction index $R_{\max}$ using the pressure method is shown as a reference. The difference between the intensity and the pressure method, Δ, is calculated for cases A0 and A3.

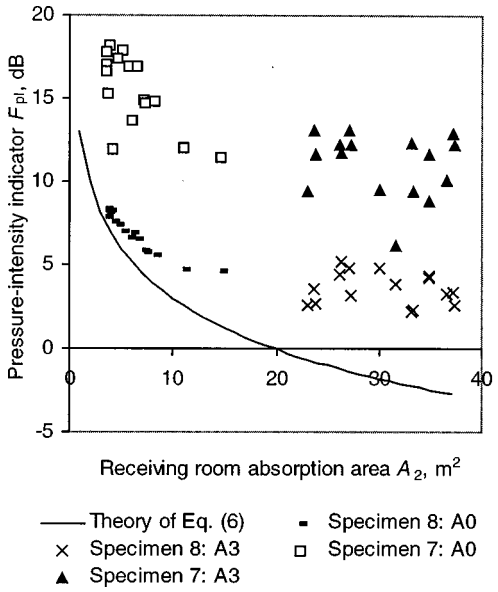

FIG. 6. The experimental verification of Eq. (6) on the basis of two extreme cases of both $R_{I,w}$ and A_2. Experimental data sets include 16 measured frequency bands simultaneously. The area of the specimen was $S = 2.5$ m^2.

and the absorption were strong, like in case A3 for specimen 7, Eq. (6) gave large underestimations. Thus, the application of Eq. (15) was justified.

On average, the fitting results were satisfactory and it can be assumed that the most important factors affecting the value of F_{pI} were included in the fitting equation. The average value of the χ^2 parameter was 1.35, varying in the range 0.004–7.60. The χ^2 parameter slightly increased with increasing receiving room absorption. In cases A0 and A1, the χ^2 parameter was independent of frequency. In cases A2 and A3, the χ^2 parameter was occasionally higher at middle frequencies. On average, the fitting was very successful even though the number of accepted data points N was quite small. It was on average 4.67, varying in the range 3–7. The value of N was not constant because the number of measured specimens in cases A0–A3 varied and some data points were rejected due to violation of Eq. (4). Examples of such points are marked with arrows in Fig. 4.

Figure 4(a) represents one of the best fitting results and Fig. 4(b) represents one of the poorest. Most fitting curves fitted the measured data as is shown in Fig. 4(a). It is notable that the fit of data was good also at low frequencies. Even though some data points were removed from the fitting data basis due to the violation of Eq. (4), the fitting curve agreed quite well with these removed points as is shown in Fig. 4(a). The theory of Eq. (15) seemed to be appropriate even at high values of F_{pI}. The values of F_{pI} above L_d did not begin to behave in a totally unexpected way.

The example in Fig. 4(b) represents one of the poorest fitting results where $\chi^2 = 6.9$. In this case, the reason for the large χ^2 value was the small values of F_{pI}. In cases A2 and A3, and above 1000 Hz, the value of F_{pI} did not always achieve the value of even 10 dB. The sound reduction indices were apparently too low for this study so that a high flanking ratio could not be achieved.

This study was carried out with a constant specimen size of $S = 2.5$ m^2. It would be interesting to know the results using a standard specimen size such as 10 m^2. According to Eq. (18), it is evident that by increasing S by a factor of 4, the sound level in the receiving room increases by 6 dB, assuming that flanking does not play an important role. The effect of specimen area is similar both with the pressure method and the intensity method: the values of $R_{\max}$ and $R_{I,\max}$ would increase by 6 dB if S is increased from 2.5 to 10 m^2. However, the value of Δ does not depend on S.

Flanking and reverberation were usually the strongest contributing factors to F_{pI}. The influence of the geometric near field on F_{pI} could not be determined. It never occurred that the geometric near-field effects were the only contributory factor of F_{pI}. When the receiving room absorption was low and the flanking ratio high, extraneous noise masked the contribution of near-field effects on F_{pI}. The average value of the fitted near field parameter, NF, increased systematically as the receiving room absorption increased. The values of NF in cases A0–A3 were -0.4, 0.1, 0.8, and 0.9 dB, respectively. The values of NF increased with increasing frequency in all cases. In cases A2 and A3, and above 630 Hz, the fitted values of NF were continuously in the range 1–3

dB. These values were probably very close to the true values of NF.

The influence of specimen absorption on the accuracy of intensity measurements was not studied experimentally because all specimens were acoustically hard, as is typical for most wall structures. Thus, the results of this study are valid only for hard specimens. However, the acoustic absorption coefficient of specimen 6 was determined with the impedance tube method to get some idea of the absorption coefficient of the specimens. The normal incidence sound absorption coefficient of specimen 6 was in the range 0.02–0.05, depending on the frequency.

If specimen absorption were to have an effect on the measured intensity of specimen 6, this effect would be dependent on the reverberation time of the receiving room. When the reverberation time was high (A0), the influence of specimen absorption would be larger than with a short reverberation time (A3) because the intensity of the extraneous noise was stronger. In case A0, the values of $L_{p,S}$ and F_{pI} were, on average, 3.6 dB higher than in case A3 because the amplitude of extraneous noise increased. However, the sound reduction indices obtained for specimen 6 were independent of receiving room absorption as could already be seen in Fig. 3. It could be assumed that case A3 represents a ''true'' result because of the lowest extraneous noise component. If the measured sound intensity were markedly contaminated by the absorbed intensity component in case A3, case A0 should have been even more contaminated because the sound pressure level originating from the receiving room increased. However, no increase of sound intensity level could be observed from case A3 to case A0. Therefore, the influence of specimen absorption is negligible for specimen 6 for all cases A0–A3. As a result, the intensity measurements were not contaminated by specimen absorption for specimens 1, 2, 4, 5, and 8, having lower sound insulation than specimen 6. It is probable that the specimen absorption did not affect the measurement accuracy of any specimens in this study.

It would be interesting to know what the effect would be of adding more absorption material to the receiving room. According to Fig. 5, $R_{I,\max}$ increased systematically, as the receiving room absorption increased. However, the difference in $R_{I,\max}$ between successive cases A0–A3 converged. In case A3, there was the highest practical amount of absorbent (22 m^2) that could be easily installed and removed. An obvious improvement of $R_{I,\max}$ would probably require more than 40 m^2 of absorbent in the receiving room, but this would no longer be easy to handle during practical measurements.

The values of Δ were smaller at the lowest and highest frequency bands than at the middle frequencies. The main reason for the smaller values of Δ at the frequency range 100–160 Hz was the violation of Eq. (4) when the heaviest specimens were measured. With a 50-mm microphone spacer, the dynamic capability index, L_d, is approximately 6.2 dB higher than with a 12-mm spacer.[27] Thus, considerably larger values of $R_{I,\max}$ would have been achieved at low frequencies if the 50-mm spacer had been used. As the upper frequency limit of the 50-mm microphone spacer is 1250 Hz, the measurement of the whole frequency range 100–3150 Hz would have required measurements both with 12- and 50-mm spacers. Because the effect of the 50-mm spacer is so evident on L_d, measurements were not repeated with two spacers.

The main reason for the small value of Δ in the high frequency range 630–3150 Hz was the small value of L_d. This could be solved by using equipment with a smaller phase mismatch, like that used by Machimbarrena and Jacobsen.[6,7] The smallest value of Δ occurred at 1000-Hz band in case A0. It was probably due to the coincidence of very long reverberation time and small dynamic capability index. In the frequency range 1600–3150 Hz, another reason was insufficient sound insulation of the specimens. The values of F_{pI} did not always achieve L_d or even 10 dB in cases A2 and A3. One example of such a situation can be seen in Fig. 4(b). In such cases, the flanking ratio was small and the desired situation, where flanking dominates, could not be obtained. As a result, the values of $R_{I,\max}$ were underestimated. Heavier specimens would have been required to determine the value of $R_{I,\max}$ correctly. However, the values of Δ in the frequency range 200–500 Hz were so convincing that additional tests with heavier structures were not found necessary.

The third possible explanation for the small value of Δ was that flanking via path Fd[28] (see Fig. 2) was not constant for successive specimens. Its strength depends on the specimen and its mounting. The influence of flanking via path Fd is that the sound reduction index of the specimen will be underestimated. It is possible that this flanking path prevented the observation of higher intensity sound reduction indices at high frequencies. This could also explain the low values of F_{pI}.

The most important factor affecting the values of Δ and $R_{I,\max}$ is the dynamic capability index of the measurement equipment, L_d. In this study, L_d was in the range 6–16 dB. The frequency dependences of L_d and Δ were very close to each other, as can be seen by comparing Figs. 3 and 5. It is probable that by increasing the value of L_d by using better phase-matched intensity measurement equipment, the values of $R_{I,\max}$ and Δ would have been higher. (The probe used in this study was manufactured in 1992 and the microphones are procured in 1997.) Thus, the development of better intensity measurement equipments is recommended.

VI. CONCLUSIONS

(1) The value of the pressure-intensity indicator during sound insulation measurements is determined by the flanking ratio, the reverberation time of the receiving room, the area of the specimen, the geometric near-field effects and the pressure-residual intensity index.

(2) When the intensity method and strong receiving room absorption are used, it is possible to measure considerably higher values of the sound reduction index than with the pressure method. This method is a significant alternative to the pressure method because expensive isolation structures between the test rooms can be partially avoided. The difference between the maximum measurable sound reduction indices obtained with the

intensity method and the pressure method depends mainly on the dynamic capability index of the intensity measurement device.

ACKNOWLEDGMENTS

We would like to thank Dr. Rauno Pääkkönen for reviewing the manuscript and Dr. Jussi Vahtera for fruitful discussions. The financial support of the Finnish Development Center for Technology (Tekes) is gratefully acknowledged.

[1] ISO 140-3:1995 (E) Acoustics, ''Measurement of Sound Insulation in Buildings and of Building Elements—Part 3: Laboratory Measurements of Airborne Sound Insulation of Building Elements'' (International Organization for Standardization, Genève, Switzerland, 1995)
[2] ISO 140-10:1991 (E) Acoustics, ''Measurement of Sound Insulation in Buildings and of Building Elements—Part 10: Laboratory Measurements of Airborne Sound Insulation of Small Building Elements'' (International Organization for Standardization, Genève, Switzerland, 1991)
[3] H. Jonasson, ''Sound Intensity and Sound Reduction Index,'' Appl. Acoust. **40**, 281–293 (1993).
[4] ISO 140-5:1996 (E) Acoustics, ''Measurement of Sound Insulation in Buildings and of Building Elements—Part 5: Field Measurements of Airborne Sound Insulation of Facade Elements and Facades'' (International Organization for Standardization, Genève, Switzerland, 1998).
[5] ISO 15186-1:1999 (E) Acoustics, ''Measurement of Sound Insulation in Buildings and of Building Elements Using Sound Intensity—Part 1: Laboratory Conditions'' (International Organization for Standardization, Genève, Switzerland, 1999).
[6] M. Machimbarrena and F. Jacobsen, ''Is there a systematic disagreement between intensity-based and pressure-based sound transmission loss measurements?'' Building Acoust. **6**(2), 101–111 (1999).
[7] F. Jacobsen, V. Cutanda, and P. M. Juhl, ''A numerical and experimental investigation of the performance of sound intensity probes at high frequencies,'' J. Acoust. Soc. Am. **103**, 953–961 (1998).
[8] S. Gade, ''Validity of intensity measurements in partially diffuse sound field,'' Brüel & Kjær Technical Review **4**, 33–31 (1985).
[9] ISO 9614-1:1993 (E) Acoustics, ''Determination of Sound Power Levels of Noise Sources Using Sound Intensity—Part 1: Measurement at Discrete Points'' (International Organization for Standardization, Genève, Switzerland, 1993).
[10] R. E. Halliwell and A. C. C. Warnock, ''Sound transmission loss: Comparison of conventional techniques with sound intensity techniques,'' J. Acoust. Soc. Am. **77**, 2094–2103 (1985).
[11] A. Cops, M. Minten, and H. Myncke, ''Influence of the Design of Transmission Rooms on the Sound Transmission Loss of Glass—Intensity versus Conventional Method,'' Noise Control Eng. J. **28**(3), 121–129 (1987).
[12] J. C. S. Lai and D. Qi, ''Sound Transmission Loss Measurements Using the Sound Intensity Technique Part 1: The Effects of Reverberation Time,'' Appl. Acoust. **40**, 311–324 (1993).
[13] H. Jonasson, ''Measurement of sound reduction index with intensity technique,'' Nordtest project 746-88, Swedish National Testing and Research Institute, SP Report 1991:23, Sweden, Borås (1991).
[14] F. J. Fahy, *Sound Intensity* (Elsevier Science, Essex, England, 1989).
[15] B. G. van Zyl and P. J. Erasmus, ''Sound Transmission Analysis in Reactive Fields by Sound Intensimetry,'' Noise Control Eng. J. **28**(3), 113–119 (1987).
[16] V. Hongisto and K. Saine, ''Sound Power Measurement of a Diesel Engine by ISO/DIS 9614-2 and ISO 3746 in Different Acoustical Conditions,'' in *Proceedings of Internoise 96*, Liverpool, 31 July–2 August 1996 (Institute of Acoustics, UK), pp. 2697–2702.
[17] B. G. van Zyl, P. J. Erasmus, and G. J. J. van der Merwe, ''Determination of Sound Reduction Indices in the Presence of Flanking Transmission,'' Appl. Acoust. **19**, 25–39 (1986).
[18] B. G. van Zyl, P. J. Erasmus, and F. Anderson, ''On the Formulation of the Intensity Method for Determining Sound Reduction Indices,'' Appl. Acoust. **22**, 213–228 (1987).
[19] V. Hongisto, V. Viljanen, H. Koskela, K. Nieminen, and M. Lindgren, ''An Automatic System and a Test Procedure for Sound Insulation Measurements Using Sound Intensity Technique,'' Noise Control Eng. J. **45**(2), 85–94 (1997).
[20] V. Hongisto, ''Experimental and Predictive Methods for Improving the Sound Insulation of Lightweight Building Elements,'' Licentiate Thesis, Tampere University of Technology, Finland, Report 1/97, 1997.
[21] R. W. Guy and J. Li, ''Intensity measurements in the presence of standing waves,'' J. Acoust. Soc. Am. **92**, 2709–2715 (1992).
[22] G. Porges, *Applied Acoustics* (Arnold, London, 1977).
[23] V. Hongisto, ''Airborne sound insulation of wall structures—Measurement and prediction methods,'' Helsinki University of Technology, Laboratory of Acoustics and Audio Signal Processing, Report 56, Doctoral Thesis, 2000, Espoo, Finland.
[24] Origin Users Manual, Version 5, 1997 Microcal Software Inc. USA.
[25] ASTM C 483-90a, ''Standard test method for impedance and absorption of acoustical materials by the impedance tube method'' (American Society for Testing and Materials, Philadelphia, 1990).
[26] ISO 717-1:1996 (E) Acoustics, ''Rating of sound insulation in buildings and of building elements—Part 1: Airborne sound insulation'' (International Organization for Standardization, 1996, Genève, Switzerland, 1996).
[27] CEI/IEC 1043:1993 Electroacoustics, ''Instruments for the measurement of sound intensity—Measurement with pairs of pressure sensing microphones (International Electrotechnical Commission, Geneva, Switzerland, 1993).
[28] E. Gerretsen, ''European developments in prediction models for building acoustics,'' Acta Acoust. **2**, 205–214 (1994).

The prediction of speech intelligibility in underground stations of rectangular cross section

Lening Yang and Bridget M. Shield
School of Engineering Systems and Design, South Bank University, London SE1 0AA, United Kingdom

(Received 23 December 1998; revised 17 July 2000; accepted 28 September 2000)

Long enclosures are spaces with nondiffuse sound fields, for which the classical theory of acoustics is not appropriate. Thus, the modeling of the sound field in a long enclosure is very different from the prediction of the behavior of sound in a diffuse space. Ray-tracing computer models have been developed for the prediction of the sound field in long enclosures, with particular reference to spaces such as underground stations which are generally long spaces of rectangular or curved cross section. This paper describes the development of a model for use in underground stations of rectangular cross section. The model predicts the sound-pressure level, early decay time, clarity index, and definition at receiver points along the enclosure. The model also calculates the value of the speech transmission index at individual points. Measurements of all parameters have been made in a station of rectangular cross section, and compared with the predicted values. The predictions of all parameters show good agreement with measurements at all frequencies, particularly in the far field of the sound source, and the trends in the behavior of the parameters along the enclosure have been correctly predicted. [DOI: 10.1121/1.1329617]

PACS numbers: 43.55.Br, 43.55.Ka, 43.55.Gx, 43.55.Hy [JDQ]

I. INTRODUCTION

Underground stations are normally long enclosures in which the theory of classical acoustics is not applicable. In recent years there has been increasing interest in the acoustics of underground stations and several investigations into the acoustics of this kind of space have been undertaken.[1–3] This work has involved acoustic measurements in both physical scale models of stations and real underground stations.

In general, underground stations are long enclosures with either a rectangular or curved cross section. A computer model for the prediction of sound in underground stations has been developed by Kang.[4] This model is based on the image source method and is suitable for an overall investigation of the behavior of the sound field, although it involves simplifying the space, as required with the image source technique.

The ray-tracing modeling method is more flexible than the image source method, and therefore more suitable for the modeling of spaces of complex construction. Ray-tracing computer models have therefore been developed by the authors for detailed investigation of the sound field in long enclosures of both curved and rectangular cross section.[5,6] Initially a model was developed for the prediction of sound propagation, early decay time, and reverberation time in a long enclosure, using hypothetical spaces to ensure that the characteristics of the sound field in a long, nondiffuse, space were correctly modeled.[7] This model has been validated using data measured in a scale-model underground station.[5,8]

This paper describes the further development of the ray-tracing model to include the prediction of acoustical parameters relating to speech intelligibility, such as clarity index and definition. The model predicts sound propagation (in terms of sound-pressure level), early decay time, clarity index C50, and definition D50. It also calculates the speech transmission index (STI) at individual frequencies and overall, at points along the enclosure.

The calculation of STI is based upon the original method of Houtgast and Steeneken,[9] which was incorporated into a ray tracing method by van Rietschote.[10] This method has been modified as described here to make it applicable for the prediction of STI in long enclosures.

The paper also describes the validation of the model using measurements made in a real station of rectangular cross section. The validation showed that the model can accurately predict all the above parameters related to speech intelligibility, including the STI.

II. THE RAY-TRACING MODEL

The ray-tracing model used here has been developed specifically for the prediction of the sound field in long enclosures. It models sound propagation throughout the space, and predicts the impulse response at any point in the space. The acoustics parameters early decay time, clarity, and definition at a receiver point are calculated from the impulse response at the point.

An initial version of the model was tested using hypothetical data to ensure that it correctly predicts the characteristics of both a diffuse space and a long nondiffuse space, in particular the decrease in sound-pressure level and increase in early decay time along a space containing a single source.[7] This model was then tested using a scale model of a station with curved surfaces, and shown to accurately predict sound-pressure levels and early decay times at all frequencies.[5,8]

The distinguishing features of this ray-tracing model, which make it appropriate for modeling the sound field in a long enclosure, are described below. They include the use of the energy discontinuity percentage to terminate the tracing of a ray, the use of a statistically based method to compensate for the lack of later reflections owing to computer limi-

tations, the inclusion of diffraction effects from the station ends around the openings to the train running tunnels, and the ability to model enclosures of both rectangular and curved cross sections. The model also includes source directivity which was applied in the case of the scale-model validation, but has not been used in the validation described in this paper, in which a real station of rectangular cross section was used.

A. Energy discontinuity percentage

The energy discontinuity percentage (EDP), defined by Dance and Shield,[11] rather than the number of reflections, is used to decide when to terminate the tracing of a ray. The EDP represents the percentage of a ray's energy lost before the termination of the tracing of the ray. The typical value of EDP required to give accurate predictions in a range of spaces has been found to lie between 90% and 99%, the lower the value, the shorter the run time of the model. In the case of diffuse spaces with uniform absorption, the relationship between the reflection order and EDP is as follows:

$$n=\frac{\ln(1-P/100)}{\ln(1-\alpha)-hl}, \tag{1}$$

where n is the reflection order; P is the energy discontinuity percentage; h is the air absorption attenuation (dB/m); l is the mean free path length, and a is the average absorption coefficient.

It was decided to use EDP to terminate the tracing of rays in the case of long enclosures, as it represents the real situation where the ending of the travel of a ray is determined by its loss of energy.

B. Late reflections

The method used to compensate for the loss of late reflections which may occur due to speed and memory limitations of the computer is the reverberation time tail correction, as used by Ondet and Barbry.[12] The feasibility of using this method in the case of long enclosures has been investigated by the authors in Ref. 7.

C. Diffraction effects

Measurements made in a scale model of a circular station showed that the platform ends had a significant effect upon both sound-pressure level and early decay times.[13] It was concluded that these effects were due to diffraction around the tunnel openings. The ray-tracing model has therefore been designed to include diffraction effects from the tunnel portals at the ends of the platform. The diffraction approximation used is that of Dance *et al.*,[14] in which a diffraction area of depth one wavelength around the tunnel opening, is defined. When a ray strikes this area it is reflected in a random direction, with no attenuation.

D. Modeling of different cross-sectional shapes

Although the model described here was validated using data from a station of rectangular cross section, it is also suitable for other long enclosures, including those with curved surfaces. Curved surfaces can be modeled using a series of planes, although in this case focusing effects caused by the curved surfaces will be partly lost.[15] Alternatively, the curved surface of a station can be modeled exactly to give more accurate results.[8]

III. CALCULATION OF SPEECH TRANSMISSION INDEX

The speech transmission index was defined in 1980 by Houtgast and Steeneken[9] and has been shown to be highly correlated with speech intelligibility.

STI is derived from the modulation transfer functions (MTF) of a room. Therefore, before calculating STI at a point in a space, the MTF first needs to be evaluated from the modulated sound intensity emitted by the source and the sound intensity at the point.

In an infinite space without background noise, the modulation index obviously does not change with the observed point as there is only direct sound in the space. However, in a real enclosed space, background noise and reflections from the boundaries of the space can reduce the modulation index of sound intensity at the receiver position. Houtgast, Steeneken, and Plomp[16] show that for a diffuse space, the modulation transfer index $m(F)$ for a given modulation frequency F can be classified into two components, the reverberation and noise components, to give

$$m(F)=M_{\text{noise}}\times M_{\text{reverberation}}, \tag{2}$$

where $M_{\text{reverberation}}$ and M_{noise} denote the reverberation and noise components of the modulation transfer function, respectively.

The noise component of the MTF can be calculated from the signal-to-noise ratio as follows:

$$M_{\text{noise}}=\frac{1}{1+10^{(-\text{S/N})/10}}, \tag{3}$$

where S/N is the signal-to-noise ratio in dB.

The reverberation component in a diffuse space can be calculated from the reverberation time RT_{60} in the space as follows:

$$M_{\text{reverberation}}=\frac{1}{\sqrt{1+\left(2\pi F\frac{\text{RT}_{60}}{13.8}\right)^2}}. \tag{4}$$

Equation (3) shows that M_{noise} is independent of modulation frequency and the shape of the space. Moreover, Eq. (3) is suitable for any space and is relatively simple to calculate when the signal-to-noise ratio is known.

However, Eq. (4) indicates that $M_{\text{reverberation}}$ depends on both the modulation frequency and the reverberation time of the space. For a given modulation frequency F, the value of $M_{\text{reverberation}}$ is only dependent on the reverberation time RT_{60} of the space. Thus, the accurate calculation of ST1 depends on the accurate calculation of reverberation time. Equation (4) assumes a purely exponential reverberation decay, which may not occur in long enclosures such as underground stations. Plomp and co-workers[10,16–18] developed a series of

methods for use in different situations including a general statistical method, an image-source method, a ray-tracing method, and a hybrid method.

Since in most underground stations the space is nondiffuse and the boundary is disproportional, and may include a curved surface, the image-source and statistical methods cannot be used for calculating acoustics parameters. The method used here for the calculation of STI is therefore the ray-tracing model of van Rietschote *et al.*,[10] which has been modified for inclusion in the basic ray-tracing model of long enclosures. The main advantage of the ray-tracing method is that with this method it is possible to predict the speech intelligibility in any spaces regardless of their complex acoustic or architectural boundaries. The modifications to the original ray-tracing method of van Rietschote *et al.*, which increase its suitability for use in predicting the STI in long enclosures, are described below.

IV. RAY-TRACING METHOD FOR CALCULATION OF STI

The reverberation time can be evaluated from the reverberation decay curve calculated from the impulse response, and subsequently the modulation index reduction at any modulation frequency can be calculated mathematically. Thus, from the MTF matrix, the STI value for any listener position can be evaluated.

A mathematical model for calculating the modulation transfer function of the reverberant component of sound by using the ray-tracing method was originally developed by van Rietschote *et al.*,[10] and is described below. The particular characteristics of the sound field in long, nondiffuse spaces necessitated that modifications be made to this MTF calculation method to make it applicable to the prediction of STI in long enclosures. The modifications, which are described in detail below, include taking into account air absorption, considering the precise values of sound intensity passing through a receiver cell, and using total ray traveling distance instead of the mean free path length to decide the critical point at which to start using a statistical method in the calculation of late reflected sound.

A. van Rietschote's ray-tracing model of STI

In the model of van Rietschote, the sound sources are treated as point sources emitting a large number of sound rays, and the receivers are represented as spheres receiving the rays.

At a receiver position, each sound ray can be written as

$$a_i[1+\cos 2\pi F(t-t_i)], \tag{5}$$

where a_i is the intensity of the ray at the receiver position, F is the modulation frequency, and t_i is the time delay due to the distance traveled.

The modulation index at the receiver position can then be calculated from all rays which hit the listener

$$m(F)_{\text{reverberation}}=\frac{\sqrt{(\Sigma_i a_i \cos 2\pi F t_i)^2+(\Sigma_i a_i \sin 2\pi F t_i)^2}}{\Sigma_i a_i}, \tag{6}$$

or

$$m(F)=\frac{\sqrt{C^2(F)+S^2(F)}}{A(F)}, \tag{7}$$

where

$$A(F)=\sum_i a_i$$

$$C(F)=\sum_i a_i \cos 2\pi F t_i \tag{8}$$

$$S(F)=\sum_i a_i \sin 2\pi F t_i,$$

where a_i is the ray intensity received by the listener with a delay time $t_i=d_i/c$; d_i is the distance the ray travels from the source to the listener, and c is the speed of sound. The summation includes all possible rays which can hit the listener. The values of $A(F)$, $C(F)$, and $S(F)$ can be divided into four parts, contributed by:

(i) direct sound;
(ii) early reflected sound;
(iii) late reflected sound; and
(iv) diffused sound.

The calculation of each of these parts is explained below.

1. Calculation of direct sound

The intensity of the direct sound rays follows the inverse square law of the travel distance from the point source to listener. If d is the distance from the source to the listener, N_{ray} the total number of rays emitted by the source, and r_0 the radius of the listener's sphere, the number of rays q hitting the listener is approximately given by

$$q=\frac{N_{\text{ray}}}{4\pi d^2}\pi r_0^2, \tag{9}$$

provided $d>2r_0$.

The direct sound components of $A(F)$, $C(F)$, and $S(F)$ are given by

$$A_1(F)=q, \tag{10}$$

$$C_1(F)=A_1(F)\cos\left(2\pi F\frac{d}{c}\right), \tag{11}$$

$$S_1(F)=A_1(F)\sin\left(2\pi F\frac{d}{c}\right), \tag{12}$$

where a spherical directivity pattern of the source has been assumed, implying an initial strength of 1 for each ray; c is the velocity of sound.

2. Calculation of early reflected sound

When a ray reaches a receiver after reflection from the boundaries, if its strength is a_i and the distance it traveled is d_i, then the components of $A(F)$, $C(F)$, and $S(F)$ contributed by early reflected rays are given by

$$A_2(F)=\sum_i a_i, \tag{13}$$

$$C_2(F)=\sum_i a_i \cos\left(2\pi F\frac{d_i}{c}\right), \tag{14}$$

$$S_2(F)=\sum_i a_i \sin\left(2\pi F\frac{d_i}{c}\right). \tag{15}$$

3. Calculation of later reflected sound using statistical approach

A statistical method is employed in the calculation of the later reflected sound. It is assumed that, between two successive reflections of a sound ray, the probability P_i of the ith ray hitting the listener is proportional to its travel distance in the space, and can be calculated from

$$P_i=\frac{\delta_i \pi r_0^2}{V}, \tag{16}$$

where δ_i is the distance between two successive reflection points. Therefore, the contribution from the later reflected sound to the listener is given by

$$A_3(F)=\sum_i a_i P_i, \tag{17}$$

$$C_3(F)=\sum_i a_i P_i \cos\left(2\pi F\frac{d_i}{c}\right), \tag{18}$$

$$S_3(F)=\sum_i a_i P_i \sin\left(2\pi F\frac{d_i}{c}\right), \tag{19}$$

where a_i and d_i refer to the halfway point of the ray between two successive reflections.

The critical number of reflections N_{sta}, after which the statistical approach needs to be used, can be estimated from

$$\frac{N_{\text{ray}}}{4\pi d^2}\pi r_0^2 \leqslant 1, \tag{20}$$

where $d=N_{\text{sta}}L_{\text{mfp}}$ is the total distance traveled and L_{mfp} is the mean free path length of the room. Finally, the critical number of reflections can be worked out, from Eq. (20), to give

$$N_{\text{sta}}=\frac{r_0}{2L_{\text{mfp}}}\sqrt{N_{\text{ray}}}. \tag{21}$$

Equation (21) shows that N_{sta} depends on the receiver diameter r_0, total ray number N_{ray}, and the mean free path length L_{mfp} associated with the room dimensions.

Combining the above three contributions of A, C, and S, the reverberation component of MTF is calculated from

$$M(F)_{\text{reverberation}}=\frac{\sqrt{\Sigma_i C_i(F)+\Sigma_i S_i(F)}}{\Sigma_i A_i(F)}. \tag{22}$$

4. Diffused sound

Diffusion was also taken into account in the model of van Rietschote *et al.* and forms the fourth component of $A(F)$, $C(F)$, and $S(F)$. However, as the sound field in long enclosures is not diffuse, it was not thought appropriate to include diffusion in the ray-tracing model developed here.

B. Development of the model for the calculation of STI in long enclosures

The method of van Rietschote, described above, has been modified as follows to make it suitable for the prediction of the speech transmission index in long enclosures.

1. Calculation of direct sound

In van Rietschote's mathematical model, the initial ray strength is assumed to be 1. For the predictions of STI in a real space, with directional sources and background noise, the precise energy of the sound source has been taken into account. Air absorption has also been included in the model, as it will have a significant effect on the sound in long enclosures. After considering the air absorption h and the distance the ith ray travels in the receiver cell, d_{icell}, the direct sound components of $A(F)$, $C(F)$, and $S(F)$ are given by

$$A_1(F)=\frac{1}{V_{\text{receiver}}}\sum_i a_{i0} d_{\text{icell}} e^{-hd_i}, \tag{23}$$

$$C_1(F)=A_1(F)\cos\left(2\pi F\frac{d}{c}\right), \tag{24}$$

$$S_1(F)=A_1(F)\sin\left(2\pi F\frac{d}{c}\right), \tag{25}$$

where a_{i0} is the initial intensity of the ith sound ray of the directional source; $V_{\text{receiver}}=\frac{4}{3}\pi r_0^3$ is the volume of the receiver sphere used as a normalizing factor; and d_i is the distance traveled by the ith ray from the source. If the source is omnidirectional, then $a_{i0}=a_{00}$, where a_{00} is the strength of each sound ray.

Thus, Eq. (23) can be simplified to

$$A_1(F)=\frac{1}{V_{\text{receiver}}} q a_{00}\,\overline{d_{\text{cell}}}\, e^{-hd}=\frac{E_0}{4\pi d^2}e^{-hd}, \tag{26}$$

where $\overline{d_{\text{cell}}}=4r_0/3$ is used as the average length of sound path in the receiver sphere, q is the number of rays hitting the listener given by Eq. (9), and $E_0=N_{\text{ray}}a_{00}$ is the total intensity of sound emitted from the source, where N_{ray} is the total number of rays.

Equation (26) is the same as the equation used to express sound intensity in a free space excited by a point source, taking into account the air absorption. It demonstrates that in this case the intensity in the ray-tracing method has the same expression as in the wave acoustics method by using the normalizing factor V_{receiver}^{-1} in the calculation of A, S, and C.

2. Calculation of early reflected sound

If a ray emitted from a source with an initial strength a_{i0} is reflected k times by boundary surfaces with different absorption coefficients α_j, and reduced by air absorption, the intensity a_i of the sound ray at the listener position can be calculated from

$$a_i=a_{i0}e^{-hd_i}\prod_{j=1}^{k}(1-\alpha_j), \tag{27}$$

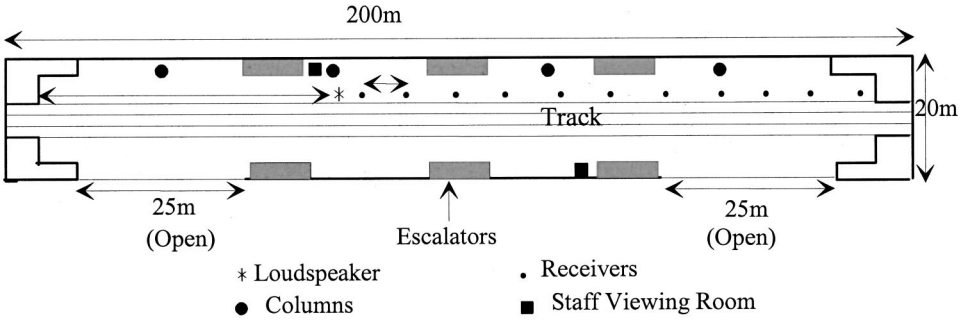

FIG. 1. Plan view of underground station.

where d_i is the travel distance of the ith sound ray. Then, the A, C, and S components in Eq. (8), contributed by reflected rays, can be deduced to give

$$A_2(F)=\frac{1}{V_{\text{receiver}}}\sum_i d_{\text{icell}}a_i, \tag{28}$$

$$C_2(F)=\frac{1}{V_{\text{receiver}}}\sum_i d_{\text{icell}}a_i\cos\left(2\pi F\frac{d_i}{c}\right), \tag{29}$$

$$S_2(F)=\frac{1}{V_{\text{receiver}}}\sum_i d_{\text{icell}}a_i\sin\left(2\pi F\frac{d_i}{c}\right). \tag{30}$$

3. Calculation of late reflected sound using statistical approach

The statistical approach is used to calculate the later reflected sound. The expressions for the late reflected sound components of A, C, and S are

$$A_3(F)=\frac{\overline{d_{\text{cell}}}}{V_r}\sum_i a_iP_i, \tag{31}$$

$$C_3(F)=\frac{\overline{d_{\text{cell}}}}{V_r}\sum_i a_iP_i\cos\left(2\pi F\frac{d_i}{c}\right), \tag{32}$$

$$S_3(F)=\frac{\overline{d_{\text{cell}}}}{V_r}\sum_i a_iP_i\sin\left(2\pi F\frac{d_i}{c}\right), \tag{33}$$

where a_i and d_i refer to the halfway point of the ray between two successive reflections; P_i is the probability of the ith ray hitting the listener.

It was decided to use inequality (20) directly to determine when to use the statistical method instead of using the mean free path length L_{mfp} to give the critical number of reflections, as the implication of using the mean free path length in long enclosures with long reflection paths has not yet been fully investigated. The critical distance d for the start of the statistical method is thus given by

$$d=\frac{r_0}{2}\sqrt{N_{\text{ray}}}, \tag{34}$$

where r_0 is the radius of the receiver sphere.

The reverberation component of the MTF can be calculated from Eq. (22)

$$M(F)_{\text{reverberation}}=\frac{\sqrt{\Sigma_iC_i(F)+\Sigma_iS_i(F)}}{\Sigma_iA_i(F)}. \tag{22}$$

C. Consideration of the ambient noise

If there is ambient noise in the space, the signal-to-noise ratio S/N needs to be taken into account as shown in Eqs. (1) and (2), to calculate the final MTF value as

$$M(F)=M(F)_{\text{reverberation}}\times\frac{1}{1+10^{(-\text{S/N})/10}}. \tag{35}$$

V. VALIDATION OF THE MODEL

Measurements were made in Hong Kong Kwai Fong Station, which is a rectangular-shaped underground station. The shape and dimensions of the station are as shown in Figs. 1 and 2.

The station is 200 m long, 20 m wide, and 5.7 m high from platform to ceiling. There are four columns along the platform, two staff viewing rooms, and six escalators, as shown in Fig. 1. Since the station is above ground, one side wall of the platform is partly opened for fresh air exchange with two gaps of length 25 m. The other side wall of the platform consists of concrete panels of height 1.1 m, and width 1.8 m. The two ends of the train running tunnels are both open.

The measurements were taken with a single source located 66 m from one end of the station, 1.5 m from the edge of the platform, and 1 m above the platform floor. The source was a loudspeaker of dimensions 0.5×0.5×0.75 m. No directivity information was available, so it was modeled as an omnidirectional source; however, given the dimensions of the source and the space it is likely that directivity would only have had a significant effect at the nearest receiver point to the speaker. The receiver positions were along the platform at 5-m intervals, at a height of 1.25 m above the plat-

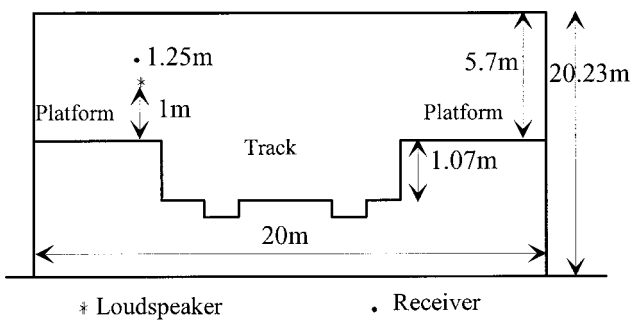

FIG. 2. Cross section of underground station.

TABLE I. Absorption coefficients of the station boundaries.

Frequency (Hz)	250	500	1000	2000	4000
Absorption coefficient	0.03	0.035	0.04	0.05	0.07

form floor and 1.5 m from the platform edge, as shown in Figs. 1 and 2.

The measuring signal was generated and received using the maximum length sequence system MLSSA, whose post-processing functions calculated most of the acoustical parameters from the measured impulse response. All parameters were measured and predicted at octave bands 125 to 4000 Hz. The speech transmission index was additionally measured and predicted in the 8000-Hz octave band.

As the surfaces along the length of the underground station are all of the same concrete, acoustically hard, material it was assumed in the model that they all have the same absorption coefficient, as shown in Table I.

Air absorption has also been taken into account in the model. The air absorption for frequencies from 125 to 8000 Hz was calculated according to the American National Standard ANSI S1-26.[19]

VI. COMPARISON OF THE MEASUREMENTS AND PREDICTIONS

The measured and predicted values of early decay time, sound propagation, clarity, definition, and speech transmission index for the 125- to 4000-Hz octave bands are shown in Figs. 3–7. The sound propagation is shown as decrease in sound-pressure level relative to the level at the receiver point 5 m from the source. Measured and predicted values of the overall speech transmission index are shown in Fig. 8.

It can be seen that the measurements of all parameters at 125 Hz showed significant fluctuations along the platform, suggesting that interference effects were occurring. As interference effects are not accounted for in this model, there were large discrepancies between predicted and measured values at certain points at this frequency, and these results have been ignored in the following discussion.

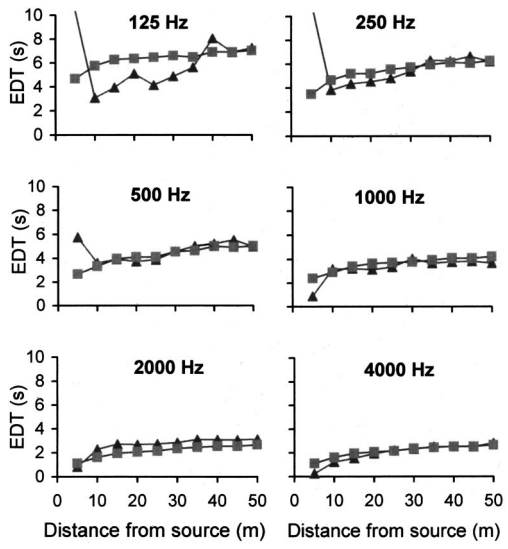

FIG. 3. Measured (-♦-) and predicted (-■-) values of early decay time in octave bands 125 to 4000 Hz.

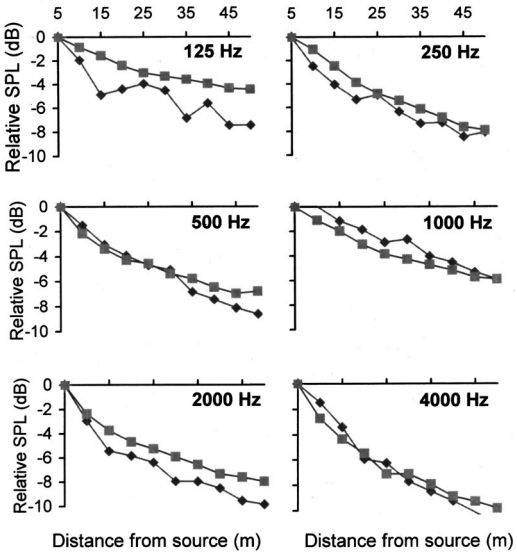

FIG. 4. Measured (-♦-) and predicted (-■-) values of sound propagation in octave bands 125 to 4000 Hz.

A. Predictions of EDT, SP, C50, and D50

It can be seen from Fig. 3 that, apart from spurious measurements at the point 5 m from the source at the lower frequencies, the measured early decay time increases with the source–receiver distance at all frequencies. The predicted values of EDT correctly followed this trend, and were generally within accepted limits.

Similarly, Fig. 4 shows that the model correctly predicted the decrease in sound-pressure level along the station at all frequencies, predictions being within 2 dB of measured levels at all points.

As with EDT and SP, the model correctly predicted the general trends in C50 and D50 along the platform at all frequencies, as can be seen from Figs. 5 and 6. However, the

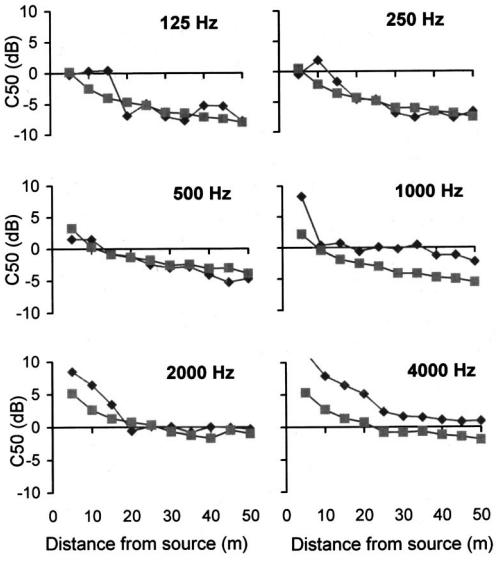

FIG. 5. Measured (-♦-) and predicted (-■-) values of clarity index C50 in octave bands 125 to 4000 Hz.

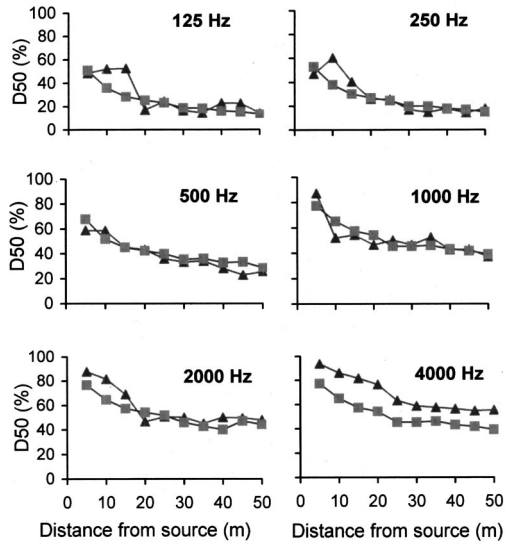

FIG. 6. Measured (-♦-) and predicted (-■-) values of definition D50 in octave bands 125 to 4000 Hz.

model underpredicted both C50 and D50 at the higher frequencies, although the predicted values of D50 are, in general, more accurate than those of C50. This is because D50 depends on the energy ratio of the first 50 ms to the overall time, but C50 depends on the energy ratio of the first 50 ms to the later 50 ms, so the calculation of C50 is more sensitive to the critical time of 50 ms.

B. Prediction of speech transmission index (STI)

The evaluation of the speech transmission quality in an enclosure is based on the final value of STI which is calculated from the individual values in the 125- to 8000-Hz octave bands. For this purpose, the individual values of STI in the octave bands have been measured and modeled. Figure 7 shows the measured and predicted STI values for the 125- to 4000-Hz octave bands. The predicted overall value was calculated from the individual values predicted in the 125- to

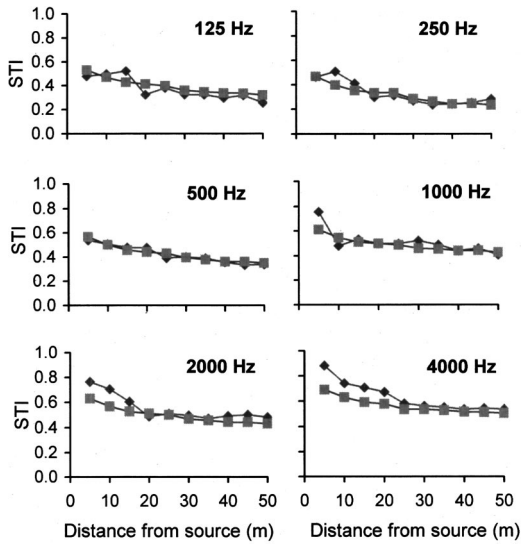

FIG. 7. Measured (-♦-) and predicted (-■-) values of STI in octave bands 125 to 4000 Hz.

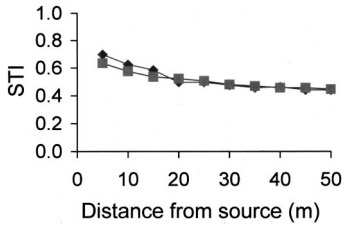

FIG. 8. Measured (-♦-) and predicted (-■-) values of overall STI.

8000-Hz octave bands. The measured and predicted values of the overall speech transmission index are shown in Fig. 8.

The figures show that, in general, the value of the STI decreases with increasing source–receiver distance. As with the other parameters this overall trend has been correctly predicted by the model. Furthermore, it can be seen that, on the whole, the model has accurately predicted the STI at individual receiver points at all frequencies, the predictions being particularly accurate in the far field of the source.

Figure 8 shows that the overall predicted values of STI are very accurate compared with the measured overall values. The deviation between predicted and measured values of overall STI is less than ± 0.01 in the far field and ± 0.03 in the near field. The larger errors in the near field are probably because the source size is considerable in the near field, but it has been simply treated as a point source in the model. Another possible source of error is the size of the receiver volume. The receivers were modeled as spheres of 1-m diameter. For greater accuracy in the near field, a smaller receiver volume is required.

VII. CONCLUSIONS

It has been shown that the ray-tracing model described for predicting the sound field, including the speech transmission index, in long enclosures accurately predicts both the values and trends of acoustics parameters at most frequencies. The model has thus been proved to be a useful tool for the prediction of acoustics parameters in long enclosures such as underground stations.

Errors occur at particular receiver points and frequencies for some of the parameters. Possible sources of error include the fact that the predictions are based on approximations of the geometry and acoustic characteristics of the space. In the validation described here, for example, the scattering of sound from edges of the escalators and staff-viewing boxes and from tracks has not been taken into account. Furthermore, the surface absorption coefficient was assumed as angle independent, but this is not the case in practice.

In general, predictions of all parameters are more accurate in the far field than the near field of the source. The loudspeaker source used for the measurements was treated as an omnidirectional point source in the model, which may be a cause of error in the near field.

The size of the receiver volume may also lead to errors in the predictions in the near field. In this particular model the receiver was assumed to be a 1-m sphere in the space. This size of receiver relative to the dimensions of the space can give reasonable results in the far field and for later reflections, but for the near field and early part of the sound it

may not give accurate results. For more accurate results, the receiver volume should be smaller, but the number of rays will then be increased significantly since it depends on the volume of the receiver, so the running time will be correspondingly increased. However, with recent and continuing increases in computer power it should be possible to develop an efficient, fast, and more accurate model simply by increasing the number of rays traced.

[1] P. W. Barnett, ''Acoustics of underground platforms,'' Proc. Inst. Acoust. **16**, 433–443 (1994).
[2] R. J. Orlowski, ''Underground station scale modelling for speech intelligibility prediction,'' Proc. Inst. Acoust. **16**, 167–172 (1994).
[3] J. Kang, ''The unsuitability of the classic theory in long enclosures,'' Arch. Sci. Rev. **39**, 89–94 (1996).
[4] J. Kang, ''Acoustics in long enclosures with multiple sources,'' J. Acoust. Soc. Am. **99**, 985–989 (1996).
[5] L. N. Yang, T. J. Cox, and B. M. Shield, ''Modelling of sound propagation in underground stations,'' Proceedings Internoise'96 (1996), pp. 3173–3176.
[6] B. M. Shield and L. Yang, ''Modelling of acoustic parameters and speech intelligibility in long enclosures,'' Proceedings 16th International Congress on Acoustics, Seattle (1998), pp. 2157–2158.
[7] L. N. Yang and B. M. Shield, ''Development of a ray tracing computer model for the prediction of the sound field in long enclosures,'' J. Sound Vib. **229**, 133–146 (2000).
[8] L. N. Yang and B. M. Shield, ''Development and validation of a ray tracing model for predicting the sound field in underground stations with curved surfaces,'' Appl. Acoust. (submitted).
[9] T. Houtgast and H. J. M. Steeneken, ''The modulation transfer function in room acoustics as a predictor of speech intelligibility,'' Acustica **28**, 66–73 (1973).
[10] H. F. van Rietschote, T. Houtgast, and H. J. M. Steeneken, ''Predicting speech intelligibility in rooms from the modulation transfer function. IV. A ray tracing computer model,'' Acustica **49**, 245–252 (1981).
[11] S. M. Dance and B. M. Shield, ''The complete image-source method for the prediction of sound distribution in non-diffuse enclosed spaces,'' J. Sound Vib. **201**, 473–489 (1997).
[12] A. M. Ondet and J. L. Barbry, ''Modelling of sound propagation in fitted workshops using ray tracing,'' J. Acoust. Soc. Am. **85**, 787–796 (1989).
[13] L. N. Yang, ''Computer modelling of speech intelligibility in underground stations,'' Ph.D. thesis, South Bank University, London (1997).
[14] S. M. Dance, J. P. Roberts, and B. M. Shield, ''Computer prediction of insertion loss due to a single barrier in a nondiffuse empty enclosed space,'' J. Build. Acoust. **1**, 125–136 (1994).
[15] B. M. Shield and L. N. Yang, ''Two methods of modelling a curved surface in a ray tracing model,'' J. Build. Acoust. **5**, 69–78 (1998).
[16] T. Houtgast, H. J. M. Steeneken, and R. Plomp, ''Predicting speech intelligibility in rooms from the modulation transfer function. I. General room acoustics,'' Acustica **46**, 60–72 (1980).
[17] R. Plomp, H. J. M. Steeneken, and T. Houtgast, ''Predicting speech intelligibility in rooms from the modulation transfer function. II. Mirror image computer model applied to rectangular rooms,'' Acustica **46**, 73–81 (1980).
[18] H. F. van Rietschote and T. Houtgast, ''Predicting speech intelligibility in rooms from the modulation transfer function. V. The merits of the ray tracing model versus general room acoustics,'' Acustica **52**, 72–78 (1983).
[19] ANSI S1-26, ''Method for the Calculation of Absorption of Sound by the Atmosphere'' (American National Standards Institute, New York, 1978).

Characterization of particle size and its distribution during the crystallization of organic fine chemical products as measured *in situ* using ultrasonic attenuation spectroscopy

Patricia Mougin and Derek Wilkinson
Centre for Molecular and Interface Engineering, Department of Mechanical and Chemical Engineering, Heriot-Watt University, Riccarton, Edinburgh EH14 4AS, United Kingdom

Kevin J. Roberts
Centre for Particle and Colloid Engineering, Department of Chemical Engineering, School of Process, Environmental and Materials Engineering, University of Leeds, Leeds LS2 9JT, United Kingdom

Richard Tweedie
2 Roundwood Avenue, Stockley Park, Uxbridge UB11 1AZ, United Kingdom

(Received 24 February 2000; revised 5 October 2000; accepted 14 October 2000)

The potential application of ultrasonic attenuation spectroscopy to the *in situ* examination of solution phase crystallization processes is examined through studies carried out on two organic compounds: urea and (*L*)-glutamic acid. For this study a commercial ultrasonic spectrometer [Ultrasizer by Malvern Instruments Ltd., F. Alba, U.S. Patent 5,121,629 (1992)] was used. A particle size analysis was carried out in an attempt to monitor the crystal size distributions of the crystals growing within the mother liquor. While this technique was found to be of limited effectiveness for the monitoring of the crystallization of urea, due to the formation of high aspect ratio needle crystals, whose long axial size is beyond the range of the technique (0.01 μm–1000 μm), good results were obtained with prismatic (*L*)-glutamic acid crystals. The size evolution of the latter during crystal growth was successfully monitored throughout the crystallization process. [DOI: 10.1121/1.1331113]

PACS numbers: 43.58.Kr, 43.35.Yb [SLE]

I. INTRODUCTION

Crystallization from solution is a unit operation which is routinely used in the fine chemicals industry for purification and separation, notably in the manufacture of products such as pharmaceuticals, agrochemicals, and speciality chemicals such as dyes and pigments. The industrial scale production of these high value-added materials usually involves batch rather than continuous manufacturing processes in which high product quality and process reproducibility are prerequisites for market success. This need demands, in turn, stringent control of the parameters that govern the process such as mother liquor supersaturation during crystallization, crystallinity and polymorphic form of the crystallized product, as well as the product's crystal size distribution (CSD) and its evolution with time due to growth. Given the inherent nonlinear growth environment within batch reactors, optimal understanding and hence control of the crystallization process can only be accomplished via the use of appropriate analytical methods which are capable of characterizing the critical process parameters on-line during processing.

Within the above perspective, controlling the CSD is particularly important, as it is a major driver in dictating product behavior downstream through its impact on unit operations such as filtration, drying, transport, and storage. Furthermore, in terms of process intensification, an ability to control particle size through the primary particle formation step would remove the need for secondary processing through comminution to satisfy customer product requirements for the CSD. However, on-line measurement and control of the CSD can be problematic, particularly due to the fact that most commercially available particle sizing methods rely on light scattering techniques which are inherently unsuitable for examining the dense crystal/solution slurries produced in batch crystallization processes. As these particle sizing methods cannot work at representatively high solid concentration levels, a difficult and time-consuming sampling step is therefore needed for the dilution of the solid/liquid suspension, a process which can, in turn, lead to significant modification of the CSD.

Ultrasonic attenuation spectroscopy (UAS) is a comparatively new characterization technique that is suitable for measurement of particle sizes within the approximate range 0.01 μm–1000 μm. In principle, it is capable of examining optically opaque or concentrated systems without the need for analyte dilution[1] and therefore is attracting some attention as a potentially useful technique for characterizing more practical particulate suspensions. However, the complexity of the theory relating ultrasonic attenuation spectra to the CSD can be a significant obstacle in its routine application for the dynamic characterization of particle formation processes, particularly in cases where the physical parameters of both the liquid medium and growing particles in suspension are constantly evolving. Experimental data are thus clearly needed in this field where so far theoretical work has predominated.

In this paper, we address this whole issue of the potential for UAS technique to be able to characterize crystalliza-

tion processes through a series of experimental measurements performed *in situ* during the crystallization of two representative organic compounds: urea and (*L*)-glutamic acid. This study used an Ultrasizer (Malvern Instruments Ltd.) ultrasonic spectrometer, but the use of ultrasonic attenuation spectroscopy to characterize dynamic processes involving the crystallization of molecular crystals is transferable to other attenuation spectroscopy devices having a similar frequency range (1–150 MHz).

II. ACOUSTIC ATTENUATION SPECTROSCOPY

The physics of ultrasound interaction with particles goes back, together with that of optics, to the work of Lord Rayleigh more than a century ago. Phenomena, which occur when light waves propagate through particulate systems, also take place when sound waves interact with particles. When a sound wave passes through a suspension, changes occur to the wave as well as to the two phases of the particulate medium. A particle presents a discontinuity to sound propagation, and the wave scatters with a redistribution of its acoustic energy throughout the volume before being detected at the receiver (scattering and diffraction losses). In addition, absorption phenomena occur when the particles move relative to the suspending medium and the mechanical energy degrades to heat (viscous losses); and temperature differences develop between phases with mechanical energy transferring into heat (thermal losses).

A. Mathematical modeling of ultrasonic data

There are a number of solutions to the modeling of acoustic propagation in dispersed systems and the reader is referred to Harker and Temple,[2] and Tebbutt and Challis[3] for a comprehensive review of the subject and the relative merits of the various approaches available. In this work, the mathematical model chosen to relate the CSD to ultrasonic attenuation measurements was the wave scattering theory of Epstein and Carhart[4] and Allegra and Hawley,[5] hereinafter referred to as the ECAH theory. This theory is based on a mathematical treatment associated with the propagation of an ultrasonic wave through a liquid containing an ensemble of particles. The ultrasonic velocity and attenuation coefficients are related to the overall phase and magnitude of this wave. As the wave travels through the liquid, its phase and magnitude are altered because of interactions with the particles in the system, in particular via the fact that:

- the compression wave is scattered into directions which are different from that of the incident wave;
- ultrasonic energy is converted into heat due to various absorption mechanisms (e.g., thermal conduction and viscosity);
- interference occurs between waves that travel directly through the particle, waves that travel directly through the surrounding medium, and waves which are scattered.

The relative importance of these different mechanisms depends on the thermo-physical properties of the component phases, the frequency of the ultrasonic wave, and the concentration and particle size of the particles. ECAH theory reveals that any of these attenuation phenomena can be accurately characterized through fundamental equations based on the laws of conservation of mass, energy, and momentum, thermodynamic equations of state, and stress–strain relations for isotropic elastic solids or viscous fluids, i.e., by formulating the wave equations that describe the interaction between sound and particulates. In this manner, the ultrasonic attenuation spectrum associated with any particle size distribution and particle concentration can be predicted for any suspension or emulsion as long as a set of *mechanical, thermodynamic*, and *transport* properties is known for each one of the suspending and suspended media. These physical properties are:

- velocity of the ultrasonic wave;
- density;
- thermal expansion coefficient;
- heat capacity;
- thermal conductivity;
- attenuation of the ultrasonic wave;
- viscosity (for the fluid phase);
- shear rigidity (for the solid phase).

B. Application of ultrasonic spectroscopy for monitoring crystallization processes

The examination of crystallization processes using ultrasonic spectroscopy is prone to specific problems due to the intermediate phase at the dynamic interface between solid and liquid. In a paper examining the influence of sound on crystallization, Akulichev and Bulanov[6] predicted that an excess of attenuation due to the phase transition would occur compared to a suspension in a steady state. However, several studies have been published since this work on dynamic systems occurring in suspensions or emulsions. Ultrasound velocity measurements have been carried out in order to monitor crystallization in oil-in-water and water-in-oil emulsion droplets,[7–10] where the solid fraction of the crystallizing emulsion droplets was estimated using a modified form of the Urick equation.[11] Other studies of dynamic systems such as flocculating emulsions are closely related and give some useful insight into how to deal with other evolving systems.[12] Recently, the potential of ultrasound as a monitoring tool in crystallization processes was shown in a study where phase velocity and acoustic attenuation measurements were carried out in the frequency range 2–7 MHz during the crystallization of copper sulfate pentahydrate.[13] However, although acoustic measurements can have significance as a primary source of information (to determine the onset of crystallization for instance), quantitative particle size information is often more useful in process technology due to the latter's importance in product formulation. For this reason a commercial ultrasonics particle sizer was used in this study both for the measurement and deconvolution of the acoustic spectra. The principle of deconvolution of acoustical measurements is presented in the following section.

C. Acoustic attenuation spectroscopy for particle sizing

Ultrasonic attenuation spectroscopy for the particle size measurement of suspensions and emulsions involves launch-

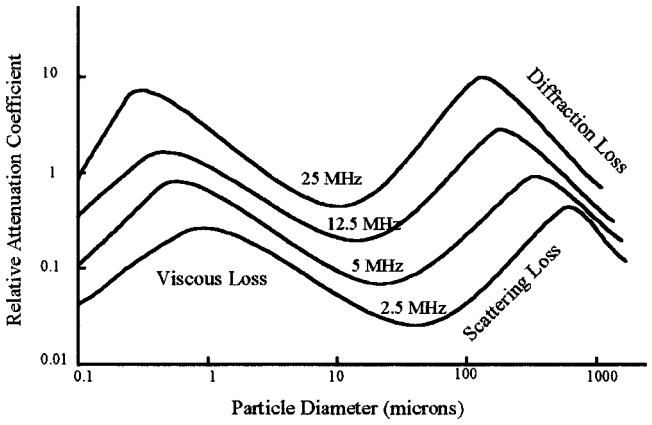

FIG. 1. Variation of ultrasonic attenuation with particle size at different frequencies.

ing ultrasound waves of different frequencies, typically from 1 MHz up to 200 MHz through a sample volume and measuring the acoustic attenuation. The relationship between spectral data and particle size plus concentration can be illustrated by considering the curves shown in Fig. 1 which are valid for the case of solid rigid high-density contrast particles suspended in water. Each curve depicts the attenuation of the sound wave of a fixed frequency as a function of the size of a monosize population with a fixed concentration. From these curves, it is clear that if the attenuation of sound was measured at a single frequency with perfect accuracy and resolution, there would only be four potential monosize distributions (two in the region of viscous attenuation, one in the Rayleigh scattering region, and a fourth in the diffraction zone) which could have produced that measured attenuation. However, measurement noise along with modeling errors lead to instabilities of the data inversion procedure, and a greater number of frequencies is therefore needed for a reliable analysis.

The actual size is determined by observing how only one of the four candidate sizes for each frequency cluster around the same value for all frequencies while the other potential sizes are irregularly dispersed. For the general case of a polysized distribution, deconvolution is more complex. A nonlinear least squares minimization is used to match the measured attenuation spectrum to the predicted attenuation spectrum of the solution particle size distribution.

The overall process by which the particle size distribution of a suspension or emulsion can be measured using acoustic spectroscopy is outlined in Fig. 2. The ECAH model is used to construct a database, the model matrix in Fig. 2, of attenuation spectra for a wide range of monodispersed particle suspensions. Two programs were used for the deconvolution of the attenuation spectra measured in this study. The procedure is split into two steps:

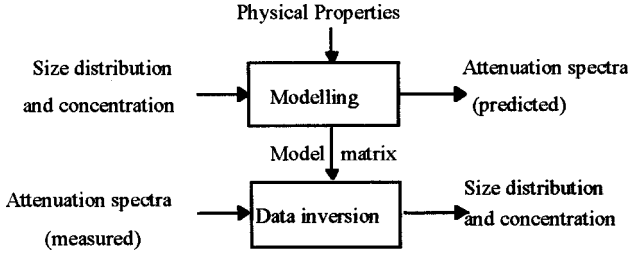

FIG. 2. Acoustical spectroscopy–key analysis steps.

- the generation of a three-dimensional matrix describing the inter-relationship between attenuation, frequency, and particle size. This matrix is obtained by calculating the attenuation spectrum associated with any particle size within the range 10 nm–1000 μm, by applying the ECAH model using the physical parameters describing the particle and liquid system. The modeling process relies on the assumption that the fundamental relationship between attenuation spectrum and physical properties exists:

$$a = K \cdot d, \tag{1}$$

  where a is the attenuation spectrum vector, K the scattering coefficients matrix, and d the particle size distribution vector. A polydisperse scattering coefficients matrix is also calculated beforehand to provide an initial estimate of the particle size distribution.
- the data inversion consisting of the determination of the particle size from an experimental acoustic spectrum. The program, which also controls the ultrasonic spectrometer, contains the data inversion subroutine.

Attenuation due to polydispersions has been assumed to be due to the combined effects of all particle sizes present:

$$\alpha(\omega) = \int_0^\infty \alpha'(\omega, D) \cdot f(D) \cdot dD, \tag{2}$$

where α is the attenuation of the polydispersion, α' is the attenuation of a monodispersion of diameter D, and $f(D)$ is the probability density function (PDF) of the polydispersion. The PDF has been assumed to be a log normal distribution or, for cases when the inversion was unsatisfactory, a combination of two log normal distributions. Thus the suspension is characterized by its concentration and either one or two log normal distributions. In the inversion scheme, data from the model matrix are weighted according to assumed PDFs in order to locate a PDF which gives a predicted attenuation spectrum which closely matches the measured attenuation spectra.

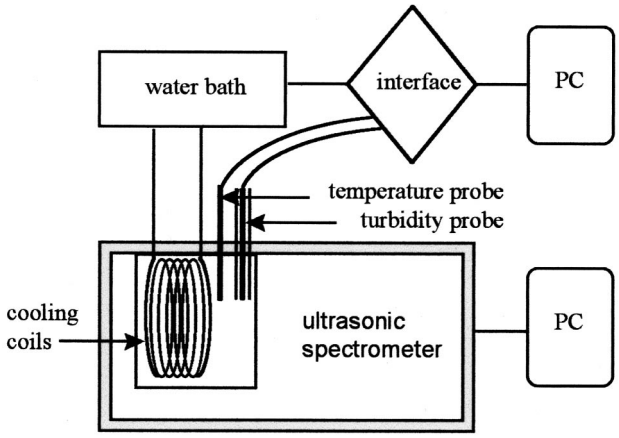

FIG. 3. Schematic of the experimental setup capable of recording ultrasonic, turbidimetric, and temperature data during temperature-programed cycles.

TABLE I. Physical properties of urea and a saturated aqueous solution of urea at 25 °C (and at T in °C for the acoustic attenuation of the mother liquor).

Property	Urea	Saturated solution of urea in water at 25 °C
Density	1.33×10^{3} kg m^{-3}	1.14×10^{3} kg m^{-3}
Sound speed	3.86×10^{3} m s^{-1}	1.7×10^{3} m s^{-1}
Thermal dilation	1.19×10^{-4} K^{-1}	2.6×10^{-4} K^{-1}
Thermal conductivity	1.08×10^{5} J m^{-1} s^{-1} K^{-1}	5.9×10^{-1} J m^{-1} s^{-1} K^{-1}
Heat capacity	3.78×10^{2} J kg^{-1} K^{-1}	4.2×10^{3} J kg^{-1} K^{-1}
Viscosity		2.6×10^{-3} N s m^{-2}
Shear rigidity	4.33×10^{9} N m^{-2}	
Attenuation	$4\times10^{-4}\times f^{1.9}$ dB m^{-1}	$(3.8\times10^{-1}-7.9\times10^{-3}\times T)\times f^{(2.7\times10^{-3}\times T+1.9)}$ dB m^{-1} where T is in °C and f in MHz[a]

[a]See Sec. IV A.

A measure of goodness-of-fit (residual) was used as a measure of the discrepancy between the experimental acoustic attenuation spectrum and the theoretical spectrum associated to ''the best particle size distribution'' as determined by data inversion. This parameter was defined as

$$\mathrm{Re}\,s=\frac{1}{N}\sqrt{\sum_{i=1}^{N}\left(\frac{\alpha_{pi}-\alpha_{mi}}{\alpha_{mi}}\right)^{2}}, \tag{3}$$

where N is the number of points in the attenuation spectrum, α_{pi} and α_{mi} are the predicted and measured attenuation, respectively, at the frequency for data point i.

III. MATERIALS AND METHODS

A. Materials

Aqueous solutions of urea and (L)-glutamic acid were prepared with distilled water. Urea and glutamic acid were purchased from BDH Chemicals Ltd. and Aldrich, respectively.

B. Experimental details for ultrasonic attenuation measurements

Ultrasonic measurements were carried out using an Ultrasizer (Malvem Instruments Ltd.) operating over a frequency range from 1 MHz to over 150 MHz and capable of characterizing a particle size range from 0.01 to 1000 μm. This instrument uses two pairs of broadband transducers driven by a continuous-wave signal to ensure accurate attenuation measurements. A measurement of the attenuation of a sound beam passing through a suspension is obtained as a function of frequency. The attenuation coefficient measured at a particular sound frequency is defined as

$$\alpha=\frac{1}{\Delta L}\ln\left(\frac{I_0}{I_1}\right), \tag{4}$$

where α is the attenuation, I_0 and I_1 are the incident intensity and the intensity after passing through the sample, respectively, and ΔL is the acoustic path length. ΔL can be adjusted to suit the attenuation characteristics of the sample under investigation (between 0.03 in. and 4 in.).

The crystallization studies were carried out by combining a computer-controlled crystallization apparatus[14] (see Fig. 3) with the ultrasonic spectrometer. A computer interface was used to control the temperature in the crystallization vessel and also to log the data recorded by the turbidimetric probe, from which the onset of crystallization could be ascertained.

C. Ultrasonic spectral data reduction and analysis

The physical properties used for the crystals and the mother liquor to calculate the scattering coefficient are given in Tables I and II. While a number of the physical properties of urea and (L)-glutamic acid are orientation dependent within the crystal, an average value was estimated in order to meet the requirement of the ECAH model, which assumes isotropic behavior for the particle. Implicit in this is the assumption that a random set of particle orientations is present within the reaction vessel. Although all physical properties are temperature dependent, all physical properties used for the size analysis were those relating to the materials at room temperature. The exception to this was the ultrasonic attenu-

TABLE II. Physical properties of (L)-glutamic acid and a saturated aqueous solution of (L)-glutamic acid at 25 °C (and at T in °C for the acoustic attenuation of the mother liquor).

Property	Glutamic acid	Saturated solution of glutamic acid at 25 °C
Density	1.54×10^{3} kg m^{-3}	1.00×10^{3} kg m^{-3}
Sound speed	4.07×10^{3} m s^{-1}	1.48×10^{3} m s^{-1}
Thermal dilation	2.0×10^{-5} K^{-1}	2.6×10^{-4} K^{-1}
Thermal conductivity	4.22×10^{-1} J m^{-1} s^{-1} K^{-1}	5.9×10^{-1} J m^{-1} s^{-1} K^{-1}
Heat capacity	1.24×10^{3} J kg^{-1} K^{-1}	4.2×10^{3} J kg^{-1} K^{-1}
Viscosity		1.0×10^{-3} N s m^{-2}
Shear rigidity	8×10^{9} N m^{-2}	
Attenuation	4×10^{-4} dB m^{-1}	$(3.2\times10^{-1}-2.2\times10^{-5}\times T)\times f^{(-2.9\times10^{-3}\times T+2.0)}$ dB m^{-1} where T is in °C and f in MHz

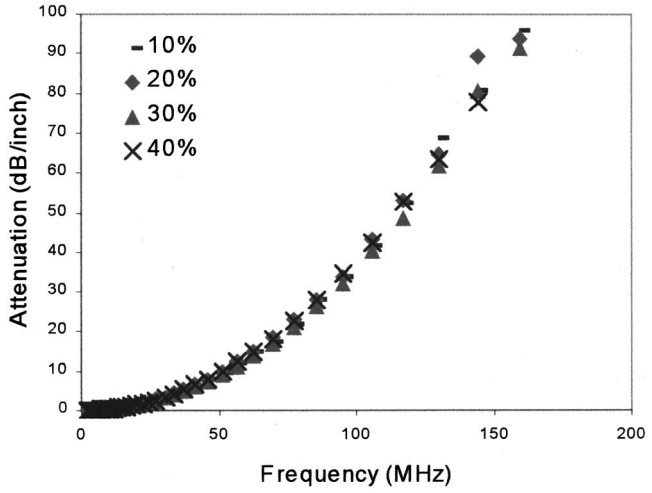

FIG. 4. Evolution of the attenuation spectra with concentration, in the concentration range 10–40 wt. %, for solutions of urea in water at 30 °C, showing the weak dependence of the attenuation spectrum of aqueous solutions of urea in water with the concentration of urea solute.

ation of the mother liquor, as its temperature dependence more strongly affects the results obtained for the acoustic attenuation of the suspension. Some of the physical properties of the organic crystal (*L*)-glutamic acid needed were not readily available, and thus had to be estimated using properties for related materials.

IV. RESULTS AND DISCUSSION

A. Crystallization of urea from aqueous solution

1. Preliminary measurements of undersaturated urea/water solutions

In crystallization experiments, several parameters are evolving:

- the crystal size;
- the particle concentration;
- the solute concentration in the liquid medium.

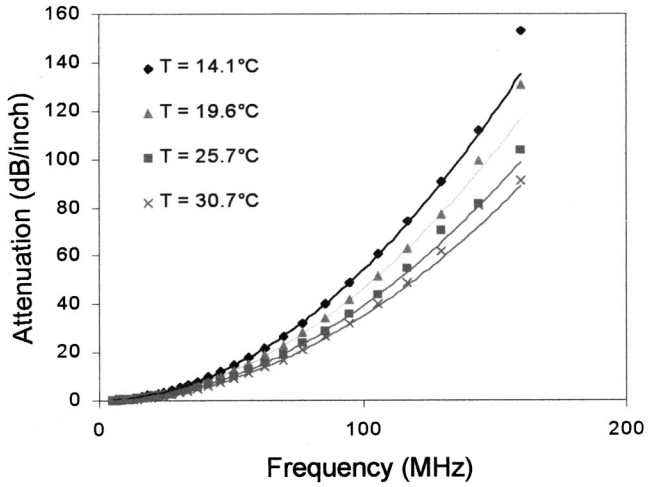

FIG. 5. Temperature dependence of the acoustic attenuation of an undersaturated solution of urea in water 30 wt. %, over the temperature range from 15–35 °C. All experimental data were fitted using a power law of the type $\alpha = a \times f^n$, using the least-squares method with all R^2 values=0.99.

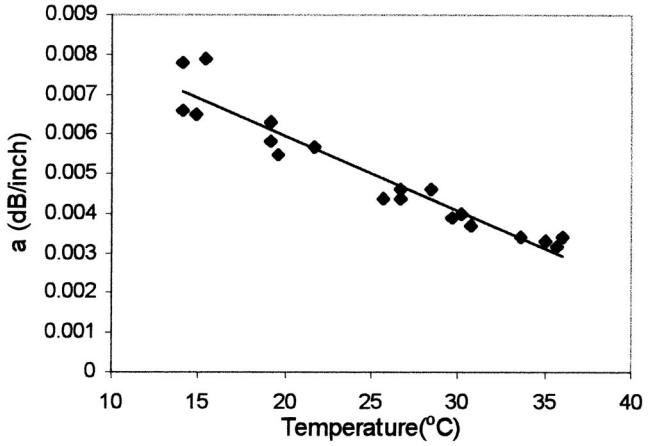

FIG. 6. Attenuation coefficient factor, *a*, for the attenuation spectrum of solutions of urea in water, measured at solute concentrations between 10 and 40 wt. % as a function of temperature. The experimental data were fitted using a linear law, using the least-squares method ($R^2 = 0.92$).

In addition, in the slow cooling crystallization process, the temperature is also allowed to vary. It is therefore necessary to know what effect all of these parameters have on acoustic attenuation, to determine those of interest, notably the CSD and the particle concentration. Thus a preliminary study was carried out, aimed to characterize the effects of changes in solute concentration and temperature on the acoustic attenuation through the liquid medium, alone. These experiments were carried out within the 2.8 liter measurement tank of the ultrasonic spectrometer, in order to study the influence of temperature and solute concentration on the attenuation by the liquid medium, for different concentrations below the level of supersaturation of urea in water. Attenuation by solutions of different concentrations of urea dissolved in water (10%, 20%, 30%, 40% mass concentration of urea dissolved in water) were measured over temperatures from 15 °C up to 35 °C. Two key conclusions can be retrieved from these experiments.

First, a weak dependence was found between the attenuation spectrum of the liquid medium and the concentration of

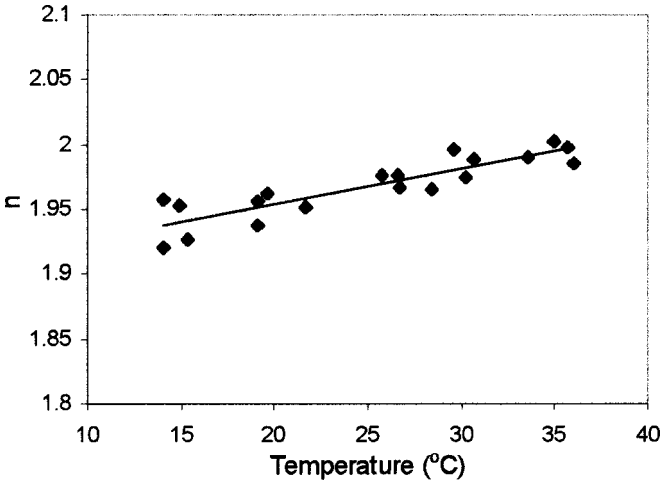

FIG. 7. Attenuation coefficient exponent *n* for the attenuation spectrum of solutions of urea in water, measured at solute concentrations between 10 and 40 wt. % as a function of temperature. The experimental data were fitted using a linear law, using the least-squares method ($R^2 = 0.79$).

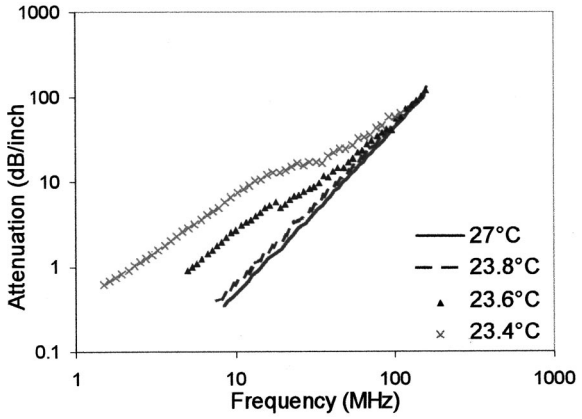

FIG. 8. Change in the acoustic attenuation spectra during the crystallization of urea in water by slow cooling of a saturated solution at 27 °C.

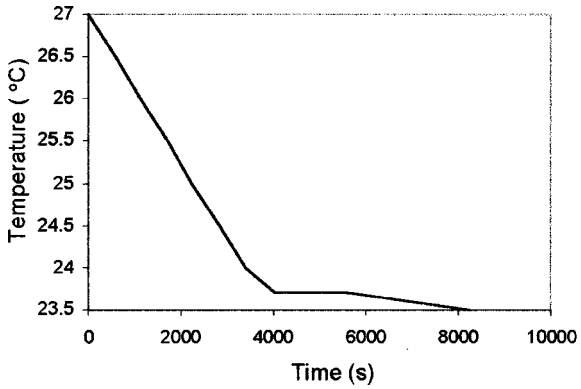

FIG. 9. Evolution of the temperature with time during the crystallization of urea in water by slow cooling of a solution saturated at 27 °C.

solute (urea). Figure 4 shows the attenuation spectra obtained at 30 °C for the four solutions at 10 to 40 wt. % of urea solute in water. The overlapping of the experimental data for the different solute concentrations was similarly found at other temperatures within the range 15–35 °C, and this suggests that the solute concentration dependence of the acoustic spectrum in the case of aqueous solutions of urea is within the error of the measurement. Experiments on other crystallizing systems suggest that this weak influence is particular to urea solutions and should not be generalized to other systems.

Second, it was found that the attenuation spectrum of the liquid medium was strongly dependent on the temperature for a given concentration. This means that, for the CSD analysis of a crystallization experiment, it is important to know how the attenuation spectrum of the liquid medium varies as a function of the temperature. The attenuation of any liquid can be presented as a function of the type:

$$\alpha = a \cdot f^n, \tag{5}$$

where α is the attenuation, a (attenuation coefficient factor) and n (attenuation coefficient exponent) are constant with respect to frequency. Figure 5 shows a series of acoustic spectra collected at various temperatures for an aqueous solution of urea at 30 wt. %. The curves were fitted with a power law ($\alpha = a \cdot f^n$) using the least-squares method, as were the curves obtained for solutions at concentrations of 10%, 20%, and 40%. The subsequent plotting of coefficients a and n as functions of temperature (Figs. 6 and 7, respectively) showed that a simple linear relationship in the temperature range 15–35 °C well described their dependence on temperature. The expression of the attenuation spectrum as a function of temperature is then derived:

$$\alpha = (-7.9\times10^{-3}\times T + 3.8\times10^{-1}) f^{(2.7\times10^{-3}T+1.9)}\ \mathrm{dB\,m^{-1}}, \tag{6}$$

where T is the temperature in °C, f is the frequency in MHz.

In practice, the change of attenuation due to the change in concentration during the crystallization process was disregarded, as it is negligible compared to the attenuation variation due to the change of temperature. The temperature dependence of the acoustic attenuation of the liquid medium was included in the calculation of the scattering coefficients matrix K (see Sec. II C) used for the deconvolution of the attenuation spectra.

2. Examination of the crystallization of urea

Crystallization of a saturated solution of urea in water at 27 °C was carried out by slow cooling at a rate of 0.05 °C/min within a measured metastable zone between 27 °C and 24 °C, and then keeping the solution at constant temperature (24 °C). The acoustic attenuation measurements were carried out using the complete range of frequencies available (1–150 MHz). Figure 8 shows the attenuation spectra obtained during crystallization by slow cooling (0.05 °C/min) of a solution of urea in water at 52 wt. % (see Table III). The corresponding cooling curve is given in Fig. 9. When a monomodal distribution was assumed to describe the CSD, the deconvolution procedure resulted in high residuals and overestimated the solid concentration compared to the concentration predicted on the basis of solubility data. A bimodal description of the distribution resulted in lower residuals. This is thought to be due to the habit of urea crystals (needles), for which a random distribution is best described

TABLE III. Analyses of the size of urea crystals for the crystallization from aqueous 52 wt.% solution by slow cooling.

T (°C)	Geometric mean 1 (μm)	Geometric deviation 2	Geometric mean 2 (μm)	Geometric deviation 2	Concentration (vol %)	Residual (%)
25	0.021	1.20			0.12	2.39
24	0.021	1.20			0.19	2.18
23.8	1.69	1.66	8.87	2.96	0.28	1.78
23.6	2.18	1.35	41.2	2.22	0.28	2.55

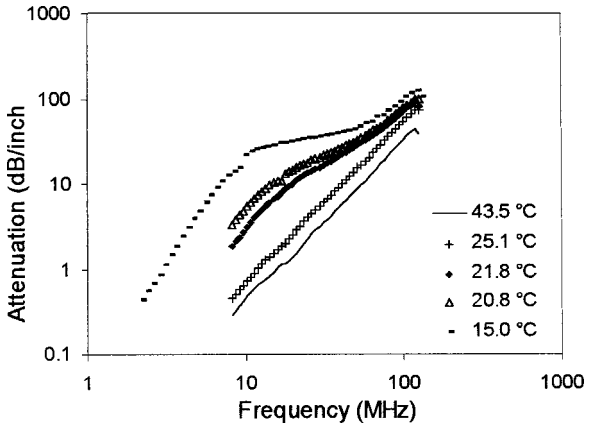

FIG. 10. Evolution of the acoustic spectra obtained during the crystallization of (*L*)-glutamic acid from aqueous solution, obtained by cooling at 0.4 °C.

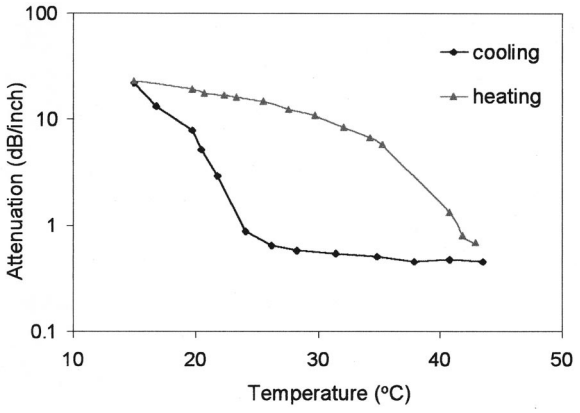

FIG. 12. Acoustic attenuation at 10 MHz measured during the crystallization of a solution of (*L*)-glutamic acid at 20 g/1000 g of water, at a linear cooling rate of 0.4 °C/min from 50 °C down to 15 °C.

as a mixture of particles whose size is distributed around the length and the width of the needles. The subsequent growth of urea crystals was difficult to follow due to the formation of a highly concentrated suspension of long needles. Although the width of the needles was within the size range of the instrument, the length of the needles, particularly toward the end of the crystallization process, was clearly beyond the capability of the instrument, with needles 3–4 mm long being formed.

B. Crystallization of (*L*)-glutamic acid from aqueous solution

Solutions at 20 g/1000 g of water (saturated solution at ~42 °C) were prepared. Crystallization experiments were carried out by linear cooling at 0.4 °C/min from 50 °C to 15 °C. The temperature was then kept constant at 15 °C until the acoustic attenuation spectra became constant. Under these conditions, (*L*)-glutamic acid crystallizes in its prismatic α-form with isometric dimensions. The temperature dependence of the acoustic attenuation spectrum of the liquid medium [saturated solution of (*L*)-glutamic acid in water at 42 °C] was estimated in a similar way as in the previous study for urea. Good quality ultrasonic data could be obtained during the whole crystallization process (see Fig. 10). The turbidity data measured during the crystallization of (*L*)-glutamic acid (Fig. 11) provided a measure of the on-set of crystallization which can, in turn, be compared to the attenuation measurements obtained at a single frequency (Fig. 12). These results show that the turbidity measurements detect the beginning of crystallization earlier than the ultrasonics measurements (~30 °C for the turbidity measurements, ~27 °C for the acoustic measurements). The evolution of the CSD and the solid concentration during the crystallization is presented in Fig. 13 and Table IV.

The two different CSD results obtained by data inversion of the acoustic spectrum at 24.1 °C (Table IV) is a typical example of the instability in the inversion procedure observed in the temperature range 27 °C–22 °C, which corresponds to the beginning of crystallization. Overestimation of the solid concentration is easily spotted, due to the disparity with subsequent attenuation spectra and analyses. The instability of the inversion procedure is thought to be due to the low particle concentration, calculated at 0.10 vol %, the minimum measurable volume concentration. However, the overestimation of the particle size and concentration in the early stage of crystallization could also originate from additional attenuation due to phase transitions, predicted by Akulichev and Bulanov[6] to be greatest for small particle sizes. The subsequent results were stable, and the CSD analysis obtained at 21.8 °C gives some indication of

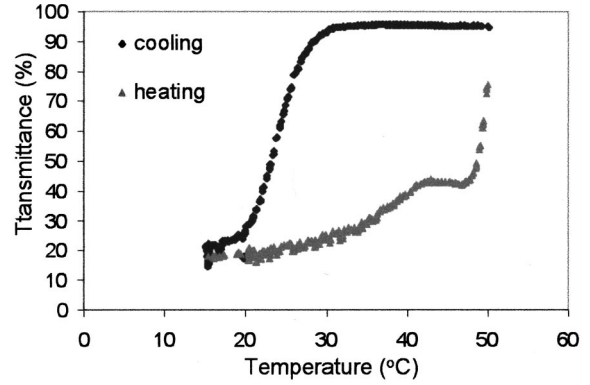

FIG. 11. Turbidity data obtained during the crystallization of a solution of (*L*)-glutamic acid at 20 g/1000 g of water, at a linear cooling rate of 0.4 °C/min from 50 °C down to 15 °C.

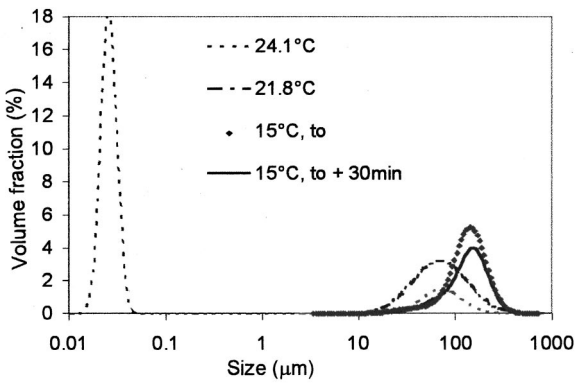

FIG. 13. Evolution of the CSD measured by ultrasonic spectroscopy during the crystallization of a solution of (*L*)-glutamic acid at 20 g/1000 g of water, at a linear cooling rate of 0.4 °C/min from 50 °C down to 15 °C.

TABLE IV. Evolution of the CSD and the concentration measured by ultrasonic spectroscopy during the crystallization of a solution of (*L*)-glutamic acid at 2 wt. % at a linear cooling rate of 0.4 °C/min from 50 °C down to 15 °C.

Temperature	24.1 °C		21.8 °C	15 °C, to	15 °C, to +15 min	15 °C, to +22 min	15 °C, to +30 min
Particle concentration (vol %)	0.10	0.59	0.18	0.79	0.80	0.81	0.81
D_{50} (μm)	0.023	0.104	64.51	126	127.5	128.3	130.8
Residual (%)	4.07	4.34	3.23	4.40	4.49	4.52	4.39
Log normal parameters							
Geo Mean (1) (μm)	0.022	0.104	64.5	51.49	60.91	68.72	75.66
Geo Deviation (1)	1.2	1.2	1.91	1.97	1.83	1.77	1.7
Proportion (1)%	83.1			12.79	17.21	20.26	30.43
Geo Mean (2) (μm)	62.07			133.1	137.5	139.6	149
Geo Deviation (2)	1.61			1.45	1.45	1.44	1.39
Proportion (2)%	16.91			87.21	82.79	79.74	69.57

the correct CSD in the range 27 °C–22 °C (as plotted in Fig. 13). After a period of 30 min at 15 °C following the end of the cooling period, the crystal size distribution stabilized to give the final distribution shown in Fig. 13. A plot of volume concentration and mean size against time (time $t=0$ taken at the beginning of the crystallization as detected by the turbidity probe), shown in Fig. 14, clearly shows the evolution of the crystallization process. In particular, it shows when it is completed, thus providing an obvious focus in terms of industrial applications in batch processing, for which a reduction in batch times is highly desirable. The micrograph presented in Fig. 15 was taken at the end of the crystallization, and it was clearly in agreement with the estimation of the size of the crystals obtained by ultrasonic measurement. The estimation of the final solid concentration is in agreement with that predicted by solubility data,[15] with a predicted solid concentration of 0.73 vol % at 15 °C at the end of the crystallization, without taking into account the partial evaporation of the solvent.

The results obtained with (*L*)-glutamic acid are very promising for the future of ultrasonic characterization of crystallization processes of organic crystals, and thus are of fundamental importance for the application of ultrasonic spectroscopy in the pharmaceutical and speciality chemicals industries.

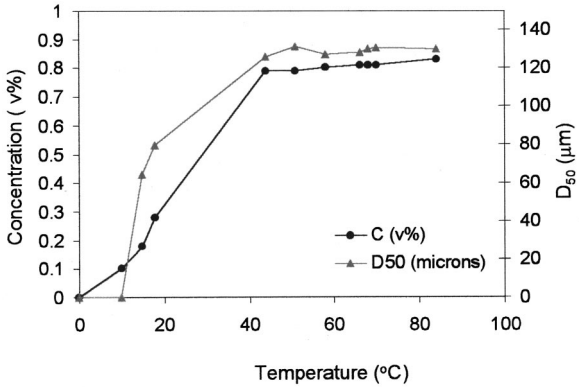

FIG. 14. Evolution of the particle concentration and the D_{50} of the size distribution during the crystallization of (*L*)-glutamic acid at 20 g/1000 g of water, at a linear cooling rate of 0.4 °C/min from 50 °C down to 15 °C.

V. CONCLUSIONS

Two examples of crystallization processes, in which attenuation measurements were carried out to characterize the evolution of the crystal growth, have been presented. Although the results obtained with urea were not conclusive in terms of estimation of particle size, it was shown with the study of the crystallization of (*L*)-glutamic acid that evolution of the CSD and the solid concentration in suspension could be effectively measured as soon as the solid concentration of the suspension reached the minimum measurable concentration of 0.1 vol %. Information on the particle size could advantageously be studied by photon correlation spectroscopy or laser diffraction in order to complete monitoring of the crystallization process at the early stage of nucleation/crystallization for concentrations lower than 0.1 vol %. It is important to note that although, from a conceptual point of view, the study of a dynamic process is different from that of a static system, as suggested by Bulanov and Akulichev,[6] it seems that in practice the CSD analysis obtained from attenuation measurements is clearly informative. For industrial applications in particular, rapid data acquisition on-line within the reactor is much more valuable than a downstream size analysis, as would be obtained from classifiers or from a sieve analysis of the product. The field of acoustic spectroscopy for on-line control is, therefore, clearly open; the next challenge is the modification of the instrumentation for routine on-line analysis of crystallization processes.

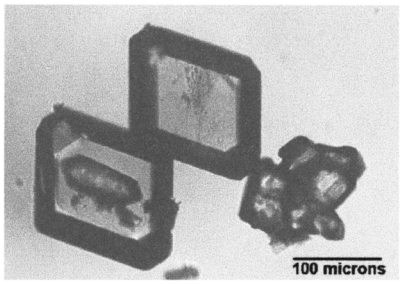

FIG. 15. Micrograph of crystal obtained at the end of the crystallization of a solution of (*L*)-glutamic acid at 20 g/1000 g of water, at a linear cooling rate of 0.4 °C/min from 50 °C down to 15 °C.

ACKNOWLEDGMENTS

This work has been carried out as part of the *Chemicals Behaving Badly* initiative, a collaborative project funded by EPSRC Grant No. GR/L/68797, together with industrial support from Astra, BASF, Glaxo-Wellcome, SmithKline Beecham, ICI, Malvern Instruments, Pfizer, and Zeneca. We gratefully acknowledge all members of this academic/industrial team for their contribution to the overall project.

[1] F. Alba, U.S. Patent 5,121,629 (1992).
[2] A. H. Harker and J. A. G. Temple, ''Velocity and attenuation of ultrasound in suspensions of particles in fluids,'' J. Phys. D **21**, 1576–1588 (1988).
[3] J. S. Tebbutt and R. E. Challis, ''Untrasonic wave propagation in colloidal suspensions and emulsions: a comparison of four models,'' Ultrasonics **34**, 363–368 (1996).
[4] P. S. Epstein and R. R. Carhart, ''The absorption of Sound in Suspensions and Emulsions I. Water Fog in Air,'' J. Acoust. Soc. Am. **25**, 553–565 (1953).
[5] J. R. Allegra and S. A. Hawley, ''Attenuation of Sound in Suspensions and Emulsions: Theory and Experiments,'' J. Acoust. Soc. Am. **51**, 1545–1564 (1972).
[6] V. A. Akulichev and V. N. Bulanov, ''Sound propagation in a crystallizing liquid,'' Sov. Phys. Acoust. **27**, 377–381 (1981).
[7] E. Dickinson, M. I. Goller, D. J. McClements, S. Peasgood, and M. Povey, ''Ultrasonic monitoring of crystallization in an oil-in-water emulsion,'' J. Chem. Soc., Faraday Trans. **86**, 1147–1148 (1990).
[8] E. Dickinson, F. J. Kruizenga, M. Povey, and M. Van der Molen, ''Crystallization in oil-in-water emulsions containing liquid and solid droplets,'' Colloids Surf., A **81**, 273–279 (1993).
[9] C. J. Kennedy, G. P. Archer, and M. Povey, ''Investigations of ice nucleation in water-in-oil emulsions using ultrasound velocity measurements,'' Cryo-Letters **17**, 391–396 (1996).
[10] V. J. Pinfield, ''Studies of creaming, flocculation and crystallisation in emulsions: computer modelling and analysis of ultrasound propagation,'' Ph.D. Thesis, Leeds University (1996).
[11] R. J. Urick, ''A sound velocity method for determining the compressibility of finely divided substances,'' J. Appl. Phys. **18**, 983–987 (1947).
[12] D. J. McClements, N. Herrmann, and Y. Hemar, ''Influence of flocculation on the ultrasonic properties of emulsions: theory,'' J. Phys. D **31**, 2950–2955 (1998).
[13] J. S. Tebbutt, T. Marshall, and R. E. Challis, ''Monitoring of copper (II) sulfate pentahydrate crystallization using ultrasound,'' Langmuir **15**, 3356–3364 (1999).
[14] A. R. Gerson, K. J. Roberts, and J. N. Sherwood, ''An instrument for the examination of nucleation from solution and its application to the study of precipitation from diesel fuels and solutions of n-alkanes,'' Powder Technol. **65**, 243–249 (1991).
[15] M. Kitamura, ''Polymorphism in the crystallization of L-glutamic acid,'' J. Cryst. Growth **96**, 541–546 (1989).

Data processing options and response scoring for OAE-based newborn hearing screening

Gabriella Tognola[a)]
CNR Centre of Biomedical Engineering and Department of Biomedical Engineering, Polytechnic of Milan, Piazza Leonardo da Vinci, 32, I-20133 Milan, Italy

Ferdinando Grandori and Paolo Ravazzani
CNR Centre of Biomedical Engineering, Polytechnic of Milan, Piazza Leonardo da Vinci, 32, I-20133 Milan, Italy

(Received 17 February 2000; revised 22 September 2000; accepted 26 September 2000)

Scoring of click-evoked otoacoustic emissions (CEOAEs) is typically achieved by the evaluation of the reproducibility of the whole emission and/or within narrow bands. Screening outcomes are influenced not only by the specific combination of the subdivision scheme (i.e., the number, position, and bandwidth of the narrow bands) and the threshold used to determine pass and refer, but also by the accuracy with which the reproducibility is estimated. This study was designed to examine what factors affect the accuracy of the reproducibility estimate and how the accuracy of the reproducibility estimate together with the choice of the subdivision scheme/thresholds affect CEOAE scoring. Simulations with real CEOAEs corrupted with synthesized noise indicated that the reproducibility estimate is influenced by time-windowing and band-pass filtering: the longer the time-window or the broader the bandwidth of the filter, the more accurate the estimate. Quantitative figures on numerical scoring were given in terms of the referral rate and were derived from CEOAEs recorded in a clinical environment from more than 3400 newborns. The narrow bands were extracted according to 12 different subdivision schemes covering the 1.5–4-kHz range. The referral rate was found to depend on the subdivision scheme being used: (i) the worst results were obtained considering four narrow bands at 1.6–2.4–3.2–4 kHz; (ii) the best results were obtained considering two narrow bands at 2.25 and 3.75 kHz; (iii) bandwidths greater than 1 kHz resulted in the lowest referral rates. Also, scoring based on the extraction of four narrow bands produced the most unstable results, i.e., a small change in the threshold might cause even a great change in the referral rate. [DOI: 10.1121/1.1326949]

PACS numbers: 43.64.Jb, 43.64.Yp [BLM]

I. INTRODUCTION

Click-evoked otoacoustic emissions (CEOAEs) are currently used in newborn hearing screening programs for the early identification of hearing impairment at birth, in order to effect appropriate intervention as early as possible. Screening of all newborns requires that babies with hearing impairments are identified rapidly and at minimal cost. CEOAEs have been shown to be a rapid, cost-effective means of quickly discharging all babies with normal auditory systems (NIH Consensus Statement, 1993). In keeping with its high sensitivity, however, the CEOAE lacks adequate specificity: it fails a relatively large number of babies whose hearing is, in fact, normal. It is for this reason that an auditory brainstem response (ABR) screen is typically performed on all babies who fail the CEOAE screen.

The literature on newborn hearing screening by means of OAEs presents various prevalence figures, yet gives little quantitative information on the procedure used to score the recordings (see, for example, White *et al.*, 1994; Maxon *et al.*, 1995; Finitzo *et al.*, 1998; McPherson *et al.*, 1998; Morlet *et al.*, 1998; Vohr *et al.*, 1998; Aidan *et al.*, 1999). Also, no consensus exists regarding the numerical criteria to be used when assessing OAE testing. On the other hand, it is well-known that screening outcomes may change even greatly depending on the decision rules separating passes from fails (Brass and Kemp, 1994; Brass *et al.*, 1994; Dirckx *et al.*, 1996; Smyth *et al.*, 1999), the acquisition procedure, and the analysis software (Vohr *et al.*, 1993; Tognola *et al.*, 1995; Maxon *et al.*, 1996; Ravazzani *et al.*, 1996; Vohr and Maxon, 1996; Ravazzani *et al.*, 1999; Tognola *et al.*, 1999).

Numerical scoring of CEOAEs is typically based on the evaluation of the reproducibility [or the signal-to-noise (S/N) ratio] of the compound emission and/or a number of narrow-band components approximately in the 1.5–4-kHz range. Scoring is influenced not only by the specific combination of the subdivision scheme (i.e., the number, position, and bandwidth of the narrow bands) and the threshold used to determine pass and refer, but also by the accuracy with which the reproducibility is estimated.

This study was designed to examine what factors affect the accuracy of the reproducibility estimate and how the accuracy of the reproducibility estimate together with the choice of the subdivision scheme/thresholds affect CEOAE scoring. Results are drawn from both simulated signals and from a population of 3415 babies bilaterally tested with CEOAEs prior to the discharge from the baby ward. The

a)Author to whom correspondence should be addressed; electronic mail: tognola@biomed.polimi.it

paper is organized as follows: Section II gives a brief description of the mathematical properties of the estimator of the reproducibility; Sec. III illustrates the material and the procedures used to the analyze the performance of the estimator of the reproducibility (Sec. III A) and OAE scoring under various testing conditions (Sec. III B); Sec. IV shows the results obtained from the simulations (Sec. IV A) and from real CEOAEs recorded with two different modalities—the ''Preset'' (Sec. IV B) and the ''QuickScreen'' mode (Sec. IV C); presented results are finally discussed in Sec. V.

II. MATHEMATICAL BACKGROUND

Numerical scoring of a CEOAE response is achieved by the evaluation of the test–retest reproducibility (or briefly, the reproducibility) between two replicate recordings of the whole response (''whole repro'') and/or selected frequency bands (''band repro''): high ''wave repro'' and ''band repro'' are associated with a ''good quality'' CEOAE.

From a mathematical point of view, the reproducibility is equal to the correlation coefficient (i.e., the zero-lag value of the cross-correlation function) expressed on a percentage base. The *cross-correlation function* for two random processes $x(t)$ and $y(t)$ is defined as

$$R_{xy}(t_1,t_2)=E[x(t_1)\cdot y(t_2)^*]$$
$$=\int_{-\infty}^{\infty} x\cdot y^*\cdot p(x,y;t_1,t_2)\,dx\,dy,$$

where the symbol * denotes complex conjugate, $E[x(t_1)\cdot y(t_2)^*]$ is the mean of $x(t_1)\cdot y(t_2)^*$, and $p(x,y;t_1,t_2)$ is the joint probability density of $x(t)$ and $y(t)$.

Two random processes $x(t)$ and $y(t)$ are called *wide-sense stationary* if their means are constant (i.e., $E[x(t)]=m$ and $E[y(t)]=n$) and their autocorrelation functions depend only on time difference, i.e., $R_{xx}(t_1,t_2)=R_{xx}(t_1-t_2)$ and $R_{yy}(t_1,t_2)=R_{yy}(t_1-t_2)$. If we introduce the lag variable τ and consider the time instants $t_1=t$ and $t_2=t-\tau$, then the above expressions become $R_{xx}(t,t-\tau)=R_{xx}(\tau)$ and $R_{yy}(t,t-\tau)=R_{yy}(\tau)$. Also, if the two processes $x(t)$ and $y(t)$ are wide-sense stationary, there follows that $R_{xy}(t,t-\tau)=R_{xy}(\tau)$, $R_{xx}(0)=E[x(t)^2]\geqslant 0$, $R_{yy}(0)=E[y(t)^2]\geqslant 0$, and $|R_{xy}(\tau)|\leqslant[R_{xx}(0)R_{yy}(0)]^{1/2}$ (McDonough and Whalen, 1995).

The *correlation coefficient* between two wide-sense stationary processes is defined as the normalized value of the cross-correlation function evaluated at zero-lag (i.e., for $\tau=0$),

$$r_{xy}=\frac{R_{xy}(0)}{[R_{xx}(0)\cdot R_{yy}(0)]^{1/2}}.$$

Since the processes $x(t)$ and $y(t)$ are known through their realizations $x(n)$ and $y(n)$ consisting of a finite sequence of N equispaced samples, the correlation coefficient can be *estimated* through this expression,

$$\hat{r}_{xy}=\frac{\Sigma_{n=1}^{N}[x(n)-\overline{x}][y(n)-\overline{y}]}{\sqrt{\Sigma_{n=1}^{N}[x(n)-\overline{x}]^2\Sigma_{n=1}^{N}[y(n)-\overline{y}]^2}},$$

where $\overline{x}$ and $\overline{y}$ are the sample means of $x(n)$ and $y(n)$. The estimate $\hat{r}_{xy}$ of the correlation coefficient is itself a random variable which has a probability density function (pdf) characterized by an expected value and a variance. Its performance in estimating the ''true'' correlation coefficient can be measured in terms of its bias and variance: the lower the bias and the variance, the better and more accurate the estimate. It can be demonstrated that $\hat{r}_{xy}$ is consistent, that is, the bias and the variance approach zero if $N\rightarrow\infty$ (Challis and Kitney, 1990).

III. MATERIAL AND METHODS

A. Estimation of the pdf of $\hat{r}_{xy}$

To provide quantitative figures on the performance of $\hat{r}_{xy}$, it is necessary to analyze what factors affect its pdf. The analytic derivation of the pdf of $\hat{r}_{xy}$ is very complicated, even for the case of well-behaved normally distributed signals [a brief discussion of this topic can be found in Hoel (1971), where expressions of the mean and variance of $\hat{r}_{xy}$ are given]. In this study, the pdf of $\hat{r}_{xy}$ was empirically derived by means of appropriate simulations to study the influence of the sample length N, the band-pass filtering, and S/N ratio.

For all simulations, ten real CEOAEs blurred into synthesized noise were considered. The ten real CEOAEs were selected among the best quality recordings having a ''whole-repro'' greater than 90% and were considered as the gold standards ($\text{CEOAE}_{\text{gold}}$). The ten $\text{CEOAEs}_{\text{gold}}$ were scaled to have all the same root-mean-square (rms) value.

The choice of the noise being used in the simulations deserves some comments. In a real CEOAE measurement the noise will probably not have a Gaussian distribution. First, the OAE measurement equipment filters the microphone signal from about 0.6 to 6 kHz. Second, most noise is generated by the test subject and has very strong low-frequency components. Third, the noise is not stationary and may contain very large transient components due to subject movements or vocalizations, or due to events occurring in the vicinity of testing. The most intense components will be rejected during acquisition but there will be less intense components that are not rejected. These features mean that the noise differs from Gaussian noise in terms of its spectrum, intensity distribution, and stationarity.

To obtain a realistic noise, representative samples of the noise were derived from a subset of 2000 newborn CEOAEs randomly chosen from all the CEOAEs analyzed in this study (i.e., more than 6800 traces). For each of the 2000 CEOAEs, the temporal waveform of the noise was off-line estimated as $(A-B)/\sqrt{2}$, where A and B are the two replicate CEOAE recordings acquired from each ear during a given test session. This calculation of noise starts from the assumption that each replicate recording is made by a signal originating from the cochlea, identical in both replicates, plus a noise of equal amplitude in both replicates (Kemp and Ryan, 1993). The 2000 representative samples of noise thus obtained were normalized to have the same rms value and stored into two separate buffers (N_A and N_B) of 1000 noisy traces each. The buffers N_A and N_B were added separately to

each $CEOAE_{gold}$, thus obtaining 1000 pairs of noisy CEOAEs for each $CEOAE_{gold}$. All signals considered in the simulations were sampled at 25 kHz and had a total length of 512 sampled points (i.e., 20.44 ms).

(a) Influence of the sample length N of the two processes $x(n)$ and $y(n)$. To analyze the influence of the sample length N, the 1000 pairs of noisy CEOAEs were windowed with time-windows of variable duration ranging from 2 to 16 ms, step 2 ms, which correspond to time-windows of variable length N ranging from 50 to 400 points, step 50 points. All the time-windows were centered around 10.5 ms. For a given value of N (i.e., for a given duration of the time-window), $\hat{r}_{xy}$ was calculated for all the 1000 pairs of noisy CEOAEs, thus obtaining a distribution of the values of $\hat{r}_{xy}$ over the 1000 pairs of noisy CEOAEs. The mean and variance of this distribution were derived and plotted as a function of N. Finally, the overall procedure was repeated for all ten $CEOAEs_{gold}$ considered here.

(b) Influence of band-pass filtering. Since the identification of a CEOAE response is achieved by the evaluation of the reproducibility in band-pass filtered components, it is interesting to examine the influence of band-pass filtering on the estimation of $\hat{r}_{xy}$. For this purpose, the 1000 pairs of noisy CEOAEs were band-pass filtered. The bandwidth of the filters was varied from 0.5 to 3 kHz, step 0.5 kHz. All the filters were centered around 3 kHz. For each value of the bandwidth, the distribution of the values of $\hat{r}_{xy}$ from all the 1000 pairs of noisy CEOAEs was obtained. The mean and variance of this distribution were derived and plotted as a function of the bandwidth. Finally, the overall procedure was repeated for all ten $CEOAE_{gold}$ considered here.

(c) Influence of the S/N ratio of the two signals $x(n)$ and $y(n)$. In the particular case of OAEs, the two signals $x(n)$ and $y(n)$ can be modeled as produced by a zero-mean deterministic component z (the same in both replicates) with variance σ_z^2 blurred into a zero-mean incorrelated random noise with variance σ_e^2, that is, $x(n)=z(n)+e_1(n)$ and $y(n)=z(n)+e_2(n)$.

Under such assumptions, it can be easily demonstrated that

$$\hat{r}_{xy}=\frac{\sigma_z^2}{\sigma_z^2+\sigma_e^2}=\frac{1}{1+\sigma_e^2/\sigma_z^2}.$$

This means that the correlation coefficient is a measure of the S/N ratio (σ_z^2 and σ_e^2 are the energy of the deterministic component—the ''true'' signal—and of the noise, respectively).

To examine the influence of the S/N ratio on the pdf of $\hat{r}_{xy}$, the noise traces in the two buffers N_A and N_B were multiplied by a scale factor of varying magnitude in order to obtain noisy CEOAEs whose S/N ratios ranged from 0 to 9 dB (step 1 dB). Similarly to the simulations presented before, at each value of the S/N ratio, the distribution of the values of $\hat{r}_{xy}$ from all 1000 pairs of noisy CEOAEs was obtained and used to derive the mean and variance of the pdf as a function of the S/N ratio. The overall procedure was then repeated for each $CEOAE_{gold}$.

B. Examination of the effects of signal processing on CEOAE scoring

1. Subjects

CEOAEs were measured during a hospital-based universal hearing screening program (the Milan Screening Program) carried out at the Neurophysiopathology Unit of the Mangiagalli Clinic in Milan (Sergi *et al.*, 2000). The Milan Screening Program consists of three stages: an initial inpatient CEOAE test where babies who failed are retested as many times as possible before discharge to reduce the number of outpatient screening and to limit the stress for families, a second outpatient CEOAE test at 15–30 days for all babies who did not pass the first stage, and a diagnostic ABR (third stage) in case of failure at the second stage. CEOAEs analyzed in this study were only those measured in the first of the three stages of the screening program. Because of the inpatient retesting procedure being implemented in the first screening stage, more than one CEOAE may be available for a given ear. In such cases, the CEOAE showing the highest whole repro was selected for the inclusion in the study material, whereas all the other duplicates were discarded.

2910 well-babies and 505 newborns coming from the Newborn Pathology Unit NPU (i.e., babies presenting morphological abnormalities, small birth weight for gestational age, hyperbilirubinemia, gestational age <37 weeks, chromosomal abnormalities, congenital infection, cardiorespiratory depression, cardiovascular and metabolic abnormalities) were considered. All babies were tested by CEOAEs between 36 and 48 hrs (or between 3 and 5 days for Caesarean section). CEOAEs coming from NPU babies were analyzed separately from the well-babies because they are typically noisier (due to the increase of endogenous noise related, for example, to a greater susceptibility of the newborn and to swallowing, snoring) and may present a different pattern.

All CEOAEs considered in this study were checked to have a stimulus stability greater than 75%, a noise level lower than 50 dB, and a stimulus dB peak (which is the intensity of the largest stimulus peak measured in the ear canal at the probe microphone) ranging from 77 to 83 dB peak. It is noted that the stimulus dB peak may differ radically from that reaching the tympanic membrane due to standing waves in the ear canal. Standing waves affect high frequencies particularly and the stimulus peak level is sensitive to high-frequency content.

2. Instrumentation

CEOAEs were recorded bilaterally using an Otodynamic ILO system, software version 5; emissions were processed and recorded according to the default settings of ILO. Clicks were presented according to the ''nonlinear'' acquisition mode (Kemp and Ryan, 1993), which employs a train of three clicks followed by a fourth click of inverse polarity and three times greater. For each trial, 260 repetitions of the click-train (4 clicks per train) were averaged into each of two

TABLE I. Summary of babies considered in this study. The ''Preset'' and the ''QuickScreen'' mode of acquisition of ILO were used.

	Preset	QuickScreen
Well-babies	1586	1324
NPU	368	137

separate buffers (A and B replicate recordings in the ILO equipment). Both the ''Preset'' and the ''QuickScreen'' acquisition mode, which employs a sweep time of 12.5 ms instead of 20 ms of the ''Preset'' mode and a higher stimulus rate, were used (see Table I for a summary of the babies analyzed in this study). Further technical details on the ILO device can be found in Bray and Kemp (1987) and in Kemp and Ryan (1993).

3. Effects of off-line processing on CEOAE scoring

CEOAE scoring is greatly influenced by the number and position of the test frequencies into which the compound emission is decomposed, their bandwidths, and the value of the thresholds for the reproducibility of the compound emission and its test frequencies. Among all the possible combinations of these factors, attention was focused on the effects of the number, central frequencies, and bandwidth of the test frequencies. A finite number of frequency settings (Table II), which entirely covered the most characteristic frequency range of newborn CEOAEs (i.e., 1.5–4 kHz) were considered. Two out of the 12 frequency combinations analyzed here were the same as used by default by ILO, specifically the subdivision into 1-kHz-wide bands centered at 2, 3, 4 kHz (''Preset'' mode) and into 0.8-kHz-wide bands centered at 1.6, 2.4, 3.2, and 4 kHz (''QuickScreen'' mode). Both nonoverlapping and partially overlapping frequency bands were taken into consideration.

CEOAEs were off-line band-pass filtered according to each of the 12 frequency combinations of Table II and numerically scored. According to the common and well-established clinical practice, a CEOAE was considered as a ''pass'' when the ''band-repro'' values of all the considered narrow-band components were greater than a threshold value and ''fail'' in all other cases. To limit the number of examined situations without losing in completeness, the band-repro thresholds were set at a same identical value for all

TABLE II. Bandwidths (kHz) considered for each of the four frequency subdivision schemes (A through D) used in the examination of decision rules. A: central frequencies at 1.6, 2.4, 3.2, 4 kHz; B: 2, 3, 4 kHz; C: 2.25, 3.75 kHz; D: 2, 4 kHz. A total number of 12 frequency combinations (3 different bandwidths×4 frequency subdivision schemes) were considered. In each of the four frequency subdivision schemes, bandwidths were selected in order to have narrow bands that do not overlap at all or have a partial overlap of about 250 and 500 Hz.

Frequency subdivision scheme			
A	*B*	*C*	*D*
0.8[a]	1[b]	1.5	2
1	1.25	1.75	2.25
1.2	1.5	2	3

[a]Default setting of ILO ''QuickScreen'' mode.
[b]Default setting of ILO ''Preset'' mode.

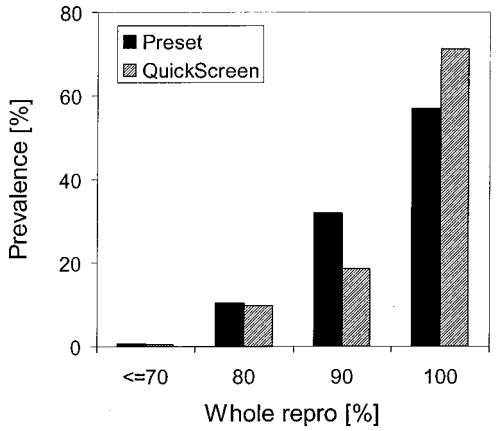

FIG. 1. Distributions of ''whole repro'' values for CEOAEs recorded with the ''Preset'' and ''QuickScreen'' mode from the newborns considered in this study. ''Preset'': 1943 babies (1583 well-babies+360 NPU babies); ''QuickScreen'': 1461 babies (1324 well-babies+137 NPU babies). All babies were tested bilaterally.

frequency bands considered at a given frequency setting. Results will be expressed in term of the referral rate, i.e., the percentage of babies that would need to be referred to a further CEOAE evaluation because of a ''fail'' CEOAE in one or both ears.

As shown in Fig. 1, in almost more than 99% of the babies analyzed in this study, the ''whole repro'' was found to be quite high and markedly well above 70%. This particular distribution of ''whole repro'' was due to the initial choice to include into the test material only those CEOAEs with the best ''whole repro'' among all the duplicate recordings available for a given ear (see Sec. III B 1). Because of this particular distribution, the ''whole repro'' does not represent a significant parameter to be analyzed in this study material.

IV. RESULTS

A. Factors affecting the pdf of $\hat{r}_{xy}$

Figure 2 shows the variance of the pdf of $\hat{r}_{xy}$ as a function of the sample length N, the bandwidth of the band-pass filter used to decompose the tested signal into narrow bands, and the S/N ratio. In all simulations, the pdf of $\hat{r}_{xy}$ presented no bias (its expected value was equal to zero) and had a finite variance. The variance was inversely proportional to N, thus meaning that the longer the sequence length the more accurate is the estimate of $\hat{r}_{xy}$. For $N \rightarrow \infty$ the variance of the pdf tends to zero. A similar trend was observed between the bandwidth and the variance of the pdf: the wider the bandwidth the better is the estimate of $\hat{r}_{xy}$. In this latter case, it is observed that the variance decreases rapidly for bandwidths smaller than some 1–1.5 kHz and tends to reach a plateau for bandwidths greater than 1–1.5 kHz. Results from these simulations revealed that windowing in the *time* and *frequency* domains produces similar effects on the variance of the pdf. Panel (c) of Fig. 2 illustrates the variance as a function of the S/N ratio. As in the two previous simulations, the variance progressively decreases for increasing S/N ratio, thus meaning that the accuracy in the estimation of reproducibility tends to decrease with bad quality CEOAEs.

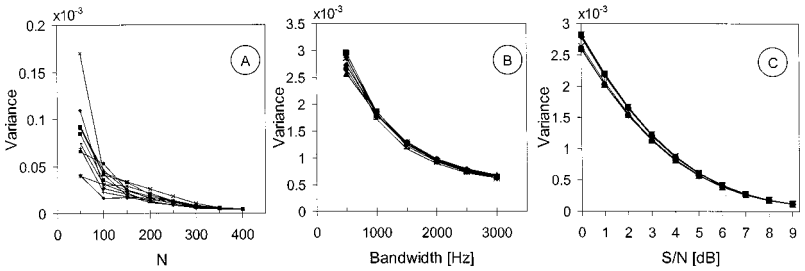

FIG. 2. Estimated variance of the pdf of $\hat{r}_{xy}$ as a function (a) of the sample length N, (b) the bandwidth (Hz) of the band-pass filters, and (c) the S/N ratio (dB). Data were calculated from 1000 pairs of noisy CEOAEs obtained by the summation of a real, good-quality CEOAE ($CEOAE_{gold}$) with 1000 pairs of representative samples of noise (see the text for details on the simulations). Results were obtained considering ten different $CEOAEs_{gold}$ and are shown superimposed on each panel.

B. Results from ''Preset'' CEOAEs

This section illustrates the effects of the frequency subdivision scheme, bandwidth, and threshold on scoring of CEOAEs recorded with the ''Preset'' mode from well-babies and NPU babies.

Figure 3, panels (a) and (c), show the referral rate as a function of the ''band-repro'' threshold for CEOAEs recorded with the ''Preset'' mode for both well-babies [panel (a)] and NPU babies [panel (c)]. Results were obtained by considering a ''band-repro'' threshold ranging from 50 to 100%. ''Band-repro'' values were calculated from band-pass filtered components extracted from the compound CEOAE. The central frequencies of the filters were set according to each of the four frequency subdivision schemes shown at the inset, whereas the bandwidths were chosen to obtain consecutive, nonoverlapping frequency components.

For both well-babies and NPU babies, the referral rate curves exhibit a very specific pattern consisting of an initial plateau (where the referral rate remains almost constant), a knee point, and a steep increase for ''band-repro'' thresholds higher than the threshold value at the knee point. The referral rates obtained evaluating the ''band-repro'' values of components centered at 1.6, 2.4, 3.2, and 4 kHz are higher than in all the other frequency subdivision schemes; the best performance is achieved with the frequency subdivision scheme 2.25–3.75 kHz. The referral rate in NPU babies is markedly higher than that obtained in well-babies, regardless of the frequency subdivision scheme and the threshold used.

Also, results obtained with the frequency subdivision scheme at 1.6-2.4-3.2-4 kHz are fairly unstable because even a small change in the numerical value of the ''band-repro'' threshold may produce a substantial change in the referral rate.

Figure 4 depicts the referral rate as a function of the bandwidth of the components extracted according to the four frequency subdivision schemes shown in the legend, for well- and NPU babies. Here, to reduce the number of varying parameters, the ''band-repro'' threshold was fixed at 60%, which corresponds to the value of the ''band-repro'' threshold at the knee points of Fig. 3. As illustrated in Fig. 4, left panel, for all the frequency subdivision schemes (with some few exceptions for NPU babies), the referral rate decreases by increasing the bandwidth of the components. The referral rate at the frequency subdivision scheme 1.6-2.4-3.2-4 kHz is greater than that obtained at the other three subdivision schemes, regardless of the bandwidth and the tested population. The referral rate obtained for the NPU babies is much greater than that observed in the well-baby population.

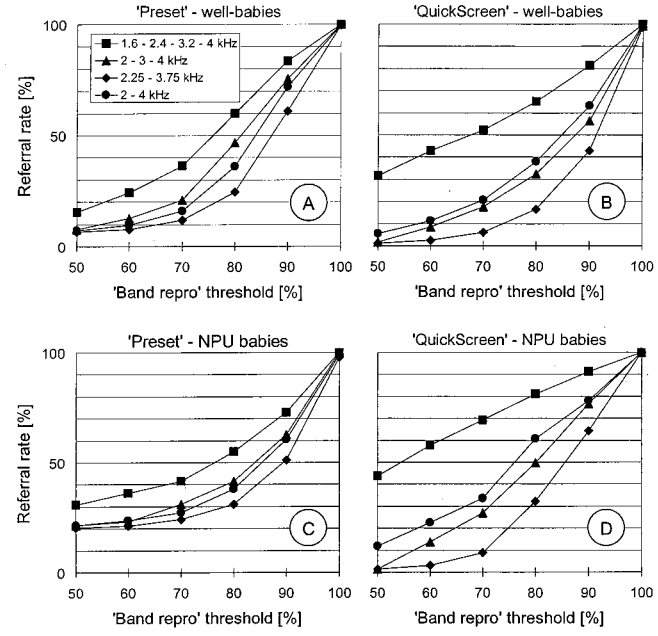

FIG. 3. Referral rate as a function of the ''band-repro'' threshold for the four frequency subdivision schemes shown in the inset. Data in panels (a) and (c) were derived from CEOAEs recorded with the ''Preset'' mode from 1586 well-babies and 368 NPU babies, whereas data in panels (b) and (d) were derived from ''QuickScreen'' CEOAEs from 1384 well-babies and 137 NPU babies. The ''band-repro'' threshold was set to the same identical value for all frequency bands considered at a given frequency subdivision scheme.

C. Results from ''QuickScreen'' CEOAEs

The referral rate as a function of the ''band-repro'' threshold for CEOAEs recorded with the ''QuickScreen'' has a similar trend as previously observed in ''Preset'' CEOAEs. Panels (b) and (d) of Fig. 3 show the referral rate as a function of the ''band-repro'' threshold for well-babies and NPU babies. As for ''Preset'' CEOAEs, the worst performance is obtained with the frequency subdivision scheme at 1.6–2.4–3.2–4 kHz: for this frequency scheme, the referral rate is found to be almost linearly related to the threshold, thus indicating that this scheme produced very unstable results, even more unstable than in ''Preset'' CEOAEs.

Figure 4, right panel, illustrates the referral rate as a function of the bandwidth for CEOAEs recorded with the ''QuickScreen'' mode. It should be noted that the increase in the bandwidth does not always produce a reduction in the referral rate, as observed in ''Preset'' CEOAEs. Also, for all the frequency subdivision schemes, but the 1.6–2.4–3.2–4 kHz, the use of the ''QuickScreen'' seems to yield to a re-

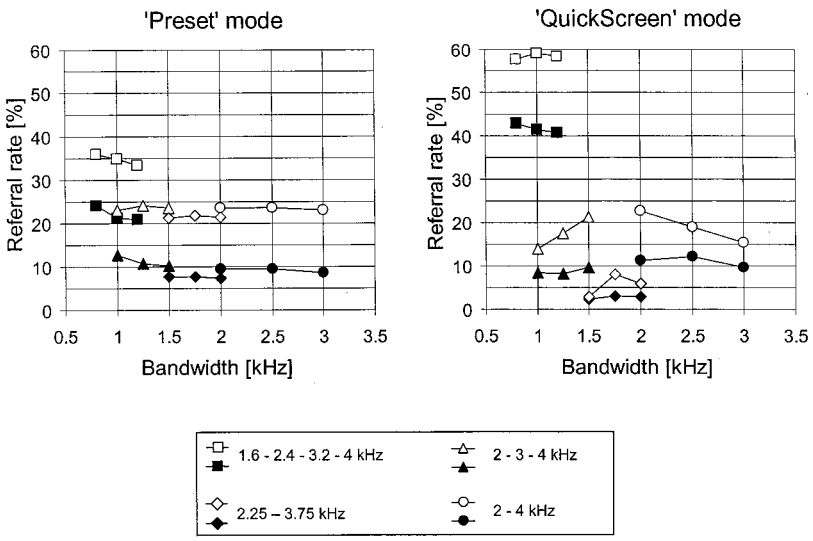

FIG. 4. Referral rate as a function of the bandwidth (kHz) of the components considered in the four frequency subdivision schemes shown in the inset. All the data were calculated by using a ''band-repro'' threshold of 60%. Results are derived from CEOAEs recorded with the ''Preset'' mode from 1586 well-babies (left panel, closed symbols) and 368 NPU babies (left panel, open symbols) and with the ''QuickScreen'' mode from 1324 well-babies (right panel, closed symbols) and 137 NPU babies (right panel, open symbols).

ferral rate better than that obtained with the ''Preset'' mode, especially in NPU babies. However, this last result must be regarded with some caution because babies tested with the ''Preset'' mode were different from those tested with the ''QuickScreen'' and the number of babies tested in the two conditions was different.

V. DISCUSSION

CEOAEs are widely used in clinical practice to assess the integrity of the outer hair cells, especially in newborn hearing screening programs; their accuracy to detect hearing damages is now well recognized (NIH Consensus Statement, 1993; White *et al.*, 1994; Maxon *et al.*, 1995; Finitzo *et al.*, 1998; McPherson *et al.*, 1998; Morlet *et al.*, 1998; Vohr *et al.*, 1998; Aidan *et al.*, 1999; Grandori and Lutman, 1999). Nevertheless, some aspects related to the influence that the acquisition procedure, the analysis software, and decision rules have on the scoring still need to be thoroughly investigated. Also, no consensus exists regarding the numerical criteria to be used to score OAE responses in a screen test.

Numerical scoring of CEOAEs is typically achieved by the evaluation of a number of quantitative parameters related to the reproducibility of the whole emission and of proper frequency bands. Therefore, screening outcomes are influenced not only by the specific combination of frequency bands/thresholds but also by the accuracy with which the reproducibility is estimated. Since the reproducibility is computed from a number of sampled realizations of the stochastic process underlying the generation of a CEOAE response, its estimate is affected by errors related to several factors, such as the length of the sampled realizations, the level of noise (or equivalently, the S/N ratio) in the recordings, and the bandwidth of the filters used to decompose the compound signal into narrow bands.

The simulations illustrated in this study show that the greater the number of sampled data points, the higher the S/N ratio, and the broader the bandwidth, the more accurate is the estimate of the reproducibility. There is a trade-off between the accuracy of the reproducibility estimate and the frequency-specific analysis of CEOAEs: to achieve a good accuracy of the reproducibility estimate the bandwidth should be as wide as possible, whereas to produce a frequency-specific analysis of CEOAEs the bandwidth of the tested components should be as narrow as possible. In particular, a bandwidth of 1 or 1.5 kHz seems to be a wise compromise between the accuracy of the estimate and the frequency-specific analysis of CEOAEs. For bandwidths narrower than 1–1.5 kHz, the error in the estimated reproducibility may be relevant.

Narrow bandwidths can lead to imprecise results due to the intrinsic distribution of frequencies in CEOAEs. As a matter of fact, CEOAE frequency spectra of normal hearing subjects are typically characterized by a series of peaks and troughs, i.e., CEOAE frequency components are not uniformly distributed and have different strengths (Kemp, 1978; Grandori *et al.*, 1990). Although the residual noise is not equal across frequency, its spectrum is almost smooth compared to the CEOAE. It follows that the S/N ratio can vary from one frequency to another. The use of too narrow bandwidths implies that the reproducibility is computed on small sections of the frequency spectra where the S/N ratio may be low, thus leading to imprecise estimates of the reproducibility.

As expected, results of this study confirmed that numerical scoring of CEOAEs is influenced by the number, the central frequency, and the bandwidth of the narrow-band components extracted from the CEOAEs being used to determine pass and refer. In this study, real CEOAEs recorded in clinical environments from more than 3400 newborns were decomposed into narrow bands according to four different frequency subdivision schemes, two of which were the same as performed by default by the ILO device. The number of components in each frequency subdivision scheme varied from a minimum of two to a maximum of four. For each frequency subdivision scheme, three different values of the bandwidth were considered. Finally, CEOAEs were numerically scored considering the 4×3 different combinations of frequency schemes and bandwidths and results were expressed in terms of the referral rate.

The most unstable and worst results were obtained when

considering the frequency subdivision scheme 1.6–2.4–3.2–4 kHz, irrespective of the thresholds separating passes from fails and the bandwidths of the extracted components. The referral rate obtained with this scheme is almost linearly related to the ''band-repro'' threshold, thus meaning that even a small change in the threshold may produce a significant change in the referral rate. For the other subdivision schemes (i.e., those with two or three test frequencies), the referral rate is more stable, remains constant for ''band-repro'' thresholds up to 60%–70%, and then increases rapidly for greater values of the threshold. The best performance is observed with the subdivision scheme using two test frequencies at 2.25 and 3.75 kHz.

The worst performance of the frequency subdivision scheme 1.6–2.4–3.2–4 kHz, mostly evident for CEOAEs recorded with the ''QuickScreen'' mode and for NPU babies, is in agreement with the simulations discussed above: the greater the number of test frequencies, the narrower the bandwidth (to assure a proper frequency specificity) and the greater the probability to obtain a ''false alarm'' due to a raw estimate of the reproducibility. Also, the choice of the number of the tested frequencies must take into account that CEOAEs exhibit a great intersubject variability (both for waveform and frequency content) and, only on average, they are present in the 1.5–4-kHz range (Bonfils *et al.*, 1988; Grandori *et al.*, 1990; Martin *et al.*, 1990; Tognola *et al.*, 1997). This mean that, a given subject, although normal, may be characterized by lack of CEOAE components in small portions of the 1.5–4-kHz range, or, in other words, the more the tested frequencies included in the evaluation, the more difficult to pass the test.

Also, the subdivision scheme using four test frequencies includes a frequency at 1.6 kHz, which is typically contaminated by the residual low-frequency noise. Results (not reported in this paper) indicate that using at 1.6 kHz a threshold lower than for the other frequencies would improve the results, although the referral rate would remain remarkably higher than for the other subdivision schemes.

Results of this study seem to indicate that the choice of the acquisition procedure (i.e., the ''Preset'' mode as opposed to the ''QuickScreen'' mode) may influence the referral rate, especially in NPU babies. As a matter of fact, CEOAEs recorded with the ''QuickScreen'' were characterized by the lowest referral rate at all frequency subdivision schemes but at 1.6–2.4–3.2–4 kHz, for both well-babies and NPU babies. Shortening the sweep time from 20 to 12.5 ms, as in the ''QuickScreen'' mode, results in decreasing the influence of noise, especially for low-frequency components (Kemp and Ryan, 1993; Tognola *et al.*, 1999). As a result, this procedure may lead to the reduction of rejected points, testing time, and fail rate (Kemp and Ryan, 1993).

It is to be noted that, although the reproducibility increases with the ''QuickScreen,'' this is at the expense of reduced degrees of freedom for the noise estimation. When the noise contains strong low-frequency components and is nonstationary (as in the case of CEOAEs), the reduction in degrees of freedom may lead to large errors. This can cause a lack of sensitivity of the test. As this study was unable to assess sensitivity and the number of babies tested with the ''QuickScreen'' was very small, the results shown here must be regarded with some caution and need more exhaustive investigations to be statistically significant.

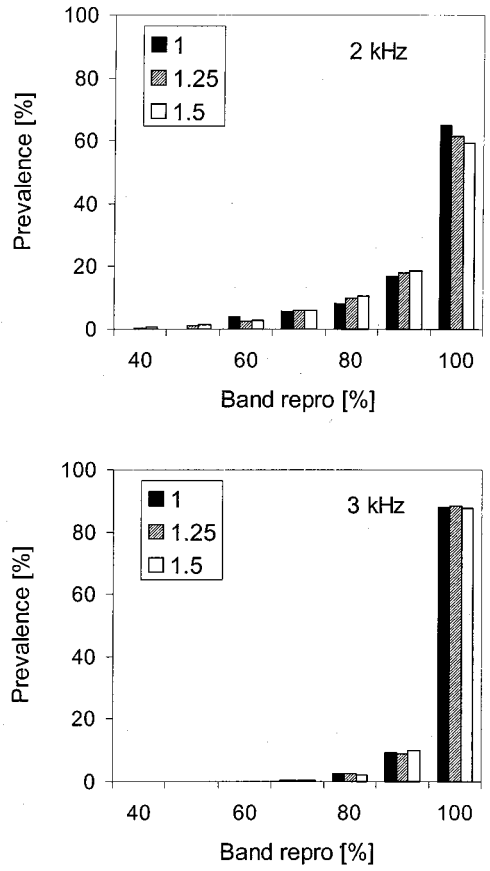

FIG. 5. Distributions of ''band-repro'' values of the components at 2 and 3 kHz for CEOAEs recorded with the ''QuickScreen'' mode (1324 well-babies+137 NPU babies). All babies were tested bilaterally. For both the components, the ''band repro'' was computed at different values of the bandwidth (in kHz), as indicated in the inset. Results obtained for the component at 4 kHz (not plotted here) were the same as for the 3-kHz component.

Generally, for CEOAEs recorded with the ''Preset'' mode the increase in the bandwidth of the tested components produces a decrease in the referral rate, especially for the subdivision scheme using four components, where the referral rate decreases from 24% to 21% for well-babies and from 36% to 33% for NPU babies. This is in agreement with data reported by Gorga *et al.* (1993), in which they showed better test performance for CEOAEs analyzed into octave bands compared to the same CEOAEs analyzed into 1/3 octave bands.

On the contrary, for emissions recorded with the ''QuickScreen'' mode, the increase in the bandwidth is often associated with an increase in the referral rate. This was mainly due to the decrease of the reproducibility at the lowest frequency bands when broader bandwidths are used. As illustrated, for example, in Fig. 5 for the components at 2 and 3 kHz, the increase in the bandwidth produces a slight but significant decrease of the reproducibility of the lowest frequency component (2 kHz), whereas for the highest component the reproducibility does not change with the bandwidth. This behavior is most probably a direct consequence of the

reduction of the sweep time from 20 to 12.5 ms performed by the ''QuickScreen.'' As described by Tognola *et al.* (1999), shortening the acquisition time-window produces an improvement of the reproducibility of the mid-to-high frequencies (i.e., the components that reached the maximal amplitude well before 12.5 ms), whereas at low frequencies this procedure may introduce no changes or even a slight decrease of the reproducibility.

The refinement of the acquisition parameters is still under investigation. In a series of simulations, Brass and Kemp (1994) found that in the objective CEOAE assessment (based on the S/N ratio of a time-limited and band-limited section of the response) time-windowing between 4 and 10 ms and filtering the response between 1.5 and 2.8 kHz performed well in comparison to the ''Preset.'' As a result, another screening device by Otodynamics—the ''Echosensor''—uses a 4–10-ms window and a band-pass filter 1.6–2.8 kHz. Tests of this device indicate that the ''Echosensor'' has a greater efficiency than the ''QuickScreen'' and the ''Preset'' (Brass *et al.*, 1994; Maxon *et al.*, 1996).

ACKNOWLEDGMENTS

CEOAEs were kindly provided by Dr. Giancarlo Pastorino and Dr. Paola Sergi from the Neurophysiopathology Unit, ICP, Milan, Italy. Dr. M. E. Lutman and an anonymous reviewer are gratefully acknowledged for their constructive and stimulating suggestions during the preparation of this article. This study was partially supported by the EC Project AHEAD (Contract No. QLRT-2000-01613).

Aidan, D., Avan, P., and Bonfils, P. (**1999**). ''Auditory screening in neonates by means of transient evoked otoacoustic emissions: A report of 2,842 recordings,'' Ann. Otol. Rhinol. Laryngol. **108**, 525–531.

Bonfils, P., Bertrand, Y., and Uziel, A. (**1988**). ''Evoked otoacoustic emissions: Normative data and presbycusis,'' Audiology **27**, 27–35.

Brass, D., and Kemp, D. T. (**1994**). ''The objective assessment of transient evoked otoacoustic emissions in neonates,'' Ear Hear. **15**, 371–377.

Brass, D., Watkins, P., and Kemp, D. T. (**1994**). ''Assessment of an implementation of a narrow band, newborn otoacoustic emission screening method,'' Ear Hear. **15**, 467–475.

Bray, P., and Kemp, D. T. (**1987**). ''An advanced cochlear echo technique suitable for infant screening,'' Br. J. Audiol. **21**, 191–204.

Challis, R. E., and Kitney, R. I. (**1990**). ''Biomedical signal processing (in four parts). Part 1: Time-domain methods,'' Med. Biol. Eng. Comput. **28**, 509–524.

Dirckx, J. J., Daemers, K., Somers, T., Offeciers, F. E., and Govaerts, P. J. (**1996**). ''Numerical assessment of TOAE screening results: Currently used criteria and their effect on TOAE prevalence figures,'' Acta Oto-Laryngol. **116**, 672–679.

Finitzo, T., Albright, K., and O'Neal, J. (**1998**). ''The newborn with hearing loss: Detection in the nursery,'' Pediatrics **102**, 1452–1460.

Gorga, M. P., Neely, S. T., Bergman, B. M., Beauchaine, K. L., Kaminski, J. R., Peters, J., Schulte, L., and Jesteadt, W. (**1993**). ''A comparison of transient-evoked and distortion product otoacoustic emissions in normal-hearing and hearing-impaired subjects,'' J. Acoust. Soc. Am. **94**, 2639–2648.

Grandori, F., Cianfrone, G., and Kemp, D. T. (**1990**). *Cochlear Mechanisms and Otoacoustic Emissions* (Karger, Basel).

Grandori, F., and Lutman, M. (**1999**). ''The European Consensus Development Conference on Neonatal Hearing Screening (Milan, 1998),'' Am. J. Audiol. **8**, 19–20.

Hoel, P. G. (**1971**). *Introduction to Mathematical Statistics* (Wiley, New York).

Kemp, D. T. (**1978**). ''Stimulated acoustic emissions from within the human auditory system,'' J. Acoust. Soc. Am. **64**, 1386–1391.

Kemp, D. T., and Ryan, S. (**1993**). ''The use of transient evoked otoacoustic emissions in newborn hearing screening programs,'' Semin Hear. **14**, 30–44.

Martin, G. K., Probst, R., and Lonsbury-Martin, B. L. (**1990**). ''Otoacoustic emissions in human ears: Normative findings,'' Ear Hear. **11**, 106–120.

Maxon, A. B., Vohr, B. R., and White, K. R. (**1996**). ''Newborn hearing screening: Comparison of a simplified otoacoustic device (ILO1088) with the ILO,'' Early Hum. Dev. **45**, 171–178.

Maxon, A. B., White, K. R., Behrens, T. R., and Vohr, B. R. (**1995**). ''Referral rates and cost efficiency in a universal newborn hearing screening program using transient evoked otoacoustic emissions,'' J. Am. Acad. Audiol **6**, 271–277.

McDonough, R. N., and Whalen, A. D. (**1995**). *Detection of Signals in Noise* (Academic, San Diego), pp. 39–46.

McPherson, B., Kei, J., Smyth, V., Latham, S., and Loscher, J. (**1998**). ''Feasibility of community-based hearing screening using transient evoked otoacoustic emissions,'' Public Health **112**, 147–152.

Morlet, T., Ferber-Viart, C., Putet, G., Sevin, F., and Duclaux, R. (**1998**). ''Auditory screening in high-risk pre-term and full-term neonates using transient evoked otoacoustic emissions and brainstem auditory evoked potentials,'' Int. J. Pediatr. Otorhinolaryngol. **45**, 31–40.

National Institute of Health (**1993**). ''Early identification of hearing impairment in infants and young children,'' NIH Consens Statement **11**, 1–24.

Ravazzani, P., Tognola, G., and Grandori, F. (**1996**). '''Derived 'nonlinear' versus 'linear' click-evoked otoacoustic emissions,'' Audiology **35**, 73–86.

Ravazzani, P., Tognola, G., and Grandori, F. (**1999**). ''Optimal bandpass filtering of transient-evoked otoacoustic emissions in neonates,'' Audiology **38**, 69–74.

Sergi, P., Pastorino, G., Ravazzani, P., Tognola, G., and Grandori, F. (**2000**). ''A hospital based universal neonatal hearing screening program using click-evoked otoacoustic emissions,'' Scand. Audiol. (in press).

Smyth, V., Kei, J., Young, J., Tudehope, D., Maurer, M., and Rankin, G. (**1999**). ''Otoacoustic emissions criteria for newborn hearing screening,'' Int. J. Pediatr. Otorhinolaryngol. **48**, 9–15.

Tognola, G., Grandori, F., and Ravazzani, P. (**1997**). ''Time-frequency distributions of click-evoked otoacoustic emissions,'' Hear. Res. **106**, 112–122.

Tognola, G., Grandori, F., and Ravazzani, P. (**1999**). ''Evaluation of click-evoked otoacoustic emissions in newborns. Effects of time-windowing,'' Audiology **38**, 127–134.

Tognola, G., Ravazzani, P., and Grandori, F. (**1995**). ''An optimal filtering technique to reduce the influence of low-frequency noise on click-evoked otoacoustic emissions,'' Br. J. Audiol. **29**, 153–160.

Vohr, B. R., Carty, L. M., Moore, P. E., and Letourneau, K. (**1998**). ''The Rhode Island Hearing Assessment Program: Experience with statewide hearing screening,'' J. Pediatr. **133**, 353–357.

Vohr, B. R., and Maxon, A. B. (**1996**). ''Screening infants for hearing impairment,'' J. Pediatr. **128**, 710–714.

Vohr, B. R., White, K. R., Maxon, A. B., and Johnson, M. J. (**1993**). ''Factors affecting the interpretation of transient evoked otoacoustic emissions results in newborn hearing screening,'' Semin Hear. **14**, 57–72.

White, K. R., Vohr, B. R., Maxon, A. B., Behrens, T. R., McPherson, M. G., and Mauk, G. W. (**1994**). ''Screening all newborns for hearing loss using transient evoked otoacoustic emissions,'' Int. J. Pediatr. Otorhinolaryngol. **29**, 203–217.

The short-wave model and waves in two directions

Egbert de Boer[a)]
Room D2-226, Academic Medical Center, University of Amsterdam, Meibergdreef 9, 1105 AZ, Amsterdam, The Netherlands

(Received 27 June 2000; accepted for publication 10 October 2000)

In the region where a sinusoidal wave in the cochlea reaches its maximum amplitude, the long-wave (or one-dimensional) model of the cochlea is deficient. In this region a short-wave model is more appropriate. However, in its current form, the short-wave model supports only waves in one direction. Therefore, it cannot cope with reflection effects associated with, e.g., inhomogeneities. Theoretical explorations of creation and internal reflection of otoacoustic emissions have almost exclusively been based on the long-wave model. In this article the road is paved for future explorations on a generalized form of the short-wave model, one that supports forward as well as backward waves, and thus can include internal reflections. © *2001 Acoustical Society of America.*
[DOI: 10.1121/1.1329623]

PACS numbers: 43.64.Kc, 43.64.Bt [LHC]

I. INTRODUCTION

In recent times several publications have appeared related to the problem of internal reflection in models of the cochlea. These explorations were inspired by the somewhat puzzling properties of otoacoustic emissions from the cochlea, in particular, distortion-product emissions. Two general classes of emission sources were distinguished, wave-fixed and location-fixed (starting with Kemp and Brown, 1983, more recent papers Schneider *et al.*, 1999; Talmadge *et al.*, 1999; Knight and Brass, 2000; Prijs *et al.*, 2000; theoretical foundation: Shera and Guinan, 1999). These classes of emissions are also different in that the former is typically associated with nonlinear phenomena, and the latter operates in linear as well as nonlinear models. Most if not all modeling work was done on the *long-wave* model, also known as the *one-dimensional* model. A few relevant publications are Talmadge and Tubis (1993), Shera and Zweig (1993), Talmadge *et al.* (1997, 1998, 1999), Shera and Guinan (1999), and the basic notion of ''coherent reflection'' was defined by Zweig and Shera (1995). The advantages of this approach are obvious: the long-wave model is described by a second-order differential equation with only two terms, and this type of equation has been thoroughly studied by mathematicians and physicists.

The long-wave model can adequately explain many properties of the cochlea, notably those related to variations of the basilar membrane impedance. It can also explain reflection phenomena, at the stapes as well as elsewhere, e.g., reflections resulting from irregularities in cochlear structure. However, the long-wave model is deficient in the ''peak region.'' To illustrate this property, data are taken from a number of experiments executed in collaboration with A. L. Nuttall (see, e.g., de Boer and Nuttall, 2000). In these experiments the velocity of the basilar membrane was measured at a location in the guinea pig cochlea that is tuned to a frequency near 17 kHz. The measured frequency response curves are converted to the place domain (x), using a standard frequency-to-place map, and the wave number $k=d\varphi/dx$, where φ is the response phase, was determined at the location of the response peak. The wave number k relates to the wavelength λ by $k=2\pi/\lambda$. According to a very conservative condition for validity of the long-wave model the wavelength λ should everywhere be larger than 2π times the height h of one cochlear channel (de Boer, 1996, Eq. 4.2.9). In terms of the wave number, the product kh should be smaller than 1. Averaged over 12 experiments in sensitive animals, the average value of the product kh at the response peak is 13.9 ± 0.9 (the height h is taken equal to 1 mm). Over the same experiments, the value of kh at the peak is 2.82 ± 0.6 for post-mortem responses. Clearly, in the live animal the condition for long waves is not met by far, and for the post-mortem condition it is not met either.

To solve a more general case, and to include long as well as short waves, two- and three-dimensional models have been developed. This development started with Lesser and Berkley (1972), and accelerated with Allen (1977), Allen and Sondhi (1979), Steele and Taber (1979, 1981), and Neely (1985). For a review of this development see de Boer (1996). In most cases solutions to these models were obtained in digital form or via the LG or Wentzel–Kramers–Brillouin (WKB) approximation. At first sight, trying to develop generalized *analytical* relations seems an impossible task in a three-dimensional setting.

In the region of the response peak the physics of the model can better be described by the *short-wave* model than by the long-wave model. In the original formulation the differential equation for the short-wave model is of the first order, even simpler than that for the long-wave model. However, this equation allows only a solution representing a wave propagating in one direction (Siebert, 1974; de Boer, 1979). In the present article it is shown that the short-wave model can be reformulated so that *it allows waves in the forward as well as the backward direction*. The result is a second-order differential equation.[1] This does not mean that all results obtained for long-wave models can be directly transposed to the short-wave model. In the physical sense the

a)Electronic mail: e.d.boer@hccnet.nl

two models are simply not equivalent. Mathematically, the two second-order equations are not equivalent either. However, it is felt that more widely applicable relations can be based on the generalized approach illustrated here. Moreover, the path to analytical solutions or useful approximations for the short-wave region is opened. It should be remembered, though, that no form of the short-wave model is adequate for the basal region.

II. DERIVATION

The model to be used has two channels, the complex variable $p(x)$ is the pressure in the upper channel (the one in which the stapes is located) and $-p(x)$ is the pressure in the lower channel. The (real) variable x denotes the coordinate in the longitudinal direction of the model, starting with zero at the stapes and round-window location. The velocity $v_{\mathrm{BM}}(x)$ is counted positive when the basilar membrane (BM) moves from the lower to the upper channel. The relation between pressure $p(x)$ and BM velocity $v_{\mathrm{BM}}(x)$ is then

$$v_{\mathrm{BM}}(x)=\frac{-2p(x)}{Z_{\mathrm{BM}}(x)}, \tag{1}$$

where $Z_{\mathrm{BM}}(x)$ the impedance of the BM. The *long-wave equation* for the pressure $p(x)$ reads

$$\frac{d^2}{dx^2}p(x)-\frac{2i\omega\rho}{h_e Z_{\mathrm{BM}}(x)}p(x)=0. \tag{2}$$

The parameters are as follows: ω is the radian frequency, ρ is the density of the fluid, and h_e is the ''effective'' height of the model.[2] Equation (2) is the equation for the *pressure*. The long-wave equation for the BM *velocity* $v_{\mathrm{BM}}(x)$ is somewhat more complicated:

$$\frac{d^2}{dx^2}v_{\mathrm{BM}}(x)+2\frac{d}{dx}\ln[Z_{\mathrm{BM}}(x)]\frac{d}{dx}v_{\mathrm{BM}}(x)+\left[U_{\mathrm{BM}}(x)-\frac{2i\omega\rho}{h_e Z_{\mathrm{BM}}(x)}\right]v_{\mathrm{BM}}(x)=0, \tag{3a}$$

with $U_{\mathrm{BM}}(x)$ given by

$$U_{\mathrm{BM}}(x)=\frac{1}{Z_{\mathrm{BM}}(x)}\frac{d^2}{dx^2}Z_{\mathrm{BM}}(x). \tag{3b}$$

The long-wave equation is valid when the wavelength of the wave in the model is ''large'' compared to the height h of the model (see Sec. I).

The other extreme occurs when the wavelength is small compared to h, this leads to the short-wave model. The *short-wave equation* for waves traveling to the ''right,'' i.e., in the direction of increasing x, reads (de Boer, 1979):

$$\frac{d}{dx}p(x)+\frac{2\omega\rho}{Z_{\mathrm{BM}}(x)}p(x)=0. \tag{4}$$

Similarly, the equation for waves to the ''left'' is

$$\frac{d}{dx}p(x)-\frac{2\omega\rho}{Z_{\mathrm{BM}}(x)}p(x)=0. \tag{5}$$

Note that each of these two equations has an analytical solution.

Let the solution to Eq. (4) be $p_1(x)$, and that to Eq. (5) $p_2(x)$. The general solution to the short-wave model equation in which waves in *both* directions are possible should be of the form

$$p(x)=\alpha p_1(x)+\beta p_2(x), \tag{6}$$

in which α and β are arbitrary constants. We desire to know the equation of which this is the general solution. To find it, first differentiate Eq. (4) once with respect to x. Use Eq. (4) again for reducing the term with $dp_1(x)/dx$ to $p_1(x)$ and the term with $p_1(x)$ to $dp_1(x)/dx$. The result is a three-term second-order differential equation with one plus and two minus signs. Use Eq. (5) in the same way for $p_2(x)$. Again, an equation results with one plus and two minus signs. Next, combine these two equations with coefficients α and β and rewrite the result in terms of $p(x)$ just as it appears in Eq. (6). It is found that the following equation in $p(x)$ fulfills the requirement (de Boer, 1983):

$$\frac{d^2}{dx^2}p(x)+\frac{d}{dx}\ln[Z_{\mathrm{BM}}(x)]\frac{d}{dx}p(x)-\left[\frac{2\omega\rho}{Z_{\mathrm{BM}}(x)}\right]^2 p(x)=0. \tag{7}$$

The solution of this equation, with the proper boundary conditions imposed at the two ends, supports forward as well as backward waves both having the character of short waves (deep-water waves).[3] It therefore also supports internal reflections, e.g., from irregularities. Equation (7) is similar in form to Eq. (3a) with two differences, (1) the factor of 2 in the second term of Eq. (3a) is missing in Eq. (7); and (2) the square of the impedance appears in Eq. (7).

About item (1), see the next section. Item (2) illustrates the well-known property of short waves in that they depend in a much stronger way on the BM impedance than long waves. In spite of these obstacles, Eq. (7) is sufficiently simple to allow analytical treatment, for instance, by a modification of the LG method. Therefore, the author feels that it is useful to reopen this formulation to theorists. It is stressed again that *in the peak region* the short-wave model describes the cochlear wave better than the long-wave model.

III. ALTERNATIVE FORMULATION

To illustrate item (1), write the pressure $p(x)$ as a product of a new unknown $q(x)$ and a coefficient function $W(x)$:

$$p(x)=W(x)q(x). \tag{8}$$

For Eq. (7) to have only two terms, $W(x)$ must satisfy

$$W(x)=\left(\frac{2\omega\rho}{Z_{\mathrm{BM}}}(x)\right)^{1/2}. \tag{9}$$

Then the two-term differential equation for $q(x)$ is

$$\frac{d^2}{dx^2}q(x)+\left[\frac{W''(x)}{W(x)}+\frac{Z'(x)}{Z_{\mathrm{BM}}(x)}\frac{W'(x)}{W(x)}-\left(\frac{2\omega\rho}{Z_{\mathrm{BM}}(x)}\right)^2\right]q(x)=0, \tag{10}$$

where $W'(x)$ stands for $dW(x)/dx$, $W''(x)$ for $d^2W(x)/dx^2$, and $Z'(x)$ for $dZ_{\mathrm{BM}}(x)/dx$. This method is one of the standard conversion methods for differential equations. In this formulation $q(x)$ does not have physical meaning. Apart from the aforementioned term $(2\omega\rho/Z(x))^2$, two extra terms appear in Eq. (10) that are related to variations of $Z_{\mathrm{BM}}(x)$ with x. In the main response region (the response peak and the regions next to it, on both sides) these terms turn out to be relatively small so that the main properties of the solution to Eq. (10) follow from those of $(2\omega\rho/Z_{\mathrm{BM}}(x))^2$.

Note added. Christopher Shera showed the author that at least one promising variation of the derivation in Sec. III on ''alternative formulation'' is possible. The author hopes that this and other variations will be developed further to give a wider scope to the theory on micro-reflections in the cochlea.

[1]This second-order differential equation, Eq. (7) of this note, has been published—without derivation—earlier, in a rather inaccessible place (de Boer, 1983).

[2]The effective height is the area of the cross section of one channel divided by the width of the BM. It is generally larger than the height h of one channel.

[3]A program set that runs in Matlab® (any Windows version from 4.0 on) can be obtained from the author. One program, SW01, shows the equivalence of solutions of Eqs. (4) and (7) for a realistic impedance function. If desired, it also shows the relative sizes of the extra terms in the bracketed part of Eq. (10). Another program, SW03, illustrates the deficiency of the long-wave model and the approximate adequacy of the short-wave model in the region of the response peak. Apply via e-mail.

Allen, J. B. (**1977**). ''Two-dimensional cochlear fluid model: New results,'' J. Acoust. Soc. Am. **61**, 110–119.

Allen, J. B., and Sondhi, M. M. (**1979**). ''Cochlear macromechanics-time domain solutions,'' J. Acoust. Soc. Am. **66**, 123–132.

de Boer, E. (**1979**). ''Short-wave world revisited: Resonance in a two-dimensional cochlear model,'' Hear. Res. **1**, 253–281.

de Boer, E. (**1983**). ''Wave reflection in active and passive cochlea models,'' in *Mechanics of Hearing*, edited by E. de Boer and M. A. Viergever (Martinus Nijhoff, The Hague, The Netherlands), pp. 135–142.

de Boer, E. (**1996**). ''Mechanics of the cochlea: modeling efforts,'' in *The Cochlea*, edited by P. Dallos, A. N. Popper, and R. R. Fay (Springer-Verlag, New York), pp. 258–317.

de Boer, E., and Nuttall, A. L. (**2000**). ''The mechanical waveform of the basilar membrane. III. Intensity effects,'' J. Acoust. Soc. Am. **107**, 1497–1507.

Kemp, D. T., and Brown, A. M. (**1983**). ''An integrated view of cochlear mechanical nonlinearities observable from the ear canal,'' in *Mechanics of Hearing*, edited by E. de Boer and M. A. Viergever (Martinus Nijhoff, The Hague, The Netherlands), pp. 75–82.

Knight, R. D., and Kemp, D. T. (**2000**). ''Indications of different distortion product otoacoustic emission mechanisms from a detailed f_1, f_2 area study,'' J. Acoust. Soc. Am. **107**, 457–473.

Lesser, M. B., and Berkley, D. A. (**1972**). ''Fluid mechanics of the cochlea. Part I,'' J. Fluid Mech. **51**, 497–512.

Neely, S. T. (**1985**). ''Mathematical modeling of cochlear mechanics,'' J. Acoust. Soc. Am. **78**, 345–352.

Prijs, V. F., Schneider, S., and Schoonhoven, R. (**2000**). ''Group delays of distortion product otoacoustic emissions: Relating delays measured with f_1- and f_2-sweep paradigms,'' J. Acoust. Soc. Am. **107**, 3298–3307.

Schneider, S., Prijs, V. F., and Schoonhoven, R. (**1999**). ''Group delays of distortion product otoacoustic emissions in the guinea pig,'' J. Acoust. Soc. Am. **105**, 2722–2730.

Shera, C. A., and Zweig, G. (**1993**). ''Order from chaos: Resolving the paradox of periodicity in evoked otoacoustic emissions,'' in *Biophysics of Hair Cell Sensory Systems*, edited by H. Duifhuis, J. W. Horst, P. van Dijk, and S. M. van Netten (World Scientific, Singapore), pp. 54–63.

Shera, C. A., and Guinan, J. J. (**1999**). ''Evoked otoacoustic emissions arise by two fundamentally different mechanisms: A taxonomy for mammalian OAEs,'' J. Acoust. Soc. Am. **105**, 782–798.

Siebert, W. M. (**1974**). ''Ranke revisited—A simple short-wave cochlear model,'' J. Acoust. Soc. Am. **56**, 594–6000.

Steele, C. R., and Taber, L. A. (**1979**). ''Comparison of WKB and finite difference calculations for a two-dimensional cochlear model,'' J. Acoust. Soc. Am. **65**, 1001–1006.

Steele, C. R., and Taber, L. A. (**1981**). ''Three-dimensional model calculations for guinea pig cochlea,'' J. Acoust. Soc. Am. **69**, 1107–1111.

Talmadge, C. L., and Tubis, A. (**1993**). ''On modeling the connection between spontaneous and evoked otoacoustic emissions,'' in *Biophysics of Hair Cell Sensory Systems*, edited by H. Duifhuis, J. W. Horst, P. van Dijk, and S. M. van Netten (World Scientific, Singapore), pp. 25–32.

Talmadge, C. L., Tubis, A., Piskorski, P., and Long, G. R. (**1997**). ''Modeling otoacoustic emission fine structure,'' in *Diversity in Auditory Mechanics*, edited by E. R. Lewis, G. R. Long, R. F. Lyon, P. M. Narins, C. R. Steele, and E. Hecht-Poinar (World Scientific, Singapore), pp. 462–471.

Talmadge, C. L., Tubis, A., Long, G. R., and Piskorski, P. (**1998**). ''Modeling otoacoustic emission and hearing threshold fine structures,'' J. Acoust. Soc. Am. **104**, 1517–1543.

Talmadge, C. L., Long, G. R., Tubis, A., and Dhar, S. (**1999**). ''Experimental confirmation of the two-source interference model for the fine structure of distortion product otoacoustic emissions,'' J. Acoust. Soc. Am. **105**, 275–292.

Zweig, G., and Shera, C. A. (**1995**). ''The origin of periodicity in the spectrum of evoked otoacoustic emissions,'' J. Acoust. Soc. Am. **98**, 2018–2047.

Binaural coherence edge pitch[a)]

William M. Hartmann[b)] and Colleen D. McMillon[c)]
Department of Physics and Astronomy, Michigan State University, East Lansing, Michigan 48824

(Received 3 March 2000; revised 19 July 2000; accepted 14 October 2000)

The binaural coherence edge pitch (BICEP) is a dichotic broadband noise pitch effect similar to the binaural edge pitch (BEP). The BICEP stimulus is made by summing spectrally dense sine wave components with random phases. The *interaural* phase angle is a constant (0 or π) for components with frequencies below (or above) a chosen edge frequency, and it is a random variable for the remaining components. The chosen edge frequency is a coherence edge because the noises to the two ears are mutually coherent within any band of frequencies on one side of the edge and they are mutually incoherent in any band on the other side. Pitch-matching experiments show that the BICEP exists for coherence edge frequencies between about 300 and 1000 Hz. It is matched by a pure-tone frequency that differs from the edge frequency by 5% to 10%. The matching frequency lies on the incoherent side of the edge, an important result that is consistent with the way that the equalization-cancellation model has been applied to binaural pitch effects, especially the BEP. The results of BICEP experiments depend upon whether the coherent components are presented in 0 or π interaural phase for some listeners but not for all. The BICEP persists if the noise to one of the ears is delayed, but it becomes weaker and less well matched as the delay increases beyond 2 ms. The BICEP does not depend on whether the component amplitudes are all created equal or are given a Rayleigh distribution. Some reliable pitch sensation exists even when the component amplitudes are entirely independent in the two ears, so long as the phase coherence conditions of the BICEP stimulus are maintained. The existence of the BICEP is a challenge for current models of dichotic pitch because none of them predicts all its features.
[DOI: 10.1121/1.1331680]

PACS numbers: 43.66.Ba, 43.66.Hg, 43.66.Pn [DWG]

I. INTRODUCTION

The binaural coherence edge pitch (BICEP) is a dichotic noise pitch effect, made with white noise wherein a particular interaural phase relationship causes a pitch to appear. Therefore, the BICEP is a member of the family of effects that began with the Huggins pitch and includes the binaural edge pitch (BEP). Like the Huggins pitch and BEP, the BICEP sounds like a narrow band of noise or like a pure tone embedded in noise.

A. The Huggins pitch

The first, and strongest, tonotopically local dichotic pitch effect is the Huggins pitch (Cramer and Huggins, 1958). It is created by dichotic broadband noise having a transition frequency region over which the interaural phase changes by 360 deg. For example, the interaural phase angle might be zero for all frequencies up to 580 Hz and 360 deg (equivalent to zero) for all frequencies above 620 Hz. Between 580 and 620 Hz is the transition region where the interaural phase changes smoothly from 0 to 360. In the center of the transition region, at a frequency of 600 Hz, the interaural phase is 180 deg. Such a stimulus produces a pitch with a frequency of about 600 Hz. The width of the transition region is a critical experimental variable. The width described above, 7% of the center frequency, is about optimal for hearing the effect (Cramer and Huggins, 1958; Hartmann, 1979).

Durlach (1962) explained the Huggins pitch in terms of his equalization-cancellation (EC) model (Durlach, 1972), in which the signals to the two ears can be binaurally added or subtracted in the central auditory system.[1] Applied to the above stimulus, the binaural subtraction operation leads to a central spectrum that is zero everywhere except in the phase transition region. Within the transition region there is a peak centered at 600 Hz, in agreement with the perceived frequency.

Evidence in favor of the EC explanation for the Huggins pitch can be found by creating a monaural analog to the Huggins effect. The analog simulates the supposed action of the binaural system by electronically subtracting the left and right signals of the dichotic stimulus to make a monaural stimulus in which most of the noise components are canceled. Perception of the resulting noise band can be compared with the percept obtained dichotically in Huggins pitch. When the noises are electronically subtracted, the peak in the monaural spectrum leads to a spectral pitch of about 600 Hz as expected. If the width of the transition region is increased, the pitch tends to disappear. As a function of transition region width, the dichotic pitch (Huggins pitch) disap-

[a)]A preliminary study of the BICEP was reported at the 107th meeting of the Acoustical Society of America at Norfolk in the spring of 1984 (Hartmann, 1984a). The noises used in that study were only 0.25 s in duration and they were not recomputed for each trial. Noises used in the experiments of the present article were much superior technically, but the results were not much different.

[b)]Electronic mail: hartmann@pa.msu.edu
[c)]Present address: Department of Physics, University of Texas, Austin, TX 78712.

pears in the same way as the spectral pitch, electronically generated by subtracting channels (Hartmann, 1979). At every value of the width, the change in pitch strength is about the same for both kinds of presentation.

B. The binaural edge pitch

The binaural edge pitch (BEP) stimulus (Klein and Hartmann, 1980) resembles the Huggins pitch stimulus, but the phase variation is only 180 deg, and the width of the transition region may be zero. Applying the cancellation process from Durlach's model leads to a central spectrum which is either a high-pass or low-pass noise band. For example, if the noise components in the two ears are in phase below the phase transition frequency and 180 deg out of phase above that frequency, then binaurally adding noises in the two ears would lead to a low-pass central spectrum, whereas subtracting noises in the two ears would lead to a high-pass central spectrum. Because noise bands with sharp spectral edges (monaural or diotic) produce pitches near the edges (Small and Daniloff, 1967; Fastl, 1971), it was predicted, by analogy with Durlach's argument, that the central spectrum created by the dichotic stimulus would also have a pitch, namely the BEP. Experiments showed that the BEP did exist, though it was weaker than the Huggins pitch. It is perhaps not extending the analogy too far to say that the BEP is weaker than the Huggins pitch by about the same amount as the spectral edge pitch is weaker than the pitch of the monaural spectral peak generated by subtracting the Huggins pitch channels.

The comparison between BEP and the pitch of a monaural spectral edge is strengthened by the results of pitch-matching experiments. A monaural noise with a spectral edge has a pitch that is close to the edge, but somewhat within the noise band itself. A low-pass noise band leads to a pitch that is a few percent below the cutoff frequency; a high-pass noise band has a pitch a few percent above the cutoff (Klein and Hartmann, 1980; Frijns *et al.*, 1986). Application of this monaural analogy to the BEP involves an ambiguity. Whether the BEP central spectrum most resembles a high-pass or low-pass noise band depends on the EC operation applied by the central auditory system, binaural addition, or subtraction. Klein and Hartmann found evidence that the BEP is bimodal, and they analyzed all their data in that way. The two peaks of the bimodal distribution compared well with spectral edge pitches that were obtained by physically combining the two channels to make high-pass and low-pass bands. Thus, the ambiguity present in the model appeared to be present in the experimental pitch matches as well.

It was conjectured that the pitches of both monaural spectral edges and binaural edges were caused by Mach bands due to lateral inhibition. In the case of a spectral edge, neurons tuned to noise components within the noise band but close to the edge would not be inhibited as much as neurons tuned to frequencies well inside the noise band. The effect of decreased lateral inhibition on these neurons near the edge of the band would produce a peak in the excitation pattern at a tonotopic place corresponding to a sine tone just inside the noise, as observed experimentally. In the case of the *binaural* edge, central neurons following the EC process would similarly reflect Mach bands. This conjecture for the binaural edge was therefore consistent with the bimodal distribution of the BEP with peaks just above and below the edge frequency. The agreement between experiment and theory was interpreted as support for the EC model. Using the EC model to explain the BEP data depended on the assumption that the binaural system would sometimes use binaural addition of channels and sometimes use subtraction.[2]

C. The binaural coherence edge pitch

A further prediction that follows from the EC model is that a central spectrum with an edge can be created by a binaural coherence edge. For example, if all the spectral components below an edge frequency are identical in amplitude and phase in the left and right channels, and all the components above the edge frequency have uncorrelated phases, then an operation that binaurally subtracts the left and right noises leads to a central edge because the low-frequency components cancel exactly while the incoherent components above the edge survive the subtraction operation. The central spectrum generated by this stimulus should resemble a high-pass noise with a sharp edge leading to a pitch. This predicted pitch is the BICEP. By analogy with monaural high-pass noise this pitch should lie above the coherence edge frequency. Similarly, noise that is coherent above an edge frequency and incoherent below the edge should lead to a pitch that is below the edge frequency.

These then are the predictions for the BICEP. If these predictions hold then the BICEP has a particular advantage over the BEP because the BICEP is predicted to be above or below the coherence edge unambiguously as determined by the stimulus. That is because only the binaural subtraction process leads to a sharp central edge with the BICEP stimulus. In contrast, either binaural subtraction or binaural addition leads to a sharp central edge with the BEP stimulus. Therefore, the BEP depends on a choice made by the central processor; the choice of binaural subtraction or addition determines whether the pitch is below or above the binaural phase edge, and that choice is not experimentally controllable. Because of this theoretical advantage of the BICEP, it is of considerable interest to know whether the BICEP exists and whether it is shifted away from the edge frequency as predicted.

II. EXPERIMENT 1—MIDDLE RANGE

A. Method

Pitch-matching experiments were done to see if the BICEP exists and, if it does exist, to check the predicted pitch shifts. The matching experiments used an alternating sequence of BICEP stimulus and sine wave matching tone. The listener could adjust the frequency of the matching tone to best match the pitch heard in the BICEP stimulus.

B. Stimuli

To make a noise with a binaural coherence edge, the left channel was created by adding 16 384 spectral components

having equal amplitudes and random phases over a 360-deg range. The components for the right channel were identical in amplitude and phase to the components for the left channel for frequencies on the coherent side of the edge. For frequencies on the incoherent side of the edge, the amplitudes were again equal, but the phases were rerandomized over a 360-deg range.

Noise computations were done in a Tucker-Davis (TDT) AP2 array processor. Noises were converted to analog form by the 16-bit DACs on a TDT DD1. The noise stimulus buffers were recomputed, with a new set of 16 384 random component phases, prior to each matching trial. For each channel, the buffer was 32 768 samples in length, and the sample rate was 20 ksps. Therefore, the cycle time was 1.6 s and the components of the noise were separated by 0.61 Hz. Thus, the transition from complete coherence to complete incoherence occurred over a frequency difference of 0.61 Hz. The noises were low-pass filtered at 8 kHz and −115 dB/octave.

The experiment was run by a microcomputer which also controlled the TDT system. The experimental matching sequence consisted of four intervals: BICEP stimulus, silent gap, matching tone in diotic noise, and silent gap.[3] All intervals were 500 ms long, incommensurate with the buffer cycle time and short enough that listeners were unaware of the 1.6-s repetition. The diotic noise presented with the matching tone had the same level as the BICEP noise, and, by adjusting the matching tone frequency and level, the listener could make the matching interval sound like the BICEP interval. The frequency and level adjustments were made with ten-turn potentiometers on the listener's response box. Potentiometer voltages were read with 16-bit ADCs and used to control a TDT WG2 pure-tone generator. The ten turns of the frequency control allowed a range of two octaves, and push buttons, also on the response box, allowed the listener to move that range up or down by arbitrarily large amounts.

The noise stimuli were presented at a level of 63 dB SPL (24-dB spectrum level) by Sennheiser HD 480 headphones. The level was high enough to produce strong binaural effects while avoiding cross talk. Listeners heard the stimuli while seated in a double-walled sound-treated room.

Matching trials were blocked as experimental runs, consisting of one match to each of five coherence edge frequencies, 550, 600, 650, 700, and 750 Hz, presented in random order. There was no time limit for making a match, and runs typically lasted 3 or 4 min. There were four different conditions: The coherent region could either be above the edge frequency or below the edge frequency, and the coherent components could be either in 0 phase (identical) or π phase (inverted). Each listener did ten runs for each condition.

C. Listeners

There were five listeners, C, J, M, T, and W. Listeners C and M were females, age 19. Listeners J, T, and W were males, ages 21, 21, and 59. Listeners C and W were the authors. All listeners had normal thresholds through 8 kHz except for W, whose thresholds were elevated above 4 kHz as typical for males of that age. Listener J was unusual, having had no musical training at any time in his life.

TABLE I. Monotonicity for five random matches. The table shows the expected percentage for which there are no (0) deviations from monotonically increasing matches with increasing boundary frequency; also the percentage of sets with one deviation, two deviations, three deviations, and four deviations.

Condition	0	1	2	3	4	Deviations
Random matches	0.8	21.7	55.0	21.7	0.8	

D. Results

Because of the predicted pitch shifts, it is not possible to judge the reliability of the pitch matches by direct comparison with the edge frequency. Alternative tests are (1) matches that are monotonic with edge frequency, and (2) matches that are mutually consistent.

1. Monotonicity statistic

The probability that five matching frequencies chosen at random are in a monotonically increasing order is 0.8 percent. Therefore, if the matches obtained experimentally rise monotonically with increasing edge frequency, there is good evidence that the listener heard a reliable pitch depending on the edge frequency. The probability that random frequencies are in ascending order except for one deviation is 21.7 percent. Therefore, if the experimental matches rise monotonically except for one deviation, then that too is evidence for a reliable pitch. This probability argument is the basis of the monotonicity statistic which is used throughout this article. The expected results for random matches are shown in Table I. This table serves as a basis for comparison for all the other tables in the article.

For experiment 1, the monotonicity statistic is given in Table II for the four conditions and five listeners.[4] A plot that corresponds to the average of the four lines of Table II appears as the dark histogram in Fig. 1 for illustration. The data in Table II indicate the presence of a pitch depending on the edge frequency for all stimulus conditions and all listeners. For instance, over all listeners and all conditions Table II shows perfectly monotonic matches for more than 50 percent of the trials, far greater than 1 percent as expected for random matches. Some listeners scored 100 percent. Statistics for monotonicity except for one deviation are similarly out of line with random performance. Although this statistic ignores the magnitude of the deviation from monotonically increasing matches, most deviations were just exchanges of neighboring positions when there was only a single violation. In summary, Table II shows unequivocal evidence for the existence of the BICEP.

TABLE II. Monotonicity for BICEP. Experiment 1. The table shows the percentage for which there were no (0) deviations from monotonically increasing matches with increasing boundary frequency; also the percentage of runs with 1 deviation, two deviations, three deviations, and four deviations. Results are averaged over five listeners, C, J, M, T, and W.

Condition	0	1	2	3	4	Deviations
Zero phase, coherent below	58	32	10	0	0	
Zero phase, coherent above	38	28	32	2	0	
Pi phase, coherent below	80	18	2	0	0	
Pi phase, coherent above	42	46	10	2	0	

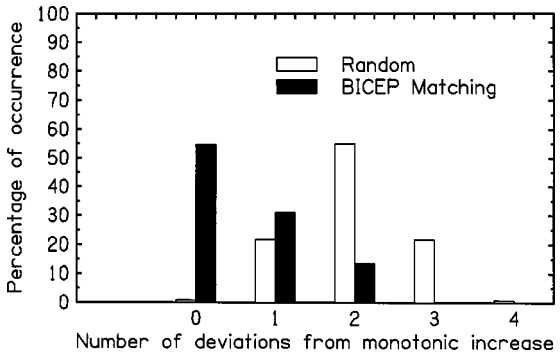

FIG. 1. Graphic example displaying the monotonicity statistic. The solid histogram shows average monotonicity statistic (five listeners and four conditions from Table II). The open histogram shows the expected monotonicity statistic for random pitch matches, Table I.

2. Pitch shifts

The pitch-matching results of the four stimulus conditions and five listeners are shown in Fig. 2. Every match is shown, with the five matches of a run connected by a line. The rising character for the lines shows the tendency for the matching frequency to increase with the edge frequency as expected from the monotonicity statistic. There is also a clear tendency for pitches to be above the edge frequency when the noise is coherent below the edge (circles), and for the pitches to be below the edge frequency when the noise is coherent above the edge (diamonds). These results are all in agreement with the original predictions based on the EC model.

Although the data as a whole all give clear evidence of the BICEP and its expected pitch shift, there are individual differences. Listeners M and W with the most musical training show the most consistent matches. Listener J with no musical training is the least consistent. Listeners C and T made more consistent matches to π-phase stimuli than to 0-phase stimuli. A model explanation for this result would be that listeners C and T are more successful in monitoring the binaural summation channel, and less successful in taking binaural differences (see Sec. E below).

E. Monaural analog

According to the EC model for BICEP, the listener binaurally subtracts or adds the noises in the two ears leading to a central spectrum with an edge. The monaural analog experiments performed noise subtraction or addition electronically and sent this noise to both ears diotically. For the purposes of this paper such a diotic noise is called ''monaural'' because each ear receives adequate information to make a pitch match. Otherwise, the monaural experiments were identical to the BICEP experiments above.

1. Noise subtraction experiment

Subtracting the two channels of the 0-phase BICEP stimulus leads to a monaural noise band with a sharp drop (measured to be 50 dB in our apparatus). If the components are coherent below the edge then the noise power vanishes below the edge and the monaural noise is high pass. If the coherent region lies above the edge then the monaural noise is low pass. Listeners C, J, and W matched the pitches of these noise bands created by subtraction. The results are shown by the monotonicity statistic in rows 1 and 2 of Table III and in Figs. 3(a), (b), (c). It is clear that listeners matched the edge pitches well and that the shifts were similar, in

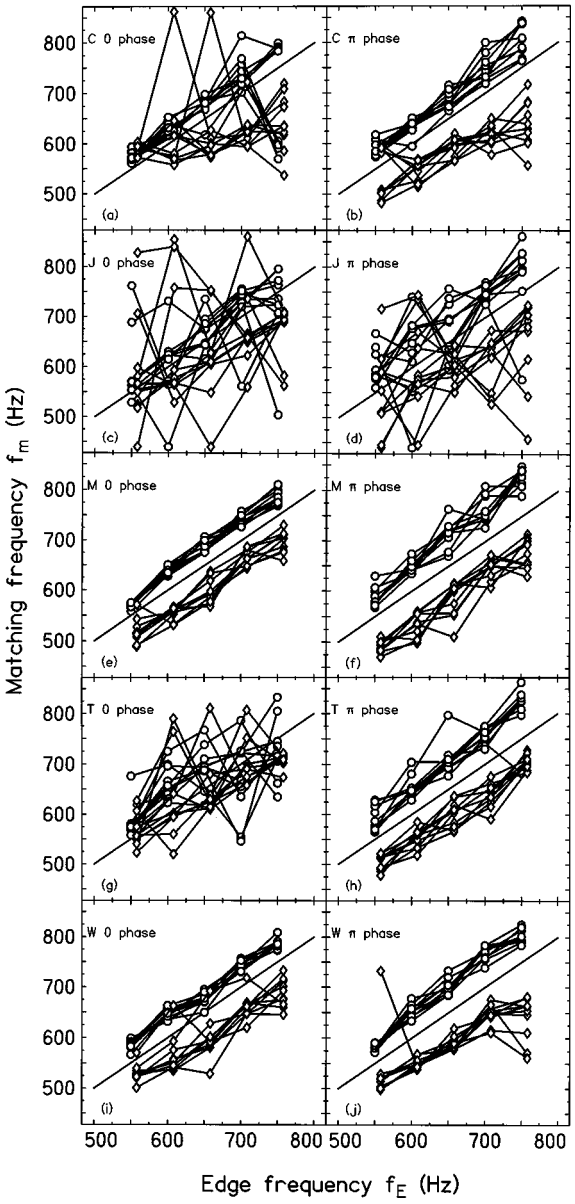

FIG. 2. Experiment 1 BICEP results. Circles show matching frequencies for BICEP noise that is coherent below the edge frequency. Diamonds show matching frequencies for BICEP noise that is coherent above the edge frequency. The diamonds have been slightly shifted to the right for clarity. The coherent noise components were identical in both ears (0 phase) or inverted (π phase). There were five listeners, C, J, M, T, and W.

TABLE III. Monotonicity, for monaural edge pitch. Experiment 1. Monaural noise was made from the difference of the two BICEP channels or the sum of the two BICEP channels with zero-phase coherence above or below the edge. Results are averaged over three listeners, C, J, and W.

Condition	0	1	2	3	4	Deviations
Difference, coherent below	77	20	3	0	0	
Difference, coherent above	90	10	0	0	0	
Sum, coherent below	3	33	47	17	0	
Sum, coherent above	10	30	43	17	0	

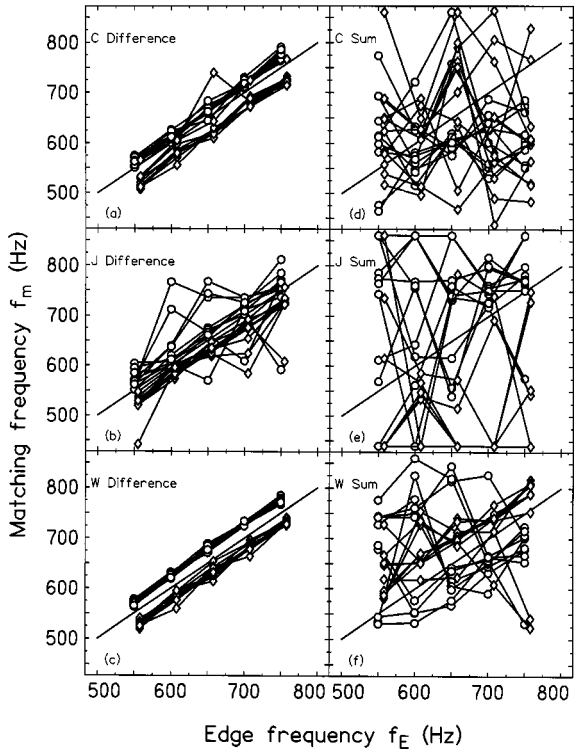

FIG. 3. Experiment 1—Monaural analog to the BICEP. Left column (a), (b), (c): Pitch matches for the *difference* of channels. Circles are for noise coherent below the edge frequency so that the difference noise is high pass. Diamonds are for noise that is coherent above the edge frequency so that the difference noise is low pass. Right column (d), (e), (f): Pitch matches for the *sum* of channels. Circles are for noise that is coherent below the edge frequency so that the summed noise has a 3-dB low-boost shelf below the edge frequency. Diamonds are for noise that is coherent above the edge frequency so that the summed noise has a 3-dB high-boost shelf above the edge frequency.

magnitude and *sign*, to the shifts observed in the BICEP experiment. This agreement suggests a similarity in mechanism between binaural and monaural experiments.

The monaural analog is conceptually similar to the monaural experiment run by Klein and Hartmann in connection with the BEP. However, the comparison of pitch shifts with the BICEP is more impressive than with the BEP. The BICEP comparison shows the auditory system to be choosing binaural addition or subtraction operations to optimize the central edge in the BICEP experiment. In contrast, it is not possible to know what is the optimum operation in the BEP experiment.

2. Noise addition experiment

Adding the two channels of the 0-phase BICEP stimulus leads to a monaural noise with an edge that is only 3 dB high. For the coherent components the amplitudes reinforce in phase, whereas for the incoherent components only the powers add. The difference is 3 dB in favor of the coherent region. Listeners C, J, and W matched the pitches of noises created by noise addition. The results are shown by the monotonicity statistic in rows 3 and 4 of Table III and in Figs. 3(d), (e), (f). Comparison with Figs. 3(a), (b), (c) shows the advantage of cancellation over reinforcement. In fact, matches to the monaural added stimulus are clearly less consistent than matches to the BICEP stimulus itself.

3. Implications for models for BICEP

In the context of the EC model, the results of the monaural experiments give every reason to believe that the optimum strategy for a binaural system attempting to fabricate a pitch is to cancel the coherent components and not to combine them so as to reinforce. That is the unambiguous binaural strategy elicited by the BICEP stimulus. For this reason it was possible to conclude above that listeners who favor coherent components in π phase, such as C and T, preferentially monitor a binaural addition channel and not a binaural subtraction channel.

III. EXPERIMENT 2—FREQUENCY LIMITS

Generally, binaural effects are strongest in the frequency region around 600 Hz (Licklider *et al.*, 1950). Binaural effects become weaker two octaves below this frequency and especially weaker two octaves above. The experiments of Sec. II were in the favorable frequency region near 600 Hz. The purpose of experiment 2 was to explore alternative frequency regions to determine the limits over which the BICEP could be heard and reliably matched.

A. Method

For the low-frequency range, edge frequencies were 100, 200, 300, 400, and 500 Hz. For the high-frequency range, edge frequencies were 800, 1000, 1200, 1400, and 1600 Hz. Except for the change in range, the experimental methods were identical to experiment 1. Equal numbers of runs were done with the coherent region above and below the edge frequency. Equal numbers of runs were done with the coherent noise in phase (0) and with phase inverted (π), a total of four different edge types. Listener C did ten runs for each edge type in the high-frequency region and four runs in the low-frequency region. Listener W did ten runs for each edge type in both the high-frequency and the low-frequency regions.

B. Results

The results for high- and low-frequency regions are shown in Fig. 4. This figure also includes the data from experiment 1 plotted in the midfrequency region. It is evident that performance was much less reliable outside the midfrequency region. Performance appears to be especially erratic in the high-frequency region, though this is partly the result of the linear frequency scale. In a log–log plot, not shown here, the low-and high-frequency regions appear with similar dispersion.

A second view of the data appears in Fig. 5, which plots the standard deviation of the matching frequencies as a percentage of the edge frequency. Although the standard deviation may be somewhat inflated by octave errors (visible at 100, 200, and 800 Hz in Fig. 4), it provides further data on the consistency of the matches.

Figures 4 and 5 show that matches to edges outside the midfrequency region were not always unreliable. In the low-

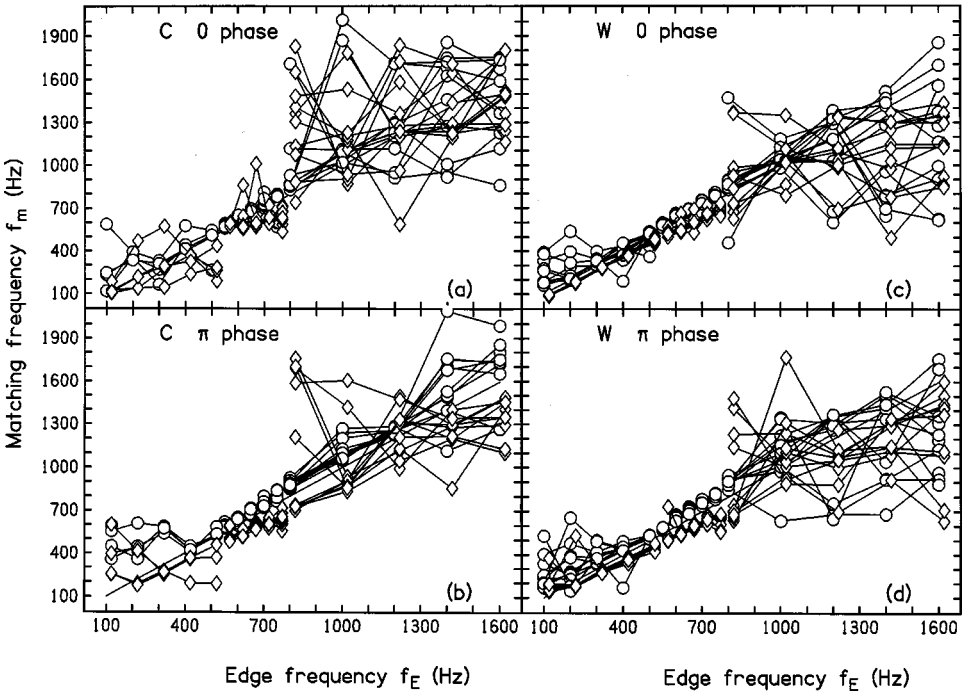

FIG. 4. Experiment 2—BICEP with extended frequency range. See the caption for Fig. 2. The data in the mid-frequency range (five edge frequencies from 550 through 750 Hz) are from experiment 1.

frequency region matches by listener W to noise that was coherent *above* the edge were almost as self-consistent as matches in the midfrequency region. Listener W exhibited excellent consistency for the 0-phase coherent noise right down to 100 Hz. For listener C, data in the low-frequency region showed no clear preference for 0-phase or π-phase coherence.

Similarly, in the high-frequency region, matches to π-phase noise that was coherent *below* the edge were consistent at 800 Hz for listener W and for edge frequencies up to 1200 Hz for listener C. The preference shown by listener C for π phase in the midfrequency region reappeared in the high-frequency region.

Because the three different frequency regions of this experiment were done separately, the data in Figs. 4 and 5 exhibit changes at the boundaries between regions that may be more pronounced than would have occurred had all frequency regions been represented in all runs. This apparent artifact was, however, not decisive. Consistent matches for coherence above a 300-Hz edge and for coherence below a 800-Hz edge were seen for both listeners. Evidently the inclusion of many difficult matches in a run did not seriously affect the ability to match at these edge frequencies in the low- and high-frequency regions. Therefore, it seems fair to present all the data in the same figures.

There are two conclusions that can be drawn from experiment 2. The first is that the BICEP is considerably more prominent in the narrow range of frequencies around 600 Hz,

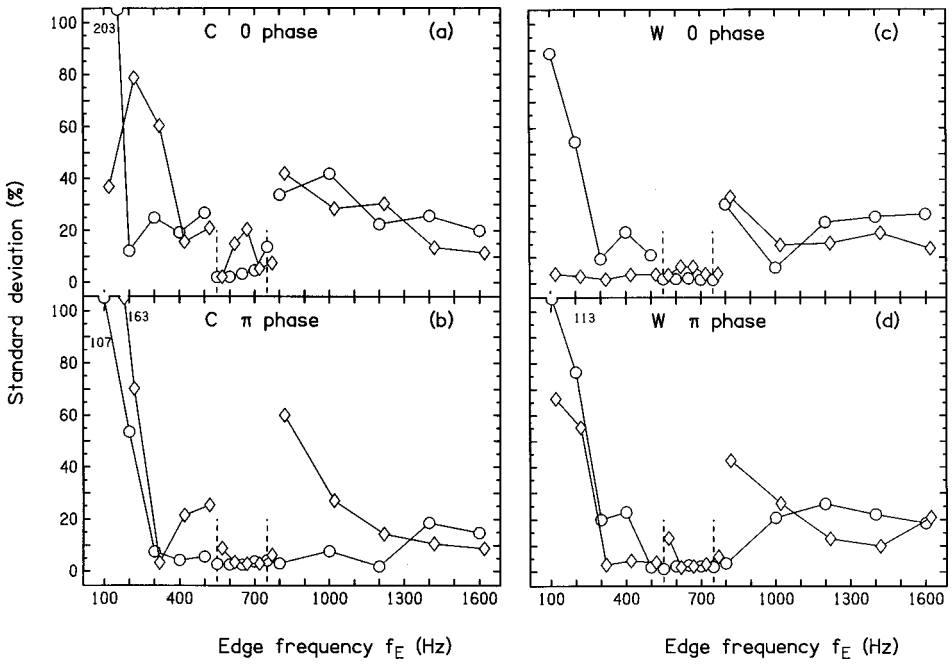

FIG. 5. Experiment 2—BICEP with extended frequency range. The ordinate shows the standard deviation ($N-1$ weight) of the matching frequencies in Fig. 4. The standard deviation is given as a percentage of the edge frequency shown on the abscissa. A few standard deviations greater than 100 percent are plotted on the top line with actual values given numerically.

where synchrony is well represented in the binaural system. Although there are exceptions, one might generalize from the data and conclude that the BICEP exists for edge frequencies in a range from 300 to 1000 Hz. This range is smaller than the range for the BEP, which can be found as high as 2.5 kHz. In the BEP the noise is coherent on both sides of the edge.

The second conclusion from experiment 2 is that when listeners are required to match edge frequencies outside the midfrequency range then the matches are more successful when the coherent region stretches into the midfrequency range, i.e., coherent above the edge for low edge frequencies and coherent below the edge for high edge frequencies. Thus, coherence in the region of best binaural synchrony seems to be important for the BICEP.

IV. EXPERIMENT 3—TIME DELAY

A. BICEP

The binaural system can obtain a central spectrum with an edge starting with the dichotic stimuli of experiments 1 or 2 by binaurally adding or subtracting the noises to the two ears. According to the standard EC model, the binaural adding operation is accomplished by a 180-deg phase shift followed by a central subtracting process. Thus, there is no central adding process *per se*. The necessary phase shift is normally attributed to an interaural delay line. It is part of the equalization stage in the EC model.

An alternative version of the EC model (Green, 1966; Henning, 1973; Bilsen and Goldstein, 1974) includes a central adding process. No delay line is required for the addition operation. Whether the central process is adding, or subtracting, or possibly both, the internal auditory delay line can be tested by a BICEP stimulus where the noise to one ear is given an external delay. Experiment 3 introduced such an external delay.

An external delay line does not change the incoherence/coherence conditions of the stimulus. For the incoherent region, adding delay maintains the incoherence. For the coherent region, adding the delay means that the (positive or negative) peak of the cross-correlation function is shifted from a lag of zero to a lag equal to the added time delay. However, the magnitude of the peak is still unity.

Delay was added with a BSS TCS-803 digital delay. (Actual values of the delay were verified ± 10 μs by a test that canceled sine tones.) The experiment was otherwise similar to experiment 1 including coherence both above and below the edge. However, the initial phase was always set to zero because it seemed superfluous to introduce a phase shift, such as π, in addition to the delay.

The results of the experiment for listeners C, M, and W are given by the monotonicity statistic in Table IV and the pitch shift plots in Fig. 6. Unlike Figs. 2, 3, and 4 which show actual matching frequencies, Fig. 6 plots each match in terms of its percentage deviation from the coherence edge frequency. Therefore, the 45-deg line in Figs. 2, 3, and 4 corresponds to the horizontal line at zero percent in Fig. 6.

The data indicate that delays as long as 1 ms have little effect on the matches except for a slight increase in variability. A delay of 2 ms sometimes disrupts pitch matching but usually does not. A delay of 3 ms produces a more dramatic increase in variability, and a delay of 4 ms increases the trends seen at 3 ms. Delays of 3- and 4 ms lead to a considerable pitch shift, in the direction of lower pitch, for listeners C and W, but not for listener M.

TABLE IV. Monotonicity for BICEP, delay in one channel. Experiment 3. Results are averaged over three listeners, C, M, and W.

Delay (ms)	0	1	2	3	4	Deviations
Coherent below						
0.0	92	8	0	0	0	
0.5	75	17	8	0	0	
1.0	50	50	0	0	0	
2.0	33	50	17	0	0	
3.0	17	25	33	25	0	
4.0	0	25	58	17	0	
Coherent above						
0.0	58	17	17	8	0	
0.5	50	50	0	0	0	
1.0	50	25	25	0	0	
2.0	8	33	59	0	0	
3.0	0	33	50	17	0	
4.0	0	16	42	42	0	

The heavy solid lines in the top panels of Fig. 6 form a

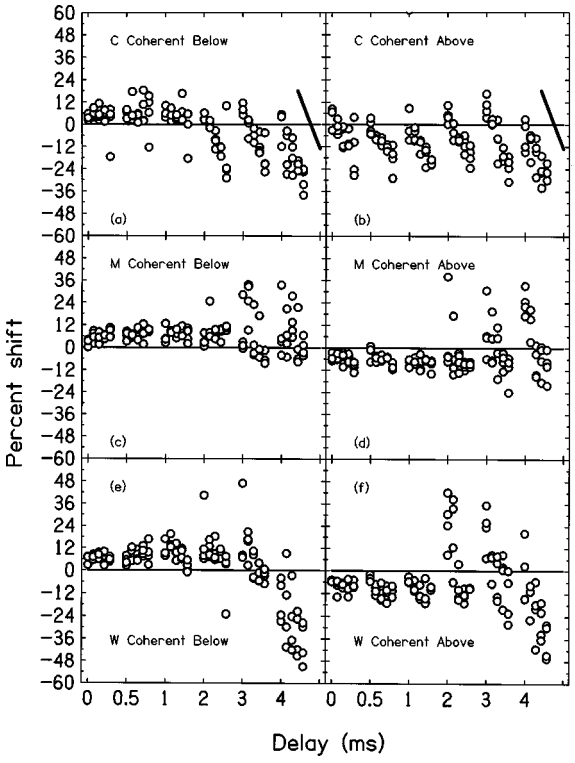

FIG. 6. Experiment 3—BICEP with one channel delayed as shown on the horizontal axis. All matches are shown. There are six blocks of data, corresponding to the six delays shown on the *x* axis. Within each block, columns, from left to right, indicate edge frequencies of 550, 600, 650, 700, and 750 Hz, the central range. Separate plots show data for stimuli that are coherent below and coherent above the edge. There were three listeners C, M, and W. The heavy lines in the top panels show the average shifts that would occur for random matches with a mean matching frequency of 650 Hz. See the text.

TABLE V. Monotonicity for the disruptive delay. Experiment 3. Results are averaged over three listeners, C, M, and W.

Condition	0	1	2	3	4	Deviations
Sum	0	22	66	12	0	
Difference	0	22	44	34	0	
BICEP	44	44	12	0	0	

reference showing the result expected for random matching with a mean matching frequency of 650 Hz, the center of the stimulus edge-frequency range. The vertical extent of the heavy line, caused by the increasing edge frequency from left to right, is less than the extent seen experimentally for long decays. The slopes of the heavy lines are similar to the slopes of the data for long delays, indicating weak correlation between matching frequency and edge frequency.

What seems most significant about this experiment is that it shows the internal delay line of the binaural system at work. The external delay can be compensated by the internal delay line so that the central spectrum has an edge, leading to a pitch, unchanged from the experiment with no external delay. This demonstration is independent of assumptions about the rule for combination, central addition, or central subtraction. The delay line begins to fail to operate in the expected way somewhere between 2 and 4 ms. This result agrees with the length of the delay line determined by binaural masking experiments (e.g., van der Heijden and Trahiotis, 1999).

B. Monaural analog

A monaural analog to the BICEP stimulus with delay adds the signals for the left and right ears. This leads to a flat noise spectrum in the incoherent region and rippled noise in the coherent region. It can be expected that listeners would have great difficulty in matching the pitch of such a noise. Unlike the binaural case, there is no way to use an internal delay line to compensate for the effects of the external delay. Particularly disruptive is a delay equal to one quarter of the reciprocal of the edge frequency.[5] For example, for an edge frequency of 650 Hz the reciprocal is 1538 μs, and the most disruptive delay is 385 μs.

1. Experiment and results

Listeners C, M, and W did three runs for the sum and three runs for the difference of the monaural delayed task with a delay of 385 μs. This delay is expected to be maximally disruptive because one quarter of its inverse is in the center of our range of edge frequencies. As always, listeners were required to make a match whether or not they could hear a clear pitch. The experiment found that sum and difference stimuli led to indistinguishable results, and both were random. The monotonicity statistic in Table V and pitch-matching plots (not shown) for sum or difference are consistent with random matches. By contrast, Table V and pitch-matching plots show monotonic or nearly monotonic matches for the BICEP with a delay of 385 μs, not different from the results with zero delay. The comparison between binaural and monaural experiments gave clear evidence for the operation of the internal delay line.

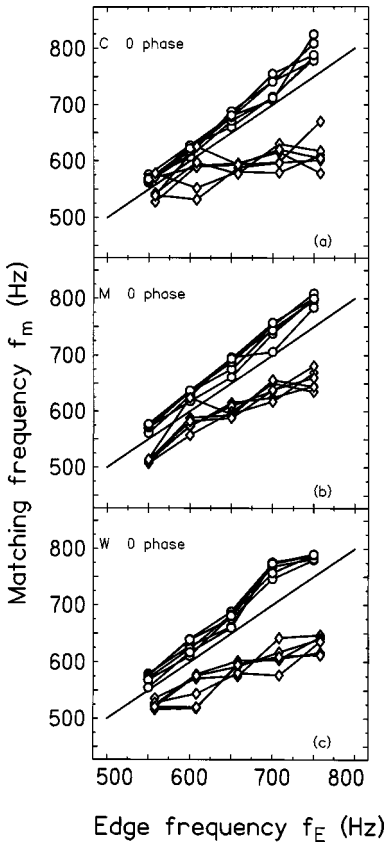

FIG. 7. Experiment 4—Matches for BICEP with random amplitudes—*identical* in both ears. See Fig. 2.

V. EXPERIMENT 4—RANDOM AMPLITUDES

Experiments 1, 2, and 3 used special noise in which every component had the same amplitude, i.e., equal-amplitude random-phase noise. However, for thermal noise the amplitudes are distributed according to a Rayleigh distribution. Experiment 4 replaced the equal-amplitude noise with such a random-amplitude noise. The conditions were otherwise the same as for experiment 1. In particular, the amplitudes of each component were the same in left and right ears. Therefore, in the phase-coherent region a subtraction operation would lead to perfect cancellation as in experiment 1. Because the spectrum is so dense, with many components in any auditory band, one expects that the change from equal amplitudes to random amplitudes should have no effect (Hartmann, 1997, p. 526). Experiment 4 was a brief test to show that this is so.

A. Results

Listeners C, M, and W each did six runs with the BICEP stimulus made with random amplitudes, both coherent below the edge and coherent above. Only the 0-phase condition was tested. The results, shown in Fig. 7, were indistinguishable from the results of experiment 1 with equal amplitudes. The monotonicity statistic in Table VI shows no degradation compared to Table II for equal amplitudes. Both tables show somewhat greater monotonicity for the ''coherent below'' condition. Although the listener populations were somewhat different, the comparison between experiments 1 and 4 gives no reason to suspect that the special choice of equal-

TABLE VI. Monotonicity for BICEP, random amplitudes. Experiment 4. Results are averaged over three listeners, C, M, and W.

Condition	0	1	2	3	4	Deviations
Zero phase, coherent below	100	0	0	0	0	
Zero phase, coherent above	50	33	17	0	0	

amplitude noise, as used in experiment 1 and in other experiments, had an important effect on the BICEP.

VI. EXPERIMENT 5—INTERAURALLY DIFFERENT AMPLITUDES

Experiment 4 used Rayleigh amplitudes that were random but were the same in left and right ears. Experiment 5 also chose amplitudes from a Rayleigh distribution, but the choices for left and right ears were made independently. Therefore, in the coherent region, only the phases of components in the left and right ears were identical. In the incoherent region both amplitudes and phases were independent across the ears. The reason for expecting that a BICEP would survive this amplitude randomization can be found in the monaural analog.

A. Monaural analog

Thermal noise is made by adding sine and cosine components with coefficients drawn from a normal distribution. If the normal distribution has variance σ^2 the amplitudes of the spectral components are Rayleigh distributed, and the noise power is half the average value of the squared amplitude or σ^2. Adding or subtracting two statistically identical but incoherent noises leads to twice the power or $2\sigma^2$. In a coherent region, where the noise phases in the two channels are the same, adding (or subtracting) the channels leads to a power given by the summed incoherent power plus (or minus) the square of the average amplitude. For a Rayleigh distribution, this is $2\sigma^2 \pm (\pi/2)\sigma^2$ (Hartmann, 1997, Appendix I). For the plus sign, the noise is 2.5 dB greater than the sum or difference of incoherent noise channels. For the minus sign, the noise is 6.7 dB less than the sum or difference of incoherent noise channels. Therefore, adding or subtracting channels leads to a spectral edge of 2.5 or 6.7 dB, respectively. It seems possible that a reliable pitch might be generated by spectral edges of this kind, especially the 6.7-dB edge created by the difference.

Listeners C, M, and W did four runs of the monaural experiment. The results are given by the monotonicity statistic in the first four lines of Table VII and by the matching graphs in Figs. 8(a)–(f). As expected, the most consistent matching occurred for the edge created by the difference, but the edge created by the sum also led to matches much better than chance.

B. Binaural experiment

Based on the good results for the difference spectrum in the monaural analog, one would expect that listeners could hear a BICEP for left and right channels made from independent noise amplitudes.

TABLE VII. Monotonicity for independent amplitudes. Experiment 5. (1) Monaural noise was made from the difference of the two zero-phase BICEP channels. (2) Monaural noise was made from the sum of the two zero-phase BICEP channels. (3) The BICEP dichotic stimulus. All were coherent below the edge or coherent above. Results are averaged over three listeners, C, M, and W.

Condition	0	1	2	3	4	Deviations
1 difference, coherent below	75	25	0	0	0	
1 difference, coherent above	75	25	0	0	0	
2 sum, coherent below	33	42	25	0	0	
2 sum, coherent above	8	75	8	0	8	
3 BICEP, coherent below	25	25	50	0	0	
3 BICEP, coherent above	9	58	33	0	0	

Listeners C, M, and W did four runs of this binaural experiment. The results are shown in the monotonicity table, Table VII—last two lines—and by Figs. 8(g)–(i). Evidently the matching performance did not rise to the level expected from the results of the monaural analog. Only listener M approached the consistency achieved with identical amplitudes in the two ears.

The poor performance with interaurally independent amplitudes is somewhat surprising. Because amplitudes are strictly positive numbers, randomizing them does not have the same effect as randomizing phases. With an identical phase spectrum in the two ears, considerable coherence remains even when the amplitudes are randomized. Therefore, good performance was expected, not poor performance. The stimulus for this experiment can be thought of as an identical-amplitude stimulus (as in experiment 4) plus added incoherent noise, albeit a rather special noise. The poor performance suggests that the BICEP is quite vulnerable to added binaurally incoherent noise.

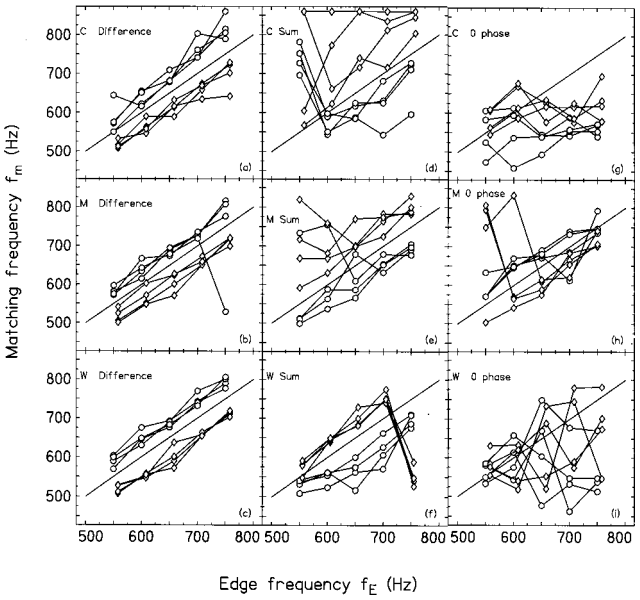

FIG. 8. Experiment 5—Pitch matches for noise with random amplitudes—*independent* in both ears. Circles are for noise coherent below the edge; diamonds are for noise coherent above the edge. Separate columns show the results for (1) Monaural experiment—difference of channels; (2) Monaural experiment—sum of channels; (3) BICEP experiment with coherent components having identical phases.

VII. SUMMARY AND COMPARISON

The most significant results of this work can be summarized in a few sentences: (1) The BICEP exists. (2) Matches to the BICEP show pitch shifts as expected based on BEP experiments and based on the model of central lateral inhibition advanced to explain the BEP (Klein and Hartmann, 1980). Therefore, BICEP and BEP are similar, but BICEP has the great advantage that the pitch shifts can be predicted unambiguously, whereas the pitch shifts for the BEP depend on a choice made by the listener's binaural system. (3) BICEP shifts agree qualitatively with the pitch shifts seen in analogous monaural experiments, concocted to simulate the imagined operation of a hypothetical EC process. Quantitatively the BICEP shifts are somewhat larger and show larger variance. (4) The BICEP continues to exist if the noise to one of the ears is externally delayed, but it becomes unreliable if the delay exceeds 2 or 3 ms. (5) The comparison of π-phase coherence and 0-phase coherence reveals a curious individual difference. Of four listeners who made very reliable matches to π-phase BICEP, only two of them retained that reliability for 0-phase BICEP.

It is natural to compare the BICEP with the BEP. The monaural analogs are essentially identical for both. However, the BEP is coherent on both sides of the edge, whereas BICEP is coherent on only one side. Therefore, the boundaries on a binaural delay-place (ITD-frequency) plot are sharper for the BEP, and, *a priori*, one might expect the BICEP to be weaker than the BEP. Listeners made informal comparisons between the BEP and BICEP in the middle range of edge frequencies, 550–750 Hz. Some of them found the BEP to be stronger and some of them did not. None of them found the difference to be striking. Apparently, what is important is the ability to cancel a coherent spectral region. The spectral region that is not canceled (coherent for BEP and incoherent for BICEP) is apparently less important, at least for favorable values of the edge frequency. It may become more important for edge frequencies that are higher than optimum. Our best evidence is that the BICEP exists over a smaller range of edge frequencies (300 to 1000 Hz) than the BEP, which persists for edges an octave higher. However, a careful head-to-head comparison between BEP and BICEP has not been done.

VIII. DISCUSSION AND CONCLUSION

Besides the EC model, there are other models that attempt to account for dichotic pitch effects like the Huggins pitch, the BEP, and the BICEP. The central activity pattern (CAP) model by Raatgever and Bilsen (1977, 1986), based on the central spectrum model (Bilsen, 1977), is a delay-place plane model for both the pitch sensation and the lateralization of the pitch. The CAP model predicts that dichotic pitches occur at the frequencies of spectral peaks prominent in the central spectrum obtained with advantageous interaural time delays. Recently Culling *et al.* (1998a, b) have developed a modified equalization-cancellation model (mEC) wherein the EC process takes place in frequency bands. The mEC model predicts binaural pitches at frequencies where the interaural phase changes so abruptly with frequency that there is a residual excitation in a filter channel following the cancellation process. These models can be compared with what we have learned about the BICEP.

On the existence of the BICEP: All three models, EC, CAP, and mEC, as they are applied to binaural pitch effects, predict that a binaural pitch occurs at a place corresponding to a peak in a central representation resembling a central spectrum. However, none of the models actually predicts a peak for the BICEP stimulus, and the most literal interpretation of the situation is that none of the models predicts the existence of the BICEP.

The mEC model has the virtue that it *does* predict a peak for the BEP stimulus. The peak occurs because auditory filters tuned to the edge frequency, where the phase changes rapidly, are the only filters in which good cancellation does not occur. Hence, a peak appears as function of place. By comparison, the original EC model predicts only an edge in the central spectrum. On the other hand, as noted by Culling *et al.*, the mEC model does not obtain a peak for the BICEP stimulus. It predicts only a broadened edge in the residual activation pattern, equivalent to the central spectrum. It was actually this situation that prompted us to resume BICEP experiments after a hiatus of 15 years.

But, although none of the models in their present form predicts a peak in the central spectrum, all of them can predict an edge. It may be reasonably argued that the remaining question is why an edge, either monaural or central, leads to a sense of pitch. Incorporating a central differentiation process with respect to place could account for both monaural and central pitches and would allow any of the binaural models to predict the existence of the BICEP. Differentiation with respect to place is here equivalent to lateral inhibition, enhancing contrast at an edge. The details of how central lateral inhibition could be incorporated into each of the models of dichotic pitch is beyond the scope of this article.

On the pitch shift of the BICEP: The experiments of this article have shown that the BICEP is shifted away from the edge frequency. The results are unequivocal on that matter. We suspect that the BEP is similarly shifted, but it is harder to prove that. Experiments on BEP made with analog stimuli by Frijns *et al.* (1986) did not find pitch shifts, but continued BEP experiments with digital stimuli in our lab continued to find shifts. The unambiguous shifts observed with the BICEP make the otherwise controversial BEP shifts more plausible.

None of the models of dichotic pitch predict the shift of the BEP. However, incorporating central lateral inhibition would predict a shift for both the BEP and the BICEP. Thus, central lateral inhibition not only allows the binaural models to predict the existence of the BEP and BICEP but it also predicts the observed shift. The EC model and the mEC model together with central lateral inhibition predict that the BICEP should be shifted into the incoherent region, in agreement with experiment. Against the hypothesized central lateral inhibition hypothesis are the results of pulsation threshold experiments (Hartmann, 1984b) which were designed to look for the effect but failed to find it. Possibly central lateral inhibition exists but has temporal properties that prevent a pulsation threshold experiment from revealing it. Possibly central lateral inhibition exists but it is such a weak effect

that it can be seen only in a pitch experiment and not in a masking (pulsation threshold) experiment.

On the advantage of π-phase coherence over 0-phase coherence: Figure 2 shows that four listeners made consistent matches to the π-phase condition but only two of them made comparably consistent matches to the 0-phase condition. The EC model and mEC model involve cancellation by central subtraction of left- and right-ear noises following an equalizing delay. As such, they should predict better performance when the coherent region has 0 phase rather than π phase because no internal delay can perfectly cancel all π-phase components within one auditory channel. The fact that two listeners performed better in experiment 1 when the coherent region was in π phase runs counter to the predictions of the EC and mEC models.

By contrast, the CAP model employs a central addition process (rather than subtraction). The apparent advantage of π-phase coherence seen experimentally would be consistent with addition as the fundamental operation because a central addition process can cancel the π-phase noise without the aid of a delay line. This result argues in favor of the CAP model. However, this argument is not consistent with the low-frequency data obtained in experiment 2. If it is really true that the π-phase advantage is caused by the delay line needed for 0-phase coherence then this advantage ought to grow as the edge frequency decreases. The lower the edge frequency the longer the required delay. Experiment 2 includes only two listeners, but both of them produce more consistent matches for 0 phase than for π phase. One of these two listeners is C, who shows an advantage for π phase at higher frequencies.

An additional clue appears in the form of the BICEP data in Fig. 2. For listeners M and W, the good performance seen with 0-phase coherence is not distinguishable from the good performance with π phase. For listeners C and T, performance is considerably worse with 0 phase. This form of the data does not suggest a central addition process that is made noisy by a delay line when the system is required to subtract. Instead, the form of the data suggests a model with two channels, one for central addition and one for central subtraction as in the version of the EC model adopted by Green (1966) and Henning (1973). Listeners may be more successful at monitoring one of these channels. Alternatively, the two channels might correspond to different paths through the delay-place plane as suggested in the CAP model. In the end, the BICEP experiments presented in this article have not enabled us to choose among competing models of dichotic pitch; the results have indicated that all the models require extension, if only to deal with the pitch shifts.

ACKNOWLEDGMENTS

We are grateful to Dr. N. I. Durlach who suggested the BICEP idea when he was a reviewer of the original BEP manuscript 20 years ago and to Dr. Brad Rakerd who programed the array processor to create BICEP noise. Dr. Quentin Summerfield and an anonymous reviewer gave useful comments on a previous version of this article. This work was supported by the National Institute on Deafness and Other Communicative Disorders. Author C. M. was supported by a Research Participation for Undergraduates Program grant from National Science Foundation to Michigan State University.

[1]In this article, the term ''addition'' is used in several ways. ''Binaural addition'' means that the auditory system as a whole operates in a way that adds the signals at the two ears. Binaural addition might possibly employ a binaural delay line to shift the phase. ''Central addition'' means that elemental rule of binaural combination is addition. By this definition the combination takes place at a stage that follows all interaural delays. ''Noise addition'' means that the experimenters have added the left and right channels to make a monaural stimulus, intended as a monaural analog to the binaural processes under study. In this article, the term ''subtraction'' is qualified in the same way as addition.

[2]The correspondence between dichotic pitch and the monaural analogy obtained by electronically simulating the operation of the binaural system does not hold perfectly for the BEP. Unpublished experiments show that when the phase transition region is broadened, the BEP survives better than the monaural analog. Although the monaural analog leads to a stronger pitch sensation than the BEP for a narrow transition region, the BEP can become stronger for wider regions (Hartmann, 1984c).

[3]Early experiments used gap intervals consisting of diotic noise. This procedure was based on the assumption that it would be easier to hear the dichotic pitch if the dichotic stimulus entered as an abrupt change in the noise as the stimulus sequence cycled. A similar temporal effect was found by Kubovy (1981) for line spectra. Experiments with a silent gap were introduced to prove that the BICEP was *not* really caused by Kubovy's effect. At that point listeners discovered that silent gaps made the BICEP easier to hear and that noise in the gaps just made the task harder. Because noise in the gaps leads to a potential Kubovy artifact, no further experiments were done with noise in the gaps, and all data reported in this article were collected with silent gaps.

[4]Expanded tables with the data from individual listeners are available from the first author. Please request Report 110SUP.

[5]If the power spectrum of the sum (or difference) of two channels is said to be 1 for the incoherent region, then in the coherent region the power spectrum of the sum of undelayed channels is 2 (because of amplitude addition), and the power spectrum of the difference is 0 (because of perfect cancellation). Delaying one of the channels by T_D before combination produces a power spectrum in the coherent region given by $2\cos^2(\pi f T_D)$ for the sum and given by $2\sin^2(\pi f T_D)$ for the difference (Hartmann, 1997, Chap. 15). When fT_D equals 1/4, these functions are both equal to 1. Therefore, if T_D is chosen according to the edge frequency, f_E, such that $f_E T_D = 1/4$ then the delay is maximally disruptive because at the edge, the power spectrum in the coherent region is exactly equal to the value of the power spectrum in the incoherent region. The spectrum in the coherent region now fits smoothly onto the spectrum for the incoherent region and there is no discontinuity, no spectral edge at all.

Bilsen, F. A. (**1977**). ''Pitch of noise signals: evidence for a central spectrum,'' J. Acoust. Soc. Am. **61**, 150–161.

Bilsen, F. A., and Goldstein, J. L. (**1974**). ''Pitch of dichotically delayed noise and its possible spectral basis,'' J. Acoust. Soc. Am. **55**, 292–296.

Cramer, E. M., and Huggins, W. H. (**1958**). ''Creation of pitch through binaural interaction,'' J. Acoust. Soc. Am. **30**, 413–417.

Culling, J. F., Summerfield, Q., and Marshall, D. H. (**1998a**). ''Dichotic pitches as illusions of binaural unmasking. I. Huggins' pitch and the 'binaural edge pitch','' J. Acoust. Soc. Am. **103**, 3509–3526.

Culling, J. F., Marshall, D. H., and Summerfield, Q. (**1998b**). ''Dichotic pitches as illusions of binaural unmasking. II. The Fourcin pitch and the dichotic repetition pitch,'' J. Acoust. Soc. Am. **103**, 3527–3540.

Durlach, N. I. (**1972**). ''Binaural signal detection—equalization and cancellation theory,'' in *Foundations of Modern Auditory Theory*, edited by J. Tobias (Academic, New York), Vol. 2, pp. 369–462.

Durlach, N. I. (**1962**). ''Note on the creation of pitch through binaural interaction,'' J. Acoust. Soc. Am. **34**, 1096–1099.

Fastl, H. (**1971**). ''Uber Tonhohenmpfindungen bei Rauschen,'' Acustica **25**, 350–354.

Frijns, J. H. M., Raatgever, J., and Bilsen, F. A. (**1986**). ''A central spectrum theory of binaural processing. The binaural edge pitch revisited,'' J. Acoust. Soc. Am. **80**, 442–451.

Green, D. M. (**1966**). ''Signal detection analysis of equalization and cancellation model,'' J. Acoust. Soc. Am. **40**, 833–838.
Hartmann, W. M. (**1979**). ''Some psychoacoustical experiments with allpass networks,'' Am. J. Phys. **47**, 29–34.
Hartmann, W. M. (**1984a**). ''Binaural coherence edge pitch,'' J. Acoust. Soc. Am. Suppl. 1**75**, S22.
Hartmann, W. M. (**1984b**). ''A search for central lateral inhibition,'' J. Acoust. Soc. Am. **75**, 528–535.
Hartmann, W. M. (**1984c**). ''The dependence of noise edge pitch and binaural edge pitch on the frequency width of the edge,'' J. Acoust. Soc. Am. Suppl. 1 **75**, S22.
Hartmann, W. M. (**1997**). *Signals, Sound, and Sensation* (AIP, Springer, New York).
Henning, G. B. (**1973**). ''Effect of interaural phase on frequency and amplitude discrimination,'' J. Acoust. Soc. Am. **54**, 1160–1178.
Klein, M. A., and Hartmann, W. M. (**1980**). ''Binaural edge pitch,'' J. Acoust. Soc. Am. **70**, 51–61.
Kubovy, M. (**1981**). ''Concurrent-pitch segregation and the theory of indispensable attributes,'' in *Perceptual Organization*, edited by M. Kubovy and J. R. Pomerantz (Erlbaum, Hillsdale, NJ).
Licklider, J. C. R., Webster, J. C., and Hedlum, J. M. (**1950**). ''On the frequency limits of binaural beats,'' J. Acoust. Soc. Am. **22**, 478–483.
Raatgever, J., and Bilsen, F. A. (**1977**). ''Lateralization and dichotic pitch a a result of spectral pattern recognition,'' in *Psychophysics and Physiology of Hearing*, edited by E. F. Evans and J. P. Wilson (Academic, London), pp. 443–453.
Raatgever, J., and Bilsen, F. A. (**1986**). ''A central spectrum theory of binaural processing. Evidence from dichotic pitch,'' J. Acoust. Soc. Am. **80**, 429–441.
Small, A. M., and Daniloff, R. G. (**1967**). ''Pitch of noise bands,'' J. Acoust. Soc. Am. **41**, 506–512.
van der Heijden, M., and Trahiotis, C. (**1999**). ''Masking with interaurally delayed stimuli: The use of internal delays in binaural detection,'' J. Acoust. Soc. Am. **105**, 388–399.

A masking level difference due to harmonicity

William C. Treurniet and Darcy R. Boucher
Communications Research Centre, Box 11490, Station H, Ottawa, Ontario K2H 8S2, Canada

(Received 22 September 1999; revised 21 February 2000; accepted 2 October 2000)

The role of harmonicity in masking was studied by comparing the effect of harmonic and inharmonic maskers on the masked thresholds of noise probes using a three-alternative, forced-choice method. Harmonic maskers were created by selecting sets of partials from a harmonic series with an 88-Hz fundamental and 45 consecutive partials. Inharmonic maskers differed in that the partial frequencies were perturbed to nearby values that were not integer multiples of the fundamental frequency. Average simultaneous-masked thresholds were as much as 10 dB lower with the harmonic masker than with the inharmonic masker, and this difference was unaffected by masker level. It was reduced or eliminated when the harmonic partials were separated by more than 176 Hz, suggesting that the effect is related to the extent to which the harmonics are resolved by auditory filters. The threshold difference was not observed in a forward-masking experiment. Finally, an across-channel mechanism was implicated when the threshold difference was found between a harmonic masker flanked by harmonic bands and a harmonic masker flanked by inharmonic bands. A model developed to explain the observed difference recognizes that an auditory filter output envelope is modulated when the filter passes two or more sinusoids, and that the modulation rate depends on the differences among the input frequencies. For a harmonic masker, the frequency differences of adjacent partials are identical, and all auditory filters have the same dominant modulation rate. For an inharmonic masker, however, the frequency differences are not constant and the envelope modulation rate varies across filters. The model proposes that a lower variability facilitates detection of a probe-induced change in the variability, thus accounting for the masked threshold difference. The model was supported by significantly improved predictions of observed thresholds when the predictor variables included envelope modulation rate variance measured using simulated auditory filters.
[DOI: 10.1121/1.1328791]

PACS numbers: 43.66.Dc, 43.66.Ba [SPB]

I. INTRODUCTION

A harmonic sound generated by melodic musical instruments such as the clarinet and harpsichord consists of partials that are integer multiples of a fundamental frequency. The sound is perceived to be quite distinct from an inharmonic sound, and may differ significantly in the structure of both the envelope and the spectrum. Since envelope structure alone is known to have an effect on masking (e.g., van der Heijden and Kohlrausch, 1995), a harmonic sound may differ from an inharmonic sound in its ability to mask a noise probe. The existence of such an effect on masking would be of theoretical importance since the underlying mechanism would not be immediately obvious. It would also be of practical importance for the design of psychoacoustic models employed in audio devices. For example, digital audio compression algorithms use such models to decide on a bit allocation strategy that minimizes the total number of bits while still ensuring that the generated quantization noise is masked by the audio signal. If the model does not take into account the harmonicity of the signal, the resulting coding noise may be more perceptible at times than expected. Since the role of harmonicity in masking is not well understood, this paper examines the relative effectiveness of harmonic maskers compared to inharmonic maskers, and describes a decision model that accounts for the observed effects.

It is generally accepted that the auditory system transforms an audio signal to a time–place representation. That is, the energy of the basilar-membrane vibration pattern at a particular location depends on the short-time spectral energy of the corresponding frequency in the input signal (Plomp, 1967). This frequency-to-place transformation is typically modeled by a tonotopically distributed bank of filters (e.g., Moore, 1997). When the signal is a complex masker composed of a number of partials, interaction of neighboring partials results in local variations of the basilar-membrane vibration pattern. The output of an auditory filter centered at the corresponding frequency would have an amplitude modulation corresponding to the vibration pattern at that location. To a first approximation, the modulation rate for a given filter is the difference between the adjacent frequencies processed by that filter. Since this frequency difference is constant for a harmonic masker, the dominant output modulation rate is also constant over all filters. For an inharmonic masker, however, the frequency difference between adjacent partials is not constant, so the modulation rates are expected to differ across filters.

The perceived effect of amplitude modulation is often studied by multiplying a carrier signal with a simple signal such as a sinusoid in order to produce amplitude fluctuations (e.g., Terhardt, 1974). A fluttering sensation perceived at low modulation rates changes to one of roughness as the modulation rate rises, and the perceived roughness increases to a

maximum around a modulation rate of 70 Hz (Zwicker and Fastl, 1999). The roughness declines with further increases in the modulation rate. Zwicker and Fastl (1999, p. 262) present a model of roughness that depends on the perceived rate of change in the sound. Terhardt (1974) showed that similar perceptual effects result from summation of two sinusoids with similar frequencies. Further, the roughness sensation arising from such modulations is not affected by sound-pressure level.

Thus, the output of a single auditory filter, which processes at least two adjacent partials of a complex signal, is associated with a roughness sensation. Although the response of an individual filter to a harmonic or an inharmonic masker may have similar roughness, the roughness distribution across filters can be quite different. An auditory filter may pass several partials that have effective amplitudes depending on their relative distances from the filter center frequency. The output modulation is dominated by the difference between adjacent partials, since these have the largest relative amplitudes. For a harmonic masker, therefore, the dominant modulation rate for each filter output is the fundamental frequency, and the variability in perceived roughness across auditory filters is negligible. On the other hand, when inharmonicity is introduced by perturbing the frequencies of the partials, the dominant modulation rate varies across filters. This variability is not negligible and it increases with increasing inharmonicity.

In general, the internal representation of a complex masker may be characterized by the variance of the modulation rates measured across a number of filters. A change in the variance should be more easily detected when the initial variance is negligible than when it is larger. As the level of a noise probe approaches the detection threshold from below, small random changes would be introduced in the relatively fixed modulation rates of the filter outputs. For a harmonic masker associated with low variability in modulation rates, a noise probe's detection threshold should be lower than for an inharmonic masker, which induces a larger variability.

An alternative cue for detecting a noise probe embedded in a complex masker could be the difference in modulation depth between a masker band and a comodulated flanking band, which has been proposed to account for the phenomenon of comodulation masking release (CMR). In CMR, the effectiveness of a masker is reduced by comodulated energy in a frequency band flanking the masker (e.g., Hall *et al.*, 1984; Hall, 1986; Hall and Grose, 1988; Grose and Hall, 1989). The reduction in masked threshold is thought to occur either because of a difference in across-frequency modulation depth due to the presence of the probe, or because the comodulated frequency bands provide cues to the occurrence of dips in the waveform envelope where the signal-to-noise ratio is highest (Hall, 1987). When a wide-bandwidth masker is harmonic and the probe has a narrower bandwidth, the masker region coincident with the probe would be comodulated with the rest of the masker if the filter output modulations were all in phase across filters. Note that the modulations are in phase only when all the harmonic partials are in phase. Such a condition might allow CMR to occur due to the presence of one of the above cues.

Ma and O'Shaughnessy (1994) found that the masked threshold of noise probes was influenced by the fundamental frequency of a harmonic masker. The threshold for narrow-bandwidth noise probes masked by wide-bandwidth harmonic maskers was a function of both the center frequency of the probe and the fundamental frequency of the masker. At lower frequencies, thresholds were reduced when the filter bandwidths were smaller than the fundamental frequency, so the limiting factor seemed to be the spectral resolution of the system. At higher frequencies, thresholds were reduced when the filter bandwidths were several times wider than the fundamental frequency. This allowed several partials to be passed by a filter, so the limiting factor seemed to be the temporal resolution available for processing the modulated waveform. However, the effects of frequency and temporal resolution should not be specific to harmonic maskers. The same effects should also occur with inharmonic maskers created by perturbing the frequencies of the partials in the harmonic complexes.

The experiments reported by Ma and O'Shaughnessy (1994) did not compare the effect of a harmonic masker to that of an inharmonic masker having roughly the same spectral energy distribution. Since a harmonic complex is characterized by particular relationships among sharp peaks in the spectrum, an appropriate baseline condition for measuring the effect of harmonicity would be a masker having a similar distribution of energy across the auditory filters, but with small perturbations in the relationships among the spectral peaks.

The following experiments were designed to study the relative effects of harmonic and inharmonic maskers on the masked threshold of noise probes, and to evaluate the viability of the envelope modulation rate variability hypothesis for predicting any observed differences. The first experiment found that a harmonic masker yielded a lower masked threshold than an inharmonic masker. Experiment 2 examined whether a ''listening in the dips'' strategy could account for the effect by taking advantage of differences in envelope modulation depth. The remaining experiments tested various predictions based on the modulation rate variability hypothesis. Experiment 3 studied the size of the effect as a function of frequency range. Experiment 4 investigated whether the effect persisted with forward masking. Experiment 5 measured the effect of varying partial separation, experiment 6 measured the sensitivity of the effect to the degree of mistuning of the harmonic partials, and experiment 7 tested for the presence of across-channel influences. Finally, a model is proposed that accounts for the observed masker harmonicity effect.

II. GENERAL METHOD

The maskers employed were based on either all or a subset of the partials of a relatively broadband harmonic masker, created by summing harmonically related sine waves. The fundamental frequency was 88 Hz, and a total of 45 equally spaced partials spanned the range from 88 to 3960 Hz. All partials had the same magnitude, and the starting phases were randomly selected. A second, inharmonic masker was constructed as a comparison condition. The 45

TABLE I. Harmonic and inharmonic masker specifications.

Partial #	Harmonic frequency	Inharmonic frequency	Phase (deg)
1	88	89	123
2	176	181	342
3	264	263	181
4	352	337	318
5	440	433	2
6	528	503	70
7	616	607	154
8	704	719	149
9	792	769	249
10	880	863	286
11	968	977	87
12	1056	1069	160
13	1144	1123	94
14	1232	1213	308
15	1320	1327	164
16	1408	1399	155
17	1496	1483	323
18	1584	1567	253
19	1672	1657	7
20	1760	1777	110
21	1848	1831	351
22	1936	1913	66
23	2024	2017	355
24	2112	2087	210
25	2200	2221	143
26	2288	2297	277
27	2376	2383	310
28	2464	2477	175
29	2552	2539	287
30	2640	2657	37
31	2728	2707	213
32	2816	2791	23
33	2904	2887	314
34	2992	2969	45
35	3080	3061	287
36	3168	3191	229
37	3256	3271	223
38	3344	3323	165
39	3432	3457	84
40	3520	2533	188
41	3608	3593	282
42	3696	3677	77
43	3784	3769	14
44	3872	3853	164
45	3960	3967	102

partials were similar to those in the harmonic masker, but the frequencies were perturbed by a small amount. In experiments 1 to 5, the new frequencies were nearby prime numbers, thus ensuring that the separation between partials was never the same. The frequencies and phases of the harmonic and inharmonic masker partials are listed in Table I. In experiments 6 and 7, the perturbations were randomly chosen from a rectangular distribution having a specified maximum value. Both procedures resulted in a distribution of frequencies similar to that of the harmonic masker. A third masker used in some experiments consisted of Gaussian noise having the same bandwidth as the harmonic and inharmonic maskers. The probe signal to be detected was an independently generated, narrow band of Gaussian noise, or was created by summing a number of equal-amplitude sinusoids having random frequency and phase sampled from a uniform distribution. In experiment 7, the probe was randomly selected from a longer sequence of noise, while in all the other experiments, the noise probe was frozen.

The effect of harmonicity was measured by comparing the masked threshold with the harmonic masker to that obtained with the inharmonic masker. The inharmonic masker was very similar to the harmonic masker with regard to the number of partials and their frequencies. However, the waveform envelopes of the two maskers were different. The harmonic masker envelope was modulated at the fundamental frequency, while the modulation of the inharmonic masker envelope was not periodic. In other respects, the maskers were qualitatively similar due to the random starting phases of the partials. Therefore, differences in masking properties might be due either to differences in envelope periodicity or the small differences in the frequencies of the partials.

A. Apparatus

Audio was generated with 16-bit linear resolution at a sampling rate of 44.1 kHz, and was presented via a Digital Audio Labs CardD digital sound card and an external Spectral Synthesis model 2218 D/A converter. The signal from the D/A converter was fed to Stax SRM-1 headphones located in an audiometric chamber. All sounds were presented diotically. A listener interacted with a computer screen through a window in the chamber using a mouse control. Software to control the experiment was developed in-house.

B. Experimental procedure

An adaptive three-alternative forced-choice psychophysical procedure was used to measure the masked thresholds. On a given trial, the masker was presented three times. One of the presentations was chosen randomly as a target interval, and the probe was added to the masker during this interval. The three audio intervals were presented sequentially in synchrony with a visual cue on the computer screen. The listener's task was to indicate which was the target interval by selecting a corresponding button on the screen with the mouse. The level of the probe was raised by a fixed amount if the response was incorrect, and it was lowered by the same amount if the response was correct on the current trial as well as on the two preceding trials. Each session consisted of a total of 12 reversals in direction. The change in signal level was 4 dB before the first two reversals and 1 dB subsequently. The measured threshold level was the mean of the levels at each of the last ten reversals. In theory, this procedure converges to the signal level on the psychometric function where 79.4 percent of signals are detected (Levitt, 1971).

Unless indicated otherwise, the masker and probe signals were each 400 ms in duration, including 25-ms raised-cosine onset and offset ramps, and were presented simultaneously. The interpresentation interval within the set of three presentations was 200 ms, and the time between successive sets was 1500 ms unless the listener failed to respond within that time. When the response was delayed, the next iteration began immediately after the response was given. The initial level of the probe was at least 5 dB higher than the overall level of the masker.

Thirteen listeners participated in some or all of the experiments. All listeners were males between the ages of 20 and 55 with no history of hearing disorders. Conditions were presented in consecutive blocks of trials in order to minimize the effect of stimulus uncertainty, and the order of conditions was randomized for each listener. For each condition, each listener's final threshold was the average of three threshold determinations.

III. EXPERIMENTS

A. Experiment 1: Masker level

The effect of masker harmonicity on detectability of a noise probe was evaluated by comparing the masked thresholds obtained with the harmonic and inharmonic maskers described above. The additional effect of the frequency spacing between the masker partials was also measured by comparing the masked thresholds obtained with the inharmonic masker and the equivalent bandwidth Gaussian noise masker. An 800-Hz bandwidth noise probe was presented centered at 700, 1800, or 2900 Hz. If the effect of masker harmonicity is mediated by the same mechanism as the sensation of roughness, it should not be significantly affected by sound-pressure level (Terhardt, 1974). Maskers were presented at overall levels of 40, 55, and 70 dB to test this prediction. Three listeners participated in the experiment.

1. Results and discussion

The trends in the data were consistent across listeners, so only average thresholds are presented. Figure 1 shows the average masked thresholds for the harmonic, inharmonic, and noise maskers for the three presentation levels. There was a trend for the masked threshold to increase with higher probe frequencies. Note that, at each presentation level, the masked thresholds for the noise masker were highest, followed by the inharmonic masker and the harmonic masker. This was the case for the individual listeners as well as the averages shown in the figure.

A repeated-measures analysis of variance found all three factors of masker level, masker type, and probe frequency to be highly significant [$F(2,4)=1579.62$, $p<0.0001$, $F(2,4)=536.24$, $p<0.0001$, and $F(2,4)=34.88$, $p<0.003$, respectively]. Multiple comparisons of means with the Scheffé test showed that the average masked thresholds for the three masker types differed significantly from each other. Further, the average masked threshold for the lowest frequency probe was significantly lower than that for the two higher frequencies, while the latter did not differ. The three-way interaction also reached significance [$F(8,16)=2.715$, $p<0.05$], indicating that the effect of masker type on masked threshold differed as a function of level and probe frequency. However, as suggested by the trends in Fig. 1, this interaction arose from the slightly different effects of level and probe frequency with the noise masker compared to the other two maskers. When the noise masker type was omitted from the analysis, the interaction was not significant [$F(4,8)=1.527$, $p>0.05$].

Figure 2 shows the masked threshold difference between the inharmonic and harmonic maskers as a function of masker level and probe center frequency. Although the figure suggests that these variables may have small effects on the masked threshold difference, the analysis showed that they are not significant in this experiment.

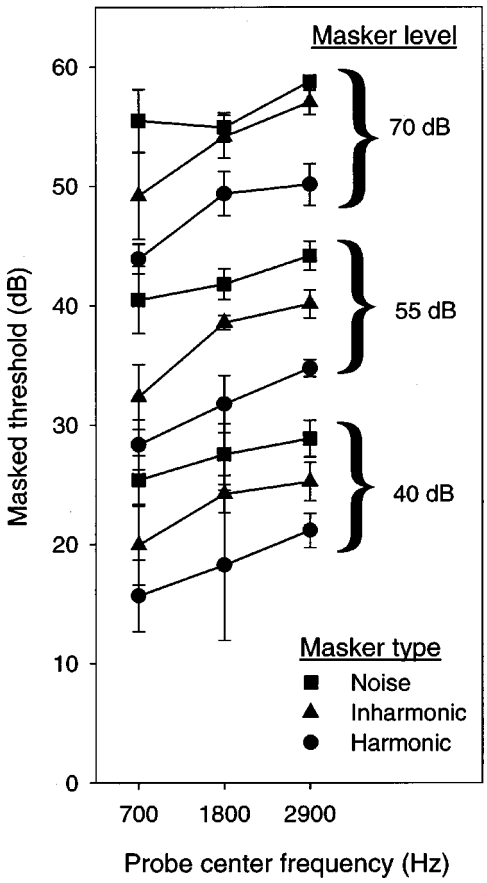

FIG. 1. Masked thresholds with harmonic, inharmonic, and noise maskers. Maskers were presented at overall levels of 40, 55, and 70 dB SPL. All thresholds are the averages of determinations obtained from the same three observers. The vertical bars indicate plus and minus one standard deviation of the threshold estimates.

2. Conclusion

The thresholds with the harmonic masker were significantly lower than the thresholds with the inharmonic masker,

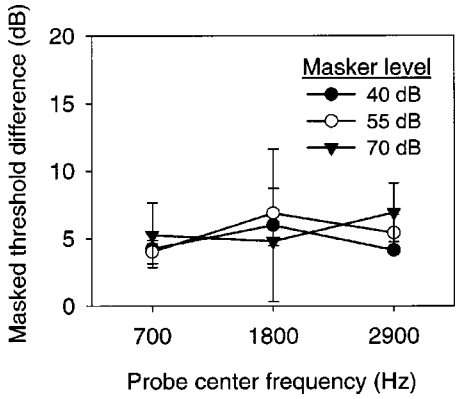

FIG. 2. Differences in masked threshold between inharmonic and harmonic maskers as a function of probe frequency with masker level as the parameter. Differences were obtained from the data shown in Fig. 1. The vertical bars indicate plus and minus one standard deviation of the threshold differences.

and these differences were relatively constant across masker levels. Further, the differences are consistent with the predictions of the envelope modulation rate variability hypothesis. The significant differences found between the inharmonic and noise masker thresholds is likely due to the comparative sparseness of the inharmonic masker spectrum. This difference confirms that the inharmonic masker is a more appropriate control condition than a noise masker for assessing the effect of harmonicity.

Any role of CMR in the harmonicity effect was precluded in this experiment since the harmonic masker partials were not in phase. Consequently, the auditory filter output modulations were not coherent across frequency and thus a condition required for CMR did not occur.

The harmonic masker is distinguished from the inharmonic masker by the precise relationship among the frequencies of the partials, as well as by the periodicity of its envelope. Kohlrausch and Sander (1995) showed that the masked threshold of a probe signal followed the envelope of a harmonic masker even when all of the masker partials were not in phase. Thus, the significantly lower thresholds for the harmonic masker could be due to the periodicity of the envelope. The following experiment investigates the possible role of envelope periodicity, which may encourage a strategy of listening in the dips in the envelope where the probe may be more easily detected.

B. Experiment 2: Listening in the dips

In experiment 1, the precise periodicity of the harmonic masker waveform might have allowed the listener to take advantage of modulation minima to converge on a lower threshold. That is, the harmonic masker yields envelope modulations which are not coherent across channels due to the random phases of the partials, but are all at the same rate. The probe energy might be more easily detected at times when the instantaneous masker energy in the frequency region of the probe is low (Buus, 1985; Kohlrausch and Sander, 1995). Further, the same-rate, across-channel modulations might help to focus attention on the dips in the region of the probe even though the modulations are not coherent.

The listening in the dips explanation of the harmonicity effect was investigated by varying the depth of the dips in the harmonic and inharmonic masker envelopes using coherent and incoherent envelope modulations across channels. Dips in the frequency region of the probe should result in lower masked thresholds, and the presence of coherent across-channel modulations should also lower thresholds (e.g., Hall, 1987). Failure to observe any effects due to changes in envelope modulation coherence and depth will argue against the listening in the dips strategy as an explanation of the harmonicity effect.

The depth of the envelope dips was increased for the harmonic masker by setting the phase of each partial in Table I to zero. The top two panels of Fig. 3 show short samples of the resulting in-phase and random-phase harmonic maskers. Note that the in-phase partials create the conditions required for CMR, which might also explain any observed reduction in threshold for this masker.

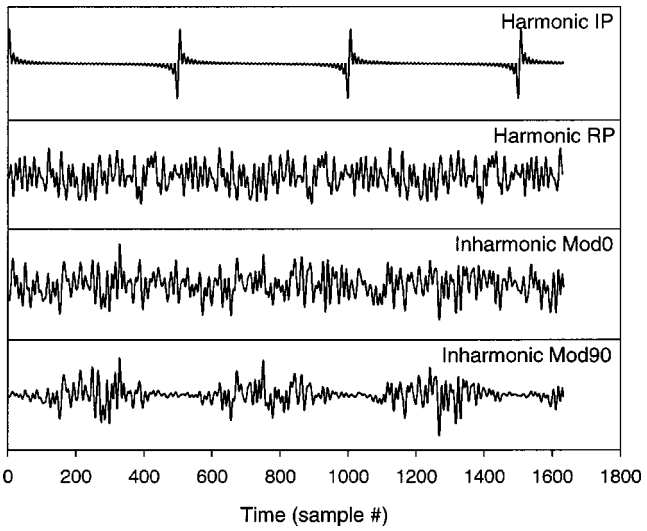

FIG. 3. Harmonic and inharmonic maskers with varying depths of waveform modulation. The abscissa represents sample number (sample rate =44 100 Hz) and the ordinate is a linear amplitude scale. *Harmonic IP*—all partials in phase; *Harmonic RP*—all partials random phase; *Inharmonic Mod0*—no amplitude modulation; *Inharmonic Mod90*—90% sinusoidal amplitude modulation.

For the inharmonic masker, envelope dips were introduced by sinusoidal amplitude modulation with an 88-Hz raised sinusoid (the fundamental frequency of the harmonic masker) to a depth of 90 percent. The lower two panels of Fig. 3 show short samples of the modulated and unmodulated inharmonic maskers. A confounding effect of amplitude modulation is the modulation components or ''sidebands'' added to the spectrum. However, the addition of sidebands should increase the spectral density of the masker, so an increase in threshold is more likely to occur than the predicted decrease. Therefore, if a reduction in threshold is observed, it would not likely be due to the increased spectral content, but would support the listening in the dips strategy.

Note that multiplying the masker with a modulating signal produces a modulation that is coherent across auditory channels, whereas the auditory filter modulations arising from summation of random-phase harmonic partials within each filter passband are not coherent across channels. However, coherent, across-channel modulation would likely allow better prediction of envelope dips in a more restricted range of channels processing the probe than would modulations that are not coherent. If a threshold reduction is not observed with coherent modulations, it would be difficult to argue that the listening in the dips strategy accounts for the lower threshold with the random-phase harmonic masker where the modulations are not coherent.

Overall levels of both the unmodulated and modulated maskers were adjusted to 55 dB SPL. All masker variations were evaluated using an 800-Hz bandwidth noise probe centered at 1800 Hz, similar to that used in experiment 1. The duration of the maskers and probe was 400 ms. Five listeners participated in the experiment.

1. Results and discussion

The average masked thresholds for the unmodulated and modulated maskers are shown in Fig. 4. A two-way

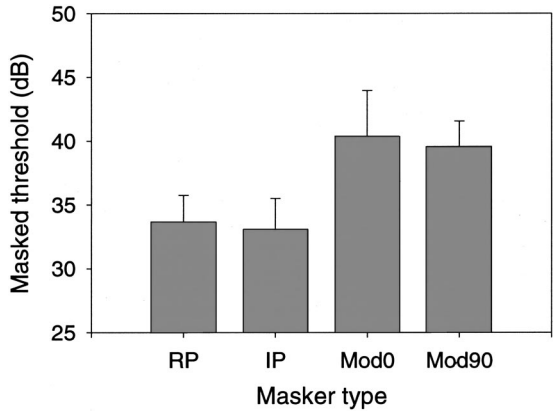

FIG. 4. Average thresholds for modulated and unmodulated maskers. Labels on the abscissa correspond to the masker labels in Fig. 3: *RP*—harmonic, random phase; *IP*—harmonic, in phase; *Mod0*—inharmonic, unmodulated; *Mod90*—inharmonic, modulated. The vertical bars indicate one standard deviation of the threshold estimates.

repeated-measures analysis of variance found a significant main effect of masker type [$F(1,4)=62.397$, $p<0.001$], but no significant effect of modulation and no significant interaction. Therefore, as in experiment 1, the harmonic masker thresholds were significantly lower than the inharmonic masker thresholds. Although there was no overall effect of modulation, one of the five listeners did appear to be sensitive to the effect of masker modulation since he consistently displayed threshold reductions of approximately 4 dB in response to either type of modulation. However, his threshold with the random-phase harmonic masker was still 5 dB lower than the threshold with the modulated inharmonic masker. Since modulating the inharmonic masker did not reduce his threshold to the level obtained with the harmonic masker, masker modulation does not account for the harmonicity effect, even for this listener.

2. Conclusion

The failure to observe a significant effect of masker modulation on masked threshold argues against the hypothesis that the threshold differences result from improved detection of the probe in periodic masker envelope dips where the probe-to-masker energy ratio is higher.

C. Experiment 3: Masker frequency

Experiment 1 found a significant effect of harmonicity on masking by measuring the detectability of a narrow-bandwidth noise probe in 4-kHz bandwidth harmonic or inharmonic maskers. The difference between the masked thresholds obtained from harmonic and inharmonic maskers was not affected significantly by masker level or probe center frequency. The lack of an effect of level is not surprising if the harmonicity effect results from differences in detectability of a change in the variability of auditory filter output modulation rates, since the modulation rates should be relatively unaffected by the overall level of the partials. Similarly, the lack of an effect of probe frequency may also be expected, since the envelope modulation rate depends on the frequency differences between the partials. This was constant for the harmonic masker at all probe positions. On the other hand, the envelope modulations for the inharmonic masker might be expected to increase in variability as a function of auditory filter width as the filter processes more partials. Therefore, the threshold difference might increase with frequency as the increased variability of the filter envelope modulations causes the change in variability due to the noise probe to be more difficult to detect.

TABLE II. Definitions of masker and probe bands.

Band ID	Masker partials (from Table I)	Probe cutoffs (Hz)	Probe f_c (Hz)
1	1–12	125–1025	575
2	7–18	643–1543	1093
3	13–24	1166–2066	1616
4	19–30	1706–2606	2156
5	25–36	2245–3145	2695
6	31–42	2752–3652	3202

The frequency dependence of the harmonicity effect was examined more closely by varying the center frequency of narrow bandwidth maskers and probes. A number of harmonic maskers and corresponding inharmonic maskers were created by selecting 12 consecutive partials from the larger sets shown in Table I. Six frequency bands with 50% overlap were chosen. Each masker band was approximately 970 Hz wide, and a 900-Hz bandwidth probe was always centered in the masker (see Table II for more details). To ensure precise control over bandwidth, each probe was created by summing 600 equal-amplitude sinusoids with both frequency and phase randomly selected from a rectangular distribution. The phases varied between 0 and 360 deg, while the frequencies were constrained to be within the bandwidths specified in Table II. Thus, although the probes were perceptually similar to the Gaussian noise probes in experiment 1, they were quite different in terms of their amplitude distributions. All maskers were presented at an overall level of 55 dB SPL.

Five listeners participated in the experiment. The experiment consisted of six sessions, each comparing harmonic and inharmonic maskers in a different frequency band, and the order of the sessions was randomly determined. The experiment was replicated three times by each listener so that the final individual thresholds were the average of three determinations. The initial sessions for two listeners were repeated after they professed difficulty with the experimental procedure. These were treated as practice sessions for these listeners only.

1. Results and discussion

The trends in masked threshold as a function of center frequency were sufficiently similar for all listeners that only mean thresholds are presented in Fig. 5. The error bars represent the standard deviations measured over listeners. A repeated-measures analysis of variance found significant main effects of frequency band and type of masker [$F(5,20)=72.81$, $p<0.0001$ and $F(1,4)=190.66$, $p<0.0001$, respectively]. Planned comparisons with t tests found that the mean threshold differences were all significantly different from zero for each frequency band. The band

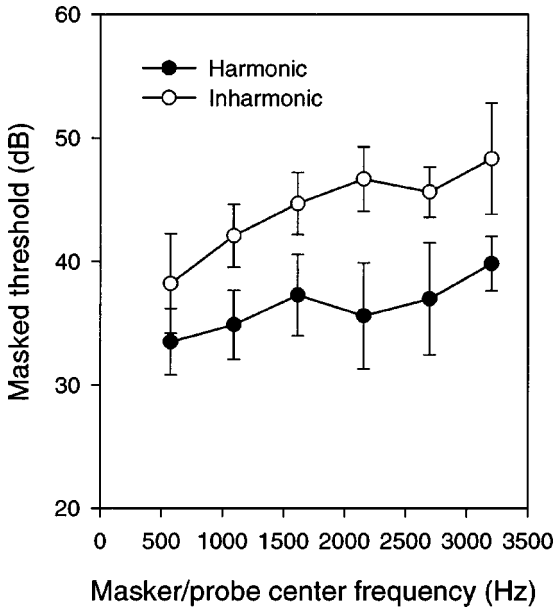

FIG. 5. Masked thresholds as a function of masker/probe center frequency (Hz). Maskers were presented at an overall level of 55 dB SPL. All thresholds are the averages of determinations obtained from five observers. The vertical bars indicate plus and minus one standard deviation of the threshold estimates.

by masker interaction [$F(5,20)=3.53$, $p<0.02$] was also significant. Figure 5 suggests that the thresholds increased more steeply with frequency for the inharmonic maskers than for the harmonic maskers. Comparisons of means using the Scheffé test found bands 1 and 2 to differ from band 6 for each masker type. However, for the inharmonic masker, band 1 also differed significantly from bands 3, 4, and 5. Thus, the slightly steeper rise for the inharmonic masker is confirmed.

The average threshold differences and associated standard deviations are shown in Fig. 6. (The model predictions shown in the figure will be discussed later.) A Scheffé test indicated that only the smallest difference in the lowest band and the largest in the fourth band were significantly different from each other. Thus, the results suggest that the effect of harmonicity is similar in all frequency bands above the lowest band where it is smaller. The larger variance across listeners in the fifth band was due mainly to one listener whose threshold with the harmonic masker was much lower than the thresholds of the other listeners.

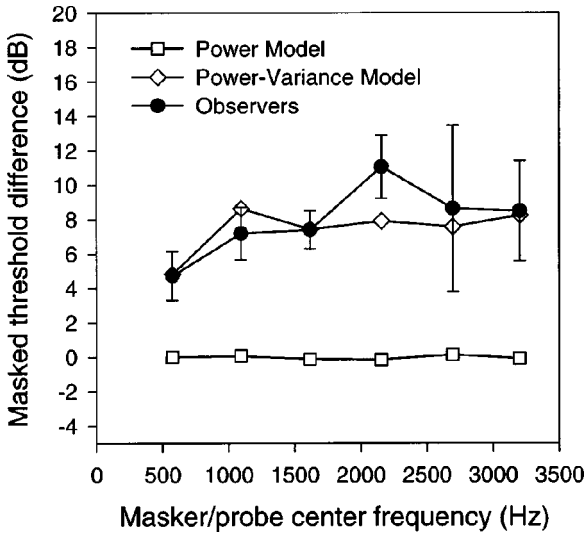

FIG. 6. Differences in masked threshold between inharmonic and harmonic maskers as a function of masker/probe center frequency (Hz). Threshold differences for observers were obtained from the data shown in Fig. 5. The vertical bars indicate plus and minus one standard deviation of the threshold differences. Model differences are those predicted by the models presented in the General Discussion.

TABLE III. Relation between partials/ERB and the threshold difference.

Band ID	Number ERBs	Partials per ERB	Threshold difference (dB)
1	11.7	1.03	4.72
2	6.6	1.82	7.19
3	4.6	2.61	7.40
4	3.6	3.33	11.06
5	2.9	4.14	8.63
6	2.4	5.00	8.49

The significant increase in masked threshold difference between the frequency band near 500 Hz and the band near 2000 Hz shown in Fig. 6 is accompanied by a widening of the auditory filters. The filter width is often expressed in terms of equivalent rectangular bandwidth (ERB) (e.g., Moore, 1997), and the number of ERBs up to a particular frequency is defined as follows:

$$\text{Number of ERBs} = 21.4 \log_{10}(4.37F_{\text{kHz}} + 1). \quad (1)$$

The number of ERBs in each frequency band is shown in Table III, as well as the number of partials per ERB and the average masked threshold difference. The table shows that the threshold difference increased with increasing number of partials per ERB up to the fourth band (i.e., about 2 kHz).

The results of this experiment appear, on the surface, to be somewhat inconsistent with those of experiment 1 where the change in masked threshold difference was not significant when the probe center frequency was varied. Note, however, that the lowest probe frequency in experiment 1 was somewhat higher than the lowest frequency in the present experiment. Further, the mean masked threshold differences for the 55-dB masker in that experiment (Fig. 2) were not very different from the mean differences found in this experiment (Fig. 6), as may be inferred by interpolating between nearby probe center frequencies. The similar threshold differences found in the two experiments suggest that the effect is not influenced significantly by the bandwidth of the masker (4000 vs 970 Hz) or by the statistics of the noise probe (Gaussian versus uniform amplitude distributions).

2. Conclusion

The size of the harmonicity effect differed significantly only between the first band where it was smallest, and the fourth band where it was largest. This difference was mainly due to a steeper rise in threshold with frequency for the inharmonic maskers compared to the harmonic maskers. The steeper rise might have resulted from increasing variability of the modulation rates with filter center frequency. That is,

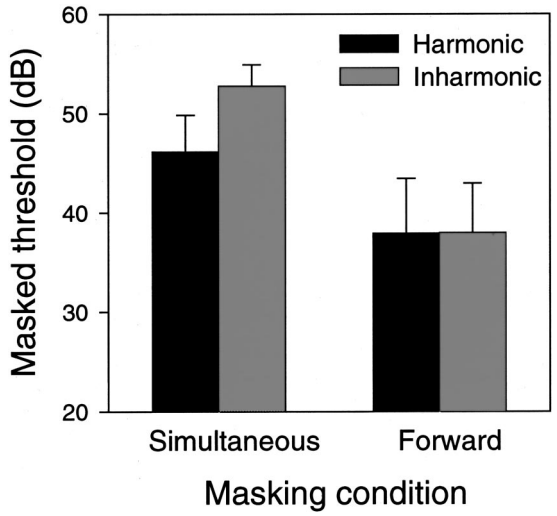

FIG. 7. Masked thresholds with harmonic and inharmonic maskers in simultaneous- and forward-masking experiments. Maskers were presented at an overall level of 55 dB SPL. All thresholds are the averages of determinations obtained from five observers. The vertical bars indicate one standard deviation of the threshold estimates.

the interaction of a larger number of inharmonic partials at higher center frequencies may yield less-consistent output modulations, resulting in increased variability of the dominant modulation rates across filters. Filter width would not have a similar effect with harmonic input, since in this case the dominant modulation rates across filters remain relatively constant. This interpretation is consistent with the hypothesis that the noise probe becomes more difficult to detect as filter modulation rates increase in variability across filters.

D. Experiment 4: Forward masking

The modulation rate variability hypothesis proposes that the cue that facilitates detection in a harmonic masker is the change in modulation rate variability over auditory filters due to the introduction of a noise probe. Such a cue requires the simultaneous presentation of both masker and probe, so the advantage associated with a harmonic masker should be lost with nonsimultaneous masking. This prediction was tested in a forward-masking experiment.

The harmonic and inharmonic maskers were as defined in Table I, and the probe to be detected was the 800-Hz bandwidth frozen, Gaussian noise signal centered on 1800 Hz that was used in experiment 1. The duration of the maskers was 400 ms and the duration of the probe was 20 ms. The maskers and probe had 10-ms raised-cosine onset and offset ramps. The probe was delayed either 300 or 400 ms from the onset of the masker, so that the effects of simultaneous-and forward masking could be compared. Five listeners participated in the experiment.

1. Results and discussion

The average masked thresholds for the simultaneous- and forward-masking conditions are shown for both types of maskers in Fig. 7. The 6.6-dB difference between masker types obtained in the simultaneous-masking condition is similar to that observed previously. However, no difference was observed in the forward-masking condition.

A repeated-measures analysis of variance found significant main effects due to probe delay [$F(1,4)=32.47$, $p<0.005$] and masker type [$F(1,4)=23.69$, $p<0.008$], as well as a significant interaction [$F(1,4)=41.11$, $p<0.003$]. Planned comparisons with t tests showed that the masked threshold difference was significant with a probe delay of 300 ms (i.e., simultaneous masking) but not when the delay was 400 ms (i.e., forward masking).

2. Conclusion

In the simultaneous-masking condition, the masked threshold difference was again observed with a probe that was much briefer than that used previously. However, this difference disappeared with forward masking as predicted by the modulation rate variability hypothesis.

E. Experiment 5: Partial separation

In the previous experiments, the harmonic maskers always had a spacing of 88 Hz between adjacent partials. This frequency separation was small enough that at least two partials fell in the range of any auditory filter. Increasing the separation between the harmonic partials would reduce the possibility of modulated filter outputs due to summation within the passbands of individual filters, and the threshold would only depend on the signal-to-noise ratios in the respective filters. The prediction follows that the harmonicity effect will decline as the distance between partials increases.

This experiment evaluated the effect of frequency separation of the partials on the masked threshold difference. The probe to be detected was the 800-Hz bandwidth Gaussian noise signal centered at 1800 Hz first used in experiment 1. Maskers consisted of the original harmonic masker with partials separated by 88 Hz (Table I), as well as new maskers constructed by selective omission of partials from the original set. Specifically, *mask135* included all odd-numbered partials and *mask246* included all even-numbered partials so that the frequency separation was 176 Hz in both cases. *Mask147* included every third partial starting with the first, *mask258* included every third partial starting with the second, and *mask369* included every third partial starting with the third. For these, the frequency separation between successive partials was 264 Hz. Corresponding partials from the original inharmonic masker were selected to create matching inharmonic maskers. All maskers were presented at an overall level of 55 dB SPL. Three listeners participated in the experiment.

1. Results and discussion

The masked thresholds averaged over listeners are shown in Fig. 8 for each harmonic and inharmonic masker. For the inharmonic maskers, the threshold declined with increases in the frequency separation between the partials. That is, the inharmonic maskers with the larger frequency gaps were less effective at masking the probe. On the other hand, the masked thresholds with the harmonic maskers were less consistently dependent on the frequency separation. At the smallest separation, the average threshold was already almost as low as the masked thresholds at the widest separation.

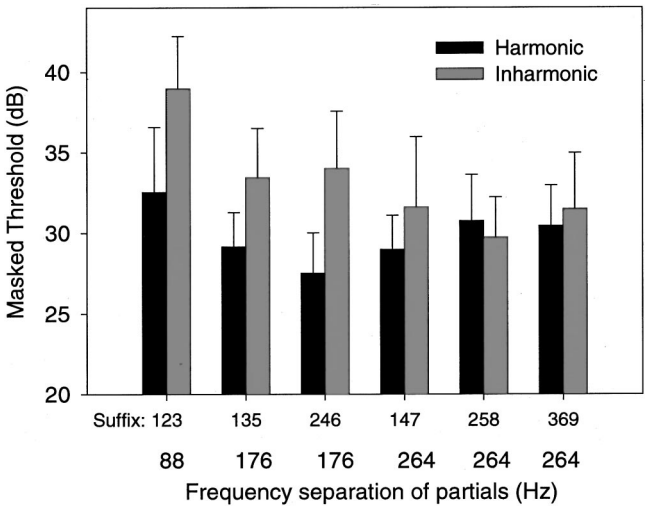

FIG. 8. Effect of partial frequency separation on masked threshold. Maskers were presented at an overall level of 55 dB SPL. All thresholds are the averages of determinations obtained from three observers. The vertical bars indicate one standard deviation of the threshold estimates. The abscissa identifies maskers described in the text by the suffixes of the masker names (e.g., *mask135*). Also shown is the corresponding frequency separation between the partials of each masker.

A repeated-measures analysis of variance found significant effects due to partial separation and type of masker [$F(5,10)=36.78$, $p<0.0001$ and $F(1,2)=71.48$, $p<0.015$, respectively], as well as a significant interaction [$F(5,10)=15.7$, $p<0.0001$]. Planned comparisons of the mean thresholds for the harmonic and inharmonic maskers at each partial separation found all differences to be significant with the exception of the *mask258* and *mask369* partial selections. Each of these maskers had a partial separation of 264 Hz.

Figure 9 shows the average masked threshold difference for each harmonic masker relative to its associated inharmonic masker. (The model data shown in the figure will be discussed later.) The differences obtained with the 176-Hz partial separation were slightly smaller than that obtained with the 88-Hz separation. However, a further increase in the separation to 264 Hz was accompanied by a marked reduction in the threshold difference. The difference was still statistically significant for the *mask147* condition, but not for the *mask258* and *mask369* conditions.

These results show that the masked threshold difference becomes small or nonexistent when the separation between partials in the harmonic series becomes large enough. This suggests that the effect depends on processing more than one partial in each auditory filter. Consistent with this interpretation, the equivalent rectangular bandwidth at the frequency of the probe (1800 Hz) is 219 Hz. Since auditory filters are not rectangular, filters in this region would likely process some energy from two partials with a separation of 176 Hz, but mainly from a single partial with a separation of 264 Hz.

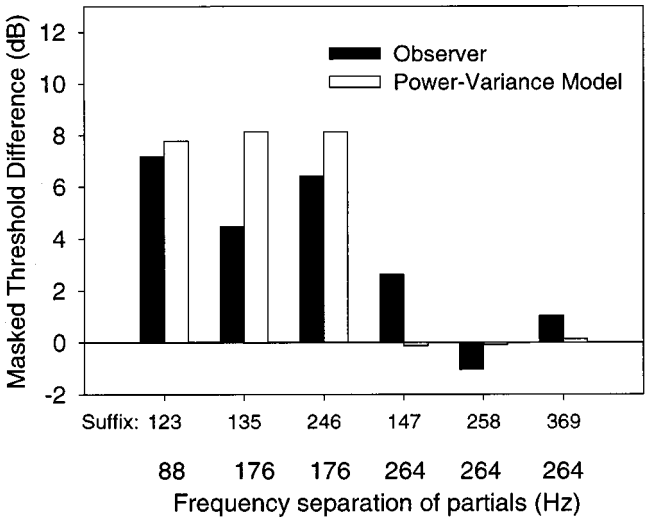

FIG. 9. Differences in masked threshold between inharmonic and harmonic maskers as a function of partial frequency separation. Threshold differences for observers were obtained from the data shown in Fig. 8. Model differences are those predicted by the power-variance model presented in the General Discussion.

2. Conclusion

In agreement with the prediction based on the modulation rate variability hypothesis, the masked threshold difference appears to depend on the interaction of at least two partials within each auditory filter.

F. Experiment 6: Degree of inharmonicity

In general, the threshold for detecting a signal embedded in a background increases with the variability of the background (e.g., Green and Swets, 1969). For the modulation rate variability hypothesis, the background is the pattern of filter output modulations due to the masker, while the signal is a change in this pattern due to the probe. Since the background is less variable for a harmonic masker than for an inharmonic masker, detection of a probe will occur at a lower level for the harmonic masker as observed in the previous experiments. Further, the detection threshold should increase in proportion to the degree of inharmonicity of the masker as reflected by the variance of filter output modulation rates.

The inharmonic masker used as a control condition in previous experiments was always as described in Table I. The frequencies of the partials were determined by perturbing harmonically related frequencies to nearby prime numbers, sometimes by as much as 25 Hz. In this experiment, a new perturbation method was devised that allowed gradations in the degree of inharmonicity. That is, the perturbation was plus or minus a randomly determined real number that was constrained to be less than a specified maximum value. The ranges of maximum perturbations were 2, 5, 10, and 25 Hz. Table IV shows the means and standard deviations of the perturbations employed for each of these ranges. Phases remained as shown in Table I. The model predicts that the masked threshold will increase monotonically as the degree of inharmonicity increases.

The harmonic masker partials were identical to those defined for the fourth frequency band in Table II, which resulted in the largest masked threshold difference in experiment 3. That is, the harmonic masker consisted of partials 19 through 30 in Table I (1672–2640 Hz), and the inharmonic

TABLE IV. Range, mean, and standard deviation of perturbations for each degree of inharmonicity.

Perturbation range (Hz)	Mean perturbation (Hz)	Stand. dev. (Hz)
2	1.16	0.423
5	2.52	1.641
10	4.94	3.037
25	11.31	9.508

maskers were this harmonic masker perturbed by the amounts indicated in Table IV. The noise probe was also identical to that used in experiment 3 for the fourth band. All maskers were presented at an overall level of 55 dB SPL. Five listeners participated in the experiment.

1. Results and discussion

Masked thresholds increased as a function of masker inharmonicity for all listeners. Therefore, only the average thresholds are presented in Fig. 10 along with the associated standard deviations. (The model thresholds shown in the figure will be discussed later.) A repeated-measures analysis of variance yielded a significant effect of perturbation range on masked threshold $[F(4,16)=28.35,\ p<0.0001]$. Planned comparisons with *t* tests showed that the mean threshold for the harmonic masker (i.e., zero perturbation) was significantly different from all the other means, as was the mean for the 25-Hz perturbation range. The 2-Hz perturbation range also differed significantly from the 10-Hz range. No significant difference was found between either the 2- and 5-Hz ranges or the 5- and 10-Hz ranges.

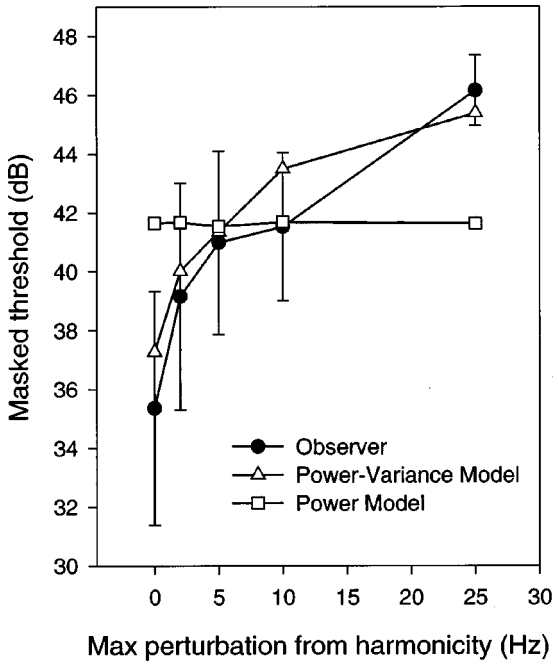

FIG. 10. Masked thresholds as a function of maximum perturbation of the masker from harmonicity. Maskers were presented at an overall level of 55 dB SPL. All thresholds are the averages of determinations obtained from five observers. The vertical bars indicate plus and minus one standard deviation of the threshold estimates. Model thresholds are those predicted by the models presented in the General Discussion.

Figure 10 shows that the variability across listeners decreased with increasing perturbation range. The threshold difference between the zero-perturbation and the 2-Hz perturbation range was roughly the same for all listeners. However, the most practiced listeners also produced the lowest thresholds in this region, suggesting that they may have learned to more effectively use cues that are normally not present with inharmonic maskers. With the largest perturbation range where such cues would presumably not be present, all listeners reached almost the same threshold.

2. Conclusion

As predicted, the masked threshold was lowest when the masker was perfectly harmonic and increased incrementally as inharmonicity increased. The results are consistent with the hypothesis that the increase in threshold with increasing inharmonicity occurs because the probe is more difficult to detect as the filter envelope modulation rate variability becomes larger. Conversely, the random perturbations due to the noise probe are easiest to detect when this variability is small.

G. Experiment 7: Across-channel effects

The envelope modulation rate variability hypothesis explicitly proposes across-channel comparisons to explain the difference in masked thresholds derived from harmonic and inharmonic maskers. That is, the variance is calculated from the envelope modulation rates of a number of auditory filter outputs. However, the previous experiments do not rule out unspecified within-channel differences between the two types of maskers that might also account for the effect on threshold. The issue is addressed in this experiment by manipulating the harmonicity of the masker in frequency bands outside the bandwidth of the probe. If the threshold difference is a within-channel effect, it should disappear under these conditions. Conversely, if it depends on across-channel information, the difference should persist.

A second issue addressed in this experiment is the relation between the fine structure of the probe and masker. In the previous experiments, the noise probes were defined prior to each experiment so that this relationship remained frozen during the experiment. Listeners' thresholds might have been biased by detection of specific interactions between the maskers and probes. For each presentation in this experiment, the 400-ms probe was extracted from a 2500-ms sequence of bandlimited Gaussian noise using a random starting position. Thus, there was never a fixed relationship between the masker and probe fine structure.

A masker band coincident with the bandwidth of the probe was either harmonic or inharmonic, and was accompanied by lower and upper flanking bands that were both either harmonic or inharmonic. The distance between the masker and the flanking bands was also varied to measure the sensitivity of any across-channel effect to frequency separation. The lower, masker, and upper bands ranged from 1408–1848, 1936–2288, and 2376–2816 Hz, or from 1056–1408, 1936–2288, and 2816–3168 Hz, respectively. A harmonic complex was created by selecting harmonic partials from Table I that were within the ranges of the masker band

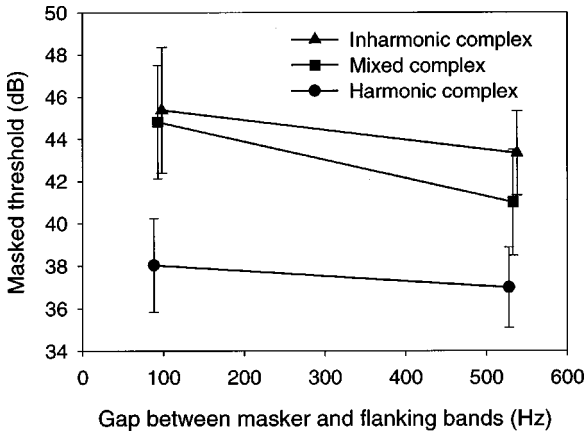

FIG. 11. Masked thresholds for the two distances between masker and flanking bands (88 and 528 Hz—points are offset slightly for clarity). Maskers were presented at an overall level of 55 dB SPL. All thresholds are the averages of determinations obtained from six observers. The vertical bars indicate plus and minus one standard deviation of the threshold estimates.

and both flanking bands. An inharmonic complex was produced by randomly perturbing each partial frequency of the harmonic complex up or down to a maximum of 22 Hz. Finally, a mixed complex was made by replacing the masker band of the inharmonic complex with the original harmonic partials. The probe was created by bandpass filtering Gaussian noise using a digital filter with very sharp cutoffs such that the spectrum level was reduced to zero within 50 Hz. It had a bandwidth of 1976–2238 Hz, which was well inside the masker band.

As in the previous experiments, the inharmonic complex is expected to yield a higher threshold than the harmonic complex. However, the threshold for the mixed complex will be higher than the threshold for the harmonic complex only if auditory channels remote from the probe influence masking (i.e., an across-channel influence). According to the modulation rate variability hypothesis, the inharmonic flanking bands should increase the overall modulation rate variance even though the masker band is harmonic.

All complexes were presented at an overall level of 55 dB SPL. Six listeners participated in the experiment. Four of the six listeners had not participated in any of the previous experiments, and they were given one practice session to familiarize themselves with the experimental procedure.

1. Results and discussion

Figure 11 shows the average thresholds for the three complexes at the two masker-flanking band distances (i.e., 88 and 528 Hz). A repeated-measures analysis of variance found flanking band distance [$F(1,5)=14.138$, $p<0.015$] and the nature of the complex [$F(1,5)=245.033$, $p<0.001$) to be significant, as well as their interaction [$F(2,10)=9.268$, $p<0.005$]. A Scheffé test showed that all means differed significantly from each other ($p<0.05$) with the exception of two pairs. That is, the threshold for the harmonic complex did not change significantly as the flanking band distance increased, and the thresholds for the inharmonic and mixed complexes did not differ significantly at the shortest distance.

The analysis showed that the masked thresholds for both the mixed and inharmonic complexes were significantly higher than the thresholds for the harmonic complex. Since the masker band was the same for the harmonic and mixed complexes, the threshold difference must be due to the nature of the flanking bands. That is, inharmonic flanking bands resulted in a higher masked threshold than harmonic flanking bands when the masker band was harmonic. Further, this difference persisted to a lesser degree even when the flanking bands were moved a considerable distance from the masker band. The threshold difference appears to be an across-channel effect since the masker and flanking bands were in different critical bands, particularly at the wider separation.

2. Conclusion

The across-channel influence is evidence that specific within-channel interactions between masker and probe fine structure are not responsible for the harmonicity effect. Further, observance of the effect with random relationships between masker and probe eliminates the possibility that consistent cues arising from frozen masker–probe interactions contributed to the effect in previous experiments.

IV. GENERAL DISCUSSION

The introduction proposed the modulation rate variability hypothesis, which predicts a decrease in the masked threshold of a noise probe due to masker harmonicity. It was recognized that partials of a complex masker interact to modulate auditory filter outputs, and that the modulation rates may vary across filters depending on the frequency differences among the partials. The hypothesis proposes that when the variability due to the masker is low, the change in variability due to a noise probe near threshold is easier to detect than when the variability due to the masker is higher. Since the expected variability for a harmonic masker is smaller than that for an inharmonic masker, the detection threshold should also be lower for the harmonic masker.

In agreement with the hypothesis, the experiments showed a consistently lower masked threshold due to masker harmonicity. Further, this difference:

(1) was not affected by masker level;
(2) was smallest when the masker and probe were below 1 kHz, and was significantly larger in the region around 2–3 kHz, possibly due to increasing modulation rate variability with the inharmonic masker;
(3) was not observed with forward masking;
(4) did not appear to be due to a listening-in-the-dips strategy since the effects of large masker modulations were not significant;
(5) disappeared when the frequency separation of the partials became excessive;
(6) increased gradually as masker inharmonicity increased; and
(7) was observed to be an across-channel effect.

Consistent with the modulation rate variability hypothesis, the experiments showed that the masked threshold dif-

ference appears to depend on interactions of partials within individual auditory filters. Such interactions produce filter output modulations that can be measured using a filter bank that simulates the auditory filters. A model of harmonicity for predicting the threshold difference is proposed based on measurements of envelope modulation rate variability.

A. A model of harmonicity

The modulation rate variability hypothesis assumes that the listener's decision process has available the array of auditory filter output modulation rates. Detecting the presence of a noise probe is facilitated by a change in the variability of these modulation rates. The variance of the modulation rates for a harmonic masker should be negligible. However, the variance for an inharmonic masker may be much larger, since the filter outputs are modulated at various rates depending on the input frequencies. The noise probe randomly alters the variance of the array of auditory filter output modulation rates, and the change in variance should be more easily discerned against a constant background due to the harmonic masker than against the more variable background due to the inharmonic masker. Therefore, a higher threshold is predicted for the noise probe embedded in an inharmonic masker than when it is embedded in a harmonic masker.

The harmonicity of a given stimulus may be measured directly by analyzing the envelope modulations of simulated auditory filter outputs. A suitable filter for this purpose, first proposed by Patterson *et al.* (1992), is the ''gammatone'' filter. A gammatone filter bank, described in detail by Slaney (1993), was implemented to process a short segment of each masker employed in the above experiments. In this implementation, the widths of the filters did not vary with input level. The center frequencies of successive filters were incremented by 10 Hz. The output of each filter was processed with the Hilbert transform to obtain the envelope. An autocorrelation applied to the envelope gave an estimate of the period of the modulation frequency.

A measure of harmonicity, R_v, was defined as the variance of the modulation rates across filters represented by the periods measured with the autocorrelation. However, this ideal was compromised somewhat in practice. An occasional problem that occurred with noise input was the failure to observe any peak in the autocorrelation function due to the absence of envelope periodicity. In this case, generating a random modulation period from a uniform distribution seemed more appropriate than ignoring the filter altogether. A second complication was the lack of an adequate criterion for selecting a peak of the autocorrelation function. For example, the peak corresponding to a rate of 44 Hz sometimes had a slightly larger magnitude than the peak corresponding to 88 Hz, the actual fundamental frequency. Thus, selection of a period based on maximum peak magnitude severely distorted the variance measurement across filters. Our solution was to select the peak with the largest magnitude, but to regard integer multiples and submultiples of the modulation periods across filters to be equivalent. This was done by calculating the mean of the minimum deviation of each filter's period from the closest integer multiple or submultiple of each other filter's period. R_v was calculated as the variance of the mean deviations over filters.

A modulation filter bank (e.g., Dau *et al.*, 1996) is a biologically plausible model for measuring modulation rates of peripheral filter outputs. A plausible mechanism to measure and take into account the effect of modulation rate variability is also desirable. However, we chose to adopt the computational methods described in this paper to investigate the importance of R_v in accounting for the harmonicity effect, and to justify consideration of more plausible implementations.

B. Simulations with an auditory model

An auditory model capable of predicting detection thresholds was constructed using the gammatone filter bank along the lines proposed by Martens (1982). Martens described a detection model based on a linear combination of three variables. The first, E_p, was the average power of the filter envelopes. The second, E_v, was the variance (in dB) of each filter envelope over time averaged over the filters, and the third was the maximum magnitude of the critical band envelope spectrum, which gives the power of the dominant modulating frequency.

Martens (1982, p. 402) considered E_p to be of primary importance for predicting the threshold of a noise probe. Accordingly, a linear regression employed E_p to predict the average observer thresholds found in experiment 1 with the noise masker. The resulting power model thresholds obtained from Eq. (2) gave a correlation of 0.99 between the thresholds predicted for the noise masker and the corresponding observer thresholds. Although this model works well given a noise masker, the thresholds observed for the harmonic and inharmonic maskers were not predicted as accurately. The correlation between the predicted and observed thresholds for the three types of maskers combined was 0.95.

$$\text{Thresh}_{\text{dB}} = E_p - 2.12. \tag{2}$$

The relationship between the power model predictions and the measured thresholds for the three masker types of experiment 1 are shown in Fig. 12. The regression lines for the harmonic, inharmonic, and noise maskers are clearly separated. For the harmonic and inharmonic maskers, the model thresholds were consistently too high. Clearly, this model fails to take into account properties of these maskers that result in lower observer thresholds. The model's threshold determinations might be rendered more accurate by incorporating the measure of harmonicity derived from the filter bank.

The additional effect of masker harmonicity on masked thresholds was calibrated using the data from experiment 1 as well as experiment 5. Note that the envelope modulation rate variance (R_v) is low when the modulations have a high amplitude and are the same for all the filters (i.e., for the harmonic maskers). It should also assume a low value, however, when the modulation amplitude is low, but still capable of producing large-amplitude peaks in the autocorrelation functions (i.e., for the maskers with widely separated partials). A suitable criterion for recognizing the occurrence of such unimportant, low-amplitude modulations is the energy

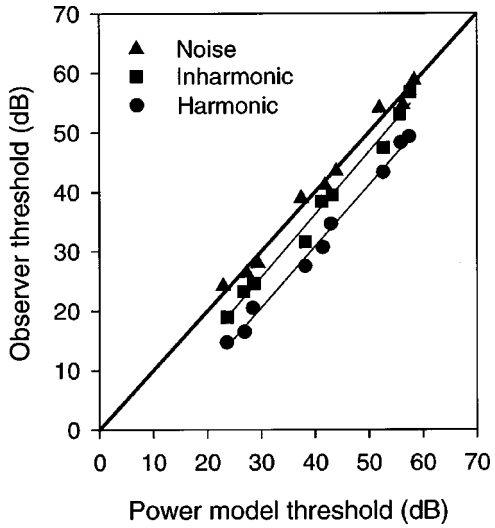

FIG. 12. Power model thresholds [Eq. (2)] versus observer thresholds as a function of noise, inharmonic, and harmonic maskers. Maskers and probes from experiment 1 were processed by the filter bank model to obtain the power measurements needed to generate the model threshold predictions.

ratio, $E_v - E_p$, which is sensitive to the average peak-to-peak amplitude relative to the average envelope energy. In practice, R_v was assigned a value of zero when $E_v - E_p$ was less than -20 dB.

The two conditions leading to a small R_v were present in the combined data taken from experiment 1 and experiment 5. Experiment 1 included harmonic, inharmonic, and noise maskers presented at three different levels. Experiment 5 included harmonic and inharmonic maskers with partial frequencies separated by more than the filter bandwidths. A linear regression was performed on the combined data sets to predict the observed thresholds using E_p and the logarithm of R_v. Since R_v increased exponentially with inharmonicity, the logarithm of R_v gave a better-fitting linear model. The result of the regression analysis is Eq. (3). The correlation between the observer thresholds for the calibration data and the corresponding thresholds given by Eq. (3) was 0.98.

$$\text{Thresh}_{\text{dB}} = E_p + 2\log_{10}(R_V + 1) - 13.75. \quad (3)$$

The performance of the power-variance model expressed by Eq. (3) was tested with independent data sets from experiment 3 and experiment 6. In these experiments, the maskers had narrower bandwidths than in experiment 1, and the harmonicity values varied somewhat with frequency band because of the associated differences in auditory filter bandwidths (experiment 3), as well as with the varying degrees of perturbation of partial frequencies (experiment 6). The upper panel of Fig. 13 shows the power model threshold estimates given by Eq. (2) versus the 17 observer thresholds, while the lower panel shows the power-variance model thresholds given by Eq. (3) versus the observer thresholds. The power-variance model predictions ($r = 0.96$, slope $= 0.84$) are an improvement over the predictions based solely on power ($r = 0.48$, slope $= 0.21$). The difference between the correlations is statistically significant ($Z = 3.76$, $p < 0.0003$) as determined using the Fisher r to Z transform (Hays, 1963).

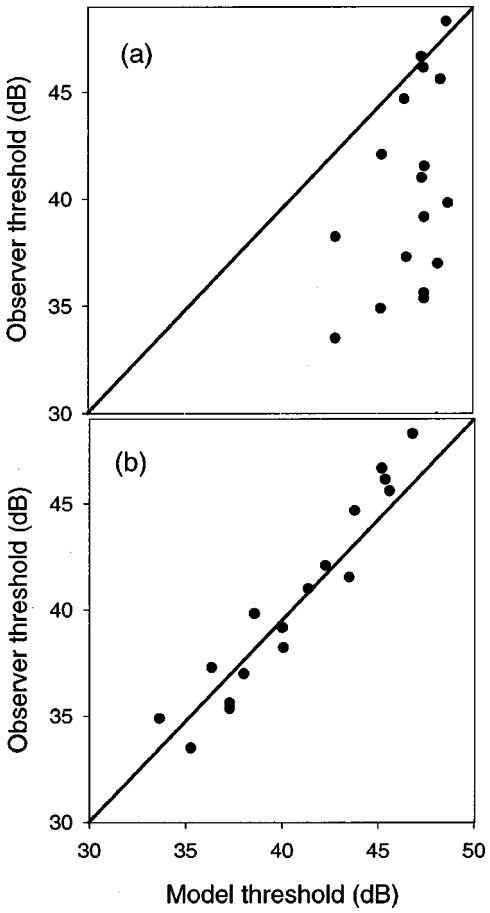

FIG. 13. Effect of the harmonicity measurement weighting on masked threshold predictions; (a) no weighting [Eq. (2), power model]; (b) weighting with harmonicity [Eq. (3), power-variance model]. Maskers and probes from experiments 3 and 6 were processed by the filter bank model to obtain the power and modulation rate variance measurements needed to generate the model threshold predictions. The diagonal represents perfect prediction.

The differences in masked thresholds predicted by the power model and the power-variance model for experiment 3 are shown in Fig. 6 to facilitate comparison with the observer data. Figure 10 shows the masked thresholds predicted for experiment 6. Clearly, much better predictions of the average observer thresholds and threshold differences were obtained from the power-variance model. Recall that the difference in masked threshold for the lowest-frequency band in Fig. 6 was thought to be significantly smaller than that in the fourth band because of a difference in envelope modulation rate variance for the inharmonic masker. Consistent with this hypothesis, the measured variance in the lower-frequency band was half that in the higher band.

The harmonicity calculation is sensitive to the separation of the partials because of the limited bandwidths of the auditory filters. Equation (3) was fitted with this in mind by including the data from experiment 5 where the separation between adjacent partials varied from 88 to 264 Hz. The harmonicity effects predicted by the power-variance model are quite close to the observer threshold differences, as can be seen in Fig. 9. In contrast, the power model predicted differences that were all close to zero. For all cases with the partial separation of 264 Hz, R_v was zero because of the small average envelope variance, E_v, relative to E_p, so the

term containing this variable in Eq. (3) was effectively eliminated. Thus, inharmonicity in the model has its effect only when partials are sufficiently close together to produce a relatively large envelope modulation in the output of the filters.

The amplitude modulation of the inharmonic masker in experiment 2 might be expected to reduce the envelope modulation rate variance found in the corresponding unmodulated masker. Instead, measurements showed only a minor decrease in $\log(R_v+1)$ with the addition of imposed modulation (Mod0=2.85 versus Mod90=2.78). Since $\log(R_v+1)$ ranges from 0.0 (e.g., for a harmonic masker) to about 3.0 (e.g., for a Gaussian noise masker), this is a relatively small change. It is consistent with the nonsignificant difference in the observed thresholds (Mod0=40.3, Mod90 =39.6), and is what would be expected according to the envelope modulation rate variability hypothesis.

An alternative hypothesis for explaining the harmonicity effect was suggested by an anonymous reviewer. Specifically, the noise probe may be detectable at lower levels with a harmonic masker because it disrupts the pitch sensation arising from the regularity in the envelope and/or the fine structure (e.g., Yost *et al.*, 1998). The inharmonic masker has neither regularity in its fine structure nor envelope periodicity. However, this hypothesis might be difficult to distinguish from the envelope modulation rate variability hypothesis since low variability is likely inseparable from periodic fine structure. Iterated rippled noise (Yost *et al.*, 1998), for example, has periodic fine structure, but also imposes a common modulation rate across a range of auditory filters. In this sense, the iterated noise stimulus is similar to a harmonic complex. It is interesting to note that an iterated noise masker also resulted in a lowered threshold for a noise probe compared to a noise masker (Patterson and Datta, 1997).

V. CONCLUSIONS

The experimental results support a model in which detection of a noise probe near threshold is facilitated by a change in the pattern of modulations over auditory filter outputs. Detection of such a change becomes more difficult as the modulation rate variance due to the masker increases. In terms of signal detection theory, the modulation rate variance is analogous to background noise level, so the threshold for detecting a change in the variance due to the probe rises as the modulation rate variance increases. The importance of envelope modulation rate variance is indicated by its role in significantly improving threshold predictions when maskers vary in harmonicity.

According to this model, a harmonic masker with a fundamental frequency smaller than the passband of the auditory filters generates filter outputs that have a dominant envelope modulation equal to the fundamental frequency. A similar inharmonic masker also generates modulated filter outputs, but the modulation rates vary across filters. A harmonicity calculation based on the variability of envelope modulation rates obtained from a gammatone filter bank reflected this difference between harmonic and inharmonic maskers. Threshold predictions based on this measure of harmonicity combined with masker energy yielded more accurate predictions of observed thresholds than the masker energy alone. The envelope modulation rate variability hypothesis successfully explains the main experimental results. In particular:

(a) For a given perturbation from harmonicity, the masked threshold difference in a given frequency band is predicted to increase with auditory filter bandwidth. This is due to the increased variability of envelope modulations for inharmonic inputs as the wider bandwidth filters pass more partials. Experiment 3 agreed with this prediction to some extent in that the difference in masked threshold in the lowest frequency band was significantly smaller than in the fourth band where the filters are wider. Further, simulations with the filter bank model found a larger modulation rate variance in the fourth band than in the first band.

(b) The measure of harmonicity is not influenced by masker level since modulation rate is not affected by level. Accordingly, experiment 1 found no significant effect of masker level on the masked threshold difference due to harmonicity.

(c) The difference in masked threshold is reduced or eliminated when the frequency separation between partials becomes larger than the passband of the auditory filters. This effect was observed in experiment 5.

(d) The model predicts the failure to obtain a difference in masked threshold with forward masking in experiment 4 since coherence of masker modulations cannot be disrupted after offset of the masker.

(e) The model predicts that thresholds will be affected by envelope modulation rate variance in auditory channels outside the bandwidth of the probe. This was observed in experiment 7 by manipulating harmonicity in bands flanking the masker.

The concept of envelope modulation rate variability offers a scale for measuring the degree to which a complex audio signal departs from harmonicity. The zero point on this scale represents a harmonic signal while the high end corresponds to a random noise signal. The experiments show that the accuracy of psychoacoustic models would be improved by incorporating this dimension.

ACKNOWLEDGMENTS

We thank the reviewers for useful comments on this manuscript, as well as all the listeners who generously gave of their time to participate in the experiments.

Buus, S. (**1985**). ''Release from masking caused by envelope fluctuations,'' J. Acoust. Soc. Am. **78**, 1958–1965.

Dau, T., Püschel, D., and Kohlrausch, A. (**1996**). ''A quantitative model of the 'effective' signal processing in the auditory system. I. Model structure,'' J. Acoust. Soc. Am. **99**, 3615–3622.

Green, D. M., and Swets, J. A (**1966**). *Signal Detection and Psychophysics* (Wiley, New York).

Grose, J. H., and Hall, J. W. (**1989**). ''Comodulation masking release using SAM tonal complex maskers: Effects of modulation depth and signal position,'' J. Acoust. Soc. Am. **85**, 1276–1284.

Hall, J. W. (**1986**). ''The effect of across-frequency differences in masking level on spectro-temporal pattern analysis,'' J. Acoust. Soc. Am. **79**, 781–787.

Hall, J. W. (**1987**). ''Experiments on comodulation masking release,'' in *Auditory Processing of Complex Sounds*, edited by W. A. Yost and C. S. Watson (Erlbaum, Hillsdale, NJ).
Hall, J. W., and Grose, J. H. (**1988**). ''Comodulation masking release for multicomponent signals,'' J. Acoust. Soc. Am. **83**, 677–686.
Hall, J. W., Hagggard, M. P., and Fernandes, M. A. (**1984**). ''Detection in noise by spectro-temporal pattern analysis,'' J. Acoust. Soc. Am. **76**, 50–56.
Hays, W. L. (**1963**). *Statistics for Psychologists* (Holt, Rhinehart and Winston, New York).
Kohlrausch, A., and Sander, A. (**1995**). ''Phase effects in masking related to dispersion in the inner ear. II. Masking period patterns of short targets,'' J. Acoust. Soc. Am. **97**, 1817–1829.
Levitt, H. (**1971**). ''Transformed up–down methods in psychophysics,'' J. Acoust. Soc. Am. **49**, 467–477.
Ma, C., and O'Shaughnessy, D. (**1994**). ''The masking of narrowband noise by broadband harmonic complex sounds and the implications for the processing of speech sounds,'' Speech Commun. **14**, 103–118.
Martens, J-P. (**1982**). ''A new theory for multitone masking,'' J. Acoust. Soc. Am. **72**, 397–405.
Moore, B. C. (**1997**). *An Introduction to the Psychology of Hearing* (Academic, New York).
Patterson, R. D., Robinson, K., Holdsworth, J., McKeown, D., Zhang, C., and Allerhand, M. H. (**1992**). ''Complex sounds and auditory images,'' in *Auditory Physiology and Perception*, edited by Y. Cazals, L. Demany, and K. Horner (Pergamon, Oxford), pp. 429–446.
Patterson, R. D., and Datta, A. J. (**1976**). ''Detecting iterated rippled noise (IRN) in IRN: The spectral position of the listening band,'' Br. J. Audiol. **31**, 131.
Plomp, R. (**1967**). ''Beats of mistuned consonances,'' J. Acoust. Soc. Am. **42**, 462–475.
Slaney, M. (**1993**). ''An efficient implementation of the Patterson-Holdsworth auditory filter bank,'' Apple Computer Technical Report #35, Apple Computer Inc.
Terhardt, E. (**1974**). ''On the perception of periodic sound fluctuations (roughness),'' Acustica **30**, 201–213.
van der Heijden, M., and Kohlrausch, A. (**1995**). ''The role of envelope fluctuations in spectral masking,'' J. Acoust. Soc. Am. **97**, 1800–1807.
Yost, W. A., Patterson, R., and Sheft, S. (**1998**). ''The role of the envelope in processing iterated rippled noise,'' J. Acoust. Soc. Am. **104**, 2349–2361.
Zwicker, E., and Fastl, H. (**1999**). *Psychoacoustics: Facts and Models* (Springer, Heidelberg, Germany).

Manipulating the "straightness" and "curvature" of patterns of interaural cross correlation affects listeners' sensitivity to changes in interaural delay

Constantine Trahiotis, Leslie R. Bernstein, and Michael A. Akeroyd
Surgical Research Center, Department of Surgery (Otolaryngology), and Department of Neuroscience, University of Connecticut Health Center, Farmington, Connecticut 06030

(Received 3 March 2000; revised 6 September 2000; accepted 28 September 2000)

The purpose of this study was to test the hypothesis that stimuli characterized by ''straight'' trajectories of their patterns of cross correlation foster greater sensitivity to changes in interaural temporal disparities (ITDs) than do stimuli characterized by more ''curved'' trajectories of their patterns of cross correlation. To do so, sensitivity to changes in ITD was measured, as a function of duration, using a set of ''reference'' stimuli that yielded differing relative amounts of straightness within their patterns of cross correlation while keeping the dominant trajectory at or near midline. The relative amounts of straightness were manipulated by employing specific combinations of bandwidth, ITD, and interaural phase disparity (IPD) of Gaussian noises centered at 500 Hz. The results were consistent with expectations in that the patterning of the threshold ITDs revealed increasingly poorer sensitivity as greater and greater curvature was imposed on the dominant, ''midline,'' trajectory. The variations in threshold ITD across the stimulus conditions can be accounted for quite well quantitatively by assuming either that the listeners based their judgments on changes in the position of the most central peak of the cross-correlation function or that they based their judgments on changes in the centroid of a second-level cross-correlation function. In a second experiment, binaural detection was measured using a subset of the reference stimuli as maskers. As expected, sensitivity was poorest with the maskers characterized by the greatest curvature, which were also those having the lowest interaural correlation. [DOI: 10.1121/1.1327579]

PACS numbers: 43.66.Pn, 43.66.Ba, 43.66.Dc [DWG]

I. INTRODUCTION

Historically, much of our understanding of binaural detection and the localization and lateralization of sounds has stemmed from investigations that focused on the roles of interaural temporal differences (ITDs), interaural intensitive differences (IIDs), and interaural phase differences (IPDs). Many of these investigations and the classical models that account for much of the data yielded by them are summarized in reviews by Colburn and Durlach (1978), Yost and Hafter (1987), Colburn (1996), and Hafter and Trahiotis (1997).

Recently, new findings have validated and extended Jeffress' (1972) contention that across-frequency consistency of information concerning interaural timing is an additional factor that influences the intracranial position of acoustic images (e.g., Stern *et al.*, 1988; Trahiotis and Stern, 1989; Buell *et al.*, 1994). The effects of across-frequency consistency of interaural timing information reported in those studies were quite dramatic. When very large external delays were applied, only stimuli having sufficiently broad bandwidths were perceived as having an intracranial locus commensurate with the external delay.

Stern *et al.* (1988) and Stern and Trahiotis (1992) suggested how across-frequency effects on lateralization can be accounted for by extending cross-correlation-based models. Their explanation was based on two aspects of a putative internal binaural representation of the stimuli: (1) ''straightness,'' which refers to the extent to which maxima in the interaural cross correlation of the stimuli are consistent in the sense that they appear at the same internal delay over a range of frequencies; and (2) ''centrality,'' which refers to the extent to which maxima of the cross-correlation function are located at or near internal delays of small magnitude. Within this framework, straightness and centrality are cast as two sometimes conflicting weighting functions that determine the relative salience of individual peaks of the cross-correlation function. For some stimulus conditions, centrality outweighs straightness and determines lateral position. For others, straightness outweighs centrality.

Now, if a listener's task were to detect a change in ITD, which can be thought of as a horizontal translation of the pattern of cross correlation, then one might expect that the change in ITD would be most discernible for the straightest trajectories. Those are the trajectories which are characterized by having the least ''variance,'' or inconsistency, along the ITD axis. Said differently, changes in the ''placement'' of the peaks of activity would be expected to be most discernible when the width or variance of a trajectory of the cross correlation which mediates performance is minimized. Such an expectation is consistent with commonly utilized mean-to-sigma relations that underlie decision statistics used in a myriad of psychophysical contexts.

We wished to test the hypothesis that ''straighter'' trajectories can foster greater sensitivity to changes in ITD than more curved trajectories. To do so, we conducted an experi-

ment in which we measured sensitivity to changes in ITD using a set of stimuli that yielded differing relative amounts of straightness. The relative amounts of straightness were manipulated by employing specific combinations of bandwidth, ITD, and IPD of Gaussian noises centered at 500 Hz.

In a previous experiment, Saberi (1995) compared threshold ITDs obtained with bands of noise that were ''comodulated'' across frequency to threshold ITDs obtained with bands of noise whose envelopes were independent across center frequency. Based on the results of Trahiotis and Stern (1994), the effects of straightness would be expected to be especially salient for comodulated bands of noise because they would produce temporally coincident activity across the channels that processed each of the individual bands of noise.

Consistent with these expectations, Saberi (1995) observed lower threshold ITDs for comodulated bands of noise and comodulated sinusoidally amplitude-modulated tones when the stimuli were centered at high spectral frequencies (2550 and 3350 Hz). The ITDs imposed on those stimuli were conveyed by their envelopes. In contrast, Saberi did not observe lower threshold ITDs for comodulated vs independent low-frequency bands of noise centered at 500 and 750 Hz, frequencies for which ITDs are conveyed by the entire waveform (i.e., fine structure and envelope). We surmised that no enhancement of performance was observed for the low-frequency stimuli because they may have fostered such great sensitivity to changes in ITD that potential additional effects resulting from the enhancement of straightness via comodulation could not be observed.

We wished to conduct an experiment that would minimize or preclude such ''floor effects,'' and perhaps reveal effects of straightness on threshold ITDs for low-frequency stimuli. In order to do so, we utilized short-duration stimuli (i.e., 20-, 60-, and 100-ms-long), for which threshold ITDs are commonly found to be elevated as compared to those obtained with longer duration stimuli (e.g., Tobias and Zerlin, 1959; Houtgast and Plomp, 1968; Ricard and Hafter, 1973). It will be seen that sensitivity to changes in ITD for low-frequency stimuli can be substantially affected by the relative straightness of their patterns of cross correlation.

II. EXPERIMENT 1

A. Procedure

Discrimination of ITD was measured using Gaussian noises centered at 500 Hz and having bandwidths of either 50, 100, 200, or 400 Hz. The duration of the noises was either 20, 60, or 100 ms (including 3-ms cosine^2 rise–decay times). For each combination of bandwidth and duration, four combinations of ITD (μs)/IPD (deg) served as ''reference'' conditions against which an increment in the ITD was to be detected. The combinations of ITD/IPD were: 0/0, $-500/90$, $-1000/180$, $-1500/270$, with positive values indicating a lead to the right ear. These four combinations of ITD/IPD produce trajectories of the cross-correlation pattern that pass through an ITD of zero at 500 Hz. These ''central'' trajectories decreased in straightness as the magnitudes of the ITD and the IPD were increased (i.e., the central trajectory was the most straight for the 0/0 combination and the most curved for the $-1500/270$ combination). It is important to note that all four of these reference stimuli were perceived as being at or near midline, independent of their bandwidth. Thus, as intended, potentially conflicting effects resulting from straightness and centrality (that do occur for other such stimuli) were effectively avoided and the central trajectories of the patterns of cross correlation for all four stimuli remained dominant.

The stimuli were presented in a four-interval, two-cue, two-alternative, temporal forced-choice task. Each trial consisted of a warning interval (400 ms) and four observation intervals separated by 300 ms. Intervals were marked by a visual display on a computer monitor. The first and fourth intervals contained a particular reference, depending on the condition being tested. The increment in ITD to be detected was imposed on the reference presented in either the second or the third interval, with equal *a priori* probability. The remaining interval, like the first and fourth intervals, contained a reference band of noise. Independent tokens of noise were presented both within and across trials. The listeners were instructed to respond according to which of the intervals was ''different,'' and that a reliable cue for doing so would be a rightward ''shift'' of the intracranial image. Correct-answer feedback was provided after each response.

The magnitude of the increment in ITD was varied adaptively in order to estimate 70.7% correct (Levitt, 1971). The initial step size of the adaptive track was 2 dB (i.e., ITD was increased or decreased by a factor of 1.58) and was reduced to 1 dB (a factor of 1.26) and to 0.5 dB (a factor of 1.12) after two reversals occurred at each of the former step sizes. A run was terminated after 12 reversals using the 0.5-dB step size and estimates of threshold were calculated using the average level of ITD across the last ten reversals. Final thresholds were calculated by averaging four estimates of threshold for each listener and for each stimulus condition.

The combinations of ITD/IPD were visited in the order: 0/0, $-500/90$, $-1000/180$, $-1500/270$. Testing began with stimuli that had a duration of 20 ms. For each combination of ITD and IPD, one of the four bandwidths was chosen at random and a pair of threshold ITDs was obtained. Next, a new bandwidth was chosen at random and another pair of threshold ITDs was obtained. This process was repeated until all four bandwidths had been utilized. The process described above was repeated with stimuli that had a duration of 100 ms. Then, a second pair of threshold ITDs was obtained as described with the order of the reference ITD/IPD combinations and the durations reversed. That is, the reference ITD/IPD combinations and the two durations were visited in a counterbalanced fashion. Finally, the process was repeated in counterbalanced fashion as described above with the duration of the stimuli being 60 ms.

All stimuli were generated digitally with a sampling rate of 20 kHz via a TDT array processor and PowerDac. All bands of noise were essentially rectangular. They were constructed in the frequency domain by setting the magnitudes of spectral components outside the nominal passband to zero

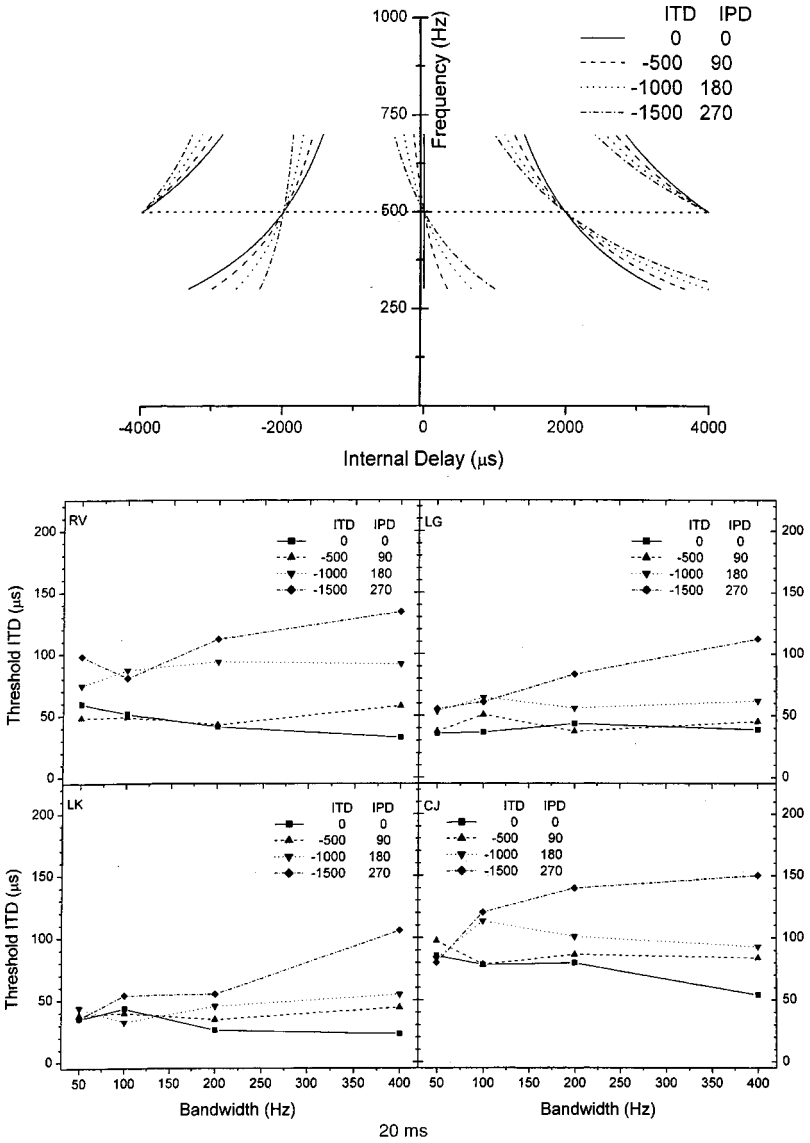

FIG. 1. Lower portion: Threshold ITDs obtained with the 20-ms-long stimuli plotted as a function of bandwidth for each of the four listeners, respectively. The parameter within each panel is the combination of ITD and IPD that was imposed on the bands of noise that served as the reference. Upper portion: Depiction of the trajectories of the cross correlation for each of the four reference stimuli.

before applying an inverse fast Fourier transform (FFT). The magnitudes of components within the passband had a Rayleigh distribution. Stimuli were low-pass filtered at 8.5 kHz (TDT FLT2) and presented via TDH-39 earphones (mounted in MX/41-AR cushions) to listeners seated in single-walled IAC booths. The level of the stimuli was 65 dB SPL. Four young adults with no evidence or history of hearing loss served as listeners. The listeners received extensive practice before the formal collection of data began.

B. Results and discussion

Figure 1 contains the threshold ITDs obtained when the duration of the stimuli was 20 ms. The top portion of the figure depicts the trajectories of the cross correlation for each of the four reference stimuli. Note that the four types of lines used to distinguish among the four reference stimuli are also used in the lower portion of the figure. The four panels in the lower portion of the figure contain the thresholds plotted as a function of bandwith for each of the four listeners, respectively. The parameter within each panel is the combination of ITD and IPD that was imposed on the bands of noise that served as the reference, against which increases of ITD were to be discriminated.

In general, the results appear to be consistent with our hypotheses. For all four listeners, the patterning of the ITD thresholds, across bandwidth, shows poorer sensitivity as greater and greater curvature is imposed on the dominant, midline, trajectory. Note that, when the reference stimuli had a bandwidth of 400 Hz, threshold ITDs increased monotonically as the combinations of ITD/IPD went from 0 μs/0° (the ''straight'' condition) to -1500 μs/270° (the maximally ''curved'' condition). In contrast, when the bandwidth was 50 Hz, the differences among threshold ITDs across the four reference stimuli were greatly reduced as compared to the differences obtained when the bandwidth was 400 Hz. This was true for all four listeners. We believe the differences across bandwidth can be understood by noting that reducing bandwidth from 400 to 50 Hz dramatically reduces the effective curvature by reducing the maximum amount of internal delay that is spanned by each trajectory. That is, with the 50-Hz-wide bands of noise, the patterns of cross correlation

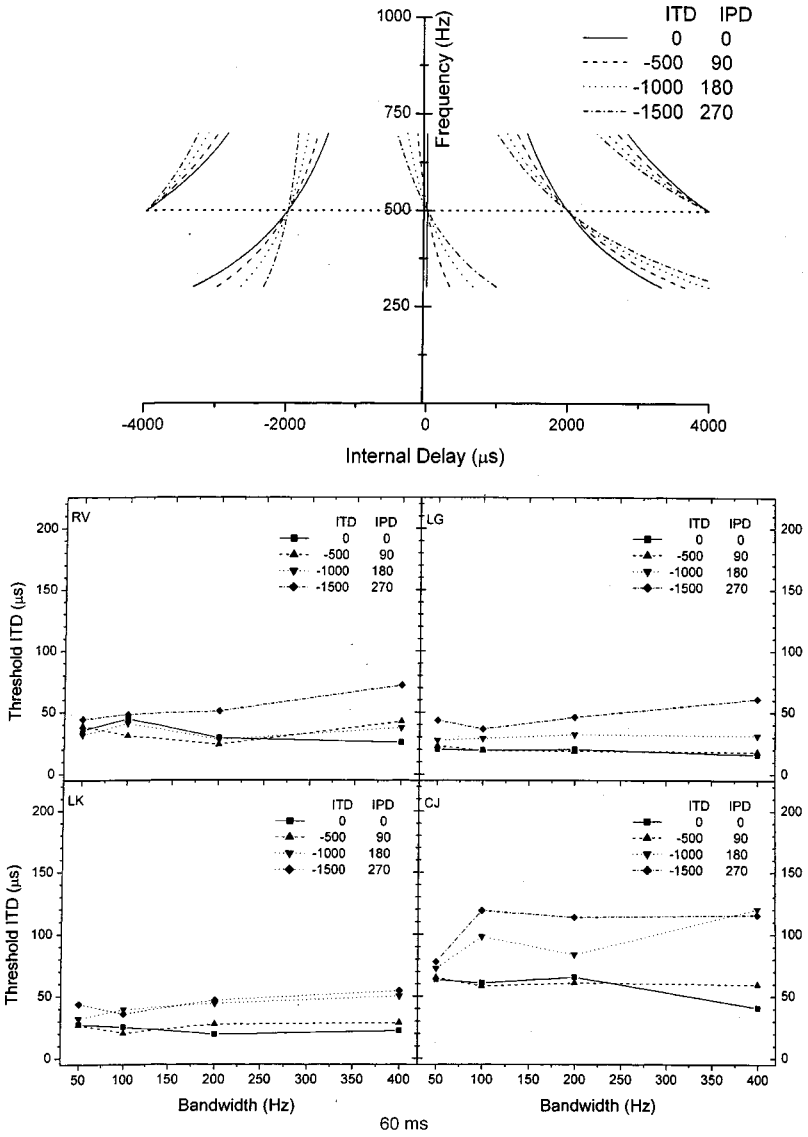

FIG. 2. Same as Fig. 1, but for the 60-ms-long reference stimuli.

are not sufficiently extended across frequency to produce enough curvature to affect performance differentially. Overall, the patterning of the data in Fig. 1 indicates that, as curvature is reduced, threshold ITDs decrease, independent of whether curvature was manipulated by changing the combination of ITD and IPD or by limiting bandwidth.

The finding that threshold ITDs *increase* up to a bandwidth of 400 Hz for the more curved reference stimuli (e.g., -1500 μs/270°) is interesting and important. It provides strong evidence that our listeners were unable to maximize performance by simply restricting their processing to the ''critical band'' centered at 500 Hz, which appears to be approximately 100 Hz wide. The finding that energy beyond the nominal (monaural) critical bandwidth can have substantial, deleterious, effects on binaural processing has been found in a variety of binaural experiments (e.g., Bourbon, 1966; Gabriel and Colburn, 1981; Heller and Trahiotis, 1995).

Essentially the same patterning of threshold ITDs was obtained with stimuli having a duration of 60 ms (Fig. 2) and 100 ms (Fig. 3). For these longer-duration stimuli, however, the increases in threshold ITD produced by imposing increasing amounts of curvature were uniformly smaller than those observed for the 20-ms-long stimuli. In addition, the values of the thresholds decreased with increasing duration. Thus, as postulated in the Introduction, longer-duration stimuli appear to foster such great sensitivity to changes in ITD that the influences stemming from the variation of straightness/curvature are attenuated or absent.

The data in Figs. 1, 2, and 3 were subjected to a three-factor, within-subjects, analysis of variance. The error terms for the main effects and for the interactions were the interaction of the particular main effect (or the particular interaction) with the subject ''factor'' (Keppel, 1973). Consistent with the evaluation of the data presented above, the main effect of the type of reference stimulus employed was highly significant [$F(3,9)=42.09$, $p<0.001$], as was the interaction of type of reference stimulus and bandwidth [$F(9,27)=15.47$, $p<0.001$]. These two outcomes, taken together, reflect the fact that the deleterious effects of increasing curvature were larger for the stimuli having the larger bandwidths. The main effect of bandwidth, however, was not significant [$F(3,9)=3.49$, $p=0.063$]. This outcome was not unexpected because, depending upon the ITD/IPD combination

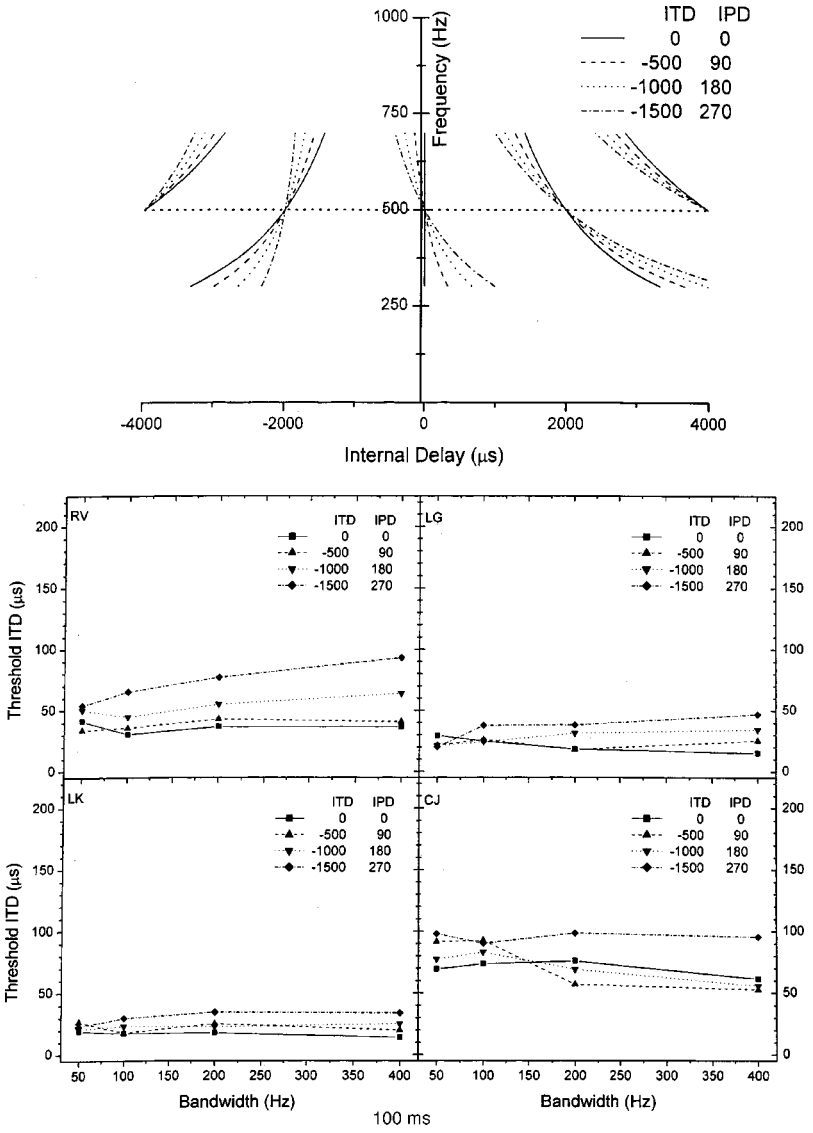

FIG. 3. Same as Fig. 1, but for the 100-ms-long reference stimuli.

that characterized the reference stimulus, threshold ITDs were expected to increase or decrease as bandwidth was increased.

The main effect of duration was highly significant [$F(2,6)=18.92$, $p=0.003$], but neither the interaction of duration and type of reference stimulus [$F(6,18)=2.34$, $p=0.076$] nor the interaction of duration and bandwidth [$F(6,18)=1.17$, $p=0.367$] were significant. These statistical outcomes reflect the general improvement of threshold ITDs with duration, a common finding in prior experiments (e.g., Tobias and Zerlin, 1959; Houtgast and Plomp, 1968; Ricard and Hafter, 1973). The triple interaction of type of reference stimulus, bandwidth, and duration was also significant [$F(18,54)=2.05$, $p=0.022$]. The statistical significance of the triple interaction validates the expectations described in the Introduction. That is, threshold ITDs are poorest for short-duration stimuli having dominant patterns of cross correlation that are curved and having sufficient bandwidth so that the curvature can be effective.

III. EXPERIMENT 2

Based on the results of experiment 1, we deemed it important to determine whether the binaural detection of tonal signals would also be affected by the relative straightness/curvature of bands of noise that serve as maskers. To that end, we measured the detectability of 500-Hz, interaurally out-of-phase ($S\pi$), tonal signals masked by bands of noise having combinations of ITD/IPD of 0 μs/0° and -1500 μs/270°. Those are the combinations of ITD/IPD used in experiment 1 that produced the straightest and the most curved trajectories, respectively, at or near the midline.

The addition of the $S\pi$ signal to the masker produces a broadening of the pattern of cross correlation at the outputs of processing bands (e.g., critical bands, listening bands, auditory filters) that contain both signal and masking noise. The listener could detect the signal by monitoring changes in the ''breadth'' of the pattern in the manner discussed recently by Bernstein and Trahiotis (1997). Such changes would have to be discriminated against the overall breadth of the cross-correlation pattern produced by the reference stimuli in the absence of the signal. If this were so, then the ''broadening'' of the pattern produced by the addition of the $S\pi$ signal would be easier to discern against the straight diotic reference stimulus than against the curved reference stimulus.

A. Procedure

Detection of 500-Hz, Sπ tones was measured in the presence of masking noises having combinations of ITD/IPD of either 0 μs/0° (more commonly referred to as No) or −1500 μs/270° and bandwidths of either 50 or 400 Hz. In order to measure masking-level differences, detection was also measured with 500-Hz, interaurally in-phase (S0) tones masked by diotic bands of noise (NoSo). The duration of the tonal signals was 20 ms (including 3-ms, cosine^2, rise/decay times) and the signals were temporally centered within the maskers, which had a total duration of 26 ms (including 3-ms, cosine^2, rise/decay times). The overall level of the maskers was 65 dB SPL.

Three new listeners, one male and two females, with no evidence or history of hearing loss were recruited. They received extensive practice before the formal collection of data began. Thresholds were obtained using the same four-interval, two-alternative, temporal forced-choice task used in experiment 1. The level of the signal was varied adaptively in order to estimate 70.7% correct (Levitt, 1971). The initial step size of the adaptive track was 4 dB and was reduced to 2 dB and to 1 dB after two reversals occurred at each of the former step sizes. A run was terminated after 12 reversals using the 1-dB step size and estimates of threshold were calculated using the average level of the signal across the last ten reversals. Final thresholds were calculated by averaging four estimates of threshold for each listener and for each stimulus condition. The bandwidths of the maskers were presented in a counterbalanced order across measurements of threshold. Within each replication, individual combinations of interaural time and interaural phase were presented in random order.

B. Results and discussion

Figure 4 contains the average S/N (in dB) required for detection, computed across the three listeners. The three left-most bars represent the thresholds obtained when the bandwidth of the masker was 50 Hz; the three right-most bars represent the thresholds obtained when the bandwidth of the masker was 400 Hz. Note that when the bandwidth of the masker was 50 Hz, thresholds obtained in the NoSπ condition were approximately 10 dB below those obtained in the NoSo condition. This 10-dB release from masking is similar to that reported earlier by Bernstein and Trahiotis (1997), who also utilized narrow-band, short-duration signals and maskers. Imposing an ITD/IPD combination of −1500 μs/270° on the masker resulted in essentially the same threshold as that obtained when the masker was diotic. This was expected because, as discussed above, the 50-Hz bandwidth of the noise is not sufficiently wide so as to produce appreciable curvature. The thresholds obtained with the 400-Hz-wide maskers, however, appear to have been affected by curvature. Note that the release from masking obtained in the NoSπ condition is about 11.5 dB, a value comparable to that obtained with the 50-Hz-wide masker. In contrast, imposing curvature led to an increase in threshold that resulted in a reduction of about 6 dB of the release from masking.

In addition, the decrease in the release from masking

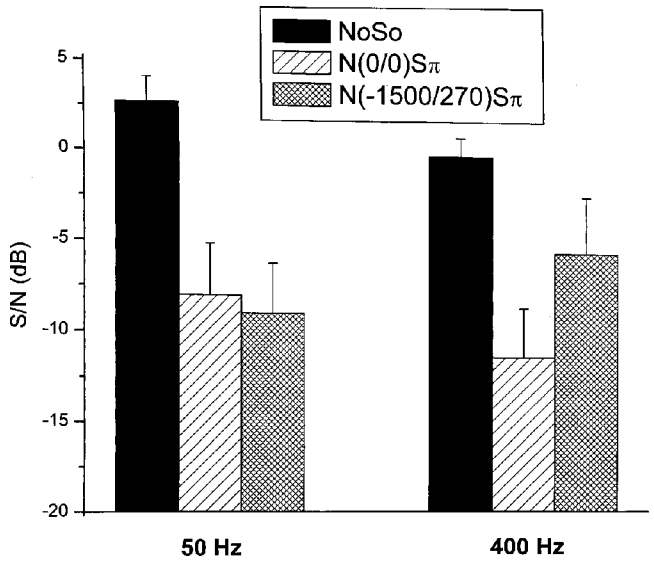

FIG. 4. The average S/N (in dB) required for detection, computed across the three listeners. The three left-most bars represent the thresholds obtained when the bandwidth of the masker was 50 Hz; the three right-most bars represent the thresholds obtained when the bandwidth of the masker was 400 Hz. The standard error of the mean is indicated atop each bar. The parameter of the plot is the particular combination of reference noise and type of signal employed.

with the 400-Hz-wide masking noise is consistent with data reported by Rabiner *et al.* (1966), who employed a masker with a spectrum extending from 100–1200 Hz. Rabiner *et al.* also measured detection thresholds for 500-Hz tonal signals. The maskers contained ITDs of up to 9 ms and compensatory IPDs, like ours, that negated the ITD at the frequency of the signal. Relative to a diotic masker, Rabiner *et al.* found that an ITD/IPD combination of 1500 μs/−270° reduced the release from masking by about 3 dB. Unfortunately, to our knowledge, there are no data for bandwidths between the bandwidth of 400 Hz that we employed and the bandwidth of 1100 Hz employed by Rabiner *et al.* Consequently, it is impossible to evaluate the dependence of the release from masking on bandwidth in these conditions. Nevertheless, the results from both studies are in qualitative agreement. The differences among the detection thresholds observed in experiment 2 are consistent with the differences in threshold ITD observed in experiment 1. Thus, in both types of tasks, it appears that listeners are adversely affected if a sufficient degree of curvature of the pattern of cross correlation is imposed on the stimuli.[1]

IV. MODELING OF THE DATA

The overall patterning of the data obtained in both experiments 1 and 2 was qualitatively in accord with our expectations in that the threshold ITDs and thresholds of detection depended upon the straightness/curvature of the patterns of cross correlation produced by the reference stimuli. In this section, we will discuss our attempts to account for the data quantitatively. The threshold ITDs obtained in experiment 1 will be considered first.

The initial attempts to account for the threshold ITDs utilized two different extensions of Stern and Colburn's (1978) ''position-variable'' model and were based on the

notion that listeners use a change in laterality in order to detect a change in ITD. The extensions, termed the ''weighted-image'' model (Stern *et al.*, 1988) and the ''extended'' position-variable model (Stern and Trahiotis, 1992, 1998) reflect explicit attempts to incorporate effects on lateralization stemming from straightness and curvature of the patterns of cross correlation. The weighted-image model is a black-box formulation. In this model, each trajectory of the cross-correlation pattern is weighted by an *ad hoc* function that is approximately proportional to the reciprocal of the variance of the internal delay spanned by that particular trajectory. This weighting provides a quantitative measure of the straightness of the trajectory. The extended position-variable model assumes that the outputs of the elements giving rise to the internal representation of the pattern of cross correlation are passed through a second level of processing. Sets of inputs to the second layer of processing are assumed to derive from first-level elements collectively tuned to a range of center frequencies (CFs), respectively, but tuned to a common internal delay.

In order to obtain predictions of threshold ITDs from both models, we first generated functions relating the lateral positions of each of the reference stimuli as a function of ITD. Then, the assumption was made that changes in ITD are detected on the basis of changes in lateral position. Under that assumption, the threshold ITD would be inversely proportional to the slope of the function relating lateral position to ITD, evaluated at the point representing the ITD applied to the reference stimulus. At best, the predictions of threshold ITDs from each of the models captured only the ordinal relations among the behavioral data. At worst, (for the -1000 μs/180° reference stimulus) the predicted thresholds could be up to an order of magnitude greater than the obtained thresholds. The amount of variance accounted for was larger for the predictions obtained from the extended position-variable model than for the predictions obtained from the weighted-image model. Still, the extended position-variable model only managed to account for about 12% of the variation in the behavioral thresholds. The inability of these two analyses, which use changes in lateralization to predict threshold ITDs, was not completely unexpected. Stern and Colburn (1978) had previously demonstrated that derivations of threshold ITDs from the slope of the function relating lateral position to ITD could lead to highly inflated predictions for large values of reference ITD of their 500-Hz tones.

Subsequently, we decided to attempt to account for the data by incorporating the token-to-token variation due to the random fluctuations inherent in the bands of noise which served as stimuli. We noted that the token-to-token variance produced a variation of the position of the peaks of the cross-correlation function that was proportional to the amount of curvature that characterized the reference stimulus. It therefore seemed reasonable to assume that threshold ITDs would vary directly with the token-to-token variation in the position of the peak.

We implemented this idea within two separate models, one based on an across-frequency averaging of the cross-correlation surface (e.g., Shackleton *et al.*, 1992; Akeroyd and Summerfield, 2000) and the other based on the second level of cross correlation used in the extended position-variable model (Stern and Trahiotis, 1992). The two models are generally similar in terms of their peripheral stages of processing but differ principally in the binaural operations that are assumed. Nevertheless, it will be shown that both models are able to account for the experimental data.

The peripheral stages of both models included bandpass filtering, rectification, low-pass filtering, and compression. All of those stages of processing have been utilized recently to enable quantitative, correlation-based predictions of binaural detection (e.g., Bernstein and Trahiotis, 1996a,b; Bernstein *et al.*, 1999). Each of 100 tokens of each of the four types of reference noise was passed through a bank of gammatone filters (see Patterson *et al.*, 1995) and the outputs of the filters were rectified, low-pass filtered, and subjected to compression in the manner described by Bernstein *et al.* (1999). In the across-frequency averaging model, the bank of filters was composed of 20 filters having center frequencies spanning the range from 100 to 1000 Hz, whereas in the second-level model the bank of filters was composed of 19 filters having center frequencies spanning the range from 47.4 to 1690 Hz. In both instances the bandwidths of the filters were as prescribed by Glasberg and Moore (1990) and the center frequencies of the filters were spaced in terms of their respective equivalent-rectangular bandwidths [i.e., according to Glasberg and Moore's (1990) ''ERB'' function]. The minor changes in the center frequencies of the filters used in the second-level model were made to foster the understanding and the interpretation of the ''second-level'' cross-correlation functions, as will be explained below.

The central, binaural, processing differed considerably across the two models. In the across-frequency averaging model, a cross correlogram (i.e., cross-correlation surface) was constructed with values of delay (τ) spanning the range -2000 to 2000 μs in 50-μs steps. Then, an across-frequency weighting was applied to the cross correlogram utilizing Stern *et al.*'s (1988) equation for the relative dominance of binaural processing. This frequency weighting emphasized the region surrounding 600 Hz or so (Bilsen and Raatgever, 1973). Next, an across-frequency average of the weighted cross correlogram was computed (Shackleton *et al.*, 1992) and the location of its most central peak was determined. This model did not include any explicit weighting function emphasizing activity at or very near midline, like the (different) ones employed by Stern and his colleagues (e.g., Blauert and Cobben, 1978; Stern and Colburn, 1978; Shackelton *et al.*, 1992; Stern and Shear, 1996). Within this model, token-to-token variation due to inherent random fluctuations in the noise results in variations in the location of the most central peak. The variability was quantified by computing the standard deviation, across 100 tokens of each of the reference stimuli, of the location of the most central peak.

In the second-level model, the same initial cross correlogram used in the across-frequency averaging model was constructed, but, in this model, the envelopes of the time-varying outputs of each delay-by-frequency (τ, f) point within the cross-correlation matrix were extracted using a Hilbert transform. The second-level cross correlogram was computed by multiplying together subsets of these enve-

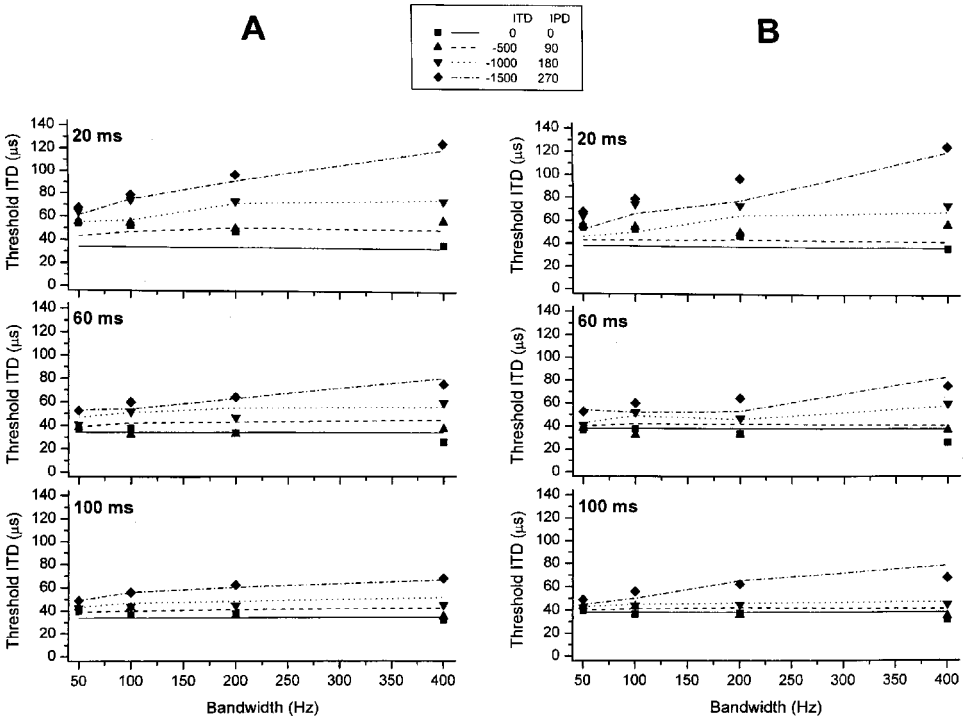

FIG. 5. (A) Average of the threshold ITDs presented in Figs. 1–3 (symbols) along with the predictions (lines) derived from the across-frequency averaging model described in Sec. IV of the text. The three panels contain data and predictions for stimulus durations of 20-, 60-, and 100 ms, respectively. The parameter within each plot is the type of reference stimulus employed. (B) Same as panel (A) with the exception that the predictions were derived from the second-level model described in Sec. IV of the text.

lopes. Each subset was defined by a common delay (τ) and a restricted range of frequency (f). This range was 9 filters wide, meaning that it extended 4 filters above and 4 filters below the center frequency of the second-level element. Representing the envelope at each point in the first-level cross correlogram as $e_1(t,\tau,f)$ and in the second-level cross correlogram as $e_2(t,\tau,f)$, where t represents time, τ represents the internal delay, and f represents frequency, the multiplication of the envelopes can be characterized as

$$e_2(t,\tau,f)=e_1(t,\tau,f-4)\times e_1(t,\tau,f-3)\times\cdots\times e_1(t,\tau,f)\times\cdots\times e_1(t,\tau,f+3)\times e_1(t,\tau,f+4).$$

Finally, each second-level envelope, $e_2(t,\tau,f)$, was averaged across the duration of the stimulus (t), in order to arrive at a single value at each point (τ,f) of the second-level cross correlogram. The reason for choosing the span of the filterbank to be 47.4 to 1690 Hz was that this choice resulted in filters having center frequencies that were spaced at 1-ERB intervals with the filterbank being centered at 500 Hz. A width of 9 filters (i.e., a width of 9 ERBs) was used because we had observed that widths of 7, 9, and 11 filters (ERBs) each resulted in predictions of lateralization that qualitatively captured the variations in lateralization with bandwidth and curvature described by Stern and Trahiotis (1992).

The resulting second-level correlogram was then weighted by Stern and Shear's (1996) centrality function and by Stern *et al.*'s (1988) frequency-dominance function. In order to calculate the position estimate for each stimulus, we calculated the centroid of each frequency channel within the second-level cross correlogram and then averaged those centroids across frequency channels. Within this model, token-to-token variation due to inherent random fluctuations in the noise results in variations in the centroids and, therefore, in the position estimate. This variability was quantified by using the standard deviation of the position estimates across 100 tokens of each of the reference stimuli.

Finally, for both models the predictions of threshold ITD, averaged across listeners, for each stimulus condition were made by assuming that the threshold ITD was linearly related to the standard deviation. This was measured by determining the linear equation for each model that simultaneously best fit (in the least-squares sense) all 48 of the threshold ITDs obtained in the experiment (i.e., with four types of reference stimuli, four bandwidths, and three durations).

Figure 5 contains the average of the threshold ITDs presented previously in Figs. 1–3, along with the predictions derived from the two models. The left column shows the predictions for the across-frequency averaging model and the right column shows the predictions for the second-level model. Within each column, the three panels contain data and predictions for stimulus durations of 20-, 60-, and 100 ms, respectively. The predictions for each reference stimulus are represented as lines, with the symbols and lines in this figure being consistent with those used in Figs. 1–3.

As can be seen, both models capture the important interactions among the combination of ITD/IPD, bandwidth, and duration. For the across-frequency averaging model, the amount of variance accounted for was 76% for the 20-ms stimuli, 82% for the 60-ms stimuli, and 85% for the 100-ms stimuli. For the second-level model, the amount of variance accounted for was generally slightly less, being 58% for the 20-ms stimuli, 78% for the 60-ms stimuli, and 78% for the 100-ms stimuli. In our opinion these differences in variance accounted for are minor and should not detract from the fact that the complex patterning within the sets of data is captured by both models. The quality of the fits is noteworthy because the two models differed greatly in terms of the cen-

tral, binaural processing, while differing only slightly in the exact center frequencies specifying the peripheral filterbank. We interpret this outcome as indicating that the primary factor determining the patterning of the threshold ITDs, as a function of curvature, bandwidth and duration, is a stimulus-based variability resulting from the random fluctuations inherent in narrow bands of noise.

When considering the ability of the models to predict the data, it should be noted that a portion of the unexplained variance in the data is the small decrease in threshold ITDs found with the diotic reference stimulus as bandwidth was increased. The location of the central peak of the cross-correlation function in the across-frequency averaging model and the position estimate in the second-level model do not vary from token-to-token for a diotic noise, regardless of the bandwidth. Therefore, both models predict that threshold ITD for a diotic band of noise is independent of bandwidth. Addressing this minor shortcoming is beyond the scope of this investigation.

A second shortcoming of the models is that we were unable to generate accurate predictions of the binaural detection data obtained in our second experiment. This became evident during computer simulations using the across-frequency averaging model while attempting to predict the detection data. The decision variable was the change in the standard deviation of the position of the central peak of the cross-correlation function produced by the addition of the $S\pi$ signal, in relation to the standard deviation of the position of the central peak in the absence of the signal. Using this approach, we were unable to account for the interactive effects in the data between the bandwidth of the masker and combinations of ITD and IPD. That is, the model did not capture the effects on detection of imposing curvature on the masker. Specifically, when the value of the decision statistic was chosen such that the model could account for the differences in $S\pi$ thresholds that were observed when the bandwidth of the masker was 400 Hz, the model also predicted large differences in $S\pi$ thresholds for a bandwidth of 50 Hz. Such differences were not observed in the data.

The detection data appear to be consistent, qualitatively, with expectations based on the notion that the listener monitors changes in the normalized correlation (i.e., the coefficient of correlation computed at $\tau=0$). Consider that the signal-to-noise ratio required to detect an $S\pi$ signal increases with decreases in the interaural correlation of the masking noise (e.g., Robinson and Jeffress, 1963). In accord with this finding, when we measured the interaural correlation of the reference stimuli that served as maskers in our experiment, we found an inverse relation between the interaural correlation of the masker, which decreased as curvature increased, and the level of the $S\pi$ signal required for detection. In addition, the differences in our masked thresholds, as a function of bandwidth, were in good qualitative agreement with thresholds of detection measured by van der Heijden and Trahiotis (1998) as a joint function of the bandwidth of the masker and its interaural correlation. Several attempts to account quantitatively for the detection data in terms of changes in the interaural correlation produced by the addition of the $S\pi$ signal proved unsuccessful in the sense that we could not discover a decision statistic (e.g., change in correlation, change in correlation relative to the sampling variability of the correlation), that could simultaneously account for the data obtained with both bandwidths of the masker. At this time, it appears that a study in which one manipulates masker duration, masker bandwidth, masker correlation, and the method by which the masker correlation is achieved is necessary. Perhaps such a parametrically generated set of data would be rich enough to enable one to formulate a successful quantitative account of how detection performance varies as a function of the relative straightness/curvature of the masker.

V. SUMMARY

We have presented data indicating that sensitivity to changes in ITD depends upon the straightness/curvature of the patterns of cross correlation of the stimuli. We found that threshold ITDs are poorest for short-duration stimuli having dominant patterns of cross correlation that are curved and having sufficient bandwidth so that the curvature can be effective. The variations in threshold ITD are accounted for quite well quantitatively by assuming that the listeners based their judgments on either the position of the most central peak of the cross-correlation function or the centroid of a set of second-level cross-correlation functions. Binaural detection of tonal signals depended on the straightness/curvature of the noises serving as maskers, but the data could not be accounted for quantitatively.

ACKNOWLEDGMENTS

The authors wish to acknowledge the continual commitment of Dr. Richard M. Stern, Jr. to fostering the modeling and understanding of binaural hearing. In this instance, Rich graciously and frequently interacted with us, providing valuable assistance and guidance concerning the implementation of the models developed by him and his colleagues. We also wish to acknowledge both reviewers and the Associate Editor, Dr. D. Wesley Grantham, for their useful comments. Special thanks are due to Dr. H. Steven Colburn, the reviewer who suggested that we include the quantitative predictions of the second-level model. Although not traditionally done, the senior authors believe it is appropriate that Dr. Michael Akeroyd's contributions to this paper be explicitly understood. Michael cheerfully took on the task of analyzing the data in terms of several quantitative approaches. His Herculean efforts included recoding and modifying the complex, cross-correlation-based models of Stern and his colleagues so that they could be utilized and evaluated via modern computing platforms. As a consequence, computational versions of these models will be readily available to the scientific community. Without minimizing the cooperation of and detailed information generously provided by our colleague, Dr. Richard Stern, Michael's efforts were, in our experience, extraordinary. This work was supported by Research Grant No. NIH DC00234 from the National Institute on Deafness and Other Communication Disorders, National Institutes of Health, and by a Medical Research Council Career Development Fellowship to Michael Akeroyd.

[1]We also measured thresholds of detection when the duration of the stimuli was 300 ms. The thresholds did not differ in any systematic fashion (i.e., they overlapped) across the four types of reference stimuli employed in experiment 1 as maskers. This outcome is consistent with how duration affects the threshold ITDs measured in experiment 1. In addition, it reinforces the notion that one must minimize or preclude ''floor effects'' (in this instance, by employing stimuli of short duration) in order to be able to observe the effects of straightness for low-frequency stimuli.

Akeroyd, M. A., and Summerfield, A. Q. (**2000**). ''The lateralization of simple dichotic pitches,'' J. Acoust. Soc. Am. **108**, 316–334.

Bernstein, L. R., and Trahiotis, C. (**1996a**). ''On the use of the normalized correlation as an index of interaural envelope correlation,'' J. Acoust. Soc. Am. **100**, 1754–1763.

Bernstein, L. R., and Trahiotis, C. (**1996b**). ''The normalized correlation: Accounting for binaural detection across center frequency,'' J. Acoust. Soc. Am. **100**, 3774–3784.

Bernstein, L. R., and Trahiotis, C. (**1997**). ''The effects of randomizing values of interaural disparities on binaural detection and on discrimination of interaural correlation,'' J. Acoust. Soc. Am. **102**, 1113–1120.

Bernstein, L. R., van de Par, S., and Trahiotis, C. (**1999**). ''The normalized correlation: Accounting for NoSp thresholds obtained with Gaussian and low-noise masking noise,'' J. Acoust. Soc. Am. **106**, 870–876.

Bilsen, F. A., and Raatgever, J. (**1973**). ''Spectral dominance in binaural lateralization,'' Acustica **28**, 131–132.

Blauert, J., and Cobben, W. (**1978**). ''Some consideration of binaural cross correlation analysis,'' Acustica **39**, 96–103.

Bourbon, W. T., Jr. (**1966**). ''Effects of bandwidth and level of masking noise on detection of homophasic and antiphasic tonal signals,'' unpublished dissertation, University of Texas, Austin, TX.

Buell, T. N., Trahiotis, C., and Bernstein, L. R. (**1994**). ''Lateralization of bands of noise as a function of combinations of interaural intensive differences, interaural temporal differences and bandwidth,'' J. Acoust. Soc. Am. **95**, 1482–1489.

Colburn, H. S. (**1996**). ''Computational models of binaural processing,'' in *Auditory Computation*, edited by H. Hawkins and T. McMullen, Volume in *Springer Handbook on Auditory Research*, edited by A. Popper and R. Fay (Springer, New York), pp. 332–400.

Colburn, H. S., and Durlach, N. I. (**1978**). ''Models of binaural interaction,'' in *Hearing, Vol. IV, Handbook of Perception*, edited by E. C. Carterette and M. P. Friedman (Academic, New York).

Gabriel, K. J., and Colburn, H. S. (**1981**). ''Interaural correlation discrimination. I. Bandwidth and level dependence,'' J. Acoust. Soc. Am. **69**, 1394–1401.

Glasberg, B. R., and Moore, B. C. J. (**1990**). ''Derivation of auditory filter shapes from notched-noise data,'' Hear. Res. **47**, 103–138.

Hafter, E.R., and Trahiotis, C. (**1997**). ''Functions of the Binaural System,'' to appear in *Handbook of Acoustics*, edited by Malcome Crocker (Wiley, New York).

Heller, L. M., and Trahiotis, C. (**1995**). ''The discrimination of samples of noise in monotic, diotic, and dichotic conditions,'' J. Acoust. Soc. Am. **97**, 3775–3781.

Houtgast, T., and Plomp, R. (**1968**). ''Lateralization threshold of a signal in noise.'' J. Acoust. Soc. Am. **44**, 807–812.

Jeffress, L. A. (**1972**). ''Binaural signal detection: Vector theory,'' in *Foundations of Modern Auditory Theory*, edited by J. V. Tobias (Academic Press, New York), Vol. 2, pp. 349–368.

Keppel, G. (**1973**). *Design and Analysis: A Researchers Handbook* (Prentice-Hall, Englewood Cliffs, NJ).

Levitt, H. (**1971**). ''Transformed up–down methods in psychoacoustics,'' J. Acoust. Soc. Am. **49**, 467–477.

Patterson, R. D., Allerhand, M. H., and Giguere, C. (**1995**). ''Time-domain modeling of peripheral auditory processing: A modular architecture and a software platform,'' J. Acoust. Soc. Am. **98**, 1890–1894.

Rabiner, L. R., Laurence, C. L., and Durlach, N. I. (**1966**). ''Further results on binaural unmasking and the EC model,'' J. Acoust. Soc. Am. **40**, 62–70.

Ricard, G. L., and Hafter, E. R. (**1973**). ''Detection of interaural time differences in short-duration low-frequency tones,'' J. Acoust. Soc. Am. **53**, 335 (A).

Robinson, D. E., and Jeffress, L. A. (**1963**). ''Effect of varying the interaural noise correlation on the detectability of tonal signals,'' J. Acoust. Soc. Am. **35**, 1947–1952.

Saberi, K. (**1995**). ''Lateralization of comodulated complex waveforms,'' J. Acoust. Soc. Am. **98**, 3146–3156.

Shackleton, T. M., Meddis, R., and Hewitt, M. J. (**1992**). ''Across frequency integration in a model of lateralization,'' J. Acoust. Soc. Am. **91**, 2276–2279.

Stern, R. M., and Colburn, H. S. (**1978**). ''Theory of binaural interaction based on auditory-nerve data. IV. A model for subjective lateral position,'' J. Acoust. Soc. Am. **64**, 127–140.

Stern, R. M., and Shear, G. D. (**1996**). ''Lateralization and detection of low-frequency binaural stimuli: Effects of distribution of interaural delay,'' J. Acoust. Soc. Am. **100**, 2278–2288.

Stern, R. M., and Trahiotis, C. (**1992**). ''The role of consistency of interaural timing over frequency in binaural lateralization,'' in *Auditory Physiology and Perception*, edited by Y. Cazals, L. Demany, and K. Horner (Pergamon, New York), pp. 547–554.

Stern, R. M., and Trahiotis, C. (**1998**). ''Binaural mechanism that emphasize consistent interaural timing information over frequency,'' in *Psychophysical and Physiological Advances in Hearing*, edited by A. R. Palmer, A. Rees, A. Q. Summerfield, and R. Meddis (Whurr, London), pp. 384–395.

Stern, R. M., Zeiberg, A. S., and Trahiotis, C. (**1988**). ''Lateralization of complex binaural stimuli: A weighted image model,'' J. Acoust. Soc. Am. **84**, 156–165.

Tobias, J. V., and Zerlin, S. (**1959**). ''Lateralization threshold as a function of stimulus duration,'' J. Acoust. Soc. Am. **31**, 1594–1595.

Trahiotis, C., and Stern, R. M. (**1989**). ''Lateralization of bands of noise: Effects of bandwidth and differences of interaural time and phase,'' J. Acoust. Soc. Am. **86**, 1285–1293.

Trahiotis, C., and Stern, R. M. (**1994**). ''Across-frequency interaction in lateralization of complex binaural stimuli,'' J. Acoust. Soc. Am. **96**, 3804–3806.

van der Heijden, M., and Trahiotis, C. (**1998**). ''Binaural detection as a function of interaural correlation and bandwidth of masking noise: Implications for estimates of spectral resolution,'' J. Acoust. Soc. Am. **103**, 1609–1614.

Yost, W. A., and Hafter, E. R (**1987**). ''Lateralization,'' in *Directional Hearing*, edited by W. A. Yost and G. Gourevitch (Springer, New York), pp. 49–84.

The influence of interaural stimulus uncertainty on binaural signal detection

Jeroen Breebaart
IPO, Center for User-System Interaction, P.O. Box 513, NL-5600 MB Eindhoven, The Netherlands

Armin Kohlrausch
IPO, Center for User-System Interaction, P.O. Box 513, NL-5600 MB Eindhoven, The Netherlands and Philips Research Laboratories Eindhoven, Prof. Holstlaan 4, NL-5656 AA Eindhoven, The Netherlands

(Received 24 August 1998; revised 15 June 1999; accepted 31 August 2000)

This paper investigated the influence of stimulus uncertainty in binaural detection experiments and the predictions of several binaural models for such conditions. Masked thresholds of a 500-Hz sinusoid were measured in an NρSπ condition for both running and frozen-noise maskers using a three interval, forced-choice (3IFC) procedure. The nominal masker correlation varied between 0.64 and 1, and the bandwidth of the masker was either 10, 100, or 1000 Hz. The running-noise thresholds were expected to be higher than the frozen-noise thresholds because of stimulus uncertainty in the running-noise conditions. For an interaural correlation close to +1, no difference between frozen-noise and running-noise thresholds was expected for all values of the masker bandwidth. These expectations were supported by the experimental data: for interaural correlations less than 1.0, substantial differences between frozen and running-noise conditions were observed for bandwidths of 10 and 100 Hz. Two additional conditions were tested to further investigate the influence of stimulus uncertainty. In the first condition a different masker sample was chosen on each trial, but the correlation of the masker was forced to a fixed value. In the second condition one of two independent frozen-noise maskers was randomly chosen on each trial. Results from these experiments emphasized the influence of stimulus uncertainty in binaural detection tasks: if the degree of uncertainty in binaural cues was reduced, thresholds decreased towards thresholds in the conditions without any stimulus uncertainty. In the analysis of the data, stimulus uncertainty was expressed in terms of three theories of binaural processing: the interaural correlation, the EC theory, and a model based on the processing of interaural intensity differences (IIDs) and interaural time differences (ITDs). This analysis revealed that none of the theories tested could quantitatively account for the observed thresholds. In addition, it was found that, in conditions with stimulus uncertainty, predictions based on correlation differ from those based on the EC theory. [DOI: 10.1121/1.1320472]

PACS numbers: 43.66.Pn, 43.66.Ba, 43.66.Dc [DWG]

I. INTRODUCTION

For a period of more than 50 years, the phenomenon of the binaural masking level difference (BMLD) has intrigued psychoacousticians. It has been shown that the interaural correlation of both the masker and the signal are important parameters influencing binaural detection thresholds. For example, when a low-frequency out-of-phase sinusoid is added to an in-phase broadband noise masker (NoSπ condition), the threshold of audibility is up to 15 dB lower compared to that for an in-phase sinusoidal signal (i.e., NoSo condition, cf. Hirsh, 1948; Hafter and Carrier, 1969; Zurek and Durlach, 1987). If the signal has an interaural correlation of +1 and an out-of-phase masker is used (i.e., an NπSo condition), BMLDs of up to 12 dB are reported (Jeffress *et al.*, 1952, 1962; Breebaart *et al.*, 1998).

In experiments where the masker correlation was varied between −1 and +1 using Sπ signals, Robinson and Jeffress (1963) found a monotonic increase in the BMLD with increasing interaural correlation. Small reductions from +1 of the interaural masker correlation in an NρSπ condition led to a large decrease of the BMLD, while for smaller correlations, the slope relating BMLDs to interaural correlation was shallower. The stimuli used by Robinson and Jeffress (1963) were composed by adding interaurally correlated noise with an interaurally uncorrelated noise. The relative intensities of both sources determined the *mean* interaural correlation. The consequence of this method for generating the stimuli is that for the masking noise alone, the interaural cues (i.e., interaural time- and intensity differences) fluctuate randomly. Moreover, because finite-length masker samples are used, the actual correlation within an observation interval can deviate considerably from the adjusted mean correlation. Thus, in terms of binaural cues, the masker contains uncertainty. The addition of the Sπ signal results in a change in the mean of the interaural cues but does not reduce the randomness of the interaural cues.

Analogous to monaural conditions (Lutfi, 1990), binaural masking can be attributed to two different sources. The first results from the limited resolution of the binaural auditory system and has been termed energetic masking by Lutfi. In models of binaural processing, this source of masking is included as internal noise. For example, the EC theory summarizes the internal errors of timing and amplitude represen-

tation in the factor k, which is directly related to the BMLD. The second source of masking results from the uncertainty associated with the trial-to-trial variation of the binaural cues used to detect the signal (called informational masking by Lutfi). This source of masking has not, as far as we are aware, been addressed explicitly so far in binaural models. In standard MLD conditions like NoSπ, the masker contains no uncertainty in terms of binaural cues: the interaural correlation is always exactly one, the energy of the difference signal between right and left masker is zero, and the interaural differences in time and intensity are always exactly zero.

Because it is well-known that the auditory system can benefit from the presence of binaural cues in a detection task, it is interesting to study the influence of uncertainty in these cues and the extent to which uncertainty limits detection. One of the possibilities to remove stimulus uncertainty is by using *frozen* noise. Thresholds for frozen binaural maskers would thus reflect the amount of energetic masking. The difference in detection performance between running noise and frozen noise indicates the amount of informational masking and this is the main topic of the present paper. Data will be presented that were measured under conditions with and without stimulus uncertainty. Three common theories for binaural processing (the change in interaural correlation, the EC theory and processing of interaural intensity differences, or IIDs, and interaural time differences, or ITDs) will be discussed for their ability to predict these data. We selected these theories because they are often used to explain binaural processing. In addition, they have been discussed recently for their ability to predict the amount of energetic masking in binaural conditions with non-Gaussian maskers (Breebaart *et al.*, 1999). Because, as we stated above, stimulus uncertainty has not been analyzed so far in terms of these models, we provide such an analysis in the following section.

II. STIMULUS UNCERTAINTY

A. Interaural correlation

It is often assumed that a change in the interaural correlation induced by adding a signal to a masker can be used as a detection cue in binaural masking experiments. Various mathematical details have been published treating changes in the interaural correlation for different experimental paradigms. For example, Domnitz and Colburn (1976) argued that models based on interaural correlation and models based on interaural differences yield similar predictions for NoSπ conditions with Gaussian noise. Breebaart *et al.* (1999) presented data with non-Gaussian noise maskers for which this close correspondence between the change in the cross correlation and the size of the interaural differences is no longer found. Durlach *et al.* (1986) determined an analytical expression for the interaural correlation in an NoSπ condition. Analytical expressions for the interaural waveform correlation and the interaural envelope correlation were derived by van de Par and Kohlrausch (1995) for NoSπ and later also for NoSm (van de Par and Kohlrausch, 1998). Bernstein and Trahiotis (1996) showed that for NoSπ stimuli, the interaural correlation of the stimuli after peripheral preprocessing did account for their NoSo vs NoSπ discrimination results for a wide range of center frequencies. Because this correlation approach is widely accepted, we will discuss stimulus uncertainty first in terms of this concept.

An interaurally partially correlated noise can be generated by adding an interaurally correlated noise $[N_0(t)]$ and an interaurally out-of-phase noise $[N_\pi(t)]$. In the following we assume that these two independent noise sources have the same rms value. To end up with a long-term normalized interaural correlation of ρ, the left-ear signal $\mathrm{L}(t)$ and the right-ear signal $\mathrm{R}(t)$ are combined as follows:

$$\begin{aligned} L(t) &= \tfrac{1}{2}\sqrt{2}\sqrt{1+\rho}N_0(t) + \tfrac{1}{2}\sqrt{2}\sqrt{1-\rho}N_\pi(t), \\ R(t) &= \tfrac{1}{2}\sqrt{2}\sqrt{1+\rho}N_0(t) - \tfrac{1}{2}\sqrt{2}\sqrt{1-\rho}N_\pi(t). \end{aligned} \tag{1}$$

Because both N_0 and N_π stem from random processes, the short-term energy estimates (i.e., integrated over one interval in a 3IFC task) of N_0 and N_π, E_0 and E_π, respectively, can deviate substantially from their expected (i.e., long-term) values provided that the product of time and bandwidth is small. Furthermore, the samples taken from the two noise sources can be partially correlated. Fluctuation of the short-term estimate of the noise energy leads to a variability in the interaural correlation for a finite-length noise interval [see the Appendix, Eq. (A2), and Gabriel and Colburn, 1981; Richards, 1987]. The interaural correlation of a finite sample will be referred to as *effective correlation*, ρ_{eff}, while the mean interaural correlation (i.e., the expected value of ρ_{eff}) will be referred to as *reference correlation*, ρ.

We determined the probability distribution for the interaural correlation for an NρSπ condition as a function of the signal-to-noise ratio, the bandwidth, and the duration of the masker. From the mathematical expressions for the effective correlation probability distribution as given in the Appendix, we found that three important factors affect the distribution for the effective correlation.

Bandwidth and duration of the noise. With increasing duration and bandwidth, the variance of the effective correlation, ρ_{eff}, will decrease as a result of the decreasing variances of E_0 and E_π (see the Appendix).

The reference correlation. For a reference correlation of $+1$ (and -1), there is no correlation uncertainty, and the effective correlation will always be $+1$ (-1). On the other hand, for reference correlations between -1 and $+1$, the effective correlation will follow a distribution rather than have a fixed value. For a reference correlation close to zero, the width of the effective correlation distribution will be widest (i.e., the correlation uncertainty is maximum).

The presence or absence of the signal. The addition of an Sπ signal results in a shift of the mean interaural correlation towards -1.

To demonstrate the effect of these properties upon the correlation uncertainty, probability density function (PDFs) for a 300-ms noise and three different combinations of reference correlation and noise bandwidth are shown in Fig. 1. Each panel shows two distributions, one for the noise alone (solid line) and one for noise plus signal (dashed line). The signal had a duration of 200 ms, was temporally centered in the noise, and had a level of 10 dB below the masker level (i.e., $\mathrm{S/N} = -10$ dB). It is clear that the *width* of the PDF

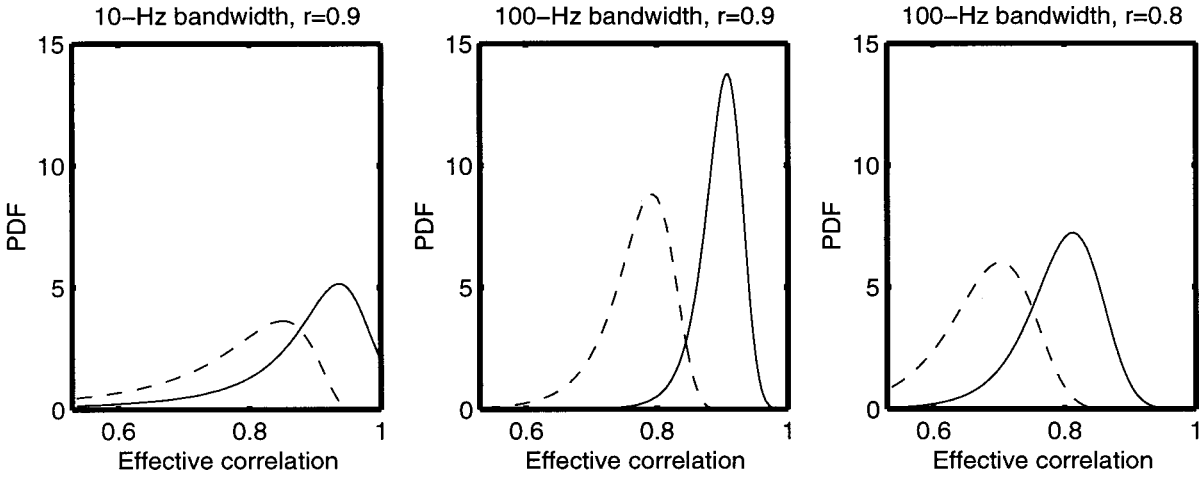

FIG. 1. Probability density functions for the effective interaural correlation. The left panel corresponds to a bandwidth of 10 Hz and a reference correlation of 0.9. For the middle and right panels, these parameters were 100 Hz, 0.9 and 100 Hz, 0.8, respectively. The solid lines represent a 300-ms masker alone; the dashed lines represent a 300-ms masker with a 200-ms Sπ signal. The distributions were calculated for the complete 300-ms interval. The signal-to-masker ratio was -10 dB.

decreases with increasing bandwidth (10 Hz in the left panel, 100 Hz in the middle and right panels) and with increasing correlation (0.9 in the left and middle panels, 0.8 in the right panel), indicating less correlation uncertainty. Furthermore, the peak of the curve migrates towards higher correlation values for decreasing bandwidth. This results from the fact that the interaural correlation is a nonlinear function of the noise energies E_π and E_o. If the mean interaural correlation is set to 0.9 and the bandwidth is 10 Hz, it can be observed in the left panel of Fig. 1 that there is a finite probability for correlation values to be smaller than 0.8, a value that differs by more than 0.1 from the mean interaural correlation. This property is highly asymmetric; correlations higher than $+1$ cannot occur. If, despite this asymmetric property, the mean correlation is 0.9, the peak of the curve must occur at a correlation greater than 0.9.

The addition of the Sπ signal results in a shift of the curves towards lower correlation values. Furthermore, the distributions show a small increase in their widths. In the left panel (10-Hz bandwidth), the shift of the curve is small compared to the width of the distributions. Thus, from a signal-detection point of view, it is likely that at this signal-to-masker ratio, interaural correlation uncertainty can influence the detection performance. For a bandwidth of 100 Hz and a reference correlation of 0.9 (middle panel), the curves for masker alone and masker plus signal show a smaller overlap. If the reference correlation is reduced to 0.8 (right panel), the amount of overlap is increased. We can conclude that both the bandwidth and the reference correlation of the noise have a strong effect on the detectability of the signal in terms of interaural correlation. If human observers indeed use the interaural correlation as a decision variable, thresholds should depend on the stimulus parameters that determine the amount of correlation uncertainty.

In fact, experimental data from Gabriel Colburn (1981) and van der Heijden and Trahiotis (1998) confirm this hypothesis. Gabriel and Colburn (1981) found that if the bandwidth of a noise stimulus is increased from 5 to 1000 Hz, the interaural correlation just noticeable difference (jnd) for a reference correlation of 0 decreases by a factor of 2. Moreover, the change in the correlation jnd was largest for bandwidth below the critical bandwidth. For masker bandwidths beyond the critical bandwidth, the correlation jnd did not change by a large amount. This might indicate that the internal interaural correlation is evaluated after filtering in the periphery of the auditory system. For a reference correlation of $+1$, the correlation jnd remained approximately constant for bandwidths up to the critical bandwidth. However, an increase in the correlation jnd was observed when the bandwidth was increased well beyond this value. Although critical band filtering seems to play a role under these conditions, this increase in thresholds is not yet understood. The data obtained by van der Heijden and Trahiotis (1998) showed that the correlation dependence of thresholds is much stronger at narrow bandwidth (3 Hz) than at large bandwidth (900 Hz). This corresponds to the notion that correlation uncertainty influences detection, because the probability density function for the correlation is wider at narrow bandwidths (see Fig. 1).

The consequences of the use of frozen noise upon correlation uncertainty are very simple. If exactly the same noise waveform is used in each trial and each token of a multiple-interval, forced-choice procedure, there is no uncertainty in the masker interval; the interaural correlation always has the same value. The addition of the Sπ signal results in a deviation from this fixed value. The actual value depends on the signal-to-noise ratio: a higher signal level results in a lower correlation.

B. The EC theory

Durlach's EC theory (Durlach, 1963) is another well-known theory to account for BMLDs. According to this theory the waveforms which arrive at both ears are modified by an interaural time delay and an interaural level adjustment in such a way that the masker waveforms are equalized (the E process). This process is performed imperfectly as a result of internal errors. Subsequently, the stimulus in one ear is

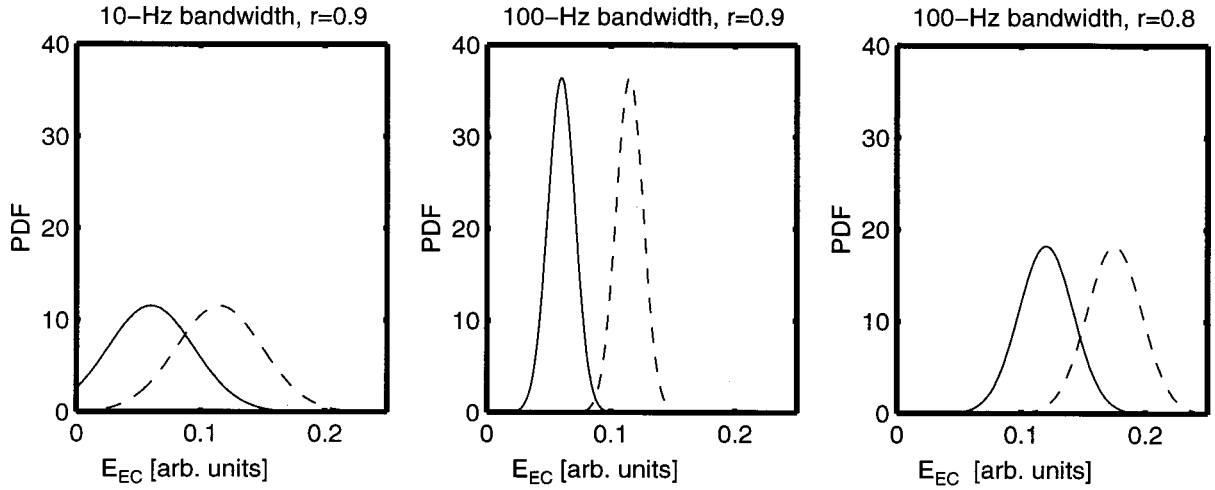

FIG. 2. Probability density functions for E_{EC} (see the text) for different values of the reference correlation and the masker bandwidth. The format is the same as in Fig. 1.

subtracted from the stimulus in the other ear (cancellation, or C process). In binaural conditions, this process often leads to an improvement of the signal-to-masker ratio and hence to the prediction of a positive BMLD. In an NρSπ condition no equalization is available that yields a signal-to-masker ratio improvement. Hence, the improvement in signal-to-masker ratio is obtained by calculating the amount of masker energy that is removed by the cancellation process. From Eq. (1), it can be seen that the common part of the masking noise will be removed and that the N_π masker portion remains. Thus, the amount of stimulus energy that remains after the EC-process equals[1]

$$E_{EC}=2(1-\rho)E_\pi+4E_S, \tag{2}$$

where E_S denotes the signal energy and E_{EC} is the energy of the difference signal between the left and right ears. The use of the difference energy as a decision variable was also suggested by Breebaart *et al.* (1999) for NoSπ stimuli with non-Gaussian maskers. If no signal is present, E_S is simply zero. Assuming that E_{EC} is used as a decision variable, stimulus uncertainty will influence the detection task because E_π is a random variable with a certain mean and standard deviation. Equations (A4) to (A6) in the Appendix give a description of the variability of E_π. A graphical representation of this description is shown in Fig. 2. The format is the same as in Fig. 1; the left and middle panels correspond to a reference correlation of 0.9, the right panel to 0.8. The bandwidth of the noise is 10 Hz in the left panel and 100 Hz in the other panels. Each panel contains two curves; the solid lines represent the PDF for E_{EC} for a masker alone, the dashed lines for masker plus signal. For simplicity it is assumed that the rms value of the noise sources equals 1 (arbitrary units) and the signal-to-masker ratio is -10 dB. The masker had a duration of 300 ms. The curves in Fig. 2 show a similar behavior as in Fig. 1; a wider bandwidth or a higher reference correlation results in a narrower distribution of E_{EC}, and hence a better detectability of the signal.

If a frozen-noise sample is used, E_π has a fixed value. Hence, no uncertainty in terms of the EC theory is present in the stimulus (the power of the difference signal is frozen) and the only limitation for detection is internal noise.

C. Interaural differences in time and intensity

The interaural differences (IIDs and ITDs) present in an interaurally partially correlated noise fluctuate as a function of time. In a running-noise condition, the random fluctuations can be described in terms of a probability distribution. We determined these probability distributions by computing a partially correlated noise in the digital domain of sufficient duration (3 s at a sample rate of 32 kHz). After a Hilbert transform of the left and right signals, the interaural intensity differences and interaural time differences were obtained. From these differences, histograms were computed which are (close) approximations of the PDFs of the IIDs and ITDs. This procedure was repeated for masker plus signal for a signal-to-masker ratio of -10 dB. The results are shown in Fig. 3. The format is the same as Figs. 1 and 2. The left panels correspond to a masker bandwidth of 10 Hz and a reference correlation of 0.9; the middle panels to a bandwidth of 100 Hz and a correlation of 0.9, and the right panels to a bandwidth of 100 Hz and a reference correlation of 0.8. The solid lines represent distributions for the maskers alone, the dashed lines for masker plus signal. The upper panels represent the interaural phase differences (IPD); the lower panels represent the IIDs.

The following facts can be observed in Fig. 3. First, if we compare the middle panels to the left panels (i.e., the effect of bandwidth), no difference is observed. Thus, the width of the PDF for the interaural differences does not depend on the bandwidth and the range of variation of the IIDs and ITDs does not change systematically with bandwidth. The *rate* of variation does, however, increase if the bandwidth is increased. This property is important for our hypothesis about stimulus uncertainty. It if often assumed that the binaural auditory system is sluggish in processing binaural cues (cf. Grantham and Wightman, 1978, 1979; Grantham, 1984; Kollmeier and Gilkey, 1990; Culling and Summerfield, 1998). Thus, because the amount of uncertainty is *not*

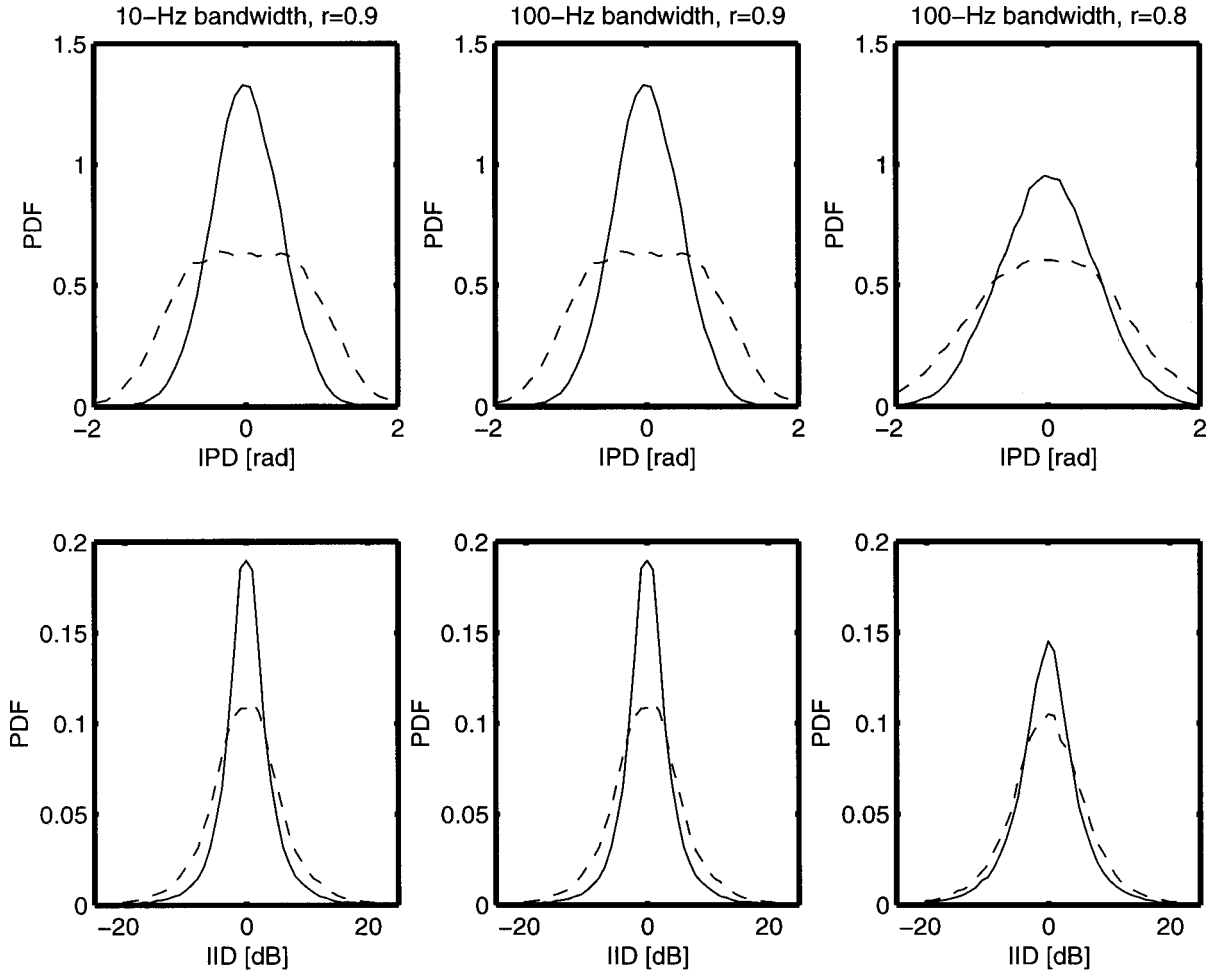

FIG. 3. Probability density functions for the IPD (upper panels) and IID (lower panels) in the same format as Figs. 1 and 2.

changed by the masker bandwidth, it is expected that thresholds will *increase* with increasing bandwidth as a result of the increase in the rate of fluctuation of the IIDs and ITDs. This is in contrast to the expectations based on the EC theory or models based on interaural correlation; these models predict a *decrease* with increasing bandwidth.

The solid line in the right panel of Fig. 3 demonstrates that a decreasing interaural correlation results in an increase in the width of the PDF, a similar effect as observed in the curves for the correlation and the EC theory. The addition of the signal has a different effect on the PDFs compared to the two other models discussed in this paper. Instead of a shift of the mean, an increase in the width of the distribution is observed. This property makes it more difficult to analyze these PDFs in terms of detectability. Nevertheless, the observation that a change in the bandwidth results in different expectations for the three theories makes it valuable also to discuss our data in terms of IIDs and ITDs.

III. EXPERIMENT I

A. Procedure and stimuli

A three-interval, forced-choice procedure with adaptive signal-level adjustment was used to determine masked thresholds. Three masker intervals of 300-ms duration were separated by pauses of 300 ms. A signal of 200-ms duration was added to the temporal center of one of the masker intervals. Feedback was provided after each response of the subject.

The signal level was adjusted according to a two-down, one-up rule (Levitt, 1971), tracking the 70.7% correct score within a 3IFC paradigm. This corresponds to $d' = 1.26$. The initial step size for adjusting the level was 8 dB. The step size was halved after every second track reversal until it reached 1 dB. The run was then continued for another eight reversals. The median level at these last eight reversals was used as the threshold value. At least three threshold values were obtained for each parameter value and subject. All stimuli were generated digitally and converted to analog signals with a two-channel, 16-bit D/A converter at a sampling rate of 32 kHz. The stimuli were presented over Beyer Dynamic DT990 headphones.

The 300-ms masker samples were obtained by adding interaurally in-phase noise and interaurally out-of-phase noise with the appropriate weighting factors [Eq. (1)]. For running-noise conditions, the noise samples for each interval were obtained by randomly selecting 300-ms segments from a two-channel, 2000-ms bandpass-noise buffer. The 2000-ms noise buffer was created in the frequency domain by selecting the desired frequency range from the Fourier transforms of two independent 2000-ms broadband Gaussian noises. After an inverse Fourier transform, and combination of the two

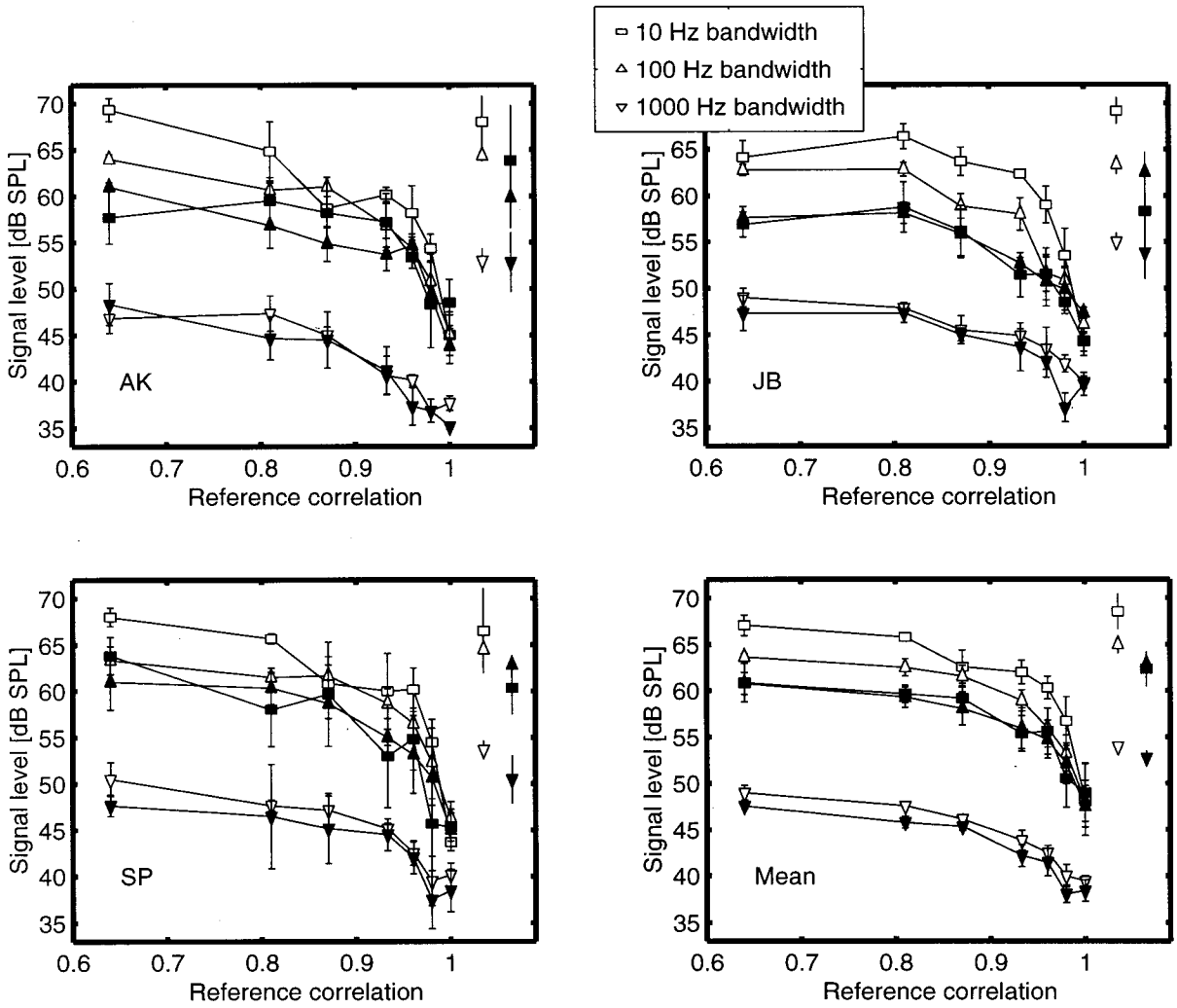

FIG. 4. Binaural masked thresholds as a function of the reference correlation. The bottom-right panel shows the mean thresholds; the other panels show individual thresholds for three subjects. The squares correspond to a masker bandwidth of 10 Hz, the upward triangles to 100 Hz, and the downward triangles to 1000 Hz. The open symbols represent running-noise conditions; the filled symbols represent frozen-noise conditions. The isolated symbols represent NoSo reference data. Error bars denote the standard error of the mean. The masker level for all three bandwidths was 65 dB.

noise signals according to Eq. (1), the two-channel (for the left and right ears) bandlimited noise buffer with the specified reference correlation was obtained. It is important to note that the specified reference correlation is the correlation of the 2000-ms noise buffer. The correlations of shorter segments (like the 300-ms noise segments used in the running-noise experiments) will in general deviate from this exact value (see Fig. 1).

For frozen-noise conditions, only one fixed 300-ms noise sample was used for which the interaural correlation was equal to the reference correlation.[2] This noise sample was generated by adding two independent bandlimited noise samples of 300 ms with a *fixed* rms value. These bandlimited noise samples were generated in the same way as the noise buffers for random-noise conditions followed by a normalization of their rms values. The partially correlated noise was then generated by combining the noises according to Eq. (1). The same noise sample was used during one run. To exclude the possibility that the frozen-noise thresholds would depend on the specific waveform of the token, a different frozen-noise sample was used for each run, and the mean threshold from these runs was used as threshold value. All noise maskers were presented at an overall level of 65 dB SPL.

The 200-ms signals were interaurally out-of-phase sinusoids with a frequency of 500 Hz. In order to avoid spectral splatter, the signals and the maskers were gated with 50-ms raised-cosine ramps. Thresholds are expressed as the means of at least three repetitions per condition and subject. Binaural masked thresholds were measured for $N\rho S\pi$ conditions, where the bandwidth of the noise was either 10, 100, or 1000 Hz. The center frequency of the noise masker was always 500 Hz. Reference correlations of $\rho = 1$, 0.98, 0.96, 0.93, 0.87, 0.81, and 0.64 were used. In addition, NoSo thresholds were also obtained. Three well-trained subjects with normal hearing participated in the experiments.

B. Results

The experimental data are shown in Fig. 4 as a function of the reference correlation. The bottom-right panel shows the mean thresholds, while the other panels show individual thresholds for the three subjects. The squares correspond to a

masker bandwidth of 10 Hz, the upward triangles correspond to 100 Hz, and the downward triangles to 1000 Hz. The open symbols represent running-noise conditions; the filled symbols represent frozen-noise conditions. The NoSo thresholds are plotted in the upper-right corners of each panel. The error bars denote the standard error of the mean.

For both running- and frozen-noise conditions, the NρSπ thresholds increase with decreasing reference correlation. This increase is strongest for the 10-Hz running-noise masker, which increases by 18.8 dB if the correlation is decreased from +1 to 0.64. For the 100-Hz-wide and 1000-Hz-wide running-noise conditions, the increase amounts to 15.5 and 10 dB, respectively. These values are in good agreement with data from van der Heijden and Trahiotis (1998). For frozen-noise maskers, the increase amounts to 12, 13.3, and 9.2 dB, for the 10-, 100-, and 1000-Hz-wide conditions, respectively.

The thresholds for frozen and running-noise maskers are approximately equal for a reference correlation of +1, while for decreasing reference correlations, the difference between frozen and running-noise maskers increases, especially for the narrow-band conditions. The reference correlations at which frozen and running-noise thresholds become different are 0.98 for a bandwidth of 10 Hz and 0.93 for a bandwidth of 100 Hz. As interaural correlation decreases the differences between running- and frozen-noise conditions reach 7 dB for the 10-Hz-wide masker, and 4 dB for the 100-Hz-wide condition. For the 1000-Hz-wide maskers, the thresholds for running and frozen noise are very similar.

The differences between the 100-Hz and 1000-Hz conditions vary considerably across reference correlations, both for running and frozen-noise conditions. For running noise, the difference in thresholds amounts to 9 dB for a reference correlation of +1 and increases up to a value of 14 dB for a reference correlation of 0.64. For frozen noise, these values are 10.6 and 13.3 dB, respectively. Because the overall masker level was kept constant, a difference of about 10 dB between 100-Hz and 1000-Hz thresholds would correspond to a constant signal-to-noise ratio at the output of an auditory filter with a bandwidth of 78 Hz [1 equivalent rectangular bandwidth (ERB) at 500 Hz, Glasberg and Moore, 1990].

The NoSo thresholds for *running* noise show a decrease with increasing masker bandwidth. The signal-to-noise ratio decreases from +4 dB at 10 Hz to 0 dB at 100 Hz and finally to −11 dB at 1000 Hz, very similar to experimental data from van de Par and Kohlrausch (1997, 1999). In contrast, for *frozen* noise, the NoSo thresholds are very similar for the 10- and 100-Hz bandwidth (S/N$=-2$ dB), while for the 1000-Hz bandwidth, the threshold is 10 dB lower. In general, the relation between running- and frozen-noise thresholds in the NoSo condition equals that for NρSπ with $\rho<0.95$. For the smallest reference correlation (i.e., $\rho=0.64$), the running-noise BMLD for a bandwidth of 10 and 100 Hz is almost zero (except for subject JB, who has a BMLD of 5 dB for this condition). For the 1000-Hz-wide condition, the BMLD is 6 dB for $\rho=0.64$, consistent with data from Robinson and Jeffress (1963).

C. Discussion

Following our hypothesis that stimulus uncertainty influences NρSπ thresholds, the difference between frozen and running-noise conditions should be larger at lower reference correlations, as a result of the fact that stimulus uncertainty increases with decreasing correlation. In addition, frozen- and running-noise thresholds should be equal for a reference correlation of +1, because no uncertainty in terms of binaural cues is present in the masker intervals. These effects are clearly visible in our data (Fig. 4) for the bandwidths of 10 and 100 Hz. For a bandwidth of 1000 Hz, there is almost no difference between the running and frozen-noise conditions for all values of the reference correlation. This suggests that for this value of the masker bandwidth, stimulus uncertainty does not influence the detection of the signal and the thresholds are limited by internal noise (similar to the frozen-noise data). Interestingly, the data that are limited by internal errors also show a dependence on the masker correlation. This implies that the net effect of the internal noise must be larger for smaller interaural correlations. One possibility to implement this property in a quantitative binaural model is given in Breebaart *et al.* (2001).

For the quantitative analysis of our data in terms of the binaural models described in Sec. II, we will concentrate on those conditions where, presumably, external variability is dominant over internal noise. In terms of the terminology used by Lutfi (1990), we are interested in conditions with a substantial amount of informational masking. As a measure for this we take the difference between running- and frozen-noise thresholds. Substantial differences are observed for a 10-Hz-wide masker and reference correlations at or below 0.98, and for a 100-Hz-wide masker at or below 0.93. For the 1000-Hz data, the difference is small at all correlation values and those data are therefore not included in the analysis.

The influence of external variability in the binaural data is stronger at 10 Hz than at 100-Hz bandwidth. This supports the expectations based on the EC theory and on correlation uncertainty, because both models predict a stronger difference between frozen and running noise at narrower bandwidths. The data are, however, not in line with the expectations based on the evaluation of IID and ITD cues. The distributions of these cues do not depend on the bandwidth, and hence no effect is expected if uncertainty is considered. Including the effect of binaural sluggishness, this should lead to an increase in threshold with an increase in masker bandwidth. This, however, is not found in the data, which show a decrease of the running-noise thresholds with increasing bandwidth.

In order to verify the hypotheses based on the EC theory and the interaural correlation quantitatively, we computed the detectability of the running-noise thresholds shown in Fig. 4 based on the two models for those conditions in which detection is apparently limited by stimulus uncertainty (i.e., $\rho\leqslant 0.98$ at 10-Hz bandwidth and $\rho\leqslant 0.93$ at 100-Hz bandwidth). For the interaural correlation, the detectability was calculated using the distribution of the interaural correlation expressed in terms of Fisher's Z (see the Appendix). The rationale for the transformation from correlation to Z lies in the fact that the correlation probability does not have a

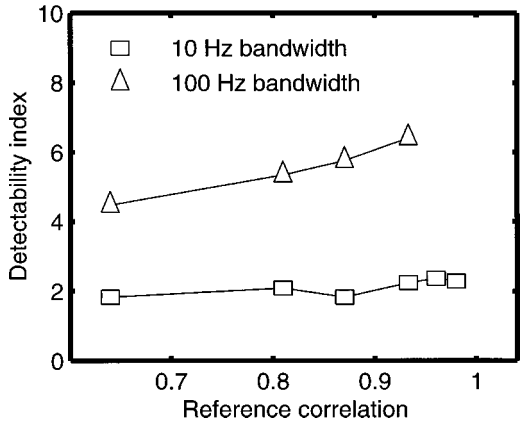

FIG. 5. Detectability index d' in terms of interaural correlation for the running-noise NρSπ conditions as a function of the reference correlation. The squares denote the 10-Hz-wide condition and the upward triangles the 100-Hz-wide condition.

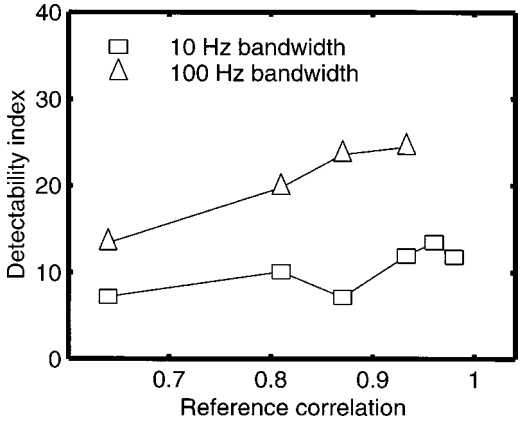

FIG. 6. Detectability index d' in terms of E_{EC} for the running-noise NρSπ conditions as a function of the reference correlation. The squares denote the 10-Hz-wide condition and the upward triangles the 100-Hz-wide condition.

Gaussian distribution, while Fisher's Z does have an approximately Gaussian distribution. For both the masker alone and the masker plus test signal at threshold, the probability distributions for Z were computed and from these distributions, the sensitivity index d' was calculated. For the sinusoidal signals, a length of 200 ms including 50-ms ramps was used to calculate the change in correlation. For the masker-alone correlation interval, a duration of 200 ms was assumed, because this corresponds to the signal length and hence the duration from which the binaural system can extract useful information concerning interaural correlation changes. Peripheral preprocessing was simulated by first filtering the signals with a fourth-order gammatone filter with a center frequency of 500 Hz and a bandwidth of 78 Hz (cf. Glasberg and Moore, 1990). The values for d' are shown in Fig. 5.

The squares denote the 10-Hz masker condition and the upward triangles the 100-Hz condition. Clearly, most values of d' are higher than the theoretical value of 1.26 that results from the applied procedure. The values of d' across reference correlations are relatively constant for 10-Hz bandwidth and increase systematically towards high reference correlations for 100-Hz bandwidth. Only the 10-Hz condition shows a fair agreement with d' in terms of the correlation uncertainty. From this simulation it appears that the correlation uncertainty is a valid statistic only for the 10-Hz-wide condition.

The large values of d' for the 100-Hz-wide conditions may indicate that, in the processing of these stimuli in the auditory system, information is lost. An optimal detector, basing its decision on the correlation change within the 200 ms of signal duration, would perform much better than the subjects, given the high values of d' for correlation discrimination. Such a loss of information might be caused by the fact that the subjects are not able to process the whole stimulus but extract a decision variable based on a shorter part of the sample.

Another possibility is that the correlation hypothesis is not correct and that detection behavior can be better described by another statistic, for example based on the EC theory. Equation (2) gives the relation between the decision variable E_{EC} and the source of stimulus uncertainty, E_π. With the help of Eqs. (A4) to (A6) and (A18) in the Appendix, the detectability index in terms of E_{EC} can be determined for the conditions limited by stimulus uncertainty. These indices are shown in Fig. 6, in the same format as in Fig. 5.

All values for d' in terms of E_{EC} are much higher than the theoretical value of 1.26. This indicates that E_{EC} is not a valid descriptor for the influence of stimulus variability.

An important remark can be made if the values for d' are compared for the correlation (Fig. 5) and the EC theory (Fig. 6). The values are completely different for these theories, the latter being much higher. This observation is particularly of interest given the analysis of Green (1992). He stated that a correlation model leads to identical predictions as an EC model in an NoSo vs NoSπ discrimination paradigm. Figures 5 and 6 show that this conclusion is not valid for conditions that are dominated by stimulus uncertainty.

In summary, both the 10-Hz-wide and the 100-Hz-wide conditions show large differences between the running and frozen-noise conditions, indicating that stimulus uncertainty dominates the detection process. This effect is smaller at 100 Hz than at 10-Hz bandwidth. The thresholds decrease with an increase in masker bandwidth in the running-noise conditions, which is not in line with expectations based on the processing of IID and ITD cues. An uncertainty analysis in terms of the EC theory revealed that an EC process fails to account for the thresholds found in the running-noise conditions.

The only close match between experimental data and predictions was found for the 10-Hz-wide conditions based on the interaural cross correlation. If one assumes that stimulus uncertainty limits the detection and the correlation is a valid statistic for describing thresholds, the psychometric function for an NρSπ condition as a function of the signal level can be predicted. To study to what extent this is true, a second experiment was performed, where predicted and measured psychometric functions were compared.

IV. EXPERIMENT II

A. Procedure and stimuli

In order to further examine the role of stimulus uncertainty in an NρSπ condition, we determined the psychomet-

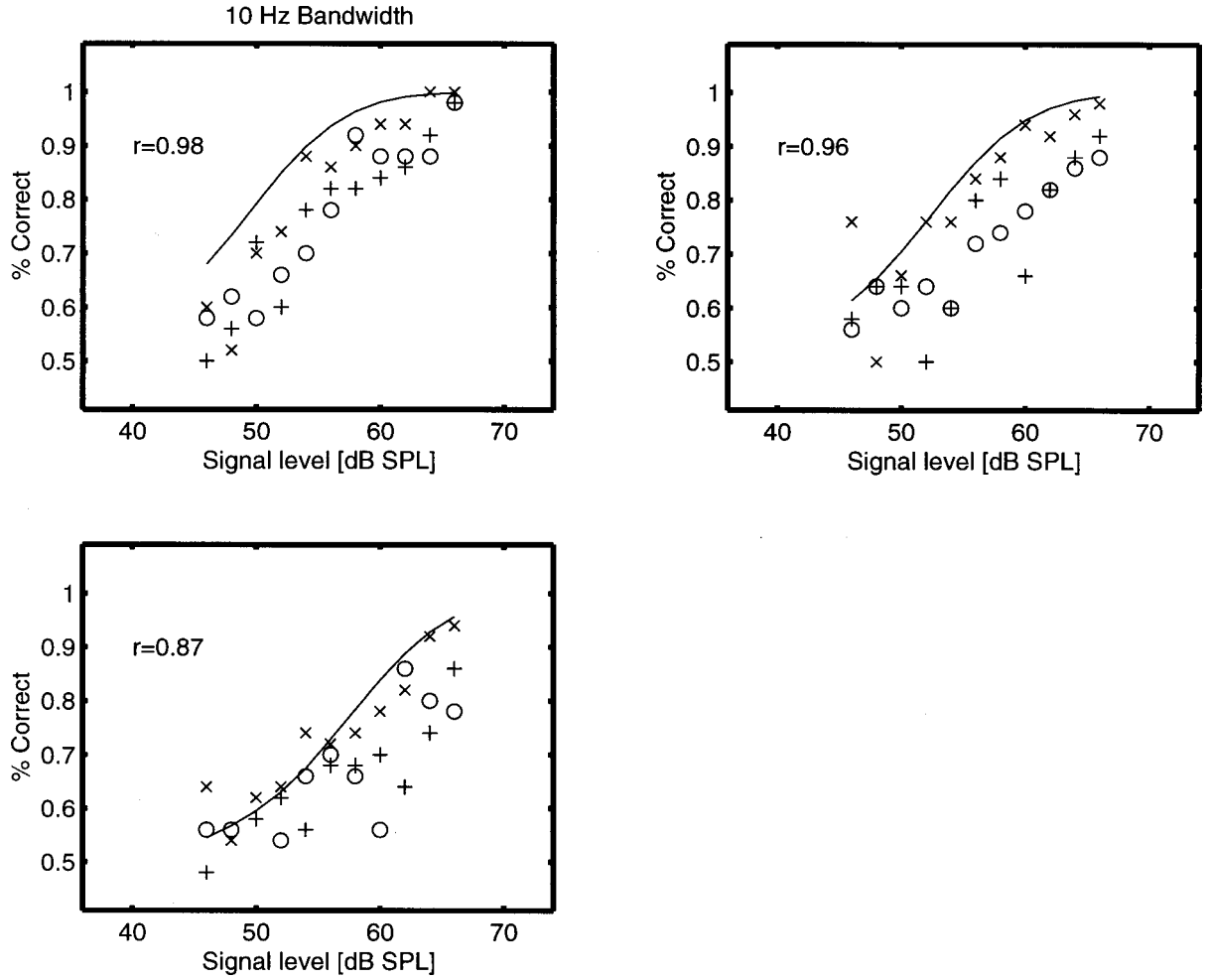

FIG. 7. Proportions correct as a function of the signal level for a running-noise NρSπ condition for $\rho=0.98$ (upper-left panel), $\rho=0.96$ (upper-right panel), and $\rho=0.87$ (lower-left panel). The different symbols represent different subjects. The bandwidth of the masker was 10 Hz. The solid line represents the predictions according to a correlation-uncertainty model (see the text).

ric functions for running-noise conditions at bandwidths of 10 and 100 Hz for reference correlations of 0.98, 0.96, and 0.87. Proportions correct were determined in a 2IFC procedure with 50 trials per condition by 3 subjects. The generation of the stimuli and the method of presentation to the subjects were similar to the method described in experiment I. The signal levels used to determine the subjects' performance were 46 to 66 dB SPL at 10-Hz bandwidth and 42 to 62 dB SPL at 100-Hz bandwidth with a step size of 2 dB.

B. Results

The proportions correct for the NρSπ condition as a function of the signal level are shown in Fig. 7 for a masker bandwidth of 10 Hz and in Fig. 8 for a bandwidth of 100 Hz. The different symbols denote different subjects. The upper-left panel represents data for $\rho=0.98$, the upper-right panel for $\rho=0.96$, and the lower panel for $\rho=0.87$. The data show an increase in the proportion of correct responses from 0.5 to 1 if the signal level is increased from 45 to 65 dB SPL at 10-Hz bandwidth and from 40 to 60 dB SPL at 100-Hz bandwidth. The solid lines represent the proportions correct based on the correlation probability density functions.

We calculated the predicted proportions correct as a function of the signal level based on the sensitivity index (d') determined from the correlation uncertainty. The values for d' were converted to proportions correct (p) by computing the area under the normal curve up to $d'/\sqrt{2}$ (see Green and Swets, 1966):

$$p=\int_{-\infty}^{d'/\sqrt{2}}\frac{1}{\sqrt{2\pi}}e^{-x^2/2}dx. \tag{3}$$

The predicted proportions correct are shown by the solid lines in Figs. 7 and 8. For a bandwidth of 10 Hz, the curves lie on top, close to the subjects' responses, indicating that the data can quite accurately be described (especially for the subject denoted by ''x'') by the stimulus uncertainty in the interaural correlation. However, at 100-Hz bandwidth, the subjects perform worse than the predictions based on the correlation uncertainty. This indicates that correlation uncertainty is not a valid descriptor for the 100-Hz data.

C. Discussion

Because of the close correspondence between the predicted and observed psychometric functions for the 10-Hz-

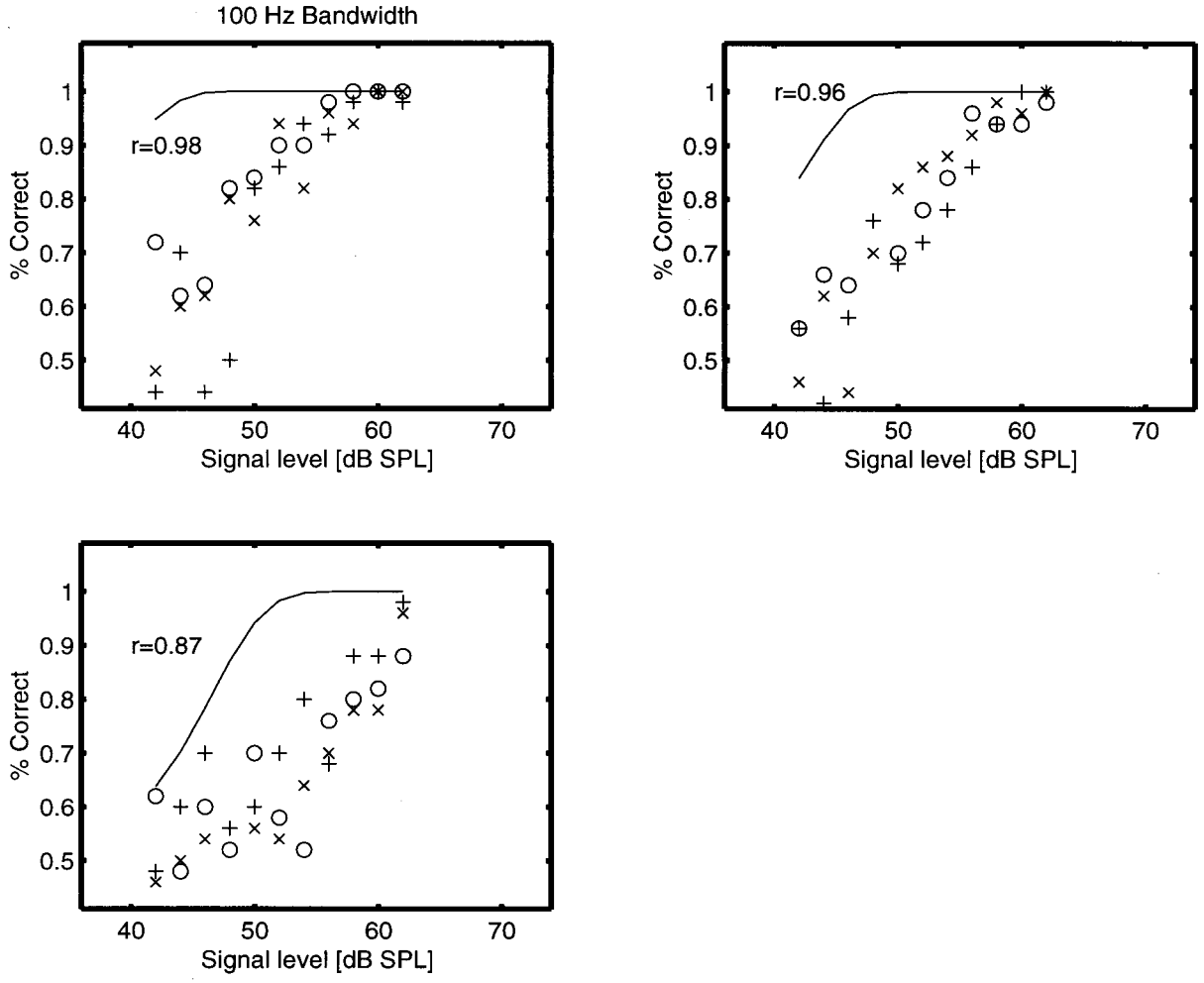

FIG. 8. Same as Fig. 7 for a masker bandwidth of 100 Hz.

wide maskers, it is likely that stimulus uncertainty limits the detection and that this uncertainty expressed in terms of the interaural correlation is a valid way to predict thresholds. For the 100-Hz condition, however, such an analysis overestimates the performance of the subjects.

We want to emphasize that although the interaural correlation is a valid detection statistic in *describing* the 10-Hz-wide running-noise conditions, this does not prove that observes indeed use this particular measure. We have shown, however, that stimulus uncertainty can play an important role in binaural detection paradigms. To further investigate the role of the interaural correlation as a detection statistic and the role of stimulus uncertainty, we performed a third experiment. This experiment is a compromise between the running-noise condition (i.e., with stimulus uncertainty) and the frozen-noise condition (i.e., absolutely no stimulus uncertainty). Two conditions were tested, which we refer to as ''fixed-ρ'' and ''interleaved.''

V. EXPERIMENT III

A. Procedure and stimuli

The following experimental paradigms were used:

(1) Fixed-ρ. In this condition, each trial consisted of three intervals which contained exactly the same noise sample. To one of these noise samples, the signal was added. For each trial, a different noise sample was calculated according to the frozen-noise algorithm described in Sec. III A. This implies that both the interaural correlation and the power of the interaural difference signal was fixed across all intervals of a run, but each noise sample was a different realization under the above constraints. Thus, across trials, the waveforms arriving at both ears were totally different, but the interaural correlation and the power of the interaural difference signal of the masker was fixed.

(2) Interleaved. Similar to the fixed-ρ condition, each trial consisted of three identical masker intervals, and again one interval contained the signal. However, the number of masker realizations was reduced to two. Thus, two frozen-noise samples were calculated as described in Sec. III A. For each trial, one of these realizations was chosen at random and used as the masker in all three intervals of this trial.

The measurement procedure, the signal durations and levels, and the method of presentation to the subjects were the same as described in Sec. III A. We measured thresholds for two masker bandwidths (10 and 100 Hz) and two masker corre-

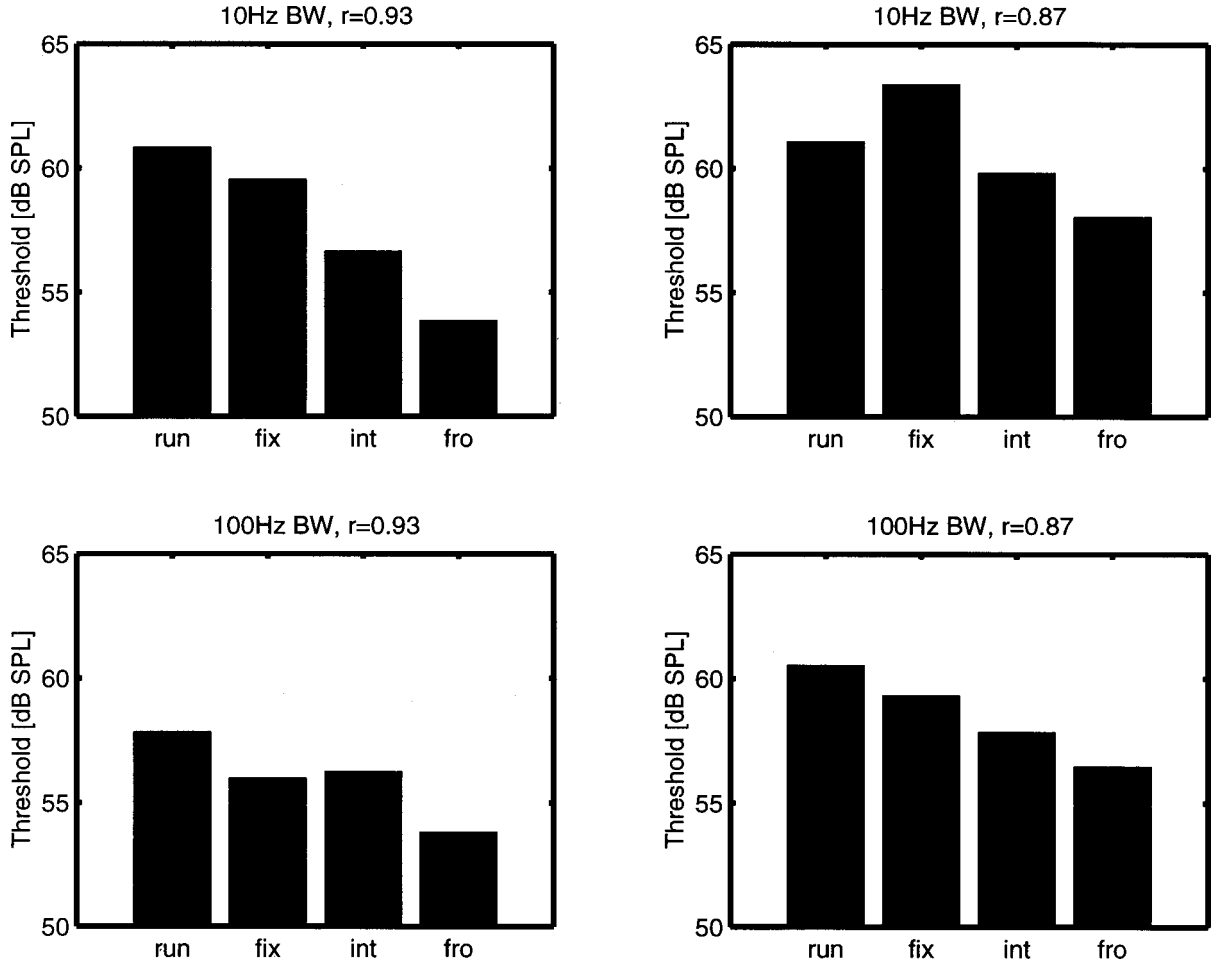

FIG. 9. Mean thresholds across three subjects for the running-noise (run), fixed-ρ (fix), interleaved (int), and frozen-noise (fro) conditions. The upper panels show thresholds for a bandwidth of 10 Hz, the lower panels for 100 Hz. The left and right panels correspond to an interaural correlation of 0.93 and 0.87, respectively.

lations (0.93 and 0.87). Three subjects participated in this experiment.

B. Results

The mean thresholds across subjects are shown in Fig. 9. The upper panels show thresholds for a masker bandwidth of 10 Hz; the lower panels correspond to 100-Hz bandwidth. The left and right panels correspond to an interaural correlation of 0.93 and 0.87, respectively. In each panel, four threshold values are shown. From left to right, these are thresholds for the running-noise condition of experiment I (labeled ''run''), the thresholds for the fixed-ρ condition (''fix''), the interleaved condition (''int''), and the frozen-noise condition of experiment I (''fro'').

As described above, these conditions reflect different levels of stimulus uncertainty. The first level corresponds to absolutely no stimulus uncertainty (frozen-noise conditions) and this condition results in uniformly lower thresholds than all other conditions. If the level of stimulus uncertainty is increased by a small step (the interleaved condition), thresholds increase by 1 to 3 dB for all tested conditions. A third level of stimulus uncertainty was to apply only one restriction to the masker stimuli: the overall interaural correlation and hence the power of the difference signal had to be constant. For three out of four conditions, this also resulted in an increase in thresholds. The differences between frozen-noise and fixed-ρ are about 6 dB at 10-Hz bandwidth and 4 dB at 100-Hz bandwidth. Finally, the highest level of stimulus uncertainty in the present experiments (i.e., running noise) resulted on average in very similar thresholds to those in the fixed-ρ conditions.[3]

C. Discussion

Some striking remarks can be made with respect to the thresholds for stimuli with a fixed interaural correlation (i.e., the fixed-ρ, the interleaved, and the frozen-noise conditions). If the binaural auditory system uses the interaural correlation of each token as a decision variable, the processing of the masker alone would result in an internal estimate of the externally presented interaural correlation. This internal value is fixed and only limited by internal noise. The addition of the signal results in a decrease of the interaural correlation and can thus be detected. Based on such an interaural-correlation processing, all the thresholds for the conditions with a fixed interaural correlation should give the same thresholds. This was not found in our data.

One reason for the differences across these conditions may be peripheral filtering. The externally presented stimu-

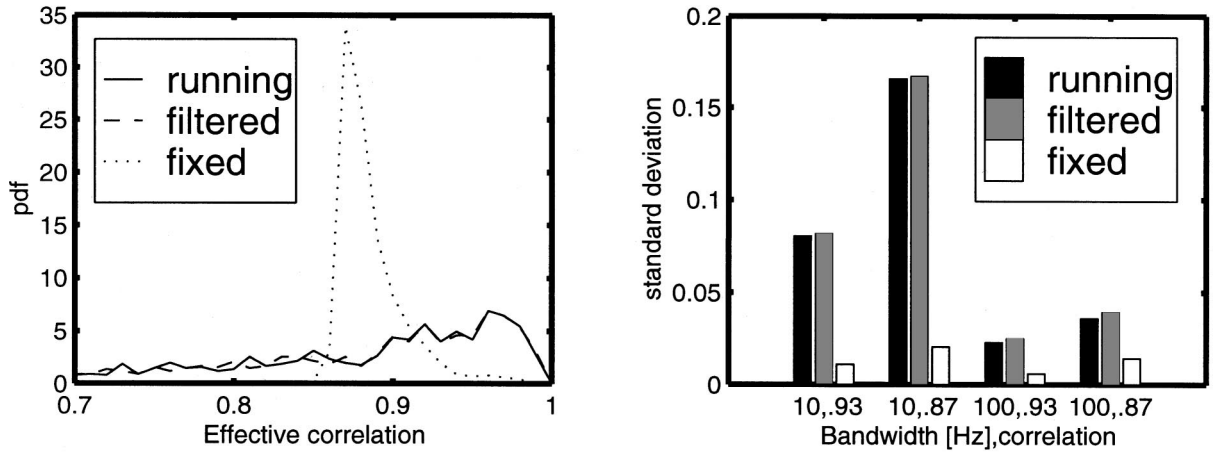

FIG. 10. Left panel: simulated correlation distribution for a 10-Hz-wide, Nρ stimulus with a reference correlation of 0.87. These distributions were obtained for running noise (running), running noise after peripheral filtering (filtered), and for fixed-ρ conditions after peripheral filtering (fixed). Right panel: standard deviations for the same stimuli as in the left panel for different values for the masker bandwidth and correlation.

lus has a fixed interaural correlation. Peripheral filtering in the cochlea results in frequency-dependent phase shifts in the presented waveforms at both ears. These phase shifts result in a change in the interaural correlation. Therefore, for the fixed-ρ condition, the interaural correlation of different tokens after peripheral filtering follows a distribution rather than having a fixed value. To evaluate this hypothesis quantitatively, we computed 1000 partially correlated noises following three different procedures:

(1) Running-noise samples which are generated in the same way as described in Sec. III A.
(2) The same running-noise samples after filtering by a fourth-order gammatone filter with a center frequency of 500 Hz. This filter simulates the effect of peripheral filtering in the inner ear; and
(3) Fixed-ρ samples generated as described in Sec. III A, also after filtering with the gammatone filter.

An example of the correlation distributions that were found with this procedure is given in the left panel of Fig. 10. In this example, the bandwidth of the noise was 10 Hz and the reference correlation was 0.87. The solid line is the distribution for running noise without filtering (i.e., procedure 1). The dashed line corresponds to procedure 2 (i.e., running noise after peripheral filtering). Clearly, these distributions are very similar, indicating that peripheral filtering does not change the statistics of the interaural correlation for running noise. The distribution for fixed-ρ after peripheral filtering is shown by the dotted line. In line with our hypothesis, the distribution has a substantially reduced standard deviation. The values for the standard deviation of the correlation distribution are shown in the right panel of Fig. 10. The black bars correspond to the running-noise procedure without filtering (number 1 in the above description); the gray bars denote running noise after peripheral filtering (2), and the white bars denote fixed-ρ samples after peripheral filtering (3). The x axis indicates the combinations of bandwidth and reference correlation of the noise for each condition. All fixed-ρ conditions have a nonzero amount of correlation uncertainty. This supports the hypothesis that peripheral filtering produces uncertainty in the interaural correlation. The magnitude of this correlation uncertainty is, however, not sufficient to explain the thresholds of the fixed-ρ condition. We computed the values for the detectability index in terms of interaural correlation for the fixed-ρ condition after peripheral filtering as described in Sec. III B. All d' values for the filtered fixed-ρ condition were above 27, indicating that subjects performed worse than expected from correlation uncertainty introduced by peripheral filtering.

An important conclusion that can be drawn from these results is that it is unlikely that the auditory system uses the interaural correlation of the complete token as a decision variable. These results also show that the overall power of the difference signal of the complete token as a decision variable is not a valid descriptor of how the auditory system processes Nρ stimuli.

A possibility to explain the results qualitatively is based on the idea of internal templates (Dau *et al.*, 1996a, b; Breebaart and Kohlrausch, 1999). Assume that listeners develop an internal representation of the interaural differences that occur as a function of time if a masker alone is presented. Such a template can be obtained from the masker-alone intervals in the 3IFC task. One possible realization would be the running average of the difference power based on a time constant that is smaller than the duration of the tokens. If such a template exists, then the task of the listener is to match the template to the internal representation of the actually presented stimuli.

For example, in an NoSπ condition, the masker alone contains no interaural differences. Hence, the template consists of a sequence of zero interaural differences. The addition of the signal results in changes in the interaural differences which can be detected. In this case, there is no uncertainty in the masker-alone representation. The same holds for the frozen-noise conditions. All masker-alone intervals are identical, resulting in the same template. The only task that a listener has to perform is to detect which interval produces an internal representation that differs from the template. This process is in principle limited by internal noise only.

If two different Nρ tokens are used in random order (i.e., the interleaved condition), detection becomes somewhat more complicated. For perfect detection, the listener has to store two templates (one for each token) and must be able to recognize which masker token is used before the templates are compared with the actual stimulus. If the wrong template is matched with the stimulus, all intervals from the trial result in an imperfect match of the template. This increases the probability of choosing the wrong interval, and hence detection performance decreases.

For the fixed-ρ condition, finally, it is only possible to derive an averaged template based on many different noise realizations. This explains the increase in thresholds with respect to the interleaved and frozen conditions, in which the template has a close relation to the actual stimulus. In such a view, fixed-ρ and running-noise conditions are equivalent with respect to the detection strategy. The fixed-ρ condition, however, does allow comparison of internal representations across the three intervals within a trial. Given our experimental data, which show no statistically significant difference between fixed-ρ and running-noise conditions, we can conclude that such an across-interval comparison does not give a significant detection advantage in our conditions.

VI. GENERAL CONCLUSIONS

The results suggest that for binaural signal detection with partially correlated noises, two factors play an important role:

(1) The reference correlation. With decreasing masker correlation, the NρSπ thresholds increase; and
(2) Stimulus uncertainty. Our results show that uncertainty in binaural cues reduces detection performance, especially in narrow-band conditions.

An unresolved issue concerning the data presented in this paper is the method of internal binaural processing. We have shown that the three theories tested (the interaural correlation, the EC theory, or the processing of IIDs and ITDs) cannot account for the results found in this study. The data suggest that the auditory system is able to use internal templates in the process of binaural signal detection. Quantitative tests to support this notion are, however, beyond the scope of this paper and have yet to be performed.

ACKNOWLEDGMENTS

We thank A. Houtsma, S. van de Par, the Associate Editor D. W. Grantham, and the reviewers for their valuable comments on earlier drafts of this paper. The investigations were supported by the Research Council for Earth and Lifesciences (ALW) with financial aid from the Netherlands Organization for Scientific Research (NWO).

APPENDIX

For the generation of an NρSπ stimulus, two independent noise sources $N_0(t)$ and $N_\pi(t)$ with the same rms value are used, which are combined as follows to yield $L(t)$ and $R(t)$ for the left and right ears, respectively:

$$L(t)=\tfrac{1}{2}\sqrt{2}\sqrt{1+\rho}N_0(t)+\tfrac{1}{2}\sqrt{2}\sqrt{1-\rho}N_\pi(t)+S(t),$$
$$R(t)=\tfrac{1}{2}\sqrt{2}\sqrt{1+\rho}N_0(t)-\tfrac{1}{2}\sqrt{2}\sqrt{1-\rho}N_\pi(t)-S(t). \quad \text{(A1)}$$

As a result of fluctuations in the energy of a finite-length interval of the Gaussian-noise samples $N_0(t)$ and $N_\pi(t)$, the effective correlation (ρ_{eff}) of the masker sample may deviate from the desired reference correlation (ρ). Because the noise sources $N_0(t)$ and $N_\pi(t)$ are independent, the effective (i.e., physically occurring) interaural correlation (ρ_{eff}) for the NρSπ stimulus can be written as (neglecting the correlation between the two independent noise sources N_0 and N_π; see also footnote 2)

$$\rho_{\text{eff}}=\frac{(0.5+0.5\rho)E_0-(0.5-0.5\rho)E_\pi-E_s}{(0.5+0.5\rho)E_0+(0.5-0.5\rho)E_\pi+E_s}, \quad \text{(A2)}$$

where E_x is defined as the energy of the stimulus of duration T, according to

$$E_x=\int_{-T/2}^{T/2}N_x^2(t)dt. \quad \text{(A3)}$$

From Rice (1959), it is known that for a Gaussian-noise sample, E is distributed normally according to:

$$p(E)=\frac{1}{\sigma_E\sqrt{2\pi}}e^{[-(E-m_E)^2]/2\sigma_E^2}, \quad \text{(A4)}$$

with

$$m_E=T\int_0^\infty \omega(f)df, \quad \text{(A5)}$$

and

$$\sigma_E^2=T\int_0^\infty \omega^2(f)df. \quad \text{(A6)}$$

Here, $\omega(f)$ refers to the spectral power density of the noise source. The relation between the energies E_0, E_π, and E_s for a certain ρ_{eff} according to Eq. (A2) is given by

$$E_0=\alpha E_\pi+\beta E_s, \quad \text{(A7)}$$

with

$$\alpha=\left(\frac{0.5-0.5\rho}{0.5+0.5\rho}\right)\left(\frac{1+\rho_{\text{eff}}}{1-\rho_{\text{eff}}}\right), \quad \text{(A8)}$$

and

$$\beta=\frac{1+\rho_{\text{eff}}}{(1-\rho_{\text{eff}})(0.5+0.5\rho)}. \quad \text{(A9)}$$

One way to realize a correlation of ρ_{eff} is to fix E_π at a certain value and compute the necessary value of E_0 according to Eq. (A7). The probability for that realization of ρ_{eff} is then equal to the product of the probabilities $p_E(E_0)$ and $p_E(E_\pi)$. Because there are many possible ways to realize a correlation of ρ_{eff}, we have to sum all possibilities of these realizations

$$p(\rho_{\text{eff}})\Delta\rho_{\text{eff}}=\sum_{E_\pi} p_E(E_0)\Delta E_0 p_E(E_\pi)\Delta E_\pi, \quad \text{(A10)}$$

which results in

$$p(\rho_{\text{eff}}) = \int_{E_\pi} p_E(\alpha E_\pi + \beta E_s) p_E(E_\pi) \frac{\partial E_0}{\partial \rho_{\text{eff}}} dE_\pi, \quad \text{(A11)}$$

and hence

$$p(\rho_{\text{eff}}) = \frac{1}{\sigma_E^2 2\pi} \times \int_{E_\pi} \exp\left(\frac{-(\alpha E_\pi + \beta E_s - m_E)^2 - (E_\pi - m_E)^2}{2\sigma_E^2} \right) \times \frac{\partial E_0}{\partial \rho_{\text{eff}}} dE_\pi, \quad \text{(A12)}$$

with

$$\frac{\partial E_0}{\partial \rho_{\text{eff}}} = \frac{0.5 - 0.5\rho}{0.5 + 0.5\rho} \frac{2}{(1-\rho_{\text{eff}})^2} E_\pi + \frac{2}{(1-\rho_{\text{eff}})^2 (0.5 + 0.5\rho)} E_s. \quad \text{(A13)}$$

In summary, if the spectral shape of the noise source and the sample duration are known, Eqs. (A5) and (A6) supply values for m_E and σ_E^2. For a given signal energy E_s and a given reference correlation ρ, Eq. (12) gives the probability density for the occurrence of a certain interaural correlation.

A difficulty arising from the probability density function given by the above equations is that for correlations close to 1, the function becomes skewed. If the distribution for the interaural correlation were Gaussian, it would be easier to calculate parameters like the detectability index d' for two different distributions. Therefore, the Fisher ρ-to-Z transformation is used. This transformation results in a probability density function that behaves approximately normal, and is given by

$$Z = 0.5 \ \ln \frac{1 + \rho_{\text{eff}}}{1 - \rho_{\text{eff}}}. \quad \text{(A14)}$$

Thus, for a given Z, the corresponding interaural correlation becomes

$$\rho_{\text{eff}} = \frac{e^{2Z} - 1}{e^{2Z} + 1}, \quad \text{(A15)}$$

and hence

$$\frac{d\rho_{\text{eff}}}{dZ} = \frac{4e^{2Z}}{(e^{2Z}+1)^2}. \quad \text{(A16)}$$

The probability density function for Z is then given by

$$p(Z) = p(\rho_{\text{eff}}) \frac{d\rho_{\text{eff}}}{dZ}. \quad \text{(A17)}$$

The detectability index for the NρSπ condition is determined by the means and the standard deviations in terms of Z as follows. The mean (μ) and standard deviations (σ) of the distributions of $p(Z)$ are determined for both masker alone and masker plus signal (μ_{N_ρ}, σ_{N_ρ}, $\mu_{N\rho S\pi}$, $\sigma_{N\rho S\pi}$, respectively). The detectability index is then obtained as

$$d' = \frac{\mu_{\text{N}\rho\text{S}\pi} - \mu_{N_\rho}}{\sqrt{\sigma^2_{\text{N}\rho\text{S}\pi} + \sigma^2_{N_\rho}}}. \quad \text{(A18)}$$

[1]We assume that the correlation between the signal S and the noise N is zero. Although this is mathematically not correct for a finite-length interval, a computational analysis revealed that the effect of these correlations is negligible in our analysis.

[2]The correlation between two finite-length samples from independent noise sources is almost never *exactly* zero. In our analysis and generation of stimuli, however, we assume that this correlation is zero. To justify this assumption, we generated 1000 intervals of interaurally partially correlated noise and determined the width of the probability density functions for the interaural correlation after (1) combination of the signals according to Eq. (1), and (2) combination of the signals according to Eq. (1) *after normalizing* the energies of the noise samples to a fixed value (i.e., there was no energy fluctuation for this case). The width of the probability density function for a reference correlation of 0 after normalization of the noise intervals was approximately 10^5 times narrower than without normalization. This indicates that for the way we generated the Nρ stimuli (i.e., with *two* independent noise sources), energy fluctuation is the main cause for correlation fluctuations. Another reason why this assumption is reasonable is the fact that the processing of the cochlea results in phase shifts in the presented stimuli. It is possible to generate a waveform with an exact interaural correlation. But, this is only possible for the waveforms arriving at the eardrums. After the processing in the peripheral hearing system, phase shifts result in changes in the correlation. It is therefore not so valuable to take the correlation between waveforms into account, because this property changes by the processing of the cochlea.

[3]A MANOVA analysis of the data shown in Fig. 9 was performed with the following independent parameters: amount of stimulus uncertainty, stimulus bandwidth, interaural correlation, and subject. The analysis revealed that bandwidth, correlation, and amount of stimulus uncertainty were statistically significant effects at a 95% confidence interval. A multiple comparison procedure (Fisher's least significant difference method) on the means for the different values of stimulus uncertainty revealed that the contrast for running noise vs fixed-ρ was not statistically significant. On the other hand, the contrasts between fixed-ρ, interleaved, and frozen conditions were all statistically significant at a 95% confidence interval.

Bernstein, L. R., and Trahiotis, C. (**1996**). ''The normalized correlation: Accounting for binaural detection across center frequency,'' J. Acoust. Soc. Am. **100**, 3774–3787.

Breebaart, D. J., van de Par, S., and Kohlrausch, A. (**2001**). ''A model for the effective signal processing in the binaural auditory system based on contralateral inhibition. I. Model setup,'' J. Acoust. Soc. Am. (submitted).

Breebaart, J., and Kohlrausch, A. (**1999**). ''A new binaural detection model based on contralateral inhibition,'' in *Psychophysics, Physiology and Models of Hearing*, edited by T. Dau, V. Hohmann, and B. Kollmeier (World Scientific, Singapore), pp. 195–206.

Breebaart, J., van de Par, S., and Kohlrausch, A. (**1998**). ''Binaural signal detection with phase-shifted and time-delayed noise maskers,'' J. Acoust. Soc. Am. **103**, 2079–2083.

Breebaart, J., van de Par, S., and Kohlrausch, A. (**1999**). ''The contribution of static and dynamically varying ITDs and IIDs to binaural detection,'' J. Acoust. Soc. Am. **106**, 979–992.

Culling, J. F., and Summerfield, Q. (**1998**). ''Measurements of the binaural temporal window using a detection task,'' J. Acoust. Soc. Am. **103**, 3540–3553.

Dau, T., Püschel, D., and Kohlrausch, A. (**1996a**). ''A quantitative model of the 'effective' signal processing in the auditory system: I. Model structure,'' J. Acoust. Soc. Am. **99**, 3615–3622.

Dau, T., Püschel, D., and Kohlrausch, A. (**1996b**). ''A quantitative model of the 'effective' signal processing in the auditory system: II. Simulations and measurements,'' J. Acoust. Soc. Am. **99**, 3623–3631.

Domnitz, R. H., and Colburn, H. S. (**1976**). ''Analysis of binaural detection models for dependence on interaural target parameters,'' J. Acoust. Soc. Am. **59**, 598–601.

Durlach, N. I. (**1963**). ''Equalization and cancellation theory of binaural masking-level differences,'' J. Acoust. Soc. Am. **35**, 1206–1218.

Durlach, N. I., Gabriel, K. J., Colburn, H. S., and Trahiotis, C. (**1986**).

''Interaural correlation discrimination: II. Relation to binaural unmasking,'' J. Acoust. Soc. Am. **79**, 1548–1557.
Gabriel, K. J., and Colburn, H. S. (**1981**). ''Interaural correlation discrimination: I. Bandwidth and level dependence,'' J. Acoust. Soc. Am. **69**, 1394–1401.
Glasberg, B. R., and Moore, B. C. J. (**1990**). ''Derivation of auditory filter shapes from notched-noise data,'' Hear. Res. **47**, 103–138.
Grantham, D. W. (**1984**). ''Discrimination of dynamic interaural intensity differences,'' J. Acoust. Soc. Am. **76**, 71–76.
Grantham, D. W., and Wightman, F. L. (**1978**). ''Detectability of varying interaural temporal differences,'' J. Acoust. Soc. Am. **63**, 511–523.
Grantham, D. W., and Wightman, F. L. (**1979**). ''Detectability of a pulsed tone in the presence of a masker with time-varying interaural correlation,'' J. Acoust. Soc. Am. **65**, 1509–1517.
Green, D. (**1992**). ''On the similarity of two theories of comodulation masking release,'' J. Acoust. Soc. Am. **91**, 1769.
Green, D. M., and Swets, J. A. (**1966**). *Signal Detection Theory and Psychophysics* (Wiley, New York).
Hafter, E. R., and Carrier, S. C. (**1969**). ''Masking-level differences obtained with a pulsed tonal masker,'' J. Acoust. Soc. Am. **47**, 1041–1047.
Hirsh, I. (**1948**). ''The influence of interaural phase on interaural summation and inhibition,'' J. Acoust. Soc. Am. **20**, 536–544.
Jeffress, L. A., Blodgett, H. C., and Deatherage, B. H. (**1952**). ''The masking of tones by white noise as a function of the interaural phases of both components. I. 500 cycles,'' J. Acoust. Soc. Am. **24**, 523–527.
Jeffress, L. A., Blodgett, H. C., and Deatherage, B. H. (**1962**). ''Masking and interaural phase. II. 167 cycles,'' J. Acoust. Soc. Am. **34**, 1124–1126.
Kollmeier, B., and Gilkey, R. H. (**1990**). ''Binaural forward and backward masking: Evidence for sluggishness in binaural detection,'' J. Acoust. Soc. Am. **87**, 1709–1719.
Levitt, H. (**1971**). ''Transformed up–down methods in psychoacoustics,'' J. Acoust. Soc. Am. **49**, 467–477.
Lutfi, R. A. (**1990**). ''How much masking is informational masking?'' J. Acoust. Soc. Am. **88**, 2607–2610.
Rice, S. O. (**1959**). *Selected Papers on Noise and Stochastic Processes* (Dover, New York), Chap. ''Mathematical analysis of random noise.''
Richards, V. M. (**1987**). ''Monaural envelope correlation perception,'' J. Acoust. Soc. Am. **82**, 1621–1630.
Robinson, D., and Jeffress, L. (**1963**). ''Effect of varying the interaural noise correlation on the detectability of tonal signals,'' J. Acoust. Soc. Am. **35**, 1947–1952.
van de Par, S., and Kohlrausch, A. (**1995**). ''Analytical expressions for the envelope correlation of certain narrow-band stimuli,'' J. Acoust. Soc. Am. **98**, 3157–3169.
van de Par, S., and Kohlrausch, A. (**1997**). ''A new approach to comparing binaural masking level differences at low and high frequencies,'' J. Acoust. Soc. Am. **101**, 1671–1680.
van de Par, S., and Kohlrausch, A. (**1998**). ''Analytical expressions for the envelope correlation of narrow-band stimuli used in CMR and BMLD research,'' J. Acoust. Soc. Am. **103**, 3605–3620.
van de Par, S., and Kohlrausch, A. (**1999**). ''Dependence of binaural masking level differences on center frequency, masker bandwidth, and interaural parameters,'' J. Acoust. Soc. Am. **106**, 1940–1947.
van der Heijden, M., and Trahiotis, C. (**1998**). ''Binaural detection as a function of interaural correlation and bandwidth of masking noise: Implications for estimates of spectral resolution,'' J. Acoust. Soc. Am. **103**, 1609–1614.
Zurek, P. M., and Durlach, N. I. (**1987**). ''Masker-bandwidth dependence in homophasic and antiphasic tone detection,'' J. Acoust. Soc. Am. **81**, 459–464.

Investigation of the relationship among three common measures of precedence: Fusion, localization dominance, and discrimination suppression

R. Y. Litovsky[a)]
Boston University Hearing Research Center, Department of Biomedical Engineering, Boston University, Boston, Massachusetts 02215

B. G. Shinn-Cunningham
Hearing Research Center, Departments of Biomedical Engineering and Cognitive and Neural Systems, Boston, Massachusetts 02215

(Received 2 January 2000; revised 7 August 2000; accepted 4 October 2000).

Listeners have a remarkable ability to localize and identify sound sources in reverberant environments. The term ''precedence effect'' (PE; also known as the ''Haas effect,'' ''law of the first wavefront,'' and ''echo suppression'') refers to a group of auditory phenomena that is thought to be related to this ability. Traditionally, three measures have been used to quantify the PE: (1) *Fusion*: at short delays (1–5 ms for clicks) the lead and lag perceptually fuse into one auditory event; (2) *Localization dominance*: the perceived location of the leading source dominates that of the lagging source; and (3) *Discrimination suppression*: at short delays, changes in the location or interaural parameters of the lag are difficult to discriminate compared with changes in characteristics of the lead. Little is known about the relation among these aspects of the PE, since they are rarely studied in the same listeners. In the present study, extensive measurements of these phenomena were made for six normal-hearing listeners using 1-ms noise bursts. The results suggest that, for clicks, fusion lasts 1–5 ms; by 5 ms most listeners hear two sounds on a majority of trials. However, localization dominance and discrimination suppression remain potent for delays of 10 ms or longer. Results are consistent with a simple model in which information from the lead and lag interacts perceptually and in which the strength of this interaction decreases with spatiotemporal separation of the lead and lag. At short delays, lead and lag both contribute to spatial perception, but the lead dominates (to the extent that only one position is ever heard). At the longest delays tested, two distinct sounds are perceived (as measured in a fusion task), but they are not always heard at independent spatial locations (as measured in a localization dominance task). These results suggest that directional cues from the lag are not necessarily salient for all conditions in which the lag is subjectively heard as a separate event.
[DOI: 10.1121/1.1328792]

PACS numbers: 43.66.Qp, 43.66.Rq, 43.66.Pn [DWG]

I. INTRODUCTION

When a sound is produced in a reverberant environment, it propagates in multiple directions and is subsequently reflected from various surfaces. The complex array of stimuli received by the listener consists of multiple sounds, each of which carries its own set of localization cues. In order to avoid localization errors, the auditory system must resolve which cues belong to the source and assign greater weight to them in the localization process. Efforts to understand how the auditory system processes sounds in complex environments have utilized simple stimulus paradigms in which a source (lead) and a single simulated reflection (lag) are presented in anechoic environments with short delays (1–5 ms for clicks, 30–50 ms for speech and music) between their onsets. Many studies have shown that the localization information in the source receives greater perceptual weight than, or has *precedence* over, the reflections; hence, this phenomenon is commonly known as the precedence effect (Cremer, 1948; Wallach *et al.*, 1949; Zurek, 1980; Blauert, 1997; Litovsky *et al.*, 1999).

Several perceptual phenomena related to the precedence effect have been quantified over the years. *Fusion* refers to the finding that at short delays listeners hear one fused auditory event, but fusion breaks apart as delays are increased (e.g., Blauert, 1997; Freyman *et al.*, 1991). *Discrimination suppression* refers to the general finding that a listener's ability to detect changes in directional cues in the lag is poor compared to sensitivity to changes in the lead (e.g., Zurek, 1980; Shinn-Cunningham *et al.*, 1993; Tollin and Henning, 1998). *Localization dominance* refers to the finding that the perceived location of a fused sound is dominated by the directional information in the lead (e.g., Wallach *et al.*, 1949; Zurek, 1980; Blauert and Divenyi, 1988; Divenyi, 1992; Shinn-Cunningham *et al.*, 1993; Litovsky *et al.*, 1997).

Studies of fusion date back to the early part of the century (cf. reviews by Blauert, 1997; Litovsky *et al.*, 1999). A common experimental paradigm presents numerous trials

a)Electronic mail: litovsky@bu.edu

with the lead–lag delay randomized; the listener reports her subjective impression of whether one or two sounds are heard on each trial. For click stimuli, at short delays (1–5 ms) most listeners report hearing only one sound on 100% of trials; at long delays (8–10 ms) most listeners report hearing two sounds on 100% of trials; at intermediate delays there is a transition in the percentage of trials in which ''two sounds'' are reported. In general, the percentage of ''two sound'' trials increases fairly steeply with delay, although the exact delay at which this sharp transition occurs varies across individuals (e.g., Freyman *et al.*, 1991). This critical delay, known as the *echo threshold*, is usually defined as the delay at which two sounds are reported on some predetermined percentage of trials (usually between 50% and 75%). Echo threshold varies with stimulus conditions, testing situation, and instructions given to the listener (Zurek, 1987; Blauert, 1997). Finally, it should be noted that the fusion task does not measure masking; listeners can detect the presence of the lag even when they do not perceive the lag as a separate auditory event.

Most localization dominance studies have been conducted under headphones using ''adjustment'' protocols. In these experiments, listeners match the position of a reference stimulus by setting interaural parameters (such as time, ITD, or level, ILD) of a test stimulus. This approach provides a quantitative measure of the relative influence of lead and lag binaural cues on lateralization (von Bekesy, 1960; Wallach *et al.*, 1949; Haas, 1951, 1972; Snow, 1954; Leakey and Cherry, 1957; Yost and Soderquist, 1984; Shinn-Cunningham *et al.*, 1993). These studies show that when the delay is a few milliseconds, the heard location of a fused image is much nearer to the position of the lead (presented in isolation) than that of the lag. Localization cues of the lag also contribute to the lateralization; however, when the delay is near or equal to zero, the perceptual influence of the lag increases until it contributes almost equally to the overall spatial impression. Although free-field measurements of localization dominance are less common, these studies also show that the lag contributes relatively little to the perceived location of the fused image (Hafter *et al.*, 1992; Litovsky *et al.*, 1997).

Studies of discrimination suppression have been conducted under headphones by measuring the just-noticeable-difference (jnd) in the ITD (e.g., Zurek, 1980; Shinn-Cunningham *et al.*, 1993; Saberi and Perrott, 1990) or ILD (Zurek, 1980; Gaskell, 1983) of the lagging source. In free field, measurements have been made for discrimination of the azimuthal direction of the lagging source (Perrott *et al.*, 1989; Freyman *et al.*, 1991; Litovsky and Macmillan, 1994; Yang and Grantham, 1997a, 1997b; Litovsky, 1997). At short lag delays, changes in the lag location (or binaural disparities) are difficult to discriminate relative to comparable differences in the lead. As the delay increases, lag discrimination performance improves dramatically, presumably because directional information in the lag becomes more salient.

Historically, the three aforementioned psychophysical measures have all been attributed to a single phenomenon, namely, the precedence effect. However, the relation among them is not well understood, in part because measures on all three tasks have never been obtained in the same listeners. Although it is often assumed that all measures reflect the fact that information in the lag is rendered perceptually inaccessible (e.g., Zurek, 1980; Freyman *et al.*, 1991), few studies have included parallel measurements of lag discrimination and either fusion or localization dominance. Comparisons that have been made do not uniformly agree. For instance, fusion and discrimination suppression are thought to reflect similar processes when single pairs of lead–lag stimuli are used (Freyman *et al.*, 1991), but not when a train of lead–lag stimuli is presented and the ''buildup of echo suppression'' occurs (Yang and Grantham, 1997a). Does the lag have to be perceived as a separate event from the lead in order for lead and lag discrimination to be equivalent? Can directional information of the lag be accessed even when the lag is still fused with the lead? While it has been suggested that localization dominance and discrimination suppression reflect similar processes (Shinn-Cunningham *et al.*, 1993), the relation of fusion and localization dominance has never been explored.

This study has two main purposes. The first is to quantify localization dominance in conditions for which two distinct sources may be perceived. Previous studies have either not allowed for responses that measure more than one source position (Shinn-Cunningham *et al.*, 1993) or have confounded temporal order confusion with localization dominance (Stellmack *et al.*, 1999). The second purpose is to directly compare fusion, discrimination suppression, and localization dominance measures in the same listeners, using similar stimuli. By directly comparing the delays at which listeners recover from ''precedence,'' as defined by each measure, we can begin to address whether a single computational mechanism underlies these three phenomena.

In order to relate the current results to previous reports, experimental procedures used in the current study are based on those commonly used in earlier experiments. Thus, whereas the discrimination suppression experiment uses an objective measure, the fusion experiment asks subjects to report their subjective impression of how many events are heard (an approach that confounds subject criteria with differences in sensitivity). In addition, the number of intervals in a trial differed across the three experiments, even though the basic stimuli were otherwise comparable. To the extent that precedence build-up may have influenced results, differences across the three experiments may be partially explained by a difference in build-up. However, despite these cautionary notes, the results reported herein are the first that allow direct within-subject comparisons of performance on all three precedence measures.

II. METHODS

A. Subjects

Six adults (two male, four female) participated as subjects in all experiments. All had pure-tone thresholds of 15 dB HL or less at octave frequencies between 250 and 8000 Hz. The ages of the listeners ranged from 19–22 years. Two

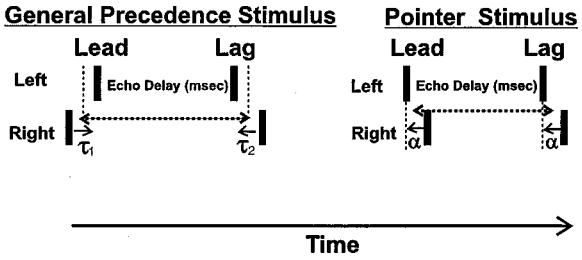

FIG. 1. General precedence stimulus (left) used for all three experiments and pointer stimulus (right) used on the localization dominance pointer task. Stimuli consisted of 1-ms Gaussian noise bursts with a 0-ms rise–decay time. The lead and lag each consisted of a pair of binaural noise bursts presented with a specified interaural time differences (ITDs), denoted as τ_1 for the lead and τ_2 for the lag. The echo delay represents the delay between the lead and lag pairs, defined as the time interval between the midpoints of τ_1 and τ_2. In the general stimulus, τ_1 and τ_2 could have ITD values that were either the same or different. In the pointer stimulus, the lead and lag pairs had the same ITD value.

listeners had previous experience in psychoacoustic tasks (S4, S5). All listeners were given a minimum of 1 h of practice on each of the tasks.

All testing was conducted in a double-walled soundproof booth. Testing was initially conducted on the fusion task, was followed by a randomized sequence of trial blocks for the discrimination and pointer tasks, and ended with a repetition of the fusion measurements.

B. Stimuli

A Tucker-Davis Technologies System II stereo analog interface was used to construct the stimuli. The output was fed through a 16-bit DAC to Sennheiser HD 520 II headphones. The general precedence stimulus (Fig. 1) was used for all three experiments. All stimuli consisted of 1-ms Gaussian noise bursts with a 0-ms rise–decay time. A lead–lag stimulus configuration consisted of two pairs of binaural noise bursts presented with various combinations of interaural time differences (ITDs) for the lead (τ_1) and lag (τ_2) pairs. Within a given interval, lead and lag were identical noise samples with new samples chosen for each interval. Delays varied from 1–15 ms.

C. Test parameters

1. Fusion

On each trial, the general stimulus was presented three times, with interstimulus intervals of 500 ms. The ITDs of the lead and lag were constant within each trial. ITDs for lead and lag were chosen from the set $(+400, 0, -400)$ μs, for a total of nine combinations. For five of the six subjects, eight delays were used (1, 2, 3, 5, 7, 10, 12, and 15 ms). The sixth subject was also tested at longer delays of 20, 30, 50, 70, and 100 ms (see Sec. III). On each trial, the ITDs and delays were randomly chosen. A total of 20 trials were presented at each delay and lead/lag ITD combination for a total of 1440 trials per listener. On each trial, listeners were instructed to report whether they perceived ''one fused auditory event'' or ''two sounds'' on the third interval. Listeners were aware of the fact that two events were always present in each interval. No feedback was provided, since two stimuli were always present. Testing was repeated both prior to (first run) and following (second run) all other experiments.

2. Discrimination suppression

On each trial, the general stimulus was presented three times in an ABX forced-choice task. In this procedure, the ''target'' ITD of the first (A) and second (B) interval differed. The target ITD of the third interval (X) was randomly chosen to equal either that of A or B with equal likelihood. The nontarget ITD and the lead/lag delay were the same in all three intervals of a given trial. Three conditions were tested that differed in the ''target'' ITD. In one condition, the target was the ITD of the lead in the general precedence stimulus (Fig. 1). In the second condition, the target was the lag ITD. The final condition was a control in which only one binaural burst was presented (i.e., the control did not use a precedence stimulus).

An adaptive procedure was used to estimate the jnd in the target ITD at different reference ITDs and delays. In each run, the delay and reference ITD were fixed. The change in the target ITD (around the reference) varied adaptively using a modified 2-down/1-up protocol with 14 reversals (Hawley, 1994). The starting ITD was 400 μs. For the first four reversals the ITD was either increased or decreased by a factor of 2; subsequent changes were by a factor of 1.4. Threshold was estimated by averaging the ITDs of the last ten reversals. Feedback was provided on every trial. Thresholds were obtained at delays of 1, 2, 3, 5, 10, and 15 ms for the two conditions (lead- and lag discrimination) using the general precedence stimulus. The reference target ITD was either 0 (center) or -400 μs (left). In each trial of lead- and lag discrimination, the ITD of the noise burst that was not being discriminated (lag and lead, respectively) was chosen randomly (from a uniform distribution ranging from -500 to 500 μs), forcing listeners to use directional information in the target to perform the task. All delay and stimulus combinations were repeated three times with the order of the conditions randomized.

3. Localization dominance

In the final task, listeners adjusted an acoustic pointer to indicate lateral positions of a target stimulus. On each trial, listeners alternated between listening to the general stimulus (target) and the pointer stimulus (Fig. 1). The pointer stimulus had the same basic structure and temporal characteristics as the general stimulus, except that the lead and lag ITDs were equal. Listeners controlled the ITDs of the pointer by adjusting a potentiometer dial. ITDs could vary between ± 1000 μs in steps of 10 μs. Subjects were asked to indicate the perceived location(s) of the lead/lag target by adjusting the pointer ITDs. Since two images are often perceived at the longer delays used in the experiment, measurements were repeated twice for all stimuli, with two separate sets of instructions. On half of the trials listeners were told to match the ''right-most'' image; on half of the trials instructions were to match the ''left-most'' image. If only one image was heard, both instructions should yield identical results. The right-most and left-most trial types remained constant within

a block, and the order of the blocks was randomized within each session. The final ITD of the pointer (the subject response) will henceforth be referred to as ''alpha'' or the ''matched ITD.''

Stimuli alternated between seven presentations of the target and nine presentations of the pointer. The pointer location could be adjusted while it was being presented. Stimuli automatically alternated between target and pointer until the listener indicated confidence in their match by pressing a button. The ITDs of the lead and lag (τ_1 and τ_2), and the delay (1, 2, 3, 5, 10, and 15 ms) varied from trial to trial, but were held constant within each trial. ITDs of both lead and lag were chosen from the set $\{+400, 0, -400\ \mu s\}$ for a total of nine combinations. Each condition was repeated five times for every listener. Presentation order of all ITD combinations and delays was randomized, and testing was conducted in blocks lasting approximately 1.5 h.

III. RESULTS

A. Fusion

Data from all six listeners are shown in Fig. 2. For S1–S5, the first and second measurements (left and right panels, respectively) are shown (S6 is discussed in more detail below). The percentage of trials on which listeners reported two sounds is plotted as a function of delay; dashed horizontal lines indicate 70.7% (echo threshold as proposed by Yang and Grantham, 1997a). Data from conditions with the same absolute difference between ITDs of lead and lag are averaged, and each plot compares data for differences of magnitude 0, 400, and 800 μs.

For all subjects, fusion was strongest at short delays, where the proportion of two sounds reported was very low. As delay increased, fusion broke down and two sounds were heard on a majority of trials. Three aspects of the data are noteworthy. First, echo threshold delay varied dramatically across listeners (see Table I). For example, in the first run, some listeners reached echo threshold at delays equal to or less than 5 ms for the majority of conditions (S2, S3, S5). Echo thresholds were slightly higher for S1 (4.7–6.5 ms) and even larger for S4 (8.7–12 ms). One listener (S6) needed extraordinarily long delays (on the order of tens of milliseconds) to recover from fusion. For this subject, additional delays were tested after the initial results had been gathered on all three tasks. Results using these longer delays are shown in the bottom-most right panel. For this subject, echo thresholds were around 45 ms.

A second interesting aspect to note is that fusion results changed for some subjects between the first and second fusion sessions (measured before and after the discrimination and localization data were gathered). For S2, S4, and S5, there was a tendency for fusion to increase during the second session compared to the first session. The echo thresholds for S3 did not seem to change. Echo thresholds for S1 showed small decreases between the first and second sessions. For S3 and S6, there was no clear effect of experience on echo threshold.

Finally, we examined the effect of spatial separation between lead and lag. In Fig. 2, results are combined across

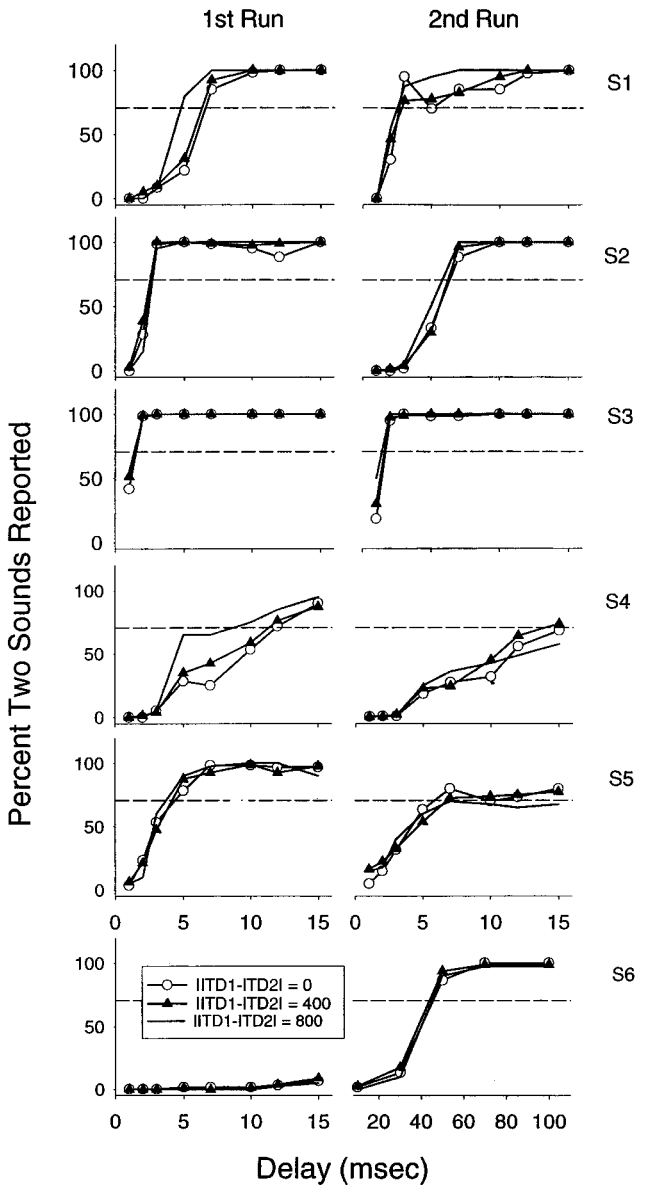

FIG. 2. Fusion results are shown for the six listeners tested. Left and right columns show data collected before and after the discrimination and pointer data, respectively. Each plot shows the percentage of trials on which the subjects reported hearing two sound images as a function of the lead–lag delay. For five subjects (S1–S5) delays ranged from 1–15 ms. For S6 the left column shows data at 1–15 ms, and the right column shows results from further testing conducted at longer delays. Within each plot the different lines show data collapsed according to the absolute value of the difference between the lead and lag ITDs.

conditions in which the spatial separation was either 0 μs (lead and lag at same location), 400 μs (lead at 0 and lag at $\pm$400, or vice versa), and 800 μs (lead at +400 and lag at −400, or vice versa). There was no consistent influence of lead/lag ITD on echo threshold in the fusion data measured in the current study.

B. Discrimination suppression

Data for the six listeners are shown in Fig. 3. Interaural-time difference (ITD) jnd's are plotted as a function of delay for lead (filled symbols) and lag discrimination (open symbols). Each data point in Fig. 3 represents the overall mean

TABLE I. Mean echo thresholds (for six subjects) for conditions in which the absolute difference between lead–lag ITDs were either 0, 400, or 800 μs. Thresholds are shown for the first and second measurements obtained before and after testing discrimination and pointer tasks, respectively.

	First run			Second run		
Subject	$\lvert\tau_1-\tau_2\rvert=0$	$\lvert\tau_1-\tau_2\rvert=400$	$\lvert\tau_1-\tau_2\rvert=800$	$\lvert\tau_1-\tau_2\rvert=0$	$\lvert\tau_1-\tau_2\rvert=400$	$\lvert\tau_1-\tau_2\rvert=800$
1	6.7	6.3	4.7	2.6	2.9	2.7
2	2.6	2.5	2.7	6.4	6.2	5.8
3	1.5	1.4	1.4	1.7	1.6	1.4
4	11.9	11.4	8.7	>15	14	>15
5	4.4	4.1	3.7	5.9	6.8	7.0
6	N/A	N/A	N/A	45.6	44.0	45.2

for the conditions at each delay. Error bars show the standard error around the means across six repetitions (three per condition). Performance depended strongly on delay for five of the six listeners and weakly for S6 (the remaining subject). At short delays lag discrimination was poor, evidenced by large ITD jnd's. In contrast, lead discrimination performance was relatively good at the short delays, as evidenced by much smaller ITD jnd's. Analyses of variance tests examining the effect of the two reference conditions (0 μs and -400 μs) found no significant difference between the conditions ($p>0.05$), as expected from the results shown in Fig. 3.

The results show that at short delays, listeners were able to use directional information in the lead much more readily than directional information in the lag. This presumably reflects the fact that for precedence effect conditions, the lead carried more perceptual weight in localization than the lag (e.g., Zurek, 1980; Shinn-Cunningham *et al.*, 1993). As delays increased, lag discrimination improved so that by 10 ms, lead and lag performance was roughly equal. This result suggests that precedence was no longer effective by 10 ms. For some listeners (S1, S3, S5), lead discrimination was actually worse than lag discrimination at delays greater than 10 ms. This reversal suggests that at these long delays (and for these subjects), the lag interfered with the lead ITD information more than the lead interfered with the lag ITD information. Finally, intersubject differences were large. For instance, the difference between lead and lag conditions was greater for three listeners (S1, S2, S3), primarily due to better lead discrimination at the shortest delays. In contrast, results for S6 suggest that lead and lag interact strongly at all delays, as evidenced by poor discrimination in both the lead and lag conditions for all measured delays.

C. Localization dominance

Figure 4 shows a sample data set for the pointer task. For brevity, we will refer to the various experimental conditions in the pointer task using two letters to denote the lateral positions (right, R; center, C; and left, L) of the lead and lag, respectively. The instructions are denoted by which letter is bold (recall that listeners were instructed to match either the right-most or left-most image). The bold letter denotes which of the bursts in the target was farther to the side indicated by the instructions. For instance, in the **R**-C condition, the lead ITD was $+400$ μs (right) and the lag ITD was 0 (center). Since, in isolation, the R stimulus is right-most compared

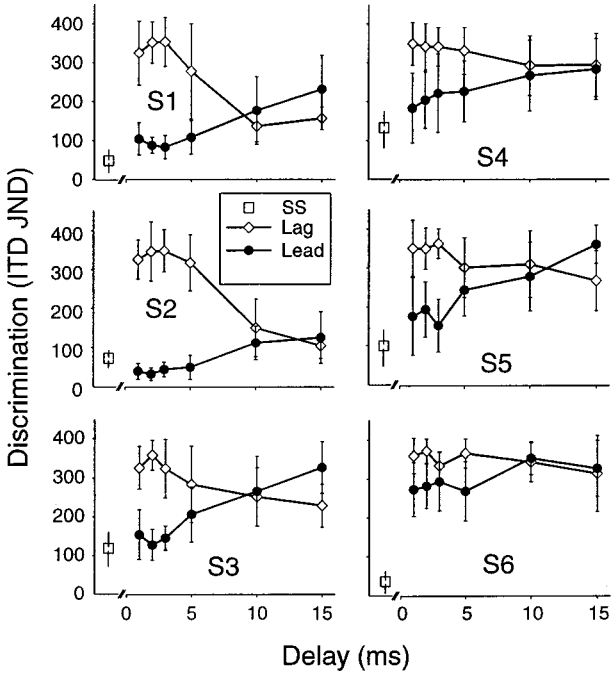

FIG. 3. Discrimination results are shown for the six listeners tested. ITD jnd's are plotted as a function of delay for lag (open symbols) and lead (filled symbols) conditions. Data were collapsed across reference ITD due to the lack of any statistically significant differences between these conditions. Means and standard error bars are based on the six data points (three at each reference ITD).

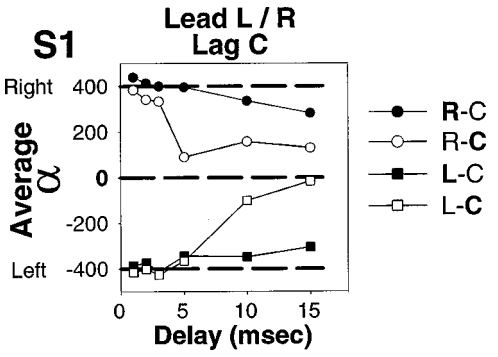

FIG. 4. Example of pointer results for subject S1 at one set of conditions in which the lead was either on the right (400 μs) or left (-400 μs) and lag was at center. The average perceived position (α), based on five repetitions at each condition, is plotted as a function of lead–lag delay. The symbol fill indicates whether instructions were to match the lead (filled) or lag (open). Symbols indicate whether the lead was on the right (circle) or left (square).

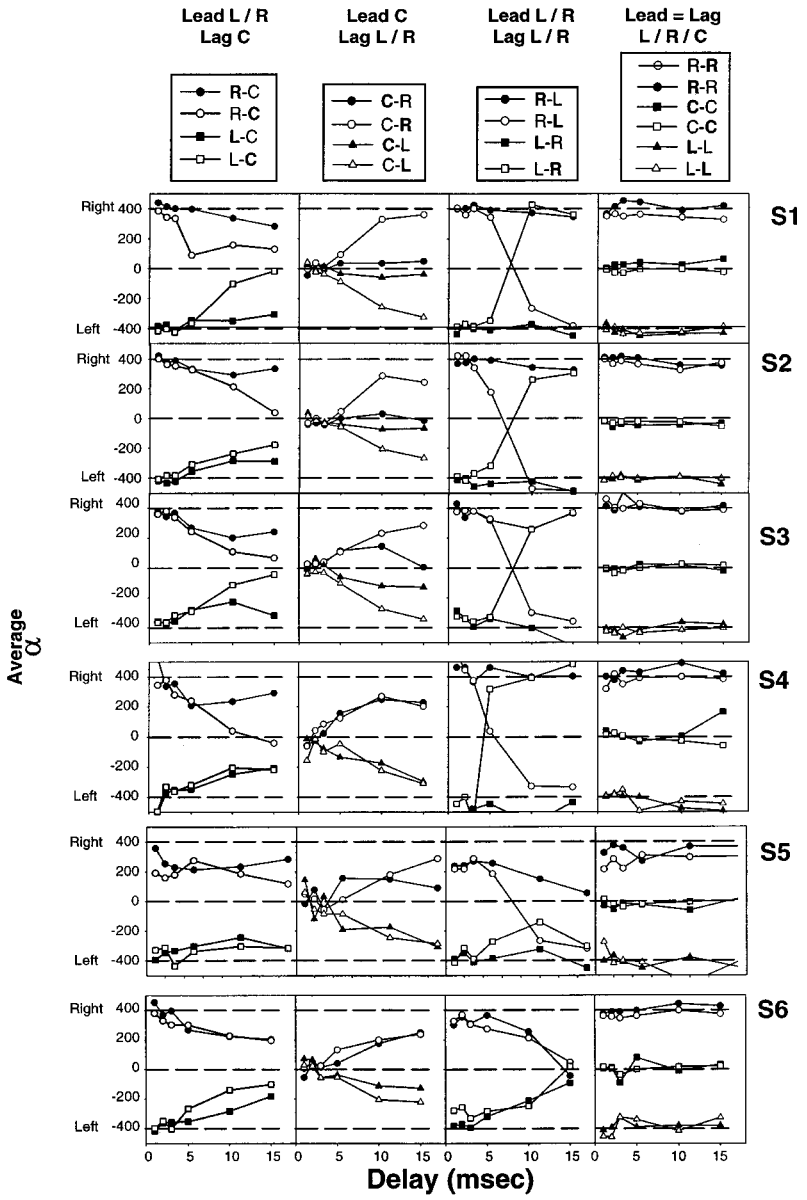

FIG. 5. Pointer results for six listeners portray the average (of five trials) alpha values—the perceived locations (ITDs) under various conditions, at delays 1–15 ms. Each row contains data from one listener. In the legend (top), lead–lag positions are denoted by order, so that R-C denotes lead on right and lag at center. Instructions included cases in which listeners were told to match the ''right-most'' or ''left-most'' auditory image in the event that more than one image was heard; the bold letter indicates whether instructions were consistent with matching the lead or lag. Each column contains data for a set of complimentary conditions. The left column shows cases in which the lead was on either the right (+400 μs) or left (−400 μs), and the lag was always at center. The second column shows cases in which the lead was always at center and the lag was either on the right or left. In the third column, both lead and lag could be on the right or left. In the right-most column, lead and lag were always at the same location, either on the right (R-R), or at center (C-C), or on the left (L-L). The dashed lines within each plot indicate the ITDs for the left, center, and right (−400, 0, 400 μs, respectively).

with the C stimulus, the R is bold when the instructions were to match the right-most. In R-**C** the C is bold because the instructions were to match the left-most. We henceforth refer to a condition such as **R**-C as one for which ''the instructions were to match the lead'' (and, similarly, R-**C** as a condition for which ''the instructions were to match the lag''), even though the instructions were always to match either the left- or right-most sound image.

In the example in Fig. 4, four conditions are shown: two with lead on right and lag at center (**R**-C and R-**C**), and two with lead on left and lag at center (**L**-C and L-**C**). Closed symbols denote cases in which the instructions were to match the lead, and open symbols denote cases in which the instructions were to match the lag. Each horizontal dashed line marks one of the noise burst (either lead or lag) ITDs.

If the listener hears two images at separate locations that are roughly equal to the locations of each burst in isolation, the same stimulus should yield different results depending on the instructions (whether or not the subject can tell the temporal order of the two images). The **R**-C matches would then be near the lead ITD at +400 μs and the R-**C** matches would then be near the lag ITD at 0. However, if the lead dominates localization, both **R**-C and R-**C** stimuli would be heard near the lead ITD at +400 μs, regardless of instructions. Similarly, in the two L-C conditions, if the lead dominates localization, match ITD should fall near −400 μs, independent of instructions. Conversely, if matches fall near the lag ITD, it indicates that directional information from the lag is influencing performance.

In Fig. 4, when instructions were to match the lead, the matched ITD (pointer ITD) was near the lead ITD at all delays. At the shorter delays, the listener matched the lead ITD regardless of instructions, consistent with a strong precedence effect. When instructions were to match the lag, the matched position only approached the lag ITD at 15 ms for the L-**C** condition. In the R-**C** condition, the matched ITD was 100 μs even for a delay of 15 ms, indicating that the lead still carried a great deal of influence in the localization process.

Figure 5 shows the entire data set for the pointer task.

Results show a strong effect of delay and a dependence on the relative ITDs of the lead and lag for all listeners. In this figure, the open and closed symbols should differ if listeners hear two distinct positions. For instance, the open symbols in the left column would fall at 0 μs if listeners matched the position of the lag (independent of the lead). Similarly, the closed symbols should remain at either $+400$ or -400 if listeners matched the position of the lead (independent of the lag).

At short delays, regardless of instructions, all listeners placed the pointer near the ITD of the lead, suggesting that they perceived one location near the lead. As delay increased, different instructions elicited different responses for the same stimulus, although not all listeners perceived two images at longer delays. In addition, the likelihood of perceiving two distinct images depends on the relative ITDs of the lead and lag. Listeners S1–S4 generally heard two separate images for delays equal to or greater than 15 ms. However, some results are asymmetric, most notably for listeners S2 and S4, who heard an image near the lag ITD when the lead was on the right, but not when the lead was on the left. Even at the longest delays measured, listeners S5 and S6 did not appear to hear two separate images. For these subjects, results are roughly independent of instructions: the open and closed symbols are near the lead ITD at short delays and are approximately midway between the lead and lag ITDs at longer delays.

When the lead was at center and lag lateral (to either the right or left; second column) three listeners (S1–S3) heard one image for delays ranging from 1 to 5 ms and two images at longer delays. The other three listeners (S4–S6) heard one image whose location was near the lead at short delays and midway between the lead and lag at longer delays.

Finally, when the lead and lag were on opposite sides (± 400 μs; third column), four listeners (S1–S4) localized two distinct images at the longer delays. The matched positions of the two images were essentially equal to the locations at which the lead and lag bursts would be perceived when presented in isolation, indicating that the lead and lag images did not interact for these subjects and conditions. Listener S5 showed some asymmetry. S5 matched two distinct images when the lead was on the right or left, but the spatial separation of these images was much smaller when the lead was on the left. Listener S6 never matched two distinct locations.

D. Match performance near echo threshold

The ability of listeners to locate two distinct images does not seem to be directly related to their subjective reports of whether one or two images are present. Fusion data (Fig. 2) show that many of the listeners reported hearing two sounds at delays near 5 ms; however, at these delays the same listeners matched a single location near the lead, independent of instructions (Fig. 5). Thus, it appears that localization dominance persists to longer delays than fusion.

To illustrate this point, Fig. 6 plots estimated matched ITD at the fusion echo threshold delay (found by interpolating matched ITDs across delay). Each plot shows data from one listener. For every lead/lag ITD and instruction combination, the matched position is plotted as a function of lead ITD. The symbol and fill indicate whether instructions were to match the lead (squares) or the lag (open circles). Filled circles are used for matches in which lead and lag ITD were equal and instructions were expected to have no effect. In Fig. 6, if the lead ITD completely dominated perception, the data would fall along the diagonal, independent of instructions or lag ITD. In other words, the matched ITD would be roughly equal to and highly correlated with lead ITD, independent of instructions. If two locations were perceived, the squares would generally be expected to fall nearer the diagonal and the open circles to be independent of lead ITD value.

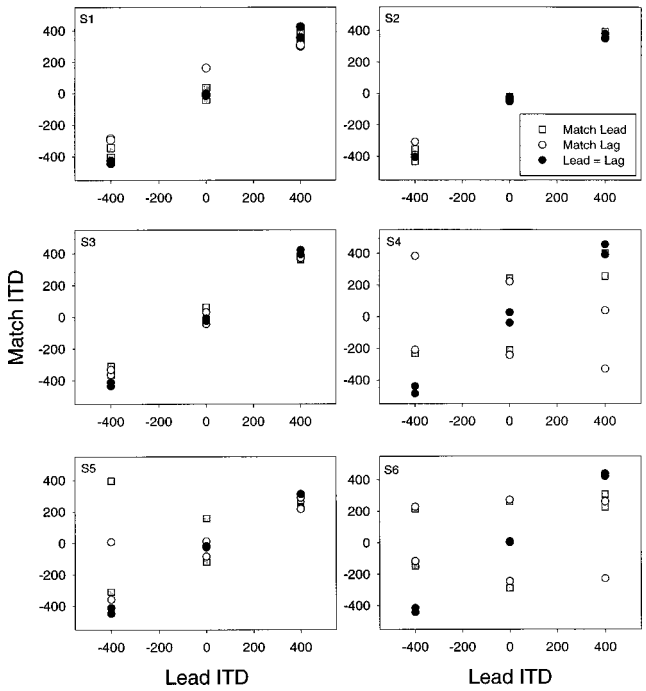

FIG. 6. Estimated matched ITD at the fusion echo threshold delay (found by interpolating matched ITDs across delay). Each plot shows data from one listener. For every lead/lag ITD and instruction combination, the matched position is plotted as a function of lead ITD. The symbol and fill indicate whether instructions were to match the side closer to the lead ITD (squares) or the lag ITD (open circles). Filled circles are used for matches in which lead and lag ITD were equal and instructions were expected to have no effect. For each condition, two data points appear with the same symbol, representing different values of lag ITD.

Table II shows correlation values between lead or lag ITD and match ITD at fusion echo threshold when instructions were to match lead or lag. For some subjects, the cor-

TABLE II. Correlations between lead (or lag) ITD and matched ITD, when instructions were to match the lead (or lag).

Subject	Lead ITD and instructions to match lead	Lead ITD and instructions to match lag	Lag ITD and instructions to match lead	Lag ITD and instructions to match lag
1	0.99	0.97	0.06	0.18
2	1.00	0.99	−0.01	0.01
3	0.99	0.99	0.06	0.10
4	0.91	0.17	0.16	0.94
5	0.57	0.88	0.57	0.30
6	0.65	0.39	0.64	0.90

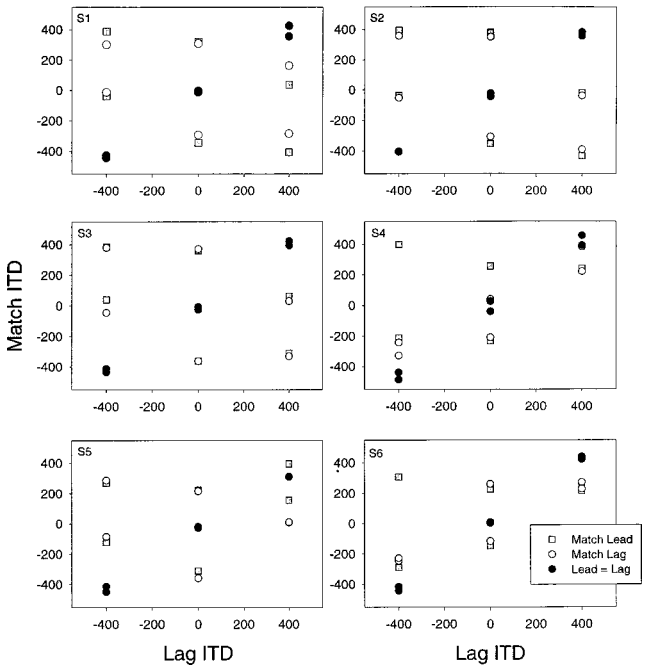

FIG. 7. Data from Fig. 6, replotted as a function of lag ITD.

relation with lead ITD was quite high regardless of instruction. For other subjects, these correlations were more modest. For all subjects, correlations were low between lag ITD and matched ITD regardless of instructions. These results suggest that, at fusion echo threshold, listeners were primarily utilizing directional cues contained in the lead.

The data are replotted in Fig. 7 as a function of lag ITD to further illustrate this point. If data fell along the diagonal, it would indicate that subjects heard a single location near the lag ITD, independent of lead ITD. If subjects heard two independent images at the lead/lag locations, open circles would fall on the diagonal (be highly correlated with the lag ITD) and squares would show little dependence on (be essentially uncorrelated with) lag ITD. Both the lack of structure in the data in the plot and the low correlation between matched ITD and lag ITD (Table II) further confirm that precedence is strong at echo threshold.

For three listeners (S1, S2, S3) the lead was clearly dominant, with the correlation between lead ITD and matched ITD close to 1.0 regardless of instructions (see Table II). Listener S4 had high correlations (a) between lead ITD and matched ITD when instructions were to match the lead, and (b) between lag ITD and match ITD when instructions were to match the lag. This result suggests that S4 was able to match the location of either source. Both S5 and S6 showed only moderate correlations with either lead or lag ITD. S5 showed some asymmetry, with matches dominated more by the lead when the lead ITD was to the right (+400 μs) than to the left (−400 μs).

E. Model estimate of precedence weight based on pointer results

The metric c (described in Shinn-Cunningham *et al.*, 1993) was calculated to quantify the relative influence of the lead and lag in localization. According to the model, the value of c is estimated by

$$c=(\alpha_p-\tau_2)/(\tau_1-\tau_2),$$

where α_p is the matched ITD and τ_1 and τ_2 are the lead and lag ITDs, respectively, for a given condition. A c value of 1.0 indicates that precedence is complete and that the lead dominates lateralization entirely. A c value of 0.5 indicates that the lead and lag both contribute equally to localization perception. A c value of 0 indicates that the lag dominates lateralization completely. In our study, instructions varied, and listeners were told to match either left or right images (see Figs. 4 and 5 for details). When told to match the lag, a c value of 0 would be expected if listeners heard two distinct images, one near the lead ITD and one near the lag ITD. If listeners were told to match the lead and a distinct image was heard near the location at which the lead would be heard in isolation, a c value of 1 is expected. Finally, if the lead and lag form a single image, then c should fall between 0 and 1 and be independent of instructions.

In Fig. 8, c values for each listener are shown as a function of delay for combinations of conditions in which the lead was lateral (L or R) and lag at center (left column), the lead at center and lag lateral (middle column), or both lead and lag were lateral (right column). The fill indicates the instructions; open and closed symbols reflect conditions in which instructions were to match the lead and lag, respectively.

Four listeners (S1–S4) showed strong precedence at delays less than 5 ms. Regardless of instructions, they matched the lead location and c values were near 1. For these subjects, as delays increased, precedence weakened. When instructed to match the side of the lead, c was high, indicating that these listeners heard the lead with little influence of the lag. However, as delay increased, two distinct images were heard. When instructed to match the lag, c was less than 0.5, indicating that subjects heard a second image that was influenced more by the lag ITD than the lead ITD. For listeners S5 and S6, c rarely fell below 0.5, indicating strong precedence at all delays tested.

The data also suggest that precedence was weaker when the lead–lag ITD difference was large. To illustrate this point, we calculated the difference between c values for pairs of conditions in which the lead ITD was identical, instructions were consistent, but the magnitude of the lead–lag ITD difference was either 800 or 400 μs. For example, we found the difference in the calculated c values for the condition **L**-R and the condition **L**-C for each subject and delay. Similar comparisons were made for **R**-L versus **R**-C, L-**R** versus L-**C**, and R-**L** versus R-**C**. For each subject, these differences are plotted in Fig. 9 as a function of delay when instructions were to match the lead. Within each plot, differences between left-center and right-center are shown separately. If the lag interferes with the lead more when lead and lag are spatially close, then the difference should tend to be positive, since we would expect c to be nearer to 1 when the lead–lag separation is 800 μs. Similar computations were conducted for the match-lag conditions, but are not plotted; statistical analyses of the data are, however, included (see Table III).

Results show that when listeners were instructed to match the lead, c values tend to be larger (precedence is

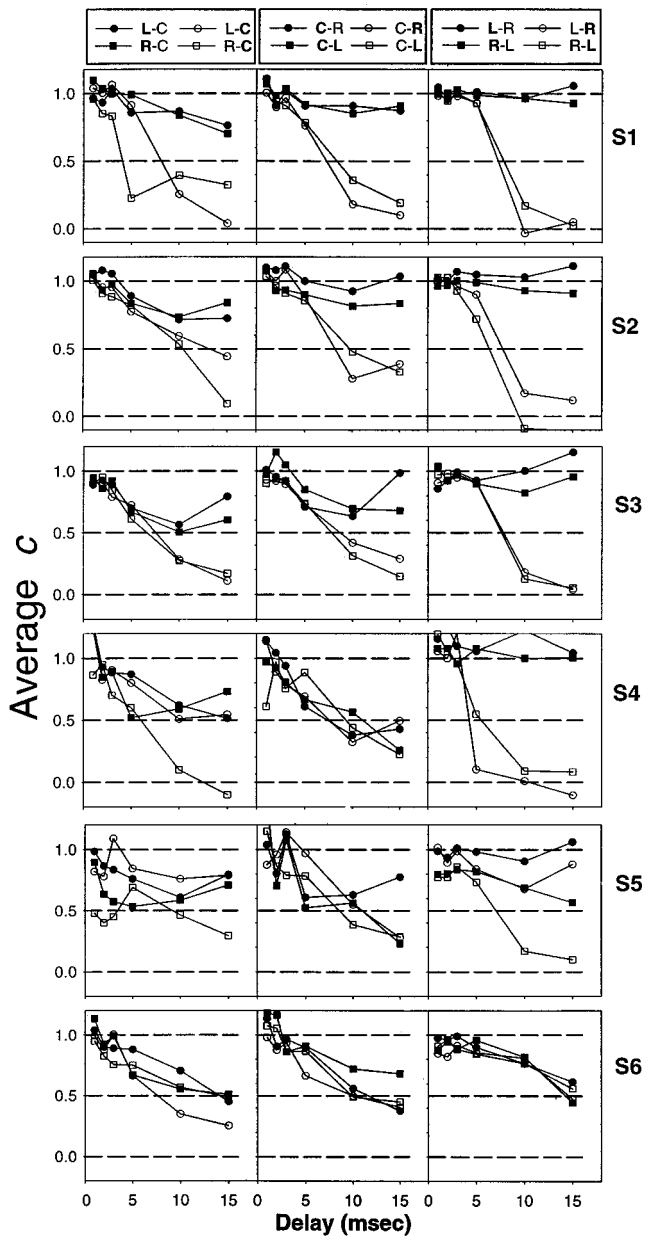

FIG. 8. Average *c* values (based on five repetitions) as a function of delay. Each row shows data for one listener. Each column contains conditions with different combinations of positions for the lead and lag. Left column: lead was lateral (L or R) and lag at center. Center column: lead at center and lag lateral. Right column: both lead and lag lateral (see legends at top of columns). For each condition, the burst that listeners were instructed to match is indicated in bold. The fill indicates the instructions; closed and open symbols reflect conditions in which instructions were to match the lead and lag, respectively.

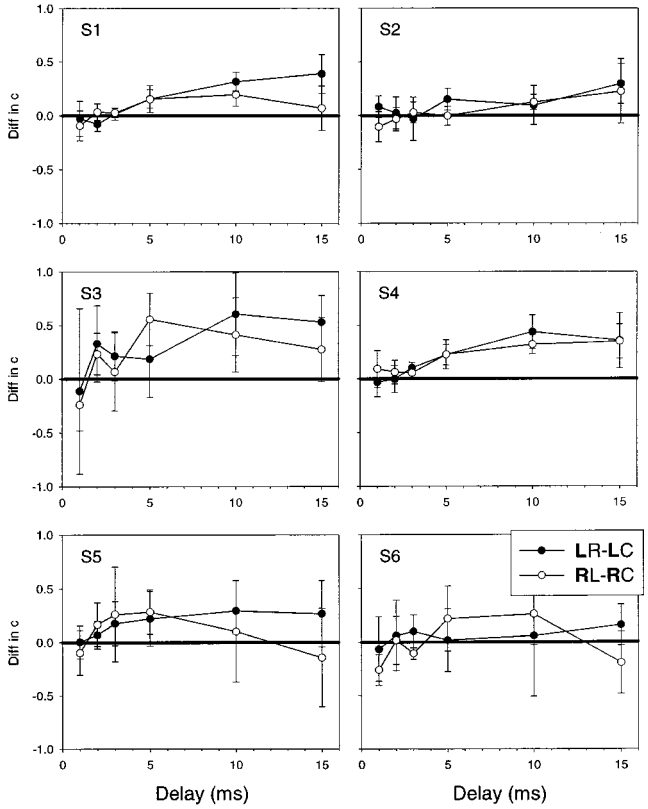

FIG. 9. Difference in *c* values for large (800 ms) and moderate (400 ms) difference between lead and lag ITD. For each subject, delay, and lateral source location, the *c* value calculated when the absolute lead–lag ITD separation is small is subtracted from the *c* value when the lead–lag separation is large. Each panel shows results for a different subject. Error bars show standard deviation in the differences. To the extent that spatial separation results in less influence of the lag on the perceived location of the primarily lead source image location, these differences will be positive.

stronger) when the lead–lag separation is 800 μs compared to 400 μs. This effect is especially pronounced at longer delays. This finding suggests that interference from the lag on the lead image is greater when the lead and lag are spatially close. However, when listeners were instructed to match the lag, there was no consistent difference between *c* values for the 800- and 400-μs lead–lag separations, suggesting that the strength of the interference of the lead on the primarily lag image was independent of spatial separation.

These observations were confirmed statistically. Left–right symmetry was assumed in a statistical analysis of the *c* values (e.g., by combining data for conditions **L**-R and **R**-L). For each subject, the pairs of conditions whose differences are plotted in Fig. 9 were compared using one-tailed, paired t tests to evaluate whether there was a statistically significant effect of the spatial separation of lead and lag on *c*. The same analyses were conducted for match-lag conditions, although the raw data are not shown in Fig. 9. Results from these analyses are shown in Table III, where comparisons yielding $p<0.001$ are indicated (X). Statistically significant differences were observed in four listeners for the match-lead conditions, and only for intermediate and long delays. Significant differences for the match-lag condition were only observed for one listener at one delay (S1, 10 ms).

In summary, when lead and lag are spatially near one another, localization dominance does not abruptly disappear; rather, a single image moves away from the lead gradually before breaking into two images, one of which grows towards the lead and one which grows towards the lag as delay increases. When lead and lag are spatial far apart (Fig. 8, right column), any second image is very near the lag ITD and is relatively unaffected by the lead ITD.

IV. DISCUSSION

Wallach *et al.* (1949) introduced the term ''precedence effect'' to describe the finding that when two pairs of di-

TABLE III. Test of significance ($p<0.001$) of difference in c values when subjects are instructed to match the source position on the side of the lead burst (A) or lag burst (B). In (A), c values for conditions **L**-R and **R**-L were compared to c values for conditions **L**-C and **R**-C in a one-tailed, paired t test. In (B), c values for conditions L-**R** and R-**L** were compared to c values for conditions L-**C** and R-**C** in a one-tailed, paired t test. Individual subject results are given in initial rows; results across subjects are shown in the bottom row.

	Delay (ms)					
Subject	1	2	3	5	10	15
(A)						
1	…	…	…	X	X	…
2	…	…	…	…	…	X
3	…	…	…	…	X	X
4	…	…	…	X	X	X
5	…	…	…	…	…	…
6	…	…	…	…	…	…
Across subs	…	…	…	X	X	X
(B)						
1	…	…	…	…	X	…
2	…	…	…	…	…	…
3	…	…	…	…	…	…
4	…	…	…	…	…	…
5	…	…	…	…	…	…
6	…	…	…	…	…	…
Across subs	…	…	…	…	…	…

chotic clicks are presented with a brief delay, they are fused into a single auditory image whose perceived direction is dominated by the interaural cues of the leading click pair. This result offered a simplified and elegant analogy to the perception of simple sounds in reverberant spaces, where information concerning the source reaches the ears first and is followed by information from the reflections or echoes. The obvious conclusion was that the auditory system minimizes confusion regarding the true location of the source by attributing greater perceptual weight to the first-arriving wavefront and minimizing the influence of later-arriving reflections. This phenomenon has also been attributed to mechanisms involved in localization dominance (e.g., Divenyi, 1992; see Litovsky *et al.*, 1999). While interaural differences in time and intensity as well as spectral cues are all important in directional hearing, the focus of the present study was on comparing various measures related to precedence, with a focus on interaural time cues.

Over the years, investigators have studied not only localization dominance, but also related perceptual phenomena using the leading–lagging stimulus paradigm. The other measurements include identifying conditions under which the sounds are perceptually fused and determining the extent to which directional changes in the location of the lagging source can be discriminated. These various measures of the perception of stimuli consisting of a direct sound and a later-arriving reflection have all been included under the umbrella term ''precedence effect.'' Although it is assumed that there is a strong relationship among these different effects, the extent to which they are mediated by the same auditory mechanisms is unclear. To address this question, the present study systematically compared all three phenomena in the same listeners.

In this discussion we first compare our data to results from previous studies, then consider the relationship between the different tasks used in the current study, and finally discuss why it may be appropriate to view the precedence effect not as a mechanism for suppressing echoes, but as a more general process for enabling robust localization.

A. Basic findings and relation to previous work

Fusion results were generally in agreement with previous reports: at short delays (<5 ms) listeners heard one fused sound image, and as the delays increased a second source emerged. The delay at which subjects perceived two sounds on 70.7% of the trials (echo threshold) varied across subjects, although the extent of the variability observed here has not been previously reported. For click stimuli measurements made in free field, echo thresholds have been in the range 5–10 ms (Ebata, 1968; Freyman *et al.*, 1991; Yang and Grantham, 1997a). In our study, thresholds for five subjects fell near or within this range; however, subject S6 had echo thresholds (45–50 ms) significantly longer than any previously reported for click stimuli (for a review, see Litovsky *et al.*, 1999). We cannot eliminate the possibility that long echo thresholds might reflect unusual central auditory processing, not unlike that reported for localization dominance in listeners with temporal lobe epilepsy (e.g., Hochster and Kelly, 1981). However, all previous studies report measurements for only a handful of subjects, and relatively little is known about the range of echo thresholds in the population at large. It is therefore premature to rule out the possibility that the ''normal'' range of echo thresholds for click stimuli can extend to 50 ms, at least when measured under headphones.

Discrimination results in the present study are in agreement with previous reports in which performance was measured at numerous delays (e.g., Zurek, 1980; Tollin and Henning, 1998; Stellmack *et al.*, 1999). For lag discrimination thresholds, the general phenomenon is illustrated with extremely high ITD jnd's at short delays. The difficulty that listeners encounter in extracting directional information from the lag is thought to reflect a suppressive mechanism that is activated by the presence of the lead. This suppressive mechanism strongly suppresses lag information at brief delays; at longer delays, performance improves as the suppressive influence of the lead becomes less effective. Lead discrimination results further suggest that, while listeners are able to ignore lag information at short delays, at longer delays the lag becomes increasingly more intrusive. This finding is consistent with one previous report (Stellmack *et al.*, 1999) which found that at long delays not only is the lag not suppressed but the lag interferes with the ability to extract lead information more than the lead interferes with the lag. However, this asymmetry (or antiprecedence) is thought to arise because subjects are (1) uncertain about the temporal order of the two auditory events, and (2) tend to be biased towards responding to the more recent stimulus in the pair.

Localization dominance measures using the pointer technique are more extensive here than in previous reports

performed either using headphones (Zurek, 1980; Shinn-Cunningham *et al.*, 1993) or in free field (Leakey and Cherry, 1957; Snow, 1954; Haas, 1951; Litovsky *et al.*, 1997). Although there are few existing parametric data for comparison, current results are generally consistent with previous reports: localization dominance is strongest at delays of 1–5 ms and weakens thereafter (for review, see Litovsky *et al.*, 1997). Unfortunately, our data set did not include delays in the range between 5 and 10 ms, which was the delay range across which lead dominance changed most dramatically for most subjects. The current data are also consistent with a previous report (Shinn-Cunningham *et al.*, 1993) which suggested that the dominance exerted by the lead is stronger when the lead and lag ITDs are similar and weaker for larger spatial separations. A similar effect was relatively strong in four (S1–S4) of our six subjects. This finding suggests that both temporal and spatial separation between lead and lag affect the strength of the precedence effect.

Current data are unique from two standpoints. First, the individual variability observed in localization dominance has not been previously reported. Although localization dominance is thought to be most effective for click stimuli at 1–5 ms, two of our listeners did not recover from this effect by 15 ms. Both of these listeners had high fusion echo thresholds (one of the subjects had an extremely large echo threshold; see above). Since instructions and testing protocol was identical for all subjects, we tentatively conclude that the widely accepted duration of the suppressive window (of 1–5 ms) does not apply to all subjects. It is therefore important that a population study be conducted to determine the range of ''normal'' behavior for localization dominance and to estimate the suppressive temporal window for normal-hearing listeners.

This study is also unique in that it quantifies localization dominance in conditions where two sources are perceived by allowing two different responses to the same stimulus conditions. In a previous study using a similar paradigm (Shinn-Cunningham *et al.*, 1993), only one matched position was measured. As a result, if two sources were heard at the longer delay, it is not clear how subjects would decide to respond to nonfused events, let alone whether their decision rule was consistent. In the current study, the pointer experiment was repeated two times with different instructions (to match either the right- or left-most image). The raw data (Fig. 5) as well as the model estimation of the strength of precedence (Fig. 8) suggest that subjects S1–S4 heard only one spatial location at shorter delays and two separate images at longer delays. However, the second (primarily lag) image was influenced by the location of the lead in several instances, especially for the condition with lag on the right or left and lead at center. Similarly, the ''lead'' image was influenced by the ''lag'' image for some conditions and subjects, particularly when the lag ITD was similar to the lead ITD. For two subjects (S5, S6) two separate images were never perceived, perhaps because these subjects were not tested at delays long enough to reveal this separation.

B. Comparison of the three precedence phenomena

No previous studies have compared performance across all three precedence tasks, and few have compared two. No previous studies have compared localization dominance and fusion results.

1. Localization dominance and discrimination suppression

Only one previous study compared localization dominance and discrimination suppression (Shinn-Cunningham *et al.*, 1993). Results of that study suggest that similar processes govern these tasks, in that discrimination performance could be predicted relatively well from localization dominance measures. In the current study, the two subjects (S5 and S6) who showed the strongest tendency to match only one source location in the localization dominance task also exhibited little change in lag and lead discrimination as a function of delay. These results are consistent with the idea that, for these subjects, localization information from the lead and lag is combined to form a single estimate of source location even for long delays. If positional changes in this single image are the only cues that S5 and S6 could use to perform the discrimination task, the interference from the nontarget burst will be pronounced and discrimination will be relatively poor, independent of delay. In other words, the current study qualitatively supports the view that localization dominance and discrimination suppression are closely related.

2. Fusion and discrimination suppression

Freyman *et al.* (1991) measured fusion and discrimination suppression in the same listeners in free field and concluded that these two aspects of precedence are related. Specifically, Freyman *et al.* found that discrimination performance was significantly above chance at a delay near echo threshold. In this free-field study, Freyman *et al.* (1991) randomly presented the lag from one of two locations, separated by 20°, and measured discrimination performance as a function of delay. These results indicate that subjects are able to extract some directional information from the lag at echo threshold; however, it must be pointed out that the detected spatial change of the lag (20°) was quite large compared with jnd's measured in the present study. The current results indicate that at echo threshold, subjects may be able to extract some directional information from the lag, but this information is combined (interacts) with information from the lead. The lead and lag information form either a single (averaged) spatial estimate or two separate images, each of which is influenced by the spatial information in both bursts. Thus, while the auditory system might be capable of extracting directional information from the lag at the fusion echo threshold, some suppression is still present at those delays and best performance is not reached until longer delays.

In a second attempt to link fusion and discrimination, Yang and Grantham (1997a) compared the same two tasks for a train of lead–lag stimuli which produce what is known as the ''build-up of echo suppression,'' whereby the strength of the precedence effect increases with the number of lead–lag pairs. This effect has been attributed to ''higher-order''

mechanisms that are involved in ongoing assessment of room acoustics (Clifton and Freyman, 1997). Yang and Grantham (1997a) found that fusion is more susceptible than discrimination to the build-up of precedence and concluded that the mechanisms mediating these two aspects of precedence are different.

Our study was not aimed at investigating aspects of the build-up effect. Both discrimination and fusion experiments presented three lead/lag intervals in each trial; however, in the fusion experiment, all three intervals were identical, while in the discrimination (ABX) paradigm, one of the intervals differed in its spatial cues. There is some evidence that build-up is affected by the ''consistency'' of the repeated stimuli (e.g., see Clifton and Freyman, 1997). As a result, there may have been less build-up in the discrimination stimuli compared to the fusion stimuli; however, any difference in build-up is likely to be small given the overall similarity of the stimuli in the discrimination and fusion experiments. We found that fusion breaks down at shorter delays than discrimination suppression. It is possible that with a longer stimulus train, using our psychophysical method, fusion would indeed be stronger than discrimination. Further tests must be conducted to reach a firm conclusion.

3. Localization dominance and fusion

The current results suggest that the delays at which listeners recover from fusion and from localization dominance differ. Although there are intersubject differences observed in both tasks, overall there emerges a consistent story regarding the relative strength of these two aspects of precedence. In general, fusion ends at relatively short delays compared with the localization dominance; at echo threshold listeners are not able to match the location of the lagging source. Intersubject variability also suggests that listeners who recover from fusion at shorter delays also tend to hear two separate positions at shorter delays (the latter always being longer than the former). For instance, the two listeners (S5 and S6) who have unusually high echo thresholds are also least likely to match two independent source locations (based on ''left'' or ''right'' instructions) in the localization dominance task.

As pointed out in the above discussion of fusion and discrimination results, it is known that fusion increases with repetitions of lead/lag stimuli. No one has ever measured whether a similar increase in suppression occurs using localization dominance measures; however, the number of presentations of the lead/lag stimuli differed in the two experiments reported here. In the localization dominance task, the ''target'' stimulus was presented as a train of seven identical lead/lag pairs, whereas in the fusion experiment, comparable stimuli were presented in a train of three identical lead/lag pairs. These differences may contribute to the trend to hear two sound events at lead/lag delays for which only one source image was localized. Further work is necessary to determine whether build-up may contribute to the observed differences between the lag at which two events are perceived and the lag at which two locations are perceived. Nonetheless, current results suggest that intersubject differences in echo threshold are qualitatively similar to intersubject differences in localization dominance.

All results are consistent with a simple model in which lead and lag information interacts perceptually and the strength of the interaction decreases with spatiotemporal separation of the lead and lag. At short delays, lead and lag both contribute to spatial perception, but the lead dominates (to the extent that only one position is even heard). At the longest delays tested, two sounds are perceived, but are not always heard at independent spatial locations. Spatial separation of lead and lag affects the degree to which two images are heard, but has no observable effect on the results of the fusion experiment performed in the current study. Overall, these results suggest that fusion and localization dominance may be mediated by somewhat different auditory mechanisms.

C. General notions regarding the precedence effect

Historically, the precedence effect has been discussed as a mechanism for suppressing directional information from echoes in order to allow robust localization of a sound source. However, there are some aspects of the precedence effect that are inconsistent with a mechanism whose primary purpose is suppression of localization information in echoes.

For instance, echoes can come from virtually any direction, independent of the source direction. However, both current and previous results (Shinn-Cunningham *et al.*, 1993) suggest that the relative directions of the lead and lag affect the strength of the suppression. Specifically, the suppression of the lag is greater when the lead and lag arise from similar directions than when they are spatially separated. In addition, the spectral content of an echo is a filtered version of the original source spectrum, so that there is always significant spectral overlap of the direct sound and any echoes. However, under some circumstances suppression occurs also when there is no spectral overlap of lead and lag (Divenyi, 1992; Shinn-Cunningham *et al.*, 1995).

If the spatial auditory system is capable of resolving the locations of both the lead and lag sources separately (i.e., there is little interference between the directional information in the lead and the lag), then there is little need to suppress lag information to preserve accurate localization of the lead. Current theories of binaural interaction (e.g., see Stern and Trahiotis, 1997) suggest that the interference between directional information from the lead and the lag may be greatest when the lead and lag give rise to similar interaural phase delays (IPDs) and excite overlapping populations of IPD-sensitive neurons. However, such interference will be reduced when the lag excites a distinct, separate population of neurons, allowing both lead and lag to be localized independently. With this analysis, the tendency for suppression to be weaker when lead and lag arrive from very different directions may reflect the fact that in this condition, the lag will cause less interference with estimation of the lead position.

There is growing evidence that localization information is combined across frequency in order to reduce ambiguity in the spatial information within any given narrow band of frequencies (Brainard and Knudsen, 1992; Trahiotis and Stern, 1989; Stern and Trahiotis, 1997). Such cross-frequency inte-

gration will be detrimental if spatial information from a lagging source is combined with information from a leading source, particularly if the spectral content of the lead and lag differs.

One interpretation of these results is that the precedence effect is a general process that enables robust localization not only in the presence of echoes, but whenever any competing information from a second source arrives before the direction of a previous source has been computed. This view suggests that echo suppression is a special case of a more general computational mechanism in the spatial auditory pathway for suppressing any information that could be disruptive to spatial auditory perception. In addition, the results suggest that the mechanisms underlying the three phenomena described here might have some general commonality, not merely at the initial stages of processing, but at later stages as well.

The current results lend further support to this view. Results from the localization dominance experiment indicate that the strength of the precedence effect as measured in a localization dominance task varies with spatial separation of lead and lag, consistent with a general mechanism for improving sound localization. Although there are links among fusion, discrimination, and localization dominance, further work is necessary to quantify how these measures relate to one another.

ACKNOWLEDGMENTS

This work was supported by NIH Grant No. R29-DC03083 to R. Y. Litovsky and ONR MURI award No. Z883402. The authors are grateful to Adam Stein and Daniel Singer for their invaluable help in programming and data collection. Dr. Miriam Valenzuela, Dr. D. Wesley Grantham, and two anonymous reviewers provided helpful feedback on an earlier draft of this paper. Portions of these data were presented at the meeting of the Association for Research in Otolaryngology, 1998.

Blauert, J. (**1997**). *Spatial Hearing: The Psychophysics of Human Sound Localization*, revised ed. (MIT Press, Cambridge, MA).

Blauert, J., and Divenyi, P. (**1988**) ''Spectral selectivity in binaural contralateral inhibition,'' Acoustica **66**, 267–274.

Brainard, M. S., and Knudsen, E. I. (**1992**). ''Neural derivation of sound source location: Resolution of ambiguities in binaural cues,'' J. Acoust. Soc. Am. **91**, 1015–1027.

Clifton, R. K., and Freyman, R. L. (**1997**). ''The precedence effect: Beyond echo suppression,'' in *Binaural and Spatial Hearing in Real and Virtual Environments*, edited by R. H. Gilkey and T. R. Anderson (Erlbaum, Mahwah, NJ), pp. 233–255.

Cremer, L. (**1948**) *The Scientific Foundations of Architectural Acoustics*, Vol. 1; cf. Blauert (1997).

Divenyi, P. L. (**1992**). ''Binaural suppression of nonechoes,'' J. Acoust. Soc. Am. **91**, 1078–1084.

Ebata, M., and Sone, T. (**1968**). ''Binaural fusion of tone bursts different in frequency,'' Proceedings, 6th International Congress on Acoustics, Tokyo, A-3-7.

Freyman, R. L., Clifton, R. K., and Litovsky, R. Y. (**1991**). ''Dynamic processes in the precedence effect,'' J. Acoust. Soc. Am. **90**, 874–884.

Gaskell, H. (**1983**). ''The precedence effect,'' Hear. Res. **12**, 277–303.

Haas, H. (**1951**). ''On the influence of a single echo on the intelligibility of speech,'' Acustica **1**, 48–58.

Haas, H. (**1972**). ''The influence of a single echo on the audibility of speech,'' Audio Eng. Soc. J. **20**, 146–159.

Hafter, E. R., Saberi, K., Jensen, E. R., and Briolle, F. (**1992**). ''Localisation in an echoic environment,'' in *Auditory Physiology and Perception*, edited by Y. Cazals, L. Demaney, and K. Horner (Pergamon, Oxford), pp. 555–561.

Hawley, M. L. (**1994**) ''Comparison of adaptive procedures for obtaining psychophysical thresholds using computer simulation,'' M.S. thesis, Boston University, Dept. of Biomedical Engineering.

Hochster, M. E., and Kelly, J. B. (**1981**). ''The precedence effect and sound localization by children with temporal lobe epilepsy,'' Neuropsychologia **19**, 49–55.

Leakey, D. M., and Cherry, E. C. (**1957**). ''Influence of noise upon the equivalence of intensity differences and small time delays in two-loudspeaker systems,'' J. Acoust. Soc. Am. **29**, 284–286.

Litovsky, R. Y., and Macmillan, N. A. (**1994**). ''Sound localization precision under conditions of the precedence effect: Effects of azimuth and standard stimuli,'' J. Acoust. Soc. Am. **96**, Pt. 1, 752–758.

Litovsky, R. (**1997**). ''Developmental changes in the precedence effect: Estimates of minimal audible angle,'' J. Acoust. Soc. Am. **102**, 1739–1745.

Litovsky, R. Y., Rakerd, B., Yin, T. C. T., and Hartmann, W. M. (**1997**). ''Psychophysical and physiological evidence for a precedence effect in the median saggital plane,'' J. Neurophysiol. **77**, 2223–2226.

Litovsky, R. Y., Colburn, H. S., Yost, W. A., and Guzman, S. (**1999**). ''The precedence effect,'' J. Acoust. Soc. Am. **106**, 1633–1654.

Perrott, D. R., Marlborough, K., Merrill, P., and Strybel, T. Z. (**1989**). ''Minimum audible angle thresholds obtained under conditions in which the precedence effect is assumed to operate,'' J. Acoust. Soc. Am. **85**, 282–288.

Saberi, K., and Perrott, D. R. (**1990**). ''Lateralization thresholds obtained under conditions in which the precedence effect is assumed to operate,'' J. Acoust. Soc. Am. **87**, 1732–1737.

Shinn-Cunningham, B. G., Zurek, P. M., and Durlach, N. I. (**1993**). ''Adjustment and discrimination measurements of the precedence effect,'' J. Acoust. Soc. Am. **93**, 2923–2932.

Shinn-Cunningham, B. G., Zurek, P. M., Clifton, R. K., and Durlach, N. I. (**1995**). ''Cross-frequency interactions in the precedence effect,'' J. Acoust. Soc. Am. **98**, 164–171.

Snow, W. B. (**1954**). ''Effect of arrival time on stereophonic localization,'' J. Acoust. Soc. Am. **26**, 1071–1074.

Stellmack, M. A., Dye, R. H., and Guzman, S. J. (**1999**). ''Observer weighting of interaural delays in source and echo clicks,'' J. Acoust. Soc. Am. **105**, 377–387.

Stern, R. M., and Trahiotis, C. (**1997**). ''Binaural mechanisms that emphasize consistent interaural timing information over frequency,'' 11th International Symposium on Hearing: Auditory Physiology and Perception, Grantham, UK.

Tollin, D. J., and Henning, G. B. (**1998**). ''Some aspects of the lateralization of echoed sound in man. I. Classical interaural delay-based precedence,'' J. Acoust. Soc. Am. **104**, 3030–3038.

Trahiotis, C., and Stern, R. M. (**1989**). ''Lateralization of bands of noise: Effects of bandwidth and differences of interaural time and phase,'' J. Acoust. Soc. Am. **86**, 1285–1293.

von Bekesy, G. (**1960**). *Experiments in Hearing* (McGraw-Hill, New York).

Wallach, H., Newman, E. B., and Rosenzweig, M. R. (**1949**). ''The precedence effect in sound localization,'' Am. J. Psychol. **LXII**(3), 315–336.

Yang, X., and Grantham, D. W. (**1997a**). ''Echo suppression and discrimination suppression aspects of the precedence effect,'' Percept. Psychophys. **59**(7), 1108–1117.

Yang, X., and Grantham, D. W. (**1997b**). ''Cross-spectral and temporal factors in the precedence effect: Discrimination suppression of the lag sound in free-field,'' J. Acoust. Soc. Am. **102**, 2973–2983.

Yost, W. A., and Soderquist, D. R. (**1984**). ''The precedence effect: Revisited,'' J. Acoust. Soc. Am. **76**, 1377–1383.

Zurek, P. M. (**1987**). ''The precedence effect,'' in *Directional Hearing*, edited by W. A. Yost and G. Gourevitch (Springer, New York), pp. 85–105.

Zurek, P. M. (**1980**). ''The precedence effect and its possible role in the avoidance of interaural ambiguities,'' J. Acoust. Soc. Am. **67**, 952–964.

Channel weights for speech recognition in cochlear implant users

Maureen A. Mehr, Christopher W. Turner, and Aaron Parkinson[a)]
Department of Speech Pathology and Audiology and Department of Otolaryngology, Head and Neck Surgery, University of Iowa, Iowa City, Iowa 52242

(Received 1 February 2000; revised 1 September 2000; accepted 5 September 2000)

The purpose of this study was to develop and validate a method of estimating the relative ''weight'' that a multichannel cochlear implant user places on individual channels, indicating its contribution to overall speech recognition. The correlational method as applied to speech recognition was used both with normal-hearing listeners and with cochlear implant users fitted with six-channel speech processors. Speech was divided into frequency bands corresponding to the bands of the processor and a randomly chosen level of corresponding filtered noise was added to each channel on each trial. Channels in which the signal-to-noise ratio was more highly correlated with performance have higher weights, and conversely, channels in which the correlations were smaller have lower weights. Normal-hearing listeners showed approximately equal weights across frequency bands. In contrast, cochlear implant users showed unequal weighting across bands, and varied from individual to individual with some channels apparently not contributing significantly to speech recognition. To validate these channel weights, individual channels were removed and speech recognition in quiet was tested. A strong correlation was found between the relative weight of the channel removed and the decrease in speech recognition, thus providing support for use of the correlational method for cochlear implant users. [DOI: 10.1121/1.1322021]

PACS numbers: 43.66.Sr, 43.66.Ts, 43.66.Yw, 43.71.Gv [KRK]

I. INTRODUCTION

Perhaps the biggest advance in cochlear implants subsequent to their initial introduction has been the employment of multiple electrodes and/or channels for simulation of the auditory nerve. The multiple electrode array presumably takes advantage of the natural tonotopic organization of the cochlea and its innervation pattern to allow the speech processor to provide ''place-frequency'' information to the listener. Considering the range of speech recognition performance among individual cochlear implant users, it may be beneficial to help determine how individual cochlear implant users understand or recognize speech. At present, besides overall recognition scores, we have very few tools available to determine how the multichannel implant is functioning. A good deal more information is required regarding what behavioral measures such as threshold, comfort level, dynamic range, and/or various electrophysiological characteristics can tell us about how well a particular electrode, and its associated nerve fibers, can transmit speech information. Because most of today's multichannel cochlear implant processors divide speech information into different frequency bands, with each frequency band corresponding to an electrode, or group of electrodes, it is desirable to investigate the extent to which individual bands or electrodes contribute to the overall understanding of speech.

Since some multichannel cochlear implant users have relatively good understanding of speech while others do not, it is important to determine the factors influencing their success. Previous studies have suggested that these differences may be attributed to signal processing (Gantz *et al.*, 1988; Tyler and Tye-Murray, 1991; Waltzman *et al.*, 1992; Wilson, 1993), individual device-programming strategies (Tyler *et al.*, 1992) and rehabilitation (Lansing and Davis, 1988). Other studies have looked at electrophysiology (e.g., Black *et al.*, 1987; Brown *et al.*, 1990; Simmons *et al.*, 1984), psychology (Knutson *et al.*, 1991; McKenna, 1991), and psychoacoustic measures (Dorman *et al.*, 1990; Hochmair-Desoyer *et al.*, 1985; Shannon, 1993; Chatterjee, 1999). Few of these previous efforts have directly investigated how speech information is transmitted to the listener through the implant beyond just measuring an overall percent score.

For example, Brown *et al.* (1990) reported that more rapid recovery functions on individual electrodes using an electrophysiological forward-masking paradigm correlated with higher overall speech recognition in implant users. On the other hand, Chatterjee (1999) found an apparently opposite relation using a behaviorally measured forward-masking task, that is, slower recovery times were related to better overall speech recognition. The actual relationships between characteristics of the implants' ability to transmit speech information and various electrophysiological or behavioral measures may have been obscured in these studies by across-subject comparisons, in which other variables such as duration of deafness, etc., were also contributing. In addition, the single dependent variable (overall speech recognition) is a function of the combination of the characteristics of all the implant users' functioning channels, whereas the behavioral and/or electrophysiological measures can be obtained individually across the multiple electrodes and/or frequencies. While there have been a few preliminary experiments in various laboratories in which the entire broadband speech

[a)]Current address: Cochlear Corporation, Englewood, CO 80112.

signal is input into individual electrodes or channels, in the present paper, we present a method which measures the ability of individual channels of the speech processor to transmit speech information appropriate for that channel under the condition of speech being presented to the implant user in their normal mode of listening.

A number of investigators have used the methods of the Articulation Index (e.g., ANSI, 1969; French and Steinberg, 1947; Fletcher and Galt, 1950) to determine frequency-importance information for listeners with acoustic hearing (both with and without sensorineural hearing loss). This method uses a quantity between zero and one to represent the proportion of speech information available in that frequency region to the listener. This available information in a particular frequency region is then multiplied by a frequency-importance, or ''weighing'' factor. To obtain frequency-importance information, a rather time-consuming process of using high- and low-pass filtering is utilized. In these filtering experiments, listeners are presented speech information under conditions of restricted frequency ranges.

An alternative approach to determining the importance of various frequency bands is offered by the correlational method (Doherty and Turner, 1996; Turner *et al.*, 1998). This is an adaptation (for speech) of the method originally described by Lutfi (1995) and Richards and Zhu (1994) for use in psychoacoustic experiments. In the correlational method, speech is presented to the listener in a broadband listening condition which is more typical in normal listening situations. Turner *et al.* (1998) showed that the relative importance of various frequency regions in understanding speech was often different, depending upon whether the listener was tested under conditions of broadband listening versus restricted frequency ranges. Another advantage to the correlational method is that all channels are able to be tested at the same time, which has the potential to be less time consuming than filtering experiments.

The knowledge of which channels within an individual's implant are functioning well for speech recognition and which are not may also have some clinical applications in terms of choosing an appropriate programming strategy for the speech processor. A study of Hanekom and Shannon (1996) showed that listeners' speech recognition performance was a function of the set of electrodes chosen from a seven-electrode speech processor. In another study by Zwolan *et al.* (1997), a reduction in the number of electrodes used resulted in some cochlear implant users having significant improvements in their speech recognition scores while others showed a decline in performance. These studies suggest that it may be possible to maximize benefits to the listener based on the number and choice of electrodes used. If we can determine which channels or electrodes are contributing most to the user's understanding of speech, it is possible that this information could then be used to ''tune'' the processor strategy in individual users to take maximum advantage of the fully functioning electrodes and/or to eliminate or redirect speech information away from the poorly functioning electrodes.

In the present study, we were interested in evaluating the application, reliability, validity, and efficiency of the correlational method in determining how important each frequency region is to the speech recognition of both cochlear implant users and normal-hearing listeners. The frequency weighting functions determined for normal-hearing listeners in the Turner *et al.* (1998) study suggested similar listening strategies among listeners. In experiment 1 we ask, ''How does the listening strategy or weighting functions of listeners with normal-hearing compare to the weighting functions determined for cochlear implant users?'' Ultimately, we would like to determine if the weighting functions can be used to specify which channels or electrodes are working most efficiently and which are not. In experiment 2 we describe the results of a test of the validity of the correlational method for use with cochlear implant users.

II. EXPERIMENT 1

In experiment 1, we obtained weighting functions from both normal-hearing listeners and cochlear implant users in order to determine how individual implant users make use of particular frequency regions as compared to normal-hearing listeners.

A. Methods

1. Subjects

Data were obtained from five listeners (four females and 1 male) with normal hearing, and with a mean age of 32 years (range from 21–48 years), having scored at least 95% correct on the speech tests presented. The audiometric thresholds for each listener were 20 dB HL or better at octave test frequencies from 250 to 8000 Hz. Seven adults (four females and three males) using the Med-El CIS-Link 6 Channel Processor and six active electrodes of the Ineraid cochlear implant were recruited through the Department of Otolaryngology at the University of Iowa. They had a mean age of 62 years (range 44–79 years) at the time of testing. The cochlear implant users had a minimum of 12 months experience with the Med-El processor.

2. Speech materials

Our speech test consisted of a subset of the UCLA version of the Nonsense Syllable Test (NST), which uses six lists of consonant-vowel syllables. The vowels /a, i, and u/ were paired with 22 different consonants and spoken by both a male and female talker for a total of 132 different speech tokens. These nonsense syllables were chosen to provide a rather large set of speech materials, which would include nearly all consonants in several vowel contexts and more than one talker, to reduce possible effects of token-specific cues for speech recognition. The various CV syllables were randomized when presented to the listener. Stimuli were digitized at 44.1 kHz (anti-alias filter of 20 kHz) and stored on a laboratory computer. The speech stimuli were digitally filtered into six frequency bands at frequencies corresponding to the configuration of the CIS speech processor programming strategy. FIR digital filters were implemented using MATLAB routines and provided less than 1 dB of passband ripple and 40 dB of stopband attenuation. This resulted in the six filtered speech bands corresponding to the

TABLE I. The filter cutoff frequencies for the six speech bands used in the correlational method.

Band number	Frequency range (in Hz)
1	300–486
2	486–791
3	791–1283
4	1283–2062
5	2062–3384
6	3384–5500

six electrodes of the cochlear implants used in this study. The frequency divisions were logarithmic and are listed in Table I.

3. Procedures

The correlational method was used for estimating speech weighting functions. On each trial, the root-mean-square (rms) level within each of the six frequency bands was calculated for the token to be presented. Six bands of noise, each filtered to match the frequency range of the corresponding speech band, were then mixed with the appropriate speech band at a randomly chosen signal-to-noise ratio. The signal-to-noise ratio in each speech band was chosen (in 2-dB steps) from a rectangular distribution that was 24-dB wide, the midpoint of which was determined from pilot testing (described below). On each trial, the signal-to-noise ratio chosen was independent of the level of noise in each of the other five bands. The six bands (speech plus noise) were then recombined and played to the listener. The weight placed upon a frequency band was estimated by a point biserial correlation between the signal-to-noise ratios in a band and the responses (whether correct or incorrect). That is, those frequency bands for which varying the signal-to-noise ratio had little or no effect on the subject's performance received a low weight, and those bands in which the varied signal-to-noise ratio had a large effect on performance received a high weight. The six raw correlations for each subject were transformed to relative weights by summing their values and expressing each band's weight as the raw correlation divided by this sum. Thus the relative weights of the six channels sum to 1.0. These six relative weights are then plotted as a function of the frequency band to yield a frequency-weighting function.

Each listener was allowed to listen to the nonsense syllables to become familiar with the consonant choices and response box. The response box consisted of 22 buttons, each labeled with one of the consonant alternatives. Listeners were given visual feedback in the form of a light located adjacent to the button corresponding to the correct answer after each trial. The listener was then presented with 6 CV lists of 50 trials each for a total of 300 trials to determine an overall percent-correct score in quiet. The listener was then acquainted with the speech stimuli that included the randomized noise added to the speech. Based on the overall percent-correct scores, a mean signal-to-noise ratio was then determined by additional preliminary testing to yield an approximate one-third decrease in recognition scores from those obtained in the quiet condition (i.e., from 60% correct to 40% correct). This is necessary because the correlational method requires that listeners make some recognition errors due to the added noise. For normal-hearing listeners, mean signal-to-noise ratio chosen was approximately 0 dB. For the majority of implant users, this level was approximately +12 dB.

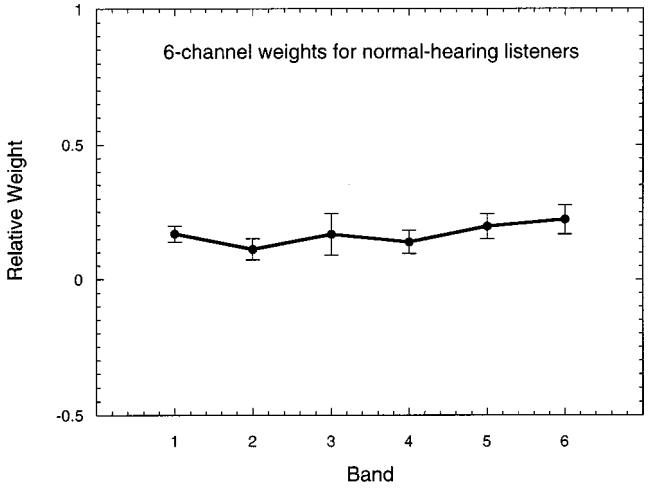

FIG. 1. The mean frequency-weighting functions for the normal-hearing listener group as estimated by the correlational method. The error bars represent plus and minus one standard deviation across the individual listener's relative weights for each channel.

Analyzed data consisted of results taken from the 132-item speech materials consisting of six lists at 200 trials each for a total of 1200 trials in the randomized noise condition. Data consisting of fewer trials were also analyzed to determine the number of trials necessary to yield a significant raw correlation in at least two or more frequency bands. Due to the occasional variability in day-to-day performance of cochlear implant users, we obtained 300-trial speech scores in quiet during each session for a baseline measure of the patient's performance on the day of testing.

Stimulus presentations and experimental records were accomplished by a Macintosh Power PC 9500 computer and DigiDesign Audiomedia III, 16-bit digital-to-analog converters. For all subjects, sound field presentation of stimuli was used in a double-walled sound-attenuation chamber (IAC). A Crown (Model D-75A) amplifier was used to drive a single three-way loudspeaker (Pyle Mfg.) located 1.5 m directly in front of the subject. The cochlear implant users wore their speech processors for the experiment. Normal-hearing listeners heard the speech stimuli at a level of 70 dB SPL. For the implant users, the presentation level was set to the highest comfortable level for each subject, attempting to ensure that the majority of the speech range was above their thresholds. From the trial-by-trial experimental record stored on the computer, correlations were calculated for each band between the signal-to-noise ratio on each trial, and whether the subject scored correctly or not. When the number of trials equals 1200, a raw correlation of $r=0.0564$ or higher is considered significantly different from zero at the $p<0.05$ level of confidence (Lutfi, 1995). We then compared the weighting

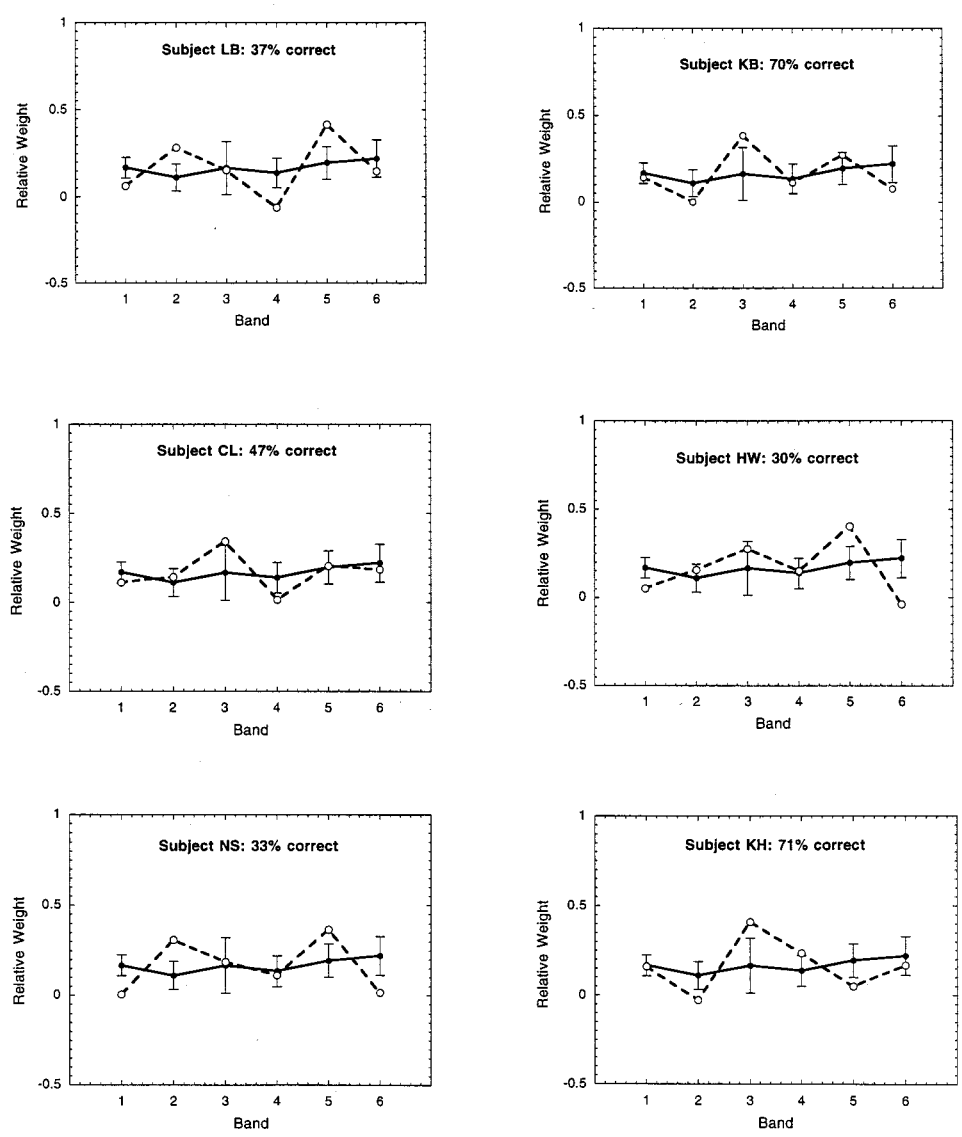

FIG. 2. The frequency-weighting functions for the six cochlear implant users. In each panel the relative weights for a single subject are shown by the dashed line, along with the average weighting function for the normal-hearing listeners (solid line). The error bars on the normal weighting function represent the 95% confidence intervals about the mean normal values. The speech recognition score in quiet is also noted in each panel for each implant subject.

functions determined for the cochlear implant users to the weighting functions determined for the listeners with normal hearing.

4. Results

Weighting functions determined for the normal-hearing listeners are plotted in Fig. 1. Similar listening strategies were demonstrated across listeners. Each channel or frequency region was approximately equal in its importance for understanding these speech tokens. Furthermore, *all* regions appeared to be making a contribution. As noted by the error bars, there was very little variation across listeners.

Weighting functions determined for six of the cochlear implant users are plotted in Fig. 2, with the solid line representing the mean normal weighting function and the dashed line representing the cochlear implant user's weighting function. The seventh cochlear implant subject's data were not used, as this subject did not yield significant raw correlations in any of the frequency bands [this was due to the subject's very low speech recognition score in quiet (18%), which made it very difficult to find an appropriate level of noise to add to the speech which would degrade the recognition score]. Because the relative weights must add to one, a relative weight greater than the normal-hearing values does not necessarily indicate that the implant user does better in using this band than normal listeners. Rather, that particular frequency region is more important for that cochlear-implant listener relative to the other frequency bands.

In contrast to weighting functions of the normal-hearing listeners, weighting functions of the cochlear implant users showed unequal weighting across the various frequency regions. Of the 36 data points for the cochlear implant users (6 channels times 6 implant users), 20 of the relative weights lie outside the 95% confidence intervals of the estimate for average normal-hearing listeners' relative weights. Channels were not contributing equally, and each implant user had at least one channel that was near zero. Four cases of negative correlations were obtained from the total of 36; however,

those negative correlations yielded negative relative weights very close to zero (the largest was −0.06). A zero weighting indicated that there was no significant relationship between the signal-to-noise ratio in that band and the subject's performance. Speech recognition scores in quiet for each of the cochlear implant users are noted on each graph in Fig. 2, with no individuals scoring near 100%.

Combined individual weighting functions of the implant users are replotted in Fig. 3, along with the averaged results of the normal-hearing listeners. Although there are large individual differences, there appears to be a general trend among cochlear implant users for a lower weighting on bands 1 and 6 and a higher weighting on band 3. It can be easily seen from this plot that the cochlear implant users' weighting functions are quite different from those for normal-hearing listeners, with each implant user having unequal weighting across the bands.

We were also interested in the reliability and efficiency of the procedure in terms of the number trials required to obtain accurate weighting functions. Because the statistical significance of the raw correlations is dependent upon the number of trials, we compared the number of significant raw correlations obtained using 600 trials versus 1200 trials. The data indicated that 1200 trials were necessary in order to yield significant raw correlations in at least two or more frequency bands for these implant users. Therefore, weighting functions based upon fewer trials may not identify every band that makes a substantial contribution to speech recognition.

Relative weights for each subject in each band determined from the first 600 trials are plotted against relative weights determined from the full 1200 trials in Fig. 4. For a relative weight in the middle range (i.e., relative weight =0.16), the 95% confidence interval of a prediction based upon 600 trials relative to the value obtained after 1200 trials was calculated to be plus or minus 0.17. Thus the relative weights determined on the basis of 600 trials would be informative primarily in the sense of showing which bands were high contributors versus which bands were low contributors.

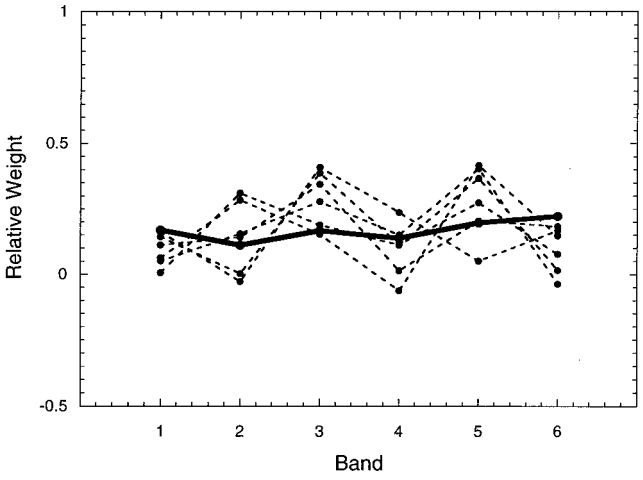

FIG. 3. The frequency-weighting functions for all six implant listeners are shown in a single graph (dashed lines), along with the group average for the normal-hearing listeners (solid line).

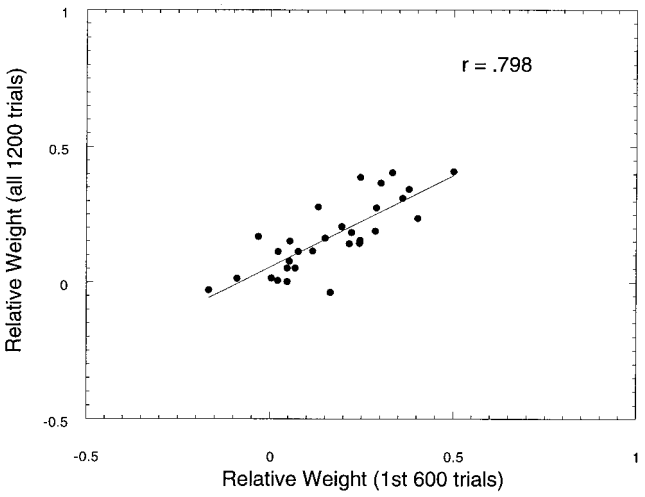

FIG. 4. The relation between the relative weight for a channel as determined by the first 600 trials and the relative weight as determined by the full 1200-trial protocol.

III. EXPERIMENT 2

In this experiment we addressed the issue of the validity of the channel weights for the implant users, as determined in experiment 1. If the relative weights obtained for an implant user are valid, then removing speech information in a band with a high relative weight should result in a substantial decrease in speech recognition performance. Furthermore, the removal of speech information in a band with a low relative weight should result in a small decrease. In experiment 2, we tested these relations.

A. Methods

1. Subjects

Three of the six adult cochlear implant users from experiment 1 provided usable data for this experiment. Experiment 2 was conducted several months following the data collection for experiment 1, and cochlear implant users were only available for a limited time block for our testing as they were visiting Iowa City for their regularly scheduled clinical checkups. Due to the elapsed time between experiments 1 and 2, each subject's actual relative weighting functions may have changed from the values originally measured. Two of the original six implant users showed a large and statistically significant increase or decrease (13%–16%) in their speech recognition in quiet performance between the time of experiment 1 and experiment 2 (implant users LB and CL). Therefore, the validity of their previously measured weighting functions at the time of experiment 2 were suspect and they were not included in experiment 2. A third implant user from experiment 1 (patient KH) was having technical difficulties with her speech processor/implant on the day of experiment 2, so we were unable to collect reliable speech recognition scores from this patient. Thus only data from cochlear implant users HW, KB, and NS were obtained in experiment 2.

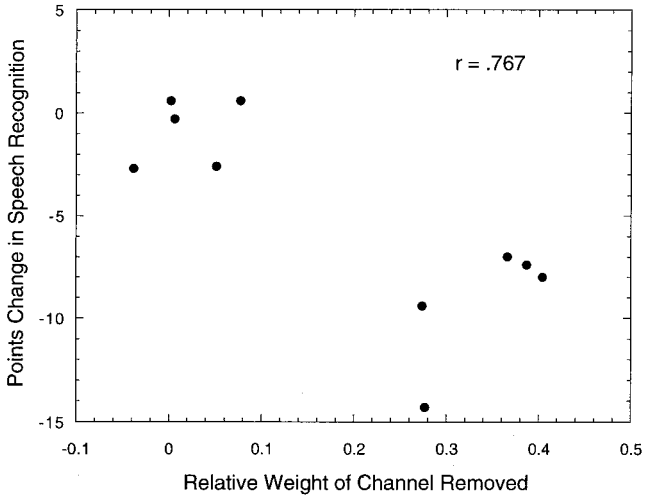

FIG. 5. The relation between the percentage points change in speech recognition (in quiet) when the speech information in a single channel was removed from the speech processor, and the relative weight of the channel removed.

2. Procedure

Individual channels were removed from the cochlear implant users' processor programs by setting the threshold (T) and comfort (C) levels of particular channels to very low levels, which were undetectable to the implant user. The other five channels were left as previously programmed. Based on the weighting function determined for each individual subject in experiment 1, we removed several individual channels for each patient, removing channels that had high weights and also those with low weights. For patient HW, channels 1, 3, 5, and 6 were removed. For NS, channels 1 and 5 were removed. Patient KB was tested with channels 2, 3, 5, and 6 removed.

Speech recognition in quiet was obtained as before, in the sound field at the same presentation level as used in experiment 1. Each of the six lists was presented for 50 trials, for a total of 300 trials per data point. A new baseline comparison condition for each subject, consisting of 300 trials in quiet with all six channels programmed to normal values, was obtained on the same day that the channel-out conditions were tested.

3. Results

The relation between the change in percentage points and the relative weight of the channels removed are plotted in Fig. 5 for each condition tested for all three implant users. As noted, there is a strong relationship ($r=0.77$) between the decrease in speech recognition measured and the relative weight of the channel removed. When the change in speech recognition with a channel removed was expressed in arcsin-transformed units (which accounts for the binomial distribution form of speech recognition scores), the relation was essentially identical ($r=0.73$). Removal of a channel with a low weighting resulted in a nominal change in percentage points. Conversely, removal of a channel with a high weighting resulted in a larger (negative) change in percentage points. While the relationship in Fig. 5 between the weight of the channel removed and its effect upon speech recognition is striking, caution should be observed due to the limited number of individuals for which data could be collected. Additional research with more cochlear implant users is warranted.

IV. DISCUSSION

Results from these experiments indicated that the correlational method can provide a method for estimating the relative weight that listeners place on various frequency bands. This procedure yields estimates of how well each ''channel'' is contributing to the implant user's understanding of speech in comparison to each of the other channels. Moreover, these measures can be obtained simultaneously for all channels in a broadband listening situation.

Results for normal-hearing listeners indicated that each listener used information in speech across frequency bands in a similar manner. This is in agreement with the similarity of band-weighting patterns across normal-hearing listeners reported in the Turner *et al.* (1998) study, which also used the correlational method. Additionally, it appears that the logarithmic frequency division of the channels produces approximately equal weights across frequency bands for the normal-hearing listeners for these speech materials. These two conclusions are further strengthened in that this same methodology yields very different weighting functions for individuals with cochlear implants. The equal-weighting across bands found for all normal-hearing listeners is not an artifact of the procedure itself. This ''flat'' weighting function and the similarity across listeners was most likely related to the large set of speech materials used in the present study. In Doherty and Turner (1996), the correlational method showed very different weights across channels and listeners. That study required the listeners to discriminate between only three speech tokens, and it was suspected that each listener developed a highly stimulus-specific strategy for the task, as opposed to a more general speech recognition strategy. We have recently begun testing a different set of speech materials (16-item, four-talker, /aCa/ consonant recognition) and have again observed approximately equal weighting across logarithmically divided bands for normal-hearing listeners.

Cochlear implant users in this study yielded very different weighting functions than did the normal-hearing listeners. This suggests that the general characteristics of electrical simulation of the remaining auditory neurons in the auditory system of deaf individuals, along with the cochlear implant devices of the present study, do not completely capture the important aspects of normal speech transmission for implant users. This may be indicated by the common pattern across implant users noted in Fig. 3, in which channel 1 produced relatively low weights and channel 3 yielded higher weights. In support of the present pattern of results, Dorman *et al.* (1989) reported that the addition of a mid-to-high frequency channel of stimulation to the most apical (low-frequency) channel produced the largest improvements in speech recognition in their group of implant users. Channel 6, which stimulates the most basal location of the cochlea, received relatively low weighting by all the implant users. This result

might reflect a lack of viable neurons in the basal end of profoundly deafened individuals. It is probably the case that implant users have real differences between the effectiveness of individual electrodes in combination with the pattern of surviving neurons. However, other factors such as speech audibility for implant users as well as the dynamic range of the implant channel in relation to the speech signal may contribute to the ineffectiveness of various channels. It may also be the case that the age differences between the normal-hearing listeners and the implant users may be a factor in the pattern of weights obtained across the two groups. Further research may help us to understand these issues and the application of the correlational method as described in this paper may be useful in these investigations.

There are, however, some limitations of the correlational procedure, as described in the present study. The correlational method may be limited by the number of channels that can be tested at one time. If too many channels are tested at once, the obtained raw correlations may not reach significance unless the number of trials is very large. One could test fewer channels of a multichannel implant, but the weighting function determined would only relate to those channels chosen, as the estimated weights are relative to one another, and the desirable characteristic of a broadband listening situation might have to be sacrificed. In the present study, we found that using 600 trials did not always yield at least two channels with significant raw correlations, whereas 1200 trials did produce at least two significant correlations. Thus the procedure as described in this paper is probably too lengthy for standard clinical application at the present time. In addition, if the listeners' speech recognition performance changes over time, weighting functions obtained at one session may not remain valid in subsequent experimental sessions. These concerns suggest that a more efficient testing procedure is desirable.

A related concern is the interaction between the difficulty of the speech materials for the range of implant users encountered, and the ability of the correlational procedure to produce significant correlations. Assigning the appropriate average noise level for each subject is very important. Too little noise will result in nonsignificant correlations. Thus the overall percent score in quiet for a patient should not be too low, otherwise the decrease in score from adding noise may result in the subject performing at chance level. This was seen in the failure of the correlational method with the seventh implant subject, for whom the speech materials were apparently too difficult.

In summary, the correlational procedure shows promise in its ability to assess the functional status and contribution to speech recognition of individual frequency bands (channels) in cochlear implant users. Additional research using this procedure may allow us to determine which factors involved in speech recognition through multichannel cochlear implants are critical in achieving optimal performance.

ACKNOWLEDGMENTS

This research was supported in part by NIDCD Grant No. 2 R01 DC00377-12. The project was the basis of an Honor's thesis for the first author in the Department of Speech Pathology and Audiology at the University of Iowa. Valuable assistance was provided by Marla Ross, Ruth Severson, Shelley Witt, and Abigail Wolaver of the Department of Otolaryngology at the University of Iowa. Helpful comments on an earlier version of this paper were provided by Paul Abbas and Bom Jun Kwon. In addition, many helpful criticisms and suggestions were provided by two anonymous reviewers as well as the associate editor.

ANSI (**1969**). ANSI S3.5-1969, American National Standards Methods for the Calculation of the Articulation Index (ANSI, New York).

Black, F. O., Lilly, D. J., Fowler, L. P., and Stypulkowski, P. H. (**1987**). ''Surgical evaluation of candidates for cochlear implants,'' Ann. Otol. Rhinol. Laryngol. **96**, 96–99.

Brown, C. J., Abbas, P. J., and Gantz, B. (**1990**). ''Electrically evoked whole-nerve action potentials: Data from human cochlear implant users,'' J. Acoust. Soc. Am. **88**, 1385–1391.

Chatterjee, M. (**1999**). ''Temporal mechanisms underlying recovery from forward masking in multielectrode-implant listeners,'' J. Acoust. Soc. Am. **105**, 1853–1863.

Doherty, K. A., and Turner, C. W. (**1996**). ''Use of a correlational method to estimate a listener's weighting function for speech,'' J. Acoust. Soc. Am. **100**(6), 3769–3773.

Dorman, M., Dankowski, K., McCandless, G., and Smith, L. (**1989**). ''Consonant recognition as a function of the number of channels of stimulation by patients who use the Symbion cochlear implant,'' Ear Hear. **10**, 288–291.

Dorman, M. F., Smith, L., McCandless, G., Dunnavant, G., Parkin, J., and Dankowski, K. (**1990**). ''Pitch scaling and speech understanding by patients who use the Interaid cochlear implant,'' Ear Hear. **11**, 310–315.

Fletcher, H., and Galt, R. H. (**1950**). ''The perception of speech and its relation to telephony,'' J. Acoust. Soc. Am. **22**, 89–150.

French, N. R., and Steinberg, J. C. (**1947**). ''Factors governing the intelligibility of speech sounds,'' J. Acoust. Soc. Am. **19**, 90–119.

Gantz, B. J., Tyler, R. S., Knutson, J. F., Woodworth, G., Abbas, P., McCabe, B. F., Hinrichs, J., Tye-Murray, N., Lansing, C., Kuf, F., and Brown, C. (**1988**). ''Evaluation of five different cochlear implant designs: Audiologic assessment and predictors of performance,'' Laryngoscope **98**, 1100–1106.

Hanekom, J. J., and Shannon, R. V. (**1996**). ''Place pitch discrimination and speech recognition in cochlear implant users,'' South African J. Commun. Disord. **43**, 27–40.

Henry, B. A., McKay, C. M., McDermott, H. J., and Clark, G. M. (**1999**). ''The relationship between speech information perceived by cochlear implantees in different spectral regions and electrode discrimination,'' J. Acoust. Soc. Am. (submitted).

Hochmair-Desoyer, I., Hochmair, E., and Stiglbrunner, H. (**1985**). ''Psychoacoustical temporal processing and speech understanding in cochlear implant patients,'' in *Cochlear Implants*, edited by R. A. Schindler and M. M. Merzenich (Raven, New York), pp. 291–304.

Knutson, J. F., Schartz, H. A., Gantz, B. J., Tyler, R. S., Hinrichs, J. V., and Woodworth, G. (**1991**). ''Psychological predictors of audiological outcomes of multichannel cochlear implants: Preliminary findings,'' Ann. Otol. Rhinol. Laryngol. **100**, 817–822.

Lansing, C. R., and Davis, J. M. (**1988**). ''Early vs delayed speech perception training for adult cochlear implant users: Initial results,'' J. Acad. Rehab. Audiol. **21**, 29–42.

Lutfi, R. A. (**1995**). ''Correlation coefficients and correlation ratios as estimates of observer weights in multiple-observation tasks,'' J. Acoust. Soc. Am. **97**, 1333–1334.

McKenna, L. (**1991**). ''The assessment of psychological variables in cochlear implant patients,'' in *Practical Aspects of Audiology, Cochlear Implants: A Practical Guide*, edited by H. Cooper (Whurr, London), pp. 125–145.

Richards, V. M., and Zhu, S. (**1994**). ''Relative estimates of combination weights decision criteria, and internal noise based on correlational coefficients,'' J. Acoust. Soc. Am. **95**, 423–424.

Shannon, R. V. (**1993**). ''Psychophysics,'' in *Cochlear Implants: Audiological Foundations*, edited by R. S. Tyler (Singular, San Diego), pp. 35–85.

Simmons, F. B., Lusted, H., Meyers, T., and Shelton, C. (**1984**). ''Electrically induced auditory brainstem response as a clinical tool in estimating nerve survival,'' Ann. Otol. Rhinol. Laryngol. **92** (Suppl. 112), 97–100.

Turner, C. W., Kwon, B. J., Tanaka, C., Knapp, J., Hubbartt, J. L., and Doherty, K. A. (**1998**). ''Frequency-weighting functions for broadband speech as estimated by a correlational method,'' J. Acoust. Soc. Am. **104**, 1580–1585.
Tyler, R. S., Opie, J. M., Fryauf-Bertschy, H., and Gantz, B. J. (**1992**). ''Future directions in cochlear implants,'' J. Acoust. Soc. Am. **16**, 151–164.
Tyler, R. S., and Tye-Murray, N. (**1991**). ''Cochlear implant signal-processing strategies and patient perception of speech and environmental sounds,'' in *Practical Aspects of Audiology, Cochlear Implants: A Practical Guide*, edited by H. Cooper (Whurr, London), pp. 58–83.
Waltzman, S. B., Cohen, N. L., and Fisher, S. (**1992**). ''An experimental comparison of cochlear implant systems,'' Semin. Hear. **13**(3), 195–207.
Wilson, B. (**1993**). ''Signal processing,'' in *Cochlear Implants: Audiological Foundations*, edited by R. S. Tyler (Singular, San Diego), pp. 36–85.
Zwolan, T. A., Collins, L. M., and Wakefield, G. H. (**1997**). ''Electrode discrimination and speech recognition in postlingually deafened adult cochlear implant subjects,'' J. Acoust. Soc. Am. **102**, 3673–3685.

Room reverberation effects in hearing aid feedback cancellation

James M. Kates[a)]
AudioLogic, A Cirrus Logic Company, 2465 Central Avenue, Suite 100, Boulder, Colorado 80301

(Received 21 April 2000; revised 28 June 2000; accepted 16 October 2000)

Room reverberation can affect feedback cancellation in hearing aids, with the strength of the effects depending on the acoustical conditions. These effects were studied using a behind the ear (BTE) hearing aid mounted on a dummy head and coupled to the ear canal via an open fitting. The hearing aid impulse response was measured for the dummy head placed at eight closely spaced locations in a typical office. The feedback cancellation in the hearing aid used a set of filter coefficients that were initialized for one location within the room, and then allowed to adapt to the feedback path measured at the same or to a different location. The maximum stable gain for the hearing aid was then estimated without feedback cancellation, for the initial set of feedback cancellation filter coefficients prior to adaptation, and for the feedback cancellation filter after adaptation. A low-order ARMA model combining a fixed set of poles with an adaptive FIR filter is shown to be effective in representing the feedback path exclusive of reverberation. Increasing the adaptive filter length has only a small benefit in improving the feedback cancellation performance due to the inability of the system to model the room reverberation. The mismatch between the modeled and actual feedback paths limits the headroom increase that can be achieved when using feedback cancellation, and varies with the location within the room.
[DOI: 10.1121/1.1332379]

PACS numbers: 43.66.Ts, 43.60.Lq [SPB]

I. INTRODUCTION

Mechanical and acoustic feedback limit the maximum gain that can be achieved in most hearing aids (Lybarger, 1982; Kates, 1988). The acoustic feedback path includes the effects of the hearing-aid amplifier, receiver, and microphone as well as the acoustics of the vent and any leaks present. The acoustic feedback path also includes the room in which the user is listening. In feedback cancellation, the feedback signal is estimated and subtracted from the microphone signal (Kates, 1999). Effective feedback cancellation requires that the adaptive filter be long enough to model all of the salient features of the feedback path, and that it adapt rapidly enough to track the changes in the feedback path as the listening environment changes. The LMS adaptation algorithm (Widrow *et al.*, 1976) is generally used to adaptively estimate the feedback path in hearing aids, as opposed to more sophisticated adaptation algorithms, because of the limited processing power available in a battery-powered device.

Computer simulations and prototype digital systems indicate that increases in gain of between 6 and 20 dB can be achieved in an adaptive system before the onset of oscillation, and no loss of high-frequency response is observed (Bustamante *et al.*, 1989; Engebretson *et al.*, 1990; Kates, 1991; Dyrlund and Bisgaard, 1991; Engebretson and French-St.George, 1993; Maxwell and Zurek, 1995; Kaelin *et al.*, 1998). In laboratory tests of a wearable digital hearing aid (French-St. George *et al.*, 1993), a group of hearing-impaired subjects used an additional 4 dB of gain when adaptive feedback cancellation was engaged and showed significantly better speech recognition in quiet and in a background of speech babble. Field trials of a feedback-cancellation system built into a behind-the-ear (BTE) hearing aid have shown increases of 8–10 dB in the gain used by severely impaired subjects (Bisgaard, 1993) and increases of 10–13 dB in the gain margin measured in real ears (Dyrlund *et al.*, 1994).

The amount of gain possible in a hearing aid is ultimately limited by the ability of the feedback cancellation system to model the actual feedback path. Room reverberation, which consists of multiple acoustic reflections at different amplitudes and time delays, can cause changes in the feedback path that can be difficult to model. Reflections cause peaks and valleys to appear in the feedback path frequency response. Hellgren *et al.* (1999) found, for example, that a wall located 10 cm from the aided ear caused peaks of up to 7.9 dB to appear at 2, 5, and 6.2 kHz in the feedback path frequency response of a BTE hearing aid, and that there were well-defined notches between the peaks. Increasing the distance from the hearing aid to the wall will reduce the strength of the reflection, reducing in turn the amplitudes of the peaks and valleys, but the number of peaks and valleys that appear in the frequency response will increase and they will be spaced more closely together. The multiple reflections that make up the reverberation will also interact, generating complicated modifications to the feedback path frequency response.

Reverberation typically persists for a much longer time than the impulse responses of the electro-mechanical components in the hearing aid or the direct acoustic path from receiver to microphone. A short adaptive filter used to model the components and the acoustic environment in the ear canal and the local vicinity of the head will not be long enough to model the room reverberation. Changes in the reverberation as the user moves about the room will change the feedback path, but the feedback cancellation filter will not be

[a)]Electronic mail: jkates@audiologic.cirrus.com

able to model them. Increasing the length of the adaptive filter may not improve performance if the filter is not long enough to include the time delays corresponding to the major room reflections. Reverberation could therefore be an important limitation to the effectiveness of feedback cancellation in hearing aids.

In this article, the effects of room reverberation on feedback cancellation will be presented. A small room is used for the experiments to give more realistic test conditions than those used by Hellgren *et al.* (1999). The design of the feedback cancellation system is first reviewed. Measurements of the feedback path in a room are then presented along with the feedback cancellation performance for an 8-, 16-, or 32-tap adaptive finite impulse response (FIR) filter in series with a five-pole nonadaptive filter. The performance limitations imposed by the room reverberation are then discussed along with the implications for hearing-aid design.

II. FEEDBACK CANCELLATION

The feedback cancellation system used for the experiments in this article is intended to compensate for acoustic feedback occurring in the vicinity of the ear and head. The feedback cancellation approach divides the feedback path model into two filters in series (Kates, 2000). The first filter represents those aspects of the feedback path that are expected to change very slowly, such as the microphone, amplifier, and receiver responses. The first part of the model is thus initialized when the hearing aid is fitted to the user, and then held constant while the hearing aid is in use. The first filter in the system used for the present experiments is an all-pole infinite impulse response (IIR) filter having five poles.

The second filter represents those aspects of the feedback path that can change rapidly, such as changes resulting from a shift in the position of the hearing aid within the ear canal. The second filter is initialized when the hearing aid is fitted to the user and then adaptively updated while the hearing aid is in use. The second filter is long enough to encompass the time delays expected when a telephone receiver is positioned close to the aided ear or a hat is put on, but it is much shorter than the typical reverberation time in a room. The second filter in the system used for the present experiments is a FIR filter having 8 to 32 taps.

A. Initialization

The initial parameter estimation procedure uses the hearing aid to acquire the raw data needed to describe the feedback path impulse response. All other signal processing tasks are performed by the host computer that communicates with the hearing aid during the initialization. The host computer generates one period of a periodic probe sequence, which is downloaded to the hearing aid. The code in the hearing aid then records the signal at the hearing-aid microphone while reading out successive periods of the probe sequence as shown in Fig. 1. The accumulated microphone signal is uploaded to the host computer, which calculates the feedback path impulse response. The feedback path signal delay is extracted from the impulse response along with an estimate

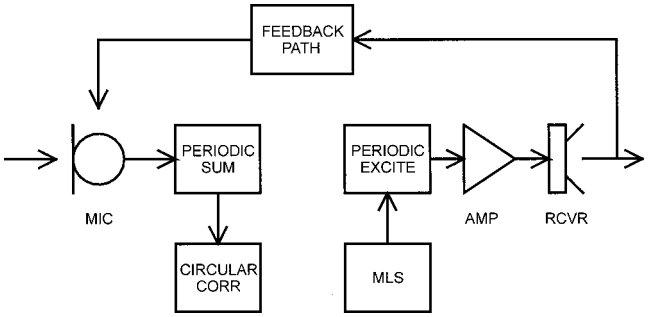

FIG. 1. Block diagram of the system used to make the initial measurement of the feedback path impulse response.

of the response signal-to-noise ratio. Using the estimated delay, the poles and zeros of a filter modeling the impulse response are then determined using system identification techniques. A description of each of these operations is given below.

1. Probe sequence and impulse response

A periodic maximal-length sequence is used to measure the feedback path impulse response. Such sequences have been successfully used to measure hearing-aid responses in laboratory measurement systems (Schneider and Jamieson, 1993). A maximal-length sequence (MLS) has only two values, $+1$ and -1. It is generated by a N-stage shift register and the period length is $M=2^N-1$ (Press *et al.*, 1986). One period of the sequence is generated and amplitude scaled in the host computer, which then downloads the scaled sequence to the hearing aid. To acquire the feedback path impulse response, the probe is read out from a circular buffer, giving a periodic excitation, and the microphone response is synchronously summed into a circular buffer having the same length as the probe signal. Because coherent averaging is used to acquire the microphone signal, the SNR for the feedback path response relative to random room noise is improved 3 dB for every doubling of the number of periods used for the excitation. Periodic room noise, such as 50- or 60-Hz hum from electrical machinery, will also be reduced by the averaging as long as the hum is not synchronized with the periodic MLS signal. Nonlinear distortion, however, can cause spurious bumps and peaks to be distributed throughout the measured impulse response (Dunn and Hawksford, 1993; Vanderkooy, 1994).

The M-point circular autocorrelation of the M-point MLS has the property that it is M for 0 lag and -1 for all other lags. To extract the feedback path impulse response, the summed microphone signal is divided by the number of periods used for the excitation and then circularly cross-correlated with one period of the MLS (Schroeder, 1979; Borish and Angell, 1983; Rife and Vanderkooy, 1989). The result is then adjusted for the amplitude of the periodic excitation. For the present system, the MLS has a period $M=255$ samples (approximately 16 msc), which is the longest possible sequence given the data memory constraints in the real-time hearing aid system. The result of the circular correlation is the impulse response of the feedback path, including the overall path delay and any residual room noise.

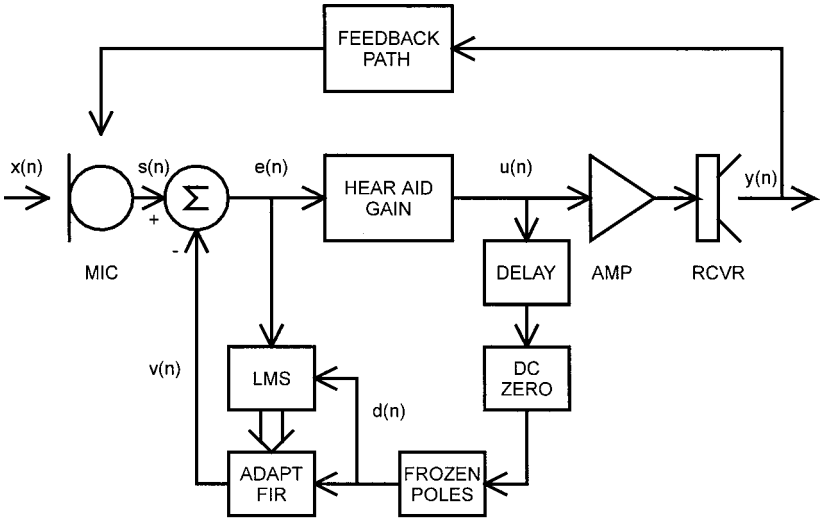

FIG. 2. Block diagram of the run-time system for the adaptive feedback cancellation.

2. PNR

The peak-to-noise ratio (PNR) is given by the ratio of the amplitude of the peak of the impulse response to the rms noise level in the tail of the impulse response. The peak is the part of the signal that is the least corrupted by the additive room noise and therefore gives the best estimate of the feedback path signal power. The impulse response is a sequence of 255 samples, but most of its energy is contained in the first 32 samples following the overall delay. Thus the tail of the impulse response consists almost entirely of room noise and reverberation, and the rms room noise is computed from the last 64 samples in the impulse response. The peak-to-rms room noise ratio thus gives an indication of the quality of the estimated feedback path impulse response. A peak-to-noise ratio of 30 dB or better has been empirically found to yield good estimates of the response poles and zeros. The peak-to-noise ratio is limited by the properties of the MLS circular convolution to a maximum of about 48 dB.

3. Feedback path delay

The feedback path delay is determined using a two-step process. The delay is first estimated by finding the peak of the impulse response and then counting backwards a fixed number of samples from the peak to locate the approximate start of the impulse response. The peak of the impulse response is used to determine the delay because it is the most robust portion of the signal in the presence of additive noise. A search is then performed using candidate delay values above and below the approximate start delay estimated from the peak. The delay value yielding the best pole-zero model fit to the measured impulse response is then selected as the feedback path delay.

4. Poles and zeros

The poles and zeros of the filter modeling the feedback path are determined from the impulse response using the ARX procedure of Ljung (1987). The ARX algorithm is a joint optimization procedure in which the pole and zero coefficients are determined at the same time. Define the following sequences:

(i) $r(n)$=the feedback path impulse response.
(ii) $q(n)$=a segment of white noise.
(iii) $t(n)$=the noise sequence $q(n)$ filtered through the dc zero filter $D(z)=1-z^{-1}$. This high-pass filtering is to duplicate the dc zero filter used in the running adaptation to remove the dc bias in the sampled data.
(iv) $z(n)=r(n)*t(n)$, the filtered noise convolved with the impulse response.

The ARX procedure is used to find the filter which, when convolved with $t(n)$, produces the closest match to $z(n)$. Define the regression vector

$$\varphi(n)=[-z(n-1),-z(n-2),\ldots,-z(n-ma),t(n-\Delta),t(n-\Delta-1),\ldots,t(n-\Delta-mb+1)]^T, \quad (1)$$

where ma is the number of poles in the model, mb is the number of zero coefficients (number of zeros plus 1), and Δ is the estimated feedback path delay. The optimal coefficient vector is then found by solving the set of linear equations $\mathbf{P}\theta=\mathbf{c}$ for the coefficient vector θ, where

$$\mathbf{P}=\left[\sum_{n=0}^{N-1}\varphi(n)\varphi^T(n)\right], \quad \mathbf{c}=\left[\sum_{n=0}^{N-1}\varphi(n)z(n)\right]. \quad (2)$$

The correlation matrix $\mathbf{P}$ is symmetric positive definite, so the set of linear equations is solved using the Cholesky factorization of $\mathbf{P}$ followed by forward and back substitution. The pole coefficients $\mathbf{a}$ are given by the first ma entries in θ and the zero coefficients $\mathbf{b}$ are given by the remaining mb entries in θ. The modeled feedback path filter transfer function is then given by

$$W(z)=z^{-\Delta}(1-z^{-1})\frac{\sum_{m=0}^{mb-1}b_m z^{-m}}{1+\sum_{k=1}^{ma}a_k z^{-k}}. \quad (3)$$

The resultant model can be considered to be a delay and a dc zero followed by an all-pole IIR filter in series with a FIR filter.

B. Running adaptation

The adaptive feedback cancellation, shown in Fig. 2, uses LMS adaptation (Widrow *et al.*, 1976) to adjust the zeros of the FIR filter that forms part of the model of the feedback path. The poles of the all-pole IIR filter remain frozen at the values determined during initialization. The adaptation proceeds closed-loop, and no additional noise is injected. The adaptive processing is implemented in block form, with the adaptive coefficients updated once for each block of data. The LMS adaptation over the block of data minimizes the error signal given by

$$\varepsilon(m)=\sum_{n=0}^{N-1} e_n^2(m)=\sum_{n=0}^{N-1}[s_n(m)-v_n(m)]^2, \tag{4}$$

where $s_n(m)$ is the microphone input signal and $v_n(m)$ is the output of the FIR filter for block m and sample n within the block, and there are N samples per block. The constrained adaptation described by Kates (1999) can also be used. The LMS coefficient update for the set of adaptive FIR filter zero coefficients $\{b_k\}$ is given by

$$b_k(m+1)=b_k(m)+2\mu\sum_{n=0}^{N-1} e_n(m)d_{n-k}(m), \tag{5}$$

where $d_{n-k}(m)$ is the input to the adaptive filter, delayed by k samples, for block m. Power normalization of the adaptation step size gives improved system performance and is implemented by setting

$$\mu=\mu_0/\langle \mathbf{d}^2(n)\rangle, \tag{6}$$

where $\mathbf{d}(n)$ is the vector of present and past adaptive filter input samples.

III. PERFORMANCE METRIC

The performance metric used in this study is the estimated maximum stable gain (MSG). Kates (1999) showed that the hearing aid will be stable if the following condition is met:

$$|H(\omega)||W(\omega)-F(\omega)|<1, \tag{7}$$

where $H(\omega)$ is the hearing aid gain, $W(\omega)$ is the feedback path model, and $F(\omega)$ is the actual feedback path response. $W(\omega)$ is given by Eq. (3) with $z^{-1}=e^{-j\omega}$. The maximum stable hearing aid gain as a function of frequency is then

$$|H(\omega)|<1/|W(\omega)-F(\omega)|. \tag{8}$$

The MSG is the maximum allowable gain value assuming a flat frequency response for the hearing aid:

$$\mathrm{MSG}=\mathrm{Min}_{\omega}[1/|W(\omega)-F(\omega)|]. \tag{9}$$

The MSG is therefore determined by the frequency at which the mismatch between the feedback model and the actual feedback path is greatest. If no feedback cancellation is used, $W(\omega)=0$ and the MSG will be determined by the peak of the measured feedback path response $F(\omega)$. In general, the greatest mismatch will occur in the vicinity of the peaks in the measured feedback path frequency response.

To compute the MSG, the impulse response of the feedback path is first measured using the MLS approach described above. The pole-zero model is then fit to the measured impulse response, resulting in the model delay, pole coefficients, and zero coefficients used in Eq. (3). The frequency response of the feedback path model is then computed along with the frequency response of the measured feedback path. The absolute value of the difference between the modeled and measured feedback path frequency responses is then computed. The absolute value of the difference is then inverted, and the minimum found and converted to dB.

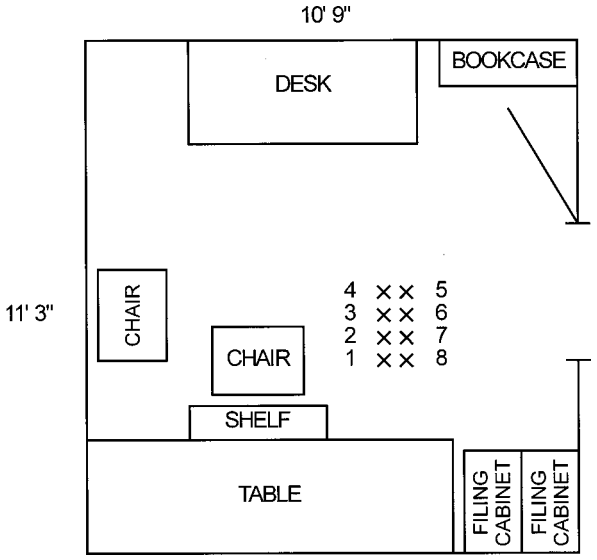

FIG. 3. Office used for the feedback path measurements. The ''Eddi'' dummy head was placed on a moveable platform. Measurements were obtained using the right ear of the dummy head at each of the numbered locations. The locations are on a grid with a six-inch spacing.

IV. METHODS

A. Test configuration

The effects of reverberation on feedback cancellation were studied for feedback path measurements made in an office. A behind-the-ear (BTE) hearing aid was mounted on the right ear of an ''Eddi'' acoustic manikin, and the manikin was placed on a wheeled platform. An open fitting, in which the earmold was replaced by the receiver tubing held in place with an annular support, was used to get the greatest possible intensity for the feedback path signal. The ear of the manikin was approximately 2.5 ft above floor level. The hearing aid was connected via a cable to a real-time digital processing system, and the sampling rate was 15.625 kHz. The ear canal in the ''Eddi'' manikin reproduces the shape of a human ear canal, but it is terminated by a rigid wall rather than by a network duplicating the acoustic impedance at the ear drum. The feedback path response measured in the ''Eddi'' manikin has been empirically determined to be about 10 dB more intense than that measured for a comparable human ear; however, it has the same general spectral shape and temporal structure.

The feedback path response was measured for a dummy head placed at eight locations in an office representative of a small room. The office floor plan is shown in Fig. 3. The ceiling consists of acoustical tile at a height of 8 ft, with the

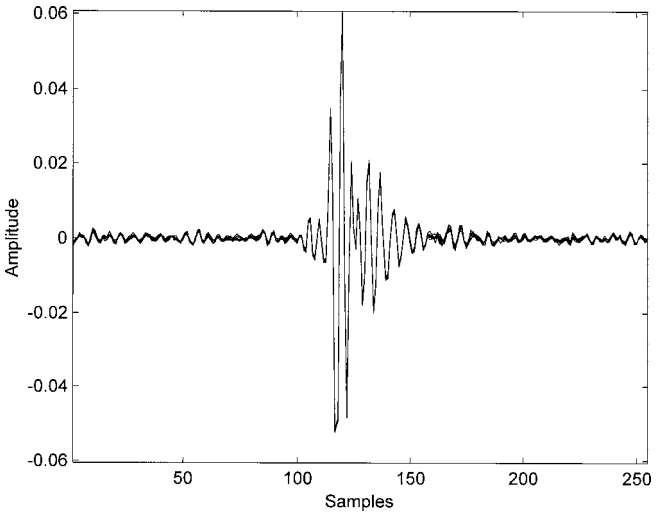

FIG. 4. Eight impulse responses obtained from repeated measurements at location 1.

plenum above the ceiling extending for another 6 ft. The office walls are painted gypsum board. The floor is carpeting with a looped pile and installed over a concrete slab. The office door was open as shown during the measurements. The effects of reverberation on the feedback path will be dominated by the early reflections from the hard walls and floor. Reflections at longer time delays will be less intense, and will tend to be subsumed into the background noise. Thus the early reflection pattern is more important than the reverberation time in assessing the room effects on the feedback path. The timing and amplitude of the early reflections will be different in different rooms; a corridor with walls close to the aided ear will typically cause larger peaks and valleys in the feedback path frequency response, while a large room with walls further from the aided ear will typically have reduced frequency response perturbations.

The eight measurement positions are indicated by the crosses in the figure, numbered from 1 through 8. At each location the right ear of the manikin was used, and the manikin always faced away from the office door. The measurement locations are on a grid with 6-in. spacing. The time delays for early reflections from the walls to either side of the manikin will shift by about 1 ms as it is moved from one location to the next, and this will shift the locations of the peaks and valleys in the feedback path frequency response perturbations caused by the reflections.

B. Initialization and measured feedback path

The feedback model initialization as described in the section above was performed for each of the eight locations. The first step in the initialization was to acquire the feedback path response to the periodic MLS excitation, after which the summed periodic response was uploaded to the host computer. The analysis and signal processing was then continued on the host computer using a MATLAB simulation of the remaining initialization steps. The filter coefficient calculations were performed using the circularly wrapped feedback path impulse response data as shown in Fig. 4. The all-pole IIR filters all had five poles, and the FIR filters had either 8, 16, or 32 taps. The use of a five-pole IIR filter has proven to be very robust in practice; the poles tend to model the receiver and tubing resonances, and the zeros model the remaining acoustic aspects of the feedback path. The feedback cancellation has proven to be effective in nearly all environments even though the poles are initialized in the hearing-aid dispenser's office.

The feedback path impulse response was obtained by the circular convolution of the MLS sequence with the summed response to the periodic 255-sample MLS excitation. The result was scaled to adjust for the excitation amplitude and the number of periods summed. An excitation amplitude of 0.016 was used as this was found to give the highest PNR, thus minimizing the possibility of distortion corrupting the reverberation measurement. A total of 10 s of data was acquired at each of the eight locations in the room. The hearing aid was left in place on the dummy head as it was moved from one location to the next to determine the effects of changing position within the room. As a control, the dummy head was placed at location 1 in the room and eight impulse responses sequentially acquired at the same location; these impulse responses showed the test/retest reliability and the effects of noise on repeated measurements.

The background noise level in the office was approximately 54 dB SPL (C weighted), measured with a Radio Shack model 33-2050 sound level meter, and was primarily due to the heating and ventilation system. The sound pressure level at the ear canal opening of the dummy head during the measurements was about 70 dB SPL (C weighted), and the level at the BTE microphone was about 57 dB SPL (C weighted). The 10-s averaging of the MLS responses improves the SNR of the measurement by about 28 dB, and the 255-point MLS itself improves the SNR by about 24 dB compared to an impulse response obtained using a single click excitation (Dunn and Hawksford, 1993). The net SNR for the measured impulse response after the circular correlation is therefore approximately $(57-54)+28+24=55$ dB.

C. Adapted MSG

A further concern is whether a system initialized at one location can effectively adapt to a different location in the room. To investigate this question, the adaptive run-time system was also simulated in MATLAB. The feedback path impulse response was computed using the MLS procedure, and the remaining initialization steps performed using the wrapped impulse response with the pole and zero filter coefficients computed using the ARX procedure and saved. Because of the periodic excitation and circular convolution, the tail of the impulse response is wrapped around to the beginning of the period. To give a causal system, the impulse response was then unwrapped, with the wrapped tail moved from the beginning to the end of each impulse response. The FIR filter coefficients were then all reset to zero, and the adaptation proceeded using the unwrapped impulse responses as shown in Fig. 6. The adaptation thus proceeded with the poles for the starting location, but with the zeros adapting to the feedback path for a second location. This procedure duplicated the effects of setting up the hearing aid in a dispenser's office, where the pole coefficients are frozen

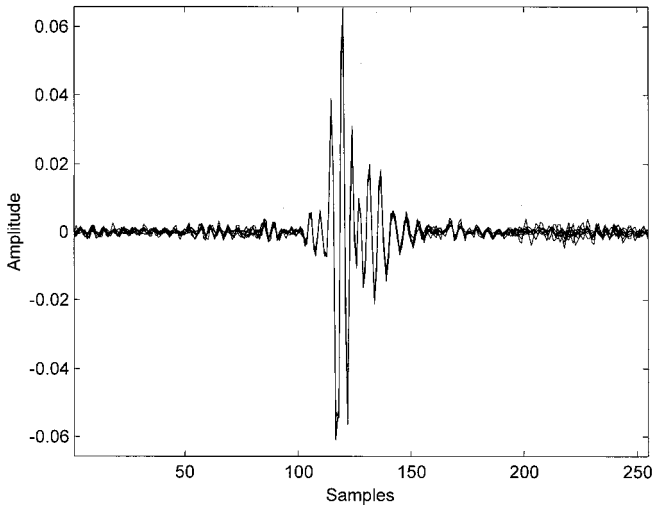

FIG. 5. Eight impulse responses consisting of one impulse response from each of the eight measurement locations.

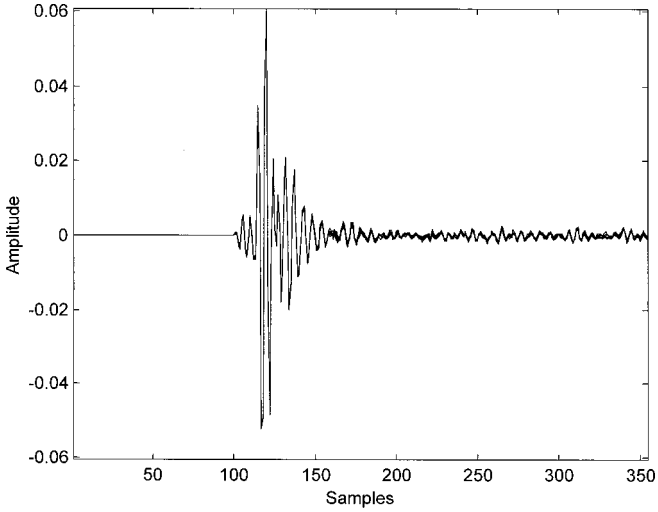

FIG. 6. Eight unwrapped impulse responses obtained from the repeated measurements at location 1.

after the initialization, and then moving to another location where the zero filter coefficients are free to adapt. A total of 4 s of white noise excitation, signal $x(n)$ in Fig. 2, was processed as the input to the simulation, with the adapted MSG obtained by averaging four samples taken during the last second of the excitation at 0.2-s intervals. The LMS adaptation time constant was set to $\mu_0 = 2.5 \times 10^{-7}$ so that steady-state feedback cancellation behavior was achieved after processing three seconds of the white noise excitation, and the block size was $N = 56$ samples.

A subset of four locations were chosen for the adaptation experiment. Full-length feedback path measurements from locations 1, 3, 5, and 7 were used for adaptive FIR filters having 8 and 16 taps. The 32-tap filter was not used because the initialization 32-tap FIR filter results were not significantly different from those of the 16-tap FIR filter. The IIR filters all had five poles. The pole and zero filter coefficients were initialized for one location within the room. The pole coefficients were frozen, and the zero filter coefficients were cleared and then allowed to adapt to the feedback path measured for the same or for a different location. The filter coefficients and the adaptation operations were quantized to 16 bits in the MATLAB simulation.

V. RESULTS AND DISCUSSION

A. Measured feedback path

The measured impulse responses determined using the MLS procedure are plotted in Fig. 4 for the eight repeated measurements at location 1 and in Fig. 5 for the eight room locations. The variance in the repeated measurements at the same location is much lower than for the set of measurements at the different room locations, indicating that the changes in the feedback path impulse response with room location are due to the changes in the reflection patterns and are not an artifact of noise or poor measurement repeatability.

The unwrapped impulse response, with the wrapped tail moved from the beginning to the end of each response, is presented in Fig. 6 for the repeated measurements at the same location and in Fig. 7 for the eight room locations. The first 100 samples represent the time delay primarily due to the digital processing algorithm used to acquire the data, with additional delays due to the A/D and D/A converters, the microphone and receiver group delay, and the acoustic delay due to the receiver tubing. It is apparent from the overlaid responses in Fig. 7 that there is very little variation during samples 100–150 of the unwrapped response as the room location is changed. This is the time interval where the ringing of the receiver resonances and the immediate acoustic effects of the ear canal and pinna would be expected to dominate, followed by the shoulder bounce (mounting board for the dummy head) approximately 20–25 samples later. These acoustic factors would not be expected to depend on the location within the room.

The first room reflection appears at about sample 160 in Figs. 6 and 7. This signal is probably due to a reflection from the opened office door, since measurements made with the door closed did not show this reflection. However, substan-

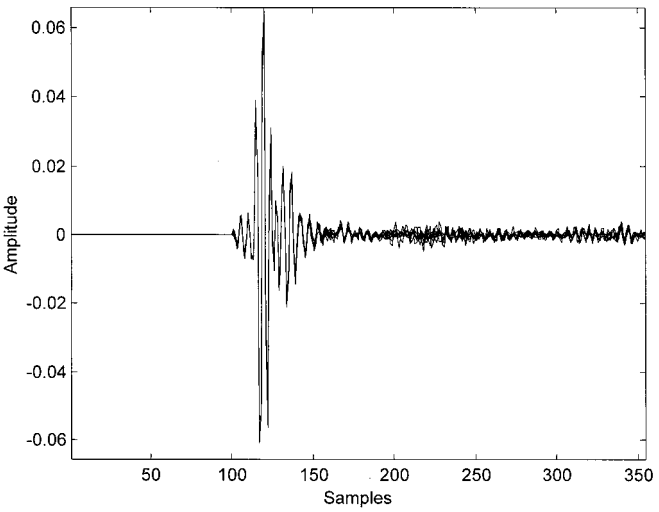

FIG. 7. Eight unwrapped impulse responses consisting of one impulse response from each of the eight measurement locations.

tial variation is seen in the interval between 180 and 250 samples in Fig. 7. As the manikin is moved within the room, there will be shifts in the distance from the hearing aid to the walls near the table and desk, as shown in Fig. 3. Thus the reflections from these two walls will arrive at different times, creating the apparent randomness in the overlaid impulse responses. There is another strong reflection with very little variance at about 340 samples, indicating a reflection path such as a ceiling reflection that would not depend strongly on the location of the manikin in the room. Reflections at longer time delays will be wrapped around the periodic response and will tend to appear as additional noise.

Distortion in the hearing aid could also cause artifacts to appear in the measured impulse response. Distortion would be caused by nonlinear responses to the excitation signal. However, the same nonlinear reactions would always occur in response to the same subsequences of the MLS sequence. Thus the distortion effects would be the same for each period of the excitation and would not depend on the location within the room. The variation in the tails of the impulse responses shown in Fig. 7 is therefore evidence that reverberation and not distortion is the dominating factor corrupting the measured feedback path impulse response.

The magnitude frequency responses computed from the feedback path impulse responses of Figs. 6 and 7 are plotted in Figs. 8 and 9, respectively. The variation in the impulse responses translates into a corresponding variation in the frequency responses. The greatest variation in dB is at the low and high frequencies where the signal is weakest, and the least variation at the frequency response peaks. The frequency response curves of Fig. 8, computed from the eight impulse responses measured at location 1, show very little variance in the vicinity of the peaks at 2.8 and 3.7 kHz, with the different responses spanning less than 0.5 dB. In contrast, the eight measurements at the different room locations span a 2-dB range in the vicinity of the response peaks. Thus small displacements within the room can result in noticeable differences in the feedback path impulse and frequency responses.

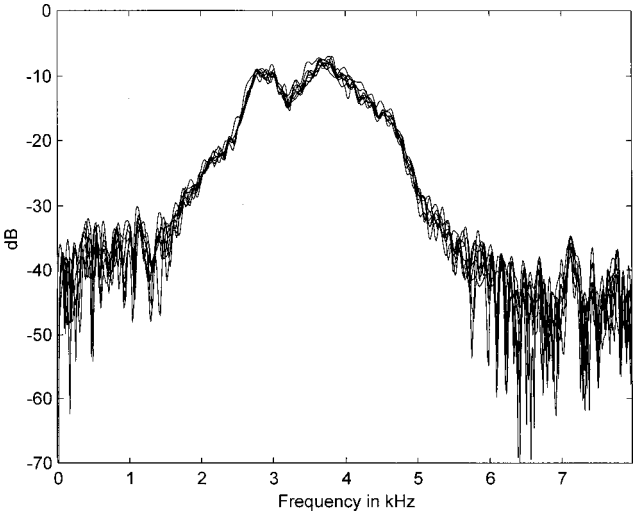

FIG. 9. Magnitude frequency responses computed from the eight feedback path impulse responses at each location shown in Fig. 5.

The reverberation effects can be minimized by temporally windowing the impulse response (Rife and Vanderkooy, 1989; Dunn and Hawksford, 1993). To apply the window, the peak of the impulse response was first located. The window consisted of a linearly rising portion starting at ten samples before the peak and rising to unity gain at the peak, followed by a 40-point section having unit gain, and then by a 25-point section linearly decreasing back to zero. The total window duration was thus 75 samples (4.7 ms). This window was applied to the eight impulse responses acquired for the different room locations and plotted in Figs. 5 and 7, and the resultant magnitude frequency responses are plotted in Fig. 10. The frequency response curves for the windowed data are much smoother than for the entire impulse response, and show much less variation with room location.

The ability of the feedback cancellation system to model

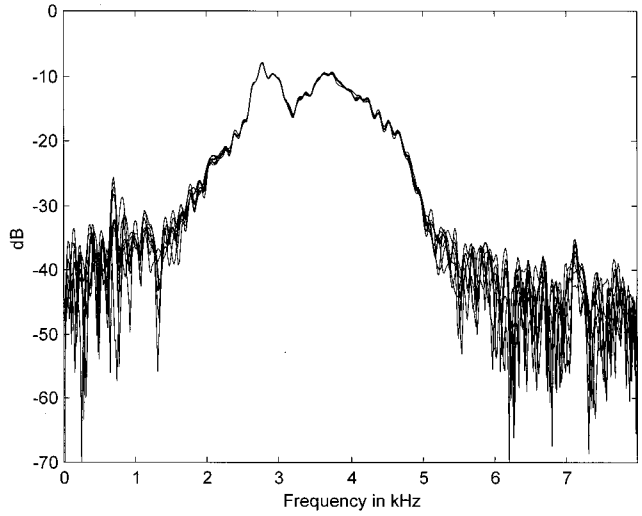

FIG. 8. Magnitude frequency responses computed from the eight repeated feedback path impulse responses shown in Fig. 4.

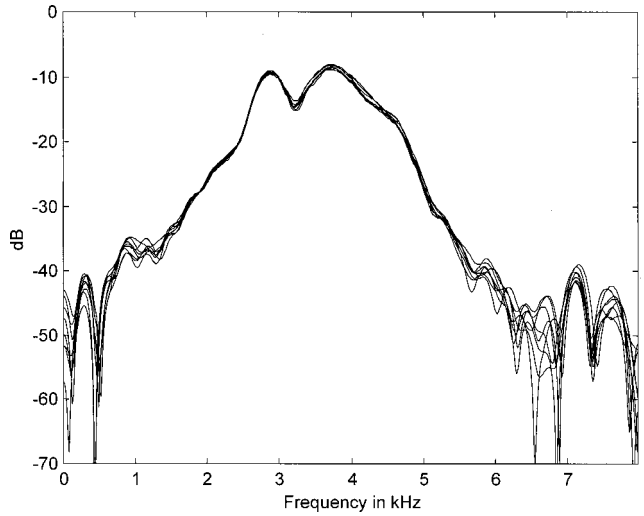

FIG. 10. Magnitude frequency responses computed from the eight feedback path impulse responses at each location shown in Fig. 5 after application of a time-domain window. The window consisted of a 10-sample linearly rising portion to the peak of the impulse response, a flat portion of 40 samples, and a linearly decreasing portion of 25 samples.

the feedback path response is illustrated in Fig. 11. The figure shows the magnitude frequency response of a feedback path measured at room location 1, along with the response of the ARX five-pole seven-zero (8-tap FIR filter) model fit to the data. The feedback path has a pair of peaks, one at about 2.8 kHz and the other at about 3.7 kHz. The model is able to accurately reproduce these peaks. The pole-zero model produced by the ARX procedure can be viewed as a smooth curve that fits the major features of the feedback path frequency response but ignores the response ripples and fine structure. The shape of the pole-zero model is similar to the frequency response of the windowed data shown in Fig. 10, indicating that the model represents primarily the feedback path in the vicinity of the ear. This smooth curve models the short-time behavior of the impulse response, which includes the microphone, receiver, ear canal, and pinna resonances, but it is too short to include the room reverberation.

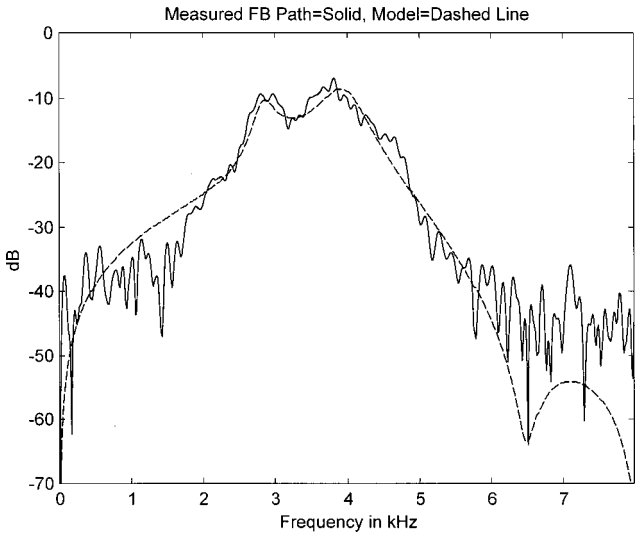

FIG. 11. Magnitude frequency response computed from a single feedback path impulse response for room location 1 (solid line) and the ARX five-pole seven-zero model fit to the response (dashed line).

B. Initial MSG

1. Impulse response with reverberation

The next question is whether the differences in the measured feedback paths cause differences in the expected feedback cancellation performance. The initialization calculations were performed for a five-pole IIR filter in series with an 8-, 16-, or 32-tap FIR filter for each of the eight locations. In addition, the PNR, the MSG without feedback cancellation, and the MSG with feedback cancellation were computed for each of the combinations of FIR filter length and location. The results are based on the ARX model fit to the data; the run-time adaptation was not used. The results are shown in Table I. The PNR ranges from 33.2 to 36.6 dB, with an average of 34.9 dB. The MSG without feedback cancellation averages 7.7 dB, while that for the 8-tap FIR filter gives 16.4 dB, the 16-tap FIR filter gives an average of 19.9 dB, and the 32-tap FIR filter gives an average of 20.7 dB. Thus the feedback cancellation using the 8-tap FIR filter results in an 8.7 dB improvement in the expected maximum gain over no feedback cancellation. Increasing the FIR filter length to 16 taps improves the expected performance by just 3.5 dB, and doubling the length again to 32 taps adds only an additional 0.8 dB.

A two-way analysis of variance (ANOVA) was performed on the data of Table I, and the results are presented in Table II. The factor of the number of taps in the FIR filter (T) was significant, but the initialization location (I) was not. A Tukey HSD *posthoc* analysis indicates that the conditions of no feedback cancellation, the 8-tap FIR filter, and the 16-tap FIR are significantly different at the 0.01 level. The 32-tap FIR filter results are not significantly different from those of the 16-tap FIR filter.

The 32-tap filter should be long enough to model the shoulder bounce, but this increased filter length did not make a significant improvement in feedback cancellation performance. Successfully modeling the reverberation within a room requires a much longer filter; acoustic echo cancellation, for example, can require a FIR filter of up to 4000 taps at an 8-kHz sampling rate to model the room reverberation, and using ARMA techniques to model the room reverberation can still require on the order of 250 pole coefficients and 450 zero coefficients (Haneda *et al.*, 1994).

An additional concern is the criterion for computing the ARX model fit, which is to minimize the mean-squared error between the observed response and the model. The model thus minimizes the average deviation, while the stability, and the related MSG criterion, is controlled by the maximum deviation, which may not be improved by the increased filter

TABLE I. Peak-to-noise ratio (PNR) and maximum stable gain (MSG) in dB for the initial feedback cancellation poles and zeroes. The test conditions are no feedback cancellation, an 8-tap FIR filter, a 16-tap filter, and a 32-tap filter. No filter adaptation has taken place.

Room location	PNR (dB)	MSG (dB)			
		No FB cancellation	8-tap FIR	16-tap FIR	32-tap FIR
1	33.7	7.0	17.1	20.4	22.1
2	34.2	7.5	18.1	18.1	21.2
3	34.5	7.6	15.7	20.5	19.2
4	35.0	7.8	15.5	19.7	19.1
5	33.2	8.0	15.3	18.6	17.4
6	36.5	7.6	15.9	21.0	21.7
7	36.1	8.1	17.4	19.7	23.4
8	36.6	8.1	16.3	21.2	21.5
Average	34.9	7.7	16.4	19.9	20.7

TABLE II. Two-factor analysis of variance (ANOVA) for the initial feedback cancellation maximum stable gain (MSG) data of Table I.

Source of variation	Sums of squares	Degrees of freedom	Mean squares	F	Signficance
Taps in FIR filter	848.17	3	282.72	219.42	0.001
Initialization location	16.42	7	2.35	1.82	0.136
$I \times T$	27.06	21	1.29		
Total	891.65	31			

length. Increasing the FIR filter length will be of minimal benefit if it cannot be made long enough to include all of the important room reverberation effects and still retain a reasonable computational load.

2. Windowed impulse response

Even though the benefit of a longer FIR filter is limited by the presence of room reverberation, there may be some conditions where increasing the filter length will lead to measurable improvements in feedback cancellation performance. In situations where reverberation is minimal, the degrees of freedom in the longer filter will not be wasted trying to model the reverberation, but will instead be available to model the feedback path in the vicinity of the head.

Reduced reverberation was simulated by windowing the measured impulse response. The window was the same as used for the magnitude frequency response curves of Fig. 10. For each of the eight locations, the MSG without feedback cancellation and the MSG with feedback cancellation using 8-tap, 16-tap, and 32-tap FIR filters were computed for the windowed impulse response data. The results are shown in Table III. The MSG without feedback cancellation averages 8.4 dB, while that for the 8-tap FIR filter gives 19.6 dB, the 16-tap FIR filter gives an average of 22.8 dB, and the 32-tap FIR filter gives an average of 28.8 dB. Thus the feedback cancellation using the 8-tap FIR filter results in a 11.2 dB improvement in the expected maximum gain over no feedback cancellation. Increasing the FIR filter length to 16 taps improves the expected performance by only 3.2 dB, and doubling the length again to 32 taps adds a further 6.0 dB.

A two-way analysis of variance (ANOVA) was performed on the data of Table III, and the results are presented in Table IV. The factor of the number of taps in the FIR filter (T) was significant, but the initialization location (I) was not. A Tukey HSD *posthoc* analysis indicates that the four test conditions of no feedback cancellation and the three different filter lengths are all significantly different at the 0.01 level.

These results confirm the supposition that the benefit of longer filters depends on the amount of reverberation. Increasing the number of taps in the filter allows a better model of either the reverberation or the residual error in the ear-level feedback path, depending on which is greater. Increasing the FIR filter length from 8 to 16 taps yielded similar results for the full-length and windowed impulse responses, which indicates that the 16-tap filter is still modeling the ear-level feedback path and not the room. The 32-tap FIR filter gave a much bigger improvement for the windowed impulse response than for the full-length response, which indicates a much better model of the ear-level response than for the shorter filters in the absence of reverberation. When reverberation is present, however, the 32-tap filter tries to model the reverberation ripples because these ripples in the frequency response are greater in magnitude than the residual errors in modeling the ear-level feedback path.

Room reverberation causes perturbations in the feedback path response that depend on the location within the room. A short feedback-cancellation filter will fit a smooth curve through the measured data, and will thus give an average improvement that will be similar everywhere in the room because the reverberation is essentially ignored in the feedback path model. The stronger the reverberation, the less the benefit because the errors between the actual feedback path and the model will be greater. A longer filter in the absence of reverberation, as simulated by the windowed response, will do a better job of modeling the ear-level feedback path and will give additional headroom. However, the longer filter will try to model the reverberation when it is present, and very little benefit will result from the increased filter length unless the filter is long enough to substantially encompass the early reflections in the room.

C. Adapted MSG

The MSG results for a system initialized at one location and allowed to adapt to the same or different location are presented in Table V. The average initial MSG values for the four selected locations are essentially the same as for the complete set of eight locations, and show an initial predicted benefit of 3.4 dB for the 16-tap FIR filter in comparison with

TABLE III. Maximum stable gain (MSG) in dB for the initial feedback cancellation poles and zeroes computed for the windowed impulse responses. The window consisted of a 10-sample linearly rising portion to the peak of the impulse response, a flat portion of 40 samples, and a linearly decreasing portion of 25 samples. The test conditions are no feedback cancellation, an 8-tap FIR filter, a 16-tap filter, and a 32-tap filter. No filter adaptation has taken place.

Room location	MSG (dB)			
	No FB cancellation	8-tap FIR	16-tap FIR	32-tap FIR
1	8.3	19.8	23.8	27.8
2	8.1	20.8	22.4	31.4
3	8.0	19.1	23.0	27.4
4	8.3	19.6	21.8	26.1
5	8.5	19.2	22.4	28.7
6	8.4	19.2	23.7	30.0
7	8.9	19.8	21.8	29.4
8	8.5	19.4	23.6	29.2
Average	8.4	19.6	22.8	28.8

TABLE IV. Two-factor analysis of variance (ANOVA) for the initial feedback cancellation maximum stable gain (MSG) data of Table III.

Source of variation	Sums of squares	Degrees of freedom	Mean squares	F	Signficance
Taps in FIR filter	1757.70	3	585.90	679.31	0.001
Initialization location	8.32	7	1.19	1.38	0.265
$I \times T$	18.11	21	0.86		
Total	1784.14	31			

the 8-tap filter. The average after adaptation shows a predicted benefit of 2.8 dB for the 16-tap FIR filter in comparison with the 8-tap filter, so the adaptation has improved the performance of the 8-tap filter slightly more than that of the 16-tap filter. The variation in the adapted MSG with room location is a result of the differences in the error between the actual and adapted feedback paths; the error is a result of the peaks and valleys in the feedback path frequency response introduced by the reverberation, and these perturbations will change with location. An individual reflection may be stronger in one location than in another, and the resultant error greater.

A three-factor analysis of variance (ANOVA) was used to analyze the data of Table V, and the ANOVA results are presented in Table VI. The factors of the adaptation location (A) and the number of taps (T) in the FIR filter were significant at $p<0.01$, as was the interaction of the adaptation location with the number of taps. The initialization location (I) and the remaining interactions were not significant.

That the adaptation location was significant, but the initialization location was not, indicates that the feedback cancellation performance is controlled by where the user is located within the room and not by the initialization location. It also indicates that the poles computed at any location are valid at any other location within the room. Thus the change in the room reverberation pattern with location within the room has only minimal effects on the computed poles, and the poles can be considered to be independent of reverberation. The reverberation primarily affects the FIR filter coefficients, and the feedback cancellation system will adapt to provide the best model of the overall feedback path that it can at any given location. The reverberation reduces the benefit of the feedback cancellation by increasing the mismatch between the modeled and actual feedback paths, and this mismatch will depend on the location within the room.

The interaction of the adaptation location and the initialization location was not significant. Thus the adapted performance of the feedback cancellation did not depend on the initialization location. This result is another argument that the poles of the feedback path model are essentially the same no matter where the initialization is performed in the room. The poles give a smooth curve fit to the feedback path frequency response, and this smooth curve represents primarily the ear-level feedback path and is independent of location.

The number of taps in the adaptive FIR filter was significant but, as noted above, the difference in going from an 8-tap to a 16-tap filter was relatively small. The interaction of the adaptation location and the number of taps was also significant. Thus the benefit of increasing the FIR filter length depends on the location within the room. The feedback path frequency response can be considered to be a smooth curve representing the hearing aid and ear effects, with superimposed ripples from the reverberation. Increasing the FIR filter length will give a somewhat better model of the smooth curve representing the hearing aid and ear, but is inadequate to model the reverberation ripples. However, the longer filter will change the amplitude and phase of the feedback path model response so that for some locations consistently greater headroom is available than for other locations.

VI. CONCLUSIONS

Room reverberation can affect feedback cancellation in hearing aids, with the strength of the effects depending on

TABLE V. Maximum stable gain (MSG) in dB for the feedback cancellation poles and zeros initialized for one location in the room, the zero coefficients cleared, and the adaptive system then allowed to adapt the zeros to the feedback path measured at a different location.

Adaptive FIR taps	Initial location	Initial MSG (dB)	Adaptive MSG in dB for room location				
			1	3	5	7	Average
8	1	17.1	18.2	17.0	15.3	18.0	17.1
	3	15.7	18.6	17.3	15.7	17.9	17.4
	5	15.3	18.7	18.0	15.9	19.0	17.9
	7	17.4	18.7	17.3	15.7	18.5	17.6
	Average	16.4	18.6	17.4	15.7	18.4	17.5
16	1	20.4	20.2	21.1	18.6	21.8	20.4
	3	20.5	20.0	21.1	18.4	22.6	20.5
	5	18.6	20.3	20.6	18.8	21.1	20.2
	7	19.7	19.5	20.2	18.3	21.2	19.8
	Average	19.8	20.0	20.8	18.5	21.7	20.3

TABLE VI. Three-factor analysis of variance (ANOVA) for the adapted feedback cancellation maximum stable gain (MSG) data of Table V.

Source of variation	Sums of squares	Degrees of freedom	Mean squares	F	Signficance
Adaptation location	37.74	3	12.58	81.87	0.001
Initialization location	0.72	3	0.24	1.57	0.263
$A \times I$	0.20	9	0.02	0.14	0.996
Taps in adapted FIR filter	60.78	1	60.78	395.56	0.001
$A \times T$	4.85	3	1.62	10.52	0.003
$I \times T$	1.79	3	0.60	3.88	0.049
$A \times I \times T$	1.38	9	0.15		
Total	107.45	31			

the acoustical conditions. These effects were studied using a BTE hearing aid mounted on a dummy head and coupled to the ear canal via an open fitting. The feedback path impulse response was measured for eight closely spaced locations in a typical office. The maximum stable gain was estimated without feedback cancellation, for the initial feedback path model filter coefficients, and after adaptation using a simulation of adaptive feedback cancellation processing.

The impulse response measurements show that the feedback path impulse response can be divided into a short-time portion consisting of the ear-level factors of the microphone, receiver, ear canal, vent, and pinna resonances, and into a long-time portion consisting of the room reverberation. The short-time portion of the feedback path response can be accurately represented using an ARMA model consisting of a five-pole IIR filter in series with an 8-tap FIR filter. The ARMA model fits a smooth curve through the feedback path frequency response, minimizing the effects of the room location and reverberation in fitting the poles and zeros. Increasing the length of the FIR filter from 8 to 16 taps improves the model accuracy, but yields only a 3- to 3.5-dB improvement in the estimated available amplifier headroom. Further increasing the FIR filter length to 32 taps yields a benefit only when reverberation is minimal.

The changes in the measured responses with room location indicate that reverberation and not distortion dominates the long-time portion of the feedback path impulse response, and major features of the tail of the impulse response correlate with reflections from surfaces in the room. Because of the length of the reverberation response, it cannot be modeled with a filter short enough to be practical in a wearable hearing aid. The mismatch between the modeled and actual feedback paths limits the headroom increase that can be achieved when using feedback cancellation to approximately 10–15 dB. The actual feedback cancellation performance depends on the room acoustics and location within the room, and will therefore vary as the user moves about.

The feedback cancellation techniques discussed in this article are covered by United States and international patent applications.

ACKNOWLEDGMENTS

The author is grateful to Boaz Rafaely of the Institute of Sound and Vibration Research, University of Southampton and to Johan Hellgren of Linköping University for comments on a draft version of this article. The work reported in this article was supported by GN ReSound.

Bisgaard, N. (**1993**). ''Digital feedback suppression: Clinical experiences with profoundly hearing impaired,'' in *Recent Developments in Hearing Instrument Technology: 15th Danavox Symposium*, edited by J. Beilin and G. R. Jensen (Kolding, Denmark), pp. 370–384.

Borish, J., and Angell, J. B. (**1983**). ''An efficient algorithm for measuring the impulse response using pseudorandom noise,'' J. Audio Eng. Soc. **31**, 478–488.

Bustamante, D. K., Worrell, T. L., and Williamson, M. J. (**1989**). ''Measurement of adaptive suppression of acoustic feedback in hearing aids,'' in Proceedings 1989 International Conference on Acoustics, Speech and Signal Processing, Glasgow, pp. 2017–2020.

Dunn, C., and Hawksford, M. O. (**1993**). ''Distortion immunity of MLS-derived impulse response measurements,'' J. Audio Eng. Soc. **41**, 314–335.

Dyrlund, O., and Bisgaard, N. (**1991**). ''Acoustic feedback margin improvements in hearing instruments using a prototype DFS (digital feedback suppression) system,'' Scand. Audiol. **20**, 49–53.

Dyrlund, O., Henningsen, L. B., Bisgaard, N., and Jensen, J. H. (**1994**). ''Digital feedback suppression (DFS): Characterization of feedback-margin improvements in a DFS hearing instrument,'' Scand. Audiol. **23**, 135–138.

Engebretson, A. M., and French-St. George, M. (**1993**). ''Properties of an adaptive feedback equalization algorithm,'' J. Rehabil. Res. Dev. **30**, 8–16.

Engebretson, A. M., O'Connell, M. P., and Gong, F. (**1990**). ''An adaptive feedback equalization algorithm for the CID digital hearing aid,'' in Proceedings 12th Annual International Conference of the IEEE Engineering in Medicine and Biology Society, Part 5, Philadelphia, PA, pp. 2286–2287.

French-St. George, M., Wood, D. J., and Engebretson, A. M. (**1993**). ''Behavioral assessment of adaptive feedback cancellation in a digital hearing aid,'' J. Rehabil. Res. Dev. **30**, 17–25.

Haneda, Y., Makino, S., and Kaneda, Y. (**1994**). ''Common acoustical pole and zero modeling of room transfer functions,'' IEEE Trans. Speech Audio Process. **2**, 320–328.

Hellgren, J., Lunner, T., and Arlinger, S. (**1999**). ''Variations in the feedback of hearing aids,'' J. Acoust. Soc. Am. **106**, 2821–2833.

Kaelin, A., Lindgren, A., and Wyrsch, S. (**1998**). ''A digital frequency-domain implementation of a very high gain hearing aid with compensation for recruitment of loudness and acoustic echo cancellation,'' Signal Process. **64**, 71–85.

Kates, J. M. (**1988**). ''A computer simulation of hearing aid response and the effects of ear canal size,'' J. Acoust. Soc. Am. **83**, 1952–1963.

Kates, J. M. (**1991**). ''Feedback cancellation in hearing aids: Results from a computer simulation,'' IEEE Trans. Signal Process. **39**, 553–562.

Kates, J. M. (**1999**). ''Constrained adaptation for feedback cancellation in hearing aids,'' J. Acoust. Soc. Am. **106**, 1010–1019.

Kates, J. M. (**2000**). ''Feedback cancellation apparatus and methods,'' U.S. Patent 6,072,884, issued 6 June 2000.

Ljung, L. (**1987**). *System Identification: Theory for the User* (Prentice–Hall, Englewood Cliffs, NJ).

Lybarger, S. F. (**1982**). ''Acoustic feedback control,'' in *The Vanderbilt Hearing-Aid Report*, edited by G. Studebaker and F. Bess, Upper Darby, PA, Monographs in Contemporary Audiology, pp. 87–90.
Maxwell, J. A., and Zurek, P. M. (**1995**). ''Reducing acoustic feedback in hearing aids,'' IEEE Trans. Speech Audio Process. **3**, 304–313.
Press, W. H., Flannery, B. P., Teukolsky, S. A., and Vetterling, W. T. (**1986**). *Numerical Recipes: The Art of Scientific Computing* (Cambridge U.P., New York), pp. 209–213 (Section 7.4: Generation of Random Bits).
Rife, D. D., and Vanderkooy, J. (**1989**). ''Transfer-function measurement with maximum-length sequences,'' J. Audio Eng. Soc. **37**, 419–444.
Schneider, T., and Jamieson, D. G. (**1993**). ''A dual-channel MLS-based test system for hearing-aid characterization,'' J. Audio Eng. Soc. **41**, 583–594.
Schroeder, M. R. (**1979**). ''Integrated-impulse method measuring sound decay without using impulses,'' J. Acoust. Soc. Am. **66**, 497–500.
Vanderkooy, J. (**1994**). ''Aspects of MLS measuring systems,'' J. Audio Eng. Soc. **42**, 219–231.
Widrow, B., McCool, J. M., Larimore, M. G., and Johnson, Jr., C. R. (**1976**). ''Stationary and nonstationary learning characteristics of the LMS adaptive filter,'' Proc. IEEE **64**, 1151–1162.

Recognition of time-distorted sentences by normal-hearing and cochlear-implant listeners

Qian-Jie Fu,[a] John J. Galvin III, and Xiaosong Wang
Department of Auditory Implants and Perception, House Ear Institute, 2100 West Third Street, Los Angeles, California 90057

(Received 16 May 2000; accepted for publication 27 September 2000)

This study evaluated the effects of time compression and expansion on sentence recognition by normal-hearing (NH) listeners and cochlear-implant (CI) recipients of the Nucleus-22 device. Sentence recognition was measured in five CI users using custom 4-channel continuous interleaved sampler (CIS) processors and five NH listeners using either 4-channel or 32-channel noise-band processors. For NH listeners, recognition was largely unaffected by time expansion, regardless of spectral resolution. However, recognition of time-compressed speech varied significantly with spectral resolution. When fine spectral resolution (32 channels) was available, speech recognition was unaffected even when the duration of sentences was shortened to 40% of their original length (equivalent to a mean duration of 40 ms/phoneme). However, a mean duration of 60 ms/phoneme was required to achieve the same level of recognition when only coarse spectral resolution (4 channels) was available. Recognition patterns were highly variable across CI listeners. The best CI listener performed as well as NH subjects listening to corresponding spectral conditions; however, three out of five CI listeners performed significantly poorer in recognizing time-compressed speech. Further investigation revealed that these three poorer-performing CI users also had more difficulty with simple temporal gap-detection tasks. The results indicate that limited spectral resolution reduces the ability to recognize time-compressed speech. Some CI listeners have more difficulty with time-compressed speech, as produced by rapid speakers, because of reduced spectral resolution and deficits in auditory temporal processing.
[DOI: 10.1121/1.1327578]

PACS numbers: 43.71.Ky, 43.66.Ts [CWT]

I. INTRODUCTION

Most normal-hearing listeners, despite a multitude of talkers, dialects, and adverse environmental conditions, easily recognize spoken language because they are provided with highly redundant speech information. While electric stimulation of the auditory nerve with a cochlear implant can partially restore hearing sensation to deaf listeners, speech recognition by CI users can be easily affected by surrounding environmental conditions. One typical adverse listening situation involves background noise. Although new speech processors and processing strategies have resulted in better recognition performance in noise (Arndt *et al.*, 1999), it remains more difficult for CI users to understand speech in noise than NH listeners (Müller-Deiler *et al.*, 1995; Fu *et al.*, 1998). The limited spectral resolution provided by the implant device is thought to be the cause of noise susceptibility among CI users (Fu *et al.*, 1998).

Another commonly encountered listening situation involves some form of temporal waveform distortion. Temporal waveform distortion characterizes reverberant speech, interrupted speech, and rapidly produced speech. Many studies have been conducted to evaluate the effect of speaking rate on speech recognition performance in NH listeners. One approach in evaluating the effect of speaking rate is to simply alter the speed of the speech playback. However, this approach also significantly distorts the speech signal's frequency content. Fairbanks *et al.* (1954) developed an electromechanical device to accelerate recorded speech without introducing the pitch change that would result from simply increasing the speed of the speech playback. Word intelligibility as a function of time compression was measured using this device (Fairbanks and Kodman, 1957). The stimulus materials were 50 phonetically balanced monosyllables with a mean duration of 180 ms per phoneme. The data showed near-perfect recognition when the stimulus words were shortened to 20% of their original duration. When the words were shortened to 10% of their original duration, intelligibility approached 50% correct. Daniloff *et al.* (1968) examined the effects of various degrees of time compression on vowel recognition. They found that time compression did not affect intelligibility appreciably until the phonemes were shortened to 30% of their original duration. Nagafuchi (1976) further investigated the intelligibility of time-distorted speech sounds by normal-hearing children, using 20 monosyllabic words. He found that discrimination was largely unaffected when the words were lengthened to 300% of their original duration. However, recognition began to gradually decrease when the words were shortened to 50% of their original duration and recognition began to rapidly deteriorate when the words were shortened to 25% of their original duration. Wilson *et al.* (1994) examined that effect of time compression on the intelligibility of Northwestern University Auditory Test No. 6. Word recognition scores dropped from 90% to 25% when the compression ratio increased from 45% to 75%. There was a gradual decrease in recognition perfor-

[a]Electronic mail: qfu@hei.org

mance (−1% correct recognition per 1% compression) as the compression ratio increased from 45% to 65%. As the compression ratio increased from 65% to 75%, there was a more rapid decrease in recognition performance (−2.8% correct recognition per 1% compression).

Recently, considerable attention has been paid to the speech recognition deficits experienced by elderly listeners and hearing-impaired listeners presented with time-compressed speech signals. Stuart and Phillips (1998) measured word recognition performance by normal-hearing young adults listeners with and without a simulated hearing loss as a function of time compression ratio. They found that word recognition scores decreased significantly as a function of increased time compression and the simulated hearing loss. There was a significant interaction between time compression ratio and the degree of hearing loss, indicating that loss of audibility alone cannot account for decrements in word recognition performance with time-altered speech. They suggested that both a loss of audibility and a loss in temporal resolution might contribute to the recognition deficits with time-compressed speech for hearing-impaired listeners. Gordon-Salant and Fitzgibbons (1993) examined the effect of time compression on speech recognition in both young and elderly listeners. To reduce the effect of context, they used the low-predictability sentences of the Speech Perception in Noise (SPIN) test. They found no performance differences between younger and elderly adult listeners when sentences were not time distorted. However, age effects were found when the sentences were time compressed at various rates (30% to 60%). The data also suggested that age and hearing impairment contributed independently to deficits in recognizing time-compressed speech.

CI listeners may have particular difficulty processing rapid speech due to the limited spectral resolution. Furthermore, a deficit of auditory temporal processing in CI listeners may also delay or disrupt processing of the acoustic cues available in rapid speech. The purpose of the present study was to investigate the effects of spectral resolution and auditory temporal resolution on the recognition of time-altered speech by normal-hearing and cochlear-implant listeners. Several hypotheses concerning auditory resolution and time-altered speech perception were explored.

The first hypothesis predicted that a loss of spectral resolution would cause listeners to perform more poorly when the speech rate was increased. A noise-band channel vocoder (Shannon *et al.*, 1995) has been used to quantify the effect of reduced spectral information on speech performance. The noise-band channel vocoder is capable of modifying any combination of pitch and spectrum of speech signals because of its independent parametric control of excitation (noise carrier bands), spectrum (amplitude envelope across channels), and pitch (the number of output samples need not be equal to the number of input samples). Sentence recognition was therefore measured in NH listeners using either 32-channel noise-band processors (fine spectral resolution) or 4-channel noise-band processors (coarse spectral resolution) as a function of time manipulation. The effect of spectral resolution was determined by comparing NH listeners' performance between the 32- and 4-channel noise-band processors.

TABLE I. Subject information for five Nucleus-22 CI listeners who participated in the present study. Frequency table refers to the frequency allocation used by the listener in their clinically assigned processor, as defined and numbered by the manufacturer. Frequency table 7 has a frequency range of 120 to 8658 Hz while frequency table 9 has a range of 150 to 10 823 Hz. Insertion depth is reported as the number of stiffening rings outside the round window from the surgical report. A full insertion would be O rings out.

Subject	Age	Gender	Cause of deafness	Duration of use (years)	Insertion depth (rings out)	Frequency table
N3	55	M	Trauma	6	3	7
N4	39	M	Trauma	4	4	9
N7	54	M	Unknown	4	0	9
N9	55	F	Hereditary	7	4	9
N19	68	M	Noise-induced	3	6	7

The second hypothesis predicted that CI listeners could perform as well as NH listeners listening to corresponding spectral conditions. The continuous interleaved sampling (CIS) strategy is a multichannel vocoder-like speech processor that has been used successfully in several implant systems (Wilson *et al.*, 1991). The cochlear implant also provides a straightforward approach in investigating the effect of time manipulation on speech recognition. Because the spectral information of speech signals is mostly conveyed by the locations of the stimulated electrode pairs, time manipulations can be achieved by simply altering each channel's temporal envelope duration. As long as the channel-to-electrode configuration is intact, this manipulation can speed or slow the speech signal without introducing distortions to the spectral content. Sentence recognition was therefore measured in CI listeners fitted with 4-channel CIS speech processors as a function of time manipulation. The sentence recognition performance of CI listeners was compared to that of NH subjects listening to 4-channel noise-band processors.

The third hypothesis predicted that the auditory temporal processing deficit of some CI listeners might also contribute to their difficulty with time-compressed speech. Gap-detection thresholds of CI listeners were therefore measured and then compared to speech recognition measures obtained for all CI subjects in an effort to quantify the relationship between speech recognition performance and auditory temporal processing.

II. METHODS

A. Subjects

Ten subjects (five NH and five CI listeners) participated in this experiment. All NH subjects had thresholds better than 15 dB HL at audiometric test frequencies from 250 to 8000 Hz (ANSI, 1989); all NH listeners were between 25 to 35 years old, except one subject who was 53 years old. The five CI subjects were postlingually deafened adults using the Nucleus-22 device. Table I shows relevant information for these five subjects.

All CI users had at least 3 years experience using the SPEAK speech-processing strategy and all were native speakers of American English. The Nucleus processor with

the SPEAK strategy divides an input acoustic signal into 20 frequency bands, extracts the amplitude envelope from all 20 bands, and then stimulates the electrodes corresponding to the 6 to 10 bands containing the maximal amplitude (Seligman and McDermott, 1995). The frequency allocation table specifies the frequency range covered by the speech processor. Three subjects (N4, N7, and N9) used frequency allocation table 9 (150–10 823 Hz) in their clinically assigned processor, and two subjects (N3 and N19) used table 7 (120 Hz–8658 Hz). All implant subjects had 20 active electrodes available for use.

B. Signal processing

For CI users, the 4-channel CIS speech processors were implemented as follows. The signal was first pre-emphasized (first-order Butterworth high-pass filter with a cutoff frequency of 1200 Hz), then band-pass filtered into four broad frequency bands using eighth-order Butterworth filters. The five corner frequencies (−3 dB down points) of the four bands were: 300, 713, 1509, 3043, and 6000 Hz. The temporal envelope of each band was extracted by half-wave rectification and low-pass filtering (eighth-order Butterworth with a 160-Hz cutoff frequency). For time-distorted speech, the temporal envelope of each band was compressed (shortened) or expanded (lengthened) in time by a linear interpolation method. For example, assume that the ratio between the duration of the manipulated sentence and original sentence is γ (ranging from 0.2 to 2.0) and the total number of samples for original sentence is N. For a given sample location n of the manipulated sentence, the output sample $y(n)$ would be

$$y(n) = x(m) + \alpha[x(m+1) - x(m)]$$
$$0 \leqslant n < N^*\gamma, \quad 0 \leqslant m < N,$$

where m is the integral part of the product n/γ, α is the remainder, and $x(m)$ is the original sample. This linear manipulation effectively shortens or lengthens the duration of the output speech relative to the input speech; speech is therefore sped up or slowed down. Seven time manipulation conditions were created, including four compressed conditions, one undistorted condition, and two expanded conditions. The ratios between the duration of the manipulated sentence and original sentence were 0.3, 0.4, 0.6, 0.8, 1.0, 1.5, and 2.0. The current level (E) of electric stimulation in each band was set to the acoustic envelope value (A) raised to the power of 0.2 (Fu and Shannon, 1998). This transformed amplitude was used to modulate the amplitude of a continuous, 500 pulse/s biphasic pulse train with a 100-μs/phase pulse duration. The pulse trains were simultaneously delivered to the four electrode pairs in an interleaved fashion; the stimulus order of the 4 channels was (3,7), (13,17), (8,12), (18,22) (or 1–3–2–4 for the selected electrode pairs). All signals were presented at comfortably loud levels through a custom implant interface system (Shannon *et al.*, 1990).

For NH listeners, 4- and 32-channel noise-band processors were implemented as follows. Speech signals were band-pass filtered into either 4 or 32 frequency bands using eighth-order Butterworth filters. The corner frequencies (−3 dB down points) of the bands were 300, 713, 1509, 3043, and 6000 Hz for 4-channel noise-band processors and 300, 338, 379, 424, 473, 526, 583, 646, 713, 787, 866, 953, 1046, 1148, 1259, 1379, 1509, 1651, 1804, 1971, 2152, 2348, 2561, 2792, 3043, 3316, 3616, 3933, 4281, 4660, 5070, 5516, and 6000 Hz for 32-channel noise-band processors. The temporal envelope of each band was extracted by half-wave rectification and low-pass filtering at 160 Hz. For time-distorted speech, the temporal envelope of each band was linearly compressed or expanded in time as above. Seven time manipulation conditions were created for the 4-channel processors; the ratios between the duration of the manipulated sentence and original sentence were 0.3, 0.4, 0.6, 0.8, 1.0, 1.5, and 2.0. In addition to these seven time distortion conditions, an extra condition (ratio=0.2) was also created for the 32-channel processors. The time-distorted envelope was used to modulate a wideband noise that was spectrally limited by the same bandpass filters used for signal analysis. The output from each band was then summed and presented to the listeners seated in a sound-treated booth via one loudspeaker (Tannoy Reveal monitors) at 70 dBA.

C. Speech test materials and procedures

Recognition of words in sentences was measured using the Hearing in Noise test (HINT) sentences recorded at the House Ear Institute (Nilsson *et al.*, 1994). The sentences contain, on average, about ten phonemes per second (equivalent to approximately 100 ms per phoneme). For HINT sentence recognition, a list was chosen randomly from among 26 lists, and sentences were chosen randomly, without replacement, from the ten sentences within that list. The subject responded by repeating the sentence as accurately as possible; the experimenter tabulated all correctly identified words. The percent correct was obtained by computing the ratio between the correctly identified words and all words of the ten sentences in each list. Two HINT sentence lists were presented for most conditions (20 sentences per condition). Because there were 15 conditions for NH listeners (thereby necessitating 30 HINT lists when only 26 were available), only one list (ten sentences) was presented for five of the 32-channel conditions (0.6, 0.8, 1.0, 1.5, and 2.0 ratios). These five conditions were extremely easy for all NH listeners, and presenting only one list for each condition ensured that speech materials would not be repeated in the more difficult conditions. The order of the time manipulation conditions and the channel conditions was randomized and counterbalanced across subjects. Two to four lists were presented for each condition for CI listeners because there were only seven time distortion conditions. The order of the time manipulation conditions and test repetitions were also randomized and counterbalanced for CI users.

D. Gap-detection thresholds procedures

A temporal gap-detection task was used to assess the auditory temporal resolution for CI listeners. Temporal gap-detection thresholds for the four stimulated electrode pairs were measured for the five CI listeners. The two markers

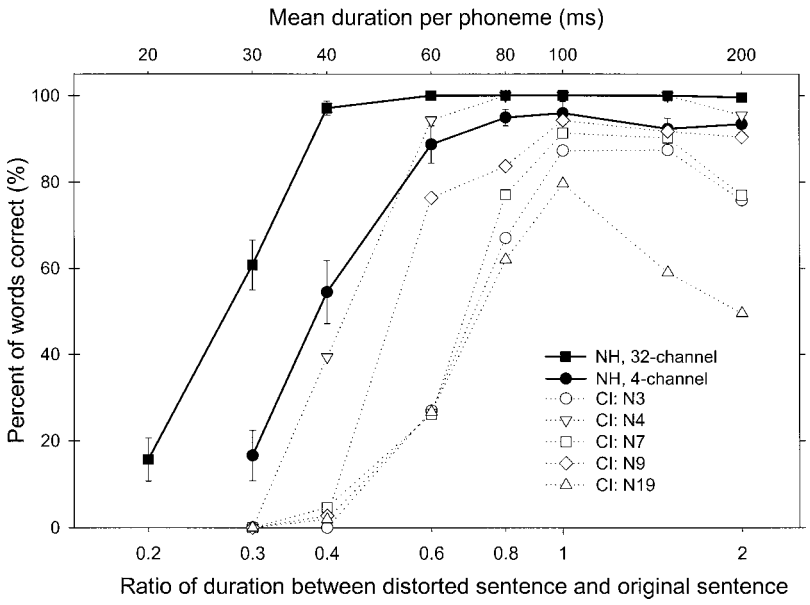

FIG. 1. Recognition scores as a function of time compression and expansion. The bottom *x* axis shows the ratio between the duration of the time-distorted sentence and the duration of the original, undistorted sentence. The top *x* axis shows the mean duration per phoneme in milliseconds for each time distortion condition. The *y* axis shows the percent of words correctly identified. The filled squares show the mean scores from five NH subjects listening to the 32-channel noise-band processor and the filled circles show the mean scores from five NH subjects listening to the 4-channel noise-band processor. The error bars represent one standard deviation. The open symbols show the individual scores from five CI users.

were 100-ms long, 100-μs/phase, 500-pps biphasic pulsatile trains fixed at comfortable level. Gap thresholds were estimated in an adaptive (three-down, one-up) two-interval, two-alternative forced-choice (2AFC) procedure. Each run consisted of 60 trials. The initial step size was generally twice the final step size, and both were set according to the anticipated threshold for each condition. The average of the last 8 out of 12 reversals was computed as the mean gap threshold for each run. The mean and standard deviation of three repetitions were calculated for each data point.

III. RESULTS AND DISCUSSION

Figure 1 shows sentence recognition scores as a function of time compression and expansion for both NH and CI listeners.

The filled squares show the mean scores for NH subjects listening to time-altered speech when fine spectral resolution was available (32-channel noise-band processor). Perfect sentence recognition was observed when sentences were not distorted in time (ratio=1). As sentences were expanded linearly in time, recognition was not affected even at the extreme 2.0 ratio ($p=0.374$; Student's *t* test on arc-sine transformed scores). As sentences were linearly time compressed, recognition was not significantly affected up to the 0.4 time ratio ($p=0.092$). However, further time compression resulted in a rapid deterioration in sentence recognition. In general, the results from the present study are in broad agreement with previous findings (Foulke and Stitcht, 1969; Orr *et al.*, 1965; Vaughan and Letowski, 1997), especially those using similar speech materials (e.g., high-predictability sentences). For example, Orr *et al.* (1965) revealed that listeners could be trained to comprehend speech at a speed of about 30 phonemes per second without temporal order confusions. Time-compressed speech remains partially intelligible even at four times (equivalent to the 0.25 time ratio in the present study) the normal rate (Foulke and Stitcht, 1969). Note that the absolute level of performance for NH listeners may highly depend on the type of speech material, the presentation level, and the method of time compression used (Gordon-Salant and Fitzgibbons, 1993; Wilson *et al.*, 1994; Vaughan and Letowski, 1997). For example, Gordon-Salant and Fitzgibbons (1993) found that recognition scores dropped significantly when the time-compression ratio changed from 30% to 60% (equivalent to 0.7 to 0.4 time ratio in the present study) when the low-predictability sentences of the Revised Speech Perception in Noise test (R-SPIN) (Bilger *et al.*, 1984) were used.

In Fig. 1, the filled circles show the mean scores of NH subjects listening to either time-compressed or-expanded speech when only coarse spectral resolution was available (4-channel noise-band processor). With reduced spectral resolution, over 90% correct recognition was achieved when no time distortion occurred (ratio=1.0), and was not significantly affected at the time-expanded ratio of 2.0 ($p=0.233$). As sentences were time compressed, there was a gradual decrease in performance beginning at the 0.6 time ratio, followed by a rapid deterioration beginning at the 0.4 time ratio. A two-way, repeated-measures analysis of variance (ANOVA) on arc-sine-transformed scores revealed significant effects of time distortion [$F(6,56)=60.51$, $p<0.001$] and spectral resolution [$F(1,56)=119.17$, $p<0.001$], and a significant interaction between time distortion and spectral resolution [$F(6,56)=4.16$, $p=0.002$]. A Student's *t* test on arc-sine-transformed scores also revealed that recognition scores with 4-channel processors were significantly lower that those with 32-channel processors for all time-distortion ratios except the undistorted condition (ratio =1.0). These results support the hypothesis that NH listeners are more susceptible to temporal waveform distortion (e.g., time compression) when the spectral resolution of speech signals is low.

The open symbols in Fig. 1 show individual scores for the five CI subjects. Compared to NH listeners, the recognition patterns of CI users were much more variable. With no time distortion (ratio=1.0), CI users, on average, could correctly recognize about 90% of sentences (about 6% lower than NH subjects listening with the spectrally corresponding

TABLE II. Temporal gap-detection thresholds of the four stimulated electrode pairs from the five CI subjects.

Subject	Electrode (18,22) (ms)	Electrode (13,17) (ms)	Electrode (8,12) (ms)	Electrode (3,8) (ms)	Mean gap threshold (ms)
N3	2.67	2.67	2.56	2.89	2.70
N4	1.11	1.33	0.80	0.81	1.01
N7	2.89	4.67	2.84	2.44	3.21
N9	1.72	1.72	0.79	1.84	1.52
N19	8.84	5.42	3.37	6.84	6.12

4-channel noise-band processor). Four out of five CI users were not significantly affected by the time-expanded 2.0 ratio; however, one subject's (N19) recognition did drop significantly at this level of time expansion. At the time-compressed 0.6 ratio, two out of five CI users (N4 and N9) were not significantly affected; however, the other three CI users (N3, N7, and N19) scored significantly lower at this level of time compression than subjects N4 and N9.

There are significant similarities as well as differences between CI and NH listeners' ability to perceive time-distorted speech. With the same coarse spectral resolution available (4 channel), the best implant user (N4) performed as well as the NH listeners. This suggests a potential commonality between acoustic hearing and electric hearing for recognizing time-altered speech. However, three CI subjects (N3, N7, and N19) performed poorer than subjects N4 and N9 did in recognizing time-distorted speech, especially time-compressed speech. It is unlikely that differences in the subjects' capability to utilize contextual cues could account for this difference because all were native English-speaking listeners. One potential explanation for this difference is that a deficit in auditory temporal processing resolution impedes these subjects' ability to recognize moderately time-compressed speech. To verify this hypothesis, gap-detection thresholds of the four stimulating electrode pairs were measured, and are shown in Table II. The data show that the gap thresholds were quite variable across electrode pairs as well as subjects, ranging from 0.8 to 8.8 ms. This high variability of temporal resolution among CI users is consistent with previous observations (Busby and Clark, 1998). Subject N4, who performed best in recognizing time-compressed speech, also performed best in detecting temporal gaps (1.01 ms). Similarly, the subjects who performed poorer in recognizing time-compressed speech (e.g., N3, N7, and N19) also performed relatively poorer in detecting temporal gaps. These results suggest that some CI users are more susceptible to time-compressed speech due to the limited spectral resolution and a deficit in temporal resolution.

One issue worth mentioning involves the potential effect of subjects' ages. A few studies have reported diminished recognition performance of temporally distorted speech signals by elderly listeners. For example, Konkle *et al.* (1977) demonstrated that recognition of time-compressed speech deteriorated with increasing age among subjects aged 54 to 84 years old. Gordon-Salant and Fitzgibbons (1993) also reported age effects (aged 20–40 years for young listeners and aged 65–76 years for elderly listeners) when the sentences were time compressed at various rates (30% to 60%). In the present study, four out of five NH subjects were 25 to 35 years old; one NH subject was 53 years old. No significant performance difference was observed among the NH listeners. The five CI users ages ranged from 39 to 68 years old. Subject N4 (39 years old), the best performer, was considerably younger than the other CI users. Conversely, subject N19 (68 years old), who was considerably older than the others, performed worst. It is possible that age-related factors, e.g., a slowing of the auditory temporal processing that could result in a poor temporal gap-detection threshold, may contribute to poor recognition of time-compressed speech by elderly subjects.

IV. SUMMARY AND CONCLUSIONS

The results of the present study imply that NH listeners can perform well in recognizing time-compressed speech at rates of about 40 ms/phoneme when the fine spectral resolution of speech is available. However, this ability to recognize time-compressed speech deteriorates with reduced spectral resolution. The best CI user exhibited recognition patterns similar to NH subjects listening to corresponding spectral conditions, indicating that a common mechanism between acoustic and electric hearing might be involved in the pattern recognition of time-distorted speech. A deficit in temporal processing may further reduce the ability to recognize time-compressed speech for some CI listeners, further increasing their difficulty in understanding rapid-rate conversational speech.

ACKNOWLEDGMENTS

We appreciate the efforts of all subjects, especially the cochlear implant users. We are grateful to Bob Shannon, Sandra Gordon-Salant, Chistopher Turner, and an anonymous reviewer for useful suggestions on an earlier draft of this paper. This research was supported by Grant No. R03-DC-03861 and Contract No. N01-DC-92100 from the National Institute of Deaf and Communication Disorders (NIDCD).

ANSI (**1989**). ANSI S3.6-1989, ''Specification for audiometers'' (American National Standards Institute, New York).

Arndt, P. L., Staller, S. J., and Skinner, M. W. (**2000**). ''Advanced encoder conversion study performance versus preference,'' Cochlear Corporation Symposium, Miami Beach, Florida, February 2000.

Bilger, R. C., Nuetel, J. M., Rabinowitz, W. M., and Rzeczkowski, C. (**1984**). ''Standardization of a test of speech perception in noise,'' J. Speech Hear. Res. **27**, 32–48.

Busby, P. A., and Clark, G. M. (**1998**). ''Gap detection by early-deafened cochlear implant subjects,'' J. Acoust. Soc. Am. **105**, 1841–1852.

Daniloff, R. G., Shrinder, T. H., and Zemlin, W. R. (**1968**). ''Intelligibility of vowels altered in duration and frequency,'' J. Acoust. Soc. Am. **44**, 700–707.

Fairbanks, G., Everitt, W. L., and Jaeger, R. (**1954**). ''Method for time or frequency compression-expansion of speech,'' Trans. IREPGA **AU2**, 7–11.

Fairbanks, G., and Kodman, Jr., F. (**1957**). ''Word intelligibility as a function of time compression,'' J. Acoust. Soc. Am. **29**, 636–641.

Foulke, E., and Sticht, T. G. (**1969**). ''Review of research on the intelligibility and comprehension of accelerated speech,'' Psychol. Bull. **72**, 50–62.

Fu, Q.-J., and Shannon, R. V. (**1998**). ''Effects of amplitude nonlinearity on speech recognition by cochlear implant users and normal-hearing listeners,'' J. Acoust. Soc. Am. **104**, 2571–2577.
Fu, Q.-J., Shannon, R. V., and Wang, X. (**1998**). ''Effects of noise and spectral resolution on vowel and consonant recognition: Acoustic and electric hearing,'' J. Acoust. Soc. Am. **104**, 3586–3596.
Gordon-Salant, S., and Fitzgibbons, P. J. (**1993**). ''Temporal factors and speech recognition performance in young and elderly listeners,'' J. Speech Hear. Res. **36**, 1276–1285.
Konkle, D., Beasley, D., and Bess, F. (**1977**). ''Intelligibility of time-altered speech in relation to chronological aging,'' J. Speech Hear. Res. **20**, 108–115.
Müller-Deiler, J., Schmidt, B. J., and Rudert, H. (**1995**). ''Effects of noise on speech discrimination in cochlear implant patients,'' Ann. Otol. Rhinol. Laryngol. **166**, 303–306.
Nagafuchi, M. (**1976**). ''Intelligibility of distorted speech sounds shifted in frequency and time in normal children,'' Audiology **15**, 326–337.
Nilsson, M., Soli, S. D., and Sullivan, J. A. (**1994**). ''Development of the Hearing in Noise Test for the measurement of speech reception thresholds in quiet and in noise,'' J. Acoust. Soc. Am. **95**, 1085–1099.
Orr, D. B., Friedman, H. L., and Williams, J. C. (**1965**). ''Trainability of listening comprehension of speeded discourse,'' J. Educ. Psychol. **56**, 148–156.
Seligman, P. M., and McDermott, H. J. (**1995**). ''Architecture of the Spectra-22 speech processor,'' Ann. Otol. Rhinol. Laryngol. **104**, Suppl. 166, 139–141.
Shannon, R. V., Adams, D. D., Ferrel, R. L., Palumbo, R. L., and Grantgenett, M. (**1990**). ''A computer interface for psychophysical and speech research with the Nucleus cochlear implant,'' J. Acoust. Soc. Am. **87**, 905–907.
Shannon, R. V., Zeng, F.-G., Kamath, V., Wygonski, J., and Ekelid, M. (**1995**). ''Speech recognition with primarily temporal cues,'' Science **270**, 303–304.
Stuart, A., and Phillips, D. P. (**1998**). ''Recognition of temporally distorted words by listeners with and without a simulated hearing loss,'' J. Am. Acad. Audiol. **9**, 199–208.
Vaughan, N. E., and Letowski, T. (**1997**). ''Effects of age, speech rate, and type of test on temporal auditory processing,'' J. Speech Lang Hear Res. **40**, 1192–1200.
Wilson, B. S., Finley, C. C., Lawson, D. T., Wolford, R. D., Eddington, D. K., and Rabinowitz, W. M. (**1991**). ''New levels of speech recognition with cochlear implants,'' Nature (London) **352**, 236–238.
Wilson, R. H., Preece, J. P., Slamon, D. L., Sperry, J. L., and Borstein, S. P. (**1994**). ''Effects of time compression and time compression plus reverberation on the intelligibility of Northwestern University Auditory Test No. 6,'' J. Am. Acad. Audiol **5**, 269–277.

Phonetically trained models for speaker recognition

Leandro Rodríguez-Liñares[a] and Carmen García-Mateo[b]
Departamento de Tecnoloxías das Comunicacións, E.T.S.E. Telecomunicación, Universidade de Vigo, 36200 Vigo, Spain

(Received 1 November 1999; revised 19 June 2000; accepted 22 September 2000)

In this paper, a speaker recognition system that introduces acoustic information into a Gaussian mixture model (GMM)-based recognizer is presented. This is achieved by using a phonetic classifier during the training phase. The experimental results show that, while maintaining the recognition rate, the decrease in the computational load is between 65% and 80% depending on the number of mixtures of the models. © *2001 Acoustical Society of America.* [DOI: 10.1121/1.1331679]

PACS numbers: 43.72.Pf [DOS]

I. INTRODUCTION

Automatic speaker recognition deals with identification of the person who utters a sentence. Two modes of operation are usually envisaged: speaker identification and speaker verification. Speaker identification is concerned with the selection of one speaker within a set of enrolled members, while speaker verification is concerned with the validation of the claimed identity of a person. Nowadays, speaker verification applications are more viable than speaker identification ones. In both cases, a recognition test can be accomplished either in a text-dependent or text-independent way. In a text-dependent system, the training and testing speech are constrained to be the same word or phrase, while in a text-independent system this restriction no longer exists.

Over the last years, several algorithms and techniques have been proposed to cope with this problem. Among them, vector quantization (VQ) and continuous hidden Markov models (HMMs) are the techniques most extensively investigated so far (Matsui and Furui, 1994). It is well known that the performance of the HMM-based systems relies on the total number of Gaussian mixtures of the model and not so much on how many states are used. Thus, single-state multiple-Gaussian mixture observation density HMMs called GMMs are one of the preferred algorithms for this task (Reynolds, 1995a, 1995b).

In Auckenthaler *et al.* (1999) and Rose and Reynolds (1990), it is stated that the discrimination among speakers provided by GMMs is in fact due to an implicit classification in broad phonetic classes. This fact can be exploited in the design of GMM-based systems for speaker recognition purposes. The introduction of some kind of explicit phonetic classification should have a positive effect on the performance of the systems. We will show that this is true specifically from the computational point of view.

Using *a priori* knowledge sources is a common strategy in speech processing systems. In the literature, many approaches for using phonetic information in the development of speech technology can be found. In speech coding, various forms of speech segmentation have been used in the past. For example, in the classical LPC vocoder (US Federal Standard, 1984), each speech frame is classified as either voiced or unvoiced, while other schemes use a more complex set of phonetic classes. In Wang (1991) and Wang and Gersho (1992) three wide, phonetically distinct categories (voiced, unvoiced, and onsets) are proposed based on acoustic and phonetic features. In García-Mateo *et al.* (1990) we used a very similar classification approach in a code excited linear prediction (CELP) coding scheme.

Regarding speaker recognition, many approaches that exploit some sort of acoustic class-dependent representation have been used. In Matsui and Furui (1991) an HMM-based binary classifier (voiced/unvoiced) is used prior to a VQ-based system, both in training and testing phase. A different strategy is presented in Auckenthaler *et al.* (1999), where phoneme likelihoods are obtained using 30 speaker-independent phoneme models. These likelihoods are weighted by a previously trained speaker dependent multilayer perceptron (MLP). In Rose and Reynolds (1990), the training data are segmented into 50 predefined acoustic–phonetic classes and these labeled observations are used to initialize the Gaussian components of an initial GMM model for expectation maximization (EM) training (Demspter *et al.*, 1977). In Savic and Gupta (1990), five-states speaker-dependent HMMs are used. In the training phase, the LPC vectors are classified by spectral analysis into five broad phonetic categories (nasal, voiced 1, voiced 2, plosive, and fricative) and the frames belonging to each class are used to train a state of the HMM. In the testing phase, Viterbi decoding is used to assign each frame to a phonetic category and a verification score is obtained for each class. In these papers, no significant improvement in recognition accuracy is achieved compared to a standard GMM-based system.

We decided to use phonetic classification in three broad phonetic categories (Wang, 1991; Wang and Gersho, 1992; García-Mateo *et al.*, 1990) in the training phase of a GMM-based speaker recognition system with the aim of reducing the computational load. The experience gained with the work presented in García-Mateo *et al.* (1990) led us to decide to use the very same approach, because it obtains a good compromise between using explicit phonetic information and training material requirements. We show that introducing phonetic information into the training procedure can main-

[a]Electronic mail: leandro@gts.tsc.uvigo.es
[b]Electronic mail: carmen@gts.tsc.uvigo.es

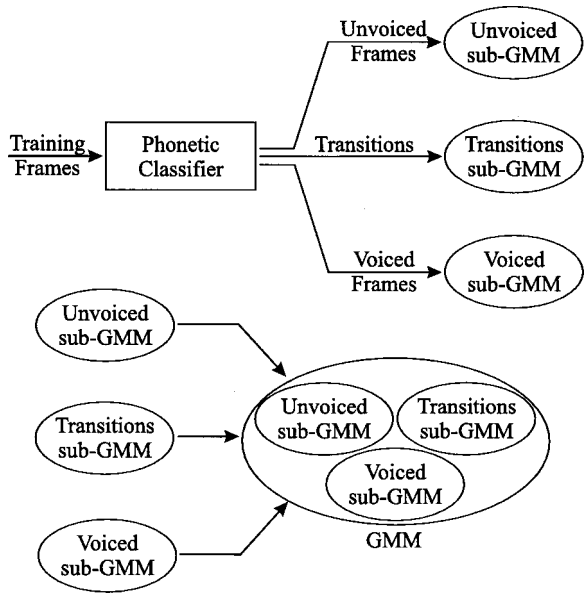

FIG. 1. PT-GMMs training procedure: The system configuration consists of GMMs obtained by combining three sub-GMMs per speaker: voiced, unvoiced, and transitions.

tain the overall performance while reducing the computational load dramatically.

The rest of the paper is organized as follows. The next section describes in depth the architecture with phonetic information. The used experimental framework is studied in Sec. III, while Sec. IV presents the obtained results. Some conclusions and comments are given at the end of the paper.

II. SYSTEM DESCRIPTION

The system configuration consists of GMMs obtained by combining three sub-GMMs per speaker. The training procedure is shown in Fig. 1 and it is performed in two stages.

(1) First, training frames are *a priori* segmented into four categories: silence and three distinct broad ''phonetic'' classes having in mind two aspects:

(i) The need of a robust speech segmentation algorithm: the more classes are considered, the less robust the algorithms are;
(ii) To get a suitable compromise between classification complexity and data requirements.

The classifier uses an algorithm similar to the one described in Tucker (1992). It considers three distinct sound classes.

(i) Voiced sounds, which have quasiperiodic waveforms and fairly harmonic spectra;
(ii) Unvoiced frames, which have aperiodic waveforms and irregular spectra;
(iii) Transitions, defined as the two first voiced frames after an unvoiced segment and the two last voiced frames before an unvoiced segment. This type of frame is characterized by a nonstationary waveform.

(2) A submodel is trained for each ''phonetic'' class. The sub-GMMs are trained using the EM (Dempster *et al.*, 1977) algorithm after a *k*-means (Linde *et al.*, 1980) initialization. Variances are tied across the mixtures due to the scarcity of training data. These models are trained in parallel, being fed by their corresponding type of frames. The three sub-GMMs are combined afterwards into a GMM called phonetically trained Gaussian mixture model or PT-GMM. This training scheme can be observed in Fig. 1. The goal of this procedure is to perform a guided training to obtain GMMs where the third part of the mixtures corresponds to each of the phonetic categories. For example, in a 48-mixture PT-GMM, 16 mixtures will correspond to voiced frames, 16 to unvoiced frames, and the rest to the transitions. In Reynolds (1995b) it is stated that there is no theoretical way to estimate *a priori* the optimal number of mixtures in a GMM-based system, but with 30 and 60 s of training speech there is no improvement over 32 mixtures. If a maximum of 32 mixtures is going to be used for each phonetic category, a total of $32\times 3=96$ mixtures will be used in the largest PT-GMMs. Then, we decided to train PT-GMM models with a number of mixtures ranging from 3 (the minimum required value) to 96 (the maximum suitable value). With this procedure, the computational load is reduced when compared to the training of GMM models (see Sec. IV).

For each test utterance O, alignment is performed using the target speaker model λ_s. In the case of speaker verification experiments, an antimodel $\lambda_{c(s)}$ is also used for score normalization purposes (Reynolds, 1995a). The verification decision is based on the score

$$\Lambda(O)=\log P(O/\lambda_s)-\log P(O/\lambda_{c(s)}).$$

The choice of antimodels for the normalized score can significantly affect the verification performance. In our experiments, we used six (three close and three far) maximally spread cohort models per speaker are obtained as described in Reynolds (1995a). The selection procedure for the cohort models is the same for the GMMs and the PT-GMMs.

Next, we describe the experiments we have carried out in order to assess the performance and computational load of the PT-models approach. We also compare it with the state-of-the-art GMM approach.

III. EXPERIMENTAL FRAMEWORK

All the experiments were conducted using our database called ''TelVoice'' (Rodríguez-Liñares and García-Mateo, 1998). It has been designed for speaker recognition purposes, and it consists of speech recorded by 46 Spanish speakers (32 men and 14 women), with six sessions each, recorded over a period ranging from 1 month to a year and a half. Time interval between sessions may vary from one speaker to another, but is never less than 3 days. It consists of telephone speech sampled at 8 kHz. The session dialogue has been carefully designed to get as much meaningful material as possible. There are ten items varying from isolated digits, strings of digits, connected digits, common phrases, and free speech. Out of TelVoice we selected the following material for carrying out these experiments:

TABLE I. Comparison of the identification error and the training time of GMMs and PT-GMMs.

	GMMs		PT-GMMs	
Number of mixtures	Training time	% Ident. error	Training time	% Ident. error
6	10.2	26.63	2.1 (−79.4%)	30.58 (+14.83%)
12	24.8	24.59	6.6 (−73.4%)	24.73 (+5.69%)
24	64.8	19.70	19.5 (−70.0%)	21.88 (+11.07%)
48	118.4	17.80	40.2 (−66.0%)	16.98 (−4.61%)
96	226.7	18.34	76.2 (−66.4%)	16.85 (−8.29%)

(1) For model training, we used data from the first and second sessions. In each session we selected:

(i) A utterance containing the digits from 0 to 9 (12 seconds);

(ii) Two fixed sentences (7 s each).
This provided us with a total of 52 s of speech (before removing silence frames) for training purposes.

(2) For testing, we used from each session four pronunciations of the Spanish identity card number, made of eight digits (5 s for each pronunciation, before removing silence frames) from sessions 3 to 6. The speakers were addressed to pronounce it naturally (digit by digit, grouping digits, or as a whole, as they usually do).

The voice was high-pass filtered with cutoff frequency of 200 Hz. The filtering was performed off-line. Liftering (Juang *et al.*, 1987) was also performed using a factor of 22. Twelve mel-cepstra coefficients and their corresponding Δ-mel-cepstra coefficients were computed using a frame length of 20 ms and a frame shift of 10 ms. Normalized log energy and its first derivative were appended up to a total of 26 coefficients per vector.

IV. EXPERIMENTAL RESULTS

It is well-known that the computational load of the EM algorithm grows exponentially with the number of mixtures. Therefore, our PT-GMM approach should show a faster training behavior than the GMM approach. In the PT-GMM, three EM passes are conducted. However, each of them has one-third of the total number of mixtures and a lesser quantity of training frames. In order to estimate the computational load of the training procedure, we observed the CPU-consumed time on a Unix Sun Sparc Station. Table I summarizes the results for the different configurations. The computational load for PT-GMM approach is much lower than for the classical GMM: the relative reduction of the computational load is approximately 70% in any configuration. This is an important issue for practical implementations.

The performance was evaluated for two text-independent tasks: speaker identification and speaker verification.

A. Speaker identification

For speaker identification experiments, every single test file is compared with all the speaker models. It yields a total of

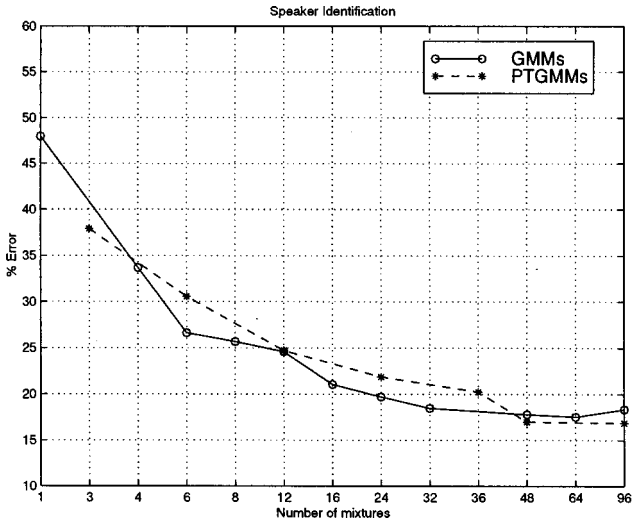

FIG. 2. GMMs vs PT-GMMs:identification error: The performance of both systems is quite similar, since both share a classification ability. The implicit classification property of the GMMs is made explicit in the PT-GMMs.

46 speakers×4 sessions/speaker×4 test files/session

=736 tests.

Figure 2 shows the identification error for the speaker identification task. As was expected, the performance of both systems is quite similar, since both share a classification ability. The implicit classification property of the GMMs is made explicit in the PT-GMMs. The main contribution of our scheme is that this *a priori* phonetic classification helps to reduce the computational load dramatically.

B. Speaker verification

For the speaker verification experiment, we need to select data for the impostor ''attacks.'' The strategy followed is explained next. Twelve utterances drawn from sessions 3, 4, and 5 of Speaker I were compared with I's model. The decoding of the data provided a set of true or ''customer'' scores. The total number of customer tests obtained was

4 sessions/speaker×4 test files/session=16 tests/speaker.

One verification utterance from session 6 of each speaker other than I was decoded using I's model to provide a set of false speaker or ''impostor'' scores. Those speakers that contribute to the target cohort model are excluded from the impostor population. It can be argued that this strategy excludes ''good'' impostors from the testing process. There are two possible solutions for this problem. The first consists of including the cohort speakers in the attacking scenario. Our experiments showed that this method is not a fair test, since these speakers are easily identified as impostors due to their similarity with the cohort models. The second solution consists of splitting the database into two sets of speakers and choosing the cohorts from one set and the impostors from the other set. In our case, we considered that the size of TelVoice was not large enough to prevent the loss of statistical significance this method would imply. Besides, this problem is palliated by the procedure used to select cohort models. We use maximally spread cohorts (Reynolds,

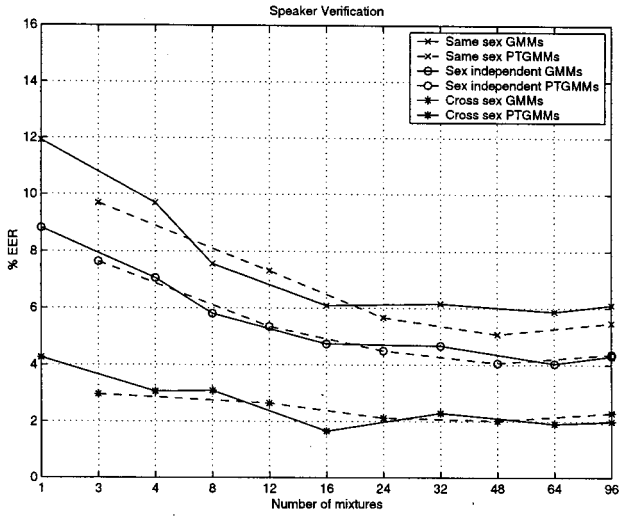

FIG. 3. GMMs vs PT-GMMs: equal error rate: PT-models perform close to the models without phonetic training. Both systems show similar robustness against attacks from speakers of the same or the opposite sex.

1995a), so cohort models are not concentrated in the vicinity of the speaker model.

In summary, for the verification, each speaker is used as a claimant, with the remaining speakers (excluding the claimant's cohort speakers) acting as impostors, and rotating through all speakers. The number of impostor tests was therefore

$$39 \text{ impostors/speaker} \times 2 \text{ test files/impostor} = 78 \text{ tests/speaker}.$$

There are 46 speakers in TelVoice. Then, the total numbers of customer and impostor tests were 736 and 3588, respectively.

Results are reported using the average equal-error rate (EER) per speaker obtained with a procedure similar to the one proposed by the COST250 to perform experiments with PolyCost (Melin and Lindberg, 1996).

(1) Three ROC (receiver operating characteristic) curves were calculated per speaker:

(i) Impostors were speakers with the opposite sex of the target speaker;
(ii) Impostors had the same sex of the target speaker;
(iii) Impostors could be either females or males.

(2) The points on the ROC curves where the false acceptance error is equal to the false rejection error are the EER points. There will be three EERs per speaker depending on the sex of the attacking impostors.

(3) The global EERs are calculated as the average of the EERs obtained for each speaker of TelVoice.

Figure 3 shows the results considering this attacking scenario.

Again, we observe that PT models perform close to the models without phonetic training under any circumstance. That is, the recognition performance remains constant in both approaches. Both systems show similar robustness against attacks from speakers of the same or the opposite sex.

TABLE II. Comparison of the identification error and the average number of millions of floating point operations needed for training one VQ and one PT-VQ.

	VQs		PT-VQs	
Number of centroids	No. of ops.	% Ident. error	No. of ops.	% Ident. error
6	0.55	29.45	0.10 (−81.7%)	41.03 (+39.32%)
12	1.27	22.42	0.23 (−82.0%)	28.13 (+25.47%)
24	2.10	19.97	0.50 (−75.1%)	23.23 (+16.32%)
48	3.53	15.49	0.91 (−74.1%)	21.38 (+38.02%)
96	5.36	16.03	1.58 (−70.5%)	16.71 (+4.24%)

The same approach can be applied to other algorithms. In Rodríguez-Liñares (1999) the possibility of using phonetic training in a VQ-based system is studied in depth. In this scheme, a VQ is trained for each phonetic class using the *k*-means algorithm (Linde *et al.*, 1980) and the three sub-VQs thus obtained are combined into a VQ called PT-VQ. The behavior of this system can be observed in the results included in Table II for the speaker identification task. Two differences between Table I and Table II deserve explanation.

(i) In Table I, the first column is the number of mixtures of the GMMs and the PT-GMMs, while in Table II this is changed to the number of centroids of the VQs and the PT-VQs.
(ii) In VQs and PT-VQs, the computational load can be approximately calculated as the number of floating point operations needed for the training process (Rodríguez-Liñares, 1999) instead of using the training time.

Although the computational load of the training phase decreases in a similar amount (70%–80%) in the PT-GMMs and the PT-VQs, the performance of the PT-VQs is sensibly lower than the case where standard VQs are used. A similar decrease in performance was shown in the speaker verification task.

The reason for this behavior can be the way a VQ models the vector space. A GMM models a complex distribution. In this case, the classification of the training frames will help the training of the GMM in the sense that mixtures of each sub-GMM will model areas with a high density of training vectors. A VQ models areas around its centroids. The phonetic classification shouldn't affect the final result of the training phase. However, there can be errors in the phonetic classification so that the frontiers among classes are not so neatly defined. While GMMs will absorb these errors, VQs will move centroids to these incorrect frames with the result that the performance of the training phase will be worse.

V. CONCLUSIONS

In this study, a novel topology that makes use of explicit phonetic information in the training phase of a speaker rec-

ognition system was introduced. We have used three broad phonetic classes (''voiced,'' ''unvoiced,'' and ''transitions'') based on a speech coding scheme. The models thus obtained were combined in a phonetically trained model (PT-GMM). The performance of the PT-model approach is similar to the performance of the model obtained without using the phonetic information.

The main advantage of our approach is the important reduction in the training load. This factor can be of importance in the design and implementation of real-world recognition systems where the training time for new enrolled customers can be an important issue. It can be argued that more complex classification schemes could have been used. However, with three phonetic classes problems of undertraining have been avoided and a good compromise between performance and computational load has been achieved.

The PT-GMM training technique is going to be implemented in the speaker authentication module of TelCorreo (Rodríguez-Liñares and García-Mateo, 2000), an e-mail client that allows Internet users to read their e-mail using speech through the telephone.

ACKNOWLEDGMENTS

This work has been supported by Spanish CICYT, Project Ref. No. TIC96-0964-C04-02.

Auckenthaler, R., Parris, E. S., and Carey, M. J. (**1999**). ''Improving a GMM Speaker Verification System by Phonetic Weighting,'' Proc. IEEE Int. Conf. Acoust., Speech, Signal Process. **1**, 313–316.

Dempster, A. P., Laird, N. M., and Rubin, D. B. (**1977**). ''Maximum Likelihood from Incomplete Data via the EM Algorithm,'' J. R. Stat. Soc. Ser. **39**, 1–38.

García-Mateo, C., Casajús, F. J., and Hernández-Gómez, L. (**1990**). ''Multi-Band Vector Excitation Coding of Speech at 4.8 Kbps,'' Proc. IEEE Int. Conf. Acoust., Speech, Signal Process. **1**, 13–16.

Juang, B. H., Rabiner, L. R., and Wilpon, J. G. (**1987**). ''On the Use of Bandpass Liftering in Speech Recognition,'' IEEE Trans. Acoust., Speech, Signal Process. **35**, 947–953.

Linde, Y., Buzo, A., and Gray, R. M. (**1980**). ''An Algorithm for Vector Quantization,'' IEEE Trans. Commun. **28**, 84–95.

Matsui, T., and Furui, S. (**1991**). ''A Text-Independent Speaker Recognition Method Robust against Utterance Variations,'' Proc. IEEE Int. Conf. Acoust., Speech, Signal Process. **1**, 377–380.

Matsui, T., and Furui, S. (**1994**). ''Comparison of Text-Independent Speaker Recognition Methods using VQ-Distortion and Discrete/Continuous HMMs,'' IEEE Trans. Speech Audio Process. **2**, 456–459.

Melin, H., and Lindberg, T. (**1996**). ''Guidelines for Experiments on the PolyCost Database,'' Proceedings of the COST250 Workshop on the Application of Speaker Recognition Technologies in Telephony, Vigo, Spain, pp. 59–69. http://circwww.epfl.ch/polycost/baseline.htm

Reynolds, D. A. (**1995a**). ''Speaker Identification and Verification using Gaussian Mixture Speaker Models,'' Speech Commun. **17**, 91–108.

Reynolds, D. A. (**1995b**). ''Robust Text-Independent Speaker Identification using Gaussian Mixture Speaker Models,'' IEEE Trans. Speech Audio Process. **3**, 72–83.

Rodríguez-Liñares, L., and García-Mateo, C. (**1998**). ''A Novel Technique for the Combination of Utterance and Speaker Verification Systems in a Text-Dependent Speaker Verification Task,'' Proceedings of the International Conference on Spoken Language Processing (ICSLP) **2**, 213–216.

Rodríguez-Liñares, L. (**1999**). ''Estudio y Mejora de Sistemas de Reconocimiento de Locutores mediante el Uso de Información Verbal y Acústica en un Nuevo Marco Experimental,'' Ph.D. thesis, ETSE de Telecomunicación, Universidade de Vigo, Spain. http://www.gts.tsc.uvigo.es/~leandro/archivos/Tesis.ps.gz

Rodríguez-Liñares, L., and García-Mateo, C. (**2000**). ''TelCorreo: A Bilingual E-mail Client over the Telephone,'' in *Lecture Notes in Artificial Intelligence* (Springer, Berlin), Vol. 1902, pp. 381–386.

Rose, R. C., and Reynolds, D. A. (**1990**). ''Text Independent Speaker Identification Using Automatic Acoustic Segmentation,'' Proc. IEEE Int. Conf. Acoust., Speech, Signal Process. **1**, 293–296.

Savic, M., and Gupta, S. K. (**1990**). ''Variable Parameter Speaker Verification System Based on Hidden Markov Modeling,'' Proc. IEEE Int. Conf. Acoust., Speech, Signal Process. **1**, 281–284.

Tucker, R. (**1992**). ''Voice Activity Detection using a Periodicity Measure,'' IEE Proceedings—I **139**, 377–380.

US Federal Standard 1015 (**1984**). Analog to Digital Conversion of Voice by 2400 bit/second Linear Predictive Coding.

Wang, S. (**1991**). ''Low Bit-Rate Vector Excitation Coding of Phonetically Classified Speech,'' Ph.D. thesis, University of California, Santa Barbara.

Wang, S., and Gersho, S. (**1992**). ''Improved Phonetically Segmented Vector Excitation Coding at 3.4 Kb/s,'' Proc. IEEE Intern. Conf. Acoust., Speech, Signal Process. (ICASSP) **1**, 349–352.

A linear relation between the compressibility and density of blood

S. H. Wang
CardioResearch, Inc., Charlottesville, Virginia 22903 and Department of Biomedical Engineering, Chung Yuan Christian University, Chung Li, 32023, Taiwan

L. P. Lee
CardioResearch, Inc., Charlottesville, Virginia 22903

J. S. Lee[a)]
Department of Biomedical Engineering, University of Virginia, Charlottesville, Virginia 22908

(Received 13 March 2000; accepted for publication 18 October 2000)

By considering the blood as a mixture of ultrafiltrate and protein concentrate, the additive nature of compressibility and density from the components is utilized to deduce a linear relation between the compressibility and density for blood. This deduction also indicates that the intercept and slope of the linear relation are independent of the hematocrit, plasma protein concentration, and hemoglobin concentration of red blood cells. To verify experimentally this linear relation, saline and plasma dilutions on porcine or canine blood flowing in an extracorporeal circuit were carried out. The hematocrit of the experiments ranges from 0% to 55% and the plasma protein concentration ranges from 10 to 90 g/l. A resonance device in the circuit measured the density ρ_b of blood at 37 °C and an ultrasound system measured the sound velocity c_b. The range of density is from 1010 to 1060 g/l and that of sound velocity is from 1530 to 1580 m/s. The linear relation that best fits the data of compressibility [computed as $(\rho_b c_b^2)^{-1}$] and density has a correlation coefficient of 0.9978. The linear relation is found to fit well the dependence of compressibility on density derived from the sound velocity data of human, horse, and porcine blood in the literature. © *2001 Acoustical Society of America.* [DOI: 10.1121/1.1333419]

PACS numbers: 43.80.Cs, 43.80.Ev, 43.80.Jz [FD]

I. INTRODUCTION

Blood is a mixture of red blood cells (RBCs) and plasma. As a result, the density or compressibility of blood is the sum of that of its components weighted by their volume fraction. This additive nature of the compressibility and density of blood shows that they are linearly related to hematocrit.[1] In applying to mixtures of the same RBCs and plasma, Urick deduced further that the compressibility is linearly related to the density.[1] He organized his measurements on blood diluted by plasma to verify that the relation between compressibility and density is indeed linear over a wide range of hematocrit. Many studies have shown a linear or nonlinear dependence of the sound velocity or compressibility of blood on its hematocrit, total protein concentration (TPC), plasma protein concentration (PPC), mean cellular hemoglobin concentration (MCHC), or density.[1–6] The question of whether the same linear relation as derived by Urick can characterize the dependence of compressibility on density for blood over a wide range of hematocrit, PPC, and MCHC remains to be determined. Our first objective is to answer this question by examining the dependence of compressibility on density for blood of different RBCs and PPCs. We also examine whether published data support the linear dependence.

In these studies,[1–6] the hematocrit and TPC were not measured online with the sound velocity. The methods to measure hematocrit or TPC have lesser resolution capability than a density measuring system (DMS) constructed from a resonance device (DMA 602W, Parr, Inc., Graz, Austria). Our second objective is to use a highly sensitive DMS and an ultrasound system to measure accurately and simultaneously the density and sound velocity of blood with the aim of establishing a more precise relationship between the density and compressibility of blood.

A saline bolus infused into the jugular vein will produce a minute transient density (or sound velocity) reduction in the aortic blood. Because the density change is proportional to the change in TPC,[7] one can therefore apply the concept of protein conservation for saline infusion (the absence of protein from that of plasma) to determine from the transient density reduction the cardiac output.[6–10] Density measurements are also shown useful for the assessment of blood volume and the amount of blood volume pooled to the microcirculation.[11–13] Severe microvascular pooling or hypovolemia can lead to poor cardiac filling, hypotension, and shock. The design of the ultrasound system may make it more suitable for patient use than the DMS, which is difficult for sterilization. Our third objective is to examine whether the ultrasound system has the resolution required to assess density changes for the quantification of these cardiovascular parameters.

a)Electronic mail: JL@virginia.edu

II. THEORY

Let H be the hematocrit of blood, ρ_{pl} be the density of plasma, ρ_r be that of RBC, κ_{pl} be the compressibility of plasma, and κ_r be that of RBC. The additive nature of blood density ρ_b and compressibility κ_b from the plasma and RBC components leads to these relations:[1]

$$\rho_b = H\rho_r + (1-H)\rho_{\mathrm{pl}}, \tag{1}$$

$$\kappa_b = H\kappa_r + (1-H)\kappa_{\mathrm{pl}}. \tag{2}$$

The elimination of the variable H yields this relation:

$$\kappa_b = a + b\rho_b, \tag{3}$$

where $a=(\rho_r\kappa_{\mathrm{pl}}-\rho_{\mathrm{pl}}\kappa_r)/(\rho_r-\rho_{\mathrm{pl}})$ and $b=(\kappa_r-\kappa_{\mathrm{pl}})/(\rho_r-\rho_{\mathrm{pl}})$. κ_{pl} and ρ_{pl} are functions of PPC and κ_r and ρ_r are functions of MCHC. Instead of concluding a and b to be variables of PPC and MCHC, they are shown later to be constants.

The plasma is a mixture of ultrafiltrate and protein concentrate, which is mostly albumin and γ-globulin, while the RBC is a mixture of the same ultrafiltrate but with hemoglobin as the protein. Suppose we can regard these proteins as having the same density ρ_{prot}. Let the density of the ultrafiltrate be ρ_u, and the volume fraction of protein concentrate in plasma be P_{pl}, and that of RBCs be P_r. The additive nature of the density of the mixture from its components yields these equations:

$$\rho_r = \rho_u(1-P_r) + \rho_{\mathrm{prot}}P_r, \tag{4}$$

$$\rho_{\mathrm{pl}} = \rho_u(1-P_{\mathrm{pl}}) + \rho_{\mathrm{prot}}P_{\mathrm{pl}}. \tag{5}$$

Since $\rho_{\mathrm{prot}}P_{\mathrm{pl}}$ is PPC, $\rho_{\mathrm{prot}}P_r$ is MCHC, and TPC is $(1-\mathrm{H})\mathrm{PPC}+\mathrm{H}\times\mathrm{MCHC}$, the substitution of Eqs. (4) and (5) into Eq. (1) yields the following linear relation between the blood density and TPC:

$$\rho_b = a_1 + b_1\,\mathrm{TPC}, \tag{6}$$

where a_1 is ρ_u and b_1 is $(1-\rho_u/\rho_{\mathrm{prot}})$. The measurements obtained for plasma, blood, and RBC concentrates verify that their densities are linearly related to their TPC,[7] justifying the consideration of plasma and RBCs as a mixture of ultrafiltrate and protein concentrate and the use of a constant density for either protein concentrate or ultrafiltrate.

The application of this mixture consideration to the compressibility of blood leads us to deduce the following linear relation:

$$\kappa_b = a_2 + b_2\,\mathrm{TPC}, \tag{7}$$

where a_2 is κ_u (the compressibility of ultrafiltrate) and b_2 is $(\kappa_{\mathrm{prot}}-\kappa_u)/\rho_{\mathrm{prot}}$, where κ_{prot} is the compressibility of protein concentrate. Because κ_u and κ_{prot} are the intrinsic characteristics of ultrafiltrate and protein concentrate, we see that Eq. (7) for a given temperature would have a_2 and b_2 as constants. Shung *et al.* had shown that the compressibility of RBCs is linearly related to its MCHC.[5] This finding serves as a partial justification of Eq. (7).

The elimination of TPC from Eqs. (6) and (7) allows us to obtain Eq. (3) with the constant a now expressed as $a_2-a_1b_2/b_1$ and the constant b expressed as b_2/b_1. These two new expressions for a and b indicate that they are independent of MCHC or PPC. This theoretical conclusion is tested here with porcine and canine blood over a wide range of hematocrit, TPC, and PPC.

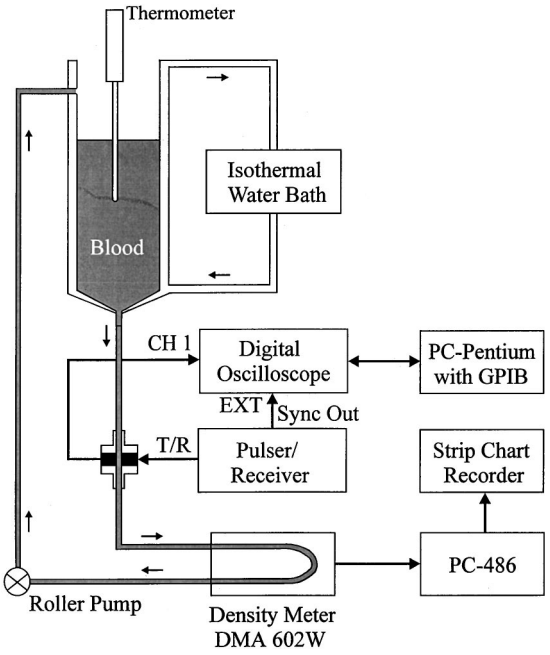

FIG. 1. The extracorporeal circuit and setup to measure the sound velocity and density of blood.

III. EXPERIMENTAL SYSTEMS AND PROTOCOLS

A. Setup

The experimental arrangement for blood dilution and the measurement of compressibility and density are shown in Fig. 1. Most of the 75 ml of blood was in a glass reservoir. The blood temperature was maintained at 37 °C by the circulation of isothermal water through the outer jacket of the reservoir. The blood first flowed through a circular Plexiglas tubing mounted with two ultrasound transducers (2 mm in inner diameter), then to the U-tube of a density meter (DMA 602W), and finally back to the reservoir via a roller pump (Cole Parmer).

The U-tube is a hollow glass tube bent to the form of U and has its two tips fixed on a heavy basis. The U-tube is excited through a solenoid and feedback system to vibrate like a cantilever beam at its resonance frequency. The fact that resonance is related to the spring constant of the U-tube and its mass (which contains the blood) forms the basis for the DMS to determine the period of resonance and then the density via a calibration protocol with fluids of known density. The density reading of blood flowing inside the U-tube is reported at a rate of five samples per second. The resolution of the DMS has been found as 0.03 g/l.[9]

The through-transmission technique was used for sound velocity measurements.[6,14] The two near identical transducers had their active surfaces in alignment with the inner surface of the Plexiglas tubing. Let L be the distance between the two active surfaces. The impulse generated by a Panametrics Pulser 5072PR at 100 Hz excited one transducer to emit a short pulse of ultrasound with a central frequency of

16 MHz. Then a digital oscilloscope (LeCroy 9350AL) acquired the signal from the receiving transducer. The signal digitized at 1 GHz was transferred to a computer with a GPIB board for the determination of T_{peak}, the time from the leading edge of the square wave generated by the pulser to the peak of the received ultrasound. With the time from the leading edge to the peak of emitting ultrasound as T_0, we calculated the sound velocity c as

$$c = L/(T_{\text{peak}} - T_0). \tag{8}$$

To assess the values of L and T_0 with the system at the preset temperature and under a flowing condition, we first obtained the average of the peak time of 20 pulses when the circuit was flowing with 37 °C distilled water. Then the average peak time for isotonic saline was similarly determined. With the sound velocity of water as 1467.9 m/s and that of isotonic saline c_s as 1521.1 m/s,[15] we employed Eq. (8) to solve for L and T_0. Afterward, we applied Eq. (8) to calculate from the average peak time of blood T_b the sound velocity of blood c_b.

Together with the blood density ρ_b measured by DMS, we calculated the blood compressibility κ_b from the following equation:

$$\kappa_b = 1/(\rho_b c_b^2). \tag{9}$$

Blood has viscosity, which can introduce an error in estimating the compressibility from Eq. (9). An analysis done by Shung *et al.* indicates the error would be smaller than 0.1% for a hematocrit of 15%, and 0.3% for a hematocrit of 45%.[5]

B. Dilution and measurement protocols

Fresh porcine blood was collected by the personnel of a slaughterhouse to a container. Acid citrate dextrose (ACD) solution (formula A) was mixed as an anticoagulant with the blood at the ratio of about 0.15 ml/ml of blood. Canine blood was exsanguinated from the carotid artery of an anesthetized dog to which we had carried out a number of blood volume measurements. Then ACD was added to the blood. The experimental protocol and exsanguination procedure for dogs have been approved by the Animal Care and Use Committee of the University of Virginia and are in conformation to NIH guidelines. Dilution experiments were carried out within the next day by first collecting plasma and RBC concentrate from the blood sediment. Then five 75-ml batches of blood were prepared to have a hematocrit of about 55%, 45%, 35%, 25%, and 15%. Each batch was placed into the reservoir for circulation to carry out the dilution measurement. After the equilibration to 37 °C as indicated by a stable blood density reading and a thermometer, the initial blood density and transit time of the ultrasound were recorded. Then a 2- to 4-ml plasma sample was pipetted into the blood reservoir. Reaching a steady state in about 1 min, the blood density and the transit time were recorded. The dilution was continued for six to eight more measurements. Then the same dilution sequence was applied to the next batch of blood. The measurement sequences with saline dilution were repeated with the five batches of blood.

Before each dilution sequence, 2 ml of blood was withdrawn for the measurement of the initial hematocrit, TPC, and PPC. The hematocrit was taken as the average of three hematocrit readings (the fraction height of the RBC column corrected by 97% to account for trapped plasma) obtained by the microcentrifugation method. TPC was the hematocrit-weighted sum of PPC, measured by the Biuret method, and MCHC, measured by Drabkin's method.[16] For each dilution, the hematocrit reduction was about 0.5%. Because this is comparable to the resolution of the microcentrifugation method to measure hematocrit, we elected, instead, to calculate the new hematocrit after each dilution from the previous hematocrit by utilizing the principle of mass conservation. Similar calculations were also made with the TPC.

The density and sound velocity of plasma were measured by filling the circuit with plasma. The plasma densities of canine and porcine blood were 1010.1 and 1023.3 g/l, respectively. Using the measured hematocrit, plasma, and blood density, we projected from Eq. (1) the density of canine RBCs as 1081.1 g/l and that of porcine RBCs as 1087.4 g/l. The RBC concentrate of human blood has a density in the range of 1084.6 to 1091.5 g/l and a MCHC of 325 to 353 g/l.[7]

IV. RESULTS

The relations between the density and hematocrit of canine blood for five plasma dilution sequences and five saline ones are shown in Fig. 2(a). For the same hematocrit decrease in each sequence, the density decrease due to saline dilution is more pronounced than that due to plasma dilution, reflecting the fact that the saline dilution also reduces the density of plasma. As shown in Fig. 2(b), the decrease in sound velocity due to saline dilution is also larger than that due to plasma dilution. The results of porcine blood, presented in Fig. 3, show a density decrease for plasma and saline dilution more pronounced than that of canine blood. This difference results from the fact that the density difference between the porcine plasma and saline is about 2.3 times that of the canine one. This difference in PPC also makes the sound velocity of porcine plasma larger than that of canine plasma, leading to a more pronounced decrease in sound velocity of porcine blood [Fig. 3(a)] than that of canine blood [Fig. 2(a)] for the dilution experiments.

The sound velocity and the calculated compressibility of canine blood are plotted against the density in Figs. 4(a) and 4(b), respectively. As shown, the different relations found for the sound velocity and hematocrit in Figs. 2 and 3 are now integrated into one relation between the sound velocity and density.

The compressibility data of canine and porcine blood are summarily presented in Fig. 5. A linear relation in Eq. (3) with a as $137.9\times10^{-12}\,\text{cm}^2/\text{dyn}$ and b as $-0.0948\times10^{-12}\,\text{cm}^2/\text{dyn}/(\text{g/l})$ is depicted as the solid line in the figure. The correlation coefficient of the fit is 0.9978. Setting B as $-b\rho_u/\kappa_u$ and recognizing κ_u as $a+b\rho_u$, we can convert Eq. (3) to the following form:

$$(\kappa_b - \kappa_u)/\kappa_u = -B(\rho_b - \rho_u)/\rho_u. \tag{10}$$

With 1000.28 g/l being the density ρ_u of ultrafiltrate at 37 °C which is identical to the density of isotonic saline, we deduce

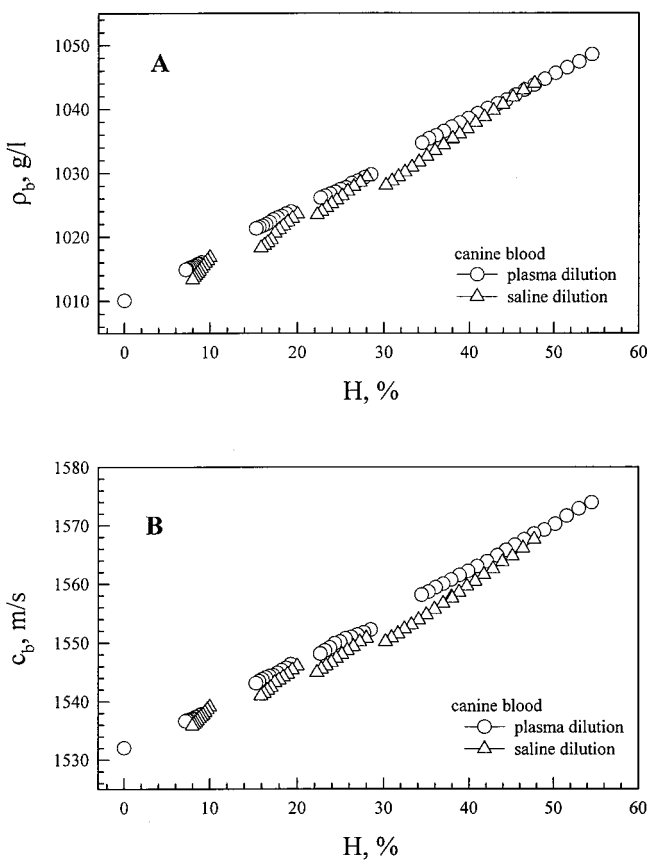

FIG. 2. (a) The dependence of the density of canine blood on its hematocrit. The data from five sequences of dilution experiments by plasma all fall into one line. Each sequence of saline dilution started from the same blood used in the plasma dilution sequence. The starting points coincide with the plasma ones. Because saline density is lower than plasma density, we see more reduction in blood density than that of plasma dilution. (b) The dependence of the sound velocity of canine blood on its hematocrit for the same five sequences of dilution experiments.

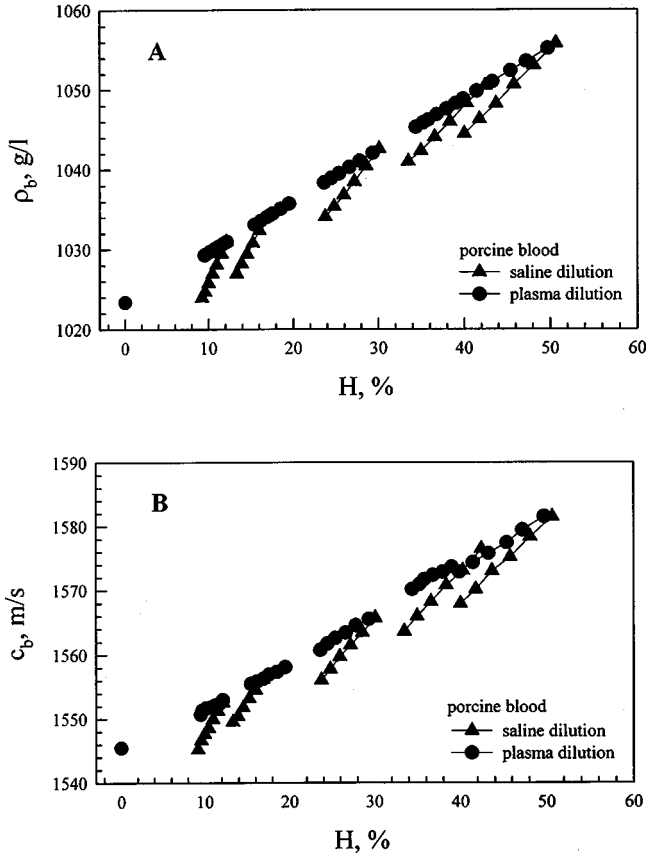

FIG. 3. (a) The dependence of the porcine blood density on the hematocrit for five sequences of dilution experiments with plasma or saline. (b) The dependence of the sound velocity of blood on its hematocrit for the same dilution experiments.

from the values of a and b that B is 2.2 and κ_u is 43.1 $\times 10^{-12}$ cm^2/dyn.

Since c_u^2 is $1/(\rho_u \kappa_u)$, Eqs. (9) and (10) can be merged to this quadratic equation between the sound velocity and density:

$$1-(c_u/c_b)^2=(B-1)(\rho_b/\rho_u-1)+B(\rho_b/\rho_u-1)^2. \tag{11}$$

The solid curve in Fig. 4(a) is Eq. (11) calculated with the previously given values of B, c_u, and ρ_u. Its fit with the data has a correlation coefficient of 0.9991. This quadratic equation allows one to convert the sound velocity measurement of blood to a reading in blood density.

The linear fit between the density and TPC of canine and porcine blood at 37 °C has a slope of 0.264 (b_1 in Eq. 6) and a correlation coefficient of 0.9994. Hinghofer *et al.* reported that the slope is 0.257($R=0.9996$) for human blood at 37 °C.[7] Since b_1 is also $1-\rho_u/\rho_{\text{prot}}$, we obtain the density of protein concentrate at 37 °C as 1359.08 g/l. The expressions we have for b_2 and b yield this identity: $b_1 b=(\kappa_{\text{prot}}-\kappa_u)/\rho_{\text{prot}}$. From the values of b_1, b, and ρ_{prot} quantified here, we deduce the compressibility of protein concentrate κ_{prot} as 9.09×10^{-12} cm^2/dyn.

Fourteen dilutions, each with the addition of 0.5 ml plasma to the blood circulating in the extracorporeal circuit, were performed in accordance to the protocol used by Gamas and Lee to assess the resolution of the DMS.[9] The data on the compressibility and density are presented in Fig. 6 and were used to determine the best linear fit and the standard deviation. As done previously, we take the value of the latter, when expressed in the unit of density, as the resolution of the ultrasound system, which is 0.06 g/l. The small total density change (3 g/l) for this dilution protocol was deliberately chosen to match the minute density change encountered in the dilution experiments to measure cardiac output. Thus we could regard the resolution as the relative error of the measuring system to assess cardiovascular parameters.

V. DISCUSSIONS

Compressibility, sound velocity, and density characterize the bulk properties of the blood. By treating the protein concentrate of RBC and plasma as one having the same density, the TPC can now be regarded as a bulk property of blood. On the other hand, the PPC and MCHC of blood are in general different, disallowing the hematocrit to be regarded as a bulk property of blood. Our results indicate that the bulk properties of blood, compressibility, sound velocity, TPC, and density of blood, have a one-to-one relation with each other. Five of these relations for blood at 37 °C are listed below for easy reference:

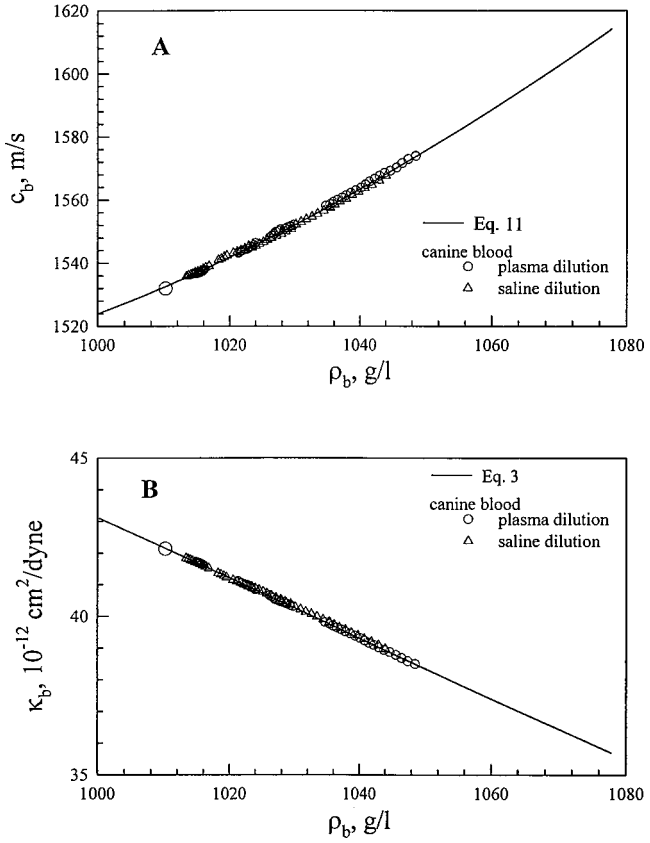

FIG. 4. (a) The dependence of the sound velocity on the density of canine blood for the data given in Fig. 2. The solid curve is calculated from Eq. (11) with the constants given in the text. The correlation coefficient of the fit with the data is 0.999. (b) The dependence of the compressibility on the density of blood. The solid line is the linear relation in Eq. (3). The correlation coefficient is 0.999.

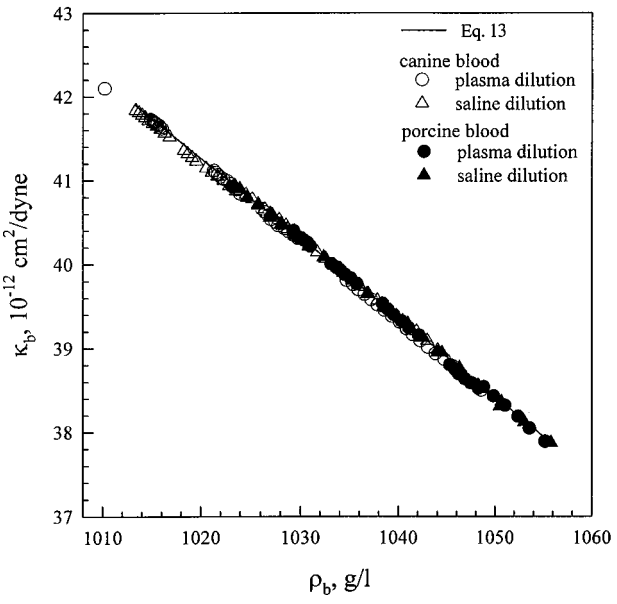

FIG. 5. The relation between the compressibility and density of porcine and canine blood. The solid line is Eq. (13) and has a correlation coefficient of 0.9978.

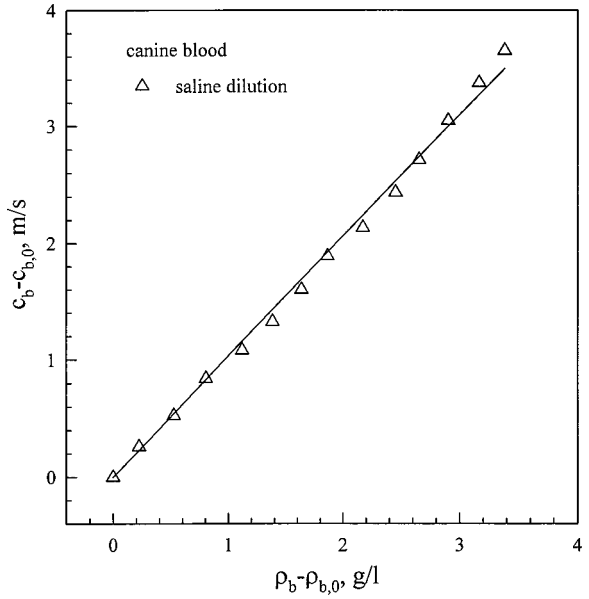

FIG. 6. The change in blood compressibility following a sequence of 0.5-ml plasma infusion into the extracorporeal circuit. The resolution of the ultrasound system to assess blood density, taken as the standard deviation of the best linear fit in the unit of density, is 0.06 g/l.

$$\rho_b = \rho_u + 0.264 \quad \text{TPC}, \tag{12}$$

$$\kappa_b = \kappa_u[1 - 2.2(\rho_b/\rho_u - 1)] \tag{13}$$

$$= \kappa_u(1 - 0.581 \ \ \text{TPC}/\rho_u), \tag{14}$$

$$1 - (c_u/c_b)^2 = 1.2(\rho_b/\rho_u - 1) + 2.2(\rho_b/\rho_u - 1)^2 \tag{15}$$

$$= 0.545(1 - \kappa_b/\kappa_u) + 0.455(1 - \kappa_b/\kappa_u)^2, \tag{16}$$

where ρ_u is 1000.28 g/l, κ_u is 43.1×10^{-12} cm^2/dyn, and c_u is 1523 m/s. The protein concentrate has ρ_{prot} as 1359.08 g/l and κ_{prot} as 9.08×10^{-12} cm^2/dyn.

The measurements obtained by Urick on various dilutions of blood by plasma indicate that the sound velocity has a one-to-one relation with the density.[1] By adding RBC concentrate to the blood (having the same plasma and RBC), Schneditz *et al.* established a single relation between the sound velocity and TPC.[6] Because these two studies imposed no change in PPC and MCHC, the scope of a valid one-to-one relation might be limited. By expanding their protocol to include saline dilutions and to use two species, we show that Eqs. (12)–(16) are valid over a wide spectrum of PPCs and two values of MCHC.

The plasma protein concentration used in the experiment ranges from 10 to 90 g/l and the hematocrit from 0% to 55%. On the other hand, the span of density change for these ranges is about 4 g/l or 4% of the mean density. The sound velocity predicted by the nonlinear fit [Eq. (11)] deviates from that predicted by the best linear fit by at most 1.1 m/s, or 2% of the span of sound velocity change. On the other hand, the nonlinearity can have significant effect on the computation of the slope. For example, the slope computed from Eq. (11) at a density of 1010 g/l is about 74% of that at a density of 1060 g/l. The data of sound velocity and TPC in g% obtained by Schneditz *et al.* are reproduced in Fig. 7(a).[6]

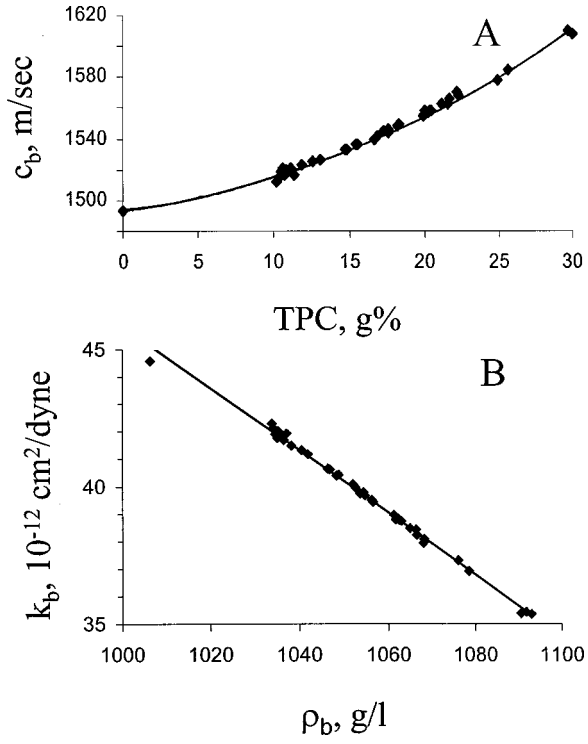

FIG. 7. (a) The dependence of sound velocity on TPC in the unit of g% obtained by Schneditz *et al.* on porcine blood at 20 °C (Ref. 6). The solid line is a second-order polynomial fit. (b) The dependence of compressibility on density computed from the data above. The solid line is the best linear fit: $\kappa_b = 159.1\times10^{-12}$ cm^2/dyn -0.1132×10^{-12} cm^2/dyn/(g/l)ρ_b.

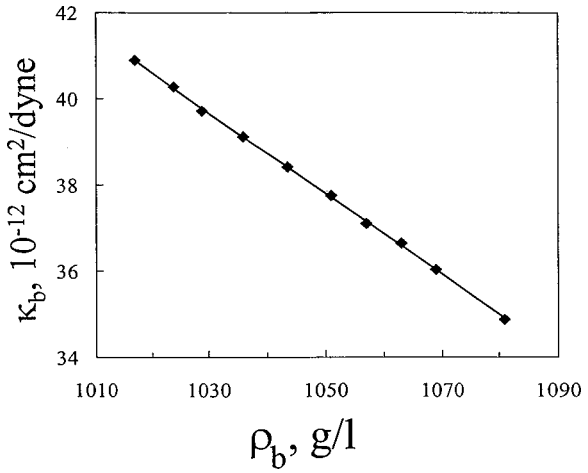

FIG. 8. The relation between the compressibility and density of horse blood obtained from a plasma dilution protocol. The solid line is the best linear fit: $\kappa_b = 135.9\times10^{-12}$ cm^2/dyn -0.0934×10^{-12} cm^2/dyn/(g/l)ρ_b. Results are calculated from the graphed data of Urick (Ref. 1).

The deviation between the linear and second-order polynomial fit (the solid line) over the range of density covered is at most 9 m/s in sound velocity or 14% of the span of sound velocity. However, the nonlinearity now projects that the slope at a TPC of 4 g% (comparable to the low density of 1010 g/l) is about 44% of that at 24 g% (comparable to the high density of 1060 g/l).

When the ultrasound system is used to assess cardiac output, the sound velocity change produced in the blood by saline dilution needs to be converted to the change in blood density. This conversion requires precise knowledge of this slope $(dc_b/d\rho_b)$. This is the reason we place considerable effort in making accurate measurements and in establishing the best fit for the conversion of sound velocity change to density change.

The microcentrifugation method has a resolution of about 0.5% in the determination of hematocrit. This level of resolution is difficult to refine because of a lack of a distinct, flat interface between the RBCs and the plasma column. The Biuret method is reported to have a resolution of 0.6 g/l on the measurement of PPC. To determine the relation between the compressibility and hematocrit (or TPC) covered in Figs. 2–5, 7, and 8 these resolutions are sufficient. The transient change in hematocrit, encountered in the protocol to assess cardiac output, is at most 1%. The corresponding change in TPC is 3 g/l, and in density 1 g/l.[11–13] The microcentrifugation and Biuret method may therefore have insufficient resolution to assess cardiac output. In contrast, the DMS can do so at ease because of a resolution of 0.03 g/l and the ability to continuously measure blood density through an extracorporeal circuit. The density resolution of the ultrasound system is 0.06 g/l, which may still be sufficient to accurately assess cardiac output.

From the results of horse blood obtained by Urick,[1] we computed the compressibility and plotted it against the density in Fig. 8. Depicted in the figure is the following linear fit:

$$\kappa_b = 42.5\times10^{-12}\ \text{cm}^2/\text{dyn}[1-2.2(\rho_b/\rho_u-1)], \qquad (17)$$

where ρ_u is taken as 1000.28 g/l. The correlation coefficient of the fit is 0.9998. The results of Schneditz *et al.* on porcine blood at 20 °C have the sound velocity plotted against the TPC in the unit of g% [Fig. 7(a)].[16] To convert their data to our format for comparison, we employed Eq. (12) to determine from the reported TPC the TPC with the unit g/l and then the density. Finally, the computation of the compressibility yields the data shown in Fig. 7(b). In contrast to the nonlinear dependence depicted in Fig. 7(a), the data on compressibility and density has a good linear fit of which the correlation coefficient is 0.9978. We estimated from Table II of the study of Schneditz *et al.*[6] that the temperature increases the value of slope b by $0.000\,97\times10^{-12}$ cm^2/dyn/(g/l) per °C and decreases the value of the intercept at the ultrafiltrate density by 0.15×10^{-12} cm^2/dyn per °C. Using these adjustments, we extrapolate from the best fit of the 20 °C data in Fig. 7(b) to the following relation for blood at 37 °C:

$$\kappa_b = 42.6\times10^{-12}\text{cm}^2/\text{dyn}[1-2.27(\rho_b/\rho_u-1)]. \qquad (18)$$

We note Eqs. (17) and (18) are quite similar to the dependence specified by Eq. (13).

Bradley and Sacerio measured the dependence of sound velocity on PPC in a 37 °C experiment for which the PPC was varied while the hematocrit was maintained at 40%.[2] They reported that the slope of the linear dependence, $dc_b/d\text{PPC}$, is 1.69 m/s(g/100 ml). Since the plasma occupies 60% of the blood volume, the change in total protein concentration of blood dTPC is 60% of dPPC. From Eq. (6), we see that $d\rho_b$ is b_1dTPC. Using the value of b_1 found in this

study (0.264), we find that the value of $dc_b/d\rho_b$ for their data is $1.067\ \text{m/s/(g/l)}[=0.169\ \text{m/s/(g/l)}\div(0.6\times0.264)]$. This value matches well with the slope 1.09 m/s/(g/l) estimated from our data at a hematocrit of 40%.

From the plasma dilution results of Figs. 2 and 3, we find that the slope dc_b/dH for the canine blood is 0.774 m/s/% and the slope for porcine blood is 0.701 m/s/%. The difference in these two slopes is simply the result of the porcine plasma protein concentration being higher than the canine one. Experiments with plasma dilution for human blood at 37 °C have been carried out by Bradley and Sacerio[2] and Bakke *et al.*[3] The former reported 0.59 m/s/% as the slope dc_b/dH, and the latter 0.98 m/s/% as the slope. The PPC and MCHC of blood employed by these groups may be different, a likely reason making the values reported for dc_b/dH different.

The compressibility of human RBC at 23 °C and in isotonic saline was assessed by Shung *et al.* as $34.8\times10^{-12}\ \text{cm}^2/\text{dyne}$.[5] The MCHC is 32.1 g%. We find this compressibility value differs by no more than 3% from that extrapolated to RBC concentrate from the results of Urick,[1] Schneditz *et al.*,[6] and ours. The volume fraction of hemoglobin in RBCs is about 25%.[17] Using the values of κ_u and κ_{prot} reported earlier, we deduce the compressibility of RBCs as $34.6\times10^{-12}\ \text{cm}^2/\text{dyn}[=(43.1\times0.75+9.08\times0.25)\times10^{-12}\text{cm}^2/\text{dyn}]$. This compressibility is consistent with the results listed here.

By increasing the osmolarity of the suspending medium to change the MCHC of RBCs, Shung *et al.* determined that the compressibility is linearly related to the MCHC with the slope as $-0.225\times10^{-12}\ \text{cm}^2/\text{dyn/(g\%)}$. Using similar protocol to change the MCHC, Weiser and Apfel reported the slope of the linear relation fitting the data of the compressibility and MCHC is $-0.4\times10^{-12}\ \text{cm}^2/\text{dyn/(g\%)}$.[4] By converting MCHC from the unit of g% to that of g/l and then to the density as done previously on the data of Schneditz *et al.*, we find that the best fit of the data of Shung *et al.* on the compressibility and density has the slope b as $-0.0674\times10^{-12}\ \text{cm}^2/\text{dyn/(g/l)}$. Assuming the same proportionality on the slope conversion, the slope of Weiser and Apfel's linear fit has the value $-0.15\times10^{-12}\ \text{cm}^2/\text{dyn/(g/l)}$. The reason leading to the large difference in b from our isotonic study $-0.0948\times10^{-12}\ \text{cm}^2/\text{dyn/(g/l)}$ is not clear. A lower pH would cause the cells to swell, changing the value of MCHC. The compressibility of the suspending medium (the ultrafiltrate) is lower for hypertonic saline, which forms a major fraction of the compressibility of RBC concentrate. The experimental difference in pH, osmolarity, and temperature may be the contributing factors to the variation in b.

VI. CONCLUSION

The consideration of blood as a mixture of ultrafiltrate and protein concentrate leads us to deduce that the compressibility of blood is linearly related to the blood density. This linear relation is supported by the experimental results ofcanine and porcine blood reported here and the measurements of horse, porcine, and human blood given in the literature. These theoretical and experimental results also indicate that the bulk properties of blood (compressibility, sound velocity, density, and total protein concentration) possess a one-to-one relation with each other.

ACKNOWLEDGMENT

This research was supported by HL 57136 of the National Heart, Lung, and Blood Institute.

[1] R. J. Urick, ''A sound velocity method for determining the compressibility of finely divided substances,'' J. Appl. Phys. **18**, 983–987 (1947).
[2] E. L. Bradley and J. Sacerio, ''The velocity of ultrasound in human blood under varying physiologic parameters,'' J. Surg. Res. **12**, 290–297 (1972).
[3] T. Bakke, T. Gytre, A. Haagensen, and L. Giezendanner, ''Ultrasonic measurement of sound velocity in whole blood,'' Scand. J. Clin. Lab. Invest. **35**, 473–478 (1975).
[4] M. A. Weiser and R. E. Apfel, ''Extension of acoustic levitation to include the study of micron size particles in a more compressible host liquid,'' J. Acoust. Soc. Am. **71**, 1261–1268 (1982).
[5] K. K. Shung, B. A. Krisko, and J. O. Ballard III, ''Acoustic measurement of erythrocyte compressibility,'' J. Acoust. Soc. Am. **72**, 1364–1367 (1982).
[6] D. Schneditz, T. Kenner, H. Heimel, and H. Stabinger, ''A sound-speed sensor for the measurement of total protein concentration in disposable, blood-perfused tubes,'' J. Acoust. Soc. Am. **86**, 2073–2080 (1989).
[7] H. Hinghofer-Szalkay, H. Leopold, T. Kenner, and H. Holzer, ''On the coefficient of thermal expansion of blood and its constituents,'' Biomed. Tech. **25**, 151–157 (1980).
[8] T. Kenner, H. Leopold, and H. Hinghofer-Szalkay, ''The continuous high-precision measurement of the density of flowing blood,'' Pfluegers Arch. **370**, 25–29 (1977).
[9] L. Gamas, and J. S. Lee, ''A density indicator method to measure pulmonary blood flow,'' J. Appl. Physiol. **60**, 327–334 (1985).
[10] L. Krivistki, ''Novel method to measure assess flow during hemodialysis by ultrasound velocity dilution technique,'' ASAIO J. **41**, M749–M753 (1995).
[11] J. S. Lee and L. P. Lee, ''A Density method for determining plasma and red blood cell volume,'' Ann. Biomed. Eng. **20**, 195–204 (1992).
[12] J. S. Lee, ''Microvascular volume change induced by exercise, heat exposure, and endotoxin injection,'' Am. J. Physiol. **267**, H1142–H1150 (1994).
[13] J. S. Lee, ''1998 Distinguished Lecture: Biomechanics of the microcirculation, an integrative and therapeutic perspective,'' Ann. Biomed. Eng. **28**, 1–14 (2000).
[14] E. L. Madsen, J. A. Zagzebski, and G. R. Frank, ''Oil-in-gelatin dispersions for use as ultrasonically tissue-mimicking materials,'' Ultrasound Med. Biol. **8**, 277–287 (1982).
[15] F. J. Millero and T. Kubinski, ''Speed of sound in sea water as a function of temperature and salinity at 1 atm,'' J. Acoust. Soc. Am. **57**, 312 (1975).
[16] A. J. Pesce and L. A. Kaplan, *Methods in Clinical Chemistry* (Mosby, St. Louis, 1987), Chaps. 11 and 12.
[17] A. C. Burton, *Physiology and Biophysics of the Circulation* (Year Book Medical, Chicago, 1965), p. 38.

Estimating source position accuracy of a large-aperture hydrophone array for bioacoustics

Magnus Wahlberg,[a] Bertel Møhl, and Peter Teglberg Madsen
Center for Sound Communication, Department of Zoophysiology, Århus University, Building 131, C.F. Møllers Alle, DK-8000 Århus C, Denmark

(Received 5 April 2000; accepted for publication 2 October 2000)

A linear error propagation analysis was applied to a hydrophone array used to locate sperm whales [see Møhl *et al.*, J. Acoust. Soc. Am. **107**, 638–648 (2000)]. The accuracy of two-dimensional (2D) and three-dimensional (3D) array configurations was investigated. The precision in source location was estimated as a function of inaccuracies in measurements of sound velocity, time-of-arrival differences (TOADs), and receiver positions. The magnitude of additional errors caused by geometric simplification was also assessed. The receiver position uncertainty had the largest impact on the precision of source location. A supplementary vertical linear array consisting of three receivers gave information on the vertical bearing and distance to the sound sources. The TOAD data from an additional receiver as well as from surface reflections were used to form an overdetermined location system. This system rendered positions within two standard deviations of the estimated errors from the original 3D array. © *2001 Acoustical Society of America.*
[DOI: 10.1121/1.1329619]

PACS numbers: 43.80.Ev, 43.80.Ka, 43.30.Yj, 43.30.Sf [WA]

LIST OF SYMBOLS AND ABBREVIATIONS

A	data matrix
δc, δs_x, etc.	error (1 s.d.) of sound velocity, source position x coordinate, etc.
b	data vector
B, *B*30	platform B; 30-m hydrophone at platform B
c	sound velocity
Cov(**b**)	covariance matrix of vector **b**
*E*1–*E*5	detonators 1–5
G, *G*30	platform G, 30-m hydrophone at platform G
GPS	Global Positioning System
m	source solution vector
MINNA	minimum number of receiver array
M, *M*30	platform M; 30-m hydrophone at platform M
N, *N*30	platform N; 30-m hydrophone at platform N
m_r	number of receivers
ODA	overdetermined array
PLA	perturbed linear array
R	receiver coordinate matrix
R, *R*30	platform R; 30-m hydrophone at platform R
r(1)–**r**(5)	receiver 1–5 coordinates
s	source position vector
s.d.	standard deviation
SVP	sound velocity profile
TOAD	time-of-arrival difference

I. INTRODUCTION

Acoustic locationing is a common technique in bioacoustics using a set of receivers (a receiver array). Usually a minimum number of receiver array (MINNA) is used. A MINNA implies that the array consists of the smallest number of receivers required to find the source location. To restrict the source to a hyperboloid surface,[1] one time-of-arrival difference (TOAD) is needed, and therefore the MINNA system consists of two receivers. To calculate the source position in 2D (two dimensions), one has to estimate two coordinates, or two independent parameters. Therefore, two TOADs are needed, and the MINNA system consists of three receivers. The same argument gives a MINNA system of four receivers when solving a 3D source location problem.[2] If there are more receivers present than what is needed for the MINNA solution, the system is denoted an overdetermined array (ODA).

It is essential to know the precision of the derived source coordinates in acoustic location studies. Location errors are induced by uncertainties in the variables used for calculating the source position, such as the sound and wind (current) velocity of the medium, time of arrivals, and receiver position coordinates. In MINNA systems the number of TOAD data is just sufficient to calculate the source position, and there are no extra TOAD data available to evaluate the precision. However, if the errors in the measured variables (sound velocity, TOADs, and receiver positions) are assessed, the magnitude of the error in source position can still be determined. The simplest methods for such an error assessment is linear error propagation (Taylor, 1997). Consider a function of N variables $f=f(x_1,x_2,\ldots x_N)$. Assume that the errors δx_i of the variables x_i $(i=1,\ldots,N)$ can be assessed. The linear error propagation model estimates the magnitude of the error in f (denoted δf) as

$$\delta f=\sqrt{\sum_{i=1}^{N}\left(\frac{\partial f}{\partial x_i}\delta x_i\right)^2}. \quad (1)$$

[a]Electronic mail: Magnus.Wahlberg@biology.au.dk

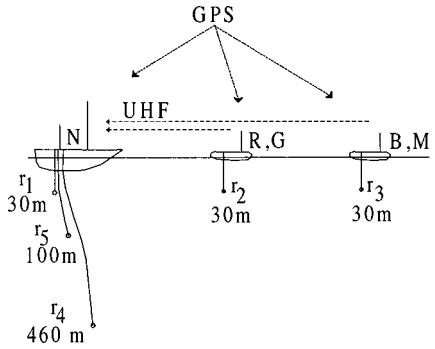

FIG. 1. The recording principle used for positioning sperm whales. Abbreviations: r=receiver, with identification and depth. GPS=Global Positioning System, UHF=Ultrahigh frequency radio link. N=main platform, G,M=auxiliary platforms in 1997, R,B=auxiliary platforms in 1998. For the recordings made in 1997, receivers 4 and 5 were not available.

If the variables x_i are correlated, Eq. (1) is modified with additional terms containing the covariances between the x_i's (Taylor, 1997).

The literature on error analysis of acoustic location systems is vast. However, for the common bioacoustic arrays with a limited amount of receivers, there are only a few examples where an error analysis has been performed. Smith *et al.* (1998) and Aubauer *et al.* (2000) performed error analyses of 2D MINNA systems, and Janik *et al.* (2000) compared acoustic- with telemetry-derived positions. Watkins and Schevill (1971) outlined an error analysis for TOAD measurement, and Cleator and Dueck (1995) made measurements on positioning error of a 3D MINNA. In this paper we extend Watkins and Schevill's (1971) approach to formulate a linear error propagation model for all the types of errors encountered when determining the position of a source. Only the wind (or current) field is not considered. The problem of wind fields has been treated extensively by other investigators (such as Spiesberger and Fristrup, 1990). The model presented here can be used for both 2D and 3D MINNA or ODA systems. It is exemplified on data on sperm whale acoustic source location presented in Møhl *et al.* (2000a).

II. METHODS

A. Field recordings

Recordings were made off the continental shelf of Northern Norway (N69°23,E15°45) in the presence of an unknown number of sperm whales during July 1997 and July 1998. In the recording area, the seafloor drops rapidly from a depth of 130 m to more than 1 km. All recordings were made in sea state 2 or below. The recording setup is described in Møhl *et al.* (2000a). In the present paper only facts relevant for estimating the precision of source positions are given. The setup is schematically outlined in Fig. 1. The array consisted of three free-floating platforms (labeled as in Møhl *et al.*, 2000a: main craft N in both 1997 and 1998, and auxiliary crafts G and M in 1997, R and B in 1998), each equipped with a hydrophone at 30 m depth. In 1998, two additional hydrophones were lowered from the N craft to depths of 100 and 460 m (receiver 4 and 5 in Fig. 1). The hydrophone signals from the two auxiliary crafts were transmitted via UHF links to the main platform. On the main platform all hydrophone signals were recorded on a Racal Store 7D multichannel instrumentation recorder. The bandwidth (−3-dB limits) of the recorded signals was 2 kHz for the radio links and 37.5 kHz for the direct recordings on the N craft. The signals were subsequently low-pass filtered (20 kHz) and digitized using a PC sound card (sampling frequency 44.1 kHz, 16-bit resolution). The position of each craft was logged every 2 s using the Global Positioning System (GPS; Garmin GPS45 receivers). Additional radar measurements of platform distances were made from the main craft at irregular intervals. In 1998, the receiver positions were calibrated using three detonators fired 3–20 m below each craft. Two additional detonators were set off 3 m below a fourth craft. The sound velocity profile (SVP) from the surface to a depth of 150 m was measured in 1998 with a custom-built *sing-around* sound velocimeter (Urick, 1983). The SVP at greater depths was calculated from salinity and temperature measurements made in the same general area during July 1997 and July 1998 (obtained from the Institute of Marine Research, Bergen, Norway).

B. Source location algorithms

Whales were located from TOADs of the same click recorded on the different receivers. TOADs were measured with a two-channel sound-editing program. Four different source location algorithms were used.

(1) A 2D MINNA algorithm was used with the 1997 field data (receivers 1–3 in Fig. 1).
(2) A 3D MINNA algorithm was used with the 1998 field data (receivers 1–4 in Fig. 1).
(3) A vertical linear array was analyzed with data from the three receivers on the N platform in 1998 (receivers 1, 4, and 5 in Fig. 1).
(4) An ODA algorithm was used with data from all five receivers in Fig. 1 as well as from surface reflections (1998 field data).

There are several mathematical ways to solve the source location problem (Watkins and Schevill, 1971; Rindorf, 1981; Spiesberger and Fristrup, 1990; Juell and Westerberg, 1993). The algebraic solution presented here is a synthesis of the methods used by Watkins and Schevill (1971) and Spiesberger and Fristrup (1990). It has the advantage of giving the same mathematical form for 2D and 3D array systems, and for both MINNAs and ODAs.

In the following, boldface letters indicate column vectors or matrices, and $^{\mathbf{T}}$ denotes the transpose operator. For a source with position vector $\mathbf{s}=(s_x,s_y,s_z)^{\mathbf{T}}$ the distances between the source and the receivers give the equations

$$(r_x(i)-s_x)^2+(r_y(i)-s_y)^2+(r_z(i)-s_z)^2 = c^2(T_1+t(i))^2, \quad i=1,2,3,mr, \tag{2}$$

where the receiver position vector of receiver i is $\mathbf{r}(i)=(r_x(i),r_y(i),r_z(i))^T$, c is the sound velocity, $t(i)$ is the TOAD between receiver i and receiver 1, and m_r is the number of receivers. The time of arrival from the source to the

receiver 1 is denoted T_1. Placing the origin of the coordinate system at $\mathbf{r}(1)$, and subtracting the $i=1$ row from the other rows in Eq. (2), we obtain (Spiesberger and Fristrup, 1990)

$$\mathbf{Am}=\mathbf{b}. \tag{3}$$

The ith row of the matrix $\mathbf{A}$ is given by $2[\mathbf{r}(i+1)^T \;\; c^2t(i+1)]$, where $\mathbf{r}(i)$ is the position vector of the ith receiver, c is the sound velocity of the medium, and $t(i)$ is the TOAD between the ith and the first receiver $(i=1,...,m_r-1)$. The vector $\mathbf{m}$ is given by $[\mathbf{s}^\mathbf{T}T_1]^\mathbf{T}$, where $\mathbf{s}=(s_x,s_y,s_z)^T$ is the source position vector, T_1 is the straight-line travel time from the source to receiver 1. The ith row of matrix $\mathbf{b}$ is given by $b_i=-c^2t^2(i+1)+\|\mathbf{r}(i)\|^2$, where $\|\mathbf{r}(i)\|$ denotes the length of the vector $\mathbf{r}(i)$.

The task is now to solve Eq. (3) for the vector $\mathbf{m}$, which contains the source coordinates.

For a 3D MINNA system, $m_r=4$. Below, Watkins and Schevill's (1971) solution is reformulated in matrix notation, which facilitates the error analysis notation. Equation (3) may be written as

$$2\mathbf{R}^T\mathbf{s}+2c^2\mathbf{t}T_1=\mathbf{b}. \tag{4}$$

Here, $\mathbf{R}$ denotes the receiver matrix

$$\mathbf{R}=\begin{pmatrix} r_x(2) & r_x(3) & r_x(4) \\ r_y(2) & r_y(3) & r_y(4) \\ r_z(2) & r_z(3) & r_z(4) \end{pmatrix},$$

and $\mathbf{t}=[t(2) \;\; t(3) \;\; t(4)]^T$. It follows that

$$\mathbf{s}=-c^2\mathbf{R}^{-T}\mathbf{t}T_1+\tfrac{1}{2}\mathbf{R}^{-T}\mathbf{b}. \tag{5}$$

Using the relationship $c^2T_1^2=\mathbf{s}^T\mathbf{s}$, we solve for T_1

$$T_1=\frac{-p\pm\sqrt{p^2-aq}}{a}, \tag{6}$$

where $a=c^4\mathbf{t}^T\mathbf{R}^{-1}R^{-T}\mathbf{t}-c^2$, $p=-c^2\mathbf{t}^T\mathbf{R}^{-1}\mathbf{R}^{-T}\mathbf{b}/2$, and $q=\mathbf{b}^T\mathbf{R}^{-1}\mathbf{R}^{-T}\mathbf{b}/4$. Equation (5) can now be solved to give the coordinates of the source.

Each set of TOADs will result in two T_1's from Eq. (6). A negative T_1 is discarded as noncausal. Two positive solutions correspond to two source positions for the given set of TOADs. If T_1 is complex there is no physical source solution.

For a 2D MINNA system, all terms with $i=4$ and z indices in Eqs. (5)–(6) are omitted.

With a linear array, the bearing and range to the source can be found in a similar manner (Møhl *et al.*, 1990). The three-receiver vertical linear array analyzed in this paper had the positions of the receivers $\mathbf{r}(4)$ and $\mathbf{r}(5)$ shifted from the vertical axes, and the three receivers were not on a line. This receiver geometry is called a perturbed linear array (PLA). With this array the intersection of the two rotated hyperboloids is not symmetric around the vertical axes. A numerical routine was constructed to plot the hyperboloid intersections. First, a vertical plane was defined in the direction from the receiver $\mathbf{r}(1)$ and the source (as obtained from the 3D algorithm). The intersection of the this plane and the hyperboloids was plotted, and the point where the two intersection lines crossed was estimated from the plot and compared with the 3D solution.

For ODA systems, the least-square solution to Eq. (3) is obtained as

$$\mathbf{m}=\mathbf{VS}^*\mathbf{U}^T\mathbf{b}, \tag{7}$$

where $\mathbf{S}^*=(\underline{\mathbf{S}}^{-1}\mathbf{0})^\mathbf{T}$ and $\mathbf{S}=(\underline{\mathbf{S}}\mathbf{0})^\mathbf{T}$, and $\mathbf{A}=\mathbf{USV}^\mathbf{T}$ is the singular value decomposition of the matrix $\mathbf{A}$ (Spiesberger and Fristrup, 1990).

C. The linear error propagation model

First, consider a MINNA system. Watkins and Schevill (1971) used a linear error propagation model on their 3D location algorithm with respect to uncertainties in TOAD measurements. Here, we expand their analysis to incorporate the impact on location errors caused by other measured variables, such as sound velocity and receiver positions. The analysis presented here also allows the effect of correlations between measured variables to be investigated. The analysis results in a covariance matrix for the source position vector, $\mathrm{Cov}(\mathbf{s})$, containing the estimated variances for each source coordinate in its diagonal, and the covariances between different source coordinates in the off-diagonal places. The total error is defined as the square root of the trace of the covariance matrix.

The covariance matrix for the source position vector is estimated as

$$\mathrm{Cov}(\mathbf{s})=\left(\frac{ds}{d(c,\mathbf{t},\mathbf{R})}\right)^T\mathrm{Cov}(c,\mathbf{t},\mathbf{R})\left(\frac{ds}{d(c,\mathbf{t},\mathbf{R})}\right), \tag{8}$$

where $(c,\mathbf{t},\mathbf{R})$ denotes a vector containing the c, $\mathbf{t}$, and $\mathbf{R}$ elements. Vector derivatives are defined as in Wunsch (1996). For the uncorrelated variables c, $\mathbf{t}$, and $\mathbf{R}$, Eq. (8) can be split up into

$$\mathrm{Cov}(\mathbf{s})=\left(\frac{d\mathbf{s}}{dc}\right)^T\mathrm{Cov}(c)\left(\frac{d\mathbf{s}}{dc}\right)+\left(\frac{d\mathbf{s}}{d(\mathbf{t})}\right)^T\mathrm{Cov}(\mathbf{t})\left(\frac{d\mathbf{s}}{d(\mathbf{t})}\right)+\left(\frac{d\mathbf{s}}{d(\mathbf{R})}\right)^T\mathrm{Cov}(\mathbf{R})\left(\frac{d\mathbf{s}}{d(\mathbf{R})}\right). \tag{9}$$

The terms on the right-hand side in Eq. (9) correspond to the contribution to the source position error from the inaccuracies in sound velocity, TOADs, and receiver position measurements, respectively.

The covariance matrix for c is simply δc^2, where δc is the standard deviation in the sound velocity estimate. The error analysis is performed analogous to Eq. (11) below.

Each TOAD is measured between the time of arrival at receiver 1 and receiver i. Assume that the time of arrivals are uncorrelated and associated with an equal measurement inaccuracy of δt (1 s.d.). Then the TOADs all include T_1 and are correlated with the amount δt^2. We obtain the TOAD covariance matrix as

$$\mathrm{Cov}(\mathbf{t})=\begin{bmatrix} 2 & 1 & 1 \\ 1 & 2 & 1 \\ 1 & 1 & 2 \end{bmatrix}\delta t^2. \tag{10}$$

The derivatives of **s** in Eq. (9) are

$$\frac{d\mathbf{s}}{d\mathbf{t}} = -c^2\left(T_1 + \mathrm{diag}(\mathbf{t}) + \frac{\partial T}{\partial \mathbf{t}}\mathbf{t}^T\right)\mathbf{R}^{-1},$$

$$\frac{\partial T}{d\mathbf{t}} = \frac{-d_t p \pm \dfrac{2p\dfrac{\partial p}{\partial \mathbf{t}} - a\dfrac{\partial q}{\partial \mathbf{t}} - q\dfrac{\partial a}{\partial \mathbf{t}}}{2\sqrt{p^2 - aq}} - T_1\dfrac{\partial a}{\partial \mathbf{t}}}{a},$$

$$\frac{\partial p}{\partial \mathbf{t}} = c^4\,\mathrm{diag}(\mathbf{t})\mathbf{R}^{-1}\mathbf{R}^{-T}\mathbf{t} - \frac{c^2}{2}\mathbf{R}^{-1}\mathbf{R}^{-T}\mathbf{b}, \tag{11}$$

$$\frac{\partial q}{\partial \mathbf{t}} = -c^2\,\mathrm{diag}(\mathbf{t})\mathbf{R}^{-1}\mathbf{R}^{-T}\mathbf{b},$$

$$\frac{\partial a}{\partial \mathbf{t}} = 2c^4\mathbf{R}^{-1}\mathbf{R}^{-T}\mathbf{t},$$

where diag(**t**) is a square 3×3 diagonal matrix with the elements of **t** in the diagonal.

The evaluation of the receiver term in Eq. (9) is made through the decomposition (receiver *x*, *y*, and *z* coordinates are assumed to be uncorrelated)

$$\left(\frac{d\mathbf{s}}{d(\mathbf{R})}\right)^T \mathrm{Cov}(\mathbf{R})\left(\frac{d\mathbf{s}}{d(\mathbf{R})}\right) = \sum_{j=x,y,z}\left(\frac{d\mathbf{s}}{dr_j}\right)^T \mathrm{Cov}(\mathbf{r}_j)\left(\frac{d\mathbf{s}}{dr_j}\right). \tag{12}$$

Each receiver coordinate is determined as the distance between the receiver *i* and receiver 1 in the coordinate direction. Each receiver coordinate is therefore correlated with the same coordinate of another receiver with the amount $\delta r_j(1)^2$. This gives the receiver covariance matrices

$$\mathrm{Cov}(r_j) = \begin{bmatrix} \delta r_j(1)^2 + \delta r_j(2)^2 & \delta r_j(1)^2 & \delta r_j(1)^2 \\ \delta r_j(1)^2 & \delta r_j(1)^2 + \delta r_j(3)^2 & \delta r_j(1)^2 \\ \delta r_j(1)^2 & \delta r_j(1)^2 & \delta r_j(1)^2 + \delta r_j(4)^2 \end{bmatrix}, \quad j = x,y,z. \tag{13}$$

The derivatives are found in a similar fashion to Eq. (11).

For the ODA solution [Eq. (7)] the error in the least-square approximation can be estimated either through linear error propagation or residual analysis. Linear error propagation is chosen for direct comparison with the MINNA analysis. Spiesberger and Fristrup (1990) used this technique for the case of TOAD measurement errors. Here, the same analysis is extended to measurement errors in sound velocity and receiver positions. The resulting covariance matrix for **m** contains the variances $\delta\mathbf{m}^2 = (\delta s_x^2, \delta s_y^2, \delta s_z^2, \delta T_1^2)^T$ in the diagonal. The total error is defined as the square root of the sum of δs_x^2, δs_y^2, and δs_z^2.

Analogous to the MINNA analysis, the covariance matrix of **m** for ODA is

$$\mathrm{Cov}(\mathbf{m}) = \mathbf{V}\mathbf{S}^*\mathbf{U}^T\mathrm{Cov}(\mathbf{b})\mathbf{U}(\mathbf{S}^*)^T\mathbf{V}^T, \tag{14}$$

where the covariance matrix of **b** is split up into its uncorrelated terms

$$\mathrm{Cov}(\mathbf{b}) = \left(\frac{d\mathbf{b}}{dc}\right)^T \mathrm{Cov}(c)\left(\frac{d\mathbf{b}}{dc}\right) + \left(\frac{d\mathbf{b}}{d(\mathbf{t})}\right)^T \mathrm{Cov}(\mathbf{t})\left(\frac{d\mathbf{b}}{d(\mathbf{t})}\right) + \left(\frac{d\mathbf{b}}{d(\mathbf{R})}\right)^T \mathrm{Cov}(\mathbf{R})\left(\frac{d\mathbf{b}}{d(\mathbf{R})}\right). \tag{15}$$

The covariance matrix of the sound velocity is given simply by δc^2, the variance of the sound velocity estimate. The components of $\partial\mathbf{b}/\partial c$ are

TABLE I. Estimated error (1 s.d.) of variables used in source positioning of the Møhl *et al.* (2000) data.

Variable/ source of error	Assumed error 1997	Assumed error 1998	Comments
Sound velocity	±10 m/s	±10 m/s	From sound velocity profile data
Time of arrival	±0.001 s	±0.001 s	Measurement accuracy of click timing
r_1x,y,z coordinate	±0 m	±0 m	Defines origin of coordinate system
r_2x coordinate	±70 m	±20–60 m	Estimated from GPS data and detonators
r_2y coordinate	±0 m	±0 m	Defines direction of *x* axis
r_3x,y coordinate	±300 m	±20–60 m	From radar, GPS, and detonators
r_4x,y coordinates	···	±10–60 m	From GPS and detonators
r_5x,y coordinates	···	±10–60 m	From GPS and detonators
r_2, r_3z coordinates	···	±2 m	From detonators
r_4z coordinate	···	±20–60 m	From detonators
r_5z coordinate	···	±20–50 m	From detonators
2D simplification	···	···	Magnitude of error depends on source–array geometry
Ray bending	···	···	Magnitude of error depends on source–array geometry

$$\frac{\partial b_i}{\partial c} = -2ct(i)^2. \tag{16}$$

The covariance matrix of **t** is given by

$$\mathrm{Cov}(\mathbf{t}) = \begin{bmatrix} 2 & 1 & \cdots & & 1 \\ 1 & 2 & & & \vdots \\ \vdots & & \ddots & & \vdots \\ \vdots & & & 2 & 1 \\ 1 & \cdots & \cdots & 1 & 2 \end{bmatrix} \delta t^2, \tag{17}$$

where δt is the standard deviation of the TOAD measurements [cf. Eq. (10)]. The time derivatives of **b** are

$$\frac{\partial b_i}{\partial t_j} = -2c^2 t(i)\,\delta_{ij}, \tag{18}$$

where δ_{ij} is the Dirac delta function ($\delta_{ij}=0$ if $i<>j$, $\delta_{ij}=1$ if $i=j$).

The covariance matrix of the receiver positions, for the same arguments given for Eq. (13), is

$$\mathrm{Cov}(r_j) = \begin{bmatrix} \delta r_j(1)^2+\delta r_j(2)^2 & \delta r_j(1)^2 & \cdots & \cdots & \delta r_j(1)^2 \\ \delta r_j(1)^2 & \delta r_j(1)^2+\delta r_j(3)^2 & & & \vdots \\ \vdots & & \ddots & & \vdots \\ \vdots & & & \delta r_j(1)^2+\delta r_j(m_r-1)^2 & \delta r_j(1)^2 \\ \delta r_j(1)^2 & \cdots & \cdots & \delta r_j(1)^2 & \delta r_j(1)^2+\delta r_j(m_r)^2 \end{bmatrix}, \quad j=x,y,z. \tag{19}$$

The derivatives of **b** are found as

$$\frac{\partial b_i}{\partial r_j(k)} = 2c^2 r_j(i)\,\delta_{ik}, \tag{20}$$

with the Dirac delta function δ_{ij} defined as above.

D. Sources of errors for acoustic location

Table I lists the sources of errors in variables used to calculate source positions in the Møhl *et al.* (2000a) data.

1. Linear error propagation variables

a. Sound velocity measurement. The measured SVP (Fig. 2) decreased from 1495 m/s at the surface to 1478 m/s at a depth of 500 m. At a depth of 800 m, the sound velocity reached a minimum of 1460 m/s. In the location algorithms a sound velocity value of 1480 m/s was used, as this is the average sound velocity for a signal traveling from a source at a depth of a few hundred meters to the receivers. In the linear error propagation model the standard deviation of the sound velocity estimate was set to ± 10 m/s, which reflects the variation observed in Fig. 2.

b. TOAD measurement. The standard deviation of TOAD measurements was set to 1 ms. Sperm whale clicks have well-defined onsets, and therefore TOADs can be measured with higher precision than 1 ms. However, the precision in timing degrades due to the use of radio links of limited bandwidth and dynamic range. There are several techniques to improve the TOAD measurements (e.g., cross correlation; Cahlander, 1967; Menne and Hackbarth, 1986). As the TOAD measurement errors turned out to have an insignificant impact on source location precision in the Møhl *et al*. (2000a) data, no effort was made to make such improvements. Water currents (maximum 1–2 knots in the present study) induce errors in TOAD measurements in the sub-ms range in the array data analyzed and were therefore not taken into account.

c. Receiver position errors. The *x* and *y* coordinates of receivers 1–3 were determined with GPS (1 s.d. positioning error ± 50 m; Kaplan, 1996), sampled with 2-s intervals. In 1997 the GPS position of receiver 3 was not recorded due to a technical failure, and the position of this craft was obtained by means of observations on a radar screen. This increased the estimated error for the coordinates of receiver 3 as compared with receiver 2 (Table I). The receiver positions from 1998 were treated in three steps to minimize the impact of fluctuations in the logged positions (Fig. 3): (1) The distances between the three platforms were calculated as a function of time; (2) Linear regression lines were fitted to each of the receiver distance curves; and (3) The regression lines

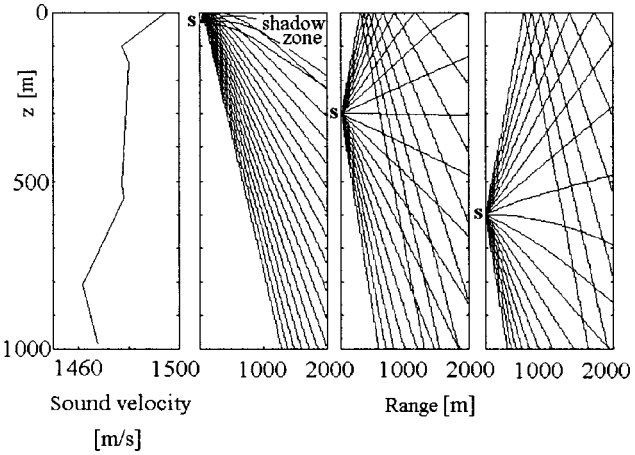

FIG. 2. The average sound velocity profile calculated from salinity and temperature measurements in the study area during July 1997 and July 1998, by the Institute of Marine Research, Bergen, Norway. Ray tracing of a sound source at depths of 30, 300, and 600 m. Ray separation: 8 degrees.

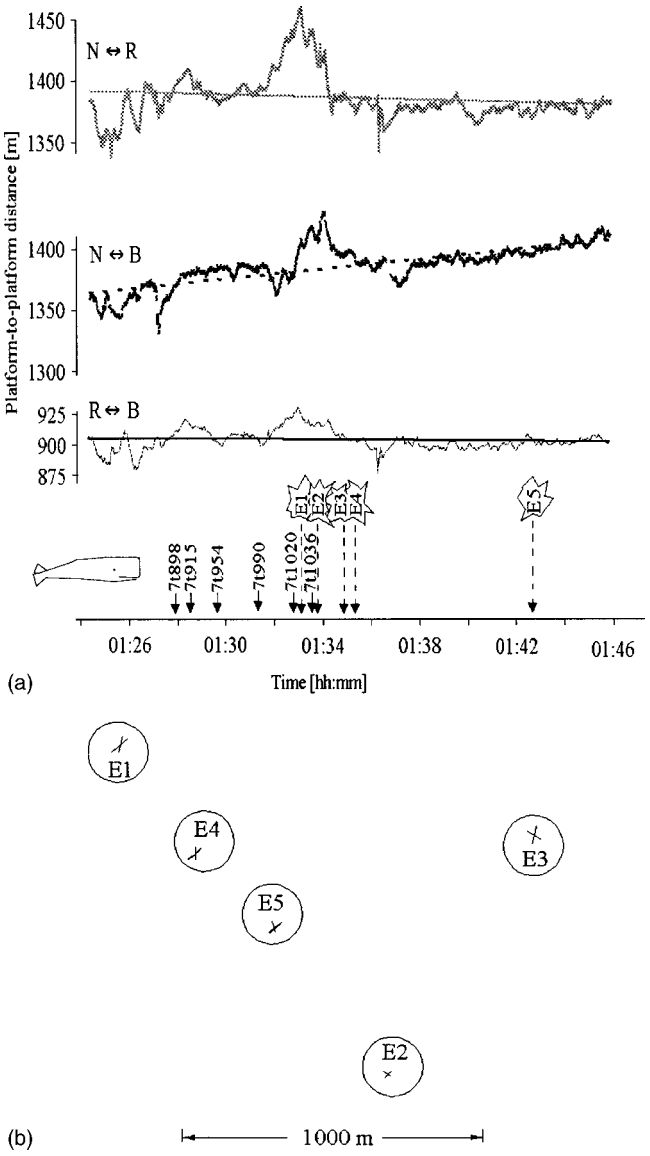

FIG. 3. (a) Distance between platforms as a function of time during the 1998 recordings. The linear regression lines for each platform distance are indicated. Six whale sequences and the detonators $E1-E5$ are indicated. (b) Calibration of recording geometry during 1998. Numbers refer to detonators $E1-E5$. Circles signify the GPS positions of the platforms, with the centers obtained through the linear regression given in Fig. 6(a). The diameter represents the 2-s.d. uncertainty in platform positions. The crosses at 1–3 are constructed from distances derived from the time of arrivals of the detonator signals to the platforms. The crosses at 4 and 5 are derived from acoustic localization of the detonators $E4-E5$. From: Møhl *et al.* (2000a), courtesy of the *Journal of the Acoustical Society of America*.

were shifted up to 30 m using the detonator data. The array geometry at the time of a whale sequence was estimated from the adjusted regression lines.

2. Errors due to geometric simplification

a. Using a 2D algorithm in a 3D source–array geometry. A geometric problem with 2D arrays occurs when the sound source is outside the plane defined by the receivers (Konagaya, 1982; Stæhr, 1982). As sketched in Fig. 4(a), the projection of the 3D position of the sound source onto the receiver plane may differ considerably from the coordinates obtained with the 2D solution. The implication of this error is that a position estimate made with a 2D algorithm is either

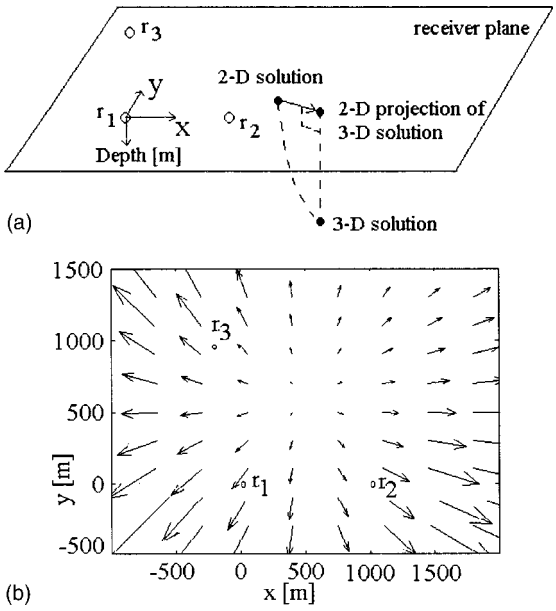

FIG. 4. (a) Illustration of the positioning error produced by locating a sound source with a 2D array, when the actual position of the source (denoted 3D solution) is not situated on the receiver plane. (b) Magnitude and direction of this error from the 1997 data. Depth of sound source: 500 m. The arrow shows the magnitude and direction of the difference between the 2D solution and the 2D projection of the 3D solution.

under- or overestimating the distances between the source and the receivers. The magnitude of this bias increases as the distance between the sound source and the receiver plane increases. In Fig. 4(b) the situation for the 2D array used in the 1997 field work is depicted for a sound source at 500 m depth.

b. Ray bending. All the location algorithms used here assume that the signal is traveling along a straight line from the source to the receiver. If the sound velocity changes with depth or otherwise, the actual sound path bends (Fig. 2; Urick, 1983). The measured TOADs then differ from those from straight path propagation. Spiesberger and Fristrup (1990) deduced an approximate formula for the deviation in time of arrival (δT) between the curved and straight path in the case of sound velocity changing linearly with depth

$$\delta T = -\left(\frac{\partial c(z)}{\partial z}\right)^2 \frac{L^3}{24 c_1^3}, \tag{21}$$

where $\partial c(z)/\partial z$ is the slope of the sound velocity profile, L is the distance between the source and the receiver, and c_1 is the sound velocity at the source depth.

E. Calibration of array configuration

The receiver array used in 1998 was calibrated using two detonators set off at 3 m depth from a separate, GPS-positioned, dinghy. The TOAD data from these detonators were used to compare acoustically derived locations with GPS positions.

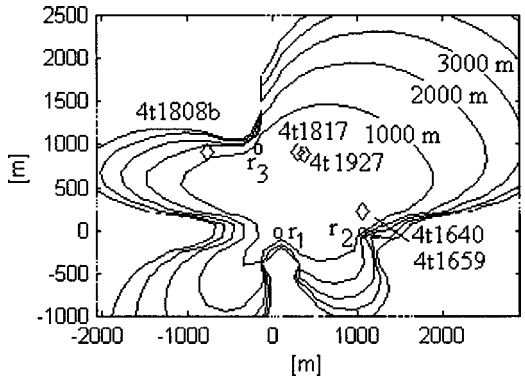

FIG. 5. Magnitude of the error in source position due to uncertainties in measurements of TOADs, sound velocity, and receiver positions applied to the 2D array data from 1997. $r(1)-r(3)$: receivers. Contour lines (spaced 1000 m) indicate the one standard deviation positioning error in m. Positions (diamonds) of five sperm whales are indicated ($4t1640$ and $4t1659$ are at the same position).

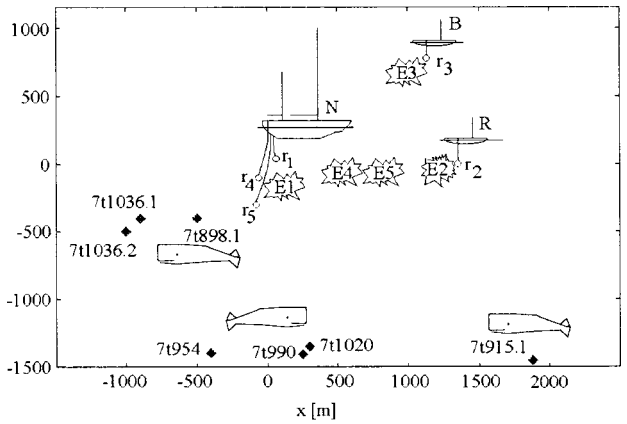

FIG. 6. Array geometry of the 1998 recordings reported in Møhl *et al.* (2000). Receivers $r(1)-r(5)$ are indicated. The positions of six whale sequences are shown as diamonds. Sequences $7t898$, $7t915$, and $7t1036$ are in a location of the array, where two source positions are found from the set of TOADs (denoted $7t1036.1$, etc.; $7t898.2$ and $7t915.2$ are outside the range of the figure). Detonations $E1-E5$ are indicated.

III. RESULTS

A. Indentifying click sequences

Click sequences were identified across receivers as consecutive clicks having the same (within 1 ms) interclick intervals on all receivers. Five click sequences from 1997 and six sequences from 1998 were analyzed. The shortest sequence consisted of five consecutive clicks, and the longest of 64. Click sequences are labeled as in Møhl *et al.* (2000a).

B. Error map of the 2-D MINNA

In Fig. 5, the result of the linear error propagation model for the 2D hydrophone array used in 1997 is shown. The contour lines (spaced 1000 m apart) indicate the magnitude of the location error (1 s.d.), using the variable errors listed in Table I. The source position of five click sequences are indicated (the sequences $4t1640$ and $4t1659$ are so close to each other that only one position is indicated). In Table II, the results from the linear error propagation model are shown for one of the whales ($4t1659$). This sequence is chosen to illustrate the error propagation analysis for a source outside the array, close to the line connecting two receivers. Errors are given in percent as the ratio of the error and the estimated source distance to $\mathbf{r}(1)$. Assuming that the whale is not situated deeper than 500 m, the maximum impact on geometric simplification is also given in Table II. Three of the sequences in Fig. 5 ($4t1640$, $4t1659$, and $4t1808b$) are situated in areas where the location error is very large. Two pairs of sequences ($4t1640-4t1659$, and $4t1817-4t1927$) almost overlap in their positions, indicating that they are from the same whale. Thus, the five sequences probably are produced by three individual whales.

C. Error of the 3D array used in 1998

Figure 6 shows the array system used in 1998. The positions of six whale sequences are indicated, as well as the positions of the five detonators fired from the platforms and an additional dinghy. The time elapsed from the first whale sequence ($7t898$) to the last transient event ($E5$) is 14 min. The sequences were probably generated by three individual whales (1: sequences $7t1036$ and $7t898$; 2: $7t954$, $7t990$, and $7t1020$; and 3: $7t915$). In Table II, the coordinates of two of the six click sequences are listed, together with the results of the error analysis.

The $E1-E3$ detonators were also used to position the deep hydrophones $\mathbf{r}(4)$ and $\mathbf{r}(5)$. In Table III, the results are presented, as well as the errors from a linear error propagation analysis.

The TOAD measurements from the two detonators $E4-E5$ were used to compare GPS and acoustic positions. The acoustically derived positions did not deviate more than 40 m from the GPS positions of the detonators.

D. Positions from the PLA compared with 3D positions

For the PLA, the intersection of each hyperboloid and the vertical plane between receiver 1 and the 3D-derived

TABLE II. The impact on source position accuracy from errors in sound velocity, TOAD measurements, and receiver positions. The sequence $7t898$ has 2 solutions. Errors are given in percent of the ratio between the standard deviation error estimates and the derived distance between the whale and the origin of the array. Geometric error is calculated for a source depth of 500 m.

Whale	Position (x,y,z) [km]	Sound velocity error [%]	TOAD error [%]	Receiver position error [%]	3D to 2D geometric error [%]	Ray curvature error [%]
$4t1659$	1.0, 0.2, −	0.6	0.4	300	30	⋯
$7t898.1$	−0.5, −0.4, 0.2	20	2	500	⋯	3
$7t898.2$	−27, −13, 0.8	700	80	4000	⋯	⋯
$7t990$	0.3, −1.4, 0.3	5	0.2	50	⋯	0.5

TABLE III. Positions of the two deep hydrophones deployed from the *N* craft derived from detonators $E1-E3$.

Receiver	x [m]	y [m]	z [m]
$r(4)$	23 ± 20	-59 ± 60	462 ± 10
$r(5)$	-2 ± 20	37 ± 50	98 ± 30

whale position are shown in Fig. 7. The curves are not symmetric around the $r1-r(i)$ axis, as this axis is not running on the whale–receiver 1 plane. The 3D solution is on the H14 curve, as receiver 4 is part of the 3D MINNA system. The H15 curve is not running through the 3D solution, probably due to uncertainties in the position of receiver 5. In Table IV, the estimated ranges and bearings are compared with the 3D MINNA results for two whale sequences. The ranges and bearings calculated with the perturbed linear array are within the error margins of the 3D solution.

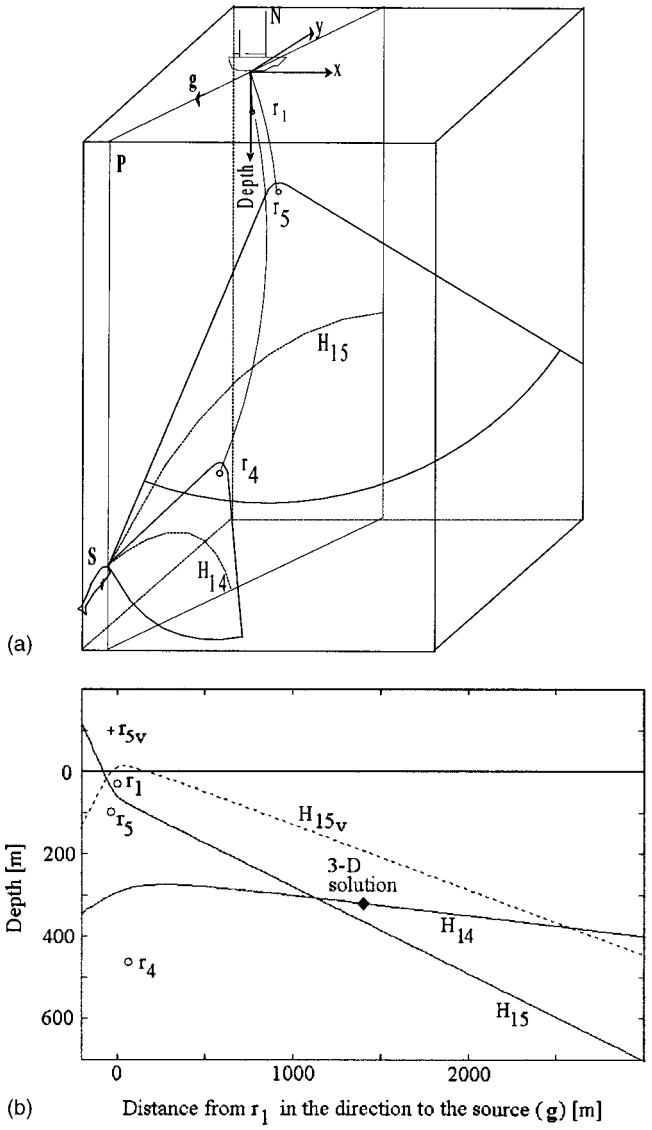

FIG. 7. (a) Geometry of the perturbed linear array analysis. x,y=coordinate system of the 3D algorithm. Abbreviations: **N**=platform. **r**(1), **r**(4), **r**(5)=receivers 1, 4, and 5. **s**=position of whale, calculated with the 3D algorithm. **g**=direction between receiver 1 and the whale in the horizontal plane. **P**=The vertical plane through **r**(1) and **s**. **H14** (**H15**): Intersection of **P** and the hyperboloid created from TOAD between receivers 1 and 4(5). (**b**) View of the receiver 1–source plane (**P** in 7a) for click sequence $7t1036$. **r(4)** and **r(5)** are projections of receivers 4 and 5 onto the plane **P**. A surface reflection is treated as recorded by an additional virtual receiver, denoted **r5v**. The curves corresponding to TOADs between receivers 1–5 and 1–4 are drawn with solid lines, and the curve corresponding to TOADs between receiver 1 and the virtual receiver is drawn with a dotted line.

Several signals contained echoes, likely generated by surface reflections. Surface reflections can be viewed as recordings made by virtual hydrophones, situated above the surface at a height corresponding to the depth of the ''real'' receiver (Urick, 1983; Møhl *et al.*, 1990; Aubauer *et al.*, 2000). Surface reflection data were incorporated into the linear array analysis. The curve generated by the TOAD from a surface reflection is shown in Fig. 7(b) as a dotted curve. The dotted curve is converging reasonably well towards the 3D solution, so the corresponding echo is regarded as a surface reflection.

The surface reflected signal is expected to be 180 deg phase shifted compared with the direct signal (Urick, 1983). This should be easily observed in the cross correlation between the direct and the surface reflected signals and could thus be a further help in the interpretation of echoes. However, in the Møhl *et al.* (2000a) there was no clear negative maximum in the cross-correlation function between click and echo, so this method could not be readily implemented.

E. The ODA compared with the 3D MINNA and the PLA solutions

In Table IV, the range and bearing to the source are shown with an ODA system using receivers 1–5 and surface reflection data. Signals were considered as originating from surface reflections if the analysis with the PLA indicated that this was plausible. The ODA solution can be compared with results from the two other location algorithms: the 3D MINNA system and the PLA (Table IV). In most cases the error estimates derived with the ODA and 3D MINNA were of similar magnitude. If the source was situated outside the array close to one of its corners, the ODA errors were smaller by up to an order of magnitude (e.g., the sequence $7t898$ in Table IV).

F. Errors due to a varying sound-velocity profile

The error from ray bending in five sequences from 1998 data was estimated. The source was assumed to be at the position given by the 3D solution, and Eq. (21) was used to compensate for the measured TOADs for ray-bending effects. Then, a new 3D position was calculated with the adjusted TOADs. The difference from the uncorrected positions was always less than 10% of the total error as derived from linear error propagation (Table II).

IV. DISCUSSION

The accuracy of source location depends on the precision of the measurements in sound velocity, TOADs, and receiver positions, as well as on source–array geometry. It is evident from Fig. 5 that the location precision is a complicated function of the bearing and range from the array to the source.

TABLE IV. Comparison of 3D MINNA, ODA, and PLA positioning for two click sequences selected from the 1998 data in Møhl *et al.* (2000). The sequence 7*t*898 has two solutions with the MINNA system. Range is the estimated distance from the source to receiver 1 in the origin of the array. Bearing is the angle between the horizontal plane and the line connecting the whale and receiver 1. Virtual hydrophones are constructed from signals interpreted as being reflected from the surface (see the text). The sequences are selected to illustrate the performance of the error analysis. All errors are standard deviations (±1 s.d.).

	3-D MINNA (Receivers 1–4)			3-D ODA (Receivers 1–5+virtual receivers)				PLA (Receivers 1, 4, and 5)		
Whale	Range to $r(1)$ [km]	Bearing [degrees]	Source depth [km]	No of virtual receivers	Range to $r(1)$ [km]	Bearing [degrees]	Source depth [km]	Range to $r(1)$ [km]	Bearing [deg]	Source depth [km]
7*t*898.1	0.7±3	18±80	0.2±0.5	0	0.7±0.7	16±6	0.2±0.7	0.7	18	0.2
7*t*898.2	30±90	1±60	0.8±30	…	…	…	…	…	…	…
7*t*990	1.4±0.6	11±21	0.3±0.6	2	2.3±0.5	10±4	0.4±0.1	1.1	15	0.3

A considerable problem with locating directional sources with a MINNA system is that there are no means to assure that the signal is correctly interpreted in terms of direct and reflected paths. In the present study the PLA data were used to confirm the range and vertical bearing to the source from the *N* platform. Still, there is a possibility that an erroneous interpretation of the signal TOADs can render similar yet erroneous results with the two location systems, as two of the linear array receivers were also a part of the 3D MINNA system. To some extent, surface reflections can be used to confirm the interpretation of the TOADs (Møhl *et al.*, 1990; Aubauer *et al.*, 2000). The problem can best be minimized through the use of an overdetermined system, where additional independent data are collected.

Overdetermined systems are also favorable in terms of reducing the positioning error. This effect is most clearly seen in the areas of the array where the ODA systems are very sensitive to errors (Table IV).

The linear error propagation analysis applied in this study gives a measure of the expected error in source location. The fact that the analysis is linear makes it unfeasible in areas of the array where the location error increases rapidly (i.e., nonlinearly). This is clearly seen in Table II. The estimated source location errors of the sequences 4*t*1659 and 7*t*898 are much larger than the location inaccuracies we would expect from repeated measurements of sound sources situated at these positions. Spiesberger (1999) deduced boundaries where the linear approximation of location errors breaks down for overdetermined acoustic location systems. A similar approach to MINNA systems would be useful to define the source–array geometries for which the linear error propagation analysis presented here is valid. The nonlinear effect is largest where the hyperboloid surfaces have large curvature or are almost parallel.

The PLA created with the hydrophones deployed from the *N* platform in 1998 gave additional vertical bearing and range data which proved useful to confirm source positions derived with the 3D algorithm [Fig. 7(b), Table IV]. In two end-fire situations (sequences 7*t*898 and 7*t*1036 in Fig. 5) the difference in the ranging estimation of the PLA and the MINNA solutions was within 20% of the range. The difference is readily explained by the uncertainties in the *N*100 and *N*460 receiver positions.

When cross-correlating a click with an assumed surface reflection, it was not possible to discern whether the cross-correlation function had a positive or a negative maximum. A likely reason for this is the observed acute directionality of sperm whale clicks (Møhl *et al.*, 2000a). The direct path and surface reflected signals originate from different directions of the sperm whale transmission beam, and therefore the frequency and phase content of the two signals may differ significantly. Additionally, inhomogeneities in the water mass between the source and the various receivers may distort the signal differently.

There are two major causes for source position uncertainty in the hydrophone array system described by Møhl *et al.* (2000a): receiver position uncertainty, and the usage of a 2D array in a 3D geometry. The second problem was eliminated during the field work in 1998 through the use of a 3D array. In addition, the errors in receiver positions were reduced through acoustic calibration by the firing of detonators. The differences between acoustically derived and GPS-logged receiver positions were well within the ±50-m error margin of the GPS system at the time [Fig. 3(b)]. This indicates that the regression performed on the GPS coordinates [Fig. 3(a)] eliminated some of the error associated with the GPS location of the platforms. The spurious jumps in the GPS locations observed in Fig. 3(a) are due to short periods where one or more of the GPS receivers lost contact with the satellites. During such circumstances the GPS receiver is estimating its position from dead reckoning. More accurate receiver positions can be obtained using differential GPS receivers (Kaplan, 1996). With such a system, the platform location error can be reduced by about one order of magnitude, leading to a similar reduction in errors in source location.

The impact of ray bending on location errors at the ranges and depths relevant for the Møhl *et al.* (2000a) data is at least an order of magnitude smaller than location errors caused by receiver position uncertainties (Table II). Figure 2 shows that the the ray tracings create no major ray bending at the distances and depths relevant for the data presented here. The largest problem with ray bending is the fact that the SVP of the present study created a shadow zone (Urick, 1983; Fig. 2) for shallow sources and receivers. This shadow zone starts a few kilometers away from the source and may cause considerable underestimation of sound levels recorded from shallow or distant whales.

The linear error propagation model is a useful tool for estimating location errors. Such an analysis can be used to obtain error estimates for derived parameters based on ranging information such as source levels (Møhl *et al.*, 2000a).

The error analysis is also an effective tool for pinpointing the factors causing the largest impact on the source position precision. This has been an important argument in developing the acoustic location systems investigated here into an overdetermined acoustic location system (Møhl *et al.*, 2000b).

ACKNOWLEDGMENTS

H. Westerberg and G. Bark gave many valuable suggestions during the development of the error propagation algorithms. A. Heerfordt and N. Kristiansen kindly helped with the analysis of the GPS data. We thank the crew on R/V NARHVALEN for great collaboration in the field. Special thanks to B. K. Nielsen and J. L. Spiesberger for constructive comments on earlier drafts of this manuscript. This project was funded by the Danish National Research Council, with additional logistic assistance received from Hvalsafari A/S in Andenes, and the Andenes Cetacean Research Unit, ANCRU.

[1]In 2D applications, the hyperboloid surface is reduced to a hyperbola curve.
[2]In some source–receiver geometries, the MINNA may render two source solutions. In these cases an extra receiver is needed to remove the ambiguity in the location of the source.

Aubauer, R., Lammers, M. O., and Au, W. W. L. (**2000**). ''One-hydrophone method of estimating distance and depth of phonating dolphins in shallow water,'' J. Acoust. Soc. Am. **107**, Pt1, 2744–2749.

Cahlander, D. (**1967**). ''Discussion,'' in *Animal Sonar Systems. Biology and Bionics*, edited by R. E. Busnel (NATO Advanced Study Institute), Vol. 2, pp. 1052–1081.

Cleator, H., and Dueck, L. (**1995**). ''Three-dimensional accuracy of a four-hydrophone array,'' 11th Biennial Conference on the Biology of Marine Mammals, 14–18 December 1995, Orlando.

Janik, V. M., van Parijs, S. M., and Thompson, P. M. (**2000**). ''A two-dimensional acoustic localization system for marine mammals,'' Marine Mammal Sci. **16(2)**, 437–447.

Juell, J.-E., and Westerberg, H. (**1993**). ''An ultrasonic telemetric system for automatic positioning of individual fish used to track Atlantic salmon (*Salmo salar L.*) in a sea cage,'' Aquacultural Eng. **12**, 1–18.

Kaplan, E. D. (editor) (**1996**). *Understanding GPS: Principles and applications*. Artech House, Inc., MA.

Konagaya, T. (**1982**). ''A new telemetric method of determining the positions of swimming fish,'' Bulletin Jpn. Soc. Scientific Fisheries **48**(11), 1545–1550.

Menne, D., and Hackbarth, H. (**1986**). ''Accuracy of distance measurement in the bat *Eptesicus fuscus*: Theoretical aspects and computer simulations,'' J. Acoust. Soc. Am. **79**, 386–397.

Møhl, B., Surlykke, A., and Miller, L. A. (**1990**). ''High intensity narhval clicks,'' in *Sensory Abilities of Cetaceans*, edited by J. A. Thomas and R. A. Kastelein (Plenum, New York), pp. 295–303.

Møhl, B., Wahlberg, M., Madsen, P. T., Miller, L. A., and Surlykke, A. (**2000a**). ''Sperm whale clicks: Directionality and source levels revisited,'' J. Acoust. Soc. Am. **107**, 638–648.

Møhl, B., Wahlberg, M., and Heerfordt, A. (**2000b**). ''A large-aperture array of nonlinked receivers for acoustic positioning of biological sound sources,'' J. Acoust. Soc. Am. (in press).

Rindorf, H. J. (**1981**). ''Acoustic emission source location in theory and in practice,'' Brüel & Kjær Technical Review No. 2.

Smith, G. W., Urquhart, G. G., MacLennan, D. N., and Sarno, B. (**1998**). ''A comparison of theoretical estimates of the errors associated with ultrasonic tracking using a fixed hydrophone array and field measurements,'' Hydrobiologia **371/372**, 9–17.

Spiesberger, J. L. (**1999**). ''Locating animals from their sounds and tomography of the atmosphere: Experimental demonstration,'' J. Acoust. Soc. Am. **106**, 837–846.

Spiesberger, J. L., and Fristrup, K. M. (**1990**). ''Passive location of calling animals and sensing of their acoustic environment using acoustic tomography,'' Am. Nat. **135**, 107–153.

Stæhr, K.-J. (**1982**). ''Passiv akustisk lokalisering af dyr. Teori og praksis,'' M.Sc. thesis, Aarhus University, Denmark (in Danish).

Taylor, J. R. (**1997**). *An introduction to Error Analysis*, 2nd ed. (University Science, Sausalito, CA), Chap. 3.

Urick, R. J. (**1983**). *Principles of Underwater Sound*, 3rd ed. (Peninsula, Los Altos, CA).

Watkins, W. A., and Schevill, W. E. (**1971**). ''Four-hydrophone array for acoustic three-dimensional location,'' Woods Hole Oceanographic Institution, Technical Report, Reference No. 71-60, unpublished manuscript.

Wunsch, C. (**1996**). *The Ocean Circulation Inverse Problem* (Cambridge University Press, New York).

Whistles of boto, *Inia geoffrensis*, and tucuxi, *Sotalia fluviatilis*

Wang Ding[a] and Bernd Würsig
Marine Mammal Research Program, Texas A & M University at Galveston, Galveston, Texas 77551-5923

Stephen Leatherwood[b]
IUCN/SSC Cetacean Specialist Group, c/o Ocean Park Conservation Foundation, Ocean Park, Aberdeen, Hong Kong

(Received 8 September 1998; accepted for publication 22 September 2000)

Whistles were recorded and analyzed from free-ranging single or mixed species groups of boto and tucuxi in the Peruvian Amazon, with sonograms presented. Analysis revealed whistles recorded falling into two discrete groups: a low-frequency group with maximum frequency below 5 kHz, and a high-frequency group with maximum frequencies above 8 kHz and usually above 10 kHz. Whistles in the two groups differed significantly in all five measured variables (beginning frequency, end frequency, minimum frequency, maximum frequency, and duration). Comparisons with published details of whistles by other platanistoid river dolphins and by oceanic dolphins suggest that the low-frequency whistles were produced by boto, the high-frequency whistles by tucuxi. Tape recordings obtained on three occasions when only one species was present tentatively support this conclusion, but it is emphasized that this is based on few data. [DOI: 10.1121/1.1326082]

PACS numbers: 43.80.Lb [WA]

I. INTRODUCTION

The platanistoid boto (*Inia geoffrensis*) and the delphinoid tucuxi (*Sotalia fluviatilis*) are sympatric throughout the Amazon River Basin and in portions of the Orinoco River Basin. (In Peru, where our work was conducted, these species are known as *bufeo colorado* and *bufeo gris*, respectively.) There are several reports characterizing vocalizations by both of these species (see below), but both species are still considered poorly known in terms of bioacoustic communication. This is in large part because of incomplete data, and some contradictions between different reports (see Nekoosa and Takemura, 1975; Best and da Silva, 1989).

From recordings of captive boto, Caldwell *et al.* (1966) and Caldwell and Caldwell (1967) recognized 12 types of vocalizations in four major categories: click trains, single intense clicks, jaw snaps, and burst-pulsed sounds. In this last category, they placed seven discrete types of sounds with frequencies well below 20 kHz (''squawk,'' ''screech,'' ''bark,'' ''whimper,'' ''crack,'' ''squeal,'' and ''squeaky-squawk''). Sonograms with an effective bandwidth of 600 Hz were presented for the first five. No whistles were recorded.

Three years later, Caldwell and Caldwell (1970) presented additional data to support the view that boto do not whistle. Norris *et al.* (1972) described a ''burst-pulsed yelp'' they recorded when a calf was present in a group of boto. Nekoosa and Takemura (1975) reported hearing whistles from boto, but Best and da Silva (1989) opined that these whistles were probably produced by tucuxi, which often were present with or near the boto.

Norris *et al.* (1972) described single whistles (approximately 0.2-s long and rising in frequency between 10 and 15 kHz) which they presumed were made by tucuxi, but they gave no sonograms or sound spectra. Alcuri and Busnel (1989) found that the frequencies of whistles from tucuxi were centered around 14 kHz; they, too, neglected to present a sonogram.

There has been some research into the high-frequency echolocation of both boto and tucuxi (e.g., Evans, 1973; Penner and Murchison, 1970; Kamminga, 1979; Kamminga *et al.*, 1993; Wiersma, 1982). However, none of the reports on this research addresses lower-frequency whistling.

This paper presents sonograms of whistles from free-ranging boto and tucuxi in single or mixed species groups in Peru, gives a detailed analysis of the whistles thought to be made by each of the two species, and presents evidence to support this conclusion.

II. MATERIALS AND METHODS

Vocalizations were recorded, from free-ranging animals of single or mixed species groups of boto and tucuxi, in tributaries of the Amazon, Marañon, and Tigre rivers in 1991, 1992, and 1993 (Table I). Recordings were made from a drifting 6-m aluminum skiff, with engine off, using a custom-made hydrophone (C. Clark, Cornell University) and a Marantz PMD-430 tape recorder. This system has a flat frequency (±3 dB) response range to 15 kHz, using TDK SA90, AVX90, or Supertape MII-90 cassette tapes. Information on species present, group size and composition, sounds heard, and behavior were noted on the narrative channel of the recorder and in field notebooks.

All tapes were analyzed with the IBM/PC-based analysis system known as ''SIGNAL'' (Engineering Design, Belmont, MA). Analysis frequency range was set between 0 and 10, 0 and 20, or 0 and 25 kHz, depending on frequency range of

[a]Current address: Department of River Dolphin Research, Institute of Hydrobiology, The Chinese Academy of Sciences, Wuhan, Hubei 430072, China.
[b]Deceased January 1997.

TABLE I. Summary of recording used for this report. All recordings were made upriver of the city of Iquitos, Peru, in the Marañon and Tigre Rivers and their tributaries (approximately 4.5° South, 74.5° West). Species are marked as present (yes) or absent (no) with no designation of numbers, since group sizes (generally 3 to 5) were estimates only.

Date	Boto	Tucuxi	No. of whistles
11 March 1991	Yes	Yes	35
12 March 1991	Yes	Yes	35
13 March 1991	No	Yes	3
14 March 1991	Yes	No	3
28 July 1992	Yes	Yes	0
30 July 1992	Yes	Yes	155
31 July 1992	Yes	Yes	0
3 August 1992	Yes	Yes	0
9 June 1993	Yes	No	2
			Grand total = 233

the signals. Sonograms were visually inspected first using a real time spectrogram (RTS) program while simultaneously listening to the original recording. All whistles with suitable signal-to-noise ratios were analyzed. Frequencies higher than the flat range of the recording system could be read and measured with the ''enhancing'' function of SIGNAL.

Sonograms were produced with a frequency resolution of 49, 98, or 122 Hz when the analysis bandwidth was 10, 20, and 25 kHz, respectively. Parameters were measured directly on the computer screen with the cursor supplied with SIGNAL. For each whistle, the following five variables were measured from its sonogram: beginning frequency, end frequency, minimum frequency, maximum frequency, and duration.

Microsoft EXCEL was used to plot the distribution of the minimum and maximum frequency measures of each whistle. The STATVIEW statistical package (Anonymous, 1986) was used to calculate means, standard deviations, and coefficients of variation for all measured variables. A one-factor analysis of variance (ANOVA) analysis program (Scheffé *F* test) was used to test differences in specific variables between two groups of whistles. SAS (Anonymous, 1985) was used to compute a percent-correct classification score for these two groups.

III. RESULTS

Analysis was based on a total of 610 min of recordings from the three years (Table I). A total of 233 whistle samples was obtained, 76 from 1991, 155 from 1992, and 2 from 1993. Group sizes of the animals recorded were generally between 3–5 individuals.

For recordings from 1991, the frequencies of most whistles (73 of 76) are below 5 kHz, and those of the other three exceed 8 kHz, which were recorded when only tucuxi were present for a session on 13 March 1991. For the session on 14 March 1991, only three low-frequency whistles were recorded when only boto were present during the recording. For the recordings from 1992, the frequencies of most whistles (152 of 155) exceed 8 kHz, and those of the other three are below 5 kHz. Two low-frequency whistles (below 5 kHz) were recorded when only boto were present on 9 June 1993.

A plot of the distribution of the minimum and maximum frequency of all the measured whistles is shown in Fig. 1. From the figure, it is clear that all whistles fall into two groups, based on differences in their maximum frequency: a low-frequency group in which all the maximum frequencies are below 5 kHz and a high-frequency group in which all the maximum frequencies are above 8 kHz, and most of these are above 10 kHz.

Descriptive statistics of the measured variables of the whistles of these two groups are shown in Table II. It can be seen that the four measured frequency variable values of the high-frequency group are much larger than those of the low-frequency group. For example, the mean value of the maximum frequency of the low-frequency group is 2.97 kHz, but the same value of the high-frequency group is as high as 15.41 kHz, almost 5.2 times higher. The duration of sounds of the low-frequency group is much longer than the one of the high-frequency group. The mean difference between

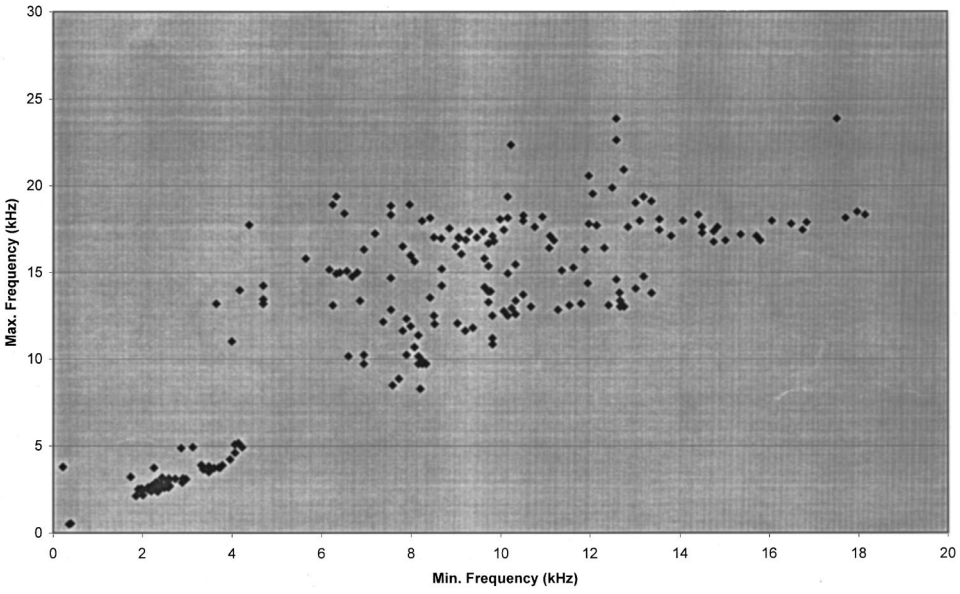

FIG. 1. Plot of max. and min. frequency of all the recorded whistles.

TABLE II. (a) Descriptive statistics for variables of 76 whistles of the low frequency group (frequency is in kHz and duration in seconds). (b) Descriptive statistics for variables of 155 whistles of the high frequency group (frequency is in kHz and duration in seconds).

Variable	Smallest	Largest	Mean	Std. dev.	C.V.
		(a)			
Beginning frequency	0.22	4.22	2.61	0.75	28.55
End frequency	0.36	4.86	2.86	0.77	27.01
Minimum frequency	0.22	4.22	2.54	0.76	29.88
Maximum frequency	0.50	5.16	2.97	0.84	28.11
Duration	0.16	4.42	1.14	1.04	91.10
		(b)			
Beginning frequency	3.65	21.21	10.76	3.53	32.77
End frequency	7.89	23.11	14.35	2.89	20.15
Minimum frequency	3.65	18.14	10.21	3.10	30.39
Maximum frequency	8.28	23.86	15.41	3.11	20.18
Duration	0.06	1.04	0.41	0.21	51.10

these groups is as high as 0.73 s, which is 1.8 times the mean duration of the high-frequency group sounds. There is a consistent pattern in coefficients of variation: all the frequency variables have the lowest coefficients of variation; duration has much higher coefficients of variation than frequency variables.

Contours of sonograms of the two groups' whistles are also different. The ones of low-frequency whistles are simple and flat, with very little frequency modulation: 0.43 kHz (defined as the range between mean maximum and minimum frequency of the whistles; see Table II and Fig. 2); the contours of high-frequency whistles are usually not flat but show some degree of loop (deep up–down or down–up) structure, with much greater frequency modulation: 5.2 kHz (see Table II and Fig. 3).

All the measured variables: beginning frequency, end frequency, minimum frequency, maximum frequency, and duration, are significantly different between the low- and high-frequency groups (one-factor ANOVA, Scheffé F Test, $P<0.001$) (Table III). The percent-correct classification score of pairwise discriminant analysis is as high as 100, which means that a discriminant function developed from the analysis can classify each whistle into its proper group easily and without errors.

IV. DISCUSSION

Dolphin whistles have been implicated in communication (Herman and Tavolga, 1980), and especially noisy bouts of whistling have been noted during high levels of social activity (Norris *et al.*, 1985). Herman and Tavolga (1980) asserted, however, that species in which individuals habitually travel alone or in small groups, such as the platanistoid river dolphins, do not whistle. They attempted to relate whistle production with special functions in large schools, such as maintaining vocal communication during food search by echolocation. There are, however, published accounts of whistling by some platanistoid dolphins.

Jing *et al.* (1981) described a whistle-like sound from baiji (*Lipotes vexillifer*). Subsequently, Wang *et al.* (1989, 1999) by analyzing vocalizations recorded in captivity and in the wild, confirmed that baiji do indeed produce whistles. Whistles were also found in recordings of susu (*Platanista gangetica*) from the Ganges River (Mizue *et al.*, 1971), although not in recordings of captive bhulan (*P. minor*) from the Indus River (Herald *et al.*, 1969). In the recordings of both baiji and susu, whistles were relatively infrequent, and such infrequency may account in part for the few reports of whistling by platanistoid dolphins.

As a platanistoid species, boto has also been thought to be one of the ''nonwhistling'' dolphins (Herman and Tavolga, 1980). But, on two recording sessions when only boto were present from this study, some low-frequency whistles (five whistles) were recorded. On one recording session when only tucuxi were present, three high-frequency whistles were recorded. In another recording session made with tucuxi on 5 July 1994, high-frequency whistles were also the only ones recorded (B. Würsig, 1994). Several lines of evidence lead us to speculate on the origins of the two frequency classes of whistles in those samples.

It has been demonstrated for at least seven species of small cetaceans (*Tursipos truncatus, Lagenorhychus acutus,*

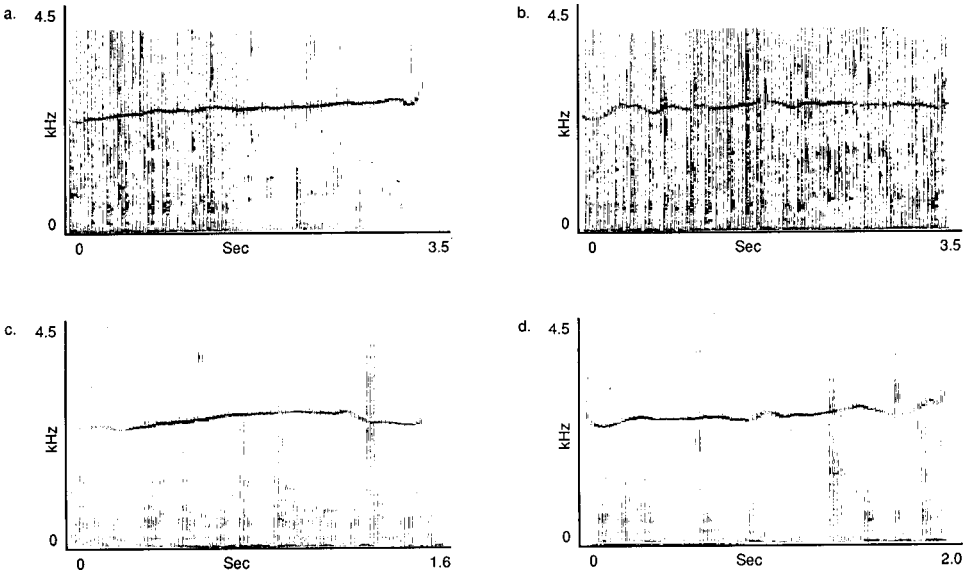

FIG. 2. Sonograms of four typical whistles from the low-frequency group: contours are simple and flat, with very little frequency modulation.

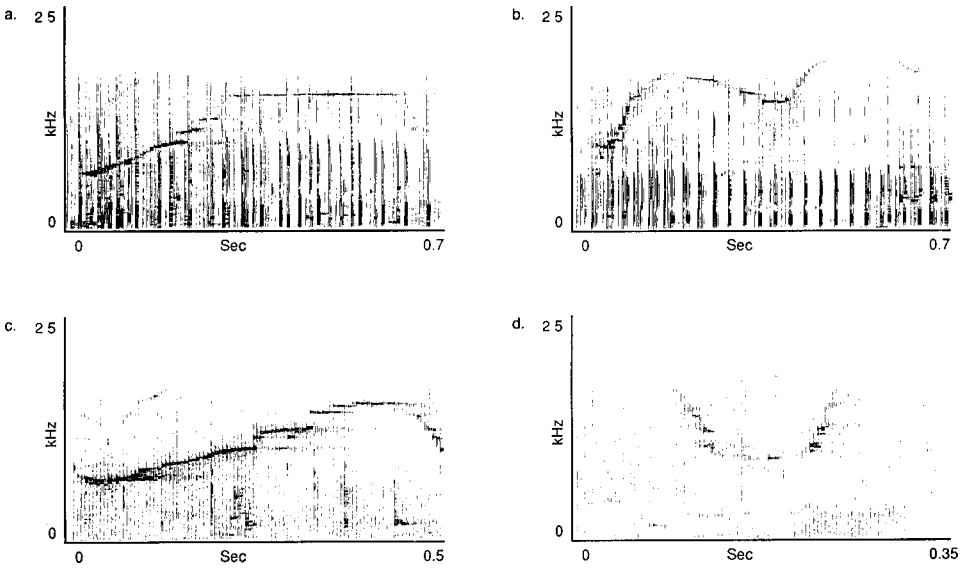

FIG. 3. Sonograms of four typical whistles from the high-frequency group: contours are usually not flat, showing some degree of loop structure, with much greater frequency modulation. Note the differences in scales: Fig. 2=4.5 kHz, Fig. 3=25 kHz.

L. obscurus, Stenella frontalis, S. longirostris, S. attenuata, and Globicephala melas) that whistles have consistent, species-specific characteristics and the frequency of whistles is the least variable acoustic parameter within that species (Steiner, 1980, 1981; Wang, 1993; Wang *et al.*, 1995a, b). If we assume that the two categories of whistles were from two species, the result of this study tallies with this conclusion, i.e., coefficients of variation of frequency variables of each group are much lower than the one of duration of the same group (Table II). Furthermore, there were significant differences between the high-frequency group and the low-frequency group in all measured frequency and duration parameters (Table III).

Contours and frequency modulation ranges of whistles in the low-frequency group are similar to those reported for baiji (Jing *et al.*, 1981; Wang *et al.*, 1989, 1999) and susu (Mizue *et al.*, 1971). The contours are simple and flat, with little frequency modulation. Contours and frequency modulation ranges of whistles in the high-frequency group are more like those of such oceanic species as bottlenose, spinner (*Stenella longirostris*), spotted (*S. frontalis*), and dusky (*Lagenorhynchus obscurus*) dolphins (Graycar, 1976; Steiner, 1980, 1981; Wang, 1993; Wang *et al.*, 1995a, b). The contours are usually not flat but with some loop structures, and exhibit much greater frequency modulation. Furthermore, the whistles in this group are similar to sounds attributed to tucuxi by Alcuri and Busnel (1989) and Norris *et al.* (1972).

TABLE III. The results of one factor ANOVA (Scheffé *F* test) comparing variables of whistles of the two frequency groups. B.F.=beginning frequency; E.F.=end frequency; Mn.F.=minimum frequency; Mx.F. =maximum frequency; D.=Duration; Mean differences of the variables between the two groups are in ( ).

Comparisons	B.F.	E.F.	Mn.F.	Mx.F.	D.
High F. group	396[a]	1158[a]	450[a]	1172[a]	72[a]
vs					
Low F. group	(8.15)	(11.49)	(7.67)	(12.44)	(−0.73)

[a]Scheffé *F* test values are significant at $p=0.001$.

From the evidence stated above, we tentatively concluded that whistles of the low-frequency group were made by boto, those of the high-frequency group by tucuxi. This conclusion is further strengthened (but not proved) by the small number of recordings we made when single-species presence was known.

Our assignation is consistent with the general pattern noted by Wang (1995b) in which, while habitats were similar, the maximum frequency of whistles in small cetaceans tended to rise as body length decreased. At approximately 1.5 m maximum length, the tucuxi is among the smallest of the delphinids. The boto reaches a maximum length of about 3 m (Leatherwood and Reeves, 1983). Meanwhile, body lengths of baiji and susu are similar but shorter than those of boto, at usually less than 2.5 m (Leatherwood and Reeves, 1983), and their whistles' maximum frequencies are also similar but higher than the assumed ones of boto, usually close to 6 kHz (Mizue *et al.*, 1971; Wang *et al.*, 1989, 1999).

In summary, we recorded and analyzed whistles from free-ranging single or mixed species groups of boto and tucuxi. Sonograms are also presented. We found two broad classes of whistles that were probably from two different species, the high-frequency ones from tucuxi, and the low-frequency ones from boto. We urge further study of the sound repertoire of these species.

ACKNOWLEDGMENTS

This work was supported by the World Wide Fund for Nature, The Chinese Academy of Sciences (Grant No. KZ951-A1-105), Oceanic Society Expeditions (OSE), and Cetacean Society International. The fieldwork was made possible by OSE as part of its natural history travels and research program, under the direction of Birgit Winning. The authors thank Randall Reeves, Thomas Jefferson, Robert Benson, and Barbara Carry for assistance with the field research, and Spencer Lynn for helping to prepare figures. We are particularly grateful for the valuable comments and fine suggestions on an earlier version of this manuscript by Laela

Sayigh, Rachel Smolker, and Peter Tyack. This represents contribution No. 72 of the Marine Mammal Research Program, Texas A&M University of Galveston.

Alcuri, G., and Busnel, R.-G. (**1989**). ''Sonar clicks and whistling signals are made by the same acoustical source in the fresh-water Amazonian dolphin *Sotalia fluviatilis* Gervais and Deville,'' C. R. Acad. Sci. Paris, Serial III **308**, 379–384.

Anonymous (**1985**). *SAS® User's Guide: Statistics*, Version 5 Edition (SAS Institute, Inc., Cary, NC).

Anonymous (**1986**). *StatView™* (BrainPower, Inc., Calabasas, CA).

Best, R. C., and da Silva, V. M. F. (**1989**). ''Amazon river dolphin, boto—*Inia geoffrensis* (de Blainville, 1817),'' in *Handbook of Marine Mammals*, edited by S. Ridgway and S. R. Harrison (Academic, London), Vol. 4, pp. 1–24.

Caldwell, M. C., and Caldwell, D. K. (**1967**). ''Intra-specific transfer of information via the pulsed sound in captive odontocete cetaceans,'' in *Animal Sonar Systems*, edited by R.-G. Busnel (Jouy-en-Josas, France), Vol. 2, pp. 879–936.

Caldwell, M. C., and Caldwell, D. K. (**1970**). ''Further studies on audible vocalizations of the Amazon freshwater dolphin, *Inia geoffrensis*,'' Los Angeles County Mus. Cont. Sci. **187**, 1–5.

Caldwell, M. C., Caldwell, D. K., and Evans, W. E. (**1966**). ''Sounds and behavior of captive Amazon freshwater dolphin, *Inia geoffrensis*,'' Los Angeles County Mus. Cont. Sci. **108**, 1–24.

Evans, W. E. (**1973**). ''Echolocation by marine delphinids and one species of freshwater dolphin,'' J. Acoust. Soc. Am. **54**, 191–199.

Graycar, P. (**1976**). ''Whistle dialects of the Atlantic bottlenosed dolphin,'' Ph.D. dissertation, University of Florida, Gainesville.

Herald, E. S., Brownell, Jr., R. L., Frye, F. L., Morris, E. J., Evans, W. E., and Scott, A. B. (**1969**). ''Blind river dolphin: First side-swimming cetacean,'' Science **166**, 1408–1410.

Herman, L. M., and Tavolga, W. N. (**1980**). ''The communication systems of cetaceans,'' in *Cetacean Behavior: Mechanisms and Functions*, edited by L. M. Herman (Wiley, New York), pp. 149–209.

Jing, X., Xiao, Y., and Jing, R. (**1981**). ''Acoustic signals and acoustic behavior of Chinese river dolphin (*Lipotes vexillifer*),'' Sci. Sin. **2**, 233–239.

Kamminga, C. (**1979**). ''Remarks on dominant frequencies of cetacean sonar,'' Aquat. Mammals **7**, 93–100.

Kamminga, C., van Hove, M. T., Engelsma, F. J., and Terry, R. P. (**1993**). ''A comparative analysis of underwater echolocation clicks of *Inia spp* and *Sotalia spp*,'' Aquat. Mammals **19**, 31–43.

Leatherwood, S., and Reeves, R. R. (**1983**). *The Sierra Club Handbook of Whales and Dolphins* (Sierra Club Books, San Francisco).

Mizue, K., Nishiwaki, M., and Takemura, A. (**1971**). ''The underwater sound of Ganges river dolphin (*Platanista gangetica*),'' Sci. Rep. Whales Res. Inst. **23**, 123–128.

Nekoosa, K., and Takemura, A. (**1975**). ''Studies on the underwater sound. VI. On the underwater calls of freshwater dolphins in South America,'' Bull. Fac. Fish. Nagasaki Univ. **40**, 7–13.

Norris, K. S., Harvey, G. W., Burzell, L. A., and Kartha, T. D. K. (**1972**). ''Sound production in the freshwater porpoises *Sotalia fluviatilis* Gervais and Deville and *Inia geoffrensis* Blainville, in the Rio Negro, Brazil,'' Invest. Cetacea **IV**, 251–260.

Norris, K. S., Würsig, B., Wells, R. S., Würsig, M., Brownlee, S. M., Johnson, C., and Solow, J. (**1985**). ''The behavior of the Hawaiian spinner dolphin, *Stenella longirostris*,'' Southwest Fisheries Center Administrative Report LJ-85-06C.

Penner, R. H., and Murchison, A. E. (**1970**). ''Experimentally demonstrated echolocation in the Amazon River porpoise, *Inia geoffrensis* (Blainville),'' Naval Undersea Research and Development Center Technical Publication 187.

Steiner, W. (**1980**). ''A comparative study of the pure tonal whistle vocalizations from five western north Atlantic dolphin species,'' Ph.D. dissertation, University of Rhode Island, Kingston.

Steiner, W. (**1981**). ''Species-specific differences in pure tonal whistle vocalizations of five western north Atlantic dolphin species,'' Behav. Ecol. Sociobiol. **9**, 241–246.

Wang, D. (**1993**). ''Dolphin whistles: Comparisons between populations and species,'' Ph.D. dissertation, Texas A&M University, and Institute of Hydrobiology, the Chinese Academy of Sciences, People's Republic of China.

Wang, D., Lu, W., and Wang, K. (**1989**). ''A preliminary study of the acoustic behavior of the baiji, *Lipotes vexillifer*,'' Occasional Papers of the IUCN Species Survival Commission (SSC) No. 3, pp. 137–140.

Wang, D., Würsig, B., and Evans, W. (**1995a**). ''Whistles of bottlenose dolphins: Comparisons among populations,'' Aquat. Mammals **21**, 65–77.

Wang, D., Würsig, B., and Evans, W. (**1995b**). ''Comparisons of whistles among seven odontocete species,'' in *Sensory Systems of Aquatic Mammals*, edited by R. Kastelein, J. Thomas, and P. Nachtigall (De Spil, Woerden, The Netherlands), pp. 299–323.

Wang, D., Wang, K., Akamatsu, T., and Fujita, F. (**1999**). ''Study on whistles of the Chinese River Dolphin or baiji (*Lipotes vexillifer*),'' Ocean. Limonol. Sin. **30**(4), 349–354.

Wiersma, H. (**1982**). ''A comparison of wave shapes of odontocete sonar signals,'' Aquat. Mammals **9**, 57–66.

Würsig, B. (**1994**). Unpublished data.

Sound localization in a new-world frugivorous bat, *Artibeus jamaicensis*: Acuity, use of binaural cues, and relationship to vision

Rickye S. Heffner,[a] Gimseong Koay, and Henry E. Heffner
Department of Psychology, University of Toledo, 2801 West Bancroft Street, Toledo, Ohio 43606

(Received 23 July 2000; accepted for publication 2 October 2000)

Passive sound-localization acuity and its relationship to vision were determined for the echolocating Jamaican fruit bat (*Artibeus jamaicensis*). A conditioned avoidance procedure was used in which the animals drank fruit juice from a spout in the presence of sounds from their right, but suppressed their behavior, breaking contact with the spout, whenever a sound came from their left, thereby avoiding a mild shock. The mean minimum audible angle for three bats for a 100-ms noise burst was 10°—marginally superior to the 11.6° threshold for Egyptian fruit bats and the 14° threshold for big brown bats. Jamaican fruit bats were also able to localize both low- and high-frequency pure tones, indicating that they can use both binaural phase- and intensity-difference cues to locus. Indeed, their ability to use the binaural phase cue extends up to 6.3 kHz, the highest frequency so far for a mammal. The width of their field of best vision, defined anatomically as the width of the retinal area containing ganglion-cell densities at least 75% of maximum, is 34°. This value is consistent with the previously established relationship between vision and hearing indicating that, even in echolocating bats, the primary function of passive sound localization is to direct the eyes to sound sources. [DOI: 10.1121/1.1329620]

PACS numbers: 43.80.Lb, 43.80.Jz [WA]

I. INTRODUCTION

A major feature of mammalian hearing is the wide, but systematic, variation in the ability of different species to localize sound. Two aspects of sound localization in particular vary in predictable ways: sound-localization acuity and the upper limit of the ability to use the binaural phase-difference cue.

First, sound-localization acuity, as revealed by minimum audible angle, extends over a wide range from the 1–2° acuity of humans and elephants, to the 25° acuity of some rodents and hoofed animals, to the inability of subterranean species to localize brief sounds (H. Heffner and Heffner, 1998). However, this variation is not due to special adaptations on the part of individual species to specific ecological niches, such as whether an animal is a predator or prey, nocturnal or diurnal. Nor is it simply related to the magnitude of the available binaural locus cues, as reflected in an animal's head size. Instead, the variation in sound-localization acuity is related to the width of the field of best vision such that animals with narrow fields of best vision have good localization acuity, whereas those with broader fields of best vision have poorer acuity (R. Heffner and Heffner, 1992b; R. Heffner, Koay, and Heffner, 1999). The explanation for this relationship is that a major function of sound localization is to direct an animal's field of best vision to the source of a sound. The accuracy with which the ears must direct the eyes depends on the width of the visual field being directed. Thus, species with narrow fields of best vision, such as humans, require more accurate information about the locus of a sound source than species with wide visual streaks, such as cattle, and those that do not use vision (subterranean mammals) do not localize sound at all.

The second feature of sound localization that shows systematic variation is the upper limit of use of the binaural phase cue, a subset of the binaural time cue that involves detecting differences in the phase of a pure tone reaching the two ears. In general, most mammals are able to use both binaural locus cues, the difference in the time of arrival as well as the difference in the intensity of a sound at the two ears, although a few species rely on only one or the other of the cues (R. Heffner and Heffner, 1989, 1992a; Koay *et al.*, 1998b). Among those species that use the binaural time cue, the upper frequency limit for using it can be measured by determining the highest frequency at which the animal can detect differences in the phase of a pure tone reaching the two ears or the highest frequency that can be localized free field using only the binaural phase-difference cue. For example, humans can use the binaural phase cue at frequencies up to 1.3 kHz (Klump and Eady, 1956) and chinchillas up to 2.4 kHz (R. Heffner *et al.*, 1994), whereas the Egyptian fruit bat (*Rousettus aegyptiacus*) can use the binaural phase cue at frequencies as high as 5.6 kHz (R. Heffner, Koay, and Heffner, 1999). This variation in the upper limit of binaural phase is not random, but is inversely related to interaural distance such that small species with close-set ears have a higher upper limit than larger species (e.g., Brown, 1994; R. Heffner *et al.*, 1999). This relationship is based on the fact that the phase cue becomes physically ambiguous at lower frequencies for larger mammals than it does for smaller mammals. However, some interaural distances may be too small to provide useful time differences and an animal may relinquish binaural time analysis altogether, as apparently has happened with some small mammals such as big brown

[a]Electronic mail: RHeffne@pop3.utoledo.edu

bats, hedgehogs, and spiny mice (Koay *et al.*, 1998b; Masterton *et al.*, 1975; Mooney, 1992).

Because an understanding of the variation in sound localization is relevant to the physiological as well as the ecological study of hearing, it is important to extend our observations to additional species. Bats, of which there are more than 950 species, are of particular interest because so many have developed the use of active sonar entailing a variety of auditory specializations. Further, bats are a diverse group ranging from the insectivores familiar in temperate and even cold climates to tropical bats that eat meat, fish, blood, fruit, and nectar—adaptations which impose different demands on sonar for orientation and feeding (Arita and Fenton, 1997). Knowledge of their passive localization abilities would broaden the sample upon which to base an understanding of mammalian sound localization. Moreover, whereas big brown bats have relinquished the use of binaural time cues, Egyptian fruit bats can extract binaural phase cues at higher frequencies than other mammals, which suggests that the study of bats may shed more light on the use of this cue in small mammals.

Accordingly, the purpose of this study was to broaden the sample on which to base a comparative analysis of the hearing of bats by determining the passive sound-localization abilities of the Jamaican fruit bat (*Artibeus jamaicensis*), a microchiropteran bat found in Central and South America. The Jamaican fruit bat is a leaf-nosed bat (*Phyllostomidae*) and, because of its very low-intensity sonar signal, is also known as a whispering bat (Griffin, 1958). Its diet consists of fruit, mainly figs, concealed in leaf clutter high in the canopy, which it locates and identifies using olfaction, although sonar may be used in the final approach to a food item (Bonaccorso and Gush, 1987; Kalko, Herre, and Handley, 1996). Nevertheless, Jamaican fruit bats rely heavily on echolocation for orientation, and their frequency-modulated sonar is comparable to that of insectivorous bats, allowing them to detect and avoid wires of 0.175 mm diameter (Griffin and Novick, 1955). These features are in contrast to those of the old-world fruit bat, *Rousettus aegyptiacus*, that makes limited use of echolocation and relies on olfaction and vision to find fruit (Kwiecinski and Griffiths, 1999). Both of these species differ, in turn, from the insectivorous big brown bat (*Eptesicus fuscus*) that relies on echolocation to identify and capture prey (Arita and Fenton, 1997). At 40–50 g, the Jamaican fruit bat is intermediate in size between the 15-g big brown bat and the 80–150-g Egyptian fruit bat.

This study was a threefold investigation of the passive sound-localization abilities of Jamaican fruit bats to determine how this species compares with other mammals as well as with other bats. First, we determined the animals' left–right sound-localization acuity (minimum audible angle) using a standard 100-ms broadband noise burst. We then examined their ability to use binaural time- and intensity-difference cues for sound localization by determining their ability to localize pure tones at a fixed angle of 60° horizontal separation. In addition, sinusoidally amplitude-modulated tones were used to explore the bats' use of envelope-based time cues. Finally, we measured the packing density of their retinal ganglion cells to estimate visual resolution throughout the retina and evaluate the relation between the width of the field of best vision and sound-localization acuity. The resulting data are compared with those for other mammals.

II. METHODS

The behavioral sound-localization tests used a conditioning procedure in which a hungry animal steadily licked a food spout while sounds were presented from a loudspeaker to its right, but suppressed ongoing eating and broke contact with the spout when sounds were presented from a loudspeaker to its left to avoid a mild shock (H. Heffner and Heffner, 1995). The anatomical procedure involved mapping the ganglion cell densities throughout the retina of a Jamaican fruit bat.

A. Subjects

Three Jamaican fruit bats (*Artibeus jamaicensis*), one female (A) and two males (B and C), were used in the behavioral tests and a fourth bat was used for the anatomical analysis of the retina. The animals were individually housed with free access to water, with vitamin and mineral supplements (Lambert Kay Avimin and Avitron), and received a food reward of fruit juice during the daily test session. The animals typically consumed 18–25 cc of juice in sessions lasting up to 2 h. The natural feeding pattern of these bats is to eat their fill quickly, digest the meal in about 20 min, and then eat at least once more. The long test sessions, accordingly, consisted of periods during which they were not working but instead digesting the food. Additional supplements of fruit juice were given as needed to maintain a healthy body weight.

B. Behavioral apparatus

Testing was conducted in a carpeted, double-walled acoustic chamber (IAC model 1204; 2.55×2.75×2.05 m), the walls and ceiling of which were lined with eggcrate foam. The equipment for behavioral control and stimulus generation was located outside the chamber and the animals were monitored via closed-circuit television.

The bats were tested in a cage (37×22×23 cm) constructed of 0.5-in. (1.26-cm) hardware cloth, mounted 93 cm above the floor on an adjustable tripod (see Koay *et al.*, 1998a, for an illustration of the test cage). A food spout (3-mm-diameter brass tube topped with a 7×8-mm ''lick'' plate) was mounted vertically so that it projected up through the bottom of the cage 6 cm above the cage floor. The spout was attached via an 80-cm-long plastic tube to a 30-cc syringe filled with fruit juice located below the cage. The fruit juice, a mixture of cantaloupe, pear juice, and sugar, finely blended and strained through a tea strainer (0.5×1.0-mm openings), was dispensed though the spout by a syringe pump similar to that described elsewhere (Thompson *et al.*, 1990). Both the syringe pump and food reservoir were housed in a high-density polyethylene plastic box (64 ×212×28 cm) lined with eggcrate foam to eliminate any noise from the pump.

During testing, the bats were placed on a small platform (13×7×7 cm) located directly behind the spout. The top of

the platform was covered with a piece of dampened carpet to facilitate traction and ensure good electrical contact while the bat ate from the spout. The tip of the food spout was placed in front of and at the same height as the platform to minimize obstructions between the animal's ears and the loudspeaker. A contact circuit, connected between the food spout and platform, detected when an animal made contact with the spout and activated the syringe pump to dispense a trickle of juice. Requiring the bat to maintain mouth contact with the spout served to fix its head within the sound field.

Finally, a mild shock was delivered by a shock generator connected between the food spout and platform. The shock was adjusted for each individual to the lowest level that produced a consistent avoidance response (backing away slightly from the spout or lifting its head away from the spout) to a readily detected signal. The bats never developed a fear of the spout, as they readily returned to it after the shock. A 25-W light, mounted 0.5 m below the cage, was turned on and off with the shock to signal successful avoidance and to indicate when it was safe to return to the food spout.

C. Acoustical apparatus

Sound-localization ability was assessed using broadband noise bursts, pure tones, and sinusoidally amplitude-modulated tones. The sounds were presented through loudspeakers mounted at ear level on a perimeter bar (102 cm radius, 101 cm height) and centered on the position occupied by an animal's head while it was drinking from the spout.

1. Broadband noise

The minimum audible angle for Jamaican fruit bats was determined using a standard 100-ms noise burst. Such a signal provides good binaural and monaural locus cues but is brief enough to minimize opportunities for scanning movements. Because echolocation was of no use in determining which speaker had been active, echolocation and scanning movements of the pinnae extinguished early in training. An additional threshold was obtained for Bat A using a train of five 2-ms noise pulses (2 ms on, 18 ms off). The noise bursts were generated by a noise generator (Stanford Research Systems 770, set to produce energy up to 100 kHz). The electrical signal was randomly attenuated over a 3.5-dB range (Coulbourn S85-08 programmable attenuator) from one trial to the next to reduce the possibility of the animals responding on the basis of small intensity differences. The signal was then sent to a rise–fall gate (Coulbourn S84-04; 0.1-ms rise/fall), split into left and right channels, amplified to 68 dB sound-pressure level (Coulbourn S82-24), and routed to one of a pair of loudspeakers. Three matched pairs of Motorola piezoelectric speakers (model KSN1005A) were used. In a single session, the bats were tested at three angles of separation then the speakers were moved to three different angles for a total of six angles in a session. The members of each pair of speakers were switched before each session to reduce the possibility that the animals might respond on the basis of speaker quality. The signal going to the speakers was monitored with an oscilloscope and calibrated at the beginning of each test session (see below). These precautions were adequate to prevent responses to nonlocus cues as attested by each animal's chance performance at small angles of speaker separation.

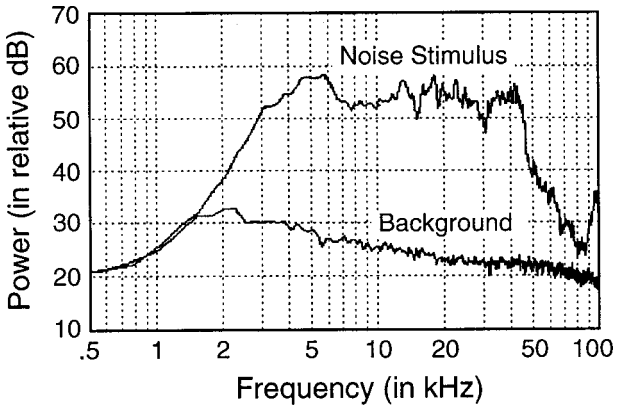

FIG. 1. Spectrum of the broadband noise stimulus used for sound localization (upper line) compared to background noise (lower line). The 100-ms noise burst included frequencies throughout all but the upper half-octave of the hearing range for this species, which at a level of 60 dB SPL extends from 2.8 to 130 kHz (Koay *et al.*, 1999).

The spectrum of the noise produced by this acoustic apparatus was monitored using a spectrum analyzer (Zonic 3525) and 1/4-in. (0.64-cm) microphone (Brüel & Kjaer 2619). As illustrated in Fig. 1, the noise spectrum was relatively flat (± 3 dB) between 3 and 45 kHz with energy above background level up to 100 kHz. Thus, the signal included frequencies throughout most of the hearing range of this species (2.8–130 kHz, Koay *et al.*, 1999). A detection threshold for this signal was behaviorally determined for Bat B and found to be -2 dB, so that the signal used for noise localization was approximately 70 dB hearing level. Lower intensities were also used with this animal to assess the effect of intensity on performance.

2. Pure tones

Sine waves were generated by a tone generator (Krohn-Hite 2400 AM/FM Phase Lock Generator) and randomly attenuated over a 3.5-dB range from one trial to the next (Coulbourn S85-08 programmable attenuator). The tones were pulsed (100 ms on and 1000 ms off, for two pulses), shaped by a rise–fall gate (Coulbourn S84-04; 10 ms rise/fall) and bandpass filtered (Krohn-Hite 3550; 1/3 octave above and below the frequency of the tone). Finally, the signal was split into left and right channels, separately amplified (Coulbourn S82-24), and sent to one of two loudspeakers (Motorola piezoelectric KSN1005A). The acoustic signal at the location of a listening bat was analyzed for overtones using a spectrum analyzer (Zonic 3525) and any harmonics in the acoustic signal were at least 40 dB below the fundamental frequency and below the animal's detection threshold. Tones were calibrated at the beginning and end of each test session (see below).

Testing was conducted with the loudspeakers placed 60° apart (30° to the left and right of midline) at the following frequencies: 4, 5.6, 6.3, 8, 12.5, 16, 20, 40, and 56 kHz. Each frequency was presented at 50 dB above the average

absolute threshold for the Jamaican fruit bat (Koay *et al.*, 1999). To assure that motivation and performance had been maintained throughout the session, each session began and ended with a few trials using a stimulus that elicited good performance.

Additional tests used sinusoidal amplitude modulation of an 8-kHz tone (Krohn-Hite 2400 AM/FM Phase Lock Generator) that provided an ongoing binaural time-difference cue in the envelope of the signal. Modulation rates ranging from 50 Hz to 2 kHz at 100% modulation depth were used. A 10-ms rise/decay was retained in order to avoid onset and offset transients.

D. Sound-level measurement

The sound-pressure levels of the stimuli (SPL *re* 20 $\mu N/m^2$) were measured and the left and right loudspeakers were equated daily with a 1/4-in. (0.64 cm) microphone (Brüel & Kjaer 4135, protective grid removed), preamplifier (Brüel & Kjaer 2619), measuring amplifier (Brüel & Kjaer 2608), and filter (Krohn-Hite 3202; bandpass range set at 250 Hz–100 kHz) and spectrum analyzer (Zonic 3525) to permit detection of any harmonics that might be present. This measuring system was calibrated with a pistonphone (Brüel & Kjaer 4230). Sound measurements were taken by placing the microphone in the position occupied by the animal's head and pointing it directly towards a loudspeaker (0° incidence).

E. Behavioral procedure

1. Training

The animals were first trained to drink steadily from the spout in the presence of a series of four 400-ms broadband noise bursts (100-ms interburst intervals), presented from a loudspeaker located 90° to the right of the animal. Next, the animals were trained to break contact with the spout (a ''detection response'') whenever the noise bursts were presented from a loudspeaker located 90° to their left to avoid a mild electric shock (0.5 s) delivered via the spout 2.0 s after left signal onset. Breaking contact with the spout indicated that the animal had detected the new locus of the sound. The light bulb located underneath the cage was turned on while the shock was on to provide feedback for a successful avoidance (since in those cases no shock was actually received by the bat) and permitted the animals to distinguish between successful avoidance of a shock and false alarms (i.e., breaking contact when the signal was presented from the right side). After the animals were trained in the basic avoidance procedure, the signals were reduced to one 100-ms noise burst per 2-s trial.

2. Testing

Test sessions consisted of a series of 2-s trials separated by 1.5-s intertrial intervals. Thus, the animals received one signal every 3.5 s and made a decision after each as to whether to break contact or to continue drinking. The response of an animal on each trial (i.e., whether or not it made a detection response) was defined as the duration of contact with the spout during the last 150 ms of each 2-s trial. If the animal broke contact for more than half of the 150-ms period, a response was recorded. The response was classified as a ''hit'' if the preceding signal had come from the animal's left side and as a ''false alarm'' if it had come from the animal's right. If the bat was not in contact with the spout during the 1 s preceding a trial, data from that trial was not recorded even though the trial proceeded as usual. This avoided using trials in which the animal was grooming or otherwise not engaged in the task.

Each trial had a 22% probability of containing a left signal. The sequence of left–right trials was quasirandom and is described in detail elsewhere (H. Heffner and Heffner, 1995). Both hit- and false-alarm rates were determined for each block of approximately 7–9 left trials and approximately 28–36 associated right trials for each stimulus type and angle. The hit rate was then corrected for the false-alarm rate to produce a performance measure according to the formula: performance=hit rate-(false-alarm rate×hit rate). This measure varies from 0 (no hits) to 1 (100% hit rate with no false alarms). Note that the calculation proportionately reduces the hit rate by the false-alarm rate observed for each block of trials in each stimulus condition, rather than by the average false-alarm rate for an session as false-alarm rates may vary within a session depending on the discriminability of the stimulus.

Noise localization thresholds were determined by gradually reducing the angular separation between the left and right loudspeakers. Blocks of trials, usually containing 7–9 left signal trials, were given at each angle until the animal could no longer discriminate reliably (that is, the hit rate no longer differed significantly from the false-alarm rate, binomial distribution, $P>0.05$). A typical session consisted of approximately 50 to 60 warning trials (plus approximately 200 to 250 associated safe trials) during which six different angles were tested. Daily testing continued until performance no longer improved at any angle, that is, asymptotic performance had been reached (eight sessions for Bats A and C, and nine sessions for Bat B). The mean of the three trial blocks with the highest scores was calculated to represent the best performance for each animal. If none of the trial blocks showed performance above chance, all scores were included in the average. These means were then plotted as the best performance curve for each individual. Threshold was defined as the angle yielding a performance score of 0.50, which was determined by interpolation. The angles tested were 180°, 120°, 90°, 60°, 45°, 30°, 20°, 15°, 10°, and 5°.

Tone localization tests were conducted at a fixed angular separation of 60° (30° to the left and right of the animal's midline), with the animal's performance calculated for blocks of trials containing 7–9 left trials (plus associated right trials). Testing was carried out using a single frequency per session for frequencies that sustained good performance. However, if an animal had difficulty or was unable to localize a particular frequency, as happened at 8 and 12 kHz, broadband noise was presented for several trials to verify that the animal was still sufficiently motivated. Each frequency was tested during at least three sessions for an average of 90–100 warning trials. The top 50% of the trial blocks

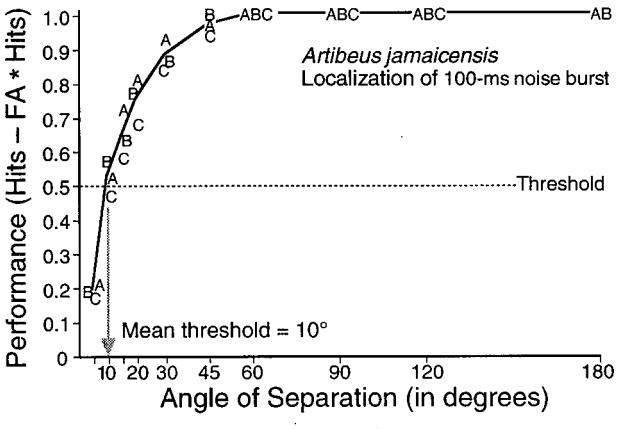

FIG. 2. Sound-localization performance of three Jamaican fruit bats for a single 100-ms burst of broadband noise. Letters indicate individual animals and the dashed line indicates the 0.50-performance level used to define threshold. The arrow indicates the mean threshold of 10°.

were averaged to represent the best overall performance the animals were capable of sustaining.

F. Anatomical procedure

One bat was anesthetized with an overdose of ketamine (80 mg/kg) plus xylazine (4 mg/kg) intramuscularly and perfused with 0.9% saline, followed by 10% formalin. The superior surface of the eyes was marked with fine suture and the eyes were removed and the retinas dissected free from the sclera. The retinas were then mounted on heavily gelatinized slides with the ganglion-cell layer uppermost, and stained with thionine (Stone, 1981). The density of the ganglion cells was determined throughout the retina in 0.1-mm steps through the regions of relatively high ganglion-cell density and 0.5-mm steps in the periphery. The number of ganglion-cell nucleoli within a sampling rectangle 33×52 μm (0.001 716 mm^2) were counted using a 100X oil-immersion objective. To make comparisons between species, the horizontal width of the region encompassing ganglion-cell densities equal to or greater than 75% of maximum density was determined as an indication of the width of the field of best vision. The maximum number of cells/deg^2 was then used to calculate the maximum theoretical resolvable spatial frequency in cycles per degree (i.e., the maximum number of cycles of a square wave grating—alternating black and white bars—that can be resolved per degree of visual angle) using Shannon's sampling theorem (e.g., DeBruyn, Wise, and Casagrande, 1980). For additional details of the method, see R. Heffner and Heffner (1992b).

These experiments were carried out with the approval of the University of Toledo Animal Care and Use Committee.

III. RESULTS

A. Behavioral results

1. Noise localization

The ability of the three Jamaican fruit bats to localize 100-ms noise bursts emitted from loudspeakers centered symmetrically about midline is illustrated in Fig. 2. The animals were capable of near-perfect performance at angles of 45° and larger. Performance began to fall at 30° and no animal performed above chance at 5°. The 50% corrected detection thresholds (to the nearest 0.5°) for animals A, B, and C were 9.5°, 9°, and 11.5°, respectively, for a mean threshold of 10°. Bat A was also tested using a 100-ms burst of five 2-ms noise pulses mimicking the temporal pattern of the echolocation call. Similar excellent performance and the same threshold of 10° were obtained with this stimulus, indicating that there is no unusual sensitivity associated with, or required for, very brief signals.

The extensive training (49 sessions), excellent performance at large and moderate angles, sharp decline in performance as threshold is approached, and close agreement between the animals suggest that the thresholds are representative for this species. As has been found for other mammals, auditory sensory abilities seem to vary little between young, healthy individuals of the same species (R. Heffner and Heffner, 1988, 1991; Koay, Heffner, and Heffner, 1997).

The effect of signal intensity on localizability was also investigated to determine whether it might have had an effect on the bats' performances. This was done by assessing the ability of bat B to localize 100-ms noise bursts of 30–68 dB SPL (32–70 dB above detection threshold) at 60° separation. The resulting performance scores were quite similar at all intensities, ranging from 0.86 to 1.00 and did not differ systematically with intensity. Thus, intensity of the noise burst had no noticeable effect on localizability of these brief broadband signals through a wide range of moderate listening levels, suggesting that any effect of the small variations in intensity used in subsequent tests would be negligible.

2. Pure-tone localization

To determine the ability of Jamaican fruit bats to use the binaural time- and intensity-difference cues for locus, two animals were tested for their ability to localize brief tone pips ranging from 4 to 56 kHz. This test is based on the absence of binaural intensity-difference cues at low frequencies, as low frequencies undergo little or no attenuation as they travel around the head and thus do not present different intensities to the two ears. Low frequencies do, however, permit the comparison of the arrival time of a pure tone at the two ears, referred to as the phase-difference cue. The phase-difference cue becomes ambiguous for pure tones at high frequencies when successive cycles are too close for the nervous system to match the arrival of the same cycle at the two ears. This occurs when more than one-half cycle of the tone occurs during the time it takes for the sound to travel from one ear to the other. Travel time, in turn, is dependent on both the distance between the ears and the distance of the sound source from midline. The calculated frequency at which the phase cue would become physically ambiguous for the Jamaican fruit bat (with a head diameter of 1.78 cm) at an angle of $\pm30°$ is 12.6 kHz, indicated by the shaded vertical bar in Fig. 3. (For a detailed discussion of phase ambiguity, see Jackson, 1996, or Saberi, Farahbod, and Konishi, 1998; for a formula for calculating the frequency of

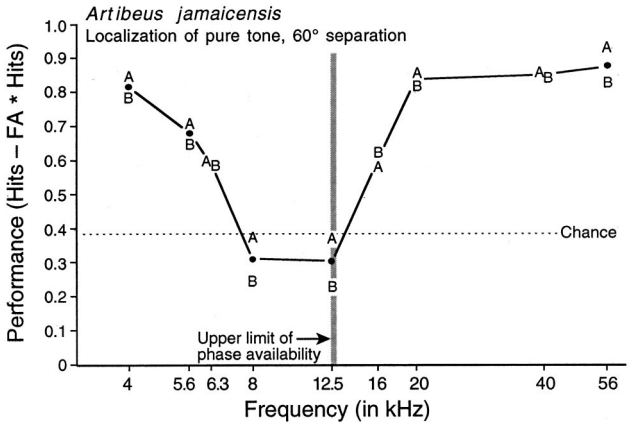

FIG. 3. Sound-localization performance for two Jamaican fruit bats as a function of the frequency of a pure-tone stimulus (two pulses of 100 ms duration, 1-s interpulse interval) at a fixed angle of separation (±30° azimuth). Letters represent individual animals; vertical bar indicates the upper limit of the physical availability of the binaural phase-difference cue at this angle for Jamaican fruit bats (12.6 kHz). Note that the animals perform well at frequencies both above and below the frequency of ambiguity, indicating that they can use both binaural phase- and intensity-difference cues. However, performance falls to chance at 8–12.5 kHz, indicating the absence of adequate locus cues in this frequency range.

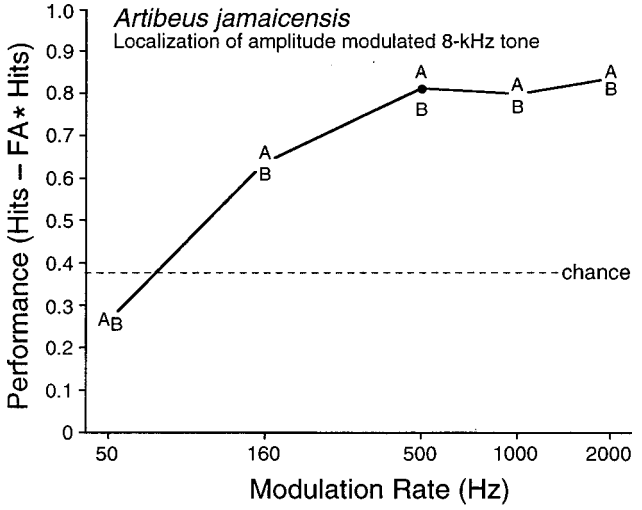

FIG. 4. Sound-localization performance for two Jamaican fruit bats as a function of the modulation rate of an 8-kHz tone at a fixed angle of separation (±30° azimuth). Without modulation, the 8-kHz tone was not localizable (cf. Fig. 3), but modulation rates of 160 Hz or higher permitted good to excellent localization in both bats.

ambiguity, see Kuhn, 1977.) Thus, above this ''frequency of ambiguity'' binaural intensity differences must provide the cue to locus.

Figure 3 illustrates the localization performances of the two Jamaican fruit bats as a function of frequency. The bats showed good agreement in their tone localization and are able to use both binaural locus cues. The bats' use of binaural phase differences is indicated by their good performance at lower frequencies of 4–6.3 kHz. (Frequencies below 4 kHz were not tested because the hearing of Jamaican fruit bats becomes too insensitive below this frequency to permit undistorted tones at 50 dB above threshold.) Performances were also good at frequencies of 20 kHz and above (ranging between 0.82 and 0.93), frequencies for which only the interaural intensity-difference cue was available. In summary, their good performances at frequencies both above and below the frequency of ambiguity demonstrated that they are capable of using both binaural phase and intensity differences for localization.

However, the performance of both animals fell markedly at intermediate frequencies—at both 8 and 12.5 kHz, Bat A performed above chance on only about half of the trial blocks, and Bat B never performed above chance at all, indicating that neither binaural cue was effective. The upper limit of their use of the binaural phase cue thus appears to be about 6.3 kHz. Wavelengths of 8–12.5 kHz tones are apparently too long for the head and pinnae to shadow and produce an effective binaural intensity difference in a bat of this size at ±30°, as earlier suggested by acoustic measures on several species of bats (Obrist *et al.*, 1993).

The chance performance at 8–12.5 kHz, at which neither binaural phase nor intensity cues were usable indicates that no other usable cues were available. This finding rules out the possibility that the bats could localize using the transient onset difference, which is the difference in the arrival time of the leading edge of a sound at the two ears. It should be noted, however, that the magnitude of the onset difference was somewhat reduced by the 10-ms rise/decay time used here to reduce the possibility of onset and offset clicks. Thus, within these limitations, there was no indication that the Jamaican fruit bats used the transient onset difference to localize sound.

3. Sinusoidal amplitude modulation

To further explore the ability of Jamaican fruit bats to use binaural time differences, we modulated the amplitude of the previously unlocalizable 8-kHz tone at rates ranging from 50 to 2000 Hz (sinusoidal modulation, 100% depth). The amplitude modulation presented the bats with an additional time cue, namely the variation in the envelope of the 8-kHz tone. However, it also resulted in the production of sidelobes, i.e., tones of frequencies equal to the 8-kHz tone plus and minus the modulation rate. For example, modulating the 8-kHz tone at 2 kHz produced sidelobes of 6 and 10 kHz. Thus, in analyzing the results, it is necessary to rule out the possibility that any improvement in performance was due to the presence of the sidelobes.

As illustrated in Fig. 4, modulating the tone markedly improved the performance of both bats. Moreover, the improvement was much greater than could be attributed to the presence of sidelobes. For example, the bats' average performance at a 500-Hz modulation rate was 0.80, whereas the interpolated performance for a sidelobe of 7.5 kHz is less than 0.50 and the 8.5-kHz sidelobe would still be unlocalizable (cf. Fig. 4). Indeed, even at the 2-kHz modulation rate, the animals' average performance of 0.83 is well above the interpolated performance for a 6-kHz sidelobe, which is approximately 0.60. Thus, it appears that the improvement in performance was due to the ability of the bats to extract a binaural time difference cue from the envelope of the amplitude-modulated signal.

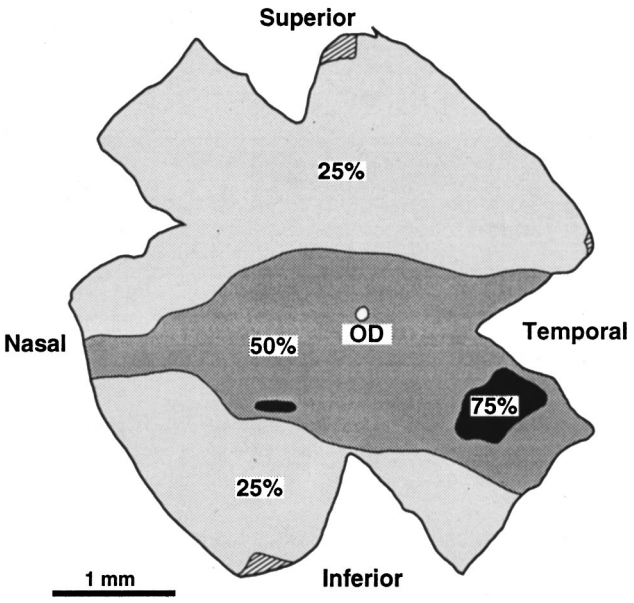

FIG. 5. Retinal ganglion-cell isodensity contours in the retina of a Jamaican fruit bat. Density is expressed as a proportion of the maximum density (9325 cells/mm^2). Density gradients are relatively shallow and remain at least 38% of maximum in the inferior retina and at least 30% of maximum in the superior retina. An unpronounced visual streak extending across the entire horizon of the retina can be seen in the region encompassing densities at least 50% of maximum. OD, optic disk; black indicates densities of 75%–100% of maximum; dark gray indicates densities of 50%–75% of maximum; light gray indicates densities of 25%–50% of maximum; hatching indicates areas not counted due to folds in the tissue.

B. Retinal analysis

The flattened retina of the Jamaican fruit bat was approximately 4.4 mm in diameter and subtended approximately 180° of arc. The ganglion-cell layer was well separated from the inner nuclear layer and was unremarkable, with cells ranging from about 4–12 μm diameter. Few small cells having the appearance of glia were observed and were not likely to have contaminated the enumeration of ganglion cells. The isodensity contours of the retina are illustrated in Fig. 5. The ganglion cells reached a relatively high peak density of 9325 cells/mm^2 that, in an eye of this size, suggests a visual acuity of only 1.1 cycles per degree. This level of acuity is very similar to the 1.35 cycles per degree previously estimated for a closely related species, *Artibeus cinereus* (Pettigrew *et al.*, 1988).

The region of greatest ganglion-cell density, and thus of best vision, is concentrated in the temporal retina. From this region, the density of the ganglion cells decreases gradually toward the periphery. Nowhere does ganglion-cell density fall below 30% of maximum. There is a visual streak across the horizon of the retina in which ganglion cell densities remain above 50% of maximum. The width of the field of best vision for this animal, as defined by the portion of the retina with ganglion-cell densities at least 75% of maximum, is 34° (Fig. 5). This value is much smaller than the 139° in the big brown bat but slightly greater than the 27° in the Egyptian fruit bat, the only other bats for which this measure is available (R. Heffner, Koay, and Heffner, 1999; Koay *et al.*, 1998b).

IV. DISCUSSION

The 10° threshold of Jamaican fruit bats falls within one standard deviation (2.4°) of the 12° mean threshold for all surface-dwelling mammals (i.e., excluding aquatic and subterranean species). Compared with other mammals, its acuity is most similar to that of Norway rats (9–11°) and sea lions (8.8°) (Kavanagh and Kelly, 1986; Kelly, 1980; H. Heffner and Heffner, 1985; Moore, 1975). Compared with other bats, the Jamaican fruit bat's acuity is slightly superior to the 14° acuity of the big brown bat and even to the 11.6° acuity of Egyptian fruit bats (R. Heffner *et al.*, 1999; Koay *et al.*, 1998b).

Of interest is how well a bat's passive sound-localization ability compares with its active echolocation. Jamaican fruit bats have been reported to reliably avoid wires as small as 0.175 mm using echolocation, although this may be due in part to their relatively slow and cautious manner of flight (Griffin and Novick, 1955). The insectivorous big brown bats, which have a passive localization acuity of 14°, are able to detect and avoid much smaller wires (0.06 mm) using echolocation (Schnitzler and Henson, 1980). In comparison, Egyptian fruit bats, the only old-world fruit bat that echolocates (albeit with tongue clicks rather than phonation) show passive localization acuity (11.6°) comparable to the Jamaican fruit bats, but avoids wires only as small as 0.5 mm using its rudimentary echolocation (Griffin, Novick, and Kornfield, 1958). Thus, among the three species for which data are available, acuities for active and passive localization appear unrelated, suggesting that the two abilities may be served at least in part by independent processes.

A. Sound localization and vision

The Jamaican fruit bats' intermediate localization acuity, coupled with a moderately broad field of best vision, provides support for the hypothesis that sound-localization acuity is driven by the requirements of the visual system. Specifically, sound-localization acuity among mammals appears to be primarily determined by the need to direct the eyes to the source of a sound (R. Heffner and Heffner, 1992b). Indeed, studies of attention support the conclusion that sounds exert a powerful effect on visual attention, but that the relationship is not symmetrical in that vision does not readily direct auditory attention (Spence and Driver, 1997). Thus, it appears that vision is exerting selective pressure on sound-localization acuity rather than the other way around.

Furthermore, just how accurate sound localization must be to direct the eyes seems to depend on the width of an animal's field of best vision. Animals with narrow fields of best vision, such as humans, require good sound-localization acuity to direct their gaze so that the visual image of the sound source falls upon their fovea, whereas animals with broad fields, such as those with visual streaks, do not require as high a degree of sound-localization acuity to direct their gaze to the source of a sound. The relationship between the

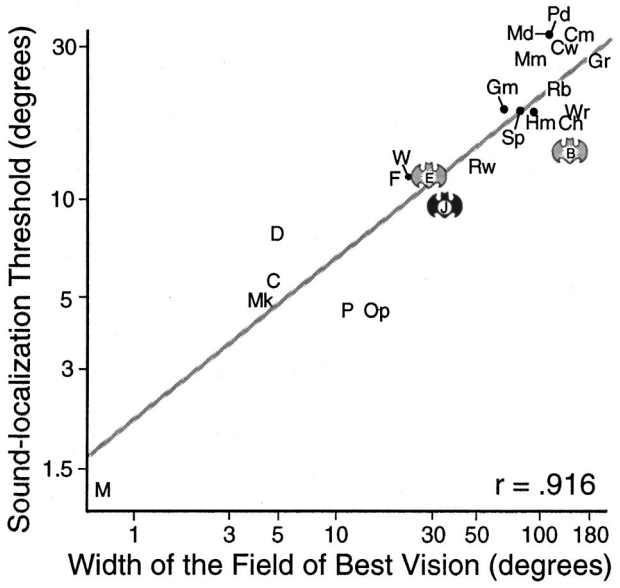

FIG. 6. Relationship between the width of the field of best vision (region of ganglion-cell densities at least 75% of maximum) and sound-localization threshold for 24 species of mammals (note logarithmic scale on both axes). Species with narrow fields of best vision have better localization acuity (smaller thresholds) than species with broad fields of best vision, $r = 0.916$, $P < 0.0001$. **B**, big brown bat (*Eptesicus fuscus*); **C**, domestic cat (*Felis domesticus*); **Ch**, chinchilla (*Chinchilla laniger*); **Cm**, chipmunk (*Tamias striatus*); **Cw**, cow (*Bos taurus*); **D**, dog (*Canis familiaris*); **E**, Egyptian fruit bat (*Rousettus aegyptiacus*); **F**, ferret (*Mustela putorius*); **Gm**, grasshopper mouse (*Onychomys leucogaster*); **Gr**, gerbil (*Meriones unguiculatus*); **Hm**, hamster (*Mesocricetus auritus*); **J**, Jamaican fruit bat (*Artibeus jamaicensis*); **M**, man (*Homo sapiens*); **Md**, domestic mouse (*Mus musculus*); **Mk**, macaque (*Macaca fuscata*); **Mm**, marmot (*Marmota monax*); **Op**, virginia opossum (*Didelphis virginiana*); **P**, pig (*Sus scrofa*); **Pd**, prairie dog (*Cynomys ludovicianus*); **Rb**, domestic rabbit (*Oryctolagus cuniculus*); **Rw**, wild norway rat (*Rattus norvegicus*); **Sp**, spiny mouse (*Acomys cahirinus*); **W**, least weasel (*Mustela nivalis*); **Wr**, wood rat (*Neotoma floridana*); for citations, see Heffner *et al.*, 1994.

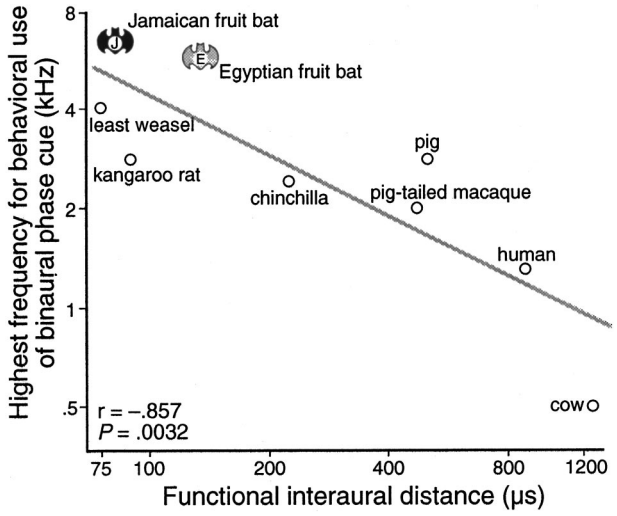

FIG. 7. Relationship between functional interaural distance and the highest frequency at which use of the binaural phase-difference cue has been demonstrated behaviorally (H. Heffner and Masterton, 1980; R. Heffner, 1981; R. Heffner and Heffner, 1987, 1989; R. Heffner *et al.*, 1994; Houben and Gourevitch, 1979; Klump and Eady, 1956). Humans and pig-tailed macaques were tested using dichotic signals; all others were tested using free-field tones.

width of the field of best vision and passive sound-localization acuity is illustrated in Fig. 6. As can be seen, mammals with narrow fields of best vision are more accurate localizers than mammals with broader fields of best vision, accounting for 84% of the variance ($r = 0.916$). Moreover, mammals that do not rely on vision, such as the subterranean pocket gopher (*Geomys bursarius*), blind mole rat (*Spalax ehrenbergi*), and naked mole rat (*Heterocephalus glaber*), and are adapted to living in dark burrows where visual scrutiny of sound sources is not possible, conform to this relationship by losing virtually all of their ability to localize sound (R. Heffner and Heffner, 1990, 1992c, 1993).

Echolocating bats are another group that one might expect to differ from typical surface-dwelling mammals because of reduced reliance on vision. As can be seen in Fig. 6, however, the three bats in the sample do not deviate from the relationship between width of the field of best vision and sound localization acuity ($P > 0.5$, t test). Thus, despite their use of active echolocation for orientation and/or prey capture, tasks accomplished largely by vision in other mammals, the bats examined so far do not appear to be unusual in the relationship between passive hearing and vision.

Although visual acuity itself is not related to sound-localization acuity (R. Heffner and Heffner, 1992b), it is of some interest to compare the visual acuity of the Jamaican fruit bat with that of other bats. The eyes of Jamaican fruit bats are smaller than those of most mammals, but larger than those of most insectivorous bats. Their estimated visual acuity of 1.1 cycles/degree, like that of other new-world fruit bats, is poorer than the visual acuity of old-world fruit bats and many other nocturnal mammals, but superior to that of insectivorous bats (e.g., Bell and Fenton, 1986; Birch and Jacobs, 1979; Pettigrew *et al.*, 1988; Suthers, 1966). They have larger and more distinct nuclei in the central nervous system for interpreting visual information than either big brown bats or the three other phyllostomid species that have been studied (Cotter, 1985; Hope and Bhatnagar, 1979). Thus, Jamaican fruit bats retain intermediate vision, probably as an aid to obstacle avoidance (Kalko *et al.*, 1996), despite their nocturnal habits and use of echolocation. However, multiple regression analysis incorporating information on the visual acuity of Jamaican fruit bats continues to indicate that absolute visual acuity is not a significant factor influencing sound localization ($P > 0.3$).

B. Use of binaural locus cues

The ability of Jamaican fruit bats to localize both low- and high-frequency pure tones indicates that they are able to use both the interaural time cue and the interaural intensity-difference cue. In this respect they are like most other mammals, including Egyptian fruit bats, that also use both binaural locus cues (e.g., R. Heffner and Heffner, 1992a). An interesting feature of the Jamaican fruit bat's ability to use the binaural phase cue, however, is that its 6.3-kHz upper limit is the highest observed so far in a mammal.

The observed upper limit of the use of the binaural phase cue in mammals spans a range greater than 3 octaves: from the 500-Hz upper limit of cattle to the 6.3-kHz upper limit of Jamaican fruit bats. As shown in Fig. 7, this varia-

tion is inversely correlated with interaural distance such that animals with large interaural distances have low upper limits and vice versa ($r=-0.857$, $P=0.0032$). The explanation for this relationship appears to lie in the physical availability of the phase cue (e.g., Brown, 1994; Jackson, 1996; R. Heffner, Koay, and Heffner, 1999). Briefly, the binaural phase cue requires the nervous system to distinguish one cycle of a waveform from another, match the portion of a cycle reaching one ear with the same portion when it reaches the other ear, and then to determine the difference in the time of arrival. At low frequencies, for which one cycle reaches both ears well before the next cycle reaches the leading ear, the phase cue is unambiguous. However, the cue becomes ambiguous when the wavelength of the tone is short relative to the distance between the ears, specifically when more than one-half cycle of the tone occurs during the time it takes for a sound to reach the two ears, because the individual cycles can no longer be distinguished with certainty. Because the maximum difference in the time of arrival depends on the interaural distance, the phase cue remains physically unambiguous at shorter wavelengths in species with shorter interaural distances. Similarly, the unambiguous wavelengths become shorter when smaller angles are presented because the time delays between the arrival of a sound at the two ears become shorter.

Although the physics of the binaural phase cue suggests that smaller animals should use the phase cue at higher frequencies, eventually an animal may become so small that the time differences available to it provide only approximate indications of locus and it may relinquish the use of binaural time cues entirely. This appears to be the case for big brown bats (*Eptesicus fuscus*), which are unable to localize frequencies below 11.2 kHz, even though its 55-μs maximum interaural time difference indicates that the binaural phase-difference cue should be unambiguous below 10.5 kHz (given maximally separated sound sources 90° from midline).

The conclusion that big brown bats cannot use binaural time cues in general was supported by the observation that its performance did not improve with amplitude modulated signals (Koay *et al.*, 1998b). Jamaican fruit bats, on the other hand, use the binaural phase cue on both a carrier signal and on an envelope. This suggests that the extraction of binaural time differences from the components of a signal and from the signal's envelope rely on the same neural mechanism. Whether animals with very small interaural distances relinquish the binaural time-difference cue because the time difference itself has become so small as to be of limited use, or because the auditory system cannot phase lock at frequencies high enough to encode phase at usefully small angles, is not known.

The results of the tone-localization tests have implications for phase locking in the mammalian nervous system. First, phase locking is used to encode the pitch of low-frequency sounds as well as to provide the basis for the binaural phase-difference cue. Because the use of phase locking for pitch may be limited to frequencies below about 1 kHz (e.g., Langner, 1997), phase locking at higher frequencies may be solely for the analysis of binaural phase differences for locus. Thus, the variation in the upper limit of binaural phase suggests that mammals may show similar variation in the upper limit of phase locking (Brown, 1994; Palmer and Russell, 1986). Second, previous studies have found that the ability of an animal to localize pure tones may decline at low frequencies (e.g., R. Heffner and Heffner, 1987). This decline has been attributed to the observation that the phase locking of neurons becomes less precise at low frequencies with multiple discharges sometimes occurring during a single cycle (Rose *et al.*, 1967). Although the performance of the Jamaican fruit bats did not decline when localizing tones (Fig. 3), this may have been because performance does not usually decline until frequency falls below 500 Hz, and the limited low-frequency hearing range of the bats prevented them from being tested below 4 kHz. However, the results of the amplitude modulation test clearly show that the performance of these animals declines for modulation frequencies below 500 Hz and that they are totally unable to extract locus from a 50-Hz modulation rate (Fig. 4). This result suggests that phase locking does indeed become less precise at low rates of modulation just as it does at low frequencies and that the use of an amplitude-modulated signal provides a demonstration of the behavioral effect of this phenomenon on sound localization, as it allows testing to be conducted at lower frequencies than can be done with pure-tone localization.

Finally, it may be noted that there is a potential localization cue that results from the transient onset difference that occurs when the leading edge of a sound reaches one ear before it arrives at the other (e.g., Tobias and Schubert, 1959). However, the Jamaican fruits bat could not localize tones from 8–12.5 kHz, where neither binaural phase or intensity cues were usable, indicating that they could not use any transient onset difference remaining in the envelope of the signal (with its 10-ms rise/decay). Although this does not rule out their ability to use a transient onset delay given more rapid signal onsets, it does suggest that they were relying on the ongoing interaural phase difference to localize the frequencies of 6.3 kHz and below rather than interaural time differences.

ACKNOWLEDGMENT

Supported by NIH Grant No. R01 DC02960.

Arita, H. T., and Fenton, M. B. (**1997**). ''Flight and echolocation in the ecology and evolution of bats,'' TREE **12**, 53–58.

Bell, G. P., and Fenton, M. B. (**1986**). ''Visual acuity, sensitivity and binocularity in a gleaning insectivourous bat, *Macrotus californicus* (*Chiroptera: Phyllostomidae*),'' Anim. Behav. **34**, 409–414.

Birch, D., and Jacobs, G. H. (**1979**). ''Spatial contrast sensitivity in albino and pigmented rats,'' Vision Res. **19**, 933–937.

Bonaccorso, F. J., and Gush, T. J. (**1987**). ''Feeding behaviour and foraging strategies of captive phyllostomid fruit bats: An experimental study,'' J. Anim. Ecol. **56**, 907–920.

Brown, C. H. (**1994**). ''Sound localization,'' in *Comparative Hearing: Mammals*, edited by R. R. Fay and A. N. Popper (Springer, New York), pp. 57–96.

Cotter, J. R. (**1985**). ''Retinofugal projections of the big brown bat, *Eptesicus fuscus* and the neotropical fruit bat, *Artibeus jamaicensis*,'' Am. J. Anat. **172**, 105–124.

DeBruyn, E. J., Wise, V. L., and Casagrande, V. A. (**1980**). ''The size and topographic arrangement of retinal ganglion cells in the galago,'' Vision Res. **20**, 315–327.
Griffin, D. R. (**1958**). *Listening in the Dark* (Yale University Press, New Haven).
Griffin, D. R., and Novick, A. (**1955**). ''Acoustic orientation of neotropical bats,'' J. Exp. Zool. **130**, 251–300.
Griffin, D. R., Novick, A., and Kornfield, M. (**1958**). ''The sensitivity of echolocation in the fruit bat, *Rousettus*,'' Biol. Bull. **115**, 107–113.
Heffner, H. E., and Masterton, B. (**1980**). ''Hearing in Glires: Domestic rabbit, cotton rat, feral house mouse, and kangaroo rat,'' J. Acoust. Soc. Am. **68**, 1584–1599.
Heffner, H. E., and Heffner, R. S. (**1985**). ''Sound localization in wild Norway rats (*Rattus norvegicus*),'' Hear. Res. **19**, 151–155.
Heffner, H. E., and Heffner, R. S. (**1995**). ''Conditioned avoidance,'' in *Methods in Comparative Psychoacoustics*, edited by G. M. Klump, R. J. Dooling, R. R. Fay, and W. C. Stebbins (Birkhäuser, Basel, Switzerland), pp. 79–93.
Heffner, H. E., and Heffner R. S. (**1998**). ''Hearing,'' in *Comparative Psychology, a Handbook*, edited by G. Greenberg and M. Haraway (Garland, New York), pp. 290–303.
Heffner, R. (**1981**). ''Sound localization and the superior olivary complex in horses and cattle,'' J. Acoust. Soc. Am. **69**, 10S.
Heffner, R. S., and Heffner, H. E. (**1987**). ''Localization of noise, use of binaural cues, and a description of the superior olivary complex in the smallest carnivore, the least weasel (*Mustela nivalis*),'' Behav. Neurosci. **101**, 701–708, 744–745.
Heffner, R. S., and Heffner, H. E. (**1988**). ''Sound localization acuity in the cat: Effect of azimuth, signal duration, and test procedure,'' Hear. Res. **36**, 221–232.
Heffner, R. S., and Heffner, H. E. (**1989**). ''Sound localization, use of binaural cues, and the superior olivary complex in pigs,'' Brain, Behav. Evol. **33**, 248–258.
Heffner, R. S., and Heffner, H. E. (**1990**). ''Vestigial hearing in a fossorial mammal, the pocket gopher (*Geomys bursarius*),'' Hear. Res. **46**, 239–252.
Heffner, R. S., and Heffner, H. E. (**1991**). ''Behavioral hearing range of the chinchilla,'' Hear. Res. **52**, 13–16.
Heffner, R. S., and Heffner, H. E. (**1992a**). ''Evolution of sound localization in mammals,'' in *The Evolutionary Biology of Hearing*, edited by D. B. Webster, R. R. Fay, and A. N. Popper (Springer, New York), pp. 691–715.
Heffner, R. S., and Heffner, H. E. (**1992b**). ''Visual factors in sound localization in mammals,'' J. Comp. Neurol. **317**, 219–232.
Heffner, R. S., and Heffner, H. E. (**1992c**). ''Hearing and sound localization in blind mole rats (*Spalax ehrenbergi*),'' Hear. Res. **62**, 206–216.
Heffner, R. S., and Heffner, H. E. (**1993**). ''Degenerate hearing and sound localization in naked mole rats (*Heterocephalus glaber*), with an overview of central auditory structures,'' J. Comp. Neurol. **331**, 418–433.
Heffner, R. S., Heffner, H. E., Kearns, D., Vogel, J., and Koay, G. (**1994**). ''Sound localization in chinchillas. I. Left/right discriminations,'' Hear. Res. **80**, 247–257.
Heffner, R. S., Koay, G., and Heffner, H. E. (**1999**). ''Sound localization in an Old-World fruit bat (*Rousettus aegyptiacus*): Acuity, use of binaural cues, and relationship to vision,'' J. Comp. Psych. **113**, 297–306.
Hope, G. M., and Bhatnagar, K. P. (**1979**). ''Effect of light adaptation on electrical responses of the retinas of four species of bats,'' Experientia **35**, 1191–1193.
Houben, D., and Gourevitch, G. (**1979**). ''Auditory lateralization in monkeys: An examination of two cues serving directional hearing,'' J. Acoust. Soc. Am. **66**, 1057–1063.
Jackson, L. (**1996**). ''The upper limit of binaural phase discrimination in the Japanese macaque (*Macaca fuscata*),'' Unpublished doctoral dissertation, University of Toledo, Toledo, OH.
Kalko, E. K. V., Herre, E. A., and Handley, Jr., C. O. (**1996**). ''Relation of fig fruit characteristics to fruit-eating bats in the new and old world tropics,'' J. Biogeog. **23**, 565–576.
Kavanagh, G. L., and Kelly, J. B. (**1986**). ''Midline and lateral field sound localization in the albino rat (*Rattus norvegicus*),'' Behav. Neurosci. **100**, 200–205.
Kelly, J. B. (**1980**). ''Effects of auditory cortical lesions on sound localization by the rat,'' J. Neurophysiol. **44**, 1161–1174.
Klump, R. G., and Eady, H. R. (**1956**). ''Some measurements of interaural time difference thresholds,'' J. Acoust. Soc. Am. **28**, 859–860.
Koay, G., Heffner, H. E., and Heffner, R. S. (**1997**). ''Audiogram of the big brown bat (*Eptesicus fuscus*),'' Hear. Res. **105**, 202–210.
Koay, G., Heffner, H. E., and Heffner, R. S. (**1999**). ''Behavioral audiogram of the neotropical fruit bat, *Artibeus jamaicensis*,'' Bat Res. News **40**, 177.
Koay, G., Heffner, R. S., and Heffner, H. E. (**1998**). ''Hearing in a megachiropteran fruit bat, *Rousettus aegyptiacus*,'' J. Comp. Psych. **112**, 371–382.
Koay, G., Kearns, D., Heffner, H. E., and Heffner, R. S. (**1998**). ''Passive sound localization ability of the big brown bat (*Eptesicus fuscus*),'' Hear. Res. **119**, 37–48.
Kuhn, G. F. (**1977**). ''Model for the interaural time differences in the azimuthal plane,'' J. Acoust. Soc. Am. **62**, 157–167.
Kwiecinski, G. G., and Griffiths, T. A. (**1999**). ''*Rousettus egyptiacus*,'' Mammalian Species **611**, 1–9.
Langner, G. (**1997**). ''Neural processing and representation of periodicity pitch,'' Acta Oto-Laryngol., Suppl. **532**, 68–76.
Masterton, R. B., Thompson, G. C., Bechtold, J. K., and RoBards, M. J. (**1975**). ''Neuroanatomical basis of binaural phase-difference analysis for sound localization: A comparative study,'' J. Comp. Physiol. Psychol. **89**, 379–386.
Mooney, S. (**1992**). ''Hearing and sound localization in the Egyptian spiny mouse and Darwin's leaf-eared mouse,'' thesis submitted as partial fulfillment of the requirements for Master of Arts in Psychology, University of Toledo, Toledo, OH.
Moore, P. W. B. (**1975**). ''Underwater localization of click and pulsed pure-tone signals by the california sea lion (*Zalophus californianus*),'' J. Acoust. Soc. Am. **57**, 406–410.
Obrist, M. K., Fenton, M. B., Eger, J. L., and Schlegel, P. A. (**1993**). ''What ears do for bats: A comparative study of pinna sound pressure transformation in chiroptera,'' J. Exp. Biol. **180**, 119–152.
Palmer, A. R., and Russell, I. J. (**1986**). ''Phase-locking in the cochlear nerve of the guinea pig and its relation to the receptor potential of inner hair-cells,'' Hear. Res. **24**, 1–15.
Pettigrew, J. D., Dreher, B., Hopkins, C. S., McCall, M. J., and Brown, M. (**1988**). ''Peak density and distribution of ganglion cells in the retinae of microchiropteran bats: Implications for visual acuity,'' Brain, Behav. Evol. **32**, 39–56.
Rose, J. E., Brugge, J. F., Anderson, D. J., and Hind, J. E. (**1967**). ''Phase-locked response to low frequency tones in single auditory nerve fibers of the squirrel monkey,'' J. Neurophysiol. **30**, 769–793.
Saberi, K., Farahbod, H., and Konishi, M. (**1998**). ''How do owls localize interaurally phase-ambiguous signals?'' Proc. Natl. Acad. Sci. U.S.A. **95**, 6465–6468.
Schnitzler, H.-U., and Henson, Jr., O. W. (**1980**). ''Performance of airborne animal sonar systems: I. Microchiroptera,'' in *Animal Sonar Systems*, edited by R. G. Busnel and J. F. Fish (Plenum, New York), pp. 109–181.
Spence, C., and Driver, J. (**1997**). ''Audiovisual links in exogenous covert spatial orienting,'' Percept. Psychophys. **59**, 1–22.
Stone, J. (**1981**). *The Wholemount Handbook* (Maitland, Sydney, Australia).
Suthers, R. A. (**1966**). ''Optomotor responses by echolocating bats,'' Science **152**, 1102–1104.
Thompson, M., Porter, B., O'Bryan, J., Heffner, H. E., and Heffner, R. S. (**1990**). ''A syringe-pump food-paste dispenser,'' Behav. Res. Methods Instrum. Comput. **22**, 449–450.
Tobias, J. V., and Schubert, E. D. (**1959**). ''Effective onset duration of auditory stimuli,'' J. Acoust. Soc. Am. **59**, 634–639.

LETTERS TO THE EDITOR

This Letters section is for publishing (a) brief acoustical research or applied acoustical reports, (b) comments on articles or letters previously published in this Journal, and (c) a reply by the article author to criticism by the Letter author in (b). Extensive reports should be submitted as articles, not in a letter series. Letters are peer-reviewed on the same basis as articles, but usually require less review time before acceptance. Letters cannot exceed four printed pages (approximately 3000–4000 words) including figures, tables, references, and a required abstract of about 100 words.

A hexahedral face element for elastoacoustic vibration problems

Alfredo Bermúdez and Pablo Gamallo
Departamento de Matemática Aplicada, Universidade de Santiago de Compostela, 15706 Santiago de Compostela, Spain

Rodolfo Rodríguez
Departamento de Ingeniería Matemática, Universidad de Concepción, Casilla 160-C, Concepción, Chile

(Received 10 August 2000; accepted for publication 16 September 2000)

A finite-element method to compute elastoacoustic vibration modes in 3D problems is analyzed. It is based on displacement formulations for solid and fluid. The discretization consists of classical isoparametric hexahedral elements for the former and hexahedral Raviart–Thomas elements for the latter, to avoid spurious modes. The meshes on fluid and solid domains do not need to coincide on the common interface, since the kinematic constraint is weakly imposed. The generalized eigenvalue problem is written in a matrix form which allows using a standard MATLAB eigensolver. Numerical results showing the good performance of the method and the convenience of using incompatible meshes are reported. © *2001 Acoustical Society of America.*
[DOI: 10.1121/1.1324677]

PACS numbers: 43.40.At, 43.40.Rj, 43.20.Ks, 43.20.Tb [CBB]

I. INTRODUCTION

The need for computing fluid–solid interactions arises in many important engineering problems. A large amount of work has been devoted to this subject during past years. A general overview can be found in the monographs (Refs. 1 and 2), where numerical methods and further references are also given.

This paper deals with one of these interactions: the elastoacoustic vibration problem. It is concerned with the determination of harmonic vibrations of an elastic structure interacting with a compressible fluid. Since the solid is generally described in terms of displacement, to choose the same variable for the fluid presents one important advantage: compatibility and equilibrium through the fluid–solid interface satisfy automatically. This approach could be in principle applied to the solution of a broad range of problems (in particular nonlinear ones)[3] and leads to sparse symmetric matrices.

In this paper we propose the use of hexahedral finite elements for the discretization: trilinear isoparametric in the solid and lowest-order Raviart–Thomas in the fluid. Fluid and solid meshes do not need to be compatible on the common interface, since the kinematic constraint (i.e., equal normal displacements for fluid and solid) is imposed in a weak sense. We give a matrix formulation yielding a generalized eigenvalue problem which can be solved with MATLAB eigensolver eigs. Finally, we present numerical results exhibiting the good performance of the method.

II. STATEMENT OF THE PROBLEM. DISCRETIZATION

We consider the problem of determining the small amplitude motions of an ideal inviscid barotropic fluid contained into a linear isotropic elastic structure which obeys Hooke's law. Let Ω_F and Ω_S be the three-dimensional domains occupied by fluid and solid, respectively, and Γ_I the interface between both media, as shown in Fig. 1. The structure is fixed on Γ_D and free on Γ_N.

When both media are described by means of displacement fields, the free vibration modes of the coupled system are the solution of the following spectral problem (see Ref. 4):

$$\text{To find } \omega>0 \text{ and } (\mathbf{U},\mathbf{W})\neq(\mathbf{0},\mathbf{0}) \text{ such that}$$

$$\mathbf{U}\cdot\boldsymbol{\nu}=\mathbf{W}\cdot\boldsymbol{\nu} \text{ on } \Gamma_I \text{ and} \tag{1}$$

$$\int_{\Omega_F}\rho_F c^2 \operatorname{div}\mathbf{U}\operatorname{div}\mathbf{Y}\,dx+\int_{\Omega_S}\boldsymbol{\sigma}(\mathbf{W}):\boldsymbol{\epsilon}(\mathbf{Z})dx = \omega^2\left(\int_{\Omega_F}\rho_F\mathbf{U}\cdot\mathbf{Y}\,dx+\int_{\Omega_S}\rho_S\mathbf{W}\cdot\mathbf{Z}\,dx\right)$$

$$\forall(\mathbf{Y},\mathbf{Z}):\quad \mathbf{Y}\cdot\boldsymbol{\nu}=\mathbf{Z}\cdot\boldsymbol{\nu} \text{ on } \Gamma_I, \tag{2}$$

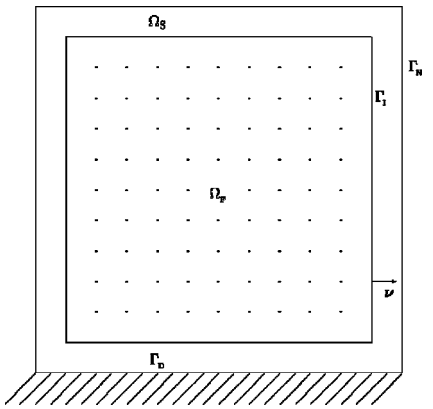

FIG. 1. Vertical section of fluid and solid domains.

where $\mathbf{U}$ and $\mathbf{W}$ are the amplitudes of fluid and solid displacements, respectively, ω is the angular vibration frequency, ρ_F and ρ_S are the fluid and solid densities, respectively, c is the sound speed in the fluid, and $\boldsymbol{\sigma}$ the stress tensor in the solid, which relates to the linearized strain tensor $\boldsymbol{\epsilon}(\mathbf{W})=\frac{1}{2}(\nabla\mathbf{W}+\nabla\mathbf{W}^t)$ by Hooke's law: $\boldsymbol{\sigma}=\lambda(\mathrm{tr}\,\boldsymbol{\epsilon})\mathbf{I}+2\mu\boldsymbol{\epsilon}$ (λ and μ being the Lamé coefficients). Notice that the kinematic interface constraint (1) is explicitly imposed on the admissible displacements in this formulation.

Let us remark that $\omega=0$ is an eigenfrequency of this problem with an infinite-dimensional eigenspace which consists of pure rotational fluid motions inducing neither vibrations in the solid nor variations of pressure in the fluid. They do not correspond to vibration modes of the coupled system, but arise because no irrotational constraint is imposed to the fluid displacements. The rest of the eigenfrequencies are strictly positive and correspond to vibrations of the coupled fluid–solid system (see Ref. 4).

To solve the variational spectral problem (1)–(2), we consider regular partitions in hexahedra of Ω_F and Ω_S, not necessarily compatible on the fluid–solid interface. The hexahedra do not need to have planar faces. They are defined by means of trilinear transformations of the unit cube. Thus, the edges are always straight segments, but each face is planar if and only if its four vertices lie on the same plane. This possibility of having curved faces allows us to obtain a better fitting of curved boundaries by judiciously choosing the vertices of the corresponding faces, with the only restriction of lying on the boundary.

The simplest method of solving problem (1)–(2) consists of discretizing each component of solid and fluid displacements by Lagrangian isoparametric trilinear finite elements.[5] However, such discretization in the fluid produces spurious rotational modes with nonzero frequencies interspersed among those of the irrotational ones. Instead we consider a different finite element for the fluid displacement field: the *lowest-order Raviart–Thomas hexahedron*.

This element discretizes, on each hexahedron, the whole vector field instead of each of its components separately. Its degrees of freedom are the mean values of the normal component of the field on each face. A detailed introduction of this element in the context of acoustics is given in Ref. 6.

Lagrangian trilinear isoparametric hexahedra are used for each component of the displacements in the solid.[5] Finally, the kinematic interface constraint (1) should be imposed somehow to the discrete displacements $\mathbf{U}_h$ and $\mathbf{W}_h$. Since doing it strongly (i.e., $\mathbf{U}_h\cdot\boldsymbol{\nu}=\mathbf{W}_h\cdot\boldsymbol{\nu}$ on Γ_I) is too stringent,[4] then we impose it weakly in the following way:

$$\int_{\mathcal{F}}\mathbf{U}_h\cdot\boldsymbol{\nu}\,dS=\int_{\mathcal{F}}\mathbf{W}_h\cdot\boldsymbol{\nu}\,dS, \tag{3}$$

for each face $\mathcal{F}$ of the fluid mesh lying on Γ_I. This constraint amounts to eliminating by static condensation the degrees of freedom of the fluid displacement corresponding to these faces.

The discrete problem has $\omega_h=0$ as an eigenfrequency with an associated eigenspace consisting of discrete rotational fluid motions. All the other eigenfrequencies of the discrete problem are strictly positive and correspond to the actual vibration modes of the coupled system.

We give a matrix description of this discrete problem, which allows us to solve it with standard eigensolvers. In particular we show a convenient way of imposing the kinematic constraint (3) on the fluid–solid interface.

Let $\{\boldsymbol{\varphi}_j\}_{j=1}^{N_F}$ be the Raviart–Thomas basis functions associated with each face $\mathcal{F}_j$ in the fluid mesh (N_F being the total number of such faces). Let $\{\boldsymbol{\psi}_j\}_{j=1}^{3N_S}$ be the standard isoparametric trilinear basis functions associated with the vertices of the solid mesh (N_S being the number of such vertices not lying on Γ_D). We write the discrete displacements in terms of these basis: $\mathbf{U}_h=\Sigma_{j=1}^{N_F}\alpha_j\boldsymbol{\varphi}_j$ and $\mathbf{W}_h=\Sigma_{j=1}^{3N_S}\beta_j\boldsymbol{\psi}_j$.

Let $\mathbf{K}_F=(K_{ij}^F)$ and $\mathbf{M}_F=(M_{ij}^F)$ be the stiffness and mass matrices of the fluid, respectively, defined by

$$K_{ij}^F=\int_{\Omega_F}\rho_F c^2\,\mathrm{div}\,\boldsymbol{\varphi}_i\,\mathrm{div}\,\boldsymbol{\varphi}_j\,dx,$$

$$M_{ij}^F=\int_{\Omega_F}\rho_F\boldsymbol{\varphi}_i\cdot\boldsymbol{\varphi}_j\,dx.$$

Let $\mathbf{K}_S=(K_{ij}^S)$ and $\mathbf{M}_S=(M_{ij}^S)$ be the corresponding matrices of the solid, with

$$K_{ij}^S=\int_{\Omega_S}\boldsymbol{\sigma}(\boldsymbol{\psi}_i):\boldsymbol{\epsilon}(\boldsymbol{\psi}_j)dx,\quad M_{ij}^S=\int_{\Omega_S}\rho_S\boldsymbol{\psi}_i\cdot\boldsymbol{\psi}_j\,dx.$$

In the absence of fluid–solid coupling, the discrete problem would read

$$\begin{pmatrix}\mathbf{K}_F & \mathbf{0}\\ \mathbf{0} & \mathbf{K}_S\end{pmatrix}\begin{pmatrix}\boldsymbol{\alpha}\\ \boldsymbol{\beta}\end{pmatrix}=\omega_h^2\begin{pmatrix}\mathbf{M}_F & \mathbf{0}\\ \mathbf{0} & \mathbf{M}_S\end{pmatrix}\begin{pmatrix}\boldsymbol{\alpha}\\ \boldsymbol{\beta}\end{pmatrix}.$$

However, to solve the coupled problem, we need to impose the kinematic constraint (3). We assume for simplicity that the first N_I basis functions in the fluid correspond to the faces lying on the interface. Each of the nodal components $\alpha_I,\ldots,\alpha_{N_I}$ can be statically condensed in terms of the nodal values of the solid displacements. If we write $\boldsymbol{\alpha}=(\boldsymbol{\alpha}^I,\hat{\boldsymbol{\alpha}})$, with $\boldsymbol{\alpha}^I=(\alpha_I,\ldots,\alpha_{N_I})$ and $\hat{\boldsymbol{\alpha}}$ the remaining nodal components, we have (see Ref. 6)

$$\boldsymbol{\alpha}^I=\mathbf{E}\boldsymbol{\beta},$$

with the entries of the matrix $\mathbf{E}$ defined by

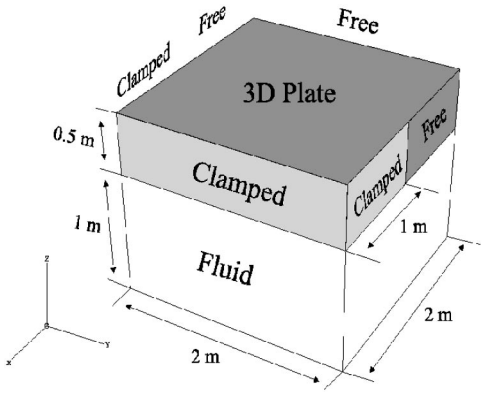

FIG. 2. Geometrical data and plate boundary conditions.

$$E_{ij}=\frac{1}{\text{area}(\mathcal{F}_i)}\int_{\mathcal{F}_i}\boldsymbol{\psi}_j\cdot\boldsymbol{\nu}\,dS.$$

If we split $\mathbf{K}_F$ and $\mathbf{M}_F$ into blocks corresponding to the unknowns $\boldsymbol{\alpha}^I$ and $\hat{\boldsymbol{\alpha}}$

$$\mathbf{K}_F=\begin{pmatrix}\mathbf{K}_F^I & \mathbf{C}_K\\ \mathbf{C}_K^t & \hat{\mathbf{K}}_F\end{pmatrix}\quad\text{and}\quad\mathbf{M}_F=\begin{pmatrix}\mathbf{M}_F^I & \mathbf{C}_M\\ \mathbf{C}_M^t & \hat{\mathbf{M}}_F\end{pmatrix},$$

then the discrete problem can be written in terms of the genuine degrees of freedom $\hat{\boldsymbol{\alpha}}$ and $\boldsymbol{\beta}$ in the following way:

$$\begin{pmatrix}\hat{\mathbf{K}}_F & \mathbf{C}_K^t\mathbf{E}\\ \mathbf{E}^t\mathbf{C}_K & \mathbf{K}_S+\mathbf{E}^t\mathbf{K}_F^1\mathbf{E}\end{pmatrix}\begin{pmatrix}\hat{\boldsymbol{\alpha}}\\ \boldsymbol{\beta}\end{pmatrix}$$
$$=\omega_h^2\begin{pmatrix}\hat{\mathbf{M}}_F & \mathbf{C}_M^t\mathbf{E}\\ \mathbf{E}^t\mathbf{C}_M & \mathbf{M}_S+\mathbf{E}^t\mathbf{M}_F^I\mathbf{E}\end{pmatrix}\begin{pmatrix}\hat{\boldsymbol{\alpha}}\\ \boldsymbol{\beta}\end{pmatrix}.$$

This is a well-posed generalized eigenvalue problem with symmetric sparse matrices. Furthermore, the matrix on the right-hand side is positive definite; hence this problem can be efficiently solved by using, for instance, MATLAB eigensolver eigs.

III. NUMERICAL RESULTS

We report in this section numerical results obtained with an implementation of the method described above by using MATLAB.

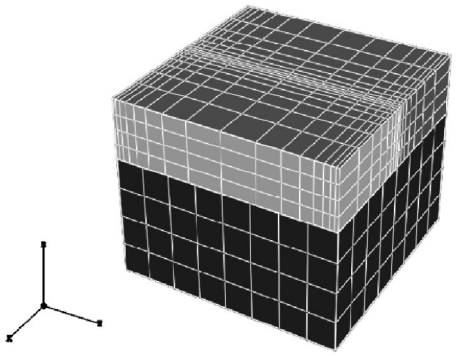

FIG. 3. An incompatible fluid–solid mesh.

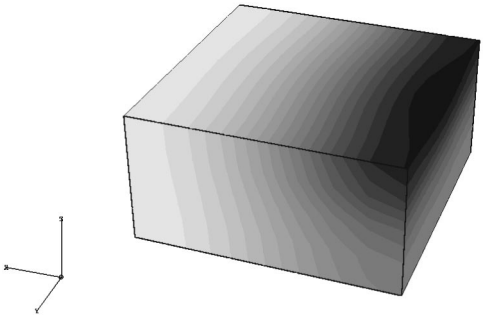

FIG. 4. Lowest-frequency mode. Pressure in the fluid.

We consider a 3D cavity completely filled with water with perfectly rigid walls and bottom, its top being a thick 3D steel plate. We have used the following values of the physical parameters:

Steel density:	$\rho_s=7700\ \text{kg/m}^3$,
Young modulus:	$E=1.44\times10^{11}\ \text{Pa}$,
Poisson ratio:	$\nu=0.35$,
Water density:	$\rho_F=1000\ \text{kg/m}^3$,
Sound speed:	$c=1430\ \text{m/s}$.

To illustrate the ability of our method to deal with fluid and solid meshes not coinciding on the common interface, we have chosen a problem for which such incompatible meshes behave better than compatible ones. We have computed the vibration modes of the fluid–solid coupled system described in Fig. 2.

The thick 3D plate on the top of the cavity is clamped only by part of its lateral walls and free on the remainder. In particular, two of these walls are half-clamped/half-free. Thus, singularities appear in the solid displacements around the edges separating the pieces of these walls supporting different boundary conditions.

Because of this, it is well known that graded meshes, highly refined in the neighborhood of these singularities (like that in the 3D plate of Fig. 3), are better for solving this problem than uniform meshes. Instead, the fluid displacements are expected to be quite regular, and so uniform fluid meshes look convenient. Furthermore, if fluid meshes compatible with the solid ones were used, a much larger number of degrees of freedom (d.o.f.) would be needed.

We have applied our method with three types of hexahedral meshes:

H_1: compatible hexahedral uniform meshes for both, fluid and solid;

H_2: compatible hexahedral meshes, graded in both media;

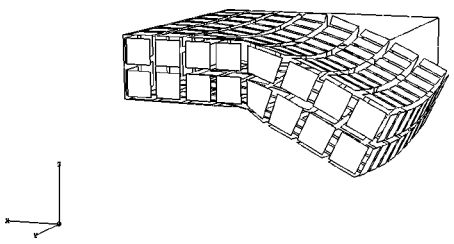

FIG. 5. Lowest-frequency mode. Deformed structure.

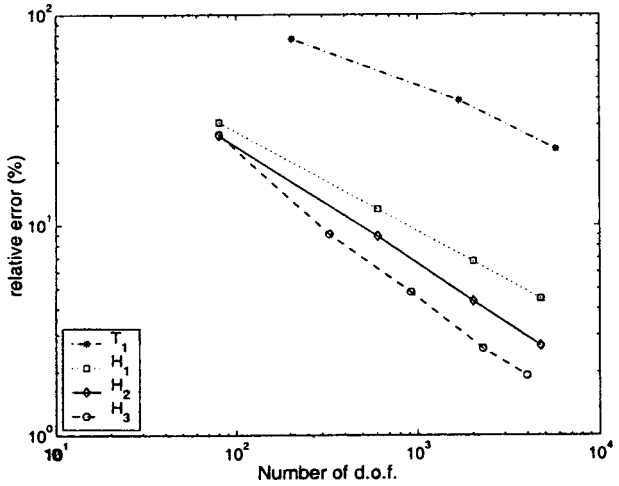

FIG. 6. Error versus number of d.o.f. (log–log scale).

H_3: incompatible hexahedral meshes, graded in the solid and uniform in the fluid.

We have also solved the problem with a method analyzed in Ref. 7, based on Raviart–Thomas tetrahedral elements in the fluid and standard linear tetrahedral elements in the solid, with the following meshes:

T_1: compatible tetrahedral uniform meshes for both media.

We present the results obtained for the lowest-frequency vibration mode of the coupled system. Figures 4 and 5 show the fluid pressure and the deformed structure, respectively, for this mode.

Figures 6 and 7 show the error of the computed vibration frequencies, for all the meshes, versus the number of d.o.f. and the computer time, respectively. We have taken as a reference ''exact'' solution the one obtained by using a Reissner–Mindlin plate model on a very fine mesh coupled with Raviart–Thomas elements for the fluid (see Ref. 8). It can be clearly seen that the method based on hexahedral meshes is much less expensive, and that incompatible meshes turn out to be the best choice in terms of computational cost.

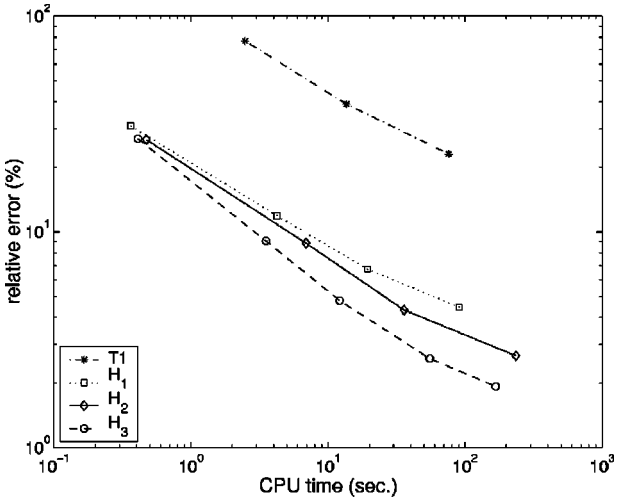

FIG. 7. Error versus CPU time (log–log scale).

IV. CONCLUSIONS

A finite element to compute 3D elastoacoustic vibrations has been analyzed: the *Raviart–Thomas hexahedron* to discretize fluid displacements, weakly coupled on the interface with isoparametric trilinear elements for solid displacements.

This method leads to symmetric sparse generalized eigenvalue problems with positive definite right-hand side matrices. Therefore, they can be efficiently solved by standard procedures like the one used in this paper: MATLAB eigensolver eigs.

Furthermore, the method does not require compatibility of fluid and solid meshes on the common interface. Thus, it can be conveniently used for problems where different degree of refinements are needed in each medium.

The numerical experiment reported in this paper shows a clearly better performance for this method than for its tetrahedral counterpart. It also illustrates the effectiveness of this method to deal with incompatible meshes and the convenience of using them for certain problems instead of compatible ones.

ACKNOWLEDGMENTS

The work of the third author was partially supported by FONDECYT Grant No 1.990.346 and Program A on Numerical Analysis of FONDAP in Applied Mathematics (Chile).

[1] H. J.-P. Morand and R. Ohayon, *Fluid Structure Interaction* (Wiley, Chichester, U.K., 1995).
[2] R. Ohayon and C. Soize, *Structural Acoustics and Vibration* (Academic, New York, 1998).
[3] X. Wang and K. J. Bathe, ''Displacement/pressure based mixed finite element formulations for acoustic fluid-structure interaction problems,'' Int. J. Numer. Methods Eng. **40**, 2001–2017 (1997).
[4] A. Bermúdez and R. Rodríguez, ''Finite element computation of the vibration modes of a fluid–solid system,'' Comput. Methods Appl. Mech. Eng. **119**, 355–370 (1994).
[5] M. Petyt, *Introduction to Finite Element Vibration Analysis* (Cambridge University Press, 1990).
[6] A. Bermúdez, P. Gamallo, and R. Rodríguez, ''A hexahedral face element for elastoacoustic vibration problems,'' (extended version) Technical Report DIM 99-12, Universidad de Concepción, Concepción, Chile, 1999 (also available in: http://lanin.ing-mat.udec.c1/~rodolfo/public.html).
[7] A. Bermúdez, L. Hervella-Nieto, and R. Rodríguez, ''Finite element computation of three dimensional elastoacoustic vibrations,'' J. Sound Vib. **219**, 277–304 (1999).
[8] R. Durán, L. Hervella-Nieto, E. Liberman, R. Rodríguez, and J. Solomin, ''Finite element analysis of the vibration problem of a plate coupled with a fluid,'' Numer. Math. **86**, 591–616 (2000).

Effects of flanking component spectral position and modulation pattern on thresholds for signals presented in the peaks of a modulated tonal masker

Roel Delahaye
Parmly Hearing Institute, Loyola University, Chicago, Illinois 60626

Deborah A. Fantini and Ray Meddis
Department of Psychology, University of Essex, Wivenhoe Park, Colchester CO4 3SQ, England

(Received 23 May 2000; revised 21 September 2000; accepted 28 September 2000)

Detection of signals added solely to the peaks of an on-frequency modulated masker has never been found to improve after adding flanking components (FCs) at remote frequencies. However, according to theories underlying comodulation masking release (CMR), adding comodulated FCs could provide cues that improve signal detection for signal-peak placement. A reason masking release was not found with peak placement might be because of processes underlying modulation detection interference (MDI). This possibility was further investigated by using FCs that could diminish MDI but still provide signal detection cues associated with theories of CMR. It seemed that a peripheral within-channel and a central across-channel mechanism underlying MDI could hinder signal detection for signal peak placement. © *2001 Acoustical Society of America.*
[DOI: 10.1121/1.1328790]

PACS numbers: 43.66.Dc, 43.66.Mk, 43.66.Rq [SPB]

I. INTRODUCTION

This study focuses on the ability of the auditory system to use signal detection cues predicted by theories of comodulation masking release (CMR) (Hall *et al.*, 1984). CMR is referred to as the detection improvement of a signal masked by a fluctuating masker (on-frequency component, OFC) after adding modulated components with the same envelope-phase relationship as the OFC to frequencies remote from the signal frequency (flanking components, FCs). One of the theories of CMR involves comparisons between masker envelopes. One aspect of the envelope comparison theory is based upon the difference in envelope amplitude, derived by subtracting the envelope at the signal frequency from the envelope at the flanking frequency (Buus, 1985; Hall, 1986).

Another theory of CMR is not based on a direct comparison between masker envelopes, but on listening for the signal during the OFC envelope when the signal-to-masker ratio is greatest. The signal-to-masker ratio is usually greatest around the OFC minima (dips). Thus, the more the dips in the OFC envelope are cued by FC dips, the more masking release there should be. This is called the dip-listening theory (Buus, 1985). An experiment conducted by Hall and Grose (1988) showed that CMR can be obtained for stimuli that contain cues based only on amplitude level differences across frequencies or contain only cues for dip listening.

The possibility of obtaining CMR for different signal detection cues is probably the reason that CMR can be found for a variety of stimuli (see also Schooneveldt and Moore, 1987; Fantini *et al.*, 1993; Fantini and Moore, 1994). Despite this, CMR has never been observed for signals placed solely in the peaks of a modulated OFC (Grose and Hall, 1989; Moore *et al.*, 1990). However, if the mechanism underlying CMR relied on an across-channel difference in envelope amplitude, some masking release would be expected even when the signal occurred only in the peaks of the masker. Moore *et al.* (1990) suggested that the reason why no masking release has been found for the comodulated signal peak-placement condition might be because of perceptual fusion of the FCs and the OFC plus signal. This fusion might be related to a mechanism underlying modulation detection interference (MDI) as described by Yost and Sheft (1989). Yost and Sheft found that if a listener had to detect the modulation of a target component in the presence of another component, it was harder to detect the modulation when the other component was also modulated.

The experiments in this study were designed to investigate if mechanisms similar to the ones underlying MDI might prevent the benefit to signal peak-placement detection of dip-listening and envelope-level cues associated with CMR. The issue of dip-listening cues was addressed by using FCs that were modulated 180° out of phase with the OFC (antiphasic FCs). The dips of the antiphasic FCs might indicate the optimum time to listen for the signal (the OFC peaks). This might give an advantage in signal detection over the no-FC condition in which no indication of the signal timing by FCs exists. The issue of envelope-level cues was addressed by using unmodulated FCs. No interference in signal detection due to common modulation of any of the masker components can take place. Therefore, across-frequency level disparities can be used as a detection cue without the mechanism underlying MDI impairing signal detection. To determine the role of peripheral and central processes, the FCs were presented ipsilaterally or contralaterally to the OFC and signal. In the first experiment, signal detection was measured as a function of the modulation pattern of six FCs. In the second experiment only one FC was used. Signal detection was measured as a function of the FC spectral position.

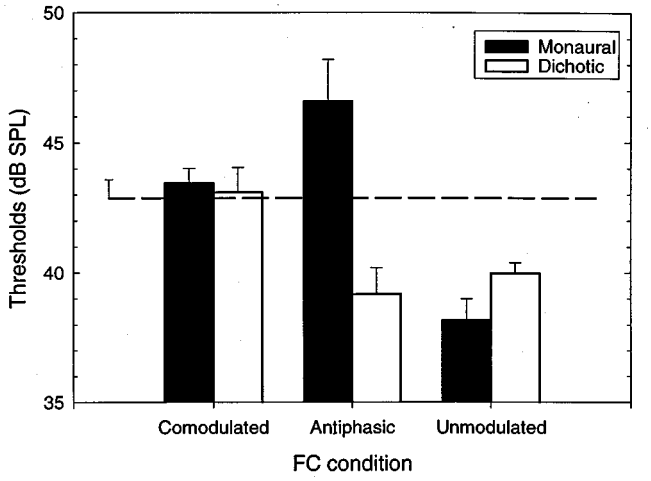

FIG. 1. The average results for monaural (filled columns) and dichotic (open columns) stimulus presentations are shown. The dashed line represents the average threshold obtained when no FCs were present. Signal detection thresholds are plotted for the different FC conditions. Error bars indicate plus one standard error of the mean.

II. METHOD

A. Listeners

Three normal-hearing listeners participated in this experiment. The first two listeners were the first two authors. The third listener was paid for her participation. All listeners were between the ages of 20 and 40 years. Data collection for experiment 1a started after a listener had at least 10 h of practice and showed a stable performance. Data for experiment 1b were collected after the listeners gained an additional amount (about 20 h) of practice by participating in similar psychoacoustical experiments. Listeners always ran individually in an IAC double-walled sound-attenuating chamber.

B. Stimuli

The stimuli were essentially the same as the ones used by Grose and Hall (1989) and Moore *et al.* (1990). The signal was a 700-Hz pure tone, which was presented as three 50-ms tone bursts, each with 20-ms raised-cosine rise and fall ramps and a steady-state duration of 10 ms. The time interval between the bursts was 50 ms. The on-frequency component (OFC) was a 700-Hz sinusoid which was 100% sinusoidally amplitude modulated (SAM) at a 10-Hz rate. The OFC had an overall duration of 500 ms, with 20-ms raised-cosine rise and fall ramps, and an overall level of 51.8 dB SPL after modulation. The signal was temporally centered on the middle three peaks of the OFC envelope and was presented in phase with respect to the OFC carrier.

Pure-tone flanking components (FCs) could be presented ipsilaterally or contralaterally to the OFC and signal. In experiment 1a six FCs were used. These FCs had carrier frequencies of 300, 400, 500, 900, 1000, and 1100 Hz. In experiment 1b a single FC was used. This FC had a carrier frequency of either 100, 300, 500, 600, 650, 750, 800, 900, 1100, or 1300 Hz. FC duration was the same as for the OFC. FCs were either modulated or unmodulated. Each unmodulated FC had an overall level of 50 dB SPL. Each modulated FC had the same level (51.8 dB SPL), SAM depth (100%), and modulation frequency (10 Hz) as the OFC. The modulation phase of the FCs with respect to the OFC envelope was varied in two different ways. First, in the comodulated condition, the FCs were modulated in phase with respect to the OFC. Second, in the antiphasic condition, the FC envelopes were 180° out of phase with the OFC envelope. A condition in which no FCs but only the OFC was present was also run. This no-FC condition was run in both experiments to account for differences in performance due to an unequal amount of practice preceding the data collection in experiments 1a and 1b.

A NeXT work station generated the stimuli digitally using a 44.1-kHz sampling rate, converted them using a 16-bit D/A, and filtered them using an antialias filter. Stimuli were presented through Sennheiser HD 340 headphones.

C. Procedure

A three-interval forced-choice adaptive-tracking paradigm, with a two-down, one-up strategy (Levitt, 1971) was used to determine the 71% correct signal detection thresholds in dB SPL. The starting level of the signal was always above threshold and the step size was 5 dB for the first four reversals. For the next eight reversals, a step size of 2 dB was used. Data collected for the first four reversals were omitted and signal levels for the last eight reversals were averaged to estimate threshold. Runs in which the standard deviations across eight reversals exceeded 5 dB were discarded and repeated. Estimates of three signal thresholds were collected for each condition. If the range of the three thresholds exceeded 3 dB another estimate was obtained. The final threshold value was the average of all the threshold estimates for each condition. A warning light preceded each block of trials. Each observation interval was indicated by a light, followed by a 500-ms silent interval. After a response was given and visual feedback was provided the next trial started immediately.

III. RESULTS

A. Experiment 1a

Signal thresholds of the three listeners were averaged and plotted in Fig. 1 for each FC condition. Filled columns represent thresholds obtained in the monaural condition and open columns represent thresholds obtained in the dichotic conditions. The dashed line represents the threshold obtained for the no-FC condition. Bars indicate plus one standard error of the mean.

Thresholds obtained in the comodulated, antiphasic, and unmodulated conditions were considered with respect to the condition in which no FCs were present. Adding comodulated FCs did not seem to have an effect on signal detection. The presence of antiphasic FCs impaired signal detection in the monaural condition but improved signal detection in the dichotic condition. Adding unmodulated FCs resulted in a signal detection improvement for both monaural and dichotic stimulus presentations.

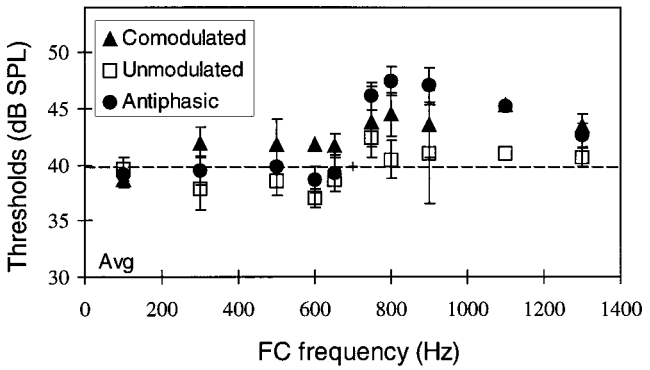

FIG. 2. The monaural average results are shown. Signal detection thresholds are plotted as a function of FC frequency. Triangles represent the comodulated conditions, circles represent the antiphasic conditions, and squares represent the unmodulated conditions. The horizontal dashed line represents the signal threshold obtained in the no-FC condition. Bars represent plus and minus one standard error of the mean. Error bars are, for clarity's sake, omitted when they did not exceed the symbol size.

B. Experiment 1b

The average results are shown in Fig. 2 for the monaural conditions. Figure 3 shows the individual results for the dichotic condition. Signal threshold is plotted as a function of the FC frequency. Triangles represent the comodulated conditions, circles represent the antiphasic conditions, and squares represent the unmodulated conditions. The horizontal dashed line represents the signal threshold obtained for the no-FC condition. Bars represent plus and minus one standard error of the mean. Error bars are, for clarity's sake, omitted when they did not exceed the symbol size.

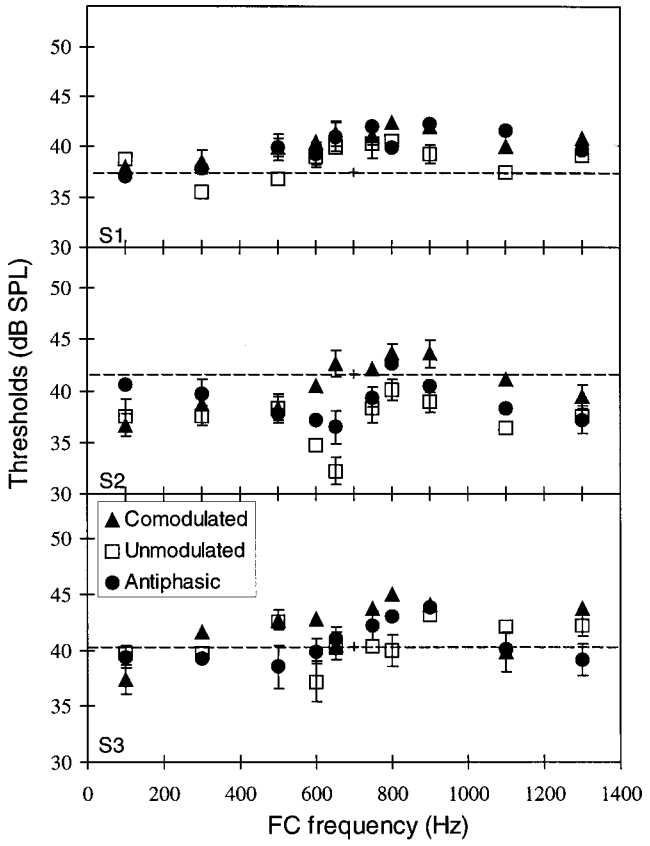

FIG. 3. As Fig. 2, but for dichotic results for the individual listeners.

First, consider thresholds obtained for the monaural conditions (Fig. 2). Only the average results are shown as the threshold patterns among individual listeners were similar. For four out of five FCs positioned below the signal frequency, the lowest average thresholds were found for the unmodulated conditions followed by the antiphasic and comodulated conditions, respectively. The threshold obtained for the no-FC condition was similar to the thresholds obtained for the antiphasic conditions. When FCs were placed above the signal frequency, thresholds were higher than those found for the no-FC condition. The lowest thresholds were found for the unmodulated conditions followed by the comodulated and antiphasic conditions, respectively. For dichotic conditions (Fig. 3), only the individual results are shown as they vary substantially among listeners. A clear distinction between the thresholds obtained for the different conditions could not be made.

For both the unmodulated and comodulated conditions, there was no clear difference between the monaural and dichotic conditions. However, for the antiphasic conditions, the difference was rather striking. Antiphasic monaural and dichotic thresholds were similar when FCs were placed below the signal frequency, but when antiphasic FCs were placed above the signal frequency, dichotic thresholds were consistently lower than monaural thresholds.

IV. DISCUSSION

Thresholds obtained in the no-FC condition of experiment 1b were on average about 3 dB lower than in experiment 1a. This might be due to additional practice obtained before commencing the second experiment. Although performance appeared stable after the initial 10 h of practice, it seemed that another 20 h of experience could still decrease thresholds in the no-FC condition. Delahaye *et al.* (1999) measured the effect of extended practice in the six-FC conditions for two of the three listeners used here. They showed that, after extended practice, thresholds obtained in the no-FC condition seem to decrease more than thresholds obtained in the FC conditions. Extended practice reduced or diminished masking release when measured with respect to the no-FC condition. However, the threshold difference between FC conditions seemed independent of practice. Therefore, Delahaye *et al.* (1999) proposed using a reference condition that also contains FCs. This proposal is taken into account in this study by not only discussing FC conditions in respect to the no-FC condition but also in respect to each other.

The lack of signal detection improvement after adding comodulated FCs (CMR) is in agreement with the findings of Moore *et al.* (1990) and Grose and Hall (1989). In fact, they showed a tendency for an increase in thresholds after adding comodulated FCs to the OFC. In experiment 1a, most similar to the experiments by Moore *et al.* (1990) and Grose and Hall (1989), such an increase was not found. However, a closer look at the results obtained in the previous studies showed that, although higher thresholds were generally found for the comodulated than for the no-FC conditions, this difference was not significant in the study by Grose and Hall (1989) and not significant in the study by Moore *et al.*

(1990) for the conditions most similar to the ones used in experiment 1a (seven-component masker). Thus, the current results are in general agreement with the previous results. If the lack of a masking release in the comodulated condition is due to a mechanism that hinders across-frequency level comparisons, this mechanism is probably involved with central across-channel interactions as no masking release is found in both monaural and dichotic conditions.

In the antiphasic condition of experiment 1a, the release from masking found in the dichotic condition is in contrast with the increase in masking found in the monaural condition. The masking release found in the dichotic condition indicates that it is produced by an across-channel mechanism. This mechanism might be related to the dip-listening theory (Buus, 1985). Antiphasic FC dips might indicate the optimal time to listen for the signal during the OFC peaks where the signal is present. This might give an advantage in signal detection over the no-FC condition. For the monaural condition it seems that the effect of dip listening is counteracted by peripheral within-channel interactions. From experiment 1b it can be seen that these peripheral within-channel interactions occur mainly for FCs placed immediately above the signal frequency.

The lack of a masking release for the monaural and dichotic comodulated conditions and the monaural antiphasic condition might be related to the MDI phenomenon as discussed by Moore and Jorasz (1996). In a monaural setting they showed that MDI could be due to both peripheral within-channel and central across-channel interactions. They argued that the MDI caused by peripheral within-channel interactions was greater when the target and flanker were antiphasic than when they were comodulated. Conversely, the MDI caused by central across-channel interactions was supposed to be greater in the comodulated than in the antiphasic condition. Also, Moore and Jorasz (1996) argued that for FCs placed above the target frequency, peripheral interactions were dominant, resulting in more MDI for the antiphasic than for the comodulated condition. For FCs placed below the signal frequency, central processes were dominant resulting in more MDI for the comodulated than for the antiphasic condition. Notice that Moore and Jorasz (1996) used only monaural stimulus conditions. However, in this study both monaural and dichotic conditions were used. It was assumed that peripheral interactions could occur only in the monaural condition as central interactions could occur in both the monaural and dichotic conditions. Therefore, the peripheral mechanism underlying MDI in the antiphasic condition is assumed to operate only in the monaural condition. In contrast, the central mechanism underlying MDI in the comodulated condition is assumed to operate in both the monaural and dichotic conditions. Therefore, the MDI effect caused by the central mechanism could be of the same magnitude in the monaural and dichotic conditions. The similarity in threshold pattern between the current experiments and the MDI experiment by Moore and Jorasz indicates that mechanisms underlying MDI might hinder signal detection for signal peak placement.

The lowest thresholds were generally found for the unmodulated conditions. In experiment 1a, adding unmodulated FCs resulted in a masking release for both the monaural and dichotic conditions. It seemed that in the unmodulated condition, MDI could not hinder signal detection as it was argued to do in the comodulated and monaural antiphasic conditions. Therefore, in the unmodulated condition across-frequency level comparisons could be used as a detection cue without the mechanism responsible for MDI impairing signal detection.

V. CONCLUSIONS

A reason why CMR has never been obtained for signal-peak placement conditions might have been due to an interfering, central across-channel mechanism associated with MDI. However, a theory associated with CMR based on amplitude level comparisons across frequencies still applies for peak-placement conditions when MDI is diminished by using unmodulated FCs. Support for another theory associated with CMR, the dip-listening theory, is found for results obtained in the dichotic antiphasic peak-placement condition. A reason no support for the dip-listening theory is found in the monaural antiphasic peak-placement condition might be due to a peripheral within-channel process underlying MDI.

Buus, S. (**1985**). ''Release from masking caused by envelope fluctuations,'' J. Acoust. Soc. Am. **78**, 1958–1965.

Delahaye, R., Fantini, D. A., and Meddis, R. (**1999**). ''Effect of practice on performance for different masking tasks,'' J. Acoust. Soc. Am. **105**, 1153.

Fantini, D. A., and Moore, B. C. J. (**1994**). ''A comparison of the effectiveness of across-channel cues available in comodulation masking release and profile analysis tasks,'' J. Acoust. Soc. Am. **96**, 3451–3462.

Fantini, D. A., Moore, B. C. J., and Schooneveldt, G. P. (**1993**). ''Comodulation masking release as a function of type of signal, gated or continuous masking, monaural or dichotic presentation of flanking bands, and center frequency,'' J. Acoust. Soc. Am. **93**, 2106–2115.

Grose, J. H., and Hall, J. W. (**1989**). ''Comodulation masking release using SAM tonal complex maskers: Effects of modulation depth and signal position,'' J. Acoust. Soc. Am. **85**, 1276–1284.

Hall, J. W. (**1986**). ''The effect of across-frequency differences on masking level on spectro-temporal pattern analysis,'' J. Acoust. Soc. Am. **79**, 781–787.

Hall, J. W., and Grose, J. H. (**1988**). ''Comodulation masking release: Evidence for multiple cues,'' J. Acoust. Soc. Am. **84**, 1669–1675.

Hall, J. W., Haggard, M. P., and Fernandes, M. A. (**1984**). ''Detection in noise by spectro-temporal pattern analysis,'' J. Acoust. Soc. Am. **76**, 50–56.

Levitt, H. (**1971**). ''Transformed up–down methods in psychoacoustics,'' J. Acoust. Soc. Am. **49**, 467–477.

Moore, B. C. J., Glasberg, B. R., and Schooneveldt, G. P. (**1990**). ''Across-channel masking and comodulation masking release,'' J. Acoust. Soc. Am. **87**, 1683–1694.

Moore, B. C. J., and Jorasz, U. (**1996**). ''Modulation discrimination interference and comodulation masking release as a function of the number and spectral placement of narrow-band noise modulators,'' J. Acoust. Soc. Am. **100**, 2373–2381.

Schooneveldt, G. P., and Moore, B. C. J. (**1987**). ''Comodulation masking release (CMR): Effects of signal frequency, flanking-band frequency, masker bandwidth, flanking-band level, and monotic versus dichotic presentation of the flanking band,'' J. Acoust. Soc. Am. **82**, 1944–1956.

Yost, W. A., and Sheft, S. (**1989**). ''Across-critical-band processing of amplitude-modulated tones,'' J. Acoust. Soc. Am. **85**, 848–857.

Sound source location by difference of phase, on a hydrophone array with small dimensions

Karsten Brensing, Katrin Linke, and Dietmar Todt
Institute of Behavioral Research, Free University of Berlin, D-12163 Berlin, Germany

(Received 11 April 2000; accepted for publication 23 October 2000)

A method for localizing calling animals was tested at the Research and Education Center Dolphins Plus in Key Largo, FL, under realistic field conditions. Experiments were performed with bottlenose dolphins (*Tursiops truncatus*) using a special hydrophone arrangement. There were two groups of hydrophones, and the two hydrophones in each group were 15 cm apart. The groups were separated by a distance of 15 m. Acoustic signals from the animals were recorded by use of a digital data acquisition system with a sampling rate of 1 MHz. All data were processed off-line. The time delay was measured by the phase difference in a single wavelength on whistles and clicks. The bearing of the signals was calculated with help of the time delay. This method has high precision and provides the possibility for analyzing overlapped signals. © *2001 Acoustical Society of America.*
[DOI: 10.1121/1.1333421]

PACS numbers: 43.80.Ev, 43.80.Jz, 43.80.Ka [WA]

I. INTRODUCTION

Until recently, the continuous observation of a large interacting dolphin group and the acoustic communication of an individual could not be carried out satisfactorily. One of the main problems is the assignment of the acoustic signals to the corresponding transmitters. Theoretically, it is possible to calculate the bearing from a sound source by the arrival time difference at different hydrophones.

In a study performed by Watkins and Schevill in 1972, a ship platform with a four-hydrophone array on a buoy system was used. This system needed to be calibrated absolutely. It was shown that the distance between the hydrophones must be about 30 m to measure biological signals. The signal amplitudes were very strongly varied on all sensors, although identically constructed hydrophones were used. The precision of this system was also very limited (Watkins and Schevill, 1972).

The first practicable system was used to investigate and estimate the population of right whales. This system measured the phase difference between the signals from a two-dimensional hydrophone array and calculates the bearing to the sound source. This system determined the direction with 12-degree resolution. By repeated determination of the direction from different positions, it was possible to locate the sound source (Clark, 1980; Clark *et al.*, 1986). However, this system was not accurate enough to investigate the communication of dolphin groups in a small area. A similar system was used to estimate sperm whale populations (Leaper *et al.*, 1992). Two hydrophones were used with a separation of 3 m. The sound source location was calculated by using bearings taken at different ship positions. Further experiments used a group of seven circularly positioned and tightly installed hydrophones. It was possible to locate the position of an acoustic source within this circle (Spiesberger and Fristrup, 1990). However, neither of the methods described above is suitable for the investigation of dolphins that are not widely separated with little spatial distribution.

Experiments in an aquarium and in a fenced ocean bay showed that the cross correlation of an entire whistle is possible (Freitag and Tyack, 1993). However, the cross correlation supplies exact results only if the signal on all hydrophones is undistorted and similar. Another solution is the use of a device attached to the animals. Small recorders and signaling lamps, which were fixed on the head of the animals, have been successfully used (Tyack, 1985). The caveat for this method is that it works only with captive and trained dolphins.

In the context of this study, it was possible to develop a disturbance-insensitive method that provides a very accurate time delay measurement, which makes it possible to successfully locate the source of a sound. This method, used at the Dolphins Plus Center, can easily be applied to the conditions in the open ocean.

II. METHODS

The data recording was carried out at the Marine Mammal Research and Education Center Dolphins Plus, Key Largo, Florida Keys. This center consists of two fenced pools, connected to an open ocean water channel between the Atlantic Ocean and the Gulf of Mexico. The recordings were made between 1 November and 15 December 1998. The observation pool (22×37 m^2) contained four females and one young male.

The location of the sound source was determined as the intersection point of two bearings, measured by four hydrophones (C50a, Cetacean Research Technology, www.cetaceanresearch.com) in two groups (Fig. 1). Most of the problems described earlier, i.e., the large distance between and the fixed arrangement of the hydrophones, or the impact of devices on the dolphins, could be solved by reducing the distance between the hydrophones in each group to approximately 15 cm. This arrangement allows analyzing the time delay of **single** cycle waves. A specially designed transient recorder (GKSS Research Center, Geestacht, Germany) with four channels and an accuracy of 1 μs was used. All four hydrophone channels were triggered simultaneously.

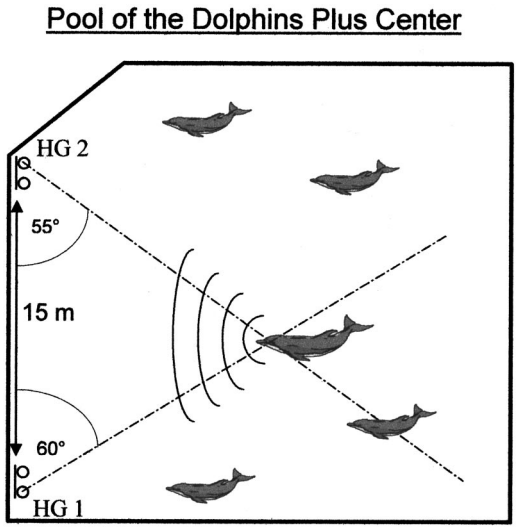

FIG. 1. Schematic diagram of the pool at Dolphins Plus Center. HG1 and HG2 are the two-hydrophone groups separated by 15 m. The distance between the two hydrophones in each group is 15 cm. The two dotted lines show the bearings with a dolphin at the intersection point. The figure is adapted to the video perspective by using an empirical formula complex.

The analog signals from every channel were digitized into an 8-bit digital data stream with a sampling rate of 1 MHz. The resulting data stream of 4 MB/ps was continuously saved for approximately 19 min on a 4500 MB SCSI hard drive for further analysis.

The two groups of hydrophones were attached to the wall of the pool with a separation distance of 15 m (Fig. 1). The exact distance between all hydrophones was determined acoustically.

Every acoustic event in the pool produces a wave front, which passes through the hydrophone groups with a distinct time delay, which depends on the bearing. This time delay between the two channels in each group makes it possible to calculate the bearing and the intersection point of the bearings of the sound source, assuming a plane wave front.

The distance between the hydrophones in each group was approximately 15 cm. A sound wave in ocean water needs a maximum of about 100 μs to travel this distance. In the case that the sound source is in line with the hydrophones the time delay will be 100 μs. The opposite case is that the phase difference is zero, meaning that the sound source is in front of the hydrophone group and the waves arrive on both channels in the same moment without a time delay [Figs. 2(a) and (b)]. The high sampling rate of the system allows us to describe a single cycle wave of 10 kHz in a 100-μs time frame with a resolution of 100 samples.

It is possible to determine the phase difference visually on a computer screen (Fig. 2) if there are less than four zero crossings in a 100-μs time frame. Therefore, it is possible to analyze frequencies of up to 20 kHz. In relation to the system's sampling rate and with the use of the Pythagorean theorem, it is theoretically possible to determine the angle up to a maximum of 0.6 degree in front of the hydrophones. This precision decreased down to 8 degrees on the sides (Fig. 3).

The sinusoidal form of the wave makes it impossible to

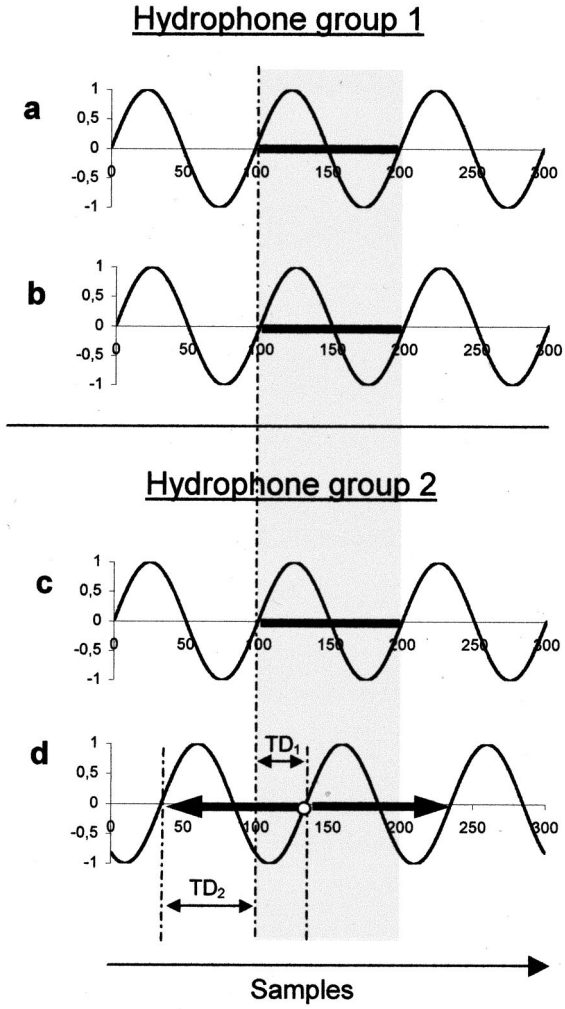

FIG. 2. Waveform view of a 300-μs (300 samples) time frame of a whistle on four different channels. The time frame includes three complete waves, which corresponds to a frequency of 10 kHz. The gray sector represents 100 μs (100 samples). This corresponds to the maximum time delay of a sound wave (sound velocity in ocean water 1500 m/s) by hydrophone separation of 15 cm. The black bars on the *x* axis show single cycles of a 10-kHz wave. There is no time delay in between a and b, meaning that the sound wave arrives on both hydrophones at the same moment or the delay is smaller than 1 μs. The phase shift between c and d is +35 samples or −65 samples, meaning that the sound wave has a time delay of +35 μs (TD_1) or −65 μs (TD_2) on channel d compared to channel c. This time delay between these hydrophones belongs to one cycle sinus wave, because the wave consists of less than four zero crossings and therefore less than two complete waves.

recognize which hydrophone was passed by the wave first. This means that two possible time delays and therefore two bearings belong to each cycle wave [Figs. 2(c) and (d)].

The position of the sound source lies on the intersection point of the bearings from the two-hydrophone groups (Fig. 1). In some circumstances, it is possible to get more than one intersection point. This depends on the possible second bearing of each hydrophone group. However, it is unlikely that there are dolphins at all intersection points. Therefore, an assignment is possible in most cases. The coordinates of the intersection were compared to the video recordings using the ''RaPid'' time code. It is not possible to correlate the intersection points directly to the video view. All photo and video sources have a distortion of perspective, depending on the angle of the camera. This distortion must be calculated in

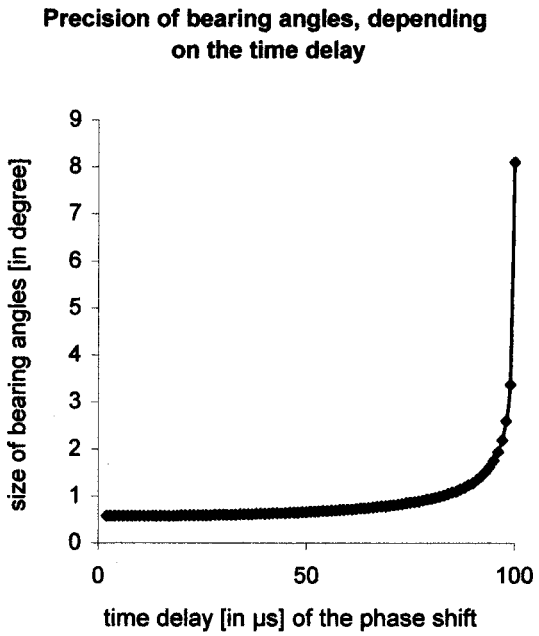

FIG. 3. This figure shows the precision of bearing angles, depending on the time delay of the phase shift, calculated using the Pythagorean theorem. The size of the bearing angles is the difference between two consecutive angles compared to the time delay in increments of 1 μs. It is possible to determine the angle with a maximum resolution of 0.6 degrees for a small time delay (in front of the hydrophones). For a time delay of 100 μs and a sound source on the sides, the resolution decreases to 8 degrees.

every case to obtain more exact positions. There are different methods to do so, all having considerable costs. In this study, an adequately exact formula complex was empirically developed.

The precision of these formulas was tested with a white PVC bar of 3.1 m. This bar was moved around the pool. Since the length of the bar is constant, the bar must always be represented by the same number of pixels in any position. One hundred thirty measurements were carried out. The bar was represented by 3.09 ± 0.38 m on average. This precision is acceptable and correlates with the quality of the data collected from the video screen. The corrected perspective of the positions of dolphins based on the calibration can be correlated to the exact position of the hydrophones and the corresponding intersection points.

III. RESULTS AND DISCUSSION

The main problem of time delay measurement is to recognize the starting point of biological signals. The beginning of a click impulse is easy to recognize by the shape of the waveform. The beginning of most biological signals, especially frequency-modulated tones, is not as obvious. To solve this problem and to get the average of the time delay, experiments with cross correlation over the whole whistles were performed (Freitag and Tyack, 1993). However, this method is very sensitive to different influences. It is practically impossible to analyze a fast-moving animal or overlapped signals in one time frame. In addition, this method requires a large distance between the hydrophones.

The first results from the data analysis found by using the method described in this publication show clearly that this theoretical principal can be used in practice. The method was used successfully for the analysis of 50 whistles and 30 broadband impulses, meaning that it was possible to identify a dolphin. Figure 1 shows one of these cases as an example. The two possible time delays on hydrophone group 2 (HG_2) are 60 μs, if the right hydrophone was passed first, and 81 μs if the left hydrophone was passed first. This corresponds to an angle of 55° to the right and an angle of 38° to the left side. The angle of 38° was not a realistic option, due to a fenced-off area for sea lions. The calculation for hydrophone group 1 (HG_1) yields an angle of 60° to the left side. The bearing on the right side is outside the pool. It can be clearly shown that there is a dolphin in the intersection point of the two remaining lines. The precision of this method seems to be very high and comparable to Fig. 3. Further analyses and statistical methods have to be employed to calculate an estimate of the precision.

The method makes it possible to analyze very small parts of signals. This way it is possible to analyze time delays independently from the speed of the animals. Another advantage is the possibility to analyze overlapped signals, if they are not completely overlapped. Early experiments show that it is also possible to filter overlapping signals by their frequency and subsequently to analyze the time delay for each filtered signal.

All analyzed sounds were undistorted signals of high intensity. Very-low-intensity signals with strong background noise are hard to analyze, because it not possible to see the signal in the amplitude directly. The reason for this is the low 8-bit data resolution. The resulting 256 values are not enough to adequately represent the dynamic range of the environment. The amplification was increased in order to get a small dynamic range with a high resolution. The disadvantage of this solution is the loss of all loud sounds, which lie outside the range of the measurement. The ideal solution for this problem would be to increase the 8 bits to 16 bits. Another solution would be the dynamic preamplification. This means that a dynamic range with a high resolution is dynamically moved over the entire dynamic range caused by the special situation. For this reason a four-channel dynamic preamplifier with a frequency range between 50 Hz and 500 kHz was developed in cooperation with GKSS. Recently some experiments with this preamplifier and the hydrophone array described in the next section were performed satisfactorily.

A further problem is that there are two time delays and two angles for a single sound wave. This makes it necessary to know which hydrophone was passed by the wave first. Earlier experiments show that it is possible to calculate these with a cross correlation of 10 to 100 wavelengths.

IV. PERSPECTIVE

The biggest advantage of the method described in this letter lies in the possibility to assemble the hydrophone groups closely together. An arrangement with two hydrophones side by side (for the horizontal angle) and two hydrophones above each other (for the vertical angle) provides the ability to measure 360° on the horizontal and the vertical angles, respectively. Therefore, this hydrophone cube is able

to measure all bearings of sound sources surrounding the array. The dimension of the cube should not exceed 20 $\times 20 \times 20$ cm^3 and can be easily attached to an underwater video system. If the aperture angle of the camera lens is known, it is easy to identify the corresponding signal transmitter in a group of animals.

This method allows for conducting experiments in the open ocean, which provides the opportunity to collect data with context-specific behavior and the individual acoustic output of dolphins or other marine mammals.

ACKNOWLEDGMENTS

Our special thanks go to Russell Leaper, who pointed us in the right direction at the beginning of this project. Particular thanks go to the engineers Jörg Burmeister and Uwe Apel from the GKSS Research Center Hamburg for all their innovative ideas. The experimental work presented here would not have been possible without the support of the Technology Foundation of the state of Schleswig–Holstein. For the various contributions in Florida, we would like to thank all of the employees of the Dolphins Plus Center in Key Largo.

Clark, C. W. (**1980**). ''A real-time direction finding device for determining the bearing to the underwater sound of Southern Right Whales, *Eubalaena australis*,'' J. Acoust. Soc. Am. **68**, 508–511.

Clark, C. W., Ellison, W. T., and Beeman, K. (**1986**). ''Acoustic Tracking of Migrating Bowhead Whales,'' in Proc. Oceans 1986, Washington DC, 23–25 September, pp. 341–346.

Freitag, L. E., and Tyack, P. L. (**1993**). ''Passive acoustic localization of the Atlantic bottlenose dolphin using whistles and echolocation clicks,'' J. Acoust. Soc. Am. **93**, 2197–2205.

Leaper, R., Gorden, J. C., and Chappell, O.P. (**1992**). ''Acoustic techniques for sperm whale survey,'' Report of International Whaling Commission.

Spiesberger, J. L., and Fristrup, K. M. (**1990**). ''Passive localization of calling animals and sensing of their acoustic environment using acoustic tomography,'' Am. Nat. **135**, 107–153.

Tyack, P. (**1985**). ''An optical telemetry device to identify which dolphin produces a sound,'' J. Acoust. Soc. Am. **78**, 1892–1895.

Watkins, W. A., and Schevill, W. E. (**1972**). ''Sound source location by arrival-times on a non-right three-dimensional hydrophone array,'' Deep-Sea Res. Oceanogr. Abstr. **19**, 691–706.

A large-aperture array of nonlinked receivers for acoustic positioning of biological sound sources

B. Møhl and M. Wahlberg
Department of Zoophysiology, Aarhus University, Building 131, C. F. Møllers Alle, DK-8000 Aarhus C, Denmark

A. Heerfordt
Computer Sciences Corporation Scandinavia, Retortvej 8, DK-1780 Copenhagen, Denmark

(Received 9 June 2000; accepted for publication 14 September 2000)

A system of independent recording units that can be used to form an arbitrarily large acoustic array is described. Position of units and timing of signals are obtained from Global Positioning System (GPS) with precisions within 2.5 m and 50 microseconds, respectively. An integrated hardware and software solution is presented and results reported from a four-unit feasibility test in shallow water. Sound sources at a distance of 2 km were located within 2 to 138 m of GPS-derived positions. [DOI: 10.1121/1.1323462]

PACS numbers: 43.80.Sh, 43.30.Sf [WA]

I. INTRODUCTION

A number of large mammals like whales and elephants produce sounds that travel over distances in the order of kilometers. Such sounds can disclose the position of the source when an array of acoustic sensors at known locations is used. The array generates a set of time of arrivals (TOAs) for the sound at the sensors. A position (fix) of the source can then be computed from this set.

There are three fundamental requirements for the method: (1) the position of the sensors must be accurately known; (2) sensor output must be recorded in synchrony, and (3) the aperture (size) of the array must be of the same order of magnitude as the range to be covered.

There are additional requirements such as knowledge of the sound velocity field and the need to identify a time marker in the signal at all sensors. This paper deals with an integrated approach to meet the three fundamental requirements listed above.

Passive, acoustic positioning techniques have largely been applied at relatively short ranges where the sensor positions can be fixed or monitored, and the sensors connected by cables to a central, multitrack recorder. When the aperture exceeds some 10 m, arrays tend to be cumbersome to deploy and operate. This restraint is particularly strong for work at high seas where fixed positions of sensors are not feasible. Watkins and Schevill (1972) have perfected a shipborne, four-sensor array with a 30-m separation of the elements, possibly the limit for a cabled, nonrigid, workable array at sea. A characteristic of such arrays is that references for sensor coordinates and synchronization are local, rather than global. As requirement (3) (aperture equal to range) is not met by such arrays, the potential for long-range positioning and tracking inherent to a number of biological sounds cannot be exploited.

The advent of GPS (Global Positioning System) has made it possible to meet requirement (1) (sensor positioning) by adoption of global coordinates. With this technique, precision of sensor positioning is made independent of their spacing, allowing for arbitrarily large apertures. Radio links can then be used to satisfy requirement (2) (recording synchrony), eliminating the need for cables. Thus, the third requirement can also be met. A number of different implementations of this principle have recently been published (Hayes *et al.*, 2000; Janik *et al.*, 2000; Møhl *et al.*, 2000).

This communication describes an extension of the GPS-based techniques, using global references for position as well as for time. The latter is obtained by synchronization with the atomic clocks onboard the GPS satellites. At each standalone unit of the array, sensor position information together with time information is recorded continuously on one track of a stereo recorder, while the sound signal is recorded on the other. An array built from a number of units satisfies the three fundamental requirements for long-range acoustic positioning of biological sound sources. Test results from such an array are described and evaluated.

II. MATERIAL AND METHODS

A. Overview

The array is constructed from a number of identical units as outlined in Fig. 1. One channel of a stereo recorder is allocated to the signal from the sensor via signal conditioning circuitry. The other channel is effectively turned into a digital channel by a frequency shift keying device (FSK). The latter transforms the stream of ASCII sentences from a GPS unit to a tone signal (much like in a telephone modem) that can be recorded by an audio recorder. The GPS unit (a Garmin GPS25 LV, 12-channel receiver) provides a 20-ms pulse synchronized to the atomic clocks onboard the satellites of the GPS system. The leading front of this pulse coincides with the 1-s increment of UTC time. The actual UTC time is identified in an ASCII sentence following the 20-ms synchronization pulse. The pulse is amplitude-modulating the tone signal from the FSK device, and is identified on the tape track as a sudden drop in amplitude of the FSK signal (see Fig. 2). To increase the positional accuracy beyond what is achievable with standard GPS, a special receiver for cor-

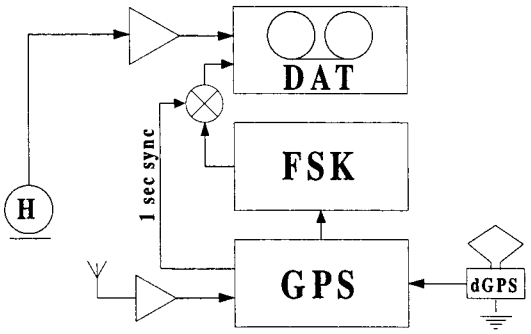

FIG. 1. Schematics of a recording unit. For explanations, see the text.

rective signals from local, ground-based radio beacons is added (dGPS, see Fig. 1.) For a general introduction to the principle of operation of this system, see Kaplan (1996).

Not shown in Fig. 1. is a palm-top computer (Psion 3MX), serving two purposes. It receives the serial output from the GPS and displays position and quality parameters of the positional fix. Second, it generates digital labels (electronic tape log) describing the recording conditions, including position of the hydrophone relative to the GPS antenna. The labels are transferred via the FSK unit to the recorder under operator control. This facility ensures that log information follows acoustic information through all subsequent copying and analyzing processes.

For data analysis, the content of the DAT tapes is transferred to CD-ROM files in WAV format, preserving the original digitization of the recorder. A standard sound-editing program (Cool Edit, Syntrillium) is used to display the tracks (Fig. 2). The time of occurrence of an event is measured from the onset of the nearest second marker. The identity of that marker, together with the coordinates (latitude, longitude) of the recording platform at that point in time, is displayed using custom software (FSK decoder, see the software section below). The FSK decoder operates on the information in the window of the sound editor (Fig. 2). Records from the other units are treated similarly, and TOAs at each sensor derived for the event. The set of TOAs is subsequently treated by the positioning software (Wahlberg *et al.*, unpublished).

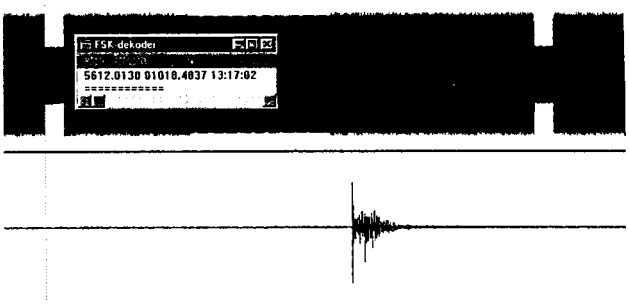

FIG. 2. Snapshot from analyzing screen. Top: FSK trace with 1-pulse-per-second markers; bottom: blasting cap signal. The insert is the decoded GPS information, showing position to be 56°12.0130′ N, 10°18.4837′ E, at 13:17:02 UTC.

B. FSK unit

The FSK unit is build around an XR-2206 chip (Exar). It converts the serial, 4800-baud signal from the GPS into a continuous tone signal consisting of a 20-kHz space tone and a 17-kHz mark tone. A sensing circuitry monitors the transmit line of the palm-top. In case of activity, the input of the FSK modulator is switched from the GPS to the palm-top by a reed relay. In this way, digital label information from the palm-top is recorded on the tape.

C. Decoding of the FSK signal

An FSK demodulator has been implemented as a set of C++ modules. The signal is stored in a WAV file as 16-bit words sampled at 48 kHz. The word stream is copied into two identical word streams. One is sent through an 18-kHz digital finite impulse response (FIR) low-pass filter, and the twin data stream is sent through an 18-kHz digital FIR high-pass filter. Each data stream is then converted to a rms stream in a software filter. The two rms values are compared in a software comparator module. If the rms value from the high-pass filter is larger than the rms value of the low-pass filter, then a 0 (space value) is output, otherwise a 1 (mark value) is output. This stream is then sent through a software state machine, which inputs a stream of bits and outputs a stream of bytes. The stream of bytes is then separated into ASCII lines. From a specific line, position and time information is extracted and output to the screen. The FSK decoding methods are not affected by amplitude modulation caused by the marker pulses.

The program for the palm-top is written in OPL language. It is menu organized and prompts the operator for information about recording and environmental conditions in a standardized way. This ensures that tape log information from all operators is uniform and linked with the sound track at all times. Additionally the program provides the operator with navigational information as well as indicators of the quality of the actual GPS fix.

D. Field test

Four recording platforms were instrumented with units as described above. The platforms were anchored in the Bight of Aarhus in an L-shaped configuration at water depths between 12 and 23 m with a separation of 1 km, on 6 May 2000. Hydrophones were lowered to a depth of 5 m. A fifth platform generating test signals was anchored 2 km away from platform 1 in a direction perpendicular to a line between recording platforms 2 and 3 (Fig. 3). The signal platform also had a stand-alone recording unit. Sensors were B&K 8101 hydrophones, supplied with power from B&K 2804 power supplies. Sensor at the source platform was a B&K 8100 hydrophone. Five Sony DAT recorders of types TCD-D3, TCD-D7, and TCD-D8 served as recorders. Anti-alias filters (see Møhl *et al.*, 2000) were used. The passband of each chain was from 0.1 to 22 kHz and deviations from flat response compensated for during analysis. Passive attenuators were used between the hydrophones and the signal conditioning circuitry when appropriate. All recording systems were calibrated with a B&K 4223 hydrophone calibra-

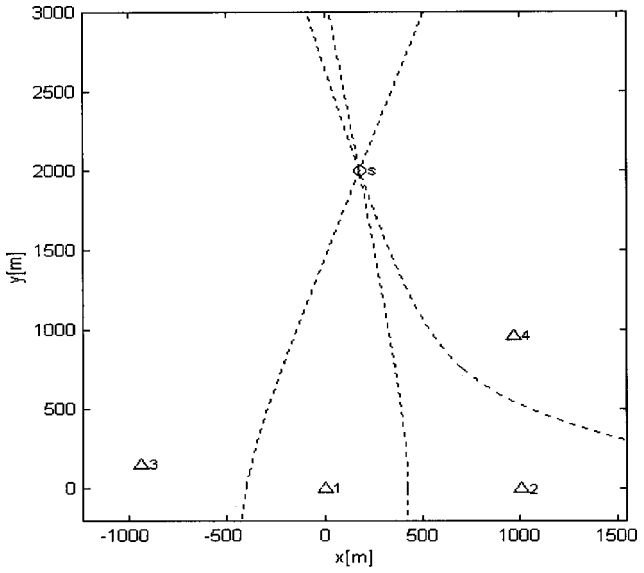

FIG. 3. Hyperbola plot for event no. 5. Receiver dGPS positions are plotted as triangles, source position as a circle.

tor. Water temperature was measured to 13.7 °C, salinity to 16.4 ppm by a Grant/YSI type 3800 water quality meter. Velocity of sound was derived from the Leroy equation (Urick, 1983), as well as from direct observation of distance and travel time of the acoustic events. Sea state was 0 to 1. Traffic from ferries and leisure crafts dominated the background noise.

A preliminary test was carried out on 12 March at the same location but with only three units. Water temperature and salinity at that occasion were 3.5 °C and 24 ppm, respectively.

E. Test signals

Five blasting caps were fired, giving rise to the acoustical events analyzed below. Source levels (SLs) for the five events were 233 dB ± 4 dB, as derived from measurements at the source platform at a distance of 3 m.

F. Analysis

Time of arrival of the events at each hydrophone was measured using CoolEdit to display the number of milliseconds since the preceding UTC second mark. The latter, as well as receiver position, was read from the FSK data with custom-built software described above. Source positioning and error analysis were derived from algorithms for 2D arrays given in Wahlberg *et al.* (unpublished).

For linear error propagation analysis, sound velocity was assumed to be known within ±10 m/s, hydrophone positions within 2.5 m for dGPS data (data from 3600 measurements with fixed antenna), 25 m for plain GPS data, and time measurements to be accurate within 1 ms, all errors given as rms errors (2 × standard deviation, or 95% of the error distribution).

TABLE I. Differences (*m*) between acoustic and GPS-derived positions for five blasting cap events. Results from the linear error propagation analysis (LEP) are added.

Event	Array configuration:	Linear	Triangular	ODA[b]
1		61	138	67 ± 16
2		37	15	34 ± 30
3		2	3	2 ± 1
4		6	30	3 ± 8
5		3	21	6 ± 4
	LEP dGPS	20[a]	100	7
	LEP plain GPS[c]	30[a]	500	70

[a]LEP analysis of a strict linear array.
[b]±rms errors calculated from residual analysis.
[c]GPS without differential correction.

III. RESULTS

Sound velocity from the Leroy equation was 1481 m/s. Direct observations yielded a mean value of 1476 ± 8 m/s. The positional results of the acoustic events, including error analyses, are listed in Table I for three different after-the-fact configurations: a quasilinear array, composed of receivers 1 + 2 + 3, a triangular array from receivers 1 + 2 + 4, and an overdetermined array (ODA) with all four receivers. The term overdetermined is used to signify the use of receivers above the minimum number required, which for a 2D array is three. Figure 3 shows a hyperbola plot for event 5.

IV. DISCUSSION

The difference between the acoustic source positioning and the dGPS positions ranges from 2 to 138 m, depending on event and array configuration (Table I). The larger differences coincide with cases where it was difficult to identify the onset of the event at some of the receivers (events 1 and 2). The consequences of the differences are quite small in situations where the calculated range is used to estimate transmission losses since if a spherical transmission situation could be assumed, the largest difference in Table I will result in an error of 0.6 dB. For the remaining events, the difference between ODA and GPS positions is of the same magnitude as the rms error of the dGPS itself.

The difference in performance of the three configurations is illustrative. The linear array is performing well for sources in broad side positions. Outside the triangular array there are areas with poor resolution. For further discussion of array geometry, see Wahlberg *et al.* (unpublished). Finally, an overdetermined array is advantageous both with regard to precision, and because it allows for a measured value for the magnitude of localization error. Addition of more units will improve the ODA properties.

The linear error propagation model (LEP), which gets its input from data known in advance of the actual experiment, predicts resolution reasonably well, though on the conservative side, for events 3 through 5. This indicates that one or more of the parameters entered in the computations is too pessimistic. TOA timing (set to 1 ms) is a likely candidate as resolution allowed by recorder bandwidth and signal waveform is somewhat better, at least for events 3 through 5.

The large LEP values for the triangular array are in part explained by problems of predicting the magnitude of positioning error in a source–receiver geometry close to an endfire situation (as discussed by Wahlberg *et al.*, unpublished). Still, as a tool for choosing the best configuration of receivers before deployment, LEP is clearly useful. The last row in Table I for a situation with plain GPS without differential correction is derived from LEP (receiver position rms errors set to 25 m). It illustrates the importance of precise knowledge of the position of the hydrophones.

The acoustic signals received at the test day of 6 May were characterized by a prolonged reverberation and at times by a poor definition of onset. This is contrary to the situation from 12 March where reverberation was low and onset well defined. Figure 2 is from a record of that day. Further, the source levels (SL) derived from measurements at the remote receivers from 12 March were within 11 dB ($n=8$) of that expected from spherical spreading losses and absorption (1 dB/1000 m), while the SLs from the 6 May test were 20 to 40 dB below expectations from such mechanisms.

Compared with a traditional, cabled array, the system has some advantages and some disadvantages. Among the advantages is that the range is restricted only by the signal-to-noise ratio of the sounds, their directionality, and their timing properties, not by the array itself. With regard to analysis, we find the present system simpler/faster to operate than conventional, multitrack data when TOAs differ by more than some 10 ms. Further, the implementation of a rigidly formatted, electronic log for each platform is found to be a time-saving asset during copying and analysis. On the negative side is the impossibility of using this system for real-time tracking. Also, operating a fair number of platforms at sea presents logistic problems, even though the platforms may not necessarily have to be manned.

The principle of a globally referenced array of independent receivers was conceived as a tool for obtaining source levels and radiation patterns of clicking sperm whales, a task where it has satisfied expectations (Møhl, unpublished). It may have potentials in fields outside bioacoustics. However, the modest costs (a unit is about $2000, the recorder being the most expensive item) make it particularly interesting for bioacousticians. With this tool it should be possible not only to obtain source levels at large distances, but also to make acoustic inventories of certain vociferate populations, to make acoustic tracking, and to study long-range acoustic interactions.

ACKNOWLEDGMENTS

We thank the following for applying their skills and giving their time in order to make the array work. N. Kristiansen designed and assembled the hardware. The platforms were operated by M. F. Christoffersen, T. Jensen, O. Krause, A. Lund, P. T. Madsen, L. A. Miller, B. K. Nielsen, T. Norup, M. H. Rasmussen, T. Schmidt, M. Simon, P. T. Sørensen, J. Tougaard, and S. Tougaard. The temperature/salinity profile was obtained from the Office of Environment, Aarhus Amt. The Danish Research Foundation through the Center for Sound Communication, Odense University, funded this work.

Hayes, S. A., Mellinger, D. K., Croll, D. A., Costa, D. P., and Borsani, J. F. (**2000**). ''An inexpensive passive acoustic system for recording and localizing wild animal sounds,'' J. Acoust. Soc. Am. **107**, 3552–3555.

Janik, V. M., Parijs, S. M. V., and Thompson, P. M. (**2000**). ''A two-dimensional acoustic localization system for marine mammals,'' Marine Mammal Sci. **16**(2), 437–447.

Kaplan, E. D., editor (**1996**). *Understanding GPS: Principles and Applications* (Artech House Telecommunications Library, Boston, MA).

Møhl, B., Wahlberg, M., Madsen, P. T., Miller, L. A., and Surlykke, A. (**2000**). ''Sperm whale clicks: Directionality and source level revisited,'' J. Acoust. Soc. Am. **107**, 638–648.

Møhl, B. ''Preliminary report of the Andenes Y. 2000 expedition'' (unpublished).

Urick, R. J. (**1983**). *Principles of Underwater Sound*, 3rd ed. (McGraw Hill, New York).

Wahlberg, M., Møhl, B., and Madsen, P. T. ''Estimating source position accuracy of data from a large aperture array for bioacoustics'' (unpublished).

Watkins, W. A., and Schevill, W. E. (**1972**). ''Sound source location by arrival times on a non-rigid three-dimensional hydrophone array,'' Deep-Sea Res. **19**, 691–706.